

# *Acta* **METALLURGICA**

**VOL. 3**

**JAN. 1955**

OL.  
3  
1955

METALLURGICA

No. 1

JAN. 1955



VOL.  
3  
1955

# Author Index to Volume 3

(References with (L) are Letters to the Editor)

- Alexander, B. H. (see Wang, C. C.)—515(L)  
 Amelinckx, S. (see Votava, E.)—89  
 Ammann, D. (see Gruhl, W.)—347  
 Ang, C. Y., Sivertsen, J., and Wert, C. Anelastic behavior in alloys of gold and nickel—558  
 Ardley, G. W. On the effect of ordering upon the strength of  $\text{Cu}_3\text{Au}$ —525  
 Åström, H. U. Isothermal measurements on the release of energy stored in cold-worked aluminium—508(L)  
 Auld, J. H. (see Garrod, R. I.)—190  
 Averbach, B. L. (see Kurtz, A. D.)—442  
 Axon, H. J. (see Mehta, M. L.)—538
- Bakish, R. Internal deformation markings in single crystals of  $\text{Cu}_3\text{Au}$ —513(L)  
 Balluffi, R. W. and Seigle, L. L. Effect of grain boundaries upon pore formation and dimensional changes during diffusion—170  
 Bangert, L. (see Köster, W.)—274  
 Bechtold, J. H. Tensile properties of annealed tantalum at low temperatures—249  
 — (see Shewmon, P. G.)—452  
 Belbeoch, B. and Guinier, A. Relation entre les structures et les propriétés des alliages aluminium-argent pendant le durcissement structural—370  
 Birnbaum, H. K. Double-valued internal friction behavior—297(L)  
 Bleakney, H. H. Internal friction in titanium and titanium oxygen alloys—103(L)  
 Blin, J. Energie mutuelle de deux dislocations—199(L)  
 Boulanger, C. (see Friedel, J.)—380  
 Bowles, J. S. and Tegart, W. J. McG. Crystallographic relationships in aged copper-beryllium alloys—590  
 Brenner, A. E. (see Uhlig, H. H.)—108(L)  
 Brinkman, J. A. Mechanism of pore formation associated with the Kirkendall effect—140  
 — On the mechanism of pore formation during diffusion—605(L)  
 Brook, G. B. and Sully, A. H. Some observations on the internal friction of polycrystalline aluminium during the early stages of creep—460  
 Buehler, E. (see Fuller, C. S.)—97(L)  
 Burgers, W. G. (see Okkerse, B.)—300(L)
- Cahn, R. W. (see Piercy, G. R.)—331  
 Calnan, E. A. (see Murphy, H. M.)—268  
 Chalmers, B. (see Thomas, W. R.)—17  
 Chipman, J. and Floridis, T. P. Activity of aluminum in liquid Ag-Al, Fe-Al, Fe-Al-C, and Fe-Al-C-Si alloys—456  
 Churchman, A. T. The yield phenomena, kink bands and geometric softening in titanium crystals—22  
 Clemm, P. J. and Fisher, J. C. The influence of grain boundaries on the nucleation of secondary phases—70  
 Cocharde, A. W. Abnormal after-effect of twisted metal wires upon heating—607(L)  
 — Schoek, G. and Wiedersich, H. Interaction between dislocations and interstitial atoms in body-centered cubic metals—533  
 Cohen, Morris (see Kurtz, A. D.)—442  
 Conard, G. P. (see Griest, A. J.)—509(L)  
 Cottrell, A. H. (see Piercy, G. R.)—331  
 Cracknell, A. Hydrogen and the yield point in steel—200(L)  
 — and Petch, N. J. Frictional forces on dislocation arrays at the lower yield point in iron—186  
 Crussard, C. (see Friedel, J.)—380
- Dejace, J. (see Lambot, H.)—150  
 Dench, W. A. (see Kubaschewski, O.)—339  
 Dekeyser, W. (see Votava, E.)—89  
 DeSorbo, W. Calorimetric investigations of a gold-nickel alloy. I. Low temperature heat capacity of gold-nickel alloy—227  
 Dickenscheid, W. Zur Rekristallisation von Eisen nach der  $\gamma$ - $\alpha$ -Umwandlung—206
- Dienes, G. J. Kinetics of order-disorder transformations—549  
 Ditzemberger, J. A. (see Fuller, C. S.)—97(L)  
 Donahoe, F. J. Effect of order on the electrical resistivity of ferromagnetic alloys—292(L)  
 Dorn, J. E. (see Frenkel, R. E.)—470  
 Doyama, M. (see Kuczynski, G. C.)—415(L)  
 Dunn, C. G. Some observations of dislocation sites in polygonized silicon-iron crystals—409(L)
- Ehrlich, G. Impurity particles and the lateral growth of cadmium iodide—201(L)  
 Eisner, R. L. Tensile tests on silicon whiskers—414(L)  
 Eshelby, J. D. The elastic interaction of point defects—487
- Fast, J. D. Solubility of nitrogen in  $\alpha$ -iron—203(L)  
 Fisher, J. C. A dislocation model for the origin of fracture cracks in metal crystals—109(L)  
 — Approximate steady-state configuration of a dislocation mill—413(L)  
 — (see Clemm, P. J.)—70  
 — and Hollomon, J. H. Dislocation glide as an aid to precipitation at low temperatures—608(L)  
 Floridis, T. P. (see Chipman, J.)—456  
 Foreman, A. J. E. Dislocation energies in anisotropic crystals—322  
 Frank, F. C. and Thompson, N. On deformation by twinning—30  
 Frenkel, R. E., Sherby, O. D., and Dorn, J. E. Activation energies for creep of cadmium, indium, and tin—470  
 Friedel, J., Boulanger, C., and Crussard, C. Constants élastiques et frottement intérieur de l'aluminium polygonisé—380  
 Fuller, C. S. Resistivity changes in silicon single crystals induced by heat treatment—97(L)
- Garrod, R. I. and Auld, J. H. X-ray line broadening from cold-worked iron—190  
 Gilman, J. J. Fine structure in zinc twins—209(L)  
 — Structure and polygonization of bent zinc monocrystals—277  
 Graham, J. (see Moore, A.)—579  
 Grewen, J. and Wassermann, G. Über die idealen Orientierungen einer Walztextur—354  
 Griest, A. J. Effect of ternary additions of silicon and aluminum on the ordering reaction in iron-cobalt—509(L)  
 Gruhl, W. and Ammann, D. Über die Abhängigkeit der Korngrenzenausscheidung von der Orientierung der benachbarten Kristalle—347  
 Guinier, A. Nouvelle interprétation des diagrammes à "sidebands"—510(L)  
 — (see Belbeoch, B.)—370
- Hannay, N. B. (see Fuller, C. S.)—97(L)  
 Hart, E. W. A uniaxial strain model for a Lüder's band—146  
 — (see Hoffman, R. E.)—417  
 Hasiguti, R. R. A tentative explanation of the accelerated growth of tin whiskers—200(L)  
 Hässner, F. (see Lucke, K.)—204(L)  
 Haynes, C. W. and Smoluchowski, R. Grain boundary diffusion in a body-centered cubic lattice—130  
 Heidenreich, R. D. Transition structure in lead-silver alloys and a dislocation mechanism—79  
 Hendrickson, A. A. and Machlin, E. S. A thermal etching technique for revealing dislocations in silver—64  
 Hibbard, W. R., Jr. (see Dunn, C. G.)—409(L)  
 Hill, M. L. and Johnson, E. W. The diffusivity of hydrogen in nickel—566  
 — (see Johnson, E. W.)—99(L)  
 Hillert, M. Solubility of cementite in liquid iron—37  
 — Some applications of isoactivity lines—34  
 Hingley, M. (see Thompson, N.)—289  
 Hoffman, R. E., Turnbull, D., and Hart, E. W. Self-diffusion in dilute binary solid solutions—417  
 Hollomon, J. H. (see Fisher, J. C.)—608(L)

- Hulme, K. F. A surface structure observed on electrolytically polished zinc—572
- Huntington, H. B. (see Wajda, E. S.)—39
- Jenkins, I. (see Robins, D. A.)—598
- Johnson, E. W. and Hill, M. L. The diffusion of hydrogen in iron and ferritic steels—99(L)
- (see Hill, M. L.)—566
- Josefsson, A. (see Lagerberg, G.)—236
- Karnik, F. (see Lindner, R.)—297(L)
- Kelley, A. Sub-grain formation in aluminum deformed at  $-183^{\circ}\text{C}$ —96(L)
- Kelly, E. M. Electron microscope study of slip bands in radiation-damaged aluminum crystals—101(L)
- Kittel, C. An electron transfer mechanism for ultrasonic attenuation in metals—295(L)
- Kleppa, O. J. A calorimetric investigation of the system silver-tin at  $450^{\circ}\text{C}$ —255
- Koehler, J. S. (see Noggle, T. S.)—260
- Köster, W. and Bangert, L. Bestimmung der Versetzungsliniendichte von verformten Eisen—274
- Kubaschewski, O. and Dench, W. A. The heats of formation in the systems titanium-aluminum and titanium-iron—339
- Kuczynski, G. C. Variation of the yield point with temperature in  $\text{AuCu}_3$ —415(L)
- Kunz, F. W. The segregation of carbon in iron single crystals as studied by torsion pendulum damping—126
- Kurtz, A. D., Averbach, B. L., and Cohen, Morris. Self-diffusion of gold in gold-nickel alloys—442
- Lagerberg, G. and Josefsson, A. Influence of grain boundaries on the behaviour of carbon and nitrogen in  $\alpha$ -iron—236
- Lambot, H., Vassamillet, L., and Dejace, J. Determination des sous-structures dans les monocristaux métalliques à l'aide des rayons X—150
- Leak, D. A., Thomas, W. R., and Leak, G. M. Diffusion and solubility of nitrogen in silicon-iron—501
- Leak, G. M. (see Leak, D. A.)—501
- Levinson, D. W. On the lattice parameter of  $\text{Mg-Li}$   $\beta$ -alloys—294(L)
- Libsch, J. F. (see Griest, A. J.)—509(L)
- Lindner, R. Diffusion von radioaktiven Kupfer in technischem Stahl—297(L)
- Lindstrand, E. A method for the measurement of elastic relaxation, and its use for determination of the solubility of carbon in  $\alpha$ -iron—431
- Lovell, L. C. (see Pfann, W. G.)—512(L)
- Lücke, K. Zur Entstehung der Rekristallisationstexturen in Aluminiumdrähten—204(L)
- MacDonald, D. K. C. and Pearson, W. B. Electron transport in copper and dilute alloys at low temperatures. I—392
- Electron transport in copper and dilute alloys at low temperatures. II—403
- Machlin, E. S. (see Hendrickson, A. A.)—64
- MacNairn, J. S. (see Uhlig, H. H.)—302(L)
- Massalski, T. B. (see Raynor, G. V.)—480
- Mehl, R. F. (see Pollock, W. I.)—213(L)
- Mehta, M. L. and Axon, H. J. The influence of thin intermediate layers on interdiffusion in copper-nickel couples—538
- Meijering, J. L. On the diffusion of oxygen through solid iron—157
- Moore, A., Graham, J., Williamson, G. K., and Raynor, G. V. An X-ray examination of crystallographic transformations in indium-rich solid solutions with thallium, lithium, and lead—579
- Moore, A. J. W. Twinning and accommodation kinking in zinc—163
- Murphy, H. M. and Calnan, E. A. The deformation of single crystals of  $\alpha$ -brass—268
- Mykura, H. An interferometric study of grain boundary grooves in tin—436
- Newkirk, J. B. Growth of cadmium iodide crystals—121
- and Sears, G. W. Growth of potassium halide crystals from aqueous solution—110(L)
- Nicholas, J. F. Comments on "Formation energies of vacancies in copper and gold" by C. J. Meehan and R. R. Eggleston—411(L)
- The mechanisms of self-diffusion in tin—178
- Noggle, T. S. and Koehler, J. S. Crystal perfection in aluminum single crystals—260
- Nowick, A. S. On the interpretation of "low-temperature" recovery phenomena in cold-worked metals—312
- Nyström, J. A possible explanation of the stability of Guinier-Preston zones—103(L)
- Calorimetric measurements during precipitation in a gold-nickel alloy—182
- Okkerse, B., Tiedema, T. J., and Burgers, W. G. Self-diffusion of lead in oriented grain-boundaries—300(L)
- Olney, M. J. Twinning in aluminium—205(L)
- Oriani, R. A. Calorimetric investigations of a gold-nickel alloy. II. The heat capacity at high temperatures and the entropy of formation—232
- Paidassi, J. Sur la précipitation d'oxyde  $\text{Fe}_2\text{O}_3$  dans les pellicules d'oxydation du fer aux températures élevées—447
- Parr, J. G. (see Polonis, D. H.)—307
- Paterson, M. S. Plastic deformation of copper crystals under alternating tension and compression—491
- Pearson, W. B. (see MacDonald, D. K. C.)—392
- (see MacDonald, D. K. C.)—403
- Perryman, E. C. W. Some observations on the relationship between vacancies, recovery and precipitation in  $\text{Al-Mg}$  alloys—412(L)
- Petch, N. J. (see Cracknell, A.)—186
- (see Cracknell, A.)—200(L)
- Pfann, W. G. Dislocation densities in intersecting lineage boundaries in germanium—512(L)
- Piercy, G. R., Cahn, R. W., and Cottrell, A. H. A study of primary and conjugate slip in crystals of  $\alpha$ -brass—331
- Pitsch, W. Die Teilchenform bei der Karbidausscheidung aus dem  $\alpha$ -Eisen—542
- Pollock, W. I. Spiral growth of cadmium crystals from the vapor phase—213(L)
- Polonis, D. H. and Parr, J. G. Isothermal decomposition kinetics of transformed-beta phase in a titanium-nickel alloy—307
- Powers, R. W. Internal friction in solid solutions of oxygen-tantalum—135
- Rapperport, E. J. Deformation processes in zirconium—208(L)
- Rawlings, R. Nitrogen in iron anelasticity and solid solubility—212(L)
- Raynor, G. V. and Massalski, T. B. The lattice spacings of close-packed hexagonal  $3/2$  electron compounds—480
- (see Moore, A.)—579
- Resnick, R. (see Seigle, L.)—606(L)
- Richards, J. T. Effect of irradiation upon beryllium copper—211(L)
- Roberts, B. W.  $\text{BiMn}$  "spire" growths induced by a magnetic field—425
- Roberts, W. T. (see Kelly, A.)—96(L)
- Robertson, W. D. (see Bakish, R.)—513(L)
- Robins, D. A. and Jenkins, I. The heats of formation of some transition metal silicides—598
- Rowland, T. J. Nuclear electric quadrupole interactions in aluminum—74
- Salkovitz, E. I. (see Weertman, J.)—1
- Schoek, G. (see Cochardt, A. W.)—533
- Schoening, F. R. L. and Van Niekerk. X-ray measurements on silver filings—10
- Schönberg, Nils. Metallic ternary phases in the  $\text{Mn-Ta-O}$  system—14
- Schuhmann, R., Jr. Application of Gibbs-Duhem equations to ternary systems—219
- Sears, G. W. A growth mechanism for mercury whiskers. I—361
- A mechanism of whisker growth. II—367

- The origin of screw dislocations—role of colloidal particles—299(L)  
 — (see Newkirk, J. B.)—110(L)  
**Seigle, L. L.** (see Balluffi, R. W.)—170  
 — and **Resnick, R.** On pore formation during diffusion—606(L)  
**Sherby, O. D.** (see Frenkel, R. E.)—470  
**Shewmon, P. G. and Bechtold, J. H.** Marker movements in titanium-molybdenum diffusion couples and the Zener theory of  $D_0$ —452  
**Shirn, G. A.** Self-diffusion in thallium—87  
 — (see Wajda, E. S.)—39  
**Sivertsen, J.** (see Ang, C. Y.)—558  
**Smith, G. C.** (see Olney, M. J.)—206(L)  
**Smoluchowski, R.** (see Haynes, C. W.)—130  
**Stanley, J. T. and Wert, C.** Internal friction of interstitial solid solutions of oxygen and nitrogen in vanadium—107(L)  
**Sully, A. H.** (see Brook, G. B.)—460
- Tambini, D.** (see Rawlings, R.)—212(L)  
**Tegart, W. J. McG.** (see Bowles, J. S.)—590  
**Thomas, W. R. and Chalmers, B.** The segregation of impurities to grain boundaries—17  
 — (see Leak, D. A.)—501  
**Thompson, N. and Hingley, M.** The formation of mechanical twins—289  
 — (see Frank, F. C.)—30  
**Tiedema, T. J.** (see Okkerse, B.)—300(L)  
**Tiller, W. A.** Grain boundary segregation—209(L)  
**Treafis, H. N.** (see Turnbull, D.)—43  
**Tuchschmid, H. E.** The lack of a crystal boundary hardening in deformed metals as revealed by microhardness measurements—215(L)  
**Turnbull, D.** Theory of cellular precipitation—55  
 — (see Hoffman, R. E.)—417  
 — and **Treafis, H. N.** Kinetics of precipitation of tin from lead-tin solid solutions—43
- Uhlig, H. H.** Effect of electric field on oxidation of copper—108(L)  
 — Formation of the intermetallic compound Pt Zn at room temperatures—302(L)
- Van Bueren, H. G.** Theory of the formation of lattice defects during plastic strain—519  
**Van Niekerk, J. N.** (see Schoening, F. R. L.)—10  
**Vassamillet, L.** (see Lambot, H.)—150  
**Vaughn, D. A.** (see Uhlig, H. H.)—302(L)  
**Vermilyea, D. A.** Space charges in anodic films—106(L)  
**Verrijp, M. B.** (see Fast, J. D.)—203(L)  
**Vogel, F. L., Jr.** Dislocations in low-angle boundaries in germanium—245  
 — Dislocations in polygonized germanium—95(L)  
**Votava, E., Amelinckx, S., and Dekeyser, W.** Indentation figures on single crystals. I—89
- Wajda, E. S., Shirn, G. A., and Huntington, H. B.** Lattice and grain boundary self-diffusion in cadmium—39  
**Walters, R. E. S.** Grain boundaries in alloys of high magnetic permeability—293(L)  
**Wang, C. C.** Hardness of germanium-silicon alloys at room temperature—515(L)  
**Warekois, E. P.** (see Warren, B. E.)—473  
**Warren, B. E. and Warekois, E. P.** Stacking faults in cold-worked alpha-brass—473  
**Wassermann, G.** (see Grewen, J.)—354  
**Weertman, J. and Salkovitz, E. I.** The internal friction of dilute alloys of lead—1  
**Wert, C.** (see Ang, C. Y.)—558  
 — (see Stanley, J. T.)—107(L)  
 — (see Wruck, D.)—115  
**Westbrook, J. H.** Note on the temperature dependence of hardness of the transition metal monocarbides—104(L)  
**Wiedersich, H.** (see Cochart, A. W.)—533  
**Williamson, G. K.** (see Moore, A.)—579  
**Winegard, W. C.** (see Tiller, W. A.)—209(L)  
**Wruck, D. and Wert, C.** The role of crystal structure of irradiation effects on metals—115

## Contents of Volume 3, 1955

### Number 1

### January

- The internal friction of dilute alloys of lead, J. Weertman and E. I. Salkovitz—1  
 X-Ray measurements on silver filings, F. R. L. Schoening and J. N. Van Niekerk—10  
 Metallic ternary phases in the Mn-Ta-O systems, N. Schönberg—14  
 The segregation of impurities to grain boundaries, W. R. Thomas and B. Chalmers—17  
 The yield phenomena, kink bands and geometric softening in titanium crystals, A. T. Churchman—22  
 On deformation by twinning, F. C. Frank and N. Thompson—30  
 Some applications of isoactivity lines, M. Hillert—34  
 Solubility of cementite in liquid iron, M. Hillert—37  
 Lattice and grain boundary self-diffusion in cadmium, E. S. Wajda, G. A. Shirn and H. B. Huntington—39  
 Kinetics of precipitation of tin from lead-tin solid solutions, D. Turnbull and H. N. Treafis—43  
 Theory of cellular precipitation, D. Turnbull—55  
 A thermal etching technique for revealing dislocations in silver, A. A. Hendrickson and E. S. Machlin—64  
 The influence of grain boundaries on the nucleation of secondary phases, P. J. Clemm and J. C. Fisher—70  
 Nuclear electric quadrupole interactions in aluminum, T. J. Rowland—74  
 Transition structure in lead-silver alloys and a dislocation mechanism, R. D. Heidenreich—79  
 Self-diffusion in thallium, G. A. Shirn—87  
 Indentation figures on single crystals. I, E. Votava, S. Amelinckx and W. Dekeyser—89  
 Letters to the Editor—95

- Dislocations in polygonized germanium, F. L. Vogel, Jr.; Sub-grain formation in aluminum deformed at  $-183^{\circ}\text{C}$ , A. Kelly and W. T. Roberts; Resistivity changes in silicon single crystals induced by heat treatment, C. S. Fuller, J. A. Ditzemberger, N. B. Hannay and E. Buehler; The diffusion of hydrogen in iron and ferritic steels, E. W. Johnson and M. L. Hill; Electron microscope study of slip bands in radiation-damaged aluminum crystals, E. M. Kelly; A possible explanation of the stability of Guinier-Preston zones, J. Nyström; Internal friction in titanium and titanium oxygen alloys, H. H. Bleakney; Note on the temperature dependence of hardness of the transition metal monocarbides, J. H. Westbrook; Space charges in anodic films, D. A. Vermilyea; Internal friction of interstitial solid solutions of oxygen and nitrogen in vanadium, J. T. Stanley and C. A. Wert; Effect of electric field on oxidation of copper, H. H. Uhlig and A. E. Brenner; A dislocation model for the origin of fracture cracks in metal crystals, J. C. Fisher; Growth of potassium halide crystals from aqueous solution, J. B. Newkirk and G. W. Sears

### Number 2

### March

- The role of crystal structure on irradiation effects in metals, D. Wruck and C. Wert—115  
 Growth of cadmium iodide crystals, J. B. Newkirk—121  
 The segregation of carbon in iron single crystals as studied by torsion pendulum damping, F. W. Kunz—126  
 Grain boundary diffusion in a body-centered cubic lattice, C. W. Haynes and R. Smoluchowski—130  
 Internal friction in solid solutions of oxygen-tantalum, R. W. Powers—135



effect, J. A. Brinkman—140  
 A uniaxial strain model for a Lüder's band, E. W. Hart—146  
 Determination des sous-structures dans les monocristaux métalliques à l'aide des rayons X, H. Lambot, L. Vassamillet and J. Dejace—150  
 On the diffusion of oxygen through solid iron, J. L. Meijering—157  
 Twinning and accommodation kinking in zinc, A. J. W. Moore—163  
 Effect of grain boundaries upon pore formation and dimensional changes during diffusion, R. W. Balluffi and L. L. Seigle—170  
 The mechanisms of self-diffusion in tin, J. F. Nicholas—178  
 Calorimetric measurements during precipitation in a gold-nickel alloy, J. Nyström—182  
 Frictional forces on dislocation arrays at the lower yield point in iron, A. Cracknell and N. J. Petch—186  
 X-ray line broadening from cold-worked iron, R. I. Garrod and H. H. Auld—90  
 Letters to the Editor—199  
 Energie mutuelle de deux dislocations, J. Blin; Hydrogen and the yield point in steel, A. Cracknell and N. J. Petch; A tentative explanation of the accelerated growth of tin whiskers, R. R. Hasiguti; Impurity particles and the lateral growth of cadmium iodide, G. Ehrlich; Solubility of nitrogen in  $\alpha$ -iron, J. D. Fast and M. B. Verrijs; Zur Entstehung der Rekristallisationstexturen in Aluminiumdrähten, K. Lücke and F. Hässner; Twinning in aluminium, M. J. Olney and G. C. Smith; Zur Rekristallisation von Eisen nach der  $\gamma$ - $\alpha$ -Umwandlung, W. Dickenscheid; Deformation processes in zirconium, E. J. Rappoport; Grain-boundary segregation, W. A. Tiller and W. C. Winegard; Fine structure in zinc twins, J. J. Gilman; Effect of irradiation upon beryllium copper, J. T. Richards; Nitrogen in iron anelasticity and solid solubility, R. Rawlings and D. Tambini; Spiral growth of cadmium crystals from the vapor phase, W. I. Pollock and R. F. Mehl; The lack of a crystal boundary hardening in deformed metals as revealed by microhardness measurements, H. E. Tuchschild

### Number 3

May

Application of Gibbs-Duhem equations to ternary systems, R. Schuhmann, Jr.—219  
 Calorimetric investigations of a gold-nickel alloy. I. Low temperature heat capacity of gold-nickel alloy, W. DeSorbo—227  
 Calorimetric investigations of a gold-nickel alloy. II. The heat capacity at high temperatures and the entropy of formation, R. A. Oriani—232  
 Influence of grain boundaries on the behaviour of carbon and nitrogen in  $\alpha$ -iron, G. Lagerberg and Å. Josefsson—236  
 Dislocations in low-angle boundaries in germanium, F. L. Vogel, Jr.—245  
 Tensile properties of annealed tantalum at low temperatures, J. H. Bechtold—249  
 A calorimetric investigation of the system silver-tin at 450°C, Q. J. Kleppa—235  
 Crystal perfection in aluminum single crystals, T. S. Nogge and J. S. Koehler—260  
 The deformation of single crystals of  $\alpha$ -brass, H. M. Murphy and E. A. Calnan—268  
 Bestimmung der Versetzungsliniendichte von verformtem Eisen, W. Köster and L. Bangert—274  
 Structure and polygonization of bent zinc monocrystals, J. J. Gilman—277  
 The formation of mechanical twins, N. Thompson and M. Hingley—289  
 Letters to the Editor—292  
 Effect of order on the electrical resistivity of ferromagnetic alloys, F. J. Donahoe; Grain boundaries in alloys of high magnetic permeability, R. E. S. Walters; On the lattice parameter of Mg-Li  $\beta$ -alloys, D. W. Levinson; An electron transfer mechanism for ultrasonic attenuation in metals, C. Kittel; Diffusion von radioaktiven Kupfer in technischem Stahl, R. Lindner and F. Karnik; Double-valued internal friction behavior, H. K. Birnbaum; The origin of screw dislocations—role of colloidal particles, G. W. Sears; Self-diffusion of lead in oriented grain-boundaries, B.

Bakish and W. D. Robertson; Hardness of germanium-silicon alloys at room temperature, C. C. Wang and B. H. Alexander

### Number 6

November

Theory of the formation of lattice defects during plastic strain, H. G. Van Bueren—519  
 On the effect of ordering upon the strength of  $\text{Cu}_3\text{Au}$ , G. W. Ardley—525  
 Interaction between dislocations and interstitial atoms in body-centered cubic metals, A. W. Cocharde, G. Shoenk and H. Wiedersich—533  
 The influence of thin intermediate layers on interdiffusion in copper-nickel couples, M. L. Mehta and H. J. Axon—538  
 Die Teilchenform bei der Karbidausscheidung aus dem  $\alpha$ -Eisen, W. Pitsch—542  
 Kinetics of order-disorder transformations, G. J. Dienes—549  
 Anelastic behavior in alloys of gold and nickel, C. Y. Ang, J. Sivertsen and C. Wert—558

H. H. Uhlig, J. S. MacNairn and D. A. Vaughn

### Number 4

July

Isothermal decomposition kinetics of transformed-beta phase in a titanium-nickel alloy, D. H. Polonis and J. G. Parr—307  
 On the interpretation of "low-temperature" recovery phenomena in cold-worked metals, A. S. Nowick—312  
 Dislocation energies in anisotropic crystals, A. J. E. Foreman—322  
 A study of primary and conjugate slip in crystals of alpha-brass, G. R. Piercy, R. W. Cahn and A. H. Cottrell—331  
 The heats of formation in the systems titanium-aluminum and titanium-iron, O. Kubaschewski and W. A. Dench—339  
 Über die Abhängigkeit der Korngrenzenauscheidung von der Orientierung der benachbarten Kristalle, W. Gruhl and D. Ammann—347  
 Über die idealen Orientierungen einer Walztextur, J. Grewen and G. Wassermann—354  
 A growth mechanism for mercury whiskers, G. W. Sears—361  
 A mechanism of whisker growth, G. W. Sears—367  
 Relation entre les structures et les propriétés des alliages aluminium-argent pendant le durcissement structural, B. Belbeoch and A. Guinier—370  
 Constantes élastiques et frottement intérieur de l'aluminium polygonisé, J. Friedel, C. Boulanger, and C. Crussard—380  
 Electron transport in copper and dilute alloys at low temperatures. I., D. K. C. MacDonald and W. B. Pearson—392  
 Electron transport in copper and dilute alloys at low temperatures. II., D. K. C. MacDonald and W. B. Pearson—403  
 Letters to the Editor—409  
 Some observations of dislocation sites in polygonized silicon crystals, C. G. Dunn and W. R. Hibbard, Jr.; Comments on "Formation energies of vacancies in copper and gold," C. J. Meehan and R. R. Eggleston; Some observations on the relationship between vacancies, recovery and precipitation in Al-Mg alloys, E. C. W. Perryman; Approximate steady-state configuration of a dislocation mill, J. C. Fisher; Tensile tests on silicon whiskers, R. L. Eisner; Variation of the yield point with temperature in AuCu, G. C. Kuczynski and M. Doyama

### Number 5

September

An interferometric study of grain boundary grooves in tin, H. Mykura—436  
 Self-diffusion of gold-nickel alloys. A. D. Kurtz, B. L. Averbach and M. Cohen—442  
 Sur la précipitation d'oxyde  $\text{Fe}_3\text{O}_4$  dans les pellicules d'oxydation du fer aux températures élevées, J. Paidassi—447  
 Marker movements in titanium-molybdenum diffusion couples and the Zener theory of  $D_0$ , P. G. Shewmon and J. H. Bechtold—452  
 Activity of aluminum in liquid Ag-Al, Fe-Al, Fe-Al-C and Fe-Al-C-Si alloys, J. Chipman and T. P. Floridis—456  
 Some observations on the internal friction of polycrystalline aluminium during the early stages of creep, G. B. Cook and A. H. Sully—460  
 Activation energies for creep of cadmium, indium and tin, R. E. Frenkel, O. D. Sherby and J. E. Dorn—470  
 Stacking faults in cold-worked alpha-brass, B. E. Warren and E. P. Warekois—473  
 The lattice spacings of close-packed hexagonal 3/2 electron compounds, G. V. Raynor and T. B. Massalski—480  
 The elastic interaction of point defects, J. D. Eshelby—487  
 Plastic deformation of copper crystals under alternating tension and compression, M. S. Paterson—491  
 Diffusion and solubility of nitrogen in silicon-iron, D. A. Leak, W. R. Thomas and G. M. Leak—501  
 Letters to the Editor—508  
 Isothermal measurements on the release of energy stored in cold-worked aluminium, H. U. Åström; Effect of ternary additions of silicon and aluminum on the ordering reaction in iron-cobalt, A. J. Griest, J. F. Libsch and G. P. Conard; Nouvelle interprétation des diagrammes à side-bands, A. Guinier; Dislocation densities in intersecting lineage boundaries in germanium, W. G. Pfann and L. C. Lovell; Internal deformation markings in single crystals of  $\text{Cu}_3\text{Au}$ , R.

The diffusivity of hydrogen in nickel, M. L. Hill and E. W. Johnson—566

A surface structure observed on electrolytically polished zinc, K. F. Hulme—572

An X-ray examination of crystallographic transformations in indium-rich solid solutions with thallium, lithium and lead, A. Moore, J. Graham, G. K. Williamson and G. V. Raynor—579

Crystallographic relationships in aged copper-beryllium alloys, J. S. Bowles and W. J. McG. Tegart—590

The heats of formation of some transition silicides, D. A. Robins and I. Jenkins—598

Letters to the Editor—605

On the mechanism of pore formation during diffusion, J. A. Brinkman; On pore formation during diffusion, L. Seigle and R. Resnick; Abnormal after-effect of twisted metal wires upon heating, A. W. Cocharde; Dislocation glide as an aid to precipitation at low temperatures, J. C. Fisher and J. H. Hollomon

VOL.  
3  
1955

OL.  
3  
955

VOL.  
3  
1955

## THE INTERNAL FRICTION OF DILUTE ALLOYS OF LEAD\*

J. WEERTMAN and E. I. SALKOVITZ†

The internal friction and Young's modulus were measured for a series of single crystals of lead containing approximately .01 to 1 atomic per cent of either Bi, Sn, or Cd. It was discovered that the internal friction was independent of strain amplitude up to a critical strain amplitude, at which point the internal friction increased and the modulus decreased with further increase in strain amplitude. At room temperature the resolved shear stress for this critical strain amplitude is approximately equal to  $.15 \mu \epsilon$  where  $\mu$  is the shear modulus,  $\epsilon$  is the fractional difference in size between the solute and solvent atoms, and  $c$  is the fraction of the total number of atoms which are solute atoms. The data also agree well with results on the change in the critical shear stress with alloying content in copper crystals reported by Linde, Lindell, and Stade.

### LE FROTTEMENT INTERNE DANS DES ALLIAGES DILUÉS DU PLOMB

On a mesuré le frottement interne et le module de Young d'une série de monocristaux de plomb contenant de 0.01 à 1 pour cent en atomes d'un des éléments suivants: Bi, Sn, Cd. Il fut constaté que le frottement interne était indépendant de l'amplitude de déformation jusqu'à une valeur critique de cette amplitude. À partir de cette valeur le frottement interne augmentait et le module de Young diminuait quand on augmentait l'amplitude de déformation. À la température ambiante, la composante de la tension de cisaillement dans le plan de glissement, pour cette amplitude de déformation, est approximativement égale à  $0.15 \mu \epsilon$ , où  $\mu$  représente le module de cisaillement,  $\epsilon$  la différence fractionnaire entre les dimensions des atomes de soluté et des atomes du solvant et  $c$  la fraction du nombre total d'atomes qui représente les atomes de soluté.

Ces données sont aussi en bon accord avec les résultats de Linde, Lindell et Stade sur le changement de la tension critique de cisaillement de cristaux de cuivre par l'addition d'éléments d'alliage.

### DIE INNERE REIBUNG VON VERDÜNNTEN BLEILEGIERUNGEN

Die innere Reibung und Young's Modulus wurden an einer Reihe von Bleieinkristallen, die zwischen etwa 0.01 Atomprozent und 1 Atomprozent Bi oder Sn oder Cd enthielten, gemessen. Es zeigte sich, dass die innere Reibung von der Verzerrungsamplitude unabhängig war, bis eine bestimmte Grenzverzerrungsamplitude erreicht wurde. Von da an nahm die innere Reibung und der Modulus ab, wenn die Verzerrungsamplitude weiter vergrößert wurde. Bei Zimmertemperatur beträgt die Wirksame Schubspannung für diese kritische Verzerrungsamplitude etwa  $.15 \mu \epsilon$ , wobei  $\mu$  der Scherungsmodulus,  $\epsilon$  der prozentuale Unterschied in der Grösse des Lösungs- und des gelösten Atomes und  $c$  der Bruchteil der Atome, die als Lösungsatome vorhanden sind, bedeutet. Die vorliegenden Daten stimmen gut mit den von Linde, Lindell und Stade mitgeteilten Ergebnissen der Änderung der kritischen Scherungsspannung beim Legieren von Cu überein.

## INTRODUCTION

Since the time of the suggestion by T. A. Read<sup>1</sup> that dislocation motion gives rise to that portion of the internal friction in metals which cannot be explained by such mechanisms as interstitial atom movement, thermoelastic currents, etc.<sup>2,3</sup> there have been many experiments on single crystals of pure metals which can be qualitatively explained using Read's idea. Most of these experiments have been concerned with cold-working and annealing the specimens. The effect of impurities on the internal friction due to dislocation motion, however, has been given very little attention. Marx and Koehler<sup>4</sup> have shown that annealing copper single crystals in a hydrogen atmosphere causes the internal friction to decrease and the modulus to increase much more rapidly than a corresponding anneal in a vacuum. Bradfield and Pursey<sup>5</sup> have shown that the addition of a slight amount of another metal to copper will cause its modulus to increase.

Since impurity atoms can interact with dislocation lines through the Cottrell mechanism, such an interaction might be expected to manifest itself in internal

friction experiments on specimens containing various amounts of impurities. With this idea in mind internal friction measurements were made upon single crystals of lead containing small amounts of either Bi, Sn, or Cd as a function of composition, strain amplitude of vibration, and temperature.

## EXPERIMENTAL TECHNIQUE

The method of measuring the internal friction that was used was that developed by Marx,<sup>6</sup> which makes use of two matched quartz piezoelectric crystals. This method is completely discussed by Marx in his paper. Figure 1 shows the experimental arrangement. The unit consists of a driver crystal, gauge crystal, a fused quartz rod, and the lead sample. The two quartz crystals, the rod, and the sample are of such a length that their resonant frequencies in longitudinal motion are about equal. The decrement (which is defined to be equal to the energy lost per cycle divided by twice the stored energy in the system) can be calculated from the measured values of the applied driver voltage and the gauge voltage when the system is vibrating at the resonant frequency. The maximum strain amplitude of vibration can be calculated from the gauge voltage. In this experiment all measurements were made at frequencies close to 30 kc.

\* Received January 20, 1954.

† Metallurgy Division, Naval Research Laboratory, Washington, D. C.



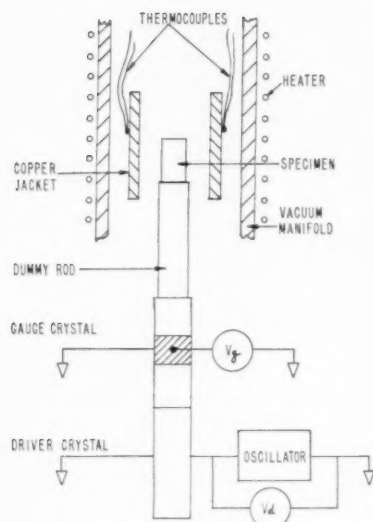


FIG. 1. Schematic diagram of composite oscillator.

The temperature was measured with thermocouples attached to a copper tube surrounding the specimen. This temperature was assumed to be that of the specimen. This assumption was valid for the slow heating and cooling rates used (approximately  $1^\circ/\text{min}$ ). Measurements were made from room temperature up to  $315^\circ\text{C}$  in *vacuo* of better than  $10^{-4}$  mm Hg.

Specimens were cut from lead single crystals grown by the Bridgman method in the form of  $1/4$  in. diameter rods of 9 in. length. The crystals were grown in graphite crucibles under *vacuo* of approximately  $10^{-6}$  mm Hg. The major impurity of the pure lead specimens (using 99.9998 per cent pure lead as starting material) after growth was carbon (.003 atomic per cent). In all cases except one the alloying addition in the alloy crystals as determined by analyses was greater than the carbon content. The one exception was sample PbCd7 $\beta$  containing .0015 per cent of cadmium.

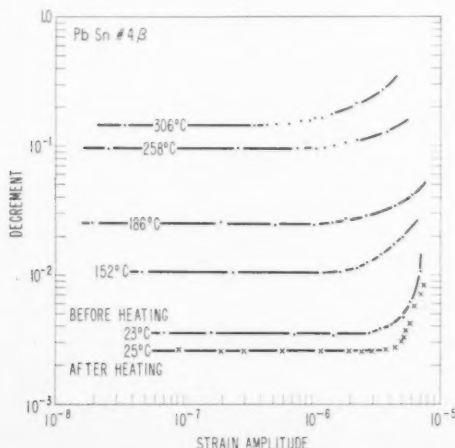


FIG. 2. Decrement vs strain amplitude of a lead specimen containing .058 per cent Sn at various temperatures.

Single crystals of dilute alloys were prepared as follows: Graphite crucibles were loaded to the approximate desired compositions and the alloys were allowed to remain in the molten state overnight. The melts were slowly cooled through a temperature gradient, thereby producing single crystals of the alloys. The material immediately adjacent to either side of the samples cut for the experiments or the samples themselves after the measurements had been made were chemically analyzed. The variation of composition from one end of the sample to the other was always less than 15 per cent. The lead-cadmium alloys were the most difficult to prepare since a major portion of the cadmium distilled away during the preparation of the crystal. The samples were cut and ground to length without being removed from the crucible. The graphite was then split away and the samples etched to remove the very fine grains produced by grinding and polishing the ends. The samples were annealed during the course of the experiment.

The quartz crystals in the composite oscillator were glued together with beeswax. In the earlier experiments

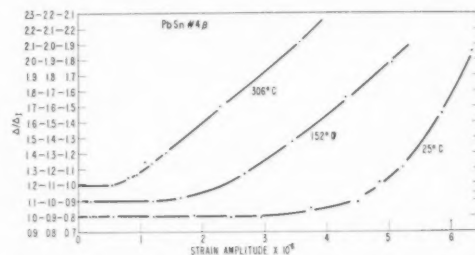


FIG. 3. Ratio of decrement divided by decrement at lowest strain amplitude vs strain amplitude of a lead specimen containing .058 per cent Sn at three different temperatures. The left-hand ordinate scale is to be used with the  $25^\circ\text{C}$  curve, the middle with the  $125^\circ\text{C}$  curve, and the right-hand scale with the  $306^\circ\text{C}$  curve.

the lead crystals were glued onto the dummy quartz rod with water glass. Since this joint often cracked, the cement suggested in the paper by Sutton<sup>7</sup> consisting of barium sulfate, sodium fluosilicate, and water glass was tried and found to be very satisfactory. The cement joint was allowed to set for at least three days before the specimen and dummy rod were glued to the dummy and gauge crystal. The results to be described were not affected by the type of cement (at least at room temperature) since identical measurements were obtained by gluing the lead specimen with beeswax. Since the cement joint is at a strain node it is not expected to affect the results even if strains are induced in it due to the difference in thermal expansion of lead and quartz.

### Experimental Results

For low strain amplitudes it was found that the internal friction of the alloys studied was independent of strain amplitude. On increasing the amplitude of vibration a region could be reached where the decrement increased with increasing amplitude of vibration. The

strain amplitude dividing these two regions, the critical strain amplitude, was found to depend on the alloying content and the temperature. Figure 2 shows the decrement as a function of strain amplitude for various temperatures for an alloy containing .15 atomic per cent Sn. In Fig. 3 the same data are plotted on a larger scale except that the ratio of the decrement divided by the decrement at the lowest strain amplitude is plotted instead of the decrement. The same type of data for three lead-bismuth alloys of different compositions is plotted in Fig. 4. A curve very similar to these has been reported by Takahashi<sup>8</sup> for pure zinc (99.996 per cent) and may be of the same origin. Figure 5 shows a curve of the critical amplitude as a function of  $1/T$ . Slopes of curves of this type give an apparent activation energy of approximately .15 ev. The data on all specimens are

summarized in Table I and Table II. Where the points are too scattered to draw a straight line through them a range of activation energies is given.

A curve of the log of the internal friction in the strain amplitude-independent region versus  $1/T$  is plotted in Fig. 6. The apparent activation energies from curves of this type in the high temperature region are approximately .3 ev. These data are also summarized in Table I. Specimens for which no straight line could be drawn through the high-temperature region data are indicated with a range of activation energies with the higher value corresponding to the highest temperature. For a 1.2 per cent Sn and a 0.053 per cent Bi specimen, Fig. 7 shows a low-temperature peak of unknown origin which was observed around 95 degrees. The peak cannot be due to a pair reorientation since it was not observed for a

TABLE I.

Sample	Decrement at room temperature ( $\times 10^{-3}$ )	Decrement at 300°C ( $\times 10^{-2}$ )	Apparent activation energy of critical strain amplitude (in electron volts)	Apparent activation energy of the strain amplitude-independent decrement (in electron volts)	Resolved shear stress at break at room temperature (dynes/cm <sup>2</sup> $\times 10^{-8}$ )	Critical shear stress (dynes/cm <sup>2</sup> $\times 10^{-8}$ )	Concentration (atomic %)
Bismuth in lead $\epsilon = .018$ $\mu$ lead = $5.0 \times 10^{10}$ dynes/cm <sup>2</sup>							
6 $\beta$ *	.7	30		.31	.37	2.3	.035
4 $\beta$ †	.6	5	.14	.34	1.2	3.8	.053
1 $\alpha$ ‡	2.4	4	.16	.34 to .39	2.6	7.0	.095
8 $\gamma$	.9	1.3	.16 to .12	.30	4.1	48.6	.65
8 $\delta$	2.0				8.9	48.6	.65
Tin in lead $\epsilon = .062$							
6 $\beta$	.85	2		.26	.41	3.4	.016
6 $\alpha$	1.2	2	.07	.26	.12 to .14	3.5	.017
4 $\alpha$	3.1	20	.10 to .07	.34 to .45	1.3	11	.051
4 $\beta$	3.5	11	.10	.37	2.4	13	.058
3 $\gamma$ †	3.9	2.6	.15	.32	2.7	18	.074
5 $\alpha$ †	.32	.25		.28	**	340	1.3
5 $\beta$	3.6				33	340	1.3
Cadmium in lead $\epsilon = .14$							
7 $\beta$	5.7	50		.18	.23	.58	.0015
8 $\alpha$	1.2	2.2	.18	.25 to .35	1.6	5.6	.011
2 $\beta$	2.8	3.8	.10		2.7	9.1	.017
Manganese in copper†† $\epsilon = .1$ $\mu$ copper = $3.2 \times 10^{11}$ dynes/cm <sup>2</sup>							
						220	.48
						240	.52
						230	.61
						290	.70
Tin in copper†† $\epsilon = .28$							
						220	.12
						320	.20
						490	.30
Indium in copper†† $\epsilon = .26$							
						350	.26
Pure lead							
~10	~30				~3††	100***	
					~4†††		
Pure copper							
					~40†††	53††	
						100†††	
						220***	

\* The decrement versus temperature curve of this sample was reversible on cooling and heating only above 150°C. At lower temperatures the decrement of the cooling curve was higher than the heating curve.

† Showed a peak in decrement-temperature curve around 90-100°C.

‡ Were grown in glass crucibles and picked up, ~.01 atm % Si.

\*\* No break up to the highest stress applied,  $\sim 1.2 \times 10^8$  dynes/cm<sup>2</sup>.

†† Data of Linde, Lindell, and Stade on critical shear stress of copper and its alloys.<sup>19</sup>

††† Stress at which irreversible changes in the decrement occur.

\*\*\* Data of Neurath and Koehler.<sup>20</sup>

†††† Stress at which irreversible changes in decrement occur. Data of Marx and Koehler.<sup>4</sup>

†††† Data of Sachs and Weerts.<sup>21</sup>

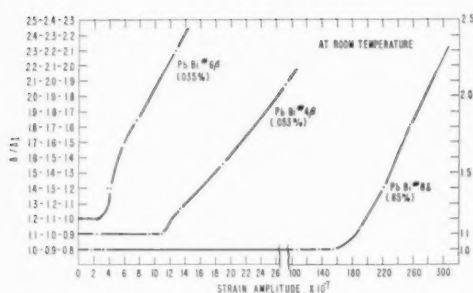


FIG. 4. Ratio of decrement divided by decrement at lowest strain amplitude vs strain amplitude for three lead-bismuth samples containing various amounts of bismuth. The left hand scale is to be used with the curve of sample PbBi8 $\beta$ , the middle with PbBi4 $\beta$ , the right hand scale with PbBi6 $\beta$ .

.65 per cent Bi sample. The Laue spots of their back-reflection patterns showed a very slight splitting so the peak may be due to a polygonized structure. Another possibility is that it may arise from a segregation of impurity atoms which Thomas and Winegard<sup>9</sup> show can occur during crystal growth.

Young's modulus was found to behave in a way analogous to the decrement. Figure 8 shows a plot of the fractional change in Young's modulus versus strain

TABLE II.

Temp. (°C)	Resolved shear stress (dynes/cm <sup>2</sup> ×10 <sup>9</sup> )	Temp. (°C)	Resolved shear stress (dynes/cm <sup>2</sup> ×10 <sup>9</sup> )
Bismuth 6 $\beta$		Tin 4 $\beta$	
29	.37	23	2.4
111	<.05	95	1.2
Bismuth 4 $\beta$		152	1.0
29	1.2	186	.8
60	.4	258	.7
102	.4	Tin 4 $\alpha$	
166	.3	31	1.3
201	.2	100	.7
272	.15	126	.6
Bismuth 1 $\alpha$		158	.5
27	2.6	218	.35
91	1.3	Tin 3 $\gamma$	
134	.8	30	2.7
204	.6	124	1.2
232	.5	171	1.0
257	.4	213	.65
308	.4	Tin 3 $\gamma$	
Bismuth 8 $\gamma$		247	.4
28	4.1	276	.35
126	.8	300	.2
206	.5	Tin 5 $\beta$	
315	.3	26	33
Bismuth 8 $\delta$		Cadmium 7 $\beta$	
28	8.9	25	.23
Tin 6 $\beta$		112	<.02
28	.41	Cadmium 8 $\alpha$	
Tin 6 $\alpha$		30	1.6
26	.12 to .24	53	.8
58	.12	155	.4
88	.095	211	.35
162	.007	260	.25
254	.0036	302	.20
		Cadmium 2 $\beta$	
		28	2.7
		120	.8
		208	.45

amplitude. In Fig. 8 the break occurs at a slightly higher strain amplitude than in Fig. 4. This difference arises because the sensitivity of the frequency measurements was low. This low sensitivity was due to the fact that the total mass of the quartz components was 15 times heavier than the sample itself. Thus a shift of 15 cycles/second in the resonant frequency of the sample corresponded to a measured change of 1 cycle/second in the total composite oscillator.

In order to increase the sensitivity of the frequency measurements, data were taken at room temperature using smaller gauge and driver crystals without a dummy rod. The results are shown in Fig. 9. A linear relationship is obtained between the decrement and the

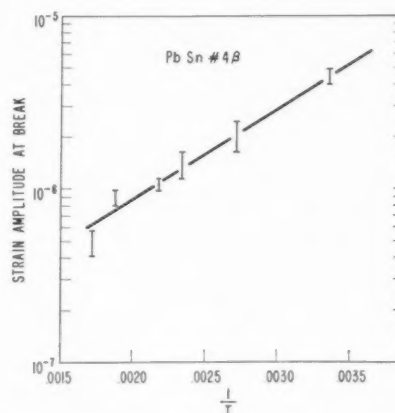


FIG. 5. Strain amplitude at break in decrement-strain amplitude curves vs reciprocal of absolute temperature for a specimen containing .058 per cent Sn.

fractional change in frequency. This relationship was first pointed out by T. A. Read many years ago.

Several curves of Young's modulus versus temperature are shown in Fig. 10. Measurements were also made upon pure lead crystals. If the measurements were made immediately after mounting the specimen in the unit, the internal friction increased with strain amplitude from the very lowest strain amplitude. If, however, the specimen was allowed to anneal overnight at room temperature while in the unit, the strain amplitude dependence disappeared at low strain amplitudes. The decrement then increased only very slowly with strain amplitude up to a resolved shear stress of about  $3 \times 10^5$  dynes/cm<sup>2</sup>. At this stress the decrement started to rise very rapidly and became irreversible. If the strain amplitude was lowered to the strain amplitude independent region the decrement was then higher than it had previously been. The increase in the decrement annealed out at room temperature. This cold-working effect was first reported by Marx and Koehler<sup>4</sup> for both copper and lead and our stress value for lead agrees with theirs. The break in the internal friction curves for the alloys differed from that of the pure lead in that going to strains higher than the strain at the break did

not cause an increase in the decrement when the strain amplitude was lowered below the critical amplitude unless one went to much larger strains.

For comparative purposes a plot of decrement versus  $1/T$  for pure lead is shown in Fig. 11.

### THEORY

The main point of interest in this experiment is the occurrence of a break in the internal friction-strain amplitude curve. We wish to give a possible explanation of this break in the light of dislocation theory.

As mentioned in the introduction the mechanism proposed by T. A. Read, namely, dissipation of energy through dislocation motion, seems to be the most reasonable for explaining that portion of the internal friction of metals which is not due to other known causes. To date, two dislocation models have been de-

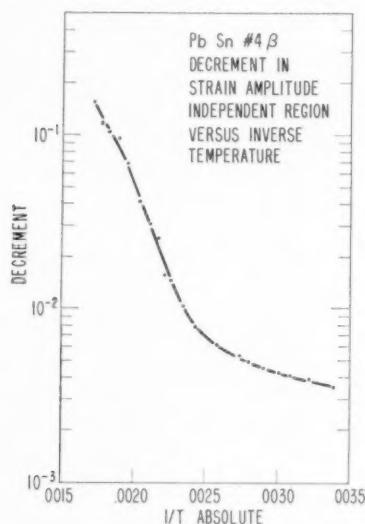


FIG. 6. Decrement as a function of temperature for a specimen containing .058 per cent Sn.

veloped using Read's idea to account for the internal friction. The one due to Koehler<sup>10</sup> pictures the dislocation lines as being pinned down along their lengths by impurity atoms. Under an alternating stress a dislocation vibrates like a violin string in its fundamental mode, restrained from motion only at the pinning points. Koehler's theory predicts that the internal friction is proportional to the frequency of vibration in the kilocycle range of frequency. Nowick<sup>3,11</sup> has pictured the process as due to a hysteresis phenomenon in which dislocations are suddenly torn from one low-energy position and moved to another. His theory predicts that the internal friction is independent of frequency. Most of the experimental evidence on frequency dependence favors Nowick's theory. Koehler's theory would correspond to Nowick's when the stress is large enough to tear dislocations from impurity atoms.

Koehler's theory as it stands cannot be used to ex-

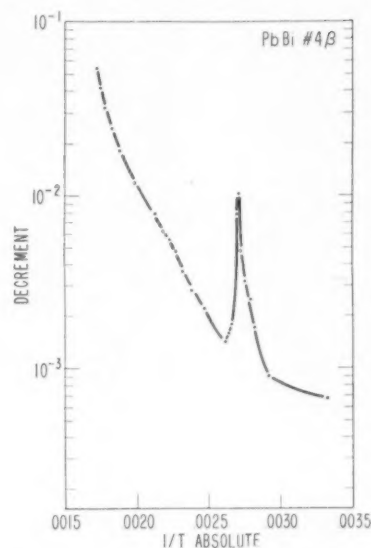


FIG. 7. Anomalous peak in the decrement-temperature curve for a specimen containing .053 per cent Bi.

plain the internal friction of the lead alloys. The binding energy of either Bi, Sn, or Cd atoms to a dislocation is so small that at room temperature, thermal stress fluctuations would keep the dislocation from being pinned down in the manner envisaged by Koehler. Cottrell<sup>12</sup> calculates that the maximum binding energy of an alloying atom with a dislocation line is equal to  $\frac{1}{2}b^2\mu\epsilon$ , where  $\mu$  is the shear modulus,  $b$  is the length of the Burger's vector, and  $\epsilon$  is equal to  $(1/a)da/dc$  where  $a$  is the lattice parameter of the alloy and  $c$  is the fraction of the total number of atoms which are solute atoms. For Bi, Sn, and Cd in lead ( $\mu = 5.25 \times 10^{10}$  dynes/cm<sup>2</sup>,  $b = 3.5 \times 10^{-8}$  cm,  $\epsilon_{Bi} = +.018$ ,<sup>13</sup>  $\epsilon_{Sn} = -.062$ ,<sup>14</sup> and  $\epsilon_{Cd} = -.14$ <sup>15</sup> the binding energies are .013, .044, and .10 ev re-

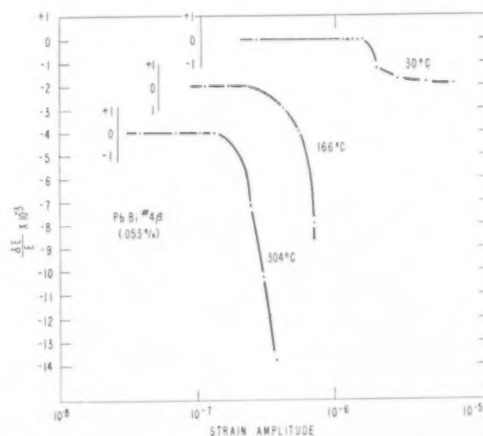


FIG. 8. Fractional change relative to the value at the lowest strain amplitude in Young's modulus vs strain amplitude for a specimen containing .053 per cent Bi at three different temperatures. The ordinate scale has been shifted for the 166°C and the 304°C curves in order to separate all three curves in the region where  $\delta E/E$  is equal to zero.



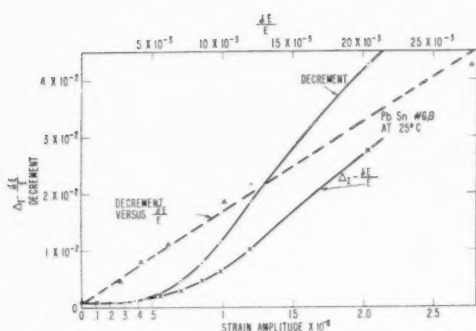


FIG. 9. Curves of decrement vs strain amplitude, fractional change in Young's modulus vs strain amplitude, and decrement vs fraction change in Young's modulus for a specimen containing .016 per cent Sn. Measurements were made at room temperature.

spectively. Since these energies are comparable with  $kT$  (.026 ev) at room temperature it is not likely that the dislocations will be pinned down as in Koehler's model. Another consequence of these low energies is that there will be no marked segregation of the alloying atoms at the dislocations.

Even though individual impurity atoms cannot pin down the dislocations in lead at room temperature, the impurities acting collectively can prevent large displacements of the dislocation under the action of small applied stresses. If the applied stress is made great enough the dislocations can be made to move through the lattice containing the dissolved impurities. Values of the critical stress to move a dislocation past the impurities have been worked out in papers by Nabarro,<sup>16</sup> Mott and Nabarro,<sup>17</sup> and Mott.<sup>18</sup> They assume that in a lattice containing randomly spaced impurity atoms there exists a stress field caused by the presence of the alloying atoms. The wavelength of this stress field,  $\lambda$ , is approximately equal to  $b/c^{1/3}$ . The mean magnitude,  $\sigma_i$ , of the stress around each impurity atom is calculated by them to be equal to  $\mu\epsilon c \ln(1/c)$ . Thus a segment of dislocation of length  $\lambda$  would feel a force  $\lambda b \mu \epsilon c \ln(1/c)$  due to this stress. Along a length of dislocation longer than  $\lambda$  this force alternates with sign in a random manner. For a dislocation of length  $n^2 \lambda$  the total force acting on the dislocation due to the impurities can be any value from zero to  $\pm n^2 b \lambda \mu \epsilon c \ln(1/c)$ . However, in moving a distance of several units of  $\lambda$  the maximum force exerted by the impurities on the dislocation would be  $n b \lambda \mu \epsilon c \ln(1/c)$  since the mean of  $n^2$  events of random sign and magnitude 1 is  $n$ . This length of dislocation would thus experience a force caused by a stress field of average amplitude equal to  $\sigma_i/n$  and average wavelength equal to  $b/c^{1/3}$ .

In order to calculate the critical stress required to move dislocations through the lattice it is necessary to have some basis for evaluating the characteristic length,  $l = n^2 \lambda$ , of dislocation line which has to be moved as a unit to obtain yielding. Since the yield stress is equal to  $\sigma_i/n$ , the longer this length the smaller the yield stress.

The longest conceivable length that can be chosen, and which Nabarro uses in his first paper,<sup>16</sup> is that of a Frank-Read source. If this length is  $L$ , the yield stress will be equal to

$$\sigma_L = \left(\frac{c^2 L}{b}\right)^{1/2} \mu \epsilon c \ln\left(\frac{1}{c}\right). \quad (1)$$

On the other hand, Mott<sup>18</sup> chooses as the characteristic length the smallest segment of dislocation line that can be moved an average distance  $\lambda$  without inducing movement in the remaining length of the dislocation line. For this case he obtains  $n = [2\pi b / \lambda \epsilon c \ln(1/c)]^{1/3}$ , and he finds that the yield stress is equal to

$$\sigma_M = (2\pi)^{-1/3} \mu \epsilon^{4/3} c^{11/9} [\ln(1/c)]^{4/3}. \quad (2)$$

Equation (1) represents a lower limit to the yield stress and equation (2) an upper limit.

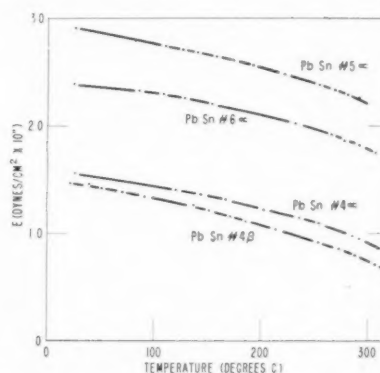


FIG. 10. Young's modulus versus temperature for four lead-tin specimens.

Dislocation motion can occur for stresses smaller than  $\sigma_M$ , but the resultant displacement will be of the order  $\lambda$ . The actual stress field that a dislocation of length  $l$  feels as it moves through the lattice will be of wavelength  $b/c^{1/3}$  but its amplitude will vary from zero to values much greater than  $\sigma_M$ . The average value of the amplitude will be approximately equal to  $\sigma_M$ . From statistical theory the number of wavelengths in the stress field felt by the dislocation having a maximum amplitude between  $\sigma$  and  $\sigma + d\sigma$  will be proportional to  $\exp(-\sigma^2/\sigma_M^2) d\sigma$ . If a stress  $\sigma < \sigma_M$  is applied some of the dislocations will be able to move but they will only be able to move a distance approximately equal to  $\lambda$ . For stress greater than  $\sigma_M$  the dislocations will be able to move large distances before they are stopped since there will be so few places in the crystal where the amplitude of the stress field is greater than  $\sigma_M$ .

If an alternating stress is applied to a crystal containing impurity atoms as is the case in an internal friction experiment, a large increase in the internal friction is to be expected when the maximum stress reaches the value  $\sigma_M$ . Under this circumstance large dislocation motion can take place and hence large

energy losses arise. The stress in the internal friction curve at which the internal friction starts to rise rapidly is thus equal to the yield stress of the material if the yield stress depends only on the impurity concentration. Actually the yield stress of a metal crystal depends on the impurity concentration and the stress required to activate a Frank-Read source. For high-impurity concentrations the effect of the impurities is predominant and Eq. (2) should give the yield stress. For low-impurity concentrations the stress required to activate a Frank-Read source is the yield stress, and Mott's equation is no longer applicable. However Eq. (2) is still applicable for calculating the break in the internal friction for this case. Thus internal friction measurements enable one to extend the measurement of that portion of the total yield stress due to impurities to values much lower than can be obtained in static tests.

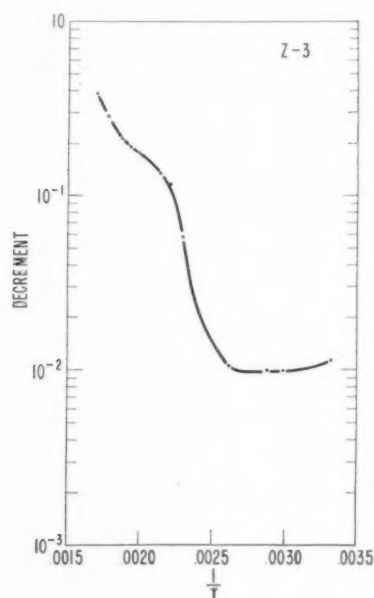


FIG. 11. Decrement as a function of absolute temperature for pure lead.

In Fig. 11 is plotted the resolved shear stress for the break at room temperature versus  $\sigma_M$ . Also plotted are points from the paper by Linde, Lindell, and Stade<sup>19</sup> on the change in the critical shear stress in copper containing small amounts of Mn, In, and Sn. This work has been discussed in the light of Mott's theory by Cottrell.<sup>12</sup> The scatter in the points is too great to permit any conclusion regarding the validity of the powers used in Mott's formula. It is clear, however, that the break-away stress is roughly proportional to the concentration,  $\epsilon$ , and  $\mu$ . The expression  $\sigma = .15\mu\epsilon c$  gives as good a plot for the lead points as Mott's expression.

Although plotting the experimental points using Mott's formula gives a linear relationship, the agreement is still not good between theory and experiment

since the magnitude of the experimental points are an order of 10 too low. Part of this discrepancy is due to thermal stress fluctuations which can help dislocations get over the stress barriers. Experimental work on the yield stress as a function of temperature<sup>20,21</sup> show an increase in the yield stress of a factor of 2 or 3 on extrapolation to absolute zero. Part of the discrepancy can also be accounted for, as pointed out by Cottrell,<sup>12</sup> if the length of the coherent piece of dislocation line was underestimated by Mott. The two earlier papers<sup>16,17</sup> used longer lengths and got smaller answers for the yield stress. A length of 3 to 5 times longer than Mott used would bring agreement between theory and experiment.

For the impurities to be effective in holding up the dislocations and thus give rise to a break in the internal friction-strain amplitude curves it is necessary from rate theory that  $\exp(-Q/kT)$  be less than  $\omega/\nu$  where  $\nu$  is the frequency of vibration of a dislocation  $\sim 10^{10} \text{ sec}^{-1}$ ,  $\omega$  is the frequency of vibration of the applied stress  $\sim 3 \times 10^4 \text{ sec}^{-1}$ , and  $Q$  is the work required to move a length of coherent dislocation line from its stable equilibrium position to the first unstable equilibrium position. The magnitude of this energy is approximately equal to  $\lambda$  times the coherent length times the average force per unit length exerted by the impurities on the dislocation. If the length is equal to  $n\lambda$  then the force per unit length is  $\sigma_c b/n$  and the energy is equal to  $n\lambda^2 b \sigma_c$ . Using a length of coherent dislocation line three times longer than used by Mott gives the expression  $3^{1/2} \mu b^3 \epsilon^{2/3}$  for this energy in the concentration range used in this experiment. For Bi, Sn, and Cd, in lead the  $Q$ 's are approximately .5, 1, and 3 ev respectively. For these values the relationship  $\exp(-Q/kT) < \omega/\nu$  holds true. If the length of coherent dislocation line had been picked from Mott's theory, the

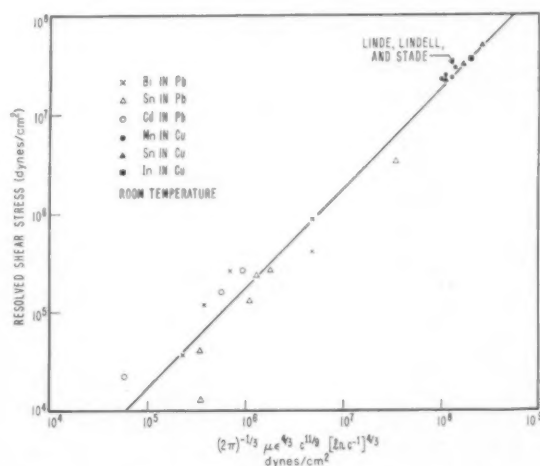


FIG. 12. Resolved shear stress at break in decrement-strain amplitude curves vs values calculated from formula  $\sigma = (2\pi)^{-1/3} \mu \epsilon^{4/3} c^{11/9} [2\lambda c^{-1}]^{4/3}$ . The full circles, triangles, and square in upper right-hand corner are taken from the paper of Linde, Lindell, and Stade on change in critical shear stress of copper single crystals with different alloying compositions.

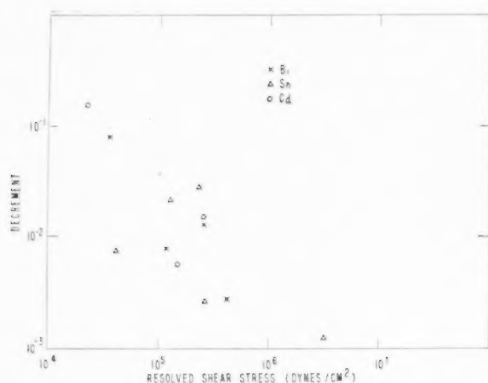


FIG. 13. Decrement vs resolved shear stress at break for various specimens. Decrement measured at 200°C and resolved shear stress at room temperature.

value of  $Q$  for Bi would have been too low and it would have been impossible to account for the break in the lead-bismuth specimens.

The strain amplitude independence of the internal friction in the low-amplitude region can also be explained using Mott and Nabarro's and Nowick's theories. As mentioned before at stresses smaller than  $\sigma_M$  some of the dislocations can move a distance of the order of  $\lambda$ . The length able to move when the stress is increased from  $\sigma$  to  $\sigma + d\sigma$  will be equal to  $A \exp(-\sigma^2/\sigma_M^2) d\sigma$  where  $A$  is a constant.  $A$  can be evaluated from the fact that

$$\int_0^{\sigma_M} A e^{-\sigma^2/\sigma_M^2} d\sigma = \frac{\sqrt{\pi}}{2} A \sigma_M \approx N,$$

where  $N$  is the total length of dislocation line in the crystal.

The energy dissipated per cycle for stresses smaller than  $\sigma_M$  will be given by

$$\text{Energy lost} = \lambda b \int_0^{\sigma_M} \sigma A e^{-\sigma^2/\sigma_M^2} d\sigma \approx \frac{2}{\sqrt{\pi}} N \lambda b \left( \frac{\sigma^2}{\sigma_M} \right).$$

Since the total energy stored in a unit cube is equal to  $\sigma^2/2\mu$ , the decrement will be given by

$$\text{Decrement} = \frac{2}{\sqrt{\pi}} N \lambda b \mu / \sigma_M,$$

as long as  $\sigma < \sigma_M$ .

At temperatures higher than 100°C there is a trend for specimens having the lowest stress at the break in the internal friction curves to have the highest decrement. Figure 13 shows a plot of the decrement at 200°C as a function of the resolved shear stress at the break. (The room temperature value of the stress at the break was used rather than that at 200°C owing to the difficulty of measuring this stress for the specimens containing the smallest amounts of impurity atoms.) An

inspection of the data in Table I show that this relationship is no longer valid at room temperature where all the specimens have about the same value of the decrement. It may be that at room temperature background losses such as losses in the cement joint are great enough to mask the true internal friction of the material; however, this appears unlikely. Also in qualitative agreement with Eq. (3) is the fact that as the stress at the break decreases with temperature the internal friction increases. The rate of change of the lowering of the shear stress at the break with increasing temperature is too great to account for by any simple theory since it appears to decrease exponentially. Theoretical expressions such as that due to Becker<sup>22</sup> on the variation of yield stress with temperature show a decrease of the stress with some power of the temperature. If the impurity atoms were fixed in the lattice and did not move about a dependence of this last type should hold true. However, impurity atoms can move about at greater speeds than the moving dislocation at high temperatures. This movement should lead to a more rapid decrease in the stress at the break than if the impurity atoms were fixed in the lattice.

Besides the hysteresis losses due to dislocations moving back and forth over potential hills there will also be a loss proportional to the frequency from dislocations that oscillate back and forth in potential wells without ever leaving them. The energy loss from these dislocations can be calculated from their equation of motion, which can be written as

$$B\ddot{x} + (\sigma_M b / \lambda)x = \sigma b \sin(2\pi\omega t),$$

where  $B$  is a dissipative force constant,  $(\sigma_M b / \lambda)x$  the approximate restoring force when the dislocation is displaced a distance  $x$  from its equilibrium position, and  $\sigma b \sin(2\pi\omega t)$  is the applied force per unit length on the dislocation. If  $M$  is the total length of dislocation contributing to the energy loss due to this process, then the decrement in the kilocycle range of frequency would be given by

$$\text{Decrement} = M \mu B 2\pi\omega \lambda^2 / \sigma_M^2, \quad (4)$$

if hysteresis losses were zero. Since  $\lambda 2\pi B \omega / b \sigma_M$  is always much less than 1 in the kilocycle range of frequency for typical values of  $\lambda$ ,  $\sigma_M$ , and for a value of  $B = 5 \times 10^{-5}$  dynes/sec,<sup>25,26,27</sup> the energy loss due to hysteresis will be much greater than that portion of the loss which is frequency dependent. Nowick's picture is thus better able to account for the energy loss in the kilocycle range of frequency than a modified Koehler approach to the problem of internal friction of single crystals of dilute alloys of lead. The frequency dependence has still to be checked to confirm this and it is hoped that work being carried out by E. W. Kammer and S. D. Hart of this laboratory will clarify this point.

The number of dislocations in a lead crystal can be estimated with the use of Eq. (3). For a value of the decrement equal to  $10^{-2}$ , of  $\lambda$  equal to  $10b$  and  $\sigma_M$  equal

to  $10^5$  dynes/cm<sup>2</sup>, the value of  $N$  is approximately  $2 \times 10^6$ . This value, although low, is not out of line with estimates of the length of dislocation lines in an annealed metal.

### CONCLUSION

The internal friction of dilute alloys of lead is independent of strain amplitude up to a critical stress at which point it starts to rise. The value of this stress can be decreased by increasing the temperature and increased by increasing the impurity content. At room temperature the magnitude of stress at the break is approximately equal to  $.15 \mu\epsilon$ . This dependence on  $\mu$ ,  $\epsilon$ , and  $c$  can best be explained in terms of the theories of Nabarro and of Mott.

### ACKNOWLEDGMENTS

We wish to thank Mr. D. Walter for making the carbon analysis, Messrs. M. Cavanagh, S. Cress, and O. Gates for the chemical and spectrographical analysis, Mr. W. Sadler for taking the Laue patterns, and Mr. J. Pasternak for growing some of the lead crystals.

### Note Added in Proof

S. Takahashi and H. Konno (private communication) have also observed breaks in internal friction-strain amplitude curves. They observed breaks in polycrystalline samples of dilute alloys of copper (Cu-Al, Cu-P, Cu-Zn). Their experimental points, covering a stress range of  $10^5$ – $10^8$  dynes/cm<sup>2</sup>, follow reasonably well the Nabarro-Mott theory.

It should also be pointed out that impurity effects similar to those found in the present work have been observed in irradiated NaCl. (D. R. Frankl and T. A. Read, Phys. Rev. **89**, 663 (1953), D. R. Frankl, Phys. Rev. **92**, 573 (1953).

C. Tysalk and G. V. Raynor (Acta Cryst. **7**, 505 (1954) have recently made lattice constant measurements on a series of lead rich alloys. Their measurement

of  $\epsilon_{Bi}$  is about the same as that of Hofe and Hanemann. Their results for  $\epsilon_{Sn}$  ( $-0.028$ ) and  $\epsilon_{Cd}$  ( $-0.045$ ) are different from those quoted in this paper. The measurements of Jenkel and Mader on Pb-Cd, however, were over a much wider range of composition than were those of Tysalk and Raynor. If the new lattice parameter data are used the bismuth and tin points in Fig. 12 are brought closer together; on the other hand the fit becomes worse for the cadmium points.

### REFERENCES

1. T. A. Read, Trans. A.I.M.E. **143**, 30 (1941).
2. C. Zener, *Elasticity and Anelasticity of Metals* (Chicago, University of Chicago, 1948).
3. A. S. Nowick, Progress in Metal Physics **4** (1953).
4. J. Marx and J. S. Koehler, Pittsburgh Conference on the Plastic Deformation of Cryst. Solids (1950), p. 171.
5. G. Bradfield and H. Pursey, Phil. Mag. **44**, 437 (1953).
6. J. Marx, Rev. Sci. Instrum. **22**, 503 (1951).
7. P. M. Sutton, Phys. Rev. **91**, 816 (1953).
8. S. Takahashi, J. Appl. Phys. **23**, 866 (1952).
9. W. R. Thomas and W. C. Winegard, Canadian Metals **15**, 26 (1952).
10. J. S. Koehler, Imperfections in Nearly Perfect Crystals (New York, John Wiley, 1952), p. 197.
11. A. S. Nowick, Phys. Rev. **80**, 249 (1950).
12. A. H. Cottrell, Dislocations and Plastic Flow in Crystals (Oxford, Clarendon Press, 1953).
13. H. Hofe and H. Hanemann, Z. Metallkunde **32**, 112 (1940).
14. W. C. Phebus and F. C. Blake, Phys. Rev. **25**, 107 (1925).
15. E. Jenkel and H. Mader, Metallwirtschaft Technik **16**, 499 (1937).
16. F. R. N. Nabarro, Proc. Phys. Soc. **58**, 669 (1946).
17. N. F. Mott and F. R. N. Nabarro, Report of a Conference on the Strength of Solids (London, Physical Society, 1948), p. 1.
18. N. F. Mott, Imperfections in Nearly Perfect Crystals (New York, John Wiley, 1952), p. 173.
19. J. O. Linde, B. Lindell, and C. H. Stade, Arkiv f. Fysik **2**, 89 (1950).
20. E. N. Da C. Andrade, Phil. Mag. **43**, 1218 (1952).
21. J. E. Dorn, P. Pietrowsky, and T. E. Tietz, Trans. A.I.M.E. **188**, 933 (1950).
22. R. Becker, Z. Physik **26**, 919 (1925).
23. P. W. Neurath and J. S. Koehler, J. Appl. Phys. **22**, 621 (1951).
24. G. Sachs and J. Weerts, Z. Physik **62**, 473 (1930).
25. J. D. Eshelby, Proc. Roy. Soc. **197A**, 396 (1949).
26. G. Leibfried, Z. Physik **127**, 344 (1950).
27. F. R. N. Nabarro, Proc. Roy. Soc. **209A**, 278 (1951).



## X-RAY MEASUREMENTS ON SILVER FILINGS\*

F. R. L. SCHOENING and J. N. VAN NIEKERK†

A Geiger counter spectrometer, with crystal-reflected  $\text{CuK}\alpha$  radiation, is used to determine the shapes and breadths of the X-ray diffraction profiles of filings from high purity (99.999 per cent) and electrolytic (99.6 per cent) silver. Because the filings recover rapidly at room temperature, the observations are made on specimens kept at  $-30^\circ\text{C}$ .

From the Fourier coefficients and breadths of the diffraction profiles, particle size and strain values are calculated. Normal strain values are found and particle size values of the order of 200 Å are obtained. No experimental evidence is found for the presence of stacking faults in plastically deformed silver.

Curves illustrating the rate of recovery (increase in intensity with time of a profile maximum) of two specimens filed under different conditions are given.

### UNE ÉTUDE DE LIMAILLES D'ARGENT, AUX RAYONS X

Les formes et largeurs des profils de diffraction des rayons X, donnés par des limailles d'argent de haute pureté (99.999 pour cent) et d'argent électrolytique (99.6 pour cent), ont été déterminées aux moyen d'un spectromètre à compteur de Geiger, en utilisant la radiation  $\text{CuK}\alpha$  réfléchi par un cristal. Étant donné que ces limailles subissent une restauration rapide à la température ambiante, les observations ont été faites sur des échantillons maintenus à  $-30^\circ\text{C}$ .

Les dimensions des particules et les valeurs de la déformation furent calculées à partir des coefficients de Fourier et de la largeur des profils de diffraction. Les valeurs trouvées de la déformation sont normales, les dimensions des particules sont de l'ordre de 200 Å. On n'a pas trouvé de preuve expérimentale de l'existence de défauts d'empilage dans de l'argent déformé plastiquement.

On présente des courbes de vitesse de restauration (accroissement de l'intensité d'un maximum de profil en fonction du temps) pour deux échantillons limés dans des conditions différentes.

### RÖNTGENOGRAPHISCHE MESSUNGEN AN SILBERFEILSPÄNEN

Die Form und Breite der Röntgenbeugungslinien von Feilspänen von Reinstsilber (99.999 Prozent) und Elektrolytsilber (99.6 Prozent) wurde mit Hilfe eines Zählrohrspektrographen und mit am Kristall reflektierten Kupfer  $\text{K}\alpha$  Strahlung gemessen. Da sich die Feilspäne bei Zimmertemperatur schnell erholen, wurden die Messungen an Proben, die eine Temperatur von  $-30^\circ\text{C}$  hatten, ausgeführt.

Die Teilchengröße und die inneren Spannungen wurden aus den Fourierkoeffizienten und aus den Linienbreiten berechnet. Es ergaben sich normale Spannungswerte und Teilchengrößen von etwa 200 Å. Das Vorhandensein von Stapelfehlern in plastisch verformtem Silber liess sich experimentell nicht nachweisen.

Es werden für zwei unter verschiedenen Bedingungen gefeilten Proben Kurven angegeben, die die Erholungsgeschwindigkeit, d.h. die Intensitätszunahme am Linienmaximum als Funktion der Zeit, angeben.

## 1. INTRODUCTION

The influence of plastic deformation on the diffraction profiles of metals has been studied extensively during recent years. Although it is generally agreed today that the broadening of the diffraction lines, which is observed when metals are cold-worked, is due to the combined effects of lattice strains and small particles, attempts to separate strain broadening from particle size broadening are still in their beginning stages. By making use of the Fourier coefficients derived from the experimentally determined diffraction line profiles, Warren and Averbach<sup>1,2</sup> have developed a method whereby strain broadening can be separated from particle size-stacking fault broadening. During the present investigation this method has been applied to the X-ray diffraction profiles obtained with silver filings.

Preliminary investigations had shown that for freshly prepared silver filings the peak intensities of the diffraction profiles, when measured at room temperature, increased continuously with time while the line breadths decreased. In order to prevent such recovery of

the specimens it was necessary, in certain cases, to make measurements from specimens kept at approximately  $-30^\circ\text{C}$ . At such temperatures recovery of the specimen was found to be negligibly small. Throughout this investigation the term recovery is used in a restricted sense and merely implies the increase in intensity with time of a profile maximum.

## 2. EXPERIMENTAL PROCEDURE

A Philips High Angle Goniometer, with monochromatic  $\text{CuK}\alpha$  radiation obtained by reflection from a curved quartz crystal, was used to measure the diffraction profiles of filings obtained from high purity (99.999 per cent) and from electrolytic (99.6 per cent) silver. The high-purity silver rods were filed mechanically under liquid oxygen and also at room temperature ( $25-28^\circ\text{C}$ ). In the latter case the filings were allowed to drop into liquid oxygen. When preparing X-ray specimens the filings were removed from the liquid oxygen, washed in alcohol, dried and sieved through a 325-mesh per inch sieve. They were then hand packed into specimen carriers. The time that elapsed between removing the filings from liquid oxygen and starting measurements

\* Received April 1, 1954; in revised form July 26, 1954.

† National Physical Laboratory, Pretoria, South Africa.

was kept at exactly one hour for all specimens. During this period the filings were exposed to room temperature and partial recovery must have taken place. While making profile measurements the filings were kept at a temperature of approximately  $-30^{\circ}\text{C}$  by blowing a controlled stream of cold, dry air onto the samples.

After all the profiles had been recorded the cold air stream was shut off and the counting rate at the maximum of the 200 reflection was measured at five-minute intervals. For these measurements the width of the Geiger counter receiving slit was increased slightly to allow for a possible shift in the peak position. The filings were left exposed to room temperature and after 8 and 33 days the line profiles were again measured, this time without cooling the specimens. The filings were then annealed for 5 hours at  $500^{\circ}\text{C}$  and these specimens were used to determine the sharp profiles.

In the case of electrolytic silver the filing was done only at room temperature and profile measurements were made on specimens kept at room temperature. The filings were then annealed and it was found that the line profiles given by such filings were identical with the profiles obtained from annealed high-purity filings.

Although all the  $hkl$  spectra obtainable with  $\text{CuK}\alpha$  radiation were measured at times, on account of the anisotropy of silver only the 111, 222, 200 and 400 reflections were investigated systematically. Profiles of the diffraction lines were obtained by measuring the counting rate at various points along the lines and plotting the results. Intervals between the points measured ranged from 0.025 to 0.5 degrees in  $2\theta$ , depending on whether the measurements were taken near the maximum or near the foot of a diffraction peak. The number of counts recorded ranged from 1600 at the base, to 25 600 at the peak maximum.

Integral line breadths of the diffraction profiles were determined by planimetry the area between a profile and its background level and dividing this by the height of the profile.

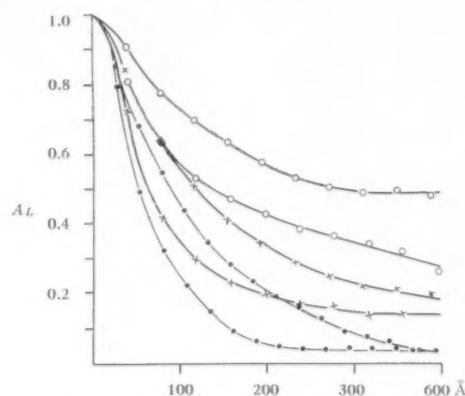


FIG. 1. Fourier coefficients of the 111 (upper) and 200 (corresponding lower) profiles plotted against distance.  $\circ$ : Electrolytic silver filed at room temperature.  $\times$ : High-purity silver filed in liquid oxygen and measured at  $-30^{\circ}\text{C}$  after one hour annealing at room temperature.  $\bullet$ : High-purity silver filed at room temperature and measured at  $-30^{\circ}\text{C}$  after one hour annealing at room temperature.

### 3. FOURIER ANALYSIS OF LINE SHAPES

The diffraction profiles were corrected for instrumental broadening according to Stokes<sup>3</sup> and Fourier coefficients were evaluated using Lipson and Beevers strips. In Fig. 1 the results obtained for some of the profiles are shown.

Warren and Averbach<sup>4</sup> have shown that for 70:30  $\alpha$ -brass, a definite distribution exists when the Fourier coefficients of the various  $hkl$  reflections are plotted against distance. They have interpreted this regular distribution as being due to stress isotropy. Because corresponding plots for electrolytic silver do not reveal a similar regularity it is inferred that stress isotropy is absent in silver. Following essentially Warren and Averbach's<sup>1,2</sup> method of separating strain broadening from particle size broadening, values as tabulated in Table I were obtained. The strain values are only very approximate, because the scattering of the points on the rms strain versus distance plots did not permit the construction of unique curves through these points.

TABLE I.

Specimen	Fourier analysis of line shapes				Analysis of line breadths			
	Particle size $\text{\AA}$		rms strain %*		Particle size $\text{\AA}$		rms strain %†	
	[111]	[100]	[111]	[100]	[111]	[100]	[111]	[100]
High purity Ag filed at $-183^{\circ}\text{C}$ and measured after:								
1 hour at room temperature	280	140	0.25	0.15	490	330	0.08	0.13
8 days at room temperature					1470	820	0.03	0.03
33 days at room temperature					1560	820	0.004	0.002
High purity Ag filed at room temperature and measured after:								
1 hour at room temperature	200	130	0.40	0.50				
Electrolytic Ag filed at room temperature and measured at room temperature	560	240	0.25	0.40				

\* Defined by  $\langle(\epsilon_L^2)\rangle^{\frac{1}{2}}$  as  $L \rightarrow 0$ .

† Defined by  $0.2\theta \cot\theta$ .

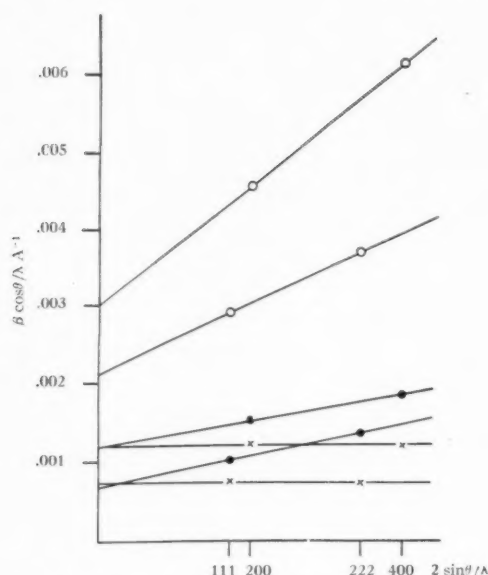


FIG. 2. Plots of  $\beta \cos \theta / \lambda$  versus  $2 \sin \theta / \lambda$  for the 111, 222, 200 and 400 reflections of high-purity silver filed in liquid oxygen.  $\circ$ : Measured at  $-30^\circ\text{C}$  after one hour annealing at room temperature.  $\bullet$ : Measured at room temperature after 8 days annealing at room temperature.  $\times$ : Measured at room temperature after 33 days annealing at room temperature.

Because the Fourier method does not separate the effects of particle size (fragmentation) from stacking faults, observations on the angular shift of the diffraction lines were made to decide between these two possibilities. For face-centered cubic crystals, gliding on the  $\{111\}$  planes, Paterson<sup>5</sup> has calculated both the direction and the amount of shift that will result for each diffraction line when stacking faults occur. Although very small angular shifts were detected during the present investigations, they did not follow the pattern predicted by Paterson.

#### 4. ANALYSIS OF LINE BREADTHS

The profiles obtained from high purity silver filings after they were left to recover at room temperature for 8 and 33 days, were too sharp to permit the evaluation of reliable Fourier coefficients. However, to obtain a qualitative picture of the happenings during recovery it was decided to apply Hall's<sup>6</sup> additive method to the observed line profiles. For this purpose the observed breadths were corrected for instrumental influence following the method described by Schoening, van Niekerk and Haul.<sup>7</sup> Using the corrected breadths plots as shown in Fig. 2 were obtained. From these particle size and strain values as tabulated in Table I were calculated.

It may be mentioned that in none of the plots obtained for the entire  $hkl$  spectrum was it possible to draw continuous curves through the points. This affords further evidence as to the anisotropy of silver.

#### 5. DISCUSSION

Referring to the results tabulated in Table I it should be stressed that the strain values are only approximate and that too much importance should not be attached to the difference in the values obtained by the two methods. Corresponding values of particle size differ on the average by a factor of two. These differences can, however, be accounted for. Williamson and Hall<sup>8</sup> have shown that the simplifying assumptions on which their method is based will lead to particle size values which are too large by a factor between 1 and  $\pi$ .

In Fig. 3 the counting rates at the maximum of the 200 diffraction peak, for two high-purity silver specimens, are shown. From these curves it is evident that after one hour's recovery at room temperature (the time required for specimen preparation) the recovery rate of the filings prepared under liquid oxygen is much higher than that of filings prepared at room temperature. Assuming that the rate of recovery did not change appreciably during the first hour, it follows that, because of its much slower recovery rate, the sample filed at room temperature will be closer to the state that prevailed immediately after filing than will be the sample prepared under liquid oxygen. The higher strain values that were obtained for the sample filed at room temperature (see Table I) are therefore not surprising.

The greater rate of recovery of the filings prepared under liquid oxygen, in spite of their lower residual strains, may be explained as follows: either the rate of recovery is not determined by the magnitude of the strains measured in the manner described in section 3, or different processes are active in the two samples. It is possible, for example, that recrystallization may already have started in the sample filed under liquid oxygen, while in the sample filed at room temperature only a slow release of the stresses, accompanied perhaps by crystal growth, may have taken place. This is a plausible explanation if, as seems very likely, it is assumed that filing at  $-183^\circ\text{C}$  will bring about more deformation than will filing at room temperature.

The particle sizes are smaller than those obtained by

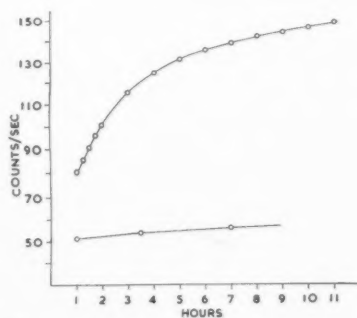


FIG. 3. Counting rate at the 200 reflection maximum plotted against time of annealing at room temperature. Points are taken from measurements made at 5 minute intervals. Upper curve is for high purity silver filed under liquid oxygen. Lower curve is for high purity silver filed at room temperature.

Wood<sup>9</sup> for silver (800 Å), nickel (1200 Å) and iron (3200 Å) and by Williamson and Hall<sup>8</sup> for aluminium (4000 Å). They can, however, be compared with values obtained by Warren and Warekois<sup>10</sup> for  $\alpha$ -brass (180 Å along [111], 80 Å along [100]) and by McKeehan and Warren<sup>11</sup> for thoriated tungsten (200 Å). For  $\alpha$ -brass the systematic shift observed in the positions of the diffraction peaks was explained as being due to stacking faults in the lattice which constitute the boundaries between these "particles." A systematic shift of this nature was not observed in silver and it is therefore concluded that, contrary to  $\alpha$ -brass, stacking faults do not contribute appreciably to the particle size broadening.

A qualitative picture of the happenings during the later stages of recovery is afforded by the results obtained from the analysis of line breadths shown in Table I. It appears that the particles grow to a certain value then remaining nearly constant, while stresses are released until the lattice strains finally approach zero. Although these latter results were obtained by using a comparatively inaccurate method, it must nevertheless be stressed that the results do not depend strongly on the type of profile assumed, but rather on the observa-

tion that the breadths of the high-angle reflections decrease more rapidly than those of the low angle reflections. Figure 2 illustrates this point.

For electrolytic silver bigger particle size values and lower strain values were found than for the high purity sample filed at room temperature.

This paper is published by permission of the South African Council for Scientific and Industrial Research.

#### REFERENCES

1. B. E. Warren and B. L. Averbach, *J. Appl. Phys.* **21**, 595 (1950).
2. B. E. Warren and B. L. Averbach, *J. Appl. Phys.* **23**, 497 (1952).
3. A. R. Stokes, *Proc. Phys. Soc.* **61**, 382 (1948).
4. B. E. Warren and B. L. Averbach, *Symposium on the Plastic Deformation of Crystalline Solids* (Pittsburgh, Mellon Institute, 1950), 113.
5. M. S. Paterson, *J. Appl. Phys.* **23**, 805 (1952).
6. W. H. Hall, *Proc. Phys. Soc.* **A62**, 741 (1949).
7. F. R. L. Schoening, J. N. van Niekerk, and R. A. W. Haul, *Proc. Phys. Soc.* **B65**, 528 (1952).
8. G. K. Williamson and W. H. Hall, *Acta Met.* **1**, 22 (1953).
9. W. A. Wood, *Proc. Roy. Soc.* **A172**, 231 (1939).
10. B. E. Warren and E. P. Warekois, *J. Appl. Phys.* **24**, 951 (1953).
11. M. McKeehan and B. E. Warren, *J. Appl. Phys.* **24**, 52 (1953).



## METALLIC TERNARY PHASES IN THE Mn-Ta-O SYSTEM\*

NILS SCHÖNBERG†

Mn-Ta-O samples have been prepared in different ways and have been examined by x-ray methods.

Two ternary phases have been found to exist, i.e., the metallic  $Mn_3Ta_3O$  phase of the  $\eta$ -carbide structure and the  $Mn_2TaO_3$  phase of a structure closely related to that of CoSn (B35 type). The abnormally great interatomic metal-metal and metal-oxygen distances indicate weak metallic as well as nonmetallic (ionic) properties for the latter phase.

The configurations of the ternary phases in the Mn-Ta-X systems, where X is any of the nonmetals C, N and O, have been discussed.

### LES PHASES MÉTALLIQUES, TERNAIRES, DANS LE SYSTÈME Mn-Ta-O

Des échantillons de Mn-Ta-O furent préparés par différentes méthodes et ensuite examinés aux rayons X.

On y a constaté l'existence de deux phases ternaires, à savoir, la phase métallique  $Mn_3Ta_3O$  ayant la structure du carbure- $\eta$  et la phase  $Mn_2TaO_3$ , dont la structure se rapproche de celle de CoSn (type B35). Dans ce dernier cas les distances interatomiques métal-métal et métal-oxygène, anormalement grandes, indiquent que la phase en question a des propriétés métalliques, ainsi que non-métalliques (ioniques) faiblement caractérisées.

On a discuté les configurations des phases ternaires dans les systèmes Mn-Ta-X, où X représente les éléments non-métalliques C, N et O.

### TERNÄRE METALLISCHE PHASEN IM SYSTEM Mn-Ta-O

Mn-Ta-O proben wurden auf verschiedene Art und Weise hergestellt und röntgenographisch untersucht.

Es wurde die Existenz von zwei ternären Phasen gefunden, und zwar die metallische  $Mn_3Ta_3O$ -Phase mit einer Karbidstruktur und die  $Mn_2TaO_3$  Phase mit einer dem CoSn (B35 Typ) nahe verwandten Struktur. In dieser Phase deuten die anormal grossen Metall-Metall und Metall-Sauerstoff Bindungen auf schwache metallische wie auch auf nicht-metallische (ionische) Eigenschaften.

Die Konfigurationen der ternären Phasen in Mn-Ta-X Systemen—wobei X eines der Nichtmetalle C, N, oder O ist—werden diskutiert.

## INTRODUCTION

A systematic investigation of  $Me'-Me''-O$  systems undertaken by the present author, where  $Me'$  and  $Me''$  are transition metals with  $Me'=Ti-Cu$  and  $Me''=Ti, Zr, Nb, Ta, Mo, W, \text{ and } Re$ , has revealed the existence of several metallic ternary oxide phases. The majority of these oxides are of the  $\eta$ -carbide structure<sup>1,2</sup> with the general formula  $Me'_3Me''_3O$ .<sup>3,4</sup> Some oxides with the metal atoms in a hexagonal close-packed arrangement ( $L'3$  type) and with the general formula  $Me'Me''O$  have also been prepared.<sup>4</sup>

Two metallic oxides exist in the binary Ta-O system ( $\beta$ - and  $\gamma$ -phases).<sup>5</sup> The  $\beta$ -phase has a metal atom arrangement obtained by an orthorhombic deformation of the body-centered tantalum lattice. The phase can dissolve oxygen up to an oxygen content corresponding to the formula  $Ta_4O$ . The  $\gamma$ -phase has the probable composition  $TaO$  and is of the B1 type.

The oxide phase with the lowest oxygen content in the Mn-O system is  $MnO$  of the B1 type. The properties of this oxide indicate that it can hardly be characterized as a metallic compound.

## EXPERIMENTAL

The starting materials used for the preparations were tantalum metal powder (Fansteel) or degassed tantalum

hydride (Metal Hydrides Inc.), manganese metal (Ferrolegeringar, Stockholm, 99.9 per cent) and manganese dioxide (Baker's analyzed). The samples were prepared in three ways:

1. The powdered metals and  $MnO_2$  were carefully mixed in different proportions, moulded into brickettes, and heated in zirconia crucibles in a high frequency vacuum induction furnace at various temperatures between 1400°C and 1800°C.
2. The same mixture of metals and oxide as above was heated in evacuated and sealed silica tubes at 1000°C for periods varying between one hour and two weeks.
3. Binary Mn-Ta alloys were prepared in a vacuum furnace starting from the powdered metals. The powdered alloys were then oxidized by means of steam in the presence of hydrogen in great excess at a temperature of about 700°C.

The best results were obtained with methods 1 and 2, although the heating of the samples in silica tubes (2) often caused reactions with the inner walls of the tube. The samples from method 3 were often heterogeneous.

The phase analysis and structure determinations were made from powder photographs taken with Cr- $K\alpha$  and Cu- $K\alpha$  radiation in a camera of the Guinier type. For measurements of the high-angle reflections, additional photographs were taken with focussing cameras of the Hägg-Phragmén type.

\* Received April 9, 1954.

† Institute of Chemistry, University of Uppsala, Uppsala, Sweden.





TABLE II. Interatomic distances in the  $Mn_2TaO_3$  phase.

Atom	Surrounding atoms	Interatomic distance, Å
Mn	3 Mn	3.07
	2 Mn	3.58
	6 Ta	3.56
	6 O	2.36
Ta	2 Ta	3.58
	12 Mn	3.56
	6 O	2.66
O	4 Mn	2.36
	2 Ta	2.66
	4 O	2.66

metallic bonds. In the case of ionic bonds the corresponding distances are calculated to be 2.23 Å and 2.16 Å, if the radius values of the  $Mn^{2+}$ ,  $Ta^{2+}$  \* and  $O^{2-}$  ions are presumed to be 0.91 Å, 0.84 Å and 1.32 Å respectively. It is evident from Table II that the actual metal-oxygen distances are considerably greater than those calculated both for metallic bonds and ionic bonds and have values intermediate between the latter ones and the radius sums: metal atom + oxygen ion. In all probability some of the *s*- and *d*-electrons in the outer shells of the metals have been displaced towards the oxygen atoms but not to such an extent that it is correct to designate the bonding as ionic. There are still electrons left for the formation of metallic bonds, although these bonds will be weak.

The  $Mn_2TaO_3$  phase exists as an intermediate oxide in the  $MnO$ - $TaO$  interval in the  $Mn$ - $Ta$ - $O$  system. The  $TaO$  phase can by analogy with the corresponding oxides of the NaCl structure among the group IV and V elements be characterized as having metallic properties. On the other hand  $MnO$  for several reasons cannot be specified to be a metallic oxide. With regard to bond type  $Mn_2TaO_3$  is intermediate between the metallic  $TaO$  phase (probably with a defective lattice) and the nonmetallic  $MnO$  phase, both binary oxides of the *B1* type and with the same lattice constants = 4.43 Å.<sup>5,12</sup>

The mean  $Ta$ - $O$  distances in  $Mn_3Ta_3O$ ,  $Ta_4O$ ,  $TaO$ ,  $Mn_2TaO_3$  and  $TaO_2$  are 2.08, 2.19, 2.22, 2.66 and 2.02 Å respectively.

A corresponding electron displacement from the transition metal towards oxygen—as in the  $Mn_2TaO_3$  phase—exists obviously in the metallic oxides  $Cr_3O$ ,<sup>13</sup>  $Mo_3O$ ,<sup>4</sup> and  $W_3O$ ,<sup>14</sup> as the interatomic metal-oxygen distances can be derived from the radius sums: metal atom + oxygen ion. Because of the low oxygen content this displacement is at most 2/3 electrons per metal atom. The remaining "free" electrons in the outer *s*- and *d*-shells form metal-metal bonds of such a nature that the intermetallic distances are almost the same as in the pure metals.

Attempts were also made to replace  $Ta$  in  $Mn_2TaO_3$  with  $Nb$ , but no analogous compound seems to exist in

\* The radius value of the  $Ta^{2+}$  ion has been derived from that of the  $Ta^{4+}$  ion ( $=0.71$  Å)<sup>5</sup> using the expression given by Pauling,<sup>11</sup>  $r_z = (nB/AZ^2)^{1/(n-1)}$ , for the calculation of the radius  $r_z$  of an ion of valency *Z*. The Born exponent is taken to be  $n \sim 9$ .

the  $Mn$ - $Nb$ - $O$  system. The only phases thereby obtained were  $Mn_2Nb$  (*C14* type),  $NbO$  and  $NbO_2$ .

A study of the  $Me'$ - $Ta$ - $O$  systems, where  $Me' = Ti$ ,  $Cr$ ,  $Fe$ ,  $Co$ , and  $Ni$ , showed that no ternary phases seem to exist for  $Me' = Ti$ ,  $V$  and  $Cr$ . For  $Me' = Fe$ ,  $Co$  and  $Ni$ , on the other hand, ternary phases were obtained, most likely having metallic character. According to the distribution of the diffraction lines they have rather complicated structures, and it was not possible to obtain them in pure states.  $Fe$  further forms the  $Fe_3Ta_3O$  compound of the  $\eta$ -carbide structure, which is not the case for  $Me' = Co$  and  $Ni$ .

#### TERNARY METALLIC $Mn$ - $Ta$ - $X$ PHASES WITH $X = C, N$ , AND $O$

It may be of interest to compare the  $Mn$ - $Ta$ - $X$  systems, where  $X$  is any of the nonmetals  $C$ ,  $N$  and  $O$ .

No homogeneous ternary  $Mn$ - $Ta$ - $C$  phase seems to exist. In a recently published paper about the formation of  $\eta$ -carbides Kuo<sup>15</sup> argued that the inability of  $Ta$  to form phases of this type with the metals of the first period of transition metals ( $Ti$ - $Cu$ ) is due to the fact that the only metal in this period suitable for such a formation must have properties intermediate between those of  $Cr$  and  $Mn$ . Thus no double-carbides  $Cr_3Ta_3C$  or  $Mn_3Ta_3C$  exist according to Kuo but triple carbides  $(Me'(1), Me'(2))_3Ta_3C$  in the combinations  $Me'(1) = Cr$ ,  $Me'(2) = Fe$ ,  $Co$ ,  $Ni$ ,  $Cu$ , and  $Me'(1) = V$ ,  $Me'(2) = Fe$ ,  $Co$ ,  $Ni$ .

Two ternary  $Mn$ - $Ta$ - $N$  phases have been prepared,<sup>16</sup> i.e.,  $MnTaN_z$  with unknown structure and  $Mn_3Ta_3N_4$  of a partially ordered "anti-TiP" structure. In the latter compound the  $N$ -atoms have octahedral surroundings of metal atoms.

The  $O$ -atoms in  $Mn_3Ta_3O$  are situated at the centers of slightly deformed  $Ta$  atom octahedra. The configuration and the nature of the  $Mn_2TaO_3$  phase have been discussed above.

#### ACKNOWLEDGMENTS

The author wishes to express his gratitude to Professor G. Hägg for his never-failing interest. A grant from Statens Tekniska Forskningsråd is gratefully acknowledged.

#### REFERENCES

1. A. Westgren and G. Phragmén, *Trans. Amer. Soc. Steel Treating* **13**, 539 (1928).
2. A. Westgren, *Jernkontorets Ann.* **117**, 1 (1933).
3. N. Karlsson, *Nature* **168**, 558 (1951).
4. N. Schönberg, *Acta Chem. Scand.* (1954). In press.
5. N. Schönberg, *Ibid* **8**, 240 (1954).
6. H. J. Wallbaum, *Arch. Eisenhütt.* **14**, 521 (1941).
7. H. J. Wallbaum, *Z. Krist.* **103**, 391 (1941).
8. N. Schönberg, *Acta. Chem. Scand.* **8**, 199 (1954).
9. G. Brauer and K. H. Zapp, *Naturwiss.* **23**, 604 (1953).
10. *Strukturbericht*, Band VI, Leipzig, 1941, p. 4.
11. L. Pauling, *The Nature of the Chemical Bond*, London, 1948, Chaps. X and XI.
12. G. R. Levi, *Rend. R. Istit. Lomb. di Sc. e. Lett.* **57**, 619 (1924).
13. N. Schönberg, *Acta Chem. Scand.* **8**, 221 (1954).
14. G. Hägg and N. Schönberg, *Acta Cryst.* **7**, 351 (1954).
15. K. Kuo, *Acta Met.* **1**, 301 (1953).
16. N. Schönberg, *Acta Chem. Scand.* **8**, 213 (1954).

## THE SEGREGATION OF IMPURITIES TO GRAIN BOUNDARIES\*

W. R. THOMAS† and B. CHALMERS‡

It has been experimentally shown that polonium segregates to grain boundaries in an alloy of lead and 5 per cent bismuth in which the polonium was present to the extent of one part in  $10^{10}$ . The results show that the amount of polonium contained in the boundary is a function of the orientation of the crystals adjacent to the boundary and of the temperature at which equilibrium is attained. The boundaries were produced by symmetrical rotations of seed crystals about the [001] direction so that the boundaries consisted mainly of edge type dislocations.

The number of polonium atoms is calculated for boundaries with  $\theta$  up to 15 degrees to be one atom of polonium in every  $2 \times 10^8$  dislocation sites; a dislocation site is the intersection of a dislocation and an atomic plane. The number increases to about four times this value for boundaries with an orientation difference of 25 degrees.

The concentration of polonium in the boundaries decreased rapidly with annealing temperature; only the high-angle boundary segregate persists at the higher annealing temperatures.

### LA SÉGRÉGATION D'IMPURETÉS DANS LES JOINTS INTERCRISTALLINS

On a montré expérimentalement qu'il y a ségrégation de polonium dans les joints inter cristallins, dans un alliage de plomb avec 5 pour cent de bismuth, contenant une part dans  $10^{10}$  de polonium. Les résultats permettent de constater que la quantité de polonium contenue dans un joint est une fonction de l'orientation des cristaux adjacents au joint et de la température à laquelle l'équilibre est atteint. Les joints furent produits au moyen de rotations symétriques de cristaux-germes autour de la direction [001], ce qui donne des joints consistants principalement en dislocations-coin. Pour des joints à angle  $\theta$  jusqu'à  $15^\circ$ , le calcul donne un atome de polonium par  $2 \times 10^8$  intersections d'une dislocation avec un plan réticulaire. Ce nombre est approximativement quatre fois plus grand pour des joints à angle  $\theta$  égal à  $25^\circ$ .

Une élévation de la température de recuit conduit à une diminution de la concentration de polonium dans les joints; aux températures de recuit plus élevées, la ségrégation ne persiste que dans les joints à grande différence angulaire.

### DIE AUSSCHIEDUNG VON VERUNREINIGUNGEN AN KORNGRENZEN

Es wird experimentell nachgewiesen, dass sich Polonium an den Korngrenzen einer Bleilegierung mit 5% Wismuth, in der Polonium in einer Konzentration von  $1:10^{10}$  vorhanden war, abscheidet. Die Ereignisse zeigen, dass die an der Korngrenze zurückgehaltene Poloniummenge eine Funktion der kristallographischen Orientierung der der Korngrenze benachbarten Kristalle und der Temperatur, bei der Gleichgewicht erreicht wurde, ist. Die Korngrenzen wurden durch symmetrische Rotationen von "Keim" kristallen um die [001] Richtung hergestellt. Infolge dessen bestanden die Korngrenzen hauptsächlich aus Stufenversetzungen.

Die Anzahl der Poloniumatome wurde für Korngrenzen mit  $\theta$ -Werten bis zu  $15^\circ$  zu einem Atom Polonium je  $2 \times 10^8$  Versetzungsstellen berechnet. Eine Versetzungsstelle ist der Schnittpunkt einer Versetzung und einer Kristallebene. Die Zahl der Poloniumatome wächst auf etwa das Vierfache, wenn die Korngrenzen ein  $\theta = 25^\circ$  aufweisen.

Die Poloniumkonzentration an den Korngrenzen nimmt schnell mit steigender Glühtemperatur ab; nur die Ausscheidung an Grosswinkelkorngrenzen ist bei höheren Glühtemperaturen beständig.

### INTRODUCTION

It has been suggested by numerous investigators on the basis of their own observations and on theoretical grounds that impurities segregate to grain boundaries. Such segregation might be expected, since at the grain boundaries there exist some regions where large foreign atoms and others where small foreign atoms will fit with less strain than they do within the crystal lattice. Therefore, the concentration of impurity should be higher at the boundary than it is within the body of the grain. The evidence for this type of segregation can be divided into two categories; indirect, where the experimental data are most easily explained by the assumption that this type of segregation exists; and direct, where

the evidence has been produced by experiments designed to measure the difference in concentration.

There are numerous examples in the literature of investigations providing indirect evidence. Spretnak and Speiser<sup>1</sup> suggest that the temper brittleness found in some steels is due to the concentration of carbon at the grain boundaries; their argument is based on the appearance of the grain boundaries in metallographic sections and on a qualitative type of thermodynamic argument. It has been found that small amounts of antimony embrittle copper at low temperature,<sup>2</sup> and although no concentration of antimony at the grain boundaries was observed metallographically, it was suggested that this was the cause of the embrittlement.

Miekk-Oja<sup>3</sup> has measured the effect of small additions of iron and phosphorus to brass on the recrystallization temperature and concluded that the manner in which these elements inhibit recrystallization is due to concentration at the grain boundaries. It is also well known

\* Received April 28, 1954.

† Department of Metallurgical Engineering, University of Toronto.

‡ Division of Applied Science, Harvard University, Cambridge, Massachusetts.

The calculation of the number of dislocations can be obtained from the equation

$$N = \frac{D \times 10^2 \sin \frac{\theta}{2}}{d},$$

where  $D$  is the length of boundary perpendicular to the line of the dislocations,  $d$  is the lattice constant, which in this case is 4.94 and  $\theta$  is the orientation difference in degrees. If it be assumed that all the dislocations are edge-type and that their lines are parallel to the emulsion, then the number of polonium atoms per dislocation of 2 mm length (the length of the slit) is calculated by dividing the total number of polonium atoms in a 2 mm length of boundary by the number of dislocation lines. The table gives the values obtained by this calculation, and the number of dislocation sites per atom of polonium, a dislocation site being the intersection of a dislocation and an atomic plane.

$\theta$ degrees	No. of dislocations	No. of $P_0$ atoms per 2 mm length of dislocation line	No. of dislocation sites per $P_0$ atom
4	$2.0 \times 10^3$	$1.8 \times 10^3$	$2.2 \times 10^3$
10	$4.9 \times 10^3$	$1.8 \times 10^3$	$2.2 \times 10^3$
15	$7.7 \times 10^3$	$1.8 \times 10^3$	$2.2 \times 10^3$
16	$8.2 \times 10^3$	$2.7 \times 10^3$	$1.5 \times 10^3$
17	$8.7 \times 10^3$	$6.5 \times 10^3$	$6.1 \times 10^2$
25	$1.3 \times 10^4$	$7.2 \times 10^3$	$5.5 \times 10^2$

### DISCUSSION

Shockley and Read have derived an expression relating the energy of the grain boundary to the angular difference of orientation of the crystals, of the form

$$\gamma = E_0 \theta (A - \ln \theta).$$

The experimental data on the energies of grain boundaries in silicon iron, lead, tin, and silver agree remarkably well with the prediction of the theory and show that the dislocation model of the boundary is satisfactory for small angle boundaries. In fact, the experimental data fit the theoretical curve far beyond the limit to which the theory should be valid. Read and Shockley state that this is probably due to a fortunate cancellation of errors although the reason for this cancellation is by no means clear.

A critical examination of the experimental data shows that the change in boundary energies from low angle to high angles may not be smooth. The results of the measurements of grain boundary energies in silicon iron<sup>10,11</sup> suggest a sharp change at 20 degrees, that for lead<sup>13</sup> at 16 degrees and that for tin<sup>14</sup> at 6 degrees. The results for silver are not precise enough to indicate any abrupt change. Achter and Smoluchowski<sup>15</sup> have studied the diffusion of silver in grain boundaries of copper and found diffusion to be absent in boundaries where the

relative orientation is less than 20 degrees and to rise sharply as the difference of orientation increases from 20 degrees to a maximum at 45 degrees.

The results of the present investigation show that an abrupt change occurs in the segregation of polonium at grain boundaries at 16 degrees in the alloy of lead and bismuth. The first portion of the curve of Fig. 3 is an approximately straight line indicating that each dislocation added to the array to produce an increment of rotation brings with it a specific number of polonium atoms.

At 15 degrees the spacing of the dislocations in the array is about 4 lattice parameters, which is the distance at which the cores of the dislocations begin to interact.<sup>16</sup> It is likely, therefore, that an increase in the number of dislocations will increase the strain in the region between the cores. The extra impurity atoms may be accommodated in the regions between the cores of the dislocations, or a higher proportion of the dislocation sites may be occupied by polonium atoms. It is probable that the curve of relative concentration *vs*  $\theta$  levels off above 25 degrees when all the single dislocations have lost their identity and the structure of the boundary is one of extreme disorder.

Cottrell<sup>16</sup> has shown that the concentration of impurity in a single dislocation can be related to the temperature, the average concentration of impurity provided it is dilute, and the strain energy of the dislocation by the function

$$C = C_0 e^{-V/kT},$$

where  $C_0$  is the average concentration and  $V$  is the strain energy. This predicts an exponential curve relating the concentration of impurity at the boundary to the annealing temperature, whereas Fig. 5 suggests that the relationship is linear. It is possible that equilibrium was not reached at the lower annealing temperatures, in which case the corresponding points would be spuriously low. If the points for the lower temperatures were higher, the exponential relationship would appear more probable.

### SUMMARY

It can be concluded that the concentration of impurities at a grain boundary is a function of relative orientation and of temperature. The results imply that the structure of the grain boundary changes abruptly as the orientation difference increases through 15 degrees. The dislocation model of the boundary is satisfactory for low angle boundaries but inadequate to completely explain the properties of high angle boundaries.

### ACKNOWLEDGMENTS

One of the authors, W. R. Thomas, gratefully acknowledges the financial assistance of the National Research Council of Canada. The authors are indebted



to Professor L. M. Pidgeon, Head of the Department of Metallurgical Engineering, University of Toronto, for facilities and encouragement.

## REFERENCES

1. J. W. Spretnak and R. Speiser, *Trans. A.S.M.* **43**, 734 (1951).
2. D. McLean, *J. Inst. Metals* **81**, 121 (1952-3).
3. H. M. Mikk-Oja, *J. Inst. Metals*, 569 (1952).
4. J. S. Smart, Jr. and A. A. Smith, Jr., *Trans. A.I.M.M.E.* **152**, 103 (1943).
5. P. E. Beck, *Trans. A.I.M.M.E.* **137**, 222 (1940).
6. P. J. E. Forsyth, G. J. Metcalfe, R. King, and B. Chalmers, *Nature (London)* **158**, 875 (1946).
7. P. Lacombe and N. Yannaquis, *Metaux et Corrosion* **22**, 35 (1947); *Revue de Met.* **3** and **4**, 68 (1948).
8. G. R. Dean and W. P. Davey, *Trans. A.S.M.* **26**, 267 (1938).
9. D. F. Clifton and G. S. Smith, *Rev. Sci. Instrum.* **20**, 583 (1949).
10. M. T. Stewart, *Phys. Rev.* **83**, 657 (1951).
11. C. G. Dunn and F. Lionetti, *Trans. A.I.M.M.E.* **185**, 125 (1949).
12. C. G. Dunn, F. W. Daniels, and M. J. Bolton, *Trans. A.I.M.M.E.* **188**, 368 (1950).
13. K. T. Aust and B. Chalmers, *Proc. Roy. Soc. A* **201**, 210 (1950).
14. K. T. Aust and B. Chalmers, *Proc. Roy. Soc. A* **204**, 359 (1950).
15. M. R. Achter and R. Smoluchowski, *Phys. Rev.* **76**, 470 (1949).
16. A. H. Cottrell, *Progress in Metal Physics*, Vol. 1 (Butterworth, 1949) 83.



# THE YIELD PHENOMENA, KINK BANDS AND GEOMETRIC SOFTENING IN TITANIUM CRYSTALS\*

A. T. CHURCHMAN†

Single crystals of titanium grown by a modification of the strain anneal technique show discontinuities in the stress strain relationship when containing 0.1 wt.% oxygen and nitrogen. The discontinuities are explained as a manifestation of the yield phenomenon modified by geometric softening taking place during the formation of kink bands. An explanation of fragmentation is suggested for materials which form kink bands.

## LES PHÉNOMÈNES D'ÉCOULEMENT, LES BANDES DE PLIAGE ET L'ADOUCCISSEMENT GÉOMÉTRIQUE DANS DES MONOCRISTAUX DE TITANE

On constate l'existence de discontinuités dans les relations tension-déformation de monocristaux de titane contenant 0.1 pour cent d'oxygène en poids, produits par une technique modifiée de déformation-recuit. Ces discontinuités sont interprétées comme une manifestation du phénomène d'écoulement, modifié par un adoucissement géométrique qui apparaît lors de la formation de bandes de pliage. On suggère une explication de la fragmentation pour les matériaux qui forment des bandes de pliage.

## FLIESSERSCHEINUNGEN, KINKBÄNDER, UND GEOMETRISCH BEDINGTE ERWEICHUNGEN VON TITANKRISTALLEN

Titaneinkristalle, die mit Hilfe einer modifizierten Spannungs-Glüh methode gezüchtet waren, zeigten Unstetigkeiten in den Spannungs-Verzerrungsbeziehungen, wenn sie 0,1 Gew. % Sauerstoff und Stickstoff enthielten. Diese Unstetigkeiten werden als Folgen von Fliesserscheinungen erklärt, die durch geometrisch bedingte Erweichungen, die bei der Bildung von Kinkbändern auftreten, modifiziert worden waren. Es wird eine Erklärung der Fragmentation von Stoffen, die Kinkbänder bilden, vorgeschlagen.

### INTRODUCTION

Yield phenomena have been observed in a number of metals in which interstitial impurities are present (notably nitrogen). The stress-strain curves for materials showing the yield phenomena have certain characteristics: (a) a drop in load is associated with the start of plastic flow in an annealed specimen; (b) a smooth stress-strain curve is obtained on immediate retesting; and (c) the discontinuous stress-strain curve is again obtained after a low-temperature annealing treatment. Curve *A* of Fig. 1 shows an idealised case. The phenomena have been known for a long time in

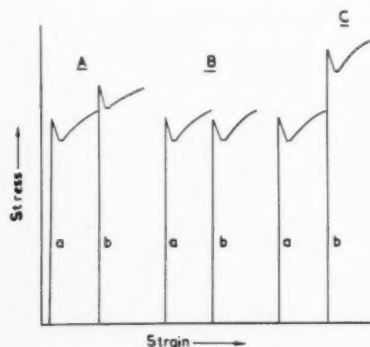


FIG. 1. Idealised stress-strain curves for single crystals of three different materials in which curves (a) represent fully annealed crystals and (b) the crystals on retesting after a low-temperature ageing treatment. *A* shows the yield phenomena alone. *B* the yield phenomena modified by recovery during ageing. *C* the yield phenomena modified by precipitation hardening during ageing.

\* Received May 6, 1954.

† Research Laboratory, Associated Electrical Industries Limited, Aldermaston, Berkshire.

polycrystalline mild steel and have been observed more recently in molybdenum<sup>1</sup> and in single crystals of  $\alpha$ -iron<sup>2</sup> both of which have a body-centered cubic structure, in zinc<sup>3</sup> and cadmium<sup>4</sup> with close-packed hexagonal crystal structures, and in  $\alpha$ -brass<sup>5</sup> and aluminium-4 per cent magnesium<sup>6</sup> with face-centered cubic structures. These phenomena have been explained in terms of an interaction between the strain field produced by the impurities in the metal lattice and the strain fields associated with dislocations. This interaction is called "Cottrell locking."<sup>7</sup> The observed stress-strain curve may differ from the simple case due to other superimposed phenomena. In the case of zinc and cadmium,<sup>3,4</sup> complete recovery occurs during strain ageing, resulting in curves of type *B* in Fig. 1. In iron, on the other hand, a form of precipitation hardening occurs during strain ageing, resulting in a curve of type *C* in Fig. 1. In all these cases, however, the basic yield characteristics are observed. Yield phenomena found in the stress-strain curves of titanium are modified by a further complication, as will be reported in this paper. An explanation on the basis of geometric softening is put forward to account for this modification.

### EXPERIMENTAL METHOD

#### Material

The titanium used in the following experiments was produced in this Laboratory by the van Arkel process, and single crystals were grown by a modification of the strain anneal technique.<sup>8</sup> Crystals of two compositions were examined with purities of 99.85 and 99.95 per cent which contained iron <0.005 per cent, silicon <0.02 per cent, tungsten, molybdenum and boron <0.0001

per cent. The difference between the two samples lay in their oxygen and nitrogen contents. The relationships between hardness and combined oxygen and nitrogen content determined from published data<sup>9</sup> was relied upon to evaluate the approximate amounts of these elements present. A gas analysis carried out at the National Physical Laboratory on two samples with a Vickers pyramid hardness of 97 gave the combined oxygen and nitrogen content as 0.014 per cent  $\pm 0.001$  per cent which is in agreement with the above relationship. The Vickers pyramid diamond hardness number of the two compositions examined were 90 and 160, which correspond to combined oxygen and nitrogen contents of 0.01 wt. per cent and 0.1 wt. per cent, respectively. The orientations of the crystals relative to the stress axis were determined by the back-reflection Laue technique.

### Testing Conditions

Shouldered strip test pieces were used with a  $5/8'' \times 1/8'' \times 1/16''$  gauge length. The gauge length consisted of one or more crystals which extended right across the cross section of the specimen and which, in the tensile test, behave free of boundary constraint. The four faces of the gauge length were electro-polished, before testing, in a 5 per cent perchloric acid acetic acid bath.<sup>10</sup> The specimens were tested in a rigid machine of the Polanyi type, being mounted by clamping into axial loading shackles. The rigidity of the machine is such that a stress relaxation of approximately 25 lb/sq in., corresponding to an 0.5 mm scale deflection, involves a specimen extension of only  $10^{-5}$  in. if the relaxation is rapid compared with the strain rate. The machine is therefore sensitive to quite small variations in the stress required for plastic flow. Test temperatures above and below room temperature were obtained by placing the specimen in a vacuum vessel containing heated silicone oil or a suitable coolant. Ageing of the specimens *in situ* was also possible in this manner.

### THE YIELD PHENOMENA: STRESS-STRAIN CURVES

Titanium crystals containing only 0.01 wt. per cent oxygen and nitrogen showed no signs of discontinuities

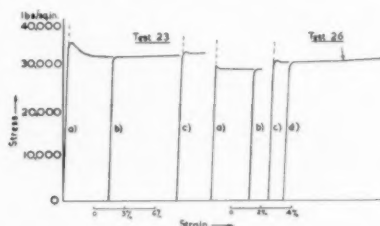


FIG. 2. Stress-strain curves for two titanium crystals containing a total of 0.1 wt. per cent of oxygen and nitrogen. In both cases the slip plane is (1010) with  $X_0 = 45^\circ$  in Test 23 and  $35^\circ$  in Test 26. Note the small initial discontinuity with the lower  $X_0$  value, although the discontinuities after ageing are similar. Note also that the curves do not apparently show any work-hardening until after the onset of duplex slip (arrowed in Test 26).

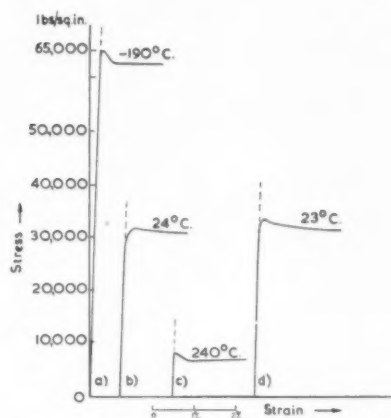


FIG. 3. The stress-strain curves of a crystal of the lower purity slipping on the (1010) system, when tested at  $-190^\circ\text{C}$ , at  $24^\circ\text{C}$  after 600 hours rest at room temperature, at  $240^\circ\text{C}$  after 18 hours at room temperature, and again at  $23^\circ\text{C}$  after 18 hours at  $240^\circ\text{C}$ .  $X_0 = 52^\circ$ . Note the negative slope of the curves except in c, where the specimen may be ageing during the test. The discontinuities at  $240^\circ\text{C}$  and  $190^\circ\text{C}$  differ very little in magnitude.

in the stress-strain curves even at  $-190^\circ\text{C}$ . On the other hand, all specimens containing 0.1 wt. per cent oxygen and nitrogen showed discontinuities during the initial test at room temperature. The yield characteristics were in evidence (see Fig. 2); that is, (1) a load drop was observed; (2) immediate reloading gave a smooth stress-strain curve; (3) annealing at  $180^\circ\text{C}$  restored the discontinuous curve. The stress-strain curves appeared to be of type (A) in Fig. 1, in which recovery and strain age-hardening are negligible factors. However, a small strain age-hardening, as measured by the difference between the flow stress immediately before annealing and the lower yield stress after annealing, was observed, but the magnitude was only of the order of 20 per cent of that observed in iron.

Complete strain ageing and the return of a yield point required an annealing treatment of from one to two hours at  $180^\circ\text{C}$ . Up to 600 hours' treatment at room temperature resulted in no detectable ageing (see Fig. 3, curve b).

A number of features distinguished the behaviour observed in titanium from that of other metals showing the yield phenomena. Thus the discontinuity produced after ageing was never so large as the initial one and the magnitude of the fall in stress appeared to depend on orientation (see curves a, Fig. 2). On the other hand, the magnitude of the fall in stress was not markedly affected by the test temperature. The stress-strain curves are shown in Fig. 3 for a crystal slipping on the (1010) system when tested at  $-190^\circ\text{C}$ , at  $20^\circ\text{C}$  after ageing at room temperature, at  $240^\circ\text{C}$ , and again at  $20^\circ\text{C}$  after ageing at  $200^\circ\text{C}$ . The actual yield stress at  $-190^\circ\text{C}$  was twice that at room temperature: this increase in strength is of the same order as that of a crystal of similar orientation, but of the higher purity, in which no signs of yield phenomena were observed. The

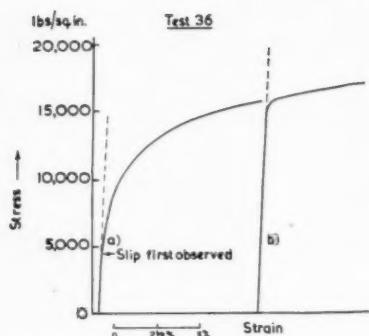


FIG. 4. The stress-strain curves obtained with a crystal containing a total of 0.01 wt. per cent of oxygen and nitrogen slipping on the  $(10\bar{1}0)$  system.  $X_0 = 43\frac{1}{2}^\circ$ . Curve (a) was taken in the fully annealed state, curve (b) after an annealing treatment of 18 hours at  $200^\circ\text{C}$ . Note that there are no discontinuities in the curves, even after ageing.

fall in stress at the start of plastic flow in the low-temperature test is only about 50 per cent above the fall in stress observed during testing at  $240^\circ\text{C}$  and at  $20^\circ\text{C}$ .

Examination of the stress-strain curves of the two types of titanium crystals revealed a difference in the apparent rates of work hardening. In the less pure crystals showing the yield phenomena the stress-strain curves after the initial drop in load were either parallel to the strain axis or had a negative slope (see Figs. 2 and 3). After considerable deformation the slope became positive and the onset of duplex slip in a crystal was usually marked by an increase in the slope of the stress-strain curve. The shape of the stress-strain curve again appeared to be orientation-dependent. In the purer crystals (see Fig. 4) the stress-strain curve was a normal one showing a positive rate of work-hardening and no discontinuities.

#### METALLOGRAPHIC EXAMINATION

The appearance of the slip lines was different in the two groups of crystals examined. In the purer crystals, flow commenced with isolated and fairly evenly spaced slip lines. As the deformation increased the spacing between the lines decreased. The deformed surfaces after 0.5 and 1.5 per cent extension were examined by electron microscopy using both "Formvar" and carbon replicas<sup>11</sup> with and without low-angle shadowing with a gold palladium alloy. In titanium no fine slip was resolved between the optically visible slip lines but these slip lines were themselves resolved into two or three finer traces (see Fig. 5).

However, in the less pure crystals the slip first appeared in groups of two or three lines (see Fig. 6). With increasing deformation the regions in which slip had taken place increased until after about 0.5 per cent extension the density of the slip lines was approximately the same all over the crystal. This behaviour is characteristic of other metals showing the yield phenomena<sup>6,4</sup> and indicates local regions of inhomogeneous deformation.

Cross-slip was occasionally observed in the less pure crystals, especially in orientations in which the stress axis was near to the  $c$ -axis (see Fig. 7).

#### KINK BANDS

Metallographic examination of specimens of the less pure crystals during tensile testing showed that the discontinuity in the stress-strain curve was associated with the appearance of tilted regions on the surface of the specimens<sup>12</sup> (see Fig. 8); these did not appear with the first slip lines on the specimens but only after extensions of approximately 0.1 per cent. Even though ageing reintroduced further discontinuities it did not normally lead, to a multiplication of the tilted regions. The tilted region did not increase appreciably in width with increasing deformation, which distinguished it from the Lüders bands associated with the yield phenomena in steels. Further microscopic and X-ray examination showed that the lattice is rotated in the tilted regions and that this rotation increased with increasing deformation. The phenomenon has been observed in other metals in which the tilted regions have been called kink bands.<sup>13</sup> The appearance and magnitude of these kink bands were related to the crystal orientation, as were a number of features of the stress-strain curves of titanium.

A large discontinuity and a negative work-hardening curve were associated with the formation of a kink band which occupied a large part of the crystal and in which there was a considerable lattice rotation. In the large bands  $(10\bar{1}0)$  slip was always involved but, at least in part, this was a consequence of the orientation effect.

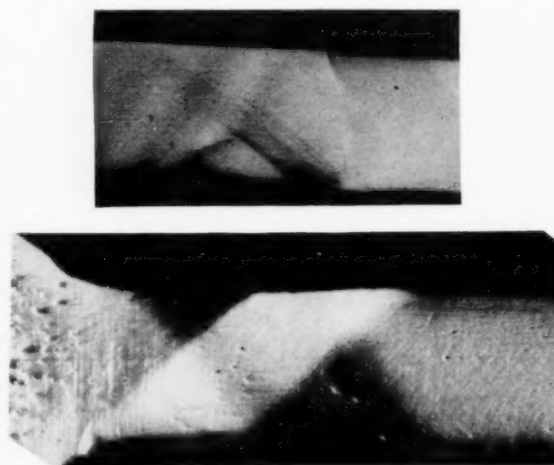
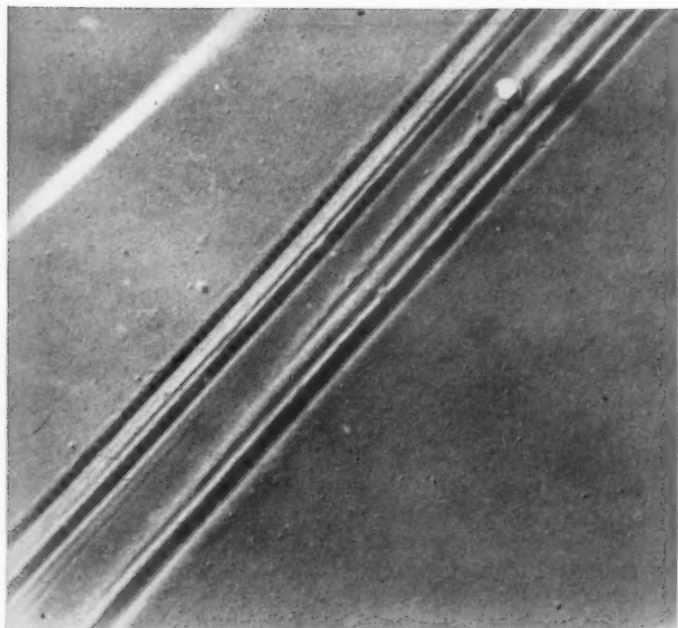
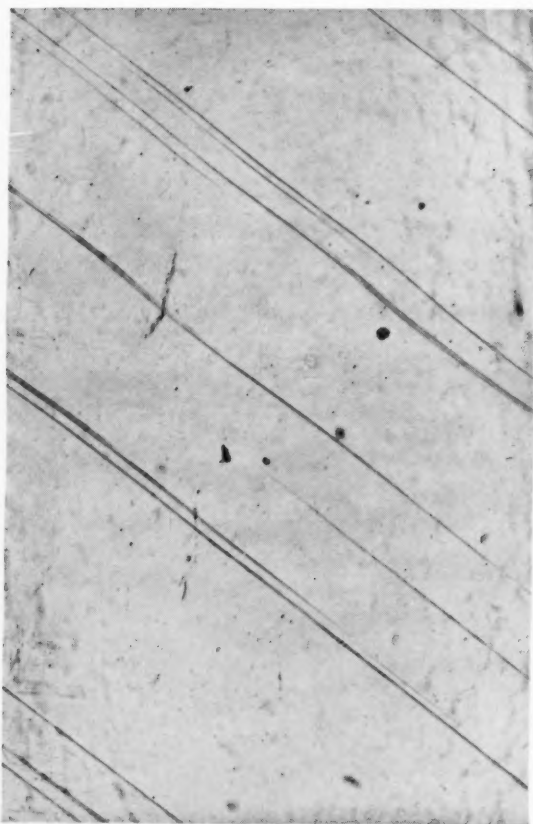


FIG. 8. Kink bands formed after  $(10\bar{1}0)$  slip in titanium crystals of the lower purity. In the case of the large band (a) the  $(10\bar{1}0)$  plane makes an angle of  $52^\circ$  with the stress axis and in the case of the multiple banding (b) the  $(10\bar{1}0)$  plane is  $37^\circ$  away from the stress axis. The bands are revealed because of the tilt which they produce at the specimen surface. In (a) the band is the light region. The dark region corresponds to heavy slip. In (b) the slip lines are coarse and can be seen. The bands here correspond to the lighter regions at  $90^\circ$  to the slip lines.  $20\times$ .



5



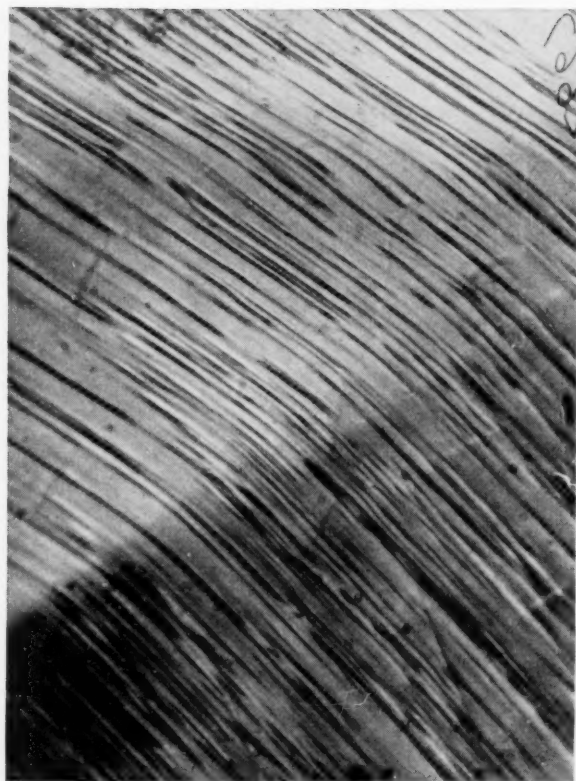
6



7

PLATE I. FIG. 5.—An electron micrograph of a  $(10\bar{1}0)$  slip trace after 0.5% extension. The trace is approximately  $1\mu$  wide and is resolved into a number of steps of different heights.  $50,000\times$ . FIG. 6.—The grouping or uneven distribution of slip traces observed in the initial stages of deformation of a crystal with a discontinuous stress strain curve.  $100\times$ . FIG. 7.—Unpredicted cross slip in titanium crystals of the lower purity. The main traces correspond to  $(10\bar{1}0)$  slip. The cross slip traces, which are not all in the same direction, can be seen joining some of the main traces.  $300\times$ .

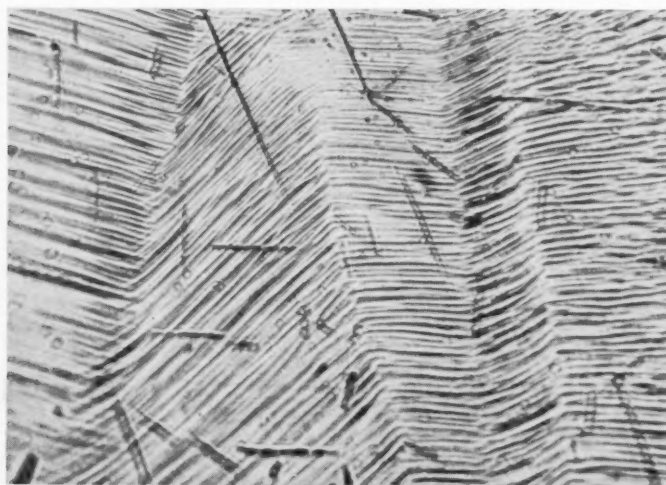




9



11



12

PLATE II. FIG. 9.—The bend plane boundary of a kink band showing the change in slip direction over a small region near to this boundary. The slip lines are straight on either side of this narrow region of bent lattice. 600 $\times$ . FIG. 11.—The boundary of a kink band in a crystal slipping on a (10 $\bar{1}$ 0) plane, after 30 per cent elongation. The main bend plane boundary is the bright line at which the direction of the slip lines changes markedly. A second boundary can be seen as a dark line inside the kink band. The angular difference between these two boundaries increases with increasing deformation. Note the second slip system operating inside the kink band. 300 $\times$ . FIG. 12.—Regions of marked change of slip direction observed in a polycrystalline titanium specimen after deformation (at 200°C) during which discontinuities were observed in the stress strain curves. 800 $\times$ .



As the  $c$ -axis approached the stress axis the slip system changed from  $(10\bar{1}0)$  to  $(10\bar{1}1)$  and then to  $(0001)$ .<sup>8</sup> With this change of orientation and slip system the bands became much less pronounced and usually more than one in number (Fig. 8), each involving only a small lattice rotation.

The bend planes bounding the tilted regions in the crystals were usually straight and approximated to traces of  $\{11\bar{2}0\}$  planes. The particular  $(11\bar{2}0)$  plane involved was found to be the one perpendicular to both the operative slip direction and slip plane.

In crystals which formed kink bands after  $(10\bar{1}0)$  slip, the lattice in the kinked region was rotated about the  $[0001]$  axis from the matrix orientation, the line of intersection of the slip plane with the bend plane. With increasing extension this rotation increased to as much as 25 degrees. The rotation in bands formed during  $(10\bar{1}1)$  and  $(0001)$  slip were, however, too small for accurate analysis; nevertheless, the rotation during kinking after basal slip appeared to be about a  $[10\bar{1}0]$  axis, which is the line of intersection of the basal plane and the bend plane. This is in agreement with recent findings on the axis of rotation of aluminium during kinking.<sup>14</sup>

The bent region of the lattice was confined to the bend plane boundary of the band (see Fig. 9) as shown by the occurrence of asterism in back-reflection Laue photographs. Inside and outside the kink band the photographs showed no asterism, indicating that the lattice is unbent in these regions, as other workers have shown for aluminium, copper<sup>15</sup> and zinc.<sup>16</sup> This is in agreement with the dislocation picture of deformation bands<sup>17</sup> which is that the bands are regions bounded by planes at which dislocations are piled up causing a fairly sharp lattice bending.

The region of the bent lattice was observed to polygonise after an annealing treatment of 12 hours at 850°C. The polygon boundaries were approximately perpendicular to the slip lines and were revealed by thermal etching which occurred during the annealing (see Fig. 10). That the polygon boundaries separated regions of slightly different orientation was shown in the back-reflection Laue photographs in which the asterism streaks were broken down into discrete spots very close together. After considerable deformation (approximately 30 per cent elongation in tension) the asterism streaks appeared to be broken into diffuse spots before annealing, which then served only to sharpen the spots. A similar phenomenon has been reported during the deformation of zinc<sup>18</sup> and molybdenum.<sup>19</sup> Aust, Maddin and Chen<sup>19</sup> ascribed the phenomenon to fragmentation, in which small units of slightly disoriented good crystal were connected by highly strained regions.

A possible mechanism for this type of fragmentation was suggested by the appearance, after considerable deformation, of a second bend plane at the kink-band boundaries (see Fig. 11). Further deformation resulted

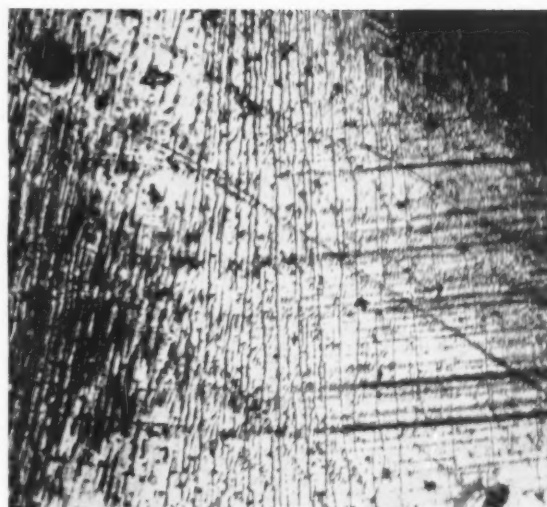


FIG. 10. The boundary region of a kink band after annealing at 850°C. The surface has thermally etched during the annealing process. The change in direction of the original slip lines can still be seen. (The lines are approximately horizontal). In the region of lattice bending a series of markings can be seen at right angles to the old slip lines. These are polygon boundaries separating regions of slightly different orientation (approximately 30 minutes of arc). 150X.

in further rotation of the lattice while the angular difference between the two components of the kink-band boundary increased. If a number of these boundaries formed during the deformation, the outcome would be slightly disoriented regions of good lattice separated by bend planes or regions of piled-up dislocations. As the disorientations would involve increasing degrees of rotation about a given crystallographic axis, the X-ray pattern would show diffuse spots lying along an arc corresponding with the asterism that would have resulted from a uniform bending of the lattice about the same axis. Complete polygonisation or sharpening of the spots would not be possible without a rise of temperature to provide the activation energy for the "climb" of dislocations from one plane to another.

#### DISCONTINUITIES IN THE STRESS-STRAIN CURVES OF POLYCRYSTALLINE MATERIAL

Polycrystalline titanium and zirconium of 99.85 per cent purity also showed discontinuities in their stress-strain curves, but only when tested at temperatures above 90°C when the criteria of the yield phenomena were observed. The temperature at which the discontinuities appear is probably a function of grain size. The grain size which corresponded to a critical temperature of 90°C was 25 grains/mm<sup>2</sup>. Microscopic examination of specimens which had been tested above 90°C showed wedge-shaped regions in which there were sharp changes in the direction of slip (see Fig. 12) resembling the bands of "secondary slip" observed by Honeycombe in aluminium.<sup>20</sup>

### THE RELATIONSHIP BETWEEN GEOMETRIC SOFTENING, KINK BANDS AND THE YIELD PHENOMENA IN TITANIUM

Differences between the stress-strain curves of titanium and those of other metals showing the yield phenomena can be explained by a combined effect of geometric softening, kink-band formation, and the yield phenomena. Kink bands were observed only in crystals of titanium showing the yield phenomena. This suggests that the kink bands are a means of relieving local lattice stresses (bending) produced by the inhomogeneous deformation associated with the yield phenomena. This hypothesis is given further support by the nonappearance of kink bands where the crystal has from an early stage in the deformation been able to slip on a second system. In such cases the local stresses are relieved by duplex slip. A second slip system was often observed in the kinked regions but this was due to the change in orientation relative to the stress axis produced by the rotation of the lattice in the kink band.

Schmid and Boas<sup>21</sup> have shown that during the deformation of a single crystal by slipping on one system, the lattice was so rotated that the slip plane and direction were brought more nearly into coincidence with the axis of the applied stress, thereby increasing the resolved stress on the slip plane. Assuming no work-hardening, they predicted a relationship between stress and strain which showed a falling applied stress to maintain flow—the actual shape of the curve being governed by the original orientation of the crystals. The larger the angle ( $X_0$ ) between the slip plane and the stress axis of the original crystal, the greater the initial rate of rise in the resolved shear stress on the plane and the lower the necessary applied stress to maintain plastic flow. Andrade and Roscoe<sup>22</sup> used this argument to explain 'stove piping' in zinc crystals with high  $X_0$  values. In zinc crystals of such orientations the rate of work-hardening was such that with increasing extension the flow stress continuously fell, thus localising the region in which deformation occurred. Such a process is a geometrical property of the mode of deformation of a crystal and should therefore be independent of the testing temperature or of low-temperature annealing treatments in which recovery does not take place.

Due to the three possible slip systems in titanium there will only be a limited range of values for  $X_0$  (less than 0 to 60 degrees): the range will differ with the purity of the crystal, for purity has been shown to affect the relative values of the critical resolved shear stress for slip on the various slip systems.<sup>8</sup> The initial rate of work-hardening of titanium is higher than that for zinc discussed by Andrade and Roscoe; this will limit further the range of orientations showing a falling stress-strain curve due solely to geometric softening. Except in a few orientations the principal effect of geometric softening will be to vary the apparent rate of work-hardening (see Fig. 4).

That the observed discontinuity in the stress-strain

curves of the crystals containing 0.1 wt. per cent of oxygen plus nitrogen is not due solely to geometric softening is shown by the reappearance of a discontinuity after a low-temperature annealing treatment and by the uneven distribution of slip in the early stages of deformation.

In crystals showing the yield phenomena, inhomogeneous deformation will result in local bend stresses between the macroscopic regions which have slipped and those which have not. In suitable orientations these stresses may be relieved by duplex slip; in others they lead to the formation of bend planes which migrate under the influence of further bend stresses into a narrow region forming a kink band. The lattice in the kink band is so rotated that the resolved shear stress on the slip plane is increased. The rate of increase will again depend on the initial orientation of the crystal. The formation of kink bands thus accentuates the effect of geometric softening and, as shown in Figs. 2 and 3, leads to an apparent negative work-hardening curve. The onset of duplex slip—whether it occurs at an early stage in the deformation, when it inhibits kinking, or in the kink bands after a certain amount of lattice rotation—results in an increased rate of work-hardening.

We can now explain the apparent anomalies in the yield behaviour of titanium. It is apparent that the yield phenomena are not very marked and are coupled with quite a high rate of work-hardening. Because of two factors the observed stress-strain curves differ from the continuous stress-strain relationship usually obtained with metals. One arises from the yield phenomena and the other from geometric softening accentuated by the lattice rotation involved in the formation of kink bands. Whereas the yield phenomena are strongly temperature-dependent<sup>7</sup> but have not been reported to be affected by orientation changes, the geometric softening is strongly orientation-dependent, and is not affected by changes in test temperature. It appears that in certain orientations the contribution from geometric softening is equal to, or greater than, that from the yield phenomena. Therefore crystals of these orientations will show a much enhanced difference between the upper yield stress and the stress required to maintain plastic flow. Herein lies the explanation for the apparent orientation dependence of the difference between the upper and lower yield stresses.

In a similar manner the temperature dependence of the magnitude of the discontinuity at the initiation of plastic flow will be smaller than expected on the basis of the yield phenomena alone and will vary with the initial orientation of the crystal.

### THE MAGNITUDE OF THE YIELD PHENOMENA

The two groups of crystals of titanium, one which shows the yield phenomena and the other which does not differ only in the oxygen and nitrogen content of the material.

Oxygen and nitrogen go into interstitial solution in

the titanium with a wide range of solubility in the  $\alpha$ -phase.<sup>23</sup> In other metals exhibiting the yield phenomena, the solubility of nitrogen in the  $\alpha$ -phase at room temperature is very low.<sup>24,3,4</sup> A wide range of solubility can arise either from a favourable size factor, when only a small distortion of the lattice is caused by solution, or from a high chemical affinity between the atoms concerned. In the case of titanium there is a very high affinity for oxygen and nitrogen, as shown by its 'gettering' properties, its reduction of nearly all oxides, and the thermodynamic stability of the solid solution of oxygen in titanium. Lattice parameter measurements of titanium containing oxygen<sup>25</sup> or nitrogen<sup>26</sup> show that the  $c$ -parameter is expanded more than the  $a$  parameter but that up to about 2 wt. per cent this results in an insignificant change of the axial ratio. Above 2 per cent the axial ratio increases with oxygen content as the  $a$  parameter does not appreciably change. The distortion produced by the nitrogen appears to be somewhat greater than that produced by oxygen atoms. Ehrlich<sup>23</sup> has shown that the interstitial oxygen atoms can occupy sites in the unit hexagonal cell corresponding to  $(2/3, 1/3, 1/4)$  and  $(2/3, 1/3, 3/4)$  when the titanium atoms are at  $(000)$  and  $(1/3, 2/3, 1/2)$ . These interstitial sites are spherically symmetrical and expansion of the lattice at a constant  $c/a$  ratio results in a simple dilation of this space. This type of distortion involving no shear has been shown to react as in face-centered cubic metals only with the stress field of the edge components<sup>7</sup> of dislocations. This results in a weak locking of the dislocations. One would expect local shear stresses to be developed when only one of the two interstitial positions was filled. The symmetrical distortion, together with the high chemical affinity of titanium for the interstitial elements, will result in a much smaller reduction in free energy by the association of interstitial atoms with dislocations and so in a much weaker locking than is the case possible in other metals.

### CONCLUSIONS

1. Single crystals of titanium containing 0.1 per cent combined oxygen and nitrogen show the yield phenomena during tensile testing.
2. The phenomena are not detected in crystals containing 0.01 per cent interstitial impurity.
3. Large kink bands are developed during the tensile testing of those crystals which show the yield phenomena but which are not suitably oriented for duplex slip.
4. The rotation of the lattice in the kink bands is such that it increases the effect of geometric softening on the stress strain curve.
5. Specimens in which kink bands are produced

during deformation show a negative work hardening curve.

6. The superposition of geometric softening and the yield phenomena results in a much smaller temperature dependence of the flow stress than is normally associated with the yield phenomena.

7. A possible mechanism for fragmentation is suggested for materials forming kink bands.

### ACKNOWLEDGMENTS

The author wishes to express his appreciation for invaluable discussions with Professor A. H. Cottrell who suggested the possible function of geometric softening. To Dr. G. A. Geach for interest and helpful discussion while preparing the manuscript and to Dr. T. E. Allibone, F.R.S., for permission to publish this paper.

### REFERENCES

1. R. Tury and S. Kraus, *Nature* **138**, 331 (1936); **139**, 30 (1937).
2. A. T. Churchman and A. H. Cottrell, *Nature* **167**, 943 (1950).
3. A. T. Churchman and H. Paxton, *Acta Met.* **1**, 473 (1953).
4. H. L. Wain and A. H. Cottrell, *Proc. Phys. Soc.* **B63**, 339 (1950).
5. D. F. Gibbons and A. H. Cottrell, *Nature* **162**, 488 (1947).
6. G. A. Ardley and A. H. Cottrell, *Proc. Roy. Soc.* **A219**, 328 (1953).
7. V. A. Phillips, A. J. Swain, and R. Eborall, *J. Inst. Met.* **81**, 625 (1953).
8. A. H. Cottrell, *Dislocations and Plastic Flow in Crystals*. Clarendon Press, Oxford, 1953.
9. A. T. Churchman, *Nature* **171**, 706 (1953), *Proc. Roy. Soc.* **A226**, 216 (1954).
10. A. E. Jenkins and H. W. Worner, *J. Inst. Met.* **80**, 157 (1951).
11. Cross, "Titanium." Report of Symposium on Titanium. Sponsored by the Office of Naval Research, U.S.A., Paper 13, December, 1948, p. 125. R. L. Bickerdike and D. A. Sutcliffe, *Selected Government Research Report*, Vol. 9, Report 10, p. 153. F. C. Holden, H. R. Ogden, and R. I. Jaffee, *J. Metals*, **5**, 238 (1953).
12. A. T. Churchman, A.E.I. Research Report. To be published.
13. D. E. Bradley, *Brit. J. Appl. Phys.* **5**, 105 (1954).
14. A. T. Churchman and G. A. Geach, *J. Metals* **5**, 1084 (1953).
15. J. B. Hess and C. S. Barrett, *J. Metals* **1**, 599 (1949). E. Orowan, *Nature* **149**, 643 (1942).
16. A. M. Gervais, J. T. Norton, and N. J. Grant, *J. Metals* **5**, 1487 (1953).
17. H. Nishimura and J. Takamura, *Tech. Rep. Eng. Res. Inst., Kyoto University, Japan* **2** (1952), Rep. 12.
18. F. I. Salkavitz and J. S. Koehler, *Acta Met.* **1**, 553 (1953).
19. F. C. Frank and A. N. Stroh, *Proc. Phys. Soc.* **65B**, 811 (1952).
20. G. B. Conard, B. L. Averbach, and M. Cohen, *J. Metals* **5**, 1036 (1953).
21. K. T. Aust, R. Maddin, and N. K. Chen, *J. Metals* **5**, 1477 (1953).
22. R. W. K. Honeycombe, *J. Inst. Met.* **80**, 49 (1951-2).
23. E. Schmid and W. Boas, *Plasticity of Crystals*. Hughes, London, 1950, p. 119.
24. E. N. da C. Andrade and R. Roscoe, *Proc. Phys. Soc.* **49**, 152 (1937).
25. P. Ehrlich, *Z. Anorg. Chem.* **247**, 53 (1941).
26. L. J. Dijkstra, *Trans. A.I.M.M.E.* **185**, 252 (1949). C. J. Smithells, *Metals Reference Book*, London, 1949, p. 318.
27. W. Rostoker, *J. Metals* **4**, 981 (1952).
28. H. T. Clark, *Trans. A.I.M.M.E.* **185**, 588 (1949).



## ON DEFORMATION BY TWINNING\*

F. C. FRANK† and N. THOMPSON

In considerations of the crystallographic directions of loading needed to operate particular twinning systems, due attention is not always paid to the distinction between the strain due to complete twinning and the macroscopic strain due to formation of a thin twin lamella. The subdivision of the orientation diagram according to the twinning system which can be operated by axial loading is a more complicated one than customarily indicated. The hypothesis of a shear stress criterion for twinning leads to a further complexity of subdivision according to the sequence of preference of the various systems permitted within any one region.

### SUR LA DÉFORMATION PAR MACLAGE

Dans les considérations sur le choix des directions cristallographiques le long desquelles on applique la charge pour faire agir un système de maillage, il n'est pas toujours suffisamment tenu compte de la différence entre la déformation due au maillage complet et la déformation macroscopique due à la formation d'une mince lamelle de macle. La subdivision du diagramme d'orientation, d'après le système de maillage qui agit lors de l'application d'une charge axiale, est plus compliquée qu'il n'est habituellement indiqué. L'hypothèse d'un critérium de tension de cisaillement pour le maillage ne fait qu'accroître la complexité du diagramme par la nécessité de subdivision d'après le degré de préférence des divers systèmes permis dans une région donnée.

### ZUR VERFORMUNG DURCH ZWILLINGSBILDUNG

In Betrachtung der kristallographischen Richtung der zur Aktivierung eines bestimmten Zwillingsystems notwendigen Belastung wird der Unterschied zwischen Verzerrungen auf Grund einer vollständigen Zwillingsbildung und makroskopischen Verzerrungen auf Grund der Bildung von dünnen Zwillingslamellen nicht immer genügend beachtet. Die Unterteilung des Orientierungsdiagramms nach Zwillingsystemen, die durch Axialbelastung aktiviert werden können, ist komplizierter als im allgemeinen angegeben. Die Hypothese eines Scherspannungskriteriums der Zwillingsbildung bedeutet eine weitere Komplizierung der Orientierungsteildigramme wegen der nun möglichen Bevorzugung der verschiedenen innerhalb eines Teildigramms auftretenden Systeme.

## INTRODUCTION

The main purpose of this note is to draw attention to a rather trivial but prolific source of error in connection with the deformation of a body by mechanical twinning. When even Barrett falls into the error, it seems necessary to signpost the danger. The essential point is this: when a crystal is *completely* converted into one of its deformation twins, this involving a non-infinitesimal shear of magnitude  $s$ , all directions lying in the (initially) acute sector between the two undeformed planes  $K_1$  and  $K_2^0$  are shortened while all directions lying in the obtuse sector are lengthened. The acute angle in question is conventionally called  $2\phi$  and is equal to  $\arctan(2/s)$ : it is less than 90 degrees by  $\arctan(s/2)$ . On the other hand, if only a thin lamina of twin on the plane  $K_1$  is formed in the crystal, then the distance apart of two points initially separated by a distance large compared with the thickness of the lamina increases or decreases according as the line joining them lies in one or other of the *quadrants* bounded by the plane  $K_1$  and the plane normal to the shear direction. Thus the following sentence, quoted from Barrett<sup>1</sup> is erroneous: "A specimen whose longitudinal axis lies in one of the two regions in the *acute* angle between  $K_1$  and  $K_2^0$  will be shortened by the formation of a twin, while a specimen in the obtuse angle between  $K_1$  and  $K_2^0$  will be

lengthened." Of the two statements in this sentence, the first is true and the second false.

Since mechanical twinning is always a progressive process rather than the sudden conversion of the whole body into its twin, much more importance attaches to the deformation produced by the formation of thin twin lamellae than to that produced by complete twinning. In particular, it is a necessary condition in order that an applied load should produce twinning of a particular kind that it should do positive work for an infinitesimal growth of the twin. This depends only on the sign of the resolved shear stress on the composition plane in the shear direction. It is possible to have an axial load which would do a positive nett amount of work on completion of twinning, but would initially be doing negative work, and therefore inhibiting the process. This is the case for axial tensions lying in the sector of angular width  $\arctan(2/s)$  between the second undeformed plane  $K_2^0$  and the plane normal to the twinning shear direction.

The condition as specified is a necessary one without prejudice to the possible significance of other stress components in influencing twinning: e.g., the possible influence of normal stress on the composition plane, or the possible prior requirement of other deformation processes before twinning commences.

Subsequent writers have been misled by the analysis of elongations in completed twinning due to Schmid and Wassermann<sup>2</sup> which is summarised by Schmid and Boas.<sup>3</sup> The latter treatment does not appear to state the

\* Received April 23, 1954.

† H. H. Wills Physical Laboratory, University of Bristol, England.

error explicitly, but its introduction under the title "Betätigung der mechanischen Zwillingsbildung" for Section 39 undoubtedly makes it a trap even for the fairly wary. There are also some independent errors:—typographical errors in equation (31/1) in the English edition only, and in the last two equations, unnumbered, on the same page in both English and German editions, and a mistake in Fig. 70 where VI and IV should be interchanged on the diagram. (These numbers may alternatively be interchanged in the legend, but continuous counterclockwise numbering appears preferable.) The figure is reproduced, with the same error, as Fig. 36 by Hall.<sup>4</sup> We reproduce it here as our Fig. 1, with this error removed, and Arabic numerals substituted for roman ones to prevent its recurrence. It shows the directions of elongation and contraction in the complete twinning of zinc. Figure 2 shows the more important distribution of elongations and contractions

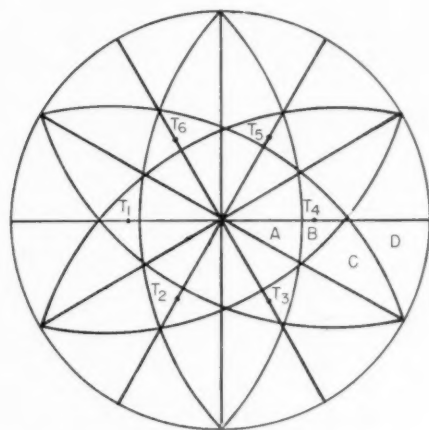


FIG. 1. Change in length as a function of orientation, consequent upon complete twinning of a zinc crystal.  $T_1$ – $T_6$  are poles of twinning planes. A—1–6 contraction. B—2, 3, 5, 6 contraction; 1, 4 extension. C—2, 5 contraction; 1, 3, 4, 6 extension. D—1–6 extension.

accompanying the formation of thin twin laminae in zinc. This diagram has twice as many boundaries and nine instead of four distinct fields in the fundamental triangle. The construction is simple enough: sector boundaries for any one twinning system are great circles 90 degrees away from the pole of its composition plane and from its shear direction respectively; and, for zinc, the elongation is in each case negative in the sector containing the hexad axis. The second boundary is absent from Fig. 1, being replaced by the trace of the second undeformed plane which coincides with the composition plane of the conjugate (or reciprocal) twinning system.

Actually, since the shear in the twinning of zinc is not very large, the additional regions are narrow (4 degrees wide), and since they are near to the boundaries, they are regions of low driving force for the twinning processes concerned. It is therefore not surprising that no one has

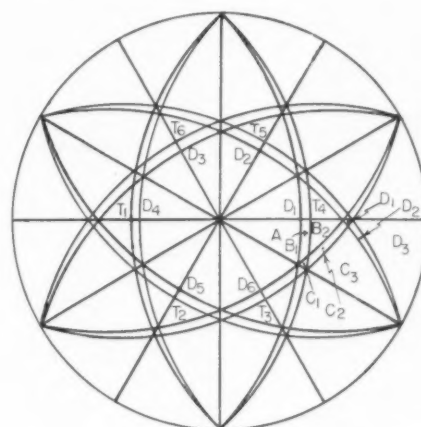


FIG. 2. Change in length as a function of orientation, consequent upon formation of a thin lamellar twin in a zinc crystal.  $T_1$ – $T_6$  are poles of twinning planes.  $D_1$ – $D_6$  are twinning directions.

Those twinning systems giving rise to an increase in length are listed: all others produce a contraction: A—none. B—1. B<sub>2</sub>—1, 4. C<sub>1</sub>—1, 6. C<sub>2</sub>—1, 4, 6. C<sub>3</sub>—1, 3, 4, 6. D<sub>1</sub>—1, 2, 4, 6. D<sub>2</sub>—1, 2, 3, 4, 6. D<sub>3</sub>—all.

pointed out the inadequacy of Schmid and Wassermann's diagram from practical observation. On the other hand, in  $\alpha$ -iron, for which the twinning shear is much larger, the sectors in which complete twinning gives elongation but formation of a thin twin gives contraction have widths of  $19\frac{1}{2}$  degrees. This is a more significant alteration: in particular, the inference from the diagram of Schmid and Boas (their Fig. 71) that tension can in general produce a greater variety of twins than compression is now denied. The appropriate revised diagram is shown here as Fig. 3. The figure is easily constructed by noting that four successive poles on a great circle, say,  $[112]$ ,  $[001]$ ,  $[112]$ ,  $[111]$  represent respectively the pole of a twinning plane, the adjacent cube pole, the pole of its second undistorted plane and its shear direction. Great circles drawn 90 degrees from the first and last of these four poles represent the required spherical quadrant boundaries, and the elongation is positive in the quadrant containing the adjacent cube pole. In the case of complete twinning the second great circle boundary is centred on the third instead of the fourth of these poles, and is itself, of course, the

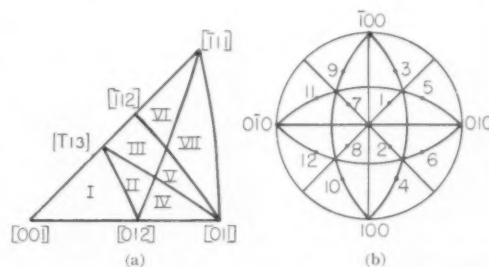


FIG. 3. Twinning in  $\alpha$ -iron. Diagram (a) shows the twinning systems (not necessarily in order of preference) operated by a tensile stress in each area of the fundamental triangle. The numbering follows the scheme of diagram (b).



trace of another twinning plane. The additional boundaries appearing on the revised diagram are the four  $\{111\}$  traces, and only one of them crosses the fundamental triangle.

### THE HYPOTHESIS OF A CRITICAL SHEAR STRESS

So far, our discussion, insofar as it has dealt with stresses, has dealt with a necessary stress condition for twinning. This condition is compatible with, though it does not necessitate, the hypothesis of a critical shear stress condition for twinning. Such a hypothesis states that twinning proceeds if and only if the resolved shear stress on the composition plane resolved in the twinning shear direction, exceeds a critical value. We may conveniently call this resolved stress component the *twinning stress*: no other stress component does any work for an infinitesimal growth of the twin. The hypothesis thus is that twinning proceeds at a critical value of the twinning stress. There is some evidence that in some circumstances (perhaps when plentiful twin nuclei already exist) this may be the case. If so, additional boundaries can be added to our diagram in some of the regions in which the necessary condition allows two or more modes of twinning, dividing these regions into sub-regions in each of which a particular twinning mode is preferred.

Such boundaries will be the loci of those directions of tensile stress which produce equal twinning stresses on two twinning systems. In a hexagonal crystal there are three types of such loci, which may conveniently be described by a nomenclature borrowed from the chemistry of aromatic compounds:

(1) *para-type*, when the two twinning planes concerned are, for example, 1 and 4. The locus has two branches which are readily seen to be (a) the diameter bisecting the line joining the poles of the two twinning planes, and (b) the circumference of the stereographic diagram. This is a trivial case, since both branches coincide with boundaries of the fundamental triangle.

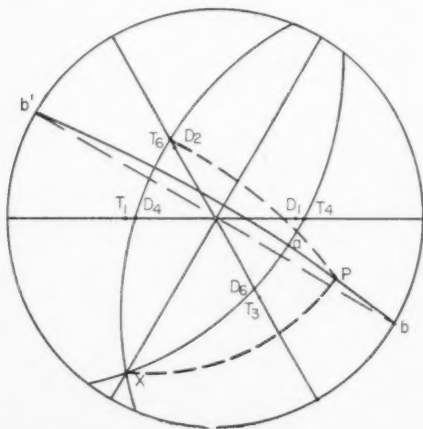


FIG. 4. Twinning in zinc. Geometrical construction to draw the locus ( $b'ab$ ) of directions which produce equal twinning stresses on systems 4 and 6.

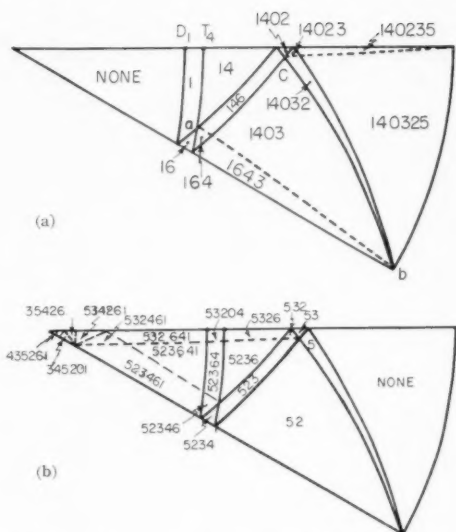


FIG. 5. Formation of thin lamellar twin in zinc. Final subdivision of fundamental triangle. Possible twinning systems are enumerated in order of preference: (a) Tensile stress. (b) Compressive stress.

(2) *meta-type*, when the twinning planes are, for example, 4 and 6. The locus again has two branches (a) the diameter bisecting the join of the two poles—again trivial; (b) a great circle drawn in Fig. 4 as  $b'ab$  and part of which is shown as the arc  $ab$  in Fig. 5a. The construction to obtain this arc is as follows: Denote by  $D_1$  the twinning direction in the plane  $T_1$ , etc. Draw the great circle through  $T_4$  and  $D_6$ ; and also that through  $T_6$  and  $D_4$ . These two will intersect in a point  $X$  which, by symmetry, will lie on the first branch of the locus. The point  $X$  is then the pole of the great circle ( $b'ab$ ) which constitutes the second branch of the locus. This branch passes through the point of intersection of the trace of the twinning plane  $T_6$ , and the zonal boundary which passes through the pole  $T_4$  (point  $a$ , Fig. 5a). A proof of these relations is given in the Appendix.

(3) *ortho-type*, when the twinning planes are, for example, 2 and 3. There are two branches as before, a trivial, diametral one, and a second, in the form of a great circle, which can be obtained by a construction analogous to that used above. The arc  $cd$  in Fig. 5a is part of this branch. Considering the case of a zinc crystal subjected to a tensile stress, these additional boundaries further subdivide four of the previous sub-regions, making a total of 13 sub-regions in all. Moreover, the hypothesis of the existence of a critical stress for twinning permits us to place the various possible modes of twinning in order of preference in each sub-region. This has been done in Fig. 5a. It should be noted that this refinement does not alter the number of permitted twinning modes for any specified direction of stressing; it simply places them in an order of preference, which varies from point to point.

For a zinc crystal subjected to uniaxial compression, Fig. 5b is appropriate. The complexity of this diagram

near the hexad axis implies that many modes of twinning are almost equally likely. Thus small variations in local stress conditions—even, for example, local stresses due to the formation of the first twin,—may start up different systems. Under these conditions we find large numbers of fine twins on many systems. On the other hand, the twins caused by tension at right angles to the hexad axis are usually larger, and in general confined to two systems. The four other systems are permitted, but, unless the stress axis lies close to the points *b* or *d* of Fig. 5a, two systems are much preferred.

## APPENDIX

A. To prove that the curve *b'ab*, Fig. 4, drawn as described in the text, is the required locus.

Let *P* be a point on the curve. Then a tensile stress *F* in the direction *P* produces a resolved shear stress on the plane *T*<sub>6</sub> and in the direction *D*<sub>6</sub>, equal to

$$F \cos PT_6 \cdot \cos PD_6.$$

A similar expression gives the twinning stress on the system *T*<sub>4</sub>, *D*<sub>4</sub>. Thus if *P* lies on the required locus, we have to prove that

$$\frac{\cos PT_6 \cdot \cos PD_6}{\cos PT_4 \cdot \cos PD_4} = 1. \quad (1)$$

Join *P* to the points *X*, *T*<sub>6</sub>, *T*<sub>4</sub>, *D*<sub>6</sub>, *D*<sub>4</sub> by great circles. (For simplicity, only the first two of these lines are drawn in Fig. 4.) Then, referring to the triangle *XPT*<sub>6</sub>, a theorem of spherical trigonometry states

$$\cos PT_6 = \cos T_6 X \cdot \cos PX + \sin T_6 X \cdot \sin PX \cdot \cos P\hat{X}T_6$$

(cf. Schmid and Boas, p. 9 Eng. ed.). But  $PX = \pi/2$ ;

$$\therefore \cos PT_6 = \sin T_6 X \cdot \cos P\hat{X}T_6.$$

Similar expressions can be obtained for the three other quantities involved in (1); the left-hand side of this equation can thus be written:

$$\frac{\sin T_6 X \cdot \cos P\hat{X}T_6 \cdot \sin D_6 X \cdot \cos P\hat{X}D_6}{\sin T_4 X \cdot \cos P\hat{X}T_4 \cdot \sin D_4 X \cdot \cos P\hat{X}D_4}$$

But  $P\hat{X}T_6 = P\hat{X}D_4$  and  $P\hat{X}D_6 = P\hat{X}T_4$  in virtue of the construction used to draw Fig. 4; also  $T_6 X = T_4 X$  and  $D_6 X = D_4 X$  from symmetry. Thus the above expression is equal to unity, and the theorem is established.

B. To prove (i) the circle *b'ab*, (ii) the zone boundary through *T*<sub>4</sub> and (iii) the trace of the twinning plane *T*<sub>6</sub> are concurrent.

Let *a'* denote the point of intersection of the two last-named lines, (ii) and (iii). Then since *D*<sub>4</sub> is the pole of line (ii),  $a'D_4 = \pi/2$ . Also  $a'T_6 = \pi/2$ . Thus *a'* is the pole of the great circle through *D*<sub>4</sub> and *T*<sub>6</sub>. But *X* lies on this great circle; therefore  $a'X = \pi/2$ . But *X* is the pole of the great circle *b'ab*; therefore *a'* lies on the line *b'ab*.

Q.E.D.

## REFERENCES

1. C. S. Barrett, *Structure of Metals* (New York, McGraw Hill 1943 ed.), p. 316; (1953 ed.), p. 383.
2. E. Schmid and G. Wassermann, *Metallwirtschaft*, 1930, V. 9, p. 698.
3. E. Schmid and W. Boas, *Kristallplastizität* (Berlin, Springer, 1935); Eng. ed. *Plasticity of Crystals* (London, F. A. Hughes & Co., 1950).
4. E. O. Hall, *Twinning* (London, Butterworth, 1954).

## SOME APPLICATIONS OF ISOACTIVITY LINES\*

MATS HILLERT†

A connection between phase boundaries and isoactivity lines in isothermal sections of ternary diagrams is shown. Thereby laws relating to these diagrams can be proved in a very simple way.

The connection between the slope of tie-lines and the change in activity along a phase boundary is demonstrated qualitatively and a quantitative formula is derived.

### CERTAINES APPLICATIONS DES LIGNES D'ISOACTIVITÉ

On indique l'existence d'un rapport entre les limites des phases et les lignes d'isoactivité dans des sections isothermes de diagrammes ternaires. De là, les lois se rapportant à ces diagrammes peuvent être démontrées très facilement.

Le rapport existant entre la pente des lignes de conjugaison et la variation de l'activité le long d'une limite de phase, est démontré qualitativement; on déduit aussi une formule quantitative.

### EINIGE ANWENDUNGEN VON ISOAKTIVITÄTSKURVEN

Es wird eine Beziehung zwischen den Phasengrenzen und den Isoaktivitätskurven in den isothermen Bereichen der ternären Diagramme gezeigt. Auf Grund dessen lassen sich die diese Diagramme betreffenden Gesetzmässigkeiten sehr einfach beweisen.

Die Beziehung zwischen der Steigung der Konoden und der Aktivitätsänderung längs der Phasengrenze wird qualitativ erläutert, und es wird eine quantitative Formel abgeleitet.

## INTRODUCTION

An isoactivity line in an isothermal section of a ternary diagram is the locus of all points which represent a certain chemical activity of a component. Such lines afford a very suitable means of presenting the results of activity measurements and have been used for this purpose by, among others, R. P. Smith<sup>1</sup> and J. Chipman.<sup>2</sup> Isoactivity lines also have some general properties which might be of practical value.

It has been shown<sup>3,4</sup> that an isoactivity line for a component cannot intersect a straight line from the component more than once. Figures 1 and 2 show a simple ternary diagram with two one-phase regions and one two-phase region. Tie-lines have been drawn in the two-phase region. The component represented by the right corner is considered. It is self-evident that each tie-line is a part of an isoactivity line, since different compositions along it consists of phases of the same compositions, only in different amounts. The continuations of these isoactivity lines in the one-phase regions

have been drawn in two different ways in Figs. 1 and 2. It is evident that Fig. 2 shows an impossible arrangement, since a straight line from the component is cut three times by an isoactivity line. The direction of tie-lines can thus give some information about isoactivity lines in one-phase regions. By means of this a better understanding has been gained of some phenomena in alloyed iron-carbon-systems.<sup>3</sup> Some other uses of isoactivity lines will be demonstrated in this paper.

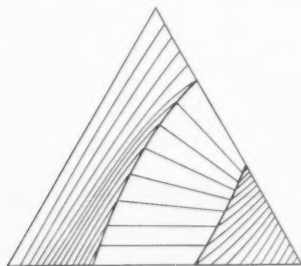


FIG. 1. Possible arrangement of isoactivity lines for the right corner component.

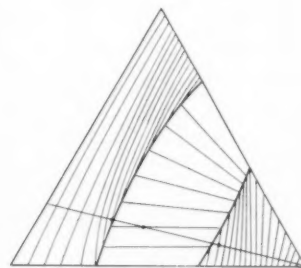


FIG. 2. Impossible arrangement of isoactivity lines for the right corner component.

### I. CONNECTION BETWEEN ISOACTIVITY LINES AND PHASE BOUNDARIES

Figure 3 shows a two-phase region. Three tie-lines have been drawn and the middle one has been extended to the right. Consider a component  $P$ , arbitrarily chosen on this extension. Each tie-line must be part of an isoactivity line for this component (as well as for all other components). Suppose the continuations of these isoactivity lines in the one-phase region form angles with the phase boundary  $ab$  as Fig. 3a demonstrates. Such a straight line can then be drawn from the component, that intersects one of the isoactivity lines twice (in  $d$  and  $e$ ). This is forbidden, as already mentioned in

\* Received May 28, 1954; in revised form June 22, 1954.

† Massachusetts Institute of Technology, Cambridge, Massachusetts.

the introduction. The only way of avoiding this error is to let the isoactivity line through  $g$  be tangent to the phase boundary at this point as Fig. 3b demonstrates.

## II. APPEARANCE OF TERNARY DIAGRAMS

The laws relating to ternary diagrams have been extensively treated by Schreinemakers.<sup>5</sup> Intersections between two phase boundaries in isothermal sections of ternary diagrams were later treated by Lipson and Wilson<sup>6</sup> in a simpler way. Section I in this paper now offers a possibility of an even simpler way of proving the laws relating to isothermal sections. Figure 4 demonstrates this for a specific case.

Consider a sample with the composition represented by the upper corner of the three-phase region. Two components,  $A$  and  $B$ , are chosen on the extensions of

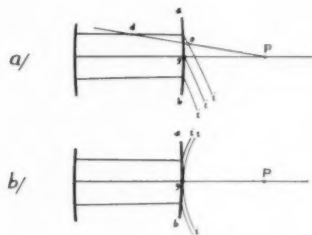


FIG. 3. Isoactivity lines ( $i$ ) for a component  $P$ , chosen on the extension of a tie-line. (a) Impossible case. (b) Possible case.

the two tie-lines from the corner. The isoactivity lines for  $A$  and  $B$  ( $i_A$  and  $i_B$ ) in the one-phase region must be tangent to the phase boundaries at the corner. The right part of Fig. 4 can thus be constructed from the left part. If the  $B$  content is increased in the sample without formation of a new phase, then the  $A$  activity is decreased, since isoactivity lines for  $A$  further away from  $A$  than  $i_A$  are reached. Thus,

$$\frac{\partial a_A}{\partial n_B} < 0 \quad \text{and} \quad \frac{\partial \ln a_A}{\partial n_B} < 0.$$

The  $B$ -activity is, however, increased if the  $A$  content is increased, since then isoactivity lines for  $B$  closer to  $B$  than  $i_B$  are reached. Thus  $(\partial \ln a_B)/(\partial n_A) > 0$ . This is impossible since the two derivatives must be equal:

$$\frac{\partial \ln a_B}{\partial n_A} = \frac{1}{RT} \frac{\partial^2 G}{\partial n_A \partial n_B} = \frac{\partial \ln a_A}{\partial n_B}.$$

The left part of Fig. 4 shows therefore an impossible case. The extensions of the two phase boundaries must lie either both within the three-phase region  $[(\partial \ln a_B)/(\partial n_A)]$  and  $(\partial \ln a_A)/(\partial n_B)$  are both negative] or one on each side  $[(\partial \ln a_B)/(\partial n_A)]$  and  $(\partial \ln a_A)/(\partial n_B)$  are both positive]. Figure 5 illustrates the last case.



FIG. 4. Impossible appearance of ternary diagram.

## III. CHANGE OF ACTIVITY ALONG PHASE BOUNDARIES

It was mentioned in the introduction that the direction of the tie-lines in a two-phase region gives some information about the direction of the isoactivity lines in the one-phase regions. At the same time, the direction of tie-lines also gives information about the change of activity along the phase boundaries.<sup>3</sup> The activity will thus decrease upwards along the phase boundaries in Fig. 1 since each point on the phase boundaries lies on an isoactivity line further away from the component (in this case the right corner) than any lower point. This change in activity can in fact be computed quantitatively.

Let  $(x, y, z)$  and  $(x', y', z')$  be the composition (in mole fraction) of two points, one on each phase boundary and both on the same tie-line. The activities  $a_1, a_2$  and  $a_3$  of the three components must be identical in the two points. The Gibbs-Duhem equation gives:

$$x d \ln a_1 + y d \ln a_2 + z d \ln a_3 = 0, \quad (1)$$

$$x' d \ln a_1 + y' d \ln a_2 + z' d \ln a_3 = 0, \quad (2)$$

$a_3$  can be eliminated:

$$(xz' - x'z) d \ln a_1 + (yz' - y'z) d \ln a_2 = 0, \quad (3)$$

$$\frac{d \ln a_1}{d \ln a_2} = - \frac{yz' - y'z}{xz' - x'z}. \quad (4)$$

Notice that  $z = 1 - x - y$  and  $z' = 1 - x' - y'$ . The coordinates for one of the points can be substituted by the slope of the tie-line, which is

$$k = \frac{y' - y}{x' - x}, \quad (5)$$

if  $x$  and  $y$  are considered as rectangular coordinates. (It is always possible to choose a right-angled triangle for a ternary representation.) The result, which is of general



FIG. 5. Possible appearance of ternary diagram.



validity, will be:

$$\frac{d \ln a_1}{d \ln a_2} = -\frac{k+y-kx}{1-y+kx} \quad (6)$$

It is easy to show geometrically that  $k+y-kx$  is equal to zero if component 1 lies on the extension of the tie-line with the slope  $k$ . Equation (6) then gives  $d \ln a_1 = 0$  and the activity of component 1 does therefore not change in the direction of the phase boundary. This is a rigorous proof of the statement in Section I that phase boundary and isoactivity lines are tangent at the end points of the tie-line, if the component has been chosen on its extension.

Equation (6) can be simplified by some approximations. Consider only dilute solutions, i.e.,  $1-y+kx \cong 1$ , and assume Henry's law holds for component 2 at the point  $(x, y, z)$ , i.e.  $d \ln a_2 = dy/y$ . Equation (6) then simplifies to

$$\frac{d \ln a_1}{dy} = -\left[\frac{k}{y}(1-x)+1\right], \quad (7)$$

which can be integrated easily if  $k/y$  is a constant [related to the partition coefficient  $K$  for component 2 between the two phases by  $k/y = (K-1)/(x'-x)$ ]. This might often be a good approximation. We integrate Eq. (7) from the end-point of the phase boundary on the

$x$ -axis, i.e.,  $y^0=0$ . Let  $a_1^0$  be the activity of component 1 at this point.

$$\ln \frac{a_1}{a_1^0} = -[k(1-x)+y], \quad (8)$$

where  $a_1$  is the activity at an arbitrary point on the phase boundary,  $k$  is the slope of the tie-line from this point and  $y$  is its mole fraction of component 2. If the mole fraction of component 1 varies along the phase boundary,  $x$  should be some mean value.

#### ACKNOWLEDGMENT

The author wishes to thank Professor E. Rudberg, Director of the Swedish Institute for Metal Research, for many valuable discussions during the course of this work and Professor C. Wagner of M.I.T. for his assistance in simplifying the derivations in Section III.

#### REFERENCES

1. R. P. Smith, J. Am. Chem. Soc. **70**, 2724 (1948).
2. J. Chipman, Disc. Faraday Soc. **4**, 23 (1948).
3. M. Hillert, Jernkontorets Annaler **136**, 25 (1952).
4. E. Rudberg, Jernkontorets Annaler **136**, 91 (1952).
5. F. A. Schreinemakers, "Die ternären Gleichgewichte." Braunschweig, 1911, 1913. (Part III of Roozeboom, "Die Heterogenen Gleichgewichte.")
6. H. Lipson and J. C. Wilson, J. Iron and Steel Inst. **142**, 107 (1940).

# SOLUBILITY OF CEMENTITE IN LIQUID IRON\*

MATS HILLERT†

From a theoretical study of the solubility of cementite in liquid iron it is shown that the solubility curves for graphite and cementite intersect at about 10°C below the eutectic temperature. A revised Fe-C diagram is presented which explains some of the solidification characteristics of cast iron.

## LA SOLUBILITÉ DE LA CÉMENTITE DANS LE FER LIQUIDE

En se basant sur une étude théorique de la solubilité dans le fer liquide on montre que les courbes de solubilité pour le graphite et pour la cémentite se rencontrent à environ 10°C en dessous de la température eutectique. Un diagramme Fe-C révisé est présenté. Ce diagramme permet d'expliquer certaines caractéristiques de la fonte.

## DIE LÖSLICHKEIT VON ZEMENTIT IN FLÜSSIGEM EISEN

Es wird auf Grund einer theoretischen Untersuchung der Löslichkeit in flüssigem Eisen gezeigt, dass sich die Löslichkeitskurven für Graphit und Zementit etwa 10°C unterhalb der eutektischen Temperatur schneiden. Es wird ein berichtigtes Fe-C Diagramm veröffentlicht, das einige der Erstarrungseigenschaften des Gusseisens erklärt.

### INTRODUCTION

The solubility of graphite in ferrite, austenite and liquid iron and of cementite in ferrite and austenite are rather well established. There is, however, relatively little information about the solubility of cementite in liquid iron. The only point on this solubility curve known with any accuracy is at the eutectic. Usually the solubility curve for cementite is drawn parallel with that for graphite.<sup>1</sup> Tentative free-energy diagrams for the Fe-C system seem to indicate, however, that the two curves should intersect below the eutectic temperature.<sup>2</sup> Additional evidence for this conclusion will now be presented.

### I. USE OF TERNARY DIAGRAMS

It has been shown that the slope of tie-lines in ternary diagrams provides information about the variation in activity along phase boundaries.<sup>3,4</sup> Figure 1 shows a part of the Fe-C-W diagram at 1085°C.<sup>5</sup> The slope of the tie-lines in the two-phase region austenite+cementite reveals that  $\gamma_1$  (alloyed austenite in equilibrium with both cementite and liquid) has a slightly lower carbon activity than  $\gamma_0$  (unalloyed austenite in equilibrium with cementite). On the other hand the slope of the tie-lines in the two-phase region liquid+cementite shows that  $l_1$  (alloyed liquid in equilibrium with both cementite and austenite) has an appreciably higher carbon activity than  $l_0$  (unalloyed, supercooled liquid in equilibrium with cementite).

$$a_C^{l_0} \ll a_C^{l_1} = a_C^{\gamma_1} < a_C^{\gamma_0}.$$

The carbon activity of the austenite  $\gamma_0$  is known to be 1.03.<sup>6</sup> The carbon activity of the supercooled liquid  $l_0$  should therefore be appreciably less than 1.03 and thus less than that of graphite, which is 1 by definition. The

supercooled liquid  $l_0$ , which is saturated with respect to cementite, is therefore not saturated with respect to graphite. This confirms that the solubility curves for cementite and graphite should intersect below the eutectic temperature and obviously above 1085°C. Thus  $l_0$  is supercooled only with respect to austenite.

The activity change along phase boundaries can be computed quantitatively by the approximate equation (8) in reference 4. It is strictly valid only for dilute solutions but if it is nevertheless applied to the Fe-C-W diagram a value of 0.6 is obtained for the carbon activity of supercooled liquid in equilibrium with cementite at 1085°C. A similar analysis of the Fe-C-P diagram at 950°C<sup>7</sup> gives an activity value 0.35 at 950°C.

### II. USE OF THERMODYNAMIC DATA

From the free-energy data for the Fe-C system compiled by Darken and Gurry<sup>8</sup> it can be deduced that cementite is formed from pure liquid iron and graphite at 1027°C with a decrease in free energy of 3590 cal/mol Fe<sub>3</sub>C. These authors also give equations for the iron and carbon activities in liquid phase. At 1027°C these will be:

$$\ln a_C = \ln x_C - 8.24(l - x_C)^2 + 7.59,$$

$$\ln a_{Fe} = \ln(l - x_C) - 8.24x_C^2.$$

Here,  $x_C$  is the carbon content of the liquid phase expressed as mole fraction. The constant 7.59 has been

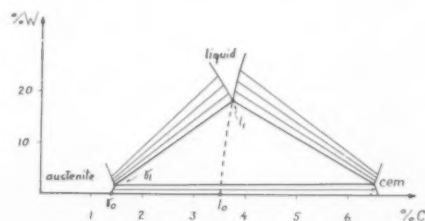


FIG. 1. Detail of the Fe-C-W diagram at 1085°C.

\* Received May 28, 1954; in revised form June 22, 1954.

† Massachusetts Institute of Technology, Cambridge, Massachusetts.

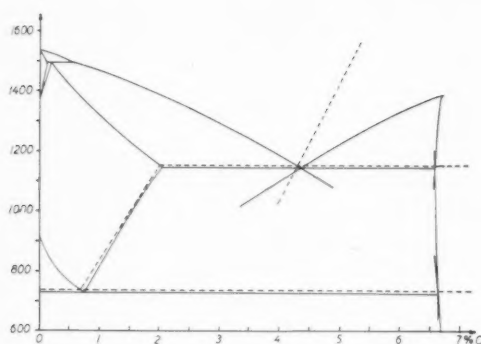


Fig. 2. Fe-C diagram showing the probable solubility curve for cementite in liquid.

found by fitting the equation to the value  $x_C=0.161$  (i.e., 3.95 per cent by weight) for the solubility of graphite in the liquid phase at 1027°C, obtained by extrapolation from higher temperatures. By successive approximations it can be found from these equations, that liquid in equilibrium with cementite at 1027°C has the carbon activity value 0.65. The carbon content of this saturated liquid is 3.4 per cent (i.e.,  $x_C=0.14$ ). The Fe-C diagram in Fig. 2 has been drawn in accordance with this value, which is considered to be more reliable than the values found in section I. The latter indicate a slightly less slope of the solubility curve for cementite.

If the activity equations given by Darken and Gurry are valid for higher carbon content than the solubility value of graphite, it is found that the melting point of cementite is as low as 1210°C. The experimental data underlying these equations are, however, rather limited and cementite has therefore, quite arbitrarily, been given a higher melting point in Fig. 2.

Since it has been shown by three different methods that the solubility curves for graphite and cementite intersect below the eutectic temperature, this may be considered a well-established fact. The temperature of intersection seems to be about 10°C below the eutectic temperature of cementite. The peritectic equilibrium between liquid, graphite and cementite at this temperature is of course metastable with respect to austenite.

### III. SOLIDIFICATION OF CAST IRON

White cast-iron contains cementite whereas grey cast-iron contains graphite. It is well known that rapid cooling and low carbon content promote white solidifi-

cation, i.e., formation of cementite. Slow cooling and high carbon content promote grey solidification, i.e., formation of graphite. These facts can now be explained by means of the Fe-C diagram.

If a eutectic liquid is cooled very slowly it precipitates graphite and austenite and it never becomes supersaturated with respect to cementite. If the liquid is cooled just below the eutectic temperature for cementite + austenite, then it becomes supersaturated with respect to cementite but is still more supersaturated with respect to graphite. The supersaturation with respect to cementite, however, increases more rapidly with further decrease in temperature than the supersaturation with respect to graphite. Below the temperature, where the two solubility curves for cementite and graphite intersect, the liquid can be said to be more supersaturated with respect to cementite than graphite. Graphite in equilibrium with liquid is here metastable with respect to cementite. Thus a rapid cooling should promote formation of cementite. It should be noted that the equilibria between graphite and liquid and between cementite and liquid are both metastable with respect to austenite at these temperatures. As soon as austenite has been formed in contact with the cementite, graphite becomes stable with respect to cementite.

The Fe-C diagram also shows that a liquid, richer in carbon, must become more supersaturated with respect to graphite before it becomes supersaturated with respect to cementite. Thus high carbon content should promote grey solidification and low carbon content should promote white solidification.

### ACKNOWLEDGMENT

The author wishes to thank Professor E. Rudberg, director of the Swedish Institute for Metal Research, for many valuable discussions during the course of this work.

### REFERENCES

1. Metals Handbook, A.S.M. 1182 (1948).
2. M. Hillert, Discussion, J. Iron and Steel Inst. **178**, 158 (1954).
3. M. Hillert, Jernkontorets Annaler **136**, 25 (1952).
4. M. Hillert, "Some Applications of Isoactivity Lines," (this issue of Acta Met.).
5. S. Takeda, Techn. Rep. of Tôhoku Imp. Univ. **10**, 42 (1931).
6. L. S. Darken and R. W. Gurry, J. Metals **3**, 1015 (1951).
7. R. Vogel, Arch. f. d. Eisenhüttenwesen **3**, 369 (1929).
8. L. S. Darken and R. W. Gurry, Physical Chemistry of Metals, McGraw-Hill, New York, 1953.

# LATTICE AND GRAIN BOUNDARY SELF-DIFFUSION IN CADMIUM\*

E. S. WAJDA,† G. A. SHIRN,‡ and H. B. HUNTINGTON‡

The bulk and grain boundary diffusion in cadmium of 99.5 per cent purity have been measured as a function of temperature. The bulk diffusion constants as measured in single crystals are given by

$$D_{\text{BH}} = 0.05 \text{ cm}^2/\text{sec} \exp(-18,200 \text{ cal/mol-RT})$$

and

$$D_{\text{GL}} = 0.10 \text{ cm}^2/\text{sec} \exp(-19,100 \text{ cal/mol-RT}),$$

where  $D_{\text{BH}}$  and  $D_{\text{GL}}$  refer respectively to diffusion parallel and perpendicular to the hexagonal axis. The grain boundary diffusion gave  $D_b = 1.0 \text{ cm}^2/\text{sec} \exp(-13,000 \text{ cal/mol-RT})$ . These results are compared with analogous values obtained for zinc. The implication for the determination of mechanism is in this case less clear cut.

## L'AUTO-DIFFUSION DANS LE RÉSEAU ET LES JOINTS INTERCRISTALLINS DU CADMIUM

On a mesuré l'auto-diffusion en fonction de la température dans le réseau et les joints inter cristallins de cadmium 99.5% pur. Les constantes de diffusion dans le réseau, mesurées dans des monocristaux, sont données par les équations suivantes:

$$D_{\text{BH}} = 0.05 \text{ cm}^2/\text{sec} \exp(-18\,200 \text{ cal/mol-RT})$$

et

$$D_{\text{GL}} = 0.10 \text{ cm}^2/\text{sec} \exp(-19\,100 \text{ cal/mol-RT}),$$

où  $D_{\text{BH}}$  et  $D_{\text{GL}}$  se rapportent respectivement à la diffusion parallèlement et perpendiculairement à l'axe hexagonal. Pour la diffusion dans les joints inter cristallins on a trouvé la valeur  $D_b = 1.0 \text{ cm}^2/\text{sec} \exp(-13\,000 \text{ cal/mol-RT})$ . Ces résultats sont comparés aux valeurs analogues, obtenues pour le zinc. Les implications menant à la détermination du mécanisme sont, dans ce cas-ci, moins bien définies.

## DIE GITTER- UND KORNGRENZENSELBSTDIFFUSION IN KADMIUM

Die Volumen- und Korngrenzendiffusion von 99.5% reinem Kadmium wurde als Funktion der Temperatur gemessen. Die folgenden Diffusionskonstanten wurden für die Volumendiffusion in Einkristallen experimentell ermittelt:

$$D_{\text{BH}} = 0.05 \text{ cm}^2/\text{sec} \exp(-18\,200 \text{ Kal/mol-RT})$$

und

$$D_{\text{GL}} = 0.10 \text{ cm}^2/\text{sec} \exp(-19\,100 \text{ Kal/mol-RT})$$

wobei sich  $D_{\text{BH}}$  und  $D_{\text{GL}}$  auf die Diffusion parallel resp. senkrecht zur hexagonalen Achse beziehen. Im Falle der Korngrenzendiffusion ergab sich ein  $D_b = 1.0 \text{ cm}^2/\text{sec} \exp(-13\,000 \text{ Kal/mol-RT})$ . Die Ergebnisse werden mit den entsprechenden Resultaten für Zink verglichen. Ihre Konsequenzen in Bezug auf die Klarlegung des Elementarvorganges sind in diesem Falle weniger augenfällig.

## I. INTRODUCTION

In a previous paper<sup>1</sup> an investigation of the self-diffusion in zinc was described showing a definite anisotropy for the diffusion process along the  $c$ -axis of the hexagonal zinc structure and perpendicular to it. In another paper<sup>2</sup> the grain boundary self-diffusion in zinc was reported. The activation energy for grain boundary diffusion turned out to be 61 per cent of that for the bulk diffusion in the case of zinc.

A similar investigation has now been carried out for cadmium which also has a hexagonal structure with a  $c/a$  ratio of 1.886, 1.6 per cent larger than that of zinc. This work herein described gives the results for the activation energy and the temperature-independent factor in the diffusivity which will be compared to those obtained for zinc.

## II. EXPERIMENTAL TECHNIQUE

The experimental techniques used in this investigation were largely the standard ones for the plating, sectioning studies of diffusion. Details available in the earlier zinc papers<sup>1,2</sup> will be omitted here.

Single crystals of cadmium were grown from 99.5 per cent purity by the Bridgman method and only those specimens whose figure axis was within 10 degrees of being either parallel or perpendicular to the specimen axis were retained. Properly oriented crystals were selected by a method suggested from the work on "punching" by Smakula<sup>3</sup> as follows. Upon indenting the surface of a crystal to be oriented with a sharply pointed tool such as a scribe, a strain pattern results which is definitely correlated with the orientation of the crystal. This correlation is easily seen when the pattern is made on a crystal of known orientation. The strain pattern in cadmium takes the form of a pair of lobes radiating from the punch mark at 180 degrees. The center line of these lobes is always perpendicular to the basal planes of the crystal. A few of these patterns suffice to orient the

\* Received June, 1954.

† Now at Department of Physics, Union College, Schenectady, N. Y.

‡ Department of Physics, Rensselaer Polytechnic Institute, Troy, New York.



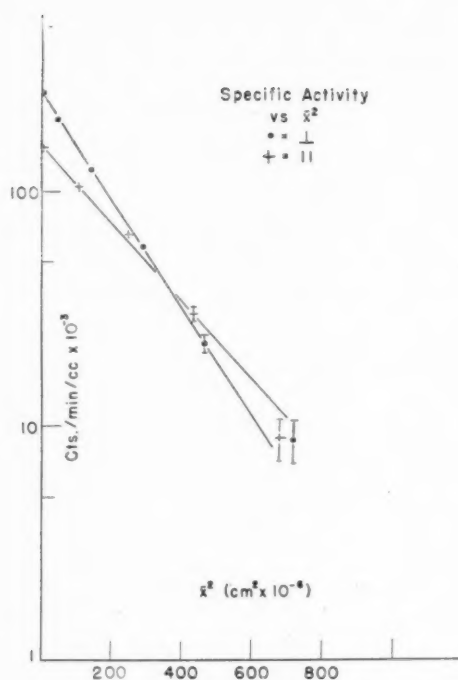


FIG. 1. Perpendicular and parallel diffusion.

crystal. This method is much faster than the X-ray technique employed on the zinc crystals in reference 1. The orientation of the crystals can be made easily to within 5 degrees, which is sufficiently accurate for this investigation. So long as the specimen axis lies within 10 degrees of either the hexagonal axis or basal plane, the orientation can be disregarded in calculating  $D_{\parallel}$  or  $D_{\perp}$  without introducing an error of more than 3 per cent.

Briefly, the properly oriented crystals were cut to size, etched to remove smear, annealed to check possible

TABLE I.

Crystal no.	$D_p$ (cm <sup>2</sup> /sec)	$1/T$ (°K) <sup>-1</sup>	Crystal orientation
3	$19.7 \times 10^{-10}$	$1.852 \times 10^{-3}$	⊥
4	23.4	1.852	
6	39.6	1.795	
8	7.29	1.961	⊥
9	10.1	1.961	
10	2.45	2.115	
11	1.89	2.115	⊥
12	0.727	2.260	
13	0.474	2.260	⊥
14	70.6	1.718	⊥
15	84.3	1.718	
18	57.0	1.757	⊥
19	73.4	1.715	⊥
20	44.3	1.786	⊥
21	0.065	2.457	⊥
25	0.045	2.490	⊥
26	0.081	2.490	

FIG. 2.  $\log D_p$  vs  $1/T$  (single crystals).  
Symbol + for  $D_{\parallel}$ ; o for  $D_{\perp}$ .

recrystallization and electrodeposited with  $\text{Cd}^{115}$ . This cadmium isotope has a half-life of 43 days and is predominantly a 0.5 Mev gamma-emitter. The plating bath used a  $\text{Cd}(\text{OH})_2\text{-NaCN}$  type and gave a thin, even deposit. The prepared specimens were diffused at various temperatures and corresponding times ranging from 5 hours to 3 months. After cutting 1 mil sections from the specimens in a lathe, the cuttings from each section were dissolved in a 50 per cent nitric acid solution and, to insure uniform geometry for counting, were sealed in glass tubes. The activity was then measured with an automatic G. M. counter.<sup>4</sup> Good counting statistics were obtained in times of the order of an hour.

The polycrystalline specimens were made by melting the 99.5 per cent purity cadmium and casting into slugs, which were quenched to achieve a small size of crystallites. These crystallites displayed a marked radial orientation just as in the case of zinc.<sup>2</sup> The size of these crystallites was about  $0.06 \text{ mm} \times 3 \text{ mm}$ . The specimens were treated exactly the same as the single crystal samples, except that lower temperatures and longer diffusion times were used. The experimental procedure was the same as outlined in reference 2.

### III. RESULTS

The single crystal data were analyzed in the standard manner as described in reference 1 by plotting the logarithm of the activity of each section against the penetration distance squared as required by the theory of homogenous diffusion. The slope of this curve is proportional to the diffusion coefficient. Typical radio-

activity-penetration curves at  $T=237^\circ\text{C}$  are shown in Fig. 1. A definite anisotropy is noted between the plots for  $D_{\perp}$  and  $D_{\parallel}$ . The measured values for the self-diffusion coefficient for the two crystallographic orientations in the temperature range from  $110^\circ\text{C}$  to  $315^\circ\text{C}$  are shown in Table I.

Under the assumption that the temperature-dependence of the diffusion constant is described by

$$D = D_0 \exp(-Q/RT),$$

one plots the logarithm of  $D$  against  $1/T$  and the slope and intercept will give the activation energy ( $Q$ ) divided by  $R$  and the temperature-independent part of the diffusivity ( $D_0$ ) respectively. A plot of the data is shown in Fig. 2. A least-square fit for these data gives the following values for the activation energy and frequency factor,

Parallel	Perpendicular
$Q = 18.2 \pm 0.3 \text{ kcal/mol}$	$Q = 19.1 \pm 0.7 \text{ kcal/mol}$
$D_0 = .05 \text{ cm}^2/\text{sec}$	$D_0 = .10 \text{ cm}^2/\text{sec}$

The polycrystalline data are here interpreted on the basis of Fisher's analysis,<sup>5</sup> which predicts a linear relation between the logarithm of the activity of the sections with the penetration distance. The analytical expression for the ratio of the volume diffusion constant to the grain boundary diffusion constant is

$$D_v/D_b = \frac{\delta(\pi D_v t)^{1/2}}{2} \left[ \frac{d \ln a}{dy} \right]^2,$$

where  $a$  is the isotope activity per unit volume, at a

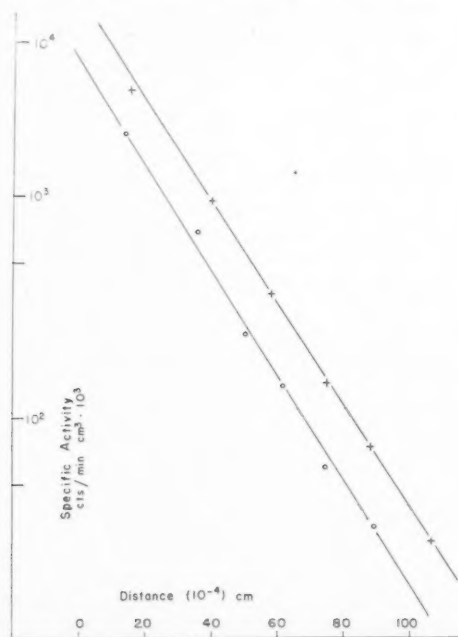


FIG. 3. Polycrystalline diffusion. Symbol + for run at  $T=105^\circ\text{C}$  with  $t=792$  hours;  $\circ$  for run at  $T=85^\circ\text{C}$  with  $t=1080$  hours.

TABLE II.

Crystal no.	(Polycrystals) $D_b$ ( $\text{cm}^2/\text{sec}$ )	$1/T$ ( $^\circ\text{K}$ ) $^{-1}$
1	$146 \times 10^{-10}$	$2.792 \times 10^{-3}$
2	1320	2.551
3	62.6	2.872
4	284	2.646
5	3540	2.383
9	61.2	2.965
11	17.1	3.086
14	275	2.732
15	272	2.732
16	30.0	3.040

distance  $y$ , measured in a direction normal to the free surface on which the original isotope was deposited;  $t$  is the diffusion time; and  $\delta$  is the thickness of the uniform grain boundary. As in the case of zinc,<sup>2</sup>  $\delta$  was assumed to be about  $5 \times 10^{-8} \text{ cm}$ . Typical activity-penetration curves for grain boundary diffusion are shown in Fig. 3. The individual diffusion measurements are given in Table II.

A plot of the logarithm of the  $D_b$  against the reciprocal temperature is shown in Fig. 4. A least-square fit, applied to the points in the low-temperature range, gives the following results for the activation energy and temperature independent factor:

$$Q_b = 13.0 \pm 1.2 \text{ kcal/mol},$$

$$D_0 = 1.0 \text{ cm}^2/\text{sec}.$$

#### IV. CONCLUSIONS

In one respect the results for the self-diffusion of cadmium give less clear information as to the mechanisms involved than did the comparable data for zinc. For zinc the difference in activation energy for  $D_{\parallel}$  and

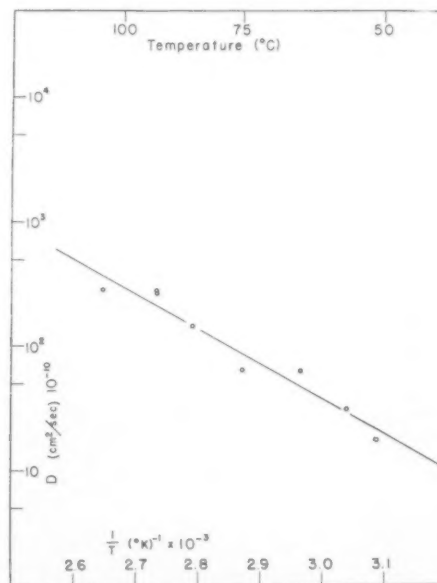


FIG. 4.  $\log D_b$  vs  $1/T$  (Polycrystals).

TABLE III.

Mechanism	$D_L/D_{II}$ (HCP) ( $c/a = 1.63$ )	$D_L/D_{II}$ (Cd) ( $c/a = 1.89$ )
1. Interstitial	1	0.75
2. Ring of four	1	0.75
3. Vacancy (non-basal)	0.25	0.187
4. Vacancy (basal)	$\infty$	$\infty$
5. Ring of three (basal)	$\infty$	$\infty$
6. Ring of three (non-basal)	0.63	0.487

(The above-mentioned mechanisms are fully described in reference (1).)

$D_L$  was considerably larger than the r.m.s. deviations for  $Q_{II}$  and  $Q_L$  as calculated statistically. For cadmium this difference is about 1 Kcal/mol and is roughly comparable to the r.m.s. deviations ( $\sigma_{II} = 0.44$  Kcal/mol and  $\sigma_L = 1.0$  Kcal/mol). Whereas for zinc it was quite unlikely that the observed results could be attributed to a single activation energy, for the case of cadmium the plots of  $\ln D_e$  vs  $1/T$  are more nearly parallel and the possibility of the single process cannot be eliminated with reasonable certainty. From statistical reasoning for random events it can be concluded that, for any observed difference in activation energies  $\Delta Q = Q_L - Q_{II}$ , the relative probability that other observed data arise from a process with a single activation rather than from two separate processes with separate activation energies is given by  $\exp\{-[(\Delta Q)^2/(\sigma_L^2 + \sigma_{II}^2)]\}$ . This quantity in the present case is .45. One concludes that there is approximately an equal statistical probability for either one or two processes on the basis of present data. It should be pointed out that this probability calculation takes into account no correlation between  $Q_{II}$  and  $Q_L$ . Since they both refer to processes in the same material and manifest in the same temperature range, such a correlation does exist and it is not surprising that, if two mechanisms are

at work here, the task of resolving them experimentally is difficult.

The effect of different mechanisms on the ratio of  $D_L/D_{II}$  in hexagonal metals has been developed from geometrical considerations. The values for  $D_L/D_{II}$  for six reasonably possible mechanisms are given in Table III for the close packed hexagonal lattice and for cadmium ( $c/a = 1.89$ ). From the table it is apparent, that if only one mechanism is operative, it may be either the interstitial mechanism (1) or ring of four (2). If the observed difference in  $Q$  is truly significant and a pair of processes is operative, then either mechanism 3 (or possibly 6) which favor  $D_{II}$  could be coupled with either of the basal mechanisms 4 or 5.

In the case of zinc it seemed reasonably clear that at least one or possibly two vacancy mechanisms were operative. Here the situation is much less clear but one is tempted to assume that analogous mechanisms are at work.

Further comparison with zinc shows that though the  $c/a$  ratio is greater for cadmium the diffusion constant is less anisotropic. As for  $Q_b$  the activation energy for grain boundary diffusion, it appears that the ratio of  $Q_b/Q_e$  is some 7 per cent higher for cadmium.

#### ACKNOWLEDGMENT

This work was supported by a contract with the Atomic Energy Commission.

#### REFERENCES

1. G. A. Shirn, E. S. Wajda, and H. B. Huntington, *Acta Met.* **1**, 513 (1953).
2. E. S. Wajda, *Acta Met.* **2** (1954).
3. A. Smakula, *Phys. Rev.* **84**, 1043 (1951).
4. G. A. Shirn and E. S. Wajda, *Nucleonics* **10**, 30 (1952).
5. I. Fisher, *J. Appl. Phys.* **22**, 74 (1951).

# KINETICS OF PRECIPITATION OF TIN FROM LEAD-TIN SOLID SOLUTIONS\*

D. TURNBULL and H. N. TREAFIS†

At all temperatures,  $T$ , and initial solute concentrations,  $X_0$ , investigated the first rapid stage of precipitation of tin,  $\beta$ , from lead,  $\alpha$ , is effected by the nucleation and growth of cells. Each cell consists of a multiplicity of  $\beta$ -plates, originating from a single nucleus, interspersed in the depleted  $\alpha$ . Independently of  $T$  and  $X_0$ , the kinetic law of precipitation is, with rare exceptions:

$$x = 1 - \exp(-bt^3).$$

This kinetic law is consistent with the hypothesis that all nuclei originate at the beginning of precipitation within a limited number of singular elements of the structure. Precipitation proceeds  $10^7$  to  $10^8$  times faster than calculated from Seith and Laird's data on the rate of diffusion of tin into lead. The precipitation rate is greatly increased by cold-working the supersaturated  $\alpha$ .

## LA CINÉTIQUE DE LA PRÉCIPITATION DE L'ÉTAIN À PARTIR DES SOLUTIONS SOLIDES PLOMB-ÉTAIN

A toutes les températures,  $T$ , et concentrations initiales,  $X_0$ , considérées, le premier stade rapide de précipitation d'étain,  $\beta$ , à partir de plomb,  $\alpha$ , s'effectue par la germination et la croissance de cellules. Chaque cellule consiste en une multiplicité de lamelles de  $\beta$  provenant d'un seul germe, qui parsèment le  $\alpha$  appauvri. Indépendamment de  $T$  et  $X_0$  la loi cinétique de la précipitation est, avec de rares exceptions:

$$x = 1 - \exp(-bt^3).$$

Cette loi cinétique est compatible avec l'hypothèse que tous les germes naissent au début de la précipitation dans un nombre limité d'éléments simples de la structure. La précipitation est  $10^7$  à  $10^8$  fois plus rapide que ne l'indique le calcul basé sur les données de Seith et Laird concernant la vitesse de diffusion de l'étain dans le plomb. La vitesse de la précipitation est considérablement accrue par l'écrouissage de l' $\alpha$  sursaturé.

## DIE KINETIK DER AUSSCHIEDUNG VON ZINN AUS FESTEN BLEI-ZINN LÖSUNGEN

Das erste, schnelle Stadium der Ausscheidung von Zinn,  $\beta$ , aus Blei,  $\alpha$ , ist bei allen untersuchten Temperaturen  $T$  und Ausgangskonzentration von  $X_0$  der gelösten Komponente, durch die Keimung und das Wachstum von Zellen beeinflusst. Jede Zelle besteht aus einer Vielzahl von  $\beta$  Plättchen, die von einem einzigen Keim ausgehen und Zwischen denen sich das verarmte  $\alpha$  befindet. Unabhängig von  $T$  und  $X_0$  ist das kinetische Gesetz der Ausscheidung mit wenigen Ausnahmen

$$x = 1 - \exp(-bt^3).$$

Dieses kinetische Gesetz steht im Einklang mit der Hypothese, dass alle Keime beim Beginn der Ausscheidung innerhalb einer begrenzten Anzahl spezieller Stellen im Gefüge entstehen. Die Ausscheidung erfolgt  $10^7$  bis  $10^8$  mal schneller als nach den Angaben von Seith und Laird über die Diffusionsgeschwindigkeit für Zinn und Blei berechnet. Die Ausscheidungsgeschwindigkeit wird durch Kaltbearbeitung des übersättigten  $\alpha$  stark erhöht.

## INTRODUCTION

Borelius and co-workers<sup>1,2,3</sup> have measured the rate of precipitation of tin ( $\beta$ -phase) from lead-rich solid solutions ( $\alpha$ -phase). Their results were shown to be apparently in agreement with the Borelius-Konobeyevski (B-K) theory of nucleation. On the other hand, Hardy<sup>4</sup> showed that the results also appeared to be consistent with the Becker theory of nucleation. (See review of Hollomon and Turnbull<sup>5</sup> for detailed discussion of these theories.) The interpretations of Borelius *et al.* and Hardy presupposed that nucleation is effected in structurally pure (excepting for point defects)  $\alpha$ -crystals. No satisfactory explanation was offered for the kinetic law of precipitation. By the kinetic law we mean  $x = f(t)$  where  $x$  is the fraction of precipitation (to be quantitatively defined later) that has taken place isothermally in time  $t$ .

\* Received June 25, 1954.

† General Electric Research Laboratory, Schenectady, New York.

Inferences about the rate of nucleation in a precipitation process are of doubtful validity in the absence of a satisfactory theory for the kinetic law. Also, there are some other important characteristics of the precipitation behavior in lead-tin that are not explained by the Borelius or Hardy interpretations.

Seith and Laird<sup>6</sup> have reported that the interdiffusion coefficient,  $D$ , of lead and tin in  $\alpha$  containing 2 atom per cent tin can be described as a function of absolute temperature,  $T$ , by the equation

$$D = 4.0 \exp[-26,000/RT] \text{ cm}^2 \text{ sec}^{-1}. \quad (1)$$

If it is assumed that the rate of diffusion of tin during precipitation is described by  $D$ , it follows that in a 10-minute period at 300°K tin could be drained from an  $\alpha$ -region having a linear extent of 2 to 3 Å. Actually, for an initial atom fraction of tin in  $\alpha$  of  $\sim 0.15$ , the first rapid stage of precipitation is nearly completed in 10 minutes and microstructural observations indicate that the thickness of the depleted  $\alpha$  region is of the order of a micron. Hence, during precipitation the diffusion coefficient



cient of tin atoms is apparently  $10^7$  to  $10^8$  times larger than is predicted by Eq. (1). The precipitation measurements were made on solutions initially much more concentrated than used in Seith and Laird's measurements; nevertheless it would be very surprising if the rate of diffusion of tin in  $\alpha$  increased by a factor of  $10^7$  when the atom fraction,  $X$ , increases from 0.02 to 0.10. Thus it is likely that the rate of precipitation of tin is many orders of magnitude larger than is predicted from the appropriate volume diffusion data. This rapid rate of precipitation might be accounted for either (a) by the presence of a much greater than equilibrium number of point defects during precipitation, as suggested by Zener<sup>7</sup> and Seitz,<sup>8</sup> or (b) by the drainage of tin from solution along diffusion short circuits sweeping the solid solution in advance of the precipitate. It has been demonstrated<sup>9</sup> that elements of incoherent grain boundaries and dislocation channels are about equally effective short circuits in self-diffusion.

Borelius *et al.*<sup>1</sup> report the time,  $\tau$ , required for the isothermal half completion of precipitation as a function of  $T$  and the initial atom fraction,  $X_0$ , of tin in  $\alpha$ . They find that  $d \ln(1/\tau)/dT$  is dependent on  $X_0$  when the temperature exceeds a characteristic value  $T'$ , but independent of  $X_0$  for  $T < T'$ .  $T'$  is a function of  $X_0$ . To explain this result, Borelius and Hardy assume that the thermodynamic part,  $\Delta G^*$ , of the potential energy barrier to nucleation becomes negligible at  $T = T'$ . However, for  $T < T'$ ,  $1/\tau$  is still strongly dependent upon  $X_0$ ; for example, at  $T = 273^\circ\text{K}$  (a temperature well below  $T'$  for  $X_0 = 0.100$ )  $1/\tau$  is 500 times larger for  $X_0 = 0.235$  than for  $X_0 = 0.100$ . For precipitation limited only by diffusion, we expect  $1/\tau$  to be at most directly proportional to  $X_0$ , so there seems to be a factor of at least 100 in the variation of  $1/\tau$  with  $X_0$  not accounted for by the Borelius and Hardy interpretations.

Because of these inadequacies in the Borelius and Hardy interpretations, we have reinvestigated the kinetics of precipitation of tin from lead-tin solid solutions for the purpose of establishing the kinetic law and its relation to the individual rates of nucleation and growth of the precipitate particles.

### EXPERIMENTAL

Precipitation was followed by measuring the resistance of the alloys as a function of time at constant temperature.

#### Preparation of Alloys

Alloys were made from American Smelting and Refining Co., 99.999 per cent pure lead, and Vulcan Detinning Co., 99.997 per cent pure tin. Wires 20–30 mils in diameter and 2–4 inches in length were made for the resistance measurements. Most of the wires (cast wires—C) were cast in Pyrex tubes of uniform capillary bore 20 to 25 mils in diameter. In this operation specified amounts of the pure metals are placed in bulb A of the

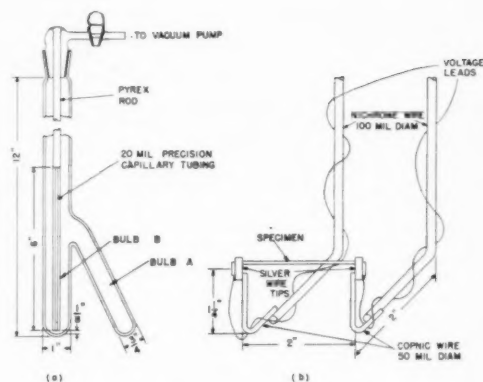


FIG. 1. Schematic diagram of (a) wire casting vessel, and (b) specimen mounting.

vessel shown in Fig. 1a. The vessel is evacuated (to 10 to 100 micron pressure of mercury) and partly immersed in a furnace held at a temperature exceeding the melting point of the alloy. The melt is then run from bulb A to bulb B and a portion of it forced into the capillary by the pressure of an inert gas. The entire apparatus is then rapidly cooled so that the alloy in the capillary solidifies. The cast wire is easily removed from a capillary tube that is clean initially. After each casting operation the vessel was thoroughly cleaned and a new capillary sealed in. The alloy remaining after preparation of the wire was analyzed for tin (to  $\pm 1$  part in 100). Before beginning a series of measurements the wire was sealed in an evacuated pyrex tube and homogenized at  $225^\circ\text{C}$  for a period of at least 15 hours.

A few of the wires were extruded (extruded wire—E) from 1/2-inch diameter specimens chill cast in a graphite coated copper mold after melting in air.

#### Resistance Measurements

An approximately 2-inch length of lead-tin wire was mounted across two silver tipped 1/16 inch diameter constantan rods as shown in Fig. 1b. The wire and copper potential leads were secured to the silver tips by solder having the same composition as the resistance specimen. The nichrome rods were held on a transite backing secured to a 1/2 inch diameter supporting rod that could be displaced vertically in either direction. (The axes of the nichrome and supporting rods were vertical.)

To determine resistance, a current of 1.000 ampere (held constant to within 1 part in  $10^5$ ) was passed through the wire and the resulting drop in potential (between the copper potential leads) was measured as a function of time. The potential determinations were accurate to about  $10^{-5}$  volt corresponding to  $10^{-5}$  ohm in resistance. The magnitude of the resistance change,  $\Delta R$ , during the rapid stage of precipitation ranged from approximately 0.002 to 0.006 ohm out of a total resistance of 0.04 to 0.08 ohm. Hence, the uncertainty in  $\Delta R$  is about 1 part in 200 to 600.

### Homogenization

For heat treating the wires, a rectangular nichrome wound furnace, having chamber dimensions 1×5 inch and 3 inch high, was positioned about 3 inch directly above the constant temperature bath. The furnace chamber was closed excepting for a small slot at the bottom that admitted the wire and its supporting rods. Argon gas, preheated by circulation through a copper coil wound around the inner surface of the furnace, was passed through the chamber during heat treatment. For temperature measurement the hot junction of a thermocouple was positioned in the vicinity of the wire midpoint. Temperatures along the whole length of the wire between the silver terminals deviated no more than 10° from the chamber temperature at 250°C. Prior to a precipitation rate measurement, the wire was heated at 250°C (about 80–100 degrees higher than the equilibrium homogenization temperature) for one hour.

### Procedure

All the necessary electrical connections for measuring  $R = f(t)$ , where  $R$  is the wire resistance, were made before homogenization. Hence, after the heat treatment the wire was plunged directly into a constant temperature bath; the standard current started and timing begun. The bath was thermostated to  $\pm 0.1^\circ\text{C}$ . Silicone oil served as the bath fluid excepting for  $0^\circ\text{C}$  an ice bath (with an arrangement to keep pieces of ice from contacting the wire) was used.

The rate of resistance change with time,  $dR/dt$ , at first increases from zero to a maximum  $(dR/dt)_m$  and then decreases as time increases. Resistance was recorded until  $dR/dt$  had fallen to a value approximately 1 per cent of  $(dR/dt)_m$ . The points to be shown in the figures were calculated from resistances read from continuous recorder curves.

We have given in Table I the initial resistance,  $R_0$ , (rounded off at the fourth place for tabulation) of a particular wire (3C) as a function of temperature. Also given is  $\Delta R$  which is defined by:

$$\Delta R = R_0 - R_f, \quad (2)$$

where  $R_f$  is the resistance at the time that  $(dR/dt)$  has fallen to  $(1/50)(dR/dt)_m$ .

TABLE I. Variation of resistance change,  $\Delta R$ , for a single wire during precipitation with  $T$ .  $X_0 = 0.147$  (Wire 3C).

$T^\circ\text{K}$	$R_0$ (ohms)	$\Delta R$ (ohms)		$\Delta R/R_0$
		Exp.	Calc.	
273	0.0728	0.0063	(0.0063)	0.087
288	0.0763	0.0063	0.0062	0.083
303	0.0806	0.0062	0.0059	0.077
320	0.0852	0.0057	0.0056	0.067
333	0.0887	0.0051	0.0052	0.057
348	0.0926	0.0045	0.0046	0.049
358	0.0952	0.0039	0.0041	0.041
373	0.0992	0.0029	0.0032	0.029

It is interesting that for a given wire:

$$\Delta R \propto X_0 - X_e, \quad (3)$$

where  $X_e$  is the equilibrium atom fraction of tin in  $\alpha$ . From the data of Borelius *et al.*,<sup>1</sup> we deduce the approximate dependence of  $X_e$  on  $T$  to be:

$$\log X_e = -\frac{1210}{T} + 2.11. \quad (4)$$

Table I also compares the experimental  $\Delta R$  at various temperatures with the value of  $\Delta R$  calculated assuming the validity of Eq. (3). For all temperatures the agreement between the two values of  $\Delta R$  is excellent.

### RESULTS

Much exploratory work was done in this investigation and it is not practicable to report all of the results in detail. Therefore, we shall describe the representative findings of most significance and state the largest deviations from these that were found.

### The Kinetic Law

We now give a more precise definition of the fraction,  $x$ , of precipitation that has occurred in time,  $t$ , as follows:

$$x = \frac{X_0 - X_t}{X_0 - X_f}, \quad (5)$$

where  $X_t$  is the "apparent" atom fraction of tin in  $\alpha$  at time  $t$ ,  $X_f$  is the "final" value of  $X$  but is not necessarily identical with  $X_e$ . In order to obtain  $x = f(t)$  we must relate some property of the precipitating system, such as resistance, to  $x$ .

It is expected that the specific energy,  $E_t$ , evolved isothermally during precipitation should be approximately proportional to the amount of precipitate per unit mass of alloy. Nystrom<sup>2</sup> measured  $E_t = f(t)$  for the precipitation of tin from lead using an isothermal calorimeter. Assuming  $x \propto E_t$ , he finds for  $x \rightarrow 0$  that

$$x = bt^n, \quad (6)$$

where  $n = 3$  for low temperatures and  $n = 4$  for "high" temperatures and initial concentrations. Equation (6) probably derives from the more general law of precipitation:

$$x = 1 - \exp(-bt^n). \quad (7)$$

Borelius *et al.*<sup>1</sup> have shown one isothermal relationship  $R = f(t)$  for  $X_0 = 0.192$  and  $T = 359$ . If it is assumed that  $x$  is related to  $R_t$  by the following equation:

$$x = \frac{R_0 - R_t}{R_0 - R_f}, \quad (8)$$

where  $R_t$  is the wire resistance at time  $t$ ,  $x = f(t)$  is described by Eq. (7) with  $n = 3.0$  for  $x \leq 0.5$ . For the

lowest initial concentrations and temperatures reported by Nystrom, and assuming the validity of Eq. (8), our results are best described by Eq. (7) with  $n=3.0$ . Hence, there is an excellent correspondence between the kinetic law calculated from calorimetric data and that obtained from resistance data with the use of Eq. (8).

On the basis of this agreement we have used Eq. (8) to convert all of our results from  $R_t = f(t)$  to  $x = f(t)$ . In this calculation  $R_f$  is defined, as before, to be the resistance at the time that  $(dR/dt)$  has fallen to  $(1/50)(dR/dt)_m$ . Hence,  $X_f$  must exceed  $X_e$ . The assumed relation between  $R$  and  $x$  is probably a poor approximation for  $x \geq 0.5$ .

We find that  $R_f$  is related to  $R_\infty$ , the resistance at  $t = \infty$ , by:

$$(R_0 - R_f) \sim 0.6(R_0 - R_\infty).$$

The very marked decrease in precipitation rate when  $\Delta R \sim 0.6(R_0 - R_\infty)$  was also observed by Borelius *et al.*<sup>1</sup> This effect is not due to a peculiarity of the electrical

TABLE II. Summary of kinetic data on some cast wires.  $T_c = f(X_0)$  is temperature at which, according to Borelius,  $\Delta G^*$  should disappear.

Temp., °K	$n$	$\dot{x}_{0.2}$ (min <sup>-1</sup> )	-Log $b$
Wire No. 17C $X_0 = 0.112$ (6.8 wt. per cent) $T_c = 298$			
273	3.2	0.0072	6.26
298	2.8	0.0167	5.04
315	2.9	0.0185	4.91
323	2.9	0.0163	4.94
330	3.0	0.0157	5.21
353	3.0	0.0041	6.98
$\bar{n} = 3.0$			
Wire No. 2C $X_0 = 0.147$ (9.0 wt. per cent) $T_c = 320$			
273	2.9	0.035	4.20
282		0.052	3.68
288		0.066	3.37
294		0.074	3.22
303	3.1	0.089	2.98
319	2.7	0.096	2.88
333	3.1	0.089	2.98
348	2.7	0.057	3.56
363		0.026	4.58
373	3.0	0.0063	6.43
$\bar{n} = 2.9$			
Wire No. 3C $X_0 = 0.147$ (9.0 wt. per cent) $T_c = 320$			
273	3.1	0.042	3.96
288	3.2	0.086	3.03
303		0.119	2.60
320		0.135	2.44
333	2.9	0.125	2.53
348	2.8	0.089	2.98
358		0.062	3.45
373	3.1	0.0159	5.23
$\bar{n} = 3.0$			
Wire No. 15C $X_0 = 0.170$ (10.5 wt. per cent) $T_c = 330$			
273	3.0 <sub>5</sub>	0.130	2.49
309		0.412	0.98
321	3.1	0.426	0.93
334		0.44	0.89
353	2.9	0.292	1.44
373	3.4	0.109	2.71
393	3.3	0.0079	6.14
$\bar{n} = 3.1_5$			

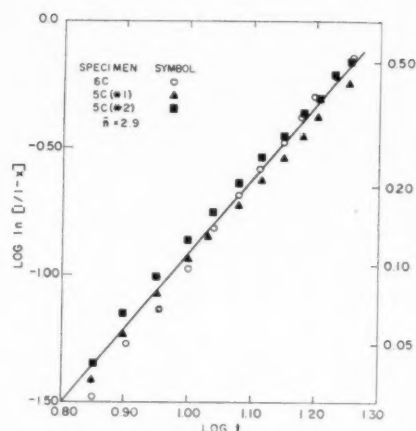


FIG. 2. Dependence of  $\text{Log ln}[1/(1-x)]$  on  $\text{log } t$  for two cast wires.  $T = 273^\circ\text{K}$ ,  $X_0 = 0.147$ .

behavior of the precipitating system, for calorimetric data, kindly sent to us by Professor Borelius, indicated a similar sharp decrease in  $dX_t/dt$  at  $X_0 - X_c \sim 0.7(X_0 - X_c)$ .

Therefore, we conclude that precipitation occurs in two stages possibly described by two kinetic laws. The first rapid stage drains 60 per cent of the thermodynamic excess of tin from solution and the remainder is drained out in a second very slow stage. It may be that drainage of tin in the fast reaction is effected primarily by diffusion short circuits but the slow reaction is limited by lattice diffusion.

We shall now describe our results on the first stage of precipitation.

Rates of precipitation,  $dx/dt = \dot{x}$ , in different cast wires or in a succession of experiments on one wire for a constant degree of precipitation  $x = c$ , temperature, and initial atom fraction of tin generally agreed to within 12 percent  $[(dx/dt)_c = \dot{x}_c]$ . However, there was a single cast wire in which  $\dot{x}_c$  differed as much as 33 per cent in a succession of experiments. Among different cast wires of the same composition the precipitation rates (shown in Table II) in wires 2C and 3C exhibit the widest disagreement (a total error of  $2\frac{1}{2}$  parts per 100 in the tin analyses would account for this disagreement). The maximum scatter in  $\dot{x}_c$  for the extruded wires ( $T$ ,  $X_0$  constant) was larger than for the cast wires and often exceeded 20 per cent. The rate measurements of Borelius *et al.* apparently scatter as widely as ours for extruded wires.

The differences in  $\dot{x}_c$  for a given specimen are often substantially larger than the measurement errors and seem to indicate changes in the specimen. A wire might change in a succession of experiments in (a) initial homogeneity of composition, (b) average composition, (c) microstructure—including such fine structural details as the dislocation distribution. We found that for a particular wire  $R_0$  was reproduced to 1 part in 4000 in a succession of experiments where  $\dot{x}_c$  differed as much as 33 per cent. Considering that the total change in  $R$  during

precipitation was 320 parts in 4000 and no trend in  $\dot{x}_c$  was discerned in successive experiments, we conclude that the scatter in  $\dot{x}_c$  is probably due primarily to microstructural changes that occur in successive homogenization and precipitation treatments.

To indicate the order of reproducibility of the data the results of three experiments at 273°K on two cast wires of the same composition ( $X_0=0.147$ ) are shown as  $\log \ln[1/(1-x)]$  vs  $\log t$  plots in Fig. 2. The linearity of the curve is consistent with Eq. (7) and the slope of the composite line  $\bar{n}=2.9$ .

If a single kinetic law (i.e., one value of  $n$ ) applies, it should be possible to superpose  $x=f(t)$  relations by multiplying the unit of time for each isotherm by a suitable factor,  $f$ , "superposition factor." All of the isothermal relations were thus superposable. Figures 3a and 3b show the superposition of representative isotherms for two cast wires. The curves were made to coincide at  $x=0.5$  with  $f=1.00$  at 273°K.

For  $x \geq 0.5$  all isotherms are satisfactorily described by a straight line relation between  $\log \ln[1/(1-x)]$  and  $\log t$  as predicted by Eq. (7). The slopes,  $n$ , of these lines for each of four cast wires, having  $X_0$  ranging from 0.112 to 0.170, at a series of temperatures are given in Table II.  $\bar{n}$ , the average  $n$  value, is also shown. The relation between  $\log \ln[1/(1-x)]$  and  $\log t$  at representative temperatures for three of the wires are shown in Figs. 4a, 4b, and 4c.

The average of all the  $n$ -values for cast wires is 3.0 with a mean deviation of  $\pm 0.15$  and, excepting for one specimen, the maximum deviation is 0.4. In a single cast

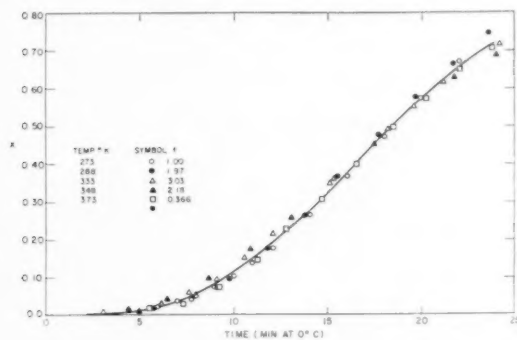


FIG. 3a. Superposition of kinetic relations for different temperatures. Wire 3C,  $X_0=0.147$ .

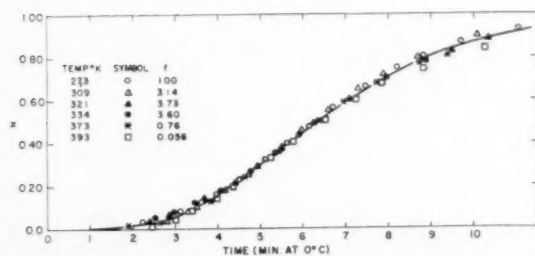


FIG. 3b. Superposition of kinetic relations for different temperatures. Wire 15C,  $X_0=0.170$ .

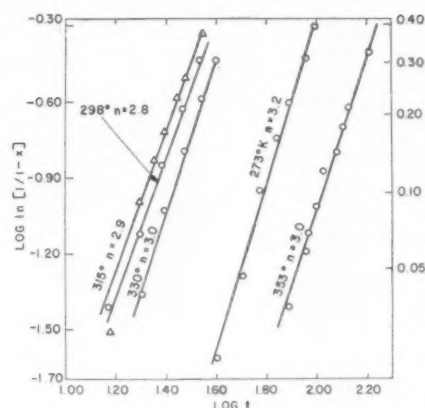


FIG. 4a. Dependence of  $\text{Log} \ln[1/(1-x)]$  on  $\log t$  at various temperatures. Wire 17C,  $X_0=0.112$ .

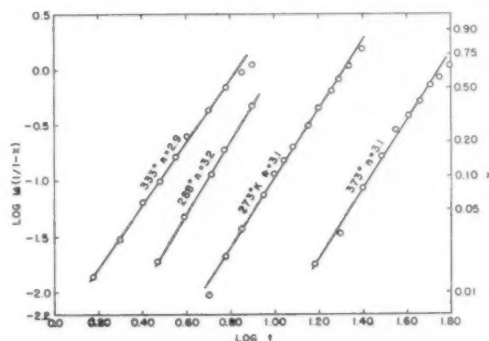


FIG. 4b. Dependence of  $\text{Log} \ln[1/(1-x)]$  on  $\log t$  at various temperatures. Wire 3C,  $X_0=0.147$ .

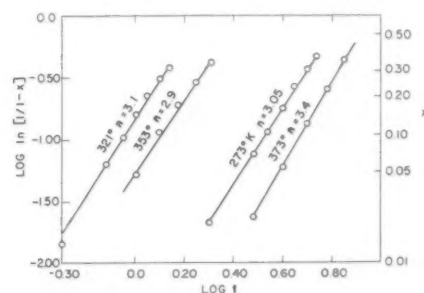


FIG. 4c. Dependence of  $\text{Log} \ln[1/(1-x)]$  on  $\log t$  at various temperatures. Wire 15C,  $X_0=0.170$ .

specimen (21C,  $X_0=0.170$ ) the maximum deviation exceeded 0.4,  $n$  being 2.3 in two successive experiments at 273°K. There is no discernible trend of  $n$  with either  $X_0$  or  $T$ .

Isotherms for the extruded wires also were well described by Eq. (7) as is shown in Fig. 5, but the slopes of these lines (see, for example, Table III) tended to scatter more widely than did those for the cast wires.

#### Dependence of Precipitation Rate on Temperature

From Eq. (7) with  $n=3$ , we obtain

$$\dot{x} = 3b^{1/3}(1-x)[- \ln(1-x)]^{2/3}. \quad (9)$$



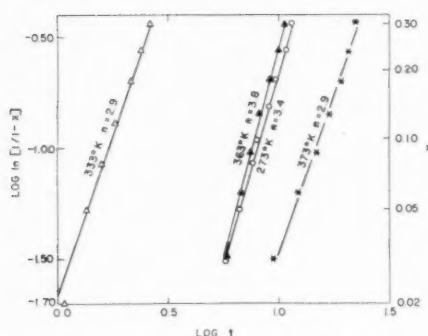


FIG. 5. Dependence of  $\text{Log ln}[1/(1-x)]$  on  $\text{log } t$  at various temperatures for an extruded wire.  $X_0=0.147$ .

Hence,

$$\dot{x}_c = A_c b^{1/3}, \quad (10)$$

where  $A_c = 3(1-c)[- \ln(1-c)]^{2/3}$ . Let  $t = \tau_c$  when  $x = c$ . It then follows:

$$1/\tau_c = B_c b^{1/3}, \quad (11)$$

where  $B_c = [\ln(1/(1-c))]^{-1/3}$ . Combining (10) and (11) we get:

$$\dot{x}_c = (A_c/B_c)(1/\tau_c). \quad (12)$$

Hence it follows for constant  $X_0$ :

$$d \ln(1/\tau_c)/d(1/T) = d \ln \dot{x}_c/d(1/T) = d \ln(b^{1/3})/d(1/T), \quad (13)$$

and for constant  $T$ :

$$d \ln(1/\tau_c)/dX_0 = d \ln \dot{x}_c/dX_0 = d \ln(b^{1/3})/dX_0. \quad (14)$$

Thus, the shapes of the  $\ln \dot{x}_c$  vs  $1/T$  or  $X_0$  and  $\ln(1/\tau_c)$  vs  $1/T$  or  $X_0$  curves will be identical for all values of  $c$ . Borelius<sup>11</sup> curves of  $\ln(1/\tau_{1/2})$  vs  $1/T$  and  $X_0$  therefore also describe the shapes of the  $\ln(b)^{1/3}$  vs  $1/T$  or  $X_0$  curves as well as the shapes of  $\ln \dot{x}_c$  vs  $1/T$  or  $X_0$  for any value of  $c$ .

$\text{Log } b$  for each of the representative isotherms is given in Tables II and III. However, for purposes of interpreting the results of thermal cycling experiments, it is more convenient to consider the variation of precipitation rate with temperature and initial tin concentration. Therefore, we have also listed in Tables II and III  $\dot{x}_{0.2}$  for each of the isotherms.

In Fig. 6,  $\ln \dot{x}_{0.2}$  is plotted against  $1/T$  for each of the initial concentrations. These points are shown as circles and the curves through them are solid. The shapes of these curves are qualitatively very like the shapes of the

TABLE III. Summary of kinetic results on an extruded wire ( $X_0=0.147$ ).

Temp. °K	$n$	$\dot{x}_{0.2}$ (min <sup>-1</sup> )	$-\text{Log } b$
273	3.4	0.062	3.45
333	2.9	0.229	1.71
363	3.8	0.068	3.33
373	2.9	0.032	4.45
$\bar{n} = 3.25$			

$d \ln(1/\tau_{1/2})$  vs  $1/T$  relations found by Borelius *et al*<sup>11</sup> at the corresponding initial concentrations. Below some temperature  $T'$  characteristic of  $X_0$ ,  $d \ln \dot{x}_{0.2}/d(1/T)$  becomes virtually independent of  $X_0$ . Our relationship between  $T'$  and  $X_0$  agrees within experimental error with  $T' = f(X_0)$  found by Borelius *et al*.

Although we are in fair agreement with Borelius *et al* on the dependence of precipitation rate on temperature and initial concentration, the absolute magnitudes of our rates are considerably less than they report. In Fig. 7,  $\ln(1/\tau_{1/2})$  vs  $1/T$  found for a cast wire (25C,  $X_0=0.124$ ) in this investigation is compared with  $\ln(1/\tau_{1/2}) = f(1/T)$  reported for the same composition by Borelius *et al*. Our  $1/\tau_{1/2}$  values are about a factor of 2 to 3 smaller than the corresponding values of Borelius *et al*. We found that the rates in extruded wires are significantly larger than in cast wires (cf. Tables II and III). Our conclusion is that the absolute magnitude of the precipitation rates are considerably dependent upon the concentration of structural impurities in the solid

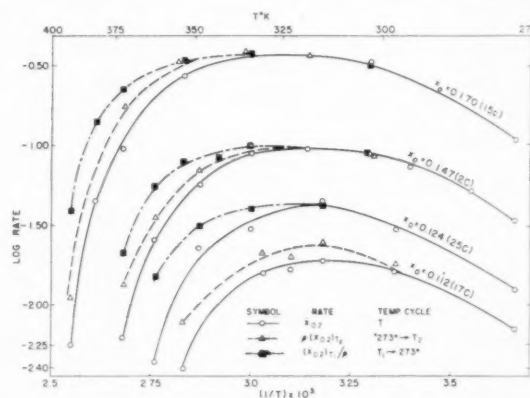


FIG. 6. Dependence of logarithm of precipitation rate (at  $x=0.2$ ), after various temperature cycling treatments, on  $1/T$ .

solution. These results further demonstrate the invalidity of interpretations of existing kinetic data for this system assuming homogeneous nucleation and growth of precipitate particles in structurally pure crystals.

### Results of Thermal Cycling Experiments

Thermal cycling experiments sometimes provide information that is useful in separating the nucleation and growth components of precipitation rates.\* In such experiments precipitation is completed at a temperature  $T_2$  after having been begun at a different temperature  $T_1$ . The initial rate of precipitation,  $\dot{x}'_i$  at the second temperature, where  $(x = x_i)_{T_2}$ , should be due only to the growth of  $\beta$  particles nucleated at  $T_1$ . Thermal cycling experiments in which the first temperature  $T_1$  is greater than the second temperature  $T_2$  will be designated as down-cycling experiments and the inverse type of ex-

\* See, for example, Wert's<sup>10</sup> experiments on the precipitation of carbide and nitride from  $\alpha$ -iron.

periment in which  $T_2 > T_1$  as up-cycling experiments. In either event the precipitation rate at the second temperature  $T_2$  and degree of precipitation  $x=c$ , will be denoted by the symbol  $\dot{x}'_c$ . Tests in which precipitation begins and goes to completion at the same temperature will be designated direct precipitation experiments and the corresponding precipitation rate denoted by  $\dot{x}_c$ . It may be possible to relate  $\dot{x}'_c/\dot{x}_c$  to  $N'/N$  where  $N'$  and  $N$  are the number of nuclei operative at  $T_2$  as a result of the thermal cycling and direct precipitation processes, respectively.

Let  $x = f(t)$  for direct precipitation at  $T_2$ , and  $x = f_1(t)$  at  $T_2$  after some prior precipitation at  $T_1$ .  $f_1(t)$  is defined to coincide with  $f(t)$  at  $x = x_i$ . Initially we calculated  $f_1(t)$  on the assumption that the resistance,  $R$ , of any wire would be a single function of  $x$ , at constant temperature, independently of thermal history. Figure 8 compares  $f(t)$  and  $f_1(t)$  so calculated from a series of experiments in which  $X_0 = 0.147$ ,  $T_1 = 373$  and  $T_2 = 273^\circ\text{K}$ .  $f_1(t)$  calculated in this way approaches a

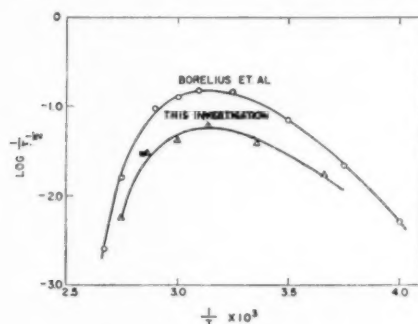


FIG. 7. Comparison between precipitation rates obtained by Borelius *et al* and in this investigation for  $X_0 = 0.124$ . (Our wire 25C).

limiting value less than unity,  $x_l$ , that is smaller the larger is  $x_i$ . Table IV gives  $1 - x_l$  for each  $x_i$ .

This failure of  $f_1(t)$  to approach unity and the apparent dependence of  $1 - x_l$  on  $x_i$  is accounted for if it is assumed that:

1. Precipitation is effected by the growth of "cells." Each cell consists of a multiplicity of  $\beta$ -particles, all originating from a single nucleus, interspersed in  $\alpha$ .
2. The atom fraction,  $X_f$ , of tin within a cell formed at temperature,  $T$ , is related to the equilibrium concentration,  $X_e$ , of tin at that temperature by the equation:

$$\frac{X_0 - X_f}{X_0 - X_e} = C, \quad (15)$$

where  $C$  is temperature independent. The basis of this relation is not yet understood.

3. Upon quenching to  $T_2$  there is no appreciable precipitation of tin within the parts of cells grown at  $T_1$ .

Until swept over by a cell boundary, the concentration of tin in the supersaturated solution remains at  $X_0$ .

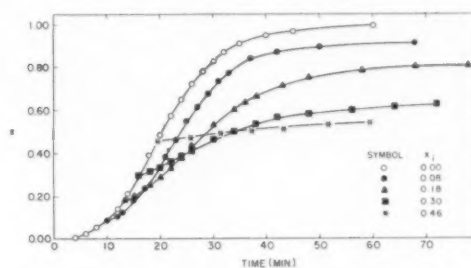


FIG. 8. Dependence of  $x$  on  $t$  at  $273^\circ\text{K}$  after prior precipitation at  $373^\circ\text{K}$  to apparent  $x = x_i$ . Wire 18C,  $X_0 = 0.147$ .

Thus,  $f(t)$  must be identified with the volume fraction of the specimen transformed by the growth of the cells. In a thermal cycling experiment, cells nucleated at one temperature will develop a two layer structure upon growth at a second temperature. This structure will consist of a "core" formed at  $T_1$ , wherein the final tin concentration  $X_f = X_0 - C[X_0 - (X_e)_1]$ , and a "shell" formed at  $T_2$ , wherein  $X_f = X_0 - C[X_0 - (X_e)_2]$ .  $X_e$  is given by Eq. (4). Since the final tin concentration within

TABLE IV. Comparison between  $1 - x_l$  and  $f_v(t) - f_1(t)$ .

$x_i$ (uncorrected)	$(1 - x_l)$	$f_v(t) - f_1(t)$
0.0	0.0	0.0
0.04	0.04	0.04
0.08	0.09	0.08
0.18	0.19	0.18
0.23	0.22	0.23
0.30	0.36	0.30
0.46	0.44	0.46

a cell element is determined by the temperature at which it formed it is evident that the specimen resistance cannot be a single function of  $x$  at constant temperature.

With the use of the assumptions explained above, we can calculate the correction that must be applied to convert  $f_1(t)$  to transformed volume fraction,  $f_v(t)$ . This correction,  $f_v(t) - f_1(t)$ , should be equal to  $1 - x_l$ .  $1 - x_l$  and  $f_v(t) - f_1(t)$ , obtained from the results on wire 18C, are in excellent agreement as may be seen from Table IV.  $f_v(t)$  from this series of experiments is plotted against  $t$  in Fig. 9. Here the initial transformed volume fractions,

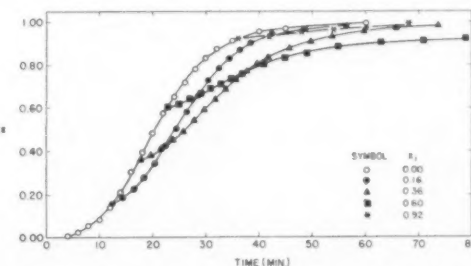


FIG. 9. Same results as Fig. 8 but with  $x$  and  $x_i$  corrected to correspond to transformed volume fraction.

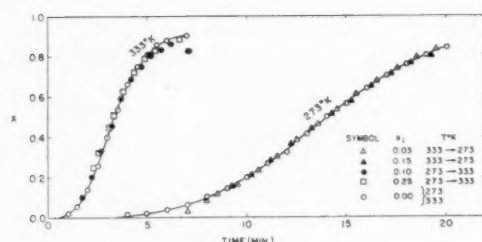


FIG. 10. Dependence of  $x$  on  $t$  at  $T_2$  after prior precipitation to  $x = x_i$  at  $T_1$ .  $T_1 < T'$  and  $T_2 < T'$ . Extruded wire,  $X_0 = 0.147$ .

$x_i$ , at  $T_2$  have been corrected by the addition of  $f_v(t) - f_1(t)$ .

Where both  $T_1$  and  $T_2$  were less than a characteristic temperature,  $T_m$ , the precipitation rate proved to be independent of the thermal cycling treatment, at least for  $x_i \leq 0.2$ . In this event,  $f_v(t) = f(t)$ . Figure 10 shows the excellent correspondence between  $f_v(t)$  and  $f(t)$  for an extruded wire cycled between 333°K and 273°K. Similar results from experiments with a cast wire are given in Fig. 11.  $T_m$  corresponds, within experimental error, to the temperature  $T'$  at which  $d \ln \dot{x}_c / d(1/T)$  becomes independent of  $X_0$ . These results indicate that the distribution of cell number with size at constant  $x$  is independent of temperature when  $T < T'$ .

When  $T > T'$ , the precipitation rate is clearly dependent upon thermal history (see Fig. 8). Figure 12 compares the kinetic relations,  $f_v(t)$  and  $f(t)$ , obtained from cycling an extruded wire from a low ( $T_1 = 273^\circ\text{K}$ ) to a higher temperature ( $T_2 = 373^\circ\text{K}$ ). For this composition ( $X_0 = 0.147$ )  $273 < T' < 373^\circ$ . At  $373^\circ$   $\dot{x}'_{0.2} / \dot{x}_{0.2} = 1.7$ .

A series of up-cycling experiments were carried out with  $T_1 = 273^\circ\text{K}$  and the initial volume fraction precipitated at this temperature,  $x_i$ , approximately equal to 0.02. The logarithms of the resulting precipitation rates at  $x = 0.2$  [ $\log \dot{x}'_{0.2} = \log \rho \dot{x}_{0.2}$ ] are shown (triangular points) as a function of  $1/T$  and  $X_0$  in Fig. 6.  $\rho$  is defined by the equation:

$$\rho = \dot{x}'_c / \dot{x}_c. \quad (16)$$

When  $T_2$  is less than the characteristic temperature, the rates at  $T_2$  resulting from up-cycling and direct precipitation are equal. However,  $\dot{x}'_{0.2} > \dot{x}_{0.2}$  when  $T_2 > T'$ .

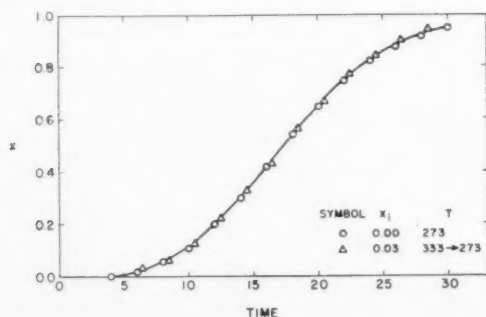


FIG. 11. Dependence of  $x$  on  $t$  at  $273^\circ\text{K}$  after prior precipitation to  $x = x_i$  at  $333^\circ\text{K}$ . Wire 4C,  $X_0 = 0.147$ .

Down-cycling experiments were carried out with  $T_2 = 273^\circ\text{K}$  and  $T_1$  varied between  $393^\circ$  and  $298^\circ\text{K}$ . Figures 13a and 13b show several down-cycling isotherms  $x = f_v(t)$  at  $273^\circ\text{K}$  corresponding to various temperatures  $T_1$  of initial precipitation for cast wire 20C,  $X_0 = 0.147$ . In these experiments  $\rho$  was evaluated from the initial rate of precipitation at  $273^\circ\text{K}$ , i.e., at  $x = x_i$ . When  $T_1$  exceeded the characteristic temperature the initial precipitation rate at  $273^\circ\text{K}$  was less than the corresponding direct precipitation rate but these rates ( $\dot{x}_i$  and  $\dot{x}'_i$ ) were equal when  $T_1 < T'$ . In Fig. 6  $\log(\dot{x}_{0.2}/\rho)$  (square points) from the down-cycling experiments is plotted against  $1/T$  for different  $X_0$ . Here  $\rho$  is evaluated at  $x = x_i$  and  $(\dot{x}_{0.2}/\rho) = f(T_1)$ .

### Effect of Cold Working

It is well known<sup>11</sup> that cold-working a supersaturated solid solution greatly increases the rate of precipitation. We did not attempt a complete evaluation of the effect of cold-working on the precipitation of  $\beta$  from  $\alpha$  but made a few experiments on this effect that are pertinent to the evolution of our interpretation.

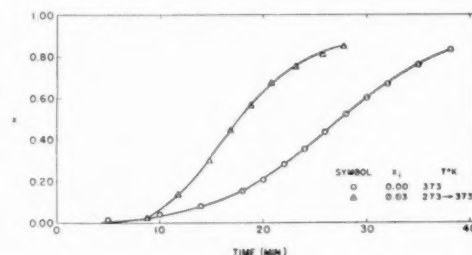


FIG. 12. Dependence of  $x$  on  $t$  at  $373^\circ\text{K}$  after prior precipitation to  $x = x_i$  at  $273^\circ\text{K}$ . Extruded wire,  $X_0 = 0.147$ .

The change of resistance of a cold-worked supersaturated solution is the sum of two factors, one due to recovery and the other to precipitation. However, we found that the displacement of resistance due to cold-working the  $\alpha$  at a low temperature is negligible in comparison with the total change in resistance due to precipitation at a low temperature, e.g.,  $273^\circ\text{K}$ . Therefore, it appears that  $x = f(t)$ , for a cold-worked specimen, calculated with the use of Eq. (8) should have at least qualitative validity.

Figure 14 shows the effect of straining an extruded wire at liquid nitrogen temperature 9 per cent in tension prior to precipitation at  $273^\circ\text{K}$ . Figure 15 compares  $x = f(t)$  for a cast wire at  $273^\circ\text{K}$  (a) without prior strain and (b) hammered flat at  $273^\circ\text{K}$  immediately after quenching from the homogenization temperature (in a period short in comparison with the precipitation time).

From these and other of our results we conclude the following:

1. Cold-working the  $\alpha$  greatly increases the rate of tin precipitation. The effect increases with strain and  $\dot{x}_c$

for a hammered specimen was as much as four times larger than  $\dot{x}_c$  for a specimen that had not been strained.

2. There is no such simple functional relationship between  $x$  and  $t$  as Eq. (7) for strained specimens. If we attempt to describe the data with Eq. (7),  $n$  is less than 3.0 and decreases with increasing  $x$ .

3. The effect of strain on  $\dot{x}_c$  is most pronounced in the early stages of precipitation. For  $x > 0.6$  there appears to be little difference between  $\dot{x}_c$  values for the hammered and unstrained specimen (see Fig. 15).

### Microstructural Observations

We deduced from the kinetic results that the precipitate must form by the growth of cells containing a

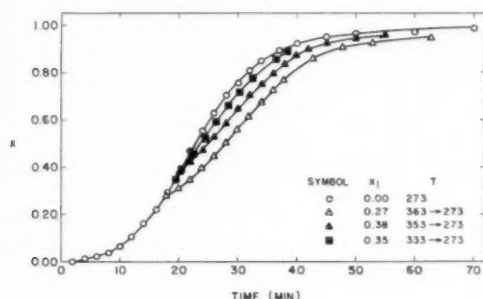


FIG. 13a. Dependence of  $x$  on  $t$  at 273°K after prior precipitation to  $x_i$  at  $T_1$ . Wire 20C,  $X_0=0.147$ .

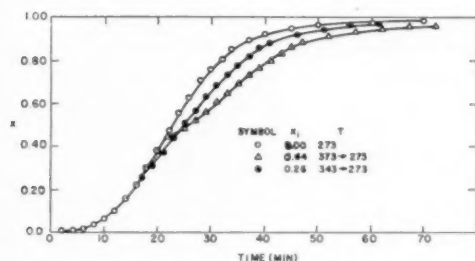


FIG. 13b. Dependence of  $x$  on  $t$  at 273°K after prior precipitation to  $x_i$  at  $T_1$ . Wire 20C,  $X_0=0.147$ .

multiplicity of  $\beta$ -particles dispersed in  $\alpha$ . Recently Tiedema and Burgers<sup>12</sup> established that such cells do indeed form and grow in  $\alpha$  lead-tin alloys. It appeared that  $\beta$ -lamellae were dispersed within the cell  $\alpha$ . Mr. Donald Wood of our laboratory independently verified the cell-like mode of precipitation in this system (see Fig. 16a) and clearly resolved (see Fig. 16b) the lamellar  $\beta$ -precipitate. Wood found that the cells nucleate preferentially at grain boundaries. Tiedema and Burgers' alloy specimens were single crystals but the cell nuclei formed at dendrite boundaries where the composition segregation would be highest. There is some possibility that these nuclei came from occluded crystals.

This cellular mode of precipitation has been observed in many systems and is known as the "recrystallization" reaction (we shall call it cellular transformation).

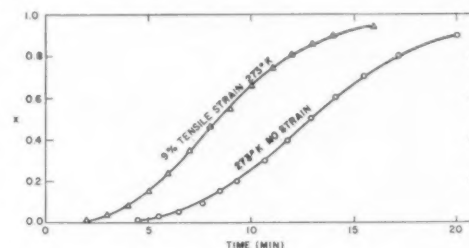


FIG. 14. Dependence of  $x$  on  $t$  at 273°K for unstrained wire and for same wire strained 9 per cent in tension at boiling temperature of liquid nitrogen. Extruded wire,  $X_0=0.147$ .

Geisler<sup>13</sup> has reviewed its essential features. Usually the cells nucleate at grain boundaries and a reorientation of the  $\alpha$  matrix accompanies their growth. In the lead-tin system there is no evidence that any mode of precipitation other than the cellular reaction is operative.

### INTERPRETATION

#### The Kinetic Law

The kinetic law for nucleation and growth transformations is usually of the form of Eq. (7) with  $n$  ranging between 1 and 4. How  $n$  is related to the mechanism of nucleation and growth has been reviewed in other publications.<sup>10,14,15</sup>

We have to account for  $n \approx 3$  with rare departures that appear to be greater than the experimental error. From microstructural results, we know that (a) the cells have a form that is nearly spherical, (b) the cell dimensions are negligible in comparison with the wire diameter, and (c) the interlamellar spacing of  $\beta$  within the cells is approximately constant. We picture a cell growing uniformly in three dimension with a constant density (as evidenced by the constant interlamellar spacing) of tin diffusion sinks ( $\beta$ -edges) in its surface. Therefore, the cells should advance linearly at a rate independent of time. How the constant surface density of  $\beta$ -edges is maintained will be discussed in a following publication.

If the cell grows linearly at a constant rate, we can only account for  $n=3$  if the number,  $N$ , of cells/volume remains constant throughout the precipitation. In this event the constant  $b$  of Eq. (7) is given by:

$$b = (4\pi/3)NG^3, \quad (17)$$

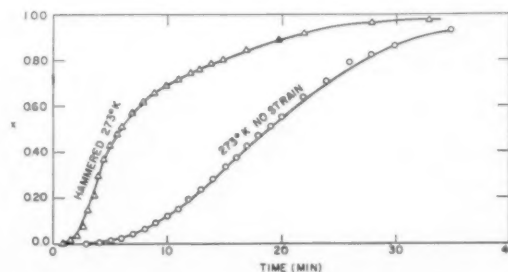


FIG. 15. Dependence of  $x$  on  $t$  at 273°K for unstrained wire and for same wire hammered flat at 273°K. Wire 6C,  $X_0=0.147$ .



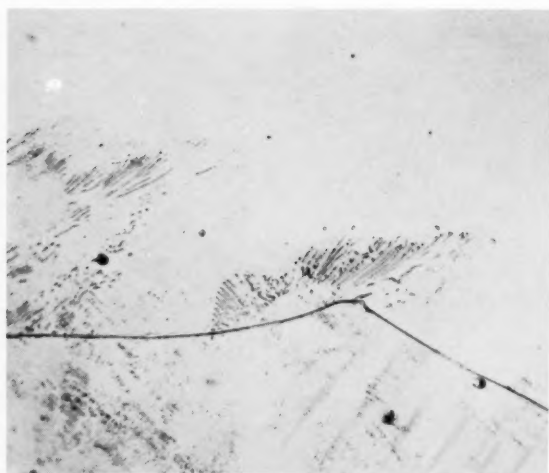


FIG. 16a. Cast film after 16 minutes at 300°K.  $X_0=0.124$ . Magnification 1000X.

where  $G$  is the linear rate of cell growth. The constancy of  $N$  implies that all the cell nuclei are formed in the earliest stages of precipitation. Since the initial supersaturation of the  $\alpha$ -matrix is not reduced until swept by a cell boundary, it follows that the nuclei must originate at a limited number of singular sites. Activation of nuclei at these sites occurs either athermally during quenching or isothermally at the beginning of transformation.  $N$  and  $G$  will depend upon  $X_0$ ,  $T$ , and strain.

Wood finds that the cells nucleate preferentially at grain boundaries. If  $N$  is of the same order of magnitude or smaller than the number,  $g$ , of solid solution grains per unit volume, we should expect  $n=3$  (for  $x$  not too large) as though nuclei had formed randomly. However, it is possible for the specific number of nuclei at grain boundaries to be so great (that is,  $N \gg g$ ) that all the grain boundary area is coated with cells while the amount of precipitation is still very small. From this point the total transformed volume should increase at a

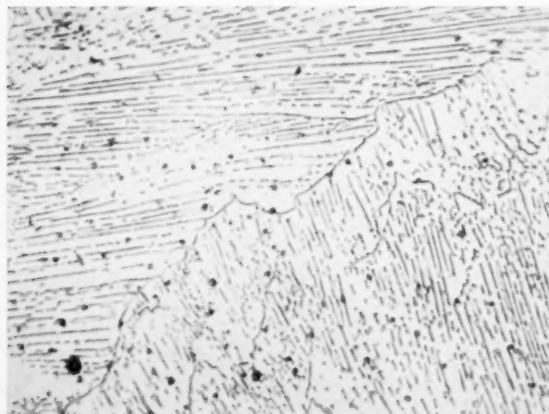


FIG. 16b. Cast film after 16 hours at 300°K.  $X_0=0.112$ . Magnification 2000X.

constant rate so that  $n$  would be unity. For the more general case,  $n$  should fall between 1 and 3 approaching 3 for  $x \rightarrow 0$  but decreasing below 3 as  $x$  increases. In our lead-tin wire,  $N$  must have been of the same order of magnitude as (or less than)  $g$  since  $n \approx 3$  for  $x \gtrsim 0.5$ .

Occasionally  $n$  found in experiments with extruded wire was significantly larger than 3.0. This result may indicate that thermal nucleation in some instances persists throughout the transformation period. Relief of the transformation strain by plastic flow of random elements of the matrix would also lead to  $n > 3.0$ .

### Kinetic Law in Thermal Cycling Experiments

In the following discussion  $\dot{x}$  will represent the rate of precipitation that results from direct quenching to  $T_2$  from the homogenization temperature while  $\dot{x}'$  will denote the rate at  $T_2$  after some precipitation at  $T_1$ . In interpreting these results it will be assumed that  $G$  is independent of thermal history.

Let precipitation proceed for time  $t$  at  $T_2$  after transformation to  $x=x_i$  at  $T_1$  ( $t=0$ ,  $x=x_i$ ). Then:

$$\dot{x}' = 4\pi(1-x)[N_1G_2(r_i+G_2t)^2 + N_2G_2^3t^2], \quad (18)$$

where

$N_1$  = number of cells nucleated at  $T_1$ .

$N_2$  = number of cells nucleated at  $T_2$ .

$$r_i = [(3/4\pi N_1) \ln\{1/(1-x_i)\}]^{1/3}; \quad (19)$$

that is,

$$r_i = \text{radius of cells at } x=x_i.$$

When  $N_2 \gg N_1$  and for  $x$  very large it may be that Eq. (18) does not adequately compensate for impingement; however, we shall draw conclusions from (18) only in limiting cases where (18) should be a satisfactory approximation. Integration of (18) gives:

$$\ln[(1-x_i)/(1-x)] = 4\pi N_1(G_2r_i^2t + r_iG_2^2t^2) + (4\pi/3)G_2^3t^3(N_1+N_2). \quad (20)$$

When  $t=0$ , (18) becomes:

$$\dot{x}'_i = 4\pi(1-x_i)N_1G_2r_i^2. \quad (21)$$

For  $x_i=0$ , we have:

$$\dot{x} = 4\pi(1-x)N_2G_2^3t^2. \quad (22)$$

We deduce from Eqs. (19), (21) and (22) that

$$\dot{x}'_i/\dot{x}_i = (N_1/N_2)^{1/3} \equiv \rho. \quad (23)$$

Equation (23) is valid if there is no precipitation or resolution of the solute in the cells formed at  $T_1$ . Provided  $x_i$  is small and  $N_1 \gg N_2$ , it follows:

$$(\dot{x}'_c/\dot{x}_c) = (N_1/N_2)^{1/3}. \quad (24)$$

Figure 17 shows the decomposition of  $f_v(t)$  for a down-cycling ( $373 \rightarrow 273^\circ$ ) experiment into two components. One of the components derives from nuclei formed at  $273^\circ$  and is calculated from the  $f(t)$  curve for  $273^\circ$  also shown in Fig. 17. The second component results from nuclei formed at  $373^\circ$  and is obtained by subtracting the

first component from  $f_s(t)$ . The second component is approximately linear over the intermediate range of  $x$  values as expected on the basis of Eq. (20). The decomposition was not carried further because the impingement correction becomes more uncertain as  $f_s(t)$  increases.

From Eqs. (13), (17), and (23) with  $X_0$  constant we can relate the rate of precipitation to the rate of cell growth as follows:

$$(\dot{x}_c/\rho)_{T \rightarrow T_s} = \gamma_c G, \quad (25a)$$

and

$$(\dot{x}_c/\rho)_{T_s \rightarrow T} = \gamma_c G. \quad (25b)$$

Here  $\gamma_c$  and  $T_s$  are constants and  $\dot{x}_c$  and  $G$  correspond to  $T$  which is variable. The subscripts refer to the thermal cycle; in (25a)  $T_1 = T$ ,  $T_2 = T_s$ , while in (25b)  $T_1 = T_s$  and  $T_2 = T$ .

Figure 6 shows  $\log(\dot{x}_{c,2}/\rho)_{T \rightarrow T_s} = f_1(1/T)$  or  $\log(\dot{x}_{c,2}/\rho)_{T_s \rightarrow T} = f_2(1/T)$  plotted against  $1/T$  for four  $X_0$  values with  $T_s = 273^\circ$  and  $T > T_s$ . For  $T$  less than the characteristic temperature, the dependence of cell growth rate on  $T$  is identical whether it is deduced from down-

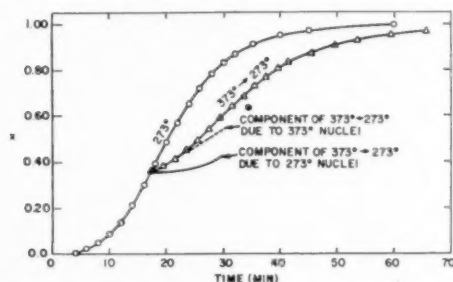


Fig. 17. Decomposition of  $x = f_s(t)$  from a down-cycling experiment into two components. Wire 18C,  $X_0 = 0.147$ .

cycling or up-cycling experiments; that is,  $f_1(1/T) = f_2(1/T)$  when  $T < T'$ . However, when  $T > T'$  the growth rate inferred from down-cycling experiments is larger than the corresponding rate inferred from up-cycling experiments [ $f_1(1/T) > f_2(1/T)$  when  $T > T'$ ]. In the down-cycling experiments ( $T \rightarrow T_s$ )  $\rho$  was calculated from (23) but in the up-cycling experiments ( $T_s \rightarrow T$ ) there was some tendency for  $\beta$  to redissolve at the highest temperatures so  $x_i$  was kept small ( $\sim 0.02$ ) and  $\rho$  evaluated from (24) with  $c = 0.2$ . Because of this resolution in up-cycling, we believe that  $f_1(1/T)$ , (Eq. 25a), may be a more satisfactory representation of the dependence of  $\log(\gamma_c G)$  on  $1/T$  than is  $f_2(1/T)$ .

In any event we can draw the following conclusions from the thermal cycling experiments:

1. At constant  $X_0$ ,  $N$  increases with decreasing  $T$  until  $T = T'$ . For  $T < T'$ ,  $N$  is constant.
2. With  $X_0$  constant,  $\ln G$  is not a linear function of  $1/T$ , possibly excepting the temperature range  $T < 273^\circ$ .  $G$  increases with increasing  $T$  to a maximum  $G = G_{\max}$  at  $T = T_{\max}$  and then decreases sharply with further in-

crease in  $T$ . At  $T = T_{\max}$  the supersaturation ratio ( $X_0/X_e$ ) is of the order of 5 or 6.

### Further Remarks

As an electrical conductor, our precipitating system consists of spherical elements (cells) having a characteristic conductivity,  $\lambda_c$ , imbedded in  $\alpha$  matrix of conductivity,  $\lambda_m$ . Landauer<sup>15</sup> has discussed the dependence of the resultant conductivity of such a system upon the concentration and size of cells. From Landauer's treatment we infer that while the validity of our Eq. (8) is questionable for  $x$  very large, it ought to satisfactorily describe the dependence of  $R$  on  $x$  when  $x \lesssim 0.4$ .

We are in essential agreement with Borelius and co-workers on the facts, so far as they determined them, of precipitation in the lead-tin system. We have shown that their  $1/\tau_{1/2}$  is proportional to  $\dot{x}_c$ , where  $c$  may range from 0 to 0.5. We are in good agreement with them on the variation of  $1/\tau_{1/2}$  with  $X_0$  and  $T$  though in absolute magnitude our  $1/\tau_{1/2}$  values on cast wires are considerably smaller than theirs. Also, we find that  $d \log \dot{x}_c / d(1/T)$  or  $d \log(1/\tau_{1/2}) / d(1/T)$  becomes independent of  $X_0$  at some temperature  $T' = f(X_0)$ —that is, about the same as found by Borelius *et al.* Their limited results on the kinetic law appear to be consistent with our findings. However, Borelius *et al.* report no microstructural or thermal cycling experiments that have given us basic information on the precipitation mechanism.

There are some important questions not resolved by our formal interpretation. These are:

1. Why, as shown by the microstructural and kinetic evidence, precipitation of tin from lead occurs at a rate  $10^7$  to  $10^8$  times greater than calculated from Seith and Laird's results on the diffusion of tin into dilute solutions of tin in lead.
2. What are the reasons for the complexity of the dependence of  $\log G$  on  $1/T$ .
3. Why does  $N$  become temperature independent below some critical temperature  $T'$ .
4. What is the mechanism of the slow reaction.

These questions will be dealt with in the following paper entitled, "Theory of Cellular Precipitation."

### CONCLUSIONS

1. Precipitation of tin from lead takes place in two distinct stages. The first stage is a "fast" reaction that drains about 60 per cent of the thermodynamic excess of tin from solution. The remaining 40 per cent of the tin is drained at a rate (slow reaction) about 2 orders of magnitude slower than the fast reaction.

2. The kinetic law for the fast reaction is:

$$x = 1 - \exp(-bt^n).$$

With rare exceptions,  $n = 3.0$  independently of temperature or initial tin concentration.

3. Precipitation is effected by the nucleation and growth of cells. Each cell consists of a multiplicity of  $\beta$ -particles, all originating from a single nucleus, interspersed in  $\alpha$ . This mode of precipitation has been referred to in the literature as the "recrystallization reaction."

4. We deduced that  $b$  is related to the number  $N$  of cell nuclei and their rate of growth  $G$  as follows:

$$b = (4\pi/3)NG^3.$$

5. The precipitation rate  $\dot{x}_c$ , at constant transformed volume and temperature, is independent of thermal cycling treatments (wherein precipitation is begun at one temperature and completed at a different temperature) when the cycling temperatures are less than a characteristic temperature,  $T'$ .  $\dot{x}_c$  is strongly dependent on the thermal history if one of the cycling temperatures exceeds  $T'$ .

6. Even for  $T < T'$  the precipitation rate is strongly dependent upon the initial concentration,  $X_0$ , of tin; for example, when  $X_0$  increases from 0.112 to 0.170,  $\dot{x}_c$  increases by a factor of about 15.

7. The kinetic law is satisfactorily interpreted if it is assumed that all cells have nucleated at the beginning of precipitation and originate from a limited number of singular sites mostly in the vicinity of grain boundaries. Therefore, interpretations of the precipitation kinetics in this system that have presupposed nucleation in structurally pure crystals have to be abandoned.

8. At constant initial tin concentration, the number of nuclei increases with decreasing  $T$  until the characteristic temperature is reached.  $N$  is constant at temperatures equal to or less than  $T'$ .

9.  $G$  increases with increasing  $T$  to a maximum  $G_{\max}$

at  $T_{\max}$  and then decreases sharply with further increase in  $T$ . At  $T_{\max}$  the supersaturation ratio is 5 or 6.

10. Precipitation takes place about  $10^7$  to  $10^8$  times faster than calculated from Seith and Laird's results on the diffusion of tin into dilute solutions of tin in lead.

11. Cold-working the supersaturated solid solution greatly increases the precipitation rate.

#### ACKNOWLEDGMENT

We express our thanks to E. W. Balis and W. W. Welbon for the tin analyses and to Donald Wood for his work on the microstructures. We are pleased to acknowledge valuable discussions with A. H. Geisler on the nature of the "recrystallization reaction." Also, we are indebted to Professor G. Borelius for sending us his unpublished calorimetric results on the isothermal precipitation of tin from lead.

#### REFERENCES

1. G. Borelius, F. Larris, and E. Ohlsson, *Arkiv Matematik, Astronomi och Fysik* **31A**, No. 10 (1944).
2. G. Borelius and K. M. Säfsten, *Arkiv Matematik, Astronomi och Fysik* **36B**, No. 5 (1949).
3. J. Nystrom, *Arkiv för Fysik*, **1**, 359 (1949).
4. H. K. Hardy, *J. Inst. Metals* **77**, 457 (1950).
5. J. H. Hollomon and D. Turnbull, *Progress in Metal Physics*, Vol. 4, 333, Pergamon Press (1953).
6. W. Seith and J. G. Laird, *Z. Metallkunde* **24**, 193 (1932).
7. C. Zener, Private communication.
8. F. Seitz, *L'Etat Solide*, Institut International de Physique Solvay, pp. 401-405 (1952).
9. D. Turnbull and R. E. Hoffman, *Acta Met.* **2**, 419 (1954).
10. C. A. Wert, *J. Appl. Phys.* **20**, 943 (1949).
11. B. L. Averbach, *Trans. A.S.M.* **41**, 262 (1949).
12. T. J. Tiedema and W. G. Burgers, *Applied Scientific Research* **4A**, 243 (1954).
13. A. H. Geisler, "Phase Transformations in Solids" (John Wiley 1951), pp. 387-545.
14. C. A. Wert and C. Zener, *J. Appl. Phys.* **21**, 5 (1950).
15. R. Landauer, *J. Appl. Phys.* **23**, 779 (1952).

## THEORY OF CELLULAR PRECIPITATION\*

DAVID TURNBULL†

The rate of cellular precipitation can be described by three parameters:  $D_B$ , the diffusion coefficient of atoms in the cell boundary;  $l$ , the spacing of the precipitate lamellae in the cell; and  $N$ , the number of cells nucleated per unit volume. In the precipitation of tin ( $\beta$ ) from lead ( $\alpha$ ), the activation energy for cell boundary diffusion is deduced to be 9–10 kcal/gm atom to be compared with the activation energy 26 kcal/gm atom for the volume diffusion of tin into lead. It is inferred that nucleation of  $\beta$  is catalyzed by structural impurities in the  $\alpha$  and that the rate of the cellular reaction should be many orders of magnitude slower in structurally perfect crystals than in ordinary polycrystalline aggregates.

The existing kinetic results on precipitation in lead-tin appear to be consistent with the Becker nucleation theory and not consistent with Borelius' theory.

### THÉORIE DE LA PRÉCIPITATION CELLULAIRE

La vitesse de la précipitation cellulaire peut être définie par trois paramètres:  $D_B$ , le coefficient de diffusion des atomes dans la paroi de la cellule;  $l$ , l'espacement des lamelles de précipité dans la cellule; et  $N$ , le nombre de cellules apparaissant par unité de volume. Dans la précipitation de l'étain ( $\beta$ ) à partir du plomb ( $\alpha$ ), l'énergie d'activation pour la diffusion dans la paroi de la cellule est de 9–10 kcal/atome-gramme, alors que l'énergie d'activation pour la diffusion de l'étain dans le réseau du plomb est de 26 kcal/atome-g. La germination de  $\beta$  paraît être catalysée par des impuretés structurales dans  $\alpha$  et, par conséquent, la vitesse de la réaction cellulaire devrait être de plusieurs ordres de grandeur plus lente dans des cristaux à structure parfaite que dans des agrégats polycristallins.

Les résultats existants sur la précipitation dans le plomb-étain paraissent être conformes à la théorie de germination de Becker et ne pas être conformes à celle de Borelius.

### THEORIE DER ZELLAUSSCHIEDUNG

Die Geschwindigkeit der Zellausscheidung lässt sich mit Hilfe der folgenden drei Größen beschreiben:  $D_B$ , der Diffusionskoeffizient der Atome in der Zellgrenze;  $l$ , dem Abstand der Ausscheidungslamellen in der Zelle und  $N$ , der Anzahl der Zellen pro Volumeneinheit. Im Falle der Ausscheidung von Zinn ( $\beta$ ) aus Blei ( $\alpha$ ) wurde die Aktivierungsenergie der Zellgrendiffusion zu 9–10 Kcal/Grammatom geschätzt und mit der Aktivierungsenergie von 26 Kcal/Grammatom für die Volumendiffusion von Zinn in Blei verglichen. Es wird angenommen, dass die Keimbildung von  $\beta$  durch Strukturfehler in  $\alpha$  katalysiert wird, und dass die Geschwindigkeit der Zellreaktion in strukturell fehlerfreien Kristallen um viele Größenordnungen geringer sein sollte als in gewöhnlichen polykristallinen Gefügen.

Die vorhandenen experimentellen Daten zur Ausscheidung in Blei-Zinn scheinen mit Beckers Keimbildungstheorie und nicht mit Borelius' Theorie übereinzustimmen.

### INTRODUCTION

In the preceding paper<sup>1</sup> the results of a kinetic investigation of the precipitation of tin ( $\beta$ ) from lead-tin solid solutions ( $\alpha$ ) are described and formally interpreted. Precipitation was effected by the nucleation and growth of cells. Each cell had a duplex structure consisting of  $\beta$  lamellae interspersed in  $\alpha$ .

This mechanism of precipitation has long been recognized and discussed<sup>2</sup> as the "recrystallization reaction." We prefer the designation "cellular precipitation" since the driving energy for the process derives from the solute supersaturation. In some systems, lead-tin being an example, cellular precipitation appears to be the only mechanism operative. In other systems the cellular reaction is preceded by "general precipitation," a reaction whereby isolated precipitate particles nucleate and grow. Apart from the investigations on lead-tin there seem to have been very few kinetic investigations of the cellular reaction. Bumm,<sup>3</sup> using a metallographic technique, measured the isothermal (350°C) rate of pre-

cipitation of silver from copper. However, he did not report any analysis of the results.

It is the purpose of this paper to further interpret the kinetic results on precipitation of tin from lead and to develop the theory of cellular precipitation in general.

Two important theories, one due to Becker and the other to Borelius and Konobeyevski (B-K theory), for the formation of precipitation nuclei from solid solution have been developed. In order to provide a background for our discussion, we shall review the salient concepts underlying each of these theories.\*

### Becker Theory of Nucleation

Let

$X$  be the atom fraction of a solute element  $B$  in the  $\alpha$  solid solution.

$\Delta G$  = the increase in free energy of the system resulting from the formation of a  $B$ -rich cluster containing  $i$   $B$ -atoms.

The composition of the cluster will be described by  $\Delta X$  which is the atom fraction of  $B$  in the cluster minus  $X$ .

\* Received June 25, 1954.

† General Electric Research Laboratory, Schenectady, New York.

\* For a more extensive review see Hollomon and Turnbull.<sup>4</sup>



In general,

$$\Delta G = f(i, \Delta X, \epsilon, e), \quad (1)$$

where  $\epsilon$  and  $e$  are parameters describing the strain and shape of the cluster, respectively. In discussing the relative merits of the two nucleation theories we shall assume, as did the original proponents, that  $\epsilon=0$  and  $e=\text{constant}$ . Hence:

$$\Delta G = f(i, \Delta X). \quad (2)$$

To become a nucleus for the  $\beta$ -precipitate a cluster must pass through a succession of states with  $i$  and  $\Delta X$  increasing.  $\Delta G$  for this succession at first increases reaching a maximum  $\Delta G^* = f(i^*, \Delta X^*)$  and then decreases.

The Becker nucleation theory assumes that the critical free energy for nucleation,  $\Delta G^*$ , is a consequence of the free energy/area,  $\sigma$ , of the interface between the nucleus and  $\alpha$ . For simplicity, Becker set  $\Delta X^* = X_\beta - X$  where  $X_\beta$  is the atom fraction of  $B$  in  $\beta$ . Then:

$$\Delta G^* = A\sigma^2/(\Delta G_V)^2, \quad (3)$$

where  $\Delta G_V$  is the free energy/volume (neglecting the interface free energy) for forming  $\beta$  from  $\alpha$  of composition  $X$ , and  $A$  is a geometrical factor determined by the nucleus shape. For an ideal or regular solution

$$\Delta G_V = -(kT/v) \ln(X/X_e) = -(kT/v) \ln S, \quad (4)$$

where  $v$  is the volume of an atom in  $\beta$ ,  $X_e$  is the atom fraction of  $B$  in  $\alpha$  in equilibrium with  $\beta$ .

Few measurements of the interfacial energies between solid phases have been reported. However, van der Merwe<sup>5</sup> and Brooks<sup>6</sup> have suggested that solid interphase boundaries can be described as dislocation arrays as can boundaries between misoriented crystals of the same phase. Hence, we expect that for a given boundary dislocation density, the energies of these two types (grain and solid interphase) of boundaries will be of the same order of magnitude. Suppose that low index planes,  $p_\alpha$  and  $p_\beta$ , of the two structures  $\alpha$  and  $\beta$ , respectively, are similar. Let  $\delta = |(a_\alpha - a_\beta)/a_\beta|$  where  $a_\alpha$  and  $a_\beta$  are the atomic spacings in  $p_\alpha$  and  $p_\beta$ , respectively. The dislocation density,  $d$ , in the  $\alpha$ - $\beta$  boundary increases with increasing  $\delta$ . When  $\delta \sim 0.10$  to  $0.15$ ,  $d$  is sufficiently large so that  $\sigma \sim \sigma_m$ , where  $\sigma_m$  is the maximum energy of the boundary between misoriented metal grains.\* We expect that  $\sigma$  will have a similar or greater magnitude if there are no low index planes similar between the two structures.

Brooks<sup>8</sup> has pointed out that when  $\sigma \sim \sigma_m$ ,  $\beta$  cannot nucleate (in a structurally pure crystal) at a perceptible rate unless the supersaturation is very high. In order to show the basis for Brooks' conclusion, we shall start with the following expression for  $I$ , the frequency of nucleation/volume derived by Turnbull and Fisher<sup>9</sup> from Becker's assumptions:

$$I = (X - X_e)n_v\nu \exp[-(\Delta G^* + \Delta G_A)/kT], \quad (5)$$

\* It is interesting that Nabarro's<sup>7</sup> estimate of  $\sigma$  for  $\delta \sim 0.10$  to  $0.15$  is of the same order as  $\sigma_m$ .

where

$n_v$  = number of atoms/cc. of solid solution.

$\nu$  = frequency of atom vibration.

$\Delta G_A$  = free energy of activation for diffusion of  $B$  in  $A$ .

Precipitation will become perceptible when  $|\Delta G^*/kT| \leq \phi$  and  $I \geq I'$ .  $I'$  will be dependent upon  $\Delta G_A$  but our fundamental conclusion will not be much affected by an inaccurate assumption on the relation between  $\Delta G_A$  and  $I'$ . Therefore, we shall set  $I' = 10^4 \text{ cm}^{-3} \text{ sec}^{-1}$  and  $\Delta G_A/kT = 10^{-15}$ . With plausible values of  $n_v$ ,  $\nu$ , and  $(X - X_e)$ , we get  $\phi \sim 30$ . Combining Eqs. (3) and (4) gives:

$$\ln S' \sim v(A/\phi)^{1/3}(\sigma/kT)^{3/2}, \quad (6)$$

where  $S \geq S'$  in order that  $I \geq I'$ .

$\sigma_m$  for lead is not known. However,  $\sigma_m$  values for other face centered cubic metals satisfy the empirical relation  $(\sigma_m/\sigma_l) > 1/3$ , where  $\sigma_l$  is the free energy/area of the liquid-vapor interface. Assuming that this inequality is generally valid, we estimate  $\sigma_m \geq 150 \text{ ergs/cm}^2$  for lead. Setting  $\sigma$  between  $\alpha$  and  $\beta$  equal to  $\sigma_m = 150$  and assuming that tin nuclei are spherical, we calculate that at  $350^\circ\text{K}$ ,  $S' \sim 50$  for the nucleation of tin in structurally pure lead crystals. This result confirms Brooks' theory that the homogeneous nucleation of incoherent interfaces (i.e., interfaces containing a high density of dislocations) is not possible unless the supersaturation is very high.

The dislocation density in the  $\alpha$ - $\beta$  interface is reduced provided the  $\beta$  nucleus is strained an amount,  $\epsilon$ , so that the difference in atomic spacing between  $p_\alpha$  and  $p_\beta$  is reduced. If  $\epsilon = \delta$ , the  $\alpha$ - $\beta$  interface (with  $p_\alpha/p_\beta$ ) is coherent (i.e., free of dislocations). The free energy of the coherent  $\alpha$ - $\beta$  interface may be very much less than  $\sigma_m$ . However, Nabarro<sup>7</sup> has shown that for  $\delta \geq 0.03$  to  $0.04$ , the coherency strain energy,  $E$ , (i.e., the strain energy in the nucleus when  $\epsilon = \delta$ ) becomes a considerable fraction of the  $\Delta G^*$  usually available. Hence, coherent nucleation is unlikely to occur at an appreciable rate unless there are similar low index planes between  $\alpha$  and  $\beta$  for which  $\delta \gtrsim 0.05$ .

Thus, according to the Becker theory, nucleation of  $\beta$  in structurally pure  $\alpha$ -crystals, if there are no simple similar planes between the two structures or if  $\delta > 0.10$ , cannot take place at an appreciable rate unless the supersaturation is extraordinarily high. Actually tin precipitates from lead quite rapidly when  $S \sim 2$ . Similarly, silver precipitates from copper ( $\delta = 0.12$ ) at an appreciable rate when the supersaturation level is quite low. These results are consistent with the Becker theory only if the precipitation nuclei originated at structural impurities in the  $\alpha$  such as grain boundaries, dislocations, or particles of an extraneous phase.

### Borelius-Konobeyevski (B-K) Theory

Borelius and Konobeyevski assume that the interfacial energy between  $\alpha$  and  $\beta$  is of no consequence in nuclea-

tion kinetics and that  $\Delta G^*$  can be identified precisely with the volume free energy change,  $\Delta G_m$ , associated with the critical fluctuation  $\Delta X$ . With  $i$  and  $T$  constant and  $X < X_c$  (at  $X = X_c$ ,  $\partial^2 G / \partial^2 X = 0$ ) the functional relation  $G = f(X)$  is of such a form that  $\Delta G = f(\Delta X)$  increases with small  $\Delta X$  to some maximum  $\Delta G_m$  at  $\Delta X_m = (X_m - X)$ .† It is assumed *ad hoc* that some critical number of solute atoms,  $i^*$ , must participate in the fluctuation and  $\Delta G^*$  is set equal to  $(\Delta G_m)_{i^*}$  with  $\Delta X_m = \Delta X^*$ . In order for the B-K theory to be consistent with experience, Borelius calculates that  $i^*$  must be of the order of several hundred atoms. This result implies that  $(\Delta G_m)_{X,T} = f(i)$  goes through a minimum at  $i = i^*$ . However, strict thermodynamical considerations require that  $\Delta G_m$  be directly proportional to  $i$  and no analysis has been offered showing that  $\Delta G_m = f(i)$  has a minimum at a large  $i$ -value.

Independently of the  $\Delta G_m = f(i)$  relation, the B-K theory does predict that  $\Delta G^*$  disappears when  $X = X_c$ . For a given  $X$  there is a temperature,  $T_c$ , at which  $X_c = X$  and below which  $X > X_c$ . Let  $\dot{x}$  be the rate of precipitation at a given fraction,  $x$ , of the sample precipitated.  $x$  is defined by:

$$x = \frac{X_0 - X_t}{X_0 - X_f} \quad (7)$$

where  $X_t$  = atom fraction of tin in solution at time  $t$ ,  $X_f$  is defined as in the preceding paper, and  $X_t = X_0$  at  $t = 0$ . Borelius assumes that  $d \ln \dot{x}_c / d(1/T)$ , ( $\dot{x}_c = \dot{x}$  when  $x = c$ ), is dependent on  $X_0$  when  $\Delta G^* > 0$  and that lack of dependence of  $d \ln \dot{x}_c / d(1/T)$  on  $X_0$  may be taken as evidence that  $\Delta G^* = 0$ . He calculated, assuming ideal entropy of mixing,  $X_c = f(T)$  for a number of systems and found that  $d \ln \dot{x}_c / d(1/T)$  appeared to become independent of  $X_0$  at temperatures  $T'$  in good agreement with  $T_c$ .

For example, Borelius and associates<sup>10</sup> have found that the temperatures  $T' = f(X_0)$  in the lead-tin system at which  $d \ln \dot{x}_c / d(1/T)$ , ( $\dot{x}_c \propto \tau_{1/2}$  where  $\tau_{1/2}$  is the time for half-precipitation), becomes independent of  $X_0$  are in excellent agreement with the values  $T_c = f(X_0)$  calculated on the assumption that lead-tin solid solutions are regular in their thermodynamic behavior.

The B-K theory leaves unresolved a serious dilemma about the form of the kinetic law when  $T < T'$ . It is expected that  $x = f(t)$  will have a form characteristic of nucleation and growth processes for  $\Delta G^* > 0$  or  $T > T'$ . However, if  $\Delta G^* = 0$ , we do not expect the precipitation mechanism and kinetic law to be describable by nucleation and growth kinetics. It appears, therefore, that the form of  $x = f(t)$  should change markedly when the precipitation temperature goes from  $T > T_c$  to  $T < T_c$ . What form  $x = f(t)$  will take when  $T < T_c$  is not

clear. Presumably precipitation would be a coarsening phenomenon (as is probably the case in the growth of Guinier-Preston zones) whereby large tin clusters grow at the expense of smaller ones. However, this process is incomprehensible unless the  $\alpha$ - $\beta$  interfacial energy is greater than zero.

## THEORY

### Kinetic Law

It has been shown<sup>10,11</sup> that precipitation of tin from lead occurs in two stages. In the first stage, designated "fast reaction," about 60 per cent of the thermodynamic excess of tin is drained from solution. The remaining 40 per cent of tin is drained in a "slow reaction" at a rate about two orders of magnitude less than in the fast reaction.

It was established<sup>1</sup> that the kinetic law for the fast reaction, at least for  $x \leq 0.5$ , is:

$$x = 1 - \exp(-bt^n), \quad (8)$$

where, with rare exceptions,  $n = 3.0 \pm 0.25$  independently of  $X_0$  or  $T$ . To account for the microstructural observations, it was assumed that all the cells have nucleated in the earliest stages of precipitation (effectively at zero time) and grow at a constant linear rate  $G$ . Therefore, when the cells have a spherical form,

$$b = (4\pi/3)NG^3, \quad (9)$$

where  $N$  is the number of cells/volume. It was further deduced that the cell nuclei originate at a limited number of singular sites\* mostly in the vicinity of grain boundaries.

These results are inconsistent with the Borelius interpretation of the precipitation kinetics in this system in the following respects:

1. The form of the kinetic law is independent (i.e.,  $n = 3.0$ ) of whether precipitation is carried out at temperatures well above or well below  $T_c$ . (See Table II of preceding paper). Hence it appears that a nucleation and growth mechanism is operative at all temperatures.

2. All cell nuclei appear to originate from structural impurities and are activated in a period negligible in comparison with the period of cell growth. Borelius assumed that tin nucleates homogeneously in structurally pure  $\alpha$ .

On the basis of Becker's theory and Brooks' treatment of interfacial energy, we concluded that homogeneous nucleation of tin from  $\alpha$  is unlikely at supersaturation ratios less than 50. In agreement with this conclusion, we have no evidence of homogeneous nucleation of tin up to supersaturation ratios at least as

† Hollomon and Turnbull<sup>4</sup> implied that  $X_m = X_c$ . This implication is erroneous and we regret that we did not discover the error until the paper was in press. However, our basic criticism of the B-K theory is not altered by correction of the mistake.

\* Professor M. Cohen, of the Massachusetts Institute of Technology, has independently established that cell nuclei in the nickel-gold system originate at a limited number of preferred sites (A.E.C. Metallurgy Information Meeting, Schenectady, New York, June 1954).

high as 30. Hence the results relating to the kinetic law are, as far as they go, consistent with the Becker theory.

### Cell Growth

In the preceding investigation the following facts were developed about isothermal formation of cells.

1. The cells are composed of  $\beta$ -lamellae interspersed in  $\alpha$  having an orientation different from the  $\alpha$ -matrix into which the cell grows.

2. The interlamellar spacing,  $l$ , is apparently constant so that the cell growth rate should be time independent.

The structure of these cells is very similar to that of pearlite nodules formed in the decomposition of austenite. Accordingly, we shall take as our starting point a theory of growth of pearlite nodules proposed by Zener<sup>11</sup> and further developed by Fisher.<sup>12</sup> Zener assumes that solute atoms reach the lamellae edges by volume diffusion and derives the following expression for  $G$ :

$$G = \frac{X_0 - X_e}{X_0} (2D/l), \quad (10)$$

where  $D$  is the volume diffusion coefficient. The assumption that the rate of growth of pearlite nodules is controlled by the volume diffusion of carbon appears to be compatible with the known facts.<sup>12</sup>

However, as noted in the first paper, tin precipitates from lead at a rate many orders of magnitude greater than calculated from the diffusion data of Seith and Laird.<sup>13</sup> Wood<sup>1</sup> has observed cells that had grown at a rate  $G \sim 10^{-6}$  cm/sec at 300°K in which  $l \sim 10^{-4}$  cm. To account for this rate assuming volume diffusion  $D \sim 10^{-10}$  cm<sup>2</sup> sec<sup>-1</sup> a number  $10^8$  times larger than the value of  $D$  at 300°K extrapolated from Seith and Laird's results.

Therefore, it appears that tin may be drained from the  $\alpha$  by diffusion along diffusion short circuits that sweep the solid solution in advance of the growing cell. It has been shown that dislocation channels and elements of incoherent grain boundaries are almost equally effective as short circuits for the self-diffusion of silver.<sup>14,15</sup> We expect that these imperfections will also short circuit the diffusion of substitutional solute atoms generally. Usually dislocations will be generated by the growth of precipitate due to transformation strains. The channels of these dislocations will facilitate the transport of solute atoms to the precipitate particle. However, in cellular precipitation the cell boundary itself probably constitutes a diffusion short circuit\* that is more important than the dislocation channels formed by cell growth. This boundary is incoherent and sweeps all elements of the solid solution completely as the cell grows.

\* The possibility that the cell boundary might be the sought-for sweeping diffusion short circuit was suggested to me by J. C. Fisher. Also, C. S. Smith<sup>16</sup> has implied that solute atoms drain preferentially along the cell-matrix boundary during cell growth.

Let  $D_B$  be the diffusion coefficient in the cell boundary and  $\lambda$  the boundary thickness. Assume that the tin is drained only by diffusion along the cell boundary. Then

$$G = [(X_0 - X_e)/X_0](\lambda/\tau), \quad (11)$$

where  $\tau$  is the time required to drain the grain boundary region of solute. But

$$\tau \approx l^2/D_B. \quad (12)$$

Therefore,

$$G = \left( \frac{X_0 - X_e}{X_0} \right) (\lambda D_B / l^2). \quad (13)$$

Now to account for the observed rate of cell growth  $D_B \sim 10^{-6}$  to  $10^{-7}$  cm<sup>2</sup> sec<sup>-1</sup>. This magnitude of  $D_B$  corresponds (assuming the applicability of the Dushman-Langmuir equation) to an activation energy,  $Q_B$ , of grain boundary diffusion equal to 9 kcal/gm atom to be compared with  $Q_l = 26$  kcal/gm atom activation energy for lattice diffusion. The ratio  $(Q_B/Q_l)$  between these numbers is 0.35 and agrees fairly well with  $(Q_B/Q_l) = 0.44$  for self-diffusion in silver.

In the preceding paper we showed how it is possible from the results of thermal cycling experiments to deduce  $\rho = (N_1/N_2)^{1/3}$  and the variation of cell growth rate with temperature. Here  $N_1$  and  $N_2$  are the number of nuclei formed on direct quenching to temperatures  $T_1$  and  $T_2$ . (In a thermal cycling experiment precipitation takes place to  $x = x_i$  at  $T_1$  and is then completed at  $T_2$ .) These deductions are valid only if  $G$  is independent of thermal history.

The results of these thermal cycling experiments (see Fig. 6 of preceding paper) showed that at constant  $X_0$  and over the temperature range  $T > 273^\circ\text{K}$ ,  $\ln G$  is not a linear function of  $1/T$ . From Eq. (13) we derive:

$$d \ln G / d(1/T) = d \ln(X_0 - X_e) / d(1/T) + d \ln D_B / d(1/T) - 2d \ln l / d(1/T). \quad (14a)$$

When  $X_0 \gg X_e$ ,

$$d \ln G / d(1/T) = -(Q_B/R) - 2d \ln l / d(1/T), \quad (14b)$$

since  $d \ln D_B / d(1/T) = -Q_B/R$ . This result shows that when  $l$  depends on  $T$  a straight line relation between  $\ln G$  and  $1/T$  is not expected.

Borelius *et al*<sup>10</sup> had also found that  $d \ln(1/\tau_{1/2})/d(1/T)$  is not constant when  $T > 273^\circ\text{K}$ . However, their results indicate that  $d \ln(1/\tau_{1/2})/d(1/T)$  for  $X_0 = 0.235$  is nearly constant over the temperature range 200 to 273°K. For these conditions  $d(\ln G)/d(1/T) = d \ln(1/\tau_{1/2})/d(1/T)$ . Assuming that constancy of  $d \ln G / d(1/T)$  implies constancy of  $l$  in this temperature range, we calculate that  $Q_B = 10$  kcal/gm atom in excellent agreement with  $Q_B \sim 9$  kcal/gm atom estimated from results of microstructural observations. Therefore, the concept that diffusion of tin atoms along the cell boundary is the rate governing step in cell growth is entirely consistent with the experimental evidence.

### The Interlamellar Spacing

We do not know whether or not the  $\beta$ -lamellae of the precipitation cells are interconnected but they do originate from one primary nucleus. The lamellation may be brought about by (a) branching of existing  $\beta$  as seems to be the case in pearlite formation, or (b) secondary nucleation of disconnected  $\beta$ -particles brought about by the transformation strain energy developed during cell growth.

Zener<sup>11</sup> has proposed that the interlamellar spacing will take on the value that maximizes  $G$ . He showed that the growth rate is a maximum when one-half of the driving free energy for precipitation is tied up in  $\alpha$ - $\beta$  interfaces. From this result the following relation between  $l$  and the supersaturation ratio,  $S$ , is deduced:

$$l = 4\sigma v / kT \ln S. \quad (15)$$

To obtain the dependence of  $l$  on  $T$  and hence on  $S$  at constant  $X_0$ , Eq. (14a) is integrated between 273°K and  $T$  to give:

$$\ln(l_{273}/l_T) = \frac{1}{2} \left\{ \ln \left[ \frac{(X_0 - X_e)_{273}}{(X_0 - X_e)_T} \right] + \frac{Q_B}{R} \left[ \frac{1}{T} - \frac{1}{273} \right] - \ln \left( \frac{G_{273}}{G_T} \right) \right\}. \quad (16)$$

The dependence of  $G$  on temperature is obtained from the results of the thermal cycling experiments (see Fig. 6, preceding paper) with 273°K as a reference temperature. From this dependence and setting  $Q_B = 10$  kcal/gm atom [from the low temperature value of  $d \ln(1/\tau_{1/2})/d(1/T)$  obtained by Borelius *et al.*<sup>10</sup>], we have calculated  $l_T/l_{273}$ , at various  $X_0$  values, as a function of temperature and the supersaturation ratio,  $S$ . In Fig. 1 we show  $l_{273}/l_T$  plotted against  $\log(S_T/S_{273})$  for three different initial concentrations of tin. The points all fall on a single straight line of slope 1.1 [a 10 per cent shift in  $Q_B$  would change the slope to the value unity predicted by Eq. (15)]. In the high temperature range, represented by the dashed portion of the line,  $(G_{273}/G_T) = f(T)$  deduced from the results of down-cycling experiments ( $T \rightarrow 273$ ) is in disagreement with  $f(T)$  calculated from the up-cycling experiments ( $273 \rightarrow T$ ). For reasons explained in the earlier paper the points shown in this temperature range (dashed line) are calculated from the down-cycling experiments. For the low temperature range (solid line of Fig. 1),  $(G_{273}/G_T) = f(T)$  is the same whether calculated from up-cycling or down-cycling experiments.

The independence on  $X_0$  of  $l_{273}/l_T$  of course implies nothing about the relation of  $l_{273}$  to  $X_0$ . The proportionality between  $l$  and  $1/\log S$  indicates, as was already assumed, that  $l$  is not strongly temperature dependent when  $S$  is very large.

Although our results are consistent with the functional relation between the interlamellar spacing and supersaturation ratio predicted by Eq. (15), the value of  $l$  required to make the equation quantitative is much smaller than observed. From microstructural observations it appears that  $l$  at 300°K and supersaturation ratio 6 is at least 100 times greater than the value  $l \sim 25$  Å predicted by the theory when the  $\alpha$ - $\beta$  interfacial energy = 150 ergs/cm<sup>2</sup>. Therefore, the Zener assumption that  $l$  is limited only by the dissipation of driving free energy in  $\alpha$ - $\beta$  interfaces appears not to be valid for cellular precipitation in lead-tin.

We may now re-examine the assumption that  $G$  is independent of thermal history. If the interlamellar spacing were always irrevocably established at the temperature of nucleation,  $G$  would be strongly dependent on thermal history. However, it seems more reasonable to suppose that  $l$  in the part of the cell that is growing is uniquely determined by the growth temperature. Consequently  $l$  in the core of a cell grown at one temperature will be different from  $l$  in the shell of the same cell formed at a different temperature. There will be a transient period during which the new interlamellar spacing is established. However, this transient appears to be very short since the precipitation rate is independent of thermal history when  $T < T'$  even though  $l$  appears still to be very temperature dependent.

It was established that the solute left in the cell  $\alpha$  at high temperatures is not drained out of solution at an appreciable rate when the temperature is lowered. This fact is explained as follows:

(a) Rapid precipitation at the cell boundary is effected by diffusion of solute atoms along the moving boundary. Within the cell solute atoms can only be drained by volume diffusion or by moving along stationary dislocation channels.

(b) The interlamellar spacing, hence the diffusion distance, is larger (see Fig. 1) in the cell core formed at high temperature than in the cell shell growing at a low temperature.

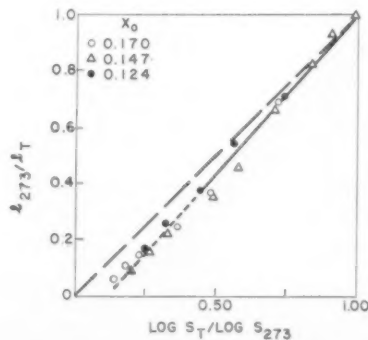


Fig. 1. Dependence of interlamellar spacing on supersaturation ratio as deduced from kinetic results.



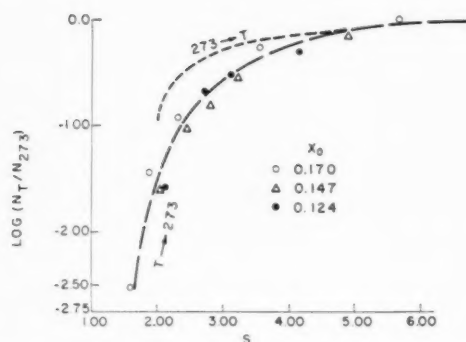


Fig. 2. Dependence of cell number on supersaturation ratio as deduced from kinetic results.

### Cell Nucleation

From the results of the thermal cycling experiments we can calculate  $N_T/N_{273}$  as a function of  $T$  or  $S$  where:

$N_T$  = number of nuclei formed on direct quenching to  $T$ , and

$N_T = N_{273}$  at  $T = 273$ .

$\log(N_T/N_{273})$  was calculated from the results summarized in Fig. 6 of the preceding paper and is plotted against  $S$  in Fig. 2. The points are from down-cycling experiments,  $T \rightarrow 273$ , and are nearly independent of  $X_0$ . Also shown is a smoothed curve of  $\log(N_T/N_{273}) = f(S)$  deduced from the results of up-cycling experiments ( $273 \rightarrow T$ ) with  $x = 0.2$ . The curves are identical when  $S \leq 4.5$  but diverge considerably at  $S > 4.5$ . However, we can certainly conclude the following:

1.  $N_T$  is independent of  $T$  and  $S$  when  $T < T'$  corresponding to  $S > 6$ .
2. When  $T > T'$ ,  $N_T$  increases with increasing  $S$  and decreasing  $T$ . As  $S$  goes from 2.0 to 6.0,  $N$  increases by a factor of at least 8 and more probably 30.
3.  $N_T/N_{273}$  appears to be dependent on  $S$  only. We do not imply that  $N_{273}$  is independent of  $X_0$ .

It is certain that  $N_{273}$  or  $l_{273}$  or both must be strongly dependent upon the initial tin concentration since the precipitation rate at  $x = 0.2$ ,  $\dot{x}_{0.2}$ , and  $273^\circ$  increases by a factor of 16 when  $X_0$  goes from 0.112 to 0.170. For  $X_0 \gg X_e$  and constant  $T$  we deduce that

$$(d \ln \dot{x}_e / d X_0)_T = (1/3) (d \ln N / d X_0)_T - 2 (d \ln l / d X_0)_T. \quad (17)$$

It is interesting that  $\log(1/\tau_{1/2})_T$  (we have shown that  $1/\tau_{1/2} \propto \dot{x}_e$ ) determined by Borelius *et al.*<sup>10</sup> varies linearly with  $1/(\log S)^2$  at all temperatures. This dependence is shown for  $273^\circ\text{K}$  in Fig. 3a and for  $356^\circ\text{K}$  in Fig. 3b. We cannot as yet interpret this result since we have no knowledge of the relative magnitude of the two terms of Eq. (17).

We have concluded that nuclei originate at certain singularities such as grain boundary elements or dislocation channels. Singular sites that have fulfilled some

critical condition of structure (or strain), composition, and size become nuclei. Suppose that nuclei form from clusters of pure tin that have collected within the singular element. Let  $i$  be the number of tin atoms in the cluster and  $\epsilon$  the strain in the element due to its deviation from structural regularity.  $\Delta G_e$ , the free energy of forming a cluster within the element is dependent upon  $i$ ,  $X_0$ ,  $T$  and  $\epsilon$ . The critical condition is fulfilled when  $i = i^*$  and  $\Delta G_e = \Delta G_e^*$ . Then:

$$i^* = f(X_0, T, \epsilon). \quad (18)$$

We can understand why the number of nuclei does not increase significantly with time at temperature if one or the other of the following hypotheses is valid:

1. Nucleation is athermal so that only those elements in which  $i \geq i^*$  upon reaching the transformation temperature become nuclei.
2. A limited number of elements become thermally activated to nuclei in a short time in comparison with the period of cell growth.

Either hypothesis implies a spectrum of singular elements such that the fraction that can be promoted to nuclei increases with increasing  $X_0$  and decreasing  $T$ . A singularity spectrum might have its origin in:

1. Variation in  $\epsilon$  among the elements.

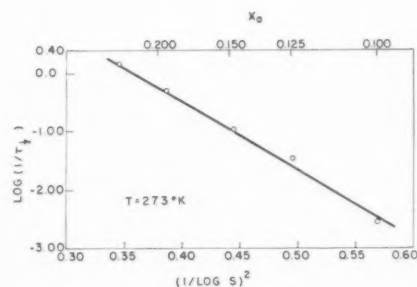


Fig. 3a. Dependence of precipitation rate on supersaturation ratio at  $T = 273^\circ\text{K}$ . (Calculated from data of Borelius *et al.*<sup>10</sup>).

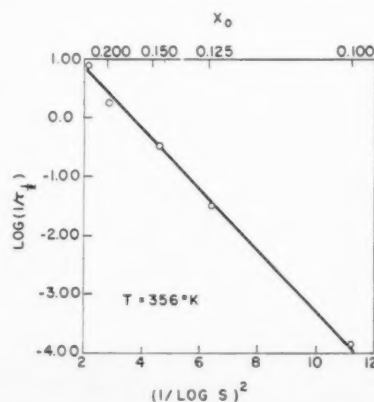


Fig. 3b. Dependence of precipitation rate on supersaturation ratio at  $T = 356^\circ\text{K}$ . (Calculated from data of Borelius *et al.*<sup>10</sup>).

2. Variation in the volume of the elements provided the total number of lattice sites within the element is of the order of  $i^*$ .

3. A size distribution of tin clusters formed by composition fluctuations at high temperatures; these fluctuations being "frozen-in" at low temperatures.

At temperature  $T'$  and below a decrease in temperature causes no further increase in  $N$ . This nucleation "cutoff" may indicate that:

1. All of the singular elements are promoted to nuclei when  $T$  is decreased to  $T'$ , or

2. There may be a kinetic condition for growth of a nucleus in addition to the thermodynamic one that  $i > i^*$ .

Suppose that this kinetic requirement is  $i > i_g$ . Then the observed nucleation cutoff would be accounted for if  $i^* > i_g$  when  $T > T'$ ,  $i^* = i_g$  at  $T = T'$ , and  $i^* < i_g$  at  $T < T'$ .

When cells nucleate at grain boundaries, the difference in orientation between the cell and matrix  $\alpha$  is readily explained by a theory due to C. S. Smith.<sup>16</sup> According to Smith, a cell may nucleate in grain  $B$  but grow into adjacent grain  $A$ . The cell does not grow into  $B$  at an appreciable rate because there is no diffusion short circuit on the  $B$  side. The driving force for the reorientation of the grain  $A_\alpha$  may come from either (1) the transformation strain energy that causes plastic deformation of  $\alpha$  as the cell grows, or (2) the surface energy differential between  $\beta$ - $B_\alpha$  and  $\beta$ - $A_\alpha$ . Since  $\beta$  nucleated in  $B$ , it is a reasonable supposition that the interfacial energy between  $\beta$  and  $B_\alpha$  is less than between  $\beta$  and  $A_\alpha$ . The orientation relationships observed in cellular precipitation apparently are consistent with Smith's theory.

According to T. J. Tiedema and W. G. Burgers<sup>17</sup> nuclei for the cellular reaction in lead-tin may sometimes form in single crystals—but at dendrite boundaries. In this case the reorientation must have been effected either by the formation of cells in occluded crystallites within the single crystal or by recrystallization of  $\alpha$  around a  $\beta$ -particle due to the transformation strain energy.

### Second Stage of Precipitation (Slow Reaction)

We shall consider three possible explanations for the slow reaction. The first is: (1) the cellular reaction slows down in its later stages to a much greater extent than predicted by Eq. (8). Such a slowing down would occur if impingement of cells along  $\alpha$  grain boundaries were complete before the  $\alpha$ -matrix cells were consumed by cell growth. However, the magnitude of the rate decrease is much greater than expected because of grain boundary impingement alone. If transformation strain energy drives the reorientation of  $\alpha$ ,  $G$  might decrease in the later stages of the cellular reaction because of the operation of strain relief mechanisms other than cell

growth. Whether or not this explanation is valid will have to be established by microstructural observations.

A second possible explanation is: (2) the chemical potential of the cellular precipitate,  $\beta'$ , exceeds that of normal  $\beta$  by virtue of either (a) its high specific surface area, or (b) a nonequilibrium structure (for example, it may be strained). Hence in order to maintain equilibrium the atom fraction,  $X'_e$ , of tin in the cell  $\alpha$  would have to exceed  $X_e$ . To account for the observed difference between  $X'_e$  and  $X_e$ ,  $\Delta\mu$ , the difference in chemical potential between  $\beta$  and the postulated  $\beta'$ , should be of the order of  $10^9$  ergs/cc. Thus the slow reaction would correspond to reversion of  $\beta'$  to  $\beta$  either by (a) coarsening or (b) transformation. From microstructural results we conclude that  $\Delta\mu \sim 10^9$  ergs/cc is several orders of magnitude greater than the specific surface energy of  $\alpha$ - $\beta$  interfaces in the cells.

If, after completion of the cellular reaction, the temperature of the wire be slightly raised, there should be a transient process in which the postulated  $\beta'$  starts to redissolve. No evidence for such a process was found; on the contrary, upon heating the wires after the cellular reaction tin continued to drain slowly from solution until a temperature was reached at which  $X_e \sim X_f$ , where  $X_f$  is the atom fraction of tin remaining in solution at the lower temperature.

A third and perhaps more attractive explanation of the slow reaction is (3) the tin is incompletely drained from an element swept over by a cell boundary. Accordingly, the cellular reaction would correspond to the extension of  $\beta$  by cell boundary diffusion and the slow reaction to the thickening of  $\beta$  by lattice diffusion of the residual thermodynamic excess of solute not collected in the cellular reaction.

As yet I have no explanation for the interesting result that  $X_0 - X_f \propto X_0 - X_e$  at all temperatures of precipitation.

### Effect of Cold-Working

Cold-working of the supersaturated  $\alpha$  greatly increases the rate of precipitation. The kinetic law of precipitation from the cold-worked solution cannot be described by Eq. (8) unless we let  $n$  decrease rapidly with time and at  $t=0$ ,  $n < 3.0$ .

Three variables,  $D_B$ ,  $l$ , and  $N$ , describe the rate of precipitation. We expect that plastic deformation will not have much effect on  $D_B$ , but the dislocation channels introduced may serve as auxiliary diffusion short circuits. Cold-working should facilitate the reorientation of  $\alpha$  in regions remote from the grain boundary with a resulting increase in  $N$ . We have no theory on how  $l$  may be affected due to cold-working.

### Further Remarks

Our results, though consistent with the Becker nucleation theory, provide no quantitative verification of it. In all experiments to date both nucleation and growth of

precipitate in lead-tin have been catalyzed by uncontrolled structural impurities in the crystal. There is no evidence that any nucleation of tin occurs in structurally perfect elements of  $\alpha$  crystals. In order to test critically the theories for nucleation of precipitate in solid solution, it will be necessary to follow the course of precipitation either in "perfect" crystals or in crystals in which the structural deviations are specified and controlled.

To the best of my knowledge, perfect solid solution crystals have not been prepared. However, crystals nearly free of imperfections might be obtained from the crystallization of very small droplets (ca 10 micron diameter) of liquid alloy. The comparative precipitation rates in these small crystals and in ordinary crystals would be of great interest. In particular, it is expected that the rate of cellular precipitation in small crystals would be greatly depressed.

It is probable that the nucleation and growth of cells is one of the most important mechanisms for the formation of incoherent precipitates. As already noted, the driving force for the  $\alpha$  reorientation may be the difference between the matrix  $\alpha$ - $\beta$  and the cellular  $\alpha$ - $\beta$  interfacial energies. However, since  $\beta$  is incoherent,  $\sigma$  is probably not very dependent upon boundary orientation. Thus branching of  $\beta$  within a cell, resulting in a greatly increased rate of growth, can be accomplished with very little increase in specific surface energy. On the other hand, a coherent precipitate is not likely to assume the lamellar habit since the interfacial energy between it and the matrix is very dependent upon boundary orientation.

General precipitation of a coherent structure often precedes and sometimes precludes the cellular reaction. However, once nucleated the cells containing incoherent precipitate grow at the expense of the generally distributed coherent precipitate particles, which are strained. In systems where coherent precipitation is energetically impossible, the cellular reaction may be the only operative mechanism.

### Conclusions

1. The facts relating to the kinetic law of precipitation in the lead-tin system are, so far as they go, consistent with the Becker theory of nucleation and inconsistent with Borelius' interpretation based on the Borelius-Konobeyevski theory.

2. It is deduced that the precipitation rate is determined by three parameters:

$D_B$ , the diffusion coefficient of atoms in the cell boundary.

$l$ , the spacing between precipitate lamellae in the cell.

$N$ , the number of cells/volume nucleated.

3. The rate of cell growth,  $G$ , can be explained with the hypothesis that the rate-limiting step is diffusion of

solute atoms along the cell boundary. When the driving free energy is very large:

$$G = \lambda D_B / l^2,$$

where  $\lambda$  is the interatomic spacing.

4. We deduced that  $l$  is inversely proportional to the specific free energy that drives precipitation. This result is qualitatively in agreement with Zener's theory for the interlamellar spacing in pearlite but the proportionality constant in the lead-tin system deviates from Zener's theory by about two orders of magnitude.

5. It seems necessary to suppose that there exists a singularity spectrum with respect to the temperature and initial concentration required to form a nucleus within the singular element.

6. The thermodynamic excess of solute is not completely drained from solution by the sweeping cell boundary. The residual thermodynamic excess drains by lattice diffusion (slow reaction).

7. The nucleation and growth of the cellular precipitate is catalyzed by structural impurities in the solid solution. It is predicted that this process will be several orders of magnitude slower in perfect than in imperfect crystals.

8. Probably cell nucleation and growth is one of the most important modes of formation of incoherent precipitates.

9. Preferential nucleation of cells at a boundary between  $\alpha$ -grains  $A$  and  $B$  may be explained with the use of the following hypotheses:

(a)  $\beta$  nucleates in  $B_\alpha$  with an orientation relationship that minimizes the interfacial energy between  $\beta$  and  $B_\alpha$  as proposed by C. S. Smith.<sup>16</sup>

(b)  $\beta$  does not grow in  $B$  because of the unavailability of diffusion short circuits.  $\beta$  does lamellate and grow into  $A_\alpha$  since the cell- $A_\alpha$  is an effective short circuit for solute diffusion that sweeps the  $A_\alpha$  as the cell grows.

10. As Smith<sup>16</sup> has suggested, the driving force for  $\alpha$  reorientation in cell growth may be the difference between the matrix  $\alpha$ - $\beta$  and cellular  $\alpha$ - $\beta$  interfacial energies though the possibility that the reorientation is driven by transformation strain energy cannot be ruled out.

11. Lamellation of  $\beta$  within a cell may be facilitated by the relatively weak dependence of the interfacial energy of the incoherent  $\alpha$ - $\beta$  boundary upon boundary orientation. Lamellation cannot occur in coherent precipitation because in this case  $\sigma$  is strongly dependent on boundary orientation.

### ACKNOWLEDGMENT

I am pleased to acknowledge the value of discussions with A. H. Geisler, E. W. Hart, and J. C. Fisher on the content of this paper.

## REFERENCES

1. D. Turnbull and H. N. Treafitis, *Acta Met.* **3**, 43 (1955).
2. A. H. Geisler, *Phase Transformations in Solids*, John Wiley (1951), pp. 387-545.
3. H. Bumm, *Metallwirtschaft* **14**, 429 (1935).
4. J. H. Hollomon and D. Turnbull, *Progress in Metal Physics*, Vol. 4, 333, Pergamon Press (1953).
5. J. H. Van der Merwe, *Proc. Phys. Soc.* **63A**, 616 (1950).
6. H. Brooks, "Metal Interfaces," *Am. Soc. Metals*, Cleveland (1952), pp. 20-65.
7. F. R. N. Nabarro, *Proc. Roy. Soc.* **175**, 519 (1940).
8. H. Brooks, Private communication (1952).
9. D. Turnbull and J. C. Fisher, *J. Chem. Phys.* **17**, 71 (1949).
10. G. Borelius, F. Larris and E. Ohlsson, *Arkiv Matematik Astronomi och Fysik* **31A**, No. 10 (1944).
11. C. Zener, *Trans. A.I.M.E.* **167**, 550 (1946).
12. J. C. Fisher, *Thermodynamics in Physical Metallurgy*, *Am. Soc. Metals*, Cleveland (1950), pp. 201-241.
13. W. Seith and J. G. Laird, *Z. Metallkunde* **24**, 193 (1932).
14. R. E. Hoffman and D. Turnbull, *J. Appl. Phys.* **22**, 634 (1951).
15. D. Turnbull and R. E. Hoffman, *Acta Met.* **2**, 419 (1954).
16. C. S. Smith, *Trans. A.S.M.* **45**, 562-571 (1953).
17. T. J. Tiedema and W. G. Burgers, *Applied Scientific Research* **4**, 243 (1954).



## A THERMAL ETCHING TECHNIQUE FOR REVEALING DISLOCATIONS IN SILVER\*†

A. A. HENDRICKSON† and E. S. MACHLIN\*\*

A thermal etching technique for revealing dislocations in silver has been developed. The technique reveals single dislocations in silver as evidenced by the close agreement between the experimentally measured area density of dislocations in bent single crystals and the area density calculated using the Cottrell formula for the excess density of dislocations as a function of the radius of curvature of the bent crystal. It has been found that the density of dislocations in recrystallized specimens and as solidified crystals is about  $2 \times 10^6$  per  $\text{cm}^2$ . A new mode of subgrain formation has been found. The type of subgrain morphology obtained is shown to be dependent upon the orientation between the crystal and the tension direction.

### UNE TECHNIQUE D'ATTAQUE THERMIQUE PERMETTANT DE RÉVÉLER LES DISLOCATIONS DANS L'ARGENT

On a développé une technique d'attaque thermique, qui permet de révéler des dislocations dans l'argent. Cette technique révèle des dislocations individuelles dans l'argent, comme le prouve le bon accord obtenu entre la densité des dislocations mesurée expérimentalement dans des monocristaux fléchis et la densité calculée au moyen de la formule de Cottrell donnant la densité des dislocations en excès, en fonction du rayon de courbure du cristal fléchi. On a constaté que la densité des dislocations dans des échantillons recristallisés et dans des cristaux solidifiés est d'environ  $2 \times 10^6$  par  $\text{cm}^2$ . Un nouveau mode de formation de sous-grains fut trouvé. On montre que le genre de morphologie des sous-grains, obtenu, dépend de l'orientation du cristal par rapport à la direction de la tension.

### EINE THERMISCHE ÄTZTECHNIK ZUM SICHTBARMACHEN VON VERSETZUNGEN IN SILBER

Es wurde eine thermische Ätztechnik zum Sichtbarmachen von Versetzungen in Silber entwickelt. Die Technik zeigt einzelne Versetzungen auf. Dies lässt sich an der guten Übereinstimmung zwischen der experimentell bestimmten Flächendichte der Versetzungen in durch Biegung verformten Einkristallen und der nach Cottrell berechneten Flächendichte zeigen. Der Berechnung liegt Cottrells Formel für die zusätzliche Versetzungsdichte eines "gebogenen" Kristalls als Funktion des Krümmungsradius zu Grunde. Es zeigte sich, dass die Versetzungsdichte in rekristallisierten und in aus der Schmelze gewachsenen Proben etwa  $2 \times 10^6$  pro  $\text{cm}^2$  betrug. Es wurde eine neue Art der Feinkornbildung gefunden. Es wird gezeigt, dass es von der relativen Orientierung des Kristalls zur Zugrichtung abhängt, welche Art von Feinkornmorphologie auftritt.

## INTRODUCTION

The concept of the dislocation has been used extensively and successfully to describe many phenomena in metals. However successful the theory has been in precisely describing the structure and properties of metals, it has lacked considerably for need of visual observation of a dislocation or of groups of single dislocations. Only recently have these observations been made in salt crystals<sup>1</sup> and in lineage boundaries in Germanium.<sup>2</sup>

Since the strain energy of a dislocation line is small, a successful etching technique to delineate it must be able to differentiate small differences in energy. The work of Chalmers<sup>3</sup> has indicated that a thermal etching of silver might well accomplish this purpose. Chalmers noted that thermal etching delineated grain boundaries at  $300^\circ\text{C}$  and at  $600^\circ\text{C}$  began to preferentially etch grooves along planes of high atomic population in order to minimize the very small surface energies involved. With

this consideration alone, thermal etching promised to be a successful method for preferential etching of dislocation singular lines.

The purpose of this research was to develop and verify a thermal etching technique for revealing dislocation lines in silver. A technique of this kind must be reproducible within the limits of laboratory control to draw any significant results. Hence it was required to show that there was an etching condition without a critical etching time to produce the same quantitative result. In addition, it had to be shown that correlations of the results of the technique with the amount of strain and geometry of deformation were consistent with the basic theory. Having established good evidence that the observed etch pits were dislocation intersections, other experiments were performed utilizing the thermal etching technique. Because of the limited application, these led to questions rather than answers in regard to the related topics of strain, recovery and recrystallization.

## SPECIMEN PREPARATION

Single crystals were grown from 99.9 per cent silver utilizing a modified Bridgman technique. Slabs were cut from the crystals with a minimum amount of distortion by the use of a cut-off wheel 0.020 in. thick. Heating of the specimens during cutting was very low since a feed

\* Received July 14, 1954.

† This paper is based on a thesis submitted by A. A. Hendrickson in partial fulfillment of the requirements for the Master of Science degree at the School of Engineering, Columbia University.

‡ Formerly Graduate Student and Research Assistant, Columbia University; now Physical Metallurgist, Ampco Metal, Inc., Milwaukee, Wisconsin.

\*\* Associate Professor of Metallurgy, Columbia University, New York, New York.

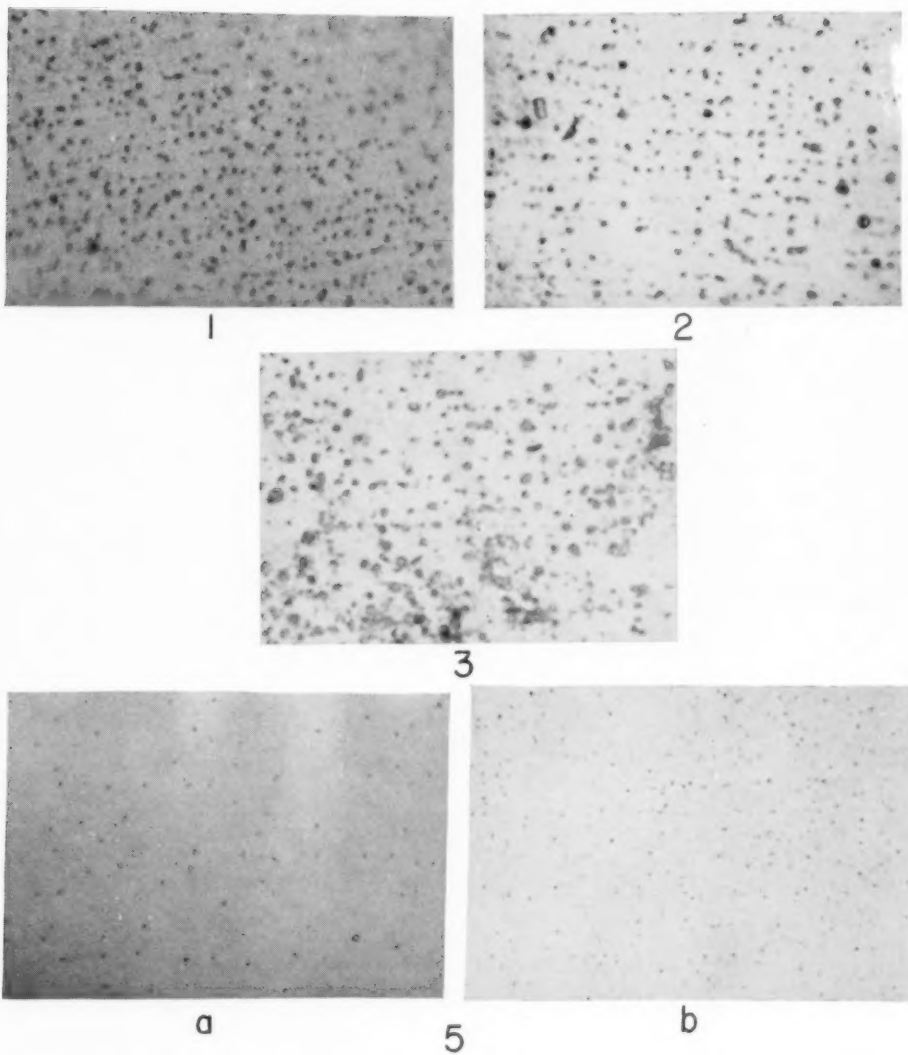


PLATE I. FIG. 1.—Appearance of a surface of a single crystal thermally etched for ten minutes at  $600^{\circ}\text{C}$  after it was bent to produce predominantly single glide and annealed at  $800^{\circ}\text{C}$  for 10 hours.  $1700\times$ . FIG. 2.—Thermally etched for 20 minutes at  $600^{\circ}\text{C}$ .  $1700\times$ . FIG. 3.—Thermally etched for 40 minutes at  $600^{\circ}\text{C}$ .  $1700\times$ . FIG. 5.—Thermally etched surfaces of silver as a function of prior amounts of bending.  $1000\times$ . (a) No prior bending (as grown from melt). (b) Bent to 1 cm radius. Annealed 5 hours at  $600^{\circ}\text{C}$ .

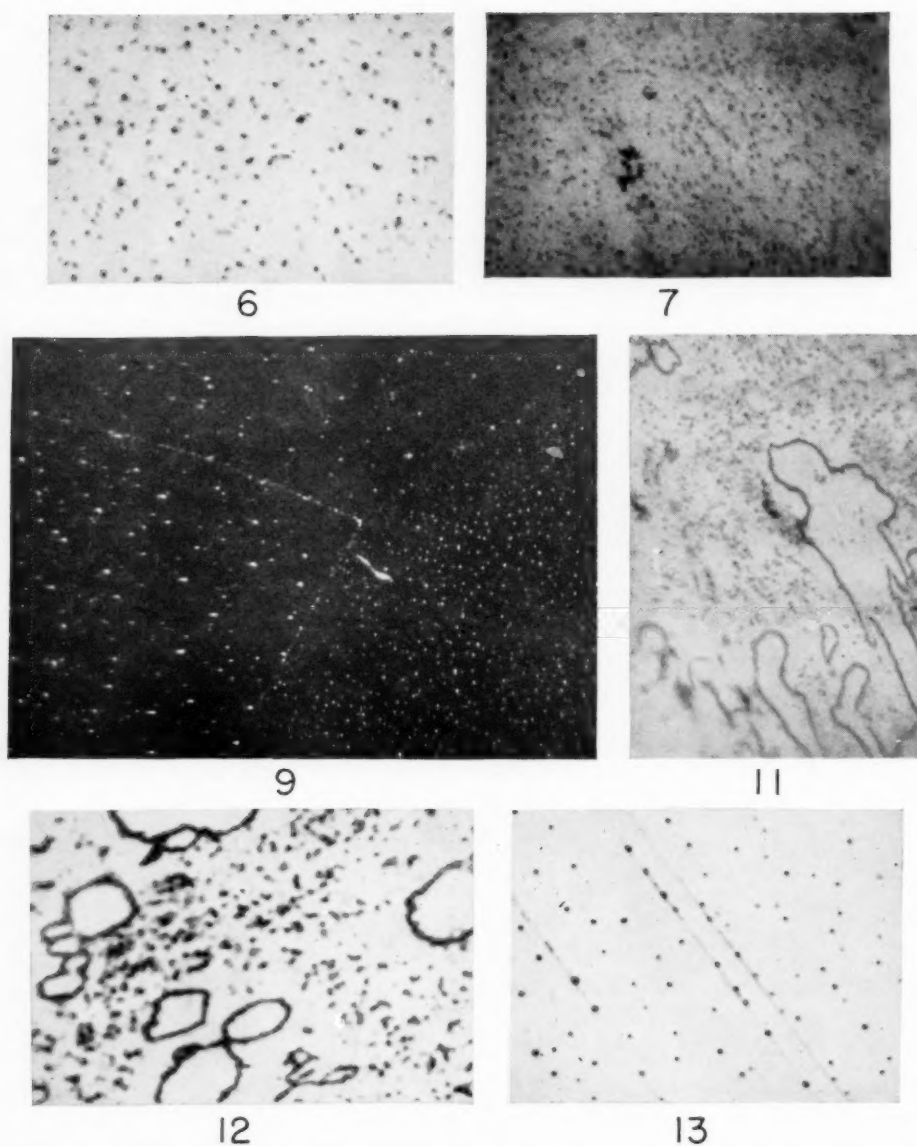


PLATE II. FIG. 6.—Crystal bent about a 1 cm bend radius. Annealed for 5 hours at 600°C. 2800X. FIG. 7.—Observed number of etch pits after bending about a 0.25 cm radius. Annealed at 850°C for 10 hours. 1700X. FIG. 9.—Photomicrograph showing etch pit density in the strained (right) and recrystallized portions of a crystal bent around a 4 cm radius and annealed for 6 hours at 550°C. 420X, polarized light. FIG. 11.—Crystal bent around a 0.25 cm radius. Annealed at 800°C for 16 hours and at 850°C for 16 more hours. 1700X. FIG. 12.—Same as Fig. 11. 2800X. FIG. 13.—Bent to 4 cm radius. Annealed at 550°C for 6 hours. Thermally etched. Electropolished. Bent some more (to about 3 cm radius). Thermally etched. 1950X.

of only 0.010 in./min was used. Before bending, all specimens were electropolished in a 9 per cent KCN solution at as high a current density as would produce a smooth, stain-free surface. This current density was about 12.5 amps per sq. in. The specimen was agitated rapidly during this polishing operation. The specimen surfaces were then washed and dried thoroughly in cold water and alcohol followed by drying rapidly in a stream of argon. At least five minutes of washing in cold water is required to produce a stain-free surface on thermal etching. Microscopic examination at 600 $\times$  insured a smooth, stain-free surface for etching.

All thermal etching was carried out in a tube furnace controlled within  $\pm 8^\circ\text{C}$  with a Tag Select-Ray multiple point controller. The specimens were etched in a thoroughly cleaned, porcelain crucible inserted into a vicor tube. The etching medium was one part of oxygen

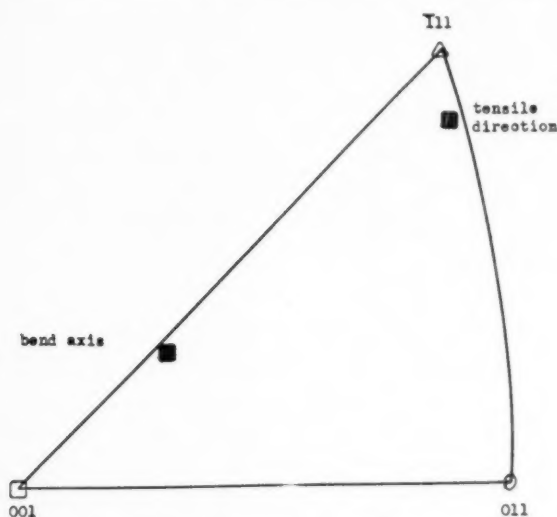


FIG. 4. Stereographic plot showing the axis of bend and tensile direction for specimens illustrated by Figs. 5a and 5b.

diluted in nine parts of argon. The gas ratio was controlled by a double connection to a water manometer. The total gas pressure of one inch of water provided satisfactory etching conditions.

The X-ray patterns were obtained by the usual back-reflection Laue techniques. Because of the small cross section of the specimens, the orientations found are accurate to only  $\pm 5^\circ$ .

#### EFFECT OF ETCHING TEMPERATURE AND TIME

Etching temperature was the first variable investigated. A high temperature, 850 $^\circ\text{C}$  was first attempted. It was found that the growth of etched areas proceeded too rapidly for good control during etching. Consequently, a lower temperature, 600 $^\circ\text{C}$ , was investigated. This temperature provided satisfactory thermal etching conditions. Figure 1 illustrates the appearance of a surface of a single crystal thermally etched for ten

TABLE I.

Radius of bend, cm	Observed etch pit density, $\text{cm}^{-2}$	Calculated dislocation density, $\text{cm}^{-2}$
no bend	$2.5 \times 10^6$	
5	$1.1 \times 10^7$	$6.9 \times 10^6$
3	$1.5 \times 10^7$	$1.2 \times 10^7$
1	$2.9 \times 10^7$	$3.5 \times 10^7$

minutes after it was bent to produce predominantly single glide and annealed at 800 $^\circ\text{C}$  for 10 hours.

It had to be shown that the number of etch pits did not vary with etching time at this temperature. The same crystal with single glide predominating was thermally etched for 10, 20 and 40 minutes. Figures 1, 2 and 3 show that the observed number of dislocation intersections with surface did not increase with etching time but only growth of the etched areas proceeded. Thus, it was illustrated that a satisfactory temperature for thermally etching dislocation intersections existed and that the number of etch pits produced at this temperature was independent of etching time.

#### EFFECT OF BEND RADIUS

The excess density of edge dislocations of the same sign to produce a certain amount of strain in bending has been calculated by Cottrell:<sup>4</sup>

$$\rho = 1/rb,$$

where  $\rho$  is the number of dislocations per unit area parallel to the bend axis,  $r$  is the bend radius at the neutral axis and  $b$  is the Burgers vector of the dislocation. In the case of silver,  $b$  is the interatomic distance in the  $\langle 110 \rangle$  direction.

In order to demonstrate that the observed density of etch pits was consistent with Cottrell's relation, four single-crystal slabs were bent around an axis given in the stereographic plot of Fig. 4. The axis of the crystal parallel to the tension direction is also given in Fig. 4. These crystals were annealed for five hours at 600 $^\circ\text{C}$  and then thermally etched. The observed and calculated density of dislocations are compared in Table I. Figures 5a and 5b illustrate the observed number of etch pits after no bending and a 1 cm bend radius respectively. In addition, a further comparison of calculated and observed densities of dislocations was made using Figs. 1, 6 and 7. In these specimens the bending geometry varied from specimen to specimen.

Table II gives the comparison between the observed and calculated dislocation densities for varying crystal orientation-bend geometry. The correlation is sum-

TABLE II.

Radius of bend, cm	Observed etch pit density, $\text{cm}^{-2}$	Calculated dislocation density, $\text{cm}^{-2}$
4	$7.3 \times 10^6$	$8.7 \times 10^6$
1.3	$8.4 \times 10^7$	$2.7 \times 10^7$
0.25	$1.8 \times 10^8$	$1.4 \times 10^8$



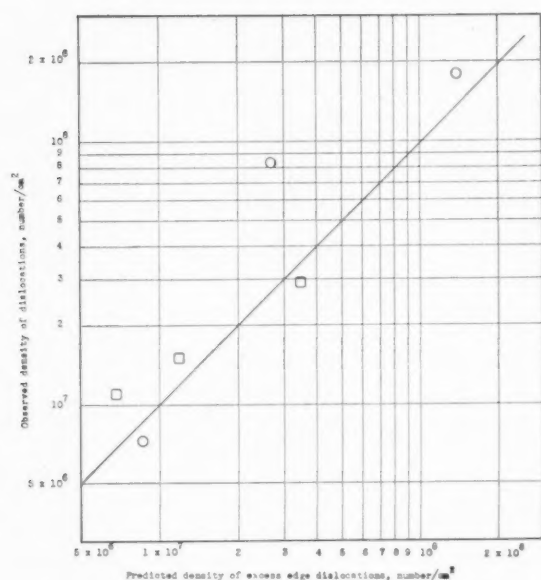


Fig. 8. Graphical correlation between predicted and observed densities of dislocations.

marized in Fig. 8. It is apparent that the agreement between calculated and observed densities is extremely good. The observed discrepancies can be accounted for in a number of ways. The calculated value may be too small in the event that the Burgers vector should correspond to the (112) direction or that wrong sign edge dislocations have been generated during the bend but have not been annihilated during subsequent anneal or that screw dislocations have been generated and intersect the surface observed. The calculated value may be too high if the Burgers vector for the dislocations is oriented away from the tension direction. The fact that good agreement has been obtained may result from a cancellation of the above affects. It is interesting to note that the worst disagreement occurs for the case where the Burgers vector (110) is parallel to the tension axis. In this case, the second factor would be negligible and the calculated value would be expected to be too low, as observed. Because the agreement is quantitative, it has been concluded that each pit corresponds to a single dislocation intersection with the surface.

Another observation that has significance is the value of the dislocation density for the annealed state. The as-grown crystal of Fig. 5a has a density of  $2.5 \times 10^6/\text{cm}^2$ . This value is in agreement with the value observed in a recrystallized grain. The density of the latter, calculated from Fig. 9, is about  $2 \times 10^6/\text{cm}^2$ . These observed values contrast with estimated values of  $10^8/\text{cm}^2$  for the annealed state.

#### EFFECT OF BENDING GEOMETRY

The effect of bending geometry was investigated superficially. The orientations of the crystals are as shown in Fig. 10. Group 1 orientation showed pre-

dominantly single glide and the appearance after annealing a specimen in this orientation after ten hours at  $800^\circ\text{C}$  is shown in Fig. 1. As shown, single glide (the existence of parallel dislocation singular lines) has led to the classical polygonized structure observed by Cahn<sup>6</sup> in hexagonal crystals, that is, dislocations aligned in nearly plane boundaries normal to the slip direction.

Multiple glide was involved in the specimens of group 2 and 3 orientations. Thus, the dislocations are not parallel in these specimens and as shown in Figs. 6 and 7, the dislocations tend to line up in curved walls. It is interesting to note that certain pits are darker than others. Although a number of explanations for this behavior may be given, it is preferred to abstain from speculation on this point. Perhaps, the most interesting observation made is shown in Figs. 11 and 12. These figures show the appearance of crystals of group 2 orientation after annealing for 16 hours at  $800^\circ\text{C}$  and 16 more hours at  $850^\circ\text{C}$ . The "dislocation-free" areas have been shown by means of Laue back-reflection diffraction patterns to be subgrains that are slightly disoriented from the deformed matrix. The rate of growth of these subgrains is extremely slow compared to the rate of migration of recrystallized-deformed crystal boundaries, such as shown in Fig. 9. It is believed that this fact implies two different mechanisms of boundary migration for the above two cases. This observation deserves further investigation. It is apparent that in order for the type of behavior illustrated in Figs. 11 and 12 to occur, it is necessary that no faster process leading to a decrease in dislocation density exist. Such processes are polygonization and recrystallization. By comparing the dislocation densities in the regions outside the subgrains shown in Figs. 11 and 12 with that determined from Fig. 7, it is found that no change in dislocation density

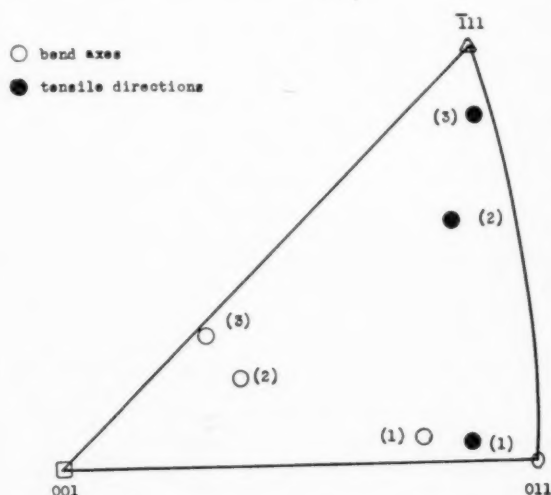


Fig. 10. Stereographic plot of the bend axes and directions of the tensile stresses for predominantly easy glide (1), complex glide (2), and greatest complexity (3).\*

\* Smallest bend radius.

with annealing time has occurred in these regions. Hence, it can be concluded that these dislocations are stuck. The question arises as to whether recrystallization is absent in this set of specimens because of the immobility of the stuck dislocations or because no recrystallization nuclei are present. It was found that the specimens in group 3 tended to recrystallize at lower deformation and temperatures than the specimens in group 2 orientation. The question arises in this case as to whether the case of recrystallization of group 3 specimens is due to the presence of recrystallization nuclei absent in group 2, or whether the dislocations are stuck in group 2 but are not stuck in group 3. The answers to these questions must await further experimentation. The observations of Lucke and Lange<sup>7</sup> on the strain hardenability of face-centered cubic crystals as a function of orientation of the tension axis are significant. They found that the resolved shear stress corresponding to a given resolved shear strain increases in the direction {110} to {111}. The fact that we have found the ease of recrystallization to increase in this direction may imply a correlation between strain hardenability and ease of recrystallization. That further experimentation is required to establish this point is obvious.

#### OBSERVATIONS OF DISLOCATIONS ALONG SLIP BANDS

The final survey made was to answer the question as to whether dislocations could be observed along slip bands using the thermal etching technique. A crystal was therefore subjected to the following treatment: Bent to 4 cm radius; electropolished and annealed at 550°C for six hours followed by thermal etching; bent some more (larger than 3 cm radius) and thermally etched without prior electropolish. The resulting surface is shown in Fig. 13. The slip direction is at a slight angle to the plane of the figure. The following observations have been made. In the regions excluding the slip bands the dislocation density is about  $9.5 \times 10^6$  dislocations/cm<sup>2</sup> (compared to  $8.7 \times 10^6$ /cm<sup>2</sup> calculated for the 4 cm radius). If the slip band region is included and a grand average density obtained the result is  $1.3 \times 10^7$ /cm<sup>2</sup> (as compared to  $1.2 \times 10^7$ /cm<sup>2</sup> for a 3 cm radius of bend). It appears therefore that new dislocations are introduced

on new slip bands rather than on bands which already have dislocations. Before this deduction can be accepted, it is desirable to investigate this phenomenon further. It can be concluded, however, that dislocation distributions along slip bands can be made visual. The utility of this technique is obvious.

#### CONCLUSIONS

1. Thermal etching of silver at 600°C in dilute solutions of oxygen produces microscopic etch pits; the number of these etch pits is independent of etching time.

2. The density of etch pits observed is proportional to the reciprocal radius of bend and correlates well with the calculated density of excess edge dislocations required for the bend radii.

3. The geometrical configuration of the etch pits varies with the complexity of deformation. Predominantly single-glide results in the etch pits lining up into straight boundaries perpendicular to the slip direction. More complex glide results in boundary formation becoming more difficult and the boundaries formed are irregular in shape.

4. A high degree of complexity in deformation may immobilize the dislocations. Long annealing at high temperatures of immobilized dislocation configurations results in the formation and growth of subgrains which are relatively free of dislocations. These subgrains are slightly disoriented with respect to the deformed matrix.

5. The density of dislocations in recrystallized and as grown crystals is about  $2 \times 10^6$ /cm<sup>2</sup>.

6. Dislocation distribution along slip bands can be revealed by thermal etching.

#### REFERENCES

1. A. H. Cottrell, "Interactions of Dislocations and Solute Atoms," Relation of Properties to Microstructure, American Society for Metals, 1954.
2. W. T. Read, "What Makes Metals So Weak?" Metal Progress, February 1954.
3. B. Chalmers and R. King, "Thermal Etching of Silver," Proc. Roy. Soc. July 21, 1948.
4. A. H. Cottrell, "Dislocations and Plastic Flow in Crystals," Oxford at the Clarendon Press, 1953.
5. R. D. Heidenreich and W. Shockley, "Report on the Strength of Solids," London Physical Society, 1948.
6. R. W. Cahn, "Conference on Strength of Metals," London, 1948; J. Inst. Metals, 1949.
7. K. Lucke and H. Lange, Z. Metall., 1952.

# THE INFLUENCE OF GRAIN BOUNDARIES ON THE NUCLEATION OF SECONDARY PHASES\*

P. J. CLEMM and J. C. FISHER†

In calculating the critical energy required for the nucleation of grains at two, three and four grain junctions it is necessary to know (1) the volume of the nucleus, (2) the surface area of the nucleus, and (3) the matrix grain boundary area which has been absorbed by the nucleus. These three quantities have been calculated as a function of (1) the dihedral angle between the surfaces bounding the nucleus and (2) the radius of curvature of the bounding surfaces.

To illustrate the use of the calculated equations the critical energy for the nucleation of ferrite from austenite at two, three and four grain junctions has been calculated.

## L'INFLUENCE DES JOINTS INTERCRISTALLINS SUR LA GERMINATION DE PHASES SECONDAIRES

Pour calculer la valeur critique de l'énergie requise pour la germination des grains nouveaux aux jonctions de grains, doubles, triples et quadruples, il est nécessaire de connaître (1) le volume du germe, (1) l'aire de la surface du germe, (3) l'aire de la surface des joints de la matrice qui ont été absorbés par le germe. Ces trois quantités furent calculées en fonction de (1) l'angle solide entre les surfaces qui limitent le germe, (2) le rayon de courbure de ces mêmes surfaces.

En vue d'illustrer l'emploi des équations déduites de cette façon, on a calculé la valeur critique de l'énergie pour la germination de la ferrite à partir de l'austenite aux jonctions des grains, doubles, triples et quadruples.

## DER EINFLUSS VON KORNGRENZEN AUF DIE KEIMBILDUNG SEKUNDÄRER PHASEN

Will man die zur Keimbildung von Kristallen an Zwei-, Drei- oder Vierkornpunkten notwendige kritische Energie berechnen, so muss man (1) das Volumen des Keimes, (2) die Grösse der Oberfläche des Keimes und (3) die Grösse der von dem Keim absorbierten Korngrenzenfläche der Wirtskörner kennen. Diese drei Grössen wurden als Funktion von (1) dem diedrischen Winkel zwischen den den Keim begrenzenden Flächen und (2) dem Krümmungsradius der begrenzenden Flächen berechnet.

Um die Anwendungsmöglichkeiten der theoretischen Gleichungen zu illustrieren, wird die zur Keimbildung von Ferrit aus Austenit an Zwei-, Drei- und Vierkornpunkten erforderliche kritische Energie berechnet.

In calculating the nucleation rate of a second phase *B* in a homogeneous solid matrix *A* the critical nucleus is spherical, and the critical energy that must be supplied by thermal fluctuations (in the absence of strain energy) is

$$W^* = \frac{16\pi\gamma_{AB}}{3\Delta f_v^2},$$

where  $W^*$  is the critical energy,  $\gamma_{AB}$  is the interfacial or grain boundary energy between phases *A* and *B*, assumed isotropic, and  $\Delta f_v$  is the difference in volume free energy between phases *A* and *B*.<sup>1</sup>

In a polygrained metal, however, the nucleation of a second phase is much more likely to take place at a grain boundary or at the junction of several grains, since at these sites the grain boundary that is eliminated by formation of a nucleus provides an energy source that can supply some of the needed critical energy for nucleation, thereby reducing the amount to be supplied by thermal fluctuations.

Let the grain boundary area that is eliminated between *A-A* grains in forming the nucleus of a new phase *B* at a grain junction of phase *A* be

$$A_{AA} = ar^2,$$

where  $r$  is the radius of curvature of the surfaces bound-

ing the new phase *B*; let the new grain boundary area formed between grains *A* and *B* be

$$A_{AB} = br^2,$$

and let the volume of the new phase *B* formed be

$$V = Cr^3.$$

Here  $a$ ,  $b$ , and  $c$  are coefficients that are functions of the *A-A* and *A-B* grain boundary energies. Then the work done in forming a nucleus of volume *V* is

$$W = \gamma_{AB}A_{AB} - \gamma_{AA}A_{AA} + \Delta f_v V,$$

or

$$W = \gamma_{AB}br^2 - \gamma_{AA}ar^2 + \Delta f_v cr^3.$$

The work of formation of the critical size nucleus corresponds to  $\partial W / \partial r = 0$ , for which

$$W^* = \frac{4}{27} \frac{(b\gamma_{AB} - a\gamma_{AA})^3}{c^2 \Delta f_v^2}.$$

The problem of grain junction nucleation then is reduced to finding the coefficients  $a$ ,  $b$ , and  $c$ , corresponding to various types of grain junction.

## TWO-GRAIN JUNCTIONS

First, the case of a simple grain boundary or two-grain junction will be considered. The grain boundary is assumed to lie in a plane, and it is assumed that all grain boundary energies are isotropic.

\* Received August 4, 1954.

† General Electric Research Laboratory, Schenectady, New York.

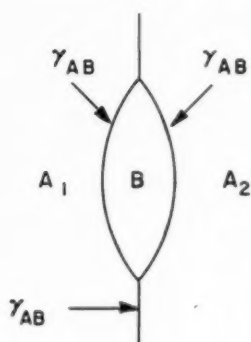


FIG. 1.

The critical nucleus of the newly formed phase *B* will have the shape of a symmetrical lens as shown in Fig. 1. The dihedral angle at the edge of the lens is determined by equilibrium of the interfacial energies.

Letting the grain boundary energy between the two *A* grains be  $\gamma_{AA}$  ergs/cm<sup>2</sup> and the grain boundary energy between *A* and *B* grains be  $\gamma_{AB}$  ergs/cm<sup>2</sup>; then the forces exerted by the grain boundaries on a length of the perimeter of the lens are as shown in Fig. 2, which is

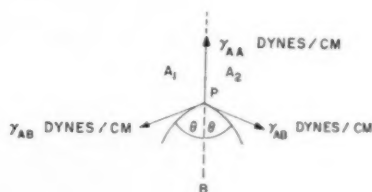


FIG. 2.

drawn perpendicular to the lens perimeter at point *P*. For equilibrium at point *P*, or at any other point along the edge, the angle  $\theta$  must be such that

$$\cos \theta = \frac{\gamma_{AA}}{2\gamma_{AB}}$$

Figure 3 shows a diametrical cross section of the lens where *PR* is the trace of the area *A*<sub>AA</sub> and *PQR* and

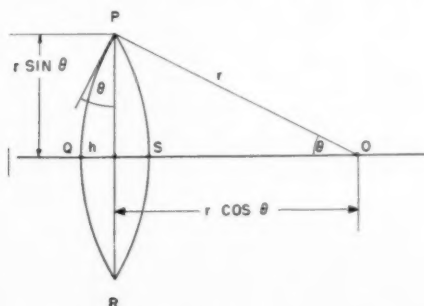


FIG. 3.

*PSR* are the traces of the area *A*<sub>AB</sub>. Then

$$A_{AA} = ar^2 \\ = \pi \sin^2 \theta r^2,$$

or

$$a = \pi \sin^2 \theta.$$

Also,

$$A_{AB} = br^2 = 2(2\pi r)h$$

$$= 4\pi(1 - \cos \theta)r^2,$$

and

$$b = 4\pi(1 - \cos \theta).$$

Further,

$$V = cr^3 = \pi h^2 \left( r - \frac{h}{3} \right)$$

$$= \frac{2\pi}{3} (2 - 3 \cos \theta + \cos^3 \theta) r^3,$$

and

$$c = \frac{2\pi}{3} (2 - 3 \cos \theta + \cos^3 \theta).$$

These equations may be represented in somewhat more convenient form if we let

$$k = \cos \theta = \frac{\gamma_{AA}}{2\gamma_{AB}}.$$



FIG. 4.

Then

$$a = \pi(1 - k^2),$$

$$b = 4\pi(1 - k),$$

$$c = \frac{2\pi}{3} (2 - 3k + k^3).$$

### THREE-GRAIN JUNCTIONS

Here the volume of the newly formed phase particle will be bounded by three equivalent spherical surfaces as shown in Fig. 4.

The dihedral angle at the edge between two surfaces will again be determined by the force diagram illustrated in Fig. 2.

For the three-grain junction the area and volume coefficients are as follows:

$$a = 3\beta(1 - k^2) - k(3 - 4k^2)^{1/2},$$

$$b = 12 \left( \frac{\pi}{2} - \alpha - k\beta \right),$$

$$c = 2 \left[ \pi - 2\alpha + \frac{k^2}{3} (3 - 4k^2)^{1/2} - \beta k (3 - k^2) \right],$$



where

$$\alpha = \arcsin \frac{1}{2(1-k^2)^{1/2}},$$

$$\beta = \arcsin \frac{k}{[3(1-k^2)]^{1/2}}.$$

#### FOUR-GRAIN JUNCTIONS

Here the volume of the newly formed phase will be bounded by four equivalent spherical surfaces. It is a spherical tetrahedron, as sketched in Fig. 5. The area

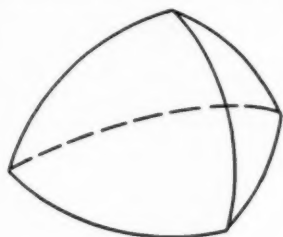


FIG. 5.

and volume coefficients are

$$a = 3 \left\{ 2\phi(1-k^2) - K \left[ \left( 1 - k^2 - \frac{K^2}{4} \right)^{1/2} - \frac{K}{\sqrt{8}} \right] \right\},$$

$$b = 24 \left( \frac{\pi}{3} - k\phi - \delta \right),$$

$$c = 2 \left\{ 4 \left( \frac{\pi}{3} - \delta \right) + kK \left[ \left( 1 - k^2 - \frac{K^2}{4} \right)^{1/2} - \frac{K}{\sqrt{8}} \right] - 2k\phi(3-k^2) \right\},$$

where

$$K = \frac{4}{3} \left( \frac{3}{2} - 2k^2 \right)^{1/2} - \frac{2}{3}k,$$

$$\phi = \arcsin \frac{K}{2(1-k^2)^{1/2}},$$

$$\delta = \arcsin \frac{\sqrt{2-k(3-K^2)}}{K(1-k^2)^{1/2}}.$$

To illustrate the use of these equations, the energy required to form a ferrite grain in an austenite matrix can be calculated and plotted as a function of the radius of curvature of the nucleus surfaces for the case of a ferrite grain nucleating

1. Entirely within an austenite grain
2. At a two austenite grain junction
3. At a three austenite grain junction
4. At a four austenite grain junction.

The numerical quantities used in the calculations are as follows:<sup>2\*</sup>

$\gamma_{AA}$  Austenite—*austenite* 850 ergs/cm<sup>2</sup>

$\gamma_{AB}$  Austenite—*ferrite* 600 ergs/cm<sup>2</sup>

$\Delta f_v$  (Austenite→ferrite),  $-4.35 \times 10^8$  ergs/cm<sup>3</sup>.<sup>3</sup>

The results when plotted are as shown in Fig. 6, showing clearly that four-grain junctions are the most favored nucleation sites for ferrite nucleation ( $W^*$  is the smallest), three-grain junctions next most favored, followed by two-grain junctions, and finally grain interiors.

Another conclusion which may be derived from the equations for  $a$ ,  $b$ , and  $c$  and from the force diagram of Fig. 2 is that when  $\gamma_{AA}/2\gamma_{AB}$  exceeds the following critical values the forces at the grain edges will no longer be in equilibrium and there will be a continuous free energy decrease as the new phase grows from zero size.<sup>4</sup>

$$\frac{\gamma_{AA}}{2\gamma_{AB}} (=k)$$

grain interior  $\infty$

2-grain junction 1

3-grain junction  $\frac{\sqrt{3}}{2} (=0.866)$

4-grain junction  $(2/3)^{1/2} (=0.817)$ .

Whenever  $\gamma_{AA}/2\gamma_{AB}$  exceeds these critical values the growth of a new phase will be controlled not by nucleation but only by its growth rate and the amount of grain boundary present per unit volume.

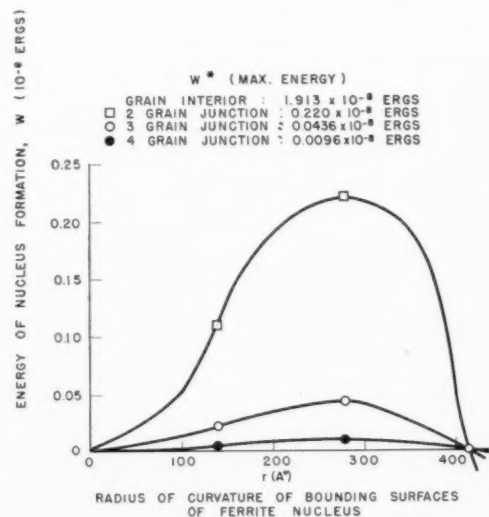


FIG. 6. Energy of ferrite nucleus formation as a function of surface curvature.

\* The temperature at which these values were determined is in the neighborhood of 1000°K.

## ACKNOWLEDGMENTS

The authors wish to extend their thanks to Dr. J. H. Hollomon for suggesting the problem, to Dr. R. L. Fullman for helpful discussions of the geometry involved and to Mrs. N. V. Doyle for performing the numerical calculations.

## REFERENCES

1. M. Vollmer, "Kinetik der Phasenbildung," Theodor Steinkopff, Dresden, 1939.
2. L. H. Van Vlack, "Intergranular Energy of Iron and Some Iron Alloys," Trans. A.I.M.E. **191**, 251 (1951).
3. J. C. Fisher, "Influence of Boron on the Hardenability of Steel," R.L. 1031, General Electric Research Laboratory, January 1954.

# NUCLEAR ELECTRIC QUADRUPOLE INTERACTIONS IN ALUMINUM\*

T. J. ROWLAND†

An experimental study of the nuclear magnetic resonance absorption of aluminum in solid solutions containing zinc or magnesium as solute is presented. The magnitude of the electric gradients caused at the Al lattice sites by the solute atoms is estimated and compared with the relative sizes of various solute atoms in a common solvent. Effects of precipitation and annealing have also been detected, and some possible applications are discussed.

## LES INTERACTIONS DES QUADRUPOLES NUCLÉAIRES, ÉLECTRIQUES DANS L'ALUMINIUM

On présente une étude expérimentale de l'absorption magnétique, nucléaire de résonance de l'aluminium en solution solide contenant du zinc ou du magnésium comme soluté. On a estimé la grandeur des gradients électriques causés par la présence d'atomes de soluté aux noeuds du réseau d'aluminium et on l'a comparé aux dimensions relatives des différents atomes dans un solvant commun. On a constaté aussi des effets de recuit et de précipitation; certaines applications possibles sont discutées.

## ELEKTRISCHE KERNQUADRUPOLEWECHSELWIRKUNGEN IN ALUMINIUM

Es wird über eine Experimentaluntersuchung der kernmagnetischen Resonanzabsorption in festen Lösungen von Zink oder Magnesium in Aluminium berichtet. Die Grössenordnung der Gradienten der elektrischen Felder, die an den Al-Gitterplätzen durch die gelösten Atome hervorgerufen werden, wird abgeschätzt und mit den relativen Abmessungen der verschiedenen gelösten Atome in einem gegebenen Lösungsmittel verglichen. Es wurden ausserdem Einflüsse von Ausscheidungen und Glühungen aufgefunden. Einige mögliche Anwendungen wurden diskutiert.

## INTRODUCTION

It has recently been shown<sup>1</sup> that nuclear magnetic resonance techniques are capable of detecting deviations from cubic symmetry on an atomic scale in metallic crystals of cubic lattice structure. The electric gradients at the nuclear sites having noncubic environment interact with the nuclear electric quadrupole moment to produce a change in energy of the nuclear spin levels from the value in the absence of the gradients. Al<sup>27</sup>, which has a nuclear quadrupole moment  $Q$  of  $+0.156 \times 10^{-24}$  cm<sup>2</sup>,<sup>2</sup> and a spin  $I$  of  $5/2$ , has a resonance line width in the pure metal which can be explained almost entirely by local field (dipole-dipole) broadening. Foreign atoms or lattice imperfections will cause additional broadening of the line in a powdered sample which, if sufficiently drastic, will cause an apparent decrease in intensity.

The difference in energy between adjacent space-quantized levels of the aluminum nucleus, when in an external magnetic field  $H_0$  and an axially symmetric electric field is to a first approximation,

$$\Delta W_{m \rightarrow m-1} = h\nu_0 - (2m-1)(1-3\cos^2\theta) \frac{3e^2qQ}{8I(2I-1)}, \quad (1)$$

where  $h\nu_0 = \mu H_0/I$ ,  $m$  and  $m-1$  are the magnetic quantum numbers of the adjacent levels,  $\theta$  is the angle between  $H_0$  and the axis of the electric field, and  $q$  is the electric gradient at the nucleus in the direction of that axis. The frequency of the  $m=1/2 \rightarrow -1/2$  transition is

seen to be unchanged according to (1). Since all angles  $\theta$  are present in the polycrystalline samples, the satellite lines (transitions  $5/2 \rightarrow 3/2$ ,  $3/2 \rightarrow 1/2$ ,  $-1/2 \rightarrow -3/2$ , and  $-3/2 \rightarrow -5/2$ ) take on a characteristic shape<sup>3</sup> and cause a broadening, though no shift, of the resonance.<sup>1</sup>

The  $m=1/2 \rightarrow -1/2$  transition will be broadened in second-order perturbation. The shift of the individual components, using the notation above, is

$$\Delta W_{1/2 \rightarrow -1/2} = h\nu_0 + A(1-9\cos^2\theta)(1-\cos^2\theta), \quad (2)$$

where

$$A = \frac{9}{64} \frac{2I+3}{4I^2(2I-1)} \frac{e^4 q^2 Q^2}{h\nu_0}.$$

The shape of the absorption line in a polycrystalline material can be determined by the straightforward process used by Pake.<sup>4</sup>

Figure 1 shows that the line broadens and its center of gravity moves to lower frequencies. The dashed curve describes the theoretical central line shape and the full curve the absorption as it might be observed when broadened by local fields and other sources of symmetrical broadening. Nierenberg and Ramsey<sup>5</sup> have discussed the same problem in molecular beam spectroscopy.

The shape of the absorptions to be discussed can be written to a good approximation as a function

$$g(\nu) = \int_{-\infty}^{\infty} P(q) \{ (9/35)g_{eq}(\nu) + (26/35)g_{\sigma q}(\nu) \} dq, \quad (3)$$

where  $P(q)$  denotes the probability that the gradient  $q$  exists at any particular lattice site of the nuclei under

\* Received August 10, 1954.

† Division of Applied Science, Harvard University, Cambridge, Massachusetts; now at Metals Research Laboratories, Electro Metallurgical Co., Niagara Falls, New York.

study and in an alloy is a function of the composition.  $P(q)$  is normalized so that  $\int_{-\infty}^{\infty} P(q) dq = 1$ , thus  $NP(q)$ , where  $N$  is the total number of nuclei of gyromagnetic ratio  $\gamma$  and quadrupole moment  $Q$ , is the number of nuclei having quadrupole coupling  $|e^2Qq/h|$ . The function  $g_{cq}(\nu)$  describes the central line shape for a gradient  $q$  and  $g_{sq}(\nu)$ , which is made up of functions representing all the satellites, describes the total resultant satellite shape for gradient  $q$ ; the functions  $g(\nu)$  are also normalized so that  $\int_{-\infty}^{\infty} g(\nu) d\nu = 1$ .

By integrating the resonance curve the total amount of power absorbed by the nuclear spin system can be determined. Experimentally the integration is usually extended over only a rather narrow region surrounding  $\nu_0$ , thus only those transitions will contribute to the observed absorption which occur within this region, say from  $\nu_0 - \Delta\nu$  to  $\nu_0 + \Delta\nu$ . The shape of the satellites suggests another simplification which will be used to interpret the data. The major satellite contribution to the observed absorption derives from their peaks, or infinities, which occur at  $\theta = \pi/2$ . The limited integration automatically excludes all those peaks contributed by nuclei at which  $q > 20h\Delta\nu/3e^2Q$  (calculated for the  $m = 5/2 \rightarrow 3/2$  transition). Let us consider a primary solid solution of  $c$  atomic fraction of solute. If we are observing the solvent resonance and a solute atom in the  $n'$ th-position causes a  $q_{n'} > 20h\Delta\nu/3e^2Q$  while that in an  $n'+1$  neighbor position causes a  $q_{n'+1} < 20h\Delta\nu/3e^2Q$  then the plot of the integrated intensity (from  $\nu_0 - \Delta\nu$  to  $\nu_0 + \Delta\nu$ ) should follow the function  $(1-c)^n$ , where  $n$  is the number of neighboring lattice sites contained in a sphere passing between the  $n'$  and  $n'+1$  neighbors. Equivalently  $n$  is the number of solvent atoms, in a sphere around a solute atom, which have an electric gradient  $q$  greater than  $20h\Delta\nu/3e^2Q$ .  $(1-c)^n$  is the probability that a solvent nucleus has no solute atom inside this sphere of critical radius, provided the solution is ideally random.

In the present experiment aluminum alloys of various zinc and magnesium contents were used to determine the extent of the influence of the solute atoms and the magnitude of the gradients caused by them in the aluminum lattice.

Pure aluminum (99.99) was alloyed with spectroscopically pure zinc to provide the Al-Zn alloys and with "commercial pure" (99.9) magnesium to provide the Al-Mg alloys used. They were made in graphite crucibles and heat treated prior to the resonance experiment in such a way as to bring about single phase equilibrium. The papers of Fink and Van Horn<sup>6</sup> and Fink and Smith<sup>7</sup> were used as a guide in establishing the desired state. Inasmuch as all of the specimens were used in the form of filings the final solution heat treatment was carried out on the cold-worked (as filed) material, immediately before use.

The detection equipment consisted of a Pound-Knight-Watkins type of radiofrequency spectrometer.<sup>8,9</sup> The external magnetic field of about 5560 gauss was

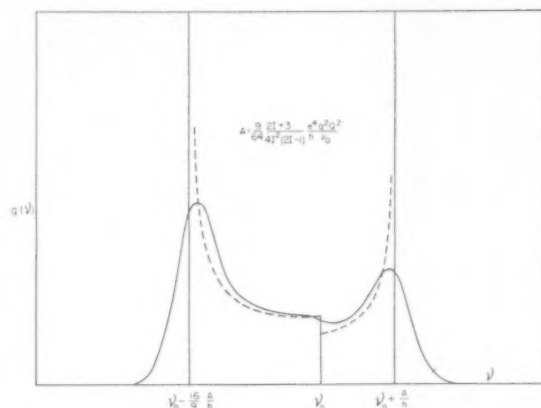


FIG. 1. The theoretical shape of the  $m = \frac{5}{2} \rightarrow \frac{3}{2}$  absorption in a powdered material when  $qQ$  is nonvanishing. Second-order quadrupole interaction broadens the line and shifts its center of gravity.

supplied by a permanent magnet. Over the volume of the sample the field inhomogeneity was less than 0.3 gauss, very small compared to the width of the Al resonance in the metal. The magnetic field was sinusoidally modulated at 280 cps with a peak amplitude of 1.1 gauss. The frequency of the r-f oscillator was slowly swept through the resonance and the oscillator output fed into a phase sensitive detector with a band width of  $1/8 \text{ sec}^{-1}$ .

The particle size of the samples was in every case smaller than the skin depth so that the experimentally observed quantities do indeed correspond to nuclear absorption only.<sup>10</sup>

## RESULTS AND DISCUSSION

The width and shape of the absorption line in Al-Zn alloys remain approximately constant over the range of composition to be considered. Consequently the integrated intensity in the region  $2\Delta\nu$  centered at  $\nu_0$  is proportional to the maximum absorption  $g(\nu_{\max})$ . In Fig. 2 these maxima are plotted as a function of the zinc concentration. They represent the absorption per Al atom in the alloy under like conditions of r-f field strength and modulation of the external magnetic field.

The absorption is seen to drop rapidly from the value characteristic of pure Al to about one-quarter of the pure Al value. Since the central line intensity is, according to theory, precisely  $9/35$  of the total of all five component lines this remaining absorption is identified with it. The lower part of Fig. 2 is a double logarithmic plot of the satellite intensity only (i.e.,  $g(\nu_{\max})/g_0(\nu_{\max}) - 9/35$ ) versus the zinc concentration. The slope of the line drawn through the experimental points determines the exponent  $n$  to be about 98; this number is to be associated with a sphere around a Zn atom outside of which  $q$  is less than approximately  $6 \times 10^{21} \text{ cm}^{-3}$ , corresponding to a  $\Delta\nu$  of about  $5 \times 10^8 \text{ sec}^{-1}$ . More precisely, two values of  $n$  corresponding to gradients necessary to



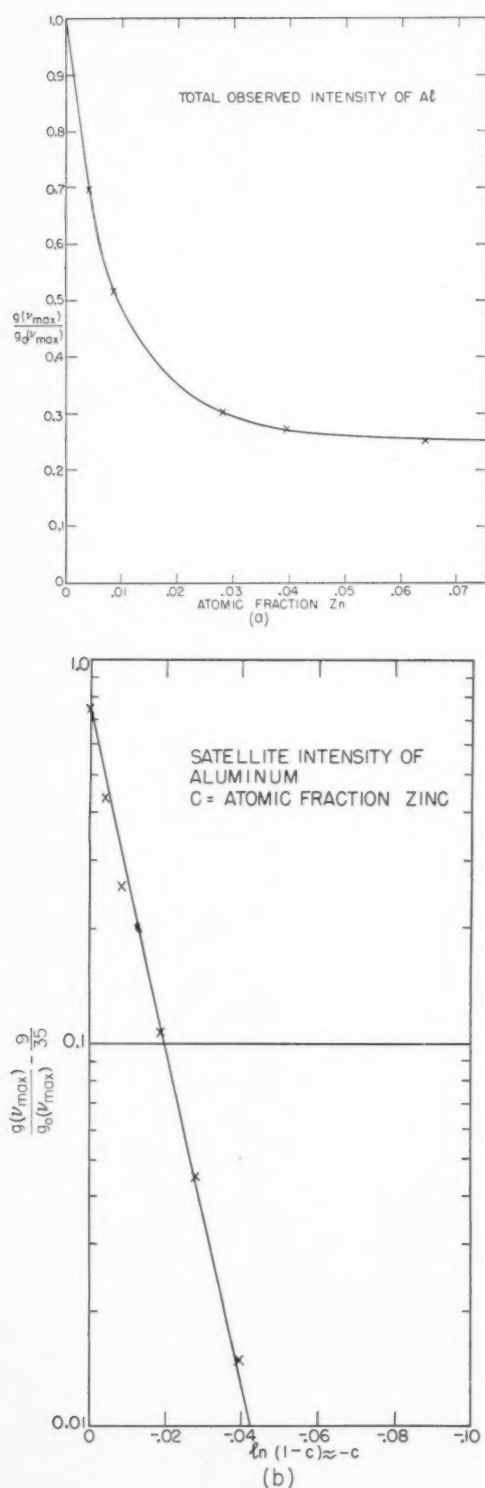


FIG. 2. (a) Intensity of absorption per Al atom as a function of the Zn content in annealed alloys. (b) The satellite intensity alone closely obeys the function  $(1-c)^{0.8}$ , the  $m = \frac{1}{2} \rightarrow -\frac{1}{2}$  transition of Al is unaffected by a near neighbor zinc atom in a 5560 gauss external field.

cause each satellite pair to fall outside of  $\nu_0 \pm \Delta\nu$  could be defined, but this is unwarranted by the data.

From the unaffected central line we can estimate an upper limit for  $q_1$ , the gradient at an Al atom with a zinc nearest neighbor. Let us say that if the central line were broadened to 2 kc/s it would show up as a broadening of the observed absorption. Then, using Eq. (2) we find that  $e^2 q_1 Q / h < 6.3 \times 10^6$  cps or  $q_1 < 1.2 \times 10^{23}$  cm $^{-3}$ , where  $\nu_0 = 6.18 \times 10^6$  cps and  $Q = 0.156 \times 10^{-24}$  cm $^2$  have been used.

From the data given above for the satellites one can estimate whether or not it is possible to satisfy both conditions simultaneously. It was stated that outside of a sphere (around an impurity) containing about 98 atoms,  $q$  is less than  $6 \times 10^{21}$  cm $^{-3}$ . This sphere will include 6th neighbors but not 7th. Let us therefore take  $q_7 = 6 \times 10^{21}$  cm $^{-3}$ . We find  $q_1 = (r_1/r_7)^3 q_7 = 18.5 \times 6 \times 10^{21} = 1.1 \times 10^{23}$  cm $^{-3}$  indicating that indeed the nearest neighbor's central line can escape broadening while 6th neighbors satellites are significantly broadened.

In two ways the data resulting from the work on Al-Mg alloys differ markedly from that on the Al-Zn discussed above. The intensity drops more abruptly with small solute additions and the  $m = 1/2 \rightarrow -1/2$  transition is affected. The latter is observed as an asymmetrically broadened line. In Fig. 3 the ratio  $g(\nu_{\max})/g_0(\nu_{\max})$  has been plotted for the Al-Mg alloys as a function of the atomic fraction Mg. The exponent  $n$ , describing the number of atoms for which  $q > 6 \times 10^{21}$ , is 130 for this case; thus magnesium atoms must cause greater strain at neighboring sites than do zinc in the aluminum lattice.

Using the simplest elasticity theory for homogeneous isotropic media<sup>11</sup> the relation between the radial strain surrounding a foreign atom and the size of this atom is  $s_r = fa^3/r^3$ , where  $f$  is the fractional difference of the radii of the impurity and the solvent atoms in the alloy,  $a$  is the solvent bulk atomic radius and  $r$  is the distance from the impurity center. The uncertainty in the meaning of  $f$  makes this of doubtful quantitative use, but perhaps as a proportionality it is valid. Let us assume that the electric gradient at a lattice point is proportional to the strain at that point. Then at points of equal  $q$  in the vicinity of two different impurity species the relation  $f_1 a^3 / r_1^3 = f_2 a^3 / r_2^3$  will hold. Of course  $r_1 = (3n_1 / 4\pi d_a)^{1/3}$ ,  $n_1$  being the experimentally determined exponent for the first impurity and  $d_a$  the atomic density of the alloy in atoms/cm $^3$ . Similarly  $r_2$  is related to  $n_2$  and thus  $f_1 / f_2 = n_1 / n_2$ . The number of nuclei affected by gradients caused by an impurity are directly proportional to the fractional difference in radius of the impurity and solvent atoms in any one solvent. If  $n_1$  pertains to Mg, of radius  $a_1$  and  $n_2$  to Zn of radius  $a_2$ , each in Al, we find  $f_1 = 1.3 f_2$ , i.e.,  $a_1 - a = 1.3(a_2 - a)$ . As mentioned above, further evidence that a Mg atom causes larger gradients than does a Zn atom is found in the shape of the central component for high Mg content. It no longer remains symmetrical, as was the case in

Al-Zn, but becomes somewhat asymmetrical and broadened and the recorded peak-to-peak amplitude drops. A higher magnetic field  $H_0$  would decrease the second-order interaction, and according to the estimate of the gradients obtained from the satellite behavior, an increase in  $H_0$  by a factor of about 1.7 should make the central line behave as it does in Al-Zn at 5560 gauss.

Because of the rather slight drop in  $g(\nu_{\max})$  and the asymmetry of the central line it is probable that its perturbation is due to nearest neighbors only. Using notation introduced previously it can be described by a shape function

$$g_c(\nu) = (1-c)^{12}g_{c0}(\nu) + [1 - (1-c)^{12}]g_{cq}(\nu), \quad (4)$$

where  $g_{c0}$  is the unperturbed central line shape. Equation (4) merely represents the second term of

$$g(\nu) = 0.743(1-c)^{130}g_{sq}(\nu) + 0.257g_c(\nu), \quad (5)$$

since the first term is less than  $10^{-3}$  for  $c$  greater than 0.05. The solid line in Fig. 3 is a plot of the function  $0.743(1-c)^{130} +$  (the dotted line in Fig. 3). The dotted and full lines coincide beyond about 4 atomic per cent Mg. Figure 1 shows  $g_{cq}$  in a powder assuming  $q$  the same at each lattice site. The present situation demands that the quadrupole width be a fraction of the dipolar broadening instead of vice versa as is represented in Fig. 1. The peak at  $\nu_0 - 16A/9h$  contains about twice the intensity of the one at  $\nu_0 + A/h$ ; consequently, when this line is superimposed on the essentially unperturbed

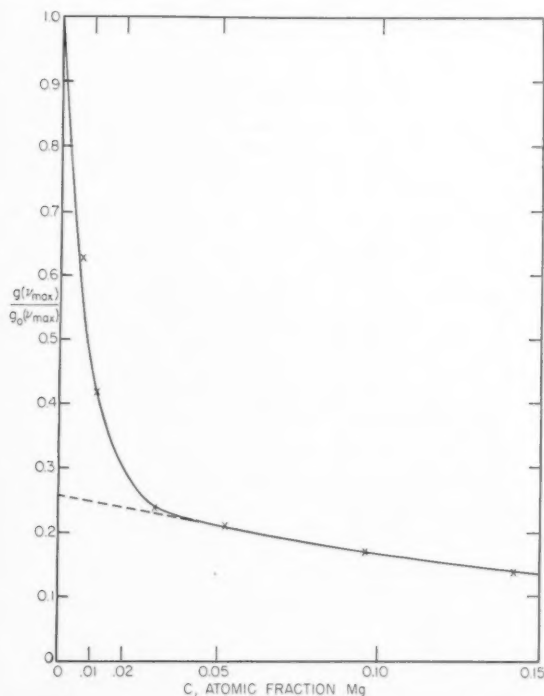


Fig. 3. Intensity per Al atom in Al-rich Al-Mg solid solutions. The satellite intensity is proportional to  $(1-c)^{130}$  showing that a Mg atom causes higher gradients at neighboring Al sites than does a Zn atom.

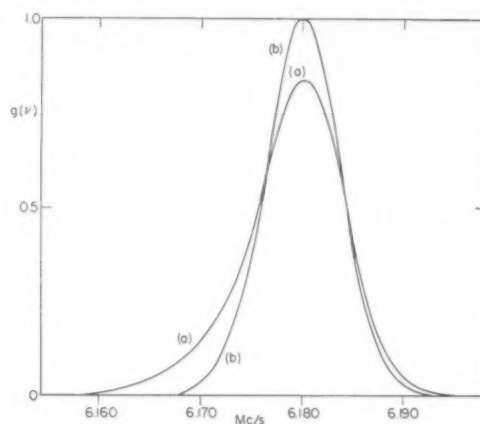


Fig. 4. Experimental absorption of Al in an alloy of Al-14 atomic per cent Mg: (a) as filed from the quenched material, (b) from the same sample after a 250°C, 5 day anneal. A Mg-rich phase precipitates.

central line, an increase in the absorption on the lower side of the line takes place.

Curve (a) of Fig. 4 illustrates this asymmetry in the central line of Al in an Al-14 atomic per cent Mg alloy. Curve (b) was obtained from the same alloy as curve (a) after it had been held at a temperature of 250°C for 5 days. During the precipitation process the Mg content of the matrix decreases so much that second order perturbation effects become unnoticeable. This is a relatively minute effect compared to that which could be expected if the impurity concentration in the solid solution should drop below that necessary for satellite disappearance. Drastic changes could then occur, and, using appropriate normalization conditions for nuclear absorption per atom in one phase of a two-phase system the precipitation process might be followed quite closely. Exact quantitative interpretation of the shape of the Al resonance in Al alloys of high Mg content is difficult, because it is probable that many Al atoms have more than one Mg neighbor.

Throughout the discussion of quadrupole effects complete randomness of the solute atoms on the lattice sites has been assumed. The extension of the theory to ordered structures is fairly straightforward and carefully chosen alloys could give much information on the ordering process and degree of ordering as a function of temperature and composition. In the experiments discussed here the effects of short range order would be slight causing a very small deviation from the straight line plot of log intensity versus log composition. Even for maximum ordering the intensity will not deviate significantly from that expected of a random solution if it is dilute. This has been calculated by Bloembergen<sup>12</sup> for a face-centered cubic lattice. Greater deviations in intensity naturally accompany higher solute concentrations, and, according to the computation referred to above, a measurable effect might be observed in alpha-brass of 10 to 30 per cent zinc.

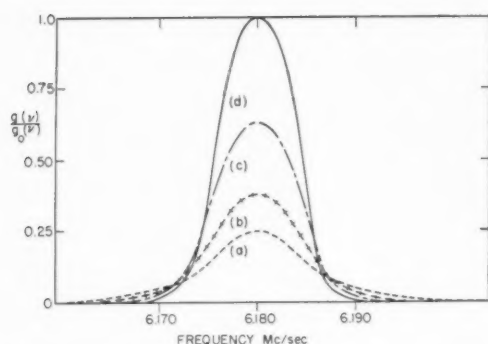


FIG. 5. Experimental result of annealing a cold-worked specimen of Al-0.64 atomic per cent Mg. The absorption curves were obtained after the following treatments: (a) as filed; (b) after a 250°C, 87-hour anneal; (c) after a 480°C, 2-hour anneal. The pure Al curve (d) is included for comparison.

Nuclear resonance provides a sensitive method of detecting lattice imperfections.<sup>12</sup> The usefulness of the technique, when applied to metals, is demonstrated by an experiment on the annealing of a low-impurity sample of Al. The result should be of interest to physical metallurgy because of the correlation between hardness and "locked-in" dislocations.<sup>13,14,15</sup> Here we have a method, superior in some ways to a conductivity study, of determining the amount of material subjected to strain due to lattice imperfections.

A powdered sample of Al-0.64 atomic per cent Mg was prepared as described before; the absorption in Fig. 5a was observed soon after filing. This sample was heated to 250°C and held there for 87 hours; it was then cooled to room temperature, and curve 5b determined. A second specimen was filed (same result) and held at 480°C for two hours. After cooling, curve 5c was obtained and further heat treatment caused no further change. Clearly the experiment involves no precipitation processes and therefore the interpretation must lie predominantly in the migration and recombination of dislocations which have been obstructed by the impurity atoms. The fact that the resonance in pure Al, Fig. 5d, shows no effect of working proves the necessity of having the impurity atoms present to tangle the dislocations. Enough of these imperfections are trapped in the 0.64 atomic per cent Mg sample to cause the complete disappearance of the satellites and to make the observed intensity fall on the dotted line in Fig. 3. The point describing the effect of the impurity atoms alone, devoid of locked dislocations, is plotted at  $c=0.0064$  near the solid curve in Fig. 3.

The present data on pure Al, which are different from nuclear resonance results in pure, cold-worked copper,<sup>1</sup> are consistent with the findings of workers in other fields. Dehlinger<sup>16</sup> first showed that the X-ray line broadening was "negligible" for pure Al and Wood<sup>17</sup> found the same result, attributable to the self-recovery during cold

work of Al. In this respect Wood found Al to behave quite differently from Cu, Ag, Ni and Mo at room temperature, and he reproduces X-ray photographs in support of his statement. A recent article on X-ray line-broadening from filed aluminum and tungsten by Williamson and Hall<sup>18</sup> shows that the lines from high-purity Al have a very low value of broadening compared to that from a commercially pure (99.7% Al) sample. Both of these breadths were much less than were produced by the cold-worked tungsten. Seeger<sup>19</sup> has recently shown that the difference between pure aluminum and copper at room temperature can be ascribed to the fact that the activation energy needed to create a jog when two dislocations lines cross each other is ten times lower in aluminum than in copper.

At room temperature the dislocations can readily move in the aluminum lattice, which consequently will have a very low random density of dislocations. On the contrary in cold-worked copper at room temperature the dislocations form a locked network and their density is high. Nuclear resonance data confirm this viewpoint.

#### ACKNOWLEDGMENTS

The author wishes to express his gratitude to Professor Bloembergen for many inspiring discussions and to Drs. Willenbrock and Redfield for reading and commenting on this paper. A stipend from the General Electric Company is also gratefully acknowledged. This work was supported jointly by the Office of Naval Research, the Signal Corps of the U. S. Army, and the U. S. Air Force.

#### REFERENCES

1. N. Bloembergen and T. J. Rowland, *Acta Met.* **1**, 731 (1953). An error in equation (6) of this paper will be corrected by multiplying the first two terms on the right hand side by a factor 2. Subsequent equations and conclusions are correct as printed.
2. H. Lew, *Phys. Rev.* **76**, 1086 (1949).
3. R. V. Pound, *Phys. Rev.* **79**, 685 (1950).
4. G. E. Pake, *J. Chem. Phys.* **16**, 327 (1948).
5. W. A. Nierenberg and N. F. Ramsey, *Phys. Rev.* **72**, 1075 (1947).
6. W. L. Fink and K. R. Van Horn, *Trans. A.I.M.E.* **99**, 132 (1932).
7. W. L. Fink and D. W. Smith, *Trans. A.I.M.E.* **124**, 162 (1937).
8. R. V. Pound and W. D. Knight, *Rev. Sci. Instr.* **21**, 219 (1950).
9. G. Watkins, Thesis, Harvard University (1952).
10. N. Bloembergen, *J. Appl. Phys.* **23**, 1383 (1952).
11. S. Timoshenko, *Theory of Elasticity* (McGraw-Hill, New York, 1934), p. 323.
12. N. Bloembergen, Report on the Bristol Conference (1954) *Proc. Phys. Soc. (London)*.
13. A. H. Cottrell and M. A. Jaswon, *Proc. Roy. Soc. A* **199**, 104 (1949).
14. A. H. Cottrell, *Dislocations and Plastic Flow in Crystals*. Oxford, The Clarendon Press, 1953.
15. A. H. Cottrell, *Progress in Metal Physics I* (Butterworths, London, 1949). Chapter II.
16. U. Dehlinger, *Z. Kristallogr.* **44**, 241 (1930).
17. W. A. Wood, *Proc. Roy. Soc. A* **172**, 231 (1939).
18. G. K. Williamson and W. H. Hall, *Acta Met.* **1**, 22 (1953).
19. A. Seeger, Report on the Bristol Conference (1954), *Proc. Phys. Soc. (London)*.

# TRANSITION STRUCTURE IN LEAD-SILVER ALLOYS AND A DISLOCATION MECHANISM\*

R. D. HEIDENREICH†

An electron metallographic investigation of lead-silver alloys in the composition range 0.009–0.23 per cent silver has demonstrated the occurrence of a transition lattice in the precipitation of silver in a lead crystal. A heat treating schedule for growing crystals of the transition structure allowed electron diffraction patterns adequate for indexing the structure as HCP with  $a=2.92\text{\AA}$ ,  $c=4.76\text{\AA}$  and  $c/a=1.63$  with an accuracy of about  $1\frac{1}{2}$  per cent. The formula is indirectly deduced to be  $\text{Ag}_4\text{Pb}$ .

The extended dislocation model in FCC crystals is employed to explain the pronounced hardening produced by the silver solute and to account for the hexagonal transition structure during precipitation of silver. The possibility of mass transport of solute to grain boundaries by means of dislocations is advanced to explain accelerated silver precipitation in grain boundaries.

## UNE STRUCTURE DE TRANSITION DANS LE SYSTÈME PLOMB-ARGENT ET UN MÉCANISME DE DISLOCATIONS

Une investigation métallographique au moyen du microscope électronique, d'alliages plomb-argent, dans l'intervalle des compositions allant de 0.009 pour cent à 0.023 pour cent d'argent, a permis de démontrer l'apparition d'un réseau de transition lors de la précipitation de l'argent dans un cristal de plomb. Un programme de traitement thermique pour la croissance de cristaux ayant la structure de transition a permis d'obtenir des diagrammes de diffraction d'électrons, permettant, à leur tour, de définir la structure comme étant hexagonale compacte avec  $a=2.92\text{\AA}$ ,  $c=4.76\text{\AA}$  et  $c/a=1.63$ , à  $1\frac{1}{2}$  pour cent près. La formule  $\text{Ag}_4\text{Pb}$  de cette structure est déduite indirectement. Le modèle étendu des dislocations dans des cristaux cubiques à faces centrées est utilisé pour expliquer le durcissement prononcé, produit par l'argent, et de justifier l'apparition de la structure hexagonale de transition lors de la précipitation de l'argent.

La possibilité de transport de soluté par des dislocations est proposée pour expliquer la précipitation accélérée de l'argent dans les joints intercrystallins.

## EINE ÜBERGANGSSTRUKTUR IN BLEI-SILBER LEGIERUNGEN UND EIN VERSETZUNGSMECHANISMUS

Eine elektronenmetallographische Untersuchung von Blei-Silber Legierungen im Konzentrationsbereich zwischen 0.009 und 0.23 Prozent Silber hat das Auftreten eines Übergangsgitters in der Silberausscheidung eines Bleikristalls gezeigt. Die zur Züchtung von Kristallen der Übergangsstruktur erforderlichen Glühungsperioden ermöglichten Elektronenbeugungsaufnahmen, aus denen sich die Struktur als eine hexagonale dichteste Kugelpackung mit  $a=2.92\text{\AA}$ ;  $c=4.76\text{\AA}$  und  $c/a=1.63$  mit einer Genauigkeit von etwa  $1\frac{1}{2}$  Prozent indizieren liess. Die Formel der Verbindung wurde indirekt zu  $\text{Ag}_4\text{Pb}$  abgeleitet.

Ein erweitertes Versetzungsmodell des kubisch-flächenzentrierten Gitters wurde herausgezogen, um die durch die Silberlösung hervorgerufenen erheblichen Härtung und das Auftreten einer hexagonalen Übergangsstruktur bei der Silberausscheidung zu erklären. Die Möglichkeit einer Massenwanderung der gelösten Atome zu den Korngrenzen mit Hilfe von Versetzungen wird diskutiert. Dies würde die beschleunigte Silberausscheidung an den Korngrenzen erklären.

## INTRODUCTION

The experimental results reported herein were obtained some years ago and although the main features were reported orally<sup>1</sup> and mentioned briefly in previous publications,<sup>2,3</sup> a full report was postponed until at least a partially satisfactory physical explanation could be proposed. Speculations concerning a mechanism for hardening and precipitation in pure lead containing only 0.01–0.02 weight per cent silver were entertained but not actually seriously considered until the paper by Suzuki<sup>4</sup> appeared and the treatment of dislocations in metals was consolidated in the books by Cottrell<sup>5</sup> and Read.<sup>6</sup> It is now felt that the experimental information can be presented as something more than just metallurgical phenomena with little in the way of physical mechanism to improve the understanding of such observations.

The interpretation of the structural features of the

precipitation of silver in a lead crystal is based on the chemical interaction of solute atoms with an extended dislocation in the F.C.C. crystal. The extended dislocation consisting of two partial dislocations separated by a stacking fault was first proposed by Heidenreich and Shockley<sup>7</sup> and is treated more fully by Cottrell<sup>5</sup> and Read.<sup>6</sup> The interaction of solute atoms with the stacking fault has been treated in detail by Suzuki.<sup>4</sup> The difficulty in assigning numerical values to thermodynamic quantities describing a stacking fault containing impurity atoms relegates the theory to a qualitative treatment. Even so, the importance of the idea is not lost and the usefulness of the model in interpreting properties will be evident.

## A. Lead-Silver System

The phase diagram for the lead-rich end of the lead-silver system has been published by Seith and Keil<sup>8</sup> and is re-reproduced in Fig. 1. In this investigation, the region of interest lies in the composition range 0–0.025

\* Received May 14, 1954; in revised form August 15, 1954.

† Bell Telephone Laboratories, Inc., Murray Hill, New Jersey.



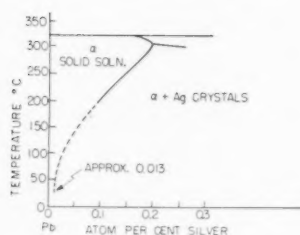


FIG. 1. Phase diagram for lead-rich silver alloys after Seith and Keil. *Z. physik. Chem.* **22**, 350 (1933). The estimated solubility at room temperature is about 0.013 atom per cent silver.

weight per cent (0–0.05 atomic per cent) silver. Both silver and lead are F.C.C. in the elemental state with the parameters exhibited in Table I. The size factor based on Table I is about 17 per cent indicating a very restricted solid solubility of silver in lead consistent with Fig. 1. The relative valency effect allows a greater solubility for Pb in Ag than vice versa while the electronegativity difference does not suggest a strong tendency for intermetallic compound formation such as is found in the Pb–Au system. No stable intermetallic compound of lead and silver is known. The equilibrium precipitation of silver in a lead crystal along the solid solubility line of Fig. 1 yields F.C.C. crystal of silver saturated with lead (of the order of 1–2 per cent Pb). A point of interest in connection with Table I and of importance later is the evidence<sup>9</sup> that with silver as a solvent, In, Tl and Pb solute atoms are completely ionized. The implication of this is that the elastic strain in a lead crystal containing dissolved silver atoms can be reduced by the formation of clusters or “clouds” rich in silver so that the interdispersed lead atoms in the cluster have their radii reduced by further ionization and so achieve a radius more compatible with silver. If the reduction in strain energy through the formation of silver-rich clusters is sufficient to compensate the mixing entropy term in the free energy, then it would be expected that the solid solution of silver in lead will not be homogeneous. Since the alloy melts at about 320°C, the mixing entropy term cannot be greatly increased over room temperature by heating the solid below the melting point and the existence of clusters at temperatures as high as 300°C is possible. As will be discussed later, the presence of dislocations and stacking faults apparently

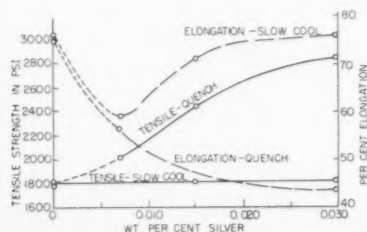


FIG. 2. Tensile properties of polycrystalline lead-silver alloys in quenched and slow cool condition as a function of silver concentration.

favor the formation of silver clusters along with the thermodynamic argument just given.

### B. Mechanical Properties\*\*

The addition of small amounts of silver to lead can produce a large effect on the mechanical properties as seen in Fig. 2 where tensile strength and elongation at failure are plotted against silver content in the range of interest here. Two points are of main concern in connection with Fig. 2. The first is that the alloys given a slow furnace cool have about the same tensile strength as pure lead and the second is that the quenched state of the alloy is the strongest. As near as can be ascertained, the tensile strength of the alloys is maximum at quench and decreases continuously thereafter with aging at room temperature. This is a significant difference from the case of age hardening alloys such as Al–Cu where the strength increases to a maximum with aging time before decreasing again as the alloy is over-aged. If the mechanism is not different (from say Al–Cu) then it will be necessary for age hardening to occur in a matter of minutes at room temperature following the quench which is difficult to accept from a diffusion standpoint. Rather long diffusion paths are necessary in dilute

TABLE I.

	Lattice constant	Crystal radius	Coordination	Valence
Pb	$a_0 = 4.94\text{\AA}$	1.74\AA	12	4*
Ag	$a_0 = 4.08\text{\AA}$	1.44\AA	12	1

\* If completely ionized. Indium, thallium and lead are thought to be only partially ionized in the elemental crystals. They may, however, become fully ionized in some alloys. Hume-Rothery<sup>9</sup> estimates that in completely ionized form, the radii of these elements should be about 0.15\AA less or a value for lead of 1.59\AA with a valence of 4.

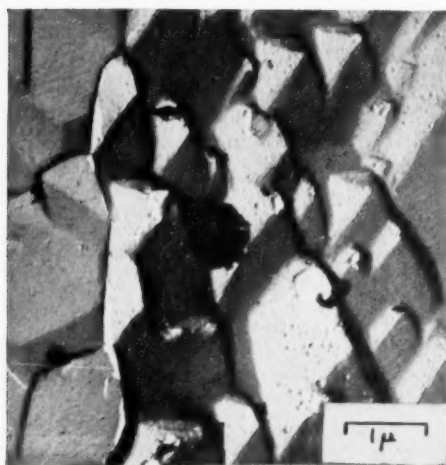
alloys. Structural evidence presented in the next section indicates that for times up to 20 minutes following the quench, the silver has not all precipitated and become immobilized as F.C.C. crystals.

In considering the mechanical properties, it must be remembered that at room temperature, lead recrystallizes readily and that such changes occur during physical testing.

### C. Structural Investigation

The structural investigation was carried out using light microscopy, electron diffraction and electron microscopy. The surfaces for examination were prepared by electropolishing in an acetic-perchloric bath and then etched either by reducing the current from the value used for polishing or removing, rinsing and etching in molybdic acid. Electron diffraction patterns were then taken of the prepared surface following which a replica for electron microscope examination was prepared. The molybdic acid etch always produces a crystallographic attack on annealed (or quenched) pure lead as seen in Fig. 3. The surfaces exposed by the etch are apparently (111).

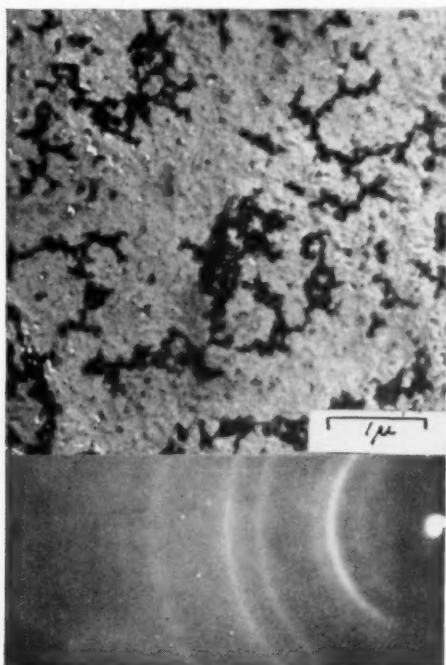
\*\* The author is indebted to Dr. R. G. Treuting of these laboratories for the data on mechanical properties.



3

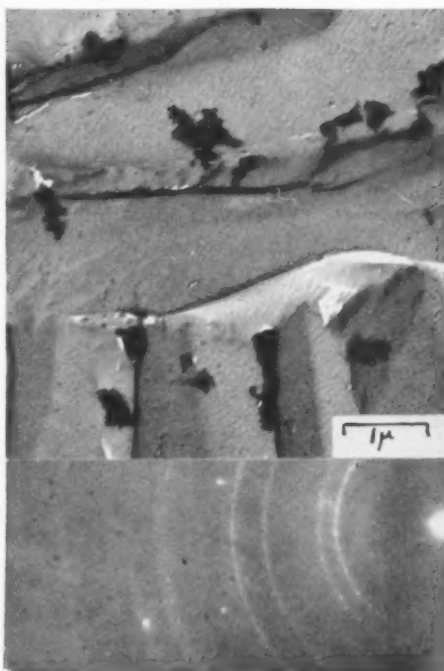


5



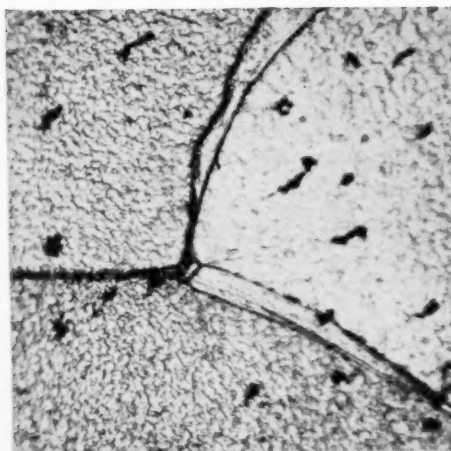
(a)

4

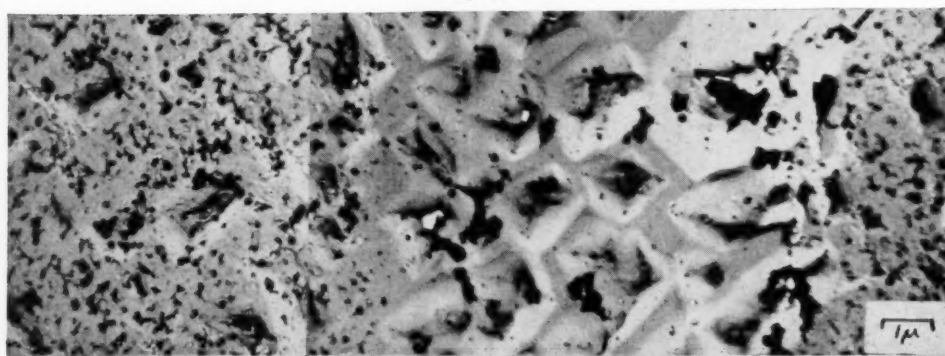


(b)

PLATE I. FIG. 3.—Crystallographic etch attack and twin boundary in high purity lead. Electropolish and molybdic acid etch. Silica replica. FIG. 4.—(a) Lead-0.01 per cent silver quenched from 260°C. Finely divided, accumulated silver appears black on the silica replica. The electron diffraction pattern exhibits broad rings indicating a crystal size of about 30A. (b) Same specimen as (a) but furnace-cooled from 260°C. Relatively few large particles of accumulated silver and a crystallographic etch attack. Sharp, grainy rings for silver and a few spots for the underlying lead crystal are seen in the diffraction pattern. FIG. 5.—Lead-0.009 per cent silver quenched from 260°C. This alloy exhibits practically no hardening. The etch attack is crystallographic with scattered regions where the attack is perturbed as seen above.

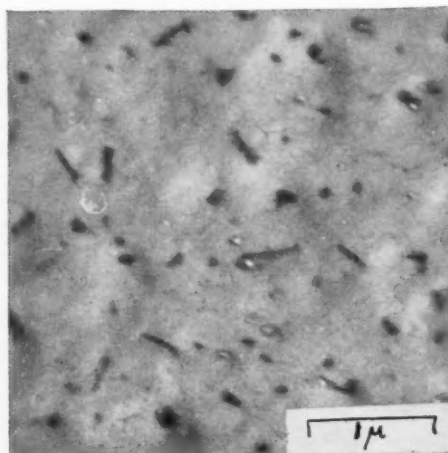


6(a)



BOUNDARY REGION

6(b)



10

PLATE II. FIG. 6.—Photomicrograph (a) and electron micrograph (b) illustrating accelerated agglomeration of silver in the grain boundary region after creep test. Lead-0.012 per cent silver. FIG. 10.—Silica replica showing transferred needle-shaped crystals of the  $\eta$  transition structure grown by the heat treatment described in the text.

When silver is present in the lead, the surface preparation described always leaves a residue of stranded or accumulated silver on the lead surface. The following conclusions were reached concerning the stranded silver.

1. The crystal and particle size of the stranded silver are a function of the thermal history of the alloy only and are independent of variations in the preparation.
2. The silver in the alloy was never actually dissolved in the etchant. The lead was chemically removed from around the silver and it was simply stranded on the newly formed surface.
3. The crystal size of the stranded silver is either the same as that in the original alloy or is a measure of the number of silver atoms occurring in a cluster or "cloud" in the alloy which condensed upon etching.

The effect of heat treatment on the state of aggregation of the stranded silver is demonstrated in Fig. 4. The alloy is 0.017 per cent\* silver and shows the fine dispersion resulting from a quench from 260°C as contrasted to the few large chunks of silver resulting from a furnace cool. The electron diffraction patterns are also displayed showing the great difference in crystal size as determined from the broad rings in Fig. 4a compared to the sharp, grainy rings in Fig. 4b. The particle size of the silver in the quenched condition is of the order of 700 Å while the crystal size as determined from diffraction line breadths is about 35 Å. The crystal size is the more important quantity as far as the alloy is concerned but the particle size and the nature of the etch attack are both indications of hardening.

The solid solubility of silver in lead at room temperature is estimated to be about 0.007 per cent. This silver content is insufficient to give a discernible electron diffraction pattern for silver while for a 0.012 per cent silver specimen good patterns are obtained. Apparently true solid solution silver does not give rise to the stranded silver particles seen in Fig. 4 nor does it interfere with the crystallographic attack.

Some experiments with single crystals containing 0.017 per cent silver showed that after quenching from 260°C the prepared surfaces exhibited a uniform dispersion of stranded silver. In polycrystalline specimens, however, occasional grain boundary regions exhibited relatively large chunks of precipitated silver even though the sample had been quenched. This accelerated precipitation of silver in the grain boundary regions was found to be greatly exaggerated in creep test specimens after a 1000 hour test. Failures in creep were predominantly intercrystalline. In addition to the large silver particles in the grain boundary areas, the lead itself exhibited a crystallographic type etch attack such as seen in the furnace cooled or pure lead samples. These

"soft" regions were often several microns wide as illustrated in Fig. 6.\*

#### D. Transition Structure

During experiments in which specimens were quenched from 260°C and then aged at various temperatures to examine the degree of segregation of silver, a new crystallographic phase was discovered in one specimen. Attempts to reproduce this structure failed until finally it was found that the controlling factor was the elapsed time between quench and anneal. From a number of experiments, it was determined that the strongest patterns for the new, transitory structure could be obtained by the following sequence.

1. Cold work +30 minutes at 260°C (in oil).
2. Quench into a light silicone oil at room temperature.
3. Stress relieve 30 minutes at room temperature.
4. Hold at 0°C (ice water) for 5-10 minutes.
5. Anneal 20 minutes at room temperature.
6. Anneal 5 minutes at 130°C or longer times at lower temperatures.

This rather peculiar sequence of treatments must be adhered to in order to grow large crystals of the transition structure† hereafter referred to as "η." The reason for (2) and (3) is simply to relieve quench strains and prevent recrystallization in the subsequent anneal. (4) turns out to be a nucleation treatment while (5) is an intermediate nucleus growth period and (6) is final growth.

The electron diffraction patterns obtained for the η structure are quite straightforward as shown in Fig. 7 and can be indexed H.C.P. with  $a = 2.92\text{Å}$ ,  $c = 4.76\text{Å}$  and  $c/a = 1.63$ . If the final anneal is omitted, the crystal size of the silver and the transition η, are so small (30-50Å) that the diffraction lines are broadened to an extent that the η lines cannot be separated.

The hexagonal indexing was checked on a number of samples and the figures quoted of  $a = 2.92\text{Å}$ ,  $c = 4.76$  and  $c/a = 1.63$  are thought to be accurate within 1½ per cent. An elemental analysis of the η crystals has not been obtained but some guesses can be made reasoning by analogy. The lattice parameters of η are nearly right for H.C.P. pure silver which apparently does not exist. This means that if η contains both lead and silver, the lead atoms must be reduced in size from the crystal radius given in Table I to fit into the structure. A number of hexagonal silver intermetallic compounds are known which lend credence to the η structure. Several of these are given in Table II. If it is now assumed that a lead atom becomes completely ionized in a silver rich environment, the reduced radius of 1.59Å (Table I) puts the η structure in the class of compounds of Table II and

\* The author is indebted to Mr. E. E. Thomas for the photomicrographs.

† This procedure works over the silver content range of .011 to .023 per cent. η lines were found in a 2.5 per cent alloy aged 2 days at room temperature.

\* Unless otherwise specified, per cent composition will be understood to be weight per cent.



TABLE II. Hexagonal close packed intermetallic compounds containing silver.

Compound	<i>a</i>	<i>c</i>	<i>c/a</i>	Crystal radius of of second metal
Ag <sub>3</sub> In	2.95	4.76	1.63	1.57
Ag <sub>4</sub> Sn	2.93	4.77	1.63	1.58
Ag <sub>3</sub> Sb	2.98	4.82	1.63	1.61
Ag <sub>3</sub> Al <sub>2</sub>	2.87	4.63	1.61	1.43

allows a packing in the crystal such as for Ag<sub>4</sub>Sn or Ag<sub>3</sub>Sb. Since tin is assigned a valence of 4, the best guess is that  $\eta$  Pb-Ag has the formula Ag<sub>4</sub>Pb. The radius of Sn given in Table II is thought to be the fully ionized radius which compares with the reduced radius of 1.59 for Pb. Until analytical data can be obtained, Ag<sub>4</sub>Pb will be taken as the formula deduced from the lattice parameters.

If  $\alpha$  denotes a disordered solid solution of silver in lead then the precipitation reaction occurring is



where  $\beta$  denotes F.C.C. silver saturated with lead. The decomposition  $\eta \rightarrow \beta$  occurs through a shear of the hexagonal lattice to form F.C.C. silver with the expulsion of lead atoms. The shear mechanism is suggested by the fact that plastic deformation accelerates the decomposition. The  $\alpha \rightarrow \eta$  reaction will be considered in the following section.

### E. Mechanism of Precipitation and Hardening

Any mechanism advanced to account for the behavior of the dilute lead-silver alloys must be capable of explaining the following salient experimental facts.

1. The large amount of hardening brought about by a solute present in an atom concentration of the order of  $3 \times 10^{-4}$ . This concentration of silver raises the tensile strength of lead from 1800 psi to nearly 2500 psi.

2. Formation of a hexagonal close-packed transition structure. When large crystals are grown, this

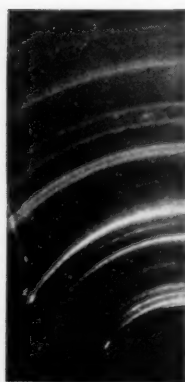


FIG. 7. Indexed electron diffraction pattern for F.C.C. silver and H.C.P.  $\eta$  Pb-Ag with *d*-values for the  $\eta$ -structure (*a* = 2.92 Å, *c* = 4.76 Å, *c/a* = 1.63).

Ag (222)	" $\eta$ "Pb-Ag (0004)	<i>d</i>
	(20 $\bar{2}$ 1)	1.21
(311)	(20 $\bar{2}$ 0)	1.25
	(10 $\bar{1}$ 3)	1.35
(220)	(10 $\bar{1}$ 2)	1.75
(200)	(10 $\bar{1}$ 1)	2.24
(111)	(0002)	2.38
	(10 $\bar{1}$ 0)	2.53

transition structure ( $\eta$ ) is indirectly deduced to be Ag<sub>4</sub>Pb.

3. Sensitivity of the  $\eta$  structure to plastic deformation.

4. Tendency for accelerated silver segregation near grain boundaries particularly under conditions of creep test.

5. Maximum hardness at the time of quench. (Aging results in softening of the alloy.)

The work of Cottrell<sup>5</sup> and Suzuki<sup>4</sup> concerning the interaction of solute atoms with dislocations offers an attractive mechanism for the lead-silver alloys.

The model is based on the extended dislocation consisting of two partial dislocations separated by a strip of stacking fault as originally advanced by Heidenreich and Shockley.<sup>7</sup> Figure 8 shows an extended dislocation on the (111) plane of an F.C.C. crystal with the two partials  $P_1$  and  $P_2$  separated by the fault of width  $\omega$ . The width of the faulted strip,  $\omega$ , in a pure crystal is determined by the repulsion between  $P_1$  and  $P_2$  balanced by the energy of the fault,  $\epsilon$ . This can be shown to be\*

$$\omega = \frac{\mu a^2}{24\pi\epsilon}, \quad (2)$$

where  $\mu$  is the shear modulus and "*a*" the interatomic distance. For copper, (2) gives a width of about 30 Å

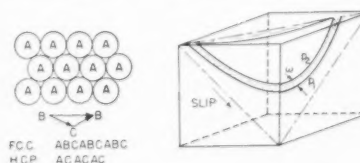


FIG. 8. An extended dislocation on the (111) plane in a F.C.C. crystal.  $P_1$  and  $P_2$  are Shockley partials separated by a strip of hexagonal stacking fault.

with  $\mu = 4 \times 10^{11}$  dynes/cm<sup>2</sup> and  $\epsilon \sim 20$  ergs/cm<sup>2</sup>. Numerical values of  $\epsilon$  are not known for lead so it is assumed that  $\omega$  for pure lead is of the same order as for copper. The stacking in F.C.C. is ABCABCABC whereas after the passage of  $P_1$  the stacking becomes ABCACABC thus producing the hexagonal close packed faulted strip. Figure 7 is the structural basis of the model. The behavior of lead-silver must now be accounted for through the interaction of the silver solute atoms with the extended dislocation.

Consider a lead crystal containing silver in atom concentration of the order of  $3 \times 10^{-4}$ . According to the phase diagram, the silver should be in substitutional solid solution at 260°C. The misfit silver atoms interact with the elastic stress fields of  $P_1$  and  $P_2$  and will be attracted to the compression side of  $P_1$  and  $P_2$  by a force varying inversely as the square of the distance between atom and dislocation.\*\* This attraction produces an atmosphere of silver atoms about the partial dislocation

\* See p. 74 of ref. 5.

\*\* See p. 56 of ref. 5.

as shown in Fig. 9b. The atmosphere of solute atoms will act as a drag on the motion of the extended dislocation as shown by Cottrell.<sup>5</sup> According to Suzuki,<sup>4</sup> there is a possibility that solute atoms will be absorbed into the fault separating  $P_1$  and  $P_2$  in a concentration depending upon the gain in free energy. The result will be an increase in the critical shear stress required to move the dislocation. Suzuki's results indicate that in F.C.C., the solute atoms in the fault promote hardening more effectively than does the atmosphere about the partials  $P_1$  and  $P_2$ , at least under conditions where the solid solution is not supersaturated. The atmosphere about  $P_1$  and  $P_2$  would serve as a reservoir for driving Ag atoms into the fault strip. Figure 9c illustrates both the atmosphere and the adsorption of silver into the fault. The consequences of the model depicted in Fig. 9c are quite far-reaching, the salient features being:

1. The hexagonal close-packed fault containing silver is a region more favorable to the formation of nuclei of " $\eta$ " crystals.
2. The critical shear stress for slip has been raised by virtue of the drag of the atmosphere\*\* about  $P_1$  and  $P_2$  and the energy of the fault.
3. At low stress levels (insufficient to tear the dislocation away from the silver atmosphere) mass transport of silver will occur with motion of the dislocation.

With the crystal still at solution temperature (260°C) consider the effect of thermal diffusion of the silver laden dislocations for which the rate is determined by the rate of diffusion of silver. At this temperature diffusive motion will occur chiefly by glide and will be away from the center of the crystal toward the boundaries. Silver-laden dislocations which reach the surface or a grain boundary and disappear will produce an enhanced local concentration of silver in the boundary region. This concentration will tend to level out either by diffusion of individual atoms back toward the center or by the formation of silver embryos if the local concentration is sufficiently high. If the latter occurs, an embryo for silver condensation is produced which will re-dissolve if given time. Thus, a dynamical situation exists with silver being transported to the boundaries by dislocations where it is "dumped" to precipitate short lived silver embryos. When the specimen is quenched, a number of these grain boundary nuclei already present relieve resulting supersaturation by condensation on these nuclei.\* This will also occur on any similar nuclei formed in the interior of the crystal by annihilation of dislocations. The model thus provides a mechanism for the nucleation of precipitate near the grain boundaries even in the absence of plastic deformation. This explains the large silver precipitate particles occasionally seen along the grain boundaries in quenched specimens.

Suppose now the specimen is quenched from 260°C.

\*\* See p. 136 of ref 5.

\* This is the commonly observed heterogeneous nucleation at grain boundaries.

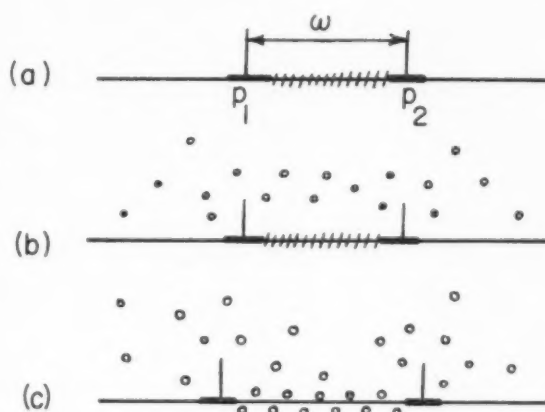


FIG. 9. (A) Edge-on view of extended dislocation showing stacking fault between partials  $P_1$  and  $P_2$ . (B) Atmosphere of solute atoms about  $P_1$  and  $P_2$ . (C) Sorption of solute atoms into the fault (Suzuki).

The situation depicted in Fig. 9c already exists and hence the quenched specimen should be harder than pure lead. The specimen is supersaturated after the quench and solute atoms in the atmosphere will find ready made embryos in the extended dislocations.

The formation of the  $\eta$  transition structure now appears straightforward. In the quenched condition, the adsorption of silver into the fault is aided by the supersaturation of the matrix and by the reduction in size of lead atoms in a silver environment as previously discussed. The fault strip is thus a favored site for nuclei of a hexagonal close packed crystal. The width of the fault strip  $\omega$  is increased due to a decrease in  $\epsilon$  and according to the diffraction line widths, attains a size of 40–50Å. The effect of deformation on the hexagonal embryo is evident. If the extended dislocation is subjected to a stress sufficient to tear it away from the silver atmosphere, the passage of  $P_2$  through the fault shifts it back to F.C.C. and it becomes a nucleus for growth of F.C.C. silver crystals rather than hexagonal lead-silver. This accounts for the effect of the stress relief period in the procedure for growing larger crystals of  $\eta$ . The ice temperature treatment increases the supersaturation to drive more silver atoms into the fault and increase its size. At this stage, the transition lattice is in the form of a ribbon separating  $P_1$  and  $P_2$ . If the temperature is now slowly raised, the surviving, ordered hexagonal regions will grow more rapidly and they can break loose from the lead lattice and grow. The growth will occur in a direction to minimize the free energy and in this case, a needle is formed as shown in the electron micrograph of Fig. 10. There is uncertainty now as to whether the observed needle was formed by growth along its  $c$ -axis (normal to the fault) or whether the needle is a segment of the original fault thickened by the heat treatment until it broke away. In the latter case, the axis of the needle is not the  $c$ -axis but was originally in the (111) plane parallel to the fault strip. Plastic deformation of the lead crystal exerts a shear on the  $\eta$  crystal which

changes it back to F.C.C. as previously found experimentally. Thus, the model is capable of accounting for points (2) and (3) as well as (1) and (5) of the original requirements.

The remaining feature to be examined is the behavior of the model under creep conditions. Suppose a polycrystalline specimen whose grains contain silver-laden extended dislocations (as shown in Fig. 9c) is submitted to a creep test (800 psi). The dislocations move slowly under the applied stress dragging the silver atmosphere and the silver in the fault along with them.\* For each unit slip occurring on a glide plane, a dislocation must traverse the entire crystal grain. Each unit of slip in which a dislocation disappears at the grain boundary in the polycrystalline specimen must result in the "dumping" of a load of silver atoms at the boundary. This results in an enhanced local supersaturation at the boundary and the likelihood of formation of a stable silver nucleus. The nucleus will proceed to drain off the solid solution silver in its vicinity until the solubility line is reached at the temperature of the test. A layer of lead containing massive silver particles and only about 0.007 per cent silver in solution (saturated) thus forms at the grain boundaries. As creep progresses, more silver nuclei will form and then grow by relieving the supersaturation to produce a slowly thickening shell of lead containing equilibrium solid solution silver and massive silver particles. Thus slow deformation results in accelerated softening at the grain boundaries and the growth of this soft region toward the center of the grain. When failure occurs, it should progress by failure in the soft material and hence be largely intercrystalline. From a qualitative standpoint, then, the dislocation model appears to be capable of explaining the mechanical and structural properties of the dilute lead-silver alloys.

The effect of silver content can be accounted for rather naturally. When the silver solid solution content is sufficient to "saturate" the atmosphere and fault of the extended dislocation, further increase in silver content will not result in more drag on the moving dislocations. The hardness should level off when an optimum degree of supersaturation is obtained and remain level until the supersaturation is sufficient to cause spontaneous nucleation of silver precipitate which reduces the solid solution silver below optimum and causes softening.

The dynamics of the system are intimately connected with the rate of diffusion of silver in lead since both the drag on the moving dislocations and the rate of growth of silver nuclei are determined by diffusion. The effects of solute atoms other than silver should be explicable using the dislocation model. Solute atoms with a lower diffusion rate should produce a lower creep rate although they would require longer times to do so since the build up of the solute atmosphere and fault concentration

\* The velocity is determined by the rate of diffusion of silver in lead (see ref. 8).

would be slower. The difference between quench hardening in lead-silver and age hardening in lead-calcium should be chiefly a matter of diffusion rate and the ability to dissolve solute in the fault strip.

The general conclusions from the experimental work and the mechanism advanced should apply to any F.C.C. alloy and particularly to dilute, age-hardening alloys. The main features of the investigation are as follows:

1. The general experimental findings in the lead-silver dilute alloys are summarized in the points at the beginning of Section E.
2. The extended dislocation consisting of two partial dislocations separated by a strip of stacking fault offers a natural mechanism for explaining both the structural and mechanical properties of the alloys.
3. The stacking fault can serve as a favored site for the formation of an hexagonal transition lattice in supersaturated solid solutions as well as increasing the critical shear stress for slip.
4. The extended dislocation tends to accumulate solute atoms and under conditions of thermal diffusion or creep results in a mass transport of solute atoms to surfaces and grain boundaries. This mass transport can lead to accelerated precipitation in grain boundary regions.

Evidently, an extension of the general dislocation model to other alloy systems such as Al-Ag, etc. is highly desirable. The generality of the hexagonal transition lattice in F.C.C. age hardening alloys must be examined in the light of competitive forces depending upon misfit on planes other than (111). If the fault energy is not lowered by dissolution and ordering of solute atoms, then the resistance to slip will not be greatly increased and precipitation may prefer other habit planes. Just how far and under what conditions this model is applicable in generally explaining both hardening and transition lattices remains to be seen.

#### ACKNOWLEDGMENT

The author is indebted to a number of members of Technical Staff for their aid and criticism and particularly to Messrs. W. T. Read, Jr. and W. C. Ellis.

#### REFERENCES

1. Gordon Research Conference, Chemistry and Physics of Metals, New Hampton, New Hampshire (1952).
2. R. D. Heidenreich, *Rev. Sci. Inst.* **23**, 583 (1952).
3. R. D. Heidenreich, *Modern Research Techniques in Physical Metallurgy*, p. 51, American Society for Metals, Cleveland, Ohio (1953).
4. H. Suzuki, *Science Reports of The Research Institute, Tohoku University* **4**, 455 (1952).
5. A. H. Cottrell, "Dislocations and Plastic Flow in Crystals," Oxford, Clarendon Press (1953).
6. W. T. Reid, Jr., "Dislocations in Crystals," McGraw-Hill, New York (1953).
7. R. D. Heidenreich and W. Shockley, "Report on Strength of Solids" (London, Physical Society) **57** (1948).
8. W. Seith and A. Keil, *Zeit. Phys. Chem.* **22**, 350 (1933).
9. W. Hume-Rothery, "Structure of Metals and Alloys," (Institute of Metals, London), 1945.

## SELF-DIFFUSION IN THALLIUM\*†

G. A. SHIRN††

The self-diffusion of single crystal thallium has been measured from 150°C to 275°C with the use of  $Tl^{204}$  as a tracer and the standard sectioning technique. For diffusion parallel to the  $c$ -axis the data were well fitted by an activation energy of  $Q=22.9$  kcal/mol and a  $D_0=0.4$  cm<sup>2</sup>/sec, and for diffusion perpendicular to the  $c$ -axis  $Q=22.6$  kcal/mol and  $D_0=0.4$  cm<sup>2</sup>/sec. The cubic phase was investigated also and resulted in the values  $Q=20.0$  kcal/mol and  $D_0$  of order 0.7 cm<sup>2</sup>/sec. Possible mechanisms are discussed.

### L'AUTO-DIFFUSION DANS LE THALLIUM

On a mesuré l'autodiffusion dans des monocristaux de thallium, entre 150°C et 275°C, en utilisant  $Tl^{204}$  comme traceur et la technique habituelle des sections. Pour la diffusion parallèlement à l'axe  $c$  les données expérimentales sont en accord avec une énergie d'activation  $Q=22.9$  kcal/mol et un coefficient  $D_0=0.4$  cm<sup>2</sup>/sec; pour la diffusion perpendiculairement à l'axe  $c$  ces valeurs sont  $Q=22.6$  kcal/mol et  $D_0=0.4$  cm<sup>2</sup>/sec. On a aussi étudié la phase cubique pour laquelle on obtient des valeurs de  $Q=20.0$  kcal/mol et  $D_0$  de l'ordre de 0.7 cm<sup>2</sup>/sec. Les mécanismes possibles sont discutés.

### SELBSTDIFFUSION IN THALLIUM

Die Selbstdiffusion in Thalliumkristallen wurde zwischen 150°C und 275°C gemessen.  $Tl^{204}$  wurde als Indikator benutzt, und es wurde eine der üblichen Schnitttechniken angewandt. Für den Fall der Diffusion parallel zur  $c$ -Achse liessen sich die Ergebnisse gut durch eine Aktivierungsenergie  $Q=22.9$  Kcal/mol und  $D_0=0.4$  cm<sup>2</sup>/sec darstellen. Für den Fall der Diffusion senkrecht zur  $c$ -Achse betrug  $Q=22.6$  Kcal/mol und  $D_0=0.4$  cm<sup>2</sup>/sec. Die kubische Modifikation wurde ebenfalls untersucht,  $Q$  betrug 20.0 Kcal/mol und  $D_0$  war von der Grössenordnung von 0.7 cm<sup>2</sup>/sec. Es wurden mögliche Elementarprozesse diskutiert.

## I. INTRODUCTION

The study of Anisotropic Diffusion initiated by the work on zinc<sup>1</sup> and followed by the work on cadmium<sup>2</sup> has been extended to thallium. Thallium was chosen for study because it has a hcp structure with  $c/a$  ratio of 1.60 which is within 2½ per cent of the ideal for close-packed spheres. This is in contrast to Zn and Cd where  $c/a$  ratio is much greater than the ideal (1.86, 1.88 respectively). Also, a suitable isotope,  $Tl^{204}$  (.76 mev  $\beta$ , 2.7 yr), is available.

As explained in reference 1, analysis of the data for operating mechanisms is based on a sufficiently comprehensive catalogue of possible mechanisms. These are reproduced in Table II along with the ratio of the contributions of each mechanism to the diffusion in the directions perpendicular and parallel to the  $c$ -axis for  $c/a=\sqrt{8/3}$  and 1.60. The mechanisms are described in reference 1.

Thallium undergoes a phase transition at about 230°C, being hcp below this temperature and probably bcc above. Data on diffusion in the bcc form were taken as a matter of general interest.

## II. EXPERIMENTAL PROCEDURE

The diffusion data were obtained by a standard sectioning technique. Single crystals of thallium were grown from 99.9+ per cent purity thallium as obtained from Belmont Smelting and Refining Works, Inc. The thallium was sealed at reduced pressure in aquadag

coated pyrex tubes and lowered through a temperature gradient. The resulting single crystals were cylinders about 3 to 4 inches long and 3/8 inches in diameter. The orientations of the cylinders were determined by back-reflection Laue pictures.

Those crystals which were suitably oriented were mounted in wax and carefully cut to size and shape with a fine jeweler's saw. The smear from the saw was removed by lathe and etching. An anneal was then made to check for recrystallization which, when it appeared, indicated incomplete etching. Plating with  $Tl^{204}$  was done with the following solution:

$TlNO_3$	40 g/l
Peptone	10 g/l
Cresol	10 cc/l

Thickness of plate was estimated at approximately  $6 \times 10^{-3}$  mm.

The specimens were allowed to diffuse at temperatures ranging from 275°C to about 135°C with diffusing times running from one hour to four months. During the diffusion anneal the specimens were sealed off in pyrex tubes at reduced pressure. No effects of evaporation were found.

After the diffusion period the specimens were mounted in the lathe and about 20 mils were removed from the cylindrical surface to remove the effects of surface diffusion. Next the crystals were sectioned in layers about .025 mm thick parallel to the plated layer. The sections were weighed and counted to determine their activity. The plot of  $\ln$  specific activity vs penetration distance squared gave the diffusion coefficient  $D$ .

\* Received August 26, 1954.

† Work supported in part by AEC Contract No. AT(30-1)-1044.

†† Rensselaer Polytechnic Institute, Troy, New York. Now at Sprague Electric Company, North Adams, Massachusetts.



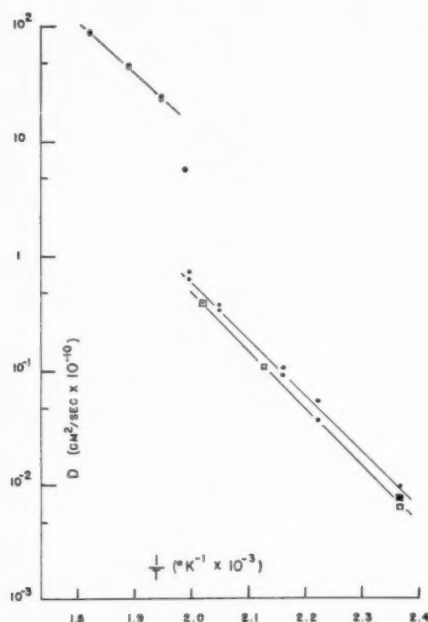


FIG. 1. Self-diffusion in thallium. ● =  $\perp$  to  $c$ -axis; □ =  $\parallel$  to  $c$ -axis; ○ = cubic phase.

### III. RESULTS AND CONCLUSIONS

The data are plotted as  $\ln D$  vs  $1/T$  in Fig. 1. From the slopes of the plots, which have been fitted with a least squares fit, the values for  $Q$  and  $D_0$  are:

TABLE I.

	$Q$	$D_0$
hcp $_{\parallel}$	$22.9 \pm 0.5$ kcal/mol	$0.4$ cm <sup>2</sup> /sec
hcp $_{\perp}$	$22.6 \pm 1$ kcal/mol	$0.4$ cm <sup>2</sup> /sec
bcc	$20.0 \pm 0.5$ kcal/mol	$0.7$ cm <sup>2</sup> /sec

The ratio  $D_{\text{cubic}}/D_{\text{hcp}}$  at transition temperature = 25.

Since the temperature range of the cubic form is so small the extrapolation to obtain  $D_0$  is not very accurate and is to be taken only as an order of magnitude.

It appears from the data that there is little or no difference between the activation energies parallel and perpendicular to the  $c$ -axis. There is a tendency for the diffusion in the perpendicular direction to be greater than that in the parallel direction. This is the opposite of what was found for zinc and cadmium and is attributed to the fact that in the cases of zinc and cadmium the  $c/a$  ratio is greater than that for the ideal case whereas for thallium the reverse is true.

TABLE II.

Mech.	$D_{\perp}/D_{\parallel}$	hcp	$c/a = 1.60$
1. Ring of 4	1	1	1.04
2. Interstitial	1	1	1.04
3. Vacancy (nonbasal)	0.25	0.25	0.26
4. Vacancy (basal)	$\infty$	$\infty$	$\infty$
5. Ring of 3 (basal)	$\infty$	$\infty$	$\infty$
6. Ring of 3 (nonbasal)	0.625	0.625	0.65

Upon applying the considerations discussed in the introduction of reference 1 to the data for the hcp form of thallium one can observe that since the activation energies for the two directions are of about the same value it is quite possible that only one mechanism is operating. Assuming that this is the case one can immediately remove the two basal mechanisms (5 and 4 of Table II) as possibilities because of their zero contribution to  $D_{\parallel}$  in the direction of the  $c$ -axis. Comparing the  $D_{\perp}/D_{\parallel}$  ratios of the rest of the possibilities with the same ratio from the data one has, respectively, 1.04 for mechanisms 1 and 2, .25 for 3, and .65 for 5 compared to 1.22 for the data. Therefore, if the assumption of only one mechanism operating is made, the interstitial or ring of four are the most probable ones.

However, the difference between the two ratios 1.22 and 1.04 is greater than the probable error of the data, making the above comparisons unsatisfactory. This leads one to suspect that possibly two mechanisms are operating, with about the same activation energy. Since  $D_{\perp} > D_{\parallel}$ , the choice of either of the basal mechanisms (4 or 5 of Table II) as one of the two mechanisms operating is required to prevent obtaining negative values for the  $D_0$ 's of the respective mechanism. Then [reference 1, Eq. (10)]

$$\left. \begin{aligned} D_{\parallel} &= A_b \exp(-Q_b/RT) \\ D_{\perp} &= A_{4,5} \exp(Q_{4,5}/RT) + \alpha_b A_b \exp(-Q_b/RT) \end{aligned} \right\} \quad (1)$$

where  $\alpha_b = D_{b\perp}/D_{b\parallel}$ ,  $b$  refers to any of the four other mechanisms, and

$$A_{4,5} \exp(-Q_{4,5}/RT) = D_{\perp} - \alpha_b D_{\parallel}. \quad (2)$$

Choosing  $Q_{4,5}$  to be the average of  $Q_{\perp}$  and  $Q_{\parallel}$  from the data and using a value of  $2.2 \times 10^{-3}$  for  $1/T$ , the values of  $A_{4,5}$  for the various  $\alpha_b$  are:

Mech.	$\alpha$	$A_{4,5}$
1 and 2	1.04	$0.06$ cm <sup>2</sup> /sec
6	0.65	$0.19$ cm <sup>2</sup> /sec
3	0.26	$0.33$ cm <sup>2</sup> /sec

Since the activation energies are about the same one expects the two mechanisms to be of the same type (i.e., vacancy, ring, etc.). Therefore, the data are satisfied by either the two vacancy mechanisms or the two ring of three mechanisms.

### ACKNOWLEDGMENT

The Author wishes to express his appreciation to Prof. H. B. Huntington for his guidance and interest in this work and to Prof. F. T. Worrell for his assistance with the x-ray problems.

### REFERENCES

- G. A. Shirn, E. S. Wajda, and H. B. Huntington, Acta Met. **1**, 513 (1953).
- E. S. Wajda, G. A. Shirn, and H. B. Huntington, Acta Met. **3**, 39 (1955).

## INDENTATION FIGURES ON SINGLE CRYSTALS. I\*

E. VOTAVA,†† S. AMELINCKX†‡ and W. DEKEYSER†

This article gives the results of an interferometric study of indentation figures on cleavage faces of mica and NaCl. In the case of mica it is found that when the pressure, exerted by a spherical indentator, is not too large, a fairly well-defined plastic deformation occurs (a bending figure). An attempt is made to explain the details of this deformation in terms of dislocations and this figure is correlated with the crack system of the pressure figure.

In the case of NaCl the phenomenon is obscured by the presence of several glide planes and no detailed explanation of the observed facts can be given.

### DES FIGURES D'EMPREINTES SUR DES MONOCRISTAUX. I

Cet article présente les résultats d'une étude interférométrique de figures d'empreintes sur les faces de clivage du mica et du NaCl.

On a constaté dans le cas du mica, que lorsqu'on exerçait une pression modérée au moyen d'une bille sphérique, une déformation plastique, relativement bien définie se produisait (figure de flexion). On a essayé d'expliquer les détails de cette déformation en termes de dislocations et on a établi une corrélation entre cette figure et le système de fissures de la figure de pression.

Dans le cas du NaCl ce phénomène est obscurci par la présence de plusieurs plans de glissement et il n'y a pas moyen de donner d'explication détaillée des faits observés.

### EINDRINGUNGSFIGUREN AUF EINKRISTALLEN. I

Die vorliegende Arbeit berichtet über die Ergebnisse einer Interferometerstudie der Eindringungsfiguren auf den Spaltflächen von Glimmer und Steinsalz. Es zeigte sich, dass in Glimmer bei nicht zu grossen Drucken (die mit Hilfe eines Kugeldruckgerätes erzeugt wurden) ziemlich klare plastische Verformung—als eine Biegungsfigur—auftrat. Es wurde versucht, die Einzelheiten dieser Verformung durch Versetzungen zu erklären, und diese Form wurde zu dem Rissystem einer Druckfigur in Beziehung gesetzt.

Im Steinsalz ist die Erscheinung durch das Vorhandensein mehrerer Gleitebenen kompliziert, und es kann keine ins Einzelne gehende Erklärung der beobachteten Tatsachen gegeben werden.

## 1. INTRODUCTION

When a small sphere of hard material is gently pressed on a crystal face, a permanent deformation is sometimes obtained, as can be deduced from the resulting topography; a so-called indentation figure. This figure is related to the symmetry of the face, provided the indentator is spherical. Indentation figures on single crystals have generally been studied macroscopically or by microscopic observation;<sup>1</sup> so far, only tin has been studied interferometrically.<sup>2</sup>

When the load, and the speed with which it is applied, is increased, pressure or punch figures are obtained. These may roughly be described as a system of cracks, presenting a symmetry which is related to that of the crystal. Since it seems logical that there must exist some relation between the indentation and punch figures, it was thought that useful information concerning crack formation could be obtained by interferometric study of indentation figures and their relation to pressure and punch figures. In what follows, we describe such observations on mica and sodium chloride. An interpretation in terms of dislocations is attempted. Further work on material with different lattices—tin, bismuth, zinc and aluminium—is in progress.

## 2. MICA; EXPERIMENTAL RESULTS

When gently indenting a mica sheet which rests on an elastic underlayer, a bending figure, barely visible by ordinary microscopy but readily detected by interferometry is obtained. When the load exceeds a certain value, pressure figures are obtained. They consist mostly of a three-armed—in rare cases, a six-armed—star. The arms of the star sometimes consist of a number of parallel cracks. It is difficult to obtain a pressure figure on a microscopic scale.

When the load is applied very quickly, a percussion figure is obtained. This is a six-branched star turned through nearly 30 degrees with respect to the pressure figure. The relation between the three figures is represented schematically in Fig. 1.

Bending figures are most conveniently studied by multiple-beam interferometry. Figures 2 and 3 are typical interferograms. They indicate that next to the central triangular depression, three other topographical features are present (see also Fig. 1). Fringes of equal chromatic order proved that they are hills.

The deformation of the lattice was deduced from Laue diagrams. Figure 4a corresponds to an undisturbed region, Fig. 4b to a deformed area. This, together with the absence of steps on the surface (see interferogram), indicates that the deformation is a pure bending about an axis lying in the (001) plane of the mica, and that only slip along the (001) planes is involved. The bending figures have a line of symmetry (the trace of the  $b$ -

\* Received February 26, 1954.

† Laboratorium voor Kristalkunde, Universiteit Gent, Belgium.

‡ Now at European Research Associates, Brussels.

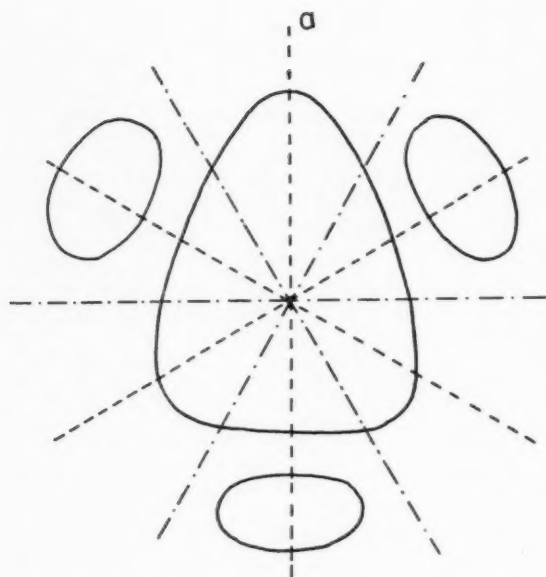


FIG. 1. Schematic drawing of the relation between bending figure, pressure figure and percussion figure in mica.

plane) in agreement with the monoclinic character of mica. Another consequence of the symmetry is the fact that the figures produced from opposite sides of the same sheet are turned through 180 degrees.

### 3. MICA; DISCUSSION

The pressure exerted by the spherical indenter causes a shear stress in the mica crystal. The direction of this shear stress is, for reasons of symmetry, radial and we have a two-dimensional state of stress. In a plane section, perpendicular to the  $c(001)$  plane, the sense of the shear stress on  $(001)$  planes is oriented outward above and inward underneath (see Fig. 5). It is evident that for diametrically opposed regions the stresses are opposite in sign. Exactly under the indenter the shear stresses on  $(001)$  are theoretically zero.

As we have seen, slip only takes place on  $(001)$  planes. It seems reasonable to admit that it occurs on the potassium layer, as the binding forces are weakest there. This layer, like every other one parallel to it in the mica structure, presents hexagonal symmetry. The glide directions being those of the most dense rows, three glide directions, making angles of 60 degrees e.g.,  $[100]$ ,  $[\bar{1}10]$ ,  $[\bar{1}\bar{1}0]$ , are to be expected.

The six corresponding glide vectors, which are equal in length, are  $[100]$ ,  $\frac{1}{2}[\bar{1}10]$ ,  $\frac{1}{2}[\bar{1}\bar{1}0]$ ,  $[\bar{1}00]$ ,  $\frac{1}{2}[110]$  and  $\frac{1}{2}[1\bar{1}0]$ . The resolved shear stress in the glide direction

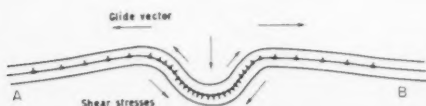


FIG. 5. Distribution of dislocations in a section perpendicular to  $(001)$  through a bending figure on mica.

will be maximum in those regions where the shear stress coincides in direction with the glide vector. Frank and Read<sup>3</sup> sources will preferentially be set in action in regions situated on lines where this condition is satisfied, and in the first place on points where the shear stress is greatest, i.e., not far from the center.

The resulting deformation pattern will exhibit a form reflecting the ease with which Frank and Read sources, with the indicated glide vectors, come into action. That differences between them must exist is roughly to be seen from the following argument.

When we consider the planes perpendicular to the glide vectors, and the distribution of ions in them, the succession in which we meet them on going from one lattice point to an equivalent one in a glide direction varies with the sense. Furthermore, this alternation of planes is not identical for the three glide directions, as is obvious from the monoclinic character of the lattice. So

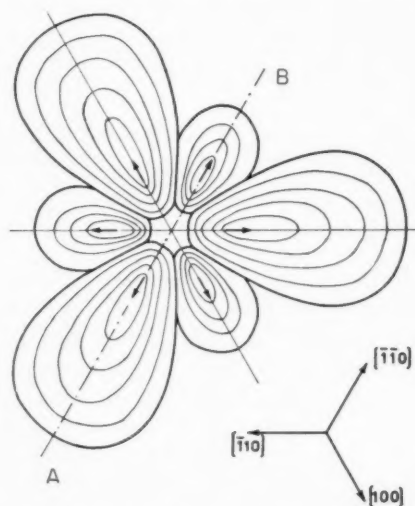
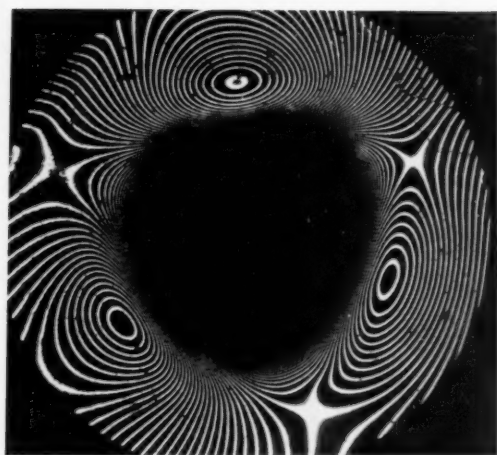


FIG. 6. Idealised distribution of dislocation lines in a  $(101)$  plane of mica.

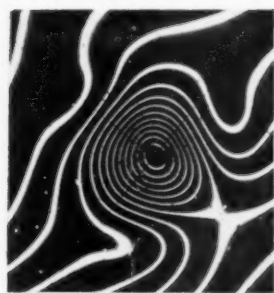
we understand that the force necessary to activate a Frank and Read generator with one of the given glide vectors will depend on the sense of this vector.

Accordingly, we should expect a deformation pattern closely related to the symmetry of the crystal, e.g., a pseudo-hexagonal one, exhibiting a line of symmetry. The fact that we only have a triangular pattern indicates, however, that three out of the six possible centers of glide are far more easy to activate than the other three. We see here that the rather slight asymmetry of the mica structure, resulting from the shift of adjacent groups of hexagonal layers at the junction of the close packed  $(O-OH)-Al-(O-OH)$  layers, has a very marked influence on the glide process.

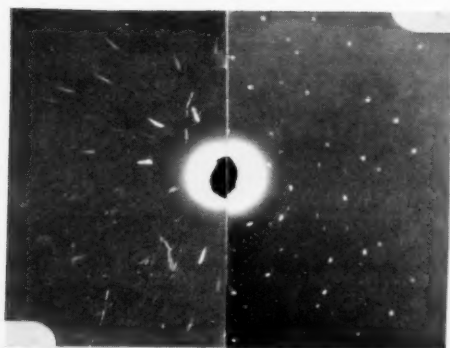
Assuming that glide in each direction proceeds more easily in one sense than in the other, a situation as shown in an idealised manner in Fig. 6 will develop.



2

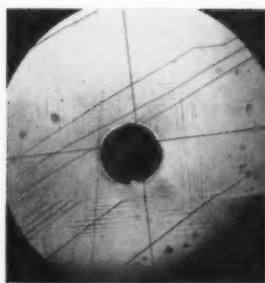


3

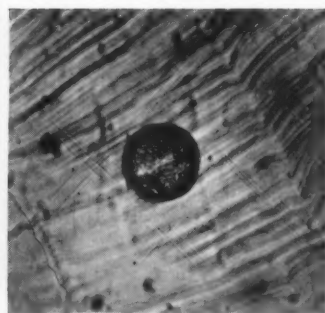


4

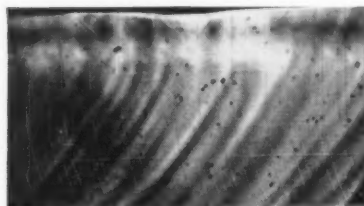
PLATE I. (All figures reduced to three-fourths in reproduction.) FIGS. 2, 3.—Interferograms of bending figure on muscovite. FIG. 4.—Laue diagrams of (a) undeformed and (b) deformed region of the bending figure.



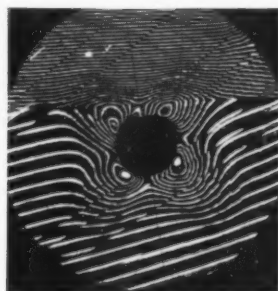
7



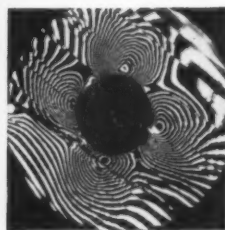
9



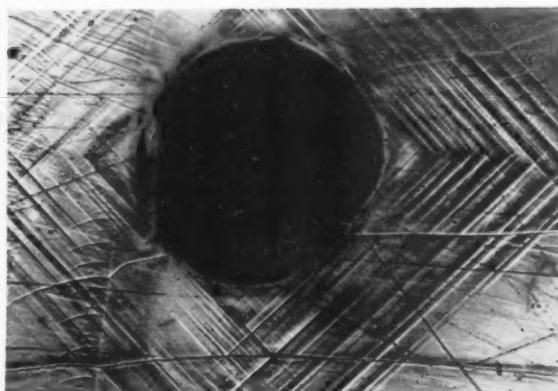
11



12



13



8

PLATE II. (All figures reduced to two-thirds in reproduction.) FIG. 7.—Surface of a NaCl crystal after indentation. Ordinary light. FIG. 8.—Surface of a NaCl crystal after indentation. Phase contrast illumination. FIG. 9.—Transmission photograph of a surface of NaCl showing the internal line system. FIG. 11.—Transmission photograph of side view of NaCl surface. FIGS. 12, 13.—Interferograms of indentation figures on NaCl.



VOL.  
3  
1955

Let us consider for the moment sources which are all situated in the same plane. The expanding loops will pile up near the center of the figure, as the shear stress is reversed there. This causes the sources to be stopped by the back stress of the dislocations piled up near the center after a limited number of loops has been formed. The loops will be approximately centered on the regions of maximum resolved shear stress. A cut *AB* along a glide direction, through the deformed mica sheet showing the distribution of dislocations is represented on Fig. 5. Sideways, the loops will meet and eventually be forced to form dislocations by the reaction  $[100] + \frac{1}{2}[110] = \frac{1}{2}[310]$ . The resultant dislocation is less mobile in the plane (001), dislocations will pile up behind the first of this kind which is formed in a plane, so giving rise to curvature of the lattice planes.

In the outward sense, the dislocations will move freely until the stress is relieved.

In the idealised case where the same symmetrical configuration of dislocation lines described here above would exist on several regularly spaced planes, this distribution would produce "polygonised" hills, as walls of dislocations, comparable to those occurring in polygonised metals would be present. In reality the sources will in general be situated in different planes, and the observed topography will result from the superposition of less symmetrical dislocation patterns. Statistically this will be comparable to the idealised case, but the hills will now be smoothly bent, as is observed. The inclination of the hills with respect to the ideal cleavage face will be smaller on the outward side, as the dislocations are more widely spaced there.

When the stress increases, the probability of having sources in the same plane increases too, and consequently the dislocations of the type with vector  $\frac{1}{2}[310]$  will be formed with greater probability. They are not freely mobile in the (001) planes, being kept in equilibrium between the dislocations piled up on both sides of them. They have screw character along their greater part, and are also submitted to the stresses of the dislocations situated in other *c*(001) planes. We can imagine that with increasing stress they are forced to move in planes, which cut the *c*(001) plane following lines which have the directions of the pressure figure.

As other dislocations lying in (001) planes are cut by such a movement, great numbers of vacancies and interstitial ions will be formed. In complicated ionic structures, as in mica, where the electrostatic neutrality in a volume as small as possible is essential, this must far more quickly lead to disruption of the lattice (a crack) than in metals, where local high temperature favors the diffusion of the neutral atoms or vacancies, so preventing, to a certain extent, agglomeration of vacancies to microcracks.

If we consider now the percussion figure, we see that the cracks are formed following  $[100]$   $[760]$   $[760]$   $[4]$  i.e., practically in the glide directions. The mechanism which is acting here must be quite different.

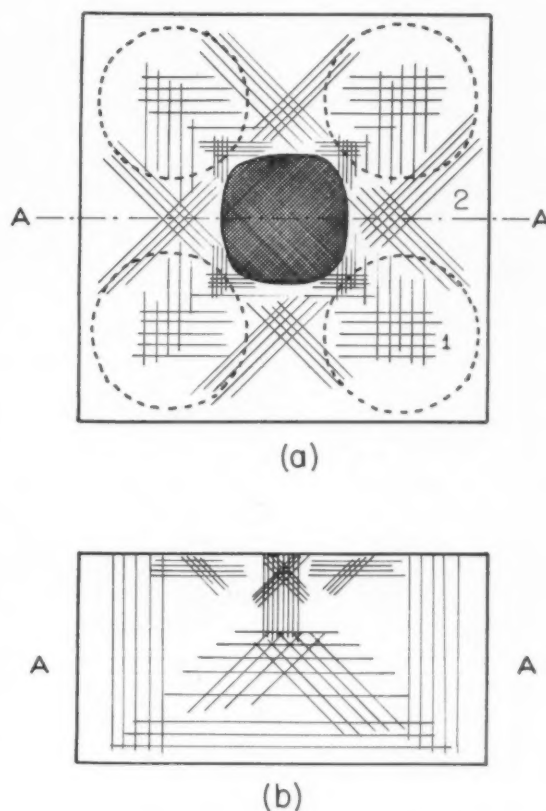


FIG. 10. Drawing of surface markings on cube face of NaCl. Top view (a) and side view (b) when an indentation is made near the edge.

#### 4. SODIUM CHLORIDE; EXPERIMENTAL

NaCl was also studied. The cleavage following (100) is perfect and small cubes with good faces can be obtained by cleaving.

As Fig. 7 (incident light) and Fig. 8 (incident phase contrast) show, slip lines parallel to  $[100]$  and  $[010]$  are formed by the slight pressure of a spherical indentator. These slip lines are faintly visible, or disappear completely in the middle. In transmission a further line system can be seen (Fig. 9) having the directions  $[110]$  and  $[1\bar{1}0]$ . As this system cannot be detected by incident phase contrast (see Fig. 2) and also not by ordinary incident light (see Fig. 7), we must conclude that it is internal. Again, the lines are faintly visible or disappear completely in the middle. Figure 10a shows schematically the observed facts.

To get further information, a pressure figure was produced near the edge of the crystal. On a (010) plane, slip lines are formed in the directions  $[001]$  and  $[010]$  and also internal lines in the directions  $[011]$ , as Fig. 11 (transmission) indicates. Figure 10b is a schematic drawing of this observation.

Figure 12 is an interferogram of the pressure figure of Fig. 7; Fig. 13 is another example. As can be seen, four

denivellations are built up, which are lying exactly in the direction  $[110]$  and  $[\bar{1}\bar{1}0]$  (marked with dotted lines in Fig. 10a). It could be proved by fringes of equal chromatic order, that these denivellations are hills.

In the case that the pressure with the spherical indentator is applied very rapidly, a percussion star is produced, lying in the directions  $[110]$  and  $[\bar{1}\bar{1}0]$  [5]. All other slip lines systems, which are present round the influence sphere of a pressure figure, can be found also round a percussion figure.

### 5. SODIUM CHLORIDE; DISCUSSION

The experimental pattern is very much more complicated than in the case of mica. This results from the action of several—possibly three—glide systems  $\{110\}$ ,  $\{100\}$ ,  $\{111\}$ , with a common slip vector  $\frac{1}{2}[110]$ .

The hills can be assumed to be built up as in the case of mica. This necessitates glide on the  $(001)$  face.

Next to the hills we observe glide lines, marked 1, which develop most markedly at the corners of the cube. Such markings can be produced by slip on  $\{100\}$  or  $\{110\}$  planes. If we consider, however, for the  $(110)$  planes the components of the applied force in the glide direction, slip on them should be most pronounced in the center. As this is not the case one has to accept that these glide lines belong to the  $(100)$  faces, but the reasons why they are active is obscure.

Furthermore, the glide markings 2 are only observed in transmission and by reflection phase contrast microscopy no evidence could be found that they reach the surface.\* When the load is applied near the edge of the crystal an intricate pattern of lines is visible as surface

steps; other lines lying at 45 degrees to the previous ones are only visible in transmission.

This indicates that interaction takes place, which alternatively set to work different sets of glide planes. Further experimental work is needed in order to determine the mechanism.

### 6. CONCLUSIONS

From these observations we can deduce, as far as ionic crystals are concerned, that the formation of cracks can proceed in two different ways, according to the velocity with which a load is applied perpendicular to a crystal face.

(a) When the load is applied very slowly and when a single slip plane is active, rupture of the lattice results primarily from interactions of dislocations with different Burger vectors, thus from the fact that different slip directions are present. Cracks are then formed in directions *not* coincident with the slip directions. When more than one slip plane is present, this stage is not developed because the stress on the less mobile interaction dislocation is released by slip on another slip system.

(b) When the load is applied more quickly, rupture proceeds nearly following the direction of easiest slip. Further work will indicate if this holds for other types of crystals.

### ACKNOWLEDGMENT

This work is part of a research scheme supported by I.R.S.I.A. (C.E.S.). One of us (E.V.) is indebted to European Research Associates for a research fellowship.

### REFERENCES

1. G. Ramman and A. Müller, *Z. f. Metallk.* **18**, 69 (1926).
2. S. Tolansky and D. G. Nicols, *Nature* **164**, 840 (1949); *Phil. Mag.* **43**, 410 (1950).
3. F. C. Frank and W. T. Read, *Phys. Rev.* **79**, 722 (1950).
4. A. J. Forty, *Research* **4**, 94 (1951).
5. A. Smakula and W. Myron Klein, *Phys. Rev.* **84**, 1043 (1951).

\* *Note Added in Proof*—These markings are most probably due to glide on  $(110)$  planes, the burgersvector being parallel to the plane of observation no steps are raised. Their visibility is due to birefringence.

## LETTERS TO THE EDITOR

### Dislocations in Polygonized Germanium

This note describes some direct observations of dislocations in bent and polygonized<sup>1</sup> germanium single crystals. The data show the effect of increasing temperature of deformation in producing the block structure and suggest that the formation of domain walls normal to the slip plane involves climb of dislocations<sup>2</sup> as well as movement along the slip plane.

Polygonized structures were obtained by bending at higher temperatures and also by bending at lower temperatures followed by annealing. Germanium single crystal bars about 3.2 cm long with 1.5 mm×1.5 mm square cross sections were cut and deeply etched to remove the strained material. The bars were oriented with  $[11\bar{2}]$  as the longitudinal axis and a (111) plane as a side face. Each specimen was bent to a radius of approximately 5 cm about a  $[111]$  axis by placing it on graphite support blocks 3 cm apart and applying equal loads at the 1 cm and 2 cm positions while heating by the passage of an electric current. The temperature at which bending occurred was controlled by proper adjustment of the load and heating current. The total time of each specimen at maximum temperature was about 1 minute. After being deformed, the specimens were lightly ground on the (111) face with 600 mesh carborundum and polish-etched with CP-4 to reveal dislocations.<sup>3,4,5</sup>

Figures 1 to 3 show the dislocation configurations which result from bending at three temperatures. At 500°C, a low temperature for deforming germanium plastically, the dislocations are aligned in the traces of the  $(\bar{1}11)$  slip planes (Fig. 1), as determined from the

known orientation of the specimen. The deformation is not distributed uniformly but rather is concentrated into separated bands. No tendency is observed, at the lowest temperature, towards the formation of a block structure. As the temperature of deformation is increased to 650°C (Fig. 2) and 800°C (Fig. 3) it appears, from the alignment of dislocations normal to the slip plane, that polygonization occurred concurrently with slip. The domain walls divide the crystal into slightly misoriented blocks approximately  $10^{-3}$  cm wide.

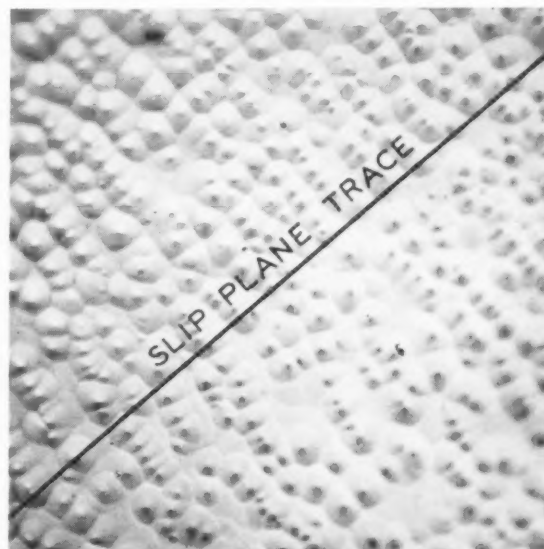


FIG. 2. Dislocations in polygonization boundaries viewed on (111) plane of crystal bent at 650°C, CP-4 etch, 1000× magnification.

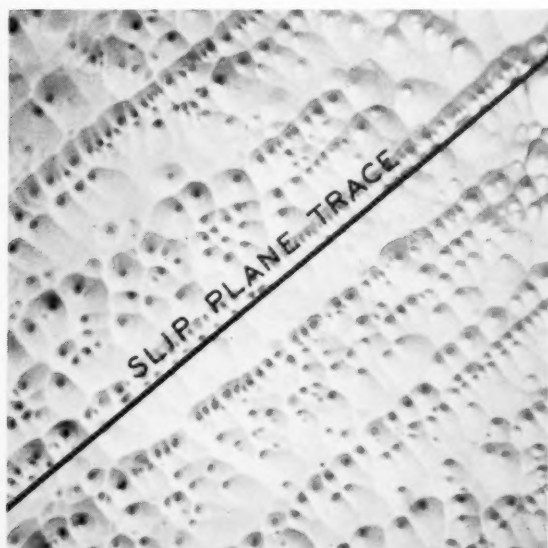


FIG. 1. Dislocations in slip lines viewed on (111) plane of crystal bent at 500°C, CP-4 etch, 1000× magnification.

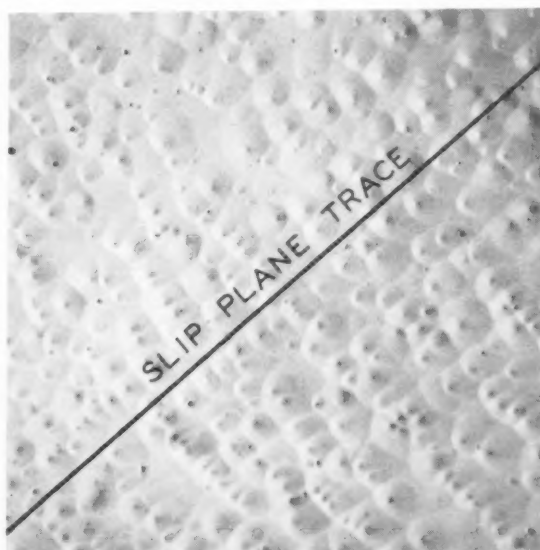


FIG. 3. Dislocations in polygonization boundaries viewed on (111) plane of crystal bent at 800°C, CP-4 etch, 1000× magnification.



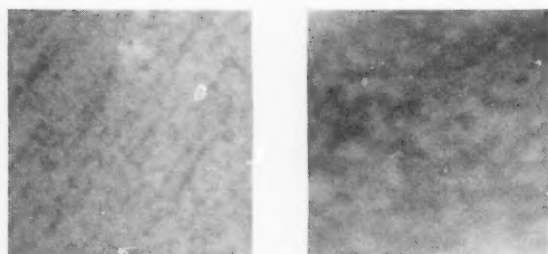


FIG. 4. 250 $\times$ —X-ray micrographs taken by Berg-Barrett technique with incident beam normal to bend axis. *a*, left, specimen bent at 500°C. *b*, right, specimen bent at 800°C. Interpretation given in text.

The presence of oriented domains in the specimen deformed at 800°C is ascertained by the Berg-Barrett<sup>6</sup> X-ray micrographs in Fig. 4. The photograph of the specimen deformed at 500°C (Fig. 4a) shows dark striations due to the slip lines. The structure is completely different with 800°C deformation (Fig. 4b). The light and dark areas here are interpreted as representing small crystal domains of varied orientations. The block size indicated by the X-ray micrograph in Fig. 4b is roughly the same ( $10^{-3}$  cm) as that shown by the light micrograph in Fig. 3.

The specimen which was bent at 500°C and showed no polygonization was subsequently annealed in vacuum at 700°C for 26 hours. Figure 5, a micrograph of the (111) surface after polish-etching, gives evidence of the occurrence of polygonization after this treatment. Comparison of Figs. 1 and 5 indicates that the polygonized structure could not be formed by migration of dislocations solely along the slip plane. It would appear necessary to invoke climb to explain the change from

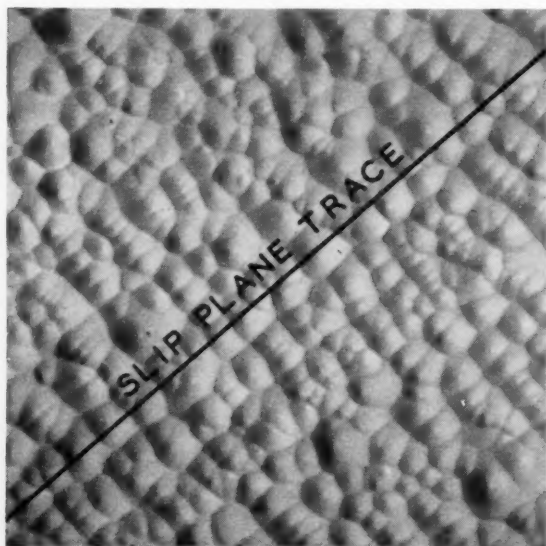


FIG. 5. Dislocations in polygonization boundaries viewed on (111) plane of crystal bent at 500°C then annealed at 700°C. CP-4 etch, 1000 $\times$  magnification.

the banded groupings of dislocations in the deformed specimen to the more uniform distribution perpendicular to the slip plane in the polygonized structures.

F. L. VOGEL, JR.

Bell Telephone Laboratories  
Murray Hill, New Jersey

#### References

1. R. W. Cahn, *J. Inst. Metals* **76**, 121 (1949).
2. N. F. Mott, *Proc. Phys. Soc.* **B64**, 729 (1951).
3. F. L. Vogel, W. G. Pfann, E. H. Corey, and E. E. Thomas, *Phys. Rev.* **90**, 489 (1953).
4. C. J. Gallagher, *Bull. Am. Phys. Soc.* **28**, 721 (1952).
5. G. L. Pearson, W. T. Read, and F. J. Morin, *Phys. Rev.* **93**, 666 (1954).
6. C. S. Barrett, *Trans. A.I.M.E., I.M.D.* **161**, 15 (1945).

#### Sub-Grain Formation in Aluminum Deformed at $-183^{\circ}\text{C}^*$

Fine-grained specimens of pure aluminum (99.99%), deformed at the temperature ( $-183^{\circ}\text{C}$ ) of liquid oxygen, have been examined by X-ray microbeam methods both at the low temperature and at room temperature immediately after deformation. In both experiments the initially annealed specimens, of grain size  $\sim 30\mu$ ,

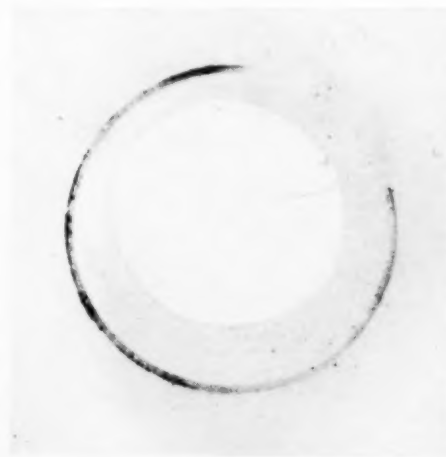


FIG. 1. X-ray microbeam back-reflexion photograph of aluminum deformed at  $-183^{\circ}\text{C}$  and examined at room temperature. Beam diameter  $30\mu$ . 422 ring-CuK $\alpha$  radiation.

were immersed in liquid oxygen for periods of up to three hours and then were either strained in tension until they broke, or were hammered under a copious stream of liquid oxygen. The specimens were then replaced in liquid oxygen for some hours before X-ray examination.

Immediate examination at room temperature, with an X-ray beam of diameter  $\sim 30\mu$ , of an aluminum specimen deformed at  $-183^{\circ}\text{C}$  showed resolution of the back reflexion ring into spots (Fig. 1). (The exposure



FIG. 2. X-ray microbeam back-reflexion photograph of aluminum deformed at  $-183^{\circ}\text{C}$ . Examination carried out at  $-183^{\circ}\text{C}$  immediately after deformation. Beam diameter  $10\mu$ . 422 ring- $\text{CuK}\alpha$  radiation.

time for microbeam photographs of this nature is 10–12 hours). These were, however, much more fuzzy and diffuse than those obtained from the material deformed at room temperature.<sup>1</sup> The sub-grain size was found from a spot count to be  $1.2\mu$ , which is considerably smaller than the value of  $\sim 2.6\mu$ , found after deformation at room temperature; no measurements of the shapes of the individual reflexions were made. The resolution of the photographs improves slightly with time at room temperature after deformation. The angular misorientations in material deformed at  $-183^{\circ}\text{C}$  appear to be approximately the same as for the material deformed at room temperature. The poorer resolution of the photographs is due to the smaller particle size, which leads to weaker reflexions and to an increase in the angular breadth of the reflexions. After two months at room temperature no growth of the particles was observed.

A microbeam back-reflexion photograph was taken of an aluminum wire which had been heavily hammered at  $-183^{\circ}\text{C}$ . During the exposure liquid oxygen was continuously spilled onto the specimen which was mounted on the specimen holder between asbestos sheets to reduce the conduction of heat from the camera. The photograph obtained with a beam of diameter  $10\mu$  is shown in Fig. 2. No sign of resolution of the Debye-Scherrer ring into spots can be seen. The photograph bears a striking resemblance to those obtained by back-reflexion microbeam methods from copper or nickel deformed heavily at room temperature.<sup>2</sup>

These experiments suggest that if particles are formed in aluminum directly on deformation at  $-183^{\circ}\text{C}$ , they are too small or too distorted to be detected by the present methods until some recovery has taken place.

The sub-grain size of  $\sim 1\mu$ , found in material deformed at  $-183^{\circ}\text{C}$  and examined at room temperature is in good agreement with that observed by Heidenreich

using electron microscopy.<sup>3</sup> It is also approximately the same as the limiting slip band spacing found by Brown<sup>4</sup> in aluminum deformed at  $-183^{\circ}\text{C}$ , and examined at room temperature. This suggests that the slip band spacing may determine the scale of separation of the deformed grains into sub-grains as is proposed elsewhere.<sup>5</sup> If this is so, the boundaries of the particles are already determined at  $-183^{\circ}\text{C}$ , but the difference between the distribution and density of dislocations in the boundaries and in the particles must be so small that the spots from the particles cannot be detected when the specimen is examined at  $-183^{\circ}\text{C}$ . The resolution of the rings into spots after warming to room temperature would then be due to the diffusion of the dislocations inside the particles to the boundaries, thus creating large local differences in the densities of dislocations. On this picture the degree and type of deformation would determine the size of the particles, while recovery would make it possible to detect the particles by accentuating the difference between the plastic distortion in the particles and in the boundaries.

The authors wish to express their thanks to the University of Wales (W.T.R.) and to the Department of Scientific and Industrial Research (A.K.) for financial support.

A. KELLY†

W. T. ROBERTS‡

Crystallographic Laboratory  
Cavendish Laboratory  
Cambridge, England

#### References

1. J. N. Kellar and P. B. Hirsch, *Acta Cryst.* **5**, 162 (1952).
2. P. Gay and A. Kelly, *Acta Cryst.* **6**, 165 (1953).
3. R. D. Heidenreich, *Bell Syst. Tech. J.* **30**, 867 (1951).
4. A. F. Brown, *J. Inst. Met.* **80**, 115 (1951).
5. P. Gay, P. B. Hirsch, and A. Kelly, *Acta Cryst.* **7**, 41 (1954).

\* Received June 25, 1954.

† Now at Department of Metallurgical Engineering, University of Illinois.

‡ Now at Research Department, I.C.I., Metals Division, Birmingham, England.

#### Resistivity Changes in Silicon Single Crystals Induced by Heat Treatment\*

Resistivity changes in germanium as a consequence of heat treatment have been known for some time.<sup>1</sup> These have recently been shown to be associated, at least in part, with the presence of copper.<sup>2</sup> We have observed analogous changes in the resistivities of silicon which, however, appear to be of different origin.

The phenomenon exhibits itself in certain single crystals of Si grown from the melt by the pulling technique.<sup>3</sup> When portions of such crystals are heated for several hours in the temperature range  $350$ – $500^{\circ}\text{C}$  increases in electron conductivity ( $n$ -type) or decreases in hole conductivity ( $p$ -type) of over  $2 \times 10^{16}$  carriers

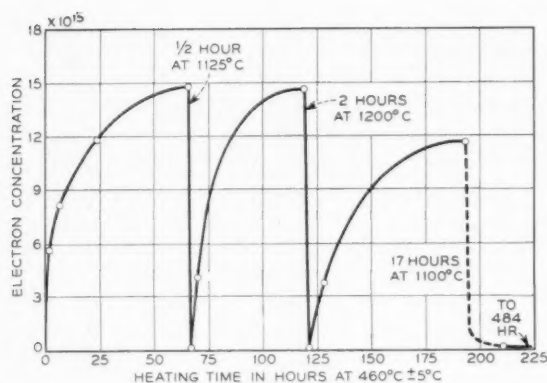


FIG. 1. Increase in electron content of silicon crystal heated at 460°C and final stabilization by long anneal at 1100°C.

$\text{cm}^{-3}$  frequently occur. These changes are reversed upon heating at 1000°C or above for a few minutes.

The rate of change in carrier concentration for a given specimen of Si depends on the temperature of heat treatment, being most rapid at about  $440^\circ\text{C} \pm 10^\circ\text{C}$ . Above and below this temperature, the rate decreases with temperature. A typical curve is shown in Fig. 1. Here the Si had an original resistivity of 25.0 ohm cm *p*-type and showed after 65 hours at 460°C an *n*-type resistivity of 0.47 ohm cm. As shown also in Fig. 1, this specimen returned to its original resistivity upon heating 1/2 hour at 1125°C. This cycle was reversible as long as the high temperature heating was short. After 2 hours at 1200°C the low temperature anneal rate was slowed and after 17 hours at 1100°C, no essential carrier increase occurred after 500 hours at 460°C. This latter behavior, which has been called "stabilization," seems to be favored by a prior low temperature anneal.

At intermediate temperatures (between 500°C and 1300°C) the resistivity changes depend on the temperature of anneal and the past heat history of the Si. If the Si crystal has been brought to the maximum electron concentration by long heating, at say 460°C, then on heating at about 500°C the electron concentration decreases monotonically, leveling off somewhat above its original value. In similar crystals, subsequently heated at 700°C, the electron concentration has been observed first to decrease, often back to its original value, and then to increase on further heating toward an intermediate value. Si specimens brought to the state of minimum electron concentration by heating to high temperature frequently show an electron increase upon heating at temperatures between 500°C and 800°C.

The above complicated changes appear to be independent of the atmosphere in which the anneals are carried out. Likewise, no role of surface impurities has yet been established. The changes occur in volume and do not appear to involve gross diffusional processes. As indicated above, we have been unable to establish that any equilibrium exists between carrier concentration and temperature.

The most striking effects of the heat treatment are connected with the crystal growth variables. When crystals grown in the normal manner<sup>3</sup> were examined after 10–20 hours anneal at 460°C it was found that the greatest changes in carrier concentration occurred in the central section of the crystals. In fact a layer of unchanged Si remained at the outside surface, the depth of which varied approximately inversely with the crystal diameter. The magnitude of the carrier increase in the central portions was also roughly inversely proportional to the diameter.

These observations indicate that the phenomena are closely associated with the fluid flow in the molten silicon during growth. Impressive support for this is furnished by the effect of rotation of the crystal during growth. This is illustrated in Fig. 2 which is a photo-



FIG. 2. Photograph of silicon crystal (original 25 ohm cm *p*-type) after heat treatment at 460°C for 20 hours. Sections A and C, grown with rotation, are 0.4 ohm cm *n*-type. Section B, grown stationary, is unchanged.

graph of a longitudinally sectioned crystal. The A and C regions were grown with the crystal rotated at 100 rpm. The center section, B, was grown without rotation. After growth the crystal was annealed for 20 hours at 460°C when the *p-n* junctions were brought out by means of barium titanate suspension applying 60 volts potential.<sup>4</sup> These lines are evident on the photograph. Sections A and C, which were rotated, showed an increase in electron content of  $1.75 \times 10^{16} \text{ cm}^{-3}$ . Section B,

which was not rotated, showed an increase of only  $4.4 \times 10^{14} \text{ cm}^{-3}$ . At intermediate rotation rates, the depth of the skin at the crystal surface, which remained unchanged by annealing at  $475^\circ\text{C}$ , increased rapidly with decreasing rotation rates.

The cause of the above described changes in resistivity is not at present understood. It is evident that the effect is intimately associated with the crystal growing process, but whether it involves lattice defects or impurities or both must await further work.

C. S. FULLER  
J. A. DITZENBERGER  
N. B. HANNAY  
E. BUEHLER

Bell Telephone Laboratories  
Murray Hill, New Jersey

#### References

1. H. C. Theuerer and J. H. Scaff, *J. Metals* **191**, 59 (1951).
2. C. S. Fuller and J. D. Struthers, *Phys. Rev.* **87**, 526 (1952).
3. G. K. Teal and J. B. Little, *Phys. Rev.* **78**, 647 (1950).
4. G. L. Pearson, Private communication.

\* Received June 21, 1954.

#### The Diffusion of Hydrogen in Iron and Ferritic Steels\*

The evolution of hydrogen from iron and ferritic steels has been reported by many investigators<sup>1,2,3</sup> to differ markedly from the behavior predicted by the usual diffusion laws. Mathematical descriptions of the evolution rate have been found to require at least two distinct rate constants differing from each other by several orders of magnitude. In some cases the hydrogen diffusing at the lower rate is termed "residual" to distinguish it from the more mobile "diffusible" hydrogen, and its rate constant is approximated as zero.<sup>2</sup> Some authors have suggested essentially that the "residual" hydrogen is partially converted into "diffusible" hydrogen on heating, but that it does not disappear completely until after traverse of the alpha-gamma transformation.<sup>1</sup>

This nonconformity of the evolution rate with diffusion theory is apparently responsible in large measure for the widespread past use of strictly empirical expressions for representing the rate of hydrogen evolution from steel. Slowly diffusing or "residual" hydrogen has not always been detected, however, and in these cases the evolution rate appears to conform satisfactorily with the theory. Thus Sykes, Burton and Gegg<sup>4</sup> reported that both their own evolution rate data and those of Andrew *et al*<sup>5</sup> are consistent with the diffusion laws, despite the substantial quantity of "residual" hydrogen postulated by the latter authors as necessary in mathematical representations of their data. More recently the diffusion laws have been applied to hy-

drogen in steel by Demarez, Hock and Meunier,<sup>6</sup> who, like Sykes *et al*, have dismissed the apparent presence of slowly diffusing hydrogen as a natural consequence of the manner in which the evolution rate theoretically varies with time.

We have investigated the evolution of hydrogen from 99.9 per cent pure iron by several experimental methods including that described by Demarez, Hock and Meunier.<sup>6</sup> Suitable solutions of Fick's equation for finite cylinders were obtained from Carslaw and Jaeger.<sup>7</sup> For a cylinder of length  $a$  and diameter  $b$  the solution of present interest is

$$\bar{C}/C_0 = \psi(a, t)\chi(b, t) \quad (1)$$

in which  $\bar{C}$  is the average concentration,  $C_0$  is the initial concentration and  $\psi(a, t)$  and  $\chi(b, t)$  are the respective functions for the time dependence of  $\bar{C}/C_0$  in an infinite slab of thickness  $a$  and an infinitely long cylinder of diameter  $b$ , respectively. Thus

$$\begin{aligned} \bar{C}/C_0 = & \frac{32}{\pi^2} \sum_{n=0}^{\infty} \frac{1}{(2n+1)^2} \exp[-(2n+1)^2 \pi^2 D t / a^2] \\ & \times \sum_{n=1}^{\infty} \frac{1}{\beta_n^2} \exp[-4\beta_n^2 D t / b^2] \quad (2) \end{aligned}$$

in accordance with the derivation of Demarez *et al*.

After a relatively short initial diffusion period  $t_0$ , Eq. (2) reduces to

$$\log \bar{C}/C_0 = \log g - D t \left( \frac{4.29}{a^2} + \frac{10.05}{b^2} \right) \quad \text{for } t > t_0 \quad (3)$$

in which  $g$  is 0.56 for finite cylinders.

As was pointed out by Demarez *et al*, the precise form of Eq. (2) is never obtained experimentally from small specimens examined at elevated temperatures because of the unavoidable hydrogen losses that occur during heating of the specimen to the experimental temperature. The diffusion coefficient  $D$ , however, is readily evaluated from the slope of the final  $\log \bar{C}$  versus  $t$  plot under a variety of conditions including those in which zero time is not precisely known and the initial concentration  $C_0$  is not uniform throughout the specimen.

The experimental evaluation of  $g$  in Eq. (3) may be approached in several ways, of which that employed by Demarez *et al*, viz., minimizing the time of heating the specimen to the experimental temperature, is one. The same effect is obtained by conducting the experiment at a sufficiently low temperature to make the heating time negligible in comparison with the total period of diffusion. In this connection we have found that extractions conducted at room temperature yield curves of theoretical form over their entire length.

The principal reason for attempting to establish agreement between experimental and theoretical values of  $g$  is apparently to validate the application of diffusion



theory. Any departure from Eq. (2) would probably result, however, from (1) non-uniformity of the initial concentration  $C_0$ , (2) control of the evolution rate by processes at the specimen surface rather than by diffusion, or (3) variation of  $D$  with concentration. The first effect does not alter the apparent or measured value of  $D$  and hence need not be considered further. The last effect can be considered to include the possible co-existence of rapidly and slowly diffusing hydrogen.

The effect of slow surface processes has been shown by Dünwald and Wagner<sup>8</sup> to be detectable from the manner in which the evolution rate varies with specimen dimensions. According to Eq. (2) the time required for evolution of a given fraction of the hydrogen from specimens of equal shape should vary directly with the square of the diameter when the evolution rate is diffusion controlled. When the rate is surface-controlled, on the other hand, this time is proportional to only the first power of the diameter. Both Derge *et al*<sup>2</sup> and Andrew *et al*<sup>5</sup> have reported in effect that the time for a given degree of hydrogen removal is proportional to the square of dimensions in specimens larger than 3/8 inch and at temperatures down to 25°C. Our own data confirm this finding, indicating that the evolution rate is entirely diffusion controlled under the conditions specified.

To permit close examination of the possible variation of  $D$  with concentration, we have employed a modified experimental procedure based on a relationship given by Geller and Sun,<sup>9</sup> of which the following form applies to finite cylinders:

$$\log(-\partial\bar{C}/\partial t) = \text{const.} - Dt \left( \frac{4.29}{a^2} + \frac{10.05}{b^2} \right) \quad (4)$$

The evolution rate  $-\partial\bar{C}/\partial t$  is actually proportional to the flow rate of hydrogen from the specimen into the collecting volume of the measuring apparatus. Hence  $D$  may be evaluated directly from the slope of a plot of  $\log(\text{flow rate})$  versus time. This method is more precise than that involving the measurement of pressures in the collecting volume, in that  $D$  is obtained directly from a plot of the experimental data themselves rather than of small differences between large quantities.

The initial experiments were on 9/32 to 3/4 inch diameter iron specimens prepared by "thermal charging," a method of introducing reproducible quantities of hydrogen that consists of saturating in a hydrogen atmosphere at from 1000 to 1350°C, and then quenching in cold water to prevent hydrogen losses during cooling. Although the quench through the transformation is known to have caused internal stresses, the subsequent evolution of hydrogen into a vacuum appeared to be normal in all respects, yielding reproducible values of  $D$  with mean deviations of from  $\pm 10$  to  $\pm 20$  per cent. Hydrogen analysis of replicate specimens by both graphite crucible and tin vacuum fusion methods indicated, moreover, that the hydrogen had been quantita-

tively evolved from these specimens at single values of  $D$  in less than one hour at 300 to 650°C. Thus no slowly diffusing or "residual" hydrogen was evident in any of these "thermally charged" specimens.

Subsequent experiments on specimens of the same material that had been hydrogen charged by a different method have indicated, however, that slowly diffusing or "residual" hydrogen is unmistakably present in specimens of less severe thermal history than those described above. Such specimens were prepared by "pressure charging," which consists of saturating with hydrogen at 650°C under a hydrogen gas pressure of up to 75 atm. The apparatus for this purpose was patterned after that described by Hobson and Sykes.<sup>10</sup> Although quenching from the saturation temperature was employed here as well as in the previous charging method, a considerably less severe internal stress level was assured by the fact that the material remained ferritic throughout the heating and quenching cycle.

The evolution of hydrogen from the "pressure charged" specimens at 385 to 575°C exhibited a behavior that departed radically from that observed in the "thermally charged" specimens. Early in the process the evolution rate decreased in the expected exponential manner and at essentially the same rate as that observed in the thermally charged specimens. After a period corresponding to the extraction of from 80 to 90 per cent of the hydrogen in the previous specimens, however, the plot of  $\log(\text{flow rate})$  versus time became nonlinear, indicating a decrease in the rate of change of  $\log(-\partial\bar{C}/\partial t)$ . Subsequent heating to 850°C, moreover, invariably resulted in a rapid evolution of additional hydrogen amounting to 20 to 50 per cent of the amount previously extracted in from 1½ to 19 hours at the lower temperature. The conditions and results of five of these experiments are listed in Table I, which indicates (1) that the quantity of hydrogen that is not evolved during several hours heating in vacuum de-

TABLE I. Vacuum extraction of hydrogen from 0.75 inch diameter  $\times 0.75$ -inch iron cylinders prepared by pressure charging.

Specimen Preparation: Hours at 650°C, 62-67 atm. H <sub>2</sub> pressure	18	18	14	14	21	21
Initial extraction: Temp., °C	385	480	575	575	575	990
Extraction time, hours	2.0	2.5	1.5	1.5	3.0	1.5
Hydrogen extracted, RV*	0.60	0.62	0.68	0.78	0.57	0.84
Additional extraction time, hrs.	—	—	—	—	16	—
Additional H <sub>2</sub> extracted, RV*	—	—	—	—	0.03	—
Final extraction at 850°C						
Extraction time, hrs.	1.3	1	0.75	0.75	1	—
Additional H <sub>2</sub> extracted, RV*	0.30	0.25	0.16	0.18	0.13	—
Total H <sub>2</sub> extracted, RV*	0.90	0.87	0.84	0.96	0.73	0.84

\* RV = Relative Volume = 12.72 ml/100 g = 0.00114 wt. %.

creases with increasing temperature, and (2) that continuation of vacuum treatment at 575°C for more than two hours is apparently ineffective in removing much additional hydrogen.

That slowly diffusing or "residual" hydrogen is not characteristic of "pressure-charged" specimens alone is indicated by numerous previous reports of a similar behavior in electrolytically charged steel<sup>11</sup> as well as in as-trepanned samples from massive sections of commercial steel.<sup>2</sup> If anything, "pressure-charged" specimens should be more representative of the interiors of thick steel sections containing hydrogen than any other specimens that can be prepared in the laboratory.

Although much information on slowly diffusing or "residual" hydrogen remains to be learned, the following conclusions are indicated by the data collected thus far:

1. Slowly diffusing or "residual" hydrogen is not a consequence of the theoretical time dependence of the diffusion rate but a real component or effect detectable only after the removal of the rapidly diffusing or "diffusible" hydrogen.
2. The amount of "residual" hydrogen appears to decrease as the specimen temperature is increased from 400 to 900°C.
3. The amount of slowly diffusing or "residual" hydrogen appears to depend on thermal history. Prominent quantities of this component were found in small iron specimens quenched from 650°C after heating in a high pressure hydrogen atmosphere, but not in specimens rapidly quenched from hydrogen atmosphere treatment above 1000°C. The amount of "residual" hydrogen present in commercial steel might therefore be expected to be appreciable in hot-rolled or forged heavy sections, but not in rapidly cooled materials such as weld metal deposits.

E. W. JOHNSON  
M. L. HILL

Westinghouse Research Laboratories  
East Pittsburgh, Pennsylvania

\* Received June 30, 1954.

#### References

1. G. A. Moore and D. P. Smith, *Trans. A.I.M.E.* **135**, 255 (1939).
2. G. Derge, W. Peifer, and J. H. Richards, *Trans. A.I.M.E.* **176**, 219 (1948).
3. J. Bleton, S. Mischonsniky, G. Coin, and P. Bastien, *Rev. Metall.* **48**, 471 (1951).
4. C. Sykes, H. H. Burton, and C. C. Gegg, *J. Iron Steel Inst.* **156**, 155 (1947).
5. J. H. Andrew, H. Lee, A. K. Mallick, and A. G. Quarrell, *J. Iron Steel Inst.* **153**, 67 (1946).
6. A. Demarez, A. G. Hock, and F. A. Meunier, *Acta Met.* **2**, 214 (1954).
7. H. S. Carslaw and J. C. Jaeger, *Conduction of Heat in Solids*, Oxford University Press (1947).
8. H. Dünwald and C. Wagner, *Z. Phys. Chem.* **B24**, 53 (1934).
9. W. Geller and T. H. Sun, *Arch. Eisenhüttenwesen* **21**, 423 (1950).
10. J. D. Hobson and C. Sykes, *J. Iron Steel Inst.* **169**, 209 (1951).
11. J. B. Seabrook, N. J. Grant, and D. Carney, *Trans. A.I.M.E.* **188**, 1317 (1950).

#### Electron Microscope Study of Slip Bands in Radiation-Damaged Aluminum Crystals\*

Jamison and Blewitt<sup>1</sup> studied the effect of radiation damage on copper, using light micrographs of the surface. The phenomenon studied was the density and spacing of slip lines. They showed that the density of slip lines was greater in damaged copper, other things being the same. Heidenreich and Shockley<sup>2</sup> studied slip bands in pure aluminum with the electron microscope and demonstrated that a single band may have a fine structure of several closely spaced bands which cannot be resolved by the light microscope. In the experiment reported here, the anode-oxide replication process as described in the latter paper was used to study the fine structure of slip bands in both irradiated and un-irradiated aluminum.

The aluminum samples were 99.996 per cent pure. After heat-treating to increase the grain size they were abraded, electro-polished, and etched, using the procedure given by Heidenreich and Shockley.

The irradiated and the control samples were strained to produce slip lines. The usual method of strain was simple bending, carried out at room temperature, -78°C, and -196°C. The time of bending was a few seconds, and the amount was such as to produce a strain of 5 to 10 per cent at the surface. The strain was computed crudely by estimating the radius of curvature of the central part of the specimen and assuming the central plane to remain unchanged in length. Because the microscopic strains vary widely from the macroscopic strain, particularly from crystal to crystal within the polycrystalline specimen, it was felt that any effort to measure strain precisely would not be profitable at this time.

The damaged samples were obtained by alpha bombardment in the Berkeley 60-inch cyclotron. The damage was produced by 39.6-Mev alpha-particles. The average bombardment was 8  $\mu\text{ah}/\text{cm}^2$ , which is equal to  $9 \times 10^{16}$  alpha-particles/cm<sup>2</sup>. The samples were kept below -100°C during and after the bombardment to prevent annealing of the damage. The temperature of one of the samples was recorded continuously by means of a thermocouple imbedded in it.

Twenty-five samples were observed, of which six had been bombarded. Each sample provided two or three replica squares, each having 50 meshes observable in the microscope. Thus the number of fields observed in the microscope was about 3000, not including faulty replicas. Of these 200 were photographed.

On the basis of the electron-microscope studies and observations with the light microscope, it is believed that irradiation at temperatures near the liquid-nitrogen point followed by straining at the liquid-nitrogen point increases the amount of slip which takes place on a given plane. The opinion is based upon the qualitative observations of many photographs similar to those in Fig. 1. Similar observations indicated no noticeable

Control



A Large Number of Very Faint Bands.

Irradiated



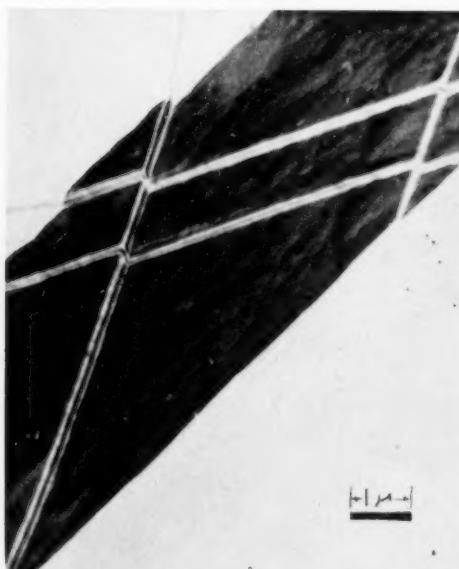
The Single Steps are About 1200 Å High.

Control



No Bands Visible in Spite of the Relative Clarity of the Picture.

Irradiated



The Largest Step is About 2000 Å High.

FIG. 1. Slip bands in samples strained at  $-196^{\circ}\text{C}$ 

difference between irradiated and unirradiated samples strained at room temperature. The results for samples strained at  $-78^{\circ}\text{C}$  were inconclusive.

This note is based on studies conducted for the Atomic Energy Commission at North American Aviation, Inc., Downey, California.

E. M. KELLY

Rheem Development Laboratory  
Downey, California

#### References

1. R. E. Jamison and T. H. Blewitt, "Slip Lines in Pile Irradiated Copper Single Crystals," Abstract D, Bull. Am. Phys. Soc., Program of the Columbus Meeting, March, 1952.
2. R. D. Heidenreich and W. Shockley, "Study of Slip in Aluminum Crystals by Electron Microscope and Electron Diffraction Methods." Report of a Conference on Strength of Solids, The Physical Society, 1948.

\* Received June 10, 1954.

VOL.  
3  
1955

### A Possible Explanation of the Stability of Guinier-Preston Zones\*

In a recent article it was shown that different mobilities of the atoms in an alloy can be the explanation to the fact that flat Guinier-Preston zones are sometimes formed in a supersaturated alloy if there is difference enough in size between the atoms.<sup>1</sup> This last requirement about the relative size of the atoms is dropped here and a more general discussion of Guinier-Preston zones will be given. Guinier<sup>2</sup> has recently published a critical review of experimental information about Guinier-Preston zones.

Assume that we have an alloy composed of a majority of *A*-atoms and a few per cent *B*-atoms and that there is higher solubility for the *B*-atoms at high temperatures. If the initially homogeneous alloy is cooled down below the two-phase boundary there will be a tendency to form a new phase, and nucleation will occur. In general we can expect the nuclei in connection with different kinds of imperfections in the crystals, for instance, at the surface and at grain boundaries. The formation of the nuclei will not be studied here but their ability to grow will be discussed. We make the assumption that diffusion takes place via vacant lattice sites.

Before we do this, imagine that we modify the original experiment of Smigelskas and Kirkendall<sup>3</sup> on a microscopic scale in the following way: Enclose a small brass grain in a copper block and heat this up enough for diffusion to take place at a reasonable rate. We can expect the brass grain to decrease in size like a salt crystal which is partly dissolved in water though the mechanism is different. We get a net flow of zinc atoms out of the grain and a flow of vacancies in the opposite direction. This will go on as long as the concentration of zinc atoms in the grain is greater than in the surrounding matrix. If we have a small copper grain inside a piece of brass we can expect a quite different behaviour. The zinc atoms of the brass move more easily than the copper atoms and we get a flow of zinc atoms towards the copper grain which grows and becomes more and more diluted with zinc. The concentration gradient will decrease and the diffusion will be slower and slower.

We go back to our alloy composed of *A*- and *B*-atoms and assume that we have obtained a nucleus of a new phase rich in *B*-atoms which is big enough to grow for thermodynamic reasons (see, for instance, reference 4). The nucleus can eventually be an enrichment of *B*-atoms coherent with the original matrix, a Guinier-Preston zone. We will now study the possibilities for the nucleus to grow. In general, it contains both *A*- and *B*-atoms, but there is always a surplus of *A*-atoms in the initial phase so they will always be available. It is different with the *B*-atoms. There must be a movement of such atoms from the inside of the old phase to the boundary between this and the nucleus. This re-

quires a certain mobility of the *B*-atoms. The boundary itself can eventually be considered as an arrangement of dislocations and other imperfections so it can act as a source or sink for vacancies. This is certainly true if the nucleus forms a new phase but it is more doubtful for a Guinier-Preston zone. If the *B*-atoms have the higher mobility, there will be a flow of these from the old phase to the boundary of the nucleus and a flow of vacancies in the opposite direction. Thus there will be *B*-atoms enough available for growth of the nucleus. Inside the nucleus itself vacancies will move towards the boundary and *B*-atoms in the opposite direction so that we get a normal growth.

If the *A*-atoms have the higher mobility, very few *B*-atoms will move towards the nucleus for two reasons: they are fewer than the *A*-atoms and they have the lower mobility. A concentration gradient will mainly be leveled out by a flow of *A*-atoms from the regions close to the nuclei where there are few *B*-atoms and the possibility for the nuclei to grow will be poor.

The conclusion from the discussion above is that if Guinier-Preston zones are formed they will very quickly grow to a precipitate if the *B*-atoms have the higher mobility and probably never be detected as such. If the *A*-atoms move more easily the zones will be much more stable, which is important in age-hardening of many technical alloys. The only alloy system known to the author where we have information about both Kirkendall effect and formation of Guinier-Preston zones is AlCu where the zones appear at the Al-rich side in agreement with the discussion above. From the discussion also follows that if we have Guinier-Preston zones at one end of a binary system we cannot expect them at the other.

J. NYSTRÖM

Department of Physics  
North Carolina State College  
Raleigh, North Carolina

\* Received June 29, 1954.

#### References

1. J. Nyström, *Appl. Sci. Res.* **A4**, 266 (1954).
2. A. Guinier, *Acta Cryst.* **5**, 121 (1952).
3. A. D. Smigelskas and E. O. Kirkendall, *Trans. Amer. Inst. Min. Met. Engrs.* **171**, 130 (1947).
4. J. H. Hollomon and D. Turnbull, *Progress in Metal Physics* **4**, 333-388 (1953).

### Internal Friction in Titanium and Titanium Oxygen Alloys\*

The paper<sup>1</sup> by Pratt, Bratina and Chalmers entitled "Internal Friction in Titanium and Titanium-Oxygen Alloys," implicitly, if not explicitly, accepts the concept of stress-relaxation across grain boundaries for which Kê<sup>2</sup> first provided experimental evidence. In particular, Fig. 2 of the paper uses that concept to explain the abnormally sharp drop in the ratio of the so-called "relaxed" to "unrelaxed" moduli of rigidity.



The evidence contained in Table I conflicts with Kê's<sup>2</sup> explanation for the sharp drop in the modulus of aluminium at elevated temperatures, and therefore conflicts with that explanation as applied to titanium, for the following reason:

In the work on both aluminium and titanium, the frequency of vibration was approximately 1 cps. Therefore, during 1/2 second, the stress on the sample rises from zero to a maximum and back to zero again. From this fact it follows that whatever stress relaxation occurs must take place in half a second or less. Kê pointed out that Zener's equation

$$G_r/G_u = \frac{2(7+5\sigma)}{5(7-4\sigma)}$$

requires that the stress relaxation be complete, and from his use of the word "slippery" to describe the grain

TABLE I. 99.99% aluminium, .033 in. diameter. Tested at 450°C by the method used by Kê to obtain his Figure 7.

Time from application of load	Deflection
0	.80 cm
30 sec	1.08 cm
60 sec	1.20 cm
2 min	1.32 cm
5 min	1.52 cm
10 min	1.72 cm
20 min	1.93 cm

boundaries, it appears that he believes complete stress relaxation will occur in the very short time available, if the temperature is high enough so that  $G_r/G_u$  satisfies the above equation. However, Table I shows that the stress-relaxation across grain boundaries—if there is such a thing—is only beginning in half a second, and is certainly less than 5 per cent complete. Table I gives the same kind of data for aluminium at 450°C as Kê's<sup>2</sup> Fig. 7 gives for 175°C. The creep shown in this figure is attributed by Kê to the same phenomenon of stress relaxation across grain boundaries as that which is supposed to explain the abnormal effect of temperature on the modulus. Therefore the evidence contained in Table I may properly be used to prove that stress relaxation across grain boundaries cannot be the explanation for the rapid drop in the modulus.

H. H. BLEAKNEY

Physical Metallurgy Division,  
Department of Mines  
Ottawa, Ontario, Canada

#### References

1. J. N. Pratt, W. J. Bratina, and B. Chalmers, *Acta Met.* **2**, 203 (1954).
2. T. S. Kê, *Phys. Rev.* **71**, 533 (1947).

\* Received June 7, 1954.

#### Note on the Temperature Dependence of Hardness of the Transition Metal Monocarbides\*

An empirical expression (1) for the hardness of metallic solids has been suggested recently by Nowotny and Vitovec,<sup>1</sup> which stems from earlier studies by Born<sup>2</sup> and Furth,<sup>3,4</sup> and relates hardness to the Lindemann frequency,  $\nu$

$$H = K'\nu$$

$$H = K \left( \frac{T_{mp} - T}{MV^{2/3}} \right)^{1/2} \quad (1)$$

In this expression  $T_{mp}$  and  $T$  are the melting temperature and test temperature respectively, expressed in °K;  $M$  is the molecular weight; and  $V$  is the molecular volume.

Nowotny and Vitovec have observed<sup>1</sup> that the temperature dependence implied by the expression (1) is identical with that derived by Becker<sup>5,6,7</sup> and by Vitovec and Nowotny<sup>8</sup> for the critical shearing stress of pure metals. They found good agreement with expression (1) for hardness data on pure metals with but few exceptions, and were even able to show that this expression will account for the decrease in hardness with increasing melting temperature observed in the monocarbides of the fourth and fifth groups. Other relations previously proposed by Bottone<sup>9</sup> and Friederich<sup>10</sup> fail to agree with experimental data in this latter respect.

Despite these rather satisfying results, the relation proposed by Nowotny and Vitovec is subject to criticism on several points. First, expression (1) predicts zero

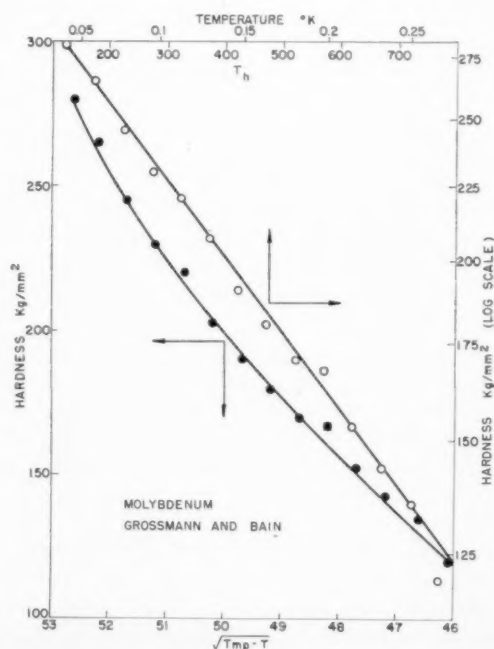


FIG. 1. Comparison of the  $\text{Log } H$  vs  $T$  and  $H$  vs  $\sqrt{T_{mp} - T}$ . Representations of the temperature dependence of hardness.

hardness at the melting temperature, whereas it has long been known<sup>11</sup> that the hardness of metals is finite and frequently quite appreciable very near the melting temperature and drops to zero only when melting has actually occurred.

Expression (1) also implies a linear dependence between  $H$  and  $(T_{mp} - T)^{1/2}$ . This relation was tested using data for molybdenum,<sup>12</sup> covering a very wide range of test temperatures. This same set of data has been previously used<sup>13</sup> to demonstrate the applicability of an expression of the form (2)

$$H = Ae^{-BT} \quad (2)$$

as compared to one implying linearity between  $H$  and  $1/T$ . In expression (2),  $A=f$  (crystal structure, melting temperature) and  $B=K/T_{mp}^n$ . Figure 1 shows a com-

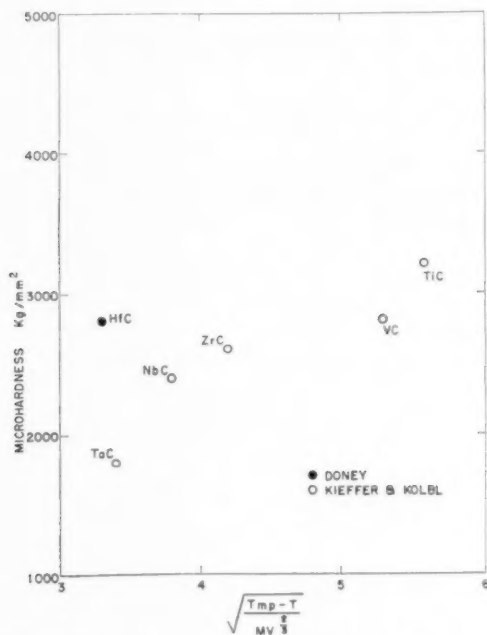


FIG. 2. Room temperature microhardness of the transition metal monocarbides as a function of the Lindemann frequency factor.

parison of the two relations for the molybdenum data, and here again, expression (2) appears to be a more satisfactory relationship.

Since the publication of the paper by Nowotny and Vitovec<sup>1</sup> a hardness value has been reported for HfC by Doney.<sup>14</sup> As shown in Fig. 2, this point does not agree with that predicted from the Lindemann frequency factor.

Still a further test may be applied to the Nowotny-Vitovec expression which will also answer the possible argument that expression (1) is more applicable to carbides than to pure metals. The hardness of TiC has recently been measured as a function of temperature. The specimen was vacuum sintered to a density of

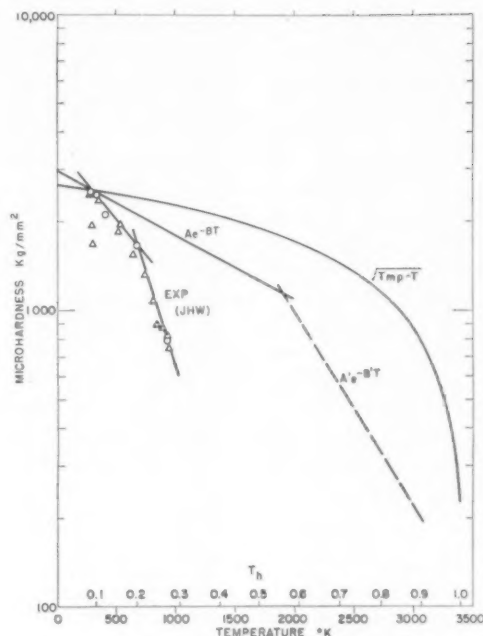


FIG. 3. Comparison of experiment with empirical prediction for the temperature dependence of hardness of TiC.

about 4.92 (about 99.5 per cent of theoretical) from carbide powder analyzing 19.03 per cent total carbon, 0.22 per cent free carbon†; no binder material was used. Testing was done *in vacuo* using a Knoop diamond indenter and 100-gram load with a modified Bergh instrument which has recently been described.<sup>15</sup> The results of the hardness tests are shown in Fig. 3, together with the hardness curves predicted from expressions (1) and (2). The latter have been normalized to agree with the hardness value measured at room temperature (2500 kg/mm<sup>2</sup>). This value agrees well with that found by other investigators,<sup>16</sup> as well as with the value (2470 kg/mm<sup>2</sup>) determined on the same sample with a standard Tukon instrument. It is considerably lower, however, than the value used in the Nowotny-Vitovec correlation (3200 kg/mm<sup>2</sup>), which apparently is taken from the work of Kieffer and Kölbl.<sup>17</sup> These differences can be attributed, in part, at least, to differences in the load and indenter used as well as to possible variation in the inherent hardness of the samples. The slope constant  $B$  used in computing the curve based on expression (2) was derived from the melting temperature correlation previously established for pure metals.<sup>10</sup>

It is obvious from Fig. 3 that neither expression (1) nor that based on expression (2) using the slope correlation established for metals, satisfactorily predicts the temperature dependence of hardness of TiC. Not only are the predicted slopes much too low, but also there is a marked change observed in the slope of the experimental curve at a rather low homologous temperature.

If TiC behaved like a pure metal, this abrupt change in slope would have occurred at about  $0.55 T_{mp}$ . It would thus appear that while the hardness-temperature plot may have a semi-logarithmic behavior, other processes or mechanisms are operative than is the case for pure metals. The Nowotny-Vitovec relation shows even poorer agreement with experiment with respect to both the slope and the homologous temperature at which the change in slope occurs.

Studies are currently in progress which, it is hoped, will improve our understanding of the temperature dependence of strength of the monocarbides. These studies will include modifications of the hot hardness instrument to provide greater accuracy in testing these extremely hard materials and to allow extension of the measurements to high temperatures, as well as the application of the method to other members of this carbide family.

J. H. WESTBROOK

General Electric Research Laboratory  
Schenectady, New York

#### References

1. H. Nowotny and F. Vitovec, "The Chemical Bond in Monocarbides and its Relation to Hardness," Plansee Proc. 1952, Metallwerk Plansee, G.m.b.H. Reutte, Tyrol 1953.
2. M. Born, "Thermodynamics of Crystallization and Melting," J. Chem. Phys. **7**, 591 (1939).
3. R. Furth, "Relation Between Breaking and Melting," Nature **145**, 741 (1940).
4. R. Furth, "A Thermodynamical Theory of the Tensile Strength of Isotropic Bodies," Proc. Roy. Soc. (London) **A177**, 217 (1941).
5. R. Becker, "Elastic Aftereffect and Plasticity," Z. f. Physik **33**, 185 (1925).
6. R. Becker, "Plasticity of Amorphous and Crystalline Substances," Phys. Z. **26**, 919 (1925).
7. R. Becker, "Plastic Strengthening and Recrystallization," Z. techn. Phys. **7**, 549 (1926).
8. F. Vitovec and H. Nowotny, "The Theory of Plastic Deformation," Z. Physik. **131**, 41 (1951).
9. Bottone, Chem. News **27**, 215 (1873).
10. E. Friederich, "The Hardness of Inorganic Compounds and of Elements," Fortsch. Chem. Phys., phys. Chem. **18**, 5 (1926).
11. P. Ludwik, "The Variation of the Internal Friction of Metals with Temperature," Z. f. physik. Chemie **91**, 232 (1916).
12. M. A. Grossmann and E. C. Bain, "High Speed Steel," 1931, p. 87, John Wiley and Sons, Inc., New York; data taken from private communication from E. S. Davenport and W. P. Sykes.
13. J. H. Westbrook, "Temperature Dependence of the Hardness of Pure Metals," Trans. A.S.M. **45**, 221 (1953).
14. L. M. Doney, "Fabrication and Properties of Hafnium Carbide," Proc. Electrochem. Soc., Wrightsville Beach, Sept. 1953.
15. J. H. Westbrook, "Micro-Hardness Testing at High Temperatures," G. E. Res. Lab. Rept. RL-1029, Feb., 1953.
16. N. W. Thibault and H. L. Nyquist, "The Measured Knoop Hardness of Hard Substances and Factors Affecting its Determination," Trans. A.S.M. **37**, 271 (1946).
17. R. Kieffer and F. Kölbl, "Tungsten Carbide Free Hard Metals," Powder Met. Bull. **4**, 4 (1949).

\* Received June 25, 1954.

† D. L. Schwartz, Carbonyl Department of the General Electric Company, was responsible for the preparation of the sample, analysis of the carbide powder, and density measurement of the sintered TiC. Sintered samples were not analyzed chemically. Carbonyl considers the chief impurities to be oxygen and nitrogen.

#### Space Charges in Anodic Films\*

Dewald<sup>1</sup> has suggested that space charges may play an important role in determining the kinetics of anodic oxidation, and has given an equation for the average field in a film when a space charge is present. It is the purpose of this note to point out that the equation predicts a dependence of average field on film thickness which is not in accord with experimental observations except under conditions where the space charge is negligible.

The equation given by Dewald for the average field is

$$\bar{E} = E_0 + \frac{kT}{aq} \left\{ -1 + \left( 1 + \frac{1}{\delta} \right) \ln(1 + \delta) \right\} \quad (1)$$

where  $E_0$  is the field when space charge is negligible,  $2a$  is the distance between interstitial positions in the oxide,  $q$  is the charge on the diffusing ion, and  $\delta$  is given by

$$\delta = \alpha D$$

where  $D$  is the film thickness and  $\alpha$  is a constant at any one formation rate and temperature. As  $\delta$  becomes very small compared to unity the second term of Eq. (1) approaches zero, and space charge is negligible. When  $\delta$  is of the same or greater order of magnitude than unity, however, the variation of average field with film thickness is great enough to be detectable experimentally.

As an example, consider the formation of an anodic film on tantalum at  $40^\circ\text{C}$  and  $1 \text{ ma/cm}^2$ . Under these conditions the field is found experimentally to be  $6.5 \times 10^6$  volts/cm. Taking  $q = 5$ ,  $a = 1.5 \times 10^{-8}$  cm,

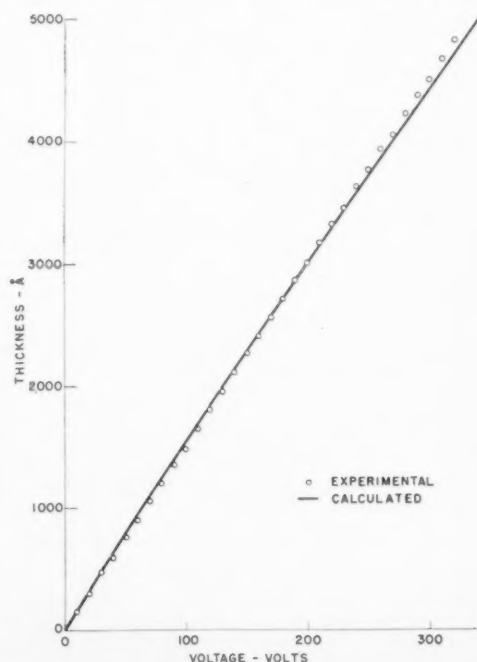


FIG. 1.

VOL.  
3  
1955

$E_0 = 6.2 \times 10^6$  V/cm and assuming that  $\alpha$  has a value such that  $\delta = 1$  at  $D = 500$  Å, the average field was calculated for film thicknesses in the range of 100–5000 Å. The voltage across the film corresponding to each thickness was then calculated from the average field. A plot of thickness versus voltage calculated in this manner is compared in Fig. 1 with experimental data obtained from measurements of capacity versus voltage under the stated conditions. It may be seen that the experimental points fall accurately on a straight line while the calculated curve is definitely nonlinear. For larger values of  $\delta$  the curvature of such a plot would be even more pronounced. Only when  $\delta$  is very small, that is, when space charge is negligible, is the variation of average field with film thickness so small as to be undetectable experimentally. It is therefore concluded that the assumption of a negligible number of ions in transit through the film is valid.

D. A. VERMILYEA

Metallurgy Research Department  
General Electric Company  
Schenectady, New York

#### References

1. J. F. Dewald, *Acta Met.* 2, 340 (1954).

\* Received June 21, 1954.

### Internal Friction of Interstitial Solid Solutions of Oxygen and Nitrogen in Vanadium\*

Internal friction arising from stress-induced diffusion of interstitial impurities has been observed in a number of the bcc transition metals. Attempts to extend these measurements to additional bcc metals are being made in several laboratories. Hence, as soon as ductile V became available, it was natural that such investigations should be made using it. This note reports on the internal friction of V containing oxygen and nitrogen; it serves in large part to confirm the observations reported earlier by Powers (1).†

In the temperature range from 25°C to 750°C, two damping peaks exist in V containing oxygen and nitrogen. These peaks are illustrated by curve *a*, in Fig. 1 for a piece of V-wire known to contain carbon, nitrogen and oxygen.‡ From an observation of the position in temperature of these two peaks, 188°C and 272°C for a frequency of 1.2 cps, combined with detailed knowledge of similar peaks in other bcc metals, one would conclude that they are probably caused by interstitial impurities. Further investigation of their behavior after various metallurgical treatments of this and other specimens showed this to be so.

Upon heating a specimen which exhibits these damping peaks to about 1500°C in a vacuum of order  $10^{-6}$ , the 188°C peak is reduced to a very low value. The 272°C peak is practically unchanged, curves *b* and *c*, Fig. 1. If a specimen annealed in this manner is now

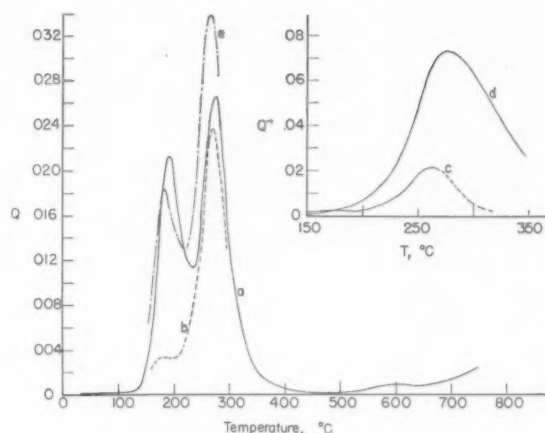


FIG. 1. Internal friction (in units  $Q^{-1}$ ) of V containing various amounts of dissolved oxygen and nitrogen. *a*. Initial specimen (frequency = 1.2 cps); *b*. and *c*. specimens annealed at high temperatures in hard vacuum (frequency  $\approx 0.7$  cps); *d*. after addition of nitrogen (frequency  $\approx 0.8$  cps); *e*. after addition of oxygen (frequency  $\approx 0.7$  cps).

heated to 1500°C in high purity nitrogen gas at a pressure of a few millimeters, the 272°C peak increases in height as is shown by curve *d*, in Fig. 1. The 188°C peak does not reappear after this treatment. Since one would expect that the nitrogen content of the specimen might well be increased by this treatment, it seems probable that this 272°C peak is indeed caused by dissolved nitrogen.

The controlled introduction of additional oxygen into the V was a more difficult problem. To prevent the accumulation of large excesses of oxide in the specimen, with its accompanying embrittlement of the metal, an oxygen atmosphere of much lower pressure is required. Numerous attempts to find the rather critical conditions necessary for an equilibrium heat treatment were not fruitful; so a simpler nonequilibrium method was used. This consisted of the forming of a thin oxide layer on the V by a short exposure of the metal at 1500°C to a few millimeters of oxygen and the subsequent dissolving of a part of this oxide in the V by a longer treatment in high vacuum at 1500°C. (This treatment must result in a rather non-uniform solution of oxygen, but it served the purpose for the present investigations). After this treatment, the 188°C peak had reappeared; a typical result is shown in curve *e*, Fig. 1. The nitrogen peak at 272°C also increased somewhat during this treatment. The increase of the nitrogen peak is apparently caused by low purity oxygen. It thus seems likely that the 188°C peak is caused by the diffusion of dissolved oxygen.

The foregoing identification of these two peaks with dissolved nitrogen and oxygen confirms the observation of Powers on the identity of these two peaks.

By carrying out the usual measurement of peak shift in temperature with frequency, one can readily determine the expression for diffusion coefficient of both of



these elements in V.<sup>2</sup> These expressions are

$$D_{\text{oxygen}} = .003 \exp(-28,200/RT)$$

and

$$D_{\text{nitrogen}} = .018 \exp(-35,100/RT).$$

The activation energies of 28,200 and 35,100 cal/mol are closely the same as those measured by Powers using the same procedure. The values of  $D_0$ , 0.003 and 0.018 cm<sup>2</sup>/sec are in the same range as those observed for diffusion in other interstitial alloys.<sup>3</sup>

If larger amounts of oxygen and nitrogen  $b$  are added, the peak height increases in the characteristic way. In addition to this, for large enough impurity additions, the peak broadens and shifts to higher temperatures as has been observed earlier for other metals.<sup>4</sup> This is apparently caused by stress arising from mutual interaction of solute atoms or by stresses about precipitated oxide or nitride.

The data presented in Fig. 1, curve  $a$ , show no grain-boundary peak. If  $V$  behaves in this regard about like other metals with comparable melting points, one might expect to see such a peak between 500°C and 750°C. The fact that no peak is seen in this range may mean that grain-boundary motion under stress is inhibited by interstitial impurities (as has been observed for Fe), although there is some possibility that the grain-boundary peak lies at a temperature even higher than 750°C.

Preliminary investigations show that the nitrogen peak decreases with time at 272°C if the nitrogen dissolved is at a high level. Hence, it appears conceivable that one might use this method to study aging of supersaturated solid solutions for this binary system as has been done earlier for other interstitial binary alloys.

This work was supported in part by the Office of Ordnance Research, U. S. Army.

J. T. STANLEY  
C. A. WERT

University of Illinois  
Urbana, Illinois

#### References

1. R. Powers, *Acta Met.* In press.
2. D. Polder, *Philips Research Reports* **1**, 5 (1945).
3. C. Ang, *Acta Met.* **1**, 124 (1953).
4. J. Marx, G. Baker, and J. Sivertsen, *Acta Met.* **1**, 193 (1953).
5. J. Stanley, Thesis, University of Illinois (1954).

\* Received May 20, 1954.

† The authors are grateful to Dr. Powers for an advance copy of his manuscript.

‡ The experimental points have been omitted for the sake of clarity. The data have been presented in a thesis by J. Stanley.<sup>5</sup>

#### Effect of Electric Field on Oxidation of Copper\*

E. K. Rideal, quoting Wilkins, stated that "electrostatic fields of the order only of 30–40 volts/cm altered the high pressure, but not the low pressure oxidation rate of copper."<sup>1</sup> Although no further details were given, and correspondence with Professor Rideal indicated

that Wilkins had not published his results nor pursued the matter further, we considered the statement sufficiently challenging to warrant a check of the facts such as might be provided by a brief investigation.

A condenser was constructed of commercial copper, the plates of which measured 2.5×2.5×0.6 cm. Separation of the plates as measured by a dial gauge was 0.5 mm. A potential difference across the plates, amounting to several hundred volts, was applied by means of a battery of dry cells.

One plate of the condenser was heated by a resistance wire coil cemented to the back face. A 12-volt storage battery supplied heating current, the regulation of which proceeded automatically by means of a chromel-alumel thermocouple embedded in the condenser plate; this operated, in turn, a relay-recorder potentiometer system. Regulation by this method maintained temperature constant at 150° within ±2°C.

The condenser was placed inside a chamber through which air, dried over calcium chloride, was circulated. The specimen surface was prepared by filing with a No. 4 Nicholson file which had been previously immersed in concentrated nitric acid, and rinsed successively in water, acetone and distilled benzene. With the field applied first in one direction, the specimen was heated for one hour at 150°C. Time of heating included the transient period of temperature rise which averaged two or three minutes in all cases. A number of experiments were run for various values of field strength, then repeated with the field applied in the opposite direction.

After the heating period, the specimen was allowed to cool to room temperature, and the thickness of Cu<sub>2</sub>O film on the surface determined by electrolytic reduction using the principle of coulometry. The procedure was that described by Campbell and Thomas,<sup>2</sup> in which the oxide was reduced at a current density of 0.06 ma/cm<sup>2</sup> in a 0.1 *N* KCl solution previously deaerated by bubbling purified nitrogen through the solution. Time was noted for the specimen to change potential corresponding to complete reduction of the oxide. The thickness in Angstroms (Å) is given by the expression  $itB/A$ , when  $i$  is in milliamperes,  $t$  is in seconds,  $A$  in square centimeters, and  $B$  is a constant equal to 12.4.

Oxide thicknesses obtained in this way for various times of heating without application of the field are

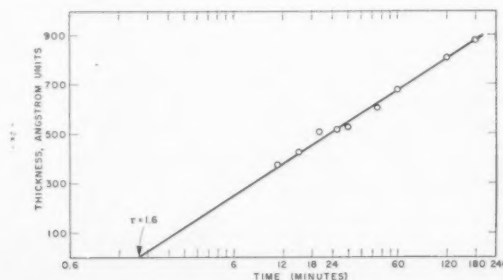


FIG. 1. Oxide film thickness on copper heated for various times at 150°C.

TABLE I. Effect of electrostatic field on oxidation of copper.

Electric field (volts/cm)	Oxide thickness, Å	
	Specimen +	Specimen -
9000	660	—
9000	675	745
14,000	660	660
14,000	740	755
15,500	650	775
15,500	675	645
Average	660	716
Standard deviation	34	60

shown in Fig. 1. The data obey the logarithmic equation  $T = k \log(1 + t/\tau)$ , where  $T$  equals thickness in Å, and  $k$  and  $\tau$  are constants equal respectively to 425 Å and 1.6 minutes.

Values of oxide thickness for heating periods of one hour in presence of an electrostatic field are given in Table I. These averages for fields with specimen positive (660 Å) and negative (716 Å) can be compared with average values in absence of field, taken from Fig. 1, equal to 675 Å. The differences are not significant. Scatter of values, in all likelihood, is a result of the unavoidable variations of surface preparation. Previous investigations have indicated that initial oxidation rates of metals very much depend on how the surface was prepared, and the presence or absence of trace impurities. Filing, like machining, appears to provide a better reproducible surface than abrading or pickling, as Volta potential measurements show.<sup>3</sup> But constancy of true surface area by this method is difficult to control; the variations are important, and probably account for some of the present scatter.

It can be concluded that within the experimental variations of the present measurements, electrostatic fields up to 15,500 volts/cm have no effect on the oxidation of copper in air.

To summarize, data on oxidation of copper in air at 150°C show that, within the experimental error, field strengths up to 15,500 volts/cm have no effect on the reaction rate.

Support of this investigation by the Office of Naval Research on Contract No. N5-ori-78 NR 036-007 is gratefully acknowledged.

H. H. UHLIG and A. E. BRENNER

Department of Metallurgy  
Massachusetts Institute of Technology  
Cambridge, Massachusetts

#### References

1. E. K. Rideal, "Surface Chemistry," Cambridge University Press (1930), p. 246.
2. W. Campbell and U. Thomas, Trans. Electrochem. Soc. **76**, 303 (1939).
3. W. Ende, Physik. Z. **30**, 477 (1929).  
H. H. Uhlig, J. Appl. Phys. **22**, 1399 (1951).

\* Received May 14, 1954.

#### A Dislocation Model for the Origin of Fracture Cracks in Metal Crystals\*

It is fairly well established that fracture cracks in metals are initiated by plastic deformation. It is possible that cracks originate in highly stressed metal near the ends of slips that have run up against grain boundaries or other obstacles to slip. In support of this idea, it is known that the stress concentration near the perimeter of a slipped region can be very large, perhaps large enough to exceed the cohesive strength of perfect crystalline material.

There is another possible mechanism whereby plastic deformation could lead to crack formation. Consider the configuration of atoms after slip on a slip plane that is pierced by a screw dislocation. Figure 1a shows the crystal before slip, with a screw dislocation passing through the plane upon which slip is to occur. Figure 1b shows the configuration after slip has occurred by the motion of edge dislocations with cross slip as a result.

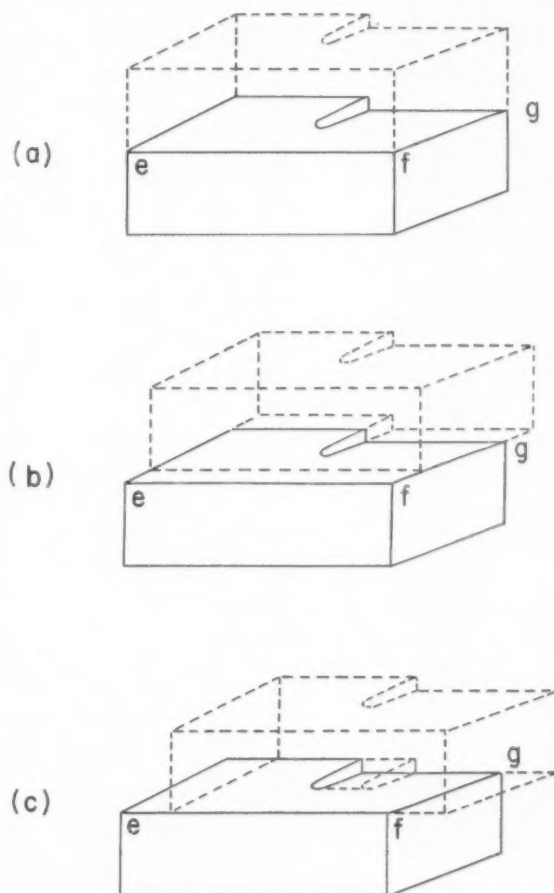


FIG. 1. A possible mechanism of crack production. (1a) A crystal containing a screw dislocation extending from top to bottom, cutting the slip planes. (1b) Slip produced by motion of an edge dislocation lying parallel to  $ef$ , with Burgers vector parallel to  $fg$ . Cross-slip can result as sketched. (1c) Slip produced by motion of a screw dislocation lying parallel to  $ef$ , with Burgers vector parallel to  $ef$ . A crack can be formed as sketched.

Figure 1c shows the configuration after slip has occurred by the motion of screw dislocations, with the resultant formation of a crack.

The crack sketched in Figure 1c may close, forming two edge dislocations, unless a normal stress of sufficient magnitude is present across it. Certainly it cannot grow in the absence of plastic deformation unless Griffith's criterion for crack propagation is satisfied. According to this criterion, a normal stress

$$\sigma \approx (E\gamma/c)^{1/2}$$

is required where  $E$  is the elastic modulus of the crystal,  $\gamma$  its surface energy, and  $c$  the crack width. Representative values of these quantities are  $E \approx 10^{12}$  dynes/cm<sup>2</sup>,  $\gamma \approx 10^8$  ergs/cm<sup>2</sup>,  $c \approx 10^{-6}$  cm for a slip of several hundred atom distances, giving

$$\sigma \approx 10^{10} \text{ dynes/cm}^2$$

or about one per cent of the elastic modulus. This value is of the same order of magnitude as the observed fracture stresses of single crystals.

The sequence of events sketched in Fig. 1 points out the importance of the normal stress across the slip plane, as well as of the slip process itself. If a hydrostatic pressure is superposed upon the tensile stress required to deform a tensile specimen, then a crack produced by screw dislocations crossing each other will tend to close up, increasing the ductility, as found experimentally by Bridgman. Conversely, superposed hydrostatic tension will tend to promote brittleness.

J. C. FISHER

General Electric Laboratory  
Schenectady, New York

\* Received June 1, 1954.

### Growth of Potassium Halide Crystals from Aqueous Solution\*

A preliminary study of the growth of potassium bromide and potassium iodide crystals from aqueous solution has shown that under the proper conditions the solid crystals can grow as thin rods, platelets, or parallelepipeds. This morphology is surprising at first since both of these salts have a cubic space lattice. However, the growth behavior may be readily explained in terms of crystal growth mechanisms which have been recently suggested.<sup>1,2</sup>

Crystals in the form of rods, thin platelets and cubes are grown concurrently in the same aqueous solution by the following method. Enough chemically pure salt is added to singly-distilled water in a test tube to saturate the solution at about 75°C. The solution is then

rapidly cooled, with or without previous superheating, to about 35°C at which temperature rods, platelets, and cubes can be easily seen with the naked eye.

It is estimated that the rods, when first visible, are about 10 microns in diameter and up to 1 cm in length. At this size they appear to be quite elastic and flexible as they swirl about in the turbulent solution. Fifteen or twenty seconds after the rods are first seen they appear to have grown in thickness, reaching a maximum diameter of about 1000 microns in about ten minutes. During this time their length increases only slightly. After thickening, the rods are weak and plastic while in solution or after they have been removed and dried in air.

The platelets appear to be rectangular and many have uniform pastel colors similar to those reported for cadmium iodide platelets growing in aqueous solution. Platelets showing characteristic interference colors are probably less than about 15,000 Å in thickness. A few of the thin colored platelets reach a maximum area of about 4 mm<sup>2</sup> before they thicken and lose their color. When they are thin, the platelets seem to be quite flexible. It has been established that the edges of a platelet and the face-normal are parallel with  $\langle 100 \rangle$  directions of the crystal structure. This has been done by means of transmission Laue photographs, made with a flat crystal which had thickened sufficiently to allow it to be handled without distortion.

Since the faces of crystals of all habits are probably parallel with  $\{100\}$ , the possibility of differential adsorption or differing nature of faces is excluded as a means of rationalizing the variation of growth rate.

It has been proposed<sup>1</sup> that a crystal nucleus should grow at constant cross section as a rod if a growth source resembling a screw dislocation is emergent on a single face. The proposal was made specifically for mercury whiskers growing on glass from the vapor. However, the assumptions were sufficiently general to include any crystalline substance growing from vapor or from solution.

It is recognized<sup>3</sup> that nucleation of crystals occurs most readily on impurity particles. We have recently found,<sup>4</sup> for example, that the growth behavior of cadmium iodide crystals from a solution which is free of colloidal particles is quite different from the growth in the presence of impurity particles. To rationalize the growth behavior of potassium bromide and iodide, it is only necessary to postulate that a salt crystallite, growing around a nucleating particle, generates a closed-loop growth step in a single face (to form a rod), a pair of closed-loop steps in a pair of mutually perpendicular faces (to form a platelet), or a spiral step emerging in one face or a pair of parallel faces. This behavior should be general for cubic materials.

Two spirals of opposite hand, emergent on a single  $\{100\}$  face, would give rise to a rod growing at constant

cross section. As longitudinal growth proceeded at a single end, the solution through which the growth occurred would be depleted of solute. The solute concentration in the depleted volume would then increase by diffusion from the surrounding solution. The concentration at the original impurity particle would increase first since the depletion occurred there first. When the concentration reached the supersaturation necessary to cause the two-dimensional nucleation on a {100} face, the rod would begin to thicken. Similarly, a spiral growth source emergent in a pair of parallel faces would give rise to a rod which would grow longitudinally by addition at both ends and would begin to thicken at its middle.

The pair of closed-loop growth sources in mutually perpendicular faces would cause the crystals to grow as thin plates. The same diffusion-controlled mechanism described for rods in the preceding paragraph would cause thickening of platelets by two-dimensional nucleation. Thickening could also be brought about by the generation of a single or double spiral growth step on a flat face. This could occur by the growth of the plate around a second impurity particle or by the intersection of two crystals.<sup>2</sup> It is possible that screw dislocations might be generated in three mutually perpendicular faces by growth around the nucleating particle. However, this would be a rare chance. Furthermore, spiral growth sources are unnecessary to grow cubes because, for these salts, two-dimensional nucleation on a perfect crystal surface requires only slight supersaturation.<sup>5</sup>

The authors are glad to acknowledge the able as-

sistance of W. G. Martin who performed most of the experimental operations discussed in this note.

J. B. NEWKIRK AND  
G. W. SEARS

Metallurgy Research Department  
General Electric Research Laboratory  
Schenectady, New York

#### References

1. G. W. Sears, *Acta Met.* **1**, 457 (1953).
2. J. C. Fisher, R. L. Fullman, and G. W. Sears, *Acta Met.* **2**, 344 (1954).
3. D. Turnbull and B. Vonnegut, *Ind. and Eng. Chem.* **44**, 1292 (1952).
4. J. B. Newkirk, "Effect of Strain on the Kinetics of Nucleation." To be published.

\* Received June 14, 1954.

#### Errata

#### The Effect of Relative Crystal and Boundary Orientations on Grain Boundary Diffusion Rates

*Acta Metallurgica* **2**, 419 (1954)

D. Turnbull and R. E. Hoffman

On p. 421, first column, fifth line down from equation (5), for " $D_L t \cong 10^{-4}$  cm": read " $(D_L t)^{1/2} \cong 10^{-4}$  cm." On p. 421, second column, second line from top, for " $D_L t = 10^{-4}$  cm": read " $(D_L t)^{1/2} = 10^{-4}$  cm."

On p. 422, caption of Fig. 4 should read: "Some typical experimental penetration curves. Open circles,  $\theta = 13^\circ$ , diffused 15 days at  $450^\circ\text{C}$ ; filled circles,  $\theta = 16^\circ$ , diffused 10 days at  $474^\circ\text{C}$ ."



## SOME CURRENT PAPERS IN OTHER JOURNALS

### *Acta Crystallographica*, Vol. 7

Part 11, November, 1954 (Partial Contents).

A theoretical possibility of correcting the collimation error in small angle X-ray scattering. Katarina Kranjc.

An X-ray diffracting method for the study of substructure of crystals. J. Intrater and S. Weissmann.

An X-ray study of the substructure of fine-grained aluminum. S. Weissmann and D. Evans.

X-ray diffraction by close-packed crystals with "growth" and "deformation or transformation stacking faults" assuming an "n-layer influence." R. Gevers.

Some calculations of atomic form factors. J. A. Hoerni and J. A. Ibers.

On the visual estimation of X-ray reflexion intensities from upper-level Weissenberg photographs. D. C. Phillips.

The status of the  $\beta$ -uranium structure. C. W. Tucker, Jr.

A method of determining the relative positions of molecules using Fourier-transform principles. C. A. Taylor.

Location of atomic centres in an electron-density synthesis. H. D. Megaw.

Aging of crushed silicon and germanium crystals. S. B. Brody.

A dynamical theory of the simultaneous reflexion by two lattice planes. III. Experimental verification. K. Kambe.

Simplified formula for calculating interplanar spacings in the rhombohedral system. W. R. McMillan.

### *Archiv für das Eisenhüttenwesen*

Heft 9-10 (September/Oktober 1954).

Modellversuche zum Schwelverhüttungs-Verfahren. H. Maetz und H.-J. Engell.

Die Bestimmung von metallischem Eisen in Schlacken und Erzen. K. Abresch und R. Dawirs.

Die Schnellbestimmung kleiner Mengen Kohlenstoff im Stahl nach dem Baryt-Schüttelverfahren. T. Heczko.

Ionenaustauscher in der analytischen Chemie. H. Specker.

### *Journal of the Chemical Society*

September, 1954 (Partial Contents).

The anodic oxidation of metals at very low current density.

Part IV. Palladium. S. E. S. El Wakkad and A. M. Shams El Din.

The anodic oxidation of metals at very low current density.

Part V. Gold. S. E. S. El Wakkad and A. M. Shams El Din.

The anodic oxidation of metals at very low current density.

Part VI. Tin. S. E. S. El Wakkad, A. M. Shams El Din, and (Miss) J. A. El Sayed.

The activation energy of electrical conductivity in fused electrolytes. R. L. Martin.

October, 1954 (Partial Contents).

The oxides of uranium. Part IV. The system  $\text{UO}_2\text{-ThO}_2\text{-O}$ . J. S. Anderson, D. N. Edgington, L. E. J. Roberts, and (in part) E. Wait.

The oxides of uranium. Part V. The chemisorption of oxygen on  $\text{UO}_2$  and on  $\text{UO}_2\text{-ThO}_2$  solid solutions. L. E. J. Roberts.

The oxidation of copper and zinc. E. R. S. Winter.

Magnetochemistry of the heaviest elements. Part VIII. Metallic plutonium. J. K. Dawson.

Tertiary alkoxides of thorium. D. C. Bradley, M. A. Saad, and W. Wardlaw.

November, 1954 (Partial Contents).

The thorium-tellurium system. R. W. M. D'Eeye and P. G. Sellman.

Adsorption from binary solutions of completely miscible liquids. Part III. Surface activity coefficients of components adsorbed from perfect solutions. G. A. H. Elton.

The hydrated tetrafluorides of uranium and plutonium. J. K. Dawson, R. W. M. D'Eeye, and A. E. Truswell.

The form of catalyst poisoning curves. E. B. Maxted and G. T. Ball.

Aluminium phosphates: Phase-diagram and ion-exchange studies of the system aluminium oxide-phosphoric oxide-water at  $25^\circ$ . R. F. Jameson and J. E. Salmon.

The oxidation of americium to the hexavalent state. M. Ward and G. A. Welch.

Thermochemistry of Organo-boron compounds. Part V. Ethoxy-chloroboranes. H. A. Skinner and N. B. Smith.

### *Journal of the Institute of Metals*, Vol. 83

Part 4, December, 1954.

Corrosion-fatigue properties of an aluminium-magnesium-silicon alloy in the unprotected, anodized, and painted conditions. N. P. Inglis and E. C. Larke.

The electrodeposition and refining of high-grade chromium. H. T. Greenaway.

The fabrication of chromium and some dilute chromium-base alloys. F. Henderson, S. T. Quaass, and H. L. Wain.

A study of the room-temperature ductility of chromium. H. L. Wain, F. Henderson, and S. T. M. Johnstone.

The surface tension of sodium. J. W. Taylor.

### *Journal of Metals*, Vol. 6

October, 1954 (Partial Contents).

Phase transformations in titanium-rich alloys of iron and titanium.

D. H. Polonis and J. G. Parr.

Quantitative substructure and tensile-property investigations of nickel alloys. B. Ancker and E. R. Parker.

Influence of boron on hardenability of steel. J. C. Fisher.

November, 1954, Section 1 (Partial Contents).

Applicability of powder metallurgy to problems of high temperature materials, with discussion. G. M. Ault and G. C. Deutsch.

Effect of subcritical rate on the brittle-fracture characteristics of structural steel. L. Mair.

November, 1954, Section 2 (Partial Contents).

Strain hardening of latent slip systems in zinc crystals. E. H. Edwards and J. Washburn.

Effect of carbon content on the  $500^\circ\text{F}$  embrittlement of tempered martensite. P. Payson.

An examination of the decrease of surface-activity method of measuring self-diffusion coefficients in wustite and cobaltous oxide. R. E. Carter and F. D. Richardson.

A colorimetric investigation of heats of formation and precipitation in some Cu-Sn alloys. J. B. Cohen, J. S. L. Leach, and M. B. Bever.

Effect of nitrogen on sigma formation in Cr-Ni steels at  $1200^\circ\text{F}$  ( $650^\circ\text{C}$ ). G. F. Tisnai, J. K. Stanley, and C. H. Samans.

Titanium-manganese phases. H. Margolin and E. Ence.

Temper embrittlement of 5140 steel. S. H. Bush and C. A. Siebert.

Stabilization of the bainite reaction. R. F. Hehemann and A. R. Troiano.

Data for one of the martensitic transformations in an 11 Pct Mo-Ti alloy. S. Weinig and E. S. Machlin.

Some observations on the tertiary stage of creep of high purity aluminum. G. R. Wilms.

### *Revue de Metallurgie* 51<sup>e</sup> Année

Numero 9, Septembre, 1954.

Recristallisation de l'uranium après passage des points de transformation. M. Pruna, P. Lehr et G. Chaudron.

Sur l'orientation des cristaux dans l'uranium laminaire. A. Wino-gradzki.

Etude du recuit de l'uranium laminé. G. Cabane et J. Petit.

Etude métallographique de la transformation  $\beta \rightarrow \alpha$  de l'uranium dans les alliages stables uranium-chrome. B. W. Mott et H. R. Haines.

Etude métallographique des inclusions d'hydruure d'uranium dans l'uranium métallique. H. Mogard et G. Cabane.

Remarques sur la solidification et l'effervescence de lingots d'acier Thomas pesant 4, 6 tonnes. J. Duflot et A. Richard.

Développement actuel des travaux sur la structure des silicates fondus. J. O'M. Bockris et J. D. Mackenzie.

Numero 10, Octobre 1954.

Quelques aspects de la métallurgie des poudres. R. Girschig.

Le module d'Young de l'aluminium et de ses alliages en fonction de la température. E. G. Stanford.

Sur la boururation, la siliciuration et la boro-siliciuration des aciers, par électrolyse. P. Blum et J. L. Andrieux.

La plasticité de métaux du système hexagonal et ses variations avec la température. S. F. Pugh.

Deux nouveaux résultats relatifs à la composition des bains de polissage électrolytique. P. Brouillet et I. Epelboin.

Le semi, microdosage du carbone dans les aciers. P. Flament et J. Marot.

Contribution à l'étude de la décarburation au four Martin. P. Vallet.

Contribution à l'étude de l'extraction électrolytique des carbures d'un acier à coupe rapide. J. Papier.

VOL.  
3  
1955

# THE ROLE OF CRYSTAL STRUCTURE ON IRRADIATION EFFECTS IN METALS\*

D. WRUCK† and C. WERT‡

The resistivity of Fe has been found to increase more than that of Co and Ni when these metals are bombarded at  $-150^{\circ}\text{C}$  by 12 Mev deuterons. The same effect was observed for Fe and Ni by neutron irradiation at room temperature. This result may be interpreted as indicating that Fe is affected to a greater extent than either Co or Ni by heavy particle bombardment, though other interpretations may also be made. Annealing of the cyclotron-irradiated samples showed that a smaller fraction of the effect produced in Fe remained after a room temperature anneal than remained in Co and Ni.

## RÔLE DE LA STRUCTURE CRISTALLINE SUR LES EFFETS DE L'IRRADIATION DANS LES MÉTAUX

La résistivité du fer est plus nettement augmentée que celle du cobalt et du nickel par bombardement à  $-150^{\circ}$  par des deutrons de 12 Mev et le même effet est observé pour le fer et le nickel par bombardement de neutrons à la température ordinaire. Ces résultats peuvent être expliqués par une action différente du bombardement sur le fer et sur le cobalt ou le nickel, quoique d'autres explications soient aussi possibles. Pour les échantillons irradiés au cyclotron, le recuit provoque une restauration moins forte à la température ordinaire dans le cas du fer que dans ceux du cobalt et du nickel.

## DER EINFLUSS DER KRISTALLSTRUKTUR AUF DIE VORGÄNGE BEI DER BESTRAHLUNG VON METALLEN

Durch Beschussung mit 12 Mev Deuteronen bei  $-150^{\circ}\text{C}$  nimmt der Widerstand von Fe stärker zu als der von Co und Ni. Die gleiche Beobachtung wurde für Fe und Ni bei Bestrahlung mit Neutronen bei Raumtemperatur gemacht. Obwohl auch andere Deutungen möglich sind, kann das vorliegende Ergebnis so ausgelegt werden, dass das Fe durch Beschussung mit schweren Teilchen mehr zu beeinflussen ist als Co und Ni. Ein Anlassen der im Zyclotron bestrahlten Proben bei Raumtemperatur zeigte, dass ein kleinerer Teil der im Fe hervorgerufenen Wirkung bei Raumtemperatur erhalten bleibt als bei Co und Ni.

## INTRODUCTION

One of the facts which seems clear from experimental studies of irradiation of metals is that different metals are affected by different amounts. It is of interest to determine what properties are responsible for this difference. Two properties which have previously been investigated in this regard are the effect of atomic number,  $Z$ , and the effect of the binding energy of the lattice. The first of these seems to be well established by measurements on Cu, Ag, and Au, metals which are quite similar except for atomic number. Marx, Cooper and Henderson observed for these metals, upon bombardment at about  $-130^{\circ}\text{C}$ , a change in resistivity which was larger the higher the atomic number.<sup>1</sup> This effect has also been observed at  $12^{\circ}\text{K}$  for these metals by Cooper, Koehler, and Marx.<sup>2</sup> If the damage (say, in terms of interstitial-vacancy, I-V, pairs) is approximately equal for equal resistivity changes in these metals, as seems reasonable, then these experiments may be readily interpreted as showing an increasing effect for increasing  $Z$ . The effect of binding energy is not so clear-cut with regard to degree of damage produced during bombardment. Although larger resistivity changes have been observed in Ni and Ta than in Cu, Ag and Au,<sup>1</sup> because of differences in other properties (electronic structure of the metals, for example) one cannot express these resistivity changes in terms of actual differences in amount of damage. An effect was observed upon annealing which was attributed to differences in binding energy.

Another property of a metal which may play a role in determining the degree of damage is the crystal structure. This property might well be a factor both in affecting the number of displacements occurring during bombardment and the amount of annealing taking place at a given temperature either during or after bombardment. Clearly, to make a valid comparison between metals of different structure type, one must choose metals which differ little from each other in all properties except this. Three metals which seem to satisfy these requirements quite well and at the same time allow comparison between the most common lattice types (for metals) are Fe, Co and Ni, respectively, b.c.c., h.c.p. (almost ideal) and f.c.c. Their atomic numbers are as close as is possible and their binding energies are about the same. They are all ferromagnetic (the importance of this feature is, of course, not known). Their electrical resistivities are not greatly different. This is of importance since this property was used in the present investigation to record the status of the damage. Some properties of these metals are listed in detail in Table I.

This paper reports on a series of measurements made on these three metals (called here the "primary group"). The results may be divided into two categories: (1) differences in damage produced by bombardment and (2) differences in annealing after bombardment. Two separate irradiations were made: (a) cyclotron irradiation with deuterons at low temperatures ( $-160^{\circ}\text{C}$  to  $-100^{\circ}\text{C}$ ) and (b) neutron irradiation at ambient pile temperature.

Ti and V were investigated under cyclotron bombardment in an effort to provide substantiating information

\* Received May 20, 1954.

† Now at Wright Field, Dayton, Ohio.

‡ University of Illinois, Urbana, Illinois.



TABLE I. Some physical properties of the metals bombarded.

Metal	Crystal type	Distance of closest approach	Z	at. wt.	$\rho_{20^\circ\text{C}}$	$T_m$	Heats of sublimation at R.T.
Iron	b.c.c.	2.48 Å	26	56	9.7 $\mu\Omega$ cm	1540°C	94 Kcal/mol
Cobalt	b.c.c.	2.50	27	59	6.2	1495	85
Nickel	f.c.c.	2.49	28	59	6.8	1455	85
Titanium	b.c.c.	2.95	22	48	~80	1820	100
Vanadium	b.c.c.	2.63	23	51	~26	1735	85

on another f.c.c. and another b.c.c. metal. Data obtained for these metals, while apparently correct, cannot at this time be used either to substantiate or refute the claims made for the primary group. This is so because one does not really know on what basis to compare them since their initial resistivities are greatly different from the others.

## EXPERIMENTAL PROCEDURE

### A. Cyclotron Bombardment

Foils of the metals were bombarded at low temperatures in the University of Illinois cyclotron. The experimental procedure was much the same as that used earlier in this laboratory.<sup>1</sup> The specimens were polycrystalline foils about 4 cm long, .2 cm wide and about .008 cm thick.\* These foils were mounted for bombardment on an aluminum block connected to a liquid-nitrogen container. The geometrical arrangement of the apparatus is shown in Fig. 1. The deuteron beam entered the apparatus through a defining slit and passed through

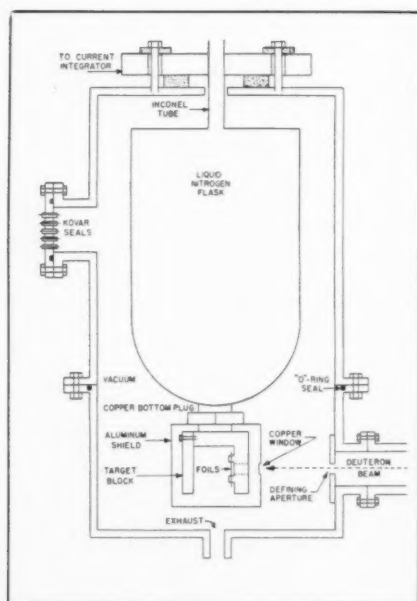


FIG. 1. Cryostat and mounting block assembly.

\* The purity of the foils was about as follows: Fe~99.95% pure, .04% O<sub>2</sub>; not much metallic impurity. Co~99+% pure; major impurities iron and nickel. Ni~99.5% pure; impurities not known. V known to contain .14% C, .12% O<sub>2</sub>, .11% N<sub>2</sub>. Ti commercial purity.

a .001 in. copper sheet before striking the foils. This copper sheet served to stop any heavy atoms that were carried along by the beam. That part of the beam not stopped in the foils was stopped by a thick block. An aluminum shield around the entire block served to collect any secondary electrons which might be produced. The flux of deuterons falling upon the samples was determined by measuring the charge collected by the foils and target block.

Since low temperatures were necessary, the entire assembly was designed to provide good heat transfer from the foils to the liquid nitrogen. The difficulty of making good thermal contact was increased by the requirement that electrical resistance measurements be made on them separately. This necessitated electrical insulation of the foils from the block at one end, which was accomplished by the use of thin mica insulating sheets between one end of the foils and the block. The foil temperatures obtained were not altogether satisfactory for all runs; it was found to be difficult to make

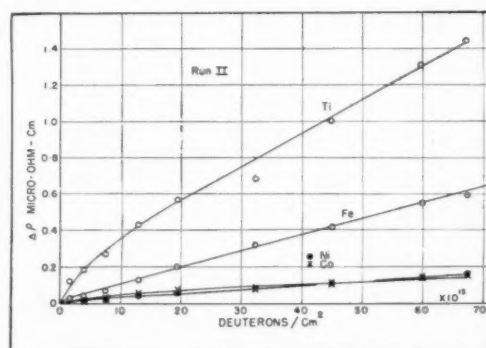


FIG. 2. Resistivity change of foils in Run II.

the thermal contact equally good for all foils. In two of the runs, one or more of the foils became as warm as -120°C with the beam on. In the final run, however, all the metals in the primary group were below -145°C. Even with higher foil temperatures on some runs, all the data show the same effect as far as the effect of crystal structure is concerned.

The resistivities of the foils were determined from measurement of the IR drop produced in them by a known current. The gauge length (about 1.2 cm) was fixed by two .010-in. Cu wires spot-welded to the foils near the end of the irradiated section. The temperature of each foil was measured by means of a Cu-constantan thermocouple spot-welded to the back of the foil in the center of the irradiated section.

### B. Pile Irradiation

Twelve specimens of iron and 12 specimens of nickel were irradiated in the Brookhaven reactor.\* The speci-

\* Cobalt was not used in this measurement because the high radioactivity resulting from neutron irradiation would have made handling of the samples difficult.

mens were coarse-grain polycrystalline wires .030 in. in diameter and about 6 in. long. The large grain-size was produced by first straining fine-grain wires about 1 per cent and then annealing them for seven days in vacuum at 850°C. The grain-size of the iron wires was about 1/4 in. and that of the nickel wires about 1/32 in. Since both the iron and nickel wires were decarburized before this treatment, they were very soft.

The resistivity of the wires at 77°K was determined over a 2-in. length of the specimens again by measuring the IR drop produced when a known current was passed through them. For measurement, the wires were mounted in a jig which was immersed directly into a bath of nitrogen. Resistivity determinations were made both before and after irradiation to determine the effect of bombardment. Further measurements were made after the specimens had been annealed at successively higher temperatures up to 500°C. Irradiation of the samples was carried out at 50°C for two months. The integrated neutron flux was  $1.25 \times 10^{19}$  neutrons/cm<sup>2</sup>.\*

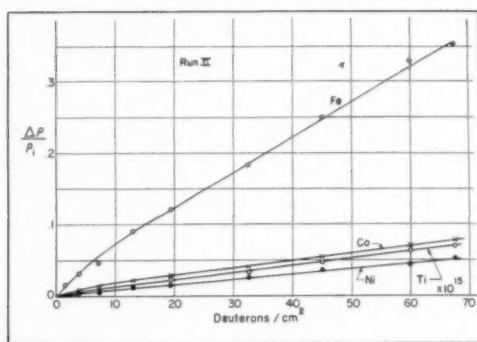


FIG. 3. Fractional change in resistivity of foils in Run II.

## RESULTS

### A. Cyclotron Irradiation

#### Bombardment

A preliminary measurement of the increase in resistivity accompanying bombardment at low temperature of Fe, Ni and Co served to demonstrate that significant differences did exist. In this determination, Run I, the

\* This pile bombardment actually had a two-fold purpose: (1) One of these was to compare the resistivity increase in iron and nickel attendant upon a given neutron irradiation. (2) The second was to see if any anelastic effects could be observed above room temperature in irradiated iron or nickel. Specifically, we thought there was a possibility of observing a relaxation peak of interstitial iron in the b.c.c. iron lattice similar to that observed for other interstitial atoms in b.c.c. lattices (for example, interstitial C and N in b.c.c. iron). Observations on nickel were expected to show no effect of this kind since this anelastic process does not occur for interstitial atoms in f.c.c. lattices. No significant changes after irradiation were observed in the anelastic behavior of either iron or nickel in the region from 25°C to 600°C. One is thus lead to the conclusion that, if interstitials are produced by bombardment, (1) they are either too few in number to change the anelastic behavior significantly; or (2) they move in iron at a temperature lower than room temperature.

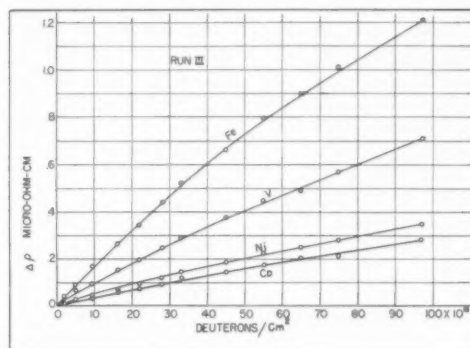


FIG. 4. Resistivity change of foils in Run III.

foil temperatures were not maintained as low as was believed desirable ( $-120^{\circ}\text{C}$  during bombardment), so further measurements were carried out with lower beam currents and better foil-mounting techniques. The second measurement (Run II) was more successful, though the Ni foil again was rather warm ( $-120^{\circ}\text{C}$ ) because of an accident in foil mounting not discovered until the end of the run. The final run (Run III) was quite successful from this point of view in that all foils were rather cold ( $<-145^{\circ}\text{C}$ ). Quite possibly the limiting factor in Runs II and III (except for Ni in Run II) was the rate of heat transfer down the specimens to the cooling block.

The changes in resistivity which were measured in Run II for the four metals Fe, Co, Ni and Ti are plotted in Fig. 2 as a function of integrated deuteron flux. Ni and Co show rather small changes in resistivity compared to those observed for Fe and Ti. The data for Ti may be somewhat misleading when comparisons are made from this plot, for the initial resistivity of Ti was at least six times that of any of the other foils. If these data are plotted as the fractional change in resistivity, as in Fig. 3, then the relative positions of Fe, Co and Ni are unchanged, but Ti also falls to a rather low level.

Similar data, Run III, for the primary group together with data for V are shown in Figs. 4 and 5. The behavior of Fe, Co and Ni is relatively the same as in Figs. 2 and 3. V behaved somewhat as Ti did; it had a

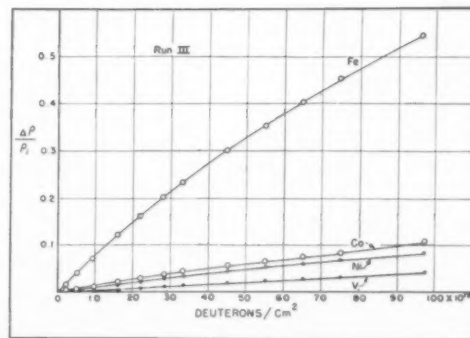


FIG. 5. Fractional change in resistivity of foils in Run III.

TABLE II. Resistivity data for four bombardments.

Metal	Temperature of foils during bombardment	Initial resistivity at $-180^{\circ}\text{C}$ $\rho_i$	$(\Delta\rho)_f$	$(\Delta\rho)_f/\rho_i$
Run I (Total flux $167 \times 10^{15}$ deut./cm $^2$ )				
Fe	$-120^{\circ}\text{C}$	$2.635 \mu\Omega \text{ cm}$	$1.193 \mu\Omega \text{ cm}$	.453
Co	$-120^{\circ}\text{C}$	2.803	.211	.075
Ni	$-120^{\circ}\text{C}$	3.493	.430	.123
Run II (Total flux $67 \times 10^{15}$ deut./cm $^2$ )				
Fe	$-150^{\circ}\text{C}$	1.647	.583	.354
Co	$-145^{\circ}\text{C}$	2.167	.169	.078
Ni	$-120^{\circ}\text{C}$	3.232	.177	.055
Ti	$-100^{\circ}\text{C}$	20.96	1.45	.069
Run III (Total flux $97 \times 10^{15}$ deut./cm $^2$ )				
Fe	$-160^{\circ}\text{C}$	2.25	1.218	.541
Co	$-150^{\circ}\text{C}$	2.67	.283	.106
Ni	$-145^{\circ}\text{C}$	4.16	.351	.084
V $_1$	$-135^{\circ}\text{C}$	17.96	.709	.039
V $_2$	$-135^{\circ}\text{C}$	16.49	.647	.039
Data of Marx <i>et al</i> <sup>1</sup> (Total flux $114 \times 10^{15}$ deut./cm $^2$ )				
Ni	$-133^{\circ}\text{C}$	3.123	.381	.122

rather high absolute change in resistivity, but a rather low fractional change because of its high resistivity. (Though Figs. 4 and 5 show only one curve for V, two foils were actually mounted and run. They behaved so similarly, however, that data for only one are plotted.)

A summary of the data pertinent for comparison purposes is given in Table II, along with a piece of data for Ni taken from the paper of Marx, Cooper and Henderson. In this table are given (1) the values of initial resistivity of the foils at  $-180^{\circ}\text{C}$ . (This was the equilibrium value of temperature obtained during measurement with about 1 ampere of current flowing through them.); (2) the highest temperatures reached by the foils during bombardment, and (3) the resistance change recorded at the end of each run expressed both in absolute value and fractional change.

With regard to Fe, Co and Ni, the chief conclusion that can be drawn from these data is that Fe undergoes a greater resistivity change upon bombardment than either Co or Ni, which behave in about the same way. The change is greater in Fe by a factor of from 3 to about 6, depending upon whether the comparison is

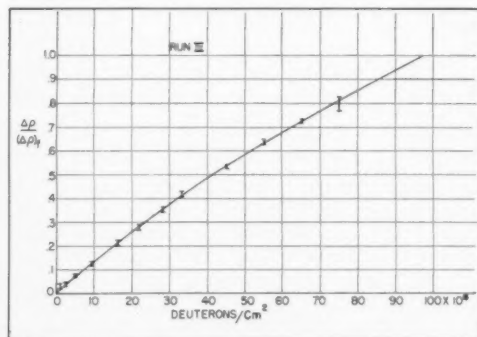


FIG. 6. Resistivity changes in Run III normalized at  $97 \times 10^{15}$  deut./cm $^2$ . All experimental points for the metals fall randomly within the ranges indicated.

made through changes in  $\rho$  or in  $\Delta\rho/\rho_i$ . Ti and V behave more like Fe or like Co and Ni, depending on the type of comparison.

The shape of the bombardment curves as a function of integrated deuteron flux is nearly the same for all of these metals. In Fig. 6 is plotted the fraction of total resistivity change *versus* integrated flux for Run III. The final point for each metal is normalized to unity. This composite curve shows that whatever is the phenomenon which causes the bombardment curve to bend over, it is constant (or changes similarly) in these four metals during the course of the bombardment.

### Annealing

At the conclusion of each bombardment, some annealing experiments were carried out. In Run I, pulse anneals were made by using the Joule heat of an ac current to maintain the foils at a given temperature for an hour or more. An accidental loss of vacuum prevented the taking of annealing data for Run II except for a room temperature anneal. A "saw-tooth" type

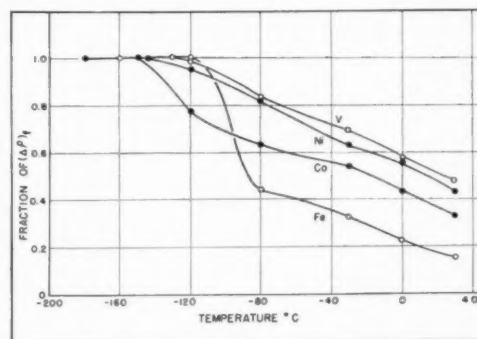


FIG. 7. Anneal to room temperature of foils in Run III.

of anneal was carried out after Run III in which the foils were allowed to warm up to a given temperature as the entire apparatus warmed up after all the liquid nitrogen evaporated. The results of the "pulse" anneal and "saw-tooth" anneal were quite similar.

The results of the anneal for Run III are presented in Fig. 7. The ordinates refer to resistivity measurements made (at  $-180^{\circ}\text{C}$ ) after the foils had warmed up to the temperature indicated. For convenience in comparing the metals, the curves are normalized. The rate of warm-up was about  $20^{\circ}\text{C/hr}$  except near room temperature, where it was much slower. In the region from  $-150^{\circ}\text{C}$  to room temperature, Fe is seen to anneal somewhat more (fractionally) than Co and Ni. The rather sudden drops at roughly  $-100^{\circ}\text{C}$  for Co and Fe were observed in the annealing measurements of both Runs I and III (also both V foils showed closely the same drop in Run III). What process this corresponds to is unknown. A summary of data obtained after room temperature annealing is given in Table III. Here are given the final resistivity change after bombardment,

$(\Delta\rho)_f$ , the resistivity change still remaining (at  $-180^\circ\text{C}$ ) after room temperature anneal,  $(\Delta\rho)_A$  and the fraction remaining after the room temperature anneal. The amount of annealing seems to increase from Ni to Co to Fe.

Some anneals above room temperature to  $500^\circ\text{C}$  were also attempted. They were not highly successful because of a large scatter of points. Within the spread of the measurements, there seemed to be no sharp temperature range in which the remaining resistivity disappeared.

### B. Neutron Irradiation

Resistivity changes in Fe and Ni following neutron irradiation at  $50^\circ\text{C}$  showed the same trend as the cyclotron measurements. Table IV shows data for six of the specimens irradiated. The absolute change in resistivity was about four to five times greater for Fe than for Ni, the fractional change, more than double this. Annealing

TABLE III. Effect of annealing at room temperature on bombarded foils.

Measurement	Metal	$(\Delta\rho)_f$ $\mu\Omega\text{ cm}$	$(\Delta\rho)_A$ $\mu\Omega\text{ cm}$	$1 - \frac{(\Delta\rho)_f - (\Delta\rho)_A}{(\Delta\rho)_f}$
Run I, 72 hrs at RT	Iron	1.193	.268	.22
	Cobalt	.211	(.026)?	(.01)?
	Nickel	.430	.145	.34
Run II, 6 hrs at RT	Iron	.583	.125	.21
	Cobalt	.169	.055	.33
	Nickel	.177	.074	.42
	Titanium	1.45	1.05	.72
Run III, 24 hrs at RT	Iron	1.218	.179	.15
	Cobalt	.283	.079	.28
	Nickel	.351	.151	.43
	Vanadium I	.709	.320	.45
	Vanadium II	.647	.315	.49
Marx <i>et al</i> (Ref. 1) 20 hrs at RT	Nickel	.385	.151	.39
		.96	.136	.35
		.264	.120	.31

measurements made on these wires were limited somewhat since two of the Fe wires broke in handling (the remainder were used in anelastic measurements). Again the annealing data obtained showed too much scatter to allow detailed analysis of the results.

### DISCUSSION

The cyclotron measurements show that Fe undergoes a much larger change in resistivity under low temperature deuteron bombardment than do Co and Ni. The data for room temperature irradiation of Fe and Ni also show the same effect for these two metals alone. In both instances the effect is so large compared to the differences one gets in making duplicate measurements on the same metal that there is small chance of its not being genuine. Interpretation of the observed effect seems not so clear-cut, however. One might suppose that either of these two extreme points of view might apply: (a) There are indeed more I-V pairs produced in Fe than in Ni and Co, or (b) The same number of I-V pairs is

TABLE IV. Effect on resistivity (at  $77^\circ\text{K}$ ) of neutron bombardment of iron and nickel.

Metal	$\rho_{\text{initial}}$	$\rho_{\text{final}}$	$\Delta\rho$	$\Delta\rho/\rho_{\text{initial}}$
Iron 1	.7786 $\mu\Omega\text{ cm}$	.8509 $\mu\Omega\text{ cm}$	.0723 $\mu\Omega\text{ cm}$	.093
	2	.7686	.8509	.0823
	3	.7410	.8192	.0782
Nickel 1	2.243	2.256	.013	.006
	2	2.423	2.445	.022
	3	2.248	2.267	.019

produced in the three, but they cause a larger resistivity change in Fe than in the other two.

In trying to decide between these two (or some combination of them), one sees that a number of possibilities exist, even for these three quite similar metals. Some of these possible factors are intrinsic physical properties of the metals themselves and some are various unresolved features of radiation damage itself. The factors which will be considered here are (1) purity of the materials, (2) energy required to produce an I-V pair, (3) electronic structure of the metals, and (4) differences in annealing behavior. Unfortunately, none of these factors can be completely eliminated as a possible explanation for the effect observed.

(1) The importance to radiation damage of the purity of the material being bombarded is not known, although a study has been made of resistivity changes accompanying bombardment of some alloys of Cu (of reasonably high alloy composition compared to normal purity of metals).<sup>3</sup> These results, reported for resistivity changes following neutron irradiation around room temperature, vary so much between alloys that no generalities were drawn about the effect of added elements. The work does indicate that there exists the possibility that impurities may be important in pinning down either vacancies or interstitials. However, since any attempt to interpret the present results in terms of the purity of the materials is virtually pure speculation at present, this effect will not be considered further.

(2) There are numerous ways in which crystal structure could play a role in radiation damage. One of these is through its effect on the energy necessary to produce an I-V pair. It is easy to see that this could be the decisive factor in explaining the present experiments. Assume that the energy necessary to produce an I-V pair in Fe is less than that required in Co and Ni. Then, under similar bombardment, more pairs would be produced in Fe than in the other two by a given number of incident particles because more of the collisions (both of the primary and secondary nature) would involve a transfer of energy greater than this minimum. Then the greater resistivity change measured for Fe would simply reflect this larger number of I-V pairs produced.

To see if this conclusion is reasonable, one must examine the assumption that the threshold energy in Fe is less than that in Co and Ni. The argument favoring



this point of view is the following: Fe, being b.c.c.; has eight nearest neighbors at a distance of about  $2.5 \text{ \AA}$ ; Co and Ni, h.c.p. and f.c.c., respectively, have 12 nearest neighbors also at a distance of about  $2.5 \text{ \AA}$ . The potential energy barrier over which a knocked-on atom must pass to be permanently displaced (even when projected in the most favorable direction), is then less in the b.c.c. lattice than in the close-packed lattices because at the saddle point it passes close to a fewer number of atoms in the b.c.c. lattice than in the close-packed lattices. In other words, for a knocked-on atom of a given energy, there is a larger solid angle of directions of projection which will result in permanent displacement in the b.c.c. lattice over that in either the h.c.p. or f.c.c. lattices.

(3) The electronic structure of the metals may play a decisive role in that the same number of I-V pairs in each might cause quite different resistivity changes in the three. Hence, the different resistivity changes observed may not actually reflect the production of more damage in Fe than in Co and Ni. Two sources from which this electronic effect might stem are these: (a) The interstitials produced might be ionized to different degrees. In such a case they would certainly scatter electrons differently and hence would contribute different resistivity changes per defect. (b) The conduction electron band may have a different configuration.

There is little experimental evidence to decide whether either of these effects is important. One piece of information which may be of some significance in evaluating the second is knowledge of the resistivity change occurring in these metals when impurities are added to them. Examination of published data shows that when a given metallic impurity is added to Fe and Ni,\* the resistivity change occurring in Fe is usually somewhat greater than that occurring in Ni. For some impurities, the effect is about the same, for others, more than twice as great in Fe. Let an average factor somewhere between 1 and 2 be considered valid. If a factor of, say, 2, is applied to the present results (there is no evidence to either support or refute the correctness of doing this), it still does not explain the difference of from 3 to 6 that is observed in the bombardment.

(4) Annealing during bombardment can arise from two sources, from thermally activated processes and from the incident particles. The details of annealing of close pairs seem obscure, but the rate of annealing of the widely separated defects is controlled by the rate at which one of them will diffuse through the lattice. Since this diffusion rate may depend markedly on the crystal type, it is reasonable to presume that the rate of annealing itself may be a function of crystal type. Unfortunately, for none of these metals is the heat of activation for motion of either defect known, although some heats of activation for self-diffusion in these metals are known.†

\* Not much data are available for Co.

† For Fe and Co these are, respectively, 60 and 62 Kcal/mol.

The annealing experiments reported in this paper can offer some information for evaluating the importance of annealing in the present discussion. After bombardment, not much thermally activated annealing is observed until the foil temperatures reach about  $-120^\circ\text{C}$ , above which the annealing is rather rapid. It is interesting to note that for Fe (which shows the greatest resistivity change upon bombardment) the fractional annealing is greatest (Fig. 7 and Table III). Hence, it appears that thermally activated annealing is not the cause of the difference in behavior upon bombardment, unless for Co and Ni annealing affects below  $-150^\circ\text{C}$  are much more important than for iron. The curve shown in Fig. 6 gives some evidence that this is not so.

A reasonable summary of these points is the following:

(1) The effect of purity is not yet established. (2) The effect of crystal structure through its effect on the threshold energy for production of defects could be the important factor. (3) Different electronic structure of the metals could account for a part or all of the observed difference. (4) The effect of annealing cannot yet be fully evaluated.

A satisfactory interpretation of the experimental effects noted must also take into account the data obtained for V (b.c.c.) and Ti (h.c.p.). If crystal structure is an important factor in determining the relative amount of damage in different metals, then one would expect V to behave like Fe and Ti like Co and Ni. In comparing them with Fe, Ni and Co, one does not know whether to compare  $(\Delta\rho)_f$  or  $(\Delta\rho)_f/\rho_i$ . Unfortunately, as an examination of Figs. 2, 3, 4 and 5 shows, neither comparison is consistent for both. However, because of the extremely large values of  $\rho_i$  for V and Ti, it is possible that no comparison is a valid one.\*

#### ACKNOWLEDGMENTS

Acknowledgment is made of assistance and advice from the entire Radiation Damage Group at the University of Illinois. The cyclotron bombardments were made possible by the cooperation of Professor Jentschke and his group. The neutron irradiation was carried out for the authors by Drs. Dienes and Fleeman of the Brookhaven National Laboratories.

This work was presented as a thesis by D. Wruck to the Graduate College of the University of Illinois in partial fulfillment of the requirements for the degree of Master of Science in Metallurgical Engineering in February, 1954, and was supported in part by the U. S. Atomic Energy Commission.

#### REFERENCES

1. J. Marx, H. Cooper, and J. Henderson, *Phys. Rev.* **88**, 106 (1952).
2. H. Cooper, J. S. Koehler, and J. W. Marx, *Phys. Rev.* In Press.
3. G. T. Murray and W. E. Taylor, *Acta Met.* **2**, 52 (1954).

\* It is probably not yet decided whether Ti and V are intrinsically poor conductors or whether they have not yet been made pure enough to be good conductors.

## GROWTH OF CADMIUM IODIDE CRYSTALS\*

JOHN B. NEWKIRK†

Fisher, Fullman and Sears<sup>1</sup> have recently proposed mechanisms by which a spiral or closed-loop growth source may originate in a growing crystal. The present paper presents experimental evidence relating to the subject of crystal growth, as discussed by the above authors, and outlines the technique by which the evidence was acquired.

### LA CROISSANCE DES CRISTAUX D'IODURE DE CADMIUM

Fischer, Fullman et Sears ont récemment proposé des mécanismes par lesquels un centre de croissance en spirale ou en boucle fermée peut apparaître dans un cristal en croissance. Cet article présente la preuve expérimentale concernant les mécanismes de croissance des cristaux discutés par les auteurs mentionnés ci-dessus, et décrit la technique grâce à laquelle cette preuve fut acquise.

### DAS WACHSEN VON KADMIUMJODIDKRISTALLEN

Fisher, Fullman und Sears postulierten kürzlich einen Prozess auf Grund dessen ein spiral-oder ringförmiges Wachstumszentrum in einem wachsenden Kristall entstehen könnte. In der vorliegenden Arbeit wird über experimentelle Beobachtungen zum Kristallwachstum im Sinne der obigen Autoren berichtet, und die angewandten Versuchsmethoden werden beschrieben.

### EXPERIMENTAL TECHNIQUE

Cadmium iodide was chosen as the subject for this investigation because of its tendency, demonstrated by Forty,<sup>2</sup> to form crystals having growth steps which are readily visible at low magnification. All of the photomicrographs reported here were made at a magnification of 150X by a method essentially similar to that described by Forty. However, Forty's method of crystal formation was modified so that the crystals were grown from an aqueous solution, saturated at 85°C, which had been heated to boiling in a separate 50 ml Erlenmeyer flask. After the mixture had been superheated in this way it was allowed to cool to 30°C in air or under flowing cold water. A drop of this solution at 30°C was then placed on a clean microscope slide at room temperature and was immediately covered with a thin glass disc. Many growing crystals, similar to those in Fig. 2a could then be seen in the liquid.

### "PERFECT" CRYSTAL PLATES

Generally, as in Fig. 1a, the crystals exhibit threefold symmetry about an axis normal to the thin plane of the platelet and many can be seen which have a uniform pastel color. This color is due to the interference of white light reflected from the top and bottom surfaces of the crystal and depends critically upon the crystal thickness. The uniformity of color is evidence that the thickness of each crystal in the (001) direction is constant. It is not necessary for these crystals to have an atomically perfect lattice; a uniform color could also result if the crystal contained a random distribution of imperfections. However, the (001) surface layer must be perfect, otherwise thickness growth would occur at any supersaturation.

Crystals of this type often grow edgewise without changing color. This is evidence that the crystals need not grow in thickness as their area increases. Figure 1b, made several minutes after 1a, shows the same crystals after they have grown edgewise. Two colored crystals which have come into direct contact in the process, have produced imperfections on their surfaces. The imperfections have provided steps by which the crystals could grow in thickness without the need for two-dimensional nucleation. Meanwhile, lacking a growth step, the single isolated crystal continued to grow edgewise at constant thickness. The crystals apparently cannot thicken continuously without a source of thickness growth steps.

### MEASUREMENT OF CRYSTAL THICKNESS

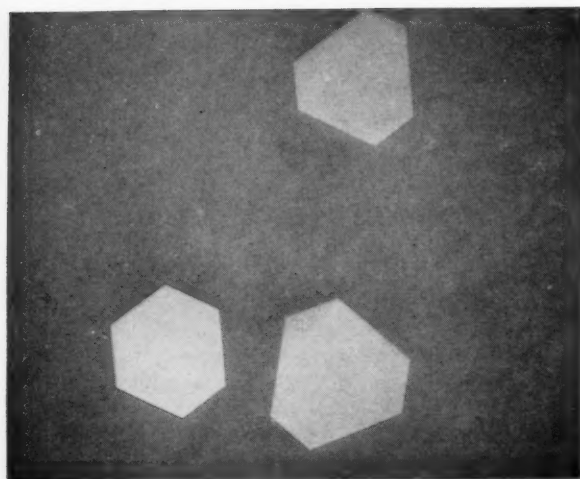
The light of the magnified image of a crystal was analyzed by means of an optical recording spectrometer. The thickness of the crystal could then be determined by the following well-known relationship:

$$h = \frac{k\lambda}{4n}$$

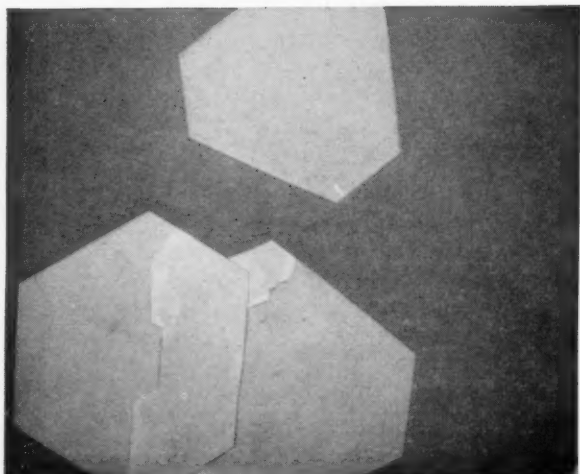
where  $h$  = thickness,  $k$  = integer,  $\lambda$  = wavelength at which a maximum or minimum intensity occurs, and  $n$  = index of refraction of platelet. Spectrometer curves for the blue and purple crystals of an overlapping pair similar to those in the middle of Fig. 2a are given in Fig. 3. Assuming  $n = 1.85$  after Forty,<sup>2</sup> the thicknesses of two overlapping crystals were found to be 5600 Å and 5500 Å, respectively. The thickness of the green overlapped portion was found to be 8600 Å or within 23 per cent of the sum of the thicknesses of the two separate crystals. Crystals thicker than about 15,000 Å were colorless. This is due to the large number of orders of interference maxima and minima which are present in the reflected light.

\* Received June 6, 1954.

† General Electric Research Laboratory, Schenectady, New York.



(a)



(b)

PLATE I. FIG. 1.—(a) Three perfect crystals grow edgewise at constant thickness in a supersaturated solution of  $\text{CdI}_2$ . (b) Having a source of growth steps, the overlapping crystals grow in thickness. The single isolated crystal, lacking a growth step, continues to grow only in the edgewise directions.

#### GENERATION OF GROWTH SPIRALS BY EDGEWISE INTERACTION OF TWO CRYSTALS\*

The sequence in Figs. 2b-d illustrates one source of growth step discussed by Fisher et al., viz., the edgewise interaction of two growing crystals whose (001) planes are slightly inclined to one another. Figure 2b was taken a few seconds after the edges of the yellow and pink crystals touched. Already a disturbance and a thickness change in the region are noticeable. The thickness continued to increase and the area affected by the contact interaction continued to spread as shown in Fig. 2c which was taken about five minutes after Fig. 2b. A

\* A 10-minute 16 mm motion picture film which illustrates this phenomenon has been made by the author and is available on request.

more disorganized step has begun to spread across the face of the pink crystal from another edge where it has met a thicker crystal in nearly perfect alignment with it.

#### GROWTH AND SOLUTION OCCURRING SIMULTANEOUSLY

Figure 2d was made two days after Fig. 2c. During this period the slide remained on the microscope stage at room temperature. Evidently the yellow crystal dissolved as the disturbed areas on the pink crystal continued to grow. Thus, the solution must have been supersaturated with respect to the thick crystal having the growth step and yet unsaturated with respect to the thin and perfect yellow crystal.

Part of the crystal at the lower right of Figs. 2b-d adhered to the glass slide. The consequent close approach of other parts of the crystal to the glass resulted in the intense interference colors. The gradual approach of crystal to glass is probably also responsible for the fringes seen in the pink crystal.

#### SINGLE SPIRAL AND CLOSED LOOP

Figures 4a-d show the progress of (1) a single growth spiral (right of photograph) and (2) a closed loop (middle of photograph) resulting from the interaction of two spirals of opposite hand. At the top of each growth hill is a dark spot of unresolved structure. On the original film (150X) the center of the single spiral appeared to be a diffuse spot having circular symmetry (Fig. 5a). Near the center of the closed loop there were two elongated spots about 0.75 mm apart similar to those in Fig. 5b. The direction of the long axis is the same for both spots within the closed loop and appears to be parallel with one of the edges of the crystal.

#### LATTICE STRAIN

Impinging crystals sometimes subject each other to large strains as they thicken. One of the crystals in Fig. 4 has been wrinkled as a result of thickness growth. A more severe case of this is shown in Fig. 6. A rough

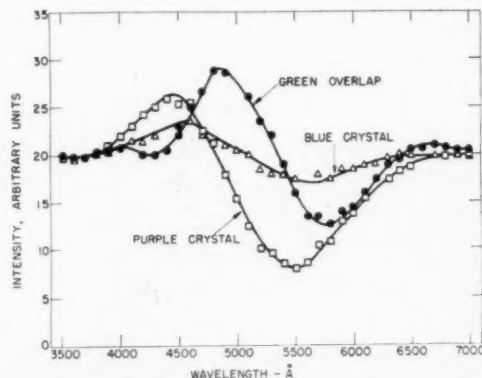
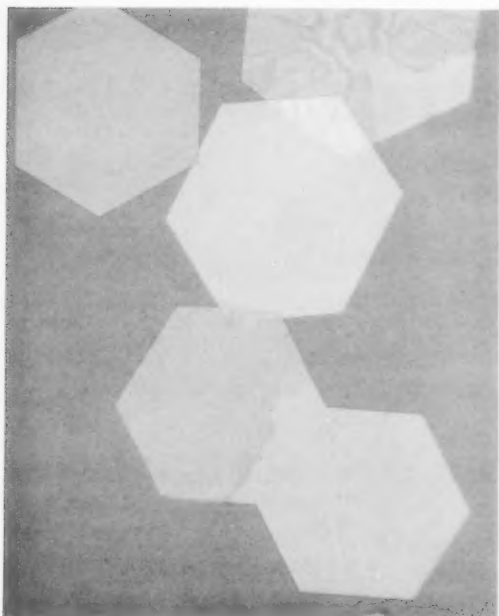
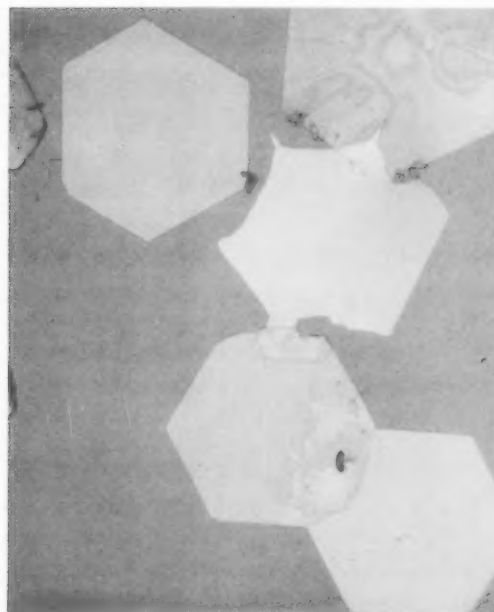


FIG. 3. Spectral distributions of light reflected from blue and purple crystals and from their green overlapped region as in Fig. 2.

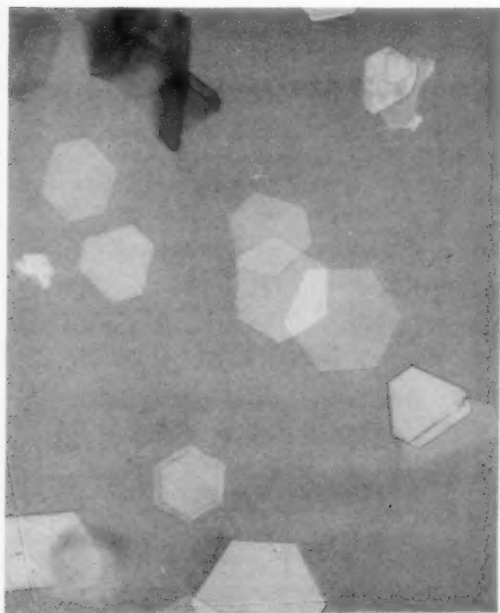


(a)



(b)

FIG. 2(a). Three overlapping crystals photographed before thickness growth started. Color is due to interference of white light reflected from the top and bottom surfaces and varies with crystal thickness. (b) Thickness growth starts where two crystals meet edge to edge. (c) Five minutes later. Thickness growth continues where a growth step is present. (d) Two days later. The solution is unsaturated with respect to the thin yellow crystal and supersaturated with respect to the thick crystal containing growth steps.



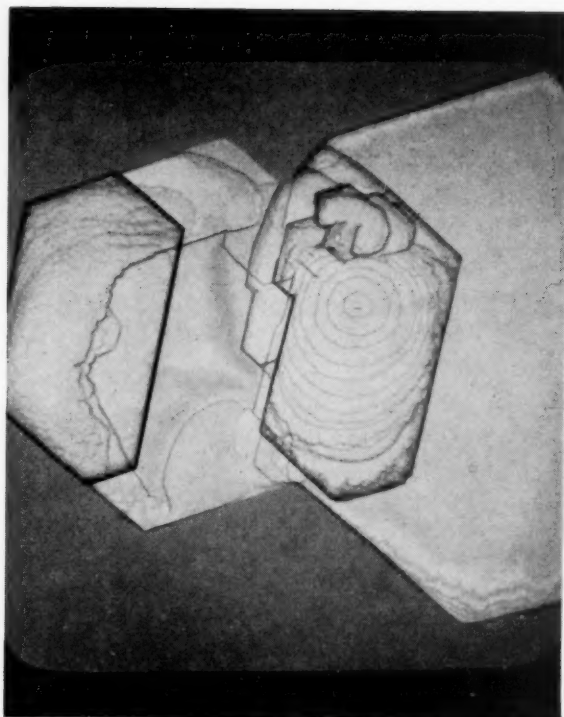
(c)



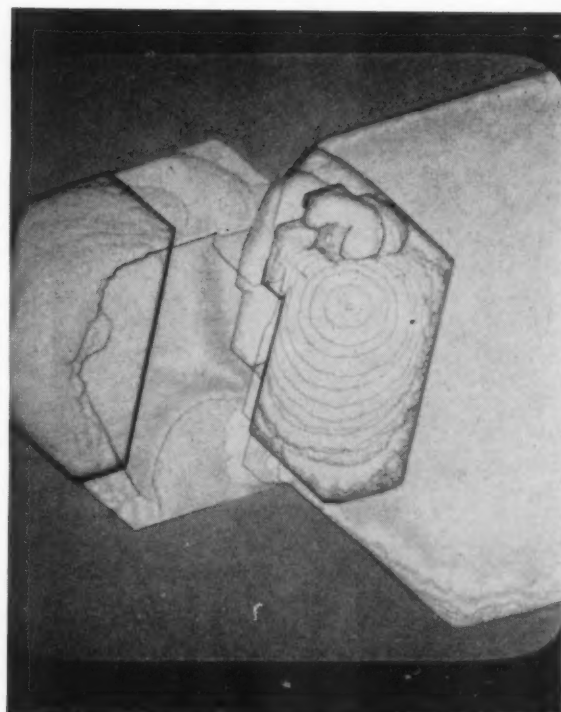
(d)



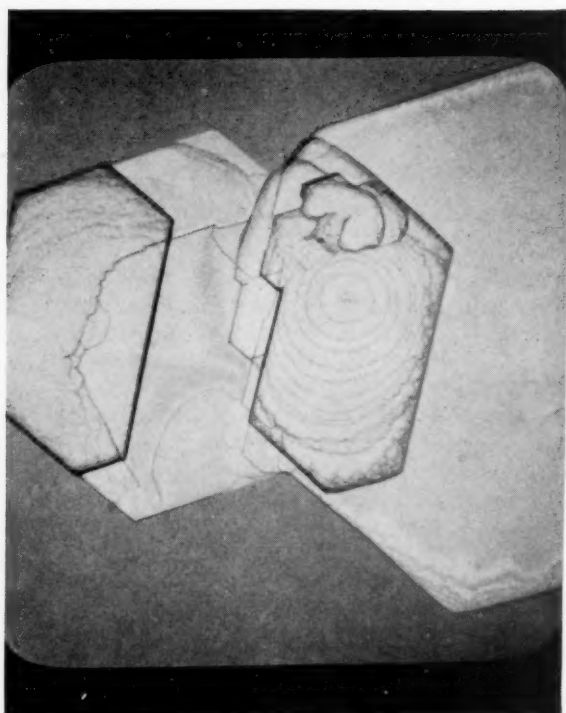
VOL.  
3  
1955



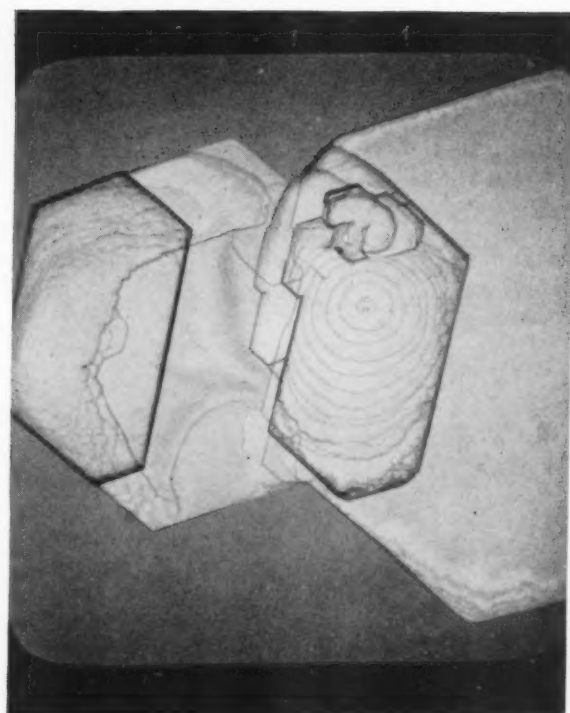
(a)



(b)



(c)



(d)

PLATE II. FIG. 4.—(a)–(d) *In right of each figure.* A spiral growth source progresses around center spot. 150X. *In middle of each figure.* Two adjacent spirals of opposite hand form successive closed loops which spread from original spots.

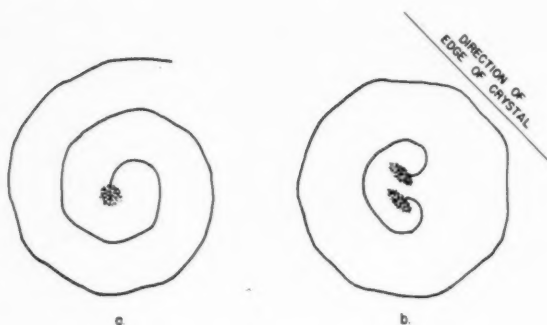


FIG. 5. Diagrammatic sketch of spiral and closed loop growth sources shown in Fig. 4.

estimate of the maximum strain suffered by the surface layer on one of the crystals of Fig. 6 may be made as follows:

$$\text{Strain} \approx \frac{\text{Thickness}}{2 \times \text{Radius}},$$

$$\text{Mag.} = 150,$$

$$\text{Estimated radius} \approx 10/150 \text{ cm} \approx 7 \times 10^{-3} \text{ cm},$$

$$\text{Estimated thickness} \approx 5 \times 10^{-5} \text{ cm},$$

$$\text{Percent strain} \approx \frac{5 \times 10^{-5}}{14 \times 10^{-3}} (100), \text{ or}$$

$$\text{Per cent strain} \approx 0.4 \text{ per cent.}$$

It is suspected that this large strain may be entirely elastic since no surface striations or other marks indicating plastic flow could be seen on the ridges or in the valleys of the wrinkled crystal. Furthermore, if plastic deformation had occurred, one would expect thickness

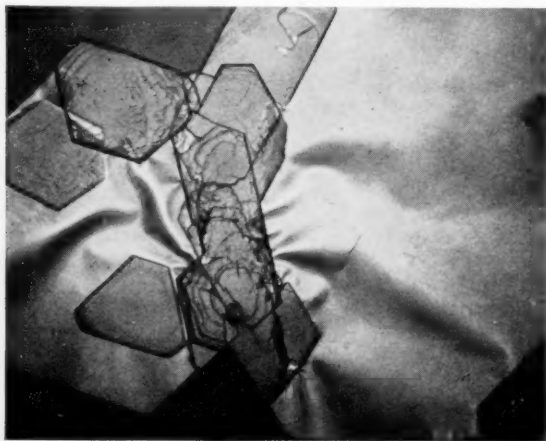


FIG. 6. Thin crystals are sometimes severely strained by thickness growth.

growth to follow in the manner demonstrated by Korndorffer et al.<sup>3</sup>

#### NON-REGENERATING GROWTH LAYER

Sometimes, a flat perfect crystal of one color appears to be resting upon a larger one, the two having their major axes parallel. This situation has been observed so frequently that it is unsatisfying to explain it on the basis of the fortuitous juxtaposition of two originally independent nuclei or platelets. An alternate and more attractive explanation is that a non-regenerating nucleus forms at a dirt particle resting on the surface of the larger crystal. It is reasonable to suppose that nucleation on a flat surface would occur at lower supersaturation where a particle is in contact with the surface. For example, if the angle between the crystal surface and the surface of a dirt particle is  $\alpha_1$  at the point of contact (see Fig. 7), new layers may deposit causing the crystal

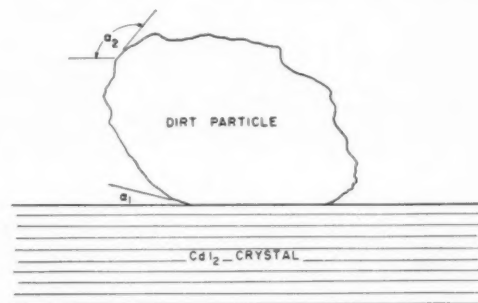


FIG. 7. Foreign solid resting on flat surface of a  $\text{CdI}_2$  crystal.

to engulf the dirt particle until the contact angle  $\alpha_2$ , between the surfaces of the crystal and the particle, reaches a critical value. This value would be determined by the supersaturation and other factors such as the shape of the particle, its composition, its crystal structure and its orientation with respect to the underlying  $\text{CdI}_2$  crystal. The step which formed in this way could then spread from the particle over the platelet in the form of a constantly expanding polygon with sides parallel to those of the parent crystal. This behavior has been observed.

#### GROWTH SPIRALS ON ONE SIDE OF A PLATE

The situation is often seen wherein two major spiral growth sources of the same hand appear to have formed at a location other than the edge of a single crystal. These sources are apparently permitting growth in the thickness direction by the usual spiral mechanism. In this case the spiral growth sources may have originated at dirt particles on the crystal surface. If the lattice planes of the newly formed  $\text{CdI}_2$  layer, which is growing around the dirt particle, are not in exact registry when

they meet on the other side of the particle, a regenerating step would be formed in the manner proposed by Fisher et al. Therefore, when a particle disturbs only one side of a platelet, a growth step would be expected to occur only on that side.

#### ACKNOWLEDGMENTS

The author is indebted to Dr. F. J. Studer and Miss G. P. Lloyd for their help in determining crystal thickness. He also has had the benefit of stimulating

discussions with Dr. D. Turnbull and Drs. Fisher, Fullman and Sears.

#### REFERENCES

1. J. C. Fisher, R. L. Fullman, and G. W. Sears, "The Origin of Screw Dislocations in Growing Crystals." Submitted to *Acta Met.* 1954.
2. A. J. Forty, "Growth of Cadmium Iodide Crystals," *Phil. Mag.* **42**, 670-2 (1951); *Phil. Mag.* **43**, 72-81, 377-92 (1952).
3. A. Korndorffer, H. Rahbeck, and F. S. A. Sultan, "The Effect of Mechanical Deformation on the Growth of Cadmium Iodide Crystals from Solution," *Phil. Mag.* **43**, 1301-6 (1952).



# THE SEGREGATION OF CARBON IN IRON SINGLE CRYSTALS AS STUDIED BY TORSION PENDULUM DAMPING\*†

F. W. KUNZ‡

The effect of quenching and straining on the segregation of carbon in single crystals of alpha iron was studied by means of torsion pendulum damping. The changes in damping observed in carburized iron single crystals during room temperature aging were explained on the basis of the Cottrell mechanism. Some mechanism of interaction between dislocations and precipitated iron carbide particles was also required to explain the changes in damping observed in iron crystals after aging at 115°C. A correlation between damping and yielding behavior during room temperature aging was also observed.

## LA SÉGRÉGATION DU CARBONE DANS LES CRISTAUX DE FER, ÉTUDIÉE À L'AIDE DU PENDULE DE TORSION

Les effets de la trempe et de la déformation sur la ségrégation du carbone dans les monocristaux de fer alpha ont été observés au moyen de mesures d'amortissement au pendule de torsion. Les variations, au cours de vieillissement à la température ordinaire, de l'amortissement dans les cristaux de fer recarburés, sont expliquées à l'aide du mécanisme de Cottrell. Une interaction entre les dislocations et les particules de carbure de fer précipitées est nécessaire pour expliquer les variations de l'amortissement lors d'un vieillissement à 115°C. Une relation entre l'amortissement et le palier a été également observée au cours du vieillissement à la température ordinaire.

## UNTERSUCHUNG DER AUSSCHIEDUNG VON KOHLENSTOFF IN EISEN EINKRISTALLEN DURCH DÄMPFUNGSMESSUNGEN MIT HILFE DES TORSIONSPENDELS

Durch Dämpfungsmessungen mit dem Torsionspendel wurde der Einfluss einer schnellen Abkühlung und Verformung auf die Ausscheidung von Kohlenstoff in  $\alpha$ -Eisen Einkristallen untersucht. Mit Hilfe des Cottrell Mechanismus wurde die Veränderung der Dämpfung bei der Alterung von aufgekühlten Eisen Einkristallen bei Raumtemperatur erklärt. Zur Erläuterung der beobachteten Änderung der Dämpfung in Eisen Einkristallen nach Alterung bei 115°C wurde eine Wechselwirkung zwischen den Gitterfehlstellen und den ausgeschiedenen Eisenkarbid-Teilchen angenommen. Zwischen der Dämpfung und dem Elastizitätsverhalten während der Alterung bei Raumtemperatur wurde ebenfalls ein Zusammenhang festgestellt.

## INTRODUCTION

The internal friction of alpha-iron containing carbon or nitrogen in solid solution has been extensively studied during the past several years.<sup>1,2,3</sup> The damping peak which occurs near room temperature at about one cycle per second has been attributed to the stress-induced interstitial diffusion of the solute atoms in the iron matrix.

By measuring the internal friction in alpha-iron, it is possible to measure the amount of dissolved solute remaining in solid solution at any time and thus quantitatively study the segregation process. This has been verified experimentally by Dijkstra,<sup>4</sup> who found that the maximum damping at room temperature is approximately equal to the weight per cent of the solute present in solution. Utilizing the damping of iron due to carbon, Harper<sup>5</sup> has recently shown that the rate of strain-induced segregation of carbon in iron is in agreement with the Cottrell mechanism of localized segregation of carbon atoms about dislocations.<sup>6</sup>

The purpose of this paper is to describe a series of experiments on the effect of quenching and straining

on the segregation of carbon in single crystals of alpha-iron. Single crystals were used because the rate of segregation of carbon may be affected by grain boundaries, and, furthermore, it is possible to obtain small homogeneous strains with carburized single crystals since the yield-point phenomenon is less pronounced for single crystals than for polycrystalline iron.<sup>7</sup>

## EXPERIMENTAL PROCEDURE

A section of high purity ingot, procured from the National Research Corporation, was worked down to 0.050-inch diameter and cold-drawn to 0.025 inch-diameter wire. Initially this material contained 0.029 wt. % O<sub>2</sub>, 0.007 wt. % N<sub>2</sub> and 0.004 wt. % C. Specimens of this wire were purified of carbon and nitrogen by annealing five hours at 720°C in a wet hydrogen atmosphere.

Single crystals were grown from this material by the following strain-anneal technique: After the decarburization process, the specimens were strained 3 per cent. A small amount of wax then was deposited on the surface of the wires, following which the specimens were sealed in evacuated quartz tubes and slowly raised through a gradient furnace at a rate of 15 mm per hour. The furnace was divided into three 8-inch temperature zones. The temperature distribution of the zones was as follows: In the lower zone, the temperature ranged from 25°C to 885°C, the middle zone was held

\* Received June 8, 1954.

† This paper is based upon a part of a thesis submitted to the faculty of the Graduate School of Siena College in partial fulfillment of the requirements for the degree of Master of Science, May 13, 1954.

‡ Knolls Atomic Laboratory, General Electric Company, Schenectady, New York.

at a constant temperature of 885°C and in the top zone of the furnace the temperature ranged from 885°C to 25°C.

After etching the wires in a 20 per cent  $\text{HNO}_3$  solution, it was found that excellent single crystals, 3 to 12 inches in length, were formed by the gradient-growth technique. These crystals contained from 0.005 to 0.008 weight per cent of carbon in solution. Crystals 6 inches in length were chosen for subsequent damping work because they were easier to handle than the longer lengths.

Several polycrystalline specimens of the same wire were marked lightly with wax, sealed in evacuated quartz tubes, and annealed at 720°C for three hours to diffuse the carbon from the decomposed wax into the specimens.

The internal friction of the single crystals and polycrystals was measured by observing the decay of the free vibrations of these specimens in a torsion pendulum similar to the apparatus used by Ké, but modified to permit annealing and quenching in situ.

In order to determine the maximum internal friction at constant room temperature, the frequency was varied by adjusting the bobs on the pendulum arms. By plotting the internal friction versus frequency of vibration for a carburized single crystal, the maximum was found to occur at about 0.6 cycle per second and this frequency was used in all the damping measurements. The background damping of the torsion pendulum assembly was determined by using a decarburized single crystal and all data have been corrected for this background damping of  $Q^{-1}=0.001$ . The longitudinal stress on the specimen was about 300 psi, a value much lower than the yield point of these crystals, which is about 7000 psi at room temperature. The maximum shear strain on the surface of the specimen at maximum deflection was  $7.5 \times 10^{-5}$ .

The general experimental procedure was as follows. The specimens were annealed for five minutes at 700°C in an argon atmosphere and water quenched in the torsion pendulum. The damping was immediately measured and also measured at various intervals of aging at 25°C. When the damping remained constant the specimens were then strained in the range from 0 to 7 per cent extension and the damping was again

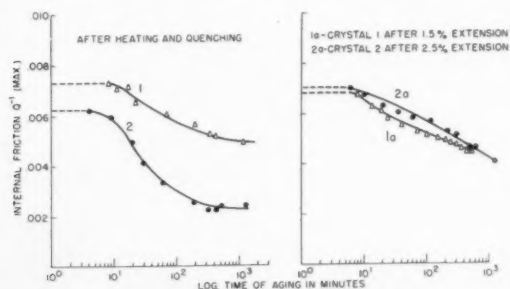


FIG. 1. The effect of aging on the damping of carburized iron single crystals.

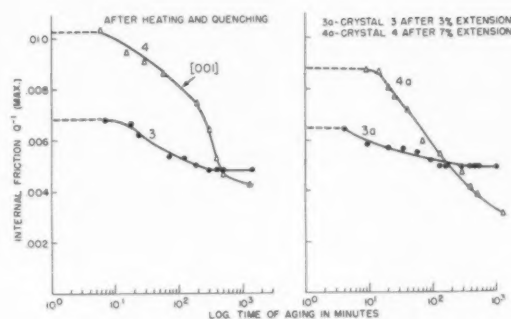


FIG. 2. The effect of aging on the damping of carburized iron single crystals.

measured after intervals of aging at 25°C. A short period of time between the initial measurement and the various treatments was necessary to make adjustments of the optical lever system.

In one instance, a rather complicated sequence of treatments was given to a carburized single crystal. It was heated to 700°C, quenched, and aged for one hour at 25°C, during which time damping measurements were made. The crystal was then aged at 115°C for one hour, quenched, and damping measurements were again made during an aging period at 25°C. The crystal was then strained 3 per cent and damping measurements were made at intervals of aging time at 25°C. After aging for a number of days, the crystal was strained an additional 2 per cent and measurements were again made during aging.

An additional experiment was performed in order to correlate the yielding behavior with the damping behavior of a carburized single crystal. A carburized single crystal was heated to 700°C and quenched to room temperature and at various aging times 1-inch sections of the crystal were tested in tension using a technique described elsewhere.<sup>8</sup>

#### RESULTS OF THE INTERNAL FRICTION MEASUREMENTS

Figures 1 and 2 are the results of plotting the internal friction  $Q^{-1}$  max. as a function of the logarithm of the aging time for four carburized single crystals of iron. In Fig. 1, after heating and quenching crystals 1 and 2, the initial values of damping were observed as 0.0073 and 0.0062, respectively, and with increasing time of aging the damping decreased to a final value of 0.0049 for crystal 1 and 0.0023 for crystal 2. After deforming 1.5 per cent and 2.5 per cent, respectively, the damping of crystal 1 and crystal 2 increased to values of 0.0068 and 0.0070, and after aging approximately  $10^3$  minutes at room temperature, the damping decreased to 0.0044 for crystal 1 and 0.0040 for crystal 2.

After heating and quenching the initial values of damping for crystals 3 and 4, as observed in Fig. 2, were 0.0068 and 0.0102, respectively, and with increasing aging time, the damping decreased to a final value

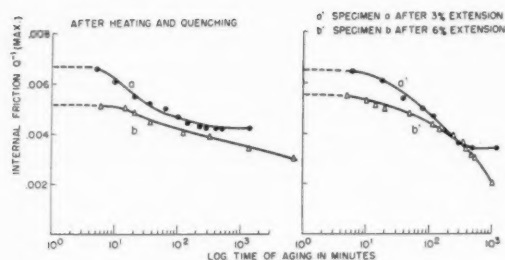


FIG. 3. The effect of aging on the damping of carburized polycrystalline iron specimens.

of 0.0048 for crystal 3 and 0.0043 for crystal 4 after aging  $10^3$  minutes. After deforming crystal 3 and crystal 4, 3 per cent and 7 per cent, respectively, it was observed that the damping increased to values of 0.0065 and 0.0088, respectively, and after  $10^3$  minutes, the damping again decreased to a value of 0.0049 for crystal 3 and 0.0030 for crystal 4.

It is apparent from Fig. 3 that the damping behavior of carburized polycrystalline iron is the same as that of the carburized single crystals. The initial values of damping for specimen (a) were observed to be 0.0067 after heating and quenching and 0.0065 after straining 3 per cent. The initial values of damping for specimen (b) were observed to be 0.0052 after heating and quenching and 0.0056 after straining 6 per cent.

The damping of a decarburized single crystal as shown in Fig. 4 was observed to have a constant value of 0.0026 even after heating and quenching and also after deforming 3 per cent. Consequently, the carbon is influencing the internal friction during the various treatments.

It should be pointed out that the height of the internal friction peak is sensitive to the orientation of the crystals, and only relative values of damping are reliable.<sup>2</sup> This is evidenced by the fact that the initial damping measurements after heating and quenching appear scattered and an exceptionally high initial damping is found in Fig. 2. In general, all the crystals contained a [110] direction nearly parallel to the wire axis with the exception of crystal number 4 (as in Fig. 2) which contained a [001] direction parallel to the wire axis. The increase in damping after deformation could not be attributed to changes in the orientations of the crystals. The change in orientation was determined by the back-reflection Laue method for a crystal deformed 10 per cent and the change observed was less than 8 degrees and consequently this small change in orientation could not account for the large change in damping observed after deformation.

The results of aging a carburized single crystal at  $115^\circ\text{C}$  are shown in Fig. 5. After quenching from  $700^\circ\text{C}$  and during aging at  $25^\circ\text{C}$ , the decrease in damping was consistent with the crystals previously examined. After additional aging at  $115^\circ\text{C}$  for one hour and quenching to  $25^\circ\text{C}$ , it was observed that the damping decreased

sharply and no change in the damping was observed during subsequent aging at  $25^\circ\text{C}$ . After straining 3 per cent, the damping was increased by an amount much smaller than had been previously experienced with the crystals strained a similar amount and aged at  $25^\circ\text{C}$ . After aging a number of days at room temperature, the crystal was given an additional 2 per cent strain and it was observed that the damping increased instantaneously followed by a gradual decrease in the damping during the room temperature aging.

The results of the tensile tests of a carburized crystal after heating and quenching are shown in Fig. 6, a plot of the nominal yield stress *versus* the logarithm of the aging time. By comparing the damping and the yield stress during aging it was observed that as the damping decreases, the yield stress simultaneously increases and after aging  $10^3$  minutes both the yield stress and the damping approach a constant value. It is interesting to note that the yielding behavior also changes with increasing aging time from a homogeneous type of yielding to a flat-type yielding and finally, at saturation, to a drop-in-load type of yielding.

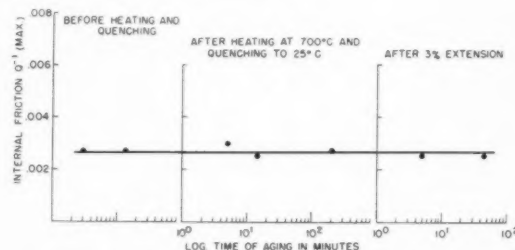


FIG. 4. The effect of quenching and strain aging on the damping of a decarburized iron single crystal.

## DISCUSSION

The results of these damping experiments may be interpreted in the following way. When a crystal of iron containing carbon is heated to  $700^\circ\text{C}$ , the thermal energy of the carbon atoms is such that they are free to diffuse quite rapidly through the iron matrix. After quenching to room temperature, the internal friction maximum is a measure only of the concentration of the interstitial carbon atoms in solid solution and not a measure of the total concentration of carbon. Consequently the decrease in the damping peak observed with increasing time of aging indicates that the carbon atoms are diffusing from their interstitial positions and are either precipitating as an intermetallic compound with the iron or are segregating about dislocations.

If the iron carbide had precipitated during room temperature aging after quenching it seems unlikely that the precipitate would have an effect on the yielding behavior of the crystals and furthermore one would not expect an increase in damping after deformation. Consequently, the Cottrell mechanism of the segregation of carbon about dislocations appears the best adapted to explain the results reported in this paper.

After quenching, the carbon atoms segregate to the dislocations and as aging time increases, the dislocations become more firmly anchored by the carbon atoms as indicated by the decrease in damping, the increase in yield stress and the change in the yielding behavior. When the dislocations have become saturated with carbon atoms, the damping becomes constant; the yield stress approaches a maximum value and one observes a drop-in-load type yielding.

During deformation, after the quench-aging treatment, the dislocations are freed from their carbon atmospheres, leaving the carbon again in solution as indicated by the immediate increase in damping after straining. Aging after deformation results in the carbon atoms again segregating to the dislocations formerly present and also to those formed during the deformation process as indicated by the decrease in damping during strain-aging.

The low value of damping, as in Fig. 5 after aging at 115°C, may be attributed to the formation of iron

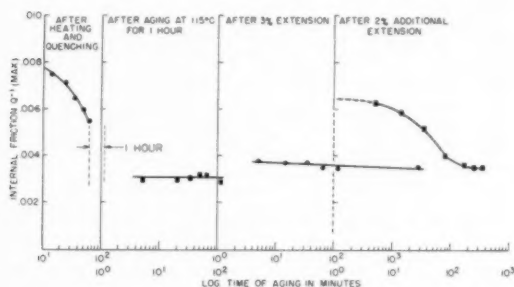


FIG. 5. The effect of aging at 115°C on the damping of a carburized iron single crystal.

carbide during aging because the damping after additional deformation increased only slightly. If the carbon had segregated at dislocations during the 115°C aging, the additional deformation should have restored the high value of damping. The slight increase in damping after deformation may be attributed to residual carbon which had not precipitated as carbide during the aging at 115°C.

When the crystal is in the condition where carbide has formed, strain followed by long-time aging at 25°C apparently dissociates the carbide and the carbon again segregates at dislocations. As a result, when the crystal is deformed after such re-segregation (as after the final 2 per cent strain in Fig. 5) the dislocations are again freed from their carbon atmospheres and an immediate increase in the damping is observed. With increasing time of aging, the carbon again segregates to the

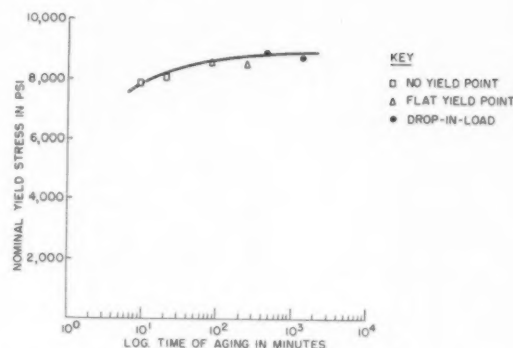


FIG. 6. The effect of quenching and aging on the yielding behavior of a carburized iron crystal.

dislocations as observed by the gradual decrease in damping.

### CONCLUSIONS

From this study one may conclude that the Cottrell mechanism can explain the changes in damping observed in carburized iron single crystals during room temperature aging. Some mechanism of interaction between dislocations and precipitated iron carbide particles is required to explain the solution of carbide once formed and the re-segregation of carbon at dislocations.

From these studies one might also postulate that the initial stage of precipitation hardening is actually the segregation of solute atoms about dislocations in the Cottrell fashion. These solute atoms then act as nuclei for the formation of the precipitate and as the equilibrium solubility is exceeded these nuclei then become critical in size and a precipitate intermetallic in nature begins to form.

### ACKNOWLEDGMENT

The author wishes to thank A. N. Holden of the Knolls Atomic Power Laboratory, B. E. Blaisdell of Siena College and J. R. Low of the General Electric Research Laboratory for their many helpful discussions and their interest in the damping problem.

This work was done under Contract No. W-31-109 Eng. 52 with the Atomic Energy Commission.

### REFERENCES

1. J. L. Snoek, *Physica* **8**, 711 (1941).
2. L. J. Dijkstra, *Philips Res. Rep.* **2**, 357 (1947).
3. T. S. Kê, *Trans. A.I.M.E.* **176**, 448 (1948).
4. L. J. Dijkstra, *Trans. A.I.M.E.* **185**, 252 (1949).
5. S. Harper, *Phys. Rev.* **83**, 709 (1951).
6. A. H. Cottrell and B. A. Bilby, *Proc. Phys. Soc. (London) Series A*, **62**, 49 (1949).
7. A. N. Holden, *J. Appl. Phys.* **22**, 1290 (1951).
8. A. N. Holden and F. W. Kunz, *J. Appl. Phys.* **23**, 799 (1952).



## GRAIN BOUNDARY DIFFUSION IN A BODY-CENTERED CUBIC LATTICE\*

C. W. HAYNES†‡ and R. SMOLUCHOWSKI†

Oriented bicrystals of a 3 per cent silicon iron alloy were prepared with a common [011] direction, and were used in a study of intergranular diffusion in the body-centered lattice. The penetration of iron at the grain boundary during diffusion was obtained by an autoradiographic technique. The penetration was found to be orientation dependent, with no preferential grain boundary diffusion being observed for relative angles of disorientation below about 10 degrees. In general the penetration increased up to a disorientation of 86 degrees with a broad minimum in the neighborhood of 50 degrees. The results can be interpreted in terms of the density of atoms of misfit at the grain boundaries although little correlation seems to exist between penetration and grain boundary energy at the cusp positions.

### DIFFUSION INTERCRISTALLINE DANS LES RÉSEAUX CUBIQUES CENTRÉS

Des bicristaux de ferro-silicium à 3% ayant une direction [011] commune ont été utilisés pour étudier la diffusion intergranulaire. La pénétration du fer le long du joint de grain pendant la diffusion est observée par autoradiographie. Elle ne dépend de l'orientation quand la différence des angles est inférieure à 10°, mais en général, la pénétration croît jusqu'à une désorientation de 86° avec toutefois un minimum étalé au voisinage de 50°. Les résultats peuvent s'expliquer en fonction d'une mesure du désordre aux joints de grains, quoique seulement une faible corrélation semble exister entre la pénétration et l'énergie superficielle lors du minimum.

### KORNGRENZENDIFFUSION IN EINEM KUBISCH-FLÄCHENZENTRIERTEN GITTER

Zum Studium der Korngrenzendiffusion im raumzentrierten Gitter wurden orientierte Zweikristalle einer Eisen-Silizium-Legierung mit 3% Silizium hergestellt. Die Wanderung des Eisens während der Diffusion entlang den Korngrenzen wurde durch ein radioaktives Isotopenverfahren verfolgt. Die Wanderung des Eisens ist orientierungsabhängig. Unter einem relativen Orientierungsunterschied von ungefähr 10° tritt keine bevorzugte Korngrenzendiffusion auf. Im allgemeinen nahm die Wanderung mit dem Orientierungsunterschied bis zu 86° zu und hatte im Bereich um 50° ein breites Maximum. Die Ergebnisse können auf Grund der Dichte von Fehlatoemen an den Korngrenzen gedeutet werden, obwohl zwischen der Wanderung und der Korngrenzenenergie an den Spitzen nur ein geringer Zusammenhang zu bestehen scheint.

## INTRODUCTION

The phenomenon of grain-boundary diffusion in metals has been known for many years and has been reported in the literature occasionally. Recently several more detailed studies of grain boundary diffusion have been made, both experimental and theoretical, stimulated by the desire for more information on the structure of the grain boundary.

Mehl<sup>1</sup> in 1936 reviewed the evidence on grain-boundary diffusion up to that time. In general, this evidence consisted of observations of the variation of over-all diffusion coefficients in polycrystalline materials with grain size. The observation of larger diffusion coefficients with smaller grain size was taken to indicate that diffusion occurred at the grain boundary more rapidly than in the lattice of the grains themselves. More recently metallographic and radiographic evidence has been presented to show preferential intergranular diffusion. Keller and Brown<sup>2</sup> obtained photomicrographs showing the copper enrichment of grain boundaries of the aluminum cladding on Alclad sheet by diffusion. Barnes<sup>3,4</sup> has made an interesting micrographic study of the diffusion of copper into nickel, with

preferential penetration at many grain boundaries but not at twin boundaries of the nickel. Hoffman and Turnbull<sup>5</sup> used a radioactive tracer technique to study the rate of self-diffusion of silver which exhibited a grain size effect. They also made a contact autoradiograph of a sectioned specimen which showed that preferential grain boundary penetration had occurred.

The orientation dependence of the diffusion of silver into columnar copper was investigated by Achter and Smoluchowski<sup>6</sup> using a metallographic technique. Diffusion couples of 4 per cent silver copper alloy *versus* columnar copper were diffused at temperatures from 673° to 725°C. These couples were sectioned parallel to the interface (normal to the columnar [001] direction) at successively greater distances and the limit of intergranular penetration between each pair of grains was determined metallographically. The results indicate that the grain boundary diffusion is markedly dependent on the relative orientation of the grains forming the boundary. It was found that if  $\theta$ , the angle between the (100) planes including the grain boundary, was less than 20 degrees or greater than 70 degrees there was no preferential grain-boundary diffusion observed; if  $\theta$  lay between 20 and 70 degrees there was preferential diffusion at the grain boundary with a maximum at  $\theta$  near 45 degrees. Flanagan and Smoluchowski<sup>7</sup> investigated the diffusion of zinc into columnar copper in a similar manner. Their results confirm the influence of

\* Received June 9, 1954.

† Carnegie Institute of Technology, Pittsburgh, Pennsylvania.

‡ Now Associate Professor of Engineering Mechanics at the University of Nebraska. Submitted in partial fulfillment of requirements for the degree of Doctor of Science at the Carnegie Institute of Technology, June 1953.

angle of disorientation between grains on intergranular diffusion and indicate an angular dependence of activation energy for the process. This led to a model<sup>8</sup> for the structure of grain boundaries for angles of disorientation higher than the range of applicability of the classical dislocation model.

Couling and Smoluchowski<sup>9</sup> have studied the anisotropy of diffusion in tilt-type grain boundaries using bicrystals of copper having parallel  $[100]$  axes and angles of disorientation in the range from 0 to 90 degrees. In addition to dependence on the angle of disorientation, an anisotropy was observed in the amount of penetration at the boundary; that is, the penetration varies with the direction of diffusion in the plane of the boundary. Theoretical treatments of grain-boundary diffusion under the assumption that the grain boundary has a uniform "thickness" and a characteristic diffusion coefficient which has a constant ratio to the volume diffusion coefficient have been given, first approximately by Fisher,<sup>10</sup> and later more exactly by Whipple.<sup>11</sup>

In view of the fact that the body-centered cubic lattice is a less closely packed arrangement of atoms than the face-centered cubic lattice, one could expect that there would be less difference between the mobility of atoms in the grain and in the grain boundary of a body-centered cubic lattice than in a face-centered lattice. If such is the case, one might also expect that preferential grain-boundary diffusion would occur to a lesser degree, if at all, in the body-centered cubic material. The investigation described in this paper was undertaken to study the possible variation of grain-boundary diffusion in a body-centered cubic lattice with the orientation of the crystals forming the boundary. The availability of a convenient radioactive isotope made a study of grain-boundary self-diffusion in iron particularly favorable. Since small amounts of silicon promote growth of large grains in iron it was decided to use this alloy. This implies the assumption that the angle of disorientation does not affect the solubility of silicon in the grain-boundary material.

#### EXPERIMENTAL

Bicrystal specimens were grown by the strain-anneal method from decarburized commercial silicon iron sheet. Strips  $1\frac{1}{8}$  inch wide by 10 inches long were cut from 0.030-inch thick sheet of silicon iron supplied through the courtesy of the Allegheny-Ludlum Steel Corporation. Chemical analysis of the material was as follows: C 0.022 per cent, Mn 0.043 per cent, P 0.011 per cent, S 0.017 per cent, Si 3.17 per cent, Sn 0.012 per cent, Al trace. The strips were decarburized in an atmosphere of moist hydrogen at a temperature of 850°C for 48 hours. They were then rolled to a thickness of 0.025 inch, and the edges ground parallel to a width of one inch. This was followed by an annealing treatment at 800°C in hydrogen for one hour which resulted in a fine grain size. The strips were strained  $2\frac{1}{2}$  per cent in tension and the ends cropped to remove the material

held in the grips. A short length at one end of each strip was recrystallized by raising it slowly into a furnace in which a steep temperature gradient existed, with the maximum temperature in the furnace (1020°C) being well above that needed for recrystallization. This procedure usually resulted in the formation of several large grains in the area recrystallized. The orientation of those grains which adjoined the unrecrystallized area was determined roughly by the etch pit method,<sup>12</sup> and the one having an orientation nearest to that desired, i.e., the (011) plane parallel to the surface, was used as a "seed" in the preparation of a bicrystal with the two grains having predetermined relative orientation. This was done by the general technique outlined by Dunn<sup>13</sup> and described in detail by Dunn and Nonken.<sup>14</sup>

The orientation of the selected seed crystal was determined accurately by means of the Laue back-reflection X-ray method. All of the recrystallized material was cut off the strip with the exception of a small amount of the seed crystal which was left on the end of a narrow neck of unrecrystallized material connecting it with the main body of the strip. The seed was then reoriented by twisting and bending the neck (which was locally heated to a dull red heat to prevent further cold-straining) in a jig to make the (011) plane parallel to the surface of the main body of the strip. Again the strip was heated progressively from the seed end, causing the seed to grow into the body of the specimen with the desired orientation. The orientation of the crystal was checked by means of the Laue back-reflection method. In order to form a bicrystal, the end of the strip was again cut, leaving seeds at the ends of two necks of unrecrystallized material. These two necks were bent about the (011) pole perpendicular to the surface of the strip so that the  $[100]$  directions of the two seeds were the desired angle  $\theta$  apart and symmetrical with respect to the axis of the strip. Growth of the two seeds into the body of the strip then resulted in a bicrystal from which Laue back-reflection X-ray photographs were made to determine the exact angle  $\theta$  between the  $[100]$  directions and the angle  $\psi$  between the (011) poles of the two crystals. The angle  $\psi$  was in all cases less than 5 degrees.

Specimens approximately  $\frac{3}{4}$  inch square were cut from the bicrystals with the grain boundary roughly parallel to and midway between the edges. The grain boundary as grown was in general far from straight. In order to straighten it and bring it to a stable low-energy position, a high-temperature annealing treatment was given to the specimens. They were packed flat in a close-fitting box machined from silicon iron to prevent loss of silicon by vaporization at the annealing temperature, and the box containing the specimens was heated to 1300°C in an atmosphere of dry argon for one week. The resulting movement of the grain boundary was mostly of microscopic order of magnitude.

The specimens were subsequently prepared for electroplating by polishing both faces on emery paper to grade 3/0. Thickness was checked on a Pratt and Whit-

ney comparator, and variations were held to  $\pm 0.0001$  inch in the area to be plated. Electroplating of the specimens was carried out by the general method described by Buffington, Bakalar, and Cohen<sup>15</sup> in which the iron is deposited from ferric chloride in a saturated solution of ammonium oxalate made slightly alkaline with ammonium hydroxide. An area, along the grain boundary, about  $5/8$  inch long by  $1/2$  inch wide was plated with iron isotope 55, obtained from the Oak Ridge National Laboratory in the form of ferric chloride solution. This isotope has a half-life of about 4 years and disintegrates by *K*-electron capture, emitting a low energy X-ray capable of exposing X-ray film. Each specimen was plated with the same amount of radioactive iron solution, to a measured activity of about  $5 \times 10^5$  counts per minute.

After plating, the specimens were placed face to face in pairs in close-fitting cells of silicon iron for the diffusion treatment. This was carried out in a ceramic tube in an atmosphere of dry hydrogen. Because of the relatively long diffusion periods, no correction was necessary for the heating or cooling time. Temperature was controlled to  $\pm 1$  degree in most cases, with a maximum variation of  $\pm 3$  degrees from values given. A trial run at  $704^\circ\text{C}$  for 144 hours using a specimen having an angle of disorientation  $\theta$  of 47 degrees showed that preferential grain-boundary diffusion was taking place and that a higher temperature or a longer diffusion period would be necessary to produce a suitable penetration. Based on published self-diffusion data for iron<sup>16,17</sup> and a diffusion period of about one week, it was calculated that a temperature of about  $825^\circ\text{C}$  would give a satisfactory amount of volume diffusion. Accordingly, the first series of specimens was diffused 176 hours at  $827^\circ\text{C}$ . In order to try to get a more pronounced difference between grain boundary and volume diffusion, later runs were made at lower temperatures and for correspondingly longer times; that is, at  $810^\circ\text{C}$  for 266 hours, at  $769^\circ\text{C}$  for 752 hours and 750 hours.

The specimens of the first ( $827^\circ\text{C}$ ) diffusion run were mounted in bakelite and a series of layers was removed from the active face by polishing on emery paper. After each layer was removed, an autoradiograph of the exposed surface was made and the activity of the surface was counted through a slit 0.25 inch by 0.030 inch. It became apparent that it was not possible to polish a specimen so that the plated area was of uniform activity away from the grain boundary, presumably because the specimen could not be kept sufficiently flat during the mounting and polishing operations. Also, the counting times involved became impractically long. It had been hoped that by positioning the slit over the grain boundary and over one of the crystals near the boundary for successive counts, a measure of the greater penetration at the grain boundary could be obtained. The differences were so small, however, that they could not be accurately determined. The autoradiographs on the other hand showed the difference between the grain

boundary and the volume diffusion quite well, and a good autoradiograph could be made in a reasonable time from a specimen from which layers were removed down to a point where the count was only slightly above background. Therefore it was decided to concentrate on the autoradiographic method for determination of the diffusion penetration. Furthermore, because of the difficulty of sectioning the specimens parallel with the interface it was decided to section intentionally at a small angle with the interface, so that the surface would be below the limit of volume diffusion at the other end. An exposure time of one week was chosen for determination of maximum penetration, Kodak No-Screen X-ray film was used for the autoradiographs, and the development of the film was standardized. Figure 1

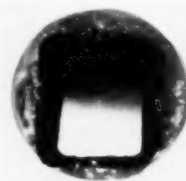


FIG. 1. Negative of an autoradiograph of a slope-sectioned bi-crystal (light areas indicate presence of radioactive isotope). Original interface greatly overexposed to show grain-boundary penetration.

shows an autoradiograph of a slope-sectioned specimen.

The location of the last visible trace of the grain boundary on the autoradiograph was determined by inspection, and its position transferred to the surface of the specimen itself by micrometer measurement. The thickness of the specimen at this location was then measured with a dial gage comparator, and the penetration calculated by difference from the original thickness to the nearest 0.0001 inch.

## RESULTS AND DISCUSSION

The depth of penetration at the grain boundary as determined by the above procedure is plotted, for the temperatures  $769^\circ\text{C}$  and  $810^\circ\text{C}$ , in Fig. 2. These results were obtained by the slope sectioning technique and are considered more reliable than the results from the set of samples diffused at  $827^\circ\text{C}$  which were sectioned approximately parallel to the interface. A comparison of the two runs at  $769^\circ\text{C}$  indicates the reproducibility of the measurements.

The corresponding amount of volume diffusion could not be determined accurately because of the difficulty in evaluating the effect of the relative areas involved in exposing the autoradiographs. The required concentration of radioactive atoms in the grain boundary would need to be much higher to give a visible image on the autoradiograph than that in the relatively broad expanse of lattice. This points out the expected low preference for grain boundary diffusion in a body-centered metal as compared to a face-centered metal. A



rough value for the volume diffusion is about 0.004 inch. The effect of grain-boundary direction was not determined because of the frequent irregularity of the grain boundary. No preferential grain-boundary penetration was observed for  $\theta=6$  and 9 degrees. Although there is considerable scatter at some angles of disorientation, several points of interest are apparent on inspection of Fig. 2. The first observation is that specimens having an angle of orientation difference below about 10 degrees show no preferential grain-boundary diffusion while those with  $\theta$  equal to 15 or 16 degrees do. Evidently at some intermediate angle the grain boundary diffusion becomes enough greater than lattice diffusion to be detected by the experimental procedure used. This confirms the general character of the angular dependence of grain-boundary penetration as observed earlier by Achter, Flanagan, Couling and Smoluchowski<sup>6,7,9</sup> although here the uncertainty in the value of the volume diffusion makes the critical angle much less pronounced. The existence of this angle was interpreted<sup>8</sup> in terms of transition from single dislocations to rod-like regions of distorted lattice at angles higher than the critical angle. It should be pointed out, however, that recent work of Turnbull and Hoffman<sup>17</sup> seems to indicate presence of preferential diffusion along dislocations. Another fact to be remembered in interpreting Fig. 2 is that the small-angle tilt-type boundary between body-centered cubic crystals with a common [011] direction is not made up solely of pure edge dislocations but the dislocations contain a screw component. The effect of the screw component on diffusion at the boundary is not known but is evidently not great in this case.

Another striking feature of the plot in Fig. 2 is the broad minimum of grain-boundary penetration near  $\theta=50$  degrees. Qualitatively, this is similar to the slight minima of penetration observed by Achter<sup>6</sup> and by Couling<sup>9</sup> in the Cu-Ag system. Quantitatively, the broad minimum in Fig. 2 is much more pronounced and more reproducible than those observed on copper in spite of the considerable scatter of the experimental points in this region. It has been often suggested that minima of grain boundary energy and of grain boundary

TABLE I. Structure of grain boundaries as cusp positions ( $0^\circ < \theta < 180^\circ$ ) and observed penetrations.

Grain boundary plane	Distance between common atoms (in $a_0$ ) $\delta$	Angle between grains in degrees	Number of channels of misfit per $\delta$	Number of misfit atoms per $\delta$	Density of misfit atoms $m$	Observed penetration beyond volume diffusion in $10^{-3}$ inch
112	0.87	109.5	0	0	0	—
332	1.66	50.5	0	0	0	.07
116	2.28	153.8	1	1	.438	—
111	2.45	70.6	1	1	.408	3.0
552	2.60	31.6	1	1	.385	2.5
114	3.00	141.1	2	1	.333	—
556	3.28	80.6	2	1	.305	3.0?
772	3.54	22.8	1	2	.564	2.7
1110	3.54	163.9	1	1	.282	—
3310	3.84	134.1	2	3	.782	—
776	4.09	62.4	2	2	.489	2.2?
334	4.13	86.7	2	2	.485	3.0
221	4.24	39.0	1 (2)	1 (2)	.236 (.472)	1.8

diffusion penetration occur whenever the distance  $\delta$  between atoms common to both grains is small. On this model the minimum for the Cu-Ag system has been interpreted in terms of coincidence of a (210) plane of each grain with a symmetrical grain boundary. The possible energy cusps for our type of grain boundaries are listed in Table I in order of increasing  $\delta$ , thus, according to Read and Shockley,<sup>10</sup> in order of increasing energy. For completeness all angles up to 180 degrees are included although only those up to about 90 degrees have been investigated. Read and Shockley seem to find a rough quantitative correlation between  $\delta$  and the depth of energy cusps as observed by Dunn and Lionetti<sup>20</sup> although they consider only the cusps (112), (332), (111), (334) and (221) and reverse the sequence of the (111) and (332) cusps. The coincidence of the normal twinning plane (112) with the grain boundary would lead to a strong minimum at  $\theta=109$  degrees, which lies outside of the range of our specimens but qualitatively agrees with the maximum penetration observed at about  $\theta=76$  degrees and the general shape of the curve. As is well known, ideal twin boundaries do not show preferential diffusion.<sup>4,18</sup> The 50-degree minimum agrees very well with the next cusp of the (332) planes. No other cusps are clearly distinguishable. This is in contrast to the energy measurements<sup>20</sup> which for angles below 90 degrees show the deepest minimum at 70 degrees and a secondary minimum near 40 degrees; presumably due to the (221) planes.

It appears thus that whether or not there is correlation between  $\delta$  and the depths of the energy minima there is little correlation between the depths of the energy minima and penetration minima though their occurrence at or near the cusps angles indicates certain common features. An inspection of the probable structure of the grain boundaries at the various cusp angles as shown in Fig. 3 indicates, however, a possible way of explaining the various penetrations. It appears that there is a pronounced difference in the "openness" of the various grain boundaries which does not seem to be related in any simple way to  $\delta$ . In Fig. 3, atoms drawn full are those which occupy essentially normal lattice

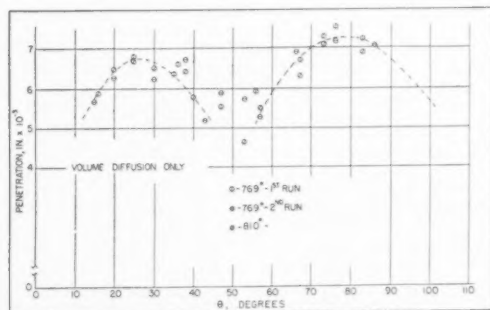


Fig. 2. Depth of grain-boundary penetration as a function of angle between cubic directions of the two grains.



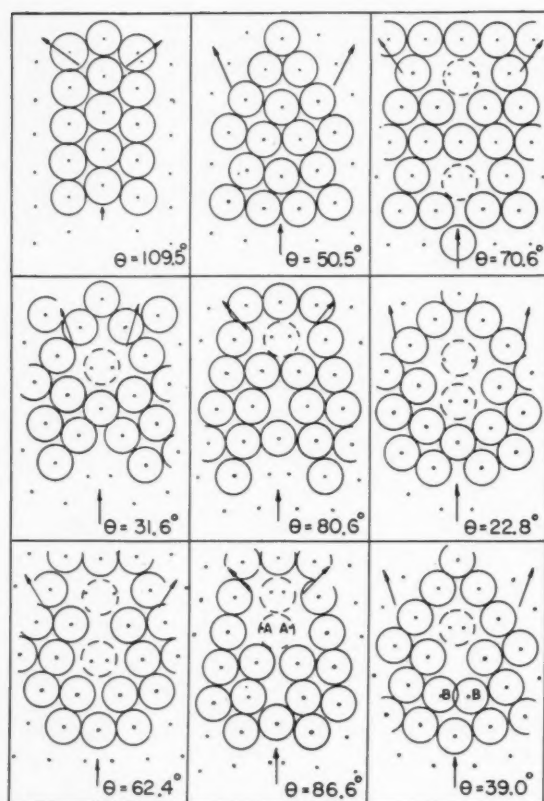


Fig. 3. Structure of grain boundaries at the most important cusp positions ( $0^\circ < \theta < 90^\circ$ ). (The atom just above the vertical arrow in the drawing for  $\theta = 86.6^\circ$  should have been drawn somewhat lower so as to have only two nearest neighbors in the plane of the drawing.)

positions. Some of them, as atoms *B* for  $\theta = 39$  degrees, may have a slightly tight fit but they have at least half of their normal contingent of first and second neighbors in proper positions. For  $\theta = 86.6$  degrees, atoms *A* would be squeezed and would have less than half the normal number of first and second neighbors and are

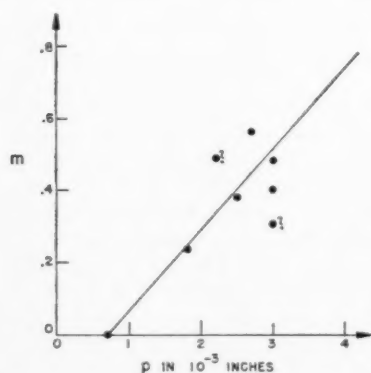


Fig. 4. Grain-boundary penetration  $p$  as a function of the density of atoms of misfit  $m$  at cusp angles.

thus considered replaced by mobile atoms. These mobile atoms do not belong to any specific grain and are indicated by dotted circles. Certain of the openings or channels are too small to accommodate any such atoms of misfit. Thus it seems plausible to try to relate the penetration to the density  $m$  of atoms of misfit in the various grain boundaries. The values of  $m$  are listed in Table I together with the best estimates of the grain-boundary penetration  $p$  beyond the limit of volume diffusion. Figure 4 shows the plot of  $m$  versus  $p$ . Question marks near the points for the (556) and (776) cusps indicate that these penetration values are much less certain than for other cusps. Apparently in spite of a large scatter of points there is an approximately linear correlation between  $m$  and  $p$ . As mentioned before, no such correlation exists with  $\delta$  or with the depths of the energy minima. In particular the relatively low value of penetration near 39 degrees, which is a high  $\delta$  cusp, and the relatively high penetration near 70 degrees, which is a low  $\delta$  cusp, seem to be understandable in terms of the density of atoms of misfit. A further check on this interpretation may be provided by extending the measurements to higher angles. In particular, at  $\theta = 164$  degrees, one would expect a cusp in spite of a rather large  $\delta$ .

#### ACKNOWLEDGMENT

The authors acknowledge with thanks the aid of S. Toney and A. Pranatis in carrying out the experimental work. They are grateful to the Allegheny-Ludlum Steel Corporation for the silicon iron used in this investigation and to the United States Atomic Energy Commission for the granting of a fellowship to one of them and also for support of part of the work by contract.

#### REFERENCES

1. R. F. Mehl, Trans. A.I.M.E. **122**, 11 (1936).
2. F. Keller and R. H. Brown, Trans. A.I.M.E. **156**, 377 (1944).
3. R. S. Barnes, Nature **166**, 1032 (1950).
4. R. S. Barnes, Metal Treatment and Drop Forging **18**, 531 (1951).
5. R. E. Hoffman and D. Turnbull, J. Appl. Phys. **22**, 634 (1951).
6. M. R. Achter and R. Smoluchowski, J. Appl. Phys. **22**, 1260 (1951).
7. M. R. Flanagan and R. Smoluchowski, J. Appl. Phys. **23**, 785 (1952).
8. R. Smoluchowski, Phys. Rev. **87**, 482 (1952).
9. S. R. L. Couling and R. Smoluchowski, J. Appl. Phys. **25**, 1538 (1954).
10. J. C. Fisher, J. Appl. Phys. **22**, 74 (1951).
11. R. T. P. Whipple, AERE Report T/R 1026, Harwell (1952).
12. C. S. Barrett, Structure of Metals, McGraw-Hill, New York (1943).
13. C. G. Dunn, J. Metals **1**, 72 (1949).
14. C. G. Dunn and G. C. Nonken, Metal Progress **64** (1953), No. 6, p. 71.
15. F. S. Buffington, I. D. Bakalar and M. Cohen, "Phys. of Powder Metallurgy," McGraw-Hill, New York (1951), Chap. 6.
16. C. E. Birchenall and R. F. Mehl, Trans. A.I.M.E. **188**, 144 (1950).
17. D. Turnbull and R. E. Hoffman, Acta Met. **2**, 419 (1954).
18. P. J. Fensham, Australian J. Sci. Res. **A3**, 105 (1950).
19. W. T. Read and W. Shockley, Phys. Rev. **78**, 275 (1950).
20. C. G. Dunn and F. Lionetti, J. Metals **1**, 125 (1949).

## INTERNAL FRICTION IN SOLID SOLUTIONS OF OXYGEN-TANTALUM\*

R. W. POWERS†

The breadth of the internal friction peak ( $Q^{-1}$  vs  $1/T$ ) arising from the diffusion of oxygen in tantalum has been found to increase monotonically with the oxygen concentration. Broadening was found to occur asymmetrically by displacement of the high-temperature branch of the damping curve. The data can be described by assuming that the experimental internal friction peak is a composite of the dilute oxygen peak found at 137°C (for  $\nu=0.6$  cps), with an activation energy of 25,000 cal/mole, and a second peak located near 162°C.

Evidence is presented which indicates that the peak previously attributed to carbon in tantalum actually is caused by oxygen at low concentrations.

In an attempt to determine the nature of the interaction giving rise to the broadening of the oxygen peak, it was observed that atoms of another element, nitrogen, can also broaden it considerably. Plastic deformation apparently did not affect the peak breadth.

### FROTTEMENT INTERNE DES SOLUTIONS SOLIDES TANTALE-OXYGÈNE

La largeur du pic de frottement interne ( $Q^{-1}$ ,  $1/T$ ) due à la diffusion de l'oxygène dans le tantale, croît de façon continue avec la concentration en oxygène. On montre que l'élargissement est dû à un déplacement de la partie de la courbe d'amortissement correspondant aux hautes températures. Les résultats peuvent être expliqués en supposant que le pic de frottement interne expérimental résulte de la superposition du maximum observé à 137° (pour  $\nu=0.6$  cps) correspondant à l'oxygène dissous avec une énergie d'activation de 25.000 cal/mol et d'un second maximum situé vers 162°.

Il est montré que le maximum précédemment attribué au carbone dans le tantale est dû à l'oxygène en faible concentration.

Pour déterminer la nature de l'interaction provoquant l'élargissement du maximum dû à l'oxygène, il a été observé que les atomes d'autres éléments comme l'azote, peuvent également l'élargir fortement. Par contre, la déformation plastique n'effecte pas cette largeur.

### INNERE REIBUNG IN FESTEN LÖSUNGEN AUS TANTAL-SAUERSTOFF

Die Breite des Maximums der inneren Reibung ( $Q^{-1}$  vs  $1/T$ ), die durch die Sauerstoffdiffusion in Tantal hervorgerufen wird, steigt gleichmässig mit der Sauerstoffkonzentration an. Bei einer Verlagerung des Hochtemperaturastes der Dämpfungskurve tritt eine unsymmetrische Verbreiterung auf. Die Ergebnisse können mit der Annahme beschrieben werden, dass sich das experimentell gefundene Maximum der inneren Reibung aus dem geschwächten Sauerstoffmaximum bei 137°C (für  $\nu=0.6$  cps) mit einer Aktivierungsenergie von 25.000 cal/Mol und einem zweiten Maximum in der Umgebung von 132°C zusammensetzt.

Es wird bewiesen, dass das Maximum, welches früher dem Kohlenstoff im Tantal zugeschrieben wurde, in der Tat durch Sauerstoff in geringen Konzentrationen hervorgerufen wird.

Bei einem Versuch, die Natur der Ursache für die Verbreiterung des Sauerstoffmaximums zu finden, wurde beobachtet, dass auch Atome eines anderen Elementes, nämlich Stickstoff, eine beträchtliche Verbreiterung verursachen können. Durch plastische Verformung wird die Breite des Maximums nicht beeinflusst.

## INTRODUCTION

Several internal friction peaks ( $Q^{-1}$  vs  $1/T$ ) have been reported to arise from the stress-induced diffusion of interstitial atoms in body-centered cubic metals.<sup>1-5</sup> For those in which the peak height or maximum damping is relatively low, the internal friction can be described rather well in terms of a single relaxation time. However, if the peak is somewhat higher, the width of the damping curve is considerably greater than that calculated assuming a single relaxation time. As shown in Fig. 1, there appears to be almost a monotonous variation in the relative widths of the several peaks with their height. The relative width is defined here as the ratio of the width of the peak in terms of  $1/T$  measured at one-half the peak height to that width calculated assuming a single relaxation time. The initial objective of this

study, consequently, was to determine if the relative width of a damping curve depends in any manner on the peak height or interstitial atom concentration. The oxygen-tantalum system was chosen for study because of a previous observation<sup>1</sup> that the peak was relatively broad, and because of the great variation in peak heights possible. In addition, the nitrogen peak, which is difficult to remove by the vacuum treatment to be described, does not overlap the oxygen peak in this metal.

## MATERIAL, APPARATUS, AND LOADING TECHNIQUE

The tantalum used in this study was of 99.9 per cent purity. Internal friction measurements were made in a low-frequency torsional pendulum similar to the one described by Kê,<sup>3</sup> utilizing specimens 0.030 in. in diameter by 12 in. in length. It was found that by heating the specimens near 1950°C for four hours *in vacuo*, the internal friction could be reduced to less than

\* Received July 20, 1954.

† General Electric Research Laboratory, Schenectady, New York.

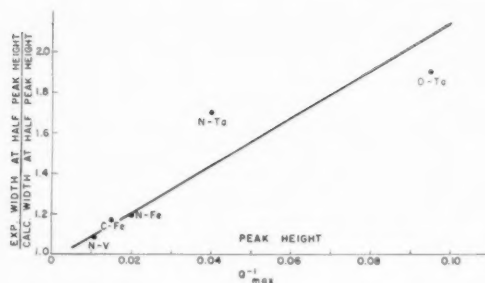


Fig. 1. Variation in the relative width of several peaks with their peak height.

0.001 in the temperature range 25–200°C. Thus all traces of the oxygen and carbon peaks previously reported to occur in this temperature range were erased.<sup>1</sup> The high vacuum system used for this treatment is depicted in Fig. 2. The tantalum wire is held in place vertically between stainless steel grips. In order to prevent bending as the tantalum is heated, the upper grip is held rigidly in place while the lower grip is left free to slide up and down along a glass rod. Large electric current leads are attached to the grips.

All the specimens used in this study first were degassed as described above and then were loaded with oxygen as follows. Variable quantities of high purity oxygen were metered into tube C (Fig. 2), in increments of the volume of the capillary tube B, by expanding oxygen from flask A into B and then into C. The tantalum wires were heated subsequently near 1600°C for several minutes during which time the pressure in the system declined to about  $10^{-4}$  mm as the oxygen was absorbed. With this technique, the danger of extra-

neous contamination was practically eliminated. The concentration of oxygen in each specimen was calculated from the known volume of the system, the oxygen pressure-drop, and the mass of the wire. It is probably known to within 10 per cent except for specimens 5 and 6. Less than one volume increment of oxygen was introduced into these specimens, and because of the relative insensitivity of the McLeod and Philips gages in the range used, the error in oxygen concentration may be 25 per cent.

## EXPERIMENTAL RESULTS

Pertinent data on the several specimens prepared are given in Table I. The internal friction of each wire was examined from room temperature up to about 250°C at a frequency near 0.6 cps. The results are plotted in

TABLE I. Pertinent data on specimens used in this investigation.

Sample No.	Oxygen peak $Q_{max}^{-1} \cdot 10^4$	Nitrogen peak $Q_{max}^{-1} \cdot 10^4$	Oxygen concentration wt %	Nitrogen concentration wt %	Comments
5	77	—	0.009	—	
6	133	—	0.016	—	
4	470	70	0.040	—	
7	880	—	0.081	—	
11	1340	80	0.121	—	
10	1670	—	0.163	—	
16	470	—	0.32	—	
9	23	—	—	—	Very broad peak Aquadag treatment. Carbon content ~0.07 wt %
20	0	—	—	—	Aquadag treatment. Carbon content ~0.09 wt %
15	386	70	0.032	0.005*	
19	275	550	0.032	0.041*	
13	258	850	0.032	0.076*	

\* Figures adjusted for estimated residual amounts of nitrogen not removed in initial degassing treatment.

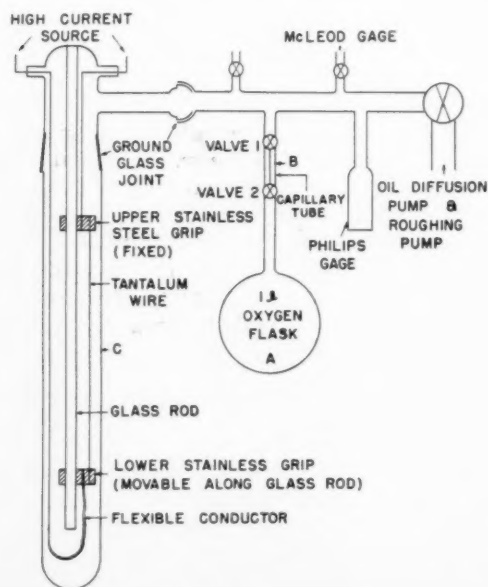


Fig. 2. Apparatus for evacuating and loading specimens.

Fig. 3 with the maximum internal friction normalized to unity in each case.

The most striking feature of this plot is the large variation in the width of the peak with oxygen concentration. This broadening is caused by the displacement of the high-temperature side of the internal friction peak since the low-temperature branches can almost be superimposed. The curve corresponding to the highest oxygen concentration (0.16 weight per cent) is about 50 per cent broader than the one corresponding to the lowest concentration investigated (0.009 weight per cent). In Fig. 4,  $W$ , the width at half the peak height, is plotted as a function of the concentration. Since the relationship is almost linear, the correlation indicated in Fig. 1 cannot be entirely fortuitous.

On extrapolating the width  $W$  to zero concentration, a value of  $0.212 \cdot 10^{-3}$  is obtained. This should represent the width of an oxygen-tantalum curve without any

"interaction" broadening. It may be readily shown\* that for an internal friction peak described by a single relaxation time,  $W$  is related to the activation energy by the expression  $E = 5.28/W$ . In this manner, assuming the width  $0.212 \cdot (10)^{-3}$  to correspond to a single relaxation time, a value of 25,000 cal/mole for the activation energy for the diffusion of oxygen in tantalum is obtained.

The experimental data in Fig. 3 can be described fairly well by assuming that in addition to the ordinary peak at 137°C ( $\nu = 0.6$  cps), there arises at 162°C another peak (hereafter called the extraordinary peak) which makes a larger and larger contribution to the measured damping as the concentration of oxygen is increased. The location of the extraordinary peak was obtained by subtracting the curve calculated for a single relaxation time from the experimental curves.

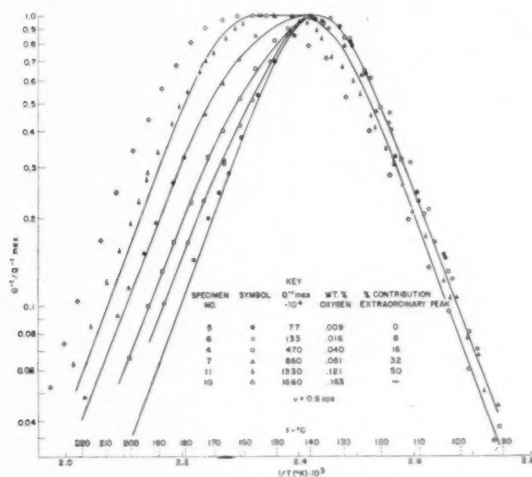


FIG. 3. Several oxygen-tantalum damping curves corresponding to different oxygen concentrations.

This extra peak corresponds, of course, to an extra relaxation time longer than the ordinary one.

By superposing two peaks, with varying weights assigned the two, the data for specimens Nos. 5, 6, 4, 7 and 11 have been approximated by the various curves shown in Fig. 3. The relative contributions of the 137°C and 162°C peaks used in calculating these curves are marked on the graph. For the purpose of curve fitting, an activation energy of 25,000 cal/mole has been

\* If only a single relaxation time,  $\tau = \tau_0 \exp E/RT$ , is operative, then

$$Q^{-1} = 2Q_{\max}^{-1} \left( \frac{2\pi\nu\tau}{1 + (2\pi\nu\tau)^2} \right) = 2Q_{\max}^{-1} \left( \frac{\exp[(1/T) - (1/T_{\text{peak}})]}{1 + \exp[2E/R(1/T - 1/T_{\text{peak}})]} \right)$$

When

$$Q^{-1} = \frac{Q_{\max}^{-1}}{2}, \quad W = 2(1/T - 1/T_{\text{peak}})$$

by definition. Solving,

$$E = \frac{5.28}{W}$$

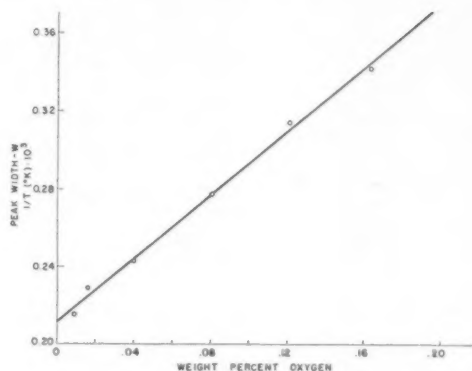


FIG. 4. Width of the oxygen-tantalum peak as a function of the oxygen concentration.

assumed for both the ordinary and the extraordinary peaks. Although Wert and Marx's correlation might indicate that a slightly higher value should be assumed for the extraordinary peak, the error introduced is not serious.<sup>6</sup>

Up to about 0.082 weight per cent oxygen, the fit in Fig. 3 is very good. Above this concentration, however, the deviation of the calculated curves from the experimental data becomes increasingly large. This deviation arises from the assumption of but one extraordinary peak rather than of a spectrum of such peaks. An indication of the breadth of the spectrum of extraordinary peaks for a specimen containing 0.32 weight per cent oxygen is furnished in Fig. 5. The width is

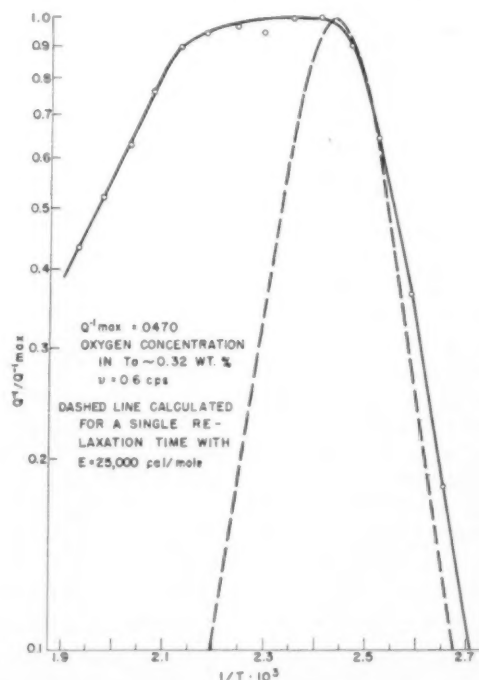


FIG. 5. An example of extreme peak broadening.



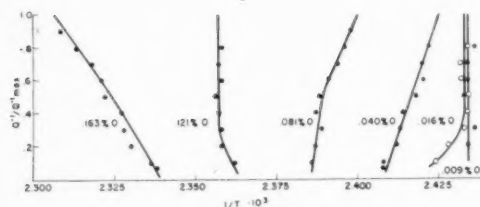


FIG. 6. The variation in skewness of the oxygen-tantalum peak with oxygen concentration.

2.7 times that calculated for a single relaxation time and the maximum internal friction is only 0.047.

It should be pointed out that the internal friction curves in Fig. 3 are not in general symmetric. This is illustrated in Fig. 6, where the normalized value of the internal friction plotted against the midpoint of the high- and low-temperature branches is employed as a measure of skewness. An internal friction peak described by a single relaxation time is symmetric about the reciprocal peak temperature. Thus in a plot such as Fig. 6, the locus of midpoints for a symmetrical peak defines a vertical line and any departure from the vertical can be used as a measure of asymmetry. Of special interest is the variation in skewness with the oxygen concentration. At low concentrations the internal friction curve is symmetric. As the concentration is increased, the curve becomes skewed from the contribution of the relatively small extraordinary peak. When the concentration reaches 0.10 per cent, the damping curve is almost symmetric again because the ordinary and extraordinary peaks are of approximately equal importance. At still higher concentrations, the curve is again skewed but in the opposite sense because now the extraordinary peak predominates.

Another consequence of the increasing contribution from the extraordinary peak with an increase in the oxygen concentration is a corresponding shift of the experimentally determined peak temperature towards higher temperatures. Peak temperatures for various oxygen concentrations were obtained by an extrapolation of the several curves in Fig. 6 to unity on the ordinate scale. This procedure has been described in more detail previously.<sup>5</sup> In Fig. 7a, the reciprocal of the peak temperature has been plotted as a function of the oxygen concentration. As is seen in Fig. 7b, the reciprocal absolute temperature of the peak is approximately a quadratic function of the oxygen concentration. Such a shift has been noted also by Marx, Baker and Sivertsen in their study at high frequencies.<sup>7</sup>

The changes in the character of the oxygen-tantalum internal friction peak with concentration explain the apparent anomaly of the carbon peak in tantalum. Whereas the carbon and nitrogen peaks in iron occur at 40 and 24°C respectively, at 1 cps, the corresponding peaks in tantalum were reported to occur at the widely separated temperatures of 150 and 350°C.<sup>1,2</sup> It is now evident that the peak previously attributed to carbon is really the

oxygen peak at low concentrations, and the broad peak previously attributed to oxygen is a composite of the ordinary and extraordinary oxygen peaks at higher oxygen concentration.

This conclusion relative to the "carbon" peak in tantalum was confirmed by the following experiments. Chemical analysis indicated the carbon content of a degassed specimen to be less than 0.01 weight per cent, the limit of the analysis. A wire previously degassed was coated with Aquadag and heated at 1100°C for 48 hours in a high vacuum. Although the carbon content was increased to 0.07 weight per cent by this treatment, the maximum internal friction was only 0.0023 at 137°C. This small peak can be readily attributed to the absorption of oxygen during carburization, as oxygen may have been absorbed on the specimen prior to coating with Aquadag. In a second experiment, a specimen was coated with Aquadag and heated at 1800°C for four hours in a high vacuum. In the temperature interval from 30–200°C, the internal friction in this specimen did not exceed 0.0008, the background damping. Chemical analysis later indicated that the carbon content of this wire amounted to 0.09 weight per cent. It should be pointed out that no carbon peak was found in vanadium either.<sup>5</sup> Moreover, the activation energy of 25,000 cal/mole determined from the extrapolated width of the oxygen-tantalum peak at zero oxygen concentration agrees exactly with that previously determined for the "carbon" peak while the activation energy for the broad oxygen peak was found previously to be 29,000 cal/mole.<sup>1</sup>

#### SOME ADDITIONAL EXPERIMENTS

Zener has considered the strain interaction between interstitial solute atoms in body-centered cubic metals.<sup>8</sup> Although his results are not in a form such that they can be directly applied to the data obtained in the present experiment, they suggested some further experiments. In order to determine whether a strain inter-

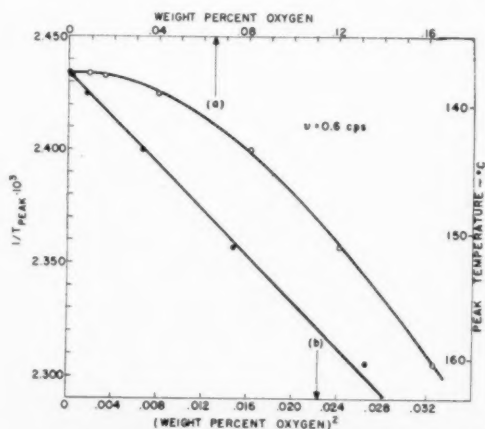


FIG. 7. Shift in the oxygen-tantalum peak temperature with oxygen concentration.

action could give rise to peak broadening, the tantalum lattice was strained by other means and the breadth of the oxygen peak was observed. The two methods of straining considered in this investigation were the presence of another kind of interstitial atom (nitrogen), and cold work. Although the experimental results leave unsettled the question of the nature of the interaction, they are nevertheless interesting in themselves and are described below.

In order to examine the effect of the presence of interstitially dissolved nitrogen on the oxygen internal friction peak, three specimens were prepared, all containing 0.032 weight per cent oxygen. The first specimen contained only a residual amount of nitrogen, estimated to be about 0.005 weight per cent. The second was loaded with an additional 0.04 weight per cent and the third with an additional 0.08 weight per cent nitrogen. The results of measurements on these specimens are found in Fig. 8. The broadening is very great. It should be pointed out that because of the large separation in temperature between the oxygen and nitrogen peaks, the contribution from the tail of the nitrogen peak has an almost negligible effect on the measurement of the oxygen peak. With nitrogen, the extraordinary peak occurs near 175°C instead of near 162°C, as in the case of oxygen alone.

In order to study the effect of cold work, 60-mil wire specimens were degassed, loaded with 0.016 weight per cent oxygen, cold-swaged to 32-mils diameter, and aged. No broadening of the internal friction peak was observed. However, other interesting effects associated with plastically deformed tantalum will form the subject of another report.

### CONCLUSION

The peak broadening and associated phenomena discussed in this report are believed to be rather general for interstitial solutions based on the  $\bar{V}B$  elements. A number of observations support this belief. A concentration-dependent skewness was noted in the internal friction peak arising from the diffusion of oxygen in vanadium.<sup>5</sup> Close inspection of Kê's data for the nitro-

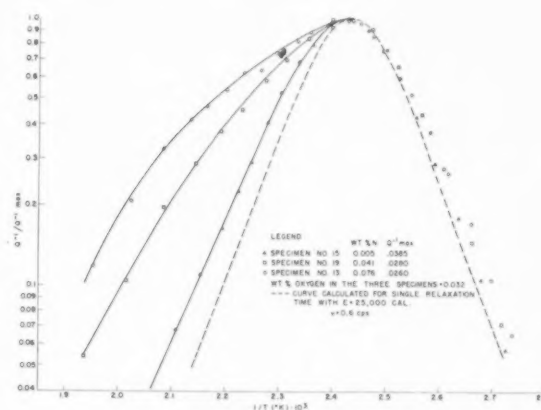


FIG. 8. The effect of nitrogen in broadening the oxygen-tantalum damping peak.

gen-tantalum peak (reference 2, Fig. 1) shows that the temperature at which the internal friction equals one-half the maximum value remains almost invariant with changes in the peak height on the low-temperature side of the peak. However, the corresponding point on the high-temperature side shifts toward higher temperature with increasing peak height. Moreover, there is the previously mentioned observation of Marx, Baker and Sivertsen on the shift in the peak temperature with concentration in several solid solutions.<sup>7</sup>

### ACKNOWLEDGMENTS

The author is very grateful to J. C. Fisher, R. H. Pry, and G. W. Ardley for reviewing the manuscript.

### REFERENCES

1. T. S. Kê, Phys. Rev. **74**, 9 (1948).
2. T. S. Kê, Phys. Rev. **74**, 914 (1948).
3. T. S. Kê, Am. Inst. Mining Met. Engrs. Tech. Publ. No. 2370 (1948).
4. C. A. Wert, in Modern Research Techniques in Physical Metallurgy, A.S.M. (1952).
5. R. W. Powers, Acta Met. **2**, 604 (1954).
6. Wert and Marx, Acta Met. **1**, 113 (1953).
7. Marx, Baker, and Sivertsen, Acta Met. **1**, 193 (1953).
8. C. Zener, Phys. Rev. **74**, 638 (1948).

# MECHANISM OF PORE FORMATION ASSOCIATED WITH THE KIRKENDALL EFFECT\*

J. A. BRINKMAN†

It is shown that a two-dimensional tensile stress is established in Kirkendall-type diffusion specimens on the side of the interface suffering a net loss of atoms. In the presence of this stress, voids larger than a critical size will grow by absorbing vacant lattice sites when the concentration of such sites is maintained at its equilibrium value. A mechanism is proposed by which the tensile stress can nucleate voids of this critical size or larger. Thus the proposed mechanism of nucleation and growth of the voids formed in connection with Kirkendall-type diffusion experiments can operate without the existence of an excess concentration of vacancies.

## MÉCANISME DE LA FORMATION DE PORES ASSOCIÉ À L'EFFET KIRKENDALL

Il est montré qu'un état bidimensionnel de contrainte de traction est créé dans l'effet Kirkendall du côté de l'interface où se produit une perte d'atomes. Sous l'action de ces contraintes, des vides plus larges qu'une certaine dimension critique grossiront en absorbant des lacunes si la concentration de celles-ci est maintenue à sa valeur d'équilibre. Un mécanisme est proposé, permettant à ces tractions de provoquer la germination de vides ayant au moins cette dimension critique. Ainsi donc, ce mécanisme de germination et de croissance des vides formés dans les expériences de Kirkendall peut se produire sans admettre une sur-saturation en lacunes.

## MECHANISMUS DER PORENBILDUNG IN VERBINDUNG MIT DEM KIRKENDALL-EFFEKT

Es wird gezeigt, dass in Diffusionsproben nach Kirkendall auf der interface eine zweidimensionale Zugspannung entsteht, die einen Nettoverlust an Atomen verursacht. Beim Auftreten dieser Spannung erreichen Hohlstellen eine größe über dem kritischen Wert durch Absorption von Gitterleerstellen, wenn deren Konzentration im Gleichgewicht gehalten wird. Es wird ein Mechanismus vorgeschlagen, durch den erklärt werden kann, dass die Zugspannung keimbildend für Hohlstellen von oder über der kritischen Grösse wirkt. Auf diese Weise kann eine Erklärung der Keimbildung und des Wachstums von Poren, die bei Diffusionsversuchen nach Kirkendall gebildet werden, ohne Annahme einer Überschusskonzentration an Fehlstellen gegeben werden.

### 1. INTRODUCTION

Seitz<sup>1</sup> has treated the development of porosity on one side of the Kirkendall interface during Kirkendall-type diffusion experiments as a result of the condensation of a superconcentration of vacancies in a region of the diffusion zone about  $10^{-2}$  cm in extent. In order that this be the formation mechanism of the voids, it was concluded that either (1) the relative excess concentration of vacancies must reach values of the order of unity, or (2) relatively large voids, imperfections, or impurities already exist, which can operate as nuclei for voids at relative excess concentrations as small as 0.01. Seitz favored the first alternative, which was shown to imply that the average vacancy lifetime was of the order of  $10^{11}$  jumps or greater.

Balluffi,<sup>2</sup> in a recent discussion of the formation of voids during dezincification of alpha-brass and Kirkendall-type diffusion experiments, concluded that it is unlikely that the relative excess vacancy concentration exceeds 0.01 over a region as large as that considered by Seitz. He favored the second of the above alternatives and presented evidence that when impurity particles are present, their location determines the location of at least a portion of the voids.

Both Seitz and Balluffi assume that some relative excess concentration of vacancies is necessary for a void

to form and grow and that the achievement of a certain critical excess concentration in a given region or in the neighborhood of a given impurity particle is the criterion determining whether or not a void will be formed. For a given spherical void the critical concentration which must be exceeded before the void can grow, according to Seitz, is given by

$$\ln \frac{N_v}{N_{v0}} = \frac{2s}{kTNr_0}, \quad (1)$$

where  $N_v$  is the vacancy concentration which must be exceeded,  $N_{v0}$  is the equilibrium vacancy concentration,  $r_0$  is the radius of the void,  $s$  is the surface energy of the void per unit area,  $N$  is the atomic density,  $k$  is Boltzmann's constant, and  $T$  is the absolute temperature. If the nuclei consist of impurity particles, it is conceivable that the effective values of  $r_0$  may be appreciably different from the actual physical dimensions of the particles when they first begin to grow, due to localized strains. However, it would seem that these strains should be relaxed before the void grows to twice the size of the impurity particle, at which time the actual physical radius of the void should become the effective  $r_0$ . Thus, one might expect the effects of any effective  $r_0$  values large relative to the actual size of the particles to be short lived and therefore negligible. According to Seitz, an excess vacancy concentration of 0.01 will produce growth of only those voids whose effective radius is of the order of 1000 atomic distances or greater. Thus, if

\* Received August 2, 1954.

† Atomic Energy Research Department, North American Aviation, Inc., Downey, California.

one accepts Seitz' criterion for growth, Balluffi's conclusion that the excess vacancy concentration does not exceed 0.01, and the above reasoning, voids with diameters of the order of 1 micron or larger must somehow be established before growth can occur by absorption of vacancies.

Seitz' criterion for the growth of voids is based upon the assumption that the change in energy of the system upon absorption of a vacancy by a void consists only of the energy decrease associated with the annihilation of one vacancy (equal to the vacancy formation energy) and the energy increase associated with the extra surface area of the void due to its increased size. The possibility of a change in the potential energy in the region around a void upon absorption of a vacancy in case a stress field is present has not as yet been considered. As will be shown below, if an appreciable number of the vacancies (interstitials) are annihilated (created) at edge dislocations, then a stress field will be established in the region in which the voids are formed; and the change in volume energy as well as the change in surface energy should be considered in deriving the criterion for growth of voids.

## 2. CALCULATION OF STRESS IN REGION OF VOID FORMATION

For convenience, the defects responsible for diffusion will be referred to in the following discussion as vacancies, although the arguments presented should be equally valid for interstitials. The stress produced by a net efflux of atoms from a region of crystal having the geometry and the constraints appropriate to the Kirkendall experiment will be calculated.

Consider an element of volume, originally in the form of a cube, on the side of the interface toward which the interfacial markers move. The boundaries of this element are to be considered as being defined by the atom sites originally just within and just without the element and will shift with time just as the interfacial markers shift. After the diffusion zone reaches this element, the equilibrium between vacancy flow in and out will be destroyed as a result of the pumping action of the chemical gradient on the vacancy current. Imagine that the particular volume element considered can be isolated from the surrounding crystal at any given time, allowing its dimensions to relax. It will have lost a net number  $\Delta N$ , of the total number,  $N$ , of atoms which it originally contained. These  $\Delta N$  atoms will have been replaced by an equal number of vacancies. The vacancies can be separated into two groups,  $\Delta N_1$  and  $\Delta N_2$ , the first of which will have been annihilated at edge dislocations while the second will have condensed on voids. The vacancies which condense on voids will continue to occupy a volume comparable with the volume which they occupied as dispersed vacancies, and therefore also comparable with the volume of atoms which they replaced. The volume originally occupied by the atoms replaced by the vacancies which were annihilated at

edge dislocations is no longer enclosed by the boundaries of our volume element, and therefore the volume of the element will have been decreased by  $\Delta N_1$  atom sites, to a first approximation. Assume that these  $\Delta N_1$  atoms have been furnished at random from the various edge dislocations in the element. The element will have shrunk in a uniform manner such that when removed from the crystal, i.e., when no stresses are acting on it, the original cubic shape will be retained. The cube edge will have shrunk from the original length,  $l$ , to a smaller length,  $l - \Delta l$ . Only first order terms in  $\Delta l$  will be retained. Then one obtains

$$\frac{\Delta N_1}{N} = \frac{3\Delta l}{l} \quad (2)$$

Now consider the same volume element again in its normal position in the crystal. Each neighboring element will experience the same tendency to shrink as does this one. However, due to the geometry associated with the Kirkendall experiment, relaxation can occur only in the direction of diffusion, i.e., the vertical direction (the interface and diffusion region are considered infinite in extent in the two horizontal dimensions). The tendency to relax horizontally will give rise to a horizontal tensile stress in the rather narrow region below the interface from which the net flow of atoms originates. This tensile stress in the volume element will now be calculated by allowing complete relaxation vertically and none horizontally.

The two equal horizontal tensile stresses,  $F$ , which must be applied to the vertical faces of the stress-free cube of side,  $l - \Delta l$ , to elastically deform it until the horizontal edges are equal in length to the initial length,  $l$ , are related to the deformation,  $\Delta l$ , through the expression

$$\Delta l = l - \frac{F}{Y}(1 - \sigma), \quad (3)$$

where  $Y$  is Young's modulus and  $\sigma$  is Poisson's ratio. One can then make use of Eq. (2) and the relationship between the bulk modulus,  $k$ , Young's modulus, and Poisson's ratio.

$$Y = 3k(1 - 2\sigma), \quad (4)$$

to obtain the desired expression for the stress in terms of the bulk modulus, Poisson's ratio, and the fraction of atom sites which have been removed from the element

$$F = k \left( \frac{1 - 2\sigma}{1 - \sigma} \right) \frac{\Delta N_1}{N} \quad (5)$$

Here only the two independent elastic constants for continuous media, rather than the three or more of crystalline metals, have been used. The justification for this choice is the fact that, as yet, no variation of the nature of the observed porosity with orientation of the grains has been established.



Inserting appropriate values in Eq. (5), this stress is found to become appreciable for relatively small values of  $\Delta N_1/N$ , approaching the yield stress of the material for  $\Delta N_1/N \sim 10^{-3}$ . Typical Kirkendall experiments yield values of  $\Delta N/N$  at least two orders of magnitude larger than this in narrow regions of the specimens parallel to the Kirkendall interface. Therefore a two-dimensional tensile stress comparable in magnitude with the yield stress of the material will be established parallel to the Kirkendall interface within such narrow regions if 1 per cent or more of the vacancies annihilate at edge dislocations and if the assumption is true that the  $\Delta N_1$  atoms have been supplied equally from all edge dislocations present in the volume element rather than preferentially from those of a particular orientation. This assumption will be considered in greater detail in the following section.

### 3. ESTIMATE OF IMPORTANCE OF DISLOCATION ORIENTATION

Contraction of the material in a direction perpendicular to the Kirkendall interface conceivably could be achieved by the annihilation of vacancies predominantly at those edge dislocations whose Burgers' vectors are perpendicular to the Kirkendall interface. Such a contraction would be one dimensional and could not tend to establish any tensile stress, since relaxation is permitted in this direction. At the beginning of the diffusion the vacancies will annihilate equally at dislocations of all orientations. However, after some of the atoms have been removed, a horizontal tensile stress will be established and there will, as a result, be some preference for subsequent atoms to be furnished by edge dislocations with Burgers' vectors perpendicular to the Kirkendall interface rather than parallel. The magnitude of this effect can be estimated as follows. (In this case the considerations differ, depending on whether interstitials or vacancies are the migrating defects.)

For the interstitial case, the net efflux of atoms originates as interstitials at the edge dislocations of the material. The rate of production of these interstitials per unit length of dislocation will be proportional to  $\exp(-E_i/kT)$ , where  $T$  represents the absolute temperature,  $k$  is Boltzmann's constant, and  $E_i$  is the energy required to form an interstitial. Nabarro has shown<sup>3</sup> that the energy necessary for the creation of a vacancy at the surface of a crystal will be increased by an amount equal to  $FV$ , where  $F$  is the normal component of the stress (positive for compression) and  $V$  represents 1 atomic volume. A similar conclusion can be drawn for the formation energy of either interstitials or vacancies which are created at edge dislocations if the corresponding surface is chosen as that containing the extra half plane of atoms associated with the edge dislocation. Thus, in the present case, the formation energy of interstitials at edge dislocations should vary from  $E_{i0}$  to  $E_{i0} + FV$ , the exact value for each dislocation depending on its orientation in the stress field. Here  $E_{i0}$

is the value of  $E_i$  in zero stress field. The ratio of the rate at which interstitials are created from the dislocations at which the required energy is least to the rate from those at which it is the greatest is given by  $\exp(FV/kT)$ , where  $F$  is the maximum stress which can be achieved due to the fact that deformation occurs. Using typical values of the yield strength of the face-centered cubic metals at high temperatures for  $F$ , a maximum value of about 1.02 is obtained for this ratio. Thus, for the case of interstitial diffusion, the rate at which atoms are supplied from edge dislocations varies with the direction of the Burgers' vector by a maximum of about 2 per cent.

For the case of vacancy diffusion, one is concerned with the relative rates of annihilation rather than the production of defects at dislocations of different orientations. As  $E_v$ , the formation energy of vacancies, is large relative to  $FV$  and  $kT$ , essentially all vacancies coming within a given distance of a dislocation (or jog, as the case may be) can be considered to be annihilated, i.e., the fraction which comes within the range of strong attraction and immediately escapes again is negligible. A "cross section" for capture of vacancies per unit length of dislocation can therefore be considered. The relationship of this cross section to the applied stress is not as simple as the dependence of the vacancy or interstitial formation energy on the applied stress; however, it seems almost certain that it will be less sensitive and that the corresponding ratio of the maximum and minimum rates of vacancy annihilation at dislocations of different orientations will be less than that for interstitials, 1.02. Thus, the assumption that the  $\Delta N_1$  atoms originate randomly from the various edge dislocations seems justified to within 2 per cent, a result which is sufficient for the present considerations.

### 4. CALCULATION OF THOMAS-GIBBS RELATION FOR VOIDS IN A THREE-DIMENSIONAL STRESS FIELD

The preceding arguments indicate that a tensile stress is established in the region of the diffusion zone in which the voids appear during a Kirkendall-type diffusion experiment. Barnes has demonstrated the presence of a stress field in the diffusion zone during such experiments.<sup>4</sup> The potential energy stored in the strained material around a given void by this stress field will be a function of the radius of the void (assumed spherical). This energy and its dependence on the size of the void will be calculated for the case of a three-dimensional stress field, rather than the actual two-dimensional stress, to simplify the geometry. The result should be of the same order of magnitude for either stress field.

Consider a sphere of material of radius,  $R$ , with a single void of radius,  $r_0$ , located at its center. The vector displacement,  $\xi$ , of any point between the surfaces  $r=r_0$  and  $r=R$  must satisfy the equation

$$\nabla^2 \xi + (1 + \lambda/\mu) \nabla(\nabla \cdot \xi) = 0, \quad (6)$$

where  $\lambda$  and  $\mu$  are the conventional elastic constants

relating the elements of the stress tensor to those of the strain tensor. The first element of the stress tensor, expressed in spherical coordinates, is

$$T_{rr} = \lambda(\nabla \cdot \xi) + 2\mu \frac{d}{dr}(\mathbf{a}_r \cdot \xi), \quad (7)$$

where  $\mathbf{a}_r$  denotes the unit vector in the radial direction. The boundary conditions to be applied are

$$\begin{aligned} T_{rr} &= -\frac{2s}{r_0} \quad \text{at } r=r_0, \\ T_{rr} &= F \quad \text{at } r=R, \end{aligned} \quad (8)$$

and because of the spherical symmetry,

$$\xi = \mathbf{a}_r \xi_r. \quad (9)$$

Solving Eq. (6) under these boundary conditions, one obtains

$$\xi_r(r) = \frac{1}{\lambda + 2\mu} \left[ \frac{FR^3 - 2sr_0^2}{R^3 - r_0^3} r + \frac{Fr_0^3 - 2sr_0^2}{R^3 - r_0^3} \frac{R^3}{2r^2} \right], \quad (10)$$

$$T_{rr}(r) = \frac{FR^3 - 2sr_0^2}{R^3 - r_0^3} - \frac{Fr_0^3 - 2sr_0^2}{R^3 - r_0^3} \frac{R^3}{r^3}. \quad (11)$$

The potential energy stored in the system is given by

$$V(r_0, R) = 2\pi R^2 T_{rr}(R) \xi_r(R). \quad (12)$$

The elementary step in the growth of a void consists of the formation of a vacancy outside the stress field, migration of this vacancy into the stress field to the void and its absorption by the void. During this process,  $\xi_r(R)$  is held constant. Thus  $F$  cannot remain constant but must be considered a function of  $r_0$  during such a step in the growth of a void:

$$F = F(r_0).$$

One can define  $F(0)$  as the stress which would exist if the void were to completely dissolve, and the resulting vacancies were to migrate out of the stressed region. Then the condition that  $\xi_r(R)$  remains constant can be applied to obtain the dependence of  $F$  on  $r_0$ :

$$F(r_0) = \frac{F(0)(R^3 - r_0^3) + 3sr_0^2}{R^3 + (1/2)r_0^3}. \quad (13)$$

The energy stored in the stress field is then found to be

$$V(r_0, R) = \frac{2\pi R^3 F(0)}{\lambda + 2\mu} \left[ \frac{F(0)(R^3 - r_0^3) + 3sr_0^2}{R^3 + (1/2)r_0^3} \right]. \quad (14)$$

The change in this energy due to the presence of the void is given by

$$\Delta V = V(r_0, R) - V(0, R). \quad (15)$$

When  $R$  is appreciably greater than  $r_0$ ,  $\Delta V$  is approxi-

mately

$$\Delta V \approx -\frac{3\pi F(0)}{\lambda + 2\mu} \left[ F(0) - \frac{2s}{r_0} \right] r_0^3. \quad (16)$$

This expression represents the volume strain energy associated with a given void of radius,  $r_0$ . As seen from Eq. (13),  $F(0)$  and  $F(r_0)$  are nearly equal when  $R \gg r_0$ . Therefore, in Eq. (16),  $F(0)$  can be taken as the actual stress present in the material.

The change in  $\Delta V$  per vacancy absorbed is

$$\frac{d(\Delta V)}{dn} = -\frac{3F(0)}{4N(\lambda + 2\mu)} \left[ 3F(0) - \frac{4s}{r_0} \right], \quad (17)$$

where  $N$  represents the atomic density and  $n$  the number of lattice sites included in the void. The change in the surface energy of the void,  $S$ , per vacancy absorbed is

$$\frac{dS}{dn} = \frac{2s}{Nr_0}. \quad (18)$$

Therefore, when a stress field is present, a volume energy term as well as the surface energy term considered by Seitz should be included in the Thomas-Gibbs relation, giving

$$\ln \frac{N_v}{N_{v0}} = \left[ \frac{2s}{r_0} - \frac{3F(0)}{4(\lambda + 2\mu)} \left( 3F(0) - \frac{4s}{r_0} \right) \right] / NkT. \quad (19)$$

If  $F(0)$  is taken to be of the order of  $10^9$  dynes/cm<sup>2</sup>, this quantity changes sign for copper when  $r_0 \sim 10^{-3}$  cm. This value of  $r_0$  is not too different from the "effective radius" of the nuclei which Seitz and Balluffi found it necessary to assume if the excess concentration did not exceed 0.01. Thus, once nuclei of this effective radius are formed, no excess concentration is required for their growth, according to Eq. (19), if a stress field of sufficient strength is present. In the next section a mechanism is proposed by which the stress field can nucleate voids in the absence of any excess vacancy concentration.

## 5. PROPOSED NUCLEATION MECHANISM FOR VOIDS

The two-dimensional tensile stress which is established in the diffusion zone will become sufficient to produce some sort of deformation of the material if more than 1 per cent of the vacancies are annihilated at edge dislocations, a situation which seems highly probable. Smith<sup>6</sup> has considered the case of deformation under such a stress in an early attempt to explain the Kirkendall effect. His stress field was postulated to arise from the change in lattice parameter, while that considered at present arises from a net efflux of atoms from a region of the crystal. The results, however, should be equally valid in the present case.

Smith points out that slip can occur but will be more difficult than in the case of a one-dimensional stress, due

to the additional constraints (hence the assumed value of  $10^9$  dynes/cm<sup>2</sup> for the tensile stress in Section 4, a value somewhat higher than the observed yield stress for polycrystalline copper pulled in uniaxial tension at high temperature<sup>6</sup>). Furthermore, he points out that it cannot completely relieve the local strain. He suggests that the most probable deformation mechanism is fissuring on a microscale in a manner analogous (except for crystalline directionality) to the cracking of a mud flat on drying. Such local cracking requires less energy than the extended slip required for relaxation of the stress through plastic flow.

Such fissures, when formed, would be long and narrow in shape but would rapidly shrink by surface diffusion minimizing their surface area. Thus, within a short time after their formation they should be nearly spherical in shape (or polyhedral if the influence of crystalline structure is sufficiently strong). These holes could conceivably be large enough for growth to continue by absorption of vacancies, even in the presence of no excess vacancy concentration. Thus it seems possible that the voids may be nucleated and grow without requiring the vacancy concentration to deviate from its equilibrium value in any region of the material. The vacancies could all annihilate at edge dislocations until voids were nucleated by the fissuring process, at which time the flow of vacancies could separate into two parts, some going to voids and others to edge dislocations.

Let us now consider the details of the fissuring process in an effort to understand the distribution of the voids. When local regions of greater than average stress concentration are present in the material, the fissures would be expected to start in such regions. If impurity particles are present, the stress field should be more concentrated around them; hence, it is possible that impurity particles will act in the same manner as the pre-existing cracks which Griffith<sup>7</sup> assumes to be present in amorphous materials. Thus fissures may start at impurity particles and extend away from them under the action of the tensile stress. Balluffi's observation that the location of the voids is influenced by the location of impurities is in agreement with this concept. A random distribution of impurity particles in the void-formation region might be expected to produce a random distribution of voids, according to this picture. Suppose, however, that no impurity particles are present and that localized stress concentrations therefore cannot be established. The region of maximum stress will then be the neighborhood close to a plane parallel to and moving away from the Kirkendall interface. It seems likely in this case that slip will commence before fissures develop. The slip pattern in this case will be rather complex, in view of the constraint requiring the deformation in two dimensions to be the same, even within grains. Multiple slip must occur from the very beginning of the deformation. Furthermore, only that portion of each slip plane which lies in the stressed

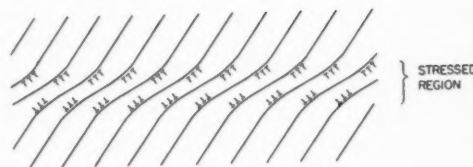


FIG. 1. Piling up of dislocations on slip planes near the edges of the stressed region of crystal within a single grain.

region can undergo slip. That is, the slip lines must terminate within the grains, rather than at grain boundaries. For low strains this results in plastic bending, and gives an orientation difference between the material in the stressed region and the remainder of the grain. This has been discussed by Mott,<sup>8</sup> and is illustrated schematically in Fig. 1 for the present situation. The diagonal lines represent slip planes, and the part of each slip plane in the stressed region has undergone slip, producing the resultant piling up of dislocations as indicated. Only a single slip system is shown, but others must operate simultaneously in the same region of crystal, producing dislocations of different orientation which tend to impede the motion of those shown.

Stroh<sup>9</sup> has investigated the formation of cracks in the neighborhood of such piled-up groups of dislocations. He concludes that in the presence of an applied stress of the magnitude occurring in cold-worked metals, cracks should form when the groups each consist of about 1000 dislocations. He further points out that it is reasonable to expect that such piled-up groups of dislocations will occur in cold-worked metals. In the present case, the stress will probably be at least as large as the typical value used by Stroh, since the occurrence of multiple slip requires a higher stress than single slip and, in general, higher biaxial than uniaxial stresses are required to initiate slip. During cold work, dislocations appear to be produced by Frank-Read generators in avalanches, each containing of the order of 1000 dislocations.<sup>10</sup> Theory indicates that this number may be as small as 300.<sup>11</sup> When such an avalanche of dislocations approaches the edge of the stressed region, it will "pile up" against other such groups on intersecting slip planes. If the avalanche consists of as many as 1000 dislocations, it seems quite probable that a crack will develop immediately, as described by Stroh, producing the necessary nucleus for further growth of a void in the presence of the equilibrium vacancy concentration. Even if there are only 300 dislocations in the avalanche, it may be possible for a crack to form by Stroh's mechanism, since the stress may be somewhat greater than he assumed, and two or more colliding avalanches of dislocations may produce additive effects in the area of intersection.

Let us now consider the other alternative—that the piled-up avalanche of dislocations is stable and unable to produce a crack immediately. Assuming 300 dislocations per avalanche, Stroh's equation (9) indicates

that, in the region within 100 Å of the lead dislocation, the stress is of the order of  $10^{11}$  dynes/cm<sup>2</sup>. In the presence of a tensile stress of this magnitude, Eq. (19) indicates that voids with "effective radii" of only 10 atom distances will grow in the presence of the equilibrium vacancy concentration. The nucleation of such small voids by condensation of a superconcentration of vacancies requires the existence of an average excess vacancy concentration over distances only as large as  $10^{-6}$  cm. Since the region in which the excess concentration must be maintained is this small, it is still possible for the average vacancy concentration to be maintained at its equilibrium value over distances as small as  $10^{-4}$  cm, as is indicated by the fact that no deviations from the  $t^{1/2}$  dependence of the diffusion have been observed as yet. One might also postulate the pre-existence of defects or impurities whose effective radii are of the order of 10 atom distances. Thus, if cracks are not formed immediately by the piled-up groups of dislocations, these groups can still be effective in nucleating voids.

From the preceding arguments it seems that, in the absence of any impurity particles, voids should still be formed and should be located in a more or less well-defined layer parallel to the Kirkendall interface. They should also be more uniform in size than those nucleated at impurity particles. This seems to agree with the pattern of voids observed by Barnes,<sup>4</sup> and is in accord with the suggestion made by Balluffi<sup>2</sup> that Barnes' material was of higher purity than that of other workers.

The experiments of Kuczynski and Alexander<sup>12</sup> provide further evidence that it is the two-dimensional tensile stress which, in the presence of the constraints present in Kirkendall-type diffusion experiments, is responsible for the formation of the voids. The constraint considered was the absence of any relaxation of the material parallel to the Kirkendall interface. This constraint would not be applicable if the interface could not be considered infinite in extent in two dimensions, i.e., if the width of the interface were not large relative to the thickness of the diffusion zone. The experiments of Kuczynski and Alexander, where the interface initially is essentially a line, provide such an example. Since the interface in this case is narrow, the material in the stressed region can relax inward from the sides, giving rise to the development of "pits" at the surface. Since, during diffusion, the region of maximum tensile stress moves progressively farther from the Kirkendall interface, the pits should progress inward and away from the interface, giving rise to "digging" of the nature observed by Kuczynski and Alexander. Furthermore, they observed no voids, a result which is in contradiction to the normal expectation if voids are formed by

vacancy condensation. If voids were present, they should have been readily observable. Seith and Kottmann,<sup>13</sup> using larger specimens, observed the development of pits at the edge, as well as voids in the center.

## 6. CONCLUSIONS

The fissuring mechanism for nucleation of voids seems to explain better the experimental observations of Kuczynski and Alexander,<sup>12</sup> Seith and Kottmann,<sup>13</sup> and Barnes,<sup>4</sup> in particular, than does a vacancy condensation mechanism. It does not depend on the presence of impurity particles but will be influenced by them if they are present. It also offers a mechanism for the development of voids of sufficiently large radii for growth to continue, rather than postulating the pre-existence of nuclei with appropriate "effective radii," as is necessary with a vacancy condensation mechanism if Balluffi's conclusions are correct.

The present modification of the growth criterion for voids permits growth of sufficiently large voids without any excess vacancy concentration. Therefore, if the presently proposed nucleation and growth mechanisms for voids are correct, no conclusions concerning the lifetime or relative excess concentrations of vacancies can be drawn from observations of voids formed during Kirkendall-type diffusion experiments. This conclusion is evident when one considers that the voids should form and grow even if the vacancy concentration is maintained at its equilibrium value and that the process should not depend strongly on any excess concentration which may be present.

## ACKNOWLEDGMENT

The author wishes to express his appreciation to J. P. Howe and D. R. Westervelt for helpful suggestions which have been incorporated in this paper.

This paper is based on studies conducted for the Atomic Energy Commission.

## REFERENCES

1. F. Seitz, *Acta Met.* **1**, 355 (1953).
2. R. W. Balluffi, *Acta Met.* **2**, 194 (1954).
3. F. R. N. Nabarro, "Report of a Conference on the Strength of Solids" (Physical Society, London, 1948), p. 75.
4. R. S. Barnes, *Proc. Phys. Soc.* **B65**, 512 (1952).
5. C. S. Smith, *Trans. A.I.M.E.* **171**, 136 (1947).
6. R. P. Carreker, Jr., and W. P. Hibbard, Jr., *Acta Met.* **1**, 654 (1953).
7. A. A. Griffith, *Phil. Trans.* **A221**, 163 (1921).
8. N. F. Mott, *Proc. Phys. Soc.* **B64**, 729 (1951).
9. A. N. Stroh, *Proc. Roy. Soc.* **A223**, 404 (1954).
10. A. F. Brown, *J. Inst. Metals* **50**, 115 (1951).
11. J. C. Fisher, E. W. Hart, and R. H. Pry, *Phys. Rev.* **87**, 958 (1952).
12. G. C. Kuczynski and B. H. Alexander, *J. Appl. Phys.* **22**, 344 (1951).
13. W. Seith and A. Kottmann, *Naturwissenschaften* **39**, 40 (1952).



# A UNIAXIAL STRAIN MODEL FOR A LÜDER'S BAND\*

E. W. HART†

An investigation of the plastic properties of Lüder's bands in tensile test specimens leads to a relatively simple description of those properties of the band which may be termed classical. It is shown that the mechanism which is responsible for the propagation of the band and which determines its velocity is independent of the classical plastic properties.

A model is proposed to explain the load-elongation test behavior for a wide range of types of materials which exhibit yield point phenomena in one form or another.

## UN MODÈLE POUR LES LIGNES DE LUDERS

L'étude des propriétés plastiques des lignes de Luders dans les éprouvettes de traction conduit à une description relativement simple de leurs propriétés que l'on désigne dans cet article sous le terme de "classiques." Il est montré que le mécanisme responsable de la propagation de des bandes, et déterminant sa vitesse, est indépendant des propriétés plastiques classiques. Un modèle est proposé pour expliquer le palier pour les divers matériaux qui présentent ce phénomène sous une forme ou sous une autre.

## EIN EINACHSIGES SPANNUNGSMODELL FÜR LÜDERSSCHE LINIEN

Eine Untersuchung der plastischen Eigenschaften Lüdersscher Linien in Zugversuch führt zu einer relativ einfachen Beschreibung derjenigen Eigenschaften der Linien, die als klassische bezeichnet werden können. Der Mechanismus, der für die Fortpflanzung und die Geschwindigkeit der Linien bestimmend ist, ist unabhängig von den klassischen plastischen Eigenschaften.

Es wird ein Modell vorgeschlagen, um die Zusammenhänge von Last und Verlängerung beim Zugversuch für eine grosse Anzahl verschiedener Materialien zu erklären, die in der einen oder anderen Form eine Streckgrenze zeigen.

### I. INTRODUCTION

Lüder's line deformation is the characteristic mode of deformation in the vicinity of the yield point for many metals exhibiting a yield point. In this process a narrow band of strain is initiated at some point in a tensile specimen, and this grows to a steady-state band which propagates along the specimen at relatively low velocity until the entire specimen is strained by the amount corresponding to the maximum strain in the band. A prominent characteristic of deformation of this type is that the load-extension curve of a specimen deforming at constant extension rate in this mode is relatively flat during the progress of the band. In other words, the Lüder's band propagates at some steady-state velocity at a constant load.

There has not appeared yet in the literature any model which would describe the steady-state structure of the Lüder's band and the dependence of its shape on the band velocity and the intrinsic stress-strain properties of the material. The purpose of this note is to present a simple model under the assumption of uniaxial strain. This assumption is certainly not justified for all regions of the band. However, there is no reason why the general features should not be adequately represented in this fashion.

### II. DERIVATION OF THE BASIC EQUATION

Consider a tensile specimen to which is attached a load  $P$ . Static equilibrium at any distance  $l$  along the

specimen requires that

$$P = \sigma A \quad (1)$$

where  $A$  is the cross section at  $l$  and  $\sigma$  is the tensile stress at the same point. Since Eq. (1) must hold simultaneously at all points  $l$ , the variation of  $P$  as a function of  $l$  must be zero. Thus

$$0 = dP/dl = A[(\partial\sigma/\partial\epsilon)_\epsilon(d\epsilon/dl) + (\partial\sigma/\partial\dot{\epsilon})_\epsilon(d\dot{\epsilon}/dl)] + \sigma(dA/dl). \quad (2)$$

Here  $\epsilon$  is the natural strain and  $\dot{\epsilon}$  the strain rate at  $l$ . The material is assumed to satisfy a classical stress-strain-strain rate relationship everywhere except where it is just going through the yield point, i.e.,  $\sigma$  is a unique function of  $\epsilon$  and  $\dot{\epsilon}$  and, perhaps, of the previous strain and strain rate history. Now,

$$(1/A)(dA/dl) = -d\epsilon/dl,$$

and so

$$(d\dot{\epsilon}/dl)/(d\epsilon/dl) = [\sigma - (\partial\sigma/\partial\epsilon)_\epsilon]/(\partial\sigma/\partial\dot{\epsilon})_\epsilon. \quad (3)$$

In order that a steady-state configuration hold such that every point of the Lüder's band appears to move with the velocity  $v$  along the specimen it is necessary that at each point

$$\dot{\epsilon} = v(d\epsilon/dl). \quad (4)$$

Substituting Eq. (4) into Eq. (3), and denoting differentiation with respect to  $l$  by primes, we obtain our final equation,

$$\epsilon''/\epsilon' = [\sigma - (\partial\sigma/\partial\epsilon)_\epsilon]/v(\partial\sigma/\partial\dot{\epsilon})_\epsilon. \quad (5)$$

The solution of this equation under appropriate bound-

\* Received August 12, 1954.

† General Electric Laboratory, Schenectady, New York.

any conditions will give the shape of the Lüder's band ( $\epsilon$  as a function of  $l$ ) as it depends on  $v$  and the intrinsic plastic properties of the material.

The boundary conditions which must be imposed depend in part on the physically observed characteristics of the band and their interpretation. The most obvious boundary conditions would be that  $\epsilon$  shall be zero at the leading edge of the band (we shall take this point to be  $l=0$ ) and that  $\epsilon'$  shall go to zero in the tail of the band (for  $l \gg 0$ ). Actually, however, the proposed boundary condition on  $\epsilon'$  for large  $l$  is not an independent boundary condition but, instead, either is or is not a property of the solutions of (5). It therefore merely prescribes the condition under which a steady-state Lüder's band will be present. It is readily verified that this condition is simply that the right-hand member of Eq. (5) be negative as  $\epsilon$  approaches its maximum value in the band. The value of the strain  $\epsilon$  for large  $l$  is, incidentally, determined by the applied load and the static stress-strain relationship which may hold when  $\dot{\epsilon}$  is zero or small. Another boundary condition is needed, then, to determine the solution, and this condition can be that  $\epsilon'$  or  $\dot{\epsilon}$  have a specified value at  $l=0$ . There is then a discontinuity of  $\epsilon'$  at  $l=0$ . A condition such as this implies that a classical stress-strain relationship fails at the advance edge of the band and Eq. (5) cannot be satisfied at that point.

### III. AN ILLUSTRATIVE EXAMPLE

These ideas are best illustrated by solving as an example a highly oversimplified material which has the plastic properties given by

$$\sigma = \sigma_c \exp(K_1 \epsilon + K_2 \dot{\epsilon}) \quad (6)$$

over the range of  $\epsilon$  and  $\dot{\epsilon}$  comprised in the band with the exception of the singular state of strain at the band edge. The unusual form of the dependence of  $\sigma$  on  $\epsilon$  for constant  $\dot{\epsilon}$  which is adopted here is chosen entirely for mathematical simplicity. For the small range of  $\epsilon$  which is encountered in a band, this dependence is essentially linear and therefore justifiable. It is not implied that this type of dependence may describe the stress-strain curve for much larger strains. Equation (5) can be rewritten in the form

$$(\ln \epsilon')' = (1/v)[1 - (\partial \ln \sigma / \partial \epsilon) \dot{\epsilon}] / (\partial \ln \sigma / \partial \dot{\epsilon}) \epsilon. \quad (7)$$

Formula (6) yields for the right-hand member the value  $(1 - K_1)/(\tau K_2)$  which we may designate by the symbol  $-K/v$ . The solution is, then

$$\epsilon = (\dot{\epsilon}_0/K)[1 - \exp(-Kl/v)], \quad (8)$$

where the zero subscript on  $\dot{\epsilon}$  denotes the value at  $l=0$ . The maximum strain  $\epsilon_1$  in the band occurs at large  $l$  and is given by

$$\epsilon_1 = \dot{\epsilon}_0/K. \quad (9)$$

This strain must be determined by the applied load and

so is not an independent parameter. For completeness, let us evaluate  $\epsilon_1$  for our simplified model. If the initial stress due to the applied load is  $\sigma_0$ , when  $\epsilon=0$ , then the stress  $\sigma_1$ , when  $\epsilon=\epsilon_1$  is given by

$$\sigma_1 = \sigma_0 \exp \epsilon_1, \quad (10)$$

and, for  $\dot{\epsilon}=0$ , Eq. (6) becomes

$$\sigma_1 = \sigma_c \exp K_1 \epsilon_1. \quad (11)$$

Equations (10) and (11) yield a value for  $\epsilon_1$  given by

$$\epsilon_1 = (K_1 - 1)^{-1} \ln(\sigma_0/\sigma_c) \quad (12)$$

which shows a rather weak dependence on  $\sigma_0$ .

This leaves one independent parameter,  $v$ , to describe the nonclassical behavior of the material at the leading edge of the band, everything else being describable classically.

### IV. DISCUSSION AND FURTHER CONSIDERATIONS

A curious feature of the stress-strain relationship in the Lüder's band is that the strain rate everywhere in the band must be just that which will make the stress satisfy the equation

$$\sigma = \sigma_0 \exp \epsilon. \quad (13)$$

This, of course, is not the stress-strain relationship for the material for any constant strain rate, but is the relationship for the special strain-strain rate history which the material undergoing Lüder's deformation follows because of the geometric requirements of the problem. This is in contradiction with the stress-strain properties which Gensamer<sup>1</sup> postulated for materials which deform by Lüder's strain. Gensamer proposed that the Lüder's lines would form for materials with a yield point and for which the initial portion of the stress-strain curve was characterized by the relationship  $d\sigma/d\epsilon < \sigma$  and that the Lüder's strain would end at the strain for which  $d\sigma/d\epsilon = \sigma$ . The treatment of the present study shows, however, that  $d\sigma/d\epsilon = \sigma$  everywhere in the band during the Lüder's strain and that the maximum strain in the band is determined only by the applied load. Note that one is concerned with total derivatives in this paragraph rather than the partial derivatives of previous sections.

One is naturally led now to a consideration of the mechanism which causes the propagation of the Lüder's band and which might explain the dependence of  $v$  on  $\sigma_0$ . It is frequently suggested that static stress concentration at the edge of the band is the feature of the band responsible for its propagation. Such a view cannot be supported since Sylwestrowicz and Hall<sup>2</sup> have shown that, if a band is stopped midway through a specimen by removing the load, and the specimen is then fully aged, the band edge will not subsequently propagate, but instead a new band may nucleate under raised stress at the same grip at which the original one started and will then propagate fully through the specimen.

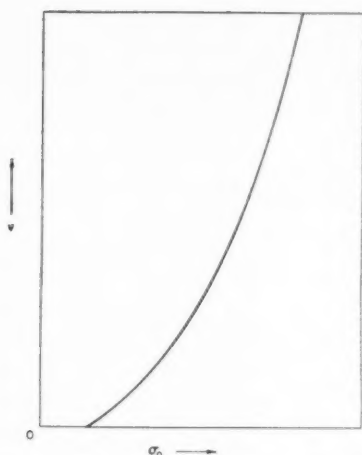


FIG. 1. The general form of the dependence of Lüder's band velocity  $v$  on the applied initial stress  $\sigma_0$ .

The considerations of this paper offer no explanation of the dependence of  $v$  on  $\sigma_0$ . The existence of such a relationship has been shown, however, by the measurements of Sylwestrowicz and Hall<sup>2</sup> and by Fisher and Rogers.<sup>3</sup> The general features of such a dependence are shown very roughly in Fig. 1. The  $v$ - $\sigma_0$  relationship can be expected to depend on the alloy composition, grain size, temperature, and state of strain hardening of the specimen. To this relationship we might add the result from Eq. (8) that the apparent breadth of the Lüder's band, which we might call  $\lambda$ , is given by a relationship of the form

$$\lambda = v/K. \quad (14)$$

If  $v$  is small, we expect the band to be very sharp, and if  $v$  is very large, the band should be quite diffuse perhaps broader than the specimen length so that the band does not even achieve its steady-state form.

These two features lead to a rather simple explanation of the presence or absence of Lüder's line deformation and the attendant characteristic load-extension curves in various specimens. Consider, for example, three specimens with different  $v$ - $\sigma_0$  curves as shown in Fig. 2, and designated severally as specimens A, B, and C. Let an applied initial stress  $\sigma_1$  be applied to each and be appropriate to nucleate one localized yielded region in each in a time comparable to the duration of the experiment. Specimen B will produce a classical Lüder's band, which would result in an observable drop in load and flat extension region if this were a constant strain rate experiment. Specimen C will yield locally, producing some extension, but since the stress is not sufficient to propagate a steady-state band, further extension must wait on further localized nucleation. The yielded region is of very small extent, and, if this were a constant extension rate experiment, a random jerky load-extension curve would result in which sudden drops in load would alternate with short sections of homogeneous strain in

the just yielded region as that region strain hardens up to the next yield stress. A typical example of this might be the jerky flow of  $\beta$ -brass crystals as reported by Ardley and Cottrell.<sup>4</sup> Specimen A will yield almost homogeneously from the beginning since the band will travel too fast to be observed. In fact the breadth of the steady-state band may be so much larger than the specimen length that the band may not even reach a steady-state configuration. It might be expected that, if the applied stress were reduced to the amount  $\sigma_2$ , a Lüder's band would now nucleate after a sufficiently long waiting time and that subsequent behavior of the same kind as specimen B would result with a band velocity appropriate to  $\sigma_2$ . The measurements on iron single crystals under static loading as reported by Gensamer and Mehl<sup>5</sup> might be an example of this case with interim strain aging as suggested by those authors. In constant extension rate test such a specimen would yield so fast that the elasticity of the machine and specimen might prevent the observation of a drop in load, especially since only a very small Lüder's strain would be required in the band to follow the imposed extension rate because of the high  $v$ .

To supplement this picture it is proposed that the band velocity for a given stress is reduced by strain hardening and by refinement of grain size.

It might be well at this point to note that the serrated load-extension curves predicted for specimen C above should not be confused with the serrated curves which may accompany Lüder's lines in strain aging alloys such as that described for aluminum by McReynolds.<sup>6</sup> Cottrell<sup>7</sup> has shown the feasibility of explaining these serrations as a result of strain aging although he does not present any explanation for the apparent anomaly of the occurrence of aging during plastic straining. It seems clear, nevertheless, that the aging must be occurring in the tail of the Lüder's band where no straining is going on. Thus if a time  $\tau$  is required for strain aging and the band velocity is  $v$ , at any instant of progress of the Lüder's band, all the strained material further behind the Lüder's front than a distance  $v\tau$  is strain aged. When the band front reaches the end of the specimen, homo-

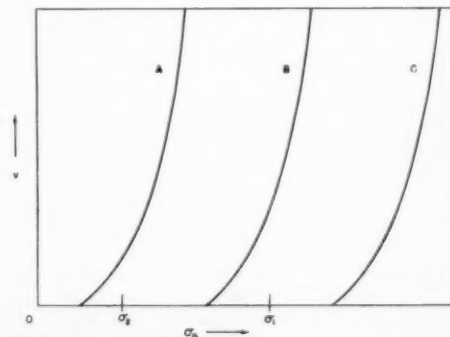


FIG. 2. Assumed  $v$ - $\sigma_0$  curves for three different specimens, all to be loaded at  $\sigma_1$ .

geneous strain proceeds in a specimen length  $v\tau$  immediately in back of the end until that portion is strain-hardened up to the yield stress of the aged section at which time another band is again nucleated. The homogeneous flow region seems to have a steep stress-strain behavior since all measurements and extension rates are referred to the full gauge length of the specimen, whereas the true gauge length for that portion of flow is only  $v\tau$ .

#### ACKNOWLEDGMENTS

The author is pleased to acknowledge helpful discussions with Drs. J. C. Fisher, J. H. Hollomon, and

J. R. Low, Jr., of the General Electric Research Laboratory. He also wishes to thank Dr. J. C. Fisher and Mr. H. C. Rogers for allowing him access to their preliminary measurements of Lüder's band velocity.

#### REFERENCES

1. M. Gensamer, Trans. A.I.M.E. **128**, 104 (1938).
2. W. Sylwestrowicz and E. O. Hall, Proc. Phys. Soc. **B64**, 495 (1951).
3. J. C. Fisher and H. C. Rogers, private communication.
4. G. W. Ardley and A. H. Cottrell, Proc. Roy. Soc. **A219**, 328 (1953).
5. M. Gensamer and R. F. Mehl, Trans. A.I.M.E. **131**, 372 (1938).
6. A. W. McReynolds, Trans. A.I.M.E. **185**, 32 (1949).
7. A. H. Cottrell, Phil. Mag. **44**, 829 (1953).



# DÉTERMINATION DES SOUS-STRUCTURES DANS LES MONOCRISTAUX MÉTALLIQUES À L'AIDE DES RAYONS X\*

H. LAMBOT†, L. VASSAMILLET††, J. DEJACE‡

La possibilité de détecter une sous-structure dans les monocristaux métalliques à l'aide de la technique de diffraction des rayons X proposée antérieurement par les auteurs<sup>14</sup> est actuellement discutée. La méthode est capable de mettre en évidence des sous-grains assez parfaits dont la taille est de l'ordre de quelques dizaines de microns et dont la désorientation mutuelle est au moins de l'ordre d'une minute d'arc.

L'étude de monocristaux d'aluminium (99.99% et 99.95%) déformés de quelques pour cent par traction a montré qu'une partie de la matrice est fragmentée en domaines possédant une bonne perfection interne tandis que le reste donne lieu à un fond diffus dans les taches de Bragg.

L'influence des traitements de revenus est la suivante: (a) le fond diffus disparaît progressivement en dessous de 450°C environ (aluminium raffiné) et 550°C environ (aluminium à 99.95%); (b) au-dessus de ces températures, la croissance de certains sous-grains pratiquement parfaits est le phénomène prépondérant.

## DETERMINATION OF SUB-STRUCTURES IN METAL SINGLE CRYSTALS BY MEANS OF X-RAYS

The possibility of detecting a sub-structure in metal single crystals by means of an X-ray diffraction technique originally proposed by the authors<sup>14</sup> is discussed in detail. The method is capable of revealing essentially perfect sub-grains whose size is of the order of tens of microns and whose mutual disorientation is at least of the order of one minute of arc.

The study of aluminium monocrystals (99.99% and 99.95%) deformed by a few per cent in tension has shown that one part of the matrix is fragmented into domains possessing a high internal perfection while the rest gives a diffuse background in the Bragg reflections.

The effect of the heat treatments is as follows: (1) The diffuse background disappears progressively below about 450°C (pure aluminium) and about 550°C (99.95% aluminium); (2) above these temperatures the growth of certain almost perfect sub-grains is the outstanding phenomenon.

## BESTIMUNG DER SUBSTRUKTUR METALLISCHER EINKRISTALLE MIT HILFE VON RÖNTGENSTRAHLEN

Die von früheren Autoren<sup>14</sup> vorgeschlagene Möglichkeit, die Substruktur metallischer Einkristalle mit Hilfe einer besonderen Röntgentechnik aufzufinden, wird erneut diskutiert. Die Methode ermöglicht es, Subkörner mit idealem Aufbau sichtbar zu machen, deren Grösse einige Zehner  $\mu$  beträgt und deren Orientierungsabweichung geringer als eine Bogenminute ist. Die Untersuchung von Aluminium Einkristallen (99.99% und 99.95%), die um einige Prozent durch Ziehen verformt worden waren, hat gezeigt, dass ein Teil der Probe in Gebiete mit idealem Gitteraufbau aufgespalten ist, während der Rest zu einer diffusen Schwärzung in den Bragg-Reflexen Anlass gibt.

Der Einfluss der Anlassbehandlung ist folgender: a) unter etwa 450°C (raffiniertes Aluminium) und etwa 550°C (99.95%) verschwindet der diffuse Untergrund allmählich; b) oberhalb dieser Temperaturen ist die auffälligste Erscheinung das Wachstum bestimmter Subkörner.

### 1. INTRODUCTION

Le problème des sous-structures dans les cristaux métalliques a fait récemment l'objet d'une mise au point par Guinier.<sup>1</sup>

Cette question a été essentiellement abordée par deux voies différentes (micrographie et diffraction des rayons X) qui ont révélé des fragmentations de nature et de taille assez variables.

Les méthodes basées sur l'emploi des microscopes optique et électronique sont évidemment les plus directes puisqu'elles permettent l'examen topographique d'une matrice monocristalline divisée en un certain nombre de domaines particuliers limités par des contours fermés. Par contre, ces techniques ne sont pas particulièrement sensibles aux désorientations réticulaires internes et au degré de perfection géométrique des

différentes parties du cristal. Nous ne pouvons évidemment discuter tous les résultats obtenus dans ce sens. Nous nous contenterons seulement de rappeler que certains travaux récents ont tenté d'élargir quelque peu la notion classique de sous-grain (région à contour fermé à l'intérieur d'un grain) en la rattachant directement au mécanisme du glissement lui-même (région comprise entre deux bandes de glissement successives). Cette conception moins simpliste semble devoir permettre une meilleure interprétation des faits en accord plus étroit avec certaines fragmentations mises en évidence par diffraction des rayons X.<sup>2</sup>

La définition précise et la mise en évidence des sous-structures par la radiocristallographie sont un peu plus délicates puisqu'elles ne reposent plus, généralement, sur une analyse topographique.\* Leur existence a d'abord été invoquée d'une manière tout à fait indirecte pour rendre compte de l'intensité diffractée par les cristaux<sup>3</sup> ou pour interpréter l'élargissement des raies de Debye-

\* Received August 13, 1954.

† Institut de Cristallographie, Université de Liège (Belgique). Actuellement à l'Université d'Illinois—Urbana (U. S. A.).

†† Fulbright Fellow à l'Université de Liège (1950–1952).

‡ Attaché au Centre National Belge de Recherches Métallurgiques (section de Liège).

\* La technique de "microscopie par rayons X" de Barrett, signalée plus loin, est une exception très importante à cette règle générale.

Scherrer obtenues avec des matériaux écrouis.<sup>4</sup> Elle a été ensuite suggérée d'une manière plus tangible par certaines applications de la méthode habituelle de Laue.<sup>5,6</sup> Enfin, les techniques de Barrett,<sup>7</sup> de Guinier-Tennevin,<sup>8</sup> de Gay-Hirsch et leurs collaborateurs<sup>9,10</sup> ont apporté des preuves plus directes de l'existence de certaines fragmentations dans les grains métalliques. Simultanément, l'interprétation des spectres de Debye-Scherrer est devenue beaucoup plus claire et précise à la suite des travaux de Warren-Averbach<sup>11</sup> et Bertaut.<sup>12</sup>

Toutefois, les résultats obtenus à l'heure actuelle présentent encore une diversité appréciable et il nous paraît impératif de préciser clairement les conditions dans lesquelles de telles sous-structures sont observées. Les techniques de diffraction des rayons X peuvent, à des degrés variables, établir une distinction entre deux parties d'un même grain à partir de leur désorientation relative, de leurs différents degrés de perfection géométrique et éventuellement de leur différence de pouvoirs d'extinction. La sensibilité particulière d'une technique vis-à-vis de l'un ou l'autre de ces facteurs lui permettra de détecter des types de sous-grains qui échappent aux autres techniques. Ainsi la méthode de Guinier-Tennevin séparera aisément deux régions d'un même grain décalées d'un angle aussi faible qu'une minute d'arc, mais à la condition que la taille de ces domaines ne soit pas inférieure à une centaine de microns et que leur imperfection interne ne soit pas trop grande. Au contraire, la technique du micro-faisceau atteindra des sous-grains, même relativement imparfaits, de taille aussi petite qu'un micron, mais elle ne possède pas une aussi bonne sensibilité aux faibles différences d'orientation. Les deux types de fragmentation ainsi révélés sont donc, à priori, de nature différente correspondant, par exemple, à ce que Julien et Cullity<sup>13</sup> appellent macro- et micro-fragmentation.

Dans un article récent,<sup>14</sup> nous avons proposé un autre dispositif utilisant la diffraction des rayons X et permettant également la mesure des faibles désorientations réticulaires dans les monocristaux. Utilisable aussi bien en réflexion qu'en transmission, la méthode possède une sensibilité légèrement inférieure à celle de Guinier-Tennevin, mais néanmoins excellente en pratique. Dans le présent article, nous voudrions envisager les possibilités qu'elle offre dans le problème de la détection des sous-grains.

## 2. SENSIBILITÉ DE LA TECHNIQUE VIS-À-VIS DE LA TAILLE DES SOUS-GRAINS

Nous avons précédemment montré comment l'utilisation d'un faisceau convergent et monochromatique irradiant une bande étroite d'un monocristal permettait d'y différencier diverses régions sur la base de leurs désorientations relatives ou de leurs différences de perfection géométrique. Pour établir une correspondance absolue entre les sous-grains observés par voie micrographique et les fragmentations mises en évidence par la diffraction des rayons X, il serait nécessaire de

savoir avec précision quelles sont les limites d'imperfection interne et de désorientation relative entre lesquelles diverses parties d'un même monocristal acquièrent la qualité de "sous-grains" nettement individualisés. Il est malheureusement impossible de résoudre complètement ce problème actuellement et c'est ce qui a conduit Guinier<sup>1</sup> à adopter des conditions très restrictives pour l'établissement d'une corrélation entre les sous-grains observés aux microscopes optique et électronique et les domaines détectés à l'aide des rayons X.

Les meilleures conditions expérimentales dans lesquelles nous pouvons certainement invoquer l'existence d'une sous-structure sont réalisées lorsque les taches de Bragg observées avec notre dispositif sont fragmentées en un nombre limité de stries très fines. Il nous est possible de séparer des stries d'environ 0.1 mm distantes de la même valeur. Cela signifie (pour une distance film-échantillon d'un mètre) que nous pouvons mettre en évidence des domaines faisant entre eux un angle de l'ordre d'une minute d'arc et dont la désorientation interne est également de cet ordre.

La largeur d'une tache de Bragg enregistrée à un mètre avec un faisceau d'un degré d'ouverture est au maximum de deux centimètres (si l'imperfection de la zone irradiée atteint cette valeur). De plus, si l'on utilise toute la hauteur du faisceau issu du monochromateur, on obtient une tache de plusieurs centimètres de hauteur ( $\approx 6$  cm). A un niveau quelconque d'une telle tache, il est donc théoriquement possible de dénombrer une centaine de stries du type décrit ci-dessus. La divergence verticale du faisceau a pour résultat pratique d'allonger les stries jusqu'à environ deux centimètres. Nous pouvons donc, grosso modo, dénombrer 300 stries sur toute l'étendue d'une telle tache. Rapporté au volume irradié, ce nombre permet d'obtenir une valeur moyenne approchée du volume occupé par un sous-grain.

A titre d'exemple, pour un volume irradié d'environ  $1.5 \cdot 10^{-6}$  cm<sup>3</sup> dans un cristal d'aluminium, la plus petite dimension linéaire décelable, calculée par ce moyen, est de l'ordre de 35 microns.

Il apparaît toutefois que cette estimation conduit très probablement à une valeur théorique trop grande. En effet, le dénombrement des stries verticales (dans une tache de Bragg équatoriale) repose sur l'excellent pouvoir de résolution que présente la technique pour les faibles décalages angulaires autour d'un axe vertical parallèle aux plans réflecteurs. Les sous-grains clairement décelables sont ceux pour lesquels ces plans réflecteurs absolument verticaux ont seulement subi l'un par rapport à l'autre une faible rotation autour de l'axe vertical. Il est facile de voir que des domaines identiques ayant subi, par rapport aux premiers, de légères rotations autour des deux axes horizontaux respectivement parallèle et perpendiculaire aux plans réflecteurs, donneront naissance à des stries qui se superposeront aux premières (qu'elles pourront tout au

plus allonger de manière imperceptible). Il pourra en être de même de certains sous-grains d'orientation plus complexe dont la composante horizontale de désorientation identique au décalage angulaire des sous-grains du premier type conduira de nouveau à une superposition de stries.

Les observations expérimentales montrent qu'un même nombre de stries est obtenu pour les différentes taches de Bragg d'un même cristal maintenu dans le même état physique. La distribution des sous-grains est donc pratiquement la même autour des différents axes et il paraît légitime de penser qu'une quantité non négligeable de sous-grains échappent à l'examen d'une seule tache de Bragg (superposition de plusieurs stries).

La manière la plus optimiste de traiter le problème consiste à repérer, à un même niveau de la tache, les stries parallèles ayant la même longueur et ne subissant aucun décalage en hauteur. Si l'on suppose que toutes ces stries sont produites par les sous-grains d'une seule couche simplement tournés mutuellement autour de l'axe vertical, on obtient dans les conditions précitées une taille limite de 5 microns. Il est clair que cette valeur constitue très certainement une limite inaccessible pour notre pouvoir de résolution. Le fait que la taille limite théoriquement accessible se situe entre les deux valeurs précitées est encore appuyé par l'évaluation suivante: si, autour d'un niveau moyen dans la tache, on tient compte du déplacement relatif des stries voisines le long de la verticale, et si, à l'aide de la divergence du faisceau, on calcule l'épaisseur moyenne de la tranche de cristal qui lui correspond, on obtient, dans les conditions indiquées plus haut, une taille limite de l'ordre de 15 à 20 microns.

Quelle que soit sa valeur exacte, la dimension moyenne la plus petite qu'il est possible d'atteindre avec notre dispositif semble certainement inférieure à celle atteinte par la méthode de Guinier-Tennevin. Il est donc possible de prolonger quelque peu la voie indiquée par ces auteurs en vue d'atteindre finalement des fragmentations de l'ordre du micron.

Il importe de remarquer que la méthode proposée

connaît également une limitation très stricte du fait qu'elle est impuissante à distinguer des domaines dont l'imperfection interne est grande et conduit à des stries larges se recouvrant mutuellement.

Afin d'illustrer ce qui précède, nous voudrions examiner les premiers résultats obtenus au cours d'une étude préliminaire de monocristaux d'aluminium légèrement déformés par traction et soumis ensuite à des revenus progressifs.

### 3. RÉSULTATS EXPÉRIMENTAUX

Au cours de ces dernières années, l'origine des sous-grains a été surtout cherchée dans le mécanisme de polygonisation, qui met en oeuvre une déformation du réseau entraînant des courbures locales, suivie d'un traitement thermique susceptible de résorber les régions courbées en domaines à contours polygonaux. Cette transformation s'interprète par le rassemblement de dislocations de même signe dans des parois planes constituant les frontières de sous-grains. Ces contours jouissent d'une certaine mobilité permettant la croissance de certains domaines polygonisés sous l'action des traitements thermiques ultérieurs.

Le problème qui a surtout retenu l'attention est celui de savoir si la formation d'une telle sous-structure exige réellement une énergie d'activation (et quel est, dans ce cas, le traitement minimum requis pour une déformation déterminée) ou si la fragmentation n'est pas plutôt une conséquence directe de la déformation.

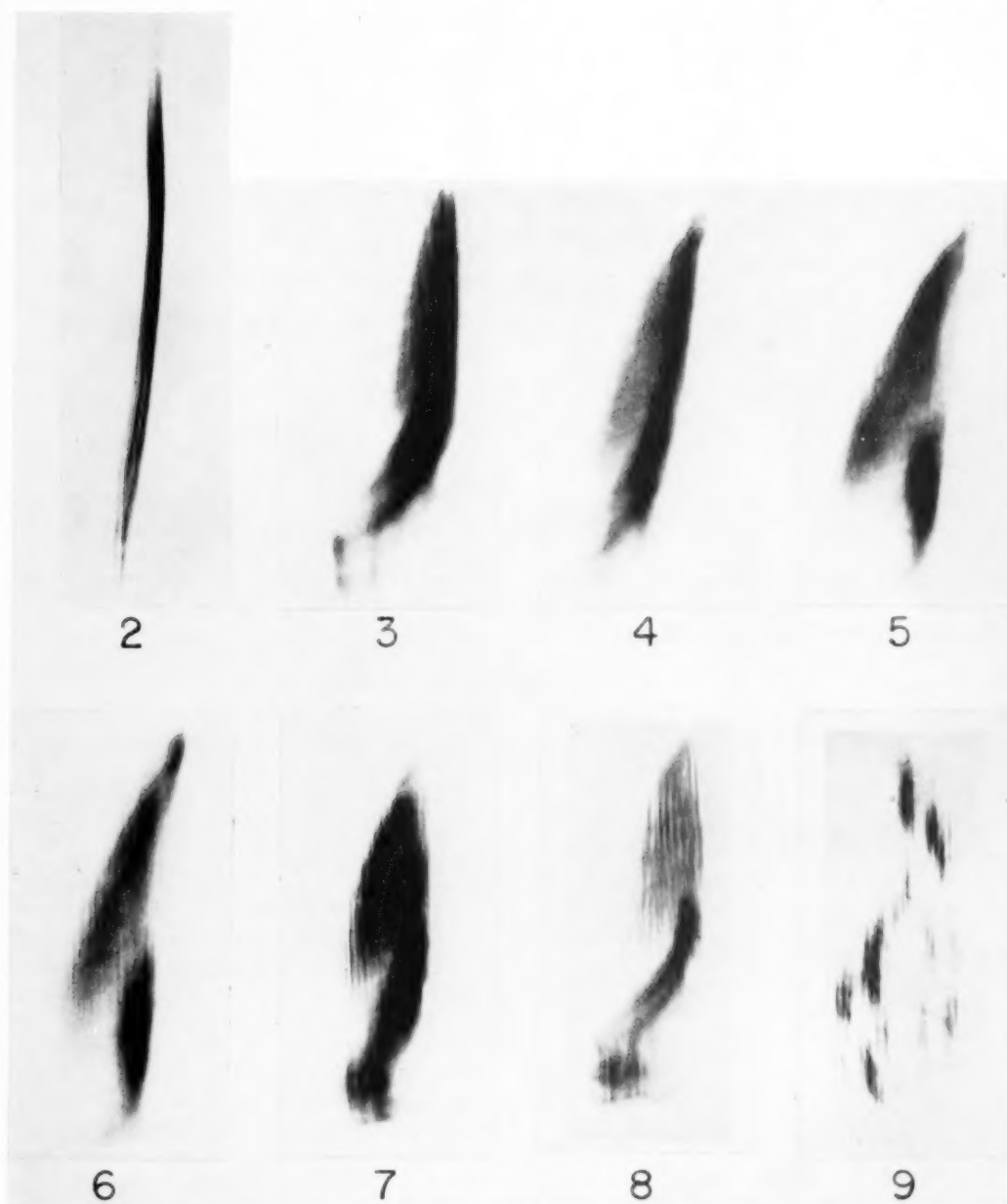
Au fur et à mesure que la sensibilité des techniques radiocristallographiques mises en oeuvre a augmenté, la température la plus basse à laquelle la polygonisation était visible (dans des monocristaux faiblement écrouis) a continuellement diminué. Alors que Cahn<sup>15</sup> et Crussard<sup>16</sup> la fixaient à environ 600°C pour l'aluminium, Guinier et Tennevin<sup>1</sup> observaient les premières traces du phénomène à 450°C. L'utilisation de notre technique<sup>17</sup> permettait ensuite d'atteindre 200°C (aluminium raffiné identique à celui de Guinier-Tennevin). Plus récemment, grâce à l'amélioration des conditions expérimentales, nous avons pu observer une striation fine des taches de Bragg obtenues avec des monocristaux identiques simplement déformés par traction de quelques pour cent à la température ordinaire. La figure 1,\* par exemple, se rapporte à un monocristal d'aluminium raffiné (99.99%) étiré de 4%. La tache révèle une structure interne à striation visible en dépit d'un fond diffus qui la masque partiellement. Un tel résultat n'est pas isolé et il est toujours plus ou moins possible d'observer des stries sur les clichés obtenus avec des échantillons faiblement déformés à la température ordinaire. Nous rappellerons ici un cas où même une déformation accidentelle donne lieu à un phénomène identique (réf. 14, fig. 10).

Des monocristaux d'aluminium raffiné (99.99%) préparés par la méthode d'Elam-Carpenter et d'orien-



FIG. 1. Tache de Bragg (111) obtenue avec un monocristal d'aluminium raffiné (99.99%) déformé de 4% par traction.

\* La difficulté de reproduction des clichés originaux entraîne une perte importante de clarté et de résolution.



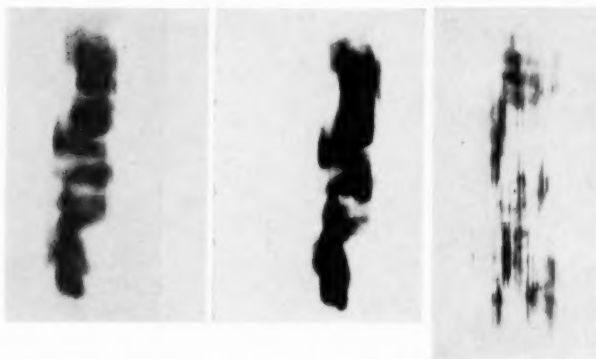
FIGS. 2 à 9. Tache de Bragg (111) obtenue avec un monocristal d'aluminium raffiné (99.99%). (2) avant déformation. (3) après traction de 2%. (4) après revenu de 24 heures à 100°C. (5) après revenu de 24 heures à 300°C. (6) après revenu de 12 heures à 400°C. (7) après revenu de 12 heures à 525°C. (8) après revenu de 12 heures à 575°C. (9) après revenu de 2 heures à 630°C.

tations diverses ainsi que des échantillons à très gros grains ont été légèrement étirés de manière à donner naissance à des taches analogues à celle de la figure 1. L'action des traitements thermiques sur de telles sous-structures de déformation a été suivie à l'aide de notre dispositif.

Les observations faites sur l'aluminium raffiné peuvent être décrites schématiquement à l'aide des figures 2 à 9. La figure 2 représente une tache (111) au

stade initial, c'est-à-dire avant toute déformation volontaire du cristal. L'imperfection maximum dans le volume irradié est d'environ 10 minutes d'arc et l'aspect général de la tache illustre à nouveau les observations mentionnées dans notre précédent article. (réf. 14, fig. 8). Lorsque le cristal a subi une déformation de 2 pour cent par traction, la même tache prend l'allure de la figure 3. L'ensemble de la tache présente un fond diffus sur lequel se détache une striation assez fine





FIGS. 10, 11 et 12. Tache de Bragg (111) obtenue avec un monocristal d'aluminium (99.95%) réformé de 2.1% par traction et soumis à des revenus. (10) 12 heures à 400°C. (11) 12 heures à 550°C. (12) 12 heures à 660°C.

clairement discernable sur les clichés originaux. La largeur accrue de la tache indique une imperfection moyenne de l'ordre du degré.

L'action des revenus successifs peut être décrite de la manière suivante. Jusqu'à 450°C (pour des durées de 12 heures), les traitements thermiques ont pour résultat de faire disparaître progressivement la partie diffuse de la tache et de rendre ainsi de plus en plus visible la striation (figs. 4, 5, 6). L'élimination du fond diffus ne devient appréciable qu'à partir de 200°C environ.

Au-dessus de 450°C et jusqu'à la recristallisation complète, le nombre de stries tend à diminuer de plus en plus (figs. 7, 8, 9).

Nous avons également eu l'occasion d'observer que la déformation se répartit souvent d'une manière très hétérogène. Le cristal initialement assez parfait dans la zone irradiée se déforme très sensiblement dans une région déterminée alors que les régions voisines gardent une assez bonne régularité géométrique. On peut à nouveau constater que, dans de tels cas, la zone déformée possède une sous-structure clairement décelable à partir des taches de Bragg. L'action des revenus est identique à celle qui a été décrite ci-dessus.

Les températures de 200°C et 450°C (pour des durées de 12 à 24 heures) ne constituent que des valeurs approchées susceptibles de varier légèrement avec l'orientation des échantillons. Il importe maintenant de préciser ces résultats par l'examen de cristaux pré-orientés et déformés suivant une direction bien déterminée.

Des expériences identiques ont été effectuées sur des monocristaux d'aluminium moins pur (99.95%). Il est également possible d'observer les traces d'une sous-structure après déformation. Mais l'élimination de la partie diffuse dans les taches de Bragg s'effectue beaucoup plus difficilement. En fait, cette transformation n'est terminée qu'au-dessus de 550°C (pour des durées identiques) (figs. 10, 11, 12). L'intervalle de températures où la striation est vraiment nette et où le nombre de traits diminue est ainsi fortement réduit.

Ces résultats permettent de rendre compte des observations antérieures. Les limites de températures indiquées ci-dessus correspondent pratiquement à celles à partir desquelles des techniques moins sensibles ont permis d'observer ce qui semblait constituer l'amorce du phénomène de polygonisation (par exemple 450°C pour Guinier-Tennevin sur l'aluminium raffiné).

Il est essentiel de signaler que la structure interne des taches de Bragg après déformation, telle qu'elle est décrite ci-dessus, n'a pu être observée au delà de quelques pour cent de traction (5 à 10%). Sans entrer dans le détail, il est possible d'affirmer que, dans ce cas, la fragmentation éventuelle ne conduit plus à la formation de domaines à faible imperfection interne.

#### 4. DISCUSSION DES RÉSULTATS

Nous avons montré plus haut comment la détection des sous-structures à l'aide des rayons X dépendait essentiellement de la sensibilité des méthodes utilisées.

*Les résultats décrits dans le présent article ne sont donc valables qu'à l'échelle du pouvoir de résolution atteint actuellement.*

Les taches de Bragg obtenues avec des monocristaux d'aluminium légèrement déformés présentent deux aspects distincts: une striation assez fine et un fond diffus.

La striation conduit immédiatement à l'idée d'une fragmentation du cristal en sous-grains relativement parfaits et bien définis. Compte tenu de la remarque de Julien et Cullity,<sup>13</sup> la formation d'une sous-structure peut donc être une conséquence directe du processus de déformation. Dans les conditions précitées et pour une partie de la matrice au moins, le mécanisme habituel de la polygonisation proposé par Cahn<sup>15</sup> et impliquant deux stades (formation de courbures locales et résorption ultérieure sous l'action de la température) n'est pas nécessairement requis pour expliquer la fragmentation du réseau. Cette observation rejoint celles d'un grand nombre d'auteurs et notamment celle de Conard, Averbach et Cohen<sup>18</sup> qui ont observé une fragmentation

des cristaux de zinc courbés à très basse température ( $-196^{\circ}\text{C}$ ) et également celles de Gay, Hirsch et Kelly<sup>2,9,10</sup> sur les métaux polycristallins sévèrement écrouis. Il importe toutefois de se rappeler que les conditions dans lesquelles nous avons travaillé sont bien différentes.

L'interprétation du fond diffus présente plus de difficulté. Il est évidemment possible de l'attribuer à la présence dans le cristal de domaines plus imparfaits (donnant lieu à un recouvrement de stries larges) ou à des régions éventuellement assez parfaites mais de tailles nettement plus petites. Il est curieux d'observer que dans des conditions toutes différentes et à une échelle de dimension nettement plus basse, la technique du micro-beam a également révélé l'existence d'un fond continu entre les taches plus ou moins définies correspondant aux sous-grains eux-mêmes. Certaines "sous-structures" correspondant à des dimensions inférieures au micron ont bien été révélées par le microscope électronique, mais leur nature exacte est encore discutée à l'heure actuelle. De toute façon, du point de vue diffraction des rayons X, il paraît trop simpliste de considérer un cristal déformé comme constitué uniquement de sous-grains bien individualisés aussi longtemps que nous ne pouvons fixer avec exactitude les caractéristiques cristallographiques qui différencient ces domaines. C'est le point de vue également défendu par Guinier<sup>1</sup> pour qui les seules sous-structures à caractères nettement définis actuellement décelables à l'aide des rayons X sont constituées de domaines assez parfaits légèrement désorientés les uns par rapport aux autres.

Un cristal constitué de régions imparfaites et d'orientations légèrement différentes contient aussi des régions frontières où divers types d'imperfections ont tendance à s'accumuler, constituant des zones à courbures locales plus ou moins continues et plus ou moins étendues. Cet aspect de la question a notamment été considéré par Jillson,<sup>19</sup> Hess et Barrett<sup>20</sup> ainsi que Gay et Kelly.<sup>21</sup>

L'étude de la restauration de l'aluminium faiblement déformé a conduit Cherian, Pietrowski et Dorn<sup>22</sup> à distinguer deux processus distincts: laméta-restauration se situant vers  $100^{\circ}\text{C}$  et l'ortho-restauration prenant place à des températures supérieures. Par contre Crussard et Jaoul<sup>23</sup> ne trouvent, avec l'aluminium raffiné, aucune discontinuité de ce genre et attribuent les résultats de Cherian, Pietrowski et Dorn à des causes accidentelles.<sup>24</sup>

Nous avons essayé de répondre au souhait de Burgers<sup>25</sup> de tenter une telle discrimination à l'aide des rayons X. Comme nous l'avons vu plus haut, les revenus à  $100^{\circ}\text{C}$  n'apportent pas de grande modification à la structure interne des taches de Bragg. Bien que mettant en jeu une grande part de l'énergie emmagasinée dans le réseau au cours de l'écrouissage,<sup>26</sup> les imperfections restaurables au cours de ces traitements (vraisemblablement des lacunes) n'ont pas d'influence visible sur l'état de perfection géométrique de la matrice. Un changement perceptible apparaît vers  $200^{\circ}\text{C}$ , mais la

modification observée est progressive et les rayons X ne permettent pas de retenir l'idée d'une discontinuité nette à ce stade de la restauration.

L'absence de modification notable dans la structure interne des taches de Bragg en dessous de  $200^{\circ}\text{C}$  conduit à la conclusion que les sous-grains existants subissent pas de croissance appréciable. Ce fait peut être rapproché des observations de Heidenreich<sup>27</sup> qui se rapportent toutefois à des domaines de taille inférieure.

La majeure partie du fond diffus disparaît entre  $200^{\circ}\text{C}$  et  $450^{\circ}\text{C}$ , ce qui indique que les imperfections mises en jeu sont plus difficilement restaurables et exigent une activation thermique non négligeable. Le nombre de stries clairement visibles augmente donc et, à l'échelle du pouvoir de résolution actuellement atteint, la seule conclusion vraiment sûre que nous puissions tirer est que nous assistons à une résorption progressive des parties imparfaites du réseau ou à une croissance continue de domaines parfaits éventuellement trop petits pour être distingués. Il est d'ailleurs très probable que ces deux phénomènes se déroulent en même temps. Cette transformation peut, en fait, correspondre à la restauration interne puis à la croissance de sous-grains ainsi qu'il a été considéré par Beck,<sup>28</sup> à la restauration des régions frontières invoquée par Gay et Kelly<sup>21</sup> ou à la polygonisation des courbures continues suivant le processus de Cahn.<sup>15</sup>

Au stade final de cette évolution, le cristal peut être considéré comme pratiquement fragmenté en sous-grains assez parfaits probablement décalés les uns par rapport aux autres d'un angle très faible.\* A partir de cet état, les traitements thermiques conduisent à une diminution progressive du nombre de sous-grains, ce qui implique la croissance de certains au détriment des autres. Immédiatement avant la recristallisation, la matrice cristalline ne comprend plus qu'un nombre limité de larges domaines et il est curieux de constater, ainsi que Guinier<sup>1</sup> l'avait fait, que la perfection de ces sous-grains, excellente jusque là, devient nettement moins bonne. L'explication de ce fait requiert une étude particulière de ce point précis.

L'interprétation des observations effectuées sur les monocristaux d'aluminium moins pur (99.95%) peut être développée dans le même sens. Il va de soi que les impuretés constituent de sérieux obstacles au mouvement des dislocations durant la restauration des régions du cristal donnant lieu au fond diffus, ce qui explique la disparition plus lente de ce dernier.

## 5. REMERCIEMENTS

Nous tenons à exprimer notre gratitude aux Professeurs P. A. Beck, H. Brasseur et A. Guinier pour l'intérêt qu'ils ont pris à ce travail. Nous remercions également Messieurs Chevigny et Saulnier de la

\* Il nous est impossible de prouver expérimentalement que deux stries voisines trouvent bien leur origine dans deux domaines réellement voisins.

Société Pechiney qui ont bien voulu mettre à notre disposition l'aluminium nécessaire.

Recherches exécutées sous les auspices de l'I. R. S. I. A. (Institut pour l'Encouragement de la Recherche Scientifique dans l'Industrie et l'Agriculture).

#### BIBLIOGRAPHIE

1. A. Guinier, "Imperfections in nearly perfect crystals" (J. Wiley, New York, 1952), 402.
2. P. Gay, P. B. Hirsch, and A. Kelly, *Acta Cryst.* (1954), sous presse.
3. C. G. Darwin, *Phil. Mag.* **27**, 315 (1914).
4. W. A. Wood and W. A. Rachinger, *J. Inst. Metals* **75**, 571 (1949).
5. C. Crussard, *Rev. Métall.* **41**, 111 (1944).
6. P. Lacombe, et L. Beaujard, *Rev. Métall.* **45**, 317 (1948).
7. C. S. Barrett, *Trans. A.I.M.E.* **161**, 15 (1945).
8. A. Guinier, et J. Tennevin, *Acta Cryst.* **2**, 133 (1949).
9. P. B. Hirsch, and J. N. Kellar, *Acta Cryst.* **5**, 162 (1952).
10. P. B. Hirsch, *Acta Cryst.* **5**, 168, 172 (1952).
11. B. E. Warren, and B. L. Averbach, *J. Appl. Phys.* **21**, 595 (1950).
12. M. F. Bertaut, *Comptes. rend., Paris*, **228**, 492 (1949). *Acta Cryst.* **3**, 14 (1950).
13. C. A. Julien, and B. D. Cullity, *Acta Met.* **1**, 588 (1953).
14. H. Lambot, L. Vassamillet, et J. Dejace, *Acta Met.* **711** (1953).
15. R. W. Cahn, *J. Inst. Metals* **76**, 121 (1949).
16. C. Crussard, *Rev. Métall.* **41**, 133 (1944).
17. H. Lambot, et L. Vassamillet, *Comptes. rend., Paris*, **235**, 1232 (1952).
18. G. P. Conard, B. L. Averbach, and M. Cohen, *Trans. A.I.M.E.* **197**, 1036 (1953).
19. D. C. Jillson, *Trans. A.I.M.E.* **188**, 1009 (1950).
20. J. B. Hess, and C. S. Barrett, *Trans. A. I.M.E.* **186**, 599 (1949).
21. P. Gay, and A. Kelly, *Acta Cryst.* **6**, 165, 172 (1953).
22. T. V. Cherian, P. Pietrowsky, and J. E. Dorn, *Metals Trans.* **185**, 948 (1949).
23. C. Crussard, et B. Jaoul, *Rev. Métall.* **47**, 589 (1950).
24. C. Crussard, 9e Congrès Solvay—R. Stoops (Bruxelles) 158 (1952).
25. W. G. Burgers, 9e Congrès Solvay—R. Stoops (Bruxelles) 82 (1952).
26. G. Borelius, 9e Congrès Solvay—R. Stoops (Bruxelles) 427 (1952).
27. R. D. Heidenreich, *J. Appl. Phys.* **20**, 993 (1949).
28. P. A. Beck, *Acta Met.* **1**, 422 (1953).

# ON THE DIFFUSION OF OXYGEN THROUGH SOLID IRON\*

J. L. MEIJERING†

Internal oxidation of three iron alloys showed—at least at 1200°C—no trace of intergranular preference. Normal interstitial diffusion of oxygen through the iron lattice must be assumed. Approximate values of the permeability (product of diffusion coefficient and solubility) of O in Fe at different temperatures are calculated from the sub-scale thickness. The permeabilities of Fe, Ni, Cu and Ag for oxygen at 85 per cent of their absolute melting temperatures are of the same order of magnitude. Discrepancies in the solubilities of O in solid Fe found by different authors are discussed.

## SUR LA DIFFUSION DE L'OXYGÈNE DANS LE FER À L'ÉTAT SOLIDE

L'oxydation interne de trois alliages de fer ne montre—du moins à 1200°C—aucune préférence pour la diffusion intergranulaire; il faut donc admettre une diffusion interstitielle de l'oxygène à travers le réseau du fer. Les valeurs approximatives de la perméabilité (produit du coefficient de diffusion par la solubilité) de l'oxygène dans le fer, ont été calculées à différentes températures à partir des épaisseurs des couches oxydées. Les perméabilités à l'oxygène du fer, du nickel, du cuivre, de l'argent, sont du même ordre de grandeur pour une température de 0,85  $T_f$  ( $T_f$ : température absolue de fusion). Les différences dans les solubilités de l'oxygène dans le fer trouvées par les différents auteurs sont discutées.

## ÜBER DIE DIFFUSION VON SAUERSTOFF IN FESTEM EISEN

Bei der inneren Oxydation von drei Eisen-Legierungen wurde wenn 1200°C keinerlei Bevorzugung der Korngrenzen festgestellt. Es muss daher angenommen werden, dass auch hier der Sauerstoff auf Zwischengitterplätzen durch das Eisen diffundiert. Aus der Dicke der Unterzunderschicht wurden Näherungswerte für die Durchlässigkeit (Produkt aus dem Diffusionskoeffizienten und der Löslichkeit) des Sauerstoffs im Eisen bei verschiedenen Temperaturen berechnet. Die Werte für die Durchlässigkeit des Eisens, Nickels, Kupfers und Silbers für Sauerstoff bei 85% ihres absoluten Schmelzpunktes sind von derselben Größenordnung. Es werden die von verschiedenen Autoren gefundenen Widersprüche in den Bestimmungen erörtert.

### 1. INTRODUCTION

A few years ago Kitchener, Bockris, Gleiser and Evans<sup>1</sup> determined the solubility of oxygen in iron, at temperatures between 1325°C and 1423°C. To prevent the possibility of FeO-formation on grain boundaries, iron was saturated with oxygen with respect to a CO<sub>2</sub>/CO mixture not sufficiently oxidizing to form FeO. The oxygen content was then determined by reducing with H<sub>2</sub>, which has the advantage that O bound by traces of Al, Si and Mn is only liberated to a more or less limited extent. The solubility in high-purity iron, over the temperature range mentioned, was found equal to the probable uncertainty of the method. Applying a 50 per cent extrapolation to the CO<sub>2</sub>/CO mixture in equilibrium with ferrous oxide, it was given as 0.003 ± 0.003 per cent by weight, and thus 0.01 ± 0.01 atomic per cent O. Higher solubilities found by previous investigators were attributed to internal oxidation of less noble elements present. Kitchener *et al* conclude that it is clear that the true solubility is quite negligible for all practical purposes, and that the mechanism of diffusion of O in Fe—necessary for the internal oxidation—is probably intergranular.

During experiments previously performed by the author, on the internal oxidation of several Fe alloys<sup>2</sup> at 1200°C, no preferential penetration along the grain boundaries was noted. The boundary of the internally oxidized rim was parallel to the metal surface, as is also

the case with Ni-alloys,<sup>3,2</sup> Cu-alloys<sup>4,5,6,3</sup> and Ag-alloys,<sup>7,3</sup> at least when the concentration of the alloying element is not too high and the oxidizing temperature not too low.

No photographs of the subscales (internally oxidized zones) in iron were published by the author, as the main purpose was a search for hardening effects. (These were not found, all oxides of alloying elements being formed in a too coarsely dispersed state.) The oxidation had been carried out in air, followed by a long diffusion anneal in nitrogen; the external oxidation of iron is rapid in comparison with the internal one, so the thickness of the subscale is greatly diminished when the atmosphere is air throughout the experiment.

In order to study the question of the existence of intergranular diffusion of oxygen somewhat further, new experiments were performed. As nitrogen is known to diffuse rapidly through iron, the possibility that the internal oxidation in air was accompanied by internal nitriding cannot be discarded. Therefore the new experiments were made in argon purified over heated magnesium turnings. During the first 15 minutes of the 6-hour anneal, 20 volume per cent O<sub>2</sub> was mixed with the argon. After the anneal, the alloys (still covered with oxide scale) were quenched in water.

Three alloys were used, vacuum-cast from high-purity materials in the apparatus of J. D. Fast:

A: 0.97% Al by weight, balance Fe.

B: 0.99% Al by weight, 30% Ni, balance Fe.

C: 0.50% Al by weight, 5% Sn, balance Fe.

\* Received September 21, 1954.

† Philips Research Laboratories, N. V. Philips' Gloeilampenfabrieken, Eindhoven, Netherlands.



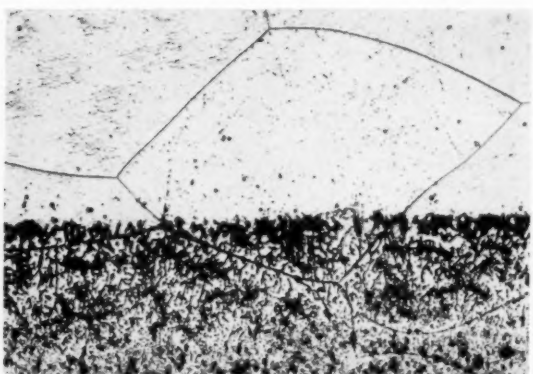
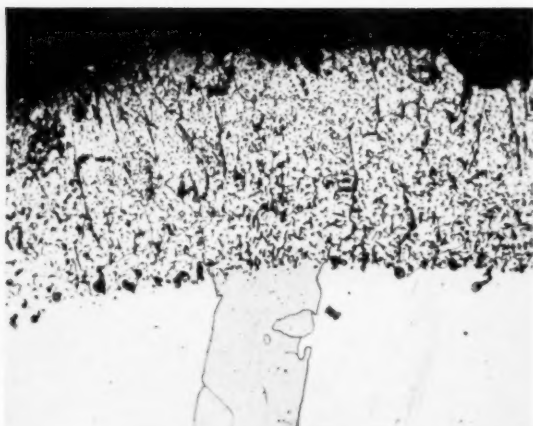


FIG. 1. Subscale of iron with 0.97% Al, heated at 1200°C  $\frac{1}{2}$  hour in argon with 20% O<sub>2</sub> followed by 5  $\frac{1}{2}$  hours in argon alone. Etched with nital. Magnification 200 $\times$ .

FIG. 2. Subscale of iron with 30% Ni and 0.99% Al. Same treatment as in Fig. 1. Etched with (NH<sub>4</sub>)<sub>2</sub>S<sub>2</sub>O<sub>8</sub>. Magnification 200 $\times$ .

The alloys *B* and *C* were examined because they have the advantage that the subscale formed at 1200 degrees retains its structure at room temperature: austenitic in the case of *B*, ferritic in the case of *C*. While Ni is more noble than Fe the affinities of Sn and Fe for O are about equal. The enthalpy of formation of  $\frac{1}{2}$  SnO<sub>2</sub> is 6 kcal more negative than that of "Fe<sub>0.95</sub>O," but, thanks to the relatively high entropy† of the latter oxide, the free enthalpy of  $\frac{1}{2}$  SnO<sub>2</sub> appears to become the higher one above about 500°C.<sup>8</sup> The low concentration of Sn (2  $\frac{1}{2}$  atomic per cent) contributes substantially to the stability of the dissolved Sn in the subscale, where the chemical potential of O is decreasing with depth from that of O in the FeO-rich scale. Thus it is to be expected that no significant amounts of Sn or Ni will be oxidized in the subscales of alloys *C* and *B* respectively.

The results of the experiments at 1200°C can be seen in Figs. 1 to 4. They do not show an appreciable influence of the crystal boundaries on the internal oxida-

tion. In the case of alloy *A*, the austenitic grain-size at 1200°C would have to be assumed very much finer than the ferritic one obtained on quenching, in order to explain Fig. 1 with the help of intergranular penetration of oxygen. This looks improbable. As the alloys *B* and *C* retain their crystal structure, Figs. 2 and 3 are still more convincing.

Similar experiments were carried out at 1050°C, 950°C and 850°C. Even at the lowest temperature no preferential penetration along the grain boundaries was appreciable in alloy *A*. In this case the depth of the subscale was only about 25 micron, with intercepts between grain boundaries of 2 mm, for instance. In alloy *C*, no grain-boundary influence was found at 1050°C and 950°C, but it was quite apparent at 850°C, the penetration being about 30 per cent greater at the boundaries. In alloy *B* this influence was seen already at 1050°C; at 950°C and 850°C it was very marked. Presumably a high nickel content favors penetration of

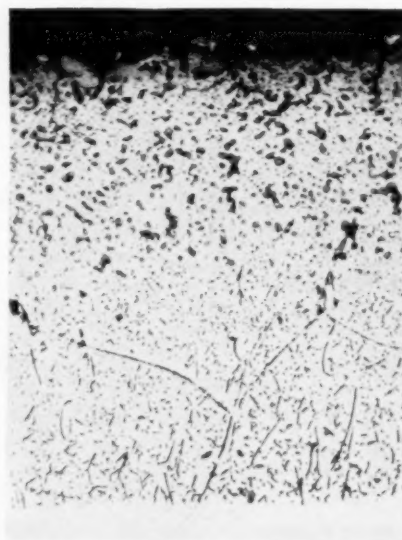
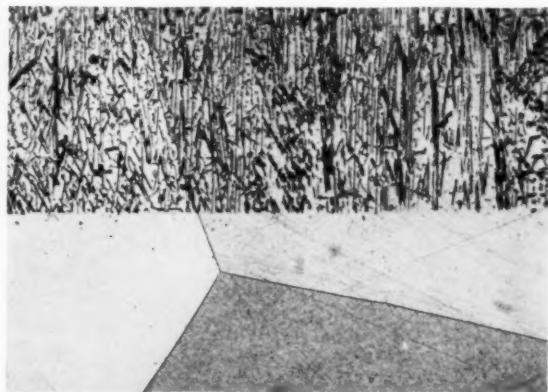


FIG. 3. Subscale of iron with 5% Sn and 0.50% Al. Same treatment, etch and magnification as in Fig. 1.

FIG. 4. Same as Fig. 2, but lightly etched. Magnification 275 $\times$ .

\* All four photographs reduced by  $\frac{2}{3}$  in reproduction.

† Which is also responsible for the stability of ferrous oxide with respect to Fe+Fe<sub>2</sub>O<sub>4</sub> above 570°C.

O along grain boundaries. It is well known that the external oxidation of nickel at, say, 700°C, is accompanied by pronounced intergranular oxidation. At 1200°C we found no appreciable influence of the grain boundaries on the subscale of Ni with, say, 0.5 per cent Al.

## 2. DISCUSSION OF THE INTERNAL OXIDATION

The experiments reported show that intergranular penetration of oxygen plays no significant role\* when the temperature is not too low. Only one possible objection seems feasible against applying this statement to iron with a much smaller percentage of Al or Si and to the diffusion of O through pure iron: Diffusion along the surface of the oxide particles could be imagined to be the main factor, especially in cases like Fig. 3, where the "needles" (probably intersected platelets) are preferentially oriented in the direction of diffusion.† This orientation was also found in the case of Ni containing Al-oxide.<sup>2,3</sup> Still, the penetration velocity was found<sup>9</sup> in good agreement with the results of Smithells and Ransley<sup>10</sup> on the diffusion of O through rather pure nickel. The internal oxidation of Cu alloys is likewise in fair agreement<sup>11,9</sup> with Ransley's results on copper.<sup>12</sup> In the case of Ag alloys<sup>7,9,13</sup> there is an appreciable deviation from the results obtained by Johnson and Larose on pure silver;<sup>14</sup> the apparent acceleration by the oxide, about a factor 2 to 5, may be due<sup>7</sup> partly to Johnson and Larose's results being too low.

We may conclude that it looks improbable that the internal oxidation of our three iron alloys is accelerated to a large extent by the presence of the oxide particles themselves. On the other hand, there appears to be no objection to assuming normal interstitial diffusion of O through the Fe lattice. A solubility of 0.01 atomic per cent is low, but, as the diffusion coefficient of interstitial solutes is very high in comparison to that of substitutional ones, it is quite sufficient for internal oxidation, even when the alloying element has a 1 atomic per cent concentration. For instance, the solubility of O in silver at 800°C, in equilibrium with air of normal pressure, is less than 0.015 atomic per cent. But even in nitrogen with 0.02 per cent O<sub>2</sub>, internal oxidation<sup>9</sup> of Ag containing 1 atomic per cent Mg was visible after 6 hours at 850°C. Under these circumstances the solubility is less than 0.001 atomic per cent O.

The main reason that Kitchener *et al* are of the opinion that the true solubility of O in  $\gamma$ -Fe will be very low appears to be a theoretical one. For instance, in their Trans. Faraday Soc. paper,<sup>1</sup> they write: "The structural reason for the very low solubility of oxygen in

iron (and in copper) as contrasted with its measurable solubility in silver and very large solubility (up to 40 atom. %) in zirconium, titanium and vanadium, is almost certainly that oxygen is too large to be accommodated interstitially in the iron lattice." Although this geometrical factor is important, and, for instance, is generally regarded as the reason for the low solubility of carbon in  $\alpha$ -Fe as compared with  $\gamma$ -Fe, it seems dangerous to omit any reference to the chemical factor. At 800°C the solubility of O in Cu (in equilibrium with Cu<sub>2</sub>O) is\* about 30 per cent of that of O in Ag (in equilibrium with 1 atmosphere O<sub>2</sub>). This means, however, that at one and the same equilibrium oxygen pressure, O is more than 10<sup>4</sup> times more soluble in Cu than in Ag. Thus, the oxygen dissolved at, say, 600°C in a eutectic Ag-Cu alloy will be virtually present in the copper-rich phase only, despite its smaller lattice parameter.

One may still expect a positive correlation between maximum obtainable solid solubility and size of the interstices by a rough line of reasoning; a strong affinity for O in the metal phase may mostly be accompanied by a great stability of its oxide. If one assumes that these two chemical factors counterbalance each other more or less, the geometrical factor remains. In this way one might argue that the oxygen solubilities in copper (in equilibrium with Cu<sub>2</sub>O) and in  $\gamma$ -iron (in equilibrium with ferrous oxide) will be roughly equal, because these metals have practically the same face-centered cubic lattice parameter.

It goes without saying that this reasoning is extremely rough. In the opinion of the author, a correlation found between solid solubilities and, for instance, the geometry of the lattice must always be interpreted very carefully, when the second phase is not the same.

Apart from this, the radii of the interstices in different metals used by Kitchener *et al* are proportional to their atomic radii, no allowance being made for the different geometries of the body-centered and face-centered cubic lattices. When this is taken into account, the geometrical circumstances in vanadium (with its rather large oxygen solubility) are *less* favourable than in Cu and  $\gamma$ -Fe. Seybolt and Fullman, in a recent note,<sup>16</sup> also appear to neglect the influence of structure on interstice dimensions. They plot solubilities of O in a number of transition metals *versus* Young's modulus over octahedral volume. The exact meaning of this volume is not quite clear, but the tabulated values are closely proportional to the volume per mole of the metals, irrespective of whether they are face-centered or body-centered cubic.

## 3. QUANTITATIVE RESULTS FOR THE PERMEABILITY OF IRON FOR OXYGEN

Using certain assumptions, the permeability can be easily calculated from the thickness of the subscale:

$$c_1 D_1 = \frac{2}{3} c_2 b^2 / 2l. \quad (1)$$

\* When the lowest of the reported determinations<sup>15</sup> is taken.

\* Note added in proof.—Recently Seybolt (J. Metals 6, 979 (1954))—from experiments on FeO precipitation—also concluded that intergranular diffusion is at least not the main process for penetration of O into  $\alpha$ -Fe.

† It should be mentioned that the etching necessary for developing the grain boundaries exaggerates the apparent size of the oxide particles. This can be seen by comparing Fig. 2 with Fig. 4, where etching was light. Here, one sees a marked difference in particle form between the interior and the exterior part of the subscale. It is not known whether we have Al<sub>2</sub>O<sub>3</sub> inside and, for instance, FeAl<sub>2</sub>O<sub>4</sub> outside.

Here  $c_1$  is the solubility of oxygen (in equilibrium with the scale) and  $c_2$  the Al-concentration of the alloy, both expressed in atomic fractions.  $D_1$  is the diffusion coefficient of O through the subscale; the product  $c_1 D_1$  will be called the permeability;  $b$  is the thickness of the subscale obtained in the time  $t$ . The main assumptions are (cf. reference 3)

1st:  $c_1$  must be small compared with  $c_2$ ; this is certainly the case here.

2nd:  $c_1 D_1$  must be large compared with  $c_2 D_2$ , where  $D_2$  is the diffusion coefficient of Al in the alloy. If not, there is enrichment of Al in the subscale by outward diffusion towards the internal oxidation boundary. Probably this condition is least fulfilled in the case of alloy C (ferrite) at 1200°C. From data calculated by Seith,<sup>17</sup> from experiments by Ageev and Vher,<sup>18</sup>  $D_2$  would be about  $2.5 \cdot 10^{-8}$  cm<sup>2</sup>/sec at 1200°C, making  $c_2 D_2$  nearly  $\frac{1}{4} c_1 D_1$ . However, in these experiments the Al concentration in the ferrite zone went up to 50 atomic per cent, and  $D_2$  may be much smaller near 1 atomic per cent. We have seen no signs of concentration gradients in the alloys beneath the subscale, but admittedly this is not a strong argument with these low Al concentrations. In any case we think the uncertainty in question is less than the next one:

3rd:  $\frac{3}{2}$  O-atoms are assumed to be bound per Al atom. If, for instance,  $\text{FeAl}_2\text{O}_4$  is formed (instead of  $\text{Al}_2\text{O}_3$ ) over the whole subscale cross section, the factor  $\frac{3}{2}$  in formula (1) should be changed to 2; this gives a possible error of 30 per cent.

4th: It is assumed that diffusion is the controlling process, the reaction at the scale/subscale interface being rapid. For the experiments at 1200°C this seems to be the case, as proportionality between  $b$  and  $\sqrt{t}$  was found\* in changing  $t$  to 25 per cent of the normal time. At the lower temperatures this check was not made; it is possible that the low value of  $c_1 D_1$  for alloy C at 850°C (see Fig. 5) is due to insufficient rapidity of the interface reaction.

5th:  $5\frac{3}{4}$  hours, the annealing time in argon, was inserted for  $t$ . The neglect of the subscale thickness obtained after  $\frac{1}{4}$  hour in  $\text{A/O}_2$  is not important, as this means a 4 per cent uncertainty in  $c_1 D_1$  at the utmost.

Three runs were made at 1200°C, two at 850°C and at 950°C, and one at 1050°C. The alloy sections (15×3 mm) were examined over the whole circumference, as irregularities appear (cf. Fig. 1), possibly due to local flaking off of the subscale together with the scale on quenching. The values of  $b$  obtained in the duplicate experiments varied only about 5 per cent from the

\* This proportionality does not exclude a reaction resistance developed by the diffusion process: during the argon anneal the interior layers of the scale lose oxygen, diffusing into the subscale. It is possible that the iron film so formed adheres somewhat poorly to the subscale proper. In unpublished preliminary experiments with Cu-alloys, the author found some evidence that (when allowance is made for external scaling) the subscale is, cet. par., thickest when the atmosphere is air throughout the heating period. This effect seems not important for our iron alloys, in view of the other uncertainties.

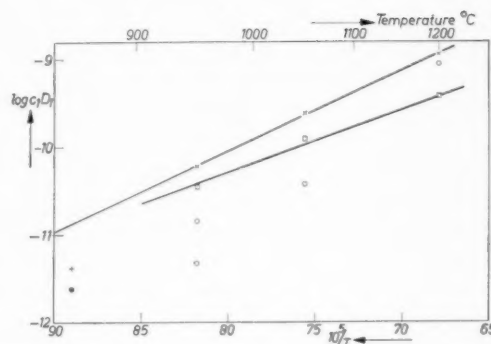


FIG. 5. Permeability  $c_1 D_1$  of three iron alloys for oxygen ( $c_1$ =solid solubility in atomic fraction,  $D_1$  in cm<sup>2</sup>/sec), as calculated from internal oxidation. + alloy A: 1.99 at. % Al, ferritic; x alloy A: 1.99 at. % Al, austenitic; o alloy B: 2.06 at. % Al, 29 at. % Ni, austenitic; x alloy C: 1.06 at. % Al, 2.4 at. % Sn, ferritic; o = o coinciding with x.

average used for calculating  $c_1 D_1$  in Fig. 5, with the exception of alloy B at 950°C, where the discrepancy was large. This will be mainly due to the pronounced intergranular penetration of O in this alloy at low temperatures (cf. Section 1). It is thought that the 1200°C point of this alloy, and the three highest points of alloys A and C, give the correct values for  $c_1 D_1$  within a factor 2. Apart from this, the values of the permeability of Fe, Fe with 30 per cent Ni and Fe with 5 per cent Sn may well be a factor 2 smaller than those of the subscales containing aluminum oxide (see Section 2).

From Fig. 5 we may conclude that the permeabilities of ferrite and austenite for oxygen are of the same order of magnitude. More precise conclusions do not appear warranted: The low value of the ferritic A point at 850°C, as compared with the austenitic A points, may be due to slow interface reaction (compare the points of alloy C, which should lie all four on one line). On the other hand, the differences between the three alloys at higher temperatures will be partly due to the influence of Sn and Ni.

The slopes of the lines drawn in Fig. 5 for alloys A and C correspond to energies of 32 and 42 kcal/mole. These are equal to the sum of the diffusion activation energy and the heat of solution of ferrous oxide in the metal.

Bramley *et al.*<sup>19</sup> have deoxidized Armco iron by heating in pure hydrogen for 100 hours at 1000°C. The analysis of subsequent layers gave nearly 0.03 per cent O by weight at the surface, the initial concentration of 0.09 per cent was reached at about 0.6 mm depth. The main part of the curve of per cent O versus depth was a straight line with a slope of 0.13 per cent per mm.

It seems rather improbable that the solubility of O in  $\gamma$ -iron would be as high as 0.09 per cent. Presumably most of the oxygen was present as ferrous oxide; the fact that its concentration did not drop sharply to a low level in a homogeneous rim must then be attributed to a slow solution velocity of ferrous oxide in the matrix. A value of roughly  $1.5 \cdot 10^{-11}$  cm<sup>2</sup>/sec can be calculated for



$c_1 D_1$  from this experiment, while from Fig. 5 one would expect  $5 \cdot 10^{-11}$  cm<sup>2</sup>/sec at 1000°C. In view of the uncertainties at both sides, this discrepancy is not disturbing.

When the permeabilities for oxygen of Fe, Ni, Cu and Ag (in air of normal pressure) at 85 per cent of the absolute melting point are calculated from the internal oxidation experiments, one finds that  $c_1 D_1$  of Fe and Ni lie between the values of Cu and Ag, which differ by a factor 5.

#### 4. THE SOLUBILITY OF O IN $\alpha$ - AND $\gamma$ -IRON

Seybolt<sup>20</sup> has determined the solubility of O in  $\alpha$ -Fe at five temperatures in the range 700°–900°C. At 900°C, about 0.029 per cent O by weight was found; this is a factor 10 more than the solubility found by Kitchener *et al* in  $\gamma$ -Fe near 1400°C. When Seybolt's linear plot of log concentration versus  $1000/T$  (heat of solution: 15.5 kcal) is extrapolated to the  $\delta$ -region, one gets a solubility that is greater than that of O in liquid iron at 1520°C. Thus it appears that his values are too high, or that the heat of solution is too large. The latter supposition is supported by the fact that Seybolt's points at 700°C and 770°C lie definitely below a line drawn through the points at higher temperatures. At 850°C, the value of the diffusion coefficient obtained by dividing the permeability  $c_1 D_1$  found in this paper by Seybolt's value for  $c_1$ , is only just sufficient for practical saturation of the strip in the time used. Therefore it looks quite possible that the lowest points are indeed too low. A line drawn through the three highest temperature points would give 10.5 kcal for the heat of solution. Extrapolation yields 0.105 per cent O at 1370°C. At this temperature the coexisting ferrous oxide becomes liquid. Subtracting 7.5 kcal for the heat of fusion,<sup>21</sup> the heat of solution decreases to 3 kcal, yielding 0.11 per cent O by weight at the three-phase temperature  $\delta$ -Fe+liquid metal+liquid oxide (about 1525°C).

This is still a large value: it is half of the oxygen concentration in liquid iron and twice the solid solubility in  $\delta$ -Fe found by Fischer and von Ende<sup>22</sup> at this temperature. In view of the long linear extrapolation from the  $\alpha$ - to the  $\delta$ -region one may say, however, that Seybolt's results at 800°C–900°C are in accord with that of Fischer and von Ende at 1520°C.

Although Kitchener *et al* distrust high solubilities of oxygen in solid iron in general, they claim their value of  $0.003 \pm 0.003$  per cent only for the  $\gamma$ -phase. Their highest temperature is at 1423°C  $\pm 20^\circ$ C. One might, therefore, accept that the solubility is much lower in  $\gamma$ -Fe than in  $\alpha$ -( $\delta$ -) Fe, as is done by Seybolt.<sup>20</sup>

This is rather unexpected, in view of the opposite state of affairs with carbon and nitrogen. A more pertinent difficulty is the following:

Fischer and von Ende's value of 0.055 per cent means, using 3 kcal for the heat of solution (see above), a solubility of 0.05 per cent O in  $\delta$ -Fe around 1400°C. In the CO<sub>2</sub>/CO mixture used by Kitchener *et al* this be-

comes 30 per cent less. When 0.002 per cent is taken for the solubility in  $\gamma$ -Fe under these conditions, and Zener's free-energy data<sup>23</sup> are used, one finds that the  $\gamma$ - $\delta$  transformation point should be decreased by about 25 degrees. Then Kitchener *et al* would have been also in the  $\delta$ -region with their determinations. It is difficult to escape the conclusion that either the results of Fischer and von Ende and of Seybolt are too high, or those of Kitchener *et al* too low.\*

In principle, a metallographic method, as used by the first authors, may give too high values. Seybolt's results cannot be attributed to internal oxidation of impurities.<sup>20</sup> Intergranular ferrous oxide could not be detected, but does not seem to be out of the question. The same author has determined solid solubilities of O in nickel.<sup>24</sup> These show a very abnormal feature: At 1200°C, 0.012 per cent by weight was found, but this increased at decreasing temperature. This would mean that the entropy of dissolution of NiO in this very dilute solid solution is negative, which is extremely improbable.† Presumably these results are due to the well-known intergranular oxidation of nickel, which becomes more pronounced at lower temperatures.

On the other hand, the only possibility for the determinations by Kitchener *et al* being too low appears to be a very slow uptake of O at the strip surface. This was found by the present author in the case of dilute copper alloys (e.g., 0.3 per cent Be at 950°C); he repeatedly tried in vain<sup>25</sup> to produce hardening by internal oxidation in atmospheres just not oxidizing enough to form Cu<sub>2</sub>O. When strips had been heated in a stream of N<sub>2</sub> containing a very small percentage of O<sub>2</sub>, a subscale was formed only beneath a skin of scale at the exposed parts of the strips; it was absent where the surface had remained metallic. Obviously oxygen enters the metal much more easily from Cu<sub>2</sub>O than from the gas atmosphere. Although the reaction resistance will have been amplified by BeO formation, there is a possibility that Fe will take up oxygen much more rapidly from a FeO-scale—as in Seybolt's method—than from the CO<sub>2</sub>–CO mixture used by Kitchener *et al*. These authors have increased their heating periods until no further increase in the oxygen absorbed was observed, but this absorption was not much greater than the "blank" value. This uncertainty might be removed by approaching the equilibrium also from the high-oxygen side: first saturating beneath an FeO scale, and then heating in the CO<sub>2</sub>–CO mixture at the same temperature. Experi-

\* Note added in proof.—In a recent investigation by F. Weber, W. A. Fischer and H. Engelbrecht, (Stahl u. Eisen), **74**, 1521 (1954), the solubility of O in  $\delta$ -Fe was found to be about 10 times smaller than in reference 22.

† When the coexisting phase is a gas (of constant pressure)—and thus has a high entropy—even a still smaller solid solubility may increase with decreasing  $T$ . This is the case for oxygen in silver below 400°C. In this temperature region the entropy (and enthalpy) of dissolution of O<sub>2</sub> in saturated Ag is negative, but it becomes positive above 400°C. The differential specific heat of O in solid silver is remarkably high. From the solubility measurements by Steacie and Johnson<sup>26</sup> one calculates about 15  $R$  per gram atom oxygen.



ments by Rees and Hopkins<sup>27</sup> show that at 950°C the solubility of O in  $\gamma$ -Fe must be less than 0.007 per cent.

It should be mentioned that in this laboratory both J. L. Snoek and J. D. Fast have sought an internal friction effect in  $\alpha$ -Fe containing oxygen, but without success. This negative result favours a very low solubility in ferrite.

#### ACKNOWLEDGMENT

The author's thanks are due to Professor J. D. Fast for supplying the high-purity alloys, and to Mr. W. Kreutzelman for assistance in the experimental work.

#### REFERENCES

1. J. A. Kitchener, J. O'M. Bockris, Molly Gleiser, and J. W. Evans, *Acta Met.* **1**, 93 (1953); *Trans. Faraday Soc.* **48**, 995 (1952).
2. J. L. Meijering, Pittsburgh International Conference on Surface Reactions, 103 (1948).
3. J. L. Meijering and M. J. Druyvesteyn, *Philips Res. Rep.* **2**, 81 (1947).
4. Cyril S. Smith, *Min. and Met.* **11**, 213 (1930); **13**, 481 (1932).
5. K. W. Fröhlich, *Z. Metallk.* **28**, 368 (1936).
6. F. N. Rhines, *Trans. A.I.M.E.* **137**, 246 (1940).
7. F. N. Rhines and A. H. Grobe, *Trans. A.I.M.E.* **147**, 318 (1942).
8. L. Brewer, *Chem. Reviews* **52**, 1 (1953).
9. J. L. Meijering and M. J. Druyvesteyn, *Philips Res. Rep.* **2**, 260 (1947).
10. C. J. Smithells and C. E. Ransley, *Proc. Roy. Soc.* **A155**, 195 (1936).
11. F. N. Rhines, W. A. Johnson, and W. A. Anderson, *Trans. A.I.M.E.* **147**, 205 (1942).
12. C. E. Ransley, *J. Inst. Metals* **65**, 147 (1939).
13. V. Gottardi, *Metallurgia Ital.* **44**, 424 (1952).
14. F. M. G. Johnson and P. Larose, *J. Am. Chem. Soc.* **46**, 1377 (1924); **49**, 312 (1927).
15. A. Phillips and E. N. Skinner, *Trans. A.I.M.E.* **143**, 301 (1941).
16. A. U. Seybolt and R. L. Fullman, *J. Metals* **6**, 548 (1954).
17. W. Seith, "Diffusion in Metallen," Berlin, 1939.
18. N. W. Ageev and Olga I. Vher, *J. Inst. Metals* **44**, 83 (1930).
19. A. Bramley, F. W. Haywood, A. T. Coopers, and J. T. Watts, *Trans. Faraday Soc.* **31**, 707 (1935).
20. A. U. Seybolt, *J. Metals* **6**, 641 (1954).
21. L. S. Darken and R. W. Gurry, *J. Am. Chem. Soc.* **68**, 798 (1946).
22. W. A. Fischer and H. von Ende, *Arch. Eisenhütt.* **21**, 297 (1950).
23. C. Zener, *Trans. A.I.M.E.* (1946), T.P. 1856.
24. A. U. Seybolt, "Metals Handbook," p. 1231, Cleveland, A.S.M. (1948).
25. Unpublished.
26. E. W. R. Steacie and F. M. G. Johnson, *Proc. Roy. Soc.* **A112**, 542 (1926).
27. W. P. Rees and B. E. Hopkins, *J. Iron Steel Inst.* **172**, 403 (1952).

## TWINNING AND ACCOMMODATION KINKING IN ZINC\*

A. J. W. MOORE†

The traces of twins and their accompanying accommodation kinks in cleavage surfaces of zinc single crystals were examined by interferometry and by optical and reflection electron microscopy. They were compared with metallographic sections cut normal to the twin trace. The results suggest that changes of shape of the twin beneath the surface determine the number and distribution of the accommodation kinks lying parallel to the twin trace. A growth history of the twin is described which conforms to these observations. The tip of the twin inside the metal may be markedly blunted giving rise to considerable internal stress.

### MACLES ET KINKING D'ACCOMMODATION DANS LE ZINC

Les traces des macles et des Kinkings d'accommodation sur la surface de clivage de monocristaux de zinc sont étudiées par interférométrie et par microscopies optique et électronique. Elles sont comparées aux coupes métallographiques perpendiculaires à la trace de la macle. Les résultats indiquent que les changements de forme de la macle au-dessous de la surface déterminent le nombre et la répartition des Kinkings d'accommodation. Un mode de croissance des macles, conforme à ces observations, est décrit. La pointe de la macle à l'intérieur du métal donne naissance à l'importantes contraintes internes.

### DIE ENTSTEHUNG VON ZWILLINGEN UND AKKOMODATIONS-KINKS IN ZINK.

Die Spuren von Zwillingen und die sie begleitenden Akkomodations-Kinks auf Spaltflächen von Zink Einkristallen wurden interferometrisch und durch optische und elektronenreflektions-mikroskopische Methoden untersucht. Sie wurden mit metallographischen Proben, die senkrecht zur Zwillingssebene entnommen worden waren, verglichen. Die Ergebnisse lassen die Vermutung zu, dass die Veränderungen in der Gestalt des Zwillings unter der Oberfläche die Anzahl und die Verteilung der zu den Zwillings Spuren parallel liegenden Akkomodations-Kinks bestimmen. Ein mit diesen Beobachtungen übereinstimmender Wachstumsablauf der Zwillingsbildung wird beschrieben. Die im Metall liegende Spitze des Zwillings kann auffallend abgestumpft sein und so zu beträchtlichen inneren Spannungen Anlass geben.

The phenomena of kinking and twinning in zinc are readily studied on faces of single crystals cleaved on the basal plane. Since this plane contains the only definitely established slip directions, the examination is not complicated by deformation due to simple slip.

The traces of twins appear on cleavage faces in three directions mutually at  $120^\circ$  (parallel to the axial directions) and are the result of a shear of about  $0.14$  ( $8^\circ$ ) on the  $10\bar{1}2$  planes. Although the atom movements are rather more complex<sup>1</sup> many of the larger scale effects of twinning can be interpreted in terms of a simple shear which causes a change of slope of  $3^\circ 58'$  on the basal plane, thus making the twin visible on cleavage faces.

Orowan<sup>2</sup> and Hess and Barrett<sup>3</sup> showed that cadmium and zinc can deform plastically by a mechanism involving a sudden bend or kink in the basal plane. The bend planes are perpendicular to the basal planes and produce sets of kinks which are either parallel to, or normal to, the  $a$ -axes and which are hence first- and second-order prismatic planes respectively.

The concept of kinking has made it possible to explain how the shear strain due to twinning may be accommodated in the lattice when the twin is not propagated right through the crystal. Jillson<sup>4</sup> pictured the process as a simple first-order kink parallel to the

twin trace on the cleavage plane as shown in Fig. 1. When the twin trace on a cleavage plane is lenticular in shape, Pratt and Pugh<sup>5</sup> have shown that the strain at the end of the twin is accommodated by a kink at right angle to the twin trace and crossing it at its tip. Moore<sup>6</sup> and Holden<sup>7</sup> have measured the angle of the first-order accommodation kink by independent methods which show that the principal kink, when fully developed, does not appear to bend the lattice by more than about  $45^\circ$ – $50^\circ$ .

The angles and dimensions of a kink are of particular interest because they are a measure of the changes of shape of the twin beneath the surface. It has been shown<sup>5,6</sup> that the same twin may have other first-order accommodation kinks parallel to the principal kink and lying between it and the twin. These have been termed

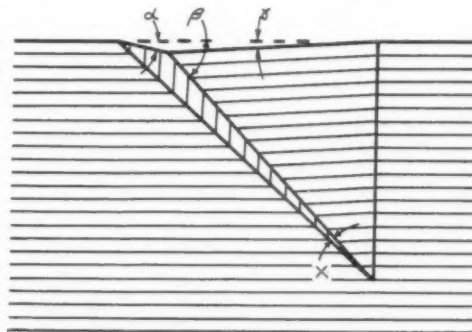


FIGURE 1.

\* Received July 6, 1954; in revised form October 6, 1954.

† Research Laboratory on the Physics and Chemistry of Surfaces, Department of Physical Chemistry, Cambridge, England, and now at Division of Tribophysics, C.S.I.R.O., Melbourne, Australia.

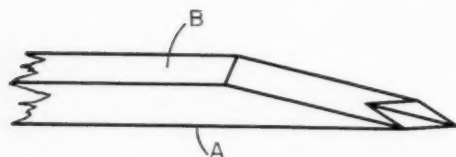


FIGURE 2.

secondary kinks in this paper. Further examples are described and compared with metallographic sections of the same twins and their possible importance in the development of the twin is discussed.

### EXPERIMENTAL

#### Preparation and Cleavage of Single Crystal Specimens

Single crystals about 15 cm long and 1 cm square cross section were grown by the method of Bridgman<sup>8</sup> from 99.998 per cent Zn (Imperial Smelting Corporation Crown Special Zinc) in graphite moulds shaped to give the pointed crystal shown in Fig. 2, under a vacuum of  $10^{-3}$  mm Hg. Crystals oriented with the specimen axis in the basal plane and the face A (Fig. 2) making an angle of  $10^\circ$  or less with the basal plane were selected and specimens 1 cm long parted off by cutting with hydrochloric acid. The faces (A and B) approximately parallel to the basal plane were soldered to the brass holders of a small tensile testing machine and cleaved by application of tensile stress approximately normal to the basal plane.

For the sectioning experiments another set of zinc crystals were made from 99.999 per cent Zn (Imperial Smelting Corporation Special High Purity Zinc) in round Pyrex glass moulds sealed *in vacuo*. Crystals were selected with the basal plane approximately perpendicular to the longitudinal axis and specimens a few millimeters thick were parted from these while at liquid air temperature by cleaving with a knife. The cleavage features on these surfaces appeared to be identical with those produced by cleavage in tension. Twins with traces in directions suitable for sectioning were produced by bending the crystal over a 6-mm diameter rod after cleavage.

#### Techniques of Examination

On the cleaved zinc surface, features such as kinks and twins can be detected only by methods sensitive to very small changes of tilt of the surface, and with the Vickers Projection Microscope the best results were obtained with the 33 mm lens and the plane glass illuminator. The use of such a low-aperture lens restricted the magnification used. For greater resolution, both in the plane of the specimen surface and in a direction normal to it, the technique of reflection electron microscopy as applied by Menter<sup>9</sup> was used. This method is very sensitive to small changes of slope, particularly when the change occurs about an axis

approximately perpendicular to the plane of incidence of the electron beam. Owing to the oblique angle of observation ( $10^\circ$ – $13^\circ$ ), the image is greatly foreshortened and a scale is given on each picture showing the magnifications in the plane of the surface in the direction of the beam, and normal to the beam. For measuring changes of slope, both a needle-type profilometer (Talysurf) and multiple-beam interferometry were used. For the latter, pieces of selected microscope slide about 2 mm square, partially silvered to give about 25 per cent reflection in order to match the reflectivity of the zinc, were used as reference flats and the specimens were observed using an illuminating system as described by Tolansky.<sup>10</sup>

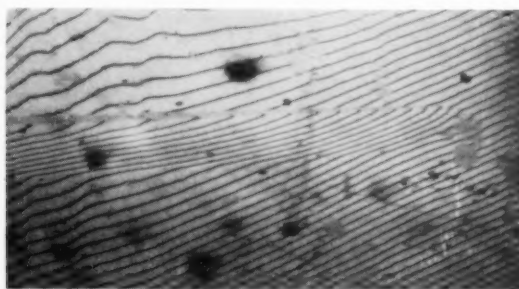
Prior to sectioning the cleavage surfaces in a direction normal to the cleavage plane and to the twin trace, the crystal was given a heavy electrodeposit of zinc and cold-mounted in plastic. The desired section was exposed by grinding under water on a 150-grade carborundum paper followed by the finer grades and subsequently diamond-polished using the technique of Samuels.<sup>11</sup> Finally, the specimen was electropolished in a phosphoric acid-alcohol bath<sup>12</sup> until all deformation due to grinding was removed. These specimens were examined in a Bausch and Lomb Metallograph under polarized light. The section was identified by means of diverging scratches drawn on the cleavage surface before plating.

Angle measurements from the sections are only approximate since if slip occurs, the shear parallel to the basal plane would have the effect of changing the angle between planes which coincided with the original twin plane and the original basal plane. If the shear is inhomogeneous the twin may appear curved.

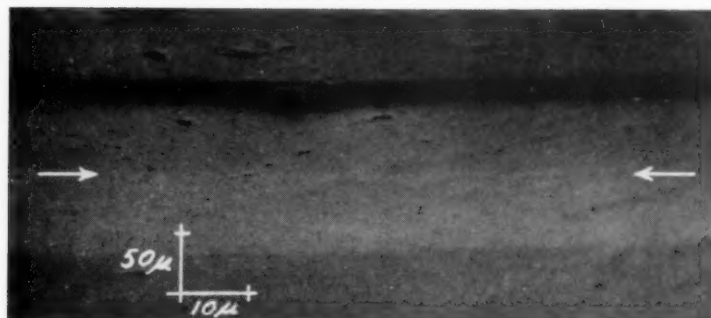
### RESULTS AND DISCUSSION

When partial cleavage occurs on a basal plane other than that on which the crystal actually parts, bending strain in parts of the crystal may cause twinning. A twin formed in this way and accompanied by marked accommodation kinking, was extensively studied both by interferometry and reflection electron microscopy.

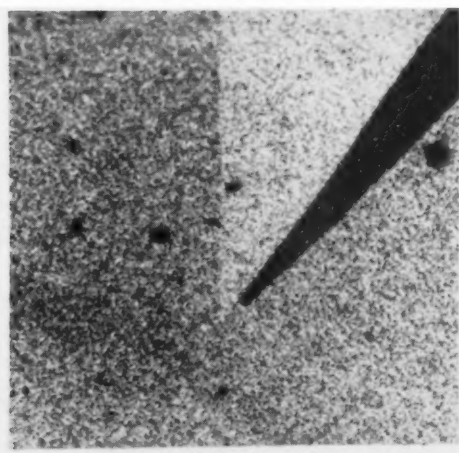
(i) *The angular relationships between a twin and its kink:* Figure 3 shows the multiple-beam interference fringes across the twin and its accommodation. The angle between the surface of the accommodation region and the undeformed surface ( $\gamma$  in Fig. 1), measured at selected points along the twin, is shown in Fig. 4. It varies between  $40'$  and  $17'$  and decreases progressively towards the thin end of the twin. On the same graph the width of the twin ( $w$ ) and the width of the accommodation ( $W$ ) are plotted. If it is assumed that the lattice relationships for the twin and its accommodation kink have the simple geometrical pattern shown in Fig. 1, then since angles  $\alpha$  and  $\beta$  are known from the lattice constants of zinc, the angle between the sides of the twin in the body of the metal (angle  $X$  in Fig. 1) can



3



5



11

FIG. 3. Interference fringes across the end of a twin and its accommodation kink. FIG. 5. Reflection electron micrograph of twin with an accommodation kink (shown by arrows) half-way across the accommodation region. FIG. 11. The tip of the twin shown in FIG. 7 at higher magnification (polarised light).

be expressed in terms of  $w$  and  $W$  by

$$\tan X = \frac{0.4654R}{0.9976 - 0.4987R}, \quad \text{where } R = \frac{w}{w+W} \quad (1)$$

This expression holds for the two conditions where the twin plane is the side of the twin nearest to, and furthest from, the accommodation kink.

This angle appears to fall from a value of about  $4^\circ$  to

about zero at the end of the twin. Twin and kink systems already illustrated in the literature can be similarly measured and they give approximate values for  $X$  of  $4^\circ 50'$ ,<sup>7</sup> and about  $5^\circ$ .<sup>8</sup>

The angle  $X$  can also be expressed in terms of the angle ( $\gamma$ ) of the principal kink

$$\tan X = \frac{6.711}{7.199 + 0.9976 \cot \gamma} \quad (2)$$



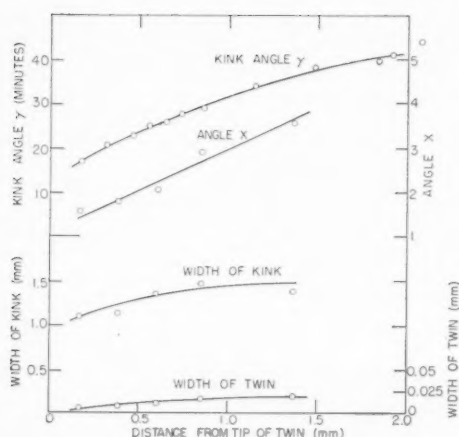


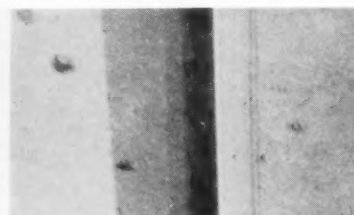
FIGURE 4.

and from this it appears that the value of  $0^{\circ}45'$  which has been suggested for the maximum angle for the principal kink of a simple twin in zinc corresponds to an angle of  $X$  of  $4^{\circ}40'$ .

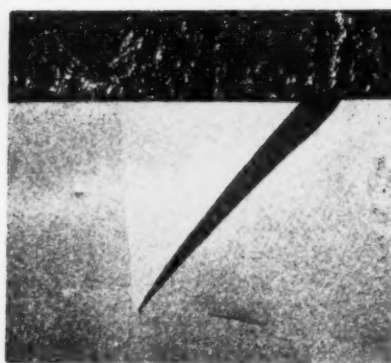
(ii) *The relationship between the shape of a twin and its kinks:* In Fig. 3 the contour lines across the accommodation zone are not straight, showing that near the twin the slope of the cleavage plane is reduced. The same phenomenon, which indicates the presence of one or more secondary kinks between the principal kink and the twin, has also been shown by using a needle-type surface profilometer.<sup>6</sup> The secondary kinks may be either in the same or the opposite sense to the principal kink increasing or reducing the slope of the basal plane respectively. Figure 5 is an electron micrograph showing another example of the latter type. It is a portion of the twin and its accommodation kink at a point about 0.4



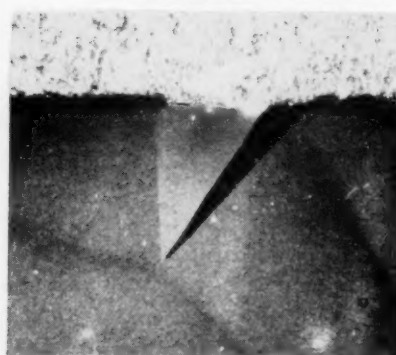
6a



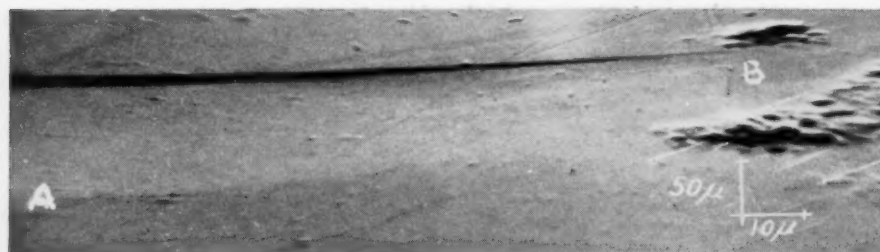
7a



6b



7b



12

FIGS. 6 and 7. Comparisons between the traces of twin kink systems on the cleavage plane, with the corresponding sections. The sections are taken with polarised light. FIG. 12. Reflection electron micrograph showing how the accommodation kink becomes indefinite near the end of the twin. The patches of corrosion near the end of the twin may be seen also in FIG. 3 as grey patches which interrupt the interference fringes.

mm from its tip, and a change in slope can be observed about half-way across the accommodation region. The intensity of the reflected electrons from the different regions shows that the secondary kink is in the opposite sense to the primary kink.

Examples of the former type of secondary accommodation are shown in the optical photomicrographs in Figs. 6a and 7a where the tones of the different regions indicate that the accommodation slope is greater nearer the twin. Talysurf records across the same regions gave the traces shown in Fig. 8. The principal kink in Fig. 8a is about  $40'$  and applies to the twin shown in Fig. 6. For Fig. 8b it is about  $50'$  and corresponds to the twin in Fig. 7, and in both cases there is a marked increase near the edge of the twin. In all cases of accommodation studied, a smooth bend was never observed but always an abrupt kink.

Equation (2) indicates that an increase in the angle between the sides of the twin should be accompanied by an increase in the angle of the accommodation kink. Thus, where there is more than one kink the angle between the sides of the twin should vary to correspond with the different kinks.

This relationship was investigated by cutting sections normal to the basal plane and to the twin trace on the basal plane. Figures 6b and 7b are sections of the twins shown in Figs. 6a and 7a and show clearly the slope of the cleavage plane due to the twinning shear, and the accommodation kink.

The side of the twin furthest from the accommodation kink appears to consist of three regions of different slope: (a) Near the surface the two sides of the twin are nearly parallel. (b) Towards the middle of the twin the sides converge sharply. (c) Furthest from the surface the sides converge more gently. Sections of several twins have been observed and the majority have shown only slopes (a) and (c). Photographs of these taken normal to the cleavage plane showed a secondary kink of sense opposite to that of the principal kink. This produced a region of low accommodation angle near the twin which corresponded to slope (a) on the twin. On the other hand some sections of twins (i.e. Figs. 6 and 7) showed slopes (a), (b), and (c) and in the few cases where these could be compared with photographs normal to the cleavage plane it appeared that the only secondary kink present was in the same sense as the principal kink. This corresponded to slope (b). The fact that a further secondary kink corresponding to slope (a) was absent appears to be

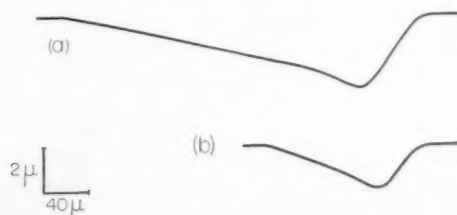


FIGURE 8.

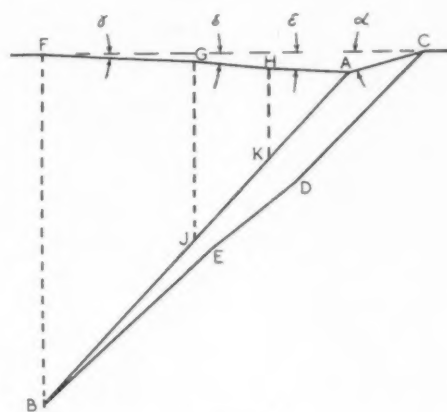


FIGURE 9.

related to the extent that the twin had grown. This is discussed later.

Figure 9 shows diagrammatically how the accommodation kinks may correspond to changes in the shape of the twin. Features giving rise to both of the above types of kink are included and they all may be summarised as follows:

1. The bend plane ( $FJ$ ) of the principal accommodation kink is a plane normal to the basal plane and lies close to the tip ( $B$ ) of the twin.

2. Other secondary accommodation kinks with bend planes  $GJ$ ,  $HK$  may occur between the principal kink and the twin. If they are of the opposite sense to the principal kink and reduce the accommodation angle to nearly zero (i.e., with kink  $H$ ,  $\epsilon < \gamma$ ) then there is a corresponding almost parallel-sided portion of the twin ( $CD$ ). If they are of the same sense and increase the accommodation angle (i.e., with kink  $G$ ,  $\delta > \gamma$ ) then there is a corresponding region of the twin where its opposite sides converge more sharply ( $DE$ ). The former type appears to be common to almost all twin kink systems, but the latter type has been observed only in certain cases.

3. The twin boundary ( $AB$ ) nearer to the accommodation kink is shown in the sections normal to the basal plane to be straighter than the boundary further from the accommodation kink. Since the two boundaries are not parallel they cannot both contain the twinning plane. It is probable, therefore, that the straighter boundary is the true twinning plane, while the boundary ( $CDEB$ ) further from the accommodation consists of a number of fine steps each consisting of a short length of true twinning plane. At any point, the length of the steps relative to their height is determined by the angle between the two sides of the twin.

(iii) *The growth of a twin*: It is possible to speculate on a scheme for various stages of growth of the twin, which will conform to the final shape shown in Fig. 9. A simple explanation which fits the general facts is as follows:

Consider a very small parallel-sided twin  $AB$  (Fig.

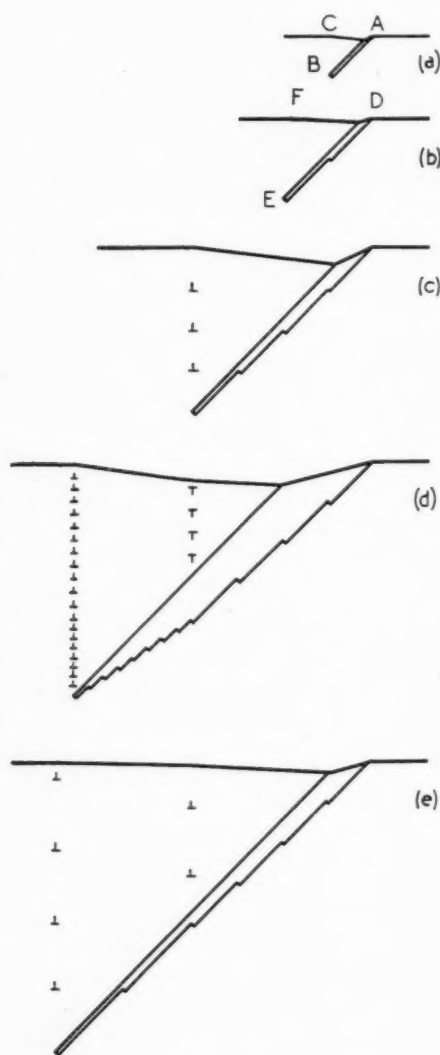


FIGURE 10.

10a) with an accommodation kink at C and with length equal to the steps referred to in 3 above. The twin grows by the production of an adjacent parallel twin DE of the same thickness as AB but two step lengths long (Fig. 10b). The kink moves outwards to its new position at EF. Further growth (Fig. 10c) proceeds by the production of additional twinned regions each a step-length longer than the previous one, the kink moving to its new position each time. A continuation of this process gives a situation similar to Jillson's conception of the simple twin and kink system shown in Fig. 1.

Since a kink is analogous to a boundary between mosaic blocks, it may be pictured as a row of dislocations of the same sign (e.g., Cottrell<sup>13</sup>). If  $45'$  is taken as a typical value of the accommodation kink angle, this corresponds to about one excess dislocation in the kink for every 75 atomic layers. If  $5^\circ$  is taken as a typical angle between the sides of the twin, then the correspond-

ing ratio of step-length to step-height is about 11. The excess dislocations could possibly arise as the twin grows and if  $n$  are assumed to arise from each new step, then the step-length would be  $(n\sqrt{2} \times 75)/11 = 9n$  atomic layers (approximately). Thus, unless  $n$  is very large, which is unlikely, there is no possibility of the steps being visible. For convenience, the dislocations have been drawn with  $n=1$ .

This scheme of growth would also conform to the observation of Pratt and Pugh<sup>14</sup> that as the twin grows wider under increasing stress, the accommodation region also becomes correspondingly wider.

The production of secondary kinks could be similar to the process shown as Fig. 10d and 10e. The twin is initially in the condition of 10c with a density  $D_1$  of positive dislocations along the kink. For the case where the secondary kink is in opposite sense to the principal kink, the secondary kink starts to form at the point where the increase in length of the twin for successive stages of growth becomes less, i.e., the ratio of step-length to step-height is reduced (Fig. 10d). If the dislocations forming the kink arise from the successive stages of growth, then the density  $D_2$  of dislocations along the new length of kink will be greater than  $D_1$ . It would appear that a kink having two different densities of dislocations along its length cannot move sideways. Instead, it splits into two kinks, one of density  $D_2$ , which becomes the principal kink and moves sideways as the twin grows, and one of density  $D_1 - D_2$ , which is fixed at the point where the twin growth changes and so becomes the secondary kink. Since  $D_1 - D_2$  is negative—i.e., an excess of negative dislocations is present—the secondary kink is of opposite sense to the principal kink. The additional positive dislocations needed to extend the principal kink to the surface of the zinc could be extracted from the region of the secondary kink, leaving an excess of negative dislocations to line up and form the kink. In crystals where there is no secondary kink to correspond to the nearly parallel-sided portion of the twin (Figs. 6 and 7), it is possible that the kink has been absorbed by the twin growing past it.

Where the principal and secondary kinks are in the same sense, the secondary kink starts to form by a similar mechanism at the point where there is a greater increase in length of the twin for successive stages of growth (Fig. 10e).  $D_1 - D_2$  is now positive and the moving principal kink extracts only some of the excess dislocations from the fixed secondary kink.

This process does not assume any particular mechanism for the formation of the small unit steps. If they should arise from a series of twinning dislocations passing down the twin plane as described by Thompson and Millard<sup>15</sup> for cadmium, then it is possible that the step-height would be the thickness of twin produced by one dislocation. The changes in the length of the steps would arise from variations in the difference between the internal stress in the zinc and the amount of stress

which has been relieved by the growth of the twin. Such variations arise from the changes in the rate of deformation and the probability that a much greater stress is needed to initiate a twin than is required to cause it to grow.<sup>16</sup>

When the sections of the tips of the twins are highly magnified (Fig. 11) they appear to be rounded or even flattened. The metal beyond the tip of the twin appears to have an abrupt and coherent boundary with the twin which has undergone a shear of 0.14. In addition, the principal accommodation kink commences from a point slightly beyond the tip of the twin. These anomalies are strong evidence of considerable internal stress around the twin. At the end of the twin trace on the basal plane, the very small change of angle in the accommodation is only just detectable even in the electron microscope. Figure 12 shows the cleavage surface at the end of the same twin shown in Fig. 3. The accommodation kink, which is seen clearly on the left-hand side at *A*, becomes rapidly ill-defined and has disappeared altogether at the tip of the twin *B*. Again, this is probably determined by the elastic stresses arising from the fact that at the end of the twin, twinned material which has been sheared must be separated from untwinned material by planes other than twin planes. It is thus clear that the internal stresses set up during twinning have to be considered more seriously than hitherto.

### CONCLUSIONS

1. Between the principal accommodation kink and the twin there may be secondary kinks. No kinks appear to be more than 40–50° when fully developed and the secondary kinks may be in the same or in opposite sense to the principal kink.

2. Sections of twins have shown that, in the side of the twin furthest from the accommodation kink, there

are changes of shape corresponding to the pattern of the kinks, and from this, speculation may be made about the mode of growth of the twin.

3. The tip of the twin in the body of the metal is markedly rounded, indicating considerable internal stress.

### ACKNOWLEDGMENTS

This paper describes work done jointly between the Research Laboratory on the Physics and Chemistry of Surfaces, Department of Physical Chemistry, Cambridge, and the Division of Tribophysics, C.S.I.R.O., Melbourne, Australia.

I thank Dr. F. P. Bowden, F.R.S., and Dr. W. Boas for their interest and encouragement and Dr. J. W. Menter for helpful collaboration, particularly with the electron microscopy.

Acknowledgement is also made to the Ministry of Supply (Air) for a grant to the Cambridge Laboratory.

### REFERENCES

1. C. H. Mathewson and A. J. Phillips, *Proc. Inst. Met. Div., Amer. Inst. Min. (Metall.) Engrs.* (1927), p. 143.
2. E. Orowan, *Nature* **149**, 643 (1942).
3. J. B. Hess and C. S. Barrett, *Trans. Amer. Inst. Min. (Metall.) Engrs.* **185**, 599 (1949).
4. D. C. Jillson, *Trans. Amer. Inst. Min. (Metall.) Engrs.* **188**, 1009 (1950).
5. P. L. Pratt and S. F. Pugh, *J. Inst. Metals* **80**, 653 (1952).
6. A. J. W. Moore, *Proc. Phys. Soc.* **B55**, 956 (1952).
7. J. Holden, *Phil. Mag.* **43**, 976 (1952).
8. P. W. Bridgman, *Proc. Amer. Acad. Arts and Sciences* **60**, 305 (1926).
9. J. W. Menter, *J. Inst. Metals* **81**, 163 (1952).
10. S. Tolansky, *Multiple Beam Interferometry* (Clarendon, Oxford, 1948).
11. L. E. Samuels, *J. Inst. Metals* **81**, 471 (1953).
12. P. A. Jacquet, *Metal Corrosion Usure* **19**, 71 (1944).
13. A. H. Cottrell, *Progress in Metal Physics I* (Butterworths, London, 1949), p. 93.
14. P. L. Pratt and S. F. Pugh, *Acta Met.* **1**, 218 (1953).
15. N. Thompson and D. J. Millard, *Phil. Mag.* **43**, 422 (1952).
16. R. L. Bell and R. W. Cahn, *Acta Met.* **1**, 752 (1953).



# EFFECT OF GRAIN BOUNDARIES UPON PORE FORMATION AND DIMENSIONAL CHANGES DURING DIFFUSION\*

R. W. BALLUFFI† and L. L. SEIGLE‡

A study has been made of the effects of grain boundaries and specimen thickness upon pore formation and dimensional changes which occur when zinc is diffused out of polycrystalline alpha brass sheets. The results are consistent with the viewpoint that the outward flux of zinc produces a supersaturation of vacancies which may either precipitate as pores or else be absorbed at sinks within the alloy causing various dimensional changes.

In thin sheets  $< \sim 0.0015$  cm in thickness it was found that vacancies were eliminated at sinks within the grains (presumably at dislocations) and also at grain boundaries. The destruction of vacancies at the boundaries tended to prevent the nucleation of porosity near the grain boundaries and caused a contraction of the specimen normal to the plane of the boundary. In thicker sheets, however, many grain boundaries acted as preferred sites for void formation and subsequent cracking. This change in the behavior of the boundaries is explained by differences in the magnitude of internal stresses which are produced in the various sheets by the restraining effect of the bulk of the specimen upon shrinkage in the diffusion zone.

## EFFET DES JOINTS DE GRAINS SUR LA FORMATION DES PORES ET LES CHANGEMENTS DE DIMENSIONS AU COURS DE LA DIFFUSION

L'effet des joints de grains et de l'épaisseur de l'éprouvette sur la formation des pores et les changements de dimensions a été étudié dans le cas du zinc diffusant en dehors de tôles polycristallines de laiton alpha. Ces résultats indiquent que le départ du zinc produit une sursaturation des lacunes qui peuvent ou précipiter sous forme de pores, ou aussi être absorbés par des puits, provoquant ainsi des changements de dimensions différents.

Dans les tôles minces (inférieures à 0.0015 cm d'épaisseur), les lacunes sont éliminées par les puits à l'intérieur des grains (probablement sur les dislocations) et aussi dans les joints de grains. La disparition des lacunes aux joints de grains empêche la germination de porosités près de ces joints de grains et provoque une contraction de l'échantillon normalement au plan de ce joint. Dans les tôles plus épaisses, par contre, de nombreux joints de grains localisent la formation de pores et finalement de fissurations. Cette modification dans le comportement des joints de grains s'explique de la façon suivante: le coeur de l'échantillon s'oppose à la contraction de la zone où se produit la diffusion et, de ce fait, les contraintes internes ne sont pas du même ordre de grandeur dans tous les cas.

## EINFLUSS DER KORNGRENZEN AUF DIE PORENBILDUNG UND DIE ÄNDERUNG DER PROBENABMESSUNGEN WÄHREND DER DIFFUSION

Der Einfluss der Korngrenzen und der Probendicke auf die Porenbildung und die Änderungen in den Probenabmessungen bei der Entzinkung von vielkristallinen  $\alpha$ -Messingblechen durch Diffusion wurde untersucht. Die Ergebnisse sind in Übereinstimmung mit der Ansicht, dass das Herausdiffundieren von Zink eine Übersättigung an Fehlstellen hervorruft. Diese Fehlstellen sind im Metall entweder in Form von Poren angesammelt oder an Löchern angelagert und verursachen verschiedene Dimensionsänderungen.

Es wurde festgestellt, dass in dünnen Blechen  $< \sim 0.0015$  cm Dicke die Fehlstellen an Löchern in den Körnern (vermutlich an Versetzungen) und ebenfalls an den Korngrenzen angesammelt werden. Die Zerstörung der Fehlstellen an den Korngrenzen wirkt im Sinne einer Verhinderung der Keimbildung für die Poren nahe den Korngrenzen und verursacht somit ein Zusammenziehen der Probe senkrecht zu der Ebene der Korngrenze. Dagegen dienen in dickeren Proben viele Korngrenzen als bevorzugte Plätze für die Entstehung von Lücken und folgender Rissbildung. Dieser Unterschied im Verhalten der Korngrenzen kann durch die unterschiedlich grossen inneren Spannungen erklärt werden, die in den verschiedenen Blechen durch die hemmende Wirkung der Probenabmessungen auf die Schrumpfung in der Diffusionszone hervorgerufen werden.

### I. INTRODUCTION

When zinc is diffused out of alpha-brass by heating *in vacuo*, it has been shown<sup>1,2</sup> that a Kirkendall effect occurs, indicating that the outward flux of zinc atoms through the brass is larger than the inward flux of copper atoms. It has also been shown that porosity forms in those volumes of the alloy which are tending to shrink due to the unequal diffusion of zinc and copper.

In order to explain this porosity it is assumed that lattice vacancies are generated or deposited in each volume of the alloy that is undergoing a loss of mass. The concentration of vacancies tends to build up above that normally in equilibrium with the lattice, and eventually voids are nucleated and grow.<sup>3,4</sup>

In previous work at this Laboratory it had been observed that grain boundaries appeared to influence the distribution of porosity in dezincified brass. Sometimes voids formed preferentially at grain boundaries, whereas at other times the grain-boundary region was preferentially free of porosity. The existence around grain boundaries of an occasional zone clear of porosity

\* Received August 4, 1954; in revised form October 18, 1954.

† Atomic Energy Division, Sylvania Electric Prod. Inc. Now with Department of Mining and Metallurgical Engineering, University of Illinois, Urbana, Illinois.

‡ Atomic Energy Division, Sylvania Electric Products, Inc., Bayside, New York.

TABLE I. Dimensional Changes in Thin Alpha-Brass Sheets during Diffusion at 800°C.

Original sheet thickness (cm)	Grain size (cm)	Treatment	% Wt. loss	% Volume decrease	% Length or width decrease	% Thick-ness de-crease	% Re-maining porosity
Part A							
0.0015	0.004	Annealed in capsule $\frac{1}{2}$ hr at 800°C; diffused 3/4 hr at 800°C	26.7	21(±1)	7.4(±.1)	7(±1)	11(±1)
0.0012	0.004		26.5	22(±1)	7.8(±.1)	7(±1)	10(±1)
0.0014	0.004		26.9	21(±1)	7.3(±.1)	7(±1)	11(±1)
0.0017	0.054	Annealed in capsule 68 hr at 880°C; diffused 3/4 hr at 800°C	27.6	16(±1)	5.0(±.1)	7(±1)	17(±1)
0.0014	0.061		28.4	19(±1)	5.2(±.1)	10(±1)	14(±1)
0.0015	0.053		28.0	18(±1)	5.1(±.1)	9(±1)	15(±1)
Part B							
0.0036	0.008	Annealed in capsule $\frac{1}{2}$ hr at 850°C; diffused 2 hr at 800°C	26.1	15(±1)	5.2(±1)	6(±1)	16(±1)
0.0031	0.008		25.7	15(±1)	5.2(±1)	6(±1)	16(±1)
0.0035	0.060	Annealed in capsule 68 hr at 880°C; diffused 2 hr at 800°C	26.7	15(±1)	4.2(±1)	8(±1)	17(±1)
0.0032	0.040		26.5	15(±1)	4.5(±1)	7(±1)	17(±1)

was especially interesting in light of the ideas of Nabarro<sup>5</sup> and Herring<sup>6</sup> concerning the diffusion of lattice vacancies to interfaces in metals. In agreement with these ideas it seemed that the supersaturation of vacancies in the matrix near a grain boundary was sometimes relieved by diffusion to the boundary, rather than by precipitation of voids. If this process occurred, in accordance with Nabarro's mechanism, it would be accompanied by a movement of the grains together normal to the plane of the boundary.

In order to study in more detail the effect of grain-boundary configuration upon structural and shape changes in dezincified brass, investigations were made of porosity formation and dimensional changes in fine and coarse grained alpha-brass sheets dezincified in vacuum at 800°C.

## II. POROSITY FORMATION AND DIMENSIONAL CHANGES IN THIN BRASS SHEETS

### A. Experimental Details

A series of thin brass sheets of varying thickness and grain size was heated *in vacuo* at 800°C for sufficient time to diffuse out essentially all of the zinc. Measurements were made of the linear shrinkages in the plane of the sheets and of the total volume shrinkages. The distribution of the resulting porosity was then observed metallographically.

All specimens were prepared from high purity brass containing less than 0.006 total percent of impurities, mainly trace amounts of Ca, Fe, Mg, Pb and Si. The sheets were made by rolling initially half-inch-diameter alpha-brass rods. Before dezincification the specimens were annealed in small evacuated quartz capsules for periods long enough to establish a grain structure that remained essentially stable during the subsequent diffusion treatment. Two different structures were used:

(1) a "fine-grained" structure in which the grain size was approximately three times the thickness of the sheets and where the grains traversed the entire thickness of the sheets, and (2) a "coarse grained" structure where the grain size was 10-40 times the sheet thickness. The "fine-grained" structure, which was found to be very persistent once formed, was easily obtained by a comparatively short anneal of the cold-rolled specimens (see Table I). The "coarse-grained" structure was developed by a grain coarsening technique which involved very slow heating to a higher temperature for longer periods.<sup>7</sup> All specimens were then diffused by heating *in vacuo* at 800°C for sufficient times to remove practically all of the zinc. The dimensional measurements in the plane of the thin sheets were made with a traveling microscope between gage marks initially scratched in the sheet surfaces. Specimen volumes were determined by weighing in air and water, and changes in the thickness dimension were calculated from the above data.

### B. Results

The results of the measurements on the diffused brass sheets are given in Table I along with estimated maximum errors. The first group is for fine- and coarse-grained foils approximately 0.0015 cm in thickness. The second group of measurements is for thicker sheets approximately 0.0033 cm thick.

#### 1. Porosity Formation

As shown in Table I, large volumes of porosity were formed in all sheets. The holes were revealed metallographically and may be seen in a number of the accompanying figures. Pore formation in alpha-brass has been observed previously<sup>1,2</sup> and the mechanism of the process has been discussed<sup>3,4</sup> in terms of the generation of excess lattice vacancies and their precipitation as holes.

According to this picture, the unequal diffusion of zinc and copper results in a tendency for the concentration of lattice vacancies to build up above the equilibrium concentration in those volumes of the diffusion couple which are losing mass. This viewpoint holds regardless of whether it is imagined that diffusion occurs interstitially or via a vacancy mechanism. If diffusion is primarily interstitial, vacancies are generated in the diffusion zone as atoms leave their lattice sites and enter the interstices. If diffusion occurs by vacancy-atom exchange, vacancies are pumped into those regions where atoms are leaving. In either case it is visualized that certain regions become supersaturated with vacancies, and when the degree of supersaturation is high enough porosity is nucleated. The evidence that hole formation occurs by a typical nucleation and growth process has been discussed in a previous article.<sup>3</sup>

In agreement with former results,<sup>2</sup> the porosity remaining in the dezincified brass (Table I) is equivalent to a substantial fraction of the atomic volume of the zinc removed. If all of the excess vacancies introduced into the specimen precipitated as voids, the volume of pores would be given by the difference between the total outward flux of zinc and the inward flux of copper at the specimen surface.<sup>8</sup> We do not have sufficient diffusion data to calculate this quantity exactly. Previous measurements<sup>9</sup> show that zinc diffuses about 5.3 times as rapidly as copper at the 28 atomic per cent zinc concentration. Assuming that the ratio of diffusivities does not change with composition, neglecting lattice parameter changes, the maximum possible pore volume may be estimated as 23 per cent of the specimen volume. The observed porosity varied from 10 to 17 volume per cent.

## 2. Dimensional Changes

If the unequal diffusion of zinc and copper were entirely compensated by porosity formation, neglecting changes in lattice parameter, the only dimensional change observable should be a shrinkage of about 5 per cent in the sheet thickness, due to the inward diffusion of copper. As shown in Table I, the actual volume of porosity was below the maximum possible, and considerable shrinkage occurred in all dimensions in both fine and coarse grained specimens.

These data may be explained by assuming that a certain fraction of the excess vacancies formed during diffusion is eliminated by absorption at dislocations and grain boundaries, in accordance with the mechanism of Nabarro. These processes occur in competition with pore formation and result in the mass movements which are observable as an over-all shrinkage. As pointed out by Nabarro, the absorption of a vacancy on an isolated edge dislocation would cause the dislocation line to move normally to its slip plane and produce a contraction in a direction normal to the dislocation line and parallel to the slip plane. In a face-centered cubic crystal the shrinkage should tend to be isotropic because of the multiplicity of slip planes and possible dislocation

orientations. These remarks, however, apply only to thin specimens such as used here, since other experiments show that, during unidirectional diffusion in massive specimens, volume shrinkages or expansions are largely restricted to the diffusion direction.<sup>9,10</sup> Even though there may be a tendency for lateral contraction or expansion to occur in the diffusion zones of the usual sandwich type couples, these are apparently restrained by the undiffused specimen bulk. However, in thin sheets such restraints are greatly reduced and lateral dimensional changes do occur.<sup>11</sup>

In the above explanation it has been implied that all shrinkage occurs during the removal of zinc from the specimen, and that there is no subsequent sintering of the porosity formed. To confirm this assumption, a number of experiments were made in which the lateral shrinkage was measured as a function of time for periods long after dezincification was essentially complete. If large sintering effects were present, significant shrinkage of the residual porosity should occur. Sheets 0.0030 cm thick with a grain size of  $\sim 0.0075$  cm were used and the average of three shrinkage curves is shown in Fig. 1. It is clear that the shrinkage is negligible after about 120 minutes when practically all of the zinc has been diffused out. We may conclude therefore, that sintering of the residual porosity is a very slow process at 800°C. This result might have been anticipated from the theoretical predictions of Herring<sup>6,12</sup> and the experimental work of Alexander and Balluffi<sup>13</sup> proving that isolated voids within grains are very stable. It is clear, of course, that the porosity formed during dezincification must eventually sinter out, and pore formation might be considered as a metastable intermediate stage in the eventual destruction of vacancies within the matrix. However, without the close proximity of a high-angle grain boundary to supply a sink for vacancies, sintering of the voids following complete dezincification is negligibly slow at 800°C. It is easy to show that pores of any observable size will grow in the presence of very small vacancy supersaturations during dezincification.

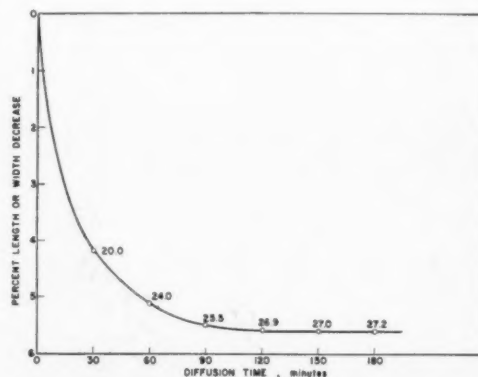


FIG. 1. Linear shrinkage of 0.0030 cm alpha-brass sheets during heating in vacuum at 800°C. Grain size, 0.0075 cm (percent weight loss at each point is indicated).

The results of Fig. 1 also proved that any shrinkage of the sheets in the lateral direction due to surface tension forces along the sheet surfaces was negligible. This phenomenon has been widely investigated elsewhere.<sup>14</sup> One additional confirmatory experiment was carried out which involved heating even thinner copper sheets under similar conditions. Pure OFHC copper sheets 0.0015 cm in thickness were annealed for 30 minutes at 800°C, thereby producing a grain size of  $\sim 0.005$  cm. The specimens were then heated for 30 minutes *in vacuo* at 800°C. Dimensional measurements proved that the linear shrinkage in the plane of the sheets during this latter treatment was less than 0.1 per cent. We therefore conclude again that shrinkages produced by surface tension forces were negligible in our experiments. Weight loss measurements also showed that no observable amount of copper was lost during these runs. Any weight losses measured during the diffusion runs were therefore exclusively caused by loss of zinc.

### 3. Effect of Grain Boundaries on Pore Formation and Dimensional Changes

The results presented in Table I indicate that the much larger number of transverse grain boundaries in the fine-grained 0.0015 cm thick sheets markedly increased the percent volume shrinkage. Metallographic examination revealed in agreement with these data that more porosity was present in the coarse-grained than in the fine-grained sheets. On the average there were fewer pores in the fine-grained sheets. Typical cross sections are shown in Fig. 2. Numerous grain boundaries were found surrounded by regions free of pores in contrast to the rather uniform distribution of porosity within the grains. Figure 3 shows several examples selected from the 0.0015-cm-thick coarse-grained foils.

These observations are, again, very satisfactorily explained on the basis of the Nabarro-Herring picture. Evidently grain boundaries can act as efficient enough sinks for vacancies so that the level of supersaturation in their vicinity remains below that required for the

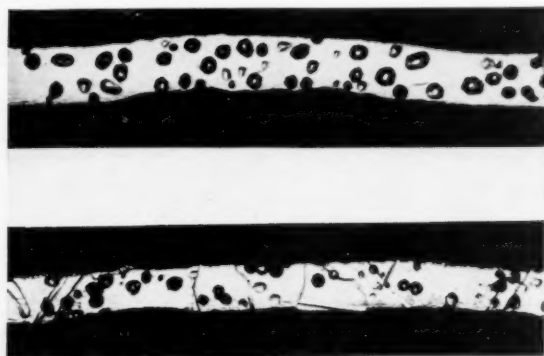


FIG. 2. 0.0015 cm thick alpha-brass sheets after heating in vacuum for 3/4 hr at 800°C. Above: coarse-grained; below fine-grained. 1000X.

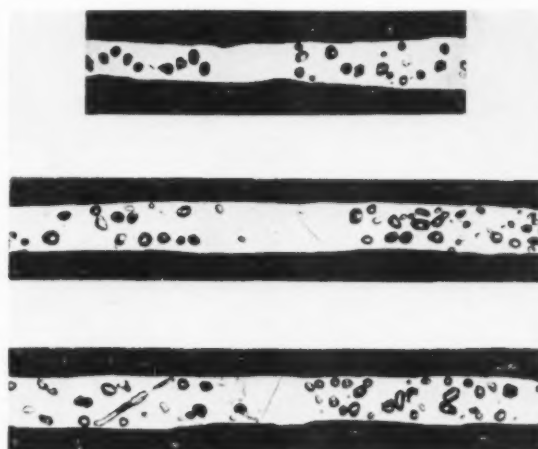


FIG. 3. Effect of grain boundaries on porosity formation in coarse-grained 0.0015 cm thick alpha-brass sheets heated in vacuum for 3/4 hr at 800°C. 1000X.

nucleation of pores. The fact that in all cases in which this effect was observed the cleared region was distributed fairly symmetrically about the boundary indicates that vacancies diffused into the grain boundary sink from both sides.

As seen in Table I, in the fine-grained sheets the amount of shrinkage in the plane of the foil is markedly increased by the additional grain boundaries, which in most cases were oriented approximately normal to the foil surface. However, the shrinkage in the thickness dimension of the fine-grained is slightly less than in the coarse-grained sheets. These results may be explained by taking account of the nature of the volume changes produced by the action of various sinks. The elimination of vacancies at grain boundaries would cause the unrestrained grains to move together producing a shrinkage which is approximately normal to the plane of the boundary. On the other hand the absorption of vacancies within the grains should in a symmetrical crystal result in a volume shrinkage which tends to be more nearly isotropic. The greater shrinkage of the fine-grained sheets in the plane of the sheet is therefore due to the elimination of vacancies at grain boundaries. The smaller shrinkage in the thickness dimension is due to the smaller number of vacancies which are absorbed in the interior of the grains of the fine-grained sheets.

The results for the sheets of approximately 0.0033 cm thickness in Table I are similar. However, in these thicker sheets no difference could be detected between the percent volume shrinkage of the fine- and coarse-grained sheets within the accuracy of the experiments. This result must be due to the longer diffusion distances involved in the thicker sheets and the fact that proportionately fewer vacancies could reach the grain boundaries. Actually, as may be seen from Table I, only a relatively small fraction of the vacancies were destroyed at grain boundaries in all of these experiments. Appar-



ently a much finer grain size would be required for the number of vacancies destroyed at grain boundaries to approach the number destroyed within the grains. However, even in the thick sheets the length measurements which were more precise than the volume measurements still prove that there is an extra increment of shrinkage normal to the grain boundaries. Metallographic work again revealed reduced pore formation in the vicinity of grain boundaries (Fig. 4).

On account of the fine grain size of some of the thin sheets used there was a suspicion that loss of zinc by diffusion along grain boundaries might have influenced the results. In order to prove that all of the effects investigated are primarily due to the diffusional loss of zinc through the volume and not along the grain boundaries of these foils, the rate of zinc loss was measured from 0.0026 cm-thick fine-grained and coarse-grained foils under identical conditions. The results are given in Fig. 5. It is apparent that the rate of zinc loss was the same in these sheets even though there was a large difference in grain size and that the effect of grain boundary diffusion must, therefore, have been negligible. No attempt was made to calculate approximate volume diffusion coefficients from these data since suitable boundary conditions and heating rates could not be attained for such short diffusion times.

### III. FORMATION OF POROSITY AND SPLITTING AT GRAIN BOUNDARIES

One of the puzzling facts which confronted us in the early phases of this work was that zones free of porosity were always present along the grain boundaries of the thin brass sheets, but in thicker specimens usually the converse was true. In many of the thicker specimens voids appeared to have formed preferentially at the grain boundaries and frequently grains had completely

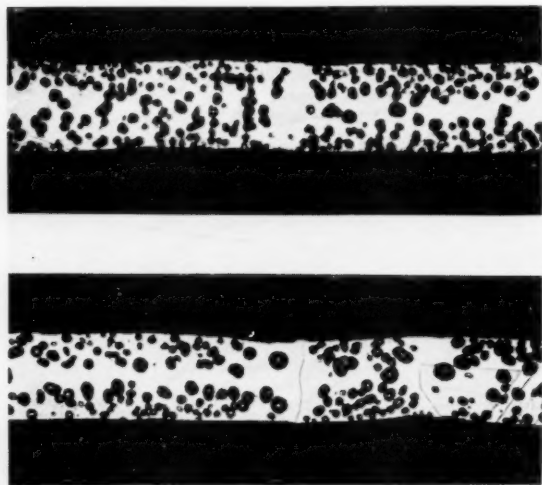


FIG. 4. Effect of grain boundaries on porosity formation in coarse-grained 0.0033 cm thick alpha-brass sheet heated in vacuum 2 hrs at 800°C. 300X.

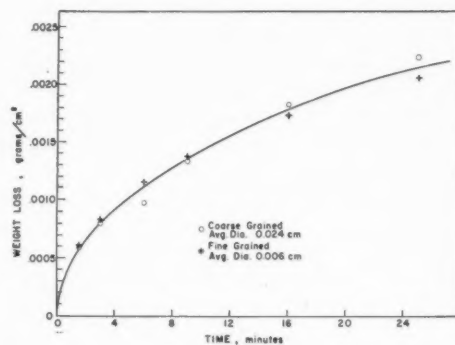


FIG. 5. Weight loss vs time for 0.0026 cm alpha-brass sheets of different grain size heated in vacuum at 800°C.

parted at their boundary. Moreover, grain-boundary splitting in dezincified brass has been reported in the past,<sup>15</sup> the occurrence of this phenomenon having led people to view with suspicion any diffusion data obtained by the sublimation of zinc from copper. Since the specimens in which grain-boundary porosity and cracking occurred were usually considerably more massive than the thin sheets discussed above, it was decided to investigate the effect of sheet thickness on the action of grain boundaries during dezincification.

Alpha-brass sheet specimens were prepared ranging in thickness from 0.003 to 0.115 cm and were annealed in evacuated quartz capsules at 800°C for sufficient periods to develop relatively stable grain structures in which the diameter of the individual grains varied from one-half to three times the sheet thickness. In these structures a large fraction of single grains traversed the sheet thickness and the majority of grain boundaries intersected the surface at angles between 45 to 90 degrees. The annealing periods required to develop these structures increased with the sheet thickness and ranged from 0.5 hr for the 0.0033-cm-thick sheets to 68 hr for the 0.115-cm-thick specimens. The sheets were then diffused by heating in vacuum at 800°C for various periods and the resulting porous structures were examined metallographically.

The metallographic examination revealed that in the thicker sheets a large percentage of the grain boundaries were not clear of porosity but instead were preferential sites for hole formation and in many cases the boundaries parted completely, forming extensive internal free surfaces. The type of behavior is shown in Fig. 6. It was generally found that no grain-boundary porosity or splitting occurred in specimens less than approximately 0.015 cm in thickness and that the tendency towards extensive grain-boundary porosity and splitting increased as the thickness increased. The splitting seemed to develop as a result of extensive pore formation at the boundaries. Many examples were found where a large number of holes formed preferentially on the boundary as in Fig. 7b, this condition apparently preceding final complete splitting. The grain-boundary

porosity and splitting phenomenon appeared quite randomly, however, and many instances were observed where some boundaries acted as preferred sites for hole formation and other boundaries acted to eliminate porosity in the same specimen. Figure 8 shows a number of boundaries in the 0.115-cm-thick sheet which behaved in the latter way.

The tendency towards increased hole formation and splitting at grain boundaries as the sheet thickness was increased may be attributed to the action of internal stresses developed during diffusion. Any small region in the specimen which is losing mass will tend to contract. A stress pattern may therefore be established early during the diffusion cycle in which the outer layers from which zinc is being removed are in tension parallel to the plane of the sheet, and the interior layers correspondingly in compression. As the thickness of the sheet is increased the relative thickness of undiffused core is increased and consequently the general level of compressive stresses in the interior decreased. Stress relaxation by creep may therefore occur more slowly in the interior of the thicker sheets, permitting the attainment of higher tensile stresses in the diffusion zone. As already shown, in accordance with Nabarro's ideas, the absorption of vacancies at a grain boundary is accompanied by a movement together of the adjacent grains. This motion, which is required in order to eliminate the vacancies, will be opposed by tensile stresses in the diffusion zone and therefore such stresses will tend to inhibit the absorption of vacancies at the boundary. On

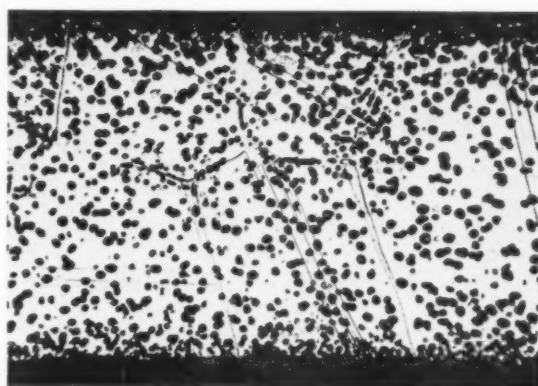
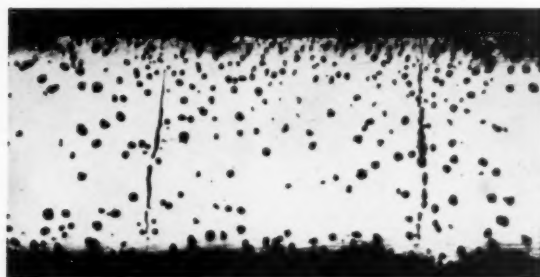


Fig. 7. Above: 0.115 cm thick alpha-brass sheet heated in vacuum 86 hrs at 800°C. 78X. Below: 0.019 cm thick alpha-brass sheet heated in vacuum 1.5 hrs at 800°C. 270X.

the other hand, tensile stresses should aid the formation of voids since the nucleation of a hole is accompanied by some stress relief. As the stress level in the diffusion zone increases, therefore, the vacancy concentration maintained at the grain boundary by the action of the grain-boundary sink increases while the critical vacancy concentration necessary for nucleation of voids decreases. Eventually, when these concentrations become equal, porosity may form in the boundary.

In attempting to analyze this problem in more detail we will use the following notation to identify the various vacancy concentrations:

$n_0$  = the equilibrium concentration of vacancies throughout the specimen. In general  $n_0$  will be a function of stress at constant temperature and composition.

$n_{gb}$  = actual concentration of vacancies maintained at the grain boundary.

$n_m$  = the actual vacancy concentration present in the matrix.

$n_{gb}^c$  = the critical concentration of vacancies necessary for pore formation at the grain boundary

$n_m^c$  = the critical concentration of vacancies necessary for pore formation in the matrix.

The relationship between stress and the concentration of vacancies maintained at the grain boundary, if the boundary acts as a perfect sink, can be obtained by

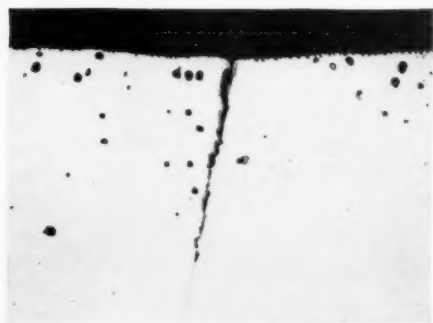


Fig. 6. Above: 0.023 cm thick alpha-brass sheet heated in vacuum 1 hr at 800°C. 240X. Below: 0.115 cm thick alpha-brass sheet heated in vacuum 1/2 hr at 800°C. 500X.

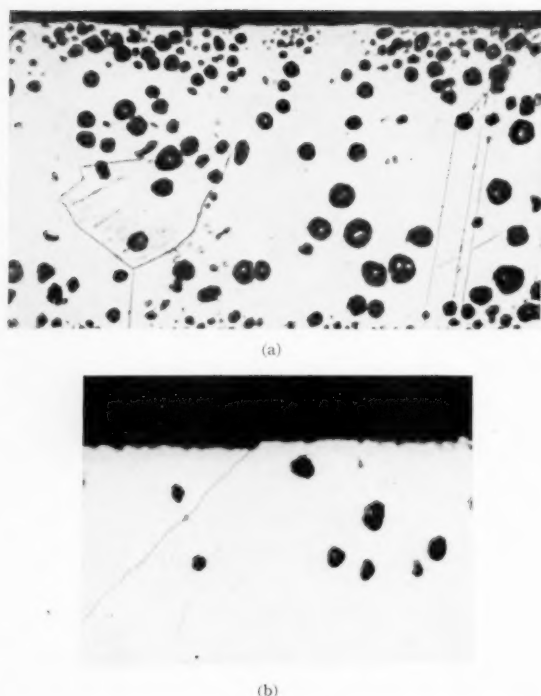


FIG. 8. Above: 0.115 cm thick alpha-brass sheet heated in vacuum 9 hrs at 800°C. 500X. Below: Region near surface of 0.115 cm thick alpha-brass sheet heated in vacuum 1/2 hr at 800°C. 1000X.

noting that the elimination at a grain boundary of a vacancy of volume  $\Omega$  will produce a contraction  $\delta x = \Omega/A$ , where  $A$  is the grain-boundary area. If the opposing normal tensile stress is  $\sigma$ ,

$$\ln\left(\frac{n_{gb}}{n_0}\right) = \left(\frac{\Omega}{KT}\right) \cdot \sigma = \left(\frac{V}{RT}\right) \cdot \sigma, \quad \text{if } n_{gb} \leq n_m, \quad (1)$$

where  $V$  is the molar volume of the alloy. It appears that  $\sigma$  is the osmotic pressure developed between the concentration  $n_{gb}$  and  $n_0$ . The effect of stress upon the critical vacancy concentration for nucleation of a void in the matrix or the grain boundary may be estimated by assuming that elastic strain energy is relaxed throughout the volume occupied by the void. For biaxial tension the strain energy density is  $[(1-\nu)\sigma^2]/E$  and the strain energy contribution to the free energy of void formation is  $-(4\pi r^3\sigma^2(1-\nu))/3E$  where  $E$  is Young's modulus,  $\nu$  is Poisson's ratio, assuming an isotropic material, and  $r$  is the radius of the void. When this term is added to the free-energy change occurring upon formation of a void, the critical supersaturation ratio for pore formation in the matrix becomes\*

$$\ln\left(\frac{n_m^c}{n_0}\right) = \frac{V}{RT} \left[ 2\gamma \left( \frac{1}{r_m^c} \right) - \sigma^2 \left( \frac{1-\nu}{E} \right) \right]. \quad (2a)$$

\* Note added in proof: A more elaborate treatment of the effect of applied stress has been carried out by J. A. Brinkman and yields approximately the same results (private communication).

For the grain boundary the equivalent expression is

$$\ln\left(\frac{n_{gb}^c}{n_0}\right) = \frac{V}{RT} \left[ \frac{11}{6} \gamma \left( \frac{1}{r_{gb}^c} \right) - \sigma^2 \left( \frac{1-\nu}{E} \right) \right]. \quad (2b)$$

In these expressions  $r_m^c$  and  $r_{gb}^c$  are the effective radii of the nuclei which must exist in the matrix and grain boundaries respectively in order for holes to form at the indicated supersaturation ratio and stress level. The critical stress,  $\sigma_c$ , for nucleation at the boundary is found by equating (1) and (2b) to yield

$$\sigma_c = \left[ \frac{11}{6} \gamma \left( \frac{1}{r_{gb}^c} \right) - \sigma_c^2 \left( \frac{1-\nu}{E} \right) \right]. \quad (3)$$

The actual magnitudes of  $\sigma_c$  and  $r_{gb}^c$  in (3) are not known. However, if we can make a reasonable estimate for  $\sigma_c$  we may calculate  $r_{gb}^c$  and then calculate the critical vacancy supersaturation ratio at the boundary ( $n_{gb}^c/n_0$ ) from (2b). According to Price<sup>16</sup> a tensile stress of  $70 \times 10^6$  dynes/cm<sup>2</sup> causes a strain rate of about 10 per cent per minute in alpha-brass at 800°C. It seems unlikely that a stress of this magnitude exists during the major portion of the diffusion cycle since the average shrinkage rate is considerably lower than 10 per cent per minute. However, stress concentrations could be present and we will therefore take  $10^8$  dynes/cm<sup>2</sup> as an upper limit for the tensile stresses acting on the boundaries. In this event equation (3) may be written as

$$\sigma_c = \frac{11}{6} \frac{\gamma}{r_{gb}^c} \quad (4)$$

since  $\sigma_c = 10^8$  dynes/cm<sup>2</sup> is small compared to the estimated value of  $E = 13 \times 10^{11}$  dynes/cm<sup>2</sup> at 800°C.<sup>17,18</sup> If  $\gamma$  is taken to be  $10^3$  ergs/cm<sup>2</sup> the lower limit of  $r_{gb}^c$  is  $= 2 \times 10^{-6}$  cm. This means that the critical supersaturation ratio according to (2b) must be  $\leq 1.006$ .

These values apply strictly only to the grain boundaries, and not necessarily to the matrix. In general it was found in the thicker specimens which developed pores at the boundaries that the density of holes along the boundaries was greater than in the grains at the same depth from the surface (see Figs. 6 and 7). This observation may be accounted for by assuming that there is a higher density of nuclei present in the boundaries than in the grains. It is difficult to tell from the present results whether there is much qualitative difference between nuclei at the boundaries and within the grains. In many cases porosity appeared sooner at the grain boundaries than in the adjacent grains as diffusion proceeded into the specimen (Fig. 6). This behavior might indicate that the nuclei in the boundaries become operative at lower supersaturations than the matrix nuclei (e.g.,  $r_{gb}^c < r_m^c$ ). However, it is possible that the pores along the boundary frequently join together, forming a continuous exit for zinc vapor to the surface. This process would cause dezincification in the boundary

region to occur ahead of dezincification in the matrix and could account for the structure of Fig. 6.

These remarks focus attention on a major problem in this work; namely, the determination of the nature of the nuclei responsible for hole formation. It seems probable that the grain boundary porosity observed here is related to the grain boundary porosity that is developed when metals and alloys are strained in the absence of chemical diffusion.<sup>19,20</sup> For instance intergranular porosity has been observed in alpha-brass at 800°C after straining at a stress of  $6 \times 10^7$  dynes/cm.<sup>20</sup> In such cases we may postulate that sufficient excess vacancies were produced during plastic flow to cause pore formation at the boundaries.<sup>21</sup> The fact that holes have often been found to occur at the boundaries but not in the grains under these conditions seems to indicate that the nuclei present at the boundaries are in general more effective than those in the matrix. The present result that  $(n_{gb}/n_0) \leq 1.006$  is consistent with a previous estimate by Balluffi<sup>3</sup> from other data that the critical supersaturation ratio in the matrix is  $\leq 1.01$ .

In many cases, in the thicker samples, it was found that porosity formed at some boundaries while other boundaries in the same specimen were completely free of holes. Possible explanations could be based upon stress differences due to elastic anisotropy<sup>18</sup> or, again, upon differences in the heterogeneous nuclei present at various boundaries.<sup>3,4</sup>

The absorption of vacancies at grain boundaries and movement together of the grains is equivalent to a subtraction of atoms from the lattice at the grain boundary. The details of the mechanism by which this occurs cannot be constructed directly from the experimental results. The grain boundaries in question are, of course, the type of "high-energy" boundaries which cannot be described by means of simple arrays of dislocations.<sup>22</sup> The atomic structure in such boundaries is highly disorganized and possibly vacancies are eliminated one by one as they enter this disorganized region by viscous flow processes. An attempt was made to find evidence of localized plastic flow near the boundaries in the thin sheets by microscopic examination but such effects were not observable. In the thick sheets surface

steps were often found where a grain intersected the surface at an acute angle as in Figs. 8a and 8b. Such steps were probably caused by grain-boundary viscous shear under the influence of the tensile stresses parallel to the specimen surface.

#### ACKNOWLEDGMENTS

The authors wish to thank Mr. R. Resnick and Mr. Anthony Martorana for assisting in the experimental work, and Mrs. Eileen Weaver for polishing and photographing the specimens. This work was sponsored by the Atomic Energy Commission and was done under Contract AT-30-1 GEN 366-7.

#### REFERENCES

1. H. N. Hersh, *J. Appl. Phys.* **23**, 1055 (1952).
2. R. W. Balluffi and B. H. Alexander, *J. Appl. Phys.* **23**, 1237 (1952).
3. R. W. Balluffi, *Acta Met.* **2**, 194 (1954).
4. F. Seitz, *Acta Met.* **1**, 355 (1953).
5. F. R. N. Nabarro, "Report of a Conference on the Strength of Solids," University of Bristol, England (Phys. Soc., London, 1948), p. 75.
6. C. Herring, *J. Appl. Phys.* **21**, 437 (1950).
7. M. Kornberg and F. Wilson, *Trans. A.I.M.E.* **185**, 501 (1949).
8. See, for example, J. Bardeen and C. Herring, "Atom Movements" (American Society for Metals, Cleveland, Ohio, 1951), p. 87.
9. R. W. Balluffi and L. L. Seigle, *J. Appl. Phys.* **25**, 5, 607 (1954).
10. L. C. C. da Silva and R. F. Mehl, *J. Metals* **191**, 155 (1951).
11. R. W. Balluffi and B. H. Alexander, *J. Appl. Phys.* **23**, 953 (1952).
12. See, for example, C. Herring "Surface Tension as a Motivation for Sintering," Chap. 8 in "The Physics of Powder Metallurgy" (McGraw-Hill, New York, 1951).
13. B. H. Alexander and R. W. Balluffi, *Trans. A.I.M.E.* **188**, 1219 (1950).
14. See, for example, H. Udin, "Metal Interfaces" (American Society for Metals, Cleveland, Ohio, 1952), p. 114.
15. R. F. Mehl, *Trans. A.I.M.E.* **122**, 11 (1936).
16. W. B. Price, "Symposium on Effect of Temperature in Properties of Metals," A.S.M.E. A.S.T.M. (1931), p. 340.
17. T. S. Ke, *J. Appl. Phys.* **19**, 285 (1948).
18. R. W. Ferm, W. R. Hibbard, and H. A. Lepper, *Trans. A.I.M.E.* **188**, 175 (1950).
19. J. N. Greenwood, D. R. Miller, and J. W. Suiter, *Acta Met.* **2**, 250 (1954).
20. J. Herenguel and M. Scheidecker, *Rev. Metall.* **48**, 179 (1951).
21. See, for example, F. Seitz, *Advances in Physics* **1**, 43 (1952); H. G. Van Bueren, *Acta Met.* **1**, 607 (1953).
22. See, for example, D. Turnbull "Atom Movements" (American Society for Metals, Cleveland, Ohio, 1951), p. 129.



# THE MECHANISMS OF SELF-DIFFUSION IN TIN\*

J. F. NICHOLAS†

The experimental data for self-diffusion in tin are analysed in terms of six possible diffusion mechanisms, viz., two vacancy, two interstitial, and two ring mechanisms. It is shown that there are four different ways of choosing a combination of two mechanisms that will adequately describe the data, none of these combinations involving a ring mechanism. For each combination, the frequency factors and activation energies of the mechanisms involved are calculated but satisfactory theoretical explanations cannot be given for these values for any of the combinations.

## MÉCANISME DE L'AUTODIFFUSION DANS L'ÉTAIN

Les résultats expérimentaux de l'autodiffusion de l'étain sont discutés en fonction de six mécanismes possibles de diffusion (deux mécanismes par lacune, deux par insertion, deux par rotation). Il est montré qu'il y a quatre moyens différents de choisir une combinaison de deux de ces mécanismes qui décrivent correctement les résultats, mais aucun de ceux-ci ne comporte de mécanisme par rotation. Pour chaque combinaison, les facteurs de fréquence et les énergies d'activation des mécanismes considérés sont calculés, mais aucune explication théorique satisfaisante ne peut être donnée pour ces valeurs.

## DER MECHANISMUS DER SELBSTDIFFUSION IN ZINN

Die experimentellen Ergebnisse über die Selbstdiffusion in Zinn werden auf Grund von sechs möglichen Diffusionsmechanismen analysiert: zwei Fehlstellen-, zwei Zwischengitterplätze- und zwei Ringmechanismen. Es gibt vier verschiedene Wege, um eine Kombination von zwei Mechanismen zu wählen, die die Ergebnisse angemessen beschreiben. Keine der Kombinationen enthält einen Ringmechanismus. Für jede Kombination wird der Häufigkeitsfaktor und die Aktivierungsenergie des eingeführten Mechanismus berechnet. Es kann jedoch für diese Werte bei keiner der Kombinationen eine befriedigende Deutung gegeben werden.

Recently, Shirn, Wajda, and Huntington<sup>1</sup> measured self-diffusion rates in single crystals of zinc and interpreted their results in terms of possible mechanisms of diffusion. They deduced that at least one vacancy mechanism was operative and that it was possible to explain all the data by two vacancy mechanisms. In this paper the results given by Fensham<sup>2</sup> for self-diffusion in tin are analysed in a similar manner. It is shown that the experimental data can be described by any one of four combinations of two mechanisms chosen from a set of two vacancy and two interstitial mechanisms but that no combination is in satisfactory agreement with theory.

The geometry of the possible mechanisms of diffusion in tin due to the movement either of vacancies or of interstitial atoms or of rings of atoms is most readily described by reference to Fig. 1.

**Vacancies:** A vacancy at *A* may move either to one of the nearest neighbour sites such as *B*, 3.02 Å away, or to one of the next nearest neighbour sites such as *C*, 3.18 Å away.

**Interstitial atoms:** The point *K*, at the centroid of *A*, *D*, *E*, and *F*, is assumed to be a typical interstitial site, the general position being  $[x(a/4), y(a/4), z(c/8)]$  with *x*, *y*, and *z* all odd integers. It seems reasonable to fit an interstitial atom on such a site as it is 2.12 Å from the nearest regular atomic site and the ionic radius of tin is just below 1 Å. The simplest movement of the interstitial atom is parallel to the *c*-axis with  $\Delta z = \pm 2$ , e.g., from *K*

to the centroid of *D*, *E*, *F*, and *C*. A second possibility is that the atom moves through the centre of such a parallelogram as *ABFC*, thereby changing either *x* or *y* by  $\pm 2$ . However, as can be seen from the figure, the movements corresponding to these four possible changes do not all involve the same configuration of atoms and so are not equally likely. Further, the changes in *z* involved in such movements are not fixed by the geometry, since rectilinear motion of the interstitial atom cannot be expected when, as in the present case, the thermal energy is much less than the activation energy. For the purposes of this paper, it will be assumed that an atom at *K* is equally likely to move through the centre of *ABFC*, of *ADGC*, or of *BFEH*, but cannot move in the fourth direction, and that either (a)  $\Delta z$  is always zero or

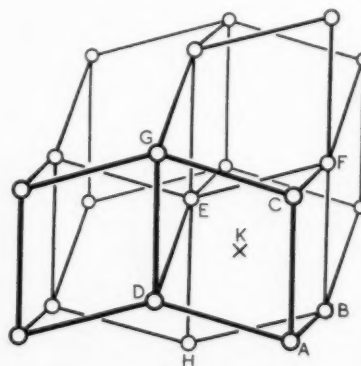


FIG. 1. Crystal structure of tin showing an interstitial site at *K*. Oblique lines join nearest neighbours; vertical lines join next nearest neighbours. The *c*-axis is vertical.

\* Received April 6, 1954; in revised form, October 20, 1954.

† Division of Tribophysics, Commonwealth Scientific and Industrial Research Organization, University of Melbourne, Australia.

(b)  $\Delta z = \pm 2$  for cases such as movement from *K* through *ABFC* and  $\Delta z = \pm 4$  for the other possibilities.

**Rings:** The rings that will be considered are (a) a 3-ring such as *ACD*, which involves one nearest neighbour pair, one next nearest neighbour pair, and one pair 3.80 Å apart and (b) a 4-ring such as *ACGD* involving two nearest neighbour pairs and two next nearest neighbour pairs.

As in the work of Shirn *et al.*, six basic mechanisms (see Table I) can be set out and, for each, we have calculated the ratio  $\gamma_i = D_{\perp}/D_{\parallel}$ , where  $D_{\perp}$  and  $D_{\parallel}$  are the rates of diffusion, perpendicular and parallel to the *c*-axis, which would be found if that mechanism alone were operative. We will assume that, in the temperature range used by Fensham, viz., 180–230°C, the diffusion is dominated by two of these mechanisms and will consider, in turn, each possible pair, eliminating those which are incompatible with experimental or theoretical data.

TABLE I.

Mechanism	$\gamma_i = D_{\perp}/D_{\parallel}$
1 Vacancy movement//[001]	0
2 Vacancy movement to nearest neighbors	$2a^2/c^2 = 6.72$
3 Interstitial movement//[001]	0
4 Other interstitial movement	
(a) assuming $\Delta z = 0$	$\infty$
(b) assuming $\Delta z = \pm 2$ or $\pm 4$	$2a^2/3c^2 = 2.24$
5 Ring of 3 atoms	$2a^2/13c^2 = 0.52$
6 Ring of 4 atoms	$2a^2/17c^2 = 0.39$

Since  $\gamma_{\text{expt}}$  ranges from 0.35 (high temperature) to 0.48 (low temperature), we must have  $\gamma_i < 0.35$  for one of the chosen mechanisms and  $\gamma_i > 0.48$  for the other. By such an argument, Shirn *et al.* reduced their possible combinations to two and they did not attempt to distinguish further. However, in the present case, only mechanism 6 can be eliminated in this way and the combinations of either mechanism 1 or 3 with any one of the mechanisms 2, 4, or 5 must be considered. On the assumption that the temperature dependence of the diffusion coefficients is of Arrhenius type, all these combinations imply that  $\ln D_{\perp}$  should be a linear function of  $1/T$ , the slope of the plot giving the activation energy of the chosen second mechanism. Further,  $\ln(D_{\parallel} - D_{\perp}/\gamma_i)$  should be a linear function of  $1/T$ ,  $i$  being 2, 4, or 5 according to the choice of the second mechanism. For  $\gamma_4$ , both the extreme values, viz., 2.24 and  $\infty$ , will be tested.

Both  $\ln D_{\perp}$  and  $\ln D_{\parallel}$  are plotted against  $1/T$  in reference 2 and the plots are reasonably linear. In Fig. 2,  $\ln(D_{\parallel} - D_{\perp}/\gamma)$  is plotted against  $1/T$  for  $\gamma = 6.7$ , 2.24, and 0.52, the points falling on straight lines in the first two cases but not in the third. Therefore, we reject mechanism 5 and are left with the combinations listed in Table II. This table also lists the activation energies,  $Q_i$ , in kcal/mol, and frequency factors,  $D_{0i}$ , in  $\text{cm}^2/\text{sec}$ , calculated from the experimental data for each combination. For mechanisms 2 and 4, only the frequency

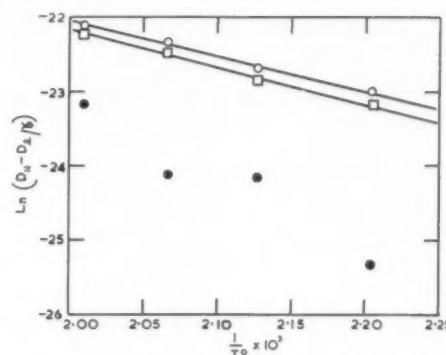


FIG. 2. Experimental values of  $\ln(D_{\parallel} - D_{\perp}/\gamma)$  plotted against  $1/T$  for  $\gamma = 6.7$  (open circles), 2.24 (open squares), and 0.52 (full circles).

factor for the component perpendicular to the *c*-axis is given. Obviously the figures in the table have no physical meaning unless the combination for which they are calculated is dominant.

In order to distinguish between these combinations, it is necessary to use theoretical expressions for  $D_0$  and for the relation between  $D_{0i}$  and  $Q_i$ . On the basis of existing theories of such relations, it can be shown (see Appendix) that, while the experimental data cannot be interpreted in terms of vacancy diffusion, they are not incompatible with interstitial diffusion, i.e., with the assumption of (3,4) as the dominant combination. However, the geometry of the interstitial movements suggests that we should find  $Q_3 < Q_4$ , in contradiction to the figures given in Table II for combination (3,4). Thus, we are forced to the rather unsatisfactory conclusion that, while any one of the combinations listed in Table II can be used to describe the experimental data, present theory cannot explain the frequency factors and activation energies found for any combination.

In an attempt to overcome these difficulties, the possibility that more than two mechanisms are operative has been considered but the experimental data are insufficient for an adequate investigation. Moreover, the assumption of three or more mechanisms implies, in general, lower frequency factors than those found when only two mechanisms are considered, so that the difficulties of explanation are increased. Another possibility would be that diffusion occurs by the movement of "crowdions" such as Paneth<sup>3</sup> suggested for the alkali metals, but such processes have not been considered.

TABLE II.

Combination	$Q_1$	$D_{01}$	$Q_2$	$(D_{02})_{\perp}$	$Q_3$	$D_{03}$	$Q_4$	$(D_{04})_{\perp}$
(1, 2)	9.6	$4 \times 10^{-6}$	6.7	$9 \times 10^{-8}$				
(1, 4)	9.4*	$4 \times 10^{-6}$						
	10.0	$6 \times 10^{-6}$					6.7	$9 \times 10^{-8}$
(2, 3)			6.7	$9 \times 10^{-8}$	9.6	$4 \times 10^{-6}$		
(3, 4)					9.4*	$4 \times 10^{-6}$	6.7	$9 \times 10^{-8}$
					10.0	$6 \times 10^{-6}$		

\* Upper figures refer to  $\gamma_4 = \infty$ , lower to  $\gamma_4 = 2.24$ .

## ACKNOWLEDGMENTS

The author would like to thank Dr. W. Boas for suggesting the work and Mr. A. D. Le Claire for helpful criticism of a previous version of the paper.

APPENDIX—THEORY OF  $D_0$ 

On general grounds (e.g., Le Claire),<sup>4</sup> we may write

$$D_0 = K\nu\delta^2 \exp(\Delta S/R), \quad (1)$$

where  $K$  is a geometrical factor depending on the crystal lattice and the mechanism of diffusion,  $\nu$  is the frequency of vibration of the diffusing atom,  $\delta$  is the jump distance, and  $\Delta S$  is an entropy change associated with the diffusion. Zener<sup>5</sup> has postulated that, for vacancy and interstitial diffusion,  $\Delta S$  should be proportional to  $Q$  and has given values for the constant of proportionality. Thus, without knowing  $\nu$ , we can calculate, in terms of the  $Q$ -values, the ratios  $D_1/(D_2)_\perp$  and  $D_0/(D_4)_\perp$ , where  $D_i = D_{0i} \exp(-Q_i/RT)$ . By comparison of these with the experimental data and by assuming that the dominant mechanisms contribute at least 90 per cent of the diffusion in each direction, the most probable combination can be shown to be (2,3), i.e., a mixed vacancy-interstitial process. However, for the experimental values found for tin, the use of Eq. (1) and Zener's theory for  $\Delta S$  leads to values of  $\nu$  which are several orders of magnitude less than the Debye frequency, so that, as has been pointed out by Le Claire (private communication), tin seems to be an exception to Zener's theory. Dienes<sup>6</sup> came to the same conclusion by taking  $\nu$  = Debye frequency and thence calculating  $\Delta S$  from Eq. (1). The negative values which he found are incompatible with Zener's theory. In his calculations, Dienes used the values of  $D_0$  given by Fensham who assumed that both  $D_{11}$  and  $D_\perp$  have a temperature dependence of Arrhenius type. However, as shown above, it is  $D_{11} - D_\perp/\gamma_i$  and  $D_\perp$ , rather than  $D_{11}$  and  $D_\perp$ , which should depend on temperature in this way so that the  $D_0$  values given in Table II are different from those used by Dienes. Nevertheless, for all mechanisms the values of  $\Delta S$  are negative when evaluated by use of Eq. (1) with  $\nu$  = Debye frequency.

In a subsequent paper, Dienes<sup>7</sup> suggested that negative values for  $\Delta S$  are not impossible, since  $\Delta S$  should be the sum of two terms, viz., a term,  $\Delta S_1$ , arising from the decrease in over-all activation energy with increasing temperature due to thermal expansion, and a term,  $\Delta S_f$ , say, arising from the altered vibration frequencies around the defect and the diffusing atom. Dienes' analysis suggested that  $\Delta S_1$  should be essentially positive but that  $\Delta S_f$  could be negative for vacancy mechanisms, a negative  $\Delta S$  thus implying  $|\Delta S_f| > |\Delta S_1|$ . However, in later work, Vineyard and Dienes<sup>8</sup> pointed out that the term  $\Delta S_1$  is really included in the vibrational entropy and therefore should not be considered separately. Thus,  $\Delta S$  can be computed solely from a consideration of changes in vibration frequencies and

this idea will be used below. In his treatment Dienes<sup>7</sup> considered two contributions to  $\Delta S_f$ , viz., (i) when a vacancy is formed the neighbouring atoms will vibrate with lower frequency and (ii) when the diffusing atom moves to the saddle point next to the vacancy, there will be regions of compression and hence of higher vibration frequency. Dienes calculated the entropy change due to (ii) and showed that it was negative but he did not give a comparable treatment for (i), and hence could not strictly compare the answers to find the sign of the net contribution to  $\Delta S$ . This separation of  $\Delta S_f$  is unnecessary since the over-all activation energy of the diffusion process ( $Q - T\Delta S$ ) is the sum of contributions from the energy of formation of a defect and from the energy for movement of this defect. Therefore,  $\Delta S$  should be interpreted as the difference between the entropy of a perfect crystal and that of a crystal with the diffusing atom at the saddle point between two lattice (or interstitial) sites.

If we consider a perfect lattice of  $L$ -atoms and the same lattice in which an atom,  $A$ , has been moved from the interior to the surface and another,  $B$  (a neighbour of  $A$  in its original position), has moved to the saddle-point next to the vacancy formed by moving  $A$ , then the change in entropy due to the changes in vibration frequencies will be given by

$$\Delta S_f = R \sum_{i=1}^N \sum_{j=1}^3 \ln(\nu_{ij}/\nu_{ij}') + R \sum_{j=1}^3 \ln(\nu_{Bj}/\nu_{Bj}'), \quad (2)$$

where  $\nu_{ij}$  is the  $j$ th vibration frequency of the  $i$ th of the  $N$  neighbours of the  $A-B$  pair in the perfect lattice,  $\nu_{ij}'$  is its value in the lattice with  $B$  at the saddle-point, and  $\nu_{Bj}$ ,  $\nu_{Bj}'$  are the corresponding quantities for atom  $B$ . In order to carry out an order of magnitude calculation similar to that given by Dienes, we assume (i) that  $\nu_{ij} = \nu_{ij}'$  except in the direction of the line joining the  $i$ th atom to  $B$ , i.e., take  $\nu_{ij} = \nu_{ij}'$  for  $j = 1, 2$  and (ii) that  $\nu_{i3}$  and  $\nu_{i3}'$  are inversely proportional to  $(r_i)^{3\gamma}$  and  $\{(r_i + r_i')/2\}^{3\gamma}$ , where  $r_i$  is the interatomic distance in the perfect lattice,  $r_i'$  is the distance from the  $i$ th atom to  $B$  (at the saddle-point), and  $\gamma$  is Gruneisen's constant. We can then write the first term of  $\Delta S_f$  in the

TABLE A-I. Changes in entropy (cal/mol/°C).

Mechanism	$N$	First term of $\Delta S_f$	$\Delta S_{\text{expt}}$	$\Delta S_{\text{Zener}}$
1	14	18	~-13	~8
	26	24		
2	16	18	-19	5
	24	29		
3	5	-10	~-7	~8
	7	-11		
	9	-9		
4	8	-10	-19	5
	12	-4		

form

$$3R\gamma \sum_{i=1}^N \ln\{(r_i+r_i')/2r_i\}. \quad (3)$$

This is almost the same as the expression used by Dienes to calculate his entropy change except that he interprets  $r_i$  as the distance between the  $i$ th neighbour and  $B$  in its original position, whereas in this calculation  $r_i$  is the distance from the  $i$ th neighbour to the nearer of  $A$  and  $B$  in their original positions. For an interstitial mechanism, we have to consider an imperfect lattice of  $L-1$  atoms on their normal sites together with the atom  $B$  at a saddle-point between two interstitial positions. Then  $\Delta S_f$  is again given by (2) and (3) if we assume that the  $N$  neighbors are the neighbours of the saddle-point,  $r_i'$  is the distance from the  $i$ th neighbour to this point, and  $r_i$  is a "mean interatomic distance" in the perfect lattice. The contribution to  $\Delta S_f$  from the second term is more difficult to estimate but is presumably of the same sign and smaller than the first term in each case.

Table A-I lists the values given by (3) for the first four mechanisms in Table I when various numbers of neighbors are considered. For comparison values of  $\Delta S_{\text{expt}}$  [obtained by substituting  $\nu$ =Debye frequency

into equation (1)] and  $\Delta S_{\text{Zener}}=8Q \times 10^{-4}$  are also given. These latter sets of values are significant only when the mechanism considered is a dominant one and the values for mechanisms 1 and 3 depend slightly on whether the other dominant mechanism is assumed to be 2 or 4. It will be seen that  $\Delta S_f$  is always positive for vacancy mechanisms and always negative for interstitial mechanisms, in agreement with physical ideas which suggest that there is a general loosening of the lattice when a vacancy is formed and a general tightening when an interstitial atom is introduced. If allowance had been made for relaxation of the atoms about the diffusing atom, the values of  $\Delta S_f$  would have been reduced in magnitude but not changed in sign, so that the figures given in Table A-I must be considered as overestimates.

#### REFERENCES

1. G. A. Shirn, E. S. Wajda, and H. B. Huntington, *Acta Met.* **1**, 513 (1953).
2. P. J. Fensham, *Aust. J. Sci. Res.* **A3**, 91 (1950); **4**, 229 (1951).
3. H. R. Paneth, *Phys. Rev.* **80**, 708 (1950).
4. A. D. Le Claire, *Acta Met.* **1**, 438 (1953).
5. C. Zener, "Imperfections in Nearly Perfect Crystals" (John Wiley, New York, 1952), p. 289.
6. G. J. Dienes, *J. Appl. Phys.* **22**, 848 (1951).
7. G. J. Dienes, *Phys. Rev.* **89**, 185 (1953).
8. G. H. Vineyard and G. J. Dienes, *Phys. Rev.* **93**, 265 (1954).



# CALORIMETRIC MEASUREMENTS DURING PRECIPITATION IN A GOLD-NICKEL ALLOY\*

J. NYSTRÖM†

An apparatus designed and built for measurements of heat evolved at high temperatures. The heat of precipitation between 400 and 500°C in a gold-nickel alloy with 26 atomic per cent nickel was determined. The results are compared with the heat of precipitation as calculated from the two-phase boundary assuming the entropy of mixing to be the same as for an ideal solution. The results are also compared with those calculated from the heat of mixing obtained elsewhere from measurements of electrolytic potentials. The kinetics of the transformation were also studied.

## MESURES CALORIMÉTRIQUES LORS DE LA PRÉCIPITATION DANS UN ALLIAGE OR-NICKEL

Un appareil pour des mesures de chaleur dégagée à hautes températures a été construit. La chaleur de précipitation d'un alliage or-nickel à 26% de nickel a été mesurée entre 400° et 500°C. Les résultats sont comparés à la chaleur de précipitation calculée à partir des limites de phase en supposant que l'énergie de mélange est la même que pour une solution idéale. Les résultats sont également comparés à ceux calculés à partir de l'énergie de mélange obtenue à l'aide des potentiels d'électrodes. La cinétique de la transformation a été étudiée.

## KALORIMETRISCHE MESSUNGEN WÄHREND DER AUSSCHIEDUNG IN EINER GOLD-NICKEL LEGIERUNG

Für kalorimetrische Messungen bei hohen Temperaturen wurde ein neues Gerät entwickelt. Die Entmischungswärme einer Gold-Nickel Legierung mit 26% Nickel wurde zwischen 400 und 500°C bestimmt. Die Ergebnisse werden mit den Werten für die Entmischungswärme verglichen, die unter der Annahme eines idealen Verhaltens der Mischungsentropie aus der Zweiphasengrenze berechnet wurden. Weiterhin wird ein Vergleich zwischen den experimentell gefundenen Ergebnissen und den an anderer Stelle auf Grund der Messung des elektrolytischen Potentials berechneten Mischungswärmen durchgeführt. Die Kinetik der Umwandlung wird ebenfalls besprochen.

### 1. INTRODUCTION

There have been many suggestions to calculate the heat of mixing for alloys. In most cases the energy has been calculated from the sum of the binding energies in pairs of nearest neighbors. Borelius,<sup>1</sup> however, assumed that groups of more than two atoms had to be taken into consideration for calculation of the energy, and gave empirical formulas. In the last few years attempts have been made to explain the heat of mixing by means of changes in the energy of the electrons in the Fermi bands<sup>2,3</sup> and from strains in the lattice.<sup>4,6</sup> The entropy of mixing for the solid solution has mostly been considered the same as for ideal solutions. Recent measurements on the gold-nickel system,<sup>4</sup> however, show that the entropy can be very different from that of ideal solutions. Detection of short-range order between the atoms above the two-phase boundary in the same alloy system<sup>5</sup> also shows that the heat of mixing can not be composed of the binding energies of pairs of nearest neighbors.

In this investigation the heat of precipitation in an alloy in the gold-nickel system was measured and compared with calculated values obtained from the heat of mixing according to the investigation mentioned above;<sup>4</sup> the kinetics of the transformation were also studied.

### 2. EXPERIMENTAL METHOD

The alloy was made of spectroscopically pure nickel from Johnson, Matthey and Co. and pure gold from Ädelmetallbolaget, Malmö, Sweden. The purity of the gold was checked by measurements of the electrical resistivity at room temperature. The metals were melted to an alloy in an evacuated quartz tube in a high-frequency furnace, rolled a little, and then annealed for 24 hours at an approximate temperature of 875°C. After quenching in cold water, it was formed into a cylinder about 2.5 cm long and 4 mm in diameter. A chemical analysis after the measurements were performed gave the concentration as 25.9 atomic per cent nickel.

The principle for the measurements was the same as for many other measurements in the same laboratory,<sup>7,8</sup> but the apparatus was designed to work at higher temperatures than had been used earlier. Two horizontal electrical tube furnaces were used, one smaller for the homogenization of the specimen and one larger for the calorimetric measurements. It was possible to move the specimen in a quartz tube going through both furnaces. For this purpose and in order to measure the temperature of the specimen, a thermocouple of silver and constantan was made with one contact inside the specimen and the two wires projecting out of the two ends of the quartz tube. A third purpose of the thermocouple was to supply Peltier heat for calibration of the measuring device (see, for instance, reference 8).

\* Received June 29, 1954; in revised form November 9, 1954.

† Royal Institute of Technology, Stockholm, Sweden, and Physics Department, N. C. State College, Raleigh, North Carolina

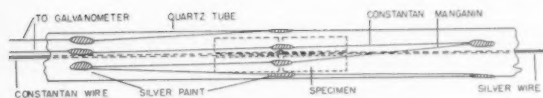


FIG. 1. Device to measure the evolution of heat in the specimen. This part of the apparatus was enclosed in a hollow copper cylinder.

The device for the calorimetric measurements is shown in Fig. 1. The part of the quartz tube seen there is placed in the center of a hollow copper cylinder in the middle of the larger furnace. The block had no metallic connections with the surroundings in order to maintain a uniform temperature. A constant temperature of the furnace was obtained by means of heating with a stabilized current. Possible variations in the temperature due to small variations in the power input and to variations in the room temperature were very slow because of the large heat capacity of the furnace. During measurements, as described herein, it is more important to keep possible variations in the temperature slow than to have the upper and lower limit for the temperature close together.

The evolution of heat in the specimen was obtained from the temperature difference between the specimen and the surroundings as measured by means of eight thermocouples made of constantan and manganin wires 0.15 mm in diameter coupled in series and connected to the outer surface of the quartz tube by means of silver paint as shown in Fig. 1. The voltage of the series of thermocouples was measured by means of a mirror galvanometer. In order to minimize errors from undesirable thermoelectric forces in the galvanometer circuit there was an electrical commutator which was thermally insulated in a wooden box.

In order to protect the specimen and the measuring device from oxidation a slow stream of a mixture of 95 per cent nitrogen and 5 per cent hydrogen was passed through the apparatus both outside and inside the quartz tube.

The solubility of nitrogen is negligible both in gold and nickel.<sup>9</sup> Hydrogen is only dissolved in nickel<sup>9</sup> but the concentration at the temperatures used is only about 0.4 atomic per cent.<sup>10</sup> Thus a heat effect due to precipitation of  $H_2$  must be negligible compared with the heat measured.

The measurements were performed in the following way: The specimen was first annealed in the smaller furnace at a temperature 60–80°C above the two-phase boundary, for a time varying between ten minutes and three hours. It was then moved to a point in the tube between the two furnaces where, during half a minute, it cooled down approximately to the temperature of the larger furnace which had been adjusted to the desired measuring temperature. Then the specimen was placed into position for measurements as shown in Fig. 1. Measurements of the galvanometer deflection could start as soon as the temperature of the specimen was within 2 degrees of the temperature of the furnace.

The time required for this was usually about five minutes. All measurements were made for both current directions through the galvanometer. In Fig. 2 the galvanometer readings for two different measurements are recorded. From these readings the evolution of heat was obtained.

The calibration was performed in the same way as in reference 8. We introduce the following symbols:

$$\begin{aligned} P &= \text{power developed in the specimen,} \\ s &= \text{change in galvanometer deflection for power} \\ &= P, \\ a, b &= \text{empirical constants,} \\ t &= \text{time.} \end{aligned}$$

The equation for the power  $P$  can be written  $P = as + b ds/dt$ . For calibration a current  $i$  was sent through the thermocouple. When equilibrium for  $s$  the equation can be written

$$P_1 = Ri^2 + \Pi i = as_1$$

and

$$P_2 = Ri^2 - \Pi i = as_2$$

for the two directions of the current where  $Ri^2$  is the ohmic part of the heat and  $\Pi i$  the Peltier heat. We get

$$a = \frac{s_1 - s_2}{2\Pi i}.$$

After the current in the thermocouple has been broken we get

$$as + b \frac{ds}{dt} = 0$$

and the relation between  $a$  and  $b$  can easily be obtained.

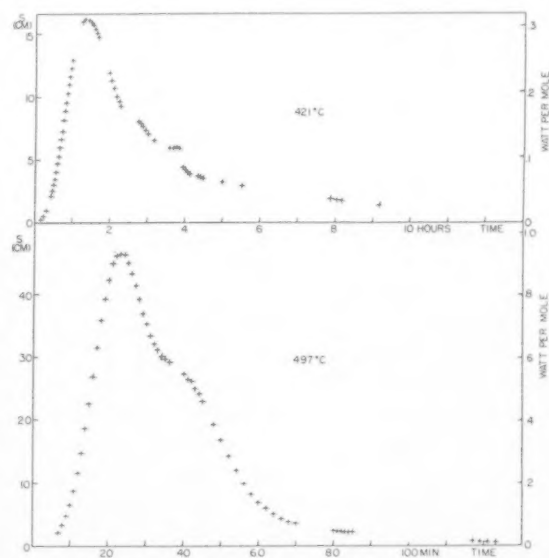


FIG. 2. Heat power evolved in the specimen as a function of time.

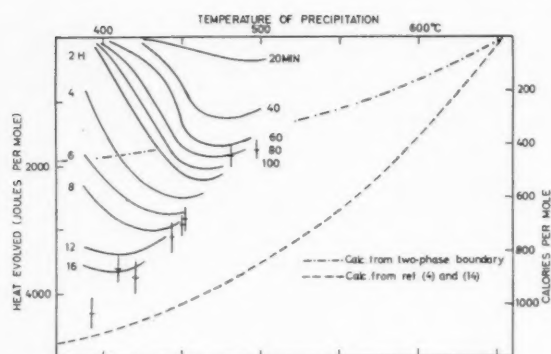


FIG. 3. Heat evolved per mole in the specimen after different lengths of time.

During the measurements the term  $b(ds/dt)$  had only to be taken into account during the first few minutes which means that the same curves could be drawn for  $s$  and  $P$  in Fig. 2.

### 3. RESULTS

In Fig. 2 two curves of the heat power in the specimen as a function of time are shown. A comparison of curves obtained at the same temperature showed that they could have different form depending on the heat treatment before the precipitation. Because of this it was not possible to give any equation of the heat evolved as a function of time and temperature. The total heat evolved, however, was the same.

The observation points in Fig. 3 show the total heat evolved, as obtained by graphical integration of curves like those in Fig. 2. The inaccuracy in the heat is indicated by the vertical lines. The temperature is measured by means of a thermocouple calibrated with an accuracy of  $\pm 2^\circ\text{C}$ . The solid curves show the heat evolved after different lengths of time. The last measurements made (at  $481^\circ\text{C}$ ) are neglected for these curves as the specimen had been heated to a higher temperature than earlier, so a slower reaction could be expected.<sup>11</sup>

### 4. DISCUSSION OF THE RESULTS

As mentioned before, the measurements showed that different homogenization conditions for the specimen could give different forms to the curves obtained at the same precipitation temperature. This can probably be explained in the following way. As Köster and Dannöhl<sup>12</sup> showed, there is grain-boundary precipitation in the system. Different time and temperature for the homogenization can give different crystal size and different form to the crystals. For large crystals it will be readily seen that if the precipitation starts at different points on different occasions, we can obtain power curves of different form. A difference in crystal size, on the other hand, cannot be expected to cause a significant difference in the internal energy of the alloy compared with the total heat of precipitation.

The heat evolved during complete precipitation can be easily calculated if we know the two-phase boundary<sup>9,13</sup> and the enthalpy of mixing as a function of concentration at the precipitation temperature. In Fig. 3 the experimental results are compared with values calculated in two different ways. For one calculation, the enthalpy of mixing is obtained directly from the two-phase boundary under the assumption that the entropy of mixing is the same as for an ideal solution. This involves the validity of Kopp-Neumann's rule. The heat of precipitation calculated under this assumption is much too low when compared with the experimental values.

The other calculated curve has been obtained from the enthalpy of mixing at  $900^\circ\text{C}$  determined by Cohen *et al.*<sup>4</sup> Starting from these values, the enthalpy of mixing at the precipitation temperature has been estimated in the following way. Oriani<sup>14</sup> has measured the specific heat of an alloy with 48 atomic per cent nickel. He found a positive deviation from Kopp-Neumann's rule and, from the deviation per mole  $\Delta C_p$ , we obtain the difference in enthalpy of mixing per mole  $\Delta H$  between  $900^\circ\text{C}$  and the temperature  $T$  for this alloy.

$$\Delta H = H_{900^\circ} - H_T = \int_T^{900} \Delta C_p dT.$$

Thus the enthalpy of mixing was found to be 5.6 per cent lower at  $600^\circ\text{C}$  and 9.3 per cent lower at  $400^\circ\text{C}$  than the values determined at  $900^\circ\text{C}$ . In order to obtain the heat of precipitation at different temperatures, the values of the enthalpy of mixing at  $900^\circ\text{C}$  were first used and a correction was made afterwards (5.6 per cent at  $600^\circ\text{C}$ , 9.3 per cent at  $400^\circ\text{C}$ ). A more exact correction would have required specific heat measurements for other concentrations also, but the accuracy in the experimental results does not justify a more elaborate correction.

We assume that the heat of precipitation calculated in this way is correct. It is then possible to compare the ratio between the heat evolved during a certain length of time and the heat of completed precipitation with the relative change in resistance with time of a gold-nickel alloy with 28 atomic per cent Ni according to Borelius.<sup>11</sup> The curves in Fig. 3 have the same form as those in reference 11. It is noticed that the reaction is extremely slow in a range of about  $100^\circ\text{C}$  below the two-phase boundary and can not be detected by means of calorimetric measurements where the sensitivity is not higher than in this investigation.

### 5. ACKNOWLEDGMENT

This investigation is a part of a general programme in progress at the Physics Department of the Royal Institute of Technology in Stockholm under the direction of

Professor G. Borelius. The author wants to express thanks to him for his interest and valuable discussions.

# REFERENCES

1. G. Borelius, *Ann. d. Physik* **24**, 489 (1935).
2. J. C. Slater, *Phys. Rev.* **84**, 179 (1951).
3. J. F. Nicholas, *Proc. Phys. Soc.* **A66**, 201 (1953).
4. L. L. Seigle, M. Cohen, and B. L. Averbach, *J. Metals* **4**, 1320 (1952).
5. P. A. Flinn, B. L. Averbach, and M. Cohen, *Acta Met.* **1**, 664 (1953).
6. B. L. Averbach, P. A. Flinn, and M. Cohen, *Acta Met.* **2**, 92 (1954).
7. G. Borelius, J. Andersson, and K. Gullberg, *Ingeniörsvetenskapsakademiens Handlingar* No. 169 (1943).
8. G. Borelius, S. Berglund, and O. Avsan, *Arkiv för Fysik* **2**, 551 (1951).
9. M. Hansen, *Der Aufbau der Zweistofflegierungen* (Springer Berlin, 1936).
10. L. Luckemeyer-Hasse and H. Schenck, *Arch. Eisenhüttenwes.* **6**, 210 (1932-33).
11. G. Borelius, *J. Metals* **3**, 477 (1951).
12. W. Köster, und W. Dannöhl, *Z. f. Metallk.* **28**, 248 (1936).
13. *Metals Handbook*, The American Society for Metals, Cleveland, Ohio, 1948.
14. R. Oriani, Private information.



# FRictional Forces on Dislocation Arrays at the Lower Yield Point in Iron\*

A. CRACKNELL† and N. J. PETCH‡

The equation  $\sigma_{l.y.p.} = \sigma_0 + k^*l^{-1/2}$ , which relates the lower yield point  $\sigma_{l.y.p.}$  of polycrystalline iron with the grain diameter  $l$ , has been confirmed. Here  $k^*$  and  $\sigma_0$  are constants and it is suggested that  $\sigma_0$  depends in part upon the frictional forces exerted by solute atoms and precipitates on the dislocation arrays that propagate the yield. In agreement, it is found that  $\sigma_0$  increases when the solute atom concentration is increased by nitriding or by sub-critical quenching and there is a further increase on ageing, followed by a decrease on over-ageing.

A linear relationship is calculated between  $\sigma_0$  and the concentration of carbon + nitrogen in solution, and this is confirmed by experimental measurements.

## FORCES DE FROTTEMENT SUR LES LIGNES DE DISLOCATIONS À LA LIMITE ÉLASTIQUE INFÉRIEURE DANS LE FER

L'équation  $\sigma_E = \sigma_0 + k^*l^{-1/2}$  qui relie la limite élastique inférieure du fer polycristallin au diamètre des grains a été vérifiée. Dans l'expression ci-dessus,  $k^*$  et  $\sigma_0$  sont des constantes et il est suggéré que  $\sigma_0$  dépend en partie des forces de frottement qu'exercent les atomes dissous et les précipités sur les lignes de dislocations. Comme vérification, il est montré que  $\sigma_0$  croît si la concentration en atomes dissous est augmentée par nitruration ou par trempe et que  $\sigma_0$  croît également par vieillissement, mais décroît pendant la phase de coalescence due à un vieillissement trop poussé. Une relation linéaire, confirmée par l'expérience, est établie entre  $\sigma_0$  et la concentration en atomes de carbone + azote dans la solution.

## REIBUNGSKRÄFTE AN VERSETZUNGSANSAMMLUNGEN AN DER UNTEREN STRECKGRENZE IN EISEN

Die Gleichung  $\sigma_{l.y.p.} = \sigma_0 + k^*l^{-1/2}$  die die untere Streckgrenze  $\sigma_{l.y.p.}$  von vielkristallinem Eisen mit dem Korndurchmesser  $l$  in Beziehung bringt, konnte bestätigt werden. Hierbei sind  $k^*$  und  $\sigma_0$  Konstanten. Es wird angenommen, dass  $\sigma_0$  zum Teil von den Reibungskräften abhängig ist, die durch gelöste Atome und Ausscheidungen an den Versetzungsansammlungen verursacht werden, die die Spannung hervorrufen. In Übereinstimmung damit wurde gefunden, dass  $\sigma_0$  grösser wird, wenn die gelösten Atomansammlungen durch eine Nitrierung oder durch unterkritisches Abschrecken vermehrt werden. Durch Alterung wird eine weitere Erhöhung von  $\sigma_0$  hervorgerufen, der ein Abfall bei der Überalterung folgt.

Zwischen  $\sigma_0$  und der Konzentration von Kohlenstoff und Stickstoff in Lösung wird eine lineare Abhängigkeit errechnet und durch experimentelle Befunde belegt.

## INTRODUCTION

The lower yield point  $\sigma_{l.y.p.}$  and the cleavage strength  $\sigma_c$  of polycrystalline iron have the same form of dependence upon the grain diameter  $l$ , namely,

$$\sigma_{l.y.p.} = \sigma_0 + k^*l^{-1/2}, \quad (1)$$

$$\sigma_c = \sigma_0 + kl^{-1/2}, \quad (2)$$

where  $\sigma_0$ ,  $k$  and  $k^*$  are constants.<sup>1,2</sup> Measurements in liquid nitrogen give the same numerical value of  $\sigma_0$  in both equations.

It has been shown that these relationships can be explained if the propagation of a Lüders band from grain to grain at the lower yield point depends upon the shear stress ahead of an array of dislocations piled up against a grain boundary by the applied stress and if cleavage depends upon the tensile stress ahead of such an array.<sup>1,2</sup>

Equations (1) and (2) are particularly powerful in the study of the yielding and cleavage of polycrystals, since they separate the factors that control  $\sigma_{l.y.p.}$  and  $\sigma_c$  into three. These are the grain size  $l$ , the stress that must be produced ahead of the array (which determines  $k^*$  and  $k$ ) and the term  $\sigma_0$ . The last of these represents a stress

that opposes the motion of the dislocations and so reduces the stress produced ahead of the array. The purpose of the present paper is to examine the nature of the internal stress that produces  $\sigma_0$ .

## FRICITION BY SOLUTE ATOMS AND PRECIPITATES

To give rise to Eqs. (1) and (2), the internal stress must either oppose the motion of the dislocations at all points along the length of the array or the wavelength of the internal stress must be very short compared to this length. The internal stress due to fine precipitates or random solute atoms fulfils this condition, so these are potential contributors to  $\sigma_0$ . Of the solute atoms, carbon and nitrogen are probably the most important because of their strong Cottrell interaction.

If fine precipitates and solute atoms do act in this way, alteration in their concentration or dispersion should alter  $\sigma_0$ , and this has been examined experimentally for a mild steel. The concentration was varied by nitriding and by sub-critical quenching, and the dispersion was varied by quench-ageing. To obtain  $\sigma_0$ , the relationship between the lower yield point at room temperature and the grain size was determined and the results are shown in Fig. 1, in which  $\sigma_0$  appears as the intercept on the yield point axis.

First, it should be noticed that these results confirm

\* Received July 29, 1954.

† Now with Imperial Chemical Industries, Ltd., Billingham, England.

‡ Metallurgy Laboratory, Leeds University, Leeds, England.

Eq. (1). Secondly, it is apparent that nitriding and quenching raise  $\sigma_0$  and that the increased dispersion produced by ageing leads initially to a further rise, followed by a fall on over-ageing when the precipitate becomes widely dispersed.

These changes are exactly those that would be expected if solute atoms and fine precipitates do contribute to  $\sigma_0$ .

Figure 1 also shows that  $\sigma_0$  was higher for the mild steel than for a Swedish iron when both were in the annealed condition. This is probably mainly due to the difference in nitrogen content (Table I), since the concentration of carbon retained in solution will be practically the same for both materials and in any case it will be much less than the nitrogen concentration<sup>3-5</sup>; also the carbides will be coarsely dispersed whereas any nitrides that precipitate will only do so below  $\sim 200^\circ\text{C}$ , which will favour fine dispersion. It is confirmed later (Fig. 2) that the observed difference in  $\sigma_0$  is in fact mainly due to the nitrogen.

This influence of the nitrogen content on  $\sigma_0$  has a direct bearing on the important yield point differences between open hearth ( $\sim 0.005\%$   $\text{N}_2$ ) and Bessemer ( $\sim 0.015\%$   $\text{N}_2$ ) steels.

The slope  $k^*$  in Fig. 1 is unaffected by any of the various treatments, showing that the shear stress ( $\tau \propto k^*$ ) required at the head of the dislocation array if yield is to propagate is unchanged. If  $\tau$  is the stress required to break a dislocation source away from its atmosphere of solute atoms, it is understandable that an increase in the concentration of atoms in solution has no

TABLE I. Composition %.

	C	Si	S	P	Mn	Ni	Cr	N <sub>2</sub>
En. 2	0.115	0.02	0.05	0.029	0.51	0.08	0.05	0.0085
Swedish Iron	0.02	<0.01	0.02	0.024	0.14	0.03	0.01	0.003

effect on this stress, since the atmosphere is already condensed before the increase takes place. However, this atmosphere should evaporate above  $\sim 700^\circ\text{K}$ ,<sup>7</sup> so that some effect on  $k^*$  might have been expected in specimens quenched from above this temperature, but none was observed. It may be that the atmosphere recondensed during quenching, since extrapolation of measurements on strain-ageing<sup>8</sup> shows that the time to condense at  $650^\circ\text{K}$  is  $\sim \frac{1}{2}$  sec and data on cooling rates<sup>9</sup> suggest that this is probably shorter than the time to cool from  $700$ – $600^\circ\text{K}$  in the present case.

#### QUANTITATIVE TREATMENT FOR C AND N ATOMS

The resistance of random C and N atoms to dislocation movement can be calculated by the method used in the Mott and Nabarro,<sup>10,7,11</sup> treatment of finely dispersed centers of internal stress.

With  $N$  carbon + nitrogen atoms per unit volume, their mean separation is  $\Lambda = N^{-1/3}$  and the dislocation is bent by the nearest-neighbor solute atoms (those within a distance of  $\sim \Lambda/2$ ) into loops of average length  $\sim \Lambda$  and of average amplitude  $F\Lambda/8\alpha\mu b^2$ . Here  $\alpha \sim 0.5$ ,  $\mu$  is the rigidity modulus,  $b$  is the Burgers vector and  $F$  is the appropriate average force exerted in the glide direction by these solute atoms.

The elementary step in the motion forwards of the dislocation is performed by a loop of length  $n^2\Lambda$ . Since there are random positive and negative forces on the constituent single loops, the average amplitude of the  $n^2\Lambda$  loops is

$$\frac{nF \cdot n^2\Lambda}{8\alpha\mu b^2}$$

With a positive edge dislocation, C or N atoms below the glide plane give interaction energy valleys, but the atoms above the glide plane give energy hills. Thus, the energy of the length  $n^2\Lambda$  varies more or less periodically with a wavelength of  $2\Lambda$  as the dislocation moves across the crystal, and the movement of the center of the compound loop from one equilibrium position to the next will be about  $2\Lambda$ . With the amplitude expression, this gives

$$n = \left( \frac{8\alpha\mu b^2}{F} \right)^{1/3}$$

To evaluate  $F$  in magnitude, we consider the force exerted on an edge dislocation in the glide direction by a solute atom situated at  $(r, \theta)$  and integrate over one quadrant.

Using the Cottrell expression for the interaction

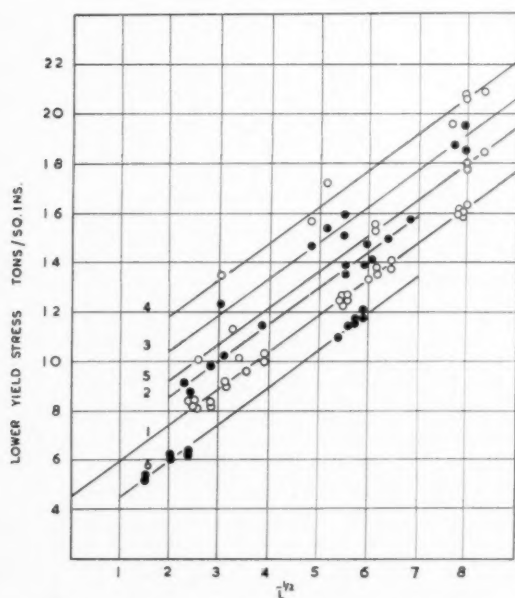
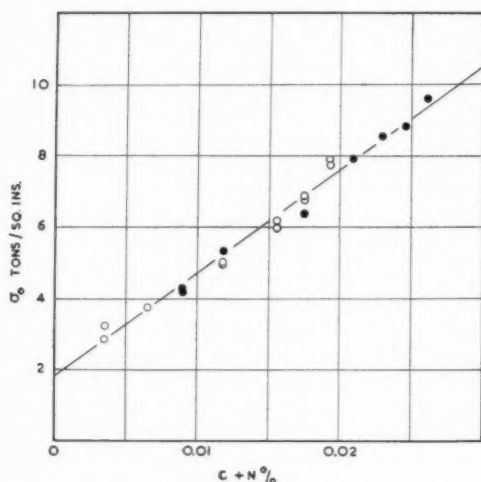


FIG. 1. Dependence of  $\sigma_{l.y.p.}$  on grain size  $l^{-1} \text{ mm}^{-1}$  for 1, annealed mild steel En. 2; 2, En. 2, nitrided; 3, En. 2, quenched from  $650^\circ\text{C}$ ; 4, En. 2, quenched, aged 1 hour at  $150^\circ\text{C}$ ; 5, En. 2, quenched, aged 100 hours at  $200^\circ\text{C}$ ; 6, annealed Swedish iron.

FIG. 2. Effect of the concentration of C+N in solution on  $\sigma_0$ .energy,<sup>12</sup>

$$F = \frac{\int_{r_0}^{\Lambda/2} \int_0^{\pi/2} \frac{2A \sin\theta \cos\theta}{r^2} \cdot r dr d\theta}{\frac{\pi \Lambda^2}{16}}$$

For  $r < r_0 \sim 2\hat{A}$ , it is considered that the interaction energy is zero.  $A$  is a constant.

$$F = \frac{16A}{\pi \Lambda^2} \ln \frac{\Lambda}{2r_0}$$

The net force  $nF$  on  $n^2\Lambda$  is equivalent to a shear stress  $F/n\Lambda b$ , so the tensile stress required at  $\sim 45^\circ$  to the glide plane to move the dislocation is

$$\sigma_0 = \frac{2F}{n\Lambda b}$$

Substitution gives

$$\sigma_0 = \frac{F^{4/3} N^{1/3}}{(\alpha\mu)^{1/3} b^{5/3}}$$

$$\sigma_0 = \frac{N^{11/9}}{(\alpha\mu)^{1/3} b^{5/3}} \left[ \frac{16A}{\pi} \ln \frac{1}{2r_0 N^{1/3}} \right]^{4/3}$$

As the concentration  $c$  increases from 0.005 to 0.025 per cent, the term  $N^{2/9} [\ln 1/2r_0 N^{1/3}]^{4/3}$  decreases by only 1 per cent, so that within this range

$$\sigma_0 \propto N \propto c.$$

With  $A \sim 1.5-3.0 \times 10^{-20}$  dyne  $\text{cm}^2$ ,<sup>13</sup>  $\sigma_0$  is 1-2 tons/sq in. at  $N = 10^{20}$  per cc (0.025% C).

## EXPERIMENTAL MEASUREMENTS

This calculation of  $\sigma_0$  has been tested experimentally. The variation in solute atom concentration was obtained

by quenching from various temperatures between 300-700°C and by using a mild steel and a Swedish iron with different "as received" nitrogen contents.

Figure 2 shows that the experimental values of  $\sigma_0$  determined at room temperature are mainly dependent upon the concentration of C+N in solution and that  $\sigma_0$  is linear with respect to this concentration in agreement with the calculation. There is, however, an intercept of  $\sim 2$  tons/sq in. at  $c=0$ .

Similar measurements in liquid nitrogen<sup>14</sup> show that the part of  $\sigma_0$  associated with the C+N in solution has little dependence on temperature, so that the magnitude of  $\sigma_0$  in Fig. 2 is directly comparable with the calculated value, which assumes no thermal activation. It is apparent that the calculated value is of the right order, but low.

This is rather to be expected. In the calculation,  $F$  is given an average value for atoms within  $\Lambda/2$  of the dislocation, but the equilibrium positions of an  $n^2\Lambda$  loop will arise because of closer proximity than average to the minimum energy positions for the single loops, and quite probably there is a consequent maximum near the equilibrium positions in the force required to move an  $n^2\Lambda$  loop. An approximate upper limit to  $\sigma_0$  can be calculated by assuming that  $F$  in the resultant force  $nF$  acting on the length  $n^2\Lambda$  has the maximum value for the displacement of a dislocation from a C or N atom, averaged for a depth of the atom below the glide plane of up to  $\Lambda/2$ . The calculation is straight-forward, although it does not give a simple result, since the interaction energy within  $r_0$  of the dislocation has to be taken as zero. At  $A \sim 1.5-3.0 \times 10^{-20}$  dyne  $\text{cm}^2$  and  $N = 10^{20}$  per cc,  $\sigma_0 \sim 4-10$  tons/sq in.

The liquid nitrogen measurements show that the  $\sigma_0$  intercept at  $c=0$  is considerably temperature-dependent, and it may well be that this contribution to  $\sigma_0$  represents the stress required to force a dislocation through intersecting dislocations.

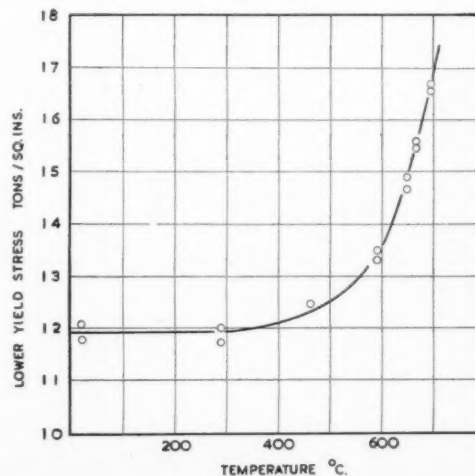
FIG. 3. Effect of quenching temperature on  $\sigma_{l.y.p.}$  for Swedish iron at constant grain size.

Figure 3 illustrates the variation with quenching temperature of the lower yield point determined at room temperature for specimens of constant grain size.

#### EXPERIMENTAL DETAILS

The compositions of the materials used are shown in Table I.

All the yield point measurements were made at room temperature on small specimens with 0.25 in. diameter ends and 1 in. gauge length of 0.125 in. diameter. The same strain rate was used in all cases (cross-head velocity = 0.34 mm/min).

Temperatures in the austenitic region of up to 1050°C and times up to 24 hours were used to obtain the various grain sizes, except for the coarser ones, which were produced by straining and annealing. The specimens were cooled over a period of 15 hours after these treatments.

Nitriding was carried out at 580°C by the Schwartzbart and Low method<sup>15</sup> using previously annealed specimens; they were cooled in the nitriding furnace.

In the quenching experiments, previously annealed specimens were heated *in vacuo* to 700°C, slowly cooled in the furnace to the required temperature, held there for 14 hours, water-quenched and then tested. To make

sure that the yield point was not affected by quenching stresses, other specimens were quenched as  $\frac{1}{4}$ -in. bar, then carefully turned into specimens and tested. The two sets of measurements agreed.

Wert's<sup>16</sup> measurements were used to give the solute atom concentration in the quenched state.

#### REFERENCES

1. E. O. Hall, Proc. Phys. Soc. **B64**, 747 (1951).
2. N. J. Petch, J. Iron Steel Inst. **174**, 25 (1953).
3. L. J. Dijkstra, J. Metals **1**, 252 (1949).
4. C. A. Wert, J. Appl. Phys. **20**, 943 (1949).
5. G. Borelius, J. Metals **3**, 477 (1951).
6. A. H. Cottrell and G. M. Leak, J. Iron Steel Inst. **172**, 301 (1952).
7. N. F. Mott, "Imperfections in Nearly Perfect Crystals," ed. W. Shockley (John Wiley, New York, 1952), p. 173.
8. F. R. N. Nabarro, Report of Conference on Strength of Solids (Phys. Soc., 1948), p. 38.
9. Metals Handbook (Amer. Soc. Metals, 1948), p. 615.
10. N. F. Mott and F. R. N. Nabarro, Report of Conference on Strength of Solids (Phys. Soc., 1948), p. 1.
11. A. H. Cottrell, "Dislocations and Plastic Flow in Crystals" (O.U.P., 1953), p. 129.
12. A. H. Cottrell, Report of Conference on Strength of Solids (Phys. Soc., 1948), p. 30.
13. A. H. Cottrell, "Dislocations and Plastic Flow in Crystals" (O.U.P., 1953), p. 134.
14. J. Heslop and N. J. Petch, unpublished work.
15. H. Schwartzbart and J. R. Low, J. Metals **1**, 637 (1949).
16. C. A. Wert, J. Metals **2**, 1242 (1950).



## X-RAY LINE BROADENING FROM COLD-WORKED IRON\*

R. I. GARROD and J. H. AULD†

Measurements of the x-ray line broadening from cold-worked iron filings, and from wire specimens prestressed by uniaxial tension to various stages in the plastic range, have been analyzed in terms of both line breadths and line shapes for a number of high angle reflections. The results indicate that heterogeneous lattice distortion is predominantly responsible for the observed broadening although some particle size broadening does occur. Values of  $\sim 10^{-6}$  and  $5 \times 10^{-6}$  cm were obtained for the minimum average particle sizes for the filings and wires, respectively. Differences in average particle sizes, root mean square strains and strain distributions were found for different directions in the deformed crystals; these effects have been interpreted qualitatively in terms of dislocation processes.

### ELARGISSEMENT DES SPECTRES DE RAYONS X DU FER ÉCROUI

L'élargissement de la forme des raies des spectres de rayons X a été analysé pour les grands angles de réflexion dans le cas de la limaille de fer écroui et dans celui de fils déformés plastiquement par traction. Les résultats montrent que l'élargissement observé est surtout dû à une distorsion hétérogène du réseau, quoiqu'un certain élargissement provienne du facteur de dimension. Des valeurs de l'ordre de  $10^{-6}$  cm et  $5 \times 10^{-6}$  cm ont été obtenues comme dimension moyenne, respectivement pour la limaille et les fils, mais les valeurs obtenues pour les dimensions moyennes de particules pour la racine carrée de la moyenne du carré des déformations et pour la distribution des déformations, varient suivant les directions; ces effets peuvent être expliqués qualitativement par la théorie des dislocations.

### VERBREITERUNG DER RÖNTGENLINIEN BEI KALTVERFORMTEN EISEN

Messungen der Verbreiterung der Röntgenlinien von kaltverformten Eisenfeilspänen und Drahtproben, die unter einachsiger Beanspruchung im plastischen Bereich um verschiedene Beträge vorgereckt wurden, sind sowohl in Bezug auf die Linienbreite als auch auf die Linienform analysiert worden. In der Hauptsache ist die Linienverbreiterung auf heterogene Gitterverzerrungen zurückzuführen, obwohl auch ein gewisser Betrag der Verbreiterung durch die Teilchengröße bewirkt wird. Die kleinste mittlere Teilchengröße wurde für die Späne zu  $\sim 10^{-6}$ , für die Drähte zu  $\sim 5 \times 10^{-6}$  cm ermittelt. In den verschiedenen Richtungen der verformten Kristalle wurden Unterschiede in der mittleren Teilchengröße, der mittleren Grösse der Ursprungsspannungen und der Spannungsverteilung gefunden; diese Erscheinungen werden qualitativ mit Hilfe von Versetzungsvorgängen gedeutet.

### INTRODUCTION

Many experiments have been carried out in different laboratories in recent years to determine the relative importance of particle-size and lattice distortion effects on the broadening of X-ray reflections from cold-worked polycrystalline metals. The theoretical background and various experimental observations have recently been summarised by Greenough<sup>1</sup> and by Williamson and Hall.<sup>2</sup>

Prior to 1950, the usual approach to the problem was to investigate the variation of true integral line breadth of high order reflections with the diffraction angle and the wavelength of the incident X-ray beam. Experiments of this type have however produced conflicting results;<sup>3-8</sup> possible reasons for this have been discussed elsewhere.<sup>9,10</sup>

Recently developed Fourier methods (Warren and Averbach)<sup>11-13</sup> for analysing the shapes of the diffraction lines provide much information which cannot be obtained from determinations of line breadth only. This type of analysis has therefore been used extensively<sup>2,11-13,15-18</sup> in spite of certain limitations<sup>10,14</sup> and exacting experimental requirements.

The present work has been undertaken with two main objects in mind:

(1) Firstly, to examine both bulk metal and filings under similar experimental conditions and with appropriate analytical procedures for assessing the results, to determine whether any radical difference in the nature of the deformation process could be detected. This point is of importance in view of previous conflicting results.<sup>19</sup>

(2) Secondly, to extend the Fourier analysis of line shapes to cases where a *mean* change in interplanar spacing occurs after plastic deformation. Previous work employing the Fourier method has been restricted to specimens that exhibit no appreciable shift in the positions of the line peaks after cold-work.

A brief account of some early results, analysed on the basis of line breadths, has already been published elsewhere.<sup>9</sup>

### EXPERIMENTAL

Iron was chosen as the material for the investigation because, (a) it exhibits relatively large residual lattice strains after uniaxial stress in the plastic range, (b) it shows no appreciable self-recovery at room temperature,<sup>7,20</sup> a point of some importance in view of the length of time involved in the experiments, and (c) by the use of different wavelengths it is possible to examine a number of different *hkl* reflections at high  $\theta$ -values.

\* Received March 22, 1954; in revised form June 1, 1954.

† Formerly at Defence Standards Laboratories, Melbourne, Australia; now at Aeronautical Research Laboratories, Melbourne, Australia.

Since unambiguous interpretation of the Fourier coefficients depends largely upon precise determination of the X-ray line profiles, especially in regions close to their "tails," it is customary to make the experimental measurements with a Geiger counter X-ray spectrometer. As this technique was not available to us, the X-ray reflections were recorded on films and the line profiles then obtained by microphotometry. As a check on the accuracy of the Fourier coefficients obtained from these experimental data, the observations were therefore analysed in terms of line breadth as well as line shape.

### (a) Preparation of Specimens

The material used was ingot iron of the following analysis:

	Per cent		Per cent
Carbon	0.03	Manganese	0.1
Sulphur	0.019	Nickel	0.005
Phosphorus	0.011	Chromium	0.01
Copper	0.02	Cobalt	<0.008

Miniature cylindrical tensile test specimens, having a gauge length of  $\frac{1}{2}$  inch and diameter of  $0.015 \pm 0.001$  inch were prepared from wire by etching and electropolishing treatments.

The specimens were then heated *in vacuo* to  $920^\circ\text{C}$ , held at temperature for 10 minutes, rapidly cooled to  $650^\circ\text{C}$  and subjected to this temperature for 30 minutes and then slowly cooled. Finally they were given a light electrolytic etch to remove any surface effects. (It is known that electrolytic etching does not produce any significant surface stresses in high purity iron.<sup>21</sup>) Stationary X-ray photographs showed that this heat treatment removed preferred orientation and internal strains.

A specimen of filings was prepared by filing one of the annealed wires in benzene, and then enclosing the powder in a cellophane tube. Part of the filings was given the same heat treatment as the wires and then also enclosed in a cellophane tube of the same dimensions as for the cold-worked sample.

### (b) X-ray Photographs

The wire specimens were examined in an 11.46 cm diameter powder camera, first in the strain-free state and then after having been strained in tension to various stages in the plastic range up to fracture. Crystal-reflected cobalt, chromium and iron monochromatic radiations and filtered molybdenum radiation were employed. Similar patterns were obtained from the cold-worked and annealed filings. In all exposures, no intensifying screens were used and the peak density of all lines was kept within the linear portion of the intensity-density characteristic of the X-ray film used (Ilford "New Ilfex").

The line profiles corresponding to values of  $\theta$  in excess of 30 degrees were determined by careful microphotometry of the films and the mean residual lattice

strains for the high-order reflections were obtained in the usual way from measurements taken on a travelling microscope, corrections being made for temperature and film-shrinkage effects.

## DETERMINATION OF LINE BREADTHS

### (a) Method

The Fourier coefficients for the true broadening profile were obtained by applying Stokes's method<sup>22</sup> to corresponding pairs of diffraction lines, after resolving each  $\alpha_1\alpha_2$  doublet by graphical means.<sup>22</sup>

Following Stokes, let  $g(x)$  and  $h(x)$  represent the experimental line profiles from a sample in the strain-free and deformed conditions, respectively, and let  $f(x)$  be the true broadening profile, where  $x$  is a linear distance on the film. Then  $g(x)$ ,  $h(x)$  and  $f(x)$  may be expressed as Fourier series of the type

$$f(x) = \sum_{-\infty}^{\infty} F(t) \exp(-2\pi ixt/a), \quad (1)$$

and similarly for  $g(x)$  and  $h(x)$ , where  $f(0)$  = peak value of  $f(x)$ ,  $t=0, \pm 1, \pm 2$ , etc. and  $\pm a/2$  are the limits for  $x$ , outside which  $h(x)$  and  $g(x)$  have fallen to the background value which is taken as zero.

If the deformation process results in no peak displacement, the same origin may be chosen for the three profiles and  $F(t) = H(t)/aG(t)$ , where  $H(t)$  and  $G(t)$  are the transforms of  $h(x)$  and  $g(x)$ , respectively. This is a close approximation for the filings, to which the method is normally applied, but may be invalid for the bulk metal plastically deformed by uniaxial stress. In the latter case, if individual origins for  $x$  for the  $g(x)$  and  $h(x)$  curves are chosen at the positions of their respective means, the origin for  $x$  in (1) will occur automatically at the position of the mean of the  $f(x)$  profile and again  $F(t) = H(t)/aG(t)$ .

In practice, however, it is more convenient to choose the origins for  $g(x)$  and  $h(x)$  at their respective peaks, rather than their means, since the peak separation may be obtained by direct measurement and is utilised in the subsequent analysis of line shapes.

In this case

$$F(t) = [H(t)/aG(t)] \exp[2\pi i(d-d_0)t/a], \quad (2)$$

where  $d$ ,  $d_0$  are the displacements of the peaks of the  $h(x)$ ,  $f(x)$  curves from the peak of the  $g(x)$  curve.

Hence if  $(d-d_0)$  is small, within the accuracy warranted in the line-breadth measurements,  $F(t) \approx H(t)/aG(t)$  and the same procedure may be used for both filings and wires.

The coefficients  $F(t)$  are complex and may be separated into real and imaginary components  $F_r(t)$  and  $F_i(t)$ , respectively, which are obtained by Stokes's method from the experimental data.

It follows from (1) that the true integral line breadth

$\beta$  is given by

$$\beta = \frac{aF_r(0)}{F_r(0) + 2 \sum_1^{\infty} F_r(l)} \quad (3)$$

The line breadths so obtained may then be used to investigate the cause of the broadening. Hall<sup>24</sup> has shown that if the particle size and distortion broadening can be regarded as additive, the total broadening  $\beta$  is related to the average particle size  $\epsilon$  and the integral breadth  $\sigma$  of the stress distribution function by

$$\frac{\beta \cos \theta}{\lambda} = \frac{1}{\epsilon} + \frac{2\sigma \sin \theta}{E \lambda}, \quad (4)$$

where  $E$  is an appropriate value of Young's modulus.

If the strain distribution in the sample is isotropic,  $\sigma/E$  is a constant independent of the order of reflection and hence a plot of  $(\beta \cos \theta)/\lambda$  against  $(\sin \theta)/\lambda$  should be a straight line with an intercept of  $1/\epsilon$ .

For elastically anisotropic metals, it is often found preferable to assume that the stress rather than the strain distribution is isotropic;<sup>5,12,25</sup> in this case,  $(\sin \theta)/E_{hkl}\lambda$  should be the function used in the plot, where  $E_{hkl}$  is the value of Young's modulus for a single crystal in the  $[hkl]$  direction. Experiments on polycrystalline metals strained in the elastic range, however, have usually not given results in agreement with either of these two limiting assumptions.<sup>1</sup> Subsidiary experiments on iron carried out during the course of the present work gave values for Young's modulus in the elastic range for several sets of  $(hkl)$  planes which agreed within  $\pm 5$  per cent with the corresponding averages,  $E_M$ , of values calculated from assumptions of either constant stress or constant strain in the aggregate. It may therefore be better to plot  $(\beta \cos \theta)/\lambda$  against  $(\sin \theta)/E_M\lambda$ .

### (b) Results

From (3) it will be seen that for line-breadth measurements, only the real Fourier coefficients  $F_r(l)$  need be determined. Applying this procedure to the experimental data for the filings and the wires, it was found that in some cases the values of  $F_r(l)$  decreased monotonically with increasing  $l$ , up to  $l \sim 12$ , but larger values of  $l$  produced maxima and minima in  $F_r(l)$ . This anomalous behaviour was due to insufficient accuracy in the measurement of the "tails" of the experimental line profiles. For determination of  $\beta$  in such cases, the curves were therefore extrapolated graphically beyond the value of  $l$  at which  $F_r(l)$  showed its first minimum.

As a check on the most appropriate value for  $E$  in (4), the values of  $\beta$  obtained for the filings and for a wire specimen strained to fracture, were used in plots of  $(\beta \cos \theta)/\lambda$  against (i)  $(\sin \theta)/\lambda$ , (ii)  $(\sin \theta)/E_{hkl}\lambda$  and (iii)  $(\sin \theta)/E_M\lambda$ . In each case, the line of closest fit was

obtained by the method of least squares and the sum of the squares of the deviations of the experimental values from the line was then computed. These values are recorded in Table I below.

TABLE I. Values of  $\Sigma \left[ \left( \frac{\beta \cos \theta}{\lambda} \right)_{\text{expt}} - \left( \frac{\beta \cos \theta}{\lambda} \right)_{\text{calc}} \right]^2$  in  $\text{mm}^{-2} \times 10^8$ .

Specimen	(i) $(\sin \theta)/\lambda$	(ii) $(\sin \theta)/E_{hkl}\lambda$	(iii) $(\sin \theta)/E_M\lambda$
Filings	8.28	12.66	5.83
Wire stressed to fracture (42.5 Kg/mm <sup>2</sup> )	1.85	2.32	1.45

These results indicate that, at least in the present work, better agreement is obtained by using the first or third relationship than the second one, and that the improvement in (iii) over (i) is perhaps just significant statistically.

The experimental results for the filings and for wires prestrained to various amounts in the plastic range are illustrated in Figs. 1 and 2. (Molybdenum radiation was used only for the filings and for a wire strained to fracture.) As pointed out previously, a linear relationship in such plots depends upon the assumption of simple addition of size and distortion broadening components. This in general will not be true; if one effect largely predominates, however, the departure from linearity will not be serious.

As is usual in these graphs, the scatter is appreciable, but the lines of best fit pass close to the origin in all cases. It therefore appears that for iron, lattice distortion is by far the predominant cause of line broadening and that there is no essential difference in the deformation

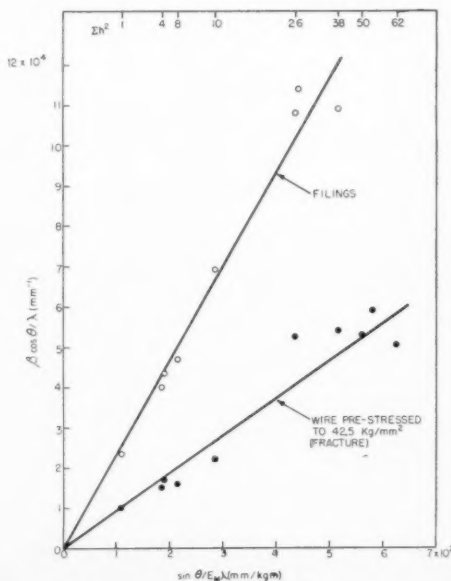


FIG. 1.  $(\beta \cos \theta)/\lambda$  versus  $(\sin \theta)/E_M\lambda$  for filings and for a wire pre-stressed to 42.5 Kg/mm<sup>2</sup> (fracture).

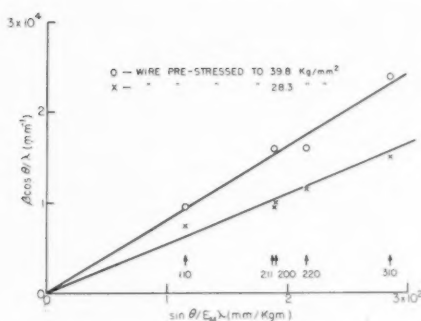


FIG. 2.  $(\beta \cos \theta)/\lambda$  versus  $(\sin \theta)/E_M \lambda$  for wires pre-stressed to 39.8 and 28.3 Kg/mm<sup>2</sup>.

process between filings and bulk metal. As pointed out by Wood and Rachinger, however,<sup>8</sup> the line breadths from the filings are larger than the corresponding values from the bulk metal strained to produce maximum broadening, the ratio here being about 2.5.

#### ANALYSIS OF LINE SHAPES

##### (a) Method

The Fourier coefficients derived for the line-breadth analysis were used to investigate in more detail the nature of the distortion process, by employing the Fourier methods referred to previously. The following analysis refers to the general case in which the experimental conditions are such that a mean displacement of the X-ray line, as well as a change in shape, may occur as a result of plastic strain.

Warren and Averbach<sup>11</sup> have shown that if any  $hkl$  reflection from a cubic crystal is transformed to the form  $00l$  with respect to appropriate orthogonal axes  $a_1 a_2 a_3$ , the true line profile from a polycrystalline sample exhibiting line broadening may be represented by the Fourier series

$$P(2\theta) = K \sum_{-\infty}^{\infty} C(n, l) \exp(-2\pi i n h_3), \quad (5)$$

where

$$h_3 = (2a_3 \sin \theta)/\lambda,$$

and  $K$  is a parameter which is sensibly constant for a given line and particular experimental conditions.

If both particle size and distortion broadening are operative

$$C(n, l) = N(n)J(n, l), \quad (6)$$

where  $N(n)$  depends only upon the size and shape of the crystallites in the sample and  $J(n, l)$  depends upon the lattice distortion.<sup>14,16</sup>

If a displacement of the peak of the line occurs, the Fourier coefficients  $C(n, l)$  are complex; i.e.,

$$C(n, l) \equiv A(n, l) + iB(n, l), \quad (7)$$

where

$$A(0, l) = 1, \quad B(0, l) = 0.$$

In these circumstances  $J(n, l)$  is complex, but  $N(n)$  is not so, since particle size broadening produces no peak displacement.

Hence

$$\begin{aligned} A(n, l) &= N(n)J_r(n, l), \\ B(n, l) &= N(n)J_i(n, l), \end{aligned} \quad (8)$$

where  $J_r(n, l)$  and  $J_i(n, l)$  are the real and imaginary components of  $J(n, l)$ .

Warren and Averbach's analysis<sup>11</sup> shows that  $J(n, l)$  is related to the strain in the crystal by

$$\begin{aligned} J_r(n, l) &= \langle \cos 2\pi l Z_n \rangle_{h_3}, \\ J_i(n, l) &= -\langle \sin 2\pi l Z_n \rangle_{h_3}, \end{aligned} \quad (9)$$

where  $Z_n/n$  is the strain in the  $[00l]$  direction in a column of unit cells of length  $na_3$ .

If the atomic displacements are small or may be approximated by a Gaussian distribution

$$J_r(n, l) \simeq \exp(-2\pi^2 l^2 \langle Z_n^2 \rangle_{h_3}), \quad (10)$$

and for small values of  $n$

$$J_i(n, l) \simeq -2\pi l \langle Z_n \rangle_{h_3}. \quad (11)$$

Hence the variation in root-mean-square displacements,  $a_3 \langle Z_n^2 \rangle_{h_3}^{1/2}$  and mean displacements  $a_3 \langle Z_n \rangle_{h_3}$  with the corresponding distances  $na_3$  in the crystal over which the averaging process is taken, may be found from a knowledge of the coefficients  $J_r(n, l)$  and  $J_i(n, l)$ .

The coefficients  $A(n, l)$  and  $B(n, l)$  may be obtained from the Fourier coefficients used in the line-breadths analysis as follows:

For comparison with (1), it is convenient to rewrite (5) in the form

$$P(2\theta) = K \sum_{-\infty}^{\infty} C(n, l) \exp[-2\pi i n (2\theta - 2\theta_0)/T], \quad (12)$$

where  $T \equiv \lambda/(a_3 \cos \theta_0)$  and  $\theta_0$  is the Bragg angle for peak intensity of the annealed material.

Stokes's method provides directly a set of coefficients  $V(t)$ , where

$$V(t) \equiv H(t)/aG(t), \quad (13)$$

i.e., from (2)

$$V(t) = F(t) \exp[-2\pi i (d - d_0)t/a]. \quad (14)$$

For compatibility with (12), however, a new set of coefficients  $\mathfrak{F}(t)$  are required given by

$$f(x - x_m) = \sum_{-\infty}^{\infty} \mathfrak{F}(t) \exp[-2\pi i t(x - x_0)/a], \quad (15)$$

where  $x_0, x_m$  are the linear positions for the peaks of the  $g(x)$  and  $f(x)$  profiles, respectively.

It can easily be shown that the real and imaginary components,  $\mathfrak{F}_r(t)$  and  $\mathfrak{F}_i(t)$  of  $\mathfrak{F}(t)$  are related to  $V(t)$  by



the expressions

$$\begin{aligned}\mathfrak{F}_r(t) &= V_r(t) \cos(2\pi td/a) - V_i(t) \sin(2\pi td/a), \\ \mathfrak{F}_i(t) &= V_i(t) \cos(2\pi td/a) + V_r(t) \sin(2\pi td/a).\end{aligned}\quad (16)$$

The coefficients  $A(n, l)$  and  $B(n, l)$  for any reflection may then be computed from these values of  $\mathfrak{F}(t)$  by equating

$$\begin{aligned}A(n) &= \mathfrak{F}_r(t)/\mathfrak{F}_r(0), \\ B(n) &= \mathfrak{F}_i(t)/\mathfrak{F}_r(0),\end{aligned}\quad (17)$$

provided that  $n$  is given the values

$$n = l \cdot T/T', \quad (18)$$

where  $T' = r/p$ ,  $r$  is the camera radius and  $p$  is the linear distance on the film corresponding to the range of integration,  $a$ , in Eq. (1). The conversion factor  $T/T'$  occurs due to the arbitrary choice of interval arising from the use of Beevers-Lipson strips to obtain the  $V(t)$  coefficients.

It then only remains to separate the particle size and distortion terms, which are given as a product by Eq. (8). It has been shown recently that the two effects may be distinguished by considering several orders of reflection from a given set of planes in the crystal.<sup>13,14,16</sup> In the present series of experiments, this method could not be used since only one order from each set of planes occurred at a high  $\theta$ -value. An approximate indication of the particle size, however, may be obtained by the following procedure.

For any 00 $l$  reflection and small values of  $n$

$$\begin{aligned}A(n) &= N(n)J_r(n) \\ &\approx (1 - n/N_3) \exp(-2\pi^2 l^2 n^2 \bar{e}^2),\end{aligned}$$

where  $N_3 a_3$  is the average particle size in the  $a_3$  direction and  $\bar{e}^2$  is the mean square strain,  $\langle Z_n^2/n^2 \rangle_{Av}$ , for a column of length  $na_3$ . If  $n$  is sufficiently small,  $\bar{e}^2$  is a constant independent of  $n$ .

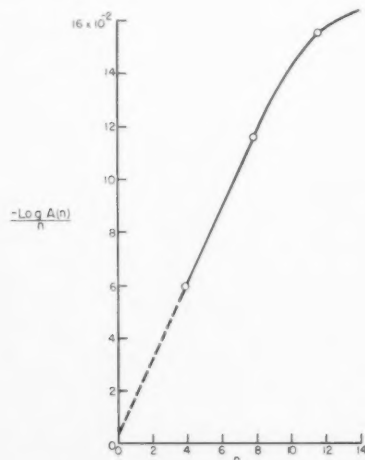


FIG. 3. Plot of  $-[\log A(n)]/n$  against  $n$  illustrating the intercept used to determine the minimum value of the average particle size in the [310] direction for filings.

Under these conditions

$$-\frac{\log A(n)}{n} \approx \frac{1}{N_3} + \left( \frac{1}{2N_3^2} + 2\pi^2 l^2 \bar{e}^2 \right) n. \quad (19)$$

Hence if  $-\log A(n)/n$  is plotted against  $n$ , for small values of  $n$ , a linear relationship should be obtained, from the intercept and slope of which,  $N_3$  and  $\bar{e}^2$  can be determined.

### (b) Results

The methods described above were applied to the experimental data for both the filings and the wires. The former represents the special case in which  $d$  and  $d_0$  in Eqs. (2), (14) and (16) are both zero. In this case, therefore, for each reflection

$$\begin{aligned}A(n) &= F_r(t)/F_r(0), \\ B(n) &= 0.\end{aligned}\quad (20)$$

#### (i) Filings

Figure 3 illustrates the results obtained from (19) for the 310 reflection. It will be observed that no truly linear range occurs for the experimental points, presumably due to the non uniformity of strains over

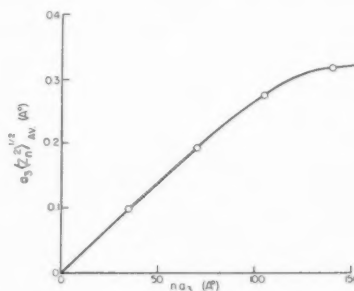


FIG. 4. Root-mean-square displacements in the [310] direction as a function of averaging distance in the crystal for filings.

distances less than 70 Å (see Fig. 4). If, however, the line joining the first two experimental points is extrapolated to  $n=0$ , the intercept so obtained represents a minimum value for the average particle size. In Fig. 3 this corresponds to a size of  $2.7 \times 10^{-5}$  cm in the [310] direction. The particle-size broadening is therefore small compared with the distortion broadening, in agreement with the conclusions from the line breadth measurements.

Minimum average particle sizes computed in this way from a number of the reflections are given in Table II. It must be emphasised, however, that the values can only be regarded as very approximate, since the intercepts were small and subject to considerable possible error.

Following Warren and Averbach, the root-mean-square displacements  $a_3 \langle Z_n^2/n^2 \rangle_{Av}^{1/2}$  (calculated directly from the values of  $A(n, l)$ , since  $N_3$  was comparatively large) have been plotted against corresponding distances  $na_3$

TABLE II. Minimum average particle sizes  $(\epsilon)^{\frac{1}{2}}$ , and root-mean-square strains  $(\bar{\epsilon}^2)^{\frac{1}{2}}$  for filings.

$hkl$	Cell length $a_3$	Radiation	$\epsilon \times 10^3$	Linear range for $(Z_n^2)_{Av}^{\frac{1}{2}}$	$(\bar{\epsilon}^2)^{\frac{1}{2}} \times 10^4$	$\frac{\beta \cot \theta}{4} \times 10^4$	$(\bar{\epsilon}^2)^{\frac{1}{2}} E_M$
	Å		cm	Å			Kg/mm <sup>2</sup>
310	9.05	Co	2.7	75	27.2	27.3	53
220	4.05	Co	0.9	60	24.0	25.5	55
220	4.05	Fe	0.8	70	22.5	21.0	52
211	7.01	Fe	1.4	90	22.2	25.0	51
211	7.01	Cr	1.7	100	16.2	18.4	39
211	7.01	Co	3.6?	80	24.8	28.2	57
200	2.86	Cr	3.2	140	24.8	28.8	46
110	4.05	Cr	0.9	60	24.2	21.0	55

in the crystal and typical results are illustrated in Fig. 4. As usual, the plots are initially approximately linear, but droop for increasing distances in the crystal over which the displacements are averaged. The initial slopes represent true root-mean-square strains and may be compared with the average values  $(\beta \cot \theta)/4$ ,<sup>7</sup> obtained from the line-breadth measurements.

Table II above summarises the results for the filings. The last column in the table lists the product of the root-mean-square strain and the average value,  $E_M$ , of Young's modulus for each  $[hkl]$  direction. If the stress is isotropic this product should be independent of  $hkl$ .

It will be seen that the results for the same direction in the crystal obtained from the use of different radiations are reasonably self-consistent, and that, in agreement with other work of this type on cold-worked metals, the strains are uniform for any particular direction over distances only  $\sim$  several cell lengths. The results also indicate that neither the stress nor the strain is truly isotropic, but that on the whole there is a closer approach to constancy of stress than constancy of strain, as was also found in the line-breadth measurements.

#### (ii) Wires

To determine the importance of the particle size effect in the wires, the relation given by (19) was applied to the experimental data for a wire stressed to fracture. The results indicated a minimum average particle size (in the  $[220]$  direction) of  $4.6 \times 10^{-5}$  cm. In consequence, within the accuracy warranted and for small values of  $n$

$$A(n, l) \simeq \exp(-2\pi^2 l^2 \langle Z_n^2 \rangle_{Av}),$$

$$B(n, l) \simeq -2\pi l \langle Z_n \rangle_{Av}.$$

The following procedure was therefore adopted.

(a) The displacement,  $d$ , for the highest-angle reflection for each radiation was measured and converted into the corresponding mean residual lattice strain in the usual way.

(b) The coefficients  $A(n, l)$  and  $B(n, l)$  for these reflections were then calculated in the way described previously. From the  $A(n, l)$  values, the root-mean-square displacements,  $a_3 \langle Z_n^2 \rangle_{Av}^{\frac{1}{2}}$ , and the true root-mean-square strains  $(\bar{\epsilon}^2)^{\frac{1}{2}}$ , were obtained. The  $B(n, l)$  coefficients

were used to obtain plots of the mean displacements,  $a_3 \langle Z_n \rangle_{Av}$ , against  $na_3$  for small values of  $n$ . The initial slopes of these curves represent the true mean strains  $\bar{\epsilon}$  for the respective directions and should thus agree with the values obtained directly from the line shifts. The measure of agreement between the two sets of values gives an indication of the reliability of the experimental data used in the analysis.

(c) For reflections other than the highest-angle line for each radiation, the line displacements were very small and could not be measured accurately. In these cases therefore,  $d$  was assumed to be negligible and the values of  $A(n, l)$  were obtained directly from the corresponding values of  $F_r(l)$  as for the filings.

Plots for the 310 reflection (cobalt radiation) from a wire strained to fracture are illustrated in Figs. 5 and 6. These two curves are qualitatively representative of most of the curves from other reflections and other wires analysed in this way. Comparing Figs. 4 and 5, it will be observed that the strains are smaller and sensibly constant over greater distances in the bulk metal than in the filings.

The plots for the mean displacements all rise to a maximum and then fall away with increasing distances  $na_3$ . From consideration of the interpretation of graphs of this type, it seems probable that this is a real effect, but in view of the fact that the curves are based on the imaginary coefficients  $\mathfrak{F}_i(l)$ , which were relatively small and subject to considerable possible error, it is at present uncertain just how much reliance may be placed

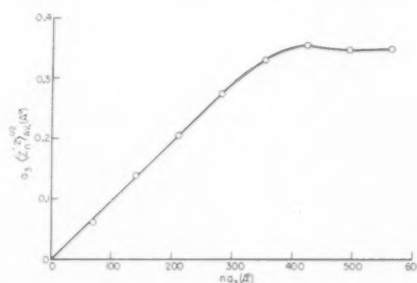


FIG. 5. Root-mean-square displacements in the  $[310]$  direction as a function of averaging distance in the crystal for wire pre-stressed to 42.5 Kg/mm<sup>2</sup> (fracture).

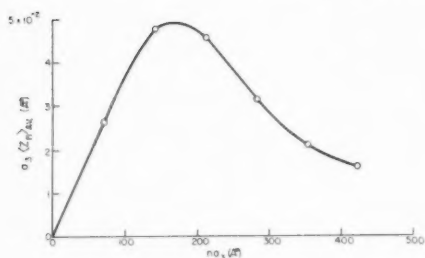


FIG. 6. Mean displacements in the  $[310]$  direction as a function of averaging distance in the crystal for wire pre-stressed to 42.5 Kg/mm<sup>2</sup> (fracture).

upon the graphs of the type shown in Fig. 6, particularly for large values of  $na_3$ .

The residual lattice strains found by direct measurement are given in Table III and the data obtained from the Fourier analysis for wires pre-stressed to given amounts are summarised in Table IV. Owing to the small degree of broadening for low plastic strains, it was found practicable to apply the Fourier analysis only to specimens which had been strained to amounts in excess of  $\sim 8$  per cent. For convenience of comparison, the results for the filings are also listed in Table IV.

#### DISCUSSION

It is interesting to examine the results described above in the light of the differences in particle sizes and strains exhibited in different crystallographic directions in the deformed metal.

Firstly, for the filings, Table II shows that the particles tend more closely to equi-axed crystallites than to long rods or lamellae. It is significant, however, that of the directions investigated, the two smallest sizes are in the  $[110]$  and  $[211]$  directions, i.e., normal to two of the slip planes operative in iron at room temperature. Conversely the maximum dimension is in the direction for maximum shear modulus. Now the effective particle size in any direction represents the limiting distance before curvature of the lattice (progressive or local) destroys the phase conditions required for coherent scattering of the X-ray beam. From general considerations of the curvature and high dislocation density

TABLE III. Residual lattice strains in wire specimens for 310, 220 and 211 reflections, taken with Co, Fe and Cr radiations, respectively.

Previously applied stress Kg/mm <sup>2</sup>	Plastic extension per cent	Residual lattice strains $\times 10^4$		
		310	220	211
42.5 (fracture)	32.3	3.5	0.0	0.8
39.8	21.4	2.1	-0.3	0.9
28.3	8.4	1.3	-0.6	0.9
21.2	0.9	0.1	-0.1	0.7
17.5	0.6	0.2	-0.1	0.4
14.0	Strained just above yield point	-0.1	0.2	-0.1

associated with the slip bands, it seems reasonable to expect that, on the average, this limiting distance would be less in directions normal to the slip planes than in the other directions, as has been found.

Secondly, in connection with current theories on the structure of a cold-worked metal and the mechanism of polygonisation and recovery,<sup>2,26-28</sup> considerable interest is attached to the *distribution* of strains in each  $[hkl]$  direction. The results in Tables II and IV are not informative in this respect; it is possible however to gain some indication on the distribution by the following approximate analysis.

Following Warren and Averbach, regard the deformed crystal (of linear dimension  $\epsilon$  in the  $a_3$  direction) as made up of a number of columns, each containing on the average  $N_3$  unit cells. Consider a representative column (Fig. 7) in which the local strains in the individual cells are  $e_0, \dots, e_z, \dots, e_{N_3}$ .

TABLE IV. Summary of results for wires and filings for 310, 220 and 211 reflections, taken with Co, Fe and Cr radiations, respectively.

Previously applied stress Kg/mm <sup>2</sup>	$hkl$	Linear range for $\langle Z_n^2 \rangle_{Av}^{\frac{1}{2}}$ Å	$\langle \epsilon^2 \rangle^{\frac{1}{2}} \times 10^4$	Linear range for $\langle Z_n \rangle_{Av}$ Å	$\epsilon \times 10^4$
Filings	310	75	27.2	—	—
	220	70	22.5	—	—
	211	100	16.2	—	—
42.5 (fracture)	310	280	9.2	140	3.7
	220	140	11.0	—	—
	211	130	10.5	85	0.2
39.8	310	220	10.1	70	1.8
	220	180	5.6	75	-0.3
	211	210	7.1	190	0.9
28.3	310	470	6.3	210	1.4
	220	160	5.6	75	-1.4
	211	500	4.6	250	0.8

If, to a first approximation, the strain is regarded as a continuous variable along the column, it may be shown that for  $n \ll N_3$  the root-mean-square relative displacement for groups of  $n$  cells is given by

$$\langle Z_n^2 \rangle_{Av}^{\frac{1}{2}} \simeq n \langle \epsilon^2 \rangle^{\frac{1}{2}} [1 - n(\alpha/4N_3 - 1/2N_3)], \quad (21)$$

where  $\alpha = (e_0^2 + e_{N_3}^2)/\bar{e}^2$  and  $\bar{e}^2$  is the mean-square strain for all the cells.

The magnitude of the parameter  $\alpha$  provides some indication of the variation in strain along the column. Thus  $\alpha$  ranges from a very small value to a value  $\rightarrow N_3$ , depending upon whether the strains at, or near to the boundaries of the crystal are small or large, respectively, relative to the strains in the interior.

The quantity  $(\alpha/4N_3 - 1/2N_3)$  determines the drooping of the curves in plots such as Fig. 4 and hence  $\alpha$  may be calculated for each  $[hkl]$  direction from the experimental data. Furthermore, if  $\bar{e}^2$  represents the mean

square value of the boundary strains, it follows that

$$(\bar{\epsilon}^2/\bar{\epsilon}_l^2)^{\frac{1}{2}} = (2/\alpha)^{\frac{1}{2}}. \quad (22)$$

Values of  $\alpha$  and  $(\bar{\epsilon}^2/\bar{\epsilon}_l^2)^{\frac{1}{2}}$  obtained from the data for filings are given in Table V, together with the corresponding percentage ratio of the linear range for  $\langle Z_n^2 \rangle_{Av}^{\frac{1}{2}}$  to the particle size  $\epsilon$  for each direction.

Whilst no undue significance may be attached to the magnitude of these results, they do indicate two interesting features. Firstly, for each direction, the local strains on the average increase in magnitude as the boundaries of the crystallites are approached. Secondly, there is a general tendency for the strains to be more uniform in directions normal to the glide planes than in the other directions. In terms of dislocations, these

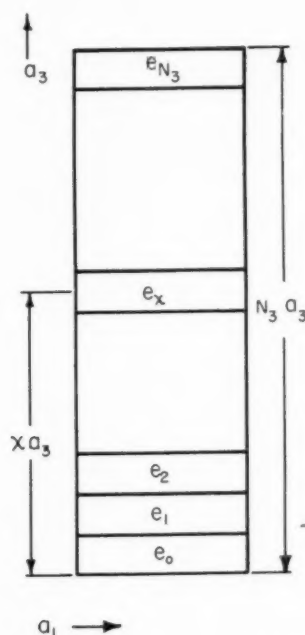


FIG. 7. Schematic diagram of a column containing  $N_3$  unit cells, each of length  $a_3$  and having individual strains  $e_0, e_1, \dots, e_{N_3}$ .

observations thus provide additional evidence for the accepted view that the density of excess dislocations in the cold worked state is greater at the boundaries than in the interior of the crystallites. They also suggest that the distribution of the dislocations is statistically more uniform in directions normal to the slip planes than in the other directions examined.

Gay, Hirsch and Kelly<sup>28</sup> have recently suggested that the particles may be identified with relatively undistorted regions between the slip bands. This corresponds to a single step process in which plastic flow creates *ab initio* a heavy density of excess dislocations in and around the slip-band regions. An alternative mechanism is for the dislocations to be first generated at random and then to migrate preferentially to form the crystallite

TABLE V. Variation of strains along the columns for different directions for filings.

hkl	$\alpha$	$(\bar{\epsilon}^2/\bar{\epsilon}_l^2)^{\frac{1}{2}}$	$\langle (Z_n^2)_{Av}^{\frac{1}{2}} \rangle_{\text{linear}}$
			$\epsilon$ per cent
310	14	0.4	3
220	5	0.7	9
211	9	0.5	6
200	12	0.4	4

boundaries. The latter explanation is generally accepted as the mechanism of recovery by polygonisation and has been used by Williamson and Hall<sup>2</sup> to account for the pronounced flattening off of their curves of  $\langle Z_n^2 \rangle_{Av}^{\frac{1}{2}}$  against  $n$ , for the higher values of  $n$ , for high-purity aluminium and for wolfram recovered at 1150°C. In the present case however, other evidence<sup>7,20</sup> suggests that self-recovery in iron is not considerable at room temperature. Furthermore, the results in Table V indicate that appreciable strains exist in the interior of the crystallites. It is therefore believed that in the present experiments the predominant mechanism is the single-step process.

#### SUMMARY

The conclusions to be drawn from the work reported here may be summarised as follows:

(a) Measurements based upon the breadths and shapes of the X-ray reflections both indicate that lattice distortion is predominantly responsible for the broadening in both the filings and the bulk metal.

(b) On the whole, the stress is more constant than the strain for different directions in the crystal.

(c) As a result of deformation, the minimum average particle size is  $\sim 10^{-5}$  cm for the filings and  $\sim 5 \times 10^{-5}$  cm for a wire strained to produce maximum broadening. These values are rather lower than those obtained for iron by Gay and Kelly<sup>20,28</sup> using a microbeam technique, but since they represent a *minimum* value to be placed on the average size this is to be expected.

(d) In the filings, smaller particle sizes are obtained for directions normal to the slip planes than in other directions. It is suggested that this arises from the high concentration of dislocations in the slip bands.

(e) The distances in the crystal over which the local strains in any direction are constant, decrease with increasing amounts of cold work down to a value, which for the filings, cannot exceed a few cell lengths. In the latter case, an analysis of the strain distribution shows that the strains are greater at the boundaries than in the interior of the crystallites, and that there is a tendency for the strains to be more uniform in directions normal to the slip planes than in the other directions.

#### ACKNOWLEDGMENTS

The authors desire to express their thanks to a number of their colleagues for helpful discussions during the



course of this work. In particular they are indebted to Mr. J. A. Macdonald for considerable assistance and advice on the mathematical aspects of the analysis and to Mrs. J. Brett and Mrs. V. Brooks for carrying out much of the tedious microphotometry and mathematical computing work. Acknowledgment is also made to the Chief Scientist, Department of Supply, Australia, for permission to publish this paper.

## REFERENCES

1. G. B. Greenough, "Progress in Metal Physics," vol. 3 (Pergamon Press, London, 1952), p. 176.
2. G. K. Williamson and W. H. Hall, *Acta Met.* **1**, 22 (1953).
3. W. A. Wood, *Proc. Roy. Soc. A* **172**, 231 (1939).
4. G. W. Brindley, *Proc. Phys. Soc.* **52**, 117 (1940).
5. A. R. Stokes, K. J. Pascoe, and H. Lipson, *Nature (Lond.)* **151**, 137 (1943).
6. C. S. Smith and E. E. Stickley, *Phys. Rev.* **64**, 191 (1943).
7. H. D. Megaw and A. R. Stokes, *J. Inst. Metals* **71**, 279 (1945).
8. W. A. Wood and W. A. Rachinger, *J. Inst. Metals* **75**, 571 (1949).
9. J. H. Auld and R. I. Garrod, *Nature (Lond.)* **169**, 579 (1952).
10. R. I. Garrod, J. F. Brett, and J. A. Macdonald, *Austr. J. Phys.* **7**, 77 (1954).
11. B. E. Warren and B. L. Averbach, *J. Appl. Phys.* **21**, 595 (1950).
12. B. E. Warren and B. L. Averbach, "Imperfections in Nearly Perfect Crystals," edited by W. Shockley *et al* (John Wiley, New York, 1952), p. 152.
13. B. E. Warren and B. L. Averbach, *J. Appl. Phys.* **23**, 497 (1952).
14. J. N. Eastabrook and A. J. C. Wilson, *Proc. Phys. Soc.* **B65**, 67 (1952).
15. R. A. Smith, *J. Iron Steel Inst.* **173**, 147 (1953).
16. M. McKeenhan and B. E. Warren, *J. Appl. Phys.* **24**, 52 (1953).
17. B. E. Warren and B. L. Averbach, *J. Appl. Phys.* **23**, 1059 (1952).
18. B. E. Warren and E. P. Warekois, *J. Appl. Phys.* **24**, 951 (1953).
19. W. A. Wood and W. A. Rachinger, *Nature (Lond.)* **161**, 93 (1948).
20. P. Gay and A. Kelly, *Acta Cryst.* **6**, 165 (1953).
21. G. B. Greenough, *J. Iron Steel Inst.* **171**, 235 (1951).
22. W. A. Rachinger, *J. Sci. Instrum.* **25**, 254 (1948).
23. A. R. Stokes, *Proc. Phys. Soc.* **61**, 382 (1948).
24. W. H. Hall, *Proc. Phys. Soc.* **A62**, 741 (1949).
25. A. R. Stokes and A. J. C. Wilson, *Proc. Phys. Soc.* **56**, 174 (1944).
26. P. B. Hirsch, *Acta Cryst.* **5**, 172 (1952).
27. A. Guinier, "Imperfections in Nearly Perfect Crystals," edited by W. Shockley *et al* (John Wiley, New York, 1952), p. 402.
28. P. Gay, P. B. Hirsch, and A. Kelly, *Acta Cryst.* **7**, 41 (1954).

Energie Mutuelle de Deux Dislocations\*

On connaît déjà l'énergie mutuelle de deux dislocations dans un certain nombre de cas particuliers.<sup>1</sup> Nous avons établi une formule générale pour cette énergie dans le cas de deux boucles de forme et de vecteur de Burgers quelconques; elle s'exprime sous forme d'intégrales effectuées le long des deux boucles. L'expression obtenue est assez simple et permet de préciser l'analogie magnétique indiquée par Peach et Koehler.<sup>2</sup>

Le corps élastique contenant les dislocations appartient à un milieu homogène et isotrope et sa surface extérieure  $S$  est rejetée à l'infini. Les deux boucles sont situées tout entières à distance finie. L'indice 1 est affecté à l'une des boucles, l'indice 2 à l'autre;  $\bar{b}$ ,  $\bar{n}$ ,  $\bar{T}$ , désignent respectivement pour chaque dislocation le vecteur de Burgers, la normale à une surface  $A$  s'appuyant sur la ligne  $\mathcal{L}$  de la dislocation et le tenseur des efforts créés dans le milieu par celle-ci. On sait que l'énergie mutuelle des deux boucles s'écrit:<sup>3</sup>

$$\mathcal{E} = \int \int_{A_1} \bar{b}_1 \cdot \bar{T}_2 \cdot \bar{n}_1 dA_1 + \int \int_S \bar{u}_1 \cdot \bar{T}_2 \cdot \bar{n}_1 dS.$$

Le terme correspondant à la surface  $S$  s'annule puisque les tensions et les déplacements créés par une boucle en un point  $M$  décroissent comme  $1/r^2$  quand la distance moyenne,  $r$ , de  $M$  à la boucle augmente indéfiniment.

Le vecteur  $\bar{b}_1 \cdot \bar{T}_2$  étant à divergence nulle, l'intégrale effectuée sur  $A_1$  peut être remplacée par une intégrale de ligne. D'autre part le tenseur pouvant lui-même s'exprimer à l'aide d'intégrales le long de  $\mathcal{L}_2$ ,<sup>2</sup>  $\mathcal{E}$  peut donc s'exprimer à l'aide d'une intégrale double le long de  $\mathcal{L}_1$  et  $\mathcal{L}_2$ .

Le calcul se développe symétriquement à partir des formules de Volterra<sup>4</sup> qui donnent le déplacement  $U$ ,  $V$ ,  $W$ , créé par une dislocation dont la surface de coupure est  $A$  et le vecteur de Burgers  $\bar{b}$ . Celles-ci sont de la forme:

$$U = \int \int_A \bar{b} \cdot \bar{i} \cdot \bar{n} dA$$

l'intégrale étant étendue à la coupure  $A$ . Le tenseur  $\bar{i}$  est celui des efforts relatifs au déplacement:

$$u = -\frac{1}{r} + \frac{\alpha}{2} \frac{\partial^2 r}{\partial x_1^2} \quad v = -\frac{\alpha}{2} \frac{\partial^2 r}{\partial x_1 \partial x_2} \quad w = -\frac{\alpha}{2} \frac{\partial^2 r}{\partial x_1 \partial x_3} \quad \alpha = -\frac{\lambda + \mu}{\lambda + 2\mu}$$

où  $r = [(x_1 - \xi_1)^2 + (x_2 - \xi_2)^2 + (x_3 - \xi_3)^2]^{1/2}$ ,  $\xi_1, \xi_2, \xi_3$ , étant les coordonnées d'un point de  $A$  et  $x_1, x_2, x_3$ , celles d'un point quelconque du milieu. On passe de  $U$  à  $V$  et  $W$  en effectuant une permutation circulaire sur  $u, v, w$ ;  $x_1, x_2, x_3$ ;  $\xi_1, \xi_2, \xi_3$ ; (formules de Somigliana, voir Love p. 245). Connaissant  $U, V, W$ , on en déduit les coordonnées du tenseur des efforts  $\bar{T}$ , relatif à une disloca-

tion, sous forme d'intégrales étendues à  $A$ .  $\mathcal{E}$  s'exprime alors sous la forme:

$$\mathcal{E} = \int \int_{A_1} \int \int_{A_2} b_{i\alpha} b_{k\alpha} \sigma_{ijkl} dA_1 dA_2$$

les indices  $i$  et  $j$  étant relatifs à  $A_1$  et  $k$  et  $l$  à  $A_2$ . Le terme  $\sigma_{ijkl}$  est naturellement symétrique par rapport aux coordonnées des points situés sur  $A_1$  et  $A_2$ . Les intégrales doubles devant se ramener à des intégrales de ligne d'après la remarque préliminaire on arrive assez facilement à exprimer le terme  $\sigma_{ijkl}$  sous la forme:

$$\sigma_{ijkl} = \frac{2\mu\alpha}{4\pi} \left( \frac{\partial^2}{\partial x_k \partial x_l} - \Delta \delta_{kl} \right) \left( \frac{\partial^2}{\partial x_i \partial x_j} - \Delta \cdot \delta_{ij} \right) r + \frac{\mu}{4\pi} \bar{n}_1 \cdot \text{rot}_x \left\{ \bar{b}_1 \left( \bar{n}_2 \cdot \text{rot}_\xi \frac{\bar{b}_2}{r} \right) \right\} - \frac{2\mu}{4\pi} \bar{n}_1 \cdot \text{rot}_x \left\{ \bar{b}_2 \left( \bar{n}_2 \cdot \text{rot}_\xi \frac{\bar{b}_1}{r} \right) \right\}.$$

Il est alors utile pour effectuer le calcul de s'appuyer sur le lemme suivant:

Quand un tenseur  $\bar{T}$  a pour coordonnées:

$$t_{ij} = \frac{\partial^2 u}{\partial x_i \partial x_j} - \Delta \delta_{ij} u$$

$u$  étant une fonction de  $x_1, x_2, x_3$ , et  $\delta$  égal à 1 si  $i=j$  et 0 si  $i \neq j$ , on a la relation:

$$\int \int_A \bar{b} \cdot \bar{T} \cdot \bar{n} dA = - \int_{\mathcal{L}} (\text{grad } u) \cdot (\bar{b} \times d\mathbf{M})$$

$d\mathbf{M}$  étant un déplacement élémentaire sur la ligne  $\mathcal{L}$  qui limite  $A$ .

En appliquant deux fois la formule de Stokes, ainsi que ce lemme, on arrive à la formule:

$$-\mathcal{E} = \frac{2\mu}{4\pi} \int \int_{\mathcal{L}_1 \mathcal{L}_2} (\bar{b}_1 \times \bar{b}_2) \frac{(d\mathbf{M}_1 \times d\mathbf{M}_2)}{r} - \frac{\mu}{4\pi} \int \int_{\mathcal{L}_1 \mathcal{L}_2} \frac{(\bar{b}_1 \cdot d\mathbf{M}_1)(\bar{b}_2 \cdot d\mathbf{M}_2)}{r} + \frac{2\mu\alpha}{4\pi} \int \int_{\mathcal{L}_1 \mathcal{L}_2} (\bar{b}_1 \times d\mathbf{M}_1) \cdot \overline{\text{grad } r} \cdot (\bar{b}_2 \times d\mathbf{M}_2) \left( \overline{\text{grad } r} \text{ désigne le tenseur } \frac{\partial^2 r}{\partial x_i \partial x_j} \right)$$

On remarque que les deux derniers termes font intervenir respectivement les composantes vis et coins de chaque dislocation. Nous avons vérifié que l'on obtenait avec ces formules les résultats classiques pour la force qui s'exerce entre deux dislocations vis ou coins.

Cette formule s'étend évidemment au cas d'un ensemble de plus de deux dislocations. Nous nous proposons de l'appliquer au calcul de la limite élastique d'un monocristal contenant des précipités très plats cohérents avec la matrice.

J. BLIN

Division des Matériaux, ONERA  
25, Avenue de la Division Leclerc  
Chatillon-s/s-Bagneux-(Seine)  
Paris, France

#### Bibliographie

1. F. R. N. Nabarro, *Advances in Physics* **1**, 306 (1952).
2. M. Peach et J. S. Koehler, *Phys. Rev.* **80**, 436 (1950).
3. B. A. Bilby, *Proc. Phys. Soc.* **363**, 191 (1950).
4. V. Volterra, *Ann. Ecole Norm. Sup.* (3) **24**, 425 (1907).
5. A. E. H. Love, *The Mathematical Theory of Elasticity*, Cambridge University Press (1927).

\* Received June 9, 1954.

### Hydrogen and the Yield Point in Steel\*

In a recent letter, Rogers<sup>1</sup> pointed out that he had produced a yield point in previously deformed steel merely by the addition of hydrogen.

We have observed that cathodic charging with hydrogen can also *eliminate* the yield point. With fifteen different annealed steels, ranging from a fairly pure iron to a 0.62% steel, the upper yield point was removed and there was progressive depression of the lower yield point and reduction of the yield elongation as the duration of electrolysis increased. In every case, the yield point was completely removed provided the time and current density were sufficient. Specimens of 1 in. gauge length,  $\frac{1}{8}$ -in. diameter, annealed after machining, charged in 4%  $H_2SO_4$  with yellow phosphorus in  $CS_2$  as poisoner and then tested in air,

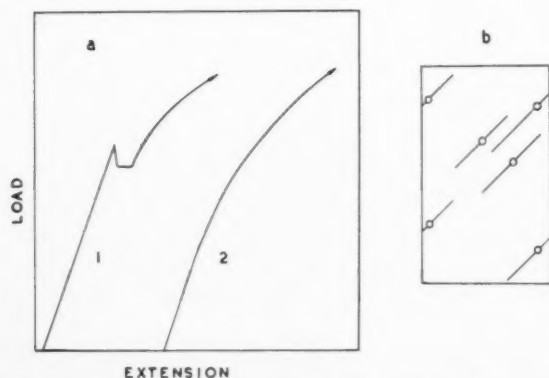


FIG. 1. (a) Load-extension curves for a mild steel (1) as annealed; (2) charged with hydrogen. (b) The spread of plastic zones from high stress regions.

required about 8 hours at 3 amps/in<sup>2</sup> for complete yield point elimination.

Figure 1a shows typical load-extension curves at room temperature.

We think that this is probably an example of yield point suppression by inhomogeneous stresses, the inhomogeneity arising from the accumulation of hydrogen under high pressure in internal cavities. Probably at least some such cavities occur even in a rolled steel; possibly they are associated with inclusions; surface blistering and diffuse X-ray patterns after hydrogen-charging have been advanced as evidence of their existence.

On this view, yielding will be initiated in the regions of high stress (during testing) and plastic zones will spread across the specimen (Fig. 1b). If the whole specimen yields in this manner before the plastic zones (Lüders bands) begin to extend sideways down the specimen, the yield point will be completely eliminated.

To make sure that stress concentration at surface irregularities produced by attack during electrolysis (which appeared to be slight) was not the important factor, the surface was carefully turned off some specimens, but this did not restore the yield point. Restoration did occur when the hydrogen was removed by annealing at 200–600°C *in vacuo*. Calculation of the hydrogen distribution showed that there did not appear to be any question of stresses due to non-uniform distribution of hydrogen in solution.

This yield point elimination took place more readily with coarse-, than with fine-grained specimens, which is in keeping with other cases of elimination by inhomogeneous stresses.

A. CRACKNELL†  
N. J. PETCH

Metallurgy Laboratory  
University of Leeds  
Leeds, England

#### Reference

1. H. C. Rogers, *Acta Met.* **2**, 167 (1954).

\* Received August 14, 1954.

† Present address: Imperial Chemical Industries, Ltd., Billingham, England.

### A Tentative Explanation of the Accelerated Growth of Tin Whiskers\*

Very interesting results were recently reported on the accelerated growth of tin whiskers under pressure by Fisher, Darken and Carroll.<sup>1</sup> According to them, the growth rate is accelerated up to 10,000 times the spontaneous rate by application of pressure up to 7500 psi. They also showed that a straightforward thermodynamical treatment fails to explain this accelerated growth. This means some additional agents are required. The present writer would like to present

VOL.  
3  
1955

a tentative explanation, assuming two additional conditions.

Fisher *et al.*<sup>1</sup> clamped the tin-plated specimen to apply the pressure on it. Considerable tin was extruded at the free side surface. They noticed, however, that whiskers seem to grow not from this extruded tin, but from the vicinity thereof.

At the region where the tin extrusion is hindered, the applied pressure,  $P$ , may be maintained without relaxation up to the very vicinity of the free surface, as if it were a hydrostatic pressure in a closed vessel. The reason why this kind of hindrance of extrusion occurs is not known, but one of the necessary conditions for it may be the thinness of plated tin between the clamps. If a Frank's spiral of whisker-producing dislocation<sup>2</sup> is situated in such a region where the tin extrusion is hindered, a whisker will grow there at an accelerated rate, which depends on the applied pressure. This whisker growth will relieve the applied stress. The basic concept of the present writer is that the stress is relieved by means of whisker growth at the region where the stress is not relieved by means of tin extrusion.

The concentration of atomic vacancies in a region of tin crystal, where the applied pressure,  $P$ , is maintained, is decreased from its normal value by a factor of  $\exp(-Pa^3/kT)$ , where  $a$  is the atomic spacing,  $k$  is Boltzmann's constant, and  $T$  is absolute temperature.<sup>3</sup> The vacancy concentration at the Frank's dislocation spiral is somewhat higher than the normal value. Then the concentration gradient of vacancies is

$$(Z/Ra^3)\{1 - \exp(-Pa^3/kT)\} \approx ZP/RkT, \quad (1)$$

where  $Z$  is normal concentration of vacancies, and  $R$  is the distance between the dislocation spiral and the region where pressure,  $P$ , is maintained. Here the vacancy concentration at the dislocation spiral was assumed to have normal value.

Now the distance,  $R$ , is assumed to be very small, say from 10 to 100 Å, because the pressure,  $P$ , is considered to be maintained up to the very vicinity of free surface. This is the first assumption.

The concentration gradient as expressed in (1) must be kept constant to secure the constant diffusion current which enables whiskers to grow at a constant rate. The concentration gradient is assumed to be kept constant by means of absorption of vacancies by edge dislocations which are situated near the end of concentration gradient. This is the second assumption.

Now the flux of vacancies is  $DP/RkT$ , if the approximate value of (1) is used. Here  $D$  is the self-diffusion coefficient of tin at the temperature  $T$ . Thus the rate of whisker growth  $G$  is

$$G = DP a^3 / RkT \quad \text{cm/sec} \quad (2)$$

Equation (2) gives a linear relation between  $G$  and  $P$ , which agrees with experimental results. Taking  $D = 10^{-12}$  cm<sup>2</sup>/sec,  $T = 300^\circ\text{K}$ ,  $a^3 = 30 \text{ Å}^3$ , and  $P = 5,000$  psi, we

obtain

$$G = 260 \text{ Å/sec} \quad (3)$$

for  $R = 10 \text{ Å}$ , and

$$G = 26 \text{ Å/sec} \quad (4)$$

for  $R = 100 \text{ Å}$ . The value (3) is ten times smaller, and the value (4) is a hundred times smaller than the experimental value, which is about 2600 Å/sec.

The calculated values of  $G$  may be increased by a factor of ten or more, if we consider two more conditions. (1) The concentration of vacancies is higher than the normal value near the Frank's dislocation spiral. This makes the concentration gradient increase. (2) Although the tin extrusion is hindered around the whisker root, it may be possible that a slow creep occurs at the vicinity of the root. If this is the case, vacancy concentration will be increased there.<sup>4</sup> This also makes the diffusion current increase.

Fisher *et al.* have shown that the whiskers may exhibit three stages of growth: (1) an induction period, (2) a period of constant growth rate, and (3) an abrupt transition to a much slower growth rate. The present writer's explanation is consistent with these three stages. Induction period is explained in the same way as in Frank's theory.<sup>2</sup> The second stage is explained as mentioned above. After some period of second-stage growth, the stress will be relieved. This will result in a deceleration of growth rate. Thus the third stage is accounted for.

R. R. HASIGUTI

Department of Metallurgy  
Faculty of Engineering  
University of Tokyo  
Tokyo, Japan

#### References

1. R. M. Fisher, L. S. Darken, and K. G. Carroll, *Acta Met.* **2**, 368 (1954).
2. F. C. Frank, *Phil. Mag.* **44**, 854 (1953).
3. F. R. N. Nabarro, *Rep. Conf. Strength of Solids*, Phys. Soc. 1948, p. 75.
4. F. S. Buffington and M. Cohen, *J. Metals*, **4**, 859 (1952).

\* Received August 19, 1954.

#### Impurity Particles and the Lateral Growth of Cadmium Iodide\*

The engulfment of impurity particles during the lateral growth of cadmium iodide plates has recently been postulated to account for the development of screw dislocations in crystals, leading to growth in thickness.<sup>1</sup> More detailed study of the growth of cadmium iodide from aqueous solution seems to indicate that the presence of impurities must also be taken into account in considering the process of lateral growth itself, through the advance of the (1010) faces.

We have observed the growth of cadmium iodide plates of uniform thickness (evidenced by the uniformity of the interference colors) formed on depositing



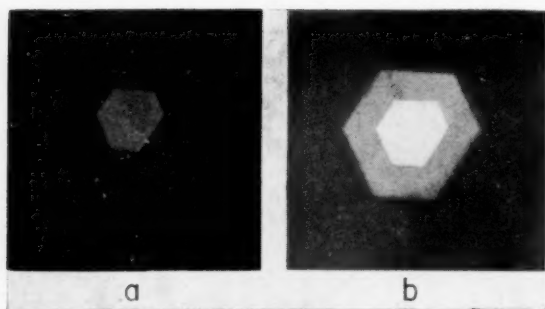


FIG. 1. Border formation in growth of cadmium iodide from aqueous solution. Magnification 340X.

a solution saturated with reagent grade material at 35.0°C in a cell<sup>2</sup> thermostated at this temperature. On lowering the temperature 5–10 degrees (giving a supersaturation ratio  $\alpha = 1.02$ –1.04), many of the plates, originally in the form of irregular hexagons, were found to grow through the addition of a layer around the prism faces of the original crystal, with an interference color different from that of the original formation (Figs. 1a, b). The step thus formed in the (0001) plane is filled in only after the border has grown to some extent, sometimes through the action of a spiral growth step.<sup>3</sup>

A sequence leading to the formation of such a border is illustrated in Figs. 2a–f. Upon lowering the temperature of the cell 9 degrees, a blue crystal plate emanates from a corner of the original red crystal. All but the (0001) face of this addition advance immediately; the equivalent faces of the original platelet remain stationary, however, and are finally engulfed (Fig. 2f). A similar sequence is apparent in Figs. 3a–d; here more than one source appears to be operating, however, sending out separate strips which join, as shown in Fig. 3b. Separate outgrowths thus formed have been found to show the same interference color, without any apparent material connection.

The formation of these borders can be rationalized by postulating the existence of a fault plane in the original crystal plate, possibly separating a region in which the layers are randomly stacked from one in which adjoining layers of cadmium iodide are so arranged as to form a C27 structure, with two  $\text{CdI}_2$  sheets per unit cell, which has been found to predominate for slow crystallization<sup>4</sup> and presumably minimizes the free energy. To account for development of crystal spokes,<sup>5</sup> we suggest that in the interval between crystal formation and the lowering of the temperature, small impurity particles present in solution are adsorbed on the platelets, primarily on the loosely packed prism faces, and that these can delay growth, as already shown by Zener for grain boundary migration.<sup>6</sup> Assuming, for simplicity, that such particles subdivide the prism faces into regions replicating the habit of the original crystal, and neglecting the contribution of impurities to the thermo-

dynamic functions in the bulk, the increase in the chemical potential,  $\mu$ , over that for a face without contamination will be<sup>7</sup>

$$\Delta\mu = \gamma \sum_i \left( \frac{l_i'}{S'} - \frac{l_i}{S} \right) \frac{\sigma}{\sin w_i} \left( \frac{\sigma_i}{\sigma} - \cos w_i \right),$$

where  $\gamma$  is the specific volume of the solid,  $\sigma$  is the surface tension of the uncontaminated face and  $w_i$  the exterior angle between it and an adjoining face  $i$ , of surface tension  $\sigma_i$ .  $S$  and  $S'$  denote, respectively, the area of the uncontaminated face and the average extent of the region delimited by impurities,  $l_i$  and  $l_i'$  the length of the edges in the two cases. For cadmium iodide the individual terms in the summation are, under our assumptions, positive quantities, so that  $\Delta\mu > 0$ . Even without taking account of the detailed mechanism by which prism faces advance, it follows that the supersaturation necessary for growth must be the greater the greater the number of impurities adsorbed on a surface. The formation of isolated outgrowths of the prism faces thus appears as a result

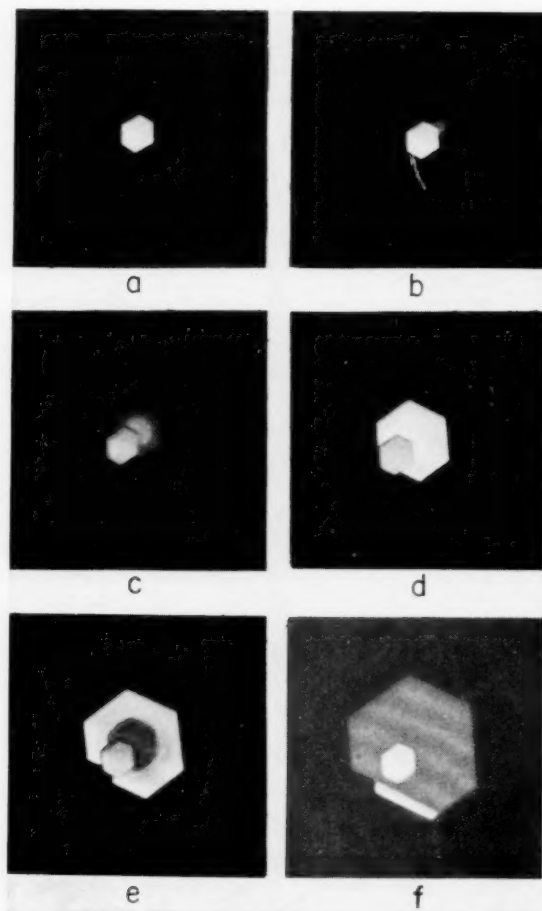


FIG. 2. Border formation in growth of cadmium iodide from aqueous solution. Magnification 340X.

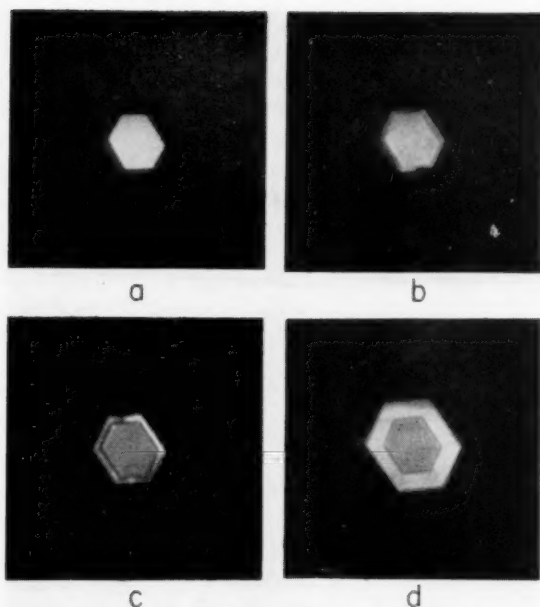


FIG. 3. Border formation in growth of cadmium iodide from aqueous solution. Magnification 340X.

of an unequal distribution of adsorbed impurities, which leaves only those sections of the prism faces free to grow at low supersaturation which have the more stable C27 structure and which are only sparsely populated with impurities. The details of the mechanism of lateral growth are not revealed by these experiments, and do not affect these conclusions since the adsorption of impurities serves only to *obstruct* growth.

G. EHRLICH

General Electric Research Laboratory  
Schenectady, New York

#### References

1. J. C. Fisher, R. L. Fullman, and G. W. Sears, *Acta Met.* In press.
2. W. H. Hartshorne and A. Stuart, "Crystals and the Polarizing Microscope (L. Arnold, London, 1950), p. 393.
3. Such bordered plates have also been reported by J. B. Newkirk, *Acta Met.* In press.
4. *Structure Reports* **11**, 491 (1951).
5. This interpretation of lateral growth arose in discussion with R. L. Fullman, for whose help I am greatly indebted.
6. C. Zener, *Trans. A.I.M.E.* **175**, 15 (1948).
7. *The Collected Works of J. W. Gibbs*, Yale University Press, New Haven, Conn. Reprinted 1948, Vol. 1, p. 321.

\* Received May 21, 1954.

#### Solubility of Nitrogen in $\alpha$ -Iron\*

In a recent "Letter to the Editor" Åström and Borelius<sup>1</sup> report on new measurements of the solubility of nitrogen in  $\alpha$ -iron in equilibrium with  $\text{Fe}_4\text{N}$  and " $\text{Fe}_3\text{N}$ ." From measurements of the elastic after-effect caused by nitrogen they deduce that the relaxation

strength is not proportional to the quantity of dissolved nitrogen (see their Fig. 1). In contrast with this conclusion the damping theory of Snoek<sup>2</sup> and Polder<sup>3</sup> anticipates proportionality between relaxation strength and N (or C) content for contents so small that interaction between interstitially dissolved atoms may be neglected. Dijkstra<sup>4</sup> substantiated this anticipation experimentally for dilute solutions of carbon in  $\alpha$ -iron.

According to Åström and Borelius' Fig. 2, the maximum solubility of nitrogen in  $\alpha$ -iron at the eutectoid temperature of 585°C is about 0, 1% by weight. According to their Fig. 1 this would mean that an iron wire containing nitrogen can never show an internal friction peak higher than  $Q_{\text{max}}^{-1} = \epsilon''/2\epsilon' \approx 0.055$  at  $-18^\circ\text{C}$  after quenching from 580°C. Our experiments show that values of  $Q_{\text{max}}^{-1}$  higher than 0.070 can easily be obtained even at room temperature by quenching iron wires containing 0.1% nitrogen from 580°C. Still higher values can be obtained by measuring at lower temperatures. The greatest peak height obtainable in principle is difficult to measure because precipitation is so rapid in iron containing 0.1%N, that part of the nitrogen has already precipitated before the first value of internal friction can be measured. The foregoing means that at least one of Åström and Borelius' curves, the solubility or the relaxation strength curve, is incorrect.

Based on their experimental relation between relaxation strength and nitrogen content (their Fig. 1), Åström and Borelius "correct" the solubility curve given by Dijkstra.<sup>5</sup> The "corrected" values agree well with those obtained by Åström and Borelius from their measurements on elastic after-effect and from their calorimetric measurements. The latter deviate strongly from the older calorimetric measurements of Borelius, Berglund and Avsan.<sup>6</sup> It is to be remarked that in their "correction," mentioned above, Åström and Borelius do not start from the curve as given by Dijkstra, but from a strongly deviating curve obtained by giving special weight to some of Dijkstra's values.

In our laboratory both the relation between quantity of dissolved nitrogen and internal friction, and the solubilities of nitrogen in  $\alpha$ -iron in equilibrium with  $\text{N}_2$  of 1 atm,  $\text{Fe}_4\text{N}$  and " $\text{Fe}_3\text{N}$ " were determined with great care, making use of a torsional pendulum system with iron wires of 0.7 mm diameter and 240 mm length as the suspension element.

In order to find the solubility of nitrogen in  $\alpha$ -iron in equilibrium with  $\text{N}_2$  of 1 atm, fine-grained, textureless wires were heated at several temperatures in the range 700 to 900°C and at 1450°C in a gas stream of the composition 99 vol %  $\text{N}_2$  + 1 vol %  $\text{H}_2$ , until, after quenching in water, a constant height of the internal friction peak was obtained.

The solubility in equilibrium with  $\text{Fe}_4\text{N}$  was determined on wires that were previously loaded with about 0.1 wt % of nitrogen at 570°C in a mixture of  $\text{NH}_3$  +  $\text{H}_2$ . These wires were heated in a pure nitrogen atmosphere

at temperatures between 380° and 580°C until a constant value of the peak height was reached. No loss or absorption of nitrogen takes place during the heating in pure N<sub>2</sub>.

The solubility in equilibrium with "Fe<sub>8</sub>N" was determined for temperatures between 125° and 225°C, using two iron wires containing 0.055 wt % and 0.026 wt % nitrogen respectively. After quenching from 570°C the value of  $Q_{\max}^{-1}$  (at about 22°C) was measured as a function of the time of heating in pure nitrogen at a temperature in the range mentioned. The heating was continued until a seemingly constant value of  $Q_{\max}^{-1}$  was reached.

Separate experiments showed that the internal friction of fine-grained, textureless  $\alpha$ -iron wires caused by nitrogen is proportional to the nitrogen content up to a concentration corresponding to the solubility at the eutectoid temperature (0.095 wt % at 585°C). The relation giving this proportionality is

$$\text{wt } \% \text{ N} = 1.26 Q_{\max}^{-1}$$

if the period of oscillation is such that the maximum of the internal friction curve lies at about 22°C. Making use of this relation and the internal friction measurements mentioned above the solubilities of nitrogen in  $\alpha$ -iron in equilibrium with "Fe<sub>8</sub>N," Fe<sub>4</sub>N and N<sub>2</sub> of 1 atm, respectively, are found to be given by the equations

$$\begin{aligned} q(\text{"Fe}_8\text{N"}) &= 3.3 \cdot 10^2 e^{-9900/RT} \text{ wt } \% \text{ N} \\ q(\text{Fe}_4\text{N}) &= 12.3 e^{-8300/RT} \text{ wt } \% \text{ N} \\ q(\text{N}_2, 1 \text{ atm}) &= 9.8 \cdot 10^{-2} e^{-7200/RT} \text{ wt } \% \text{ N} \end{aligned}$$

From the last two equations the dissociation pressures of Fe<sub>4</sub>N are calculated to be given by

$$p_{\text{N}_2}(\text{Fe}_4\text{N}) = 1.6 \cdot 10^4 e^{-2200/RT} \text{ atm},$$

in fairly good agreement with measurements of Emmett, Hendricks and Braunauer,<sup>7</sup> but strongly deviating from measurements of Lehrer.<sup>8</sup>

The results of our investigations will be given and discussed in full detail in a paper planned for publication in the *Journal of the Iron and Steel Institute*.

J. D. FAST

M. B. VERRIJF

Philips Research Laboratories  
N. V. Philips Gloeilampenfabrieken  
Eindhoven, Netherlands

#### References

1. H. U. Åström and G. Borelius, *Acta Met.* **2**, 547 (1954).
2. J. L. Snoek, *Chem. Weekblad* **39**, 454 (1942).
3. D. Polder, *Philips Research Reports*, **1**, 5 (1946).
4. L. J. Dijkstra, *Philips Research Reports*, **2**, 357 (1947).
5. L. J. Dijkstra, *Trans. Amer. Inst. Min. Met. Eng.* **185**, 252 (1949); *J. Metals*, March 1949.
6. G. Borelius, S. Berglund, and O. Avsan, *Arkiv för Gysik*, **2**, 551 (1951).
7. P. H. Emmett, S. B. Hendricks, and S. Brunauer, *J. Am. Chem. Soc.* **52**, 1456 (1930).
8. E. Lehrer, *Z. Elektrochem.* **36**, 383 (1930).

\* Received October 25, 1954.

#### Zur Entstehung der Rekristallisationstexturen in Aluminiumdrähten\*

In der Entstehung der Rekristallisationstextur stehen sich im Augenblick zwei Ansichten gegenüber.<sup>1,2</sup> Die eine Theorie, wie sie hauptsächlich durch Beck vertreten wird, sieht in der Rekristallisationstextur das Ergebnis einer Wachstumsauslese. Danach hat man sich vorzustellen, dass zunächst Rekristallisationskeime aller möglichen Orientierung gebildet werden, dass aber infolge der Abhängigkeit der Wachstumsgeschwindigkeit von der Orientierungsdifferenz zwischen wachsenden und aufgezehrt werdenden Kristall Keime in besonderer Orientierung zur Textur der Matrix eine wesentlich höhere Wachstumsgeschwindigkeit zeigen und somit die Rekristallisationstextur bestimmen (Theorie des orientierten Wachstums). Hingegen geht man in der hauptsächlich von Burgers und Tiedema vertretenen Theorie der orientierten Keimbildung von der Annahme aus, dass die Rekristallisationstextur zumindest zusätzlich auch dadurch bestimmt wird, dass die entstandenen und Wachstumsfähigen Keime selbst bereits eine bevorzugte Orientierung besitzen.

Im Rahmen einer grösseren Arbeit<sup>3</sup> sind nun einige Ergebnisse gewonnen worden, die in diesem Zusammenhang von Interesse sind.

Als Ausgangsmaterial diente ein polykristalliner technisch reiner Aluminiumdraht (0, 18% Fe, 0, 11% Si) von 0, 33 mm Durchmesser und einer mittleren Korngrösse von 0, 02 mm, der eine [111]-Verformungstextur mit einem Streubereich von  $\pm 10^\circ$  besass. An ihm wurde nach einer Dehnung von 16, 8 bzw. 4, 6% die Wachstumsgeschwindigkeit und die Orientierung der Rekristallisationskeime bei verschiedenen Glühtemperaturen bestimmt. In einer ersten Versuchsreihe wurde der gedehnte Draht mit einer Schere durchgeschnitten, wodurch die Keime bevorzugt an der hochverformten Schnittstelle entstanden, das messbare Wachstum aber in dem gleichmässig verformten Gefüge erfolgte (Erzwungene Keimbildung). In einer zweiten Versuchsreihe wurden alle Schnittstellen sorgfältig abgeätzt, sodass die Keimbildung etwa gleichmässig über die ganze Länge des Drahtes auftrat (Freie Keimbildung).

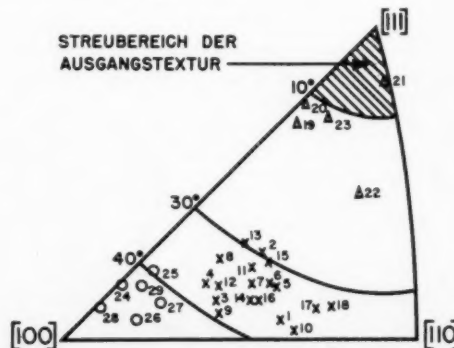


ABB. 1. Orientierung der untersuchten Keime.

TABELLE I.

Keim Nr.	Entstehungsart des Keimes	Dehnung in %	Glüh-temperatur in °C	Wachstums-geschwin-digkeit in cm/sec
1	Erzwungene Keimbildung	16,8	350	$9,3 \cdot 10^{-5}$
2				
3				
4				
5				
6				
7				
8	Erzwungene Keimbildung	16,8	370	$2 \cdot 10^{-4}$
9				
10				
11				
12				
13				
14				
15	Erzwungene Keimbildung	4,6	480	$3,9 \cdot 10^{-3}$
16				
17				
18				
19				
20				
21				
22	Erzwungene Keimbildung	16,8	370	$9 \cdot 10^{-5}$
23				
24				
25				
26				
27				
28				
29	Freie Keimbildung	16,8	390	$5,3 \cdot 10^{-4}$
30				
31				
32				
33				
34				
35				

Dabei ergab sich, dass die Wachstumsgeschwindigkeit von Keim zu Keim beträchtliche Schwankungen aufweisen konnte; sie ist für die Keime, deren Orientierung bestimmt wurde, in Tabelle I angegeben. Während bei der erzwungenen Keimbildung sowohl Keime jeweils maximaler (Keim Nr. 1 bis 13 bzw. 14 bis 18) als auch solche mit relativ niedriger Wachstumsgeschwindigkeit (Nr. 19 bis 23) untersucht wurden, konnten bei der freien Keimbildung nur die Keime maximaler Wachstumsgeschwindigkeit herausgefunden und vermessen werden.<sup>3</sup> Die Orientierungen der Keime sind in Bild 1 mit der betreffenden Keimnummer versehen in stereographischer Projektion eingezeichnet, wobei die aufgezeichneten Messpunkte die Lage der Drahtachse relativ zum Gitter des Kristalles darstellen.

Durch Vergleich von Tabelle I mit Bild 1 erhält man folgende Ergebnisse:

1. Die Keime maximaler Wachstumsgeschwindigkeit gehören sowohl für die erzwungene (Keim Nr. 1 bis 18) als auch für die freie Keimbildung (Nr. 24 bis 29) in einem begrenztem Orientierungsgebiet an, d.h. in beiden Fällen entsteht eine Rekristallisationstextur.

2. In beiden Fällen scheint die Orientierung nicht systematisch von der angewandten Glüh-temperatur abzuhängen.

3. Der Vergleich zwischen den Keimen Nr. 1 bis 13 und 14 bis 18 zeigt, dass im Rahmen dieser Messungen auch der Verformungsgrad keinen wesentlichen Einfluss auf die Orientierung hat.

4. Die Keime mit niedriger Wachstumsgeschwindigkeit (Nr. 19 bis 23) zeigen deutlich eine von den Keimen maximaler Wachstumsgeschwindigkeit (Nr. 1 bis 19) abweichende Orientierung. Dies lässt die Gültigkeit der Beck'schen Vorstellungen über die Orientierungsabhängigkeit der Wachstumsgeschwindigkeit auch in diesem Fall erkennen. Die Orientierung dieser Keime ist sehr ähnlich der Ausgangstextur, und für kleine Orientierungsdifferenzen wird auch die Wachstumsgeschwindigkeit klein.

5. Die Orientierungsgebiete der Keime maximaler Wachstumsgeschwindigkeit sind verschieden für erzwungene (Nr. 1 bis 13) und für freie Keimbildung (Nr. 24 bis 29). Der Abstand von der [111]-Achse beträgt im ersten Falle 28° bis 38°, im zweiten hingegen 38° bis 48°. Es kann also in diesem Beispiel die Wachstumsgeschwindigkeit nicht allein der auslesende Faktor sein, denn sonst wäre es nicht einzusehen, warum im Falle der freien Keimbildung nicht auch Keime des Orientierungsgebietes der erzwungenen Keimbildung entstehen sollten, zumal für diese die Wachstumsgeschwindigkeit ebenso gross oder sogar noch etwas grösser ist. Es müssen vielmehr Keime besonderer, von der Verformungsart abhängiger Orientierung bevorzugt gebildet bzw. schneller wachstumsfähig gemacht werden.

In diesen Messungen liegt also ein Beispiel dafür vor, dass trotz der zweifellos vorhandenen Orientierungsabhängigkeit der Wachstumsgeschwindigkeit die Rekristallisationstextur durch die orientierte Keimbildung bestimmt ist.

K. LÜCKE  
F. HÄSSNER

Mitteilung aus dem Institut für  
allgemeine Metallkunde  
Universität Göttingen  
Göttingen, Germany

#### Literatur

1. P. A. Beck, Acta Met. 1, 230 (1953).
2. W. G. Burgers und T. J. Tiedema, Acta Met. 1, 234 (1953).
3. F. Hässner und K. Lücke, Z. f. Metallkunde, erscheint demnächst.

\* Received July 19, 1954.

#### Twinning in Aluminium\*

It is well known that with most face-centered cubic metals, hot-working, or cold-working followed by recrystallization, produces extensive twinning. Alumin-



ium is, however, an exception to this otherwise general rule, although isolated cases of twinning have been reported. Elam,<sup>1</sup> working with large-grained specimens strained 10%, and followed by recrystallization, found twins fulfilling all the necessary crystallographic requirements. Lacombe<sup>2</sup> obtained twins in pure aluminium which had been rolled and recrystallized. These specimens were etched for 25–30 days in 10% HCl after which time the grain boundaries were found to be attacked but not the twin boundaries.

As stated by Hall,<sup>3</sup> it appears that face-centered cubic metals do not form twins under stress because the composition plane is the slip plane and slip is always preferred. Instead, twins are assumed to grow from small nuclei during annealing; these nuclei taking the form of hexagonal stacking faults formed during slip. This latter theory is due to Mathewson.<sup>4</sup>

Fullman<sup>5</sup> has measured the ratio of the interfacial free energy of a twin boundary to the mean grain boundary energy for copper and aluminium, obtaining the values  $0.036 \pm 0.006$  and  $0.21 \pm 0.05$ , respectively. He has shown that the lower ratio in the case of copper leads to the fact that twinning should be much more extensive on annealing than in aluminium.

In the course of some work on the structures of thick films of evaporated metals, it has been observed that twins are found frequently in pure aluminium obtained by evaporation in high vacuum. Figure 1, ( $\times 500$ )

shows the structure of such a specimen, after electropolishing and etching with 2% HF. Prolific twinning has also been observed in silver and copper evaporated under similar conditions. The formation of twins in electrodeposited metals, such as copper, is quite common (see, for example, Barrett<sup>6</sup>) and is usually attributed to stacking faults generated during growth, each twin boundary representing a mistake in the stacking of (111) planes.

It would seem that a similar mechanism can operate during the formation of a deposit from the vapor phase, and that metal atoms can build on to the lattice almost as readily in the twinned position as in the normal untwinned position.

M. J. OLNEY  
G. C. SMITH

Department of Metallurgy  
Cambridge University  
Cambridge, England

#### References

1. C. F. Elam, Proc. Roy. Soc. **A121**, 237 (1928).
2. P. Lacombe, "Report of Conference on Strength of Solids, Bristol, 1947," Phys. Soc., 1948, p. 91.
3. E. O. Hall, "Twinning and Diffusionless Transformations in Metals" (Butterworths, London, 1954) p. 99.
4. C. H. Mathewson, Trans. A. S. M. **32**, 38 (1944).
5. R. L. Fullman, J. Appl. Phys. **21**, 1069 (1950).
6. C. S. Barrett, "Structure of Metals" (McGraw-Hill, New York, 1953) p. 526.

\* Received September 7, 1954.

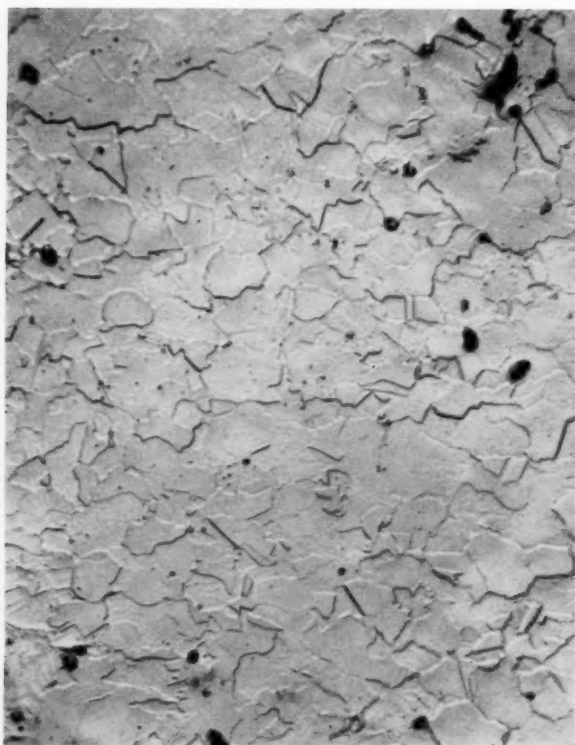


FIG. 1.

#### Zur Rekristallisation von Eisen nach der $\gamma$ - $\alpha$ -Umwandlung\*

Vor einiger Zeit berichtete G. Masing<sup>1</sup> über Rekristallisationsversuche an reinem Eisen nach der  $\gamma$ - $\alpha$ -Umwandlung. Es handelte sich um dünne Bleche, die auf dem Sinterwege aus Karbonyl-Eisenpulver hergestellt waren. Die Proben wurden oberhalb der Temperatur der  $\gamma$ - $\alpha$ -Umwandlung geglüht, in Wasser mit 10% Natronlauge abgeschreckt und dann bei 800°C angelassen. Es zeigte sich, dass das schnelle Durchlaufen der  $\gamma$ - $\alpha$ -Umwandlung einen Zwangszustand hervorruft, der rekristallisationsfähig ist. Das Anlassen bei 800°C ergab in allen Fällen eine bedeutende Zunahme der Korngrösse.

Im Rahmen von Untersuchungen an reinsten Eisen-Kohlenstoff-Legierungen mit 0,02 und 0,04% C wurden von uns ähnliche Beobachtungen gemacht.<sup>2</sup> Die Proben wurden bei unseren Versuchen jeweils von 930°C in Wasser abgeschreckt und dann bei 700°C—also unterhalb des  $A_1$ -Punktes—angelassen. Bei den Versuchen von G. Masing<sup>1</sup> lag dagegen die Rekristallisationstemperatur bei 800°C, also zwischen  $A_1$  und  $A_3$ . In diesem Falle ist darauf zu achten, dass der Kohlenstoffgehalt der Proben die Sättigungskonzentration des Ferrits bei 800°C—etwa 0,01% C—nicht überschreitet, weil sonst das Material nicht mehr rein ferritisch ist, sondern einen gewissen Prozentsatz Austenit enthält.

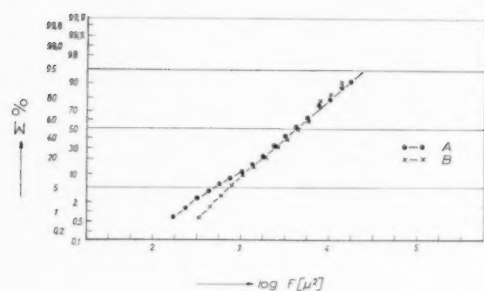


ABB. 1. Kornquerschnittverteilung von Fe+0,04%C nach  $\gamma$ - $\alpha$ -Umwandlung. Kurve A: 1 h 700°C, Kurve B: 3 h 700°C.

Eine solche Heterogenität kann unter Umständen die von der  $\gamma$ - $\alpha$ -Umwandlung herrührenden Effekte beeinflussen.

Bei unseren Untersuchungen interessierte nicht nur die mittlere Korngröße, sondern die statistische Verteilung der Kornquerschnittsgrößen. Die Ermittlung derselben wurde nach dem Verfahren von R. Dederichs und H. Kostron<sup>3</sup> vorgenommen. Die Auswertung und Darstellung der Ergebnisse erfolgte in gleicher Weise wie in früheren Mitteilungen.<sup>4,5</sup>

In der Abb. 1 ist auf der Abszisse der Logarithmus der Korngröße in  $\mu^2$  aufgetragen, während die Ordinate einen Häufigkeitsmassstab trägt, der entsprechend dem Gauss'schen Fehlerintegral geteilt ist. Die nach beendeter Rekristallisation aufgenommene Verteilungskurve B (3 Stunden Anlassen bei 700°C) ist eine gerade Linie, stellt also eine Gauss'sche Normalverteilung dar. Die nach 1 Stunde Anlassen bei 700°C aufgenommene Kurve A hat dagegen einen etwas anderen Verlauf; sie weicht für Korngrößen unterhalb von 1000  $\mu^2$  deutlich von der Kurve B ab. Man kann sich die Abweichung so entstanden denken, dass der Kurve B, d.h. also der Verteilung am Ende der Rekristallisation zunächst ein Teilkollektiv B' im Bereich der kleinen Körner überlagert ist. B und B' ergeben also zusammen die Verteilung A nach Beginn der Rekristallisation. Der ganze Vorgang besteht danach im Abbau des Teilkollektivs B', das der Gesamtverteilung im Bereich der kleinen Körner überlagert ist. Eine Verschiebung der Gesamtverteilung zu größeren Querschnittswerten hin trat dagegen nicht ein. Dies kann an der im Vergleich zu den Versuchen von G. Masing<sup>1</sup> um 100° niedrigeren Rekristallisationstemperatur liegen.

Für den eigentlichen Abschreckzustand konnte keine Korngrößenverteilung bestimmt werden. Es zeigte sich hier nämlich ein Gefüge mit derart bizarren Konturen, dass eine sichere Abgrenzung einzelner Körner unmöglich war. Die Kurve A beschreibt also einen Zustand, der bereits eine gewisse Homogenisierung hinter sich hat. Die Entstehung dieses Abschreckzustandes ist im wesentlichen von Keimbildungsvorgängen beherrscht. Im späteren Stadium des Anlassvorganges spielen dann noch andere Effekte eine Rolle, wie es auch bei sonstigen Rekristallisationsvorgängen der Fall

ist. Hier dürfte u.a. die Oberflächenspannung der Körner von Bedeutung sein. Ob der vorstehend beschriebene Vorgang zu der bei normalen Rekristallisationsvorgängen auftretenden Kornvergrößerung in Parallele gesetzt werden kann, lässt sich ohne weiteres nicht sagen; es sei darauf hingewiesen, dass bei Reinstaluminium die Kornvergrößerung ohne Änderung der Verteilungsbreite abläuft.<sup>4</sup>

Die vorstehend beschriebene Erscheinung wurde bei reinstem Eisen mit 0,02 und 0,04% Kohlenstoff nach dem Abschrecken in Wasser beobachtet. Die Proben waren kleine Drahtstücke von 3 mm Durchmesser und etwa 10 mm Länge. Dass die Proben so klein sind, bzw. dass die Abkühlungsgeschwindigkeit genügend hoch ist, ist zur Erzielung des Effektes wichtig. Proben mit etwa der 10-fachen Masse zeigten die Erscheinung nicht. Ebenso scheint es notwendig zu sein, dass der Kohlenstoffgehalt der Proben unter einem bestimmten Wert liegt. Versuche, das Teilkollektiv bei einem unruhigten und einem beruhigten Stahl mit etwa 0,1% Kohlenstoff nachzuweisen, verliefen negativ.

Wir weisen in diesem Zusammenhang noch auf eine Bemerkung von G. Masing<sup>1</sup> hin, der bei seinen Untersuchungen ebenfalls—allerdings nur auf Grund qualitativ-mikroskopischer Beobachtung—feststellte, dass die Kristalle nach dem Abschrecken anscheinend eine von der normalen statistischen Verteilung abweichende Größenverteilung haben.

Von Einfluss ist wahrscheinlich auch der Kohlenstoffgehalt. Wie J. Talbot, C. de Beaulieu und G. Chaudron<sup>6</sup> mitteilen, ist es bei reinstem Eisen mit einem Kohlenstoffgehalt von etwa 0,002%C nicht möglich, durch kritische Verformung und Rekristallisation in der üblichen Weise Einkristalle zu züchten. Erst nach Aufkohlung auf 0,035%C lässt sich dies dann in der normalen Weise erzielen. Für unseren Fall ergibt sich daraus der Hinweis, dass der von uns beschriebene Effekt nicht nur bei zu hohem, sondern möglicherweise auch bei sehr niedrigem Kohlenstoffgehalt ausbleibt.

W. DICKENSCHIED

Institut für Metallforschung  
Saarbrücken 24, Saarland

#### Literatur

1. G. Masing, Arch. Eisenhüttenw. **21**, 49 (1950).
2. Das Material wurde uns von Herrn J. D. Fast, Philips' Gloeilampenfabrieken, Eindhoven (Holland), zur Verfügung gestellt. Siehe auch: Stahl u. Eisen **73**, 1484 (1953).
3. R. Dederichs und H. Kostron, Arch. Metallkunde **3**, 193 (1949) und "Zwei Schnellverfahren zur Kornquerschnittbestimmung." Verlag Chemie, Weinheim (Bergstrasse), 1950.
4. W. Dickenscheid und H. J. Seemann, Z. Metallkde. **44**, 211 (1953).
5. W. Dickenscheid, Métaux **24**, 14 (1954).
6. J. Talbot, C. de Beaulieu, und G. Chaudron, Comptes rendus **236**, 818 (1953).

\* Received August 3, 1954.

### Deformation Processes in Zirconium\*

A study is in progress at Massachusetts Institute of Technology to determine the deformation processes in zirconium. Research to date includes a satisfactory method of obtaining relatively large stress-free grains of the  $\alpha$ -phase (h.c.p.) of iodide crystal bar zirconium, and an examination of the slip and twin systems of five crystals in a sample deformed in tension at 20°C. Observed slip plane and twin planes are shown in Table I along with calculated values of the other twin elements. The twin planes observed were the  $\{10\bar{1}2\}$ ,  $\{11\bar{2}1\}$ ,  $\{11\bar{2}2\}$ , and  $\{11\bar{2}3\}$ ; the slip plane was  $\{10\bar{1}0\}$ . The principles of the calculations and the notation used in Table I are the same as those used by Hall,<sup>1</sup> and these calculations made for zirconium check with those given by Hall for titanium. Calculated values of Table I are currently being checked by experiment.

The samples were carefully machined from Westinghouse Grade I zirconium, hand polished, chemically etched, and electrolytically polished before heat treatment. They were then heat treated, as described below, and the orientations of usable grains determined by back reflection Laue technique. Dihedral angles between the faces of the crystals were measured optically, and the crystals were pulled in tension in a fixture designed for the purpose. After deformation the surfaces were examined metallographically and the slip plane and twin planes were found by use of both single surface and two surface traces. The crystals were pulled in strain increments to a total strain of 2.2 percent with metallographic examination after each deformation. Table II gives the number of twin and slip traces definitively analyzed for each plane, and a general description of each system.

The heat treatment used to obtain large crystals of  $\alpha$ -zirconium from the crystal bar samples was based on grain growth considerations. The samples were wrapped in tantalum foil and put into a long quartz tube sealed at one end, which was then evacuated to about  $10^{-6}$  mm Hg. The samples were then heated to 840°C at a rate of about 100°C/hr with a vacuum system constantly removing the hydrogen evolved from the

TABLE I. Slip and twin indices in  $\alpha$ -zirconium tested at 20°C.  $K_1$  was observed and the other indices calculated.\*

Twins $K_1$	$\eta_1$	$K_2$	$\eta_2$	$S$	Theoretical shear
(10 $\bar{1}2$ )	[ $\bar{1}011$ ]	(10 $\bar{1}2$ )	[ $\bar{1}0\bar{1}1$ ]	0.167	$[3 - (c/a)^2]/[\sqrt{3}c/a]$
(11 $\bar{2}1$ )	[ $\bar{1}126$ ]	(0001)	[ $\bar{1}120$ ]	0.628	$a/c$
(11 $\bar{2}2$ )	[ $\bar{1}123$ ]	(1122)	[ $\bar{1}123$ ]	0.965	$(c/a)[1 - (a/c)^2]$
(11 $\bar{2}3$ )	[ $\bar{1}122$ ]	(0001)	[ $\bar{1}120$ ]	1.883	$3a/c$
Slip	Plane (observed)	Direction (calculated)			
	{10 $\bar{1}0$ }	{11 $\bar{2}0$ }			

\*  $K_1$  is the twin plane, or composition plane.

$K_2$  is the second undistorted plane in the twinned area.

$\eta_1$  is the direction in  $K_1$  perpendicular to intersection of  $K_1$  and  $K_2$ .

$\eta_2$  is the intersection of  $K_2$  and the plane through  $\eta_1$  perpendicular to  $K_1$ .

$S$  is the shear in the twinned area.

TABLE II. Occurrence and general description of slip and twin planes on the surfaces of five crystals of  $\alpha$ -zirconium tested at 20°C.

Twins	No. of grains in which plane was definitely found	No. of times plane was defi- nitely found	General description
{10 $\bar{1}2$ }	5	6	Somewhat lenticular
{11 $\bar{2}1$ }	5	6	Needle
{11 $\bar{2}2$ }	2	4	Somewhat needle
{11 $\bar{2}3$ }	3	3	Somewhat needle
Slip {10 $\bar{1}0$ }	5	9	Extremely straight fine lines

decomposition of zirconium hydride in the samples. The dynamic vacuum maintained was of the order of  $10^{-6}$  mm Hg, at a temperature of 840°C, for a period of about seven days. An annealing temperature of 840°C was chosen because it was close to the  $\alpha$ - $\beta$  transformation temperature of 863°C for zirconium. After annealing, the samples were cooled to room temperature at a rate of about 100°C/hr. The treatment did not deform the samples and no machining or paper polishing was necessary after annealing. This method gave about one usable sample for every four or five processed, and the best results to date have been crystals of square cross-section, about  $\frac{1}{4}$  in. on a side and  $\frac{1}{2}$  in. long. The sharp Laue spots were considered indicative of good crystals.

The five grains tested had roughly the same orientation in that the  $c$ -axis was, in all cases, within 18 degrees of being perpendicular to the tension axis of the sample. This particular orientation may account for the absence of basal-plane slip. In future experiments, an attempt will be made to obtain a more random distribution of orientation for tests in compression as well as tension and to investigate the occurrence of basal slip.

This work was done in the Department of Metallurgy, Massachusetts Institute of Technology, under A.E.C. contract AT(30-1)-981, and is part of a doctoral thesis being supervised by Professor A. R. Kaufmann.

E. J. RAPPERPORT

Massachusetts Institute of Technology  
Cambridge, Massachusetts

### Reference

1. E. O. Hall, "Twinning and Diffusionless Transformations in Metals" (Butterworth's Scientific Publications, London, 1954) pp. 56-75.

\* Received September 14, 1954.

### Grain-Boundary Segregation\*

Grain-boundary segregation of polonium in lead-bismuth alloys has been observed by Stewart *et al*<sup>1</sup> and

studied quantitatively using an autoradiographic technique by Thomas and Chalmers.<sup>2</sup>

Recent experiments by DeMaio<sup>3</sup> have shown that polonium also segregates to the grain boundaries of high purity lead crystals. As in the previous work with lead-bismuth alloys, the concentration of polonium was approximately  $10^{-9}$  percent and it was necessary to anneal the specimens at an elevated temperature before enough segregation occurred to be visible on an autoradiograph. Figure 1 is a typical autoradiograph of a lead-specimen after annealing at 175°C for 48 hours.

The segregation of silver to the grain boundaries of tin specimens has been observed using a radioactive isotope of silver. In this case, however, the segregation appears to have taken place during the solidification process, since the boundary was visible on an autoradiograph of the crystal immediately after solidification. The explanation for this segregation during solidification may be found by considering the alloy equilibrium diagram and the shape of the solid liquid interface of a bicrystal.

Because of the energy of the grain boundary and the forces existing at the interface in the boundary region, the boundary appears as a groove to the liquid, Fig. 2(a), the depth of which is a function of the orientation difference between the crystals. Let us now consider growth in an alloy system. It has been shown by Tiller *et al.*<sup>4</sup> that a build-up of solute will occur at the interface which depends upon " $k$ ," the distribution coefficient of the solute in the solvent. The presence of a grain-boundary groove in an otherwise smooth interface will produce lateral diffusion of solute to fill the groove, i.e., the grain boundary will act as a solute sink. The concentration of solute in the liquid at the interface varies inversely with " $k$ " and thus the amount segregated to the boundary region must depend upon " $k$ ."

Silver has a " $k$ " value of approximately  $10^{-3}$  in tin; thus, the concentration of silver in the melt near the interface would be large. Since small amounts of silver lower the melting-point of tin considerably, the

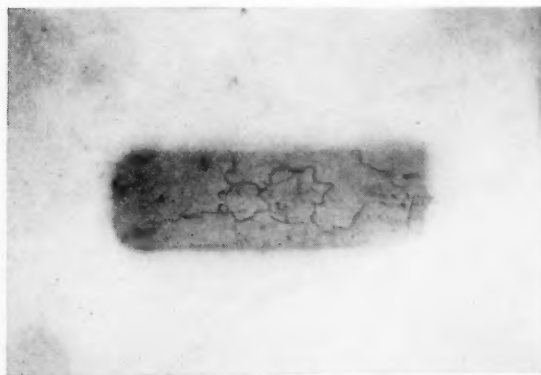


FIG. 1. Autoradiograph showing grain boundary segregation after annealing at 175°C for 48 hours.

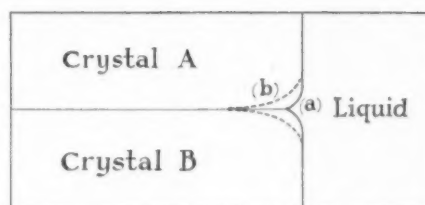


FIG. 2. (a) Grain-boundary groove in the solid-liquid interface. (b) Effect of solute on the grain-boundary groove.

increased concentration of silver in the boundary groove will have a tendency to further depress the boundary groove, Fig. 2(b). This in turn will allow more solute to segregate in the boundary region. The depth of the groove will reach a maximum value which depends upon both the freezing temperature of the alloy in the groove and the conditions of solidification. Thus, it may be seen that the amount of solute segregation to the grain boundary during solidification depends primarily upon the value of " $k$ ."

W. A. TILLER

W. C. WINEGARD

Department of Metallurgical Engineering  
University of Toronto  
Toronto, Canada

#### References

1. M. T. Stewart, R. Thomas, K. Wauchope, W. C. Winegard, and B. Chalmers, *Phys. Rev.* **3**, 657 (1951).
2. W. R. Thomas and B. Chalmers, *Acta Met.* **3**, 17 (1955).
3. F. DeMaio, Thesis, Department of Metallurgy, University of Toronto.
4. W. A. Tiller, K. A. Jackson, J. W. Rutter, and B. Chalmers, *Acta Met.* **1**, 428 (1953).

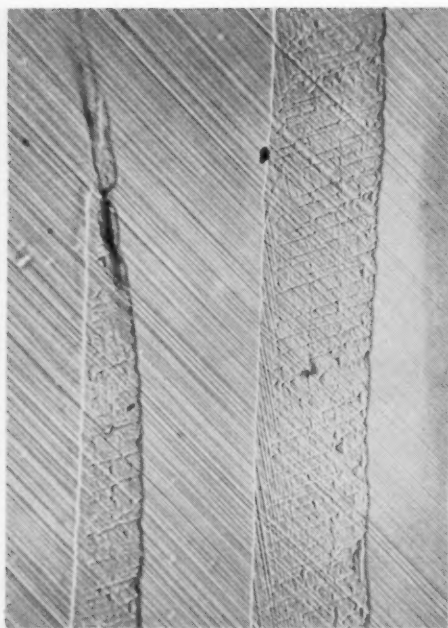
\* Received August 24, 1954.

#### Fine Structure in Zinc Twins\*

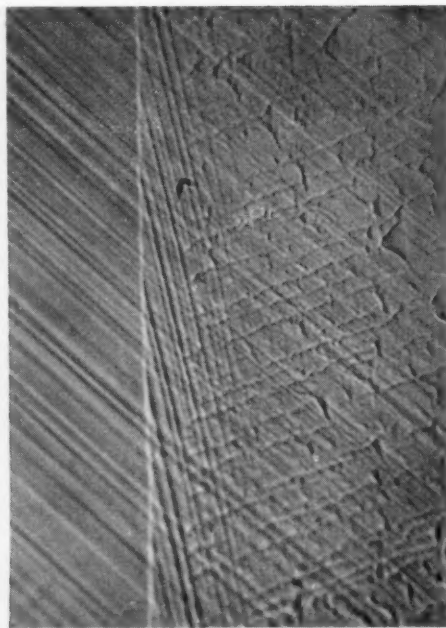
Figure 1a shows two twins that formed in a zinc crystal that had previously been strained in tension about 100% (glide strain  $\approx 1.9$ ). There are two sets of markings within the twin on the right. Analysis showed that the steeply inclined lines near the left edge of the twin correspond to slip on the basal planes of the twin. The other set of markings seems to be something new. These markings are observed only in twins that form in crystals with large amounts of prior glide-strain on the basal planes.

The crystal picture in Fig. 1 was initially square in cross section (6×6 mm) and about 8 cm long. The basal plane was oriented so that the plane containing the hexagonal axis, the slip direction, and the specimen axis was parallel to one of the sides. The basal plane initially made an angle of about 35 degrees with the specimen axis. Figures 1a, b, and d were taken normal to the "front" face (through which the hexagonal axis emerged). Fig. 1c was taken on the side face.





(a)



(b)



(c)



(d)

FIG. 1. Fine structures in twins. (a) Fine structure in twins formed in zinc crystal ( $100\times$ ). Plane of slip direction and tension axis shown by arrow. Slip plane makes angle of  $16^\circ$  with plane of paper. Prior glide strain, approximately 1.9. (b) Same as (a) at  $400\times$ . (c) Same twins as (a) but seen on side of square crystal. ( $100\times$ ). Note the absence of unusual markings. (d) Same twin as (a) after crystal was deformed further in tension ( $100\times$ ).

The unusual markings seem to delineate small regions of the matrix that did not twin along with the rest of the twin band. This is indicated in two ways: first, the markings seem to trail from the irregular right-hand edge of the twin band (this was the moving side of the twin during its growth); second, further deformation caused many of the markings to disappear (shown in Fig. 1d). The fine structure markings (Fig. 1a) seem to lie along a crystallographic plane, but the plane could not be determined because the markings were not present on the other face of the crystal.

The author is unaware of any previous description of this fine structure in twins. Although the significance of the structure is not clear at the present time, it is of some interest for two reasons. First, the fine structure is observed only in twins that form in prestrained crystals; this indicates a strong effect of the perfection of the matrix on the growth of twins. Second, the fact that the markings seem to correspond to untwinned remnants of the matrix shows that the twinning process is not as homogeneous as some theories consider it to be.<sup>1</sup>

J. J. GILMAN

General Electric Research Laboratory  
Schenectady, New York

#### Reference

1. E. O. Hall, "Twinning" Butterworths, London 1954.

\* Received August 27, 1954.

#### Effect of Irradiation upon Beryllium Copper\*

Precipitation and retrogression processes in beryllium copper are sufficiently complex, so that it is not possible to explain completely all of the resulting property changes by existing theories. Consequently, the situation is further complicated by superimposing upon it the effects of irradiation.

Recently Murray and Taylor<sup>1</sup> have shown the influence of neutron irradiation on beryllium copper and have demonstrated the similarity between this influence and low-temperature aging. There are, however, several features of this interesting study that require further consideration.

First, the authors refer to the observed increase in density accompanying their hardening experiments as "anomalous." Early work on beryllium copper by Masing and Dahl<sup>2</sup> as well as later work by Thomas<sup>3</sup> indicates an increase in density upon aging at low (100–200°C) or moderate (300–400°C) temperatures. In fact, Thomas<sup>3</sup> shows extremely close correlation between changes in hardness and length or density. For example, aging an alloy containing 1.85 percent Be at 170°C causes a length decrease of 0.12 per cent with an increase in hardness. Subsequent aging for five minutes at 280°C produced a length increase of 0.05 per cent and a decrease in hardness; however, after 10

to 15 minutes the trend is reversed, so that at five hours the hardness has increased substantially while the over-all contraction reaches 0.20 per cent. Recent precise determinations<sup>4</sup> of the density of commercial beryllium copper cold-drawn rod give an increase in density of 0.51 per cent upon aging for two hours at 315°C.

The use of binary beryllium copper—notorious for its erratic heat-treating behavior—is perhaps the cause of the non-uniform hardening response shown in the authors' curves (note the variation between the solution-annealed curves in Figs. 13 and 14). This lack of aging stability plus difficulty in controlling grain-boundary precipitate prompted commercial producers to add 0.25 per cent Ni or Co to beryllium copper. Consequently, use of the binary alloy is reserved for fundamental studies (such as the present); however, investigators should carefully consider whether the advantages of the binary alloy offset the important disadvantages.

Comparison of the authors' Fig. 12 with Guy, Barrett and Mehl's Fig. 14<sup>5</sup> reveals a marked similarity. Note in particular that the shape of the water-quenched curve for the latter investigation compares favorably with the irradiated curve in the present study. Guy and co-workers attribute the difference between the hot and cold quenched curves to the presence of greater quenching stresses in the cold-quenched specimen. This suggests that cold work or residual stresses may play a greater role in the irradiation phenomenon than indicated by the present authors.

In addition, the apparent effects of cold work resulting from irradiation are clearly brought out in another manner in Figs. 12, 13 and 15. There is no reason to believe that premature nucleation will lead to a higher maximum hardness upon aging, although cold work can account for the 10–20 points higher hardnesses on the DPH scale observed for irradiated specimens. Both premature nucleation and cold work, however, will account for the more rapid aging response and the earlier peak. Figure 15 is particularly informative, since the premature nucleation resulting from low-temperature aging gives a later hardness peak which is approximately 20 points lower than the irradiated specimen.

Geisler<sup>6</sup> has recently called attention to the similar effects produced by cold work and the coherency strains between the transition precipitate and the matrix. Although the distribution and magnitude of these strains will vary, the overall effect may be similar. Geisler has also demonstrated that cold-working provides an increase in electrical resistivity of the same magnitude as coherency strains. At the same time, the retrogression in hardness and resistance resulting from aging can be due, at least in part, to stress relief or recovery.

The choice between precipitate nucleation and cold work is a difficult one, although the answer may well

be a combination of the two. It is hard to explain the increase in density accompanying irradiation by cold work, since usual deformation resulting from cold-rolling or drawing beryllium copper<sup>7</sup> causes a decrease in density. Of course, it has not been determined whether the density increase noted by Thomas<sup>8</sup> at low temperatures is due to precipitation or complex strain patterns. Another factor to consider is the variation in precipitation rate with location in beryllium copper. It is well known, for example, that grain boundary areas may overage before the grain center has even attained maximum hardness. Unfortunately, the authors obtained average rather than local data through the use of hardness and electrical resistivity tests.

Perhaps the most convincing argument in favor of cold work over precipitate nucleation is to be found in the work of Billington and Siegel.<sup>8,9</sup> These earlier investigators observed hardness increases in stainless steel, monel, brass and other strain-hardening materials exposed to neutron radiation. In the case of annealed monel, the improvement in hardness approached that observed in beryllium copper. Consequently, the similarity between irradiation and low-temperature aging may well be coincidental. In any event, more detailed retrogression curves would be helpful, since the present authors have only shown broken lines without intermediate points in their curves. This greater detail would then permit comparison with earlier work on retrogression in beryllium copper.<sup>10,11,12</sup>

It is difficult to understand how the resistivity of beryllium copper aged for maximum hardness (or overaged) can be increased by further precipitation—as suggested by the present authors. Billington and Siegel<sup>8</sup> have shown that irradiation of material in this condition causes a slight increase in hardness, as might be expected from additional cold work. As shown by Gruhl,<sup>12</sup> low-temperature aging after heat treating for maximum hardness will not cause an increase in resistivity.

On the basis of evidence presented by Murray and Taylor,<sup>1</sup> as well as earlier investigators, it appears that most of the phenomena resulting from neutron irradiation can be explained by the "cold work" hypothesis.

J. T. RICHARDS

Penn Precision Products, Inc.  
501 Crescent Avenue  
Reading, Pennsylvania

#### References

1. G. T. Murray and W. E. Taylor, *Acta Met.* **2**, 52 (1954).
2. G. Masing and O. Dahl, "Beryllium," translated by R. Rimbach and A. Michel (Chemical Catalog Company, New York, 1932), p. 151.
3. H. Thomas, *Z. Metallk.* **36**, 12 (June 1944).
4. J. T. Richard, "Symposium on Elastic Constants," Amer. Soc. Test Mats., Special Technical Publication No. 129 (1952), p. 71.
5. A. Guy, C. Barrett, and R. Mehl, *Trans. A.I.M.E.* **175**, 216 (1948).
6. A. Geisler, J. Mallery, and F. Steigert, *J. Metals* **4**, 307 (1952).

7. J. T. Richards, *Wire and Wire Products* **27**, 257 (1952).
8. D. Billington and S. Siegel, *Metal Progress* **58**, 847 (1950).
9. J. T. Richards, *Metal Progress* **59**, 249 (1951).
10. G. Masing and L. Koch, *Z. Metallk.* **25**, 137 (1933).
11. H. Unkel, *Metall No.* 19/20 (October 1948), p. 319.
12. W. Gruhl, *Metall No.* 11/12 (June 1951), p. 231.

\* Received September 27, 1954.

#### Nitrogen in Iron Anelasticity and Solid Solubility\*

Although it has been known for some time that nitrogen and carbon in solid solution both give rise to anelasticity in  $\alpha$ -iron,<sup>1</sup> quantitative correlation is still needed. Polder<sup>2</sup> calculated the anelasticity for the case of carbon in a single crystal of  $\alpha$ -iron when the stress is applied in the direction of the cube edge. Dijkstra<sup>3</sup> confirmed the calculated value by experiments on single crystals. He also measured the anelasticity due to nitrogen. This was about 30 per cent less than that due to carbon. Using the values for the lattice constants for martensite given by Bose and Hawkes,<sup>4</sup> this also agrees well with the calculated value (0.032 observed by Dijkstra, 0.0335 our calculated value for .01% N). For polycrystalline strip, Dijkstra<sup>3</sup> found a poor correlation between carbon content and anelasticity. Later, Dijkstra<sup>5</sup> stated that the internal friction maximum was equal to the solute content to within 10 per cent in the case of both carbon and nitrogen. This does not agree with his previous results using a single crystal.

More recently Borelius *et al*<sup>6</sup> have obtained a quantitative correlation between nitrogen content and the anelasticity at  $-17^{\circ}\text{C}$ . The relationship obtained is not linear. Polder's theory<sup>2</sup> predicts a linear relationship provided the ratio of solute atoms to iron atoms is small and provided that there is no interaction between the solute atoms. One would expect these conditions to be observed when only 0.1 per cent solute is present. As Åström and Borelius point out their results at  $-17^{\circ}\text{C}$  cannot be compared directly with those made at room temperature. According to Polder, the anelasticity (due to solute atoms) varies inversely with absolute temperatures, and this has been confirmed by Fast<sup>7</sup> (but for only a short range of temperature). Allowing in this way for temperature, the results of Åström and Borelius have been plotted for room temperature ( $17^{\circ}\text{C}$ ). To them are added some results we obtained by the torsional pendulum method at  $17^{\circ}\text{C}$ , the starting material being a high purity iron supplied by British Iron and Steel Research Association.\* The nitrogen content was obtained by analysing a strip which was nitrided at the same time as the wire used for internal friction measurements. The wire was 2 in.  $\times$  0.020 in. in diameter, while the strip was 2 in.  $\times$  0.0017  $\times$  0.25 in. The wire, weighing only 0.09 gm, was too small to be analysed but the nitrogen content of the strip could be determined to  $\pm 0.002$  per cent,

TABLE I.

Run No.	Nitrogen content of strip %	Nitrogen content of wires %	Internal friction
A68	0.036 <sub>2</sub>	0.034 <sub>1</sub>	0.027 <sub>4</sub>
A69	0.031 <sub>2</sub>	0.031 <sub>6</sub>	0.025 <sub>2</sub>

or better. To verify that the wires contained the same nitrogen content as did the strip, ten wires were nitrided together with a strip and analysed for nitrogen. One of the wires was quenched and the internal friction determined. The result shown in Table I shows that there was little difference between the nitrogen content of the strip and that of the wire. These results are plotted as solid circles. The internal friction measurements were repeatable to 0.0002 except for high nitrogen contents when precipitation took place within minutes of quenching. Thus, if the results are incorrect the values for internal friction would be low. It can be seen that our results give a straight line as predicted, the actual relationship being

$$(\text{N}) \text{ wt.}\% = 1.28 \times \text{internal friction at } 17^\circ\text{C}.$$

Without knowing the details of the method used by Åström and Borelius, it is not easy to give reasons for the large discrepancies at high nitrogen contents between their work and ours. In view of the agreement at low nitrogen contents and of the known rapid precipitation at high nitrogen values, it may be suggested that their specimen weighing 200 gm was rather large to obtain an efficient quench.

In considering the solubility of  $\text{Fe}_4\text{N}$  in iron, Åström and Borelius appear to have overlooked the work of Paranjpe<sup>8</sup> *et al.* Below  $500^\circ\text{C}$ , these workers obtained much lower values for the solubility of  $\text{Fe}_4\text{N}$  than did either Dijkstra<sup>4</sup> or Åström and Borelius. They criticised Dijkstra's results on the ground that he could not have had complete precipitation in his specimen. To verify

this, we nitrided a wire (which originally contained very little nitrogen) at  $400^\circ\text{C}$  until a constant value for internal friction was obtained. The internal friction was 0.0240 (0.0307% N) compared with 0.0247 (0.0316% N) by Dijkstra and 0.02% N by Cohen, (extrapolating his results from higher temperatures). Since the same result (within about 1%) has been obtained whether equilibrium is approached from above or below, it would appear to be accurate. To check that the nitrided specimen was saturated at  $400^\circ\text{C}$ , it was quenched after heating to  $700^\circ\text{C}$  for a half-minute. The internal friction was then 0.0384. The investigation is being extended to other temperatures, and it is hoped to determine also the effect of temperature on anelasticity.

R. RAWLINGS  
D. TAMBINI

Department of Metallurgy and Fuel Technology  
University College of South Wales and Monmouthshire  
Cardiff, Wales

#### References

1. J. L. Snoek, *Physica* **8**, 711 (1941).
2. D. Polder, *Phil. Res. Rep.* **1**, 1 (1945).
3. L. J. Dijkstra, *Phil. Res. Rep.* October 1947, p. 357.
4. Bose and Hawkes, *Trans. A.I.M.E.* **188**, 307 (1950).
5. L. J. Dijkstra, *Trans. A.I.M.E.* **185**, 252 (1949).
6. H. U. Åström and G. Borelius, *Acta Met.* **2**, 547 (1954).
7. J. D. Fast and J. Verrijp, *J. Iron Steel Inst.* **176**, 24 (1954).
8. V. G. Paranjpe, M. Cohen, M. B. Bever, and C. F. Floe, *Trans. A.I.M.E.* **188**, 261 (1950).

\* Received August 20, 1954.

† B.I.S.R.A. Mark A.G.B.1. Typical analysis 0.004% C, 0.02% Si, 0.004% S, 0.28% O. (Some of the carbon will be lost during the nitriding.)

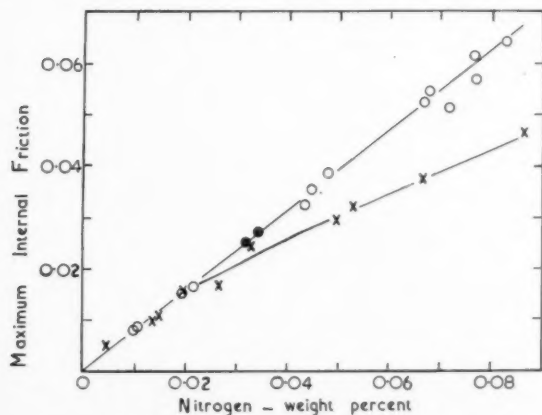


FIG. 1. The dependence of the maximum internal friction of  $\alpha$ -iron, upon the concentration of nitrogen in solid solution.  $\times$  Åström, Borelius;  $\circ$  strip analysed;  $\bullet$  wire analysed.

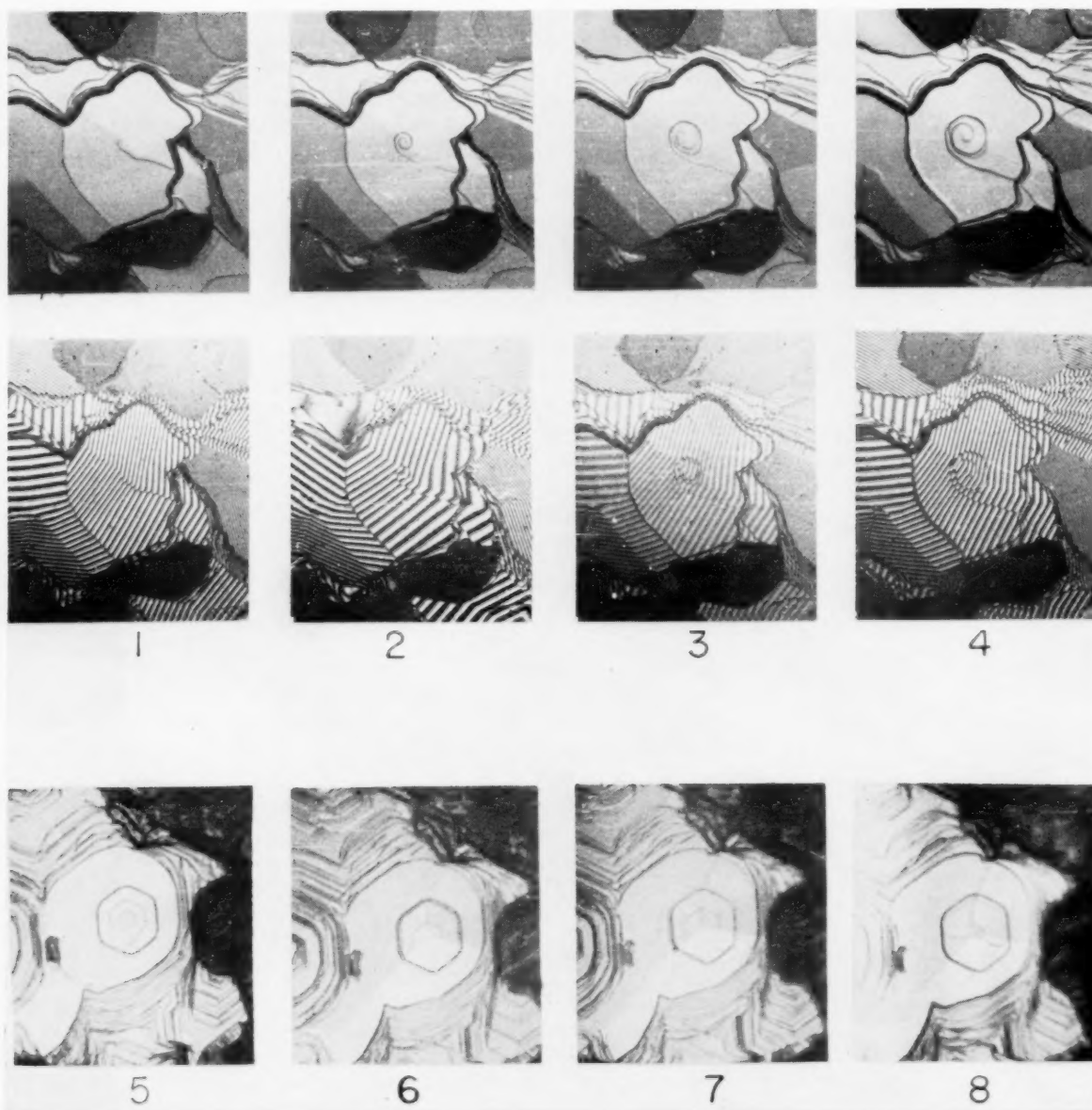
#### Spiral Growth of Cadmium Crystals from the Vapor Phase\*

McNutt and Mehl<sup>1</sup> have studied the growth of cadmium crystals in cadmium vapor by direct observation during growth, including interferometric measurement of the height of growth steps. Continued investigations have now disclosed growth spirals.

Photographs with corresponding interferograms have been taken of the start and of the growth of a spiral on a basal hexagonal plane. Figures 1 through 4 are representative photographs taken at 20 minute intervals at  $75\times$  showing step heights of 1000 to  $1500\text{\AA}$ ; in some experiments growth has been observed continuously over a period of 24 hours. Interpretation of the total series reveals the initial formation of a "solid-louver" on a surface containing a "ridge boundary"<sup>1-4</sup> this "solid-louver" develops into a step which grows spirally<sup>5</sup> and exhibits hexagonal symmetry. The "solid-louver" could possibly be a step connecting two screw dislocations of opposite handedness and of large Burgers vector.

Figure 5 is from a sequence of growth photographs which show another hexagonal spiral; Fig. 6 is 45





FIGS. 1-4. Photographs with corresponding interferograms of the start and of the growth of a spiral of cadmium taken at 20-minute intervals at 75 $\times$ .

FIGS. 5-8. Photographs from a sequence of growth of a hexagonal spiral of cadmium at 75 $\times$ . Note text.

seconds later and Fig. 7 is 15 seconds still later. The series shows that spiral growth normal to the hexagonal surface has stopped but simple lateral growth of layers has occurred. This simple lateral growth continues to the edges of the crystal, resulting in an essentially flat surface. Further observations have revealed (1) that the origin of the spiral is considerably "off-center," (2) that during simple lateral growth the point of origin of the spiral moves to the edge of the crystal (3) that the movement of the point of origin is along a "ridge boundary," and (4) a new spiral subsequently

starts at or near the point of origin of the primigenial spiral (note Fig. 8 which was taken 30 seconds after Fig. 7).

These spirals occur at low supersaturations as predicted for idealized screw dislocations. They are sporadic; spiral growth does not occur on all observed surfaces. Growth by layer formation is also observed. The origin of spirals appears to be associated with types of crystal imperfections in a manner not yet elucidated.

A full account of these experiments and their interpretations will be published soon.

This research was sponsored by the Office of Ordnance Research, U. S. Army.

W. I. POLLOCK  
R. F. MEHL

Metals Research Laboratory  
Carnegie Institute of Technology  
Pittsburgh, Pennsylvania

#### References

1. J. E. McNutt and R. F. Mehl. To be published.
2. The boundary across a crystal which separates two regions that differ slightly in orientation as evidenced by a small angle between their basal surfaces has been designated a "ridge boundary" by McNutt.
3. J. B. Newkirk. Unpublished data. These findings were presented at the Spring Meeting, American Physical Society, April 29, 1954.
4. J. C. Fisher, R. L. Fullman, and G. W. Sears, *Acta Met.* **2**, 344 (1954).
5. Note, for example, Fig. 6.5, page 75, in W. T. Read, *Dislocations in crystals* (McGraw-Hill, New York, 1953).

\* Received September 21, 1954.

#### The Lack of a Crystal Boundary Hardening in Deformed Metals as Revealed by Microhardness Measurements\*

Dehlinger<sup>1</sup> originated an explanation for the difference in strength between the polycrystal and the so-called "mean" single crystal by assuming a hardening in the crystal boundaries on deformation (Korngrenzverfestigung). He clarified his notion in outlining that at the boundaries takes place an accumulation of a particular kind of internal stresses giving rise to a very intensive work-hardening. This picture has been taken over and further developed mainly by Kochendörfer in his theoretical work on strength and related phenomena.

An experimental proof of the Dehlinger statement has hardly been given yet. However, the drift of Vickers hardness along a line crossing the microstructure of deformed, coarse-grained aluminium tensile specimens, measured by Boas and Hargreaves,<sup>2</sup> seems to show that there must be a somewhat different behavior at the crystal boundaries in comparison with the bulk of the individual crystals. These results stimulated the investigations to be outlined in the following.

To study the effect of crystal boundaries, and especially of precipitations therein, on the inhomogeneity of work-hardening in a polycrystalline aggregate it was decided to measure the distribution of microhardness in the single crystals. The resulting "hardness topographies" were expected to be in close relation with the microstructure itself.

For the experiments, two different alloys were used, one being a hot-rolled chromium-nickel steel (Fe-Cr18-Ni8) from the current production of Firth-Vickers in Sheffield England and the other a pure aluminum-magnesium alloy (Al-Mg5) cast especially for this work by the research laboratories of the Aluminum

Industry Limited in Neuhausen, Switzerland. Of each alloy a set of six samples, differing from one another by an increase in crystal boundary precipitation, was produced by heat treatment. This caused the crystals to grow up a rather big size, having a diameter of about 1 to 2 mm.

From each sample, three bars of circular cross section and a gauge-length of 6.5 mm were deformed on a Chevenard microtensile machine: one to fracture, another one up to maximum load and a third one reaching the yield "point." The use of micro-specimens permits a thorough microscopical study of the entire gauge-length within a reasonable time. For microscopical examination and microhardness testing, the deformed bars were ground down to an axial plane and then polished and etched electrolytically. The tester of Reichert, Wien, served to measure the microhardness. The constant load was 25g with the chromium-nickel steel and 5g with the aluminium alloy. So, in the mean, there was achieved a 12 microns diagonal of the impression.

The experiments led to the following essential results and conclusions:

1. Microhardness measurement is found to be insensitive for detecting small work-hardening differences, as they may exist between different localities within a microstructure (e.g., crystal centre *versus* boundary). The deviation of values caused by focusing the microscope and centering the graticule in the microscope eye-piece when measuring the hardness impression—the only deviation to be easily determined by experiment—is about  $\pm 3$  per cent for the diagonal length and  $\pm 6$  per cent for the hardness number. Only by statistical analysis of a great many of microhardness measurements one may get a definite information.

2. Such a statistical analysis has shown that in the deformed chromium-nickel steel as well as in the stretched aluminum-magnesium alloy there is no crystal boundary hardening perceptible by microhardness measurements.

That hardening being the backbone of the already mentioned hypothesis by Dehlinger,<sup>1</sup> this latter seems not to describe adequately the natural phenomenon of polycrystalline strength, if work-hardening is understood to be detectable by hardness measurement.

3. Nevertheless, the general drift of Vickers hardness along a straight line, as revealed by Boas and Hargreaves,<sup>2</sup> can be confirmed by these microhardness measurements, in spite of a different experimental arrangement: There is a steady increase or decrease of hardness when following a crystal's diameter and, moreover, some connection of the work-hardening extends between neighbouring crystals.

4. Having in mind the undetermined significance of hardness values with regard to the mechanism of deformation on testing, particular care must be taken when making inferences from the results reported here, as well as from any other hardness measurements.

A detailed description in German of the work, from which a version of main topics has been given here, is published elsewhere.<sup>3</sup>

H. E. TUCHSCHMID

Swiss Federal Institute of Technology  
Laboratory for Testing Materials and Research  
Zurich, Switzerland

#### References

1. U. Dehlinger, Z. Metallk. **34**, 197 (1942).
2. W. Boas and M. E. Hargreaves, Proc. Roy. Soc. **A193**, 89 (1948).
3. H. E. Tuschmid, Untersuchung der Kristallgrenzen in verformten Metallen, insbesondere durch Mikrohärtemessungen. Solothurn: Vogt-Schild. Thesis, Swiss Federal Institute of Technology, Zurich. Also: Schweiz. Arch. angew. Wiss. Techn. **20** (1954) (in press).

\* Received July 14, 1954.

## SOME CURRENT PAPERS IN OTHER JOURNALS

### Acta Crystallographica, Vol. 7

Part 12, December, 1954 (Partial Contents).

The crystal structure of  $WAl_{12}$ ,  $MoAl_{12}$  and  $(Mn, Cr)Al_{12}$ . J. Adam and J. B. Rich.

A fast digital computer for Fourier operations. J. Monteath Robertson.

The diffraction of X-rays by a cylindrical lattice. I. E. J. W. Whittaker.

The geometrical basis of crystal chemistry. Part 3. A. F. Wells.

The geometrical basis of crystal chemistry. Part 4. A. F. Wells.

The determination of the crystal structure of the  $\sigma$ -phase in the iron-chromium and iron-molybdenum systems. G. Bergman and D. P. Shoemaker.

### Acta Crystallographica, Vol. 8

Part 1, January, 1955 (Partial Contents).

The theory of sign relations between structure factors. W. Cochran and M. M. Woolfson.

Some observations on the probability distribution of X-ray intensities. A. Hargreaves.

The rhodium-germanium system. I. The crystal structures of  $Rh_2Ge$ ,  $Rh_3Ge_2$  and  $RhGe$ . S. Geller.

The structure of titanium oxydifluoride. K. Vorres and J. Donohue

The production of fibre diagrams with the optical diffraction spectrometer. A. R. Stokes.

The geometrical basis of crystal chemistry. Part 5. A. F. Wells.

Unit-cell dimensions of lithium fluoride made from  $Li^6$  and  $Li^7$ . J. Thewlis.

The structure of  $T(AlFeBe)$ . P. J. Black.

The structure of  $FeAl_3$ . I. P. J. Black.

On the relations between structure and morphology of crystals. I. P. Hartman and W. G. Perdok.

Fourier syntheses of electron-diffraction data. H. Viervoll.

$\beta$ -uranium. J. Thewlis and H. Steeple.

A one-dimensional integrating method for estimating the intensities on upper-level equi-inclination Weissenberg photographs. E. Stanley.

Re-investigation of the crystal structure of  $CsI_3$ . H. A. Tasman and K. H. Boswijk.

The symmetry of the normal equations for least squares. D. M. Burns and J. Iball.

On the use of slope and curvature maps in refinement of crystal structures. E. L. Eichhorn.

### Archiv für das Eisenhüttenwesen

Heft 11/12, (November/Dezember, 1954).

Untersuchungsergebnisse alter Rennfeuerschlacken. W. Oelsen und E. Schürmann.

Verschlacken von Titan aus Stahlschmelzen im sauren und basischen Hochfrequenzofen unter verschiedenen Schlacken. P. Bardenheuer und W. A. Fischer.

Die elektrische Leitfähigkeit der Schlacken im festen und flüssigen Zustand. H. Hofmann und B. Marinček.

Der Angriff eisengesättigter Zinkschmelzen auf siliziumhaltiges Eisen. D. Horstmann.

Toleranzen und Fehler bei der Temperaturmessung mit Thermoelementen. K. Guthmann.

Die Titration mit Hochfrequenz. K. Cruse.

Das Dämpfungsverhalten von gerecktem technischem Eisen. W. Köster, L. Bangert und R. Hahn.

Einfluss von Wechselbeanspruchungen auf Diffusions- und Ausscheidungsvorgänge in unlegierten Stählen. H. Schenck und E. Schmidtman.

Zugversuche an sehr langen Proben. W. Jäniche und W. Puzicha.

Der Kraftverlauf während der Einschnürung der Zugprobe. A. Krisch.

Zur Frage des Auftretens von  $Ti_2Fe$ . W. Gruhl und D. Ammann.

Die Insilizierung von Stahl als Oberflächenschutz. Die Insilizierung über flüchtige Halogenverbindungen. E. Fitzer.

Anwendung der Zephirolätzung bei Untersuchungen über Anlassversprödung, Alterungsversprödung und Spannungskorrosion von Stählen. H. K. Görlich, E. Koerfer, G. Obelode und H. Schenck.

Atomistische Vorstellungen über die Vorgänge bei der Verformung und Rekristallisation von Metallen. A. Schäfer.

### Journal of the Chemical Society

December, 1954 (Partial Contents).

The preparation of polonium metal and polonium dioxide. K. W. Bagnall and R. W. M. D'Eye.

Mixed liquid crystals. J. S. Dave and M. J. S. Dewar.

January, 1955 (Partial Contents).

The production of active solids by thermal decomposition. Part V. The sintering of active magnesium oxide. S. J. Gregg, R. K. Packer and K. H. Wheatley.

The production of active solids by thermal decomposition. Part VI. The calcination of magnesium hydroxide. S. J. Gregg and R. K. Packer.

The heat capacity of nickel carbonyl and the thermodynamics of its formation from nickel and carbon monoxide. J. E. Spice, L. A. K. Staveley and G. A. Harrow.

The extraction and purification of scandium. E. C. Vickery.

### Journal of the Institute of Metals, Vol. 83

Part 5, January, 1955

The effect of internal oxidation on the fatigue properties of copper alloys. J. W. Martin and G. C. Smith.

An apparatus for electropolishing specimens for metallographic examination. E. C. Sykes, V. J. Haddrell, H. R. Haines and B. W. Mott.

Surface nucleation in the recrystallization of aluminium single crystals. C. D. Graham, Jr. and R. Maddin.

The influence of sub-structure on the slip observed in pure aluminium and some aluminium alloys when subjected to fatigue stresses. P. J. E. Forsyth and C. A. Stubbington.

The constitution of aluminium-rich alloys containing copper, manganese, and silicon. A. P. Bagchi and H. J. Axon.

A study of the behaviour of titanium-rich alloys in the titanium-tin and titanium-aluminium systems. A. D. McQuillan.

An attempt to separate titanium from oxygen by vacuum sublimation, and some measurements of evaporation rates. A. B. Osborn.

The solubility of vanadium in gold. D. Summers-Smith.

A note on the influence of grain-boundary flow in the creep of a lead-0.5% tin alloy. P. Brock.

### Journal of Metals, Vol. 7

January, 1955 (Partial Contents).

Structure and properties of Ti-C alloys. H. R. Ogden, R. I. Jaffee, F. C. Holden.

Solution rate of solid aluminum in molten Al-Si alloy. C. M. Craighead, E. W. Cawthorne and R. I. Jaffee.

Mobilities in diffusion in alpha-brass. G. T. Horne and R. F. Mehl.

Energy stored during fatigue of copper. L. M. Clarebrough, M. E. Hargreaves, A. K. Head and G. W. West.

Titanium-lead system. P. Farrar and H. Margolin.

Effect of alpha-solutes on the heat-treatment response of Ti-Mn Alloys. H. R. Ogden, F. C. Holden and R. I. Jaffee.

Selected isothermal sections in the titanium-rich corners of the systems Ti-Fe-O, Ti-Cr-O, and Ti-Ni-O. W. Rostoker.

Heat treatment and mechanical properties of Ti-Cu alloys. F. C.



Holden, A. A. Watts, H. R. Ogden and R. I. Jaffee.  
 Autoradiography determination of the self-diffusion of silver. H. Krueger and H. N. Hersh.  
 Chromium-rich portion of the chromium-nickel phase diagram. C. Stein and N. J. Grant.  
 Stress analysis of a single crystal in pure torsion. N. Brown.  
 Solubility and decomposition pressures of hydrogen in alpha-zirconium. E. A. Gulbransen and K. F. Andrew.  
 X-ray crystallographic data on  $As_2Te_3$ . J. Singer and C. W. Spencer.  
 Metallographic study of equilibrium relationships in 3S aluminum alloy. P. R. Sperry.  
 Influence of additives in the production of high coercivity ultra-fine iron powder. E. W. Stewart, G. P. Conard, II, J. F. Libsch.  
 Resistance sintering under pressure. F. V. Lenel.  
 Physical and mechanical properties of rhenium. C. T. Sims, C. M. Craighead and R. I. Jaffee.  
 Effects of tensile stress on the austenite to ferrite transformation in eutectoid steel. L. S. Birks and E. F. Bailey.  
 Some characteristics of the isothermal martensitic transformation. C. H. Shih, B. L. Averbach and M. Cohen.  
 Melting point of germanium and constitution of some Ge-Ga alloys. E. S. Greiner and P. Breidt, Jr.  
 Contribution of crystal structure to the hardness of metals. W. Chubb.  
 Thermal conductivity of uranium and several uranium alloys. J. L. Weeks.  
 Study of the effect of boron on the decomposition of austenite. C. R. Simcoe, A. R. Elsea and G. K. Manning.  
 Dispersion hardening of copper-chromium alloys, W. R. Hibbard, Jr. and E. W. Hart.  
 Plastic deformation of germanium and silicon by torsion. E. S. Greiner.  
 Purification of gallium by zone-refining. D. P. Detwiler and W. M. Fox.  
 Study of a new mode of plastic deformation in zinc crystals. J. J. Gilman.  
 Isothermal austenite grain growth. H. B. Probst and M. J. Sinott.

#### Revue de Métallurgie 51<sup>e</sup> Année

Numéro 11, Novembre, 1954.

Etude dilatométrique de l'uranium filé. J. Bernard.  
 Recherche d'une méthode nouvelle de déchiffrement des diagrammes de Debye-Scherrer. G. A. Homès et J. Gouzou.

Contribution à l'étude de la recristallisation de l'uranium dans le domaine  $\alpha$ . Données caractéristiques concernant la recristallisation et la croissance des grains d'uranium  $\alpha$ . M. Englander.  
 Etude de l'effet Kirkendall-Smigelskas dans les couples cuivre-laiton en présence d'impuretés. A. Accary.  
 Méthode de différenciation de  $Cu_2O$  et  $Cu_2S$  sur les micrographies de cuivre. L. A. Boschi, H. Destaillets, J. A. Sabato, J. M. Valls et A. Varsavsky.  
 Etude de l'influence du revenu sur la microstructure et les propriétés mécaniques à froid et à chaud d'aciers au chrome-molybdène. A. Constant et G. Delbart.  
 Signal d'arrêt de l'opération Thomas. Mesure et enregistrement de la température vraie de la flamme du convertisseur. P. LeRoy, J. Galey et M. Denis.

Numéro 12, Décembre, 1954.

Ruptures fragiles et résistance suivant l'épaisseur des aciers. W. Soete.  
 Résultats pratiques de l'application de l'analyse spectrale en métallurgie. V. Mathien, A. Hans, B. Rosen et A. Hannick.  
 Sur quelques aspects de l'oxydation du fer à haute température et sous basse pression d'oxygène permettant l'introduction d'une méthode d'étude micrographique de la structure du fer  $\gamma$ . J. Bardolle.  
 Sur la polygonisation du fer très pur. J. Talbot, C. de Beaulieu et G. Chaudron.  
 Commission d'étude des métaux à chaud de l'IRSID. Propriétés à chaud des aciers à 0,6% Cr et 0,6% Mo, 2,25% Cr et 1% Mo, 22% Cr et 18% Ni. G. Delbart et A. Constant.  
 Etude statistique de la dispersion de l'essai MICUM et de l'essai IRSID des cokes. J. Ulmo (Mlle), Ch. G. Thibaut, P. Vigneron et B. Menuet-Guilbaud.

#### Erratum

Dans l'appendice dû à Madame A. R. Weill et faisant suite aux Mémoires de Mr. P. A. Jacquet (Acta Met. 2, 752-796 (1954) et intitulé "Examens qualitatifs aux rayons X de la polygonisation d'une solution solide cuivre-zinc à 65/35," nous nous excusons d'une erreur matérielle qui a eu pour effet d'intervertir les secteurs (a) et (d) de la figure 5.

## APPLICATION OF GIBBS-DUHEM EQUATIONS TO TERNARY SYSTEMS\*

R. SCHUHMAN, JR.†

A new method is presented for calculating activities, activity coefficients, and other partial molal properties for two components of a ternary system from experimental measurements of this property for the third component. A quantitative relation is derived between tangent intercepts of isoactivity curves for the various components, and this relation is the basis of a graphical procedure of constructing isoactivity curves. The derived relations are used to calculate activities of  $\text{SiO}_2$ ,  $\text{FeO}$ , and  $\text{O}$  in ternary iron silicate slags.

### APPLICATION DES ÉQUATIONS DE GIBBS-DUHEM AUX SYSTÈMES TERNAIRES

L'auteur propose une nouvelle méthode pour calculer l'activité, le coefficient d'activité et autres caractéristiques de deux des constituants d'un système ternaire, à partir des mesures de cette caractéristique pour le troisième constituant. Une relation quantitative déterminée par la tangente aux courbes d'isoactivité des différents constituants est proposée qui est la base d'une méthode graphique de construction des courbes d'isoactivité. Application au calcul de l'activité de  $\text{SiO}_2$ ,  $\text{FeO}$  et  $\text{O}$  dans un silicate de fer.

### ÜBER DIE ANWENDUNG DER GIBBS-DUHEMSCHEN GLEICHUNG AUF TERNÄRE SYSTEME

Zur Berechnung der Aktivitäten, Aktivitätskoeffizienten und anderer partieller molarer Größen zweier Komponenten eines ternären Systems auf Grund experimenteller Bestimmungen dieser Eigenschaften an der dritten Komponente, wird eine neue Methode vorgeschlagen. Aus den Achsenabschnitten der Tangenten an die Kurven gleicher Aktivität für die verschiedenen Komponenten wird eine quantitative Beziehung abgeleitet. Diese Beziehung dient als Grundlage für ein grafisches Verfahren zur Konstruktion von Kurven gleicher Aktivität. Die abgeleiteten Beziehungen werden zur Berechnung der Aktivitäten von  $\text{SiO}_2$ ,  $\text{FeO}$  und  $\text{O}$  in ternären Eisen-Silikat Schlacken herangezogen.

The Gibbs-Duhem relation is a fundamental cornerstone of the thermodynamic study of binary solutions and is particularly useful for calculating activity or partial molal free energy of one component from experimental data on activity or partial molal free energy of the other component. Details of various calculation procedures were summarized recently by Darken and Gurry,<sup>1</sup> and instances of these calculations can be found many places in metallurgical literature (see, for example, Chipman<sup>2</sup> and Elliott and Chipman<sup>3</sup>).

Darken<sup>4</sup> recently showed how the Gibbs-Duhem equation can be applied to ternary systems, to calculate partial molal free energies of two components from experimental data on the partial molal free energy of the third component. Wagner<sup>5</sup> has given another solution of the same problem. These solutions of the Gibbs-Duhem equation for ternary systems have been applied successfully to a number of ternary systems of metallurgical interest,<sup>6,7,8</sup> and have paved the way for further researches and thermodynamic studies on the many ternary systems which are important in metallurgy.

The principal avenue of study of ternary systems in the past has been phase diagrams. The application of the Phase Rule to ternary diagrams has been studied in some detail<sup>9,10</sup> and many diagrams have been determined experimentally. However, little has been done to develop quantitative relationships between the phase equilibrium diagrams and the thermodynamic

properties of ternary systems. In principle, however, it should be possible to utilize phase diagram data in calculating certain thermodynamic properties of ternary systems just as is done already with binary diagrams.

This paper gives another general solution of the Gibbs-Duhem equation for ternary systems, which is in somewhat simpler form than the previous solutions of Darken and of Wagner and should be easier to use for some types of calculations. This new derivation leads further to the demonstration of an interesting geometric relationship of isoactivity curves plotted on the usual composition triangle. This relationship seems potentially useful in the construction and study of ternary diagrams, even in the absence of direct experimental activity data. The original stimulus for this theoretical study came from attempts to interpret experimental activity data and phase diagrams on various ternary slag systems, on Cu-Fe-S mattes, on gas solubility in alloys, and on steel deoxidation equilibria. Activity calculations for ternary slags composed of  $\text{FeO}$ ,  $\text{Fe}_2\text{O}_3$ , and  $\text{SiO}_2$  are presented to illustrate the application of some of the derived relationships.

### INTEGRATIONS OF GIBBS-DUHEM EQUATIONS

The Gibbs-Duhem equation for a system of three components at constant pressure and constant temperature may be written

$$n_1 d\mu_1 + n_2 d\mu_2 + n_3 d\mu_3 = 0 \quad (1)$$

in which  $n_1$ ,  $n_2$ , and  $n_3$  represent moles of components 1, 2, and 3, respectively, and  $\mu_1$ ,  $\mu_2$ , and  $\mu_3$  represent the chemical potentials or partial molal free energies of the

\* Received September 2, 1954.

† School of Chemical and Metallurgical Engineering, Purdue University, W. Lafayette, Indiana.

respective components. To maintain simplicity in the mathematical presentation, all subsequent derivations will be expressed in terms of the three chemical potentials. Most of the subsequent equations can be expressed conveniently in terms of activities ( $a_i$ ) by substituting  $d \log_{10} a_i$  for  $d\mu_i$ , since  $d\mu_i = RT d \ln a_i$  and the constant  $2.303RT$  cancels out of the equations. Also, many of the subsequent derivations are valid for other partial molal properties and for activity coefficients ( $\gamma_i$ ) using the substitution of  $d \log \gamma_i$  for  $d\mu_i$ .

Choice of components will depend on convenience and on the nature of the available experimental data. In most cases, components 1, 2, and 3 will be three chemical elements but for some purposes calculations are much simplified by choosing real or unreal compounds as components (e.g., FeO, Fe<sub>2</sub>O<sub>3</sub>, and SiO<sub>2</sub> instead of Fe, Si, and O). Such choices have no effect on the validity of the Gibbs-Duhem equation if the proper internal consistency is maintained in the calculations.

Dividing Eq. (1) by  $dn_2$  and considering a path along which  $\mu_1$  and  $n_3$  are constant,

$$n_2 \left( \frac{\partial \mu_2}{\partial n_2} \right)_{\mu_1, n_3} + n_3 \left( \frac{\partial \mu_3}{\partial n_2} \right)_{\mu_1, n_3} = 0. \quad (2)$$

Differentiating Eq. (2) with respect to  $\mu_1$ , with  $n_2$  and  $n_3$  constant,

$$n_2 \left( \frac{\partial^2 \mu_2}{\partial \mu_1 \partial n_2} \right)_{n_3} + n_3 \left( \frac{\partial^2 \mu_3}{\partial \mu_1 \partial n_2} \right)_{n_3} = 0. \quad (3)$$

This equation will be combined with another equation derived from Eq. (1) by a different procedure, as follows: First, dividing Eq. (1) by  $d\mu_1$  and considering a path along which  $n_2$  and  $n_3$  are constant,

$$n_1 + n_2 \left( \frac{\partial \mu_2}{\partial \mu_1} \right)_{n_2, n_3} + n_3 \left( \frac{\partial \mu_3}{\partial \mu_1} \right)_{n_2, n_3} = 0. \quad (4)$$

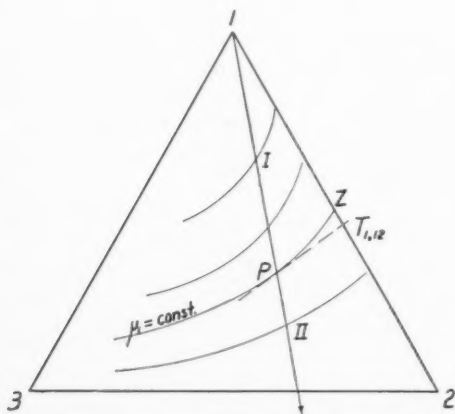


FIG. 1. Ternary isotherm showing typical integration path  $I \rightarrow II$  and tangent intercept procedure of determining  $(\partial n_1 / \partial n_2)_{\mu_1, n_3}$  from isoactivity curves for component 1.

Now, differentiating Eq. (4) with respect to  $n_2$ , with  $\mu_1$  and  $n_3$  constant,

$$\left( \frac{\partial n_1}{\partial n_2} \right)_{\mu_1, n_3} + \left( \frac{\partial \mu_2}{\partial \mu_1} \right)_{n_2, n_3} + n_2 \left( \frac{\partial^2 \mu_2}{\partial n_2 \partial \mu_1} \right)_{n_3} + n_3 \left( \frac{\partial^2 \mu_3}{\partial n_2 \partial \mu_1} \right)_{n_3} = 0. \quad (5)$$

Comparison of Eqs. (3) and (5) gives the following important equation:\*

$$\left( \frac{\partial \mu_2}{\partial \mu_1} \right)_{n_2, n_3} = - \left( \frac{\partial n_1}{\partial n_2} \right)_{\mu_1, n_3}. \quad (6)$$

Equation (6) is the principal form of the Gibbs-Duhem equation to be discussed in this paper, and thus needs to be examined rather carefully.

Equation (6) can be integrated through a one-phase field along a path of constant  $n_2$  and  $n_3$ , which means a compositional path of constant ratio  $n_2/n_3$ . On a composition triangle, such a path follows a straight line which passes through the corner corresponding to pure component 1. Both Darken's and Wagner's integrations make use of this same kind of compositional path. The integration of Eq. (6) can be expressed:

$$\left[ \mu_2^{II} - \mu_2^I - \int_{\mu_1^I}^{\mu_1^{II}} \left( \frac{\partial n_1}{\partial n_2} \right)_{\mu_1, n_3} d\mu_1 \right]_{n_2/n_3}, \quad (7)$$

in which the integration path extends from point  $I$  to point  $II$  in the ternary isotherm, at which points the  $\mu$ 's have the values corresponding to the respective superscripts (see Fig. 1). This integration can be carried out to evaluate  $\mu_2^{II}$  when  $\mu_2^I$  at the starting point is known and when experimental data on  $\mu_1$  are sufficiently complete that we can evaluate the partial derivative,  $(\partial n_1 / \partial n_2)_{\mu_1, n_3}$  as a function of  $\mu_1$  along the entire path of integration.

The partial derivative appearing in the right-hand terms of Eq. (6) and Eq. (7) is a particularly interesting type of variable which plays several important roles in subsequent derivations, and thus deserves close ex-

\* An alternative derivation goes back to the definition of partial molal quantities and to the principle that order of differentiation is immaterial.

$$\mu_1 = \left( \frac{\partial F}{\partial n_1} \right)_{n_2, n_3}; \quad \mu_2 = \left( \frac{\partial F}{\partial n_2} \right)_{n_1, n_3} \quad (a)$$

$$\left( \frac{\partial \mu_2}{\partial n_1} \right)_{n_2, n_3} = \left( \frac{\partial^2 F}{\partial n_1 \partial n_2} \right)_{n_3} = \left( \frac{\partial^2 F}{\partial n_2 \partial n_1} \right)_{n_3} = \left( \frac{\partial \mu_1}{\partial n_2} \right)_{n_1, n_3} \quad (b)$$

Also,

$$\left( \frac{\partial \mu_1}{\partial n_2} \right)_{n_1, n_3} = - \left( \frac{\partial \mu_1}{\partial n_1} \right)_{n_2, n_3} \left( \frac{\partial n_1}{\partial n_2} \right)_{\mu_1, n_3} \quad (c)$$

and

$$\left( \frac{\partial \mu_2}{\partial n_1} \right)_{n_2, n_3} = \left( \frac{\partial \mu_2}{\partial \mu_1} \right)_{n_2, n_3} \left( \frac{\partial \mu_1}{\partial n_1} \right)_{n_2, n_3} \quad (d)$$

Substituting (c) and (d) in (b), and simplifying, we obtain Eq. 6.

amination. In the first place,  $(\partial n_1/\partial n_2)_{\mu_1, n_3}$  is a quantity which describes the direction of the isoactivity curve for component 1 ( $\mu_1$  constant), or more accurately the direction of the tangent to the isoactivity curve at a given point. In nonmathematical language, it is the composition of a binary mixture of 1 and 2, expressed as the ratio of moles of component 1 to moles of component 2, which can be added to the system without changing the activity of component 1. In other words, this partial derivative tells the direction in which the composition can be changed without affecting  $\mu_1$ .

Figure 1 illustrates the graphical determination of  $(\partial n_1/\partial n_2)_{\mu_1, n_3}$  for a given point  $P$  in the path  $I-II$ . First, the available data on  $\mu_1$  as a function of composition are plotted on the composition triangle in the form of isoactivity curves along which  $\mu_1$  is constant. Then at  $P$ , a tangent is drawn to the isoactivity curve and is extended to intersect the 1—2 side of the triangle. The point of interception,  $T_{1,12}$ , represents the composition of a binary mixture of 1 and 2 which can be added to the solution represented at  $P$  in infinitesimal amount without changing  $\mu_1$ . The composition at  $T_{1,12}$  is read from the composition scale along 1—2 and converted to a mole ratio of component 1 to component 2, which then is  $(\partial n_1/\partial n_2)_{\mu_1, n_3}$  for point  $P$ . For convenience, we may label this general graphical procedure of evaluating partials of the form  $(\partial n_i/\partial n_j)_{n_k}$  the "tangent intercept procedure." In making a complete Gibbs-Duhem integration along a path such as  $I-II$  in Fig. 1, the operations of the tangent intercept procedure must be repeated at a sufficient number of points along  $I-II$  to establish the curve of  $(\partial n_1/\partial n_2)_{\mu_1, n_3}$  against  $\mu_1$ . The integral in Eq. (7) is simply the area under this curve as  $\mu_1$  varies from  $\mu_1^I$  to  $\mu_1^{II}$ .

For negative values of  $(\partial n_1/\partial n_2)_{\mu_1, n_3}$ , the intercept falls on an extension of the side 1—2 outside of the composition triangle, as shown in Fig. 2. Thus, determination of negative tangent intercepts requires linear extension of the weight % scales either in a positive direction above 100 percent or in a negative direction below 0 per cent. Point  $T_{1,12}'$  in Fig. 2 thus corresponds to the imaginary composition of -40 per cent component 1 and +140 per cent component 2. If the respective molecular weights of components 1 and 2 were say 25 and 50, then we would find

$$\left(\frac{\partial n_1}{\partial n_2}\right)_{\mu_1, n_3} = \frac{-40/25}{+140/50} = -0.57.$$

This means that for each mole of component 2 added to a large quantity of the solution  $P'$ , we would have to remove 0.57 mol of component 1 in order to maintain  $\mu_1$  constant.

An alternative to the tangent intercept procedure is to plot the isoactivity curves on a right-angled diagram, using  $\alpha = n_1/n_3$  and  $\beta = n_2/n_3$  as composition coordi-

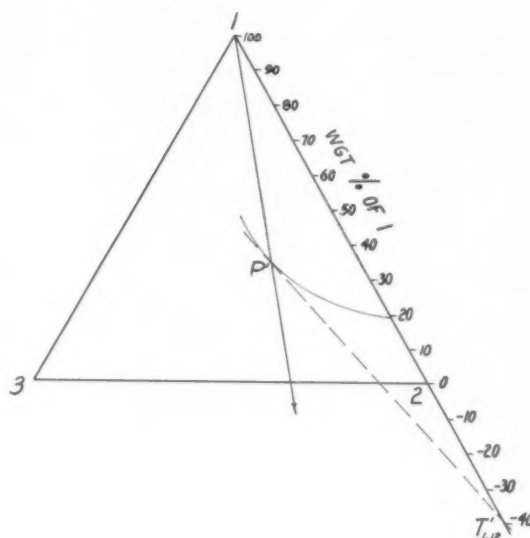


FIG. 2. Construction for negative tangent intercepts.

nates. On such a diagram,  $(\partial n_1/\partial n_2)_{\mu_1, n_3} = (\partial \alpha/\partial \beta)_{\mu_1}$  and thus is found as the slope of the isoactivity curve on this type of plot.

The special case of  $n_3=0$  reduces Eqs. (6) and (7) to the familiar Gibbs-Duhem equations for binary systems:

$$\frac{d\mu_2}{d\mu_1} = -\frac{n_1}{n_2} \quad \text{and} \quad \mu_2^{II} - \mu_2^I = \int_{\mu_1^I}^{\mu_1^{II}} \frac{n_1}{n_2} d\mu_1. \quad (8)$$

Also, referring to Fig. 1, it can be seen that as  $n_3$  approaches zero and as the integration path approaches the binary system 1—2, the tangent intercept  $T_{1,12}$  will approach the intercept  $Z$  of the isoactivity curve. That is,  $(\partial n_1/\partial n_2)_{\mu_1, n_3} \rightarrow n_1/n_2$  as  $n_3 \rightarrow 0$ . Thus, the proposed Gibbs-Duhem equation for ternary systems is mathematically very similar to the ordinary binary form, the principal difference being the use of an  $n_1/n_2$  ratio found as a tangent intercept instead of an  $n_1/n_2$  ratio corresponding directly to the solution composition.

Obviously a number of other equations of the same form as Eq. (6) can be derived, simply by interchanging the relative roles of the three components in the derivation. For example, if we have complete activity data on component 1, but now wish to evaluate  $\mu_3$  we can use

$$\left(\frac{\partial \mu_3}{\partial \mu_1}\right)_{n_2, n_3} = -\left(\frac{\partial n_1}{\partial n_3}\right)_{\mu_1, n_2}. \quad (9)$$

That is, the integration to determine  $\mu_3$  is just the same as that to determine  $\mu_2$  except that the tangent intercept ( $T_{1,13}$ ) is measured on the 1—3 side of the triangle instead of on the 1—2 side.

*Integration in Two-Phase Regions.* Equations (6) and (7), the derived Gibbs-Duhem equation and its integration, are not limited to single-phase regions of the ternary isotherm. In two-phase regions, the calculations



of  $\mu_2$  and  $\mu_3$  from experimental data on  $\mu_1$  can be made according to Eq. (7), and the graphical intercept procedure can still be used to find the necessary values of the partial derivatives  $(\partial n_1/\partial n_2)_{\mu_1, n_3}$  and  $(\partial n_1/\partial n_3)_{\mu_1, n_2}$ . However, for the two-phase region the intercepts of the tie-lines are used instead of the intercepts of tangents to the isoactivity curves. In principle, of course, any tie-line in a two-phase region of a ternary diagram is an isoactivity "curve" for all three components.

Furthermore, the restriction that the integration must follow a line of constant  $n_2/n_3$  is unnecessary in a two-phase region, so that the integration indicated by Eq. (7) is readily carried out over the entire region. All that is needed is the analytical data for the tie lines and experimental values of  $\mu_1$  for a sufficient number of tie lines. As a result, the presence of a two-phase region simplifies the Gibbs-Duhem integration for a ternary system.

When the Gibbs-Duhem integration follows a composition path of constant  $n_2/n_3$  extending from a one-phase region into a two-phase region, an abrupt discontinuity or step will be found in the curve of  $(\partial n_1/\partial n_2)_{\mu_1, n_3}$  or  $(\partial n_1/\partial n_3)_{\mu_1, n_2}$  versus  $\mu_1$ , corresponding to the abrupt change in direction of the isoactivity curve at the boundary of the two-phase region.

If one of the two phases has essentially constant or stoichiometric composition, the same integration procedure can be retained. In this case the tie-lines radiate from the point corresponding to the phase of constant composition. However, a simpler procedure in two-phase regions of this kind may be to consider the phase of constant composition as one of the components. If the composition of the system is calculated consistently on the basis that component 3 is the phase of fixed composition,  $\mu_3$  is constant and  $d\mu_3=0$  throughout the two-phase region so that the Gibbs-Duhem equation is reduced to that for a binary system of components 1 and 2. That is,  $(\partial n_1/\partial n_2)_{\mu_1, n_3}$  becomes  $n_1/n_2$  and can be obtained directly from the composition of the saturated solution without using the tangent intercept procedure. This procedure has been used for Gibbs-Duhem integrations along Fe- and  $\text{SiO}_2$ -saturation curves in the  $\text{FeO-Fe}_2\text{O}_3\text{-SiO}_2$  system.<sup>11,12</sup>

**Inherent Limitations.** The Gibbs-Duhem integrations for ternary systems involve the same inherent difficulties as the binary integrations when the integration path in a one-phase region approaches the composition of the pure component. Thus, even with complete and reasonably accurate activity data for component 1 over the entire diagram of a homogeneous ternary system, calculations of  $\mu_2$  and  $\mu_3$  taking the pure components as standard states may prove inaccurate and unsatisfactory, or may require assumptions as to the behavior of the solution as the composition approaches that of pure component 1. This limitation is compounded by the fact that even with complete activity data on component 1 throughout a single-phase system, the Gibbs-

Duhem equation can be integrated only along composition paths of constant  $n_2/n_3$ , which of course intersect each other only at the corner of the diagram corresponding to pure component 1. Thus, if we wish to find  $\mu_2$  in the interior of the diagram, based on  $\mu_2=0$  for pure component 2, we must first perform a binary integration along the binary system 2→1 to find the behavior of 2 in infinitely dilute solution in 1 and then we must perform a second integration from this infinitely dilute solution along a line of constant  $n_2/n_3$  to the desired point. Such a two-step path of integration thus has to go into and then come out of the composition region near pure 1 where  $n_1/n_2$  and  $n_1/n_3$  approach  $\infty$  and the Gibbs-Duhem integrations become uncertain.

The above-discussed difficulties are eliminated or greatly mitigated in calculations on heterogeneous ternary systems, where the paths of integration intersect two- and three-phase regions on the isotherm. In such systems, standard states other than the pure components can sometimes be used without reducing the value of the calculations for practical purposes. Calculations of this kind are illustrated in the last section of this paper.

**Modified Integrations.** Darken and Gurry<sup>1</sup> have described improved Gibbs-Duhem integration procedures for binary systems which permit more accurate graphical evaluations, especially at the extremes of the composition range. These procedures are based on the Gibbs-Duhem equation for the activity coefficients. Correspondingly, Eqs. (6) and (7) for ternary systems can be rewritten in terms of activity coefficients as follows:

$$\left(\frac{\partial \log \gamma_2}{\partial \log \gamma_1}\right)_{n_2, n_3} = -\left(\frac{\partial n_1}{\partial n_2}\right)_{\gamma_1, n_3} \quad (10)$$

$$\left[\log \gamma_2^{II} = \log \gamma_2^I - \int_{\log \gamma_1^I}^{\log \gamma_1^{II}} \left(\frac{\partial n_1}{\partial n_2}\right)_{\gamma_1, n_3} d \log \gamma_1\right]_{n_2/n_3} \quad (11)$$

Evaluation of  $(\partial n_1/\partial n_2)_{\gamma_1, n_3}$  as a function of  $\log \gamma_1$  for the graphical integration requires that the tangent intercept procedure be applied to curves of constant activity coefficient on the composition triangle.

A further improvement is obtained through the following integration of Eq. (10):

$$\left\{\log \gamma_2^{II} = \log \gamma_2^I - \left[\alpha y(1-y) + \int y d\alpha\right]_{y^I}^{y^{II}}\right\}_{n_2/n_3} \quad (12)$$

in which

$$y = \frac{1}{1 + \left(\frac{\partial n_1}{\partial n_2}\right)_{\gamma_1, n_3}}$$

$$\alpha = \frac{\log \gamma_1}{y^2} = \log \gamma_1 \left[1 + \left(\frac{\partial n_1}{\partial n_2}\right)_{\gamma_1, n_3}\right]^2$$

Equation (10) simplifies directly to a form recommended by Darken and Gurry for binary systems, if  $n_3=0$  and  $n_1/n_2$  is substituted for the partial derivative  $(\partial n_1/\partial n_2)_{\gamma_1, n_3}$  in the above definitions. Just as in the binary integrations,  $\alpha$  turns out to be a generally well-behaved function over the entire composition range in ternary systems. Moreover, it should be noted that the integration expressed by Eq. (12) is mathematically somewhat similar to the ternary integrations of Darken<sup>4</sup> and of Wagner,<sup>5</sup> although the function  $\alpha$  is defined differently.

*Comparison of Ternary Gibbs-Duhem Integrations.* Whatever Gibbs-Duhem integration is used, Darken's method, Wagner's method, Eq. (7), Eq. (10), or Eq. (12), the calculations for a new system are likely to require a good supply of graph paper, a calculating machine, and a painstaking approach to the study of the data. Careful thought needs to be given in each instance to the accuracy of the experimental data and to the effects of experimental errors on the calculated results.

When relatively complete activity data are available for one component over the entire ternary composition range, the integrations of Darken, of Wagner, and of Eq. (12) appear to be substantially equivalent in accuracy and in amount of mathematical labor. All three require an integration step and differentiation steps (slope or intercept measurements). With Darken's method the integration is performed first and the differentiations second, whereas the reverse order is used in Wagner's method and in Eq. (12). All three take full advantage of the good behavior of  $\alpha$ -functions of the form  $\log \gamma_i/(1-N_i)^2$ .

The integration of Eq. (12) was applied to the data of Elliott and Chipman<sup>6</sup> on the Cd-Pb-Bi system and gave results which seem to be of the same precision as those Elliott and Chipman obtained by the Darken integration. Both methods apparently encountered comparable difficulties in the same composition regions. For example, the close approach of the Cd-Bi binary to ideality makes the calculations of  $\gamma_{Pb}$  from experimental data on  $\gamma_{Bi}$  quite uncertain for solutions low in Pb and high in Bi. This uncertainty appears to be inherent in the experimental data and the Gibbs-Duhem equation, rather than in the methods of integration.

For the various special situations of incomplete data and heterogeneous systems which are encountered, Eqs. (7), (10), and (12) seem simpler and may have some advantages over Darken's and Wagner's equations. These potential advantages stem in large measure from the simplicity of the tangent-intercept procedure carried out on the ternary composition triangle. The FeO-Fe<sub>2</sub>O<sub>3</sub>-SiO<sub>2</sub> system discussed later in this paper and the Cu-Fe-S system recently investigated by Krivsky<sup>13</sup> are illustrative of systems wherein Eq. (7), the simplest integration of all, is entirely adequate.

### GEOMETRIC RELATIONSHIP OF ISOACTIVITY CURVES

Since the Gibbs-Duhem equation shows that the manner in which one chemical potential can vary with composition is closely related to the manner in which the other two chemical potentials vary with composition, it is reasonable to expect that the directions or "slopes" of the three isoactivity curves at a given point must be related in a simple fashion. Such a relationship is readily demonstrated, and, as is shown below, can be expressed as a simple algebraic relationship between tangent intercept values for the three isoactivity curves. This algebraic relationship is the basis for a simple and useful geometric construction which can be used to draw isoactivity curves for one component when the directions of those of the other two components are known.

Any tangent to an isoactivity curve will have three intercepts, one with each edge of the composition triangle or its extension. These three intercepts for component 1 ( $T_{1,12}$ ,  $T_{1,13}$ , and  $T_{1,23}$ )\* are numerically related, as follows:

$$\left(\frac{\partial n_1}{\partial n_2}\right)_{\mu_1, n_3} = -\left(\frac{\partial n_1}{\partial n_3}\right)_{\mu_1, n_2} \left(\frac{\partial n_3}{\partial n_2}\right)_{\mu_1, n_1} \quad (13)$$

The negative sign in Eq. (13) reflects the fact that a tangent to an isoactivity curve will have positive intercepts on two sides of the triangle but will have a negative intercept on the extension of the third side of the triangle. Similar relations can be written for the three intercepts of the  $\mu_2$ -tangent ( $T_{2,12}$ ,  $T_{2,13}$ , and  $T_{2,23}$ )\* and for those of the  $\mu_3$ -tangent ( $T_{3,12}$ ,  $T_{3,13}$ , and  $T_{3,23}$ )\*. Also an equation of the same form is a necessary condition for the intercepts of any straight line drawn through the composition triangle:

$$\left[\left(\frac{\partial n_1}{\partial n_2}\right)_{n_3} = -\left(\frac{\partial n_1}{\partial n_3}\right)_{n_2} \left(\frac{\partial n_3}{\partial n_2}\right)_{n_1}\right]_{\text{straight line}} \quad (14)$$

Sometimes it is easier to measure one tangent intercept accurately and calculate the others, using the coordinates of the point of tangency in the following relations:

$$\left(\frac{\partial n_1}{\partial n_3}\right)_{\mu_1, n_2} = \frac{n_1}{n_3} - \frac{n_2}{n_3} \left(\frac{\partial n_1}{\partial n_2}\right)_{\mu_1, n_3} \quad (15)$$

$$\left(\frac{\partial n_2}{\partial n_3}\right)_{\mu_1, n_1} = \frac{n_2}{n_3} - \frac{n_1}{n_3} \left(\frac{\partial n_2}{\partial n_1}\right)_{\mu_1, n_3} \quad (16)$$

The following sequence of equations is a derivation of the cross relation between three tangent intercepts for

\* The tangent intercepts are conveniently designated by subscripts on  $T$ , the first subscript indicating the isoactivity curve and the pair after the comma indicating the intercepting side of the composition triangle.

the three components:

$$\left(\frac{\partial n_3}{\partial n_2}\right)_{\mu_1, n_1}, \left(\frac{\partial n_1}{\partial n_3}\right)_{\mu_2, n_2} \text{ and, } \left(\frac{\partial n_1}{\partial n_2}\right)_{\mu_3, n_3},$$

corresponding to  $T_{1,23}$ ,  $T_{2,13}$ , and  $T_{3,12}$ , respectively. This particular intercept for each component is the intercept of the tangent with the side of the triangle opposite the corner for the component: e.g.,  $(\partial n_1/\partial n_2)_{\mu_3, n_3}$  or  $T_{3,12}$  is the tangent intercept for component 3 on the 1—2 side of the triangle.

First, three cross-relations are developed, based on the definition of partial molal quantities and on the principle that order of differentiation is immaterial:

$$\mu_i = \left(\frac{\partial F}{\partial n_i}\right)_{n_j, n_k}; \quad \mu_j = \left(\frac{\partial F}{\partial n_j}\right)_{n_i, n_k} \quad (17)$$

$$\left(\frac{\partial \mu_i}{\partial n_j}\right)_{n_i, n_k} = \left(\frac{\partial^2 F}{\partial n_j \partial n_i}\right)_{n_k} = \left(\frac{\partial \mu_j}{\partial n_i}\right)_{n_j, n_k} \quad (18)$$

Therefore,

$$\begin{aligned} \text{(a)} \quad & \left(\frac{\partial \mu_3}{\partial n_2}\right)_{n_1, n_3} = \left(\frac{\partial \mu_2}{\partial n_3}\right)_{n_1, n_2} \\ \text{(b)} \quad & \left(\frac{\partial \mu_1}{\partial n_3}\right)_{n_1, n_2} = \left(\frac{\partial \mu_3}{\partial n_1}\right)_{n_2, n_3} \\ \text{(c)} \quad & \left(\frac{\partial \mu_2}{\partial n_1}\right)_{n_2, n_3} = \left(\frac{\partial \mu_1}{\partial n_2}\right)_{n_1, n_3} \end{aligned} \quad (19)$$

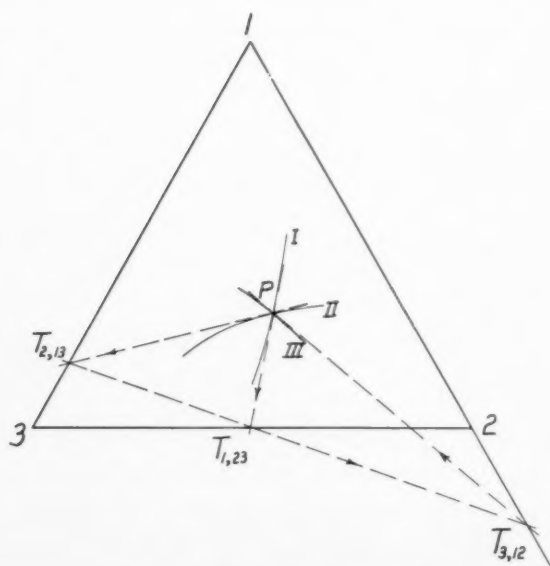


FIG. 3. Geometric relationship of tangent intercepts for three components.

Multiplying all three parts of Eq. (19) together and then rearranging the resulting equation,

$$\frac{\left(\frac{\partial \mu_3}{\partial n_2}\right)_{n_1, n_3} \left(\frac{\partial \mu_2}{\partial n_3}\right)_{n_1, n_2} \left(\frac{\partial \mu_1}{\partial n_2}\right)_{n_1, n_3}}{\left(\frac{\partial \mu_3}{\partial n_1}\right)_{n_2, n_3} \left(\frac{\partial \mu_2}{\partial n_1}\right)_{n_2, n_3} \left(\frac{\partial \mu_1}{\partial n_3}\right)_{n_1, n_2}} \quad (20)$$

Dividing out each of the three pairs of partial derivatives, we obtain the desired relation of the three tangent intercepts:

$$\left(\frac{\partial n_1}{\partial n_2}\right)_{\mu_3, n_3} = - \left(\frac{\partial n_1}{\partial n_3}\right)_{\mu_2, n_2} \left(\frac{\partial n_3}{\partial n_2}\right)_{\mu_1, n_1} \quad (21)$$

This equation shows that the directions of the three isoactivity curves for three respective components are indeed closely related. Comparison of this equation with Eq. (14) shows in fact that the three tangent intercepts  $T_{1,23}$ ,  $T_{2,13}$ , and  $T_{3,12}$  must fall on a single straight line. Thus, we have the basis of a rather simple geometrical procedure for constructing isoactivity curves.

Figure 3 illustrates the graphical determination of the direction of the isoactivity curve for component 3 at a point  $P$ , when the directions of the isoactivity curves for components 1 and 2 are known. First, the tangent to the isoactivity curve  $I$  for component 1 is extended to find the tangent intercept  $T_{1,23}$  on the side 2—3. Similarly, the tangent intercept  $T_{2,13}$  is found for component 2 on side 1—3. Then a straight line is drawn through points  $T_{1,23}$  and  $T_{2,13}$  and the tangent intercept point  $T_{3,12}$  is found where this line intersects side 1—2. The line connecting point  $P$  and  $T_{3,12}$  gives the direction of the isoactivity curve for component 3. An application of this method will be considered in the following section of this paper. Elliott and Chipman<sup>6</sup> have presented rather complete sets of isoactivity curves for several ternary systems, and these can be recommended to the reader for practice in this graphical procedure.

#### APPLICATION TO FeO-Fe<sub>2</sub>O<sub>3</sub>-SiO<sub>2</sub> SYSTEM

Measurements of oxygen activities in iron-silicate slags have been reported for slags saturated with solid iron<sup>11</sup> and for slags saturated with solid silica.<sup>12</sup> These previous papers give data on activities of FeO, Fe, and SiO<sub>2</sub> for iron- and silica-saturated slags obtained by Gibbs-Duhem integrations and by other straightforward thermodynamic calculations. Also, a phase diagram for these slags has been reported.<sup>14</sup> Application of the methods described in the present paper to the previously published activity and phase equilibrium data makes it possible to develop a complete set of activity

curves covering the entire composition range of the ternary slags. The general line of attack is first to utilize the phase diagram to estimate the geometric configuration of some of the isoactivity curves and then to combine these geometrical estimates with the limited activity data to obtain a complete Gibbs-Duhem integration over the whole range of ternary slag compositions.

The 1350°C isotherm of the FeO-Fe<sub>2</sub>O<sub>3</sub>-SiO<sub>2</sub> system<sup>14</sup> is given in Fig. 4. For the purposes of the present calculations, the significance of this diagram is that it gives four different saturation curves, showing the respective compositions of slags saturated with silica, magnetite, wüstite, and iron. Such saturation curves are in reality special cases of isoactivity curves. That is, a tangent to a saturation curve at a given point gives the direction in which the melt composition can be changed infinitesimally without changing the activity of the solid compound in equilibrium with the melt. Moreover, there are four points, at the four corners of the melt field, where the isoactivity curves intersect. At these four points we can use the tangent intercept procedure described in the last section and illustrated in Fig. 3 to determine directions of still other isoactivity curves.

The simplest starting point is to estimate the isoactivity curves for SiO<sub>2</sub>. One already available is the SiO<sub>2</sub> saturation curve at the left side of the melt field, a straight line with a constant tangent intercept value of  $(\partial n_{\text{Fe}_2\text{O}_3}/\partial n_{\text{FeO}})_{\mu_{\text{SiO}_2}, n_{\text{SiO}_2}} = 2.9$  (see point  $T_s'$  in Fig. 4). Figure 4 shows the construction for estimating another isoactivity line for SiO<sub>2</sub> at point  $P$ , the intersection of the magnetite and wüstite saturation curves. For this estimate an auxiliary composition triangle  $WMS$  is utilized, considering Fe<sub>3</sub>O<sub>4</sub>, SiO<sub>2</sub>, and wüstite of composition  $W$  as the three components. The tangents to the two saturation curves at  $P$  are extended to find the tangent intercept points  $T_W$  and  $T_M$ , corresponding, respectively, to  $(\partial n_{\text{SiO}_2}/\partial n_{\text{Fe}_3\text{O}_4})_{\text{wüst}}$  and to  $(\partial n_{\text{wüst}}/\partial n_{\text{SiO}_2})_{\text{Fe}_3\text{O}_4}$ . A straight line through  $T_W$  and  $T_M$  intersects the base line  $WM$  at points  $T_S$ . Point  $T_S$  according to the demonstration of the previous section is the tangent intercept point for silica at  $P$ , and the line  $T_S P$  gives the isoactivity direction for SiO<sub>2</sub> at point  $P$ . The tangent intercept of SiO<sub>2</sub> for point  $P$  at the right of the melt field is not greatly different from that for the SiO<sub>2</sub> saturation curve at the left of the melt field. Noting also the lack of curvature of the experimentally determined SiO<sub>2</sub> saturation curve, the proximity of  $P$  to the % SiO<sub>2</sub> side of the triangle, and other geometric features, it seems reasonable to estimate that the SiO<sub>2</sub> isoactivity curves in the melt field are a family of straight lines with  $(\partial n_{\text{Fe}_2\text{O}_3}/\partial n_{\text{FeO}})_{\mu_{\text{SiO}_2}, n_{\text{SiO}_2}}$  changing uniformly from 2.9 to 1.5 across the melt field. Activities of SiO<sub>2</sub> are known quantitatively along the iron-saturation curve at the bottom of the melt field

from the data of Schuhmann and Ensio.<sup>11</sup> Hence, the SiO<sub>2</sub> isoactivity lines can now be drawn in and are shown as dashed lines in Fig. 4.

Activity of FeO is determined throughout the melt field by Gibbs-Duhem integrations along lines of constant  $n_{\text{Fe}_2\text{O}_3}/n_{\text{FeO}}$  according to Eq. (7). The lower limits of integration are the activities in SiO<sub>2</sub>-saturated slags, which are established by the data of Michal and Schuhmann.<sup>12</sup> Thus,

$$\left[ \log a_{\text{FeO}} = (\log a_{\text{FeO}})_{\text{SiO}_2 \text{ saturation}} - \int_1^{\log a_{\text{SiO}_2}} \left( \frac{\partial n_{\text{SiO}_2}}{\partial n_{\text{FeO}}} \right)_{\mu_{\text{SiO}_2}, n_{\text{Fe}_2\text{O}_3}} d \log a_{\text{SiO}_2} \right]_{n_{\text{Fe}_2\text{O}_3}/n_{\text{FeO}}} \quad (22)$$

The evaluations of  $(\partial n_{\text{SiO}_2}/\partial n_{\text{FeO}})_{\mu_{\text{SiO}_2}, n_{\text{Fe}_2\text{O}_3}}$  by the tangent intercept procedure are easily made from the SiO<sub>2</sub> isoactivity lines and the integral is quite well-behaved, so there is no need to consider other more complicated Gibbs-Duhem integrations. Oxygen activities are found by a similar integration of Eq. (7) along the same paths, but with FeO, O, and SiO<sub>2</sub> regarded as the three components.

$$\left[ \log \frac{p_{\text{CO}_2}}{p_{\text{CO}}} = \left( \log \frac{p_{\text{CO}_2}}{p_{\text{CO}}} \right)_{\text{SiO}_2 \text{ saturation}} - \int_0^{\log a_{\text{SiO}_2}} \left( \frac{\partial n_{\text{SiO}_2}}{\partial n_{\text{O}}} \right)_{\mu_{\text{SiO}_2}, n_{\text{SiO}_2}} d \log a_{\text{SiO}_2} \right]_{n_{\text{O}}/n_{\text{FeO}}} \quad (23)$$

The partial derivative under the integral in Eq. (23) is easily calculated from the SiO<sub>2</sub> tangent intercept values

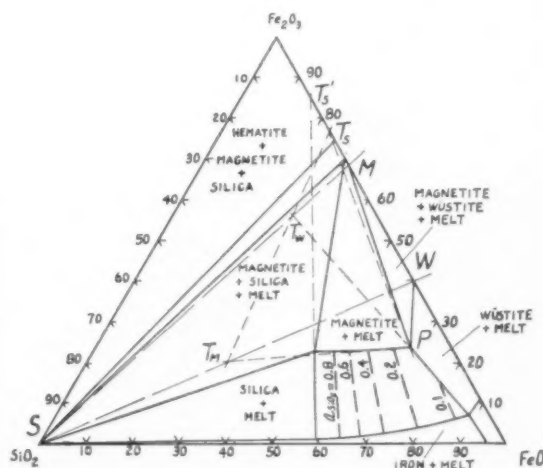


FIG. 4. Estimation of SiO<sub>2</sub>-isoactivity curves in FeO-Fe<sub>2</sub>O<sub>3</sub>-SiO<sub>2</sub> system.



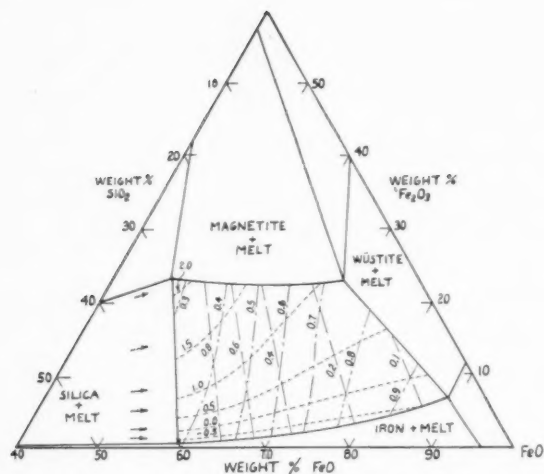


FIG. 5. Isoactivity curves for FeO, O, and SiO<sub>2</sub> in iron silicate slags at 1350°C. (Arrows at bottom left indicate paths of Gibbs-Duhem integrations.) — SiO<sub>2</sub>: Labels give  $a_{\text{SiO}_2}$  referred to tridymite as standard state. --- FeO: Labels give  $a_{\text{FeO}}$  referred to FeO in liquid iron oxide saturated with solid  $\gamma$ -iron. - - - O: Labels give  $\log_{10}(p_{\text{CO}_2}/p_{\text{CO}})$  for equilibrium gas mixtures.

in the FeO-Fe<sub>2</sub>O<sub>3</sub>-SiO<sub>2</sub> triangle:

$$\begin{aligned} \left( \frac{\partial n_{\text{SiO}_2}}{\partial n_{\text{O}}} \right)_{a_{\text{SiO}_2}, n_{\text{FeO}}} &= - \left( \frac{\partial n_{\text{SiO}_2}}{\partial n_{\text{FeO}}} \right)_{a_{\text{SiO}_2}, n_{\text{O}}} \left( \frac{\partial n_{\text{FeO}}}{\partial n_{\text{O}}} \right)_{a_{\text{SiO}_2}, n_{\text{SiO}_2}} \\ &= - \left( \frac{\partial n_{\text{SiO}_2}}{\partial n_{\text{FeO}}} \right)_{a_{\text{SiO}_2}, n_{\text{O}}} \left[ \left( \frac{\partial n_{\text{FeO}}}{\partial n_{\text{Fe}_2\text{O}_3}} \right)_{a_{\text{SiO}_2}, n_{\text{SiO}_2}} + 2 \right]. \quad (24) \end{aligned}$$

Results of the Gibbs-Duhem integrations are plotted in Fig. 5, as isoactivity curves for SiO<sub>2</sub>, FeO, and  $p_{\text{CO}_2}/p_{\text{CO}}$ . The reference states of unit activity for SiO<sub>2</sub> and FeO, respectively, are solid silica (tridymite) and metastable liquid iron oxide of the composition in equilibrium with  $\gamma$ -iron.

It should be emphasized that these calculations are all based on experimental data, except for the interpolated directions of the SiO<sub>2</sub>-isoactivity lines. That is, the calculations depend on estimating one quantity,  $(\partial n_{\text{Fe}_2\text{O}_3}/\partial n_{\text{FeO}})_{a_{\text{SiO}_2}, n_{\text{SiO}_2}}$ , which varies over a relatively narrow range. Moreover, a study of the calculations shows that the results are quite insensitive to errors in this tangent intercept. In fact, repetition of the calculations making the gross assumption

that  $(\partial n_{\text{Fe}_2\text{O}_3}/\partial n_{\text{FeO}})_{a_{\text{SiO}_2}, n_{\text{SiO}_2}}$  has a constant value of 2 (instead of interpolating from 1.5 to 2.9) yields a final plot of isoactivity curves hardly distinguishable from Fig. 5 when the two plots are placed side by side.

In the final analysis, the principal uncertainties in the experimental data on which Fig. 5 is based are in % Fe<sub>2</sub>O<sub>3</sub>. Difficulties in accurately establishing the Fe<sub>2</sub>O<sub>3</sub> content of Fe-saturated slags<sup>11</sup> were discussed previously. The similar error in the determination of the ternary isotherms was estimated to fall in the range of -1 to -3% Fe<sub>2</sub>O<sub>3</sub>, resulting from absorption of Fe by Pt crucibles.<sup>14</sup> Within these experimental errors, the results of carrying the Gibbs-Duhem integrations all the way across the melt field, from SiO<sub>2</sub>-saturation to wüstite saturation, check very satisfactorily the activity data available at the two ends of the wüstite saturation curve. Thus, for the equilibrium wüstite-magnetite-melt, interpolation on Fig. 5 indicates  $\log p_{\text{CO}_2}/p_{\text{CO}} = 0.92$ , but if the Fe<sub>2</sub>O<sub>3</sub> content of the melt were 3 per cent greater we would read  $\log p_{\text{CO}_2}/p_{\text{CO}} = 1.1$ , which is the result obtained by Darken and Gurry<sup>15</sup> for the wüstite-magnetite equilibrium at 1350°C. Similarly, Fig. 5 indicates that  $\log p_{\text{CO}_2}/p_{\text{CO}}$  in the iron-wüstite corner is slightly greater than -0.5 whereas previous data<sup>11</sup> indicate  $\log p_{\text{CO}_2}/p_{\text{CO}}$  should be a little below -0.5.

#### REFERENCES

1. L. S. Darken and R. W. Gurry, *Physical Chemistry of Metals*, (McGraw-Hill Book Co., New York, 1953), pp. 258-266.
2. J. Chipman, *Activities in Liquid Metallic Solutions*, *Discussions of the Faraday Society*, The Physical Chemistry of Process Metallurgy (1948), pp. 23-49.
3. J. F. Elliott and J. Chipman, *Trans. Faraday Soc.* **47**, 138-148 (1951).
4. L. S. Darken, *J. Amer. Chem. Soc.* **72**, 2909-2914 (1950).
5. C. Wagner, *Thermodynamics of Alloys* (Addison-Wesley Press, 1952), pp. 19-22.
6. J. F. Elliott and J. Chipman *J. Amer. Chem. Soc.* **73**, 2682-2693 (1951).
7. S. Mellgren, *J. Amer. Chem. Soc.* **74**, 5037-5040 (1952).
8. H. R. Larson and J. Chipman, *Trans. A.I.M.E.* 759-762 (1954); *J. Metals* (June 1954).
9. G. Masing (Translated by B. A. Rogers), *Ternary Systems* (Reinhold Publishing Corp., 1944).
10. W. Hume-Rothery, J. W. Christian, and W. B. Pearson, *Metallurgical Equilibrium Diagrams*, Institute of Physics, London (1952).
11. R. Schuhmann, Jr. and P. J. Ensio, *Trans. A.I.M.E.* **191**, 401-411 (1951); *J. Metals* (May 1951).
12. E. J. Michal and R. Schuhmann, Jr., *Trans. A.I.M.E.*, **194**, 723-728 (1952); *J. Metals* (July 1952).
13. W. A. Krivsky, *The Thermodynamics of the Cu-Fe-S System at Matte Smelting Temperatures*, Sc.D. Thesis, Massachusetts Institute of Technology (1954).
14. R. Schuhmann, Jr., R. G. Powell, and E. J. Michal, *Trans. A.I.M.E.*, 1097-1104 (1953); *J. Metals* (Sept. 1953).
15. L. S. Darken and R. W. Gurry, *J. Amer. Chem. Soc.* **67**, 1398-1412 (1945).

# CALORIMETRIC INVESTIGATIONS OF A GOLD-NICKEL ALLOY. I. LOW TEMPERATURE HEAT CAPACITY OF GOLD-NICKEL ALLOY\*†

WARREN DESORBO‡

The heat capacity of gold-nickel alloy containing 52 atomic per cent gold has been measured in the temperature region 13° to 300°K. The lack of conformity of the data to the Kopp-Neumann rule has been shown. The excess entropy, arising mostly from the change in the vibrational spectrum upon alloy formation, is  $0.62 \pm 0.09$  cal/g-atom/deg at 300°K. The data have been analyzed in terms of the simple Debye continuum model.

The values of the thermodynamic functions, entropy, enthalpy and free energy have been evaluated and tabulated at regular intervals of temperature up to 300°K for the Au-Ni alloy. The entropy of this material at 298.16°K is  $9.83 \pm 0.07$  cal/g-atom/deg, of which 0.10 was obtained by extrapolating below 13°K.

## RECHERCHES CALORIMÉTRIQUES SUR UN ALLIAGE OR-NICKEL. I. CAPACITÉ CALORIFIQUE À BASSE TEMPÉRATURE D'UN ALLIAGE OR-NICKEL

La capacité calorifique d'un alliage or-nickel à 52 At. % d'or a été mesurée dans l'intervalle de 13° à 300°K. Il y a désaccord avec les résultats de la loi de Kopp-Neumann. L'entropie supplémentaire due à la modification du spectre des vibrations par formation de l'alliage est  $0.62 \pm 0.09$  cal/g-atome/deg. à 300°K, les résultats étant interprétés dans le modèle d'un milieu continu de Debye.

Les valeurs des fonctions thermodynamiques, entropie, enthalpie et énergie libre, ont été calculées pour des températures régulièrement réparties jusqu'à 300°K dans le cas de l'alliage Au-Ni. L'entropie de cet alliage est à 298.16°K de  $9.83 \pm 0.07$  cal/g-atome/deg, tandis que, par extrapolation au-dessous de 13°, on obtient 0.10.

## KALORIMETRISCHE UNTERSUCHUNG GEN AN EINER GOLD-NICKEL-LEGIERUNG. I. WÄRMEINHALT EINER GOLD-NICKEL-LEGIERUNG BEI TIEFEN TEMPERATUREN

Der Wärmeinhalt einer Gold-Nickel-Legierung mit 52 At % Gold wurde in einem Temperaturbereich von 13 bis 300°K gemessen. Die Werte zeigen keine Übereinstimmung mit der Regel von Kopp-Neumann. Die Abweichung von der idealen Entropie, die in erster Linie durch die bei der Legierungsbildung auftretende Veränderung des Schwingungsspektrums verursacht wird, beträgt bei 300°K  $0.62 \pm 0.09$  Cl. Die Ergebnisse werden auf Grund der Kontinuum Theorie von Debeye diskutiert.

Für die Gold-Nickel-Legierung wurden die Werte der thermodynamischen Funktion, wie die Entropie, Enthalpie und die freie Enthalpie in regelmässigen Abständen bis zu 300°K ermittelt und zusammengestellt. Bei 298.16°K hat die Entropie dieses Materials folgenden Wert:  $9.83 \pm 0.07$  Cl, woraus für Temperaturen unter 13°K durch Extrapolation 0.10 erhalten wurde.

## INTRODUCTION

Recent publications by Cohen, Averbach and co-workers<sup>1,2</sup> have presented studies on the thermodynamic properties of solid gold-nickel alloys. Thermodynamic activities were found to deviate considerably (positive) from Raoult's law; entropies of mixing were found to be larger than those for ideal solutions; and enthalpies of mixing were found to be positive (heat is absorbed). These investigators have postulated that the excess entropy arises from a change in the vibrational spectrum which is reflected in the change in the heat capacity, i.e., in addition to the configurational entropy there would be a contribution due to the alteration of the modes of the frequency spectrum. This investigation was undertaken in order to determine the heat capacity of a 50 atomic per cent solution of Au-Ni (actually 48.3 atomic per cent nickel) in the temperature range 13° to 300°K. Such a study would elucidate

the degree of conformity of this alloy with the Kopp-Neumann rule for additivity of heat capacities below 300°K and would also afford a study of the effects of temperature on the Debye characteristic temperature.

## EXPERIMENTAL

The Au-Ni alloy sample was obtained from Professor Morris Cohen, Department of Metallurgy, Massachusetts Institute of Technology. A chemical analysis showed the sample to consist of 48.3 atomic per cent nickel. The specimen consisted of machined filings whose shorter dimensions were approximately 1-2 mm wide and roughly 0.3-0.7 mm thick averaging several mm in length.

Care was taken in maintaining this specimen size after each homogenization treatment which tended to agglomerate the sample. The homogenization treatment consisted of heating the specimen in high vacuum at approximately 900°C for several hours followed by an immediate quench in ice-water mixture.\* This causes the single solid solution to be retained at room tempera-

\* Received September 14, 1954.

† Presented in part before the A.E.C. Solid State Conference, General Electric Research Laboratory, Schenectady, New York, June 16-17, 1954.

‡ General Electric Research Laboratory, Schenectady, New York.

\* This operation was carried out by William K. Murphy.

ture. Photomicrographs were taken of the samples immediately before sealing the specimen in the calorimeter container as well as after removal of the specimen from the calorimeter upon conclusion of the experiment, in order to check for the formation of the second phase.†

The cryostat, copper calorimeter and accessory apparatus used in this experiment have been used previously and are described elsewhere.<sup>3</sup> The temperature scale in this investigation has been reestablished by intercomparing the copper-constantan thermocouple with a platinum resistance thermometer (Leeds and Northrup Co.; serial No. 736954) calibrated by the Bureau of Standards. A complete recalibration of the empty copper calorimeter was also undertaken for the experiment. In the first experiment 171.030 g of sample were used; while in the second experiment the weight of the alloy used was 99.838 g. Both weights refer to weights *in vacuo*.

### RESULTS

The heat capacity data, extending from 13°K to 299°K, are presented in Table I. Two independent determinations were carried out in this temperature region. The temperature drifts after each energy input were somewhat larger than those experienced in previous studies on monatomic solids. This is indicative of the poorer thermal conductivity of the alloy and is reflected in the over-all accuracy referred to below.

The values of the thermodynamic functions listed in Table II were obtained from a smooth curve of large graphs of heat capacities *versus T* and of heat capacities *versus log T*. Simpson's rule was used to evaluate entropy and enthalpy functions. The entropy of the alloy at 298.16°K referred to the alloy at 0°K is  $9.83 \pm 0.07$  cal/g-atom/deg. The extrapolated portion below 13°K has been obtained by applying an anisotropic continuum Debye model where

$$S_0^{13^\circ\text{K}} = \frac{4}{3} \pi^4 \frac{RT^3}{\theta_3 \cdot \theta_2^2}; \text{ where } \theta_3 = 45^\circ \text{ and } \theta_2 = 280^\circ. \quad (1)$$

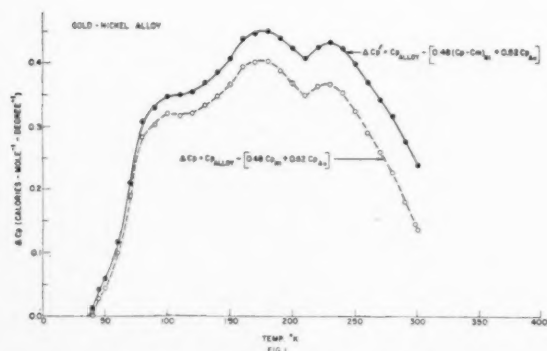


Fig. 1. The change in heat capacity,  $\Delta C_p$ , and  $\Delta C_p'$ , accompanying alloy formation for Au-Ni alloy.

† These photomicrographs were taken by Miss Dorothy Kontoleon.

TABLE I. Molal heat capacity of gold-nickel alloy, mol. weight 130.3.

Mean temp., °K	$\Delta T$	$C_p^*$ cal/deg	Mean Temp., °K	$\Delta T$	$C_p^*$ cal/deg
Data of April, 1953, sample, 1.3126 mole					
12.89	1.886	0.134	84.29	3.317	4.037
14.53	1.442	0.184	86.20	2.787	4.106
16.12	1.671	0.257	87.57	3.228	4.146
17.83	1.729	0.326	90.79	3.146	4.257
19.45	1.414	0.392	99.90	2.969	4.504
20.88	1.161	0.477	109.70	3.244	4.784
22.47	1.811	0.546	119.85	3.601	4.968
24.56	2.254	0.658	129.83	3.466	5.163
26.65	1.887	0.770	139.77	3.343	5.356
28.61	2.002	0.889	153.65	3.193	5.567
30.85	2.392	1.019	159.65	3.139	5.643
33.25	2.349	1.194	169.73	3.554	5.754
35.78	2.629	1.360	179.91	3.474	5.846
38.56	2.898	1.563	190.73	2.926	5.860
41.05	2.977	1.713	199.13	2.877	5.958
43.89	2.675	1.901	203.06	2.514	5.925
46.63	2.791	2.055	205.67	2.482	5.940
49.65	3.201	2.235	210.70	2.933	6.111
52.71	2.907	2.458	210.77	3.241	6.052
55.73	3.084	2.578	220.86	3.177	6.079
55.86	2.702	2.572	230.57	3.122	6.089
58.66	2.882	2.765	240.49	2.786	6.136
58.73	2.883	2.772	251.22	1.432	6.201
61.67	3.099	2.968	260.15	1.868	6.021
61.73	3.098	2.994	265.11	1.820	6.281
64.91	3.243	3.142	270.99	1.806	6.253
68.33	3.543	3.292	281.24	2.130	6.276
71.81	3.372	3.488	284.56	2.144	6.103
75.11	3.207	3.676	292.51	1.564	6.305
78.28	3.092	3.825	294.96	1.690	6.656
80.13	5.112	3.860	297.14	2.039	6.513
80.90	3.419	3.918	298.46	1.679	6.661
Data of January, 1954, sample, 0.7662 mole					
20.98	0.987	0.474	184.21	2.372	5.868
31.58	0.690	0.998	199.73	2.667	5.949
32.57	1.129	1.267	219.42	2.971	6.225
39.55	1.857	1.654	240.61	2.876	6.233
51.89	2.406	2.417	258.71	2.798	6.169
57.20	1.927	2.771	267.37	1.911	6.253
72.69	1.893	3.412	272.89	1.887	6.303
78.91	2.049	3.794	273.19	2.688	6.577
79.13	3.072	3.776	277.61	2.106	6.587
81.89	2.389	4.003	279.00	1.824	6.567
99.14	2.132	4.472	286.48	1.708	6.750
119.41	2.007	4.910	289.47	1.484	6.515
141.84	2.221	5.266	294.13	1.932	6.631
159.58	2.475	5.600	298.80	1.467	6.490
179.55	2.407	5.721			

\* The "defined thermochemical calorie" = 4.1840 absolute joule has been used.

This formula gives  $S_0^{13^\circ\text{K}} = 0.096$  cal/g-atom/deg. It neglects the contribution due to any magnetic effects below 13°K (see below).

Table III presents the data showing the temperature variation of  $\Delta C_p$ , the change in heat capacity accompanying alloy formation. The results show that above approximately 50°K,  $\Delta C_p$  has a positive value. For magnetic nickel the following expression was used to evaluate the change in heat capacity due to alloy formation:

$$\Delta C_p = C_{p \text{ alloy}} - (0.483 C_{p \text{ Ni}} + 0.517 C_{p \text{ Au}}). \quad (2)$$

In order to refer the heat capacity of the alloy to a mixture of gold and of nonmagnetic ( $\beta$ ) nickel, the

magnetic contribution,  $C_m$ , to the heat capacity of nickel, as evaluated by Stoner,<sup>4</sup> must be subtracted. Hence

$$\Delta C_p' = C_{p\text{alloy}} - [0.483(C_{p\text{Ni}} - C_m) + 0.517 C_{p\text{Au}}]. \quad (3)$$

The values of the heat capacity of nickel ( $C_{p\text{Ni}}$ ) are those reported by Busey and Giauque.<sup>5</sup> The purity of their sample was reported to be approximately 99.98 per cent. The specimen had been annealed at 1100–1200°C before sealing in the calorimeter. The heat capacity values for gold used in the calculations are those obtained by Geballe and Giauque.<sup>6</sup> This sample was reported by the authors to be a single crystal and to have a purity of 99.99 per cent.

The  $\Delta C_p$  and  $\Delta C_p'$  values calculated by applying Eqs. (2) and (3) are presented in Fig. 1. The value is essentially zero between 13°K and 45°K. Small and non-uniform negative values in this temperature region are probably due to accumulative errors of the various experiments involved. The  $\Delta C_p$  and  $\Delta C_p'$  values reach a maximum value at about 170°K and then decrease with increasing temperature.

The entropy increment corresponding to the deviation from the Kopp-Neumann rule has the following value: From Eq. (2)

$$\Delta S_{13}^{298.16^\circ\text{K}} = \int_{13}^{298.16} \Delta C_p d \ln T \\ = 0.51 \pm 0.07 \text{ cal/g-atom/deg.}$$

This excess entropy for gold-nickel solid solution arises mostly from a change in the vibrational spectrum upon alloy formation over and above the configurational entropy. For gold-nickel referred to  $\beta$ -nickel the excess entropy has the following value:

$$\Delta S_0^{298.16^\circ\text{K}} = 0.62 \pm 0.09 \text{ cal/g-atom/deg.}$$

The enthalpy of mixing of the alloy solution associated with the change in the specific heat upon alloy formation, considering the enthalpy values of Au-Ni,

TABLE II. Thermodynamic functions of Au-Ni based on the smooth curve of heat capacity.

Temp., °K	0°C = 273.16°K		Mol. weight = 130.3		
	$C_p$ cal/g-atom/deg	$H^\circ - H_0^\circ$ cal/g-atom	$\frac{H^\circ - H_0^\circ}{T}$	$S^\circ$ cal/g-atom/deg	$-\left(\frac{F^\circ - H_0^\circ}{T}\right)$ cal/deg-g-atom
15	0.207	1.270	0.085	0.116	0.032
25	0.680	5.546	0.222	0.322	0.101
50	2.270	42.39	0.848	1.283	0.435
75	3.668	117.01	1.560	2.474	0.914
100	4.540	220.32	2.203	3.656	1.453
125	5.079	340.83	2.727	4.737	2.011
150	5.500	473.34	3.156	5.694	2.539
175	5.812	615.19	3.515	6.567	3.052
200	5.983	762.89	3.815	7.356	3.541
225	6.130	914.12	4.063	8.071	4.008
250	6.222	1068.7	4.275	8.722	4.448
275	6.269	1225.5	4.456	9.318	4.862
298.16	6.290	1370.4	4.596	9.826	5.230
300	6.290	1381.9	4.606	9.865	5.259

TABLE III.  $\Delta C_p$  of formation Au-Ni.

Temp., °K	$\Delta C_p$ cal/g-atom/deg (magnetic nickel)	$\Delta C_p'$ cal/g-atom/deg ("non-magnetic" nickel)
20	-0.016	-0.011
40	+0.002	+0.013
60	0.100	0.117
80	0.285	0.309
100	0.321	0.350
120	0.322	0.356
140	0.349	0.387
160	0.396	0.439
180	0.404	0.452
200	0.370	0.425
220	0.365	0.426
240	0.355	0.424
260	0.292	0.371
280	0.228	0.318
298.16	0.146	0.247
300	0.137	0.240

$\beta$ -nickel and gold, has the following form:

$$\Delta H_0^{298.16^\circ\text{K}} = (H^\circ - H_0^\circ)_{\text{Au-Ni}} \\ - \{0.483[(H^\circ - H_0^\circ)_{\beta\text{Ni}} - 0.517(H^\circ - H_0^\circ)_{\text{Au}}]\}.$$

Enthalpy for gold ( $H^\circ - H_0^\circ$ )<sub>Au</sub> at 298.16°K is that given by Geballe and Giauque<sup>6</sup> while that for  $\beta$ -nickel is the value reported by Busey and Giauque<sup>5</sup> from which the "magnetic contribution" has been subtracted (as per reference 4), i.e.,  $H^\circ - H_0^\circ$  at 298.16 for  $\beta$ -nickel = 1105.3 cal/g-atom. The enthalpy of Au-Ni has been determined from the data of this research. The extrapolation below 13° to 0°K has been approximated by an anisotropic continuum model. Considering all of these values  $\Delta H_0^{298.16^\circ\text{K}} = 95.1$  cal/g-atom.

## DISCUSSION OF RESULTS

The Kopp-Neumann rule is a simplified way of treating solid-solution statistics in that it assumes the vibrational characteristic of the solution to be independent of configuration. The partition function is thus factored into configurational and vibrational contributions.<sup>7</sup> According to the rule,  $\Delta C_p$ , the change in heat capacity accompanying alloy formation is zero. Although there is no theoretical justification for the rule, it is used rather extensively. The reason for this is the rarity of reliable heat capacity data for alloys. The results presented in Fig. 1 and Table III clearly present the inaccuracy of the rule for this alloy. When the magnetic component of the specific heat of nickel,  $C_m$ , is taken into account, the deviation is somewhat enhanced. In this work  $C_m$  for nickel has been approximated by a method\* used by Stoner<sup>4</sup> based on the Weiss treatment, i.e.,

$$C_m = 0.1402a\{-\sigma_T(\partial\sigma_T/\partial T)\}, \quad (4)$$

\* An alternative method is to evaluate the various components making up the specific heat of nickel (lattice vibration term  $C_L$ , thermal expansion term  $(C_p - C_v)$ , and electronic term  $C_e$ ). Then, the total subtracted from experimental data gives the magnetic term,  $C_m$ .



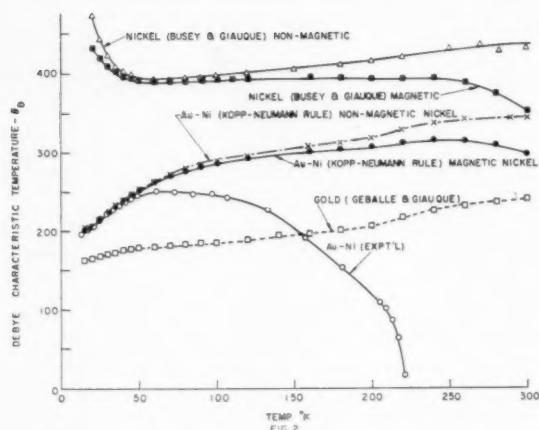


FIG. 2. Debye characteristic temperatures as a function of temperature for Au-Ni alloy, nickel and gold.

where  $\sigma_T$  is the intrinsic magnetization at the temperature  $T$ .†

In order to understand the deviation of the specific heat shown in Fig. 1, it would be necessary to study in detail the various components contributing to the specific heat of Au-Ni alloy, nickel and gold, respectively, as a function of temperature, especially to study in detail the change in vibrational spectrum accompanying alloy formation. At this stage of the problem, this analysis is difficult to carry out, particularly since basic information—such as elastic constants—is not readily available to permit an attempt to apply the rigorous dynamical methods of Born and von Karman,<sup>8</sup> Blackman,<sup>9</sup> Montroll,<sup>10</sup> Shibuya and co-workers<sup>11</sup> and others. Better than these approximate theoretical calculations would be to obtain, if possible, the complete elastic spectrum by means of diffuse X-ray scattering and to calculate the specific heat directly from the measured spectrum. Since this information is not available, the remaining alternative is the customary analysis of the specific heat in terms of the general Debye theory. Despite its theoretical limitations, this theory is still quite useful for the purpose of general description and tends to serve as a sort of reference state which can reflect variation of specific heats especially in the low temperature region.

In Fig. 2 are presented the results of an analysis of the specific heat of Au-Ni alloy, nickel and gold based on the Debye model where the Debye characteristic temperatures are presented as a function of temperature. The  $C_v$ -values for the alloy have been obtained from the experimental  $C_p$  values by applying the Nernst-Lindemann approximate relation  $C_p - C_v = 0.0214 C_p^2 (T/T_m)^{12}$  where  $T_m$  is the melting point

† Stoner discusses the variation in the value of  $a$ . For this work  $a$  has been assumed equal to 1.

\* In contrast to the correct thermodynamic relationship,  $C_p - C_v = \alpha^2 TV/\beta$ , where  $\alpha$  is the coefficient of thermal expansion,  $\beta$  the coefficient of compressibility, and  $V$  the molar volume of the crystal.

of the alloy ( $\sim 950^\circ\text{C}$ ). Since the electronic contribution to the specific heat is not available, this factor has not been accounted for.† For gold, the lattice contribution of the specific heat was calculated from  $C_p$ -values reported by Geballe<sup>6</sup> minus the electronic specific heat. The coefficient of the linear term of electronic specific heat used is that reported by Corak and Garfunkel<sup>14</sup> (i.e.,  $\gamma = 1.60 \times 10^{-4}$  cal mole<sup>-1</sup> deg<sup>-2</sup>). The  $C_p$ -values for nickel were determined by subtracting from the  $C_p$ -values, reported by Busey,<sup>5</sup> the thermal expansion term,  $C_p - C_v$ , obtained by Stoner.<sup>4</sup> The lattice vibration specific heat  $C_L$  was then obtained from  $C_p$  by subtracting the electronic specific heat values reported by Keesom<sup>15</sup> ( $\gamma = 1.744 \times 10^{-3}$  cal mole<sup>-1</sup> deg<sup>-2</sup>).

The variation of the Debye characteristic temperature with temperature is quite pronounced in this gold-nickel alloy. The  $\theta_D$  values increase with increasing temperature reaching a maximum at about  $60^\circ\text{K}$  and then decreasing with increasing temperature above  $100^\circ\text{K}$ . Above  $225^\circ\text{K}$  the values actually become negative (Dulong and Petit rule violated). The temperature variation of the Debye characteristic temperatures for gold and nickel are also presented in Fig. 2. The variations in these curves are typical of those for most f.c.c. materials.<sup>15</sup> Two curves are presented for nickel, one reflecting the lattice vibrations only; while the "magnetic" curve presents the  $\theta_D$  for the lattice vibrations plus the magnetic component,  $C_m$ . However, since the Debye model refers to 3N modes of vibration, the latter curve is incorrect and is presented for the purpose of comparison only. Also in Fig. 2 the curves represented by solid circles and crosses represent the temperature variation of  $\theta_D$  for an hypothetical gold-nickel alloy that conforms to the Kopp-Neumann rule. Again, two curves are presented merely for purposes of comparisons—one curve is for such an alloy referred to gold and magnetic nickel while the other (crosses) is for the same alloy but referred to  $\beta$ -nickel.

Flinn and co-workers<sup>17</sup> in their study on local atomic arrangements in gold-nickel alloys have shown them to form a continuous series of f.c.c. solid solutions above  $840^\circ\text{C}$ . At lower temperatures the solutions transform into two f.c.c. solutions—one gold rich and the other nickel rich. The variation of  $\theta_D$  versus  $T$  for Au-Ni reported here does not conform to the variation exhibited by most f.c.c. monatomic lattices<sup>16</sup> but more nearly resembles the behavior of  $\theta_D$  for f.c.c. materials and other isotropic monatomic solids that have some form of lattice irregularity. For such lattices the Debye characteristic temperature decreases with decreasing temperature below the liquid-nitrogen temperature region. The variation for this alloy, in this low-temperature region, is such that the frequency spectrum

† It will be assumed that, as in the monatomic metallic lattices, the neglect of the electronic specific heat has a negligible influence on the  $\theta$ -values in the temperature region of interest in this report. Goldman<sup>13</sup> has recently reported  $\gamma$ -value for  $\text{Ni}_3\text{Mn}$ :  $\gamma = 2.2 \times 10^{-3}$  for disordered alloy and  $\gamma = 1.2 \times 10^{-3}$  for the ordered phase.

can be approximated by two distribution functions,  $v^2 dv(\theta_3 = 45^\circ)$  and  $vdv(\theta_2 = 280^\circ)$ . It should be remarked that the physical significance of the amenability of the data to such an analysis is not readily apparent. Flinn and co-workers<sup>17</sup> have also presented studies, by diffuse X-ray scattering techniques, showing the size variation of each constituent atom in gold-nickel solutions of varying compositions and have presented evidence showing the size of each atom to vary with composition. The imperfect close-packing of large and small ions in the solid solution lattices could be responsible for the observed variation in  $\theta_D$  below liquid-nitrogen temperatures. For a given alloy system, such as gold-nickel, no systematic studies have been reported which show the effect of composition, as well as the variation in the size of each constituent atom, on the Debye characteristic temperature or on the change in force constants reflected in the change in the vibrational spectrum.

The portion of the  $\theta_D$  versus  $T$  curve above liquid-nitrogen temperatures for Au-Ni alloy in Fig. 2 (decrease in  $\theta_D$  with  $T$ ) is even more difficult to interpret since the Debye model becomes more inadequate in describing specific heat variations in this temperature region. The model fails completely in accounting for any specific heat contribution due to extra "internal" modes, strain energies, magnetic effects, etc. Low temperature specific heat data examining these variables have not been carried out. Furthermore, the effect of neglecting the anharmonic interaction terms in the partition function and an exact determination of the electronic specific heat for this alloy system have not been studied.

In evaluating the thermodynamic functions entropy  $S^\circ$  and enthalpy  $H^\circ - H_0^\circ$  at 298.16°K the anisotropic continuum model has been used instead of the three-dimensional Debye equation (since the former equation describes the data better) in extrapolating the data from 13° to 0°K. These thermodynamic properties, then, refer to a Au-Ni sample where contributions due to any magnetic effects between 13° and 0°K have been neglected. However, there is evidence from some experimentally determined values of magnetic permeability in the liquid hydrogen and liquid-helium temperatures<sup>18</sup>

that Au-Ni studied in this report does have a magnetic transformation point below the lowest experimental data point (13°K). The determination of the contribution to the thermodynamic properties by this transformation must await calorimetric investigations at liquid-helium temperatures.

#### ACKNOWLEDGMENTS

The author thanks Mrs. E. L. Fontanella for her assistance in the experimental work and for carrying out much of the data computation; and also G. E. Nichols, who assisted in the computation work involved in the recalibration of the thermocouple. Criticism of the manuscript by David Turnbull and J. W. Stout (University of Chicago) is also gratefully acknowledged.

This work was supported by the U. S. Atomic Energy Commission under Contract No. W-31-109-ENG-52.

#### REFERENCES

1. L. L. Seigle, M. Cohen, and B. L. Averbach, *Trans. A.I.M.E. J. Metals* **4**, 1320 (1952).
2. B. L. Averbach, P. A. Flinn, and M. Cohen, *Acta. Met.* **2**, 92 (1954).
3. W. DeSorbo, *J. Amer. Chem. Soc.* **75**, 1825 (1953).
4. E. C. Stoner, *Phil. Mag.* **22**, 81 (1936).
5. R. H. Busey and W. F. Giauque, *J. Amer. Chem. Soc.* **74**, 3157 (1952).
6. T. H. Geballe and W. F. Giauque, *J. Amer. Chem. Soc.* **74**, 2368 (1952).
7. R. H. Fowler and E. A. Guggenheim, "Statistical Thermodynamics," Cambridge University Press, Cambridge, 1939, p. 568.
8. M. Born and T. von Karman, *Physik, Z.* **13**, 297 (1912); **14**, 15 (1913).
9. M. Blackman, *Proc. Roy. Soc. (London)*, **A148**, 384 (1935); **A159**, 416 (1937).
10. E. W. Montroll, *J. Chem. Phys.* **10**, 218 (1942); **11**, 481 (1943).
11. Y. Shibuya, Y. Fukuda, and T. Fukuroi, *Sci. Rep. RITV*, A-Vol. 3, No. 1.
12. W. Nernst, and F. Lindemann, *Z. Elektrochem.* **17**, 817 (1911).
13. J. E. Goldman, Eighth Conference on Cryogenics, General Electric Co., Schenectady, New York, October 6-7, 1952.
14. W. S. Corak and M. P. Garfunkel, Eighth Annual Calorimetry Conference, University of Chicago, September 11-12, 1953.
15. W. H. Keesom and W. C. Clark, *Physica* **2**, 513 (1935).
16. W. DeSorbo, *Acta. Met.* **2**, 274 (1954).
17. P. A. Flinn, B. L. Averbach, and M. Cohen, *Acta. Met.* **1**, 664 (1953).
18. C. P. Bean, and W. DeSorbo, Unpublished data.

# CALORIMETRIC INVESTIGATIONS OF A GOLD-NICKEL ALLOY. II. THE HEAT CAPACITY AT HIGH TEMPERATURES AND THE ENTROPY OF FORMATION\*†

R. A. ORIANI‡

The literature of measurements of the heat capacity of alloys is critically reviewed. A Bunsen ice calorimeter is employed to measure the cumulative enthalpy difference between the solid solution  $Au_{0.517}Ni_{0.483}$  and the corresponding weights of the pure metals; differentiation of the temperature curve yields the deviation of the heat capacity of the alloy from the Kopp-Neumann rule. The positive value of this deviation and the large magnitude of the vibrational entropy of solution are related to the loosening of the lattice that accompanies formation of the solid solution.

## MESURES CALORIMÉTRIQUES SUR UN ALLIAGE OR-NICKEL. II. CAPACITÉ CALORIFIQUE À HAUTES TEMPÉRATURES ET ENTROPIE DE FORMATION

Discussion de la littérature sur les mesures de capacité calorifique des alliages. Emploi d'un calorimètre de Bunsen pour mesurer les différences d'enthalpie entre les solutions solides  $Au_{0.517}Ni_{0.483}$  et les métaux purs correspondants, en fonction de la température. La capacité calorifique de cet alliage ne suit pas la règle des mélanges. La valeur positive de l'écart et la grande entropie de vibration de cette solution sont attribuées au relâchement du réseau qui accompagne la formation de la solution solide.

## KALORIMETRISCHE UNTERSUCHUNGEN AN EINER GOLD-NICKEL-LEGIERUNG. II. WÄRMEINHALT BEI HOHEN TEMPERATUREN UND BILDUNGSENTROPIE

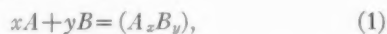
In der Literatur mitgeteilte Methoden zur Messung des Wärmeinhaltes werden kritisch besprochen. Die Differenz der Restenthalpie zwischen der festen Lösung  $Au_{0.517}Ni_{0.483}$  und den entsprechenden Gewichten der reinen Metalle wurde mit einem Eiskalorimeter nach Bunsen gemessen; die Differentiation der Temperaturkurve enthält die Abweichung von der Kopp-Neumannschen Regel. Der positive Wert dieser Abweichung und der grosse Wert der Schwingungsentropie bei der Lösung werden auf die Auflockerung des Gitters zurückgeführt, die die Bildung der festen Lösung begleitet.

### INTRODUCTION

The deviation of the heat capacity of a solid compound from that computed by assuming additive contributions from the several components (Kopp-Neumann rule) is usually small, and the error made in using this assumption to derive values of heat capacities of compounds is usually insignificant in most thermochemical calculations.<sup>1</sup>

Nevertheless, the deviation from the Kopp-Neumann rule and the dependence of the deviation on temperature are important information not only for the lattice theory of specific heats but also for the theory of solutions.

In the formation of a solution from its pure components according to the reaction



the change in heat capacity accompanying the process at any one temperature is

$$\Delta C_p = C_{pA_xB_y} - (xC_{pA} + yC_{pB}). \quad (2)$$

In these expressions,  $x$  and  $y$  are the mole fractions of species  $A$  and  $B$  respectively, while  $C_p$  represents the molar heat capacity at constant pressure; the change in

heat capacity,  $\Delta C_p$ , is the deviation from the Kopp-Neumann rule. The entropy change at constant pressure accompanying reaction (1), the entropy of solution  $\Delta S$ , may be thought of conveniently as being composed of three parts: that due to the change in configuration, depending chiefly on the spatial distribution of the atoms in the solution, that due to the change in volume in the solution process, and that due to changes in the character of the lattice vibrations accompanying the solution process. The configurational entropy change for a gram atom of solution cannot be larger than the value for random mixing,  $-R \sum_i x_i \ln x_i$ , except for a factor very nearly unity applicable to the mixing of spheres of unequal size.<sup>2,3</sup>

The change in entropy due to the change in volume in forming the solution may be evaluated<sup>4</sup> by the relation  $\int_V^{V+\Delta V} (\partial S / \partial V)_T dV = \int_V^{V+\Delta V} (-\alpha / \beta) dV$ . However, the relevant data for the thermal expansion coefficient,  $\alpha$ , and for the isothermal compressibility,  $\beta$ , are usually not available.

The configurational part of the entropy of solution would be the only contribution to the  $\Delta S$  of reaction (1) at 0°K. At any other temperature, another contribution would be that associated with the change in lattice vibrations. For a solution of spatial configuration independent of temperature, this factor is expressed by  $\int_0^T \Delta C_p d \ln T$ , in which  $\Delta C_p$  must be evaluated as a function of temperature, and it should be noted that this factor includes the volume contribution discussed above. A positive term of this sort has been invoked to

\* Received September 14, 1954; in revised form December 14, 1954.

† This material was presented in part at the A.E.C. Solid State Conference, June 16, and 17, 1954, and at the Calorimetry Conference, September 17, and 18, 1954, both at the General Electric Research Laboratory.

‡ Metallurgy Research Department, General Electric Research Laboratory, Schenectady, New York.

rationalize the larger-than-ideal entropies of mixing in the cases of several liquid metal binaries,<sup>5,6</sup> solid gold-nickel alloys,<sup>7</sup> solid cobalt-platinum alloys,<sup>8</sup> and some compositions of solid gold-copper alloys.<sup>9</sup> However, when either of the pure components, or the resulting solid solution, or both, have magnetic processes at some temperature, the observed entropy of solution will have an additional term due to the difference between the accumulated magnetic entropy of the alloy and that of the pure component multiplied by its mole fraction. In order to obtain from calorimetric measurements the vibrational contribution to the entropy of solution, it is necessary to be able to subtract out the magnetic contribution to the heat capacities of the substances in question. The present investigation on one composition of gold-nickel solid solution was undertaken\* in order to obtain an estimate of the vibrational contribution to the entropy of mixing, and to furnish careful measurements of the deviation from the Kopp-Neumann rule. Paper I<sup>10</sup> describes the measurements in the low-temperature region, and this paper extends the measurements to close to the solidus temperature of the alloy.

#### PREVIOUS WORK

Perusal of Kelley's compilation<sup>11</sup> shows that measurements of the heat capacity of alloys are quite rare. The bulk of such work has been furnished by four sets of investigators: Schimpff<sup>12</sup> (1910), Schübel<sup>13</sup> (1914), Kubaschewski<sup>14</sup> (1941-43), and Jaeger and collaborators<sup>15</sup> (1932-40). The first two investigators claimed an accuracy of 1 to 2 per cent in the heat capacity, so that a  $\Delta C_p$  of 1 per cent or less would be almost unrecognizable. Kubaschewski's measurements of enthalpy as a function of temperature, not carried out specifically for this purpose, do not have sufficient accuracy to justify a calculation of  $\Delta C_p$  from them. The work of Jaeger and collaborators, both on pure metals and on alloys, was done with great care by means of a drop calorimeter. However, a serious oversight was consistently made which somewhat vitiates their measurements on pure metals and completely spoils their attempt to determine the deviation from the Kopp-Neumann rule. This error consists in attempting to determine the heat effect due to the platinum capsules in which the samples were enclosed by multiplying the specific enthalpy change as tabulated for platinum by the weight of the capsule employed. The proper procedure is<sup>16</sup> to perform blank runs on the empty capsule, since only in this way can proper account be taken of the heat lost by radiation and convection during the descent of the capsule from the furnace to the calorimeter.†

Investigations on alloys not collated by Kelley in-

clude those on seven solid copper-manganese alloys,<sup>17</sup> on various solid alloy steels,<sup>18</sup> and on a liquid bismuth-lead alloy,<sup>19</sup> but all of these studies achieved too low an accuracy to permit a determination of  $\Delta C_p$ . The heat capacities of three liquid potassium-sodium alloys have been measured<sup>20</sup> by a Bunsen ice calorimeter, and the deviations from the Kopp-Neumann rule have been carefully established in the low-temperature region for the three superlattices of the Cd-Mg system.<sup>21</sup>

#### EXPERIMENTAL

The gold-nickel sample was analyzed at the Massachusetts Institute of Technology and in this Laboratory, the results being 48.37 and 48.2 atom per cent nickel, respectively; the figure of 48.3 will be taken as the nickel content.

The present investigation was carried out in the Bunsen drop calorimeter described previously,<sup>22</sup> the only difference in operating technique being that an electronic controller was used to regulate the temperature of the furnace. Photomicrographic studies showed that precipitation of second phase would occur to an observable extent during the lengths of time required for calorimetric investigation at furnace temperatures above about 100°C. Consequently, the temperature region from 100° to 790°, the boundary of the miscibility gap at this composition, was not amenable to study. On the other hand, it was found that the conditions under which the sample is quenched in the Bunsen calorimeter are sufficiently rapid so that when the furnace temperature is maintained between 790°C and the solidus temperature of the alloy (about 950°C), the homogeneous one-phase alloy is retained, and no abnormal thermal effects are observed. This temperature region therefore becomes accessible to study by Bunsen calorimetry.

For the high-temperature calorimetry, 14.5809 grams of alloy were sealed under helium into a platinum capsule. The reference, or blank, runs were subsequently carried out on 11.4089 grams of 99.99 per cent gold plus 3.1723 grams of carbonyl nickel held together, but unalloyed, in the same platinum capsule. A separate experiment had shown that the amount of alloying between these two metals, or between either and the capsule, at the highest furnace temperature was completely negligible. At any one furnace temperature, the heat released to the Bunsen calorimeter by the capsule plus alloy minus the heat released by the capsule plus pure metals (the difference is labeled  $\Delta[\Delta H]_{273}^T$  in Table I is equal to  $\int_{273}^T \Delta C_p dT$ , where the  $\Delta C_p$  is the same quantity as appears in Eq. (2). Hence, a graphical differentiation of the curve of  $\Delta[\Delta H]_{273}^T$  versus  $T$  yields  $\Delta C_p$ .

#### EXPERIMENTAL RESULTS

The results of the high-temperature calorimetry are given in Table I. The values of  $\Delta[\Delta H]_{273}^T$  are mean values of three or more determinations at any one

\* This has been done at the request of Professor Morris Cohen, of the Massachusetts Institute of Technology, who also furnished the alloy.

† Our judgment of these authors' experimental procedure has been corroborated by Dr. K. K. Kelley. (Private communication.)



temperature on the alloy plus capsule, and a similar number of determinations on the separated pure metals plus capsule. These data refer to magnetic or to non-magnetic nickel, depending on the state of the pure nickel in the capsule during the reference runs. The third column lists the standard deviations of the  $\Delta[\Delta H]_{273}^T$  values. The  $\Delta C_p$  values of the fourth column were obtained by a graphical method, and are similarly referred to pure nickel having the magnetic state characteristic of the experimental temperature.

A calorimetric value for the nonconfigurational portion of the entropy of mixing that would be directly comparable to the excess entropy of mixing,  $\Delta S^{(x)}$ , observed by Seigle, Cohen, and Averbach<sup>7</sup> could be obtained only if helium-region calorimetric data were available for the magnetic transformation in this gold-nickel alloy.<sup>10</sup> In the absence of such data, one can only attempt an estimate of the lattice vibrational contribution to the entropy of mixing. This can be done if one assumes that the alloy exhibits no magnetic contribution to its heat capacity above its Curie temperature, and that the magnetic contribution to the heat capacity of nickel may be approximated by the method of Stoner.<sup>23</sup> The fifth column of Table I lists the cumulative increments of  $\Delta S$ , from the ice temperature to the temperature in question, referring to nonmagnetic alloy and to nonmagnetic ( $\beta$ ) nickel; these values are therefore increments in the vibrational contribution to the  $\Delta S$  of solution.

The manner of calculation of these values is open to error not only because of the above assumptions, but also because of the lack of experimental data in the temperature region from 373° to 1076°K. Nevertheless, an approximation is made possible by the existence of three relevant experimental facts:  $\Delta C_p = 0$  and 0.22 at 373° and 1076°K, respectively, and  $\Delta[\Delta H]_{373}^{1076} = \int_{373}^{1076} \Delta C_p dT = 191.3$ , where the  $\Delta C_p$  is referred to the kind of nickel actually existing at the temperatures in question. Interconnecting the above two ( $\Delta C_p, T$ ) points

by a straight line, and evaluating  $\int_{373}^{1076} \Delta C_p dT$  along such a line leads to a number much smaller than the experimental value of 191.3, so that it is evident that the  $\Delta C_p(T)$  curve, referred to  $\beta$ Ni must go through a maximum within this temperature interval. Consequently, the alloy must exhibit a behavior somewhat as shown by the dashed curve in Fig. 1, and for ease in analytical treatment, a sine curve was added to the straight line interconnecting the two data points at 373° and 1076°K. The condition that the curve for the alloy join smoothly into the experimentally determined segments of  $\Delta C_p(T)$ , determined the wavelength of the sine function; whereas its amplitude was determined by the condition that  $\int_{373}^{1076} \Delta C_p dT = 191.3$ . Referring to Fig. 1, the area between the  $C_p(T)$  curve for the actual mixture of pure metals in the reference runs and the  $C_p^\beta(T)$  curve for a mixture of nonmagnetic nickel and gold, i.e., areas  $Q+R$ , is given from the work of Stoner<sup>23</sup> as  $x_{Ni}\Delta H = 0.483(190 \pm 40)$  cal/g-atom. On the other hand, from the present work,  $\int_{373}^{1076} \Delta C_p dT = P - Q = 191.3$  cal/g-atom. Therefore, the sum  $P+R$  can be obtained, fixing the amplitude of the sine function. Then, integrating numerically the values of  $\Delta C_p^\beta$  given by the sine function plotted against  $\ln T$  gives 0.38<sub>3</sub> for the temperature interval 373° to 1076°K, an entropy increment referred to gold and nonmagnetic nickel.

A plot of  $C_{p, alloy}$  against temperature, obtained by adding the  $\Delta C_p^\beta$  to the weighted heat capacities of Au and  $\beta$ Ni, shows a very slight hump by about 1 percent in the region 850° to 950°K. Since  $C_p(T)$  cannot have a negative slope in the absence of a second-order phase transition, and there is no reason to expect such a transition in the nonmagnetic alloy, this indicates that our choice of a sine curve overweighs the high-temperature end slightly, so that the  $\Delta S$  accumulated from 373° to 1076°K is probably slightly larger than the 0.38<sub>3</sub> calculated above. However, this difference can be neglected.

## DISCUSSION

The heat capacity of pure, nonmagnetic nickel is higher than the Dulong-Petit value even at relatively low temperatures, presumably because of electronic transitions between close-lying energy levels. Diluting nickel with gold, which much more nearly obeys the Dulong-Petit rule, would be expected to cause the heat capacity of the alloy to relax towards the classical value, especially since one may reasonably expect that electrons from the added gold atoms would go to fill vacancies in the  $d$ -shell of the nickel atoms. It therefore seems unlikely that the observed positive increment of the heat capacity of the alloy at high temperatures over the additive value can be of electronic origin.

Averbach, Flinn, and Cohen<sup>24</sup> have interpreted their X-ray diffraction data from gold-nickel solid solutions as showing that the gold and the nickel atoms are smaller and larger, respectively, than are the atoms

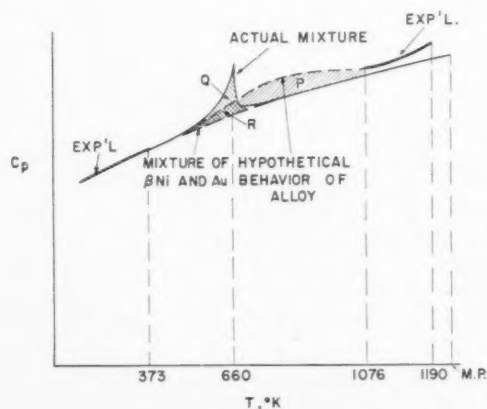


FIG. 1. Schematic representation of experimental results and of construction used to evaluate the  $\Delta S$  in the temperature region inaccessible to experiment.

TABLE I. Experimental and calculated results of Bunsen calorimetry for alloy Au<sub>0.517</sub>Ni<sub>0.483</sub>.

Temp., °K*	$\Delta[\Delta H]_{273}^T$ cal/g-atom	% deviation†	$\Delta C_p^\ddagger$ cal/deg g-atom	$\Delta[\Delta S]_{273, \text{vib}}^{T**}$ cal/deg g-atom
299.4	-1.2	±290	~0	~0
347.4	-5.2	± 80	~0	~0
373.2	0.0	∞	~0	~0
1075.8	191.3	±2.4	0.22	0.38 <sub>5</sub> ††
1105.1	201.0	+3.5	0.52	0.39 <sub>2</sub>
1138.3	226.6	±2.4	0.92	0.41 <sub>5</sub>
1163.9	252.9	±4.2	1.29	0.43 <sub>5</sub>
1189.8	292.1	±2.8	1.75	0.47 <sub>1</sub>

\* Temperature obtained by calibrated Pt-Pt, 10% Rh thermocouple and after correction for slight inequality between thermocouple and sample.

† Standard deviation as a percentage of the values listed in the second column. This considers reproducibility figures for both the principal and the reference runs, but does not include error in temperature measurement or that in chemical analysis of the alloy.

‡ Obtained by graphical differentiation of  $\Delta[\Delta H]$  versus  $T$ .

\*\* Calculated as

$$0.38_2 + \Delta[\Delta S]_{1075.8}^T = 0.38_2 + \left\{ \frac{\Delta[\Delta H]_{1075.8}^T}{T} + \int_{1075.8}^T \frac{\Delta[\Delta H]_{1075.8}^T}{T^2} dT \right\}.$$

†† Calculated as per text, by assuming a tilted sine curve for the variation of  $\Delta C_p - T$  curve between 373.2 and 1075.8°K.

of the pure metals. Such a deformation of the electronic orbitals must have a significant effect on the force constants that bind the atoms in the lattice. It must be concluded from the present data that the result is a net decrease in the magnitude of the average force constant, leading to a relative loosening of the lattice, an increased heat capacity, and a large vibrational entropy of solution. This is consistent with the finding of Ellwood and Bagley<sup>25</sup> that gold-nickel solid solutions deviate positively from Vegard's law. The rather fast increase of  $\Delta C_p$  above 1076°K may be connected with the nearness of the alloy to its melting temperature, an effect that has been noted for pure metals by Ginnings, Douglas, and Ball<sup>26</sup> and Pochapsky.<sup>27</sup>

The galvanic cell measurements of Seigle, Cohen, and Averbach<sup>7</sup> have yielded an excess molar entropy of solution,  $\Delta S^{(x)}$  (i.e.,  $\Delta S_{\text{observed}} - \Delta S_{\text{ideal solution}}$ ), referred to gold and nickel, of about 1.4 cal/deg-g atom at 900°C. Since gold-nickel solid solutions have been shown to exhibit short-range order,<sup>24</sup> the configurational entropy change in forming the solid solution of the present composition will be somewhat smaller than that calculated for the ideal solution, so that the non-configurational entropy of solution should be somewhat larger than the  $\Delta S^{(x)}$ , perhaps 1.4<sub>5</sub>. Combining with the present data the results of DeSorbo<sup>10</sup> for the vibrational contribution to the  $\Delta S$  of solution up to room temperature, the  $\Delta S$  (vibrational 1173°K is  $(0.62 \pm 0.09) + (0.45 \pm 0.1) = 1.07 \pm 0.2$  cal/deg-g atom. This number is not strictly to be compared with the nonconfigurational entropy of solution of 1.4<sub>5</sub>, since the latter is larger than the former by an amount  $[S_{\text{magn}}(\text{alloy}, 1173^\circ) - X_{\text{Ni}} S_{\text{magn}}(\text{Ni}, 1173^\circ)]$ . This quantity is probably small, though it cannot be evaluated with any precision at present.

The large value of the heat of solution<sup>7</sup> reflects the deformation suffered by the electron clouds of the atoms in going from the pure metals to the solution. The portion of the heat of solution that may be called strain energy, as being an effect that would not exist in a liquid solution and approximately calculable from elasticity theory, is small.<sup>28</sup> It is interesting to observe that a gold-nickel solid solution of the present concentration would not be stable relative to the pure components were it not for the loosening of the lattice, and hence the large vibrational entropy that occurs.

#### ACKNOWLEDGMENT

It is a pleasure to acknowledge the assistance of W. K. Murphy with the operation of the calorimeter. Criticism of the manuscript by Professor J. W. Stout, of the University of Chicago, is gratefully acknowledged. This work was supported by AEC Contract No. W-31-109-Eng-52.

#### REFERENCES

- O. Kubaschewski, and E. L. Evans, *Metallurgical Thermochemistry*, Academic Press, New York, 1951.
- J. H. Hildebrand, and R. L. Scott, *The Solubility of Non-electrolytes*, 3rd ed., Reinhold, 1950.
- E. A. Guggenheim, *Thermodynamics*, Interscience, 1949.
- G. Scatchard, *Trans. Far. Soc.* **33**, 160 (1937).
- O. J. Kleppa, *J. Amer. Chem. Soc.* **72**, 3346 (1950).
- O. J. Kleppa, *J. Am. Chem. Soc.* **73**, 385 (1951); **74**, 6052 (1952).
- L. L. Seigle, M. Cohen, and B. L. Averbach, *J. Metals, Trans. A.I.M.E.* **4**, 1320 (1952).
- R. A. Oriani, *Acta Met.* **1**, 144 (1953).
- R. A. Oriani, *Acta Met.* **2**, 608 (1954).
- W. DeSorbo, *Acta Met.* This issue.
- K. K. Kelley, U. S. Bureau of Mines, *Bull.* **476** (1949).
- H. Z. Schimpff, *Phys. Chem.* **71**, 257 (1910).
- P. Schübel, *Z. anorg. Chem.* **87**, 81 (1914).
- O. Z. Kubaschewski, *Elektrochem.* **47**, 475 (1941); *Z. phys. Chem.* **192**, 292 (1943).
- F. M. Jaeger and J. A. Bottema, *Proc. Roy. Soc. (Amsterdam)* **35**, 352 (1932); *ibid.* **35**, 916 (1932). F. M. Jaeger *et al.*, *Trans. Roy. Acad. (Amsterdam)* **35** (Part 2) 916, 929 (1932). T. J. Poppema and F. M. Jaeger, *Proc. Roy. Acad. (Amsterdam)* **35** (Part 2) 822, 833, 836 (1935). F. M. Jaeger and T. J. Poppema, *Rec. trav. chim.* **55**, 492 (1936). A. J. Zuithoff, *Rec. trav. chim.* **59**, 131 (1940).
- D. C. Ginnings and R. J. Corrucini, *J. Research Natl. Bur. Standards* **38**, R.P. 1797, 593 (1947).
- B. F. Naylor, U. S. Bur. Mines, R.I. 3835 (1946).
- T. B. Douglas and J. L. Dever, *Natl. Bur. Standards Rep.* 2302 (1953).
- T. B. Douglas and J. L. Dever, *Natl. Bur. Standards Rep.* 2544 (1953).
- T. B. Douglas, A. F. Ball, D. C. Ginnings, and W. D. Davis, *J. Amer. Chem. Soc.* **74**, 2472 (1952).
- C. B. Satterthwaite, R. S. Craig, and W. E. Wallace, *J. Amer. Chem. Soc.* **76**, 232 (1954). L. W. Coffer, R. S. Craig, C. A. Krier, and W. E. Wallace, *ibid.* **76**, 241 (1954).
- R. A. Oriani and W. K. Murphy, *J. Amer. Chem. Soc.* **76**, 343 (1954).
- E. C. Stoner, *Phil. Mag.* **22**, 81 (1936).
- B. L. Averbach, P. A. Flinn, and M. Cohen, *Acta Met.* **2**, 92 (1954).
- E. C. Ellwood and K. Q. Bagley, *J. Inst. Metals* **80**, 617 (1952).
- D. C. Ginnings, T. B. Douglas, and A. F. Ball, *J. Res. Natl. Bur. Standards* **45**, 23 (1950).
- T. E. Pochapsky, *Acta Met.* **1**, 747 (1953).
- R. A. Oriani, *Acta Met.* To be published.

# INFLUENCE OF GRAIN BOUNDARIES ON THE BEHAVIOUR OF CARBON AND NITROGEN IN $\alpha$ -IRON\*

G. LAGERBERG and ÅKE JOSEFSSON†

The internal friction has been studied as a function of the concentration of carbon or nitrogen in  $\alpha$ -iron at two different grain sizes and upon quenching from various temperatures. It is found that grain boundaries reduce the mobility of the interstitial atoms and that carbon probably is enriched in grain boundary films with rather high carbon content, both phenomena decreasing the internal friction. The solubility of carbon in  $\alpha$ -iron increases the smaller the grain size. The influence of 0.08 per cent of manganese contained in the test material is briefly discussed, and a calculation of the influence of preferred orientation on the internal friction is given.

## INFLUENCE DES JOINTS DE GRAIN SUR LE COMPORTEMENT DU CARBONE ET DE L'AZOTE SUR LE FER $\alpha$

L'influence de la concentration du carbone et de l'azote dans le fer  $\alpha$  sur le frottement interne a été étudiée pour deux grosseurs de grains après trempe à différentes températures. Les joints de grain diminuent la mobilité des atomes interstitiels et le carbone se rassemble de préférence aux joints de grain; ces deux effets diminuent le frottement interne. La solubilité du carbone dans le fer  $\alpha$  croît d'autant plus que le grain est plus fin. L'influence de la teneur en manganèse (0,08%) du matériau étudié est discutée rapidement et un calcul du rôle de la texture sur le frottement interne est donné.

## DER EINFLUSS DER KORNGRENZEN AUF DAS VERHALTEN VON KOHLENSTOFF UND STICKSTOFF IN $\alpha$ -EISEN

An  $\alpha$ -Eisen wurde die innere Reibung in Abhängigkeit von der Kohlenstoff-oder Stickstoffkonzentration für zwei unterschiedliche Korngrößen und verschiedene Abschrecktemperaturen untersucht. Es wurde festgestellt, dass die Korngrenzen die Beweglichkeit der Einlagerungsatome herabsetzen und dass der Kohlenstoff in Korngrenzenfilmen vermutlich sehr stark angereichert wird. Beide Erscheinungen setzen die innere Reibung herab. Die Löslichkeit von Kohlenstoff in  $\alpha$ -Eisen nimmt mit kleiner werdendem Korn zu. Der Einfluss eines Zusatzes von 0,08% Mangan zum untersuchten Material wird kurz diskutiert und eine Berechnung für den Einfluss einer Vorzugsorientierung auf die innere Reibung gegeben.

## INTRODUCTION

Internal friction measurements have proved to be very useful for the study of diffusion, solubility and precipitation in solid solutions of carbon and nitrogen in  $\alpha$ -iron, and our present knowledge of these phenomena is largely based on such measurements.

The internal friction is mostly manifested as damping and is due to the elastic after effect caused by the strain-induced interstitial diffusion of the atoms dissolved in the body-centered-cubic  $\alpha$ -iron. Assuming that the mutual interaction of these atoms could be neglected, Polder<sup>1</sup> showed that the elastic after effect should be proportional to the concentration of either carbon or nitrogen in solid solution. This was experimentally verified for single crystals at low concentrations by Dijkstra.<sup>2</sup>

In the internal friction method developed by Kê,<sup>3</sup> which is the technique most commonly used, the specimen is a wire constituting the suspension element in a torsional pendulum with a period of vibration of about 1 second. The damping of the vibrations, which is dependent on the temperature, is given by  $Q^{-1}$  = the logarithmic decrement/ $\pi$  and this quantity is directly proportional to the elastic after effect.‡ The maximum

of damping occurs at 36°C for carbon and at 20°C for nitrogen. For polycrystalline specimens Dijkstra,<sup>5</sup> by means of resistivity measurements, found that the corresponding  $Q_{\max}^{-1}$  value was equal to the percentage of weight of carbon or nitrogen in solid solution with an accuracy of 10 per cent.

This relationship between concentration and maximum internal friction has been accepted in most works published within the field concerned. No attention has generally been paid to the possibility that interstitial atoms may be trapped by grain boundaries which thus will influence the results. As a rule, however, the test materials have been rather pure, probably leading to coarse-grained structures. The grain-boundary area per unit of volume has then been small, and the neglect of the grain-boundary effect might have been justified.

The present investigation, which deals with the grain-boundary effect mentioned, originated from the observation that the preceding heat treatment of a specimen could influence considerably the internal friction measured upon quenching from a certain temperature,\* which at first seemed rather confusing. The variations of internal friction could be traced back to differences in grain size, which was further checked by

\* Received September 28, 1954.

† Stora Kopparbergs Bergslags Aktiebolag, Domnarvet, Sweden.

‡ The relation between damping and elastic after effect has been mathematically analyzed by Polder<sup>1</sup> and Fast and Dijkstra.<sup>2,4</sup>

\* Thus two specimens, both containing 0.020 per cent C and 0.002 per cent N, which had been furnace cooled from 1100° and normalized from 950°C, respectively, exhibited widely different internal friction values upon quenching from 700°C, the former treatment giving the higher value.

measurements on specimens given different grain sizes by cold work and recrystallization. Thus a smaller grain size was accompanied by a lower internal friction, other factors being constant.

As to the mechanism of this effect two different ways were conceivable:

(a) A small grain size might promote nucleation of carbides or nitrides and consequently, when quenching the specimen precipitation from the supersaturated solid solution could not be avoided.

(b) Grain boundaries might trap or absorb adjacent interstitial atoms.

If a precipitate was formed, according to the first explanation, it would certainly accelerate the precipitation during a subsequent aging process. No such effect could be observed, so the second explanation seemed to be the more likely. In order to establish this conception it became necessary to study the variation of the internal friction with the concentration of carbon or nitrogen at different grain sizes.

## EXPERIMENTS

### Specimen Preparation

The material used had the following basic composition:

C	Si	Mn	P	S	N
0.020	nil	0.08	0.014	0.010	0.002 per cent

The remaining metallic impurities were insignificant, Cu and Co traces, Cr and Ni nil. Mo, V and Ti have not been determined in this heat but are probably less than 0.005 per cent. The oxygen content is not known, but slag inclusions were rather frequent as is seen from the micrographs shown in Fig. 1.

Four different series of specimens in the form of wires 0.7 mm in diameter and 320 mm in length were prepared in accordance with the following procedures.

(a) *Coarse-grained specimens containing carbon.* Wires of the final shape were purified from carbon and nitrogen by treatment in wet hydrogen at 700° for 3 hours. This was followed by furnace cooling from 1100° (at a rate of 200°C per hour) in an argon atmosphere, the grain size achieved being 0.5 to 2 mm. Different amounts of carbon were then introduced by treating specimens at 710°C for different periods (8 to 50 minutes) in hydrogen saturated with n-heptane at room temperature. A final anneal at 710°C for 30 minutes in argon insured the uniform distribution. The resulting structure is shown in Fig. 1a.

(b) *Fine-grained specimens containing carbon.* A wire 3.53 mm in diameter was treated at 700°C in wet hydrogen until the contents of carbon and nitrogen

were less than 0.001 per cent by chemical analysis. It was carburized in hydrogen saturated with n-heptane, at first at 700° for 3 hours and then at 950° for 5 minutes, and further annealed at 950° and 700° in argon for some hours. The wire was cold-drawn to 0.7 mm corresponding to a reduction of area of 96 per cent and recrystallized at 750° for 30 minutes in argon. After these treatments the carbon content was 0.070 per cent, and the grain size varied from 15 to 50 microns from the surface to the center of the wire. This somewhat non-uniform grain-size distribution shown in Fig. 1b was probably due to a higher carbon content in the surface region. A treatment of wires of this material at 680°C in wet hydrogen for different intervals (16 to 30 minutes) produced specimens with different carbon contents. As for the material in (a), this was followed by annealing at 710°C for 30 minutes in argon.

(c) *Coarse-grained specimens containing nitrogen.* The same procedure as for (a) was followed, but instead of carburizing the wires were treated for 3 hours at 580°C in an ammonia-hydrogen mixture. Specimens of different nitrogen contents were produced by using different partial pressures of the ammonia gas.

(d) *Fine-grained specimens containing nitrogen.* Cold-drawn wires (96 per cent reduction of area) 0.7 mm in diameter were recrystallized at 750°C for 30 minutes in argon and purified in wet hydrogen at 700° for 3 hours. The resulting grain size was 15 to 25 microns, and the structure is seen in Fig. 1c. Nitrogen was introduced by treating these wires together with the specimens of the (c) series.

Specimens belonging to one and the same series were found to have the same grain size.

The most subtle problem regarding the specimen preparation was to get the carbon uniformly distributed along the wire. When carburizing the specimens in (a), this could only be done if the temperature along the heating zone did not vary more than  $\pm 2^\circ\text{C}$ . A rather high gas velocity also seemed to be favourable. For some unknown reason, it was not possible to introduce carbon uniformly in fine-grained specimens by this method, and that was the reason why the more complicated procedure of the (b) series had to be applied.

Any heterogeneous distribution of carbon or nitrogen along the specimen was found to lower the internal friction measured. Therefore, several specimens from each of the four series were cut and analyzed for carbon or nitrogen, respectively, in the center part as well as in the two ends. The longitudinal variations were  $\pm 0.0015$  per cent for series (a),  $\pm 0.001$  per cent for (b), and  $\pm 0.001$  per cent below and  $\pm 0.002$  per cent above 0.020 per cent for series (c) and (d). For series (a) and (b) the radial distribution was checked under the microscope by examining specimens aged at 200°C. In all instances a uniform distribution of precipitate existed all over the section of the wire. Applying the formula given by Fast and Verrijp<sup>6</sup> the time of treat-



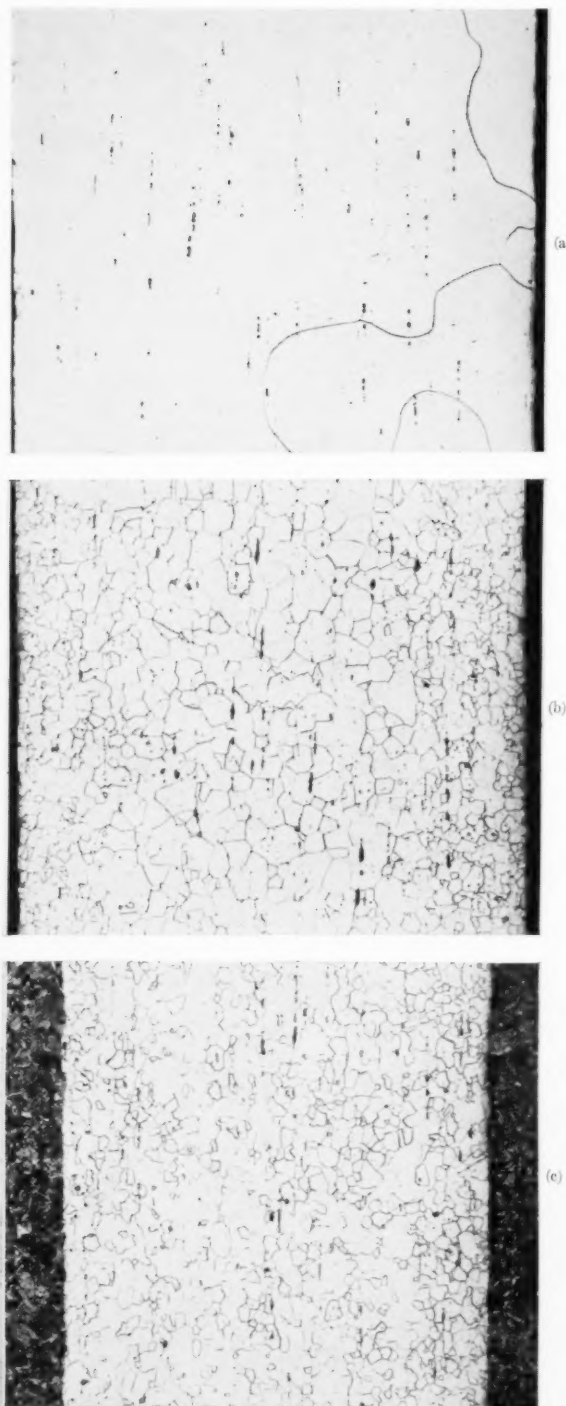


FIG. 1. Microstructures: (All figures reduced to three-fourths in reproduction.) (a) Coarse-grained carburized specimen. Grain size 0.5–2 mm. (b) Fine-grained carburized specimen. Grain size 15–50 microns. (c) Fine-grained nitrided specimen. Grain size 15–25 microns. Magnification 150X.

ment when nitriding series (c) and (d) would correspond to a radial degree of segregation of 1 per cent.

### Internal Friction Measurements

Prior to measurement the specimen was solution treated in a specially designed vertical tube furnace, the heating zone of which had a temperature that did not vary more than  $\pm 2^\circ\text{C}$  along the specimen. The furnace atmosphere consisted of argon or nitrogen depending, respectively, on whether carburized or nitrided specimens were treated. These gases were purified of oxygen, hydrogen, and water vapor before passing through the furnace. The solution treatment was interrupted by rapid quenching attained by a special arrangement, causing the specimen to fall directly from the furnace into a 10 per cent aqueous sodium hydroxide solution at room temperature.

Carburized specimens were quenched from 710 and 630°C. Five minutes of solution treatment were found sufficient. Nitrided specimens were quenched from 710, 580, and 450°C, the times of treatment being 10, 15

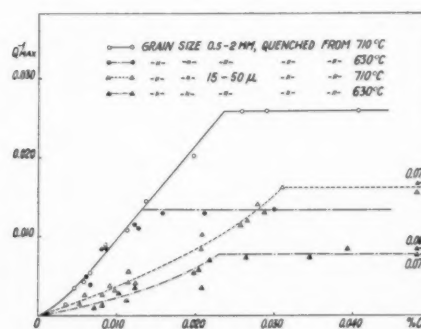


FIG. 2. Internal friction,  $Q_{\max}^{-1}$ , versus carbon content.

and 30 minutes, respectively. Solution treatments at lower temperatures were performed in a lead-bismuth bath, the time of treatment generally being 24 hours.

Immediately upon quenching the internal friction was measured by using a device similar to that described by Ké.<sup>3</sup> The frequency of vibration was 0.8 period per second. The results were corrected for a small background damping of 0.0008.

### Chemical Analysis

The specimens measured for internal friction were analyzed for carbon and nitrogen, respectively.

Carbon was determined according to the method developed by Oelsen, Haase and Graue,<sup>7</sup> using electro-metric titration. On a 0.5-gram sample the accuracy was  $\pm 0.0005$  per cent carbon. Generally, the whole internal friction specimen was used, giving 1-gram samples.

Nitrogen was determined by a titration method of Kempf and Abresch.<sup>8</sup> A weight of sample of 3 grams

allowed for an accuracy of  $\pm 0.0005$  per cent nitrogen. Since an internal friction specimen weighed only 1 gram, the sample had to be made up by three identically treated specimens. This might involve some uncertainty, as the internal friction value measured will be representative for only one-third of the sample. It was found, however, that the  $Q_{\max}^{-1}$  values of specimens identically treated did not differ more than about  $\pm 0.001$ , and judging from the fairly good agreement in the relation between internal friction and concentration (see below) the nitrogen contents probably did not differ more than about  $\pm 0.001$  per cent either.

### RESULTS

In Fig. 2 the  $Q^{-1}$  values obtained after quenching from 710 and 630°C are plotted *versus* carbon content for the two different grain sizes.

For the coarse-grained material (a) the values, with a fairly good precision, fall on a straight line having the slope of 1.2. The extrapolation of this line intersects the concentration axis at about 0.002 per cent, which might indicate that the first few thousands of the percentage of carbon will only cause internal friction to a minor extent. When the carbon content exceeds the solubility limit at the quenching temperature, cementite is formed, and the internal friction will, consequently, be constant for a further increase of carbon concentration. The point of intersection between the horizontal and the sloping parts of the curve will thus denote the carbon solubility.

The remarkably high  $Q_{\max}^{-1}$  value of 0.026 obtained on specimens saturated on carbon at 710°C has not been reported earlier for carbon in  $\alpha$ -iron and may be due to the extremely coarse grain size.

The curves for the fine-grained material (b) differ from those for the coarse-grained material (a) in four essential respects.

1. At the same quenching temperature and composition the fine-grained material yields a considerably lower internal friction value. Also, the value corresponding to saturation is lower.
2. The sloping parts of the curves do not seem to be straight lines, the increase of internal friction being greater at higher concentrations.
3. There is a marked influence of quenching temperature. Quenching from 630°C is accompanied by a lower internal friction than quenching from 710°C, even at C contents below the solubility limit.
4. The points of intersection indicating the solubility of carbon lie at higher concentrations.

Figure 3 shows the relation between internal friction and quenching temperature for specimens with carbon contents well above the solubility limit. The values obtained lie on curves well defined for each of the two grain sizes. The corresponding solubilities as given by the intersections in Fig. 2 are also indicated by dotted

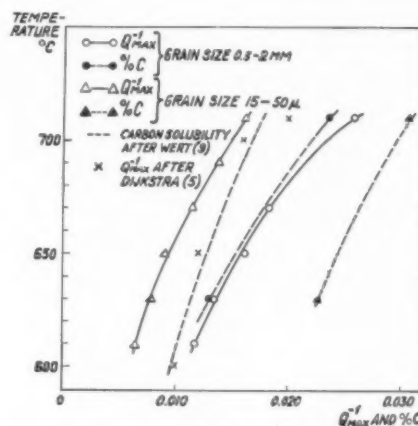


FIG. 3. Internal friction,  $Q_{\max}^{-1}$ , and carbon solubility *versus* quenching temperature.

curves. It is clearly demonstrated that the smaller grain-size is accompanied by the higher carbon solubility whereas for the internal friction the opposite is true. For comparison the solubility curve for carbon in  $\alpha$ -iron according to Wert<sup>9</sup> is shown. In the range of temperature considered he based this curve on internal friction measurements by Dijkstra<sup>5</sup> (whose results are plotted in Fig. 3) and on chemical analysis of ferrite in equilibrium with cementite from the work by Stanley.<sup>10</sup>

The internal friction as a function of the nitrogen concentration at the two different grain sizes is shown in Fig. 4. Quenching temperatures of 710, 580 and 450°C were employed. All measurements refer to individual specimens.

As for carbon the smaller grain size is accompanied by a lower internal friction. In both cases, however, the curves are approximately straight lines bending somewhat to the concentration axis at higher nitrogen contents. This form is in agreement with the results of Åström and Borelius.<sup>11</sup> The slopes are about 1.0 and 0.7, respectively.

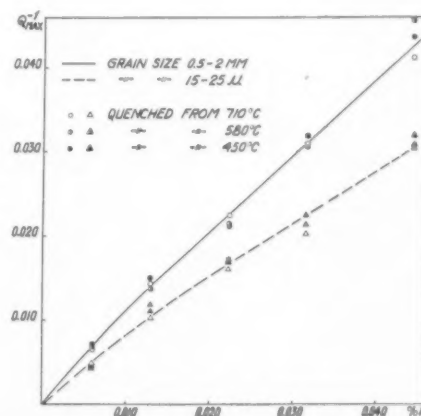


FIG. 4. Internal friction,  $Q_{\max}^{-1}$ , *versus* nitrogen content.

Contrary to the findings for fine-grained specimens containing carbon the internal friction is not influenced by the quenching temperature. There is no tendency in the spread of the plotted values, which increases somewhat with raised nitrogen content and is due to differences between the individual specimens. This independence of quenching temperature was found to be true even at 350, 300 and 250°C, provided that the nitrogen content was below the solubility limit. Thus, specimens with 0.006 per cent nitrogen quenched from these temperatures (24 hours at temperature) showed no decrease of damping with quenching temperature at any of the two grain sizes.

It should be emphasized that coarse-grained and fine-grained specimens that were nitrided together had exactly the same nitrogen content by chemical analysis. Accordingly, at one and the same nitrogen activity the concentration and hence the solubility of nitrogen in  $\alpha$ -iron is unaffected by grain size.

### DISCUSSION

As demonstrated, the grain size influences the internal friction due to either carbon or nitrogen, but the nature of the effect is somewhat different for the two elements. Thus the solubility of carbon is affected, whereas for nitrogen this is not so.\*

Since the internal friction is a measure of the entire number of movable interstitial atoms we might interpret the results in the way that the mobility of the atoms is reduced by grain boundaries. In addition, the boundaries seem to be capable of absorbing more carbon atoms than the ferrite of the grain interior.

As for the restriction of the mobility the following picture is probable. The lattice adjacent to a grain boundary is thought to be more strained than that of the grain interior. A small external stress will then not be able to move the interstitial atoms located in the strained regions into other interstices and hence these atoms will not cause internal friction. Obviously, a smaller grain size involves a greater amount of strained volume and a lower internal friction.

The markedly higher solubility of carbon in the fine-grained material as compared to the coarse-grained one\*\* shown in Figs. 2 and 3 must be attributed to

some sort of grain-boundary absorption. This is also indicated by the form of the curves for the fine-grained material in Fig. 2. Hence, the carbon atoms seem to prefer sites where they do not cause internal friction. This preference is most evident at low concentrations. At higher concentrations an increasing proportion of the atoms will enter interstices where they are freely movable; the grain boundaries become successively less prone to absorption. There seems to be an equilibrium distribution between the movable and the absorbed atoms and this equilibrium is shifted towards a greater amount absorbed when the temperature is lowered.

At a first sight this behavior of carbon might be thought to be in excellent agreement with the Cottrell theory,<sup>12</sup> if the grain-boundary zones are regarded as an arrangement of dislocations. In the strained volume near grain boundaries the carbon atoms would be trapped and enriched. The trapping is illustrated by the different  $Q_{\max}^{-1}$  values at saturation for the two grain sizes and the enrichment by the corresponding different solubilities.

However, it is not very likely that we should be able to observe a Cottrell effect at 700°C for carbon, as we cannot do this for nitrogen even at 250°. As a consequence, we conclude that the enrichment of carbon is due to the formation of a grain-boundary film rich in carbon, the nature of which might be quite separate from that of ferrite. This is consistent with the findings of Tsou, Nutting, and Menter,<sup>13</sup> who showed by means of electron diffraction that the grain-boundary ridges seen on the etched surface of a mild steel specimen had the structure of austenite. A high carbon content of grain-boundary ridges has also been proposed by Trotter, McLean, and Clews.<sup>14</sup> Moreover, the different behaviors of carbon and nitrogen agree with the observations of Hultgren *et al.*<sup>15</sup> who found that the amount of raised veins in ferrite sub-boundaries produced by hot-deformation was clearly related to the carbon content, whereas the influence of nitrogen was less evident.

If, in conformity with Tsou, Nutting and Menter, we assume that the thickness of the grain boundary film is of the magnitude of 1000 Å and that carbon is enriched solely in the volume occupied by this film, its carbon content  $X$  at the carbon activity of cementite may be calculated:

Carbon solubility of coarse-grained material (approximately the solubility of ferrite free from grain boundaries) at 710°C (Fig. 2)	0.023 pct
Carbon solubility of fine-grained material at 710°C (Fig. 2)	0.031 pct
Mean area per grain on etched surface of fine-grained material (Fig. 1b)	0.000256 mm <sup>2</sup>
Corresponding grain boundary area according to <sup>16</sup>	150 mm <sup>2</sup> /mm <sup>3</sup>
Corresponding volume of grain boundary film per mm <sup>3</sup> of specimen volume	150 · 10 <sup>-4</sup> mm <sup>3</sup>

was deposited much earlier on the former. Obviously the coarse-grained ferrite reached saturation more rapidly—that is, at a lower concentration.

\* It might be advocated that the fine-grained specimens were prepared in different ways, the final grain sizes being obtained by recrystallization of carburized material in the case of carbon and purified material in the case of nitrogen. This might be thought to produce different grain-boundary structures that would be responsible for the different behaviours of carbon and nitrogen. It was found, however, that our observations regarding nitrogen were valid even if the nitrided specimens were prepared by recrystallization in the nitrided state.

\*\* There are additional records of this fact. Two specimens with the original composition of the test material were sealed in silica tubes. One was normalized and the other furnace cooled from the  $\gamma$ -range, and no change of composition occurred during these treatments. They were both quenched from 700°C. In the furnace-cooled specimen that had a grain size of about 250 microns some grain-boundary cementite could be seen whereas in the normalized specimen having a grain size of 50 microns no cementite could be detected. It was also observed that on simultaneous carburization of coarse-grained and fine-grained decarburized materials carbon

We get the equation:

$$X \cdot 150 \cdot 10^{-4} + (1 - 150 \cdot 10^{-4}) \cdot 0.023 = 0.031 \quad X \approx 0.5\%$$

This compares to the carbon content of the grain-boundary austenite found by Tsou, Nutting and Menter, the lattice spacing of which corresponded to 0.85–1.7 per cent carbon.

It might also be of interest to compute the thickness of the supposed strained regions adjacent to a grain boundary. We assume that the strains are too low to cause any enrichment of carbon as was found in the case of nitrogen. Except for the grain-boundary film, the ferrite will have the same composition at the carbon activity of cementite for both grain sizes. Upon quenching from 710°C of saturated specimens the fine-grained material exhibits a 38 per cent lower internal friction value as compared to the coarse-grained one. The grain-boundary area of the former is 150 mm<sup>2</sup>/mm<sup>3</sup>; for the latter it might be neglected. The thickness will then be

$$\frac{0.38}{150} = 0.0025 \text{ mm} = 2.5 \text{ microns,}$$

which is a minimum value, since there is probably a continuous transition from the trapped to the movable state of the carbon atoms from the very boundary surface and inwards. This value is far above the dimensions of the grain boundary ridges, seen under the microscope.

We will finally discuss some factors that might be thought to have influenced our results.

The test material contains 0.08 per cent manganese, the presence of which is known to influence the internal friction due to both carbon and nitrogen according to Wert<sup>17</sup> and Dijkstra and Sladek,<sup>18</sup> respectively. Although the mechanism seems to be somewhat different for the two elements, 0.5 per cent of manganese is reported to decrease the  $Q_{\max}^{-1}$  values in both instances. Moreover, the maximum internal friction caused by nitrogen is shifted from 20 to 27°C. The slopes of the curves in Figs. 2 and 4 are therefore likely to be less than what would have been obtained on a pure iron. However, the manganese content is probably too low to cause any considerable difference, and on all measurements the nitrogen peak occurred at 20°C.

Therefore, the observed grain-size effect probably also applies to pure iron. Indications of that were obtained by measurements on electrolytic iron remelted in high-vacuum and containing no manganese. A bar of this material, 6 mm in diameter, was carburized to 0.022 per cent carbon. By cold work and recrystallization, internal friction specimens with grain sizes of about 0.2 mm and 30 microns, respectively, were produced. The heat treatments were performed in sealed silica tubes, the composition being unchanged according to chemical analysis. Upon quenching from 710° the  $Q_{\max}^{-1}$  values were 0.016 for the coarse-grained and

0.004 for the fine-grained specimen. The same wires were then carburized to about 0.040 per cent of carbon and again quenched from 710°C. The  $Q_{\max}^{-1}$  value of the coarse-grained specimen remained unchanged, whereas that of the fine-grained one increased to 0.008. These values fit into the picture outlined for the less pure material. The coarse-grained specimen might be considered saturated with carbon at 0.022 per cent and hence will not change its internal friction on a further increase in carbon content, while the contrary is probable for the fine-grained one. However, the increase of the internal friction of the latter might partly have been due to a slight grain growth during the carburizing treatment; the grain size increased from 30 to about 35 microns. As a whole, it proved to be difficult to keep a small grain size stable in this material, and that was why a more thorough investigation could not be performed.

Another factor that might have affected the measurements is the possible presence of preferred orientation, since the elastic after-effect is an anisotropic property. The coarse-grained material that was furnace cooled from the  $\gamma$ -range could be expected to exhibit a lower degree of preferred orientation than that of the fine-grained one, recrystallized in the  $\alpha$ -range. An approximate calculation given in the Appendix shows that the internal friction value of a wire with a [110]-texture (the texture of a cold-drawn iron wire) is 15 per cent higher as compared to a wire with grains of random orientations. Hence, any effect of preferred orientation in fine-grained specimens would be opposite to that observed. However, the difference is relatively small and since X-ray diffraction failed to reveal any preferred orientation in the wires recrystallized in the  $\alpha$ -range, we might have been justified in neglecting its influence.

#### ACKNOWLEDGMENTS

The authors want to express their indebtedness to the Stora Kopparbergs Bergslags Aktiebolag for the permission to publish this paper, and to Professor Bo Kalling, Head of the Research Department, for his interest and support.

Thanks are further due to Mr. Eric Hedlund who carried out most of the experimental work and to Mr. Hans U. Åström for valuable discussions.

#### REFERENCES

1. D. Polder, Philips Res. Rep. **1**, 5 (1945).
2. L. J. Dijkstra, Philips Res. Rep. **2**, 357 (1947).
3. T. S. Kê, Phys. Rev. **71**, 533 (1947).
4. J. D. Fast and L. J. Dijkstra, Philips Techn. Rundschau **13**, 181 (1951).
5. L. J. Dijkstra, J. Metals **1**, 252 (1949).
6. J. D. Fast and M. B. Verrijp, J. Iron Steel Inst. **176**, 24 (1954).
7. W. Oelsen, H. Haase, and G. Graue, Arch. f. d. Eisenh. wesen **22**, 225 (1951).
8. H. Kempf and K. Abresch, Arch. f. d. Eisenh. wesen **14**, 255 (1940–41).
9. C. A. Wert, J. Metals **2**, 1243 (1950).
10. J. K. Stanley, J. Metals **1**, 752 (1949).
11. H. U. Åström and G. Borelius, Acta Met. **2**, 547 (1954).



12. A. H. Cottrell, Progress in Metal Physics, Vol. 4, p. 205.
13. A. L. Tsou, J. Nutting, and J. W. Menter, J. Iron Steel Inst. **172**, 163 (1952); Proc. Phys. Soc. **B65**, 305 (1952).
14. J. Trotter, D. McLean, and C. J. B. Clews, Symposium on Metallurgical Applications of the Electron Microscope. Inst. Met. London, Nov. 16, 1949, p. 75.
15. A. Hultgren, A. Josefsson, G. Lagerberg, and E. Kula. To be published.
16. A.S.M. Metals Handbook, 1948 ed. p. 405.
17. C. A. Wert, J. Metals **4**, 602 (1952).
18. L. J. Dijkstra and R. J. Sladek, J. Metals **5**, 69 (1953).
19. C. S. Barrett, Structure of Metals, 2nd ed. London, 1953, p. 532.

## APPENDIX

Influence of preferred orientation on the internal friction due to carbon or nitrogen in solid solution in  $\alpha$ -iron as measured with the torsional pendulum.

According to Polder<sup>1</sup> the magnitude of the elastic after-effect  $\lambda_2/\lambda_1$  for a single crystal is given by

$$\frac{\lambda_2}{\lambda_1} = -\frac{2E \cdot V}{3RT} C_0 \left( \frac{e_{zz} - e_{xx}}{C_z} \right)^2 [1 - 3(x^2y^2 + y^2z^2 + z^2x^2)], \quad (1)$$

where

$x, y, z$  = the direction cosines with respect to the cube axis

$E$  = elastic modulus in the direction  $x, y, z$

$V$  = volume of one mole of Fe

$R$  = gas constant per mole

$T$  = absolute temperature

$3C_0$  = number of gram atoms of C or N per gram atom of Fe

$C_z$  = number of gram atoms of C or N in the  $z$ -interstices per gram atom of Fe

$e_{zz}, e_{xx}$  = relative deformations in the  $z$ - and  $x$ -directions respectively caused by  $C_z$  on the condition that the crystal is not externally stressed and  $C_x = C_y = 0$ .

The internal friction value  $Q_{\max}^{-1}$  is related to  $\lambda_2/\lambda_1$  by the equation

$$\frac{\lambda_2}{\lambda_1} = 2Q_{\max}^{-1}. \quad (2)$$

When only considering the anisotropy of the elastic

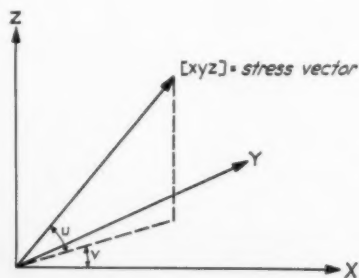


Fig. 5. Locus of stress vector in a wire with random orientation.

after-effect, Eq. (1) might be rewritten as:

$$Q_{\max}^{-1} = A \cdot E [1 - 3(x^2y^2 + y^2z^2 + z^2x^2)] = A \cdot E(1 - 3F). \quad (3)$$

$A$  is a coefficient and

$$F = x^2y^2 + y^2z^2 + z^2x^2. \quad (4)$$

Now the sum of the squared direction cosines is equal to one

$$x^2 + y^2 + z^2 = 1. \quad (5)$$

Eliminating  $z$ , Eqs. (4) and (5) give

$$F = x^2 + y^2 - x^2y^2 - x^4 - y^4. \quad (6)$$

The elastic modulus  $E$  has a directional variation, which according to Barrett<sup>19</sup> is given by

$$\frac{1}{E} = s_{11} - 2[(s_{11} - s_{12}) - \frac{1}{2}s_{44}](x^2y^2 + y^2z^2 + z^2x^2). \quad (7)$$

Here  $x, y$  and  $z$  retain their previous meanings, and  $s_{11}, s_{12}$  and  $s_{44}$  are elastic constants having the following values for  $\alpha$ -iron at room temperature.

$$s_{11} = 0.757 \cdot 10^{-12} \text{ cm}^2/\text{dyne}$$

$$s_{12} = -0.282 \cdot 10^{-12} \text{ cm}^2/\text{dyne}$$

$$s_{44} = 0.862 \cdot 10^{-12} \text{ cm}^2/\text{dyne}.$$

We insert these figures in Eq. (7) and obtain

$$E = \frac{10^{12}}{0.757(1 - 1.608F)}. \quad (8)$$

Equation (3) should consequently be written

$$Q_{\max}^{-1} = C \cdot \frac{1 - 3F}{1 - 1.608F}, \quad (9)$$

where  $C$  is a coefficient. This equation accounts fully for the anisotropy of the elastic after-effect.

When using the torsional pendulum the principal stress directions will form a  $45^\circ$  angle with the axis of the wire specimen. We assume that the  $Q_{\max}^{-1}$  measured on a polycrystalline specimen is made up by the sum of the effects deriving from all the individual grains the number of which is large. The contribution of a grain will depend on its orientation with respect to the principal stress as determined by Eq. (9).

We want to compare the measured internal friction of a specimen with randomly oriented grains with that of a specimen with a  $[110]$ -texture. (This is the texture of a cold-drawn iron wire and it is generally assumed to be retained after recrystallization.) This involves an evaluation of the corresponding mean values of  $Q_{\max}^{-1}$  according to Eq. (9) with regard to the weighted amount of material in each orientation direction.



When no preferred orientation, we obtain

$$F_{\text{mean } 0} = \frac{1}{4\pi} \int_0^{\pi/2} \int_0^{\pi/2} F(u, v) \cos u \cdot du dv = \frac{1}{5}$$

and

$$Q_{\text{max mean } 0}^{-1} = A \cdot E \left(1 - \frac{3}{5}\right) = A \cdot E \cdot \frac{2}{5}.$$

In the same way, we get for [110]-texture

$$F_{\text{mean } [110]} = \frac{1}{\pi} \int_0^{\pi} F(w) dw = \frac{23}{128}$$

and

$$Q_{\text{max mean } [110]}^{-1} = A \cdot E \left(1 - 3 \cdot \frac{23}{128}\right) = A \cdot E \cdot \frac{59}{128}.$$

Hence,

$$\frac{Q_{\text{max mean } [110]}^{-1}}{Q_{\text{max mean } 0}^{-1}} = \frac{59}{128} \cdot \frac{5}{2} = 1.15.$$

Accordingly, a specimen with a fully developed [110]-texture exhibits a 15 per cent higher internal friction value than a specimen with randomly oriented grains.

# DISLOCATIONS IN LOW-ANGLE BOUNDARIES IN GERMANIUM\*

F. L. VOGEL, JR.†

A more complete account is given in this paper of previously reported observations of dislocations in low-angle boundaries in germanium single crystals. At higher magnifications these boundaries appear as regularly spaced conical pits. X-ray and microscopic studies, which revealed an excellent correlation between the dislocation spacings in the boundary and the observed pit spacing, are described. It is concluded that the pits occur at the points of emergence of edge dislocations.

## DISLOCATIONS DANS LES LIMITES DE SOUS-GRAINS DU GERMANIUM

Cet article donne une description complète des observations antérieures sur les dislocations dans les limites de sous-grains des monocristaux de germanium. A fort grossissement, ces limites apparaissent comme des piqûres coniques régulièrement espacées. Une excellente corrélation est observée entre l'écartement de ces piqûres et celui des dislocations obtenu par micrographie et par rayons X. On en conclut que les piqûres se produisent aux points où débouchent les dislocations-coins.

## VERSETZUNGEN AN KLEINWINKELKORNGRENZEN BEI GERMANIUM

In der vorliegenden Arbeit wird eine vollständigere Beschreibung von früher bereits mitgeteilten Beobachtungen über Versetzungen an Kleinwinkelkorngrenzen ("low-angle" Korngrenzen) in Einkristallen aus Germanium gegeben. Bei grösserer Auflösung erscheinen diese Korngrenzen als regelmässig verteilte konische Grübchen. Es werden röntgenografische und mikroskopische Untersuchungen beschrieben, die einen sehr guten Zusammenhang zwischen den Versetzungsabständen an der Korngrenze und den beobachteten Lochabständen zeigen. Die Grübchen treten an den Stellen auf, wo sich Stufenversetzungen befinden.

## INTRODUCTION

The dislocation model of a low-angle crystal boundary proposed by Burgers<sup>1</sup> is shown schematically in Fig. 1. The boundary occupies a (010) plane in a simple cubic lattice and divides two parts of the crystal which have a [001] axis in common. This is referred to as a pure tilt boundary, since the existing misorientation can be described by a small rotation ( $\theta$ ) of one part of the crystal relative to the other about the common [001] axis. The boundary is represented in Fig. 1 as an array of edge dislocations of the same sign having a spacing  $D = b/\theta$  where  $b$  is the Burgers vector of the dislocations.

Recent theoretical and experimental developments have substantiated this model. Read and Shockley<sup>2</sup> derived a theory of crystal boundary energies based on Burgers' model, which states that the interfacial energy is a function of the angle of tilt. Numerous observations by Dunn<sup>3</sup> and by Aust and Chalmers<sup>4</sup> have shown excellent agreement with this theory. A more direct verification of Burgers' model resulted from observations by Lacombe<sup>5</sup> on sub-boundaries in an aluminum single crystal. These sub-boundaries appeared as rows of streaks or elongated pits. The associated Laue back-reflection photograms had split spots which permitted an estimate to be made of the orientation difference between neighboring sub-grains. The dislocation spacing to be expected in the aluminum sub-grains was calculated<sup>6</sup> using a reasonable value for the Burgers vector, and agreement to an order of magnitude ( $10^{-3}$  cm) was found with the spacing of pits in the sub-

boundaries. A more explicit interpretation of the low angle boundary in terms of dislocations has been given for germanium single crystals,<sup>7</sup> the details of which will be given here.

Low-angle boundaries appear in polished and etched cross sections of zone-melted germanium single crystals. The degree of misorientation associated with the boundaries is extremely small—of the order of a minute. Figure 2 is a macrograph of a short low-angle boundary in germanium. At higher magnification, significant detail becomes apparent, as shown in Fig. 3. The boundary appears here, not as a continuous line, but as a

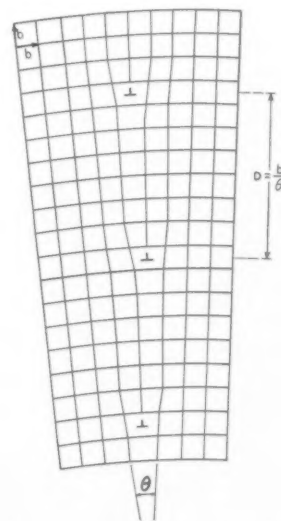


FIG. 1. Low-angle tilt boundary after Burgers.

\* Received October 1, 1954.

† Bell Telephone Laboratories, Murray Hill, N. J.



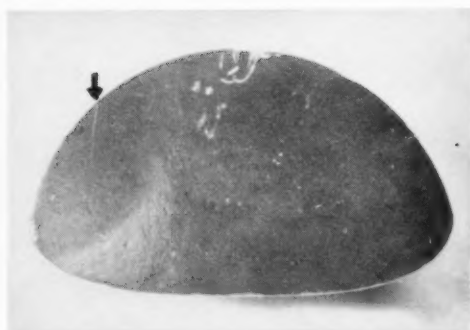


FIG. 2. Cross section of  $\langle 100 \rangle$  grown germanium single crystal showing (under arrow) low-angle boundary.  $2\times$  magnification. CP-4 Polish-etch.

series of discrete overlapping conical pits of regular spacing. Each etch pit is characterized by a definite center. To prove that these pits mark the places on the surface where edge dislocations emerge, the difference in lattice orientation on either side of the boundary was measured by means of X-rays, and the dislocation spacing calculated from this, using Burgers' model, was compared with the pit spacing measured in the microscope.

#### EXPERIMENTAL

The zone-melted germanium crystals<sup>8</sup> were prepared with a  $[100]$  as the growth direction. The low-angle boundaries appeared on  $(100)$  faces normal to the growth direction when the cross section was polished-etched in CP-4 solution (a mixture composed of 25 ml  $\text{HNO}_3$ , 15 ml  $\text{HF}$ , 15 ml glacial  $\text{CH}_3\text{COOH}$  and a few drops of  $\text{Br}_2$ ). The plane of the boundaries was the  $(011)$  in the zone of the growth axis. Cubical specimens were cut with  $(100)$  as one surface and a  $(011)$  as another surface. After lightly grinding these two surfaces on 600-mesh carborundum, each specimen was im-

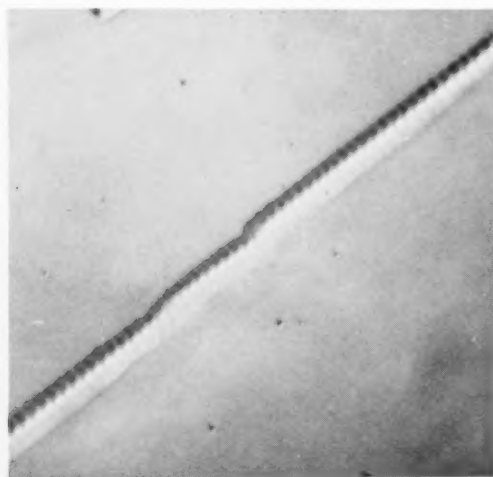


FIG. 3. Dislocation pits in low-angle boundary in germanium.  $1000\times$  magnification. CP-4 Polish etch.

mersed in CP-4 for two minutes. The conical etch pits were found to be well developed on the  $(100)$  face, but were not visible in the  $(011)$  surface. The pit spacings along the low-angle boundary were then measured with a microscope at  $1000\times$  on the  $(100)$  surface about 0.005 inch from the  $(011)$  surface. Spacings were averaged over several thousandths of an inch. The accuracy of these measurements was estimated as better than  $\pm 10\%$ . Material was then removed to a depth of 0.005 inch from the  $(011)$  surface by light grinding followed by etching. This was done so that the X-ray measurements could be made on a strain-free surface at the same distance from the original surface that the microscopic measurements were made.

A schematic diagram of the X-ray equipment that was used is shown in Fig. 4. The X-radiation from a copper target tube was reflected from the  $(011)$  planes of a quartz reference crystal and then onto the specimen.

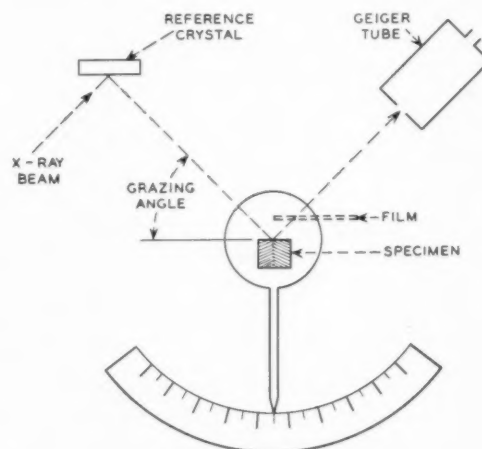


FIG. 4. Schematic diagram of double crystal X-ray spectrometer.

The beam emanating from the reference crystal contained the  $K\alpha_1$  and  $K\alpha_2$  components, each highly collimated but slightly divergent with respect to the other. The specimen was mounted in the quarter-circle goniometer so that the  $(011)$  planes received the incident radiation at the grazing angle ( $g$ ), determined by Bragg's Law. The intensity of the  $(220)$  reflection was measured by a Geiger tube set at twice the diffraction angle to the incident beam. The Geiger tube was equipped with a slit wide enough to register the diffracted intensity regardless of small lateral displacements of the planes under examination. Simultaneous readings of the diffracted intensity and the grazing angle in the vicinity of the diffracting position provided a rocking curve. Since the angles of tilt were quite small (of the same order of magnitude as the diffracted line widths), the rocking curves of both sides of the boundary were superposed. Therefore, in making the measurements it was necessary to obtain the rocking curve of

each side of the boundary with the other side shielded from the beam. This is shown in Fig. 5, which illustrates a typical result. The angle of tilt is given by the difference in angular positions of corresponding peaks of the two curves. The response of the Geiger tube was not a linear function of the X-ray intensity it received; and therefore the ordinate in Fig. 5 is distorted. This had no effect, however, on the values obtained for the angles of tilt. The angular position of the peak of the diffraction curves or the centers of the curves at half-intensity could be determined to within  $\pm 2.5$  seconds.

A graphic portrayal of the tilt of the atom planes was obtained by placing a film in a position to record the diffracted beam as shown in Fig. 4. Figure 6 shows two photographs obtained in this way. In these photographs the boundary lies in a plane normal to the page which separates the light and dark regions. The grazing angle differed in the two exposures by a rotation of 25 seconds of arc about the  $[100]$  axis. The reversal of intensity of diffraction which was observed indicates

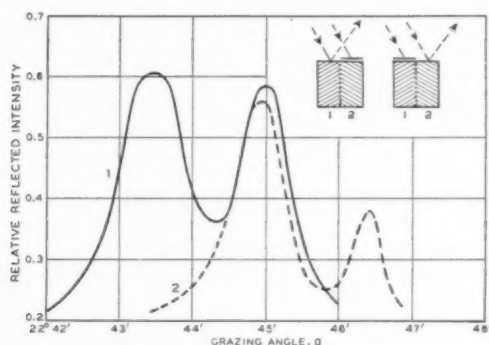


FIG. 5. Rocking curves for typical tilt boundary specimen. Ordinate not corrected for non-linear response of Geiger tube.

that in one photograph the (011) planes on only one side of the boundary were in a position to diffract, while, in the second photograph, only the (011) planes on the other side were in a position to diffract strongly. There is another feature visible in these photographs which merits consideration because it illustrates the sensitivity of this X-ray technique. In both photographs, in the upper part to the right of the main boundary, there appears a small but definite change in blackening along a line parallel to the main boundary. Also, the difference in intensity across the main boundary is greater at the bottom than at the top of the photographs. These observations are consistent with the pit spacings observed on the end (100) faces in that these were slightly lower on the face at the bottom of the photograph. Also, on the (100) end face, at the top of the photograph, there was a sparsely pitted boundary to the right of the main boundary. The difference in orientation at this smaller boundary was about 5 seconds.

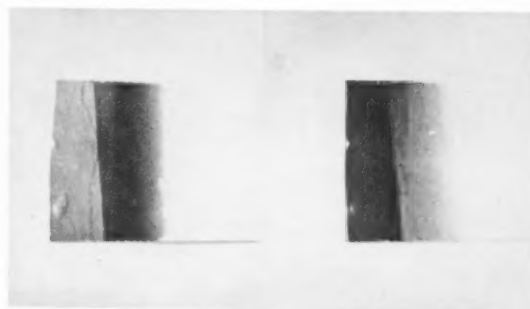


FIG. 6. X-ray diffraction photographs of (220) reflection of tilt boundary specimen. Specimen rotated 25 seconds about common axis parallel to reflecting planes.  $4\times$  magnification.

The possibility exists that the shift of the diffraction peak in Fig. 5 was due to a difference in interplanar spacing on either side of the boundary. Figure 7 illustrates how it was proved that the shift was due to a tilt of the lattice planes and not a difference in interplanar spacing. If the diffracting planes are rotated 180 degrees about their own normals, the diffraction peaks of the two sides of the boundary will reverse positions if the peak shift is due to a tilt of the planes. The peaks will not so reverse if the shift is caused by a difference in interplanar spacing. This criterion was applied to the specimens studied and it was thus ascertained that the shift was caused by a tilt of the lattice planes, rather than by a difference in interplanar spacing.

It was also necessary to prove that there existed no other component of rotation of the lattices with respect to each other. This was accomplished by measurements analogous to the measurement of  $\theta$ , except that other axes of rotation at right angles to the angle of tilt were examined. Since other rotations were not found to exist, it was concluded that only pure tilt boundaries were encountered in this investigation.

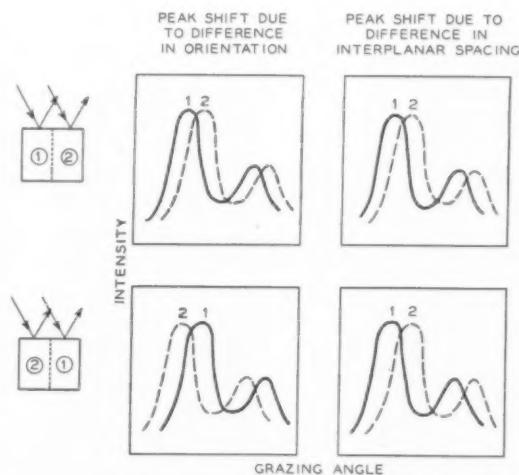


FIG. 7. Method of proof that rocking curve shift was due to tilt of lattice planes and not to difference in interplanar spacing across boundary.

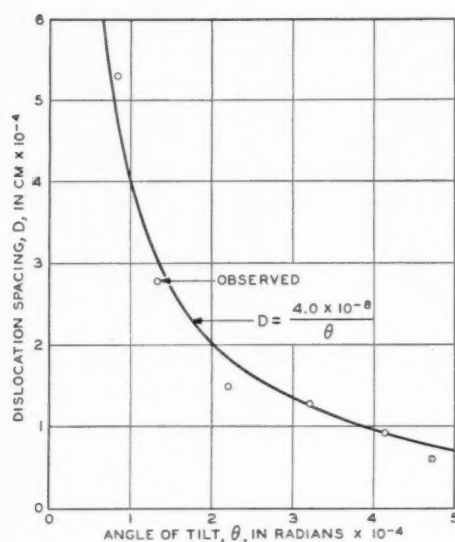


FIG. 8. Plot of dislocation spacing calculated from angle of tilt versus observed pit spacings. Angles range from 17.5 to 85 seconds.

In a pure tilt boundary, the edge dislocations lie parallel to the axis of tilt. In this case, therefore, the line of the dislocations was a  $[100]$ . The interaction energy of an array of edge dislocations of like sign with parallel Burgers vectors is minimized when they align themselves in a plane normal to the Burgers vector.<sup>9</sup> Since the boundaries occupied  $(0\bar{1}1)$  planes, the Burgers vectors must be the shortest lattice translation vectors normal thereto or  $\mathbf{b} = 1/2 a [110]$ . The Burgers vector therefore has the magnitude  $(\sqrt{2}/2)a_0 = 4.0 \text{ \AA}$ . It is interesting that this deduction is consistent with the experimentally determined Burgers vector in the slip process<sup>10</sup>. By coincidence, the picture of Fig. 1 applies equally well for this case in depicting the atom positions on a  $(100)$  plane in germanium with a low-angle boundary in a  $(0\bar{1}1)$  plane.

## RESULTS AND CONCLUSION

Six specimens were examined as described above. The pit spacings, as measured with the microscope, are shown in Fig. 8 together with the corresponding angles of tilt measured by X-rays. The data cover the range of values that can be investigated conveniently by the methods used. These limits are spacings of  $1 \times 10^{-4}$  cm as determined by the light microscope and angles of  $1 \times 10^{-4}$  radian as determined by the double crystal X-ray spectrometer.

From the excellent agreement between the calculated dislocation spacings and the observed pit spacings, it is concluded that the etch pits mark the places on the surface where edge dislocations emerge.

## ACKNOWLEDGMENT

The author is indebted to many associates for their parts in bringing this work to a successful conclusion: To W. G. Pfann for discussions which lead to this investigation, to W. L. Bond for use of his special X-ray equipment, to E. E. Thomas for help with the micrographic work, to W. T. Read for discussions on dislocations. H. E. Corey's observations on etching of germanium stimulated this work. Miss L. C. Lovell, K. M. Olsen and C. F. Larkin kindly supplied the crystals.

## REFERENCES

1. J. M. Burgers, Proc. Phys. Soc. (London) **52**, 23 (1940).
2. W. T. Read and W. Shockley, Phys. Rev. **78**, 275 (1950).
3. C. G. Dunn and F. Lionetti, Trans. A.I.M.E. **185**, 125 (1949).
4. K. T. Aust and B. Chalmers, Proc. Roy. Soc. (London) **A-201**, 210 (1950).
5. P. Lacombe, Report on Conference on Strength of Solids (The Physical Society, London, 1948).
6. W. Shockley and W. T. Read, Phys. Rev. **75**, 692 (1949).
7. F. L. Vogel, W. G. Pfann, H. E. Corey, and E. E. Thomas, Phys. Rev. **90**, 489 (1953).
8. W. G. Pfann and K. M. Olsen, Phys. Rev. **89**, 322 (1953).
9. W. T. Read, Dislocations in Crystals (McGraw-Hill, New York, 1953).
10. R. G. Treuting, Private communication.

## TENSILE PROPERTIES OF ANNEALED TANTALUM AT LOW TEMPERATURES\*

J. H. BECHTOLD†

The tensile properties of annealed tantalum, like those of other body-centered-cubic metals, were found to depend markedly on test temperature. The yield strength increased sharply from about 39 000 psi at room temperature to over 125 000 psi at  $-195^{\circ}\text{C}$ . However, a transition from a ductile to a brittle type of fracture was not observed in this temperature range. The marked temperature dependence of the yield strength is believed to be due to the ordering of carbon and nitrogen atoms into preferred interstitial sites around dislocations.

### PROPRIÉTÉS MÉCANIQUES À BASSE TEMPÉRATURE DU TANTALE RECUIT

Les propriétés mécaniques du tantale recuit dépendent fortement de la température d'essai. Comme pour tous les autres métaux cubiques centrés, la limite élastique croît de 39.000 psi à température ordinaire à plus de 125.000 psi à  $-195^{\circ}\text{C}$ . Toutefois, il n'a pas été observé dans cet intervalle de point de transition pour la rupture. L'influence de la température sur la limite élastique serait due à une répartition ordonnée des atomes de carbone et d'hydrogène en insertion autour des dislocations.

### DIE DEHNUNGSEIGENSCHAFTEN VON ANGELASSENEM TANTAL BEI NIEDRIGEN TEMPERATUREN

Die Dehnungseigenschaften von angelassenem Tantal hängen stark von der Prüftemperatur ab, wie dies auch schon für andere kubisch-raumzentrierte Metalle gezeigt werden konnte. Die Streckgrenzenspannung steigt scharf von 27,42 kg/mm<sup>2</sup> bei Raumtemperatur auf über 87,89 kg/mm<sup>2</sup> bei  $-195^{\circ}\text{C}$ . Ein Übergang vom Verformungs- zum Sprödbruch wurde jedoch in diesem Temperaturbereich nicht beobachtet. Die auffallende Temperaturabhängigkeit der Streckgrenzenspannung scheint auf die Einordnung von Kohlenstoff- und Stickstoffatomen auf bevorzugte Zwischengitterplätze in der Umgebung von Versetzungen zurückzuführen zu sein.

## INTRODUCTION

The mechanical properties of metals with the body-centered-cubic crystal structure undergo marked changes at low temperatures. These changes are usually characterized by a large increase in the yield strength and a sharp transition from a ductile to a brittle type of fracture. When tested in uniaxial tension at slow strain rates, these changes usually occur near  $-150^{\circ}\text{C}$  in iron,<sup>1</sup> near room temperature in molybdenum<sup>2</sup> and at about  $250^{\circ}\text{C}$  in tungsten.<sup>3</sup> Similar marked changes in mechanical properties have not been observed in metals with the face-centered-cubic crystal structure.

The effects of temperature on the mechanical properties of tantalum, which is body-centered-cubic, have not been examined in detail. Tests by Druyvesteyn<sup>4</sup> indicate that work-hardened tantalum retains some ductility as low as  $-180^{\circ}\text{C}$ . The purpose of the present investigation was to determine the flow and fracture characteristics of tantalum to establish if temperature affects its mechanical properties in the same way as it does other body-centered-cubic metals and to disclose any major differences that might exist.

## MATERIAL AND TEST PROCEDURE

The tantalum was purchased from the Fansteel Metallurgical Corporation as 0.300-inch diameter swaged rod. Tensile specimens with the dimensions shown in Fig. 1 were machined from the as-received rod and then annealed for one hour at  $1700^{\circ}\text{C}$  in a vacuum

of  $5 \times 10^{-6}$  mm of Hg. This anneal resulted in a completely recrystallized grain structure averaging 450 grains/sq mm. No second phases were observed in the microstructure; however, the center of the rod was quite porous, apparently the ingot had not been sintered to a very high density and subsequent working did not close up all of the micro voids. The chemical analysis of the tantalum and of several other metals with which it will be compared are listed in Table I.

The test procedure was the same as that outlined previously for studying the tensile properties of molybdenum<sup>2</sup> and tungsten.<sup>3</sup> For tests below room temperature, the specimens were cooled in gaseous nitrogen by the method of Wessel and Olleman.<sup>5</sup> The rate of elongation was held constant throughout the test at  $2.8 \times 10^{-4}$  sec<sup>-1</sup> unless otherwise specified. The proportional limit taken from the autographically plotted load-elongation curves is used herein as the criterion for yielding and referred to as the yield strength. Reduction in area determined from area measurements after fracture is taken as the criterion of ductility. Significant test data for several test temperatures are listed in Table II.

TABLE I. Chemical analysis.

Metal	Oxygen	Nitrogen	Carbon	Others
Tantalum	*	0.01	0.010	99.9 tantalum (estimated)
Molybdenum <sup>2</sup>	0.0017	0.0056	0.014	99.9% molybdenum†
Tungsten <sup>3</sup>	*	0.008	0.02	99.9 tungsten (estimated)
Iron <sup>1</sup>	0.058	0.002	0.02	99.7% iron
Nickel	*	0.013	0.013	99.0% nickel+cobalt†

\* Not determined.

† Supplier analysis.

\* Received October 18, 1954.

† Westinghouse Research Laboratories, East Pittsburgh, Pennsylvania.



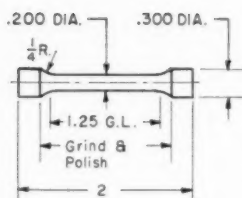


FIG. 1. Tensile test specimens for tantalum.

### RESULTS

The load-per cent elongation curves in Fig. 2 reveal the marked temperature dependence of the tensile properties of tantalum. The rapid increase in yield strength is readily evident from the curves of tests below room temperature. The percent elongation at fracture also varies significantly with temperature, being a maximum at about 25°C and decreasing at both higher and lower temperatures. The reduction in area at fracture, Table II, however, does not change greatly with temperature. The fractures at all temperatures were dull, fibrous, ductile types of failures.

One of the more striking effects of test temperature is on the over-all shape of the load-elongation curves. The curves at -78°C and above are similar to those usually observed for annealed, polycrystalline body-centered-cubic metals. Yielding is discontinuous, as revealed by upper and lower yield points at most temperatures, and a distinct yield-point elongation at all temperatures. The yield-point elongation increases with decreased test temperature. After the yield-point elongation, the load increases as the specimen elongates uniformly until a maximum, the ultimate tensile strength, is reached. Additional elongation occurs at decreasing load as the specimen necks down.

Below -130°C, the pronounced upper and lower yield points again indicate that initial yielding is discontinuous. At the lower yield point stress, several per cent elongation occurs at essentially constant load and then the load decreases rapidly instead of increasing as it does at higher temperatures. A load-elongation

curve of this type indicates that there was no uniform elongation of the gage-length section of the specimen and diameter measurements after test along the gage-length section revealed that all of the deformation was concentrated in a relatively narrow necked-down region adjacent to the rupture. This type of stress-strain curve has not been observed in previous studies of molybdenum and tungsten. Although the percent elongation at fracture was considerably less than at higher temperatures, the reduction in area in the necked-down region was not significantly smaller than at high temperatures and the fractures at all temperatures were dull, fibrous ruptures. In iron, molybdenum and tungsten, bright, brittle fractures are always observed at low temperatures.

The strain-hardening behavior of most body-centered-cubic metals can be expressed approximately by the relation:

$$\sigma = K\delta^n, \quad (1)$$

where  $\sigma$  = true stress;  $\delta$  = natural strain;  $K$  = a constant, the stress at unit natural strain; and  $n$  = a constant, usually referred to as the strain-hardening exponent. Figure 3 shows that this equation expresses quite well the relation between stress and strain from the strain at the limit of the yield-point elongation to the strain maximum load point. True stress and natural strains could not be calculated for tests below -78°C since the specimens did not elongate uniformly. The work-hardening exponents are relatively small for an annealed metal, especially below room temperature, and decrease with decreasing test temperature. If the decrease continues at the same rate below -78°C as it does above, the work-hardening exponents must be very small below -78°C. The abnormal appearance of the load-elongation curves at -130, -180 and -195°C probably results from these very low work-hardening exponents and the large difference between the upper and lower yield points.

Several indications of strain aging were observed at 200°C and 400°C. The load-elongation curves at these temperatures had numerous small irregularities such as found in the load-elongation curves of age hardening aluminum alloys. These irregularities were too small to be reproduced in the curves in Fig. 2. The relatively large decrease in uniform and total elongation and increase in the work-hardening exponent above room temperature is believed to be further evidence of a strain-aging reaction. Strain aging in this temperature range due to the precipitation, during testing, of traces of carbon, nitrogen, or oxygen, can be predicted from the internal friction studies of Kê.<sup>6</sup> Strain-aging phenomena are observed in all of the body-centered-cubic metals, usually in the temperature range slightly above that at which the yield strength increases most rapidly with decreasing test temperature.

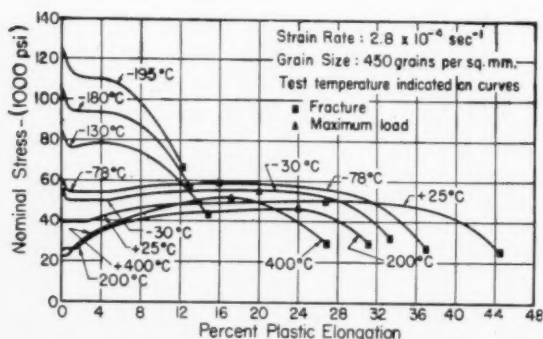


FIG. 2. Nominal stress-per cent elongation curves for annealed tantalum.

TABLE II. Tensile properties of annealed tantalum.

Spec. no.	Test temp. (°C)	Strain rate (in./in./sec)	Yield strength* (1000 psi)	Yielding		Maximum Load		Fracture	
				Upper yield point (1000 psi)	Lower yield point (1000 psi)	Ultimate tensile strength (1000 psi)	Uniform elongation (per cent)	Total elongation (per cent)	Total reduction in area (per cent)
Ta-6	-195	$2.8 \times 10^{-4}$	124.0	124.6	110.0	(a)†	0	12.4	75
Ta-2	-180	$2.8 \times 10^{-4}$	104.5	105.2	94.0	(a)†	0	13.4	78
Ta-9	-130	$2.8 \times 10^{-4}$	82.7	84.2	76.0	(a)†	0	15	81
Ta-3	-78	$2.8 \times 10^{-4}$	60.3	61.0	54.5	58.7	16.0	37	89
Ta-8	-30	$2.8 \times 10^{-4}$	56.5	56.5	50.2	55.7	20.0	34	86
Ta-1	+25	$2.8 \times 10^{-4}$	39.3	(b)‡	39.7	49.8	28	45	86
Ta-10	+200	$2.8 \times 10^{-4}$	26.2	(b)‡	26.2	46.8	24	31	86
Ta-4	+400	$2.8 \times 10^{-4}$	22.4	(b)‡	22.4	52.2	18	27	84
Ta-7	-195	$9.2 \times 10^{-3}$	127.0	128.5	110.0	(a)*	0	11.3	71
Ta-5	-195	$5.0 \times 10^{-1}$	—	139.5	—	(a)*	0	11	76

\* Yield strength defined as the stress at which the load-per cent elongation curve deviates from linearity.

† These specimens did not have ultimate tensile strengths in the usual significance attached to the term since the load did not increase after the yield point elongation (see Fig. 2).

‡ No pronounced upper yield point, but a definite yield point elongation.

### DISCUSSION

The effects of temperature on the yield strength and ductility of tantalum and of several other metals are compared in Figs. 4 and 5. The curves in Fig. 4 show the marked temperature dependence of the yield strength of body-centered-cubic metals and the relatively small effect of temperature on the yield strength of nickel, which is representative of face-centered-cubic metals. The yield strengths of iron, molybdenum and tungsten cannot be determined by the tensile tests below about  $-195^{\circ}\text{C}$ ,  $-75^{\circ}\text{C}$  and  $+150^{\circ}\text{C}$  respectively, since brittle fracture will occur before plastic yielding. However, if the yield curves are extrapolated to lower temperatures, a very high yield strengths are predicted for absolute zero. In addition to a marked dependence on temperature, the yield strength is quite sensitive to changes in strain rate. This can be seen by comparing specimens Ta5, Ta6 and Ta7 in Table II. The strain rate effect in tantalum is not as marked as it is in tungsten<sup>7</sup> or molybdenum<sup>2</sup> but slightly greater than in iron. Strain rate has a very small effect on the yield strength of nickel at low temperatures and presumably of other face-centered-cubic metals.

The reduction in area curves, Fig. 5, illustrate the sharp change from ductile-to-brittle behavior in iron, molybdenum and tungsten. Similar changes in ductility do not occur in the face-centered-cubic metals, nor was it observed in tantalum in the temperature range examined. The reason tantalum remains ductile is discussed later.

Previously, a qualitative correlation has been observed between the temperature of the ductile-to-brittle transition and the melting points for the metals iron, molybdenum and tungsten. Tungsten melts at  $3410^{\circ}\text{C}$ , molybdenum at  $2620^{\circ}\text{C}$ , and iron at  $1540^{\circ}\text{C}$ . This correlation obviously does not exist for tantalum, which melts at  $3000^{\circ}\text{C}$ , and whose ductile-to-brittle transition occurs at a lower temperature than any of the above metals. There does appear to be, however, some correlation between the ductile-to-brittle transi-

tion temperature and the modulus of elasticity. The moduli of elasticity of tungsten, molybdenum, iron and tantalum are about  $55 \times 10^6$  psi,  $45 \times 10^6$  psi,  $30 \times 10^6$  psi and  $27.5 \times 10^6$  psi, respectively. No good reason for such a correlation is known.

The marked temperature dependence of the yield strength and the predicted very high values at absolute zero must arise from anchoring of dislocations by trace impurities, since, according to dislocation theory, the stress required to move a free dislocation is relatively insensitive to temperature and should be small even at low temperatures. The major impurities present in these metals are the interstitial solutes, mainly carbon and nitrogen. Nabarro<sup>8</sup> has pointed out that carbon (and other interstitial solute atoms) can interact with dislocations in iron (and other body-centered-cubic metals) by at least three mechanisms. The first is by ordinary precipitation hardening, in which particles of the metal carbide (or nitride, etc.) are formed. The second arises from the relief of hydrostatic stresses around the dislocation by the solute atoms segregating into the close vicinity of the dislocation. The third

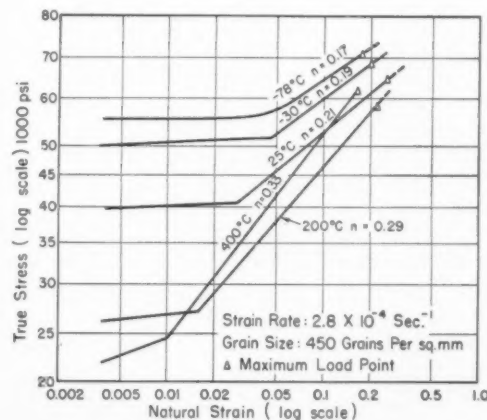


FIG. 3. Flow curves—tantalum.

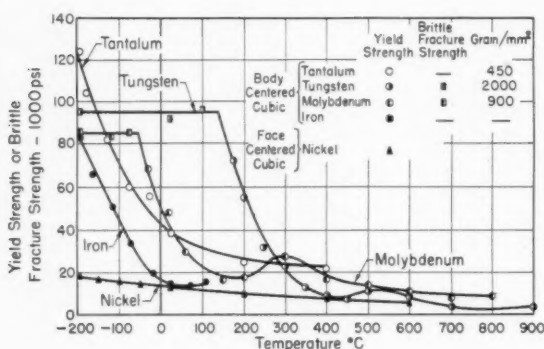


FIG. 4. Effect of temperature on yield strength.

arises from the relief of shear stresses around the dislocation by the solute atom ordering into preferred interstitial sites. It is very unlikely that the first mechanism could account for a marked temperature dependence of the yield strength, or, considering the very small concentrations of solute atoms, for the magnitude of the yield strength approaching absolute zero.

Cottrell<sup>9</sup> has treated the second mechanism and shown that solute atoms which contract or expand the crystal lattice can interact with dislocations, since hydrostatic stresses can be relieved by the solute atoms segregating into the vicinity of the dislocation. Interaction due to relief of hydrostatic stresses occurs only with the edge dislocations, since the stress field of the screw dislocations is ideally a pure shear. The special case of carbon in  $\alpha$ -iron, which is representative of interstitial solute atoms in body-centered-cubic metals, has been treated quantitatively by Cottrell and Bilby.<sup>10</sup> Carbon causes a very marked expansion of the  $\alpha$ -iron lattice, which leads to a very strong interaction with dislocations. Since carbon diffuses relatively easily through the  $\alpha$ -iron lattice, carbon atoms readily segregate to the dislocation and are believed to form a "condensed atmosphere" of carbon atoms. Cottrell and Bilby visualize this "condensed atmosphere" as a single row of carbon atoms lying parallel to the dislocation line and approximately one lattice spacing below the center of the (positive edge) dislocation. Dislocations are very strongly anchored by a "condensed atmosphere." Cottrell and Bilby estimate that a stress of about  $7 \times 10^8$  psi is required to release an anchored dislocation line in the absence of thermal activation. Since it is based on elasticity theory, their treatment undoubtedly overestimates yield strength at absolute zero, but it does show that the anchoring forces are sufficiently strong to account for the observed yield strengths. The anchoring forces, although strong close to the dislocation, extend only over a short distance along the slip plane, and the activation energy for the release of an anchored dislocation line is relatively small. The yield strength should, therefore, change rapidly with temperature from very high values at low temperatures to low values at higher temperatures where thermal

fluctuations aid the release of the dislocations and the "condensed atmosphere" has very little effect. The amount of carbon necessary for a "condensed atmosphere" in an annealed metal is extremely small,  $\sim 10^{-6}$  wt %, and the full effect of an atmosphere can be expected even in the purest metals currently available.

It is doubtful, however, if the relief of hydrostatic stress around dislocations can by itself account for the low-temperature yield behavior of the body-centered-cubic metals, since screw dislocations will not be anchored. The yield behavior of a crystal in which the edge dislocations are anchored but the screw dislocations are not, has not been treated, but probably the unanchored screw dislocations would initiate the release of the edge dislocations at relatively low stresses. To interact with screw dislocations, solute atoms must be able to relieve shear as well as hydrostatic stresses.

There is a mechanism by which interstitial solute atoms in the body-centered-cubic lattice can relieve shear stresses. Carbon atoms in  $\alpha$ -iron, and presumably interstitial solute atoms in other body-centered-cubic metals, may be in either the face-centers or the mid-points of the cube edges. If the carbon atoms are at the centers of (001) faces or mid-points of the edges perpendicular to (001), the lattice becomes tetragonal with (001) as the square base. If the carbon atoms jump to neighboring (010) interstitial sites, the lattice becomes tetragonal with (010) as the square base. Carbon atoms can therefore relieve shear stresses by arranging themselves in preferred interstitial sites, forming essentially an ordered array around the dislocation lines. This interaction should be about as strong with screw as with edge dislocations so that the entire dislocation line is anchored. The shear interaction, like the hydrostatic interaction, will cause the interstitial atom to migrate towards the dislocations forming a higher than average concentration of solute atoms in the close vicinity of the dislocation line. Consequently, the effect should be marked even in relatively dilute solutions. The mechanism is essentially the same as that of Snoek's<sup>11</sup> analysis of internal friction in  $\alpha$ -iron except that the ordering stress is internal stress instead of externally applied stress. Dislocations in face-centered-cubic metals will not be anchored by this mechanism, since neither interstitial nor substitutional solute atoms can relieve shear stresses by migrating into preferred lattice sites in the face-centered-cubic lattice. This is believed to be the reason for the pronounced differences in the low-temperature yield properties of body-centered and face-centered-cubic metals.

The yield strength of metals in which the dislocations are anchored by solute atoms in preferred interstitial sites should depend markedly on temperature and strain rate. At high temperatures, thermal fluctuations will permit the interstitial atoms to reorientate themselves into new preferred interstitial positions as the dislocation proceeds through the crystal. Consequently they will have very little effect on the yield strength. At low

temperatures thermal fluctuations alone are not sufficient for the solute atoms to move to new preferred interstitial sites as the dislocation proceeds through the crystal and either the solute atoms must be reoriented by a high externally applied stress or the dislocation must be pulled bodily through the high energy field of the solute atoms. To account for the yield strengths at absolute zero, undoubtedly some segregation of solute atoms into the close vicinity of the dislocations must occur though probably not to the extent of a "condensed atmosphere."

The effect of the ordering of interstitial solute atoms on mechanical properties should be observed at lower temperatures than the previously described hydrostatic interaction mechanism since the diffusion distances involved are much smaller. The upper limit of the temperature range where the effect of ordering on tensile properties can be expected to first occur should coincide quite closely with the temperature of the peaks, due to interstitial solute atoms, in the internal friction spectrum, since these peaks give the temperature at which the jump frequency of the interstitial solute atom is in phase with the strain frequency. When internal friction is determined by the ordinary torsional pendulum, the outer fibers of the specimen spend about the same time interval in a given strain increment as in the ordinary tension test. Table III shows that the temperature at which the rapid increase in yield strength occurs does, in fact, coincide rather closely with the temperature of the internal friction peaks due to carbon and nitrogen. If the upper and lower yield point phenomenon is assumed to be related to the segregation of interstitial atoms to edge dislocations due to relief of hydrostatic stresses, the upper and lower yield points should be observed at higher temperatures. Column 4 in Table III shows that this is actually observed.

Briefly the marked temperature and strain rate dependence of the yield strength of body-centered-cubic metals is believed to arise from the migration of interstitial solute atoms into the vicinity of the dislocation (but not necessarily to the extent of a Cottrell atmosphere) and there forming an ordered array in preferred interstitial sites. The interaction of interstitial atoms with edge dislocations due to relief of hydrostatic stress around the edge dislocation may cause additional strengthening evidence by an upper and

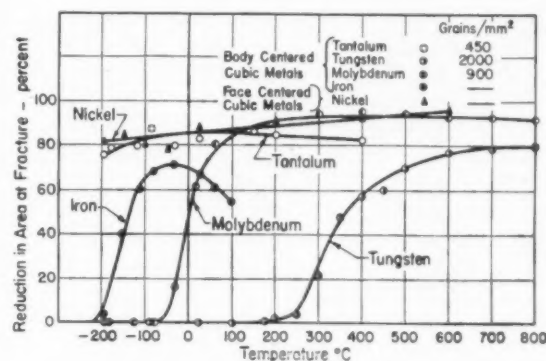


FIG. 5. Effect of temperature on ductility.

lower yield point superimposed on the shear interaction strengthening.

Although the yield strength of tantalum, like that of other body-centered-cubic metals, is highly temperature dependent, the ductility and fracture behavior are not. The ductility of iron, molybdenum and tungsten decreases sharply in the same temperature range in which the yield strength increases rapidly, and the fracture changes from a dull, fibrous, ductile rupture to a bright, brittle, crystalline fracture. This ductile-to-brittle transition arises from the combination of a rapid increase in yield strength and a relatively low stress required for brittle fracture. Completely brittle fracture occurs at the temperature where the yield strength exceeds the stress for brittle fracture. Figure 4 shows this brittle fracture strength is about 85 000 and 95 000 psi for molybdenum and tungsten, respectively.\* The brittle fracture strength of tantalum when in a somewhat comparable condition apparently is considerably higher than this, since brittle fracture did not occur at yield strengths as high as 140 000 psi. This is the reason ductile-to-brittle transition was not observed in tantalum; however, one might occur at lower temperatures or higher strain rates.

The mechanism of brittle fracture is not well enough understood to explain why the brittle fracture strength of tantalum should be higher than that of iron, molybdenum or tungsten. In iron, molybdenum and tungsten brittle fracture is probably related to the segregation of impurities, notably oxides, at grain boundaries and formation of a separate grain boundary phase.<sup>15</sup> One possible explanation of the absence of brittle fracture in tantalum is that oxides do not segregate to grain boundaries as readily as they do in other metals, since the solubility of oxygen in tantalum is considerably higher (approximately 0.9 wt % 1050°C<sup>16</sup>) than it is believed to be in iron, molybdenum and tungsten, and undoubtedly greater than the amount in the specimens tested. If a grain boundary impurity theory of brittle

\* The stress for brittle fracture is not a unique stress but depends on grain size, prior strain, and purity. In molybdenum and iron a smaller grain size, higher purity, or prior strain hardening usually results in a higher fracture stress.<sup>14</sup>

TABLE III.

	Temperature of internal friction peaks (1 cps)	Temperature at which yield strength begins to increase rapidly	Temperature at which discontinuous yielding appears
Iron	Nitrogen <sup>12</sup> ~20°C Carbon <sup>12</sup> ~40°C	~25°C	~250°C
Molybdenum	Carbon <sup>12</sup> ~250°C	150-200°C	400-600°C
Tantalum	Carbon <sup>6</sup> ~150°C	100-200°C	Above 400°C
Tungsten	—	~400°C	—



fracture is correct, brittle fracture would probably be observed in less pure tantalum.

Another possible, though less likely, reason for the absence of brittle fracture may be that tantalum is less prone to mechanical twinning than the other body-centered-cubic metals. Bruckner<sup>17</sup> and others have postulated that brittle transgranular fracture in iron may, in some cases, be related to mechanical twinning. The twins providing local high stress regions which initiate brittle, transgranular fracture at stresses well below the theoretical cleavage strength of the metal. In previous work on molybdenum<sup>2</sup> and tungsten<sup>3</sup> mechanical twins have been found in specimens that fractured in a brittle manner at low temperatures. However, no evidence of any mechanical twinning was found by metallographically examination in any of the tantalum specimens. If there is a relation between mechanical twinning and brittle fracture, the absence of mechanical twinning may be the reason for absence of brittle fracture in tantalum.

#### SUMMARY AND CONCLUSIONS

The yield strength of tantalum, like that of other body-centered-cubic metals, increases rapidly with decreased test temperature. The increase in yield strength is believed to be due to the ordering of interstitial solute atoms into preferred interstitial sites around dislocations.

Tantalum, like iron, molybdenum, and tungsten, exhibits a pronounced upper and lower yield point. Some evidence of strain aging was also observed around 200–400°C.

Unlike iron, molybdenum, and tungsten, tantalum did not exhibit a transition from ductile-to-brittle fracture at temperatures as low as  $-195^{\circ}\text{C}$ . The reason for this is a very high stress for brittle fracture. A possible explanation of this high brittle fracture strength is the relatively high solubility of oxygen in tantalum which

prevents the segregation of oxides at grain boundaries. However, an alternate explanation could be a high critical stress for mechanical twinning. Mechanical twins were not observed in tantalum, although they have been observed in iron, molybdenum and tungsten at low temperatures.

#### ACKNOWLEDGMENTS

The writer acknowledges the assistance of D. D. Lawthers who annealed the tensile specimens, and R. D. Olleman and M. Manjoine for making the tensile tests.

#### REFERENCES

1. G. W. Geil and N. L. Carwile, *J. Research Natl. Bur. Standards* **45**, 129 (1950).
2. J. H. Bechtold, *J. Metals* **5**, 1469 (1953).
3. J. H. Bechtold and P. G. Shewmon, *Trans. A.S.M.* **46**, 349 (1954).
4. M. J. Druyvesteyn, "Experiments on the Effect of Low Temperature on Some Plastic Properties of Metals," *Applied Scientific Research*, Vol. 1, Section A, 1947–1949, p. 66.
5. E. T. Wessel and R. D. Olleman, "Apparatus for Tensile Testing at Sub-Atmospheric Temperature," *A.S.T.M. Bulletin*, No. 187, January 1953, pp. 56–60.
6. Ting-Sui Ké, *Phys. Rev.* **74**, 9 and 914 (1948).
7. J. H. Bechtold, "Strain Rate Effects in Tungsten." To be published *Transactions AIME*.
8. F. R. N. Nabarro, "Mechanical Effects of Carbon in Iron." Report of a conference on Strength of Solids, The Physical Society of London, 1948.
9. A. H. Cottrell, "Effect of Solute Atoms on the Behavior of Dislocations." Report on a Conference on Strength of Solids, The Physical Society of London, 1948.
10. A. H. Cottrell and B. A. Bilby, *Proc. Phys. Soc. (Lond.)* **A62**, 49 (1949).
11. J. L. Snoeh, *Physica* **8**, 711 (1941).
12. C. Wert, "The Metallurgical Use of an Elasticity," *Modern Research Techniques in Physical Metallurgy*, A.S.M., 1953, pp. 225–250.
13. "A Metallurgical Study of Molybdenum," Summary Report to ONR, Battelle Memorial Institute, August 1, 1951, p. 147.
14. J. H. Bechtold, *Trans. A.S.M.* **46**, 1449 (1954). N. J. Petch, *J. Iron and Steel Institute* **174**, 25–28 (1953).
15. W. P. Rees and B. E. Hopkins, *J. Iron and Steel Institute* **72**, 403–409 (1952). J. H. Bechtold, Unpublished data for molybdenum.
16. R. J. Wasilewski, *J. of A.C.S.* **75**, 1001 (1953).
17. W. H. Bruckner, *Welding Journal* **29**, 467-S (1950).

## A CALORIMETRIC INVESTIGATION OF THE SYSTEM SILVER-TIN AT 450°C\*

O. J. KLEPPA†

By use of a new high-temperature calorimeter the heats of formation of solid and liquid alloys of silver-tin were determined at 450°. The results for liquid alloys were obtained by reacting solid silver with liquid tin in the calorimeter. For mole fractions of silver up to 0.2 the results may be represented by the expression

$$\Delta H^M = 15.02 x_{Ag} - 13.33 x_{Ag}^2 \text{ kilojoule/g-atom.}$$

The results are compared with those obtained in earlier calorimetric and equilibrium studies.

The heats of formation of 10 different solid alloys ranging in composition from 75 to 94 atomic per cent silver were derived from the heats of solution of the alloys in liquid tin. The minimum heat of formation ( $\Delta H$ ) was found for the nearly stoichiometric  $\gamma$ -phase ("Ag<sub>3</sub>Sn"), where two alloy samples of very nearly the same composition gave heats of formation of  $-6.06 \pm 0.23$  and  $6.19 \pm 0.23$  kilojoule/g-atom, respectively. From the results for this phase and for the neighboring  $\beta$ -phase we find for the hypothetical process

$$(\gamma)_{x_{Ag}=0.75} \text{ (orthorhombic)} = (\beta)_{x_{Ag}=0.75} \text{ (hexagonal)}$$

a  $\Delta H$  of transformation of about 1.2 kilojoule/g-atom at 450°.

### RECHERCHES CALORIMÉTRIQUES SUR LE SYSTÈME ARGENT-ÉTAIN À 450°

Les chaleurs de formation des alliages solides et liquides Ag-Sn ont été mesurées à 450° avec un nouveau calorimètre pour hautes températures. Les mesures sur les alliages liquides sont obtenues par réaction de l'argent solide avec l'étain liquide dans le calorimètre. Jusqu'à une concentration atomique de 20% d'argent, les résultats peuvent être représentés par l'expression

$$\Delta H^M = 15.02 x_{Ag} - 13.33 x_{Ag}^2 \text{ kilojoule/g-atome.}$$

Ces résultats sont comparés avec les mesures calorimétriques antérieures et le diagramme d'équilibre.

Les chaleurs de formation de 10 alliages solides entre 75 et 94 at% d'argent sont déduites des chaleurs de dissolution de ces alliages dans l'étain liquide. La chaleur de formation minimum ( $\Delta H$ ) est obtenue pour une composition correspondant sensiblement à la phase  $\gamma$  (Ag<sub>3</sub>Sn), pour laquelle deux échantillons ayant sensiblement la même composition ont comme chaleur de formation  $6.06 \pm 0.23$  et  $6.19 \pm 0.23$  kilojoule/g-atome. A partir des résultats pour cette phase  $\gamma$  et pour la phase  $\beta$  voisine, nous trouvons pour la réaction

$$(\gamma)_{x_{Ag}=0.75} \text{ (orthorhombic)} = (\beta)_{x_{Ag}=0.75} \text{ (hexagonal)}$$

une chaleur de formation d'environ 1.2 kilojoule/g-atome à 450°.

### EINE KALORIMETRISCHE UNTERSUCHUNG DES SYSTEMS SILBER-ZINN BEI 450°C

Mit Hilfe eines neuen Hochtemperatur-Kalorimeters wurden die Bildungswärmen von festen und flüssigen Legierungen im System Silber-Zinn bei 450°C bestimmt. Die Ergebnisse für die geschmolzenen Legierungen wurden durch Zugabe von festem Silber zu flüssigem Zinn im Kalorimeter erhalten. Für Molenbrüche bis zu 0,2 Silber können die Ergebnisse durch folgende Formel ausgedrückt werden

$$\Delta H^M = 15,02 x_{Ag} - 13,33 x_{Ag}^2 \text{ kilojoule/g-atom}$$

Die Ergebnisse werden mit älteren kalorimetrischen Bestimmungen und Gleichgewichtsuntersuchungen verglichen.

Die Bildungswärmen von 10 verschiedenen erstarrten Legierungen im Konzentrationsbereich von 75 bis 94 At% Silber werden aus den Lösungswärmen der Legierungen in flüssigem Zinn abgeleitet. Die kleinste Bildungswärme ( $\Delta H$ ) liegt nahe der stöchiometrischen Zusammensetzung der  $\gamma$ -Phase ("Ag<sub>3</sub>Sn"), bei der zwei Proben mit nahezu gleicher Zusammensetzung Bildungswärmen von  $-6,06 \pm 0,23$  bzw.  $6,19 \pm 0,23$  kilojoule/g-atom ergaben. Auf Grund der Ergebnisse für diese und die benachbarte  $\beta$ -Phase fanden wir für den hypothetischen Prozess,  $(\gamma)_{x_{Ag}=0,75} \text{ (rhombisch)} = (\beta)_{x_{Ag}=0,75} \text{ (hexagonal)}$  ein  $\Delta H$  von ungefähr 1,2 kilojoule/g-atom bei 450°C.

### INTRODUCTION

In recent years the increasing interest in the thermochemistry of alloys has initiated the development of new and more powerful calorimetric techniques suitable for determination of heats of formation of alloys.<sup>1-4</sup> A particularly interesting and important development has been the introduction of liquid tin as a solvent for solution calorimetry at elevated temperatures.<sup>2</sup> This method shows promise of providing more accurate data

on heats of formation in alloy systems than has been possible by earlier work in the field.

The author has adopted the tin solution technique for a study of the heats of formation in alloys of group 1B metals (Cu, Ag, Au) with other group B metals (Zn, Cd, etc.). A preliminary note on some aspects of this work has been published recently,<sup>5</sup> while the present report on the silver-tin system is the first detailed discussion of experimental details and results obtained. Another report, dealing with the silver-cadmium, silver-indium and silver-antimony systems, will be published later. Work is also in progress on other alloy systems.

\* Received October 18, 1954.

† Institute for the Study of Metals, The University of Chicago, Chicago, Illinois.

The equilibrium phase diagram for silver-tin<sup>6</sup> indicates that at 450° the following phases are stable:

$\alpha$ , f.c.c.	: 0-10 atomic per cent tin
$\beta$ , c.p. hex.	: 12-22 atomic per cent tin
$\gamma$ , orthorh.	: 24.6-25 atomic per cent tin
$l$ , liquid	: 58-100 atomic per cent tin

The investigation of this system by the tin solution technique logically falls into two parts:

- Determination of the heats of formation of liquid silver-tin alloys by reaction of solid silver with liquid tin in the calorimeter at 450°.
- Preparation of solid silver-tin alloys of known, uniform composition, followed by measurement of the heat of solution of these alloys in liquid tin. The heats of formation of each solid alloy are then obtained as the difference between the observed heat of solution and the heat of formation (obtained under (a) above) of the liquid silver-tin alloy resulting from the solution experiment. Clearly the heats of formation of the solid alloys will be associated with much greater experimental uncertainties than will be the case for the liquid alloys.

### EXPERIMENTAL

The construction of the calorimeter and the details of its operation when used for simple liquid mixing experiments have been discussed elsewhere at considerable length.<sup>4</sup> The only significant changes in procedure adopted in the present work were dictated by the fact that one of the reacting samples was in the solid state. This, first of all, called for the preparation of samples of pure, solid silver and of solid silver-tin alloys with a size and shape suitable to fit the available annular space of the charging and stirring device.<sup>4</sup>

The samples of pure silver were cast in graphite molds from electrolytic silver (assay: 99.9<sub>2</sub> per cent Ag, balance mainly copper) in the shape of hollow cylinders of about 0.5 in. o.d. and about 0.25 in. i.d. After the graphite core had been drilled out, half-cylindrical

specimens of the desired weight were cut from the cast slug.

The silver-tin alloys were prepared by melting known amounts of silver and tin (99.9+ per cent purity) of total weight 15-20 g in a graphite crucible sealed in vycor tubing at a rotary pump vacuum. After the liquid alloy had been homogenized in a slowly tilting furnace for a period of not less than two hours at a temperature 50° or more above the liquidus, the whole alloy was chill-cast while still under vacuum into the desired cylindrical shape. The solid slug was finally annealed for 12-48 hours at 450°, or above. In most samples the uniformity of composition was checked by chemical analysis (Ag as AgCl). The deviation of individual samples from the weighed in composition was always of the order of the analytical precision (0.1 per cent or less).

TABLE I. Molar integral heats of formation of liquid silver-tin alloys from solid silver and liquid tin at 450±2°.

Total, g-atoms	Composition, $x_{Ag}$	$\Delta H^M$ , joule/g-atom	$\Delta H^M/x_{Ag}$ kilojoule	
			Exp.	Calc., Eq. (1)
2.1394	0.0128 <sub>0</sub>	190 <sub>8</sub>	14.91	14.85
0.9734	0.0200 <sub>0</sub>	298	14.90	14.75
0.8550	0.0220	317	14.41	14.73
0.7650	0.0235	(365)	(15.53)	14.71
1.1202	0.0253	371	14.66	14.68
0.8550	0.0281	412	14.66	14.65
0.9645	0.0286	427	14.93	14.64
0.9730	0.0298	439	14.73	14.62
1.1851	0.0300	438	14.60	14.62
0.9191	0.0305	448	14.69	14.61
1.0112	0.0312	448	14.36	14.60
0.9131	0.0358	520	14.53	14.54
0.8917	0.0383	554	14.47	14.51
0.2558	0.1047	1418	13.54	13.62
0.2414	0.1869	2351	12.58	12.53
0.2893	0.3212	3416	10.64	—
0.2724	0.3281	3437	10.48	—
0.2607	0.3402	3407	10.02	—
0.2758	0.3604	3392	9.41	—

Mean deviation of experiments from Eq. (1): 0.11 kJ.

The liquid tin bath used in the calorimetric experiments contained about 100 g metal. The tin was cut from 0.5 in. cast sticks, the surface cleaned by scraping, and the metal then introduced into the calorimeter as described.<sup>4</sup> The weight of the alloy sample was adjusted to yield a liquid alloy containing 2-3 per cent silver.

Throughout the calorimetric experiments the over-all calorimeter temperature was maintained at 450±2°, as measured by a chromel-alumel thermocouple calibrated at the melting point of zinc. The long time fluctuations in temperature had no detectable influence on the observed heat effects.

### RESULTS

#### Liquid Silver-Tin Alloys

The molar heats of formation obtained in 19 separate experiments are given in Table I, which also contains

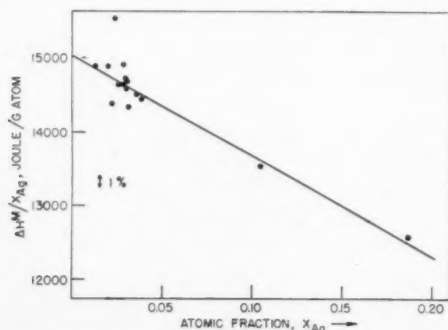


FIG. 1. Molar heats of formation ( $\Delta H^M$ ) of liquid silver-tin alloys at 450°C.

information on the total number of g-atoms of liquid alloy formed in each experiment. It will be noted that the experiments cover alloys with silver contents ranging from about 1 per cent to 36 per cent ( $x_{Ag} \sim 0.01$  to 0.36) with the greatest number of experiments in the important range 2–3 per cent. In Table I will also be found values of the quantity  $\Delta H^M/x_{Ag}$  calculated from the experimental results. This quantity is plotted *versus*  $x_{Ag}$  in Fig. 1. For moderate values of  $x_{Ag}$  such a plot may be expected to yield a straight line, and we note that this seems to hold true within experimental precision for the plotted data up to  $x_{Ag} \sim 0.2$ . The straight line drawn in the figure may be represented by the equation

$$\Delta H^M/x_{Ag} (\text{solid silver}) = 15.02 - 13.33x_{Ag} \text{ kilojoule}, \quad (1)$$

which was derived from a least-squares treatment of the data. For comparison with experimental data we have included values calculated by this equation in the last column of Table I. We find that out of the 15 experiments on alloys containing less than 20 atomic per cent of silver 11 experiments deviate from the given straight line by one per cent or less. Equation (1) has been adopted for the calculations required to evaluate the heats of formation of solid silver-tin alloys. All results on the molar heat of formation of the liquid alloys have been included in Fig. 2, where  $\Delta H^M$  is plotted *versus* composition in curve A. In order to facilitate comparison of the present data with those of earlier investigations (below), Fig. 2 also includes a plot of the molar heat of mixing for liquid silver-tin alloys from liquid tin and undercooled liquid silver at 450° (curve B). For calculation of this curve we have adopted the value for the heat of fusion of silver given by Kubaschewski and Evans,<sup>7</sup> 2.69 kcal or 11.25 kJ/g-atom. We have also, for simplicity, assumed that the heat of fusion is independent of temperature between the melting point (960°) and 450°. The error possibly introduced by this assumption will not affect our discussion in a significant way. By using the adopted value for the heat of fusion in Eq. (1) we get for the heat of mixing of liquid silver and liquid tin at low silver concentrations

$$\Delta H^M/x_{Ag} (\text{liquid silver}) = 3.77 - 13.33x_{Ag} \text{ kilojoule}. \quad (2)$$

We note that the curve for the heat of mixing shows small positive values for low silver concentrations (below  $x_{Ag} \sim 0.28$ ), while negative values are obtained at higher concentrations. It is very interesting to note that Koerber<sup>8</sup> appears to have found a somewhat similar behavior for the heat of mixing in liquid copper-tin alloys at 1150°.

#### Solid Silver-Tin Alloys

In Table II are recorded the values for the heats of formation obtained in 32 solution experiments for 10 different silver-tin alloys containing from 75 to 94

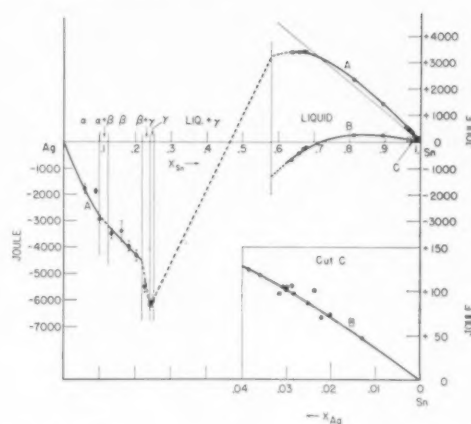


FIG. 2. Molar heats of formation of silver-tin alloys at 450°C. A:  $(1-x)\text{Ag}(s) + x\text{Sn}(l) \rightarrow \text{Ag}_{1-x}\text{Sn}_x(s \text{ or } l)$ . B:  $(1-x)\text{Ag}(l_s, \text{undercooled}) + x\text{Sn}(l) \rightarrow \text{Ag}_{1-x}\text{Sn}_x(l)$ .

atomic per cent silver. In the calculations required to evaluate these data use was made of Eq. (1) above. It will be noted that with each alloy two to five separate experiments were performed. This permits averaging of the individual results and establishes the order of magnitude of experimental precision. The appropriate average is given in the last column of Table II along with the calculated mean deviation. In most cases the mean deviation is about 0.2 kJ/g-atom, independent of alloy concentration. This imposes a practical lower limit on the heats of formation which can be studied with profit in the present apparatus. The average values of the molar heat of formation (with indicated mean deviations) are plotted in Fig. 2 along with the data on liquid alloys.

#### COMPARISON WITH EARLIER DATA. DISCUSSION

The liquid system silver-tin was studied calorimetrically at 1050° by Kawakami,<sup>9</sup> and by the e.m.f. cell method at 900°K by Frantik and McDonald.<sup>10</sup> More recently, Ticknor and Bever<sup>2</sup> have reported on the heat of solution of solid silver in tin at 240° and 300°. According to the data given by Kawakami the  $\Delta H$  of mixing for liquid silver-tin alloys should be negative for all concentrations, with a minimum of about 1.2 kcal/g-atom around 65–70 per cent silver. Frantik and McDonald in their e.m.f. investigations of liquid alloys containing up to 60–70 per cent silver calculate the integral heat of mixing (undercooled liquid silver plus liquid tin) to be positive for all alloy concentrations with a maximum of 1.4 kcal around 50 per cent silver. The discrepancy between these two sets of data can in part be explained by the results obtained in the present work. The experimental basis for the work of Frantik and McDonald was their measurement of the partial molal heat content of tin  $\bar{L}_{Sn}$ , relative to pure liquid tin. In the concentration range covered in their investigation they found positive values for  $\bar{L}_{Sn}$ , which is in



TABLE II. Molar integral heats of formation of solid silver-tin alloys from solid silver and liquid tin at  $450 \pm 2^\circ$ .

Alloy Composition $x_{Ag}$ , phase	g-atoms	Tin + alloy, g-atoms	Observed, joule	$-\Delta H^M$ , kj/g-atom	
				Result	Average
0.94 <sub>0</sub> , $\alpha$	0.02917	0.7702	455.5	1.94	1.74 $\pm$ 0.20
	0.03020	0.8721	460.8	1.54	
0.90 <sub>9</sub> , $\alpha$	0.02665	0.8536	402.8	1.81	1.86 $\pm$ 0.05
	0.03113	0.7883	471.2	1.91	
0.89 <sub>9</sub> , $\alpha$	0.03524	0.8727	568.9	3.08	2.94 $\pm$ 0.14
	0.03079	0.9004	490.6	2.80	
0.86 <sub>6</sub> , $\beta$	0.03620	0.9346	584.9	3.54	3.49 $\pm$ 0.20
	0.03529	0.7599	578.0	3.83	
	0.03305	0.7696	520.8	3.18	
	0.04184	0.9514	668.3	3.40	
0.83 <sub>8</sub> , $\beta$	0.03072	0.7878	497.7	3.98	3.37 $\pm$ 0.40
	0.03864	0.7961	589.7	3.13	
	0.02868	0.7585	437.3	3.01	
0.81 <sub>7</sub> , $\beta$	0.03049	0.9098	477.4	3.68	3.97 $\pm$ 0.20
	0.03248	0.8258	516.1	3.96	
	0.03399	0.8155	553.6	4.38	
	0.03091	0.8429	489.1	3.87	
0.79 <sub>6</sub> , $\beta$	0.03061	0.7558	477.8	4.00	4.31 $\pm$ 0.23
	0.02766	0.7731	437.6	4.17	
	0.03243	0.9173	517.7	4.31	
	0.03361	0.7578	549.1	4.76	
0.77 <sub>5</sub> , $\beta + \gamma$	0.04122	0.8747	676.3	5.18	5.53 $\pm$ 0.24
	0.02717	0.8652	463.2	5.70	
	0.03083	0.9538	526.0	5.72	
0.75 <sub>5</sub> , $\gamma$	0.03039	0.9259	515.6	5.84	6.19 $\pm$ 0.23
	0.02871	0.8939	493.0	6.04	
	0.03280	0.8931	576.5	6.45	
	0.03413	0.9578	588.6	6.11	
	0.03009	0.9207	531.1	6.52	
0.75 <sub>0</sub> , $\gamma$	0.03632	0.9459	624.6	6.22	6.06 $\pm$ 0.23
	0.03003	0.7964	517.5	6.25	
	0.02940	0.7534	490.4	5.71	

agreement with the results of the present investigation. However, in order to evaluate the partial molal properties for silver and the integral heat data these authors were forced to extrapolate their data into the concentration range beyond 60–70 per cent silver. They did not realize that in this range  $\bar{L}_{Sn}$  exhibits a maximum and then falls to negative values for lower concentrations of tin. Such a behavior is clearly indicated by the present results (see, for example, curve B, Fig. 2). Lacking our present knowledge they carried out a smooth extrapolation for  $\bar{L}_{Sn}$  and thus obtained incorrect values for  $\bar{L}_{Ag}$  and for the integral heats of mixing. It is, on the other hand, quite possible to compare Frantik and McDonald's data for  $\bar{L}_{Sn}$  with the results of the present investigation. From our data we find that the relative partial molal heat content of tin for moderate silver concentrations should be given by the expression

$$\bar{L}_{Sn} = 13.33x_{Ag}^2 \text{ kilojoule.}$$

For  $x_{Ag}=0.1$  at  $450^\circ$  we find  $\bar{L}_{Sn}=133$  joule in good agreement with Frantik and McDonald's value at  $900^\circ K$  of 35 cal (146 j). For  $x_{Ag}=0.2$  we get  $\bar{L}_{Sn}=532$  j which is compared with their value of 165 cal (690 j).

The data reported by Kawakami, although correctly giving negative values for the heat of mixing at high silver concentrations, do not suggest any anomalies for low silver contents.

Ticknor and Bever measured the heat of solution of silver in tin by dropping small pieces of silver maintained at  $0^\circ$  into a tin bath at  $240^\circ$  and  $300^\circ$ . After correcting for the heat required to bring their silver samples from  $0^\circ$  to  $240^\circ$  (or  $300^\circ$ ) they report for the limiting heat of solution of solid silver in tin values of 3800–3900 cal/g-atom (15900–16300 j). They estimate their accuracy to be about 150 cal. According to our Eq. (1) we get the corresponding value of 15020 j/g-atom at  $450^\circ$ . Based on the deviations of the experimental data from Eq. (1) we estimate the uncertainty in this figure to be of the order of 150 j. It is, as pointed out previously,<sup>5</sup> quite possible that a major part of the difference between our value and that of Ticknor and Bever is due to the effect of temperature on the heat of solution. The difference would be entirely accounted for by a relative partial molal heat capacity of silver in its dilute solutions in tin of the order of  $-5$  j/deg g-atom. Relative partial molal heat capacities of this order of magnitude have been observed by the author in the liquid systems cadmium-tin and tin-zinc.

The solid alloys of silver-tin have not previously been thermochemically explored. The system has only two intermetallic phases:

$\beta(\epsilon)$ , with a close packed hexagonal structure similar to  $\epsilon$ -brass, and

$\gamma(\epsilon')$ , which according to the X-ray powder investigation by Nial, Almin and Westgren<sup>11</sup> is a slightly distorted  $\epsilon$ -brass structure of orthorhombic symmetry.

These investigators state that it was not possible to say whether  $\gamma$  represents an ordered form of  $\beta$  due to the similarity of the scattering powers of the silver and tin atoms. However, the phase diagram does suggest that this is actually the case, although the unordered  $\beta$ -phase of composition equal to  $\gamma$  ( $x_{Ag}=0.75$ ) cannot be realized. (Note:  $\gamma$  becomes unstable with respect to  $\beta$  and liquid at  $480^\circ$ .) This view is also to some extent supported by the thermochemical data for the two phases obtained in the present work. For the hypothetical process

$$(\gamma)_{x_{Ag}=0.75} = (\beta)_{x_{Ag}=0.75}$$

our results indicate a heat of transformation of about 1.2 kj/g-atom at  $450^\circ$ . This heat effect is of course too small for a complete disordering process which, for this composition and temperature, would involve 3.5–4.0 kj. The present heat data therefore suggest

extensive disorder in the  $\gamma$ -phase and/or a high degree of short-range order in the  $\beta$ -phase at 450°. This is in general agreement with observations on disorder processes, where the disordering entropy frequently is accumulated over a considerable range in temperature. It would seem desirable to reinvestigate the structure of the  $\beta$ - and  $\gamma$ -phases by single crystal X-ray diffraction techniques. Under these conditions super-structure X-ray reflections might possibly be detectable.

#### ACKNOWLEDGMENTS

The author is indebted to Dr. N. H. Nachtrieb for comments on the manuscript of the present paper. The chemical analyses were performed by Mr. M. Kaplan. This work was supported in part by the Office

of Naval Research through Contract No. N-6ori-02004 with the University of Chicago.

#### REFERENCES

1. R. L. McKisson and Le Roy A. Bromley, *J. Metals* **4**, 33 (1952).
2. L. B. Ticknor and M. Bever, *J. Metals* **4**, 941 (1952).
3. F. E. Wittig, *Z. Metallkunde* **44**, 427 (1953).
4. O. J. Kleppa, *J. Phys. Chem.* **59**, 175 (1955).
5. O. J. Kleppa, *J. Am. Chem. Soc.* **76**, 6028 (1954).
6. *Metals Handbook*, American Society for Metals, 1948.
7. O. Kubaschewski and E. L. Evans, *Metallurgical Thermochemistry*, London, 1951.
8. F. Koerber, Stahl, and Eisen, **56**, 1401 (1936).
9. M. Kawakami, *Science Repts. Tôhoku Imp. Univ. I.* **19**, 521 (1930).
10. R. O. Frantik and H. J. McDonald, *Trans. Electrochem. Soc.* **88**, 253 (1945).
11. O. Nial, A. Almin, and A. Westgren, *Z. phys. Chem.* **B14**, 83 (1931).

## CRYSTAL PERFECTION IN ALUMINUM SINGLE CRYSTALS\*

T. S. NOGGLE† and J. S. KOEHLER‡

A high resolution X-ray diffraction technique has been employed on annealed single crystals of aluminum in order to arrive at an estimate of dislocation densities and distributions. This work indicates that in annealed aluminum crystals the majority of the dislocations are present in an essentially random array with densities of the order of  $10^6$  lines/cm<sup>2</sup>. Small-angle boundaries, which are commonly present, contribute about  $10^4$  to  $10^5$  lines/cm<sup>2</sup> to the dislocation density. Comparison of crystals obtained by growth from the melt and by recrystallization indicates that there are no basic differences in the degree of crystal perfection obtained using the two methods of growth.

### QUALITÉ DE MONOCRISTAUX D'ALUMINIUM

La densité et la distribution des dislocations sont évaluées dans des monocristaux d'aluminium recuit par une technique de diffraction de rayons X à haut pouvoir de résolution. Ce travail montre que la plupart des dislocations sont réparties au hasard avec une densité de l'ordre de  $10^6$  lignes par cm<sup>2</sup>. Les limites de sous-grains qui existent couramment introduisent  $10^4$  à  $10^5$  lignes de dislocation par cm<sup>2</sup>. Il n'y a pas de différence essentielle dans la qualité des cristaux obtenus par recristallisation ou à partir de l'état liquide.

### ÜBER DEN IDEALAUFBAU VON ALUMINIUM-EINKRISTALLEN

Angelassene Aluminium-Einkristalle wurden mit Hilfe eines Röntgenverfahrens, das sich durch besonders hohe Auflösung auszeichnet, untersucht, um eine Abschätzungsmöglichkeit für die Versetzungsdichte und -verteilung zu bekommen. Die Arbeit zeigt, dass in angelassenen Aluminium-Einkristallen der grösste Teil der Versetzungen in einer im wesentlichen regellosen Anordnung vorliegt. Die Versetzungsdichten liegen in der Grössenordnung von  $10^6$  Linien/cm<sup>2</sup>. Die meist vorhandenen Kleinwinkelkorn Grenzen ("small-angle" Korn Grenzen) tragen mit ungefähr  $10^4$  bis  $10^5$  Linien/cm<sup>2</sup> zur Versetzungsdichte bei. Ein Vergleich von Einkristallen, die aus der Schmelze gezogen wurden und durch Rekristallisation hergestellten Einkristallen zeigt, dass durch die beiden Verfahren keine wesentlichen Unterschiede im Kristallaufbau hervorgerufen werden.

## INTRODUCTION

It is generally accepted at the present time that a type of crystal imperfection called a dislocation plays a very important role in determining many of the properties of crystals. The influence of dislocations on the properties of crystals arises as a result of the inherent properties of a dislocation and its interaction with other dislocations or other types of lattice defects. Despite the recognized importance of the role of dislocations on properties such as mechanical strength, damping and electrical resistance, there has been but little work done toward obtaining direct estimates of dislocation distributions and densities. This state of affairs is primarily due to the lack of completely satisfactory methods of measuring dislocation densities and distributions. Recently developed X-ray diffraction techniques<sup>1,2,3</sup> offer hope of improving this situation, and as applied particularly to metal crystals, are capable of giving semiquantitative estimates of dislocation densities. In addition these methods can detect the presence of and measure the magnitude of a particular type of dislocation distribution commonly referred to as a small-angle boundary. Information of this kind is of importance in the interpretation of physical behavior in terms of dislocation theory.

The present investigation was carried out to assess the possibilities of using X-ray measurements to de-

termine the dislocation structure of reasonably well-annealed aluminum single crystals. In addition, single crystals of aluminum obtained by different growing methods were examined to ascertain if there were measurable differences in the degree of crystal perfection and if any basic differences in the type or distribution of the imperfections could be detected.

## GENERAL CONSIDERATIONS

X-ray diffraction theory predicts that reflection of X-rays from a set of lattice planes in a perfect crystal should occur over an angular range of a few seconds of arc. In practice, it is found that most crystals give reflections over an angular range in excess of one minute. This spread in the angular range can be interpreted in terms of a mosaic block structure in which the angular range of orientations is given by the spread of the reflection. This concept of a mosaic structure was initially introduced by Darwin<sup>4</sup> to account for the observed intensities of reflections from real crystals. Theory indicated that the observed intensities could be accounted for by a mosaic block size of mean diameter  $10^{-4}$  to  $10^{-5}$  cm. This mosaic structure can be interpreted in terms of dislocation distributions in which the boundaries between the blocks are defined by dislocations, and for the block sizes above would give dislocation densities of  $10^8$  to  $10^{10}$  lines/cm<sup>2</sup>.

In addition to the spread in the reflection angle which arises from the tilting of the blocks, contributions to the angular range of the reflections should arise due to the

\* Received November 3, 1954.

† University of Illinois, Urbana, Illinois.

‡ Now at Oak Ridge National Laboratory, Oak Ridge, Tenn.

size of the mosaic blocks and from the strains associated with the presence of dislocations.

Cottrell<sup>5a</sup> discusses the interpretation of the spread of X-ray reflections in terms of possible dislocation models for the case of tilting of the mosaic blocks. The type of model that he indicates should give the most reliable estimates of dislocation densities consists of a linear array of blocks of mean size  $l$ , each block tilted by the angle  $\alpha$  relative to its neighbors,  $\alpha$  being randomly positive or negative. For this case, the probable angular deviation  $\varphi$  between two points in the crystal separated by the distance  $L$  is given by:

$$\varphi = \alpha(L/l)^{1/2}. \quad (1)$$

Assuming that the angle  $\alpha$  is due to a single dislocation in the block boundary, the probable angular deviation is related to the dislocation density by the relation:

$$\varphi = b\rho^{1/2}(L)^{1/2}, \quad (2)$$

where  $b$  is the Burgers vector of a dislocation and  $\rho$  is the dislocation density in lines/cm<sup>2</sup>.

Extension of this theory to the two-dimensional case and to a derivation of the distribution function of the one-dimensional model leads to results similar to Eq. (2) in that the mean-square deviation increases with increasing sample size. The conclusion from this is that if dislocation distributions are essentially random, then the expected angular deviations will increase with increases in the crystal size or of the region investigated. This point can be checked experimentally. In addition, the tilting block model indicates that this source of angular spread of the reflections is independent of the reflection angle and offers the possibility of sorting out its contributions from other sources of line-broadening which are dependent on the diffraction angle.

The particle-size broadening equation gives the increase in the angular spread of the reflection associated with the size of the coherently reflecting region.<sup>6</sup> This relation is:

$$w - w_0 = \frac{0.9\lambda}{l \cos \theta}, \quad (3)$$

where  $w$  is the experimental line width,  $w_0$  is the instrumental line width,  $\lambda$  is the wavelength of X-rays reflected by the crystal,  $\theta$  is the Bragg angle, and  $l$  = mean particle size. This equation predicts an increase in the line width due to decrease in the particle size. For a given system ( $\lambda$ ,  $l$  constant) the line width observed will vary as a function of  $\sec \theta$ . In practice, the application of this relationship to the interpretation of experimental data requires accurate knowledge of the instrumental line widths—particularly in the case of annealed crystals where  $l$  is relatively large and the expected changes in line width are small.

The influence of lattice strains on the angular range of the reflections arises from the change in the diffrac-

tion angle with changes in the interplanar spacing. The shift in the reflection angle is given by:

$$\Delta\theta = -\epsilon \tan \theta, \quad (4)$$

where  $\epsilon$  is the strain and  $\theta$  is the diffraction angle. A uniform strain will simply produce a shift in the diffraction angle without any change in the angular range of the reflection. However, a non-uniform strain will give a contribution to the line width due to variation in  $\epsilon$ . The line-width increase  $\Delta w$  due to a range of strain  $\Delta\epsilon$  is given by:

$$\Delta w = \Delta\epsilon \tan \theta. \quad (5)$$

In order to relate Eq. (5) to dislocation theory, the mean strain due to dislocations in a crystal can be estimated by averaging the strain due to a single dislocation over the region surrounding the dislocation to points midway between adjacent dislocations. This type of calculation can be carried out for edge type dislocations and gives:

$$(\bar{\epsilon}^2)^{1/2} = \frac{b}{R} \left( \log \frac{R}{r_0} \right)^{1/2}, \quad (6)$$

where  $\bar{\epsilon}^2$  is the mean-square tensile or compressive strain,  $b$  is the Burgers vector of a dislocation,  $R$  is the radius of the region occupied by the dislocation, and  $r_0$  is the radius of a region around the core of the dislocation in which equation (6) is not applicable due to failure of the elasticity equations from which (6) is derived, in the region of large strains near the center of the dislocation. This region extends several atomic dimensions around the dislocation and is given a value of  $6 \times 10^{-8}$  cm in subsequent calculations. Equation (6) gives the mean tensile strain in the region below a positive edge dislocation, or the mean compressive strain in the region above the dislocation. Thus, the range of strain will be twice the mean strain. Taking this into account, and also that  $R \approx \frac{1}{2}l$ , we get:

$$\Delta w = 4b\rho^{1/2} \left( \log \frac{1}{2r_0\rho^{1/2}} \right)^{1/2} \cdot \tan \theta. \quad (7)$$

The increase in line width predicted by this equation would be due only to edge-type dislocations since screw-type dislocations introduce no dilation of the lattice.<sup>5b</sup>

In addition to the sources of line-broadening discussed above, small-angle boundaries are usually present in metal crystals and are detected readily by high angular resolution X-ray diffraction techniques.<sup>6</sup> They are observed in an X-ray reflection as a displacement between one portion of the reflection and another. The angle associated with this displacement is a direct measure of the angular misorientation occurring at the boundary. The simplest type of boundary that can be constructed using dislocations consists of a sheet of parallel-edge-type dislocations of the same sign with a mean spacing  $h$  between the dislocations. For small



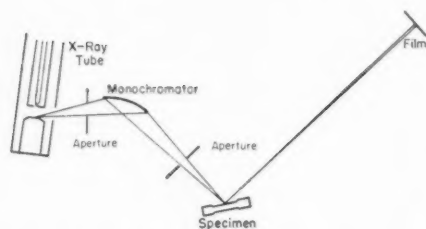


FIG. 1. Schematic diagram of experimental set-up.

angular misorientations, the angle of tilt of the boundary is:

$$\alpha = \frac{b}{h}, \quad (8)$$

where  $\alpha$  is the tilt angle of the boundary and  $b$  is the Burgers vector of the dislocations.

High-resolution X-ray diffraction methods have been applied to metal single crystals by several investigators, and their results have indicated that a higher degree of crystal perfection than heretofore expected sometimes exists in carefully handled single crystals obtained by recrystallization. Guinier and Tennevin,<sup>1</sup> using a focusing Laue method, reported a maximum disorientation in certain aluminum specimens of less than 30 seconds of arc over regions involving about 30 mm<sup>3</sup>. In terms of the tilting-block model for estimating dislocation densities (Eq. 2), this gives a dislocation density of  $\rho = 2.3 \times 10^8$  lines/cm. Lambot, Vassamillet, and Dejace,<sup>2</sup> employing a method similar to that used in the present investigation, reported for Al and Fe single crystals a maximum disorientation of 50 seconds of arc. This corresponds to a dislocation density of about  $7.5 \times 10^6$  lines/cm<sup>2</sup>. Gay, Hirsch and Kelly,<sup>3</sup> using a micro-beam technique, report the upper limit for the dislocation densities in annealed aluminum as  $3 \times 10^8$  lines/cm<sup>2</sup>. Since their work was carried out on polycrystalline material, it is not clear that their results are comparable to results obtained on single crystals.

#### EXPERIMENTAL METHODS

High-purity aluminum single crystal specimens were prepared in the form of square tensile specimens 1 cm square by 6 cm long in the reduced section of the bars. One group of specimens was prepared by the strain-anneal method of Schwope, Shober, and Jackson.<sup>7</sup> The other group of specimens were prepared by the "soft mold" method.<sup>8</sup> Both groups of specimens were prepared from the same bars of "hi-purity" aluminum (99.99+% Al).\*

After the appropriate crystal growing cycles had been carried out, the specimens were etched in a macro-etch solution<sup>9</sup> which was capable of showing orientation differences of about 1/2 degree. The presence or absence

of visible disorientations on the etched specimens was used as a criterion for sorting them into satisfactory and unsatisfactory categories. Most of the specimens processed by the strain-anneal method required an anneal of 20–50 hours at 650°C to eliminate isolated grains that remained after the growing cycle. The yield of satisfactory specimens was about the same for each method, being slightly better than 50 per cent.

#### X-RAY METHODS

The X-ray method used was essentially the same as that described by Lambot, Vassamillet, and Dejace.<sup>2</sup> Our experimental set-up is indicated schematically in Fig. 1. It employed a G.E. CA7, copper target, X-ray tube with the beam taken from the line focus port at about 4 degrees to the plane of the target. A bent crystal monochromator intercepted this beam and reflected a monochromatic beam which was convergent in the horizontal plane and divergent in the vertical plane. When properly adjusted the monochromator gave a fine-line focus in which the Cu-K $\alpha$  doublet was

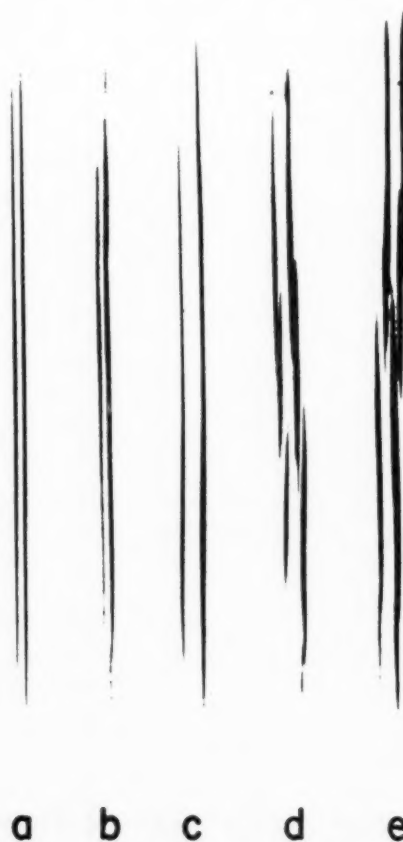


FIG. 2. *a.* Quartz ( $2\bar{1}0$ ); *b.* Al specimen D (111); *c.* Al specimen 18 (311); *d.* Al specimen 10 (220). *e.* Al specimen S (220). (Numbered specimens obtained by strain anneal, lettered specimens from the melt.)

\* Supplied by Aluminum Research Laboratories, Aluminum Company of America.

clearly resolved. The characteristics of the beam obtained from the monochromator are listed in Table I.

Specimens were held in a goniometer which could be adjusted so that the plane of the surface being investigated coincided with the vertical axis of rotation of the goniometer, which in turn had been adjusted to coincide with the monochromator focus. The orienting of specimens to obtain reflections was facilitated by prior knowledge of the orientation obtained by the back-reflection method.

In the adjusting of the monochromator, it was found convenient to employ a long focal length microscope to observe the focus on a fluorescent screen. Use of this method improved the speed and reproducibility of adjustment over that of the photographic method. In addition, the use of a portable Geiger counter to detect and locate the reflection from the specimen facilitated the accurate adjustment of the specimen for maximum intensity of reflection.

Reflections were registered on film at a distance of 1 meter from the specimen. Exposure times varied from 10 minutes for the (111) reflection from aluminum to about two hours for the (333) reflection. The films were scanned on an L and N microphotometer and line widths measured at one-half the maximum film density. Figure 2 shows several reflections obtained by this method. Figure 3 shows a typical microphotometer record obtained from an aluminum specimen.

Aperturing of the incident beam was carried out to test the predictions of the theory based on the tilting block model. This was accomplished by inserting lead slits into the path of the incident beam at a point about 1 mm in front of the specimen. By this means the vertical height of the beam at the specimen could be varied from 0.1 mm to the full beam height without disturbing the monochromator or specimen adjustments and without sensibly affecting the angular aperture of the incident beam. These aperturing tests were carried out on aluminum specimen D, grown from the melt, which fortuitously combined the attributes of a good degree of crystal perfection and an orientation such that the (111) reflection could be obtained under nearly optimum experimental conditions. In addition, similar tests were carried out on a quartz crystal using the (210) reflection. This reflection occurs at a Bragg angle very nearly the same as the (111) reflection from aluminum.

In order to determine the angular dependence of the line widths, a number of reflections which covered the

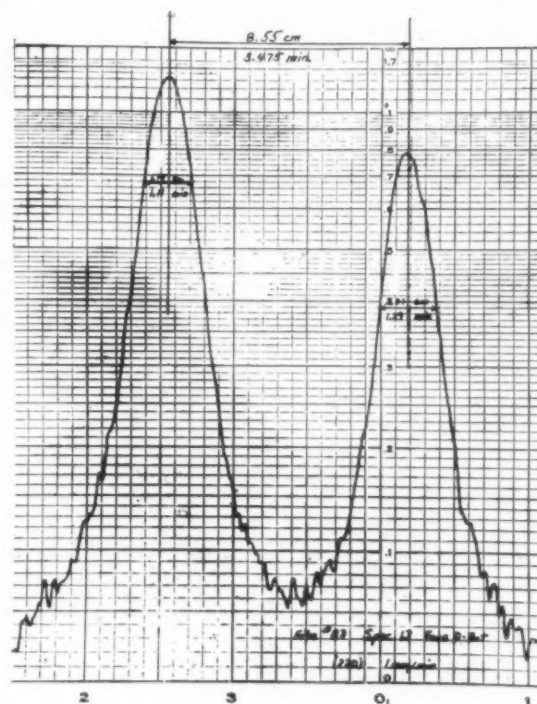


Fig. 3. Typical microphotometer record obtained from films.

range of reflection angles possible were obtained from one face of aluminum specimen D. All reflections were obtained from the same region of the specimen. Three reflections covering about the same angular range were obtained from the quartz crystal for comparison.

A survey was carried out on a number of aluminum specimens for comparison between the strain-anneal and the melt-grown specimens. Reflections were obtained from each of the four faces of a specimen, usually near the central region along the length of the specimen. Six specimens, three of the strain-anneal and three of the melt-grown, were checked at two different positions separated by about 3 cm along the length of the specimen. No significant differences in the degree of crystal perfection were observed between the top and bottom regions, so the balance of the specimens were examined only near the center.

## RESULTS

**Aperturing Tests.** The results of the aperturing tests on line widths are tabulated in Table II and summarized graphically in Fig. 4. The interpretation of the behavior observed is reasonably direct, but requires some understanding of the geometry of the experiment.

If all possible paths are considered by which a ray can arrive at and be reflected from a point on the specimen that is centrally located with respect to one of the lines in the focus, it is found that there is a vertical angular range (vertical angular aperture) of about  $3/4$  degree over which this can occur. As a result, the

TABLE I.

Separation of $K\alpha_1$ and $K\alpha_2$	.085 mm
Width of $K\alpha_1$ at one-half maximum intensity	.068 mm
Width of $K\alpha_2$ at one-half maximum intensity	.058 mm
Full width at background intensity level	.20 mm
Vertical height	10 mm
Horizontal angular aperture . . . approximately	$1^\circ$
Vertical angular aperture . . . approximately	$3/4^\circ$

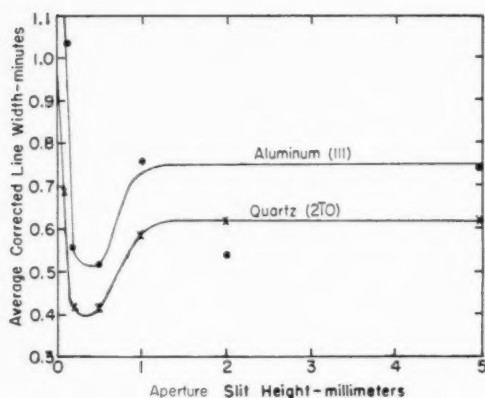


FIG. 4. Effect of aperturing on the line widths of the (111) reflection from aluminum and the (210) reflection from quartz.  $\text{CuK}\alpha$  radiation.

reflection from this point is registered on the film as a short arc whose vertical length corresponds to about  $3/4$  degree and whose horizontal width is determined by the material giving the reflection and by the spectral range present in the X-ray beam. Points on the specimen which are close enough to each other will give reflections which overlap and reinforce the intensity at the film. This condition varies with the vertical position along the focus. For reflection from points above and below the midpoint of the focus, the vertical angular aperture is reduced, and the direction of the ray producing the center of the reflected arc will no longer be horizontal, but will have a small vertical inclination. At the extremities, the vertical aperture is very small and the mean paths are inclined at about 2 degrees to the horizontal. This can be seen in the reflections shown in Fig. 2 in which the lines taper off in intensity at either end due to the reduction of the vertical aperture at the top and bottom ends of the focus. The central portions of the lines which are uniform in intensity are from the central region of the focus where changes in the vertical aperture and the inclination of the mean path are small. This region of uniform intensity in the reflection is estimated to correspond to the center 4 mm of the focus, and this is the region in which the slits were used to define the beam height. In this portion of the reflection, the experimental line width is determined

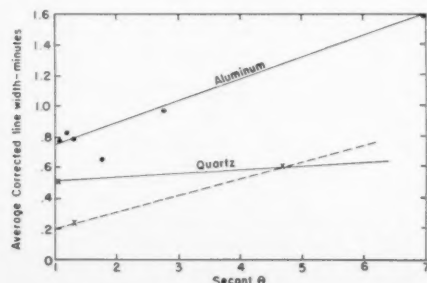


FIG. 5. Variations in line widths as a function of secant  $\theta$ .

by instrumental contributions\* and by the angular variations present in the material in an area defined by the focal width and about 1 mm of length along the focus.

Inserting a slit to define the beam height at the specimen will not affect the line width in the central part of the reflection until the slit height becomes less than the maximum separation distance of points giving overlapping reflections. For slits less than this critical size, the area contributing to the reflection is reduced. In the aperturing experiments, this critical size corresponds to about 1 mm, and for slits in the range of 0.5 to 1.0 mm the variation in the line widths qualitatively follows the behavior predicted by Eq. (2). Below 0.5 mm, the gradual upturn and sharp increase in the line width is believed due to scattering of the incident beam at the edges of the slit. This factor would become relatively more pronounced with decreasing slit heights as is evident in the large values of the line widths for the 0.1 mm slit.

Due to the limited range of slit sizes for which the line widths vary, it is not possible to check in detail whether

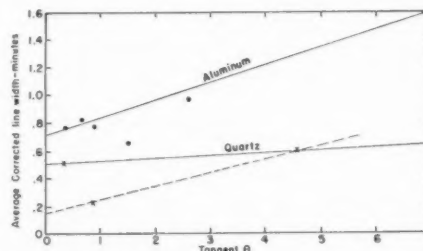


FIG. 6. Variations in line widths as a function of tangent  $\theta$ .

these changes follow the square-root relation of Eq. (2). A rough check can be made from the ratio of the line widths for the 1.0 mm and 0.5 mm slit sizes. This ratio is 1.46 for the aluminum specimen and 1.40 for the quartz. The ratio expected from Eq. (2) is 1.41. The agreement between experiment and the tilting block model theory is surprisingly good, particularly in view of serious doubts that arise as to the applicability of a theory based on a one-dimensional model to a three-dimensional (or at best quasi-two-dimensional) system. The important result of these measurements is that the behavior observed is qualitatively consistent with the behavior expected from a system containing a random dislocation distribution.

Further consideration of the applicability of Eq. (2) to observations made during this investigation reveal some features which are of interest. If we use Eq. (2) to calculate probable angular deviations for widely

\* The instrumental contributions to the widths of reflections obtained with our experimental set-up have been treated in some detail by Lambot, Vassamillet, and Dejacé.<sup>3</sup> Except for the contribution due to spectral width, the instrumental contributions for the reflections observed in the aperturing tests are quite small and lead to no serious errors if neglected.

separated points in the crystal ( $L=1$  cm) for dislocation densities in the range of  $10^6$  lines/cm<sup>2</sup> to  $10^8$  lines/cm<sup>2</sup>, we obtain the following values for the probable angular deviation:

$$\varphi_{\rho=10^6}=2.9', \quad \varphi_{\rho=10^7}=17', \quad \varphi_{\rho=10^8}=1^\circ 30'.$$

When the full beam is employed, the reflection obtained comes from a region on the specimen along a line about 1 cm in length. We can readily detect horizontal deviations in the position of the reflection of about 1 minute and vertical deviations of about 10 minutes. In the absence of small-angle boundaries, no horizontal deviations from the mean-reflection position were observed that amounted to more than 1 or 2 minutes. No vertical deviations were detected. This indicates that either the dislocation densities of the specimens observed were of the order of  $10^6$  lines/cm<sup>2</sup> or less, or that the tilting block model from which

TABLE II.

Specimen	Aperture slit height, mm	Line widths in minutes				
		$\alpha_1$	$\alpha_2$	$\alpha_3$	$\alpha_4$	Average corrected width
Aluminum D	0.1	1.72	1.27	1.42	.82	1.04
	0.2	1.10	.65	1.08	.48	.56
	0.5	1.07	.62	1.01	.41	.52
(111) Reflection	1.0	1.23	.78	1.33	.73	.76
	2.0	1.08	.63	1.05	.45	.54
	5.0	1.29	.84	1.23	.63	.74
Quartz (210)	0.1	1.28	.83	1.15	.55	.69
	0.2	.95	.50	.93	.33	.42
	0.5	.93	.48	.95	.35	.42
Reflection	1.0	1.08	.63	1.15	.55	.59
	2.0	1.07	.62	1.23	.63	.62
	5.0	1.09	.64	1.21	.61	.62

\* Average of three microphotometer scanings on the lines.

Eq. (2) is derived is not a good representation of the situation in a real crystal.

*Variation of Line Width with Diffraction Angle.* The results of the measurements made to determine the dependence of the line width on the diffraction angle are tabulated in Table III and summarized graphically in Figs. 5 and 6. It is not possible to decide from these graphs whether the data follow the tangent  $\theta$  relation for strain broadening, or the secant  $\theta$  relation for particle size broadening. The results obtained on the quartz are somewhat indefinite due to scatter in the points obtained. Dislocation densities calculated from the slopes of the curves in Figs. 4 and 5 are tabulated in Table IV along with the values calculated from Eq. (2). The agreement between the dislocation densities estimated in the aluminum specimen by the tilting block model and the particle size relation is quite good.

The low dislocation densities obtained from the

TABLE III.

Specimen and reflection	Average line widths in minutes			
	Experimental width $\alpha_1$	Corrected* width $\alpha_2$	Experimental width $\alpha_3$	Average corrected width
Aluminum Specimen D				
(111)	1.32	1.38	.83	.74
(220)	2.09	1.65	1.21	.49
(222)	2.15	2.26	.93	.66
(331)	2.88	3.12	.86	.45
(422)	4.82	5.44	1.26	.70
(333)	11.16	14.30	2.16	1.04
Quartz				
(210)	1.08	1.09	.59	.45
(410)	1.50	1.80	.29	.20
(524)	7.36	8.53	1.16	.04

\* Corrected for spectral width and vertical aperture. See Ref. 2.

strain broadening relation as compared with the densities estimated from the tilting block model and from the particle size relation indicates that strains of the type considered in the derivation of Eq. (6) are quite small. The dislocation densities tabulated in Table IV for particle size broadening are calculated under the assumption that strain broadening is negligible, and the strain broadening values assume that particle size broadening is negligible. If the value for dislocation densities given by the tilting block model and by the particle size broadening relation are accepted as the most reliable estimates of the dislocation density in the aluminum crystal examined, the low dislocation density obtained using the strain broadening relation can only be consistent with tilting block and particle size densities if the dilations present are much smaller than one would expect from most dislocation arrangements. It can be consistent if:

1. Screw type dislocations predominate in annealed crystals. This appears to be a reasonable possibility, since the strain energy of an edge type dislocation is about 50 percent greater than that of a screw dislocation.

2. Edge type dislocations, when present in annealed crystals are in arrays which minimize the strain energy of the crystal. One dislocation array which is commonly observed in metal crystals is the small angle boundary.

*Survey of Aluminum Single Crystals.* Comparison of the strain-anneal specimens (numbered series) with the melt-grown specimens (alphabet series) from the survey

TABLE IV.

Specimen	Dislocation densities			
	Tilting block I	Tilting block II	Particle size	Strain
Aluminum D	$4.2 \times 10^6$	$7.6 \times 10^6$	$6.5 \times 10^6$	$1.1 \times 10^6$
Quartz	$2.4 \times 10^6$	$4.4 \times 10^6$	$2.1 \times 10^6 - 3.4 \times 10^6$	$2.1 \times 10^6 - 6.2 \times 10^6$

I.  $L = 7.6 \times 10^{-3}$  cm = average width of beam at the specimen  
 II.  $L = 1 \times 10^{-1}$  cm = effective vertical beam height at the specimen



TABLE V.

Specimen	Reflection	Mean line widths in minutes				Avg. no. of small angle boundaries*	Average boundary angle	Maximum disorientation
		Uncorrected		Corrected for spectral width				
		$\alpha_1$	$\alpha_2$	$\alpha_1$	$\alpha_2$			
7	220	1.45	1.52	.63	.42	1.8	1.1'	3.0'
10	220	1.42	1.36	.60	.26	5.0	1.2'	6.2'
	311	1.34	1.55	.29	.15			
13	220	1.39	1.43	.57	.33	2.8	0.9'	3.4'
14	311	1.51	1.74	.46	.34	2.3	1.2'	2.4'
15	220	2.12	1.83	1.30	.73	1.3	0.9'	1.4'
18	200	1.04	0.90	.51	.19	1.0	0.7'	1.5'
	311	1.29	1.49	.24	.09			
22	311	1.62	1.81	.57	.41	0	—	—
	111	1.32	1.38	.87	.78			
D	220	2.09	1.65	1.27	.55	.7	.8'	1.5'
	311	1.87	2.14	.82	.74			
E	220	1.60	1.73	.78	.63	1.4	.8'	.8'
F Annealed	220	1.30	1.45	.48	.35	1.7	4.8'	34.4'
	311	1.58	1.83	.53	.43			
H	311	2.32	2.46	1.27	1.06	.8	2.5'	5.5'
L	311	1.50	1.62	.45	.22	1.0	2.25'	4.1'
M	200	1.77	1.64	1.24	.93	.3	.7'	.7'
	311	1.33	1.58	.28	.18			
N	311	1.61	1.87	.56	.47	6.2	3.4'	13.5'
	220	1.67	1.68	.85	.28			
P	311	1.91	1.93	.86	.53	1.5	1.4'	2.61'
Q	311	1.99	2.02	.94	.62	3.0	1.72'	5.16'
S	220	1.63	1.65	.81	.55	4.5	1.7'	14.4'
T	200	1.12	1.10	.59	.39	1.4	2.8'	7.4'
	220	1.22	1.36	.40	.20			
V	220	2.18	2.10	1.13	1.00	2.2	1.8'	7.4'
	311	1.63	1.55	.58	.15			
PCI	220	1.75	1.66	.93	.56	2.0	1.6'	5.2'
	311	2.10	2.16	1.05	.76			

\* These values are obtained by counting the discontinuities on each of the films obtained from a given specimen and dividing this count by the number of films. This gives approximately the average number of small angle boundaries that would be intersected by a line on a crystal 1 cm in length.

results as tabulated in Table V indicates that on the average the former show a slightly better degree of crystal perfection. The rather surprising aspect of this survey is that there were a number of melt-grown specimens which were comparable in all respects to the strain-anneal specimens. In general, the degree of crystal perfection present in the melt-grown specimens is much better than would be expected from information available in the literature.

In the melt-grown specimens, the number of small-angle boundaries intercepted by the beam was determined in part by the angle the line of the focus made with the specimen axis. When the focus was perpendicular to the specimen axis, it intercepted on an average three times as many boundaries as when it was parallel to the specimen axis. This indicates that the boundaries tend to run parallel to the specimen axis (and the growth direction). No indications of a preferred direction of the boundaries was observed in the strain-anneal specimens.

The density of dislocations in the small-angle boundaries is comparatively small. For the strain-anneal specimens, the average density of dislocations in boundaries\* is  $4.6 \times 10^4$  lines/cm<sup>2</sup>, and for the melt-

grown specimens  $1.0 \times 10^5$  lines/cm<sup>2</sup>. The line widths of the strain-anneal specimens tend to be slightly smaller than those of the melt-grown specimens. Annealing of several melt-grown specimens produced no detectable changes in the line widths. The average corrected line widths for both groups of specimens are 0.62' for the melt specimens and 0.45' for the strain-anneal specimens. The latter value is about the same as observed for the (210) reflection from the quartz. The dislocation densities corresponding to these line widths are  $2.9 \times 10^6$  lines/cm<sup>2</sup> for the melt specimens and  $2.3 \times 10^6$  lines/cm<sup>2</sup> for the strain-anneal specimens.

Some insight as to one of the sources of variation in line widths from specimen to specimen is given by a series of microphotometer measurements of the (111) reflection from specimen D and the (210) reflection of the quartz. Each reflection was scanned at 0.5 cm intervals along its length over the central 5 cm of the line where the film density in the reflection was uniform. The root-mean-square deviation of the measurements from the aluminum specimen amounted to 20 per cent of the corrected line width, while the deviation for the quartz was 2 per cent. Close visual examination of the aluminum lines indicated that small bulges were present

\* From the survey results, the average boundary angle and the average number of boundaries per cm are known. The total length of boundaries in a square centimeter can be estimated and calcu-

lation of the number of dislocations associated with boundaries obtained from  $\rho_B = (\bar{\alpha}/b)L$ , where  $\bar{\alpha}$  is the mean boundary angle and  $L$  the total length of boundary per square centimeter.

on the lines (compare *a* and *b* in Fig. 2). Some, but not all of the melt-grown specimens gave reflections with this type of variation in the lines, whereas the strain-anneal specimens rarely showed this type of variation. These variations are thought to correspond to small angle boundaries which are not resolved and represent angular disorientations of less than about 20 seconds of arc.

The comparable degree of perfection observed in the quartz and aluminum specimens is consistent with previous work which employed this X-ray method.<sup>2</sup> Comparison of our results, which were obtained by reflection, with previous results obtained in transmission<sup>2</sup> do not indicate any sensible differences in the degree of crystal perfection observed. This point is of some importance, since the reflection method "sees" only a thin layer at the surface and the question naturally arises as to whether these surface observations are also applicable to the interior of the crystal. Since the transmission measurements mentioned above were made on 0.5 mm thick specimens, it appears that our measurements in reflection are representative of the material to a depth comparable to this.

The unexpected high degree of crystal perfection in the melt-grown specimens is probably associated with the crystal growing method employed. No attempt has been made to date to ascertain which of several possible factors are of importance. The factors that are different in the "soft-mold" method from more conventional methods are the strength (or softness) and the radial thermal insulation provided by the mold material. The softness of the mold material reduces the possibility of strain due to differential thermal contraction in specimens "keyed" in the mold, and in addition, permits easy removal without the danger of accidentally damaging a specimen. The radial thermal insulation provided by the mold material combined with extraction of heat by conduction from the bottom of the mold favors a truly axial heat flow in the specimen during solidification. This last factor is thought to be the more important of those discussed.

## CONCLUSIONS

The use of high-resolution X-ray diffraction methods on annealed crystals offers good possibilities of obtaining considerable information about the dislocation densities and distributions. The present work indicates that in annealed aluminum single crystals, the majority of the dislocations are present in essentially random arrays and in densities of about  $10^6$  lines/cm<sup>2</sup>. Small-angle boundaries contribute but little to the over-all dislocation density, contributing on the average about  $10^4$  to  $10^5$  lines/cm<sup>2</sup>.

No basic differences were observed between aluminum single crystals prepared by the strain anneal method and those grown from the melt. The major difference between the two types of crystals is that *on the average* the number and angular range of small-angle boundaries is less in the strain anneal crystals.

Additional work is needed to confirm and expand the results of this investigation. Extension of the work on the statistics of dislocation distributions—both experimental and theoretical—is particularly desirable. Experimental techniques different from those employed in this work should be investigated.

## ACKNOWLEDGMENTS

The authors are grateful to Professor A. Guinier for help with this method during his period of residence as Visiting Professor of Metallurgy in the Department of Mining and Metallurgy at the University of Illinois.

This work was supported by the Office of Naval Research under Contract Nb ORI 071(54).

## REFERENCES

1. A. Guinier and J. Tennevin, *Acta Cryst.* **2**, 133 (1949).
2. H. Lambot, L. Vassamillet, and J. Dejace, *Acta Met.* **1**, 711 (1953).
3. P. Gay, P. B. Hirsch, and A. Kelly, *Acta Met.* **1**, 315 (1953).
4. C. G. Darwin, *Phil. Mag.* **27**, 315 and 675, (1914).
5. A. H. Cottrell, *Dislocations and Plastic Flow in Crystals* (Oxford University Press, London, 1953) (a) p. 100; (b) p. 40.
6. A. Guinier, *Imperfections in Nearly Perfect Crystals* (John Wiley and Sons, New York, 1952) p. 402.
7. A. D. Schwoppe, F. R. Shober, and L. R. Jackson, *Creep in Metals*, N.A.C.A. TN 2618, 1952.
8. T. S. Nogge, *Rev. Sci. Instrum.* **24**, 184 (1953).
9. P. A. Beck, J. C. Kremer, L. J. Demar, and M. L. Holzworth, *Trans. A.I.M.E.* **175**, 372 (1948).

## THE DEFORMATION OF SINGLE CRYSTALS OF $\alpha$ -BRASS\*

HEATHER M. MURPHY and E. A. CALNAN†

Single crystals of  $\alpha$ -brass deformed in tension have been studied by X-ray and micrographic methods. The connection between the orientation dependence of cross-slip and the unequal hardening of active and latent slip planes has been demonstrated. The two types of deformation bands observed are discussed. An explanation of the deformation differences between copper and copper solid solutions is proposed in terms of the locking of the dislocation sources in the alloy by solute atoms. This inhibits the development of the "fine structure" of elementary slip lines and so favors continued slip on parallel primary planes rather than on intersecting planes.

### DÉFORMATION DE MONOCRISTAUX DE LAITON $\alpha$

Des monocristaux de laiton  $\alpha$ , déformés par traction, ont été étudiés par rayons X et micrographie et une relation entre l'orientation des cross-slips et la différence de consolidation des systèmes actif et latent a été établie. Les deux types de bandes de déformation observés sont discutés. Le comportement différent du cuivre et de ses solutions solides lors d'une déformation est expliqué par le blocage des sources de dislocations par les atomes dissous qui empêche le développement de la structure fine des lignes de glissement et favorise le glissement continu sur des plans parallèles, plutôt que sur une autre famille de plans.

### DIE VERFORMUNG VON EINKRISTALLEN AUS $\alpha$ -MESSING

Mit Hilfe von röntgenografischen und mikroskopischen Methoden wurden durch Ziehen verformte Einkristalle aus  $\alpha$ -Messing untersucht. Der Zusammenhang zwischen der Orientierungsabhängigkeit der Doppelgleitung und der ungleichmässigen Verfestigung der aktiven und der latenten Gleitebenen konnte gezeigt werden. Zwei verschiedene Typen von Gleitlinien, die beobachtet wurden, werden erörtert. Für die Unterschiede bei der Verformung von Kupfer und kupferreichen Mischkristallen wird eine Deutungsmöglichkeit vorgeschlagen, die auf einer Bewegungshemmung der Versetzungsquellen in der Legierung beruht. Durch sie wird die Ausbildung eines "Subgefüges" (fine structure) der elementaren Gleitebenen unterbunden und so ein kontinuierliches Gleiten auf parallel liegenden, primären Gleitebenen mehr begünstigt als das Gleiten auf sich schneidenden Gleitebenen.

The deformation behavior of single crystals of  $\alpha$ -brass has been studied by a number of previous investigators. The operative slip system,  $\{111\} \langle 110 \rangle$ , was determined by Elam<sup>1</sup> who also noted that slip continued on the primary system alone until the crystal had rotated a considerable distance beyond the symmetrical position where the conjugate slip system should begin to operate. This phenomenon of unequal critical shear stresses on active and latent slip systems was investigated further by Masima and Sachs<sup>2</sup> who showed for a variety of crystal orientations that the critical shear stress for the conjugate slip system at the point where it became active was about 25 per cent greater than that for the primary system. Goler and Sachs<sup>3</sup> demonstrated the variation of the shear stresses with the composition of the brass, the latent hardening being approximately proportional to the zinc content. More recently, Maddin, Mathewson, and Hibbard<sup>4,5</sup> established the presence of cross-slip in single crystals so oriented that they should have deformed on only the primary system. They showed that the cross and primary systems corresponded to slip on different planes but in a common slip direction. Shear hardening was found to be negligible until all the surface of the crystal was covered with slip lines, then with additional slip on the existing primary and cross slip lines rapid hardening

took place, this hardening preceding the advent of conjugate slip.

It was felt that certain features of this earlier work might now be correlated in the light of recent ideas on dislocations, cross-slip, and the effect of solute atoms, and to this end X-ray and micrographic examinations were made of single crystals of particular orientations deformed in tension. The results obtained together with some interpretation of the earlier observations are described herein.

### EXPERIMENTAL

Single crystals of nominal composition 70 per cent copper, 30 per cent zinc, were grown in the form of 1/8-in. diameter rods approximately 6 in. long by slow solidification from the molten state, using seed crystals inclined to the axis of the rod to give the desired orientation. After electropolishing in a chromic acid solution the orientation of the crystals was determined by the standard X-ray back-reflection Laue method.

The crystals were extended in a simple tensile testing machine, the load being applied at the ends through friction grips which were constrained to prevent any twisting about the axis of the specimen. Optical micrographs and orientation measurements were taken at various stages in the deformation.

Details of the chemical analyses of the individual crystals will be given in the results but it may be mentioned that high accuracy carbon determinations on two crystals yielded contents of 0.004 wt % and 0.0048

\* Received November 5, 1954.

† National Physical Laboratory, Teddington, England.





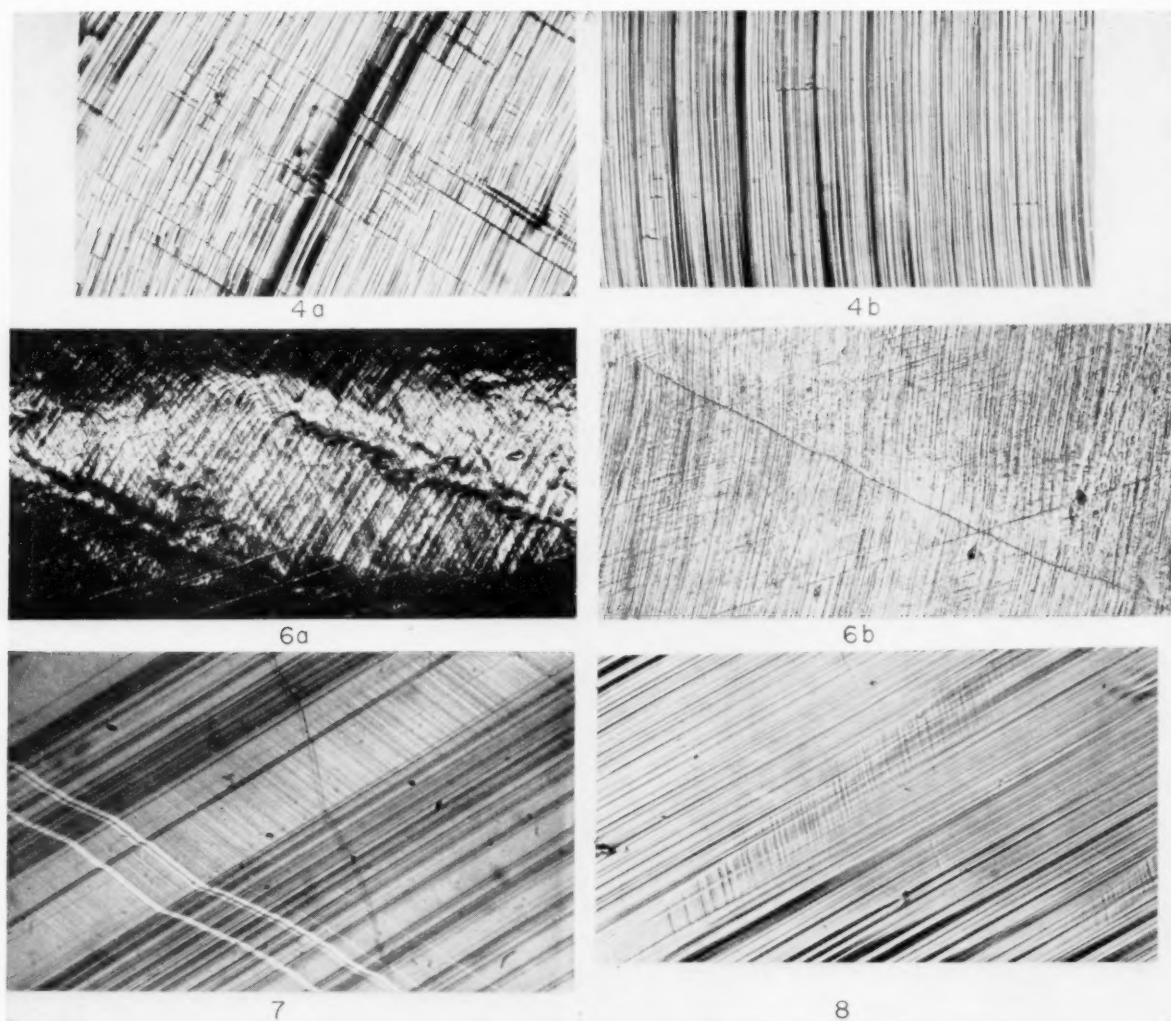


PLATE I. (All figures reduced by one-half in reproduction.) FIG. 4A.  $3^\circ$  from (100) showing much cross slip. Crystal No. 28. 14 per cent extension.  $350\times$ . FIG. 4B.  $33^\circ$  from (100) showing little cross slip. Crystal No. 43. 17 per cent extension.  $350\times$ . FIG. 6A. Rumpled band similar to kink band (low magnification)  $70\times$ . FIG. 6B. Band similar to Fig. 6A at high magnification.  $700\times$ . FIG. 7. Band of conjugate slip. Crystal No. 40. 7 per cent extension  $750\times$ . FIG. 8. Band of secondary slip. Crystal No. 43. 17 per cent extension.  $350\times$ .

close together only short cross-slip lines are formed. Figure 5 shows evidence of cross-slip on the conjugate system, the same cross-slip plane operating as with primary cross-slip but slipping in a different direction, namely, the conjugate slip direction, which is common to the conjugate and cross-slip planes.

The term *deformation band* has been used to describe various types of deformation inhomogeneity. The bands in aluminum which have been studied in some detail, Cahn,<sup>6</sup> Honeycombe,<sup>7</sup> and Calnan,<sup>8</sup> are of two distinct types: king bands and bands of slip on a plane other than the primary slip plane (secondary slip). In the present work two types of bands have also been observed, i.e., the bands of secondary slip, which might be expected and which are similar to those in aluminum, and other bands closely related to kink bands. The latter have

apparently not been observed before and in fact Kuhlmann-Wilsdorf and Wilsdorf<sup>9</sup> suggest an explanation why kink bands proper should not appear in  $\alpha$ -brass. Their argument is based on the fact that the slip lines in brass are too far apart for dislocations on adjacent lines to interact and form a kink array. The present authors thought that although this may be true throughout most of the deformation, there might be a hint of kink bands after considerable extension when slip lines were close together over the whole surface. Crystals were accordingly examined after severe deformation and rumpled markings similar to kink bands were found cutting across the primary slip lines, Fig. 6A. The planes on which these bands were lying were not, however, those normal to the operative slip direction, or in fact to any slip direction, as is the case

in aluminum. They were found to correspond to the plane of another slip system, one of the unpredicted slip lines observed early in the deformation. Confirmatory evidence of this was the fact that at high magnifications the position of the "rumple" band showed only as another slip line crossing the primary system, Fig. 6B. It should be pointed out that the apparent direction of the slip line formed in the initial stages of deformation is generally not the correct crystallographic plane after it has been displaced by subsequent shear, and due allowance for this effect must be made. It thus appears that the Wildorfs' explanation of the absence of kink bands proper is valid although in fact features closely akin to kink bands develop for another reason. In connection with the additional slip lines it may be noted that there was a tendency for them to appear as pairs, of spacing about one micron, Fig. 7. This phenomenon is unexplained.

The second type of deformation band, the bands of secondary slip, were similar to those in aluminum in having edges slightly inclined to the adjacent slip lines. This characteristic, commented on briefly by the authors,<sup>10</sup> has been considered in detail by Kitajima,<sup>11</sup> who attributes it to the bending stress in the specimen brought about by primary slip. An example is shown in Fig. 8.

#### DISCUSSION

A convenient way of discussing cross-slip is provided by the idea proposed by Calnan<sup>8</sup> for the explanation of additional slip systems in single crystals. On account of the inhomogeneity of stress which develops in a crystal undergoing plastic deformation, the effective stress direction in any small part of the crystal is not necessarily the same as the applied stress direction. It is suggested that it can be represented by a simple tensile stress,  $T_e$ , initially coincident with the applied stress direction but which under increasing applied stress

moves to a point of lower resolved shear stress. This movement continues until an element of slip occurs, which takes place on the most favorable system or systems corresponding to the orientation of  $T_e$ . Figure 9 shows the contours of the resolved shear stress function  $\cos\chi \cos\lambda$ , where  $\chi$  and  $\lambda$  are the angles which the stress axis makes with the primary slip direction and the primary slip plane normal, respectively. If the critical shear stress on the primary system is less than that for the other systems, then the boundary between the primary and the other systems will be removed from  $[111][100]$  to a position  $STUV$ . If, however, the cross-slip system has the same critical shear stress as the primary, lower than that for the other two systems, then the boundary will be  $ST100$ , the boundary between the cross and fourth systems now being  $TV$ . Thus for a crystal of applied stress direction  $p$  the path of the effective stress to a minimum is either  $pXU$  or  $pWT$  corresponding to these two cases. The former should display primary slip, the fourth system, and possibly a little cross-slip, while the latter primary and cross-slip and possibly a little of the fourth and conjugate systems. These are general trends of behavior and there may well be isolated regions of material which have such constraints as to cause them to behave otherwise. However, the experimental observations leave little doubt that there is an overwhelmingly greater amount of cross-slip than of the fourth system, that is to say,  $\alpha$ -brass corresponds to the second of the cases above in having lower critical shear stresses on the primary and cross-slip systems than on the other two systems. It will be seen immediately on this basis that for crystals of initial stress axis orientation well removed from  $[100]$ —for instance  $q$ —the path of  $T_e$  is  $qYT$ , and thus comprises considerable lengths of primary slip ( $qV$ ), and primary and conjugate slip, ( $YT$ ). Therefore cross-slip is correspondingly much less likely for such an orientation. In this way the orientation dependence of cross-slip observed is explained qualitatively. By a similar process it may also be shown that cross-slip should again

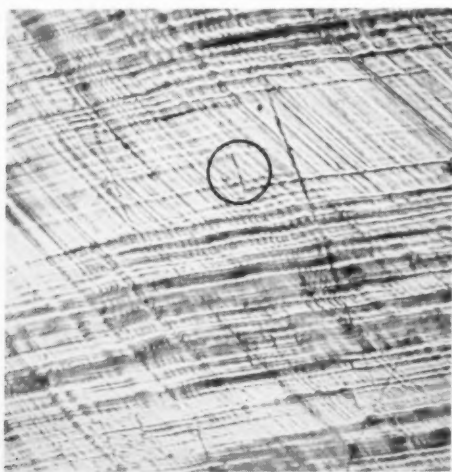


Fig. 5. Cross slip on conjugate system particularly evident within encircled area. Crystal No. 45B. 38% extension. 350 $\times$ .

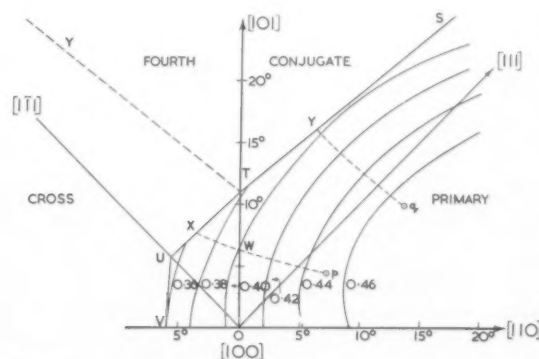


Fig. 9. Resolved shear stress contours on primary slip system in vicinity of  $[100]$ . Most favorable slip systems for various regions indicated by primary, conjugate, cross and fourth.

TABLE II. Concentrations of various solute atoms in copper to produce brass type polycrystalline deformation textures, after Hibbard *et al.*<sup>12</sup>

	Atomic radius, <i>r</i>	Size factor, $\epsilon = \frac{r - r_{Cu}}{r_{Cu}}$	Concentration, %
Cu	1.278	—	—
Ni	1.245	-0.026	>32
Zn	1.332	0.042	5-8
Al	1.431	0.120	2-4

become prevalent in the immediate vicinity of the [111] direction. In the present work, however, these orientations have not been investigated.

The next point to be considered is why the cross-slip is more extensive in  $\alpha$ -brass than in aluminum, for example. One reason is apparent from the preceding section. The probability of cross-slip occurring depends on the length of the path of  $T_e$  common to the primary slip and cross-slip triangles, i.e., the line from  $T$  towards [100]. In aluminum this line is non-existent, or very short, because there is virtually no difference in the critical shear stresses on the active and latent slip systems, and there is accordingly comparatively little cross-slip. A second reason is attributed to the absence in  $\alpha$ -brass of the "elementary structure" of fine lines found in aluminum and copper by Kuhlmann-Wilsdorf and Wilsdorf.<sup>9</sup> The present experimental observations suggest that, in general, cross-slip extends from the primary slip line where it is initiated to the next adjacent primary slip line. In aluminum there are elementary slip lines all over the specimen so that the cross-slip lines will be correspondingly shorter than in brass where there are large open spaces between adjacent slip lines. Of course, as the deformation of the brass proceeds the open spaces are increasingly filled with lines, and cross-slip in the later stages should be restricted to short lengths, which was in fact observed.

It thus appears that the cross-slip phenomena in brass are the result of lower critical shear stresses on the primary and cross-slip systems than on the other two systems. After conjugate slip has begun, the lattice rotations towards the conjugate slip direction, [110], indicate that the conjugate slip system alone is active. This in turn implies that the critical shear stress on the conjugate system is now lower than that on the primary. So the effects may be summed up by stating that the critical shear stresses on the active and cross-slip systems are lower than those on the latent systems.

Before discussing how this inequality comes about, the influence upon it of concentration of the solute atoms will be considered. First, there are the direct measurements of the orientations where marked conjugate slip begins which give the ratio of the resolved shear stresses on the primary and conjugate systems.<sup>2,3,1</sup> These indicate quite clearly that the ratio rises continuously from unity for pure copper up to a value of about 1.3 for a 30 per cent concentration of zinc in

copper. Secondly, there are some indirect measurements which may be worthy of further experimental investigation in the future. It has been proposed by one of the authors, Calnan,<sup>12</sup> that the difference between the polycrystalline deformation textures of copper and  $\alpha$ -brass stems directly from the "overshooting" phenomenon. Hibbard *et al.*<sup>13</sup> have studied the textures in various copper solid solutions and determined the concentrations required to produce the brass-like texture. These are listed in Table II, together with the size factors of the solute atoms, the atomic radius here being half the closest distance of approach in the parent lattice. It will be seen that there is some evidence that to produce the brass texture, which presumably implies a certain amount of "overshooting," the concentration varies inversely as the size factor.

A satisfactory explanation of the deformation of copper solid solutions must thus explain (a) why the active and cross-slip systems have lower critical shear stresses, (b) the increase of this effect with increased solute concentration, and (c) the variation with size factor of the solute atom. Koehler<sup>14</sup> has suggested that the vacancies produced in the slip line diffuse outwards from it and erase impurity stresses in a band bordering the slip line. A parallel line may then be propagated through it more easily. One experiment immediately presents itself. If the slip behavior is governed by a diffusion process, then at a low temperature the diffusion rate should be so reduced as to eliminate almost entirely the softened region on either side of the slip line and the overshooting should therefore disappear.

Two crystals, Nos. 2 and 4, were extended in liquid nitrogen. It will be seen from Fig. 1 and Table I that the overshoot is not significantly different from that obtained at room temperature, and accordingly the vacancy diffusion hypothesis must be discarded.

The following explanation, however, appears to be more in agreement with the experimental facts as known at present. It is suggested that in the pure metal the activation energies for the dislocation sources lie within a fairly sharply defined band, whereas in the alloy there is a very broad band of energies due to widely differing locking of the sources by correspondingly wide variations of solute concentration in the immediate vicinity. Then in the pure metal a large number of sources are activated at the same stress level and a closely spaced system of slip lines develops in contrast to the alloy case where only a few isolated sources are active. (To produce equivalent shear in the alloy, many more dislocations must be emitted by these few sources. This may accord with the observations that from the earliest stages of deformation in brass large well-marked slip lines develop.) The closely spaced system of slip bands (referred to as the elementary structure) may be considered to leave behind a "forest" of dislocations which impede equally further primary slip or intersecting conjugate slip, that is to say, the active and latent systems harden equally. The

widely spaced lines in the alloy, however, may be described as leaving "avenues" of dislocations which give no obstacle to additional parallel active but which oppose intersecting lines. It may be remarked that if a conjugate line develops in a region between two widely spaced primary lines it will oppose other primary lines and the band will fill up with parallel conjugate lines. Such may be the explanation of the band shown in Fig. 7 from Crystal No. 40 whose initial orientation near the  $[111][100]$  boundary (Fig. 1) makes the early development of stray conjugate lines particularly likely.

In the above explanation it thus appears that the fundamental cause of the alloy phenomena is the locking of the dislocation sources. The precise way in which the sources are locked might well be that proposed by Suzuki<sup>15</sup> who explains the hardening of face-centered-cubic alloys by the interaction of the solute atoms with the stacking fault separating two partial dislocations. In favor of this mechanism is the fact that it has the right concentration dependence and it seems likely that a solute atom-size factor effect could be introduced into the treatment when appropriate experimental data permit.

*To sum up:* In the pure metal there are stacking faults but no locking; therefore an elementary structure develops and there is equal hardening of active and latent slip systems.

In the alloy the solute laden stacking faults lock the dislocation sources and no elementary structure develops; therefore, the active plane is unhindered while

the dislocations left behind by the active lines oppose intersecting slip and unequal hardening results.

#### ACKNOWLEDGMENTS

The authors wish to thank Dr. S. Harper of the British Non-Ferrous Metals Research Association for his valuable assistance in making available apparatus for growing the single crystals.

The work described above has been carried out as part of the general research program of the National Physical Laboratory, and this paper is published by permission of the Director of the Laboratory.

#### REFERENCES

1. Elam, Proc. Roy. Soc. **115**, 133 (1927).
2. Masima and Sachs, Zeit. f. Physik. **50**, 161 (1928).
3. Goler and Sachs, Zeit. f. Physik. **55**, 581 (1929).
4. R. Maddin, C. H. Mathewson, and W. R. Hibbard, Jr., Trans. A.I.M.E. **175**, 86 (1948).
5. R. Maddin, C. H. Mathewson, and W. R. Hibbard, Jr., Trans. A.I.M.E. **185**, 527 (1949).
6. R. W. Cahn, J. Inst. Metals **79**, 129 (1951).
7. R. W. K. Honeycombe, J. Inst. Metals **80**, 45 (1951).
8. E. A. Calnan, Acta Cryst. **5**, 557 (1952).
9. D. Kuhlmann-Wilsdorf and H. Wilsdorf, Acta Met. **1**, 394 (1953).
10. H. M. Murphy and E. A. Calnan, J. Inst. Metals, **6**, 665 (1954).
11. S. Kitajima, Bulletin of Naniwa University, **A2**, 71 (1954).
12. E. A. Calnan, Acta Met., (1954) In press.
13. W. Hibbard, *et al*, J. Inst. Metals **77**, 581 (1950).
14. J. S. Koehler, Acta Met. **1**, 508 (1953).
15. H. Suzuki, Science Reports of the Research Institutes, Tohoku University, **A4**, No. 5, 455 (1952).



# BESTIMMUNG DER VERSETZUNGSLINIENDICHTE VON VERFORMTEM EISEN\*

W. KÖSTER und L. BANGERT†

An einem Kohlenstoff- und Stickstoff-haltigen Eisen wurden Dämpfung-Temperatur-Kurven in Abhängigkeit vom Angebot an Fremdatomen in fester Lösung und vom Reckgrad aufgenommen. Die Höhe des Dämpfungsmaximums bei 200° erreicht bei gegebenem Verformungsgrad einen Grenzwert, der durch die Sättigung der Versetzungen mit Fremdatomen gegeben ist. Aus der Messung dieser Sättigungskonzentrationen wurde die Änderung der Versetzungsliniendichte mit steigendem Verformungsgrad bestimmt.

## DETERMINATION OF THE DISLOCATION DENSITY IN DEFORMED IRON

In iron containing carbon and nitrogen, damping-temperature curves were investigated in relation to foreign atoms in solid solution and the degree of cold work. The maximum of damping at 200°C, with a given degree of cold work, reaches a limiting value, which is caused by the saturation of the dislocations with foreign atoms. Measurements of the saturation concentration permitted the determination of the change of the dislocation line density as a function of the degree of deformation.

## DÉTERMINATION DE LA DENSITÉ DES LIGNES DE DISLOCATION DANS LE FER DÉFORMÉ

Les courbes amortissement-température d'un alliage fer-carbone-azote ont été déterminées en fonction de la concentration et du taux d'érouissage. Pour une valeur donnée de la déformation, la valeur du maximum de l'amortissement à 200° atteint une limite qui est déterminée par la saturation des dislocations en atomes étrangers. De la mesure de cette saturation, la variation de la densité des lignes de dislocation avec des déformations en fonction du taux de déformation.

Die Dichte der Versetzungslinien von verformtem Eisen ist von Harper<sup>1</sup> auf der Grundlage einer theoretischen Überlegung berechnet worden. Ausgehend von einer von Cottrell und Bilby<sup>2</sup> durchgeführten Analyse der Reckalterung durch die Versetzungstheorie hat er für verschiedene Reckgrade die Geschwindigkeit der Ausscheidung von Kohlenstoff in verformtem Eisen gemessen. Für den Bruchteil des ausgeschiedenen Kohlenstoffs bezogen auf den anfänglichen Gehalt an

gelöstem Kohlenstoff gilt:

$$\frac{C_0 - C_t}{C_0} = 1 - \exp[-\alpha L (ADt/kT)^2]. \quad (1)$$

Es bedeuten  $C_t$  und  $C_0$  die Menge des gelösten Kohlenstoffs zur Zeit  $t$  bzw.  $t=0$  je  $\text{cm}^3$ ,  $\alpha$  und  $A$  je eine Konstante,  $L$  die Zahl der Versetzungslinien je  $\text{cm}^2$ ,  $D$  die Diffusions-,  $R$  die Boltzmann-Konstante und  $T$  die absolute Temperatur. Wird also die Verarmung des  $\alpha$ -Mischkristalls an Kohlenstoff mit Hilfe der Dämpfungsmessung bei gegebener Temperatur zeitlich verfolgt, so kann die Versetzungsliniendichte berechnet werden. Das Ergebnis der Messungen von Harper enthält Tabelle I.

Dabei ist aber zu berücksichtigen, dass die Theorie, ihrer Herleitung entsprechend, nur angenäherte Zahlen geben kann: insbesondere beruht der Wert der Konstanten  $A$  auf einer Abschätzung.

In dem vorliegenden Bericht wird ein Weg zur unmittelbaren Bestimmung der Versetzungsliniendichte beschrieben. Er beruht auf folgender Erkenntnis:

In der grundlegenden Arbeit, in der Snoek<sup>3</sup> die Deutung für das wenig oberhalb Raumtemperatur auftretende Dämpfungsmaximum von Kohlenstoff- und

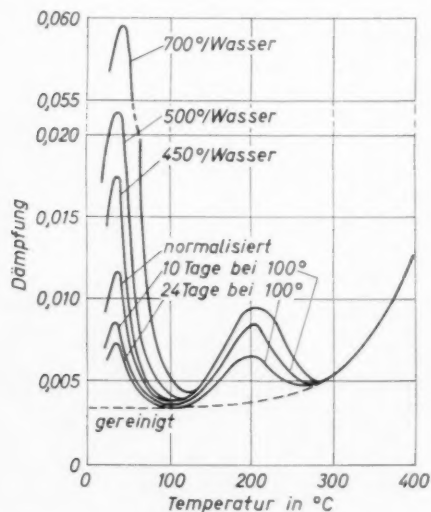


Bild 1: Einfluss des Kohlenstoff- und Stickstoffangebotes auf die Höhe des Dämpfungsmaximums bei 200°.

\* Received November 8, 1954.

† Max-Planck-Institut für Metallforschung, Stuttgart, Germany.

TABELLE I. Versetzungsliniendichte gereckten Eisens nach S. Harper.

Reckgrad %	Zahl der Versetzungslinien je $\text{cm}^2$
5	$1,86 \cdot 10^{11}$
10	$2,46 \cdot 10^{11}$
15	$3,72 \cdot 10^{11}$

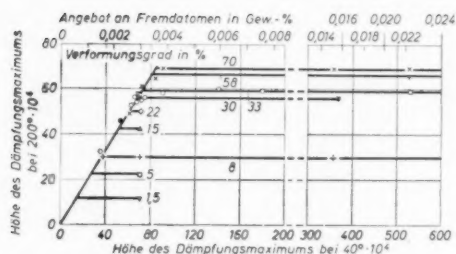


Bild 2: Einfluss des Angebots an Fremdatomen auf die Höhe des Dämpfungsmaximums bei 200° bei unterschiedlichem Verformungsgrad.

Stickstoff-haltigem Eisen gegeben hat, hat er kurz mitgeteilt, dass an kaltverformtem Eisen ein Maximum in der Gegend von 200° beobachtet wird. West<sup>4</sup> und Kê<sup>5</sup> sowie neuerdings Köster, Bangert und Hahn<sup>6</sup> haben diese Erscheinung näher studiert. Sie ist durch eine Wechselwirkung zwischen Versetzungen und den von ihnen eingefangenen Fremdatomen bedingt. Sie ist als spannungsinduzierte Diffusion von Fremdatomen in den von diesen stabilisierten beweglichen Versetzungen anzusehen. Die Aktivierungsenergie des Relaxationsvorganges bei 200° liegt bei etwa 36 000 cal/Mol.

Es hat sich nun gezeigt, dass das Maximum bei 200° bei gegebenem Verformungsgrad proportional zur Menge der ursprünglich gelösten Fremdatome bis zu einem Grenzwert ansteigt, oberhalb dessen es auch bei gesteigertem Angebot an Fremdatomen im Ausgangszustand nicht erhöht wird. Hieraus darf geschlossen werden, dass der maximale Dämpfungsbetrag durch die Zahl der Versetzungen gegeben ist und dann erreicht wird, wenn diese mit Fremdatomen abgesättigt sind. Aus der gemessenen Sättigungskonzentration kann also die Versetzungsliniendichte ohne Zuhilfenahme anderer Konstanten als des Atomebenenabstandes entnommen werden.

#### VERSUCHSDURCHFÜHRUNG

Für die Versuche wurde Draht aus einem Siemens-Martin-Stahl folgender Zusammensetzung benutzt:

0,08% C, 0,01% Si, 0,31% Mn, 0,2% Cu, 0,06% Mo,  
... 0,05% Al, 0,038% P, 0,027% S, 0,004% N.

Vor der Verformung auf 1 mm Dmr. wurden die Drähte auf verschiedene Weise wärmebehandelt, um die Menge der in Lösung befindlichen Fremdatome zu variieren. Die Messungen des logarithmischen Dekrements  $\vartheta$ ; Dämpfung genannt, wurden mit einem Torsionspendel ausgeführt, das von Kê<sup>7</sup> beschrieben worden ist. Die Schwingungsdauer betrug etwa eine Sekunde. Die Messungen an den düsengezogenen Proben wurden 10 bis 15 Min nach der Verformung begonnen. Die Aufheizgeschwindigkeit betrug 2 bis 2,5° je Min.

#### VERSUCHSERGEBNISSE

Bild 1 zeigt die Dämpfung-Temperatur-Kurven des um 33% verformten Stahles nach verschiedener Vor-

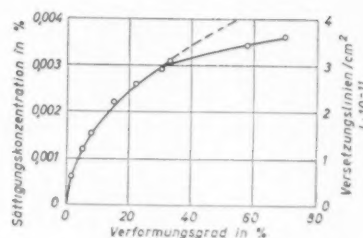


Bild 3: Sättigungskonzentration und Dichte der Versetzungslinien in Abhängigkeit vom Verformungsgrad

behandlung. Die Menge an gelösten Fremdatomen ergibt sich aus der Höhe des Dämpfungsmaximums bei 40°. Die Höhe des Maximums bei 200° steigt zunächst mit wachsender Konzentration des  $\alpha$ -Mischkristalls an Fremdatomen an, wird dann aber oberhalb eines gewissen Betrages vom Angebot an Fremdatomen unabhängig. Das gleiche Ergebnis brachten Versuche mit anderen Verformungsgraden zwischen 1,5 und 70%.

In Bild 2 ist die Höhe des Dämpfungsmaximums bei 200° in Abhängigkeit von der Höhe des Maximums bei 40° aufgetragen. Das Maximum bei 200° nimmt unabhängig vom Reckgrad proportional zum Angebot an Fremdatomen zu, bis ein Maximalwert erreicht wird, der, mit steigendem Verformungsgrad anwachsend, bei weiterem Angebot von Fremdatomen beibehalten wird. Ist einmal die Neigung der Anfangsgeraden bekannt, so kann der Sättigungswert für jeden beliebigen Verformungsgrad durch einen einzigen Messpunkt bestimmt werden, sofern die Konzentration des gelösten Fremdstoffes grösser als der Sättigungswert ist. Er ergibt sich als Schnittpunkt der durch den Messwert zur Abszisse gezogenen Parallele mit der vom Nullpunkt ausgehenden Anfangsgeraden.

Am oberen Rand von Bild 2 ist der Gehalt an gelösten Kohlenstoff- und Stickstoff-Atomen angegeben. Dabei wurde eine Eichung von Pitsch<sup>8</sup> zugrunde gelegt, der zufolge  $1,33\vartheta_{\max}/\pi$  der Menge an gelösten Fremdatomen in Gewichtsprozent zahlengleich ist.

Tabelle II enthält die Sättigungskonzentration und die aus ihr sich ergebende Versetzungsliniendichte in Abhängigkeit vom Verformungsgrad. Die Werte stimmen der Größenordnung nach mit denen von Harper<sup>1</sup> überein, liegen aber etwas niedriger.

Bis rund 30% Verformung lässt sich der Kurvenverlauf (Bild 3) durch eine parabolische Beziehung wiedergeben

$$L = 0,54 \cdot 10^{11} \cdot \epsilon^{\frac{1}{2}} \quad (2)$$

Bei höheren Verformungsgraden liegen die Werte unterhalb der gestrichelt verlängerten Parabel. Aus theoretischen Erwägungen an Leitfähigkeitsmessungen ist van Bueren<sup>9</sup> zu der Ansicht gelangt, dass die Dehnung mit dem Exponenten  $3/4$  statt  $1/2$  in die Gleichung eingehen sollte.

Bekanntlich folgt die Kinetik der Verarmung des  $\alpha$ -Mischkristalls bis zu hohen Ausscheidungsbeträgen

TABELLE II. Sättigungskonzentration und Versetzungsliniendichte von gezogenem Eisen.

Reckgrad %	Sättigungskonzentration Gew. % C+N	Zahl der Versetzungslinien je $\text{cm}^2 L \cdot 10^{11}$
1,5	0,0006	0,6
5	0,0012	1,2
8	0,0015	1,5
15	0,0022	2,2
22	0,0026	2,6
30	0,0029	2,9
33	0,0030	3,0
58	0,0034	3,4
70	0,0036	3,6

dem  $\frac{1}{2}$ -Gesetz, das auf der Vorstellung beruht, dass die Versetzungen eine anziehende Kraft auf die gelösten Fremdatome ausüben. Es ist jetzt klar zu Tage getreten, dass die verfügbaren Fremdatome sich in zweifacher Weise an den Versetzungen anordnen. Zunächst Bruchteil in die Versetzungen wirdein atomar eingebaut; nach. A. H. Cottrell dürfte ein einziges Fremdatom je Versetzung zu ihrer Verankerung genügen. Nach

dessen Einbau bleibt das Spannungsfeld der Versetzungen weitgehend erhalten, sodass eine Sogwirkung auf die überschüssigen Atome bestehen bleibt. Diese scheiden sich dann entlang den Versetzungslinien je nach der Anlasstemperatur in Abständen von 1 bis  $4 \cdot 10^{-4}$  cm aus. Dafür sprechen Gefügebilder von Kraftwirkungsfiguren,<sup>10</sup> die Zunahme der Koerzitivkraft<sup>11</sup> und die Abnahme des elektrischen Widerstandes.<sup>12</sup>

## LITERATUR

1. S. Harper, Phys. Rev. **83**, 709 (1951).
2. A. H. Cottrell und B. A. Bilby, Proc. Phys. Soc. **62A**, 49 (1949).
3. J. L. Snoek, Physica **8**, 711 (1941).
4. W. A. West, Trans. A.I.M.E. **167**, 192 (1946).
5. T. S. Ké, A.I.M.E. Techn. Publ. Nr. 2370 (1948).
6. W. Köster, L. Bangert und R. Hahn, Arch. Eisenhüttenw. **25**, 569 (1954).
7. T. S. Ké, Phys. Rev. **71**, 533 (1947).
8. W. Pitsch, Göttinger Dissertation. 1954.
9. H. G. van Bueren, Z. Metallkde **46**, 272 (1955).
10. W. Köster, Arch. Eisenhüttenw. **3**, 637 (1929/30).
11. W. Köster, Arch. Eisenhüttenw. **4**, 289 (1930/31).
12. A. H. Cottrell und A. T. Churchman, J. Iron Steel Inst. **162**, 271 (1949).

## STRUCTURE AND POLYGONIZATION OF BENT ZINC MONOCRYSTALS\*

JOHN J. GILMAN†

The geometry of bent zinc crystals is discussed. It is found that the slip planes in bent zinc crystals have the shape of involutes with the hexagonal axes of the lamellae parallel to tangents of the evolute. This concurs with other investigators' results for bent corundum-crystals and with theory.

Evidence is presented to show that bent crystals, especially sharply bent ones, are not necessarily polygonized immediately after bending. They sometimes contain low-angle grain-boundaries which may or may not form during the bending process. The normal structure of a homogeneously bent zinc crystal is believed to consist of a network of meandering dislocation lines connecting short segments of dislocation walls.

Quantitative data on the kinetics of polygonization in cylindrically bent zinc crystals are presented. Polygonization, in the absence of inhomogeneous stresses, does not occur below about 170°C in "chemically-pure" zinc and this temperature is raised somewhat by contamination with 0.1 at. % Cd. At a given temperature, the polygon angles increase in proportion to the logarithm of the time. The temperature dependence of the growth rate,  $d\theta/dt$ , at constant angle, varies with temperature. If an Arrhenius equation is used to describe it at temperatures below 250°C,  $Q$  is  $\sim 60$  kcal/mol and at temperatures from 250 to 325°C,  $Q$  is  $\sim 20$  kcal/mol.

The effect of several variables on the polygon growth rate were investigated:

1. Stress after annealing: causes boundaries to coalesce.
2. Twins: on compression side they markedly inhibit polygon growth.
3. Bending temperature: variations from  $-196^\circ\text{C}$  to  $225^\circ\text{C}$  had no marked effect.
4. Surface condition: no effect as long as surface was macroscopically smooth.
5. Intermittent *versus* continuous anneals: no effect.
6. Skew bending: no effect for small amounts of skewness.
7. Radius of curvature: polygon size is roughly inversely proportional to radius of curvature at constant time and temperature.

The theory of polygonization is discussed and it is pointed out that the rate of climb of unit dislocations does not seem to be the only factor that controls the growth rate.

## STRUCTURE ET POLYGNISATION DU ZINC COURBÉ

La géométrie des cristaux de zinc courbé est discutée et il est montré que les plans de glissement ont la forme des développantes, tandis que les axes hexagonaux des lamelles sont parallèles aux tangentes de la développée. Ceci concorde avec les résultats des autres chercheurs pour les cristaux de corundon courbés et avec la théorie.

Il est montré que les cristaux courbés et même ceux pliés ne sont pas nécessairement polygonisés immédiatement après la déformation; ils contiennent parfois des frontières de sous-grains qui peuvent s'être ou ne s'être pas formées pendant la courbure. La structure normale d'un cristal de zinc courbé uniformément consiste en un réseau de lignes de dislocation reliant de petits éléments de parois de dislocation.

Des données quantitatives sur la cinétique de la polygonisation sont présentées. La polygonisation, en l'absence de contraintes hétérogènes, ne se produit pas au-dessous de  $170^\circ$  dans le zinc pur et cette température est élevée par 0,1 at. % de cadmium. A une température donnée, les angles des polygones croissent proportionnellement au logarithme du temps. L'effet de la température sur la vitesse de grossissement pour un angle constant dépend de la température; on obtiendrait une énergie d'activation de l'ordre de 60 kcal/mol au-dessous de  $250^\circ$  et de l'ordre de 20 kcal/mol entre 250 et  $325^\circ$ .

Le rôle de plusieurs variables sur la vitesse de croissance des polygones a été étudié:

1. *Contraintes après recuit*: Provoque la coalescence des frontières.
2. *Macles*: Sur le côté en compression, empêche le grossissement.
3. *Température de déformation*: Sans influence marquée entre  $-196$  et  $225^\circ\text{C}$ .
4. *État de surface*: Sans influence pour autant que la surface soit macroscopiquement lisse.
5. *Interruption du recuit*: Sans effet par comparaison au recuit ininterrompu.
6. *Courbure oblique*: Pas d'effet quand l'obliquité est faible.
7. *Rayon de courbure*: La dimension des polygones est en première approximation proportionnelle à la courbure pour une température et un temps donnés.

La théorie de la polygonisation est discutée et il est remarqué que la vitesse de "climb" des dislocations n'est pas le seul facteur qui détermine la vitesse de grossissement.

## ÜBER DAS GEFÜGE UND DIE POLYGNISATION BEI GEBOGENEN ZINKPROBEN

Die geometrischen Verhältnisse bei gebogenen Zinkkristallen werden diskutiert. Es wurde festgestellt, dass die Gleitebenen in gebogenen Zinkkristallen die Form einer Evolvente haben. Die hexagonale Achse liegt parallel der Tangente an die Evolute. Dieser Befund ist mit den Ergebnissen anderer Autoren für gebogene Karborundkristalle und mit der Theorie in Übereinstimmung.

Es wird gezeigt, dass gebogene Kristalle, vor allem wenn sie sehr stark gebogen sind, nicht unbedingt sofort nach dem Biegen polygonisiert sind. Sie enthalten manchmal Kleinwinkelkorngrenzen ("low-angle" Korngrenzen), die sich u.U. während der Biegung gebildet haben. Das normale Gefüge eines homogen

\* Received November 13, 1954.

† General Electric Research Laboratory, Schenectady, New York.



verformten Zinkkristalles besteht vermutlich aus einem Netzwerk von gebogenen Versetzungslinien, die auf kleinen Abschnitten Versetzungswälle enthalten.

Für die Kinetik der Polygonisation in zylindrischen, gebogenen Zinkkristallen werden quantitative Daten mitgeteilt. Sind keine inhomogenen Spannungen vorhanden, so tritt bei "chemisch reinem" Zink unter 170°C keine Polygonisation auf. Diese Temperatur wird durch Verunreinigung mit 0,1% Cd etwas erhöht. Bei einer bestimmten Temperatur vergrössern sich die Winkel der Polygone proportional dem Logarithmus der Zeit. Für einen gegebenen Winkel ist das Mass des Wachstums,  $d\theta/dt$ , temperaturabhängig. Wird zur Erklärung der Temperaturabhängigkeit eine Arrhenius'sche Formel herangezogen, so beträgt für Temperaturen unter 250°C,  $Q \sim 60$  kcal/mol und bei Temperaturen von 250 bis 325°C,  $Q \sim 20$  kcal/mol.

Weiterhin wurden mehrere verschiedene Möglichkeiten untersucht, durch die das Wachstum der Polygone zu beeinflussen ist:

1. Spannung nach dem Anlassen: bewirkt ein Zusammenwachsen der Korngrenzen.
2. Zwillinge: auf der Druckseite hemmen sie das Wachstum der Polygone sehr stark.
3. Biegetemperatur: Temperaturänderungen zwischen -198 und 225°C bringen keine wesentlichen Effekte.
4. Oberflächenbeschaffenheit: kein Einfluss, so lange die Oberfläche makroskopisch glatt war.
5. Unterbrechung der Anlassbehandlung: kein Einfluss.
6. Schräges Biegen: kein Einfluss bei kleinen Abweichungen.
7. Biegeradius: die Grösse der Polygone ist umgekehrt proportional dem Radius der Biegung bei Konstanthaltung der Zeit und der Temperatur.

Die Theorie der Polygonisation wird diskutiert und dabei herausgestellt, dass nicht nur das Steigungsmass von Einheitsversetzungen das Wachstum beeinflusst.

Until recent years, there had been relatively few systematic investigations of plastic bending in monocrystals. Work on this topic was greatly stimulated, however, when Cahn,<sup>1</sup> Orowan,<sup>2</sup> and Cottrell<sup>3</sup> elucidated the process which is now known as "polygonization."

The mechanics of bending in monocrystals has been a particularly neglected subject. The author is aware of only three investigations of this subject: those of Kidani,<sup>4</sup> Held, Loercher, and Kochendoerfer,<sup>5</sup> and of Yen and Hibbard.<sup>6</sup> These authors concluded that mechanical bending phenomena can be satisfactorily interpreted in terms of pure tension phenomena with suitable corrections for the different stress patterns that exist. One exception is that strain-hardening is more rapid in bending<sup>5</sup> than in tension.

The crystallography of bent monocrystals was first clearly demonstrated by the experimental work of West<sup>7</sup> on  $\text{Al}_2\text{O}_3$  (synthetic sapphire). The experimental results were elegantly rationalized by Nye.<sup>8</sup> West found that the slip lamellae in bent  $\text{Al}_2\text{O}_3$  crystals had the shape of involutes and the optic axes in bent crystals lay parallel to tangents of the generating circles of the involutes. Nye recognized that this was a natural consequence of the lamellar nature of slip and gave a detailed interpretation of the phenomenon in terms of dislocations. He also considered the bending of crystals with more than one active slip system. Previous workers had believed<sup>4,5</sup> that the slip lamellae had the shape of cylindrical arcs.

Early workers on polygonization<sup>1,9</sup> assumed that the excess dislocations that bending introduces into a crystal were more or less randomly arrayed on the slip planes and that annealing was necessary to cause them to rearrange between "polygons" (see Fig. 1). This assumption has since been questioned by Guinier and Tennevin,<sup>10</sup> Jillson,<sup>20</sup> and by Conard, Averbach, and

Cohen<sup>11</sup> who believe that the structure may be polygonized immediately after deformation (even at low temperatures) and that only growth of the polygons occurs subsequently. This point will receive detailed attention in the present paper.

Although polygonization in monocrystals has been observed in a wide variety of metals, as well as in non-metallic crystals such as rock salt<sup>1</sup> and  $\text{Al}_2\text{O}_3$ ,<sup>12</sup> there have been no quantitative investigations of the kinetics of the phenomenon. Fragmentary data for zinc were presented by Cahn,<sup>1</sup> and for silicon-iron by Dunn and Daniels.<sup>13</sup> It is a primary purpose of this paper to discuss the kinetics of polygonization in detail and to compare the results with existing theories.

Reviews of the literature have been given by Cahn,<sup>14</sup> and Cottrell<sup>15</sup> and Guinier<sup>16</sup> so no review will be attempted here.

## EXPERIMENTAL

This investigation became feasible when it was discovered that polygonization could be observed with particular ease on the cleavage surfaces of bent zinc monocrystals. A typical specimen is shown in Fig. 2, while Fig. 3 shows how polygon boundaries look on a bent cleavage surface.

The crystals were grown by the Bridgman method in round (5/32 in. I.D.) and square (6×6 mm) precision Pyrex tubes. The raw material was 99.999+ per cent zinc from the New Jersey Zinc Company. Orientation control was obtained by means of seeding; most of the crystals had  $\chi_0 = 35^\circ$ .

After the Greninger back-reflection X-ray method had been used to determine a crystal's orientation, it was cut into 1½ in. specimens. One end of each specimen was cleaved at -196°C to make a sharp wedge that was flat on one side. The flat side was used to align the crystal in a bending jig so that the bending axis

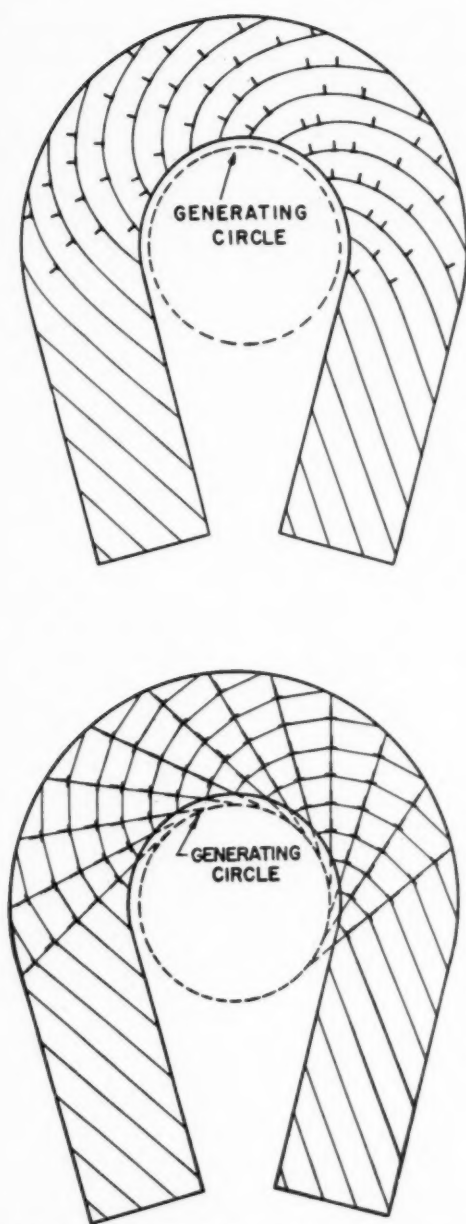


FIG. 1. Dislocations in as-bent zinc crystal and in polygonized zinc crystal.

could be fixed relative to the crystal axes. The crystals were bent at room temperature (except when it is noted otherwise). Then they were cleaved along their bent cleavage surfaces by applying a reverse bending moment to their ends at  $-196^{\circ}\text{C}$ . This technique, when carefully performed, yielded smoothly bent cleavage surfaces (except for the inevitable cleavage steps).\*

\* The following conditions were found to favor good smooth cleavages: (1) low temperatures, (2) high ratio of normal to shear stress resolved onto the cleavage surface, (3) surface polished to macroscopic smoothness, (4) polished surface lightly etched with HCl.



FIG. 2. Typical bent and cleaved zinc monocrystal.

When it was desirable to polish a specimen, one of two solutions was used: (a) 50%  $\text{HNO}_3$ —fast action but tended to pit and was difficult to control; (b) a special formulation of the standard chemical polish for zinc which was found by experiment to give optimum results. The latter polishing solution was composed of: 160 g  $\text{CrO}_3$ ; 20 g  $\text{Na}_2\text{SO}_4 \cdot 10 \text{H}_2\text{O}$ ; 500 cc  $\text{H}_2\text{O}$ . The crystal (after thorough cleansing in HCl) was immersed in the chemical polish with gentle agitation for 10 seconds; washed; and the process was repeated a few times to obtain the highest polish.

Annealing treatments were carried out in furnaces that were controlled to within  $\pm 2^{\circ}\text{C}$  of the desired temperatures. The furnace atmosphere was air and it was found that the cleavage surfaces remained free of appreciable oxide up to about  $350^{\circ}\text{C}$ . Tests made with a thermocouple embedded in a typical specimen showed that about three minutes was required for the specimen to approach within 10 degrees of the annealing temperature. Therefore, this amount of time was subtracted from the total time that a specimen was in a furnace in order to obtain the net annealing times reported in the data.

The local radii of curvature of the bent cleavage planes were measured by a microscopic method. When a cylindrical surface is observed with a metallurgical microscope, only a narrow band of the surface is illuminated. For a fixed aperture of the lighting system, it can be shown that the width of the illuminated band should be proportional to the radius of curvature of the surface. Therefore, a calibration curve was constructed by measuring the widths of the illuminated bands on polished drill-rods. A graph of bandwidth *versus* drill-rod radius was linear as predicted, and was used to find the radius of curvature of cleavage planes.

To find the polygon angles, the average spacings of the boundaries were measured and divided by the radius of curvature. To obtain representative data it was necessary to repeat the process on different specimens and then average the results. The method allowed the detection of polygon angles as small as  $10^{-3}$  radian

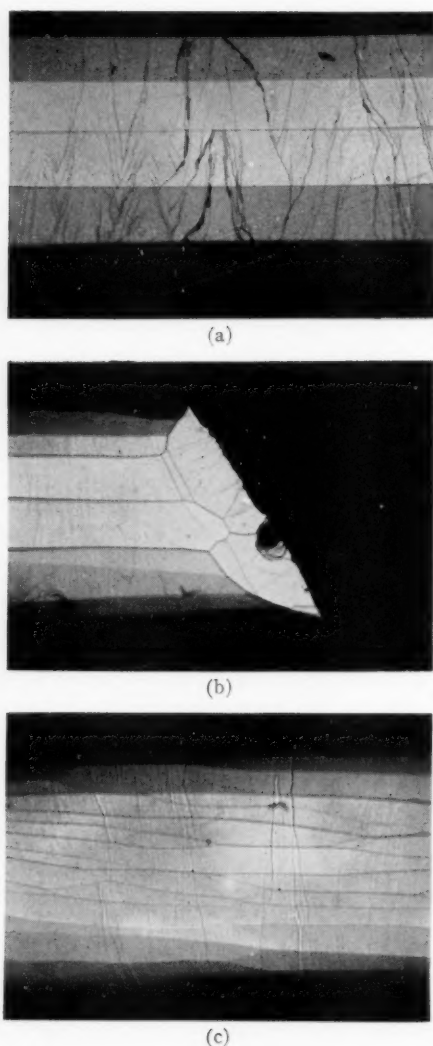


PLATE I. FIG. 3—(a) Example of well-formed polygons. Crystal-heated 10 000 min at 325°C. (b) Showing polygon boundaries "piled-up" at edge of crystal. (c) Crystal was bent skewly with respect to slip direction and specimen axis. Heated 5 min at 350°C.

consistently. Under somewhat dubious conditions angles as small as  $3 \times 10^{-4}$  radian were detected.

Some mention should also be made of the back-reflection Laue technique. Although this X-ray method is usually considered to be a low resolution method, its resolving power must be reconsidered for the special case of a severely bent crystal. Figure 4 shows the experimental arrangement. If the crystal were nominally flat with a mosaic fine structure, any part of the incident beam might strike a mosaic with a particular angle. Therefore, the resolving power would be limited by the total divergence angle of the incident beam,  $d/L$  radians. However, when a severely bent crystal is irradiated, only very limited regions of the specimen have any particular angle with respect to the

beam so that the effective divergence of the beam becomes  $d/(D+L/2)$  radians. Thus, by increasing the film-specimen distance,  $D$ , one can increase the resolving power to a very high value. This seems to be limited only by the intensity of the Laue reflections and the line breadth of reflections from bent crystals. In the present work the X-ray method could detect polygon angles of  $10^{-3}$  radian and, therefore, was about equal in sensitivity to the optical method.

## RESULTS AND DISCUSSION

The description of the results is divided into three parts: (a) the crystallography of bent zinc crystals; (b) the distribution of dislocations in freshly bent zinc crystals; (c) the kinetics of polygonization. Then the theoretical significance of the results is discussed in general.

### (a) Crystallography of Bent Zinc Monocrystals

The geometry of the majority of the specimens that were used in this investigation is shown in Fig. 5. The (0001) slip planes of the rod-shaped crystals made angles of about 35 degrees with the rod-axes and a [1210] direction was aligned in a plane parallel to the rod-axes. The crystals (unless otherwise specified) were bent about an axis lying in the (0001) plane at right angles to the rod-axis. A jig was used to insure accuracy in producing this type of bending.

The result of bending a zinc crystal is shown schematically in Fig. 1. The (001) slip planes assume the shape of cylindrical involutes and the hexagonal axes lie on tangents of the generating cylinder. This geometry for bending by simple slip was first determined by West<sup>7</sup> for the case of bent sapphires. It is shown in more detail in Fig. 6. The various symbols in the figure may be used to express the relations between the parameters of interest. As West pointed out, the equations for the

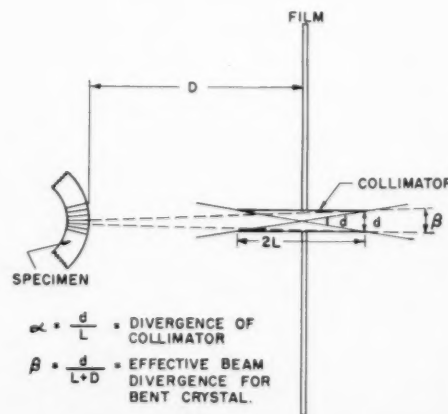


FIG. 4. Schematic drawing of back-reflection X-ray camera for bent crystals.

involutes which define the slip planes are:

$$\begin{cases} x = a(\cos\psi + \psi \sin\psi) \\ y = a(\sin\psi - \psi \cos\psi) \end{cases}, \quad (1)$$

where  $a = R \sin\chi_0$  = the radius of the generating circle. The radius of curvature of the slip planes at any point is a  $\psi = c$  and since:

$$L = (x^2 + y^2)^{1/2} = a(1 + \psi^2)^{1/2}$$

we have:

$$c = (L^2 - a^2)^{1/2}. \quad (2)$$

Since a bent crystal can support only small elastic stresses (of the order of the critical resolved shear stress) most of the strains are relieved by excess dislocations.<sup>1</sup> The local dislocation density has been shown by Cahn<sup>1</sup> and by Nye,<sup>8</sup> using somewhat different methods, to be:

$$n = 1/bc, \quad (3)$$

where  $b$  is the Burger's vector. It is assumed in the derivation of (3) that  $D$ , the slip plane spacing, is small compared to  $c$ .<sup>\*</sup> The average dislocation density is a quantity that is sometimes desired. By means of Eq. (3) it can be obtained if the average radius of curvature is known. The average radius of curvature,  $\bar{c}$ , is given exactly by:

$$\bar{c} = \frac{1}{L} \int_{r_2}^{r_1} (L^2 - a^2)^{1/2} dL$$

but it may be estimated from the value of  $R$  without taking the trouble to evaluate the integral. If  $L \approx R$ , Eq. (2) may be rewritten:

$$c = (R^2 - R^2 \sin^2\chi_0)^{1/2} = R \cos\chi_0 \approx \bar{c}.$$

Since  $c$  increases for  $I < R$  and decreases for  $L > R$ , it can be seen that this is a fairly good approximation provided  $(r_1 - r_2)$  is small compared with  $R$  and  $\chi_0$  is not large.

Consideration of Fig. 6 will show that the slip planes become perpendicular to the surface of  $r_2 = a$ . As West<sup>7</sup> and Nye<sup>8</sup> have discussed, this imposes a limitation on

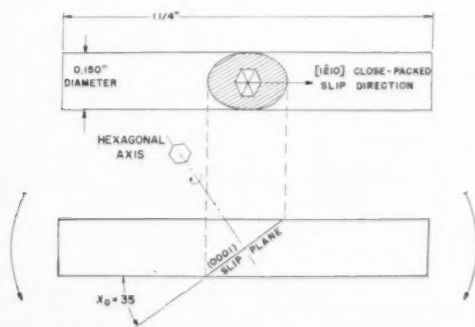


Fig. 5. Schematic drawing of crystals prior to bending.

<sup>\*</sup> Otherwise, the expression should be:  $n = (2c + D)[2cb(c + D)]$  which reduces to (3) for  $D \ll c$ .

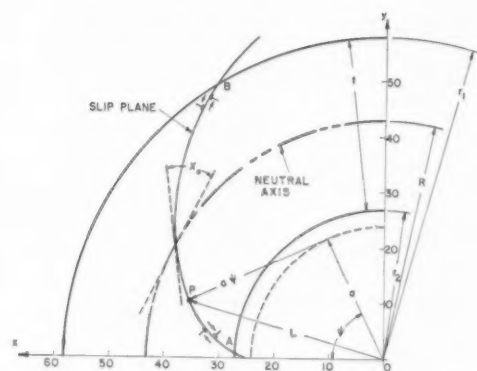


Fig. 6. Geometry of slip planes in bent crystals (after West).

the minimum value that  $R$  can have for deformation of a single slip system. However, for the case of zinc, and probably for other crystals with similar structures, the minimum value of  $R$  is limited by another factor. The additional factor is the onset of twinning. As is well known,<sup>17</sup> zinc can be twinned by compression parallel to the hexagonal axis. Since the ratio of the resolved compressive stress to the resolved shear stress on the (0001) plane increases as the (0001) plane approaches perpendicularity with the surface of a bent crystal, twinning eventually becomes preferred over slip as the mode of deformation. Thus, factors that affect the ratio of the twinning stress to the slip stress (such as temperature and impurities), also affect the minimum  $R$  obtainable.

With the above discussion in mind, we proceed to calculate the minimum value of  $R$ , for a given crystal thickness,  $t$ , and orientation,  $\chi_0$ . The method is that of Nye<sup>8</sup> since the method used by West<sup>7</sup> is unrealistic in that it ignores the change in thickness of the crystal during bending. The volume of a length,  $l_0$ , of unbent crystal of unit width is  $l_0 t$ . After bending, the volume is  $l/a(R^2 - a^2)$ . Since the volume should remain constant during the deformation, the volumes may be equated so that:

$$a^2 = R(R - t)$$

but:

$$a = R \sin\chi_0$$

so:

$$R_{\min} = \frac{t}{\cos^2\chi_0}.$$

Thus, crystals with  $\chi_0 = 90^\circ$  cannot be bent at all whereas it should be possible to bend crystals with  $\chi_0 = 0^\circ$ , until  $R = t$ . Again, however, a complication in the form of twinning presents itself.

Zinc can be twinned by tension applied parallel to the (0001) plane.<sup>17</sup> Therefore, when  $\chi_0$  is less than about 15 degrees, there is a strong tendency for a crystal that is under bending stresses to twin. The component of maximum tensile stress parallel to the (0001) planes is large compared to the shear stress and such crystals



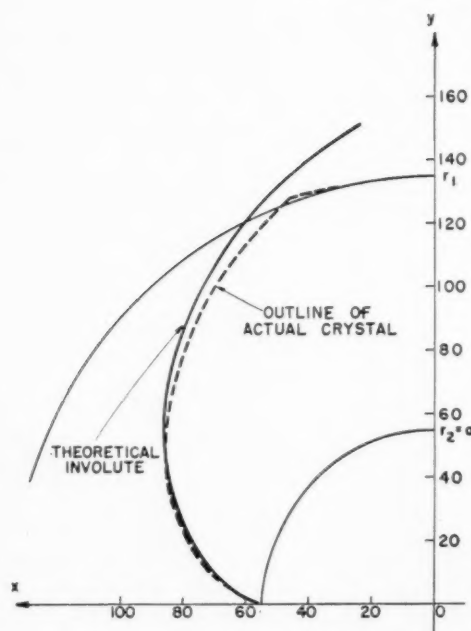


FIG. 7. Comparison of the shape of the slip planes of an actual bent zinc crystal with the calculated shape.

can be bent very little at room temperature without forming twins.

The fact that  $\chi_0$  had to be greater than a certain value for bending to occur in a crystal and that  $R_{\min}$  increased with increasing  $\chi_0$ , required that a compromise be made in the choice of  $\chi_0$  for the present specimens. It was found, by trial, that crystals with  $\chi_0$  equal to about  $35^\circ$  could be bent to smaller radii without tensile or compressive twinning, than crystals with either larger or smaller,  $\chi_0$ 's.

In order to determine how closely the theory of Nye might approximate the geometry of an actual crystal, the comparison illustrated in Fig. 7 was made. The shape of a bent and cleaved crystal was outlined from an enlarged photograph. This outline is shown in the figure. The value of  $R$  was taken as the radius of the center fiber of the bent crystal. Since this fiber made an angle of  $\chi_0 = 35^\circ$  before and after bending, it was concluded that it remained the neutral fiber throughout the bending process. The theoretical involute of Fig. 7 was calculated by means of Eq. (1). (Note that the crystal was bent until  $r_2 = a$ .) Considering all of the possibilities for error in magnification of the outline of the actual crystal and the possibility that the neutral axis shifted slightly inward, it is felt that the agreement between the two curves is quite good. Other crystals were checked with as good or better agreement between theory and experiment as shown in Fig. 7.

Another prediction of the theory is that the hexagonal axes of the bent crystal lamellae should lie along tangents to the generating circle of the involutes. West<sup>7</sup> showed that this was true for corundum crystals by

optical methods. It is shown to be true for zinc crystals in Fig. 8. This photograph shows the etch pits that formed along polygonization boundaries in a bent zinc crystal. As Cahn<sup>1</sup> pointed out, these boundaries lie approximately parallel to the hexagonal axes. It can be seen that the boundaries in Fig. 8 are indeed straight and that they seem to lie tangent to a curve which is an ellipse in this case because the curvature of the crystal was not uniform.

The final point to be discussed before the discussion of the crystallography of bending is concluded is the dislocation movements that occur during the bending process. Near A and B in Fig. 6, the dislocation movements that occur during bending are sketched schematically. Since the number of positive edge dislocations must equal the number of negative ones in an unbent crystal, it can be seen that the motion of negative dislocations out of a crystal is equivalent to the motion

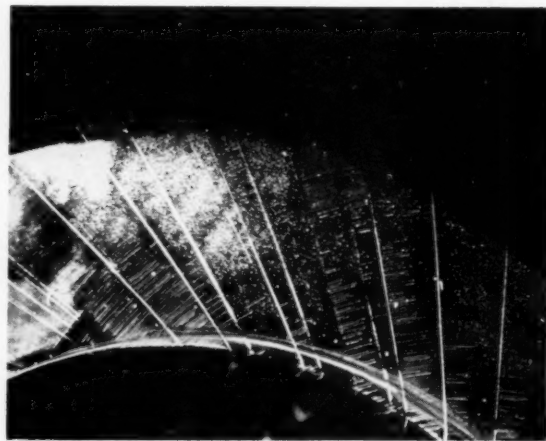


FIG. 8. View along intersections of slip planes with polygon boundaries in a polygonized zinc crystal. (Bent crystal annealed 65 hrs. at  $350^\circ\text{C}$ —etched electrolytically in 0.2% sodium thiosulfate—boundary angles approx.  $3-4^\circ$  ( $7\times$ )).

of positive ones into the crystal during bending. Note also that no dislocations should flow past the neutral axis from either side. This means that only the excess dislocations need move to their final positions in order to produce the observed glide strains. However, since strain-hardening is observed during bending,<sup>5</sup> the number of dislocations that move is probably somewhat greater.

#### (b) Structure of Bent Crystals Prior to Annealing

During a discussion of the structure of plastically bent crystals some important points must be kept in mind. These are made explicit here because the subject might become confused if these points are ignored. First, polygonization is only one of at least three processes by which sub-boundaries may be introduced into a crystal. The other two occur during solidification<sup>18</sup> and during ortho-kinking.<sup>19</sup> Second, plastic-bending

introduces many dislocations into a crystal: some of these (equal numbers of positive and negative ones) contribute towards strain-hardening but not to polygonization; others (excess positive ones) eventually cause polygonization to occur but may or may not contribute to strain-hardening.

In view of the above discussion, it should be clear that the simple observation of discontinuous X-ray reflections from a bent crystal is not sufficient evidence to show that it has polygonized (in the classical sense of the term, of course). An array of sub-grains is only one of the possible structures that can yield discontinuous X-ray reflections and there is more than one way in which an array of sub-grains may form.

In the present investigation a considerable effort was made to try to separate the various components of the structure of bent zinc crystals. Microscopic as well as various X-ray techniques (including a precision spectrometer, the high-resolution Laue-Technique, and the Berg-Barrett method of X-ray micrography) were used.

In agreement with the results of Conard, Averbach, and Cohen,<sup>11</sup> it was found that weakly bent crystals ( $R \geq 2$  cm) sometimes yielded discontinuous Laue reflections. This was never the case for strongly bent crystals ( $R \leq 1$  cm). In some cases it was possible to correlate the discontinuous X-ray reflections with visual observations of markings on the cleavage surfaces of the crystals. In other cases the X-ray reflections were discontinuous but the cleavage surfaces appeared to be perfectly smooth under the microscope.

The visual observations detected small angle grain-boundaries that seemed to have been formed in various ways. Some of them were simply "optical mosaic" boundaries that had formed when the crystals were grown, and had subsequently increased in angle during deformation. Others formed at inhomogeneities in the crystal (usually pits, etc., near the surface). In still other cases, collections of very small-angle boundaries were found adjacent to larger boundaries; suggesting that dislocations had piled up there. Finally, in some crystals, especially those with low angles ( $\chi_0 = 15-35^\circ$ ), a sort of "macro-polygonization" was observed. This seems to correspond with the phenomenon observed by Jillson.<sup>20</sup> In these crystals, the bent cleavage planes were made up of facets roughly  $1/32$  in. in width, but the boundaries between the facets were not sharp. Also, when the crystals were annealed, polygonization occurred in them on a microscopic scale.

The various markings, described above, were found in much greater density in the center two quarters of the length of the cleavage planes; that is, near the neutral axis. The outer two quarters of the cleavage surfaces were commonly free of all markings except cleavage steps. Furthermore, it was found that impure crystals (0.1 at. % Cd) seldom exhibited sub-boundary markings prior to annealing.

In the cases where discontinuous Laue reflections

were obtained from crystals that showed no optically observable substructure, another cause was suspected. It was felt that inhomogeneous "Taylor-rotations" within the slip bands might be responsible for the discontinuous X-ray spots. In order to show that this was a possibility, the photographs of Fig. 9 were taken. The crystals were placed in the reflecting position at the back-focus of a bent crystal monochromator. The line focus of a GE CA-7 Copper X-ray tube was placed at the front focal point of the monochromator. The diffracted beams from the crystals were recorded on films. As Fig. 9 shows, it was found that the X-ray reflection from a crystal pulled in simple tension (no macroscopic bending of the slip planes) was just as discontinuous as the reflection from a bent crystal. (To make the strains comparable, the outer fibers of the bent crystal had about the same elongation as the tensile specimen.) Furthermore, it was noted that the "segments" of the reflection from the as-bent crystal became more finely segmented when the crystal was annealed.

It is concluded that weakly bent zinc monocrystals are not necessarily polygonized immediately after they have been bent. Observations of X-ray reflections alone do not constitute satisfactory evidence of polygonization. Thus the conclusions of Conard, Averbach, and Cohen<sup>11</sup> are open to question.

Next, consider the structure of sharply bent crystals. The question to be decided is: are the excess dislocations in a sharply bent crystal distributed in a random or in an ordered array? Laue photographs of such crystals (taken under conditions allowing mis-orientations of  $10^{-3}$  rad to be detected) almost invariably consisted

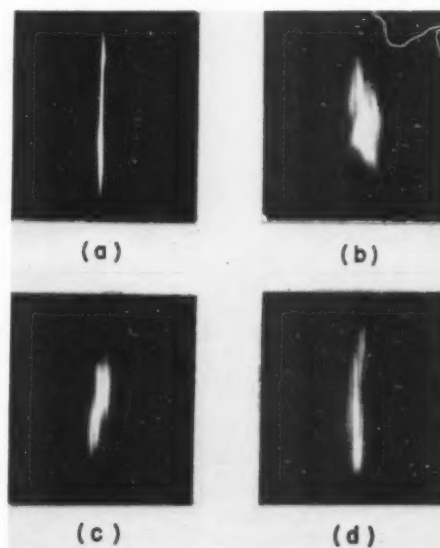


FIG. 9. (a) Undeformed zinc crystal. (b) Crystal bent to give approx. 25% El. of outer fiber.  $\chi_0 = 35^\circ$  (polished after cleavage). (c) Crystal pulled to 25% El. in tension.  $\chi_0 = 35^\circ$  (polished after cleavage). (d) Bent crystal after 10 min at  $225^\circ\text{C}$ .

of continuous asterisms. Similar results have been obtained by the very high resolution method (resolves 15 seconds of arc and sizes down to 0.01 mm) of Guinier and Tennevin.<sup>10</sup> Instead of trying to increase further the resolution of the observations, a new approach was made to the problem in this investigation. The method was to try to maximize the possible polygon angles in a crystal.

For a given dislocation density, the dislocations can be arranged in the two ways illustrated by Fig. 10. On the left, the dislocations are closely spaced on widely spaced slip planes. There is no way of distinguishing polygon boundaries in the array so that only short-range polygonization is possible. On the other hand, when  $d = D$ , as it is in the array at the right in Fig. 10, it is possible to distinguish clearly from a random array of excess dislocations. The minimum possible angle is equal to  $(b/r)^{1/2}$ , and some values are given in the table at the bottom of Fig. 10.

It has already been stated that the minimum polygon angle that could be detected by the methods of this investigation was about  $10^{-3}$  rad. The table of Fig. 10 shows that this would be the minimum possible angle in a crystal with  $c = 0.27$  mm. Some specimens with this small radius of curvature were made by polishing crystals down until their diameters were less than 1 mm. These crystals could then be bent until  $R$  was about 2 mm and  $c = 0.25$  mm. Microscopic and X-ray examinations of such crystals showed no polygonization in them in the as-bent condition.

It is concluded that sharply bent zinc crystals (bent at room temperature) are not normally polygonized except over very short distances of a few atomic spacings. Prior to bending, the crystals must be "good," of course, and they must be carefully bent to avoid heterogeneous bending.

Another aspect of the fine structure of bent crystals is the distribution of slip lines in them. The stress gradients that exist during bending and the excess

positive dislocations that are present might be expected to make the slip-band distribution in a bent crystal different from that in a crystal strained the same amount in tension. However, such a difference in slip-band distribution would probably not exist during the first few per cent of plastic strain. It would be more likely to exist in crystals that had been appreciably strained. Therefore, two polished crystals (one to be bent, one to be pulled in tension) were deformed to surface elongations of about 30 per cent; then some of the slip lines were preserved with stop-off lacquer while the others were polished off the surfaces; finally the crystals were deformed additionally and the sets of slip lines were compared. No qualitative differences could be found between the two sets of slip lines.

### (c) Kinetics of Polygonization

Figure 11 presents examples of the appearance of a zinc cleavage surface during polygonization. It can be seen that the polygon boundaries are straight over large distances throughout most of the growth process. In the very early stages of polygonization ( $\theta < 10^{-3}$  rad) the boundaries were fragmentary and there seemed to be many cross-links between the fragments. The boundaries were difficult to see, however, so the details of the cross-linking are not clear. After the boundary angles reached about  $10^{-3}$  rad in size, they were straight over distances large compared with their separation. From this stage onward they grew by the mechanism that was first discussed by Dunn and Daniels,<sup>13</sup> and which is outlined in Fig. 12. In this mechanism, two boundaries coalesce to form a single boundary of twice the angle, but less energy than the sum of the energies of the original boundaries. The average polygon angle is  $\theta = \theta_0(2)^n$  where  $\theta$  is the initial angle and  $n$  is the number of times that two boundaries coalesce. Thus, only a few growth events are required to change polygon angles of a few minutes of arc into angles of a few degrees. The "Y"-junctions of the polygon angles were observed to move at rates of the order of mm/sec at roughly 300°C.

Before the detailed kinetic studies were undertaken some of the variables that might have confused the results were investigated. These were:

1. *Effect of stress following annealing*—The results of Parker and Washburn<sup>21</sup> indicated that the polygon boundaries would be highly mobile under applied stresses. Figure 13 shows that this is indeed the case. Therefore, the polygonization specimens had to be carefully handled and could not be cleaved after the annealing treatments.\*

2. *Effect of twins introduced during bending*—It was found that twins, which sometimes formed on the compression side of the specimens, greatly inhibited or

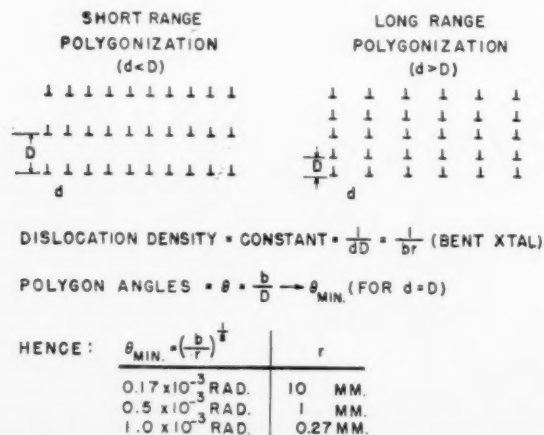


FIG. 10.

\* Figure 13 provides an additional indication that as-bent crystals are not polygonized. If an as-bent crystal were polygonized, then, under stress, the highly mobile boundaries should rapidly coalesce to form larger visible boundaries. This is not observed.

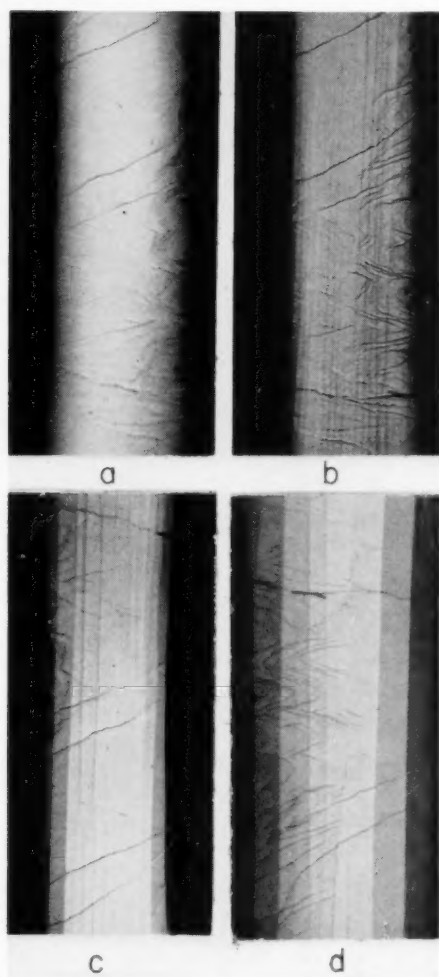


FIG. 11. Polygonization in zinc at constant temperature. Radius of curvature of cleavage surface was 3.7 mm. (a) As cleaved. (b) After 10 min in 250°C fce. (c) After 100 min in 250°C fce. (d) After 1000 min in 250°C fce.

completely stopped polygonization at ordinary temperatures. Therefore, it was necessary to avoid forming twins in the specimens used in the kinetics study. Twins also gave trouble sometimes by causing recrystallization to occur.

3. *Effect of bending temperature*—It was stated by Cahn<sup>1</sup> that zinc crystals bent at  $-196^{\circ}\text{C}$  do not polygonize when they are heated at  $400^{\circ}\text{C}$ . In order to check this point, several crystals were bent at  $-196^{\circ}\text{C}$  and then annealed at  $250^{\circ}\text{C}$ . It was difficult to obtain good specimens because the crystals tended to cleave prematurely while they were being bent and it was difficult to avoid forming twins in them. However, a few satisfactory specimens were prepared, and it was found that these polygonized at the normal rate at  $250^{\circ}\text{C}$ . It is suspected that Cahn's specimens did not polygonize because they contained unobserved twins.

Cottrell<sup>15</sup> suggests that polygonization should be

accelerated in the presence of an applied stress, because vacancies created during slip would facilitate climb of the polygonizing dislocations. This is a difficult point to prove because an applied stress would also tend to move and thereby coalesce polygon boundaries as in Fig. 12. Nevertheless, it was felt that the effect of high temperature deformation should be checked. This was done by bending crystals slowly while they were immersed in silicone oil at  $160\text{--}225^{\circ}\text{C}$ . No evidence of polygonization was found on either their external or cleavage surfaces immediately after they were bent. During subsequent annealing treatments they polygonized somewhat more slowly than normal specimens.

It is concluded that polygonization, which occurs above about  $175^{\circ}\text{C}$  in zinc, is not sensitive to the temperature at which the crystal was originally bent.

4. *Effect of surface condition*—It might be suspected that two polygon boundaries would be able to coalesce more readily near the surface of a crystal than in the interior. If this were true, the rate of growth of polygons would depend on how the surface of a specimen had been prepared. In order to test the effect of surface preparation, bent crystals were annealed after four different surface preparations had been given them. Some had polished surfaces, some etched, some oxidized, and some had surfaces plated with copper. It was found that the state of the surface had no measurable

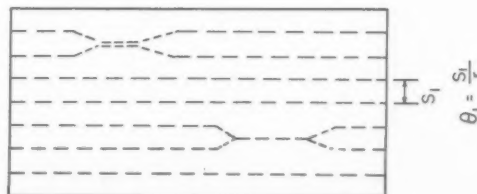
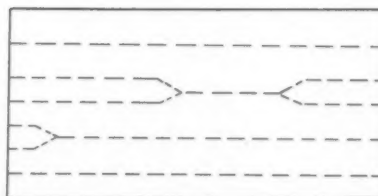
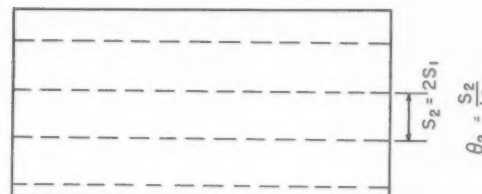


FIG. 12. Schematic growth of polygons.



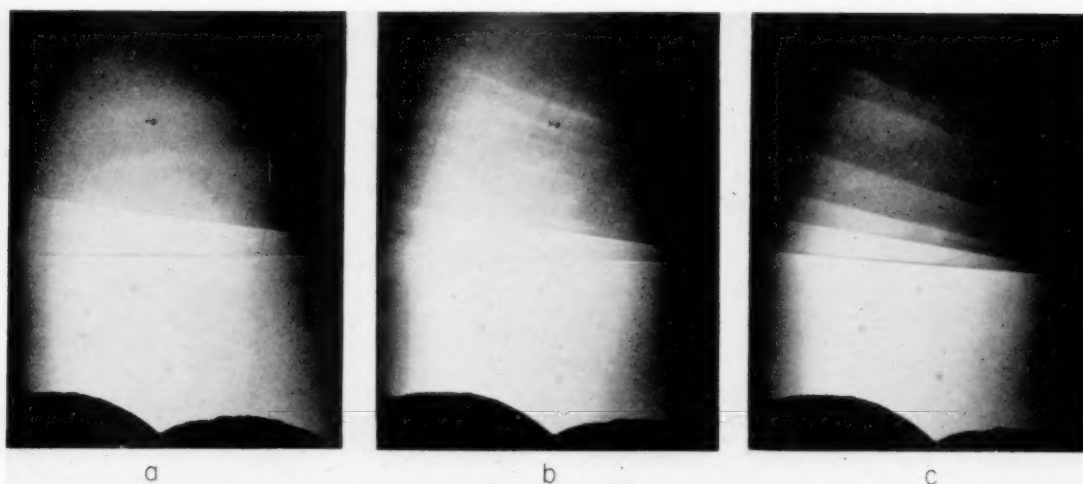


PLATE II. FIG. 13—Stress-induced motion of polygonization boundaries in a zinc monocrystal.

effect on the rate of polygonization at 250°C. The reason for this is that the growth precesses initiate in the bulk of a crystal rather than near an external surface. This does not mean that the surface has no effect at all on polygon boundaries; under some conditions boundaries that have already coalesced within a crystal become stuck near the surface as shown in Fig. 3b.

5. *Effect of intermittent annealing*—Since it was planned to anneal repeatedly the same crystal at each temperature in the kinetics study, it was necessary to compare continuously annealed crystals with crystals annealed cumulatively for the same amount of time. No measurable difference was found.

6. *Effect of bending about skew axis*—If a zinc crystal is bent about an axis that is not parallel with the (0001) slip plane, purely cylindrical bending of the slip planes does not result. Hence, the crystal will contain more than one kind of excess edge dislocations, and will not polygonize in the normal way. A few crystals that had been bent about skew axes were investigated in order to see just how critical accurate bending might be in a study of polygonization kinetics. It was found that skewly bent crystals polygonized readily. However, in accordance with expectations, the polygon boundaries were never straight as in Fig. 1a, but were always cross-

linked (Fig. 3c) and sometimes incomplete. It was evident that small amounts of skewness of bending would have no appreciable effect on the present results; nevertheless, care was always taken to obtain reasonably accurate cylindrical bending.

7. *Effect of radius of curvature*—In a preliminary study of polygonization kinetics the effect of radius of curvature was ignored because it was believed that the polygon angle,  $\theta$ , would be independent of radius of curvature for a given specimen, annealing time, and temperature. After considerable data had been collected, it was found that this was not the case, and that  $\theta$  varied in a systematic way with the radius of curvature,  $c$ . The dependence of  $\theta$  on  $c$  was not investigated in detail but, roughly,  $\theta$  was inversely proportional to  $c$  for values of  $c$  from about 0.5 mm to 20 mm; after a given annealing treatment.

In the final study of polygonization kinetics, to be described shortly, the data were measured at the constant radius of curvature, 2 mm.

Figure 14 presents data on the polygonization of pure zinc monocystals and on crystals with approximately 0.1 at. % Cd as impurity. It can be seen that at low temperatures the polygon angles at particular temperatures depended logarithmically on the time at temperature. At higher temperatures the polygon angles increased rapidly to about  $45 \times 10^{-3}$  radian and then remained constant. It was difficult to obtain reproducible data at temperatures above 325°C; therefore, the high temperature curves should be considered to be approximate.

The data show that cadmium, as an impurity, had little effect on the rate of polygonization at 300°C, but had a distinct inhibiting effect at 225°C.

The polygon angles as a function of temperature after constant annealing time are shown in Fig. 15. The graph shows that no polygon growth occurred below 170°C in zinc of the present purity (nominally 99.999+

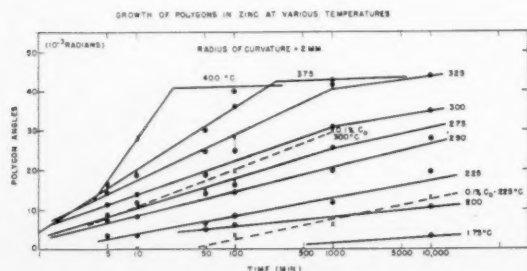


FIG. 14. Growth of polygons in zinc at various temperatures.

% pure). This suggests that polygonization is not present in crystals deformed at low temperatures.

The data of Fig. 14 were analyzed to find the rate of change of the average polygon angles with time. The rate was measured at constant angle ( $\theta = 0.01$  rad). The rate data are plotted against the reciprocal annealing temperature in Fig. 16. It is interesting that the temperature dependence of the polygonization was different below about 250°C than above. The possible significance of the different temperature dependences will be discussed in the next section.

#### (d) Polygonization Theory

Communication on the subject of polygonization has become difficult in recent times because of loose use of the term. Therefore, the meaning of the term, to the present author, will be defined at the outset of this discussion. First of all, polygonization is a *process*. Consequently, one cannot know that a material has polygonized if only its final state can be described. Second, as the name implies, polygonization is a process by which a curved line in a crystalline material becomes a polygonal line. The curvature of the line must have the same sign throughout the region under consideration, although the region may be quite small. In the simplest case, the line is part of a cylindrical surface; in more complex situations it may belong to a spherical surface.

Low-angle grain boundaries can be introduced into an undeformed zinc crystal in at least two distinct ways. One of these ways is by the unit kink-process<sup>19</sup> which results in kink-planes, accommodation-bands, and sub-boundaries in polycrystals. The other is bending followed by polygonization. The reasons why these two methods of reaching the same result seem to be distinct is not clear at present, but in the former case the formation of the dislocation walls seems to be activated by stresses, whereas, in the case of bending followed by polygonization, the process seems to be thermally activated.

It is believed that ample evidence has been presented in the present paper to show that "good" zinc crystals can be bent in such a way that they are not polygonized immediately after they are bent. They no doubt contain a sort of short-range polygonization consisting of isolated segments of dislocation walls threaded together by meandering dislocations. This is a state distinct from long-range polygonization, however, and is relatively stable below about 150–175°C in the absence of applied stresses.

Since it is well known that zinc crystals undergo rapid recovery at room temperature,<sup>17,22</sup> it is puzzling that a bent zinc crystal does not immediately polygonize. Two clues are available to guide speculation on this question. First, there is evidence that in certain stress fields polygonization does occur at room temperature in zinc. This was observed in some crystals of the

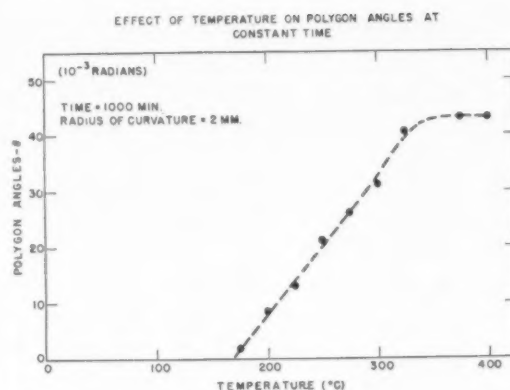


FIG. 15. Effect of temperature on polygon angles at constant time.

present investigation, and previously at tensile kink bands.<sup>23</sup> Second, at high temperatures the activation energy for polygon growth is about 20 kcal/mol (or approximately equal to that for recovery<sup>22</sup> and self-diffusion<sup>24</sup> parallel to the *c*-axis), but at lower temperatures the activation energy increases to about 60 kcal/mol.

It seems likely that the excess dislocations in a bent crystal must climb out of their slip planes for polygonization to occur.<sup>15</sup> Mott<sup>27</sup> had derived an expression

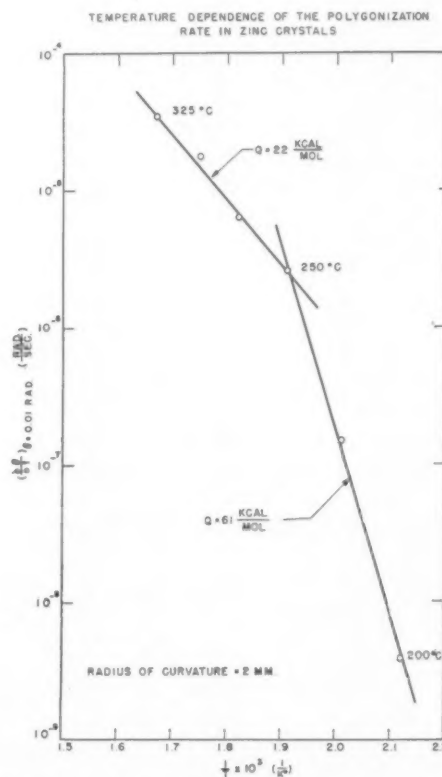


FIG. 16. Temperature dependence of the polygonization rate in zinc crystals.

for the rate of climb of unit dislocations:

$$\text{climb rate } \left( \frac{\text{cm}}{\text{sec}} \right) \simeq \nu b \left( \frac{b^2 F}{kT} \right) e^{-(W+U)/kT}$$

where:

$$\nu = 10^{13}/\text{sec}$$

$$b = \text{Burger's vector}$$

$$= 3 \times 10^{-8} \text{ cm}$$

$$F = \sigma_b = \text{force causing climb}$$

$$U = \text{activation energy to form jog}$$

$$W = \text{activation energy for self-diffusion.}$$

Now boundaries of angle  $\theta = 10^{-3}$  rad are observed to double in about 10 sec at 200°C. In such boundaries the half-distance between dislocations is about  $10^{-5}$  cm. Hence, the required climb rate is estimated to be  $10^{-6}$  cm/sec. If  $\sigma$  is taken to be a reasonable value:  $10^9$  dynes/cm<sup>2</sup>, and  $(U+W)$  is 20 kcal/mol (its value for recovery which seems to be climb-controlled), then Mott's expression yields a climb rate of about  $2 \times 10^{-6}$  cm/sec. On the other hand, if  $(U+W)$  is given the experimental value of 60 kcal/mol then the climb rate becomes impossibly small. It is concluded that the rate of climb of unit dislocations does not limit the polygonization rate at low temperatures. Some other factors must be introduced.

One factor that might limit the rate of the polygonization process is the fact that edge dislocations in zinc are dissociated to form extended dislocations.<sup>25</sup> The extended dislocations must recombine to form unit dislocations before they can climb. Stroh<sup>26</sup> has discussed the energy required for recombination in detail, and has estimated the energy required. In the absence of stress gradients, the energy would be 20–120 kcal/mol, depending on the width of the extended dislocation. Since the additional energy that is required in the present case is about 40 kcal it is not unreasonable that recombination of extended dislocations should control the polygonization rate. The activation energy should be much reduced by stress gradients and this accords with observation.

The shape of the polygonization isotherms should be considered next. Dunn and Daniels<sup>13</sup> proposed that the

"Y"-junctions are all formed early in the process and then are gradually exhausted as polygonization proceeds. This would qualitatively predict the observed dependence of the polygon angles on  $\ln t$ , and is consistent with the other results of this investigation. Another possible mechanism would be the nucleation of new boundaries by the coalescence of two old boundaries. Calculations of the present author show that this is a very unlikely occurrence, however, even in the presence of high stress gradients.

## REFERENCES

1. R. W. Cahn, *J. Inst. Metals* **76**, 121 (1949).
2. E. Orowan, *Dislocations in Metals*, A.I.M.E. (1954) p. 176.
3. A. H. Cottrell, "Theory of Dislocations," *Prog. in Metal Physics*, Vol. 1, (Butterworths, London, 1949) p. 77.
4. Y. Kidani, *J. Fac. Eng., Tokyo University*, **19**, 1–15 (1929).
5. A. Kochendoerfer, *Plastische Eigenschaften von Kristallen*, (Springer, Berlin, 1941) p. 147.
6. M. K. Yen and W. R. Hibbard, *Trans. A.I.M.E.* **185**, 710 (1949).
7. C. D. West, *Optical Study of Monocrystal Bent Corundum Rods*, Technical Report, ONR Contract N7onr39102.
8. J. F. Nye, *Acta Met.* **1**, 153 (1953).
9. R. W. K. Honeycombe, *J. Inst. Metals* **80**, 45 (1951).
10. A. Guinier and J. Tennevin, "Researches on the Polygonization of Metals," *Prog. Met. Phys.*, Vol. 2, (Butterworths, London, 1950) p. 177.
11. G. P. Conard, B. L. Averbuch, and M. Cohen *Trans. A.I.M.E.* **197**, 1036 (1953).
12. M. L. Kronberg, Private communication.
13. C. G. Dunn and F. W. Daniels, *Trans. A.I.M.E.* **191**, 147 (1951).
14. R. W. Cahn, "Internal Strains and Recrystallization," *Prog. Met. Phys.*, Vol. 2, p. 151, (Butterworths, London, 1950).
15. A. H. Cottrell, "Dislocations and Plastic Flow in Crystals" (Oxford, 1953) p. 180.
16. A. Guinier, "Substructures in Crystals," *Imperfections Symposium*, (J. Wiley & Sons, New York, 1952) p. 402.
17. E. Schmid and W. Boas, "Plasticity of Crystals," (F. A. Hughes & Co., 1950) pp. 94–100.
18. C. A. Cinnamon and A. B. Martin, *J. Appl. Phys.* **11**, 87 (1940).
19. J. J. Gilman, *J. Metals*, 621 (May 1954).
20. D. C. Jillson, *Trans. A.I.M.E.* **188**, 1009 (1950).
21. J. Washburn and E. R. Parker, *Trans. A.I.M.E.* **194**, 1076 (1952).
22. R. Drouard, J. Washburn, and E. R. Parker, *Trans. A.I.M.E.* **197**, 1226 (1953).
23. J. J. Gilman and T. A. Read, *Trans. A.I.M.E.* **197**, 49 (1953).
24. G. A. Shinn, E. S. Wajda, and H. B. Huntington, *Acta Met.* **1**, 513 (1953).
25. W. T. Read, "Dislocations in Crystals," (McGraw-Hill, New York, 1953).
26. A. N. Stroh, *Proc. Phys. Soc.* **67**, 427 (1954).
27. N. F. Mott, *Proc. Phys. Soc.* **64B**, 729 (1951).

## THE FORMATION OF MECHANICAL TWINS\*

N. THOMPSON and M. HINGLEY†

Measurements have been made of the stress required to cause the appearance of twins in single crystals of cadmium, both in tension and in compression. The results are consistent with the view that, if a twin nucleus is present, the shear stress in the twinning plane which is needed to cause it to grow is independent of the normal stress across the twinning plane.

### FORMATION DES MACLES MÉCANIQUES

Mesures de la contrainte nécessaire pour former des macles dans les monocristaux de cadmium par tension et compression. Les résultats confirment que, s'il y a un germe de macle, le cisaillement dans le plan de macle, nécessaire pour provoquer son grossissement, est indépendant de la contrainte normale.

### DIE ENSTEHUNG VON VERFORMUNGSZWILLINGEN

An Einkristallen aus Cadmium wurden die für das Auftreten von Zwillingen benötigte Spannung sowohl unter Zug- als auch unter Druckbeanspruchung gemessen. Die Ergebnisse sind mit der Theorie in Übereinstimmung, dass bei Anwesenheit eines Zwillingskeimes die zum Wachstum benötigte Schubspannung in der Zwillingsene unabhängig von der Normalspannung quer zur Zwillingsene ist.

## INTRODUCTION

In a previous paper<sup>1</sup> the question of the criterion for the production of mechanical twins was considered. Evidence was presented in support of the view that, in cadmium at least, the proper criterion was that the shear stress on the twinning plane, resolved in the twinning direction, should reach a certain critical value. At room temperature this critical shear stress was stated to be 140 gm/mm<sup>2</sup> although there was a considerable scatter ( $\pm 40$  gm/mm<sup>2</sup>) about the mean value.

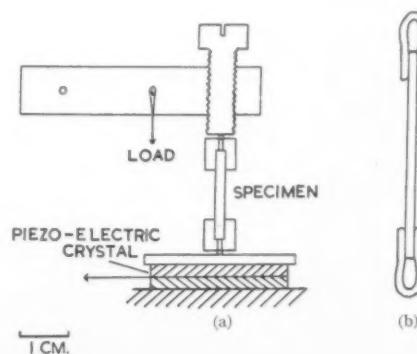
Subsequent work<sup>2</sup> has cast some doubt upon the validity of this criterion. One of the weaknesses of the experimental evidence was the limited range of crystal orientations that could be used. It was necessary that the angle between the axis of the (tensile) specimen and the basal plane of the crystal should be less than about 6 degrees; if this were not the case, then the crystal slipped on the basal plane before twinning, and it is likely that the occurrence of previous slip will affect the subsequent twinning behavior.<sup>3</sup> However, a stringent test of the hypothesis that the *shear* stress on the twinning plane is the important factor is possible, if measurements are also made in compression: for under these circumstances the normal component of stress will have changed sign. Only a limited range of crystal orientations is again possible; the angle between basal plane and compression axis must lie within the range 84°–90°, if previous slip is to be avoided.

## EXPERIMENTAL

Observations have been made on single crystals of cadmium in compression with the object of testing this hypothesis. In order to change the other conditions of measurements as little as possible, cylindrical specimens 1.8 mm in diameter were used as before. To avoid mechanical instability these had to be kept short, and

the unsupported length was never more than 17 mm. To transmit the load to the specimen, and to ensure, as far as possible, that it was applied along the axis, small brass knobs were attached at each end (see Fig. 1a). The crystal was an easy fit in the holes in the knobs and was held in place by a suitable cement, being held in a jig while the cement was hardening. Two small ball-bearings, as shown, resting in smaller holes drilled coaxial with the others, ensured axial loading. The load was applied by slowly adding water to a vessel, using the lever arrangement indicated in Fig. 1a. The lower end of the specimen rested on a piezo-electric crystal, which was used to detect the onset of twinning as before. The presence or absence of twins was, however, always confirmed by microscopic examination.

In spite of the use of cement to distribute the load over a considerable area of the specimen surface, it was frequently found that twins were first formed near the ends inside the brass knobs. This was presumably due to the increased local stress where the irregular end of the specimen rested on the brass. The occurrence of such twins was not significant to the observations, but they were, of course, indistinguishable from those formed in



\* Received November 12, 1954.

† H. H. Wills Physical Laboratory, University of Bristol.



the free gauge length, as far as the piezo-electric detector was concerned. In the results given below, attention is paid only to twins formed in the free gauge length.

### RESULTS

The procedure adopted was to increase the applied load smoothly until the piezo-electric detector indicated the formation of a twin. Loading was then stopped as quickly as possible, and the crystal removed and examined to see if the twin were visible, or at the end. If not visible, the specimen might be replaced, and the load further increased. Finally the knobs were removed by dissolving the cement, and the whole surface examined for twins.

The most striking result was that it was found possible, in some cases, to apply shear stresses considerably in excess of the expected critical value, without any detectable twinning, whereas with other specimens twins formed readily. Table I summarizes the results obtained from 113 specimens. They are grouped according to the maximum resolved shear stress on the twin plane to which they were subjected, and each group is subdivided into those which showed no twins at all; those which had no twins in the center portion, but only at the ends; and those which had twins in the center portion. A number of specimens which buckled before the test was stopped are not included in the totals. It will be observed that 48 out of the 113 specimens withstood a stress of more than 200 gm/mm<sup>2</sup> without forming twins in the gauge length—a figure in excess of the upper limit given by Thompson and Millard for tensile specimens. On the other hand, of the 30 specimens which *did* show twins, the largest single group (14) required a stress in the range 95–145 gm/mm<sup>2</sup> to produce them.

It was accordingly decided to repeat the observations in tension, using a simple apparatus in which the specimen was suspended from a stirrup resting on the piezo-electric detector. Connection to the specimen was by means of wire loops soldered to each end as shown in Fig. 1b. The results obtained from 16 specimens are shown in Table II; in this case there is no question of any stress concentration at the ends, as the wire loops, if anything, confer extra strength. It will be seen that all the specimens withstood stresses of at least 200

gm/mm<sup>2</sup> without twinning (one was taken up to 700 gm/mm<sup>2</sup>), while the stress to produce twins when they did appear ranged from 225 to 405 gm/mm<sup>2</sup>. This confirmed the results of Bell and Cahn that some crystals can withstand high shear stresses without twinning, and showed that the earlier results were not peculiar to the condition of compressive loading.

### DISCUSSION

It remains to consider why some crystals twin much more readily than others, and to reconcile these results with the earlier findings of Thompson and Millard. The possibility of off-axis loading cannot be ignored, but is unlikely to be sufficient to account for the very large range of stresses. The crystals were not all grown at the same rate, but examination of the results failed to show any correlation between growth rate and twinning behavior. In fact, with one exception to be mentioned shortly, no regularity whatever could be detected in the experimental results.

One hypothesis which seems to account for all the facts, as at present known, is that the critical stresses measured by Thompson and Millard in tension, and those observed in the 14 compression specimens which gave results in the same range, both represent the stress required to cause an existing twin nucleus to grow. This was, in fact, suggested in the earlier paper. The nucleus could possibly be produced by growth conditions<sup>4</sup> or by previous plastic deformation.<sup>2</sup> If no adequate nucleus is present, greater stresses will be required to initiate the twinning, either by one of the mechanisms proposed by Bilby and Entwisle,<sup>5</sup> or otherwise. Two points emerging from the present work lend support to this suggestion: (a) Of the five tensile specimens which did show twinning, two were known to have been accidentally bent a little before the observations began. (b) Of the compression specimens which did show twinning, one half of the total, being all those giving a critical stress in the range 95–145 gm/mm<sup>2</sup>, were to be found in the first 40 specimens tested. It is suggested that this, the only noticeable regularity, is to be explained by the greater skill and care shown in carrying out the later observations, rather than any change in the physical conditions. One deduction from this hypothesis would be that all Millard's specimens had received some plastic deformation before the test

TABLE I. Compression experiments.

Range of max shear stress on twin plan (gm/mm <sup>2</sup> )	No. of specimens	No. with no twins	No. with no twins in center	No. with twins in center
100	1	—	—	1
100–150	29	8	8	13
150–200	25	8	11	6
200–250	30	14	13	3
250–300	19	8	4	7
300–350	7	6	1	—
350–400	1	1	—	—
400	1	1	—	—

TABLE II. Tension experiments.

Range of max shear stress on twin plan (gm/mm <sup>2</sup> )	No. of specimens	No. with no twins	No. with twins in center
200–250	2	1	1
250–300	4	3	1
300–350	3	2	1
350–400	1	—	1
400–450	2	1	1
450	4	4	—

began. In view of his method of mounting specimens in his apparatus, and of the considerable care in handling which was used in the later stages of the present observations, this is considered to be not impossible. An unsatisfactory feature is the apparent existence of a wide range of twinning stresses; if the above suggestion represented the whole truth, one would expect either a low stress (nucleus present) or a very high stress (no nucleus). Some further refinement is clearly necessary.

If this general explanation is accepted, then it would be reasonable to suggest that the process observed by Thompson and Millard in tension is the same as that

concerned in the appearance of twins in compression under the lowest stresses. One could then conclude that at least the growth of a twin nucleus is mainly determined by a critical shear stress criterion, and that the normal component of stress across the twinning plane has little effect.

#### REFERENCES

1. N. Thompson and D. J. Millard, *Phil. Mag.* **43**, 421 (1952).
2. R. L. Bell and R. W. Cahn, *Acta Met.* **1**, 752 (1953).
3. W. Boas, and E. Schmidt, *Z. Physik.* **54**, 16 (1929).
4. D. S. Oliver, *Research* **5**, 45 (1952).
5. B. A. Bilby and A. R. Entwisle, *Acta Met.* **2**, 15 (1954).

## LETTERS TO THE EDITOR

### Effect of Order on the Electrical Resistivity of Ferromagnetic Alloys\*

The changes in electrical resistivity of order-disorder alloys provide one of the classic methods for studying the ordering process. In non-ferromagnetic alloys, these changes are related only to the degree of long-range order and, for a given degree of order, are temperature-independent. For an  $AB_3$  type alloy, such as  $AuCu_3$ , theory predicts a discontinuous change in order parameter, and consequently in the resistivity, at the critical temperature. This has been observed experimentally.<sup>1</sup>

The situation is more complex in ferromagnetic order-disorder alloys. Two critical temperatures appear, the Curie temperature  $\theta_f$  at which ferromagnetism vanishes and the critical temperature  $T_c$  at which long-range lattice order vanishes. Experiment shows that the resistivity is much more directly sensitive to the degree of magnetic order than to the degree of lattice order. The latter affects the resistivity chiefly through its influence on  $\theta_f$ . If the position of  $\theta_f$  changes with lattice order, a fixed temperature of measurement below  $\theta_f$  corresponds to a different magnetic reduced temperature, and large changes in resistivity occur. To the extent that short-range order is able to produce changes in  $\theta_f$  it will cause similar changes in resistivity. The behavior of the resistivity on ordering will depend on the relative positions of  $\theta_f$  and  $T_c$ , and upon the direction of

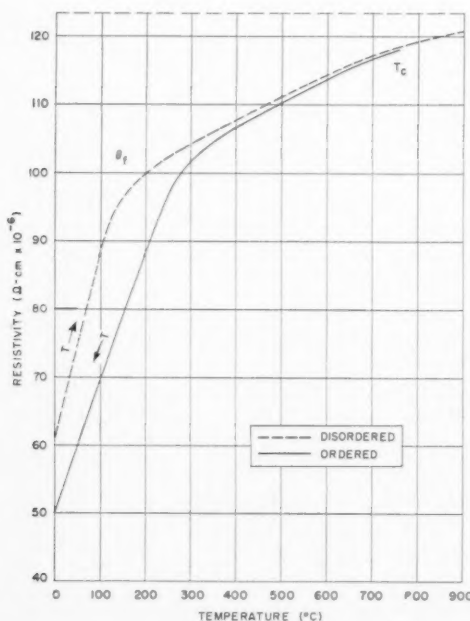


FIG. 1. Resistivity-temperature diagram for 30 atom % platinum-iron alloy  $T_c > \theta_f$ ;  $\partial\theta_f/\partial S > 0$ .

change of  $\theta_f$  with order, represented by  $\partial\theta_f/\partial S$ , where  $S$  is an order parameter. Four cases are to be distinguished:

1.  $T_c > \theta_f$ ;  $\partial\theta_f/\partial S > 0$ : The  $Fe_3Pt$  alloys are an example of this situation. Figure 1 shows the appearance of the resistivity-temperature diagram for a 30 atom % Pt alloy. No resistivity anomaly was observed in the heating and cooling curves above  $\theta_f$ , confirming the results reported by Kussmann.<sup>2</sup> Isothermal anneal studies conducted here show a very small decrease in resistivity,  $\sim 1\%$  or about  $1\mu\Omega\text{-cm}$ , as the alloy passed from the disordered to the ordered state.<sup>3</sup> Below  $\theta_f$  the resistivity is almost uniquely determined by the reduced magnetic temperature  $T/\theta_f$ .

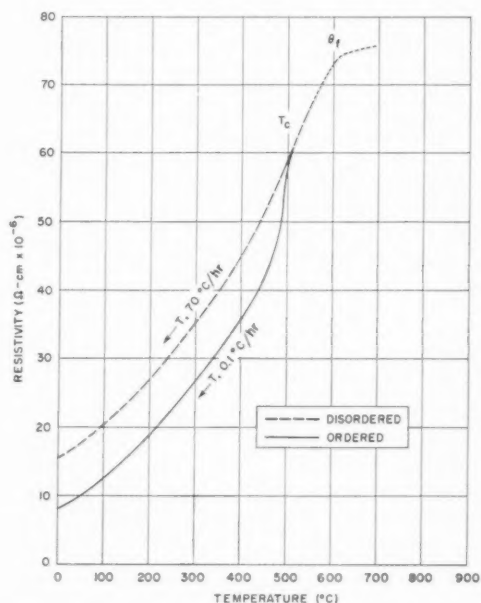


FIG. 2. Resistivity-temperature diagram for  $FeNi_3$  after Wakelin and Yates.<sup>4</sup>  $\theta_f > T_c$ ;  $\partial\theta_f/\partial S > 0$ .

2.  $\theta_f > T_c$ ;  $\partial\theta_f/\partial S > 0$ : An example of this situation is the alloy  $FeNi_3$ . Figure 2 is the resistivity-temperature diagram given by Wakelin and Yates.<sup>4</sup> Although the decrease in resistivity over a small temperature interval is large, a discontinuous change was not found at the critical temperature, contrary to theory and to experience with  $AuCu_3$ . The data points are too widely spaced to permit the conclusion that no discontinuity exists, but, from the point of view of this note, a discontinuous decrease in resistivity starting from the disordered curve is not to be expected. Since the resistivity change is primarily due to the change in  $\theta_f$ , the persistence of short-range order causes a tailing-off of the resistivity change above  $T_c$ . If any discontinuity in resistivity occurs, it will begin after appreciable resistivity changes have taken place.

3.  $T_c > \theta_f$ ;  $\partial\theta_f/\partial S < 0$ : In the FePd<sub>3</sub> alloys, order produces an increase in  $\theta_f$  in alloys containing less Fe, and a decrease in  $\theta_f$  in alloys with more Fe than the stoichiometric 1:3 ratio.<sup>5</sup> For the latter case, we expect a resistivity-temperature diagram of the form shown in Figure 3. That is, a very small decrease in resistivity above  $\theta_f$  as the alloy passes from the disordered to the ordered state, and an increase in resistivity at fixed temperature below  $\theta_f$ .

4.  $\theta_f > T_c$ ;  $\partial\theta_f/\partial S < 0$ : This case should produce a resistivity-temperature diagram of the type shown schematically in Fig. 4. If examples of this type exist, they are not known to us, but there is no *a priori* reason to rule out the possibility.

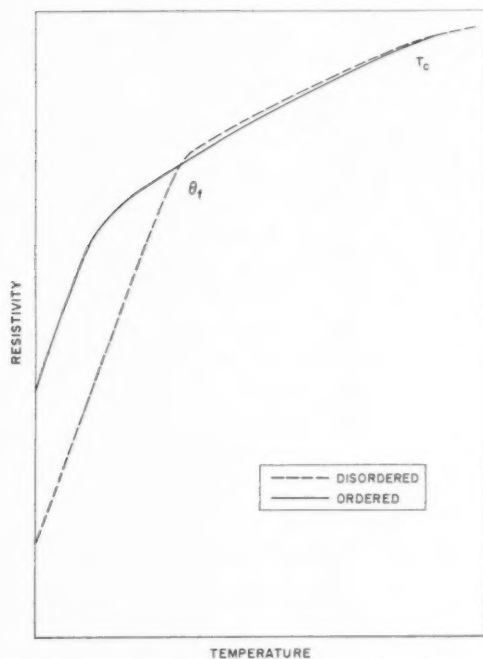


FIG. 3. Resistivity-temperature diagram (schematic) of type expected when  $T_c > \theta_f$ ;  $\partial\theta_f/\partial S < 0$ .

Departures from the ideal behavior pictured above may be expected when the occupancy of the *d*-shells changes during the ordering reaction. For the examples cited, variations in *d*-shell occupancy are apparently very small, as witness the fact that the saturation moments of the ordered and disordered alloys are almost identical when extrapolated to 0°K. There is a dearth of experimental data for alloy systems in which large differences in the ordered and disordered moments are found at 0°K. The meagre evidence available for such systems of types 1 and 3 suggest that above  $\theta_f$  the behavior is substantially as illustrated in Figs. 1 and 3.

This work was supported by the United States Air

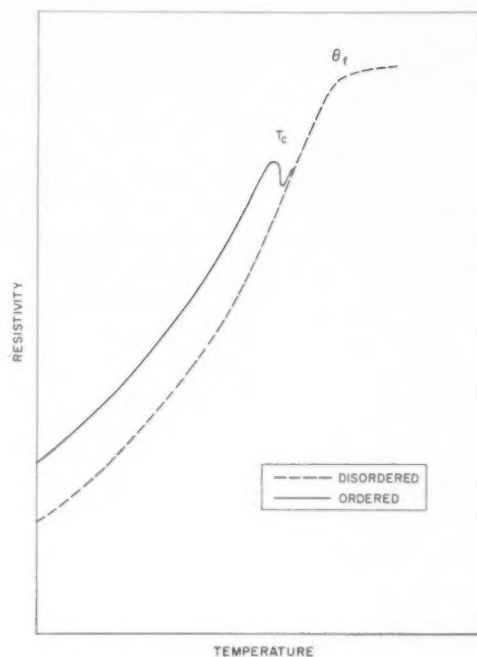


FIG. 4. Resistivity-temperature diagram (schematic) of type expected when  $\theta_f > T_c$ ;  $\partial\theta_f/\partial S < 0$ .

Force through the Office of Scientific Research of the Research and Development Command.

F. J. DONAHOE

Franklin Institute Laboratories  
Philadelphia, Pennsylvania

#### References

1. F. C. Nix and W. Shockley, *Rev. Mod. Phys.* **10** (1938).
2. A. Kussmann and G. Countess of Rittberg, *Metallkunde* **41**, 470 (1950).
3. R. P. Steijn and F. J. Donahoe, *Phys. Rev.* **94**, 1432 (1954).
4. R. J. Wakelin and E. L. Yates, *Proc. Phys. Soc.* **B60**, 221 (1953).
5. M. Fallot, *Ann. de Phys.* **10**, 291 (1938).

\* Received November 13, 1954.

#### Grain Boundaries in Alloys of High Magnetic Permeability\*

The development of high magnetic permeability in nickel-iron-copper-molybdenum alloys of the Mumetal or Permalloy-C type is achieved by annealing in pure hydrogen at temperatures above 1000°C. The functions of the anneal are believed to be (i) mechanical softening through recrystallization and grain growth, and (ii) removal of impurities such as carbon, nitrogen, and oxygen.

The idea that grain boundaries are regions of low permeability is supported by the observation that the highest permeabilities are developed in specimens annealed at the highest temperatures, i.e., those with the



largest crystals. To determine precisely, however, the dependence of magnetic behavior on grain size, specimens of different grain size, but constant purity, are needed.

An alloy containing 77 per cent nickel, 14 per cent iron, 5 per cent copper, and 4 per cent molybdenum was made by sintering a mixture of metal powders at 1350°C for five hours in pure hydrogen. The billet was cold-rolled from  $\frac{1}{4}$  in. to  $\frac{1}{8}$  in. and annealed under the same conditions. It was then reduced by cold rolling, with intermediate anneals of a few minutes at 800°C in hydrogen after every 50 per cent reduction. When the strip was 100 microns thick it was coated with alumina powder, wound into a coil, and annealed for 30 hours at 1050°C. The purpose of this anneal was to extract the greater part of the carbon, nitrogen, and oxygen remaining after the earlier heat treatments. The strip was chemically reduced to about 75 microns to remove any surface contamination resulting from contact with the alumina, and was rolled to 35 microns.

Specimens were annealed at various temperatures to produce a wide range of grain sizes, and their initial permeabilities ( $\mu$ ) and mean grain diameters ( $D$ ) were determined. The results are given in Table I.

Grain boundaries are expected to be regions of low permeability because of their irregular structure and low purity. A polycrystalline soft magnetic alloy can be regarded as consisting of crystals of mean diameter  $D$  cm, having high permeability  $\mu_1$ , separated by a film  $d$  cm thick, having low permeability  $\mu_2$ . Since there are  $1/D$  crystals per cm, we can write:

$$\frac{1}{\mu} = \frac{1}{D} \left( \frac{D}{\mu_1} + \frac{d}{\mu_2} \right)$$

$$= \frac{1}{\mu_1} + \frac{d}{D\mu_2},$$

where  $\mu$  = measured permeability.

The predicted linear relation between  $1/\mu$  and  $1/D$  is exhibited quite well by the results of Table I, as shown in Fig. 1. The intercept on the vertical axis indicates a crystal permeability of 140 000, while the slope

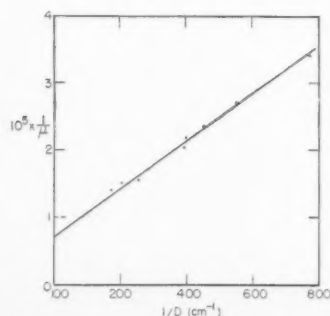


FIG. 1.

TABLE I.

Annealing conditions		$10^{-4} \times \mu$	$10^5 \times \frac{1}{\mu}$	$10^4 \times D$ (cm)	$1/D$ (cm <sup>-1</sup> )
Temperature (°C)	Time (hours)				
750	20	2.94	3.40	13.2	763
800	20	3.74	2.67	18.4	544
850	15	4.31	2.32	22.1	453
900	3	4.62	2.17	25.0	400
900	20	4.96	2.02	25.4	394
1050	3	6.45	1.55	39.2	255
1150	3	6.66	1.50	48.0	208
1300	5	7.10	1.41	58.0	172

( $3.6 \times 10^{-8}$ ) suggests a much lower permeability at grain boundaries; for, if  $d/\mu_2 = 3.6 \times 10^{-8}$ , and  $d$  is  $< 1000$  atomic spacings ( $\sim 3 \times 10^{-5}$  cm), then  $\mu_2 < 1000$ .

R. E. S. WALTERS

Post Office Engineering Department  
Research Branch  
Dollis Hill, London, England

\* Received October 25, 1954.

#### On the Lattice Parameter of Mg-Li $\beta$ Alloys\*

Studies of the variation in lattice parameter of body centered cubic magnesium-lithium alloys have been made in the magnesium-rich portion of the stable phase field<sup>1,2</sup> in the course of phase diagram studies and of a search for an order-disorder transformation in these alloys. The decrease in parameter associated with additions of lithium to the magnesium saturated composition has been rationalized in terms of a size factor effect. A study of the variation of lattice constant of these alloys over the entire range of stability (0-70 atomic per cent magnesium) has shown the previous rationale to be incorrect.

Alloys were prepared for X-ray diffraction study by melting in an inert atmosphere under a flux blanket of molten LiCl-LiF and were chill-cast. Minus 200-mesh powder was obtained by filing under an inert atmosphere and all alloys were given a stress relief anneal in the capillaries prior to the X-ray study. The melting and powdering techniques are more fully described in a forthcoming publication.<sup>3</sup> Patterns were obtained in 14 cm powder cameras and the data were extrapolated to  $\theta = 90^\circ$  using the well known extrapolation function of Nelson and Riley. The results of the study are shown in Fig. 1. In instances in which duplicate runs yielded parameters differing by much more than one part in 2000, all of the values obtained are plotted.

Consideration of Fig. 1 indicates the normal effect of adding magnesium to lithium is to decrease the lattice parameter. This trend is followed until 50 atomic per cent solute is reached, at which point the behavior

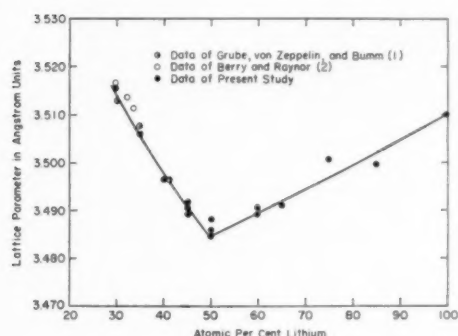


FIG. 1.

is reversed. This is a striking example of the effect of a Brillouin Zone overlap on the lattice constant of a solution since addition of divalent magnesium to monovalent lithium increases the electron-atom ratio. It may be readily shown<sup>4</sup> that the first Brillouin Zone overlap in the BCC structure occurs at  $e/a \cong 1.5$  and it is known that attending the overlap an expansion of the lattice may occur normal to the bounding planes of the first Zone. The bounding planes in the BCC structure are 110 planes and such an expansion would be thus expected to produce general expansion of the lattice. If both the lithium and the magnesium are fully ionized, the electron-atom ratio of 1.5 is reached at 50 atomic per cent magnesium and Fig. 1 shows that it is indeed at this point that the lattice begins to expand, reversing the previous trend. Some of the earlier data are included for comparison.

The author wishes to express his appreciation of the sponsorship of this research by the Metallurgy Research Laboratory, Frankford Arsenal, Philadelphia, Pennsylvania, and for permission to publish this note. The work was supported on Contract No. DA-11-022-ORD-906.

D. W. LEVINSON

Armour Research Foundation  
Illinois Institute of Technology  
Chicago, Illinois

## References

1. G. Grube, H. von Zeppelin, and H. Bumm, *Z. Elektrochem.* **40**, 160-164 (1934).
2. R. Berry and G. V. Raynor, *Nature* **171**, 1078-1079 (1953).
3. D. W. Levinson and D. J. McPherson, "Phase Relations in Mg-Li-Al Alloys." To be published.
4. G. V. Raynor, "The Electron Theory of Metals," *Inst. of Metals Monograph No. 4* (1949), p. 57.

\* Received November 18, 1954.

### An Electron Transfer Mechanism for Ultrasonic Attenuation in Metals\*

In a recent letter Bömmel<sup>1</sup> has given experimental results on ultrasonic attenuation in single crystals of superconducting and normal conducting lead crystals

at frequencies between 9 and 25 Mc/s and at temperatures between 2 and 18°K. He observed a marked decrease in attenuation on cooling through the transition temperature to the superconducting state. The decrease lends support to the plausible suggestion made earlier by Hulm<sup>2</sup> that lattice phonons are not scattered by superconducting electrons. If superconducting electrons are not scattered by phonons, it is not unreasonable that phonons should not be scattered by superconducting electrons. Hulm's suggestion was based on thermal conductivity studies and is supported strongly by recent work by K. Mendelssohn.<sup>3</sup>

It would appear reasonable to consider the change  $\Delta\alpha$  in attenuation at a given temperature between the normal and superconducting states as a measure of the phonon attenuation caused in the normal state by interaction with conduction electrons. We can fit the results of Bömmel on lead at 4.2°K by the relation

$$\Delta\alpha = 1.2 \times 10^{-16} f^2 \text{ nepers/cm}, \quad (1)$$

where  $f$  is the frequency in cycles/sec.

We now consider the possible origin of this attenuation. We have calculated a theoretical expression for attenuation by collisions with conduction electrons in which an electron absorbs or emits a phonon. The result for the energy attenuation is

$$\alpha = \frac{C^2 m^{*2} \Delta}{M \hbar^3 v^2} f, \quad (2)$$

where  $m^*$  is the effective mass of a conduction electron;  $\Delta$  is the atomic volume;  $M$  is the atomic mass;  $v$  is the velocity of sound; and  $C$  is the usual electron-lattice interaction constant (Wilson,<sup>4</sup> Eq. 9.3.8) and for many metals has values between 1 and 10 eV. Equation (2) is applicable only if the acoustic wavelength is much smaller than the mean free path of a conduction electron, a requirement not satisfied in the frequency range covered by Bömmel. In his range the residue of the phonon-electron attenuation is included in the well-

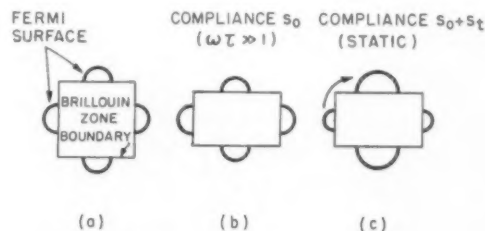


FIG. 1. Illustration of the effect of conduction electron transfer on the elastic constants of a metal. (a) Unstressed metal, showing the relation of the Fermi surface and a zone boundary. (b) Immediately after the application of an instantaneous stress, before the electrons have taken up a minimum energy arrangement in the zone. (c) Reduction of energy by electron transfer, giving an equilibrium Fermi surface appropriate to the stressed crystal.

known viscosity attenuation

$$\alpha_{vis} = \frac{16\pi^2}{3} \frac{\eta}{\rho v_0^3} f^2, \quad (3)$$

where  $\eta$  is the viscosity of the electron gas. The application of this mechanism to metals has been considered recently by W. P. Mason;<sup>5</sup> it had apparently been first treated by A. Akhieser.<sup>6</sup> The viscosity mechanism accounts quite well for the principal features of the attenuation observed in lead, but, as we show below, it is not unique in this respect.

We suggest that a part of the attenuation may be provided by an electron transfer mechanism. When polyvalent metals are deformed elastically, electrons in states near the Fermi surface are redistributed to a certain extent in  $k$ -space because of the deformation of the Brillouin zones, as shown in Fig. 1. Leigh<sup>7</sup> has calculated that electron transfer processes of this character in aluminum should make a really major contribution to the shear constants. Mott<sup>8</sup> has suggested that such processes may be important in all polyvalent metals except the transition metals. The transfer process may occur to a lesser extent in monovalent metals; formally, the only prerequisite is that the form of Fermi surface should depend on the state of strain of the lattice.

We now give a phenomenological discussion of the effect of electron transfer on ultrasonic attenuation. We suppose that the effective elastic compliance constant  $s$  may be written as

$$s = s_0 + \frac{s_t}{1 + i\omega\tau}, \quad (5)$$

where  $s_0$  is the elastic compliance which would obtain if the electrons in the metal did not change their position in the Brillouin zone during deformation;  $s_t$  represents the compliance which results from electron transfer. The transfer process is limited by a relaxation time  $\tau$  which is likely to be of the order of magnitude of the relaxation time describing electrical conductivity. Different compliance constants  $s_{ij}$  will have different transfer contributions, but we consider only a simple example. We discuss a one-dimensional model, for which the wave equation is

$$s\rho \frac{\partial^2 u}{\partial t^2} = \frac{\partial^2 u}{\partial x^2}, \quad (6)$$

where  $u$  is the displacement of a volume element and  $\rho$  is the density. Substituting  $u = e^{i(\omega t - kx)}$ , we have  $k^2 = \omega^2 \rho s$ . If we write  $k = k_1 - ik_2$ , the energy attenuation constant  $\alpha$  is equal to  $2k_2$ . For  $\omega\tau \ll 1$ , we have

$$k_1^2 \cong \omega^2 \rho (s_0 + s_t) = \omega^2 / v_0^2, \quad (7)$$

where  $v_0$  is the sound velocity in the low frequency limit. Further,

$$\alpha = 2k_2 \cong \frac{\omega^2 \tau v_0 s_t \rho}{1 + (\omega\tau)^2}. \quad (8)$$

If  $\omega\tau \ll 1$ ,

$$\alpha \cong f^2 (2\pi)^2 \tau v_0 \left( \frac{1}{v_0^2} - \frac{1}{v_\infty^2} \right), \quad (9)$$

where  $v_\infty = (\rho s_0)^{-1/2}$  is the velocity in the high frequency limit  $\omega\tau \gg 1$ . For lead we estimate

$$\alpha \approx f^2 (\tau \times 10^{-4}) \text{ nepers/cm.} \quad (10)$$

We take  $\tau \approx 10^{-12}$  sec at 4°K, which is of the correct order of magnitude to account for the electrical conductivity. We have then

$$\alpha \approx 1 \times 10^{-16} f^2 \text{ nepers/cm.} \quad (11)$$

This is in reasonable concord with the experimental value for longitudinal waves,  $\alpha = 1.2 \times 10^{-16} f^2$  nepers/cm. Our estimate is based on the assumption that the electron transfer process is reasonably important in lead; we assumed specifically that for longitudinal waves the effective compliances  $s_0$  and  $s_t$  are equal, giving  $v_0 = 2 \times 10^5$  cm/sec and  $v_\infty = 2.8 \times 10^5$  cm/s.

We note that the attenuation associated with the transfer mechanism will have roughly the same temperature dependence as the electrical conductivity, as the conductivity is also proportional to  $\tau$ . The increase in  $\Delta\alpha$  at low temperatures as observed by Bömmel can be accounted for satisfactorily by the increase in the electrical conductivity. This feature is common to both the viscous and the transfer mechanisms. Also common to the two mechanisms is the prediction of different attenuations for shear and for longitudinal waves, although it is possible that detailed studies of mode dependence can separate out the contributions of the two mechanisms. The separation cannot necessarily be decided from the order of magnitude of the attenuation, as both processes unfortunately give closely the same order of magnitude in polyvalent metals. It is not unlikely that the viscous mechanism may be more important than the transfer mechanism in monovalent metals.

The present work suggests that in the superconducting state groups of electrons participate in the transfer process without interaction with lattice phonons, provision for energy conservation presumably being made by an internal energy of the group. The transfer process must go on even in the superconducting state if the elastic constants are to be essentially continuous through the transition.

I have profited from discussions with R. Karplus and H. W. Lewis and from correspondence with K. Mendelssohn; G. Dresselhaus has kindly checked the calculation leading to Eq. (2).

C. KITTEL

Department of Physics  
University of California  
Berkeley, California

VOL.  
3  
1955

## References

1. H. E. Bömmel, *Phys. Rev.* **96**, 220 (1954).
2. J. K. Hulm, *Proc. Roy. Soc. A* **204**, 98 (1950); further references are given in the review paper by J. L. Olsen and H. M. Rosenberg, *Phil. Mag. Suppl.* **2**, 28 (1953).
3. K. Mendelssohn and C. A. Renton, *Phil. Mag.* **44**, 776 (1953); K. Mendelssohn, *Physica* **19**, 775 (1953).
4. A. H. Wilson, *Theory of Metals*, Cambridge University Press, 2nd ed., 1953.
5. W. P. Mason, unpublished.
6. A. Akhieser, *J. Phys. U.S.S.R.* **1**, 289 (1939).
7. R. S. Leigh, *Phil. Mag.* **42**, 139 (1951).
8. N. F. Mott, *Progress in Metal Physics* **3**, 76 (1952).

\* Received November 24, 1954.

\* This research was supported in part by the U. S. Office of Naval Research and the U. S. Signal Corps.

### Diffusion von radioaktiven Kupfer in technischem Stahl\*

Im Zusammenhang mit technischen Fragestellungen (Versprödung von Kupfer-Eisen-Schweisstellen) erhob sich die Frage nach den Diffusionsverhältnissen im System Kupfer/Eisen. Hierzu führten wir folgende Versuche durch:

Zylindrische Stahlplatten (mit 0,63% Mn; 0,16% Cu; 0,13% C; weniger als 0,1% Si, Ni, Cr, S, P.) von 10 mm  $\phi$  und 3 mm Dicke wurden auf ihrer polierten Stirnseite auf folgende Art mit einer dünnen, nur Bruchteile von Milligramm wiegenden Schicht radioaktiven Kupfers versehen:

Ein Wattebausch wurde mit einer verdünnten Lösung radioaktiven Kupfersulfates getränkt, und damit die zu aktivierende Fläche eingerieben, worauf durch elektrochemischen Austausch die Ausfällung einer gleichmässigen und fest haftenden Schicht eintrat. Die Menge der von der Stirnseite der Proben ausgesandten  $\beta$ -Strahlung wurde in üblicher Weise durch Messung mit einem Geiger-Müller-Zählrohr-Verstärker bestimmt, und die Proben wurden in einer Wasserstoff-Atmosphäre in den Ofen zur Erhitzung auf die Diffusionstemperatur eingeführt. Nach entsprechenden Zeitabschnitten wurden die Aktivitätsmessungen wiederholt und die Minerung der Aktivität durch Diffusion und Absorption im festen Stoff festgestellt. Der zeitliche Verlauf folgte in guter Näherung dem theoretischen Verlauf, der durch den Ausdruck:

$$A = A_0 \exp(\mu^2 D t) [1 - \psi(\mu D^{1/2} t^{1/2})];$$

$\mu$  = Absorptionskoeffizient

wiedergegeben wird. Die auf diese Art ermittelten Diffusionskonstanten sind in Fig. 1. in logarithmischer Darstellung als Funktion der reziproken absoluten Temperatur wiedergegeben. Es resultiert eine Gerade, die dem Ausdruck:  $D = 3 \exp(-61\,000/RT)$   $\text{cm}^2 \text{sec}^{-1}$  entspricht.

Bei tiefen Temperaturen (nicht in der Figur wiedergegeben) wurde die Kontaktmethode<sup>1</sup> verwendet. Die so erhaltenen Werte liegen auf der Verlängerung der

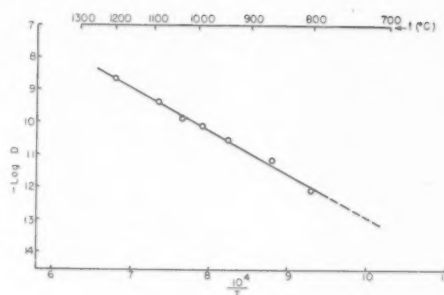


Fig. 1.

Geraden in Fig. 1 und bestätigen die Temperaturfunktion.

R. LINDNER†  
F. KARNIK‡

Göteborg, Schweden  
Södertälje, Schweden

## Reference

1. R. Lindner, *J. chem. Soc. (London)* 395 (1949).

\* Received November 27, 1955.

† Chalmers Techniske Hochschule.

‡ A. B. Svenska Maskinverken.

### Double-Valued Internal Friction Behavior\*

In the study of amplitude-dependent internal friction of single crystals, two types of double valued behavior of the internal friction *versus* strain amplitude have been reported. The first which shall be called type I was reported by Read<sup>1</sup> in zinc single crystals. This type of behavior is characterized by a single-valued internal friction *versus* strain amplitude curve as the driving voltage to the composite oscillator is increased and a large hysteresis loop as the driving voltage is decreased. The second type of double-valued behavior was reported by Frankl<sup>2</sup> in sodium chloride single crystals and shall be called type II. The type II double-valued behavior is a result of a rapid increase in damping as the driving voltage to the composite oscillator is increased. This rapid increase in decrement causes the amplitude to decrease even though the driving voltage is increased, thereby giving the curve its double-valued nature. Upon decreasing the driving voltage the initial curve was repeated; i.e., there was only a slight hysteresis loop.

The present work is an extension of the study of this double-valued behavior. The materials used were sodium chloride, silver, and aluminum single crystals. The measurements were made by the composite piezoelectric oscillator method.

Figure 1 is an example of the double-valued internal friction *versus* strain amplitude behavior in sodium chloride. The crystal had been vacuum annealed at 750°C and slowly cooled at the rate of 50°C/hr to room



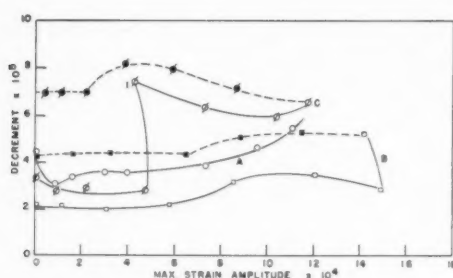


Fig. 1. Effect of heat treatment on internal friction in sodium chloride crystals A: 750°C anneal, cooled at 50°C per hour. B: 500°C anneal, cooled at 300°C per hour. C: 19 hours at 25°C.

temperature. It was then heated to 500°C and cooled at 300°C/hr to room temperature. As shown in curve B, the crystal then exhibited a double-valued behavior and a large hysteresis loop. Curve C shows the behavior of the crystal after it had annealed at room temperature. At point 1 on curve C, the driving voltage was shut off for about 30 seconds before the next driving voltage was applied. This short anneal altered the nature of the curve markedly in that the type II behavior was removed. In every case of double-valued behavior found in NaCl, the crystal exhibited a large hysteresis loop as the driving voltage was decreased. This hysteresis was not observed in the crystal initially and was not observed in Frankl's work. This type of behavior combines the features of type I and II behavior in that it exhibits a large hysteresis loop and a double valued behavior as the driving voltage is increased. In Frankl's data the maximum strain amplitude was of the order of  $3 \times 10^{-6}$  while these experiments employed strain amplitude of the order of  $14 \times 10^{-4}$ . This may account for the differences in the observations.

Figure 2 indicates the nature of the double-valued behavior in a silver single crystal. Curve B indicates the double-valued behavior obtained after a static torsional deformation of  $4 \times 10^{-4}$  in./in. maximum torsional shear strain. On annealing at room temperature, the double-valued behavior was removed as shown in curve C. On further static torsional deformation of  $16 \times 10^{-4}$  in./in. maximum torsional shear strain, and annealing for 70 minutes at room temperature, the double-valued behavior was recovered as indicated in curve D. The strain amplitude at which the crystal exhibited the rapid change in decrement increased with the amount of deformation. The behavior in the silver single crystal is characteristic of type II behavior. No hysteresis loop was observed on decreasing the driving voltage.

Figure 3 indicates the double-valued behavior in an aluminum single crystal which is typical of type II behavior. The room temperature curve indicated a large increase of the decrement with strain amplitude. On cooling to  $-196^\circ\text{C}$  in vacuum, the crystal exhibited a double-valued behavior of the decrement with strain amplitude. The double-valued behavior was also found

at  $-186^\circ\text{C}$ ,  $-167^\circ\text{C}$ ,  $-147^\circ\text{C}$ . At all these temperatures, no hysteresis loop was observed. On testing at  $-125^\circ\text{C}$ , the specimen no longer exhibited a double-valued behavior. The strain amplitudes at which the large increase in decrement occurred decreased as the temperature of testing was increased. On retesting at  $-196^\circ\text{C}$  the double-valued behavior was not obtained, although the amplitude dependence of the decrement was very large.

It is of interest to consider the behavior of an edge dislocation under the conditions of the internal friction measurement. The dislocation may be considered as pinned by dislocation intersections and points at which the dislocation line leaves the slip plane, and surrounded by a Maxwellian atmosphere of solute atoms. The concentration of solute atoms about the dislocation varies as  $C = C_0 e^{U/RT}$ , where  $C_0$  is the average solute concentration and  $U$  is the interaction energy of the solute atom and the dislocation. At temperatures above  $T_0 = U_{\text{max}}/K \ln(1/C_0)$  the atmosphere has a Maxwellian distribution.<sup>3</sup> Under the oscillating stress of the internal friction measurement, a stress

$$\sigma_c = 112CN\mu\epsilon r_s^3$$

is required to free the dislocation from the influence of its dilute atmosphere.<sup>3</sup> ( $N$  is the number of atoms per unit volume,  $b$  is the Burgers vector,  $\epsilon$  is the strain due to the solute atoms,  $r_s$  is the radius of the matrix atom.) Even if the dislocation is freed from the influence of its dilute atmosphere, it is still pinned by dislocation intersections, and by those points at which the dislocation leaves the slip plane. Its extent of motion is limited by these pinning points.

The type II behavior where no hysteresis was observed may be due to the pinning of the dislocation by intersections, while the large increase in damping may be due to the freeing of the dislocation from its dilute

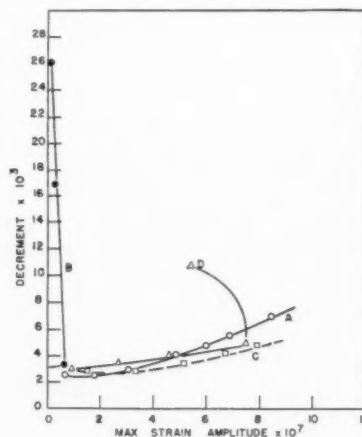


Fig. 2. Variation of internal friction with deformation of Ag single crystal. A: As grown. B:  $4 \times 10^{-4}$  in./in. torsional strain. C: 12 hours at 25°C. D:  $16 \times 10^{-4}$  in./in. torsional strain. 70 minutes at 25°C.

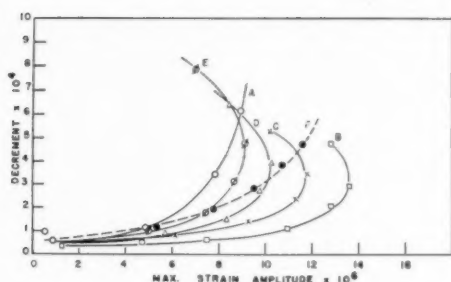


FIG. 3. Variation of internal friction with temperature in Al single crystal. A: 28°C. B: -196°C. C: -180°C. D: -167°C. E: -147°C. F: -125°C.

solute atmosphere. Since the dislocation remains geometrically fixed in the crystal, the repinning time for the solute atmosphere is quite short. The large hysteresis loop of the type I behavior may be expected when the dislocation is freed from its pinning points and is displaced geometrically in the crystal. In order to reform the solute atmosphere about the dislocation in this case, diffusion will have to occur over greater distances so the repinning time will be longer. Therefore, during the period of the internal friction measurement the specimen should exhibit a hysteresis behavior.

For the aluminum used in these experiments  $T_0$  is of the order of 0°K so the solute atmosphere may be considered dilute at all the temperatures considered. For this material,  $A$  is  $10^{-23}$  dyne cm<sup>2</sup> and  $C_0$  is  $8.65 \times 10^{-4}$ . The stress at which the double-valued behavior occurred was  $3.9 \times 10^6$  dynes/cm<sup>2</sup> at -196°C and  $2.5 \times 10^6$  dynes/cm<sup>2</sup> at -147°C. The calculated stress for freeing the dislocation from its atmosphere is of the order of  $4 \times 10^5$  dynes/cm<sup>2</sup>.

For the sodium chloride crystals used in these experiments,  $A$  is  $6.2 \times 10^{-21}$  dynes cm<sup>2</sup> and  $C_0$  is  $10^{-2}$ .  $T_0$  is calculated to be -100°C. The solute atom interaction energy with the dislocation is greater for the sodium chloride than for the aluminum crystals. The stress at which the double-valued behavior was observed was of the order of  $4 \times 10^8$  dynes/cm<sup>2</sup>. The calculated stress required to free the dislocation from its dilute atmosphere is of the order of  $14 \times 10^8$  dynes/cm<sup>2</sup>. The large hysteresis found in the sodium chloride may be explained on the basis of the much larger stress amplitudes used for this crystal.

The probability of observing the double-valued behavior appears to be greater in those specimens where loosely pinned dislocations have been produced by heat treatment or cold work, or in those materials in which the dislocation pinning is weak. If the dislocation density is increased by plastic deformation the dislocations may become more strongly pinned by dislocation intersections and the stress to produce the double-valued behavior increases as shown in Fig. 2. The hysteresis behavior of crystals may also be suppressed by increasing the dislocation pinning by cold work and annealing.

This work was supported by the Office of Ordnance Research. The author wishes to express his appreciation to Professor T. A. Read and M. Levy for their helpful discussions.

H. K. BIRNBAUM

Department of Mining and Metallurgy  
University of Illinois  
Urbana, Illinois

#### References

1. T. A. Read, Phys. Rev. **58**, 371 (1940).
2. D. R. Frankl, Phys. Rev. **92**, 573-579 (1953).
3. A. H. Cottrell, *Dislocation and Plastic Flow in Crystals* (Oxford Press, 1953).

\* Received December 6, 1955.

#### The Origin of Screw Dislocations— Role of Colloidal Particles

When proposing the screw dislocation mechanism of crystal growth, Frank<sup>1</sup> made a number of suggestions to account for the genesis of screw dislocations in growing crystals. None of these furnished a satisfactory genetic mechanism. Recently Fisher, Fullman, and Sears<sup>2</sup> have postulated a satisfactory mechanism for the origin of screw dislocations in growing crystals. Newkirk<sup>3</sup> has presented experimental data on the growth of CdI<sub>2</sub> platelets from solution, which data strongly support the proposed genetic mechanism.

Very thin platelets of CdI<sub>2</sub> grow at constant thickness to a width of perhaps 1 mm. In this size range, screw dislocations can be observed to commence operation as growth mechanisms for platelet thickening. In the language of dislocation theory a component of the Burgers vector is normal to the large faces. The dislocations form in the interior of the large faces as well as at their periphery.

It has been proposed that the dislocations originate when the originally perfect platelet impinges upon and grows around a second crystal. The latter crystal is sometimes a platelet of CdI<sub>2</sub>, slightly tilted with respect to the first crystal. This accounts for the origin of screw dislocations at the platelet periphery. Most of the screw dislocations originating in CdI<sub>2</sub> platelets, however, form in the interior of the large faces. To account for interior dislocations it was necessary to postulate the impingement of platelets with microscopically invisible colloidal particles and the subsequent platelet growth around these particles.

The postulated role of colloidal particles was supported by several facts. Aqueous solutions are notorious for the ubiquity of colloidal particles. The appearance rate of screw dislocations was in agreement with a reasonable concentration of colloidal particles in solution. Newkirk<sup>3</sup> occasionally observed a colloidal particle trapped between overlapping platelets.

A critical experiment for the validity of the postu-

lated role of colloidal particles in the genesis of interior screw dislocations is apparent. If perfect platelets are grown in the absence of colloidal particles, then screw dislocations with a Burgers vector normal to the large face should only form peripherally by impingement of two platelets, never in the interior of a face.

Such an experiment has already been reported. Kowarski<sup>4</sup> in 1933 described the growth of perfect platelets of paratoluidine from the vapor. Translated into current terminology Kowarski reported that very thin platelets of para-toluidine grew at constant thickness on the surface of condensation from the vapor. The interference color of a given platelet was constant over long periods of time. Occasionally screw dislocations were generated on the extended faces and thickening occurred. He observed that the screw dislocations were always generated at the periphery of the platelets, and only at the point of intersection when neighboring platelets came into contact with one another during growth.

He stated that the neighboring platelets were tilted slightly with respect to one another, which agrees exactly with observations of Newkirk on  $\text{CdI}_2$ <sup>3</sup> and the theoretical postulate.<sup>1</sup> Since the growth occurred from the vapor phase, there can be no argument as to the absence of colloidal particles.

The objection may be raised that there is some fundamental difference between growth from solution and from vapor. The accumulated evidence at this Laboratory appears to definitely eliminate the possibility. However, work is in progress to observe the growth of  $\text{CdI}_2$  platelets from a solution free of colloidal particles.

G. W. SEARS

General Electric Research Laboratory  
Schenectady, New York

#### References

1. F. C. Frank, *Disc. Far. Soc.* **5**, 48 (1949).
2. J. C. Fisher, R. L. Fullman, and G. W. Sears, *Acta Met.* **2**, 344 (1954).
3. J. B. Newkirk, to be published.
4. L. Kowarski, *J. Chem. Phys.* **32**, 303 (1935).

\* Received December 9, 1954.

#### Self-Diffusion of Lead in Oriented Grain-Boundaries\*

It is now generally accepted that there are three paths for diffusion in polycrystalline metals, namely, through the lattice (lattice diffusion), along grain-boundaries (grain-boundary diffusion) and over the surface (surface diffusion). Diffusion experiments are of interest as they can give information about the properties of metals and because of the fact that diffusion plays a prominent role in many processes which can take place in metals (e.g., precipitation).

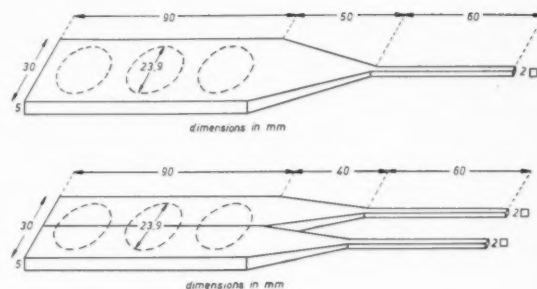


FIG. 1.

In order to avoid mathematical and experimental difficulties in investigating the complete diffusion behavior of a metal, it is advisable to study if possible, the different diffusion phenomena separately. Though it is easy to eliminate the complications due to surface diffusion, experiments on grain-boundary diffusion are practically always interfered with by lattice diffusion. This might give difficulties in analysing the experimental results obtained. For the case, however, that grain-boundary diffusion is relatively important and provided that the number of atoms diffused along the boundaries is much larger than the number of atoms diffused through the lattice, Fisher<sup>1</sup> has worked out a method which enables the analysis of the penetration curves, deviating from those obtained by homogeneous diffusion.

With the aid of this method Hoffman and Turnbull<sup>2</sup> and Slifkin, Lazarus and Tomizuka<sup>3</sup> calculated the grain-boundary diffusion constant for silver. For zinc this was done by Wajda<sup>4</sup> and for lead by Okkerse.<sup>5</sup> Smoluchowski *et al*<sup>6-9</sup> have shown by means of an etching method that the penetration of silver and zinc in copper is a function of the orientation difference between neighboring grains. Similar observations, but explained in a different way, were made by Turnbull and Hoffman.<sup>10</sup> One of the corollaries of the dislocation model is that the diffusion coefficient may be expected to be different in different directions, relative to the position of the dislocation lines in the grain-boundary. As a matter of fact such an anisotropy of the grain-boundary diffusion was demonstrated by Couling and Smoluchowski<sup>11</sup> by means of autoradiographs.

Because of the fact that in our laboratory grain-boundary and lattice diffusion in lead were investigated with the aid of the sectioning technique and as it turned out to be possible to distinguish between these two phenomena, it seemed worth while to try to determine the influence of the structure of the boundary on the self-diffusion of lead in oriented grain-boundaries. In what follows a description of the technique applied and of the results obtained will be given.

In order to have the disposal of grain boundaries with a well-defined structure, lead bicrystals were prepared after the method of Tiedema and Kooy.<sup>12</sup> The dimensions of these bicrystals were: length 90 mm, width 30

mm and thickness 6 mm. From the so-obtained bicrystalline "bars" cylinders with a diameter of 23 mm and a thickness of 5 mm were prepared by carefully sawing and machining (see Fig. 1). The specimens were only slightly deformed as appeared from Laue back-reflection diagrams. After an anneal at 310°C in vacuum for 10 days, the deformed layer disappeared in most cases as was proved by Laue back-reflection photographs. This means a complete recovery of the deformed bicrystals.

The method by which the penetration curves were obtained was the same as that used for single crystalline and polycrystalline specimens by Okkerse.<sup>5</sup> The specimens were activated in the normal way with thorium B. Then they were annealed in vacuum at a temperature of 220°C for about 70 hours. After this diffusion-anneal, sections with a thickness of approximately 10  $\mu$  were turned off on a lathe. The radioactivity of each section was determined by means of a bell-shaped Geiger counter. In each case, 25 sections were examined. After the appropriate corrections, the penetration curve could be obtained from the weight and the activity of each section.

The bicrystals were grown with orientations as given in Fig. 2. Figure 2a represents the orientations of bi-

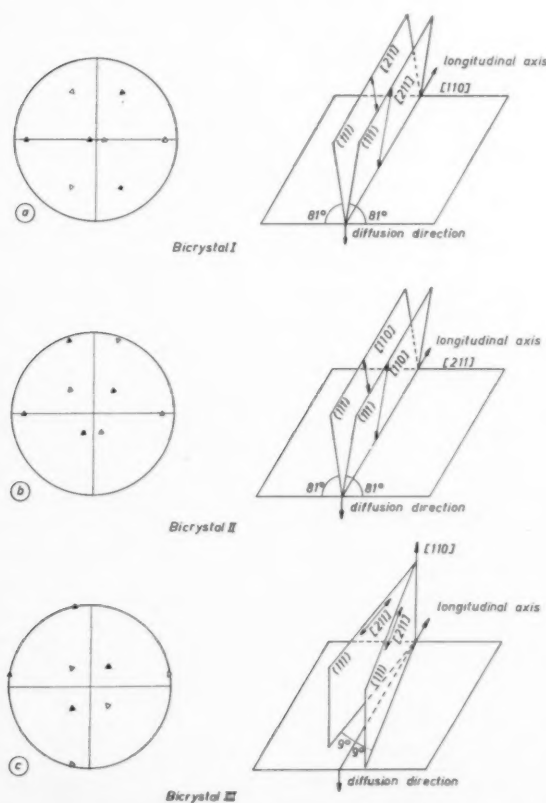


FIG. 2.

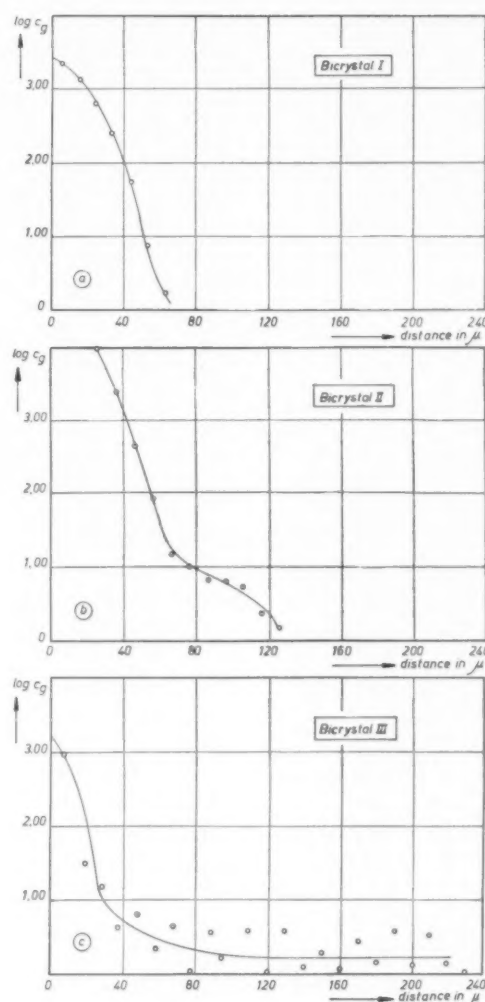


FIG. 3.

crystal I. As can be seen from the drawings, both crystals have a common  $[110]$ -direction which coincides with the longitudinal direction of the specimen, whereas each crystal has a  $(111)$ -plane which makes an angle of 81 degrees with the surface of the specimen.

In bicrystal II (Fig. 2b) both crystals have a common  $[211]$ -direction coinciding with the longitudinal direction of the specimen. Again a  $(111)$ -plane of each crystal makes an angle of 81 degrees with the surface.

Finally in bicrystal III (Fig. 2c) the two crystals have a  $(111)$ -plane perpendicular to the surface of the specimen making angles of 9 degrees with the longitudinal direction. They have a common  $[110]$ -direction perpendicular to the surface.

From bicrystal I, two specimens were examined whereas from the bicrystals II and III three specimens were analysed. The penetration curves of different



specimens from the same bicrystal were very similar. Typical curves for each bicrystal are shown in Fig. 3.

From the results obtained it seems to us that the following conclusions can be drawn:

a. In bicrystal I no detectable grain-boundary diffusion occurs. If the penetration curve is analysed in the normal way a lattice diffusion constant of  $5.20 \times 10^{-12}$  cm<sup>2</sup>/sec can be calculated. This value is 17 percent higher than the value calculated from the equation  $D = 1.17 \exp(-25700/RT)$  cm<sup>2</sup>/sec as given by Okkerse.<sup>5</sup> This deviation is within the accuracy of the experiments. In the case of bicrystal I the dislocation lines are expected to be perpendicular to the diffusion direction.

b. The deviating penetration curves obtained for the bicrystals II and III can neither be analysed in the normal way, nor by the method of Fisher.<sup>1</sup> As far as we can see this must be ascribed to the fact that the conditions required for the availability of Fisher's method are not satisfied. Still, there is a marked difference between the curves II and III. The penetration is much larger in the last case. Now in bicrystal III the dislocation lines are expected to be parallel to the diffusion direction. For bicrystal II it is not so easy to say what the position of the dislocation lines is with respect to the diffusion direction. It is, however, clear that diffusion in the boundary is much faster than for bicrystal I but slower than for bicrystal III.

c. From these experiments it follows that the diffusion in grain-boundaries is influenced strongly by the position of the dislocation lines with respect to the diffusion direction. For the case that the lines are parallel to the diffusion direction (bicrystal III) diffusion goes much faster than for the case that these lines are perpendicular to the diffusion direction.

B. OKKERSE  
T. J. TIEDEMA  
W. G. BURGERS

Laboratory for Physical Chemistry,  
Technical University,  
Delft, Netherlands

#### References

1. J. C. Fisher, *J. Appl. Phys.* **22**, 74 (1951).
2. R. E. Hoffman and D. Turnbull, *J. Appl. Phys.* **22**, 634, 984 (1951).
3. L. Slifkin, D. Lazarus, and T. Tomizuka, *J. Appl. Phys.* **23**, 1032 (1952).
4. E. S. Wajda, *Acta Met.* **2**, 184 (1954).
5. B. Okkerse, *Acta Met.* **2**, 551 (1954).
6. R. Smoluchowski *et al*, *Phys. Rev.* **76**, 470 (1949).
7. R. Smoluchowski *et al*, *Phys. Rev.* **83**, 163 (1951).
8. R. Smoluchowski *et al*, *J. Appl. Phys.* **22**, 1260 (1951).
9. R. Smoluchowski *et al*, *J. Appl. Phys.* **23**, 785 (1952).
10. D. Turnbull and R. E. Hoffman, *Acta Met.* **2**, 419 (1954).
11. L. Couling and R. Smoluchowski, *Phys. Rev.* **91**, 246 (1953).
12. T. J. Tiedema and C. L. Kooy, *Ned. T. Nat.* **2**, 419 (1954).

\* Received December 27, 1954.

#### Formation of the Intermetallic Compound PtZn at Room Temperature\*

After zinc was electrodeposited on platinum, early chemists concerned with electroanalysis of brasses and similar alloys observed that when the electrodeposit was removed in acid, a black residue remained firmly attached to the platinum. This deposit was unattacked by nitric or hydrochloric acids, and was stated to be platinum black.<sup>1,2,3</sup> A similar residue was not observed when copper was electrodeposited instead, accounting for the recommendation that a layer of copper on platinum precede electrodeposition of zinc.

With zinc, the residual film, although strongly resembling platinum black, was not analyzed by those who stated its composition, the identification being based solely on appearance and lack of attack by acids. If the compound is platinum black, as claimed, the mechanics of its formation at such low temperatures (25–60°C) and within short times (one to several hours) is of some interest and, hence, appeared to deserve further investigation.

A commercial zinc plating bath was prepared based on zinc sulfate<sup>4</sup> employing a current density of 1.5 amp/sq cm. Platinum cathodes were cleaned in nitric acid, washed in water, and then heated to a bright red temperature in an oxygen-gas flame. Immediately after cleaning, the platinum was plated with zinc for a period of 15 minutes at room temperature. This provided a deposit approximately  $7 \times 10^{-4}$  cm thick. The zinc-plated platinum was then either aged at room temperature for a definite period of time, or heated somewhat above room temperature under specified conditions. Following this period, the zinc was removed by dissolution in 15 vol.% nitric acid at room temperature. In all cases, a black or gray residue remained on the platinum, insoluble in hot concentrated nitric or hot concentrated hydrochloric acids. The residual film, however, was attacked by aqua regia.

It was apparent visually that the longer the time of aging, or the higher the temperature of heating, the darker was the film. But even when the film was stripped immediately after plating, evidence of a superficial residue was faintly apparent. This meant that aging at room temperature for 15 minutes sufficed to produce

TABLE I. Effect of aging on weight gain of Zn-plated Pt cathodes after immersion in HNO<sub>3</sub>.

Aging temperature	Aging time	Weight gain per cathode (30 cm <sup>2</sup> )
Room	0 (15 min)*	0.0 mg
Room	24 hrs	1.0
56°C	1 hr	0.2
80°C	1 hr	1.3
100°C	1 hr	2.8

\* Time in plating bath.

VOL.  
3  
1955

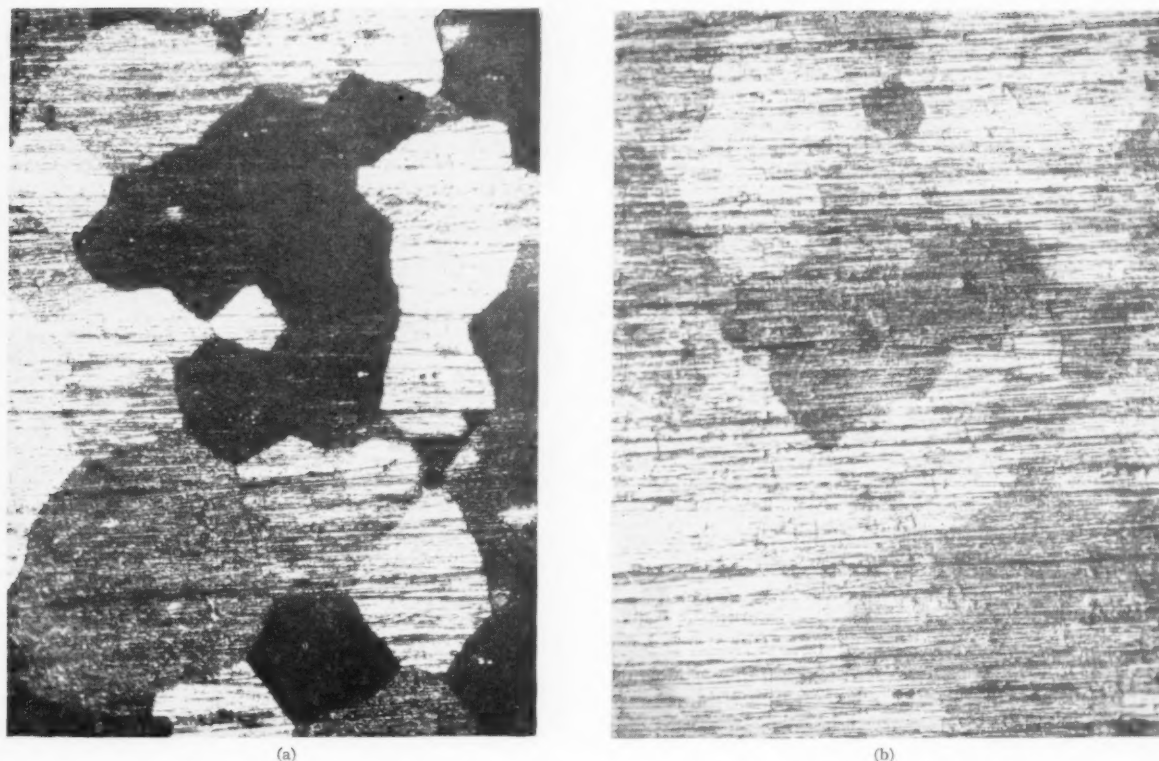


FIG. 1. Residual film after immersion of Zn-plated Pt in 15 vol. %  $\text{HNO}_3$ . Plating time, 15 minutes, room temperature. (a) Aged 1 hour,  $80^\circ\text{C}$ ; (b) aged 15 minutes, room temperature.

some amount of the film substance. The residue was darker on some grains of the base metal than on others, suggesting that rate of formation of the film substance depended on preferred crystal orientation (Fig. 1).

Further examination furnished evidence that the residue was not platinum black. By weighing platinum cathodes before and after stripping the zinc coating, it was noted that the platinum gained weight, and that the weight gain was greater the longer the aging period. Data are given in Table I.

Final identification was obtained by electron diffraction studies of the film *in situ*, and was supplemented by scraping off some of the residue and subjecting it to X-ray diffraction. The patterns were established as that of the intermetallic compound, PtZn, in accord with previous identification by Nowotny *et al.*<sup>5</sup> Weak lines of  $\text{Pt}_5\text{Zn}_2$  and Pt were also evident, but the major reaction product was PtZn.

From values of weight gain and a calculated density for PtZn of 15.4, the average thickness of film after an aging period of 1 hour at  $100^\circ\text{C}$  is about 600 Å. On some grains, the value of thickness would be considerably larger than this average. Growth of a film so thick at so low a temperature and within so short a time presents an interesting problem in diffusion, the answer

to which is not immediately obvious. Making use of the approximate relation<sup>6,7</sup>  $S^2 = 2Dt$ , where  $S$  is the thickness of PtZn (600 Å),  $D$  is the diffusion constant and  $t$  is the time (1 hr), the calculated diffusion constant at  $100^\circ\text{C}$  is equal to  $5.0 \times 10^{-15} \text{ cm}^2 \text{ sec}^{-1}$ . This value can be compared with the diffusion of zinc into copper, the activation energy for which (24–29% Zn–Cu) is given as 35 000 cal/mole and  $A$  of the Arrhenius equation is equal to 0.096.<sup>8</sup> The corresponding value of the diffusion constant at  $100^\circ\text{C}$  is calculated to be  $4 \times 10^{-22} \text{ cm}^2 \text{ sec}^{-1}$ , i.e., many orders of magnitude smaller than the value corresponding to formation of PtZn.

The high value of  $D$  for the Pt–Zn system can hardly be accounted for by rise of surface temperature through heat of reaction, in view of the good conductivity of both metals. One possibility is a very high diffusion rate of Zn or Pt through the intermetallic compound. This can be weighed against the stability of the compound exposed to hot concentrated acids and the corresponding reluctance of reactive zinc atoms to leave the lattice. An alternative explanation is the surface diffusion of zinc through pores of the compound PtZn, followed by reaction of zinc with platinum at the interface of the two metals to form more compound. Rate of surface

diffusion is typically more rapid than rate of lattice diffusion. Since surface reaction rates of this kind are logically related to the particular crystal face of platinum exposed, this mechanism would also explain the variations of film thickness over the platinum surface.

H. H. UHLIG  
J. S. MACNAIRN  
D. A. VAUGHN†

Department of Metallurgy  
Massachusetts Institute of Technology  
Cambridge, Massachusetts

#### References

1. G. Vortmann, Ber. der Deutsch. Chem. Ges. **24**, 2754 (1891).
2. E. Rüdorff, Z. Angewandte Chemie **7**, 197 (1892).
3. E. F. Smith, *Electrochemical Analysis*, 6th ed. (Blakiston Press, Philadelphia, 1918).
4. W. Blum and G. Hogaboom, *Electroplating and Electroforming* (McGraw-Hill, New York, 1949), p. 310.
5. H. Nowotny, E. Bauer, A. Stempf, and H. Bittner, Monatshefte für Chemie **83**, 221 (1952).
6. W. Jost, *Diffusion* (Academic Press, N. Y., 1952), p. 25.
7. O. Kubaschewski and B. Hopkins, *Oxidation of Metals and Alloys* (Academic Press, N. Y., 1953), p. 20.
8. O. Kubaschewski, Trans. Faraday Soc. **46**, 713 (1950).

\* Received June 29, 1954.

† Battelle Memorial Institute, Columbus, Ohio.

## SOME CURRENT PAPERS IN OTHER JOURNALS

### Acta Crystallographica, Vol. 8

Part 2, February, 1955 (Partial Contents).

- The crystal structure of  $\text{Co}_2\text{Si}$ . S. Geller.  
The geometry of lattice planes. I. M. A. Jawsom and D. B. Dove.  
Calculation of geometrical structure factors for space groups of low symmetry. I. E. W. Radoslovich and (in part) Helen D. Megaw.  
Vibrational modifications of the electron distribution in molecular crystals. II. Mean square amplitudes of thermal motion. P. W. Higgs.  
Integrated X-ray intensity measurements from a solid solution of copper-gold. R. A. Coyle and B. Gale.  
The concentration of the solution round a growing crystal. S. P. F. Humphreys-Owen.  
Al-Th intermetallic compounds. I. P. B. Braun and J. H. N. van Vucht.  
Neutron-diffraction study of  $\text{Al}_2\text{Th}$ . A. F. Andresen and J. A. Goedkoop.  
The crystal structure of copper hydride. J. A. Goedkoop and A. F. Andresen.  
 $\beta$ -Uranium. J. Thewlis and H. Steeple.  
On the unit cell of  $\text{YCrO}_3$ . L. Katz.

Part 3, March, 1955 (Partial Contents).

- The crystal structure of chalcophanite,  $\text{ZnMn}_3\text{O}_7 \cdot 3\text{H}_2\text{O}$ . A. D. Wadsley.  
The structure of  $\text{FeAl}_3$ . II. P. J. Black.  
On the treatment of unobserved reflexions in the least-squares adjustment of crystal structures. W. C. Hamilton.

### Archiv für das Eisenhüttenwesen

Heft 1, Januar, 1955 (Partial Contents).

- Der Heisswind-Kupolofen im Stahlwerk. T. Kootz und H. Rellermeyer.  
Einfluss der Inhomogenität auf die Strahlung leuchtender Flammen. W. Pepperhoff und G. Grass.  
Die thermodynamische Analyse von Zwei- und Mehrstoffs-systemen. W. Oelsen, E. Schürmann und G. Heynert.  
Messung der elektromotorischen Kräfte bei  $1500^\circ$  und Röntgenuntersuchungen im System Eisenoxyd-Aluminiumoxyd. W. A. Fischer und A. Hoffmann.  
Zur Frage der Eigenspannungen in statisch beanspruchten Stäben. H. Bühler.  
Wachstumsgesetz gekoppelter Ausscheidungen. O. Krisement.  
Das Zeitgesetz des Ausscheidens neuer Phasen in Mischkristallen. B. Ilschner.

Heft 2, Februar, 1955 (Partial Contents).

- Messung der elektromotorischen Kräfte bei  $1500^\circ$  und Röntgenuntersuchungen im System Magnesiumoxyd-Aluminiumoxyd. W. Fischer und A. Hoffmann.  
Der gegenwärtige Stand der Forschung über die Alterung weicher Stähle. W. Wepner.  
Orientierungszusammenhänge zwischen Austenit, Zwischenstufengefüge und Martensit. W. Hofmann und G. Schuhmacher.  
Über die Kristallisation des Ledeburit-Eutektikums. E. Scheil und D. Pohl.  
Gerichtete Ausscheidungen von Sekundärgraphit in Grauguss. W. Hofmann und J. M. Sistiaga.  
Gefügeuntersuchungen an Stahl mit einem Klein-Elektronenmikroskop. E. Kinder.  
Die Aktivierungspotentiale von Eisen-Chrom-Legierungen und ihre Beziehungen zu der chemischen Beständigkeit in Schwefelsäure. H. J. Rocha und G. Lennartz.

### Journal of the Chemical Society

February, 1955 (Partial Contents).

- The enrichment of crude erbium and holmium. J. K. Marsh.  
Quantitative analysis of mixtures of sodium, potassium, magnesium, and calcium by paper chromatography. D. R. Tristram and C. S. G. Phillips.

March, 1955 (Partial Contents).

- The chemistry of silica surfaces. P. F. Holt and D. T. King.

### Journal of the Institute of Metals, Vol. 83

Part 6, February, 1955.

- Assessment of quality of wrought products. W. G. Shilling.  
The control of quality in heat-treatment and final operations in the production of rolled, extruded, and drawn aluminium and aluminium alloys. A. J. Field and J. Salter.  
Heat-treatment and finishing operations in the production of copper and aluminium rod and wire. H. J. Miller.  
The control of quality in the heat-treatment and finishing of copper and copper-base alloys. V. B. Hysel and T. W. Collier.  
The production of light-alloy drop-forgings, their heat-treatment, inspection, and testing. W. T. Edmunds and R. C. Lloyd.  
The heat-treatment, inspection, and testing of wrought nickel and nickel alloys. W. Betteridge and T. C. Cound.  
Pseudo-binary phase sections between laves phases in ternary alloys of uranium. G. B. Brooks, G. I. Williams, and (Mrs.) E. M. Smith.  
The constitution of uranium-zirconium alloys. D. Summers-Smith.  
The choice and construction of monolithic linings for twin-bath induction furnaces for melting aluminium alloys. E. J. Thackwell.  
The use of refractories in low-frequency induction furnaces for melting copper alloys. M. Cook, C. L. M. Cowley, and E. R. Bradford.

Part 7, March, 1955.

- Attempts to improve aluminium reduction since Héroult and Hall. A. von Zeerleder.  
Porosity and permeability changes during the sintering of copper powder. G. Arthur.  
Aluminium-copper-cadmium sheet alloys. H. K. Hardy.  
A hot impact tensile test and its relation to hot-working properties. E. A. Leech, P. Gregory, and R. Eborall.  
Lattice spacings of the aluminium-rich solid solution containing magnesium and silicon. R. B. Hill and H. J. Axon.  
Some observations on isothermal transformations of eutectoid aluminium bronzes below their  $M_s$  temperatures. R. Haynes.  
The metallographic detection of deformation in copper and alpha-brasses. L. E. Samuels.

### Journal of Metals, Vol. 7

February, 1955, Part 1 (Partial Contents).

- Hydrogen affects critical properties in commercial titanium. H. D. Kessler, R. G. Sherman and J. F. Sullivan.  
General physical metallurgy of titanium reviewed. R. I. Jaffee.  
Oxygen solubility and oxide phases in the Fe-Cr-O system. D. C. Hilty, W. D. Forgeng, and R. L. Folkman.

February, 1955, Section 2.

- Embrittlement of molybdenum by neutron radiation. C. A. Bruch, W. E. McHugh, and R. W. Hockenbury.  
Solid solubility of calcium in magnesium. E. C. Burke.  
A study of the room temperature fatigue properties of molybdenum. W. L. Bruckart and W. S. Hyler.  
Allotropic transformation at high temperatures—a discussion. A. G. Metcalfe (Reply by J. O. McCaldin, P. Duwez).  
Molybdenum deposition on titanium. S. Tour, A. Styka, and G. Fischer.  
Continuous multistage separation by zone-melting. W. G. Pfann.  
An evaluation of dissociated ammonia and hydrogen atmospheres for sintering stainless steel. H. S. Kalish and E. N. Mazza.  
Relation of strength, composition, and grain size of sintered WC-Co alloys. J. Gurland and P. Bardzil.  
Microstructures of pyrophoric alloys. R. D. Reiswig and D. J. Mack.  
A study of the microstructure of titanium carbide. H. Blumenthal and R. Silverman.  
High temperature vacuum etching on pure titanium. W. D. Bennett.  
Influence of heat treatment on the ductile-brittle transition temperature of semikilled steel plate. R. H. Frazier, F. W. Boulger, and C. H. Lorig.  
Isoembrittlement in chromium and molybdenum alloy steels during tempering. G. Bhat and J. F. Libsch.  
Oxidation of cobalt metal. R. E. Carter, F. D. Richardson (with an addendum by C. Wagner).



- Ductility of vacuum heat-treated molybdenum wires. W. E. Few and G. K. Manning.
- Vanadium-zirconium alloy system. J. T. Williams.
- Gallium-antimony system. I. G. Greenfield and R. L. Smith.
- Effect of boron on the relative interfacial tension of gamma-iron. A. M. Adair, J. W. Spretnak, and R. Speiser.
- Magnesium-rich corner of the magnesium-lithium-aluminum system. J. A. Rowland, Jr., C. E. Armantrout, and D. F. Walsh.
- Magnetic properties of manganese-germanium alloys. R. J. Quigg, G. P. Conard, and J. F. Libsch.
- Structure and magnetic properties of some transition metal nitrides. G. W. Wiener and J. A. Berger.
- Preliminary investigation of the system Ti-Mg. J. W. Fredrickson.
- Recrystallization characteristics of superpurity base Al-Mg alloys containing 0 to 5 pct Mg. E. C. W. Perryman.
- Some aspects of the crystallization and recrystallization of vapor-deposited vitreous selenium. N. E. Brown and F. L. VerSnyder.
- On the relationship of texture changes of cold-rolled face-centered-cubic metals during recrystallization. Y. C. Liu and W. R. Hibbard, Jr.
- Effect of zinc content on the rolling texture and annealing texture of alpha-brass. A. Merlini and P. A. Beck.
- Crystal structure and some properties of the compound  $Zr_3Al$ . J. H. Keeler and J. H. Mallory.
- Preferred orientations in beta-annealed zirconium. J. H. Keeler and A. H. Geisler.
- Cold-rolled textures of silicon-iron crystals. P. K. Koh and C. G. Dunn.
- Cellular structure in high purity zinc. R. P. Steijn.
- Formation of cold-worked regions in fatigued metal. R. Webeler.
- Crystal structure of neodymium metal. F. H. Ellinger.
- Temper brittleness of some Fe-Ni-Cr alloys. L. D. Jaffe.
- Decomposition of beta titanium. F. R. Brotzen, E. L. Harmon, Jr., and A. R. Troiano.
- Sigma-phase in the molybdenum-ruthenium system. D. S. Bloom.
- A calorimetric investigation of the energy relations in alloys of composition  $Cu_3Au$ . L. R. Rubin, J. S. Ll. Leach, and M. B. Bever.
- Metallographic techniques for Cu-Au alloys. R. Bakish and W. D. Robertson.
- March, 1955 (Partial Contents).
- Chemistry of the ammonia pressure process for leaching Ni, Cu, and Co from Sherritt Gordon sulphide concentrates. F. A. Forward and V. N. Mackiw.
- Acid pressure leaching of uranium ores preparation and arc melting of high purity iron. G. W. Rengstorff and H. B. Goodwin.
- Fuming of zinc from lead blast furnace slag. A thermodynamic study. R. C. Bell, G. H. Turner, and E. Peters.
- Solubility of oxygen in liquid nickel and Fe-Ni alloys. H. A. Wriedt and J. Chipman.
- Electrical conduction in molten Cu-Fe sulphide mattes. G. M. Pound, G. Derge, and G. Osuch.
- Activities in the iron oxide-silica-lime system. J. F. Elliott.
- Elastic and plastic strains and watt losses in grain-oriented 3 pct Si iron. P. W. Neurath and R. E. Waite.

# ISOTHERMAL DECOMPOSITION KINETICS OF TRANSFORMED-BETA PHASE IN A TITANIUM-NICKEL ALLOY\*

D. H. POLONIS† and J. GORDON PARR‡

The decomposition kinetics of the transformed- $\beta$  phase during isothermal heat-treatment has been studied by measuring the rate of precipitation of  $Ti_2Ni$ . The reaction follows the type of equation suggested by Johnson and Mehl, and an activation energy of 84,000 cal/mole has been determined. On the basis of the values of the coefficient "n" it is suggested that  $Ti_2Ni$  precipitates as plates at temperatures up to 525°C. Above this temperature there appears to be a tendency for the formation of spheroidal precipitates. A model for the reaction is proposed in which the rate controlling process is the self-diffusion of titanium.

## CINÉTIQUE DE LA DÉCOMPOSITION ISOTHERME DE LA PHASE- $\beta$ DANS UN ALLIAGE TI-NI

La cinétique de la décomposition de la phase- $\beta$  pendant un traitement isotherme est étudiée en mesurant la vitesse de précipitation de  $Ti_2Ni$ . La réaction suit l'équation de Johnson et Mehl et une énergie d'activation de 84.000 cal/mol a été déterminée. De la valeur de l'exposant "n," il semble que  $Ti_2Ni$  précipite en plaquettes jusqu'à 525°; au-dessus de cette température, il y aurait tendance à une précipitation en sphères. Il est suggéré que la réaction est contrôlée par l'autodiffusion du titane.

## DIE KINETIK DER ISOTHERMEN ENTMISCHUNG DER UMGEWANDELTEN BETA-PHASE EINER TITAN-NICKEL-LEGIERUNG

Die Kinetik der Entmischung der umgewandelten  $\beta$ -Phase bei einer isothermen Wärmebehandlung wurde durch Messung der Ausscheidungs menge von  $Ti_2Ni$  untersucht. Die Reaktion verläuft nach dem Gyp der Gleichung von Johnson und Mehl. Die Aktivierungsenergie wurde zu 84.000 cal/mol bestimmt. Auf Grund des Koeffizienten "n" wird vermutet, dass sich  $Ti_2Ni$  bei Temperaturen bis 525°C plattenförmig ausscheidet. Oberhalb dieser Temperatur eine Neigung zur Bildung von sphärolitischen Ausscheidungen zu bestehen. Es wird ein Modell für die Reaktion vorgeschlagen, bei dem der massgebende Vorgang für den Reaktionsablauf die Selbstdiffusion des Titans ist.

## INTRODUCTION

The tempering kinetics of some important ferrous alloys have been explored in detail<sup>1-6</sup> by applying theories of diffusion and precipitation developed by Johnson and Mehl<sup>6</sup> and Zener.<sup>7</sup> The work has included decomposition studies of retained and martensitically transformed austenite as well as graphitization in cast-irons. Most of the research has been concerned with interstitial alloying elements in materials of complex commercial composition.

The present work is an analysis of the tempering kinetics of transformed- $\beta$  solid solution (hexagonal close-packed) in a 7.2 weight per cent (6 per cent atomic) nickel alloy of titanium. It was possible to produce 100 per cent transformed- $\beta$  (called  $\alpha'$ ) in titanium-nickel alloy powders (-200 mesh) containing up to 7.2 per cent nickel<sup>8</sup> by quenching them from 1,000°C with a blast of purified argon gas. Specimens containing more nickel showed some retained  $\beta$  after quenching. Metallographic examination of completely transformed specimens revealed pronounced strain patterns (Fig. 1) which are typical of martensitic structures observed in

other titanium alloys.<sup>9,10,11</sup> The absence of any other phase was confirmed by X-ray diffraction studies. The 7.2 per cent nickel alloy was selected for the present study since, on tempering to produce equilibrium structures, phase-ratios could be assessed more accurately than with lower compositions. In addition, this alloy corresponds approximately to eutectoid composition. (See phase diagram, Fig. 2.)

The phase diagram shows that the approach towards equilibrium during tempering yields the phase  $Ti_2Ni$ .

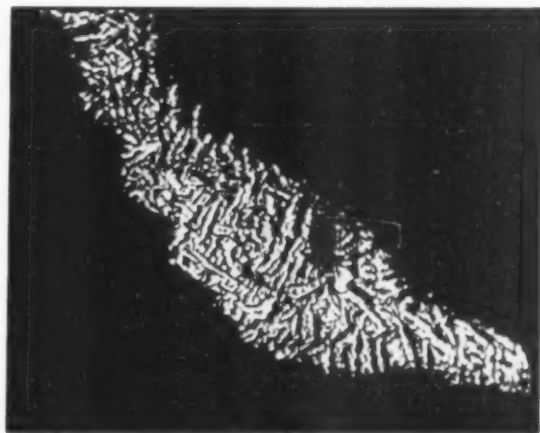


FIG. 1. Magnification 2000X. Etchant 5 per cent HF in glycerin, followed by nitric acid rinse. 7.2 per cent Ni alloy. Powder quenched in argon gas from 1000°C

\* Received December 13, 1954.

† School of Mineral Engineering, University of Washington, Seattle, Washington. Formerly, Department of Mining and Metallurgy, The University of British Columbia, Vancouver, Canada.

‡ Department of Mining and Metallurgy, University of Alberta, Edmonton, Canada. Formerly, Department of Mining and Metallurgy, The University of British Columbia, Vancouver Canada.

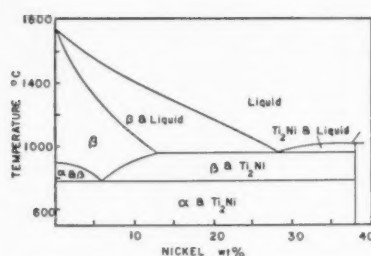


FIG. 2. Phase diagram of the titanium-nickel system after Margolin *et al.*<sup>13</sup>

During the formation of  $Ti_2Ni$  the  $\alpha'$  phase is depleted of nickel until its composition conforms to that of equilibrium  $\alpha$  at the tempering temperature. It probably contains less than 0.1 per cent nickel at 500°C.

#### EXPERIMENTAL METHOD

The titanium alloy was prepared from iodide titanium and Johnson Matthey spectrographic standard nickel by levitation-melting.<sup>12</sup> The method by which filled powders were quenched has been described elsewhere,<sup>9</sup> and the usual precautions against contamination were observed. Sufficient quenched powder of the 7.2 per cent nickel alloy was prepared for the subsequent isothermal heat-treatments which were made upon samples sealed in evacuated fine bore silica tubing. Temperature control during tempering was  $\pm 3^\circ C$ . Where heat-treatments were of less than 15 minutes' duration, a thermocouple was attached to the specimen-tube and time was measured from the instant the thermocouple reached temperature. In all cases temperature was attained in 15 to 20 seconds.

The extent of the tempering reaction after heat-treatment was determined by computing from X-ray data the amount of  $Ti_2Ni$  formed. In order to assess this quantitatively the ratio of the line intensities  $Ti_2Ni_{511}^{333}:\alpha_{101}$  was first obtained on Geiger-spectrometer plots for each of several Ti-Ni alloys ranging from 0 to 10 per cent nickel which had been heat-treated to produce equilibrium structures. The percentage  $Ti_2Ni$  for each alloy was determined from the phase diagram

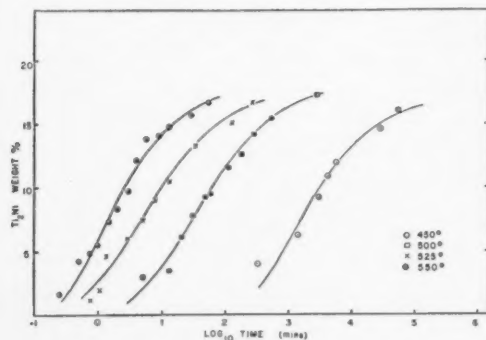


FIG. 3. Graph showing percentage by weight of  $Ti_2Ni$  formed versus  $log_{10}$  time.

and plotted against the corresponding ratio of intensities  $Ti_2Ni_{511}^{333}:\alpha_{101}$ . Hence, relative line intensities obtained after heat-treating the quenched alloy could be translated into phase ratios. It should be noted that both the 101  $\alpha$  line and 101  $\alpha'$  line are coincident about  $\theta = 20^\circ$ . Consequently, it is necessary to assume that  $\alpha$  and  $\alpha'$  phases have equal structure factors. This introduces a small error since  $\alpha'$  contains 6 atomic per cent nickel in the alloy used, and its structure factor differs from that of equilibrium  $\alpha$ , which is practically pure titanium. However, calculations based on the assumption of random nickel distribution in  $\alpha'$  reveal the error to be less than 2 per cent—a figure that is no greater than the inherent errors involved in the technique.

#### EXPERIMENTAL RESULTS

The tempering reaction in the alloy was followed at temperatures of 450°C, 500°C, 525°C and 550°C. The weight percentages of  $Ti_2Ni$  formed during the reaction are plotted as a function of  $log_{10}$  time in Fig. 3. The curves possess the familiar 'S'-shape (although the early

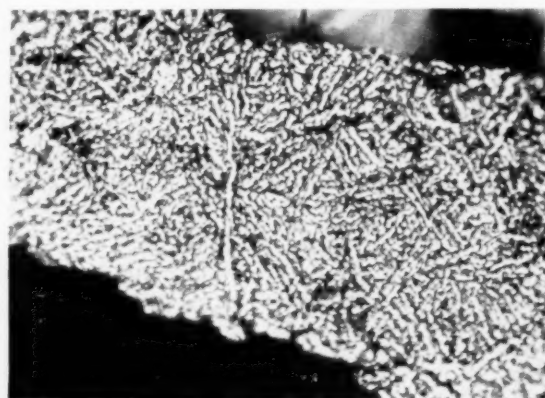


FIG. 4. Magnification 2000X. Etchant 5 per cent HF in glycerin, followed by nitric acid rinse. 7.2 per cent Ni alloy. Powder quenched and transformed 90 per cent at 500°C.

stages of the reaction could not be measured) and may be reasonably superimposed by translation along the  $log_{10}$  time axis. Once the reaction is initiated the amount of  $Ti_2Ni$  formed is approximately proportional to  $log_{10}$  time up to the concluding stages of the reaction (i.e., when more than 14 per cent  $Ti_2Ni$  has precipitated) at which juncture the rate decreases quite appreciably. Complete transformation would be at 18.9 per cent  $Ti_2Ni$ .

Tempered specimens were examined metallographically in order to detect any changes due to diffusion and precipitation. The original strained structure appeared to be transformed to a Widmanstätten precipitation type. Figure 4 shows a typical microstructure for 90 per cent transformation at 500°C. The structure is fine and acicular. Since  $Ti_2Ni$  is not resolvable at a magnification of 2,000 times, it is presumably very finely dispersed. At 550°C the structure is a little coarser

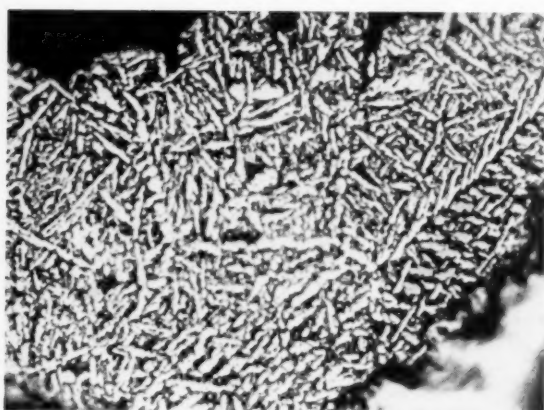


FIG. 5. Magnification 2000 $\times$ . Etchant 5 per cent HF in glycerin, followed by nitric acid rinse. 7.2 per cent Ni alloy. Powder quenched and transformed 90 per cent at 550°C.

(Fig. 5), but no definite precipitation of  $Ti_2Ni$  can be seen. Microscopic examination of a specimen heated at 750°C for 15 minutes revealed a spheroidal precipitate of  $Ti_2Ni$  in a matrix of  $\alpha$  (see Fig. 6).

#### DISCUSSION OF RESULTS

The general shape of the curves in Fig. 3 suggests a type of nucleation and growth process that was quantitatively analysed by Johnson and Mehl.<sup>6</sup> They proposed an equation of the following form for a rate of nucleation  $N$  and a rate of growth  $G$ :

$$f(t) = 1 - \exp\left(-\frac{\pi}{3} \cdot N \cdot G^3 \cdot t^4\right), \quad (1)$$

where  $f(t)$  represents the fraction transformed in time  $t$ .

A more general form of Eq. (1) is

$$f(t) = 1 - \exp(-kt^n), \quad (2)$$

which yields

$$\frac{df(t)}{dt} = kn t^{n-1} \cdot e^{-kt^n} = kn t^{n-1} (1-f). \quad (3)$$

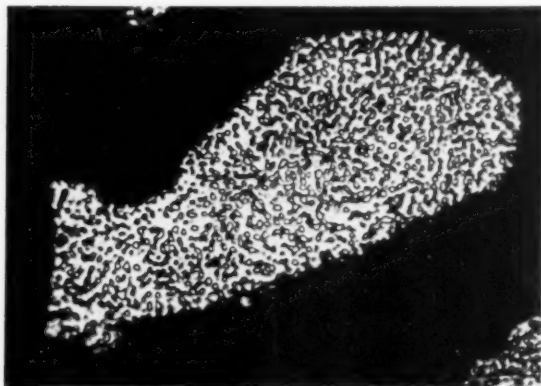


FIG. 6. Magnification 2000 $\times$ . Etchant 5 per cent HF in glycerin, followed by nitric acid rinse. 7.2 per cent Ni alloy. Powder quenched and transformed 100 per cent at 750°C.

The coefficients  $k$  and  $n$  are constants for a particular process. If logarithms are taken in Eq. (2),

$$\log_e(1-f(t)) = -kt^n \quad (4)$$

and

$$\log_{10} \log_{10} \frac{1}{1-f(t)} = \log_{10} \frac{k}{2.3} + n \log_{10} t. \quad (5)$$

Cohen *et al.*<sup>1</sup> have proposed the following equation which serves to define the specific rate constant  $K$  and is merely another form of Eq. (2):

$$\frac{df(t)}{dt} = K(1-f)t^m, \quad (6)$$

where  $m = n - 1$ .

Comparison of Eqs. (3) and (6) shows

$$nk = K. \quad (7)$$

Substituting Eq. (7) in (5),

$$\log_{10} \log_{10} \frac{1}{1-f(t)} = \log_{10} \frac{K}{2.3n} + n \log_{10} t. \quad (8)$$

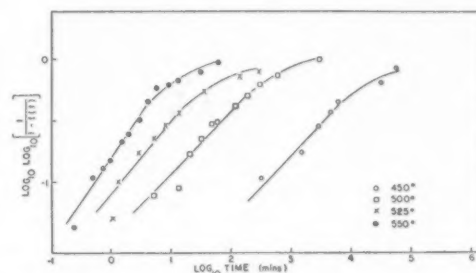


FIG. 7. Graph of  $\log_{10} \log_{10}[1/(1-f)]$  versus  $\log_{10}$  time.

From (8) it can be seen that if the tempering reaction is to obey the relationship, then a plot of  $\log_{10} \log_{10}[1/(1-f(t))]$  versus  $\log_{10} t$  will yield a straight line. The experimental values for the current investigation are plotted in Fig. 7 and produce reasonably straight lines up to the late stages of the reaction. The curves deviate from linearity at approximately the same ordinate values, suggesting the possibility of some structural feature that inhibits the growth process.

Reference to Eq. (8) shows that the slopes of the curves in Fig. 7 are equivalent to the values of  $n$  for each temperature. The values are listed in Table I,

TABLE I.

Temperature °C	$n$	$\log_{10}(K/2.3n)$
450	0.53	-2.40
500	0.51	-1.45
525	0.52	-1.02
550	0.7	-0.8



where it is seen that, except for the value of 0.7 at 550°C,  $n$  is fairly constant about 0.52.

The values of  $\log_{10}(K/2.3n)$  for each temperature have been obtained from the log time=0 intercepts of Fig. 7, and are listed in Table I. From basic rate theory, it is known that:

$$K_t = Ae^{-Q_t/RT}, \quad (9)$$

where  $K_t$  is the specific rate constant in units  $\text{time}^{-1}$ ,  $Q_t$  is the activation energy, and  $A$  is a frequency factor if the reaction is first order. If  $\log K_t$  is plotted against the reciprocal of the absolute temperature then a linear relation should exist and the slope will equal  $Q_t/2.3R$ . (This is the standard Arrhenius method of obtaining activation energy.)

From Eq. (7) the rate constant for a precipitation reaction as defined by Eqs. (6) and (8) is

$$k = \frac{K}{n}$$

Consequently, the values of  $\log_{10}(K/2.3n)$  have been plotted against  $1/T$  as shown in Fig. 8. An excellent linear

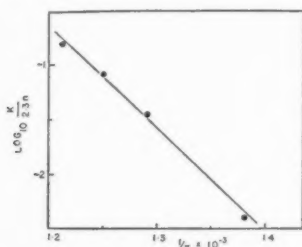


FIG. 8. Graph of  $\log_{10}(K/2.3n)$  versus  $1/T$ .

relationship yields an activation energy  $Q_k = 43,500$  cal/mole. From Eq. (8) it can be seen that the rate constant  $K$  is expressed in the units  $\text{time}^{-n}$ , but the corresponding activation energy  $Q_k$  must be evaluated in terms of  $K$  in units  $\text{time}^{-1}$  before any comparisons may be drawn with other rate processes. The conversion can be made automatically by plotting  $(1/n) \log_{10}(K/2.3n)$  versus  $1/T$ , or more simply by using the relationship  $Q_t = Q_k/n$  where  $Q_t$  is the energy of activation for the controlling process. In this investigation,  $Q_t = 43,500/n = 84,000$  cal/mole, where  $n$  is 0.5.

Alternatively, the activation energy  $Q_t$  for the tempering process may be obtained (5) from the slope of a graph of log time against  $1/T$  for a specific fraction of decomposition (e.g., 50 per cent) as shown in Fig. 9. This method gives the same value for  $Q_t$  as the above calculation.

#### DIFFUSION MODEL

The following experimental results and conclusions have been considered in proposing a model for the tempering of transformed- $\beta$  in the 7.2 per cent nickel alloy:

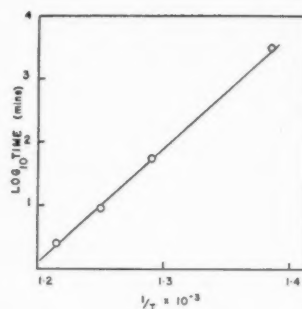


FIG. 9. Graph of  $\log_{10}$  time versus  $1/T$  for 50 per cent transformation.

1. The reaction is a growth process which can be adequately described by the equation:

$$f(t) = 1 - \exp(-k \cdot t^n),$$

where  $n = 0.5$  at 450°C, 500°C and 525°C = 0.7 at 550°C.

2. In the tempering treatments carried out at 450°C to 550°C the phase  $\text{Ti}_2\text{Ni}$  is not microscopically resolvable; however, at 750°C the precipitate appears clearly spheroidal. It is concluded that at the lower heat-treating temperatures, growth of many more dispersed nuclei occurs than at higher temperatures.

3. At the three lower tempering temperatures the coefficient  $n$  is approximately 0.5, which suggests that growth occurs by advancement of planar interfaces of  $\text{Ti}_2\text{Ni}$ . Cohen has indicated a similar process in his treatment of first stage tempering in steels.<sup>2</sup>

4. The later stages of the reaction do not comply with Eq. (2). This is perhaps due to the impingement of adjacent  $\text{Ti}_2\text{Ni}$  precipitates.

5. Diffusion in this system is by substitution. Growth of a  $\text{Ti}_2\text{Ni}$  precipitate requires that Ni atoms be transported through the  $\alpha'$  lattice to the interface. There is a great difference in nickel concentration between  $\alpha$  and  $\text{Ti}_2\text{Ni}$  at the interface and consequently it is to be expected that the rate of movement of interface will be slow. In addition, a countercurrent diffusion of Ti atoms away from the interface, in the same direction as the  $\text{Ti}_2\text{Ni}$  growth, must occur in order to create vacancies for Ni atoms to form  $\text{Ti}_2\text{Ni}$ .

6. The activation energy for the controlling diffusion process has been determined as 84,000 cal/mole.

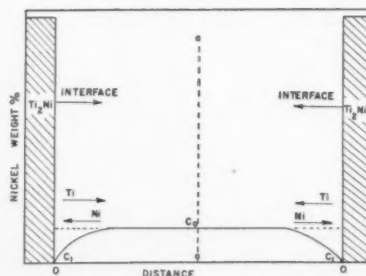


FIG. 10. Proposed model for growth process.

On the basis of these observations, it is proposed that at 450°C to 550°C (and probably below this range) growth of  $Ti_2Ni$  proceeds in plate-like form as shown in Fig. 10.  $Ti_2Ni$  is envisaged as advancing into the  $\alpha'$  solid solution with a depletion of nickel ahead of the interface. The gradient of nickel concentration in  $\alpha'$  will be determined by the diffusion coefficient of the reaction and by the maximum and minimum nickel concentrations indicated by  $c_0$  and  $c_1$  respectively. The line 'aa' represents the centre-line between the midpoints of two growing  $Ti_2Ni$  plates. Towards the end of the decomposition process the concentration  $c_0$  at line 'aa' will start to diminish, resulting in a subsequent decrease in concentration gradient. In this model the product should consist of  $\alpha$  regions surrounded by fine, well-dispersed plates of  $Ti_2Ni$ . At low tempering temperatures (less than 550°C) it is probable that the growth of many nuclei will proceed with eventual impingement which results in the nonlinearity of the upper parts of the curves  $\log_{10} \log_{10}[1-f(t)]$  versus  $\log_{10} t$ . Thus, the Widmanstätten type of  $\alpha$  precipitate seems reasonable on the basis of this model, and  $Ti_2Ni$  formations would be manifested as an apparent thickening of  $\alpha$  boundaries. Calculations based on cylindrical  $\alpha$  needles and uniform distribution of  $Ti_2Ni$  as surface layers around  $\alpha$  show that the thickness of the  $Ti_2Ni$  layer is in the order of 0.05 microns—which would not be resolvable under the microscope. At 550°C the increased value of  $n$  (0.7) implies that precipitation occurs in thicker units, since as  $n$  approaches 1.5 spheroidal precipitates are expected. Although no measurements have been made at temperatures higher than 550°C, the photomicrograph of a specimen treated at 750°C (Fig. 6) supports this view.

The diffusion coefficient for the controlling process, as calculated from

$$D = \frac{1}{6} a^2 \nu \exp - Q/RT,$$

(where  $a$  is interatomic spacing, and  $\nu$  the thermal oscillation frequency) is in the order of  $10^{-25}$  cm<sup>2</sup> per sec in the temperature range 450°C to 550°C. Such a small value implies a slow diffusion rate which will favour the formation of a very fine and well-dispersed precipitate.

Since the proposed model requires countercurrent diffusion of Ti atoms and Ni atoms, the self-diffusion of Ti to create vacancies for the Ni may well be the rate-controlling factor. Although no figure exists for the activation energy of self-diffusion in titanium ( $Q_s$ ), an analysis of self-diffusion data for several metals indicates that  $Q_s$  is roughly proportional to the melting point  $T_f$ . In Fig. 11, the available values of  $Q_s$  are plotted against  $T_f$  and a reasonably straight-line relationship is obtained. From Fig. 11 the activation energy of self-diffusion of titanium is estimated to be about 77 000 cal/mole. This value corresponds remarkably well to the activation energy for the rate-controlling step of the tempering reaction in the titanium-nickel alloy.

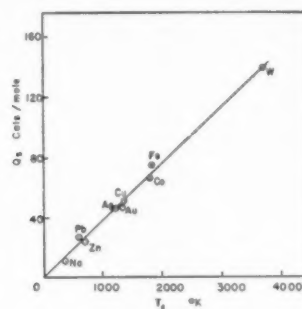


Fig. 11. Graph showing activation energy of self-diffusion,  $Q_s$ , versus melting temperature,  $T_f$ , for several metals.

### CONCLUSION

A model for the tempering kinetics of transformed- $\beta$  in a 7.2 per cent nickel alloy of titanium has been proposed. This model is based on growth of plates of  $Ti_2Ni$  during isothermal heat-treatments between 450°C and 550°C. At temperatures above 525°C there is a tendency for the precipitation of thicker units and eventually spheroids.

The reaction, to 85 per cent completion, is satisfactorily described by the rate equation based upon the work of Johnson and Mehl, Cohen and Zener. On the basis of the proposed model and the activation energy of the process, it appears that the self-diffusion of titanium is the major rate controlling factor.

### ACKNOWLEDGMENTS

This work was carried out as part of a project (No. 425) sponsored by the Defence Research Board of Canada. A fellowship awarded to one of the authors (D. H. P.) by the International Nickel Company of Canada, Limited, is gratefully acknowledged. The authors wish to thank Professors F. A. Forward and W. M. Armstrong for their encouragement, their colleagues for helpful discussion, and Mr. R. G. Butters for his assistance with certain aspects of the experimental work.

### REFERENCES

1. B. L. Averbach and M. Cohen, Trans. A.S.M. **41**, 1024 (1949).
2. C. S. Roberts, B. L. Averbach, and M. Cohen, Trans. A.S.M. **45**, 576 (1953).
3. C. A. Wert, J. App. Phys. **20**, 943 (1949).
4. W. S. Owen, Trans. A.S.M. **46** (1954) preprint.
5. J. Burke and W. S. Owen, J. Iron and Steel Inst. **176**, 147 (1954).
6. W. A. Johnson and R. F. Mehl, Trans. A.I.M.M.E. **135**, 416 (1939).
7. C. Zener, J. App. Phys. **20**, 950 (1949).
8. D. H. Polonis and J. G. Parr. To be published.
9. D. H. Polonis and J. G. Parr, Trans. A.I.M.M.E. **200** (1954); J. Metals, 1148 (October, 1954).
10. D. H. Polonis and J. G. Parr, J. Inst. Metals, 162 (October, 1954). (Letter to the Editor).
11. D. H. Polonis and J. G. Parr, J. Metals. To be published.
12. D. H. Polonis, R. G. Butters, and J. G. Parr, Research **7**, 10, s. (1954).
13. H. Margolin, E. Ence and J. P. Nielsen, Trans. A.I.M.M.E. **197**, 243.

# ON THE INTERPRETATION OF "LOW-TEMPERATURE" RECOVERY PHENOMENA IN COLD-WORKED METALS\*

A. S. NOWICK†

The "low-temperature" recovery range is defined as the range of temperatures in which equilibrium atomic diffusion is too slow to be the rate controlling process in recovery. A survey of various low-temperature recovery phenomena is carried out in order to determine to what extent effects due to point defects (vacancies, interstitial atoms, etc.) and to dislocations may be separated from one another. It is concluded that both annealing out of point defects and regrouping of dislocations occur in the very early stages of annealing. Of the various physical properties for which recovery data have been obtained, electrical resistivity seems to be the most sensitive to point defects, while internal friction and elastic modulus are affected most by the earliest stages of the rearrangement of dislocations. Studies of the latter properties show, in fact, that considerable dislocation recovery takes place at room temperature in very short times after deformation, even for high melting point metals. This recovery effect is believed to be the early stage of the same process that also leads to the release of stored energy and eventually to X-ray line sharpening.

In the quantitative interpretation of recovery data it is convenient to regard recovery as a superposition of elementary first-order processes, each having a unique recovery time. The pre-exponential factor in the Boltzmann expression for the recovery time generally falls close to  $10^{-11}$  sec. For point defect phenomena, this result implies that the mean lifetime of a defect in a cold worked lattice is of the order of  $10^2$  to  $10^3$  jumps.

## SUR L'EXPLICATION DE LA RESTAURATION À BASSE TEMPÉRATURE POUR LES MÉTAUX ÉCROUIS

Le domaine de la restauration à basse température est défini comme le domaine de température pour lequel la diffusion atomique est trop faible pour régir la restauration. En passant en revue les divers phénomènes de restauration à basse température, l'auteur cherche à distinguer les effets des défauts ponctuels (lacunes, atomes interstitiels, . . .) de ceux des dislocations et il conclut que, pendant les premiers stades de revenu, il y a à la fois destruction des défauts ponctuels et regroupement des dislocations. Des différentes propriétés physiques qui permettent de mesurer la restauration, la résistivité semble être la plus sensible aux défauts ponctuels, tandis que le frottement interne et le module d'élasticité sont affectés plus particulièrement par les premiers réarrangements de dislocations. L'étude de ces dernières propriétés montre en effet qu'une restauration importante due aux dislocations se produit à température ordinaire, immédiatement après les déformations, même pour des métaux à point de fusion élevé; c'est le même effet qui tendrait à libérer l'énergie accumulée et, éventuellement, à affiner les lignes de rayons X.

Dans l'interprétation quantitative de la restauration, il est commode de la considérer comme la superposition de diverses réactions du premier ordre ayant un même temps de relaxation. Le coefficient avant l'exponentielle dans l'expression de Boltzmann, pour ce temps de relaxation, est généralement voisin de  $10^{-11}$  sec. Pour les phénomènes liés aux défauts ponctuels, ce résultat suppose que la vie moyenne d'un défaut dans un métal écroui est de l'ordre de  $10^2$  à  $10^3$  sauts.

## BEITRAG ZUR KLÄRUNG DER PHÄNOMENE DER "TIEF-TEMPERATUR"- ERHOLUNG BEI KALTVERFORMTEN METALLEN

Der Bereich der sog. "Tief-Temperatur"-Erholung wird als derjenige Temperaturbereich definiert, bei dem die Gleichgewichtsdiffusion der Atome zu langsam ist, um für den Erholungsvorgang die steuernde Komponente zu sein. Um festzustellen, inwieweit die auf örtlich begrenzte Fehler (Leerstellen, Zwischengitteratome, etc.) von den durch Versetzungen hervorgerufenen Effekten zu trennen sind, wird eine kritische Betrachtung der Phänomene der "Tief-Temperatur"-Erholung durchgeführt. Es wird festgestellt, dass die Auflösung der örtlich begrenzten Fehler, sowie die Wiederanhäufung der Versetzungen in den frühen Stadien des Anlassens stattfindet. Der elektrische Widerstand ist von den physikalischen Eigenschaften, die zur Erholungsmessung herangezogen werden konnten, die empfindlichste in Bezug auf die örtlich begrenzten Fehler, während die innere Reibung und der E-Modul durch die Anfänge der Wiederanhäufung am meisten beeinflusst werden. Eine Untersuchung der letzteren Eigenschaften zeigt in der Tat, dass eine beträchtliche Versetzungserholung kurze Zeit nach der Verformung bei Raumtemperatur vorsichgeht, auch bei Metallen mit hohem Schmelzpunkt. Man nimmt an, dass dieser Erholungseffekt das Anfangsstadium desselben Prozesses ist, der auch zum Freiwerden der aufgespeicherten Energie, sowie zur Verschärfung der Röntgenlinien führt.

Bei der quantitativen Auswertung der Ergebnisse von Erholungsversuchen ist es üblich, die Erholung als eine Überlagerung von elementaren Vorgängen erster Ordnung zu betrachten, von denen jeder eine individuelle Erholungszeit hat. Der vorexponentielle Faktor in der Boltzmann'schen Gleichung für die Erholungszeit liegt im allgemeinen bei  $10^{-11}$  sec. Für örtlich begrenzte Phänomene sagt das Ergebnis aus, dass die mittlere Lebenszeit einer Fehlstelle im kaltverformten Gitter in der Größenordnung von  $10^2$  bis  $10^3$  Sprüngen liegt.

\* Received July 28, 1954; in revised form, December 23, 1954.

† Hammond Metallurgical Laboratory, Yale University, New Haven, Connecticut.

## I. INTRODUCTION

The modification of the properties of a cold-worked metal produced by annealing, when no change in grain structure (recrystallization) takes place, is known as recovery. Recovery phenomena have been observed for many years, but systematic investigations of these effects and attempts to understand the mechanism of recovery appear only very recently. Investigations of recovery may be roughly subdivided into two categories. First, there are effects which occur below the range of temperatures in which recrystallization normally takes place. Such "low-temperature" recovery is the principal concern of the present paper. In the second category there is recovery which occurs in and above the recrystallization range. This process competes with recrystallization as a mechanism of softening and may only be observed when recrystallization is avoided. This "high-temperature" recovery is now fairly well understood in terms of a mechanism of *polygonization*, which involves the grouping of excess dislocations of like sign into subgrain (small-angle) boundaries, and subsequent subgrain growth. The subject of polygonization has been adequately reviewed.<sup>1</sup>

In view of the great sensitivity of recrystallization temperatures to such factors as degree of deformation and purity of the metal, the above distinction between low-temperature and high-temperature recovery ranges may seem somewhat artificial. A more meaningful definition of the ranges may be obtained in terms of atomic diffusion. Such a definition is based on the belief that high-temperature recovery takes place through a mechanism of dislocation climb<sup>2</sup> where lattice diffusion is the rate controlling process.\* The "low-temperature" recovery range may then be regarded as the range in which normal atomic movement has become too slow to contribute to the recovery process. A reasonable (though somewhat arbitrary) definition is obtained by separating the low and high temperature ranges at that temperature at which the mean time between atom jumps,  $\tau$ , is greater than or equal to  $10^3$  seconds. This choice is based on the fact that for appreciable recovery by means of a diffusion controlled mechanism at least several atom jumps will be required, on the average. Thus, if  $\tau \geq 10^3$  sec, recovery by such a mechanism begins to require an unreasonably long time. Since  $\tau$  is given by

$$\tau = \tau_0 e^{Q/RT}, \quad (1)$$

where  $Q$  is the "activation energy" for normal lattice diffusion, and  $\tau_0$  is of the order of magnitude of  $10^{-15}$  sec,<sup>4</sup> the temperature,  $T_0$ , at which  $\tau = 10^3$  sec is given by

$$T_0 = Q/41.4R. \quad (2)$$

For many of the common cubic metals  $Q/T_m \cong 36$  cal/mole/K, where  $T_m$  is the melting point. Equation

(2) therefore becomes

$$T_0/T_m \cong 0.44. \quad (3)$$

In accordance with the above discussion,  $T_0$  defined by Eq. (2) or (3) may be regarded as the dividing point between "low-" and "high-temperature" recovery. (Typical values for  $T_0$  are  $135^\circ\text{C}$  for aluminum and  $310^\circ\text{C}$  for copper.<sup>†</sup>) The importance of recovery in the process of creep is illustrated by the fact<sup>5</sup> that creep of many metals may be described in terms of an activation energy very nearly equal to that for self-diffusion when  $T > 0.45T_m$ .

A discussion of the structural changes that are responsible for low-temperature recovery must start from a description of the cold worked state. The structure of a cold-worked metal has been described alternatively as a rather uniformly strained lattice<sup>6</sup> or as a lattice fragmented into unstrained crystallites or subgrains.<sup>7</sup> Recent evidence<sup>8-12</sup> favors the compromise viewpoint that subgrains do exist after deformation, but that the boundaries are poorly defined and the interiors highly strained. In terms of dislocation theory, dislocations may be distributed more or less uniformly throughout a region, producing internal strains, or may be collected into small angle boundaries to form a substructure. A variety of evidence<sup>13</sup> indicates that, in addition to the dislocations, a deformed crystal contains "point defects" (e.g., vacancies, interstitial atoms, and paired vacancies) in amounts considerably in excess of their equilibrium concentrations. Seitz<sup>13</sup> suggests that these point defects are generated through the movement of dislocations during plastic flow.

The recovery of electrical resistivity in the low-temperature range is attributed<sup>2,13</sup> primarily to the annealing out of point defects. This conclusion is based principally on the fact that the resistivity shows substantial recovery at temperatures so low that there are no corresponding changes in ordinary mechanical properties (e.g., yield strength or hardness). On the other hand, the energy of a network of dislocations may be lowered by mutual annihilation of dislocations of opposite sign or by regrouping of excess dislocations of the same sign into more stable configurations. Such redistribution of dislocations should also lead to recovery effects in the low-temperature range provided that dislocations move primarily through glide (i.e., motion along the slip plane) rather than through a climb mechanism which requires diffusion. For example, the recovery of X-ray line breadth, to the extent to which it occurs in the low-temperature range, is most reasonably attributed to such a dislocation mechanism.

The present paper has as its purpose the reexamination of various low-temperature recovery phenomena in order to see to what extent recovery effects due to dislocations and to point defects may be separated from

\* Actually Mott<sup>3</sup> indicates that the activation energy for dislocation climb might be somewhat higher than that for self-diffusion.

† For Cu, Eq. (2) is preferred since  $Q$  for self-diffusion has been measured; for Al it is necessary to use Eq. (3).



each other. It will be shown that significant redistribution of dislocations as well as the annealing out of point defects takes place in the very earliest stages of recovery. In carrying out this survey of recovery, it is desirable to obtain as much quantitative information as possible from available data. Various observers report an average activation energy for recovery in a given temperature range. It is shown here (Sec. II) that analysis of recovery as a superposition of first-order decay processes permits one to obtain an additional parameter ( $\theta_0$ ) from recovery data.

Because of the existence of several excellent reviews<sup>14-16</sup> of specific aspects of recovery phenomena, no attempt is made here to present a complete survey of low-temperature recovery. Only experiments which pertain to the objectives of the present paper will be quoted.

## II. THE RECOVERY SPECTRUM

Various attempts have been made to study recovery quantitatively by utilizing a specific model of the process to derive a corresponding recovery equation.<sup>17-19</sup> The present approach is more phenomenological; it is simply assumed that the low-temperature recovery data may be regarded as a superposition of recovery effects which obey first-order kinetics. Thus, the property  $P$  is taken as the sum of elements  $P_\theta$ , each of which recovers with its individual recovery time,  $\theta$ , and therefore obeys the differential equation

$$dP_\theta/P_\theta = -dt/\theta. \quad (4)$$

Values of  $\theta$  may vary over a continuous range or spectrum.\* It is usually appropriate to assume that each value of  $\theta$  varies with temperature according to

$$\theta = \theta_0 e^{\Delta H/RT}, \quad (5)$$

where  $\Delta H$  is the appropriate activation energy and  $\theta_0$  a constant factor with dimensions of time. When only a single  $\theta$ -value is operative, combination of Eqs. (4) and (5) shows that recovery takes place in a very narrow temperature range. The introduction of a recovery spectrum enables one to take into account the fact that recovery generally takes place over a broad range (or several broad ranges) of temperature. The existence of a spectrum of values of  $\theta$  may be due to a distribution in the activation energy  $\Delta H$ , in  $\theta_0$ , or in both these quantities.

The quantity  $\theta$  which is effective at any stage of recovery may be obtained from experimental recovery data in one of two ways. (a) In the special case of a sharp recovery spectrum,  $\theta$  is simply the time for the recoverable increment in the resistivity to fall to  $e^{-1}$  of its initial value. (b) If the recovery spectrum is very broad,  $\theta$  may be obtained at any point on an isothermal

recovery curve by setting it equal to the total time,  $t$ , to reach the desired point. This method assumes that for a sufficiently broad spectrum, all recovery for which  $\theta \ll t$  has already taken place, while that for  $\theta \gg t$  has essentially not yet begun. Thus, the principal contribution to recovery at time  $t$  comes from that part of the spectrum near  $\theta = t$ . A more quantitative demonstration of this result is given in the Appendix.

The most complete quantitative information required to describe the recovery process phenomenologically consists of the recovery spectrum itself plus the values of  $\theta_0$  and  $\Delta H$  at each point of the spectrum. Present experimental results do not permit one to obtain such complete information directly; usually a single value of  $\Delta H$  is reported as a mean value for a given recovery range. This value of  $\Delta H$  is obtained either from the shift in isothermal recovery curves as a function of temperature, from the shift in isochronal curves (plots against temperature) for two different annealing times, or from the change in slope of an isothermal curve when the temperature is abruptly changed. It is then possible to obtain  $\theta_0$  from Eq. (5) if  $\theta$  is known for the state of recovery at which the experimental value of  $\Delta H$  applies. The recovery time  $\theta$  may be obtained in each case by the use of either method (a) or method (b) described above, whichever is the more appropriate.

## III. EFFECTS ATTRIBUTABLE PRINCIPALLY TO POINT DEFECTS

### A. Recovery of Resistivity

Theoretical calculations suggest that point defects created during plastic deformation account for a large part of the resistivity increase after cold working.<sup>15</sup> This conclusion seems to be especially true if deformation is carried out at liquid nitrogen temperature, since a substantial recovery of resistivity occurs between 80°K and room temperature in metals such as copper.

Most measurements of the recovery of resistivity after deformation indicate a broad recovery spectrum. Manintveld,<sup>20</sup> however, reports sharp annealing ranges at approximately -100°C and 0°C for deformed Cu, Ag and Au. These latter observations are especially interesting since they imply the presence of two distinct types of point defect which anneal out each in its own temperature range. The results of Eggleston<sup>21</sup> (on Cu) in the same range of temperatures are quite different; the recovery spectrum observed is quite broad and barely resolvable into two broad stages. A summary of the results of these workers is included in Table I. Also included are the results of other measurements<sup>22-24</sup> on the low temperature recovery of resistivity which are such as to permit the determinations of reasonably precise values of  $\Delta H$ . The quantity  $\theta_0$  is calculated in each case by the method of Sec. II;  $T$  is the temperature at which  $\Delta H$  and  $\theta_0$  are calculated. From the results of Table I, all values of  $\theta_0$  fall within the range

$$-\log \theta_0 = 11.0 (\pm 1.0)$$

\* The recovery spectrum at a given temperature may be defined specifically as the distribution function which gives the relative magnitude of recovery per unit range of  $\ln \theta$ .

TABLE I. Resistivity recovery data for cold-worked samples.

Reference	Metal	Temp. of deformation	Stage	$\theta$ (sec)	$T$ ( $^{\circ}\text{K}$ )	$\Delta H$ (kcal/mole)	$-\log \theta_0$	$T_1$ ( $^{\circ}\text{K}$ )
Eggleston <sup>21</sup>	Cu	liq He	I	600	163	10.2	10.9	160
			II	900	243	15.5	11.0	242
Manintveld <sup>20</sup>	Cu	liq N <sub>2</sub>	I	900	178	4.6	2.7	177
			II	900	293	20.2	12.1	292
	Ag	liq N <sub>2</sub>	I	900	133	4.1	3.8	132
			II	900	238	15.0	10.8	237
	Au	liq N <sub>2</sub>	I	900	198	6.7	4.4	197
			II	900	288	16.0	9.1	287
Bowen <i>et al.</i> <sup>22</sup>	Cu	room	—	4400	423	28.8	11.2	442
Dugdale <sup>23</sup>	Pt	room	—	$2.3 \times 10^6$	343	27.6	11.2	424
Corrucini <sup>24</sup>	Pt	room	—	3200	625	40.0	10.5	650

( $\theta_0$  in seconds), with the exception of the results from Stage I of Manintveld's work on Cu, Ag and Au for which values of  $-\log \theta_0 = 2.7$  to 4.4 are obtained. These latter results are not in agreement with the data of Eggleston in a similar temperature range. In fact, Eggleston (private communication) has attempted to reproduce in copper the sharp annealing ranges obtained by Manintveld by duplicating the temperature, manner and degree of deformation as well as the annealing procedure used by Manintveld; however, he was unable to obtain annealing curves which show two sharp stages. It therefore appears that the occurrence of distinct stages and of abnormally high values of  $\theta_0$  may be very sensitive to impurity content or to the manner of deformation. Further experiments are evidently needed to clarify this point. For most cases, however, the value of  $\theta_0 = 10^{-11}$  sec appears to be valid for the recovery spectrum obtained from resistivity data over a wide range of temperatures.

Figure 1 gives a convenient alternative representation of the results of Table I showing, in effect, both the value of  $\theta_0$  and the range of temperature in which each measurement is made. Since different observers use different annealing times, the data are first adjusted (by

means of the known values of  $\Delta H$ ) to a common value of  $\theta = 10^3$  sec. The graph is then a plot of  $\Delta H/R$  against  $T_1$ , where  $T_1$  is defined as the temperature at which  $\theta = 10^3$  sec (values given in the last column of Table I). From Eq. (5) it follows that for constant  $\theta_0$  this graph will be a straight line through the origin. The solid line in the figure represents  $\theta_0 = 10^{-11}$  sec, and is in good agreement with all data for the recovery of cold-worked specimens, with the exception of Manintveld's Stage I (the group of triangles below 200 $^{\circ}\text{K}$ ).

If it is assumed that these low-temperature recovery effects result from the removal from the lattice of excess point defects created during plastic flow, then each recovery time,  $\theta$ , may be related to the mean jump time of a defect,  $\tau_d$ , through the equation

$$\theta = N\tau_d, \quad (6)$$

where  $N$  is the mean number of jumps that the defect must make before it becomes ineffective, i.e., anneals out of the lattice. The temperature dependence of  $\tau_d$  is given by the usual rate equation

$$\tau_d^{-1} = Ae^{-\Delta H/RT}, \quad (7)$$

where  $\Delta H$  is the activation energy for motion of the defect. A reasonable value<sup>4</sup> for the "frequency factor,"  $A$ , is  $10^{13}$  to  $10^{14}$  sec<sup>-1</sup>. From Eqs. (5), (6) and (7) it follows that

$$N = A\theta_0. \quad (8)$$

Substitution of  $\theta_0 = 10^{-11}$  sec and  $A = 10^{13}$  to  $10^{14}$  sec<sup>-1</sup> gives, for the mean number of jumps,  $N$ , required to anneal out a defect, a value between  $10^2$  and  $10^3$ . This result is perhaps a surprisingly small number. It certainly indicates that defects need not go far (e.g., to internal boundaries) to be effectively removed from the lattice, but that either dislocations or other point defects must serve as sinks.

\* For a point defect capable of producing diffusion, the atomic jump time,  $\tau$  (Equation (1)), is  $\tau_d$  multiplied by the mole fraction of defects.<sup>4</sup>

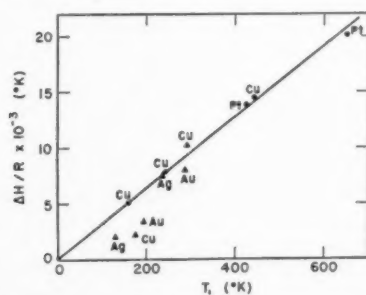


FIG. 1. Variation of the activation energy for recovery of electrical resistivity with the temperature at which the activation energy is measured (for a fixed recovery time of  $10^3$  sec). Slope of the solid line = 32.2. The triangles are from Manintveld's data (Table I).

In order to attempt to establish more definitely whether the low-temperature recoverable resistivity in deformed metals is due to point defects, it seems appropriate to compare the above results with similar data for specimens quenched from high temperatures, and those irradiated with high-energy particles. In these latter cases, it may be reasonably assumed that dislocations are not present in large numbers and therefore that only point defects contribute appreciably to the resistivity. Samples quenched rapidly from elevated temperatures seem to preserve the large number of defects present in thermodynamic equilibrium at the high temperatures,<sup>26</sup> and therefore should show an abnormally high resistivity which can be annealed out. Unfortunately, only preliminary measurements of this type have been reported for pure metals<sup>26</sup> and for alpha-brass.<sup>16</sup> Irradiated crystals also contain point defects, but among these are various types of defects having high energies of formation, which would not form thermally to any appreciable extent. Thus the situation is more complex than for quenched specimens. Resistivity studies of irradiated metals are reviewed by Broom.<sup>15</sup> Examination of the data on the annealing of irradiated copper<sup>27</sup> and platinum<sup>28</sup> shows that values of  $\theta_0$  for irradiated specimens range from  $10^{-9}$  to  $10^{-10}$  sec. This result implies a larger value of  $N$  [Eq. (8)] than in cold-worked samples, which is consistent with the lower dislocation density in the irradiated samples. The recovery spectrum of cold-worked and irradiated samples seems to be very nearly the same in copper and platinum. In the case of copper it is striking that the isochronal recovery curves for specimens irradiated near liquid nitrogen temperatures,<sup>27,28</sup> and specimens cold-worked at liquid helium temperatures<sup>29</sup> are quite similar in shape, and that all these curves show only a small amount of recovery in the range 0°C to 100°C.

It should be noted that in general the recovery spectra discussed above are quite broad, so that it is possible to observe almost any value of  $\Delta H$  depending on the temperature range in which one makes his observations. Thus, when irradiated and cold-worked samples show essentially the same value of  $\Delta H$  in a given temperature range, it is incorrect to conclude (as Mott<sup>2</sup> has done) that this particular  $\Delta H$  value represents the activation energy for the motion of a fundamental defect. Such an agreement in  $\Delta H$  values means only that  $\theta_0$  is nearly the same for the two samples.

### B. Release of Stored Energy

Seitz<sup>13</sup> claims that a large part, perhaps the major part, of the energy stored in cold-working may be due to the formation of point defects. Recent work by Clarebrough *et al.*<sup>30</sup> seems to support this conclusion, in demonstrating that 40 per cent of the energy stored in the deformation of nickel is released before any reduction in hardness occurs, and in the same temperature range as the recovery of resistivity. However, these

same measurements and others to be quoted in Sec. IV, indicate that the annealing of dislocations also contributes appreciably to the release of stored energy.

## IV. EFFECTS ATTRIBUTABLE PRINCIPALLY TO DISLOCATIONS

### A. X-Ray Observations

Various observers have found that the line-broadening of the Debye rings obtained from a cold-worked polycrystalline metal often begins to recover below the range of temperatures at which visible recrystallization occurs. The older of such observations are reviewed by Barrett.<sup>14</sup> More recently, Lutts and Beck<sup>31</sup> have shown that under suitable conditions line breadth in cold-worked aluminum may recover completely before softening sets in. The work of Hall and Williamson<sup>12</sup> shows that for deformed Al and W, line breadth recovers relatively early compared to the background intensity. Line broadening may be related to the long-range stress field about a dislocation, while the background appears related to atoms near dislocation centers which undergo relatively large displacements. It therefore seems reasonable to conclude that extensive rearrangement of dislocations may take place before the number of dislocations is affected. It is noteworthy that the recovery of line breadth is considerably slowed down by the presence of impurities.

Another X-ray approach to the study of low temperature recovery is by means of the microbeam method of Hirsch and Kellar<sup>8,32</sup> and later by Gay and Kelly.<sup>33</sup> This method uses a narrow beam which irradiates a sufficiently small volume of material as to produce spotty Debye rings. From the number of spots and the shape of the spots the mean size of subgrain particles and the distortion within them may be obtained. For pure aluminum extensive recovery of strains within subgrains takes place in a period of about one year at room temperature. During this period the subgrain size remains practically unchanged at about  $2\mu$ . Hirsch<sup>32</sup> suggests that the formation of the subgrain boundaries must take place either during cold-working or immediately thereafter and that the recovery process involves continued migration of dislocations into the boundaries to reduce internal stresses. For impure aluminum, a smaller particle size is obtained; this is interpreted to mean that impurities interfere with the migration of dislocations.

### B. Observations by Electron and Optical Microscopy

Heidenreich<sup>9</sup> has applied electron microscopy to the study of cold work and recovery in aluminum. His results lead to the conclusion that after cold work a subgrain structure is present for pure aluminum, where the mean subgrain size is about  $2\mu$  and the interior is highly strained. Appreciable recovery of the internal

strains is observed in periods of the order of days with essentially no change in subgrain size. These results are very similar to those obtained by the microbeam X-ray method. Here again impure aluminum shows a much smaller subgrain size.

The metallographic observations of Perryman<sup>11</sup> on high purity aluminum are consistent with the results of Heidenreich and of Hirsch. A subgrain structure (size  $1-2\mu$ ) is observed after cold working; this structure becomes considerably sharper on annealing for one year at room temperature or for five minutes at  $100^\circ\text{C}$ . Furthermore, the presence of an impurity (magnesium) decreases the size of the subgrains to the point where they cannot be seen.

### C. Recovery of Mechanical Properties

The recovery of such mechanical properties as hardness and tensile strength generally takes place relatively late in the annealing process—usually in the high-temperature recovery range, or coincidentally with recrystallization. Inasmuch as relief of strains within subgrains can take place in the low-temperature recovery range, as indicated by the results already quoted, it might be suspected that a finer examination of mechanical properties would show low-temperature recovery phenomena. Such recovery was in fact demonstrated by Cherian, Pietrokowsky and Dorn<sup>34</sup> in commercially pure aluminum. Experiments carried out at room temperature and at  $100^\circ\text{C}$  show that the initial flow stress recovers at these temperatures. The effects of recovery are readily wiped out, however, when deformation is resumed. From the evidence presented, a broad recovery spectrum is indicated. Recovery of an entirely different nature is observed in the high-temperature range. This latter recovery leaves a permanent effect (in that further deformation does not bring the stress-strain curve back to the original curve). Furthermore the activation energy associated with this second stage is 33 kcal/mole, which is close to the activation energy for self diffusion in aluminum. This latter result is in agreement with the definition of the high-temperature recovery range presented in the Introduction.

Indirect evidence for the recovery of mechanical properties comes from a study of the effect of temperature and rate of deformation on the stress-strain curves of single crystals. From the fact that the rate of work hardening is strongly temperature dependent over a wide range of temperatures, Schmid and Boas<sup>35</sup> conclude that work hardening involves a thermal recovery process superimposed on an athermal deformation process. More recent work<sup>36</sup> on aluminum single crystals shows that the rate of work hardening is strongly temperature dependent even near liquid nitrogen temperature. This result indicates that recovery plays an important part in the deformation process down to very low temperatures.

### D. Recovery of Dynamic Modulus and Internal Friction\*

It was first observed by Köster and co-workers<sup>37-40</sup> that freshly deformed metals may show very high values of internal friction which recover rapidly at room temperature and even more rapidly at elevated temperatures. Simultaneously with the recovery of the internal friction, the dynamic Young's modulus of the metal may increase by as much as several per cent. Both of these properties usually achieve constant values before the recrystallization region is reached. \*\* Figure 2,

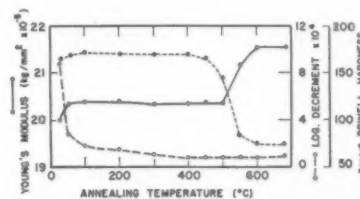


FIG. 2. Isochronal recovery curves (1/2 hour anneals) of dynamic Young's modulus, internal friction, and hardness, for deformed Armco iron. Recrystallization occurs near  $500^\circ\text{C}$ . After Köster.<sup>38</sup>

taken from Köster's work on iron,<sup>38</sup> demonstrates these low-temperature recovery effects. The rise in internal friction and the decrease in dynamic modulus resulting from the deformation has been termed the *Köster effect*.<sup>41</sup> The internal friction under discussion is to be distinguished from other types of internal friction in cold-worked metals;<sup>41</sup> in addition to its rapid recovery, it is characterized by amplitude independence at low strain amplitudes, and by only a mild dependence on frequency and temperature (not yet studied in detail). Observations of the Köster effect have been reported by various investigators for iron,<sup>38</sup> brass,<sup>39,42</sup> aluminum,<sup>40</sup> nickel-chrome,<sup>43</sup> copper<sup>44</sup> (all deformed at room temperature). Measurements are usually in the kilocycle range of frequencies, but the same type of behavior has also been demonstrated at lower frequencies.<sup>43</sup>

Isothermal plots of internal friction or dynamic Young's modulus show rapid changes at room temperature in very short periods of time following the deformation. Such behavior takes place even for relatively high melting-point metals. For example, in the work of Köster on heavily deformed iron, from which Fig. 2 is taken, isothermal data show that recovery of internal friction is essentially complete after about 10 hours at room temperature or a few minutes at  $100^\circ\text{C}$ . As another example, some new measurements of low-frequency internal friction of a cold-worked platinum wire (diam. .025 in.), are given in Fig. 3. The cold-working in this case was carried out by bending the wire

\* For convenience, dynamic elastic modulus and internal friction are here classified as distinct from other mechanical properties.

\*\* The dynamic modulus usually shows a second rise during recrystallization (see Fig. 2), but the interpretation of this latter effect is complicated by the changes in texture which accompany recrystallization.



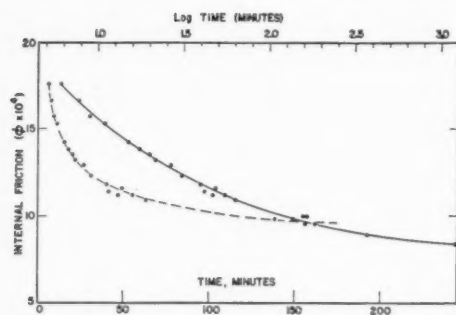


FIG. 3. Recovery of internal friction ( $\phi$ =phase angle= $Q^{-1}$ ) of a freshly deformed platinum wire at room temperature. Solid curve:  $\phi$  vs  $\log t$ ; dashed curve:  $\phi$  vs  $t$ . Frequency, 0.73 c.p.s.

about a 1/4-inch diameter cylinder and then straightening the wire in such a way as to avoid kinks. It should be noted that although measurements are begun only six minutes after the deformation, it is not possible to extrapolate the curve to zero time. This is especially clear from the plot against log time (the solid curve) which shows positive curvature over the entire range, whereas it must undergo inflection and revert to negative curvature before we can obtain an extrapolated value corresponding to  $t=0$ . This same characteristic of the isothermal recovery curves, in both internal friction and dynamic modulus, has appeared in most of the curves obtained by Köster and in unpublished work in this laboratory in measurements on deformed bars (in the kilocycle range). Such evidence implies that considerable recovery takes place in minutes or even seconds after deformation and that the recovery spectrum must be very broad.

The only precise determination of an activation energy for recovery of the Köster effect is that of A. D. N. Smith,<sup>44</sup> from dynamic modulus measurements in deformed copper. He finds as much as an 8 per cent recovery of the dynamic modulus of O.F.H.C. copper extended by 1 per cent. The mean activation energy for this recovery, which is studied between 47° and 100°C, is 25 kcal/mole. The first line of Table II lists the information required for the calculation of  $\theta_0$  [Eq. (5)] from these data. The value of  $\theta_0$  obtained is in fairly good agreement with the corresponding values from resistivity measurements (Table I).

The large recoverable decrease in modulus upon deformation has been attributed<sup>44</sup> to the elastic oscillation under stress of dislocation segments pinned at the

TABLE II. Recovery data for dynamic modulus and release of stored energy in copper (deformed at room temperature).

Reference	Property measured	$\theta$ (sec)	$T$ (°K)	$\Delta H$ (kcal/mole)	$-\log \theta_0$
Smith <sup>44</sup>	Elastic modulus	10 <sup>8</sup>	354	25	12.4
Borelius <sup>50</sup>	Release of energy	1800	373	29	13.5

ends. The damping, on the other hand, must be due either to a thermally controlled release of these segments at their pinning points or to the natural damping of a moving dislocation.<sup>45</sup> The recovery process has been associated with the annihilation of mobile screw components of dislocation loops.<sup>44</sup> In view of the low temperatures at which these recovery effects occur and in view of the large modulus changes involved, these experiments seem to be of fundamental importance in the study of low-temperature recovery. It therefore appears desirable to reexamine possible interpretations of the Köster effect and of its recovery, especially with regard to the possibility that point defects play a major role in these phenomena.

First, it seems worth considering the possibility that point defects created by the deformation might be responsible for the Köster effect. Such defects could produce a large contribution to the internal friction in a pure metal through a stress-induced reorientation of the defect, similar to the internal friction due to carbon in  $\alpha$ -iron.<sup>46</sup> An effect of this sort, which could be obtained only for a defect that produces noncubic distortion of the surrounding lattice, would involve a strong temperature and frequency dependence in the form of a simple internal friction peak. The Köster internal friction does not show such behavior.<sup>41</sup> The internal friction could also be due to defects, if the defects could be induced by stress to flow to boundaries in the crystal, such as grain boundaries or slip bands; however, the Köster effect is obtained at too low a temperature and at too high a frequency to permit such long-range defect diffusion during one oscillation. Furthermore, it is not possible to see how large modulus changes, of the order of several per cent, can be due to defects created by plastic flow. It seems therefore that the Köster effect may be sensibly attributed only to dislocations. The oscillation of dislocation loops is known,<sup>47,48</sup> to be capable of lowering the elastic modulus by 1 to 2 per cent in well-annealed high purity metals. It is therefore to be expected that such dislocation loops affect the modulus in cold-worked specimens. More quantitatively, it may be shown<sup>48</sup> that the change in shear modulus,  $G$ , due to  $N$  dislocations per  $\text{cm}^2$  pinned to form loops of average length  $L$  is

$$\Delta G/G = -NL^2/6\alpha, \quad (9)$$

where  $\alpha$  is a slowly varying function of  $L$  of the order of magnitude unity. Upon substituting the reasonable value  $N=10^{11} \text{ cm}^{-2}$ , and an average experimental value of 5 per cent for  $\Delta G/G$ , we obtain  $L \sim 10^{-6} \text{ cm}$ , for a cold-worked metal, where the pinning points are presumably intersections with other dislocations. Such a value is quite reasonable. The limitation to the magnitude of  $\Delta G/G$  probably lies in the difficulty of developing a large  $N$  without considerably decreasing  $L$ .

If it is granted that oscillating dislocation loops are responsible for the Köster effect, separate consideration must now be given to the question of how the recovery,

or immobilization of these dislocations, takes place. Immobilization may result from the movement of the dislocations themselves to new positions involving tighter binding with other dislocations, or by the movement of solute atoms or point defects to the dislocations to produce further pinning and decreased  $L$ -values. The possibility that substitutional\* solute atoms can be responsible for such pinning of dislocations is eliminated when it is noted that considerable recovery may take place at room temperature in several minutes, even for the higher melting metals. (The data already quoted for iron and platinum illustrate this point.) The requirement that solute atoms undergo appreciable movement in these metals in a short time at room temperature is in disagreement with known diffusion measurements. It is desirable to consider next the possibility that point defects created by the plastic flow are responsible for the pinning of the dislocations. Such a viewpoint is suggested, for example, by the work of Blewitt<sup>56</sup> which shows that a sharp yield point may be developed in a copper crystal deformed at 78°K and then annealed at 300°K. The following series of arguments is intended to show that the recovery of the Köster effect cannot be attributed to point defects.

1. If the recovery of the Köster effect were due to point defects, it should be capable of correlation with the recovery of electrical resistivity. Yet there is no evidence for appreciable recovery of resistivity in high melting-point metals, such as iron<sup>49</sup> and platinum<sup>28,49</sup> near room temperature. In the case of copper large recovery effects are obtained in the Köster effect (after room temperature deformation) between 25°C and 100°C, whereas the resistivity of cold-worked and irradiated copper shows relatively little change in this range.

2. The dynamic modulus recovers readily even after 1 per cent deformation; furthermore, a substantial increase in the amount of deformation does not appreciably change the character of the recovery curves.<sup>44</sup> These results are difficult to reconcile with the theory that point defects are responsible for the recovery, especially in view of the work of Blewitt,<sup>56</sup> which indicates that very few point defects are created by small amounts of cold work.

3. Pinning of dislocations by defects should result in a *hardening* effect, as far as mechanical properties are concerned. Instead, the results quoted in Sec. IV(C) indicate that, in the usual situation, softening occurs in the early stages of annealing.

4. The other recovery effects, quoted in Secs. IV(A), (B), and (C), show that regrouping of dislocations can and does occur in the low-temperature recovery range. It therefore seems quite reasonable that recovery of a property which measures the oscillation of individual

dislocations (viz., elastic modulus or internal friction) should take place much more quickly than the recovery of internal stresses within the subgrains, as observed by microscopy and X-rays.

5. There is some evidence in the work of Smith<sup>44</sup> that higher purity copper shows more rapid recovery of dynamic modulus than copper of lesser purity. This behavior is in agreement with the effect of impurities in retarding recovery of internal strains, as indicated in the microscopy and X-ray work quoted earlier. There is no evidence that impurities affect the recovery of point defects in this way.

In view of the above arguments it does not seem probable that the recovery of internal friction and elastic modulus after deformation can be related to the segregation of point defects at dislocations. On the contrary, it seems necessary to conclude that immobilization of dislocations occurs through their own migration to more stable positions. From data, such as in Fig. 3, it may then be further concluded that considerable rearrangement of dislocations takes place in very short periods of time after the deformation.

### E. Release of Stored Energy

In the discussion of experiments on the release of stored energy, given in Sec. III(B), it was noted that not all such measurements may be interpreted in terms of the annealing out of point defects. Now that it has been established that some of the early stages of recovery are due to dislocation movements, it is to be expected that some release of stored energy will accompany such movements. Borelius and co-workers<sup>50</sup> have shown that a significant release of energy may take place at 60°C and at 100°C in room-temperature deformed copper. The annealing curves indicate a broad recovery spectrum. The range of temperature in which these effects are observed is one in which the resistivity of irradiated samples shows no significant annealing. It therefore seems most reasonable to conclude that this energy release measures the reduction in strain energy associated with the same regrouping of dislocations that produces recovery of the Köster effect. From the observation of Borelius that in the release of stored energy in copper, 45 hours at 60°C correspond to 0.5 hour at 100°C, one may calculate  $\Delta H$  and  $\theta_0$  as given in Table II. The agreement between this value of  $\theta_0$  and the value obtained from the modulus recovery experiments of Smith is quite good, considering the fact that the Borelius experiments are still of a preliminary sort.

Suzuki<sup>51</sup> has measured specific heat curves for cold worked copper and found that energy is released in two stages in the low temperature recovery range. The first stage appears to be the simpler of the two; it involves an evolution of heat proportional to the prior plastic strain. Suzuki attributes this recovery effect to the movement of dislocations to more stable positions. He also observes a change in mechanical properties in the

\* The generality of the recovery of the modulus and damping after deformation tends to eliminate the possibility that interstitial solutes are responsible. Also, some of the arguments presented here to show that point defects are not responsible for this recovery effect can be applied as well to solutes.

preplastic range which accompanies this recovery and which might be attributed to a change in the anelastic properties (e.g., internal friction) of the metal.

## V. DISCUSSION

The principal result of the last section is that redistribution and possibly annihilation of dislocations take place in the very early stages of annealing. The range in which such effects are detectable depends greatly on the nature of the property being measured. It is apparent that internal friction and dynamic modulus are more sensitive to changes in individual dislocations than the other properties considered. Measurements of the release of stored energy are also capable of detecting an early stage of dislocation recovery. Microscopy and X-ray measurements, on the other hand, observe the strain over regions of the lattice that are large on an atomic scale and therefore are sensitive to still later stages of dislocation annealing. Finally, ordinary mechanical properties such as hardness and tensile strength are not greatly affected by "low-temperature" annealing. However, as indicated in Sec. IV(C), the rate of work-hardening in a tensile test at low temperatures is probably controlled by recovery.

It is possible to reexamine the theory of the formation of a substructure in the light of the present conclusion that substantial dislocation recovery takes place immediately after deformation. Conrad, Averbach and Cohen<sup>52</sup> and also Beck<sup>53</sup> have decided that the formation of subboundaries must take place during deformation and without thermal activation, rather than after deformation. This conclusion is based on experiments which show substructure formation in various metals after deformation at temperatures far below their melting points. According to the present discussion, however, a substantial recovery of dislocations is demonstrated by the Köster-effect experiments, even for high melting-point metals deformed at room temperature. It is not unreasonable, therefore, to suppose that the substructure can form as a very rapid recovery phenomenon, with comparatively low activation energy, directly after low-temperature deformation. Such a possibility is in accord with Mott's recent suggestion<sup>54</sup> that dislocation climb is not necessary to the start of polygonization, based upon his analysis of experiments on "fine slip."

In the case of the low-temperature resistivity measurements, the similarity in recovery spectrum of a cold-worked and an irradiated sample seems to indicate that the recovery of resistivity is principally due to the annealing out of point defects. It is quite possible, however, that careful resistivity measurements can also detect the regrouping of dislocations during recovery following deformation. For example, Weyerer<sup>55</sup> finds that recovery of the resistivity of copper deformed at room temperature may be observed by raising the temperature a few degrees. He further observes that this recovery effect is more noticeable in pure copper than

in impure copper, a result which may be characteristic of dislocation annealing (see discussion below).

Inasmuch as it is possible to obtain substantial rearrangement of dislocations without a significant change in the usual mechanical properties, it is not valid to assign an interpretation in terms of point defects to all recovery phenomena which take place at low temperatures. It is therefore important to attempt to find some criteria to distinguish between effects due to the annealing of point defects and of dislocations. One possible criterion is the value of  $\theta_0$ . It has been shown, for the recovery of resistivity of cold worked metals, that  $\theta_0 = 10^{-11}$  sec. This result has been interpreted to mean that the mean lifetime of a defect is about  $10^8$  jumps in a heavily cold-worked lattice. Now consider values of  $\theta_0$  obtained from measurements that have been attributed to dislocations (Table II). These values seem to be slightly lower than the corresponding values obtained from the resistivity measurements, although the difference may not really be experimentally significant. The interpretation of  $\theta_0$ , when recovery is due to dislocation movements, is as follows. The quantity  $\theta_0^{-1}$  is the frequency factor associated with the oscillation in its potential well of that segment of dislocation which must break loose from its pinned position in order to free an entire dislocation loop. This frequency factor is reasonably expected to be somewhat lower than the frequency factor  $A$  [Eq. (7)] associated with motion of a point defect. Thus, it appears that the value of  $\theta_0$  cannot serve as a criterion to distinguish dislocation from defect recovery, since in both cases it is of about the same order of magnitude.

One respect in which dislocation and point defect contributions to recovery may differ greatly is in the sensitivity of recovery to impurities. In the case of each recovery phenomenon which is dependent on redistribution of dislocations (described in the last section) there was some experimental evidence that the presence of impurities slows down recovery. In the case of defect phenomena there is no clear-cut experimental evidence. It seems quite reasonable that slight impurities may be a relatively unimportant factor in recovery due to point defects. This proposal, made at present in a somewhat speculative vein, suggests that the effect of impurities be studied more carefully in future recovery experiments.

## VI. CONCLUSIONS

1. The concept of recovery as a superposition of first-order decay processes involving a spectrum of recovery times is very useful in the analysis of recovery data. It makes possible a calculation of the pre-exponential factor,  $\theta_0$ , in the Boltzmann expression for the recovery time,  $\theta$ .

2. The fact that the value of  $\theta_0$ , obtained from data on low-temperature recovery of electrical resistivity, is essentially a constant independent of the state of recovery implies that the broad recovery spectrum is due



to a distribution in values of the activation energy,  $\Delta H$ . The experimentally observed value of  $\Delta H$  is determined by the temperature range in which the annealing experiment is carried out.

3. The low temperature recovery of resistivity may be attributed primarily to the annealing out of point defects created by the deformation. The numerical value  $\theta_0 = 10^{-11}$  sec obtained from almost all resistivity recovery experiments implies that point defects make, on the average,  $10^2$  to  $10^3$  jumps before they anneal out of the lattice.

4. The annealing out of point defects is not the only mechanism of recovery in the low-temperature range. The recovery of the dynamic elastic modulus and internal friction directly after deformation are attributed to the redistribution of dislocations. This recovery process is believed to be the early stage of the same process that also leads to the release of stored energy and eventually to X-ray line sharpening.

5. The very rapid rate of recovery of elastic modulus and internal friction (even of high melting-point metals) directly after deformation at room temperature shows how closely thermally activated dislocation rearrangement follows deformation. This result is consistent with the fact that the rate of work hardening in a tensile test is strongly temperature dependent to very low temperatures. It also tends to negate the concept that the substructures observed in metals deformed at low temperatures must arise from an athermal process.

#### ACKNOWLEDGMENTS

The author wishes to express his gratitude to Mr. A. E. Roswell for taking the measurements reported in Fig. 3, and to the Office of Ordnance Research, United States Army, for supporting the program of which the present work is a part.

#### APPENDIX

The total recovery of a Property  $P$  is given by a superposition of solutions of Eq. (4), or

$$P(t) = \int_{-\infty}^{\infty} f(\theta) e^{-t/\theta} d \ln \theta,$$

where  $f(\theta)$  is the distribution function. The effective  $\theta$  at any given time may be defined as that value which makes a maximum contribution to  $dP/dt$  at that time. The contribution of any element  $d \ln \theta$  of the spectrum to  $dP/dt$  is

$$-f(\theta) e^{-t/\theta} / \theta.$$

Under the assumption that  $f(\theta)$  is a slowly varying function of  $\theta$  (i.e., that the spectrum is broad) the last expression is a maximum for  $\theta = t$ .

#### REFERENCES

1. Symposium on Polygonization, Progress in Metal Physics II. (Interscience, 1950), B. Chalmers, Ed.
2. N. F. Mott, Phil. Mag. **43**, 1151 (1952).
3. N. F. Mott, Proc. Phys. Soc. **B64**, 729 (1951).
4. C. Zener, J. Appl. Phys. **22**, 372 (1951); Imperfections in Nearly Perfect Crystals (Wiley, New York, 1952), p. 289.
5. O. D. Sherby, R. L. Orr, and J. E. Dorn, J. Metals **6**, 71 (1954).
6. B. E. Warren and B. L. Averbach, Imperfections in Nearly Perfect Crystals (Wiley, New York, 1952), p. 152; J. Appl. Phys. **20**, 885 (1949); **21**, 595 (1950).
7. W. A. Wood, Proc. Roy. Soc. **A172**, 231 (1939).
8. J. N. Kellar, P. B. Hirsch, and J. S. Thorp, Nature (Lond.) **165**, 554 (1950).
9. R. D. Heidenreich, Bell Syst. Tech. J. **30**, 867 (1951).
10. B. E. Warren and B. L. Averbach, J. Appl. Phys. **23**, 497 (1952).
11. E. C. W. Perryman, Acta Met. **2**, 26 (1954).
12. W. H. Hall and G. K. Williamson, Proc. Phys. Soc. **64B**, 937, 946 (1951); Acta Met. **1**, 22 (1953).
13. F. Seitz, Advances in Physics **1**, 1 (1952).
14. C. S. Barrett, Structure of Metals (McGraw-Hill, New York, 2nd ed., 1953), p. 436.
15. T. Broom, Advances in Physics **3**, 26 (1954).
16. P. A. Beck, Advances in Physics **3**, 245 (1954).
17. D. Kuhlmann, Z. Phys. **124**, 468 (1947).
18. A. H. Cottrell and V. Aytakin, J. Inst. Metals **77**, 389 (1950).
19. W. Betteridge, J. Inst. Metals **82**, 149 (1953-4).
20. J. A. Maninveld, Nature (Lond.) **169**, 623 (1952).
21. R. R. Eggleston, J. Appl. Phys. **23**, 1400 (1952).
22. D. Bowen, R. R. Eggleston, and R. H. Kropschot, J. Appl. Phys. **23**, 630 (1952).
23. R. A. Dugdale, Phil. Mag. **43**, 912 (1952).
24. R. J. Corruccini, J. Res. Nat. Bur. Stds. **47**, 94 (1951).
25. A. E. Roswell and A. S. Nowick, J. Metals **5**, 1259 (1953).
26. J. W. Kauffman and J. S. Koehler, Phys. Rev. **88**, 149 (1952).
27. A. W. Overhauser, Phys. Rev. **90**, 393 (1953).
28. R. R. Eggleston, Acta Met. **1**, 679 (1953).
29. R. R. Eggleston, Unpublished data, reproduced in Fig. 8(a), ref. 16.
30. L. M. Clarebrough, M. E. Hargreaves, and G. W. West, Phil. Mag. **44**, 913 (1953).
31. A. H. Lutts and P. A. Beck, J. Metals **6**, 257 (1954).
32. P. B. Hirsch and J. N. Kellar, Acta Cryst. **5**, 162, 168, 172 (1952).
33. P. Gay and A. Kelly, Acta Cryst. **6**, 165, 172 (1953).
34. T. V. Cheria, P. Pietrowsky, and J. E. Dorn, J. Metals **1**, 948 (1949).
35. E. Schmid and W. Boas, Kristallplastizität (Berlin, Springer, 1935), p. 167.
36. F. D. Rosi and C. H. Mathewson, J. Metals **2**, 1159 (1950).
37. F. Förster and W. Köster, Z. Metallk. **29**, 116 (1937).
38. W. Köster, Arch. Eisenhüttenw. **14**, 271 (1940-41).
39. W. Köster and K. Rosenthal, Z. Metallk. **30**, 345 (1938).
40. W. Köster, Z. Metallk. **32**, 282 (1940).
41. A. S. Nowick, J. Appl. Phys. **25**, 1129 (1954).
42. H. I. Fushfeld, Phys. Rev. **82**, 769A (1951); Frankford Arsenal Report No. R-1038.
43. Ch. Boulanger, Compt. Rend. **226**, 1170 (1948).
44. A. D. N. Smith, Phil. Mag. **44**, 453 (1953).
45. A. H. Cottrell, Dislocations and Plastic Flow in Crystals (Oxford, 1953), p. 66.
46. A. S. Nowick, Progress in Metal Physics **IV** (Interscience, 1953), p. 1, B. Chalmers, Ed.
47. G. Bradfield and H. Pursey, Phil. Mag. **44**, 437 (1953).
48. J. Friedel, Phil. Mag. **44**, 444 (1953).
49. G. Tammann, Z. Metallk. **28**, 6 (1936).
50. G. Borelius, S. Berglund, and S. Sjöberg, Arch. f. Fysik **6**, 143 (1952).
51. T. Suzuki, Sci. Rep. Res. Inst. Tohoku Univ. **1**, 193 (1949).
52. G. P. Conrad, B. L. Averbach, and M. Cohen, J. Metals **5**, 1036 (1953).
53. P. A. Beck, Acta Met. **1**, 422 (1953).
54. N. F. Mott, Phil. Mag. **44**, 741 (1953).
55. H. Weyerer, Z. Metallk. **44**, 51 (1953).
56. T. H. Blewitt, Phys. Rev. **91**, 1115 (1953).



# DISLOCATION ENERGIES IN ANISOTROPIC CRYSTALS\*

A. J. E. FOREMAN†

A detailed calculation is made of the elastic energy of a straight dislocation in a cubic or hexagonal crystal, for various orientations in the crystal of the dislocation line and its Burgers vector. For both crystal systems there are a limited number of cases where the equations of anisotropic elasticity theory yield a completely analytic solution, and these are listed for several different types of Burgers vector; numerical solution of the equations is necessary for several other dislocations which are of interest. The results, which are most complete for the face-centered cubic metals, do not indicate a very marked correlation between the observed slip planes and the planes of lowest elastic dislocation energy. Finally, the inelastic energy contribution from the dislocation core is discussed on the basis of the Peierls model of a dislocation.

## ENERGIE DES DISLOCATIONS DANS LES CRISTAUX ANISOTROPE

Calcul détaillé de l'énergie élastique d'une dislocation rectiligne dans un cristal cubique ou hexagonal pour différentes orientations de la ligne de dislocation et de son vecteur de Burgers. Dans les deux systèmes, il existe un nombre limité de cas où les équations de l'élasticité anisotrope donnent une solution analytique complète et ceux-ci sont rassemblés pour les différents types de vecteurs de Burgers. Une solution numérique des équations est nécessaire pour les autres dislocations intéressantes. Ces résultats, qui sont plus complets pour les métaux cubiques à faces centrées, n'indiquent pas une corrélation marquée entre les plans de glissement observés et les plans d'énergie élastique minimum pour les dislocations. Finalement, la partie inélastique de l'énergie provenant du centre de la dislocation est discutée en partant du modèle de Peierls.

## VERSETZUNGSENERGIEN IN ANISOTROPEN KRISTALLEN

Eine genaue Berechnung der elastischen Energie einer geraden Versetzung in einem kubischen oder hexagonalen Kristall wird für verschiedene Orientierungen der Versetzungslinie im Kristall und ihren Burgers Vektor durchgeführt. Für beide Kristallsysteme gibt es eine begrenzte Anzahl von Fällen, bei denen die Gleichungen der anisotropen Elastizitätstheorie eine vollständige analytische Lösung ergeben. Sie werden für verschiedene Typen von Burgers' Vektoren aufgeführt. Für einige andere Versetzungen, die von Interesse sind, ist eine numerische Lösung dieser Gleichung erforderlich. Die Ergebnisse, die für das kubischflächenzentrierte System am vollständigsten sind, zeigen keine sehr ausgeprägte Beziehung zwischen den beobachteten Gleitebenen und den Ebenen niedrigster elastischer Versetzungsenergie. Zum Schluss wird der Anteil der unelastischen Energie des Versetzungszentrums auf Grund des Peierls'schen Modells einer Versetzung besprochen.

### 1. INTRODUCTION

In many problems relating to the dislocation theory of plastic deformation it has been customary to make use of the properties of a dislocation in an elastically isotropic material. Most of the common metals, however, exhibit a marked degree of anisotropy in their single crystal elastic behaviour and it is therefore more desirable to calculate the properties of a dislocation on the basis of anisotropic elasticity theory.

In this paper we shall consider in particular the elastic energy of a dislocation and investigate the dependence of this on the orientation in the crystal of the dislocation line. Dislocation solutions to the differential equations of anisotropic elasticity theory have been derived by several authors. Burgers<sup>1</sup> treated the problem of a dislocation loop in a cubic crystal, and Eshelby<sup>2</sup> considered the two-dimensional problem of an edge dislocation in an anisotropic medium. Eshelby, Read and Shockley<sup>3</sup> subsequently developed a more elegant mathematical solution for the problem of a straight dislocation line of either edge, mixed or screw character in an anisotropic crystal, and also made a correction to the earlier paper.

Other investigations of the properties of dislocations in anisotropic crystals have been made by Leibfried<sup>4</sup> and Seeger and Schöck.<sup>5</sup> The extension of the static theory to include a uniform motion of a straight dislocation through anisotropic media is given by Bullough and Bilby.<sup>6</sup>

In the present paper we consider the elastic energy of a dislocation and also briefly discuss the inelastic contribution from the dislocation core. In calculating the purely elastic contribution the notation and theory of Eshelby *et al* is adopted, the important results of which are outlined in section 2. In section 4 we discuss the most general case where the elasticity theory yields a completely analytic solution and in sections 5-7 the results are used to calculate the elastic energies of some dislocations in the cubic and hexagonal systems. In section 8 the possible inelastic contributions to the energy from the dislocation centre are discussed on the basis of the Peierls model of a crystal dislocation.

### 2. ELASTIC DISLOCATIONS

The components of stress and displacement for a straight dislocation lying along the  $x_3$  axis have been derived by Eshelby *et al*. In their elastic solution the quantities  $A_{kl}$  and  $p_l$  ( $k, l = 1, 2, 3$ ) are defined in

\* Received December 22, 1954.

† Atomic Energy Research Establishment, Harwell, Berks., England.

terms of the elastic constants  $C_{ijkl}$  by the three homogeneous equations\*

$$A_k[C_{i1k1} + p(C_{i1k2} + C_{i2k1}) + p^2 C_{i2k2}] = 0, \quad (1)$$

which have a solution for  $A_1, A_2, A_3$  provided that the determinant of the coefficients vanishes. This yields a sextic equation for  $p$  having six complex roots denoted by  $p_{(1)}, p_{(2)}, p_{(3)}$  and complex conjugates, and corresponding to these roots equation (1) has six solutions for  $A_k$  denoted by  $A_{k(1)}, A_{k(2)}, A_{k(3)}$  and complex conjugates. The quantities  $D_{(l)}$  are then given by

$$\Re \sum_{l=1}^3 A_{i(l)} D_{(l)} = b_i, \quad (2)$$

$$\Re \sum_{l=1}^3 B_{i2(l)} D_{(l)} = 0, \quad (3)$$

where  $\Re$  denotes *real part of*,  $\mathbf{b} = (b_1, b_2, b_3)$  is the Burgers vector of the dislocation, and we have introduced the notation

$$B_{ij(l)} = A_{k(l)} (C_{ijk1} + p_{(l)} C_{ijk2}). \quad (4)$$

The components of stress  $\tau_{ij}$  and displacement  $u_k$  are given in terms of these quantities by

$$\tau_{ij} = \Re \frac{1}{2\pi i} \sum_{l=1}^3 (\pm)_{(l)} B_{ij(l)} \frac{D_{(l)}}{z_{(l)}}, \quad (5)$$

$$u_k = \Re \frac{1}{2\pi i} \sum_{l=1}^3 (\pm)_{(l)} A_{k(l)} D_{(l)} \ln z_{(l)}, \quad (6)$$

where  $z_{(l)} = x_1 + p_{(l)} x_2$  is a complex variable and  $(\pm)_{(l)}$  is the sign of the imaginary part of  $p_{(l)}$ .

If the dislocation is generated by cutting the elastic material on the plane  $x_2=0$  and giving a relative displacement  $\mathbf{b}$  to the faces of the cut then the energy per unit length of dislocation line is†

$$E = - \int_{r_0}^R b_i \tau_{i2}(x_1, 0) dx_1, \quad (7)$$

where  $r_0$  is the inner core radius at which Hooke's law and linear elasticity break down, and  $R$  has the dimensions of the crystal. From equation (5)  $\tau_{i2}(x_1, 0)$  is inversely proportional to  $x_1$  so that the integral (7) gives

$$E = \frac{K b^2}{4\pi} \ln \frac{R}{r_0}, \quad (8)$$

where the factor  $K$  is given by

$$K b^2 = g b_i \sum_{l=1}^3 (\pm)_{(l)} B_{i2(l)} D_{(l)}, \quad (9)$$

\* Summations over repeated subscripts are inferred, except for those over  $l$  which are always shown explicitly.

† The energy contributions arising from the non-zero surface stresses at the inner and outer boundaries are self-cancelling.

in which  $g$  denotes *imaginary part of*. It may be verified that by virtue of Eq. (1) the same expression for  $K$  is derived if the dislocation is formed by cutting the elastic material on the plane  $x_1=0$  instead of on  $x_2=0$ .

The factor  $K$  is the only part of the energy equation (8) which depends directly on the elastic constants, and therefore on the orientation in the crystal of the dislocation line and its associated Burgers vector. The elastic constants are of course referred to the *dislocation axes*, i.e., to a set of orthogonal axes with the  $x_3$  axis along the dislocation line, which are not in general identical with the normal crystal axes. We shall adopt the notation of Seeger and Schöck<sup>5</sup> and denote elastic constants referred to crystal axes by heavy type, so that from the law for the transformation of a fourth-order tensor we have

$$C_{ijkl} = \alpha_{ip} \alpha_{jq} \alpha_{kr} \alpha_{ls} \mathbf{C}_{pqrs}, \quad (10)$$

where  $\alpha_{ij}$  is the cosine of the angle between the  $x_i$  dislocation axis and the  $x_j$  crystal axis.

The equations (2) and (3) may be solved in determinantal form for  $D_{(l)}$ , so that on substituting for  $D_{(l)}$  in (9) the energy factor  $K$  can be expressed in terms of  $A_{k(l)}$  and  $p_{(l)}$ . The result may be reduced to the form

$$K b^2 = \phi_{jk} b_j b_k, \quad (11)$$

where  $\phi_{jk} = D_{jk}/iD$ , in which  $D$  is the  $6 \times 6$  determinant

$$D = \begin{vmatrix} A_{k(l)} & A_{k(l)}^* \\ B_{k2(l)} & B_{k2(l)}^* \end{vmatrix} \quad (12)$$

and  $D_{jk}$  is the determinant  $D$  with the  $k$ 'th row replaced by  $(\pm)_{(l)} B_{j2(l)}$ . This shows clearly that  $K b^2$  is a quadratic combination of the slip vector components  $(b_1, b_2, b_3)$ , since both the  $A_{k(l)}$  and  $B_{k2(l)}$  are functions only of the elastic constants.

### 3. COMPONENT INTERACTION ENERGIES

In calculating the energy of any particular dislocation it is sometimes possible to choose the dislocation axes so that the separate dislocation energies of the slip vector components are known. It is not in general true, however, that the separate component energies are additive, as is the case for isotropic materials, but they may be so if the dislocation axes lie along suitable symmetry directions in the crystal.

One such condition for vanishing interactions is that the  $x_2 x_3$  plane be a symmetry plane of the crystal; a crystallographically equivalent condition is that the  $x_1$  axis has a twofold rotational symmetry, i.e., is a diad axis of the crystal. In this case it may be shown that the expression for the energy factor  $K$ , which we have seen from equation (11) to be quadratic in the slip vector components, contains no cross-terms in  $b_1 b_2$  or  $b_1 b_3$ , i.e.,  $\phi_{12} = \phi_{21} = \phi_{13} = \phi_{31} = 0$ . Terms in  $b_2 b_3$  are not necessarily absent, however, unless further symmetry conditions are satisfied.

The above result may be proved either from the general expression (11) for the energy factor  $K$ , or more simply from symmetry arguments. Suppose that the  $x_2x_3$  plane is a plane of symmetry and that we generate the dislocation by cutting the elastic material in this plane. Then the elastic energy is

$$E = -\frac{1}{2} \int_{r_0}^R [b_1\tau_{11}(0, x_2) + b_2\tau_{12}(0, x_2) + b_3\tau_{13}(0, x_2)] dx_2. \quad (13)$$

Reflecting the entire crystal and dislocation structure in the  $x_2x_3$  plane changes the sign of some stress components, giving  $\tau_{11}'(0, x_2) = \tau_{11}(0, x_2)$ ,  $\tau_{12}'(0, x_2) = -\tau_{12}(0, x_2)$ ,  $\tau_{13}'(0, x_2) = -\tau_{13}(0, x_2)$ , and generates a new dislocation with Burgers vector  $\mathbf{b}' = (b_1, -b_2, -b_3)$ , as may be seen by reflecting the Burgers circuit in the  $x_2x_3$  plane. Since the components of stress are a linear function of the slip vector components we conclude that the stresses on the plane  $x_1=0$  take the form

$$\left. \begin{aligned} \tau_{11}(0, x_2) &= \alpha_{11}(x_2)b_1 \\ \tau_{12}(0, x_2) &= \alpha_{22}(x_2)b_2 + \alpha_{23}(x_2)b_3 \\ \tau_{13}(0, x_2) &= \alpha_{32}(x_2)b_2 + \alpha_{33}(x_2)b_3 \end{aligned} \right\} \quad (14)$$

so that the energy integral (13) contains no terms in  $b_1b_2$  or  $b_1b_3$ , although the  $b_2b_3$  term does not in general vanish.

Thus if the  $x_1$  axis is normal to a symmetry plane, i.e., is a diad, then we have  $\phi_{12} + \phi_{21} = \phi_{13} + \phi_{31} = 0$ . Similarly, if the  $x_2$  axis has this property then  $\phi_{12} + \phi_{21} = \phi_{23} + \phi_{32} = 0$ , so that if both the  $x_1$  and  $x_2$  axes are diads (this implies that  $x_3$  is also a diad) there are no interaction energies between any of the three dislocation components and the separate component energies are therefore additive. The above condition is however not a unique one, since it may be shown that a sixfold symmetry about any one dislocation axis is also a sufficient condition for the interaction energy terms to vanish.

#### 4. ANALYTIC SOLUTION TO THE ELASTICITY EQUATIONS

In calculating the elastic energy of a dislocation we require to find the most general case where the elasticity solution outlined in section 2 yields a completely analytic result. The remaining cases of interest must then of necessity be evaluated numerically.

The analysis given below follows closely that of Eshelby *et al*, but for the edge dislocation we do not restrict the dislocation line to a  $\langle 100 \rangle$  direction in a cubic crystal. The calculation of the energy factor for a screw and edge dislocation is therefore only briefly outlined.

The condition for the edge and screw component solutions to be separable is that  $C_{\alpha\beta\gamma\delta} = 0$  ( $\alpha, \beta, \gamma = 1, 2$ ), or in the contracted notation  $c_{14} = c_{15} = c_{24} = c_{25} = c_{46} = c_{56} = 0$ ,

for the equation (1) then reduces to

$$\left. \begin{aligned} A_1(c_{11} + 2p c_{16} + p^2 c_{66}) \\ + A_2(c_{16} + p[c_{12} + c_{66}] + p^2 c_{26}) = 0 \\ A_1(c_{16} + p[c_{12} + c_{66}] + p^2 c_{66}) \\ + A_2(c_{66} + 2p c_{26} + p^2 c_{22}) = 0 \\ A_3(c_{55} + 2p c_{45} + p^2 c_{44}) = 0, \end{aligned} \right\} \quad (15)$$

in which  $A_3$ , which is associated with the  $u_3$  (screw) component of displacement, is clearly independent of  $A_1$  and  $A_2$ .

For a pure screw dislocation  $A_1 = A_2 = 0$ ,  $A_3 \neq 0$ , so that from (15) we have a quadratic equation for  $p$  giving the complex root  $c_{44}p_{(1)} = -c_{45} + i(c_{44}c_{55} - c_{45}^2)^{1/2}$ . For the slip vector  $(0, 0, b)$  equations (2) and (9) reduce to

$$\Re A_{3(1)} D_{(1)} = b, \quad (16)$$

$$Kb = \Im A_{3(1)} D_{(1)} (c_{45} + p_{(1)} c_{44}), \quad (17)$$

and since  $c_{45} + p_{(1)} c_{44}$  is purely imaginary this gives

$$K = (c_{44}c_{55} - c_{45}^2)^{1/2}. \quad (18)$$

This is the energy factor for a pure screw dislocation when the array of elastic constants takes the form

$$\begin{array}{cccccc} c_{11} & c_{12} & c_{13} & 0 & 0 & c_{16} \\ & c_{22} & c_{23} & 0 & 0 & c_{26} \\ & & c_{33} & c_{34} & c_{35} & c_{36} \\ & & & c_{44} & c_{45} & 0 \\ & & & & c_{55} & 0 \\ & & & & & c_{66} \end{array} \quad (19)$$

A twofold symmetry about the dislocation line (i.e., the  $x_3$  axis is a diad axis) is sufficient to give this array with also  $c_{34} = c_{35} = 0$ .

There is no slip plane associated with an elastic screw dislocation so that a degree of freedom exists in orientating the  $x_1$  and  $x_2$  axes. It may be verified that  $c_{44}c_{55} - c_{45}^2$  is invariant for a rotation of the axes about the dislocation line ( $x_3$  axis).

For an edge dislocation we set  $A_3 = 0$  in equation (15); the determinantal condition gives a quadric equation for  $p$ , which if we let  $c_{16} = c_{26} = 0$  reduces to the quadratic equation in  $p^2$

$$c_{22}c_{66}p^4 + (c_{11}c_{22} - c_{12}^2 - 2c_{12}c_{66})p^2 + c_{11}c_{66} = 0.$$

The roots are written in the form  $p_{(1)} = \lambda e^{i\alpha}$ ,  $p_{(2)} = -\lambda e^{i\alpha}$ , where  $\lambda^4 = c_{11}/c_{22}$  and

$$\alpha = \frac{1}{2} \cos^{-1} \left[ \frac{2c_{12}c_{66} + c_{12}^2 - \bar{c}_{11}^2}{2\bar{c}_{11}c_{66}} \right], \quad (20)$$

in which  $\bar{c}_{11} = (c_{11}c_{22})^{1/2}$ . The remaining analysis is similar to that of Eshelby *et al* for an edge dislocation along a cube direction, but with  $c_{44}$  replaced by  $c_{66}$ ,  $c_{11}$  by  $\bar{c}_{11}$  and the additional quantity  $\lambda$  introduced. We let

$A_{1(l)} = 1$ ,  $A_{2(l)} \equiv A_{(l)}$  ( $l=1, 2$ ), where  $A_{(l)}$  is given by

$$A_{(2)} = -A_{(1)} = \lambda \frac{c_{66}e^{i\alpha} + \bar{c}_{11}e^{-i\alpha}}{(c_{12} + c_{66})}. \quad (21)$$

The equations (2) and (3) for  $D_{(l)}$  reduce for a  $(b, 0, 0)$  slip vector to

$$\left. \begin{aligned} \Re(D_{(1)} + D_{(2)}) &= b \\ \Re(D_{(1)} - D_{(2)})A_{(1)} &= 0 \\ \Re(D_{(1)} - D_{(2)})\left(\frac{A_{(1)}}{\lambda} + e^{i\alpha}\right) &= 0 \\ \Re(D_{(1)} + D_{(2)})\left(c_{12} + \bar{c}_{11}e^{i\alpha}\frac{A_{(1)}}{\lambda}\right) &= 0, \end{aligned} \right\} \quad (22)$$

which have the solution

$$D_{(1)} = D_{(2)} = -\frac{ib}{2 \sin 2\alpha} \left\{ \frac{\bar{c}_{11}e^{2i\alpha} - c_{12}}{\bar{c}_{11}} \right\}. \quad (23)$$

The energy factor  $K$  given by Eq. (9) reduces to

$$K = 2\lambda c_{66}g \left\{ D_{(1)} \left( e^{i\alpha} + \frac{A_{(1)}}{\lambda} \right) \right\}, \quad (24)$$

which after some analysis gives

$$K = (\bar{c}_{11} + c_{12}) \left[ \frac{c_{66}(\bar{c}_{11} - c_{12})}{c_{22}(\bar{c}_{11} + c_{12} + 2c_{66})} \right]^{\frac{1}{2}}. \quad (25)$$

This is the energy factor for an edge dislocation with slip vector  $(b, 0, 0)$  when the array of elastic constants takes the form

$$\begin{array}{cccccc} c_{11} & c_{12} & c_{13} & 0 & 0 & 0 \\ & c_{22} & c_{23} & 0 & 0 & 0 \\ & & c_{33} & c_{34} & c_{35} & c_{36} \\ & & & c_{44} & c_{45} & 0 \\ & & & & c_{55} & 0 \\ & & & & & c_{66} \end{array} \quad (26)$$

A twofold symmetry about the dislocation line is not in this case sufficient to give the required array, since it does not imply that  $c_{16} = c_{26} = 0$ . The array of elastic constants takes the form (26) if either

- (i) each dislocation axis has a twofold symmetry,
- or (ii) any one axis has a sixfold (hexagonal) symmetry.

Both these conditions imply that  $c_{34} = c_{35} = c_{36} = c_{45} = 0$ .

We can now give the general analytic formula for the energy factor  $K$  of a straight dislocation with slip vector  $\mathbf{b} = (b_1, b_2, b_3)$ , whose components are along (orthogonal) dislocation axes in the crystal satisfying either of the condition (i) or (ii) given above. From Sec. 3 the component energies are seen to be additive, so that

we have

$$Kb^2 = K_1 b_1^2 + K_2 b_2^2 + K_3 b_3^2, \quad (27)$$

where

$$K_1 = (\bar{c}_{11} + c_{12}) \left[ \frac{c_{66}(\bar{c}_{11} - c_{12})}{c_{22}(\bar{c}_{11} + c_{12} + 2c_{66})} \right]^{\frac{1}{2}},$$

$$K_2 = \left( \frac{c_{22}}{c_{11}} \right)^{\frac{1}{2}} K_1,$$

$$K_3 = (c_{44}c_{55})^{\frac{1}{2}},$$

and

$$\bar{c}_{11} = (c_{11}c_{22})^{\frac{1}{2}}.$$

The value of  $K_2$  is found here by using the result (25) with axes rotated through an angle  $\pi/2$  about the  $x_3$  axis.

For an isotropic material the elastic constants are the same for all orientations of the dislocation axes, and are  $c_{11} = c_{22} = \lambda + 2\mu$ ,  $c_{12} = \lambda$ ,  $c_{44} = c_{55} = c_{66} = \mu$ . This gives

$$K_1 = K_2 = \frac{2(\lambda + \mu)\mu}{(\lambda + 2\mu)} = \frac{\mu}{1 - \nu}, \quad K_3 = \mu, \quad (28)$$

where  $\mu$  is the shear modulus and  $\nu$  is Poisson's ratio.

## 5. DISLOCATIONS IN CUBIC CRYSTALS

We shall apply the results of the theory outlined in Sec. 4 to crystals with cubic symmetry and shall consider all types and orientations of dislocations for which the elasticity theory equations yield an analytic solution. The condition for this to be so in the cubic system is that the dislocation axes shall lie along directions of twofold symmetry in the crystal. For a cubic crystal there are only two essentially different sets of axes which satisfy this condition, namely (1) the cubic axes and (2) the axes generated by rotating the cubic axes through an angle  $\pi/4$  about any one axis, e.g.,  $0x_1 = [10\bar{1}]$ ,  $0x_2 = [010]$ ,  $0x_3 = [101]$ . In one case the location line ( $x_3$  axis) lies along a  $\langle 100 \rangle$  direction and in the other along a  $\langle 110 \rangle$  direction. Thus we conclude that a dislocation line in a cubic crystal with an arbitrary Burgers vector has an analytic elastic solution only if it lies along either a  $\langle 100 \rangle$  or  $\langle 110 \rangle$  direction in the crystal. In other cases of interest it is necessary to solve the equations outlined in Sec. 2 entirely numerically.

In considering the different dislocations for which an analytic expression for the energy factor  $K$  may be derived we shall restrict the choice of Burgers vector to  $\langle 100 \rangle$ ,  $\langle 110 \rangle$  and  $\langle 111 \rangle$  directions in the cubic system.

The energy factor for a dislocation with Burgers vector  $\mathbf{b} = (b_1, b_2, b_3)$  and the cubic axes as dislocation axes is from (27) given by

$$Kb^2 = K_1' b_1^2 + K_2' b_2^2 + K_3' b_3^2, \quad (29)$$



TABLE I. The energy factor  $K$  for five types of dislocation lying along an  $[001]$  direction in a cubic crystal.

Type of dislocation	$b$	$K$
Screw	$[001]$	$K_3'$
Edge in $\{100\}$	$[100]$	$K_1'$
Edge in $\{110\}$	$[110]$	$\frac{1}{2}(K_1' + K_2')$
Mixed in $\{100\}$	$[101]$	$\frac{1}{2}(K_1' + K_3')$
Mixed in $\{110\}$	$[111]$	$\frac{1}{3}(K_1' + K_2' + K_3')$

where

$$K_1' = K_2' = (c_{11} + c_{12}) \left[ \frac{c_{44}(c_{11} - c_{12})}{c_{11}(c_{11} + c_{12} + 2c_{44})} \right]^{\frac{1}{2}},$$

$$K_3' = c_{44}.$$

There are five slip vector directions which give essentially different types of dislocation. These are listed in Table I, together with the type of dislocation and slip plane, and the value of  $K$  in terms of  $K_1'$ ,  $K_2'$  and  $K_3'$  given above; these results correspond to those given by Read.<sup>7</sup>

Secondly, we consider the set of dislocation axes

$$0x_1 = [10\bar{1}], \quad 0x_2 = [010], \quad 0x_3 = [101],$$

where  $0x_3$  is the dislocation line. The elastic constants for these axes are

$$\left. \begin{aligned} c_{11} &= \frac{1}{2}(c_{11} + c_{12} + 2c_{44}) \\ c_{22} &= c_{11} \\ c_{12} &= c_{12} \\ c_{44} &= c_{66} = c_{44} \\ c_{55} &= \frac{1}{2}(c_{11} - c_{12}), \end{aligned} \right\} \quad (30)$$

and therefore from (27) the energy factor is given by

$$Kb^2 = K_1''b_1^2 + K_2''b_2^2 + K_3''b_3^2, \quad (31)$$

where  $K_1''$ ,  $K_2''$ ,  $K_3''$  are given by the  $K_1$ ,  $K_2$ ,  $K_3$  of equation (27) with the expressions (30) for the elastic constants substituted. For the screw component

$$K_3'' = \left[ \frac{1}{2}c_{44}(c_{11} - c_{12}) \right]^{\frac{1}{2}} = \frac{c_{44}}{(A)^{\frac{1}{2}}}, \quad (32)$$

where  $A = 2c_{44}/(c_{11} - c_{12})$  is the "anisotropy factor" of

TABLE II. The energy factor  $K$  for seven dislocations having a  $[101]$  line direction in a cubic crystal.

Type of dislocation	$b$	$K$
Mixed in $\{100\}$	$[100]$	$\frac{1}{2}(K_1'' + K_3'')$
Edge in $\{110\}$	$[010]$	$K_2''$
Edge in $\{100\}$	$[10\bar{1}]$	$K_1''$
Mixed in $\{111\}$	$[110]$	$\frac{1}{3}(K_1'' + 2K_2'' + K_3'')$
Screw	$[101]$	$K_3''$
Mixed in $\{110\}$	$[111]$	$\frac{1}{3}(K_2'' + 2K_3'')$
Edge in $\{112\}$	$[1\bar{1}1]$	$\frac{1}{3}(2K_1'' + K_2'')$

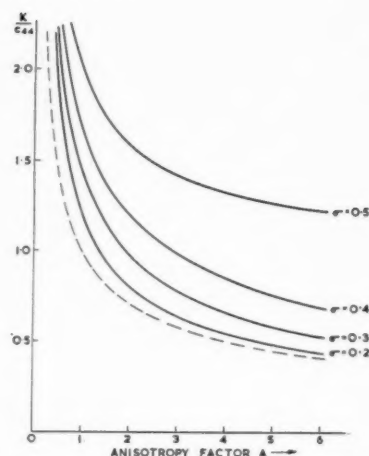


FIG. 1. Variation of  $K$  with the anisotropy factor  $A$  for a dislocation in a  $\{111\}$  plane and at an angle  $\pi/3$  to its Burgers vector, where  $\sigma = c_{12}/(c_{11} - c_{12})$  is Poisson's ratio for a  $\langle 100 \rangle$  extension. The broken curve is for a  $\langle 110 \rangle$  screw dislocation (independent of  $\sigma$ ).

Zener.<sup>8</sup> For these axes there are seven slip vectors which give essentially different types of dislocation; these are listed in Table II.

Thus for the cubic system there is a total of twelve dislocations with  $\langle 100 \rangle$ ,  $\langle 110 \rangle$  or  $\langle 111 \rangle$  slip vectors which have completely analytic solutions to the equations of elasticity. Only the expressions for the energy factor  $K$  have been listed here but we could if required set out the complete expressions for the components of stress and displacement in each case, using the equations of Sec. 2 and Sec. 4.

The energy factor  $K$  is plotted in Fig. 1 against the anisotropy factor  $A$  for two dislocations with  $\langle 110 \rangle$  slip vectors, namely (a) a pure screw dislocation, and (b) a mixed dislocation in the  $\{111\}$  plane, with an angle  $\pi/3$  between the slip vector and dislocation line. For cubic metals  $A$  exceeds unity so that the energy is less than would be predicted by the isotropic approximation.

## 6. FACE-CENTERED CUBIC CRYSTALS

In the face-centred cubic lattice the dislocations of principal interest are those with Burgers vectors in the  $\langle 110 \rangle$  direction, since this is both the shortest lattice vector and the observed slip direction.

From Sec. 5 it will be seen that we can calculate the energies of five dislocations of this type, these being

- (1) a pure screw dislocation (no slip plane),
- (2) and (3) an edge and a mixed ( $\theta = \pi/4$ ) dislocation in the  $\{100\}$  plane,
- (4) an edge dislocation in the  $\{110\}$  plane,
- (5) a mixed dislocation ( $\theta = \pi/3$ ) in the  $\{111\}$  plane,

where  $\theta$  is the angle which the  $\langle 110 \rangle$  Burgers vector makes with the dislocation line.

To obtain a more complete picture of how the dislocation energy varies with orientation of dislocation line

in a face-centred cubic metal we have computed the energy factors for the following cases:

- (i) edge dislocation ( $\theta = \pi/2$ ) in the  $\{111\}$  plane,
- (ii) mixed dislocation ( $\theta = \pi/6$ ) in the  $\{111\}$  plane,
- (iii) and (iv) mixed dislocations  $\cos^2\theta = \frac{2}{3}$  and  $\frac{1}{3}$  (respectively) in the  $\{110\}$  plane.

For cases (i) and (ii) we set up the dislocation axes  $0x_1 = [0\bar{1}1]$ ,  $0x_2 = [111]$ ,  $0x_3 = [211]$ , and calculate from the transformation law (10) the elastic constants relative to these axes. Since the  $x_1$  axis has a twofold symmetry and the  $x_2$  axis a threefold symmetry the array of constants takes the form

$$\begin{array}{cccccc} c_{11} & c_{12} & c_{13} & c_{14} & 0 & 0 \\ & c_{22} & c_{12} & 0 & 0 & 0 \\ & & c_{11} & -c_{14} & 0 & 0 \\ & & & c_{44} & 0 & 0 \\ & & & & c_{55} & c_{14} \\ & & & & & c_{44} \end{array} \quad (33)$$

in which  $c_{55} = \frac{1}{2}(c_{11} - c_{13})$ . These are given in terms of the elastic constants for the cubic axes by

$$\begin{aligned} c_{11} &= c_{11} + \phi, & c_{22} &= c_{11} + (4/3)\phi, \\ c_{12} &= c_{12} - \frac{2}{3}\phi, & c_{14} &= -\frac{\sqrt{2}}{3}\phi, \\ c_{44} &= c_{44} - \frac{2}{3}\phi, & c_{55} &= c_{44} - \frac{1}{3}\phi, \end{aligned}$$

where  $\phi = c_{44} - \frac{1}{2}(c_{11} - c_{12})$ . For case (i) the slip vector components are  $b(1,0,0)$  and for (ii)  $b(\frac{1}{2}, 0, \sqrt{3}/2)$ . The elasticity equations are solved numerically in each case for the metals copper and gold, taking the following values for the single crystal elastic constants (units of  $10^{12}$  dynes/cm<sup>2</sup>).

	$c_{11}$	$c_{12}$	$c_{44}$	Reference
Cu	1.710	1.239	0.756	Lazarus <sup>9</sup>
Au	1.87	1.57	0.436	Schmid and Boas <sup>10</sup>

The cases (iii) and (iv) are evaluated numerically in a similar manner, and using the same set of dislocation axes as above, but with interchanges in  $(x_1, x_2, x_3)$ . For case (iii) the axes are  $0x_1 = [111]$ ,  $0x_2 = [0\bar{1}1]$ ,  $0x_3 = [211]$ , and for case (iv)  $0x_1 = [211]$ ,  $0x_2 = [0\bar{1}1]$ ,  $0x_3 = [111]$ .

The following are the computed values of the energy factor  $K$  (units of  $10^{12}$  dynes/cm<sup>2</sup>) for these four cases.

	(i)	(ii)	(iii)	(iv)
Cu	0.745	0.519	0.485	0.569
Au	0.507	0.328	0.314	0.382

On combining these numerical results with the analytic cases described in section 5 we can form quite a detailed

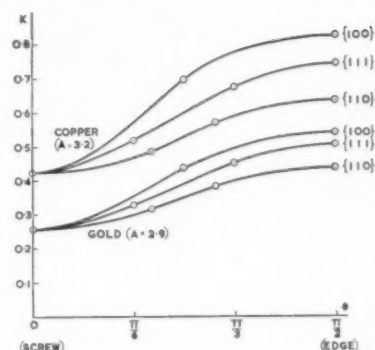


FIG. 2. The variation of  $K$  (units of  $10^{12}$  dynes/cm<sup>2</sup>) with the edge-screw composition angle  $\theta$ , for three types of dislocation slip plane in copper and gold.

picture of the way in which the energy factor for a dislocation with a  $\langle 110 \rangle$  slip vector varies with its orientation in the crystal.

Figure 2 shows the variation of  $K$  with the edge-screw composition of dislocations in the  $\{100\}$ ,  $\{110\}$  and  $\{111\}$  planes of copper and gold, with curves of best fit drawn through the calculated points. In Fig. 3 are plotted the similar curves of  $K/c_{44}$  for copper, aluminium, and isotropy ( $\nu = \frac{1}{3}$ ); the curves for gold would lie near to those for copper on this graph and are omitted for the sake of clarity.

## 7. CLOSE-PACKED HEXAGONAL CRYSTALS

In the hexagonal system we restrict our calculations to dislocations having  $\langle 11\bar{2}0 \rangle$  Burgers vectors. As for the cubic system these are a limited number of cases when the elasticity theory yields a completely analytic solution. These are (1) the screw dislocation, (2) the edge and any mixed dislocation in the basal plane, and (3) the edge dislocation in the prismatic plane.

The energy factors for these cases are easily found on erecting suitable dislocation axes and applying the

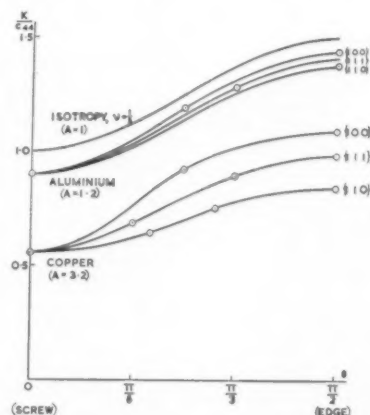


FIG. 3. Curves of  $K/c_{44}$  against the edge-screw composition angle  $\theta$  for copper, aluminium and isotropy ( $\nu = \frac{1}{3}$ ).

results of Sec. 4. In each case the  $x_3$  axis is along the dislocation line and one of the axes is in the  $c$ -direction of the crystal; from Sec. 4 an analytic solution exists if one of the dislocation axes has a sixfold symmetry, and the component dislocation energies are additive. The elastic constants for the dislocation axes are calculated in terms of those for the crystal axes, and on using Eq. (27) we find that

$$K_{\text{screw}} = \left[ \frac{1}{2} c_{44} (\mathbf{c}_{11} - \mathbf{c}_{12}) \right]^{\frac{1}{2}} = \frac{c_{44}}{(A)^{\frac{1}{2}}}, \quad (34)$$

$$K_{\text{edge}}(\text{basal}) = (\bar{\mathbf{c}}_{11} + \mathbf{c}_{13}) \left[ \frac{c_{44} (\bar{\mathbf{c}}_{11} - \mathbf{c}_{13})}{c_{33} (\bar{\mathbf{c}}_{11} + \mathbf{c}_{13} + 2c_{44})} \right]^{\frac{1}{2}}, \quad (35)$$

where  $\bar{\mathbf{c}}_{11} = (\mathbf{c}_{11} \mathbf{c}_{33})^{\frac{1}{2}}$  and

$$K_{\text{edge}}(\text{prismatic}) = \frac{c_{11}^2 - c_{12}^2}{2c_{11}}. \quad (36)$$

The hexagonal lattice is uniaxial in that the elastic constants are invariant for a rotation of the reference axes about the  $c$ -axis, so that the energy factor for a mixed dislocation in the basal plane is given by the isotropic relation

$$K_{\text{mixed}}(\text{basal}) = K_{\text{edge}}(\text{basal}) \sin^2 \theta + K_{\text{screw}} \cos^2 \theta, \quad (37)$$

where  $\theta$  is the angle between the slip vector and dislocation line.

Another plane of interest in the close-packed hexagonal system is the  $\{10\bar{1}1\}$  pyramidal plane. There is no analytic solution for an edge dislocation in this plane and the energy factor has therefore been computed for the metals zinc and beryllium, using the following values for the single crystal elastic constants (units of  $10^{12}$  dynes/cm<sup>2</sup>) and axial ratios.

	$c_{11}$	$c_{33}$	$c_{44}$	$c_{12}$	$c_{13}$	Reference	$c/a$
Zn	1.630	0.623	0.379	0.256	0.508	Schmid and Boas <sup>10</sup>	1.856
Be	3.08	3.57	1.10	-0.58	0.87	Gold <sup>11</sup>	1.568

The numerical values for the energy factors of the above dislocations are given in the Table III. It will be noted that there is a marked difference in the general behaviour of the energy factor for the two metals. The almost constant values of  $K$  for different slip planes and

TABLE III. Values of  $K/c_{44}$  for edge and screw dislocations in the close packed hexagonal metals zinc and beryllium.

Metal	Type of dislocation	Slip plane		
		Basal	Prismatic	Pyramidal
Zn	Screw	1.346	1.346	1.346
	Edge	1.462	2.098	1.982
Be	Screw	1.290	1.290	1.290
	Edge	1.307	1.350	1.281

types of dislocation in beryllium liken it to an isotropic material with zero Poisson's ratio. The energy factor for the basal plane dislocations in zinc is fairly constant also, but in the prismatic and pyramidal planes there is a more marked variation between the edge and screw dislocations.

## 8. THE PEIERLS MODEL OF A DISLOCATION

In deriving Eq. (8) for the energy of a dislocation the elastic solution is excluded from a cylinder of radius  $r_0$ , inside which both Hooke's law and linear elasticity theory break down. The energy contribution from this core region is difficult to calculate precisely but may be estimated from a Peierls-type dislocation model, in which deviations from Hooke's law for large shear strains are taken into account along the dislocation slip plane. A detailed summary of the properties of this model has been given by Nabarro.<sup>12</sup>

The essential feature of the Peierls model is the interatomic force-displacement law which is postulated for the shear displacement of neighbouring planes of atoms. Peierls and Nabarro took this to be a sinusoidal function with the periodicity of the lattice and a slope for small shear strains equal to the shear modulus of the crystal, and Eshelby<sup>2</sup> has shown how the results of their analysis may be modified for anisotropic elastic media. If the dislocation line does not lie along a symmetry direction of the crystal, however, it is not strictly correct to ascribe a shear modulus to the slip plane, since from Hooke's law each component of shear stress is in general coupled to all six strain components instead of only to the one shear strain component, as in the isotropic case. As a first approximation we may neglect these coupling terms on the slip plane and take the shear moduli as  $c_{44}$ ,  $c_{55}$  and  $c_{66}$ .

The analysis of Peierls and Nabarro has been extended by Foreman, Jaswon and Wood,<sup>13</sup> who considered a more general law of force in which the amplitude may be varied, but the initial slope is kept constant. When the solution is modified for anisotropic elasticity the total energy of an edge dislocation may be shown to be\*

$$E = \frac{Kb^2}{4\pi} \left[ \ln \frac{R}{2a\zeta} + 1 + \frac{a-1}{a} + \left( \frac{a-1}{2a} \right)^2 \right], \quad (38)$$

where the parameter  $a$  controls both the force law amplitude and the dislocation width,  $K$  is the energy factor for the corresponding elastic dislocation, and  $\zeta = \frac{1}{2} cK/c_{66}$  where  $c$  is the spacing of the planes of atoms which are parallel to the slip plane. The identical result holds for the screw dislocation except that  $c_{66}$  is replaced by  $c_{44}$ , if we take the slip plane to be the plane  $x_2 = 0$ . For both the screw and edge cases the Peierls-Nabarro dislocation with a sinusoidal law of force corresponds

\* The term  $(a-1)/a$  was omitted from the result given by Nabarro.<sup>12</sup>

to  $a=1$ . In Fig. 5 we plot the variation of the energy with the dislocation width for values of  $w$  greater than the Peierls-Nabarro width  $2\zeta$ .

A similar analysis (unpublished) has been made for a second harmonic type force law, i.e., one in which a second harmonic term is added to the sine function assumed by Peierls, the linear combination being such that the initial slope is equal to the appropriate shear modulus. The energy *versus* relative displacement for such a law of force then takes the form shown in Fig. 4, there being a metastable equilibrium position at a relative displacement of  $\frac{1}{2}b$  when the second harmonic term predominates. This is a first approximation to the situation in the octahedral planes of the face-centred cubic lattice where a stacking fault position exists midway between, but *not* in direct line with, the normal close packed positions. When the second harmonic term predominates in the law of force the solution represents two half dislocations (i.e. each with a slip vector  $\frac{1}{2}b$ ) connected by a "stacking fault." The width of the complete dislocation is approximately equal to the spacing of the halves and for large widths varies inversely as the stacking fault energy, as predicted by a purely elastic model. The total energy of the dislocation may be expressed directly in terms of the width  $w$ , giving

$$E = \frac{Kb^2}{4\pi} \left[ \ln \frac{R}{2\sigma} + 1 - \frac{1}{2} \ln \frac{w}{2\zeta} \right], \quad (39)$$

where  $w=2\zeta$  corresponds to the narrow Peierls-Nabarro dislocation. The energy again decreases with increasing width, as may be seen from Fig. 5, but not so rapidly as for the previous type of dislocation.

Seeger and Schöck<sup>5</sup> have made a detailed investigation of the problem of an edge or screw dislocation in a close-packed plane, using the Peierls model with anisotropic elasticity and deriving solutions by the approximate variational technique of Leibfried and Dietze. Both edge and screw components of displacement are involved, so that the Peierls type force law is replaced by an energy surface with minima at the equilibrium and stacking fault positions. The resulting expression for the total dislocation energy is a rather complicated

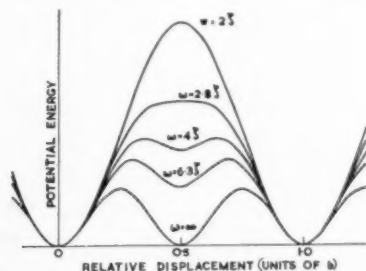


FIG. 4. Family of curves of potential energy against relative displacement for the second harmonic type law of force, showing the widths of the corresponding dislocations ( $w=2\zeta$  is the Peierls-Nabarro case).

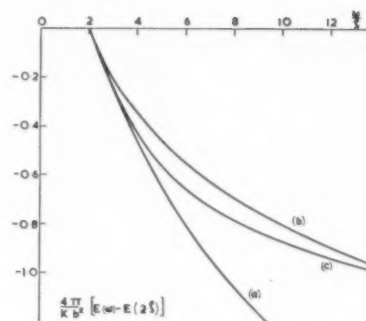


FIG. 5. Variation of dislocation energy with width  $w$  for (a) the Foreman, Jaswon and Wood force laws, (b) the second harmonic type of force law, and (c) an extended dislocation in a close packed plane (Seeger and Schöck).

function of the parameters involved but may be simplified somewhat since the total misfit energy of the slip plane atoms is a constant,<sup>12</sup> which is independent of the law of force and is equal to  $Kb^2/4\pi$  for the anisotropic case.\* With this simplification the energy is given by

$$E = \frac{Kb^2}{4\pi} \left[ \ln \frac{R}{2\sigma} - \frac{3-\chi}{12} \ln(1+\rho^2) + 1 \right], \quad (40)$$

where  $\rho$ ,  $\sigma$  and  $\chi$  are functions of the elastic constants and the stacking fault energy. In Fig. 5 we show the variation of this energy with the dislocation width, defined as in the previous two cases, for the case  $\chi=1$ ; the form of the curve is not very sensitive to the value of  $\chi$  in the range plotted. This curve lies reasonably close to that for the two dimensional second harmonic approximation, although for very large widths they must differ due to the different lengths of the dissociated slip vectors for the two cases.

As has been pointed out by Lomer and Nye<sup>14</sup> the Peierls model of a dislocation must of necessity neglect such effects as the "cracking" which may occur in the tensile side of the dislocation slip plane. This would be expected to modify the above estimate of the core energy, but these effects are, however, difficult to investigate without making a detailed lattice calculation.

## SUMMARY AND DISCUSSION

The energy per unit length of a straight dislocation line of either edge, mixed or screw character in an elastically anisotropic crystal is given by

$$E = \frac{Kb^2}{4\pi} \ln \frac{R}{r_0}, \quad (41)$$

where  $R$  is the radius of the dislocation strain field (the radius of the crystal for a single dislocation) and  $r_0$  is

\* The expression given by Seeger and Schöck for the slip plane misfit energy differs by only a few per cent from  $Kb^2/4\pi$ .



an effective core radius. The factor  $K$  is a function of both the single crystal elastic constants and the orientation in the crystal of the dislocation line and its Burgers vector, and has been calculated for a variety of dislocations in the cubic and hexagonal systems. The effective core radius  $r_0$  is more difficult to determine since it depends upon the nature of the inelastic interatomic forces acting in the dislocation core, but in the absence of a detailed lattice calculation of the core structure it may be estimated from the Peierls dislocation model discussed in Sec. 8.

The results for the energy factor  $K$  are most complete for the face-centred cubic lattice (Figs. 2 and 3), where it will be seen that for the metals so far considered the  $\{110\}$  plane is associated with lower values of  $K$  than is the observed  $\{111\}$  slip plane. If the criterion for determining the planes of slip in a crystal is that of minimum dislocation energy, then this suggests [Foreman and Lomer<sup>15</sup>] that core effects and dissociation on a close packed plane may be the more important factors.

For the hexagonal system the results in Table III show that for zinc the energy factor  $K$  takes the lowest values in the observed basal slip plane. Since this is a close packed plane there should be a further reduction in energy due to the dislocations becoming extended in this plane, the magnitude of this effect depending on the stacking fault energy. In contrast to zinc the values of  $K$  for beryllium are remarkably constant for the three dislocation slip planes considered.

It will be noted that the variations of  $K$  with the dislocation orientation are in general less than the

changes in the value of  $b^2$  due to alternative choices of the Burgers vector. Thus the anisotropy effects do not interfere with the well known result that the energy of a dislocation, which is proportional to  $Kb^2$ , is minimised by choosing its Burgers vector to be the shortest lattice vector of the crystal.

#### ACKNOWLEDGMENTS

The author wishes to acknowledge the benefit of valuable advice and encouragement from Dr. W. M. Lomer during the course of this work, and also to S. F. Pugh and Dr. J. W. Glen for stimulating discussions. I am also much indebted to E. B. Fossey and other members of the Harwell Computing Group for performing the numerical analysis in this paper.

#### REFERENCES

1. J. M. Burgers, Proc. Acad. Sci. Amst. **42**, 378 (1939).
2. J. D. Eshelby, Phil. Mag. **40**, 903 (1949).
3. J. D. Eshelby, W. T. Read, and W. Shockley, Acta Met. **1**, 251 (1953).
4. G. Leibfried, Zeit. fur Physik **135**, 23 (1953).
5. A. Seeger and G. Schöck, Acta Met. **1**, 519 (1953).
6. R. Bullough and B. A. Bilby, Proc. Phys. Soc. **B67**, 615 (1954).
7. W. T. Read, "Dislocations in Crystals" (London, McGraw-Hill Ltd., 1953), p. 120.
8. C. Zener, "Elasticity and Anelasticity of Metals" (Chicago University Press, 1948), p. 16.
9. D. Lazarus, Phys. Rev. **76**, 545 (1949).
10. E. Schmid and W. Boas, "Plasticity of Crystals," Eng. transl. (London, Hughes, 1950), p. 19.
11. L. Gold, Phys. Rev. **77**, 390 (1950).
12. F. R. N. Nabarro, Advances in Physics **1**, 269 (1952).
13. A. J. E. Foreman, M. A. Jaswon, and J. K. Wood, Proc. Phys. Soc. **A64**, 156 (1951).
14. W. M. Lomer and J. F. Nye, Proc. Roy. Soc. **A212**, 576 (1952).
15. A. J. E. Foreman and W. M. Lomer, Phil. Mag. **46**, 73 (1955).

# A STUDY OF PRIMARY AND CONJUGATE SLIP IN CRYSTALS OF ALPHA-BRASS\*

G. R. PIERCY,† R. W. CAHN† and A. H. COTTRELL‡

When a single crystal of alpha-brass is strained in tension the conjugate slip system does not become fully active until the tensile axis has "overshot" the  $[100]$ - $[111]$  symmetry line appreciably. Experiments on such crystals described in the present paper show that the amount of overshoot is substantially independent of the temperature and rate of straining, and is unaffected by intermediate strain ageing treatments. Easy glide in these crystals is accompanied by the passage of Lüders bands along the specimen and so cannot be distinguished from yield elongation. When two Lüders bands on different slip systems meet, each forms a barrier to the passage of the other which is impenetrable until the applied stress reaches the level at which conjugate slip normally propagates. An explanation of latent hardening and overshoot is proposed on the basis of these results.

## ETUDE DES GLISSEMENTS PRIMAIRES ET SECONDAIRES DANS LES CRISTAUX DE LAITON $\alpha$

Quand un monocristal de laiton  $\alpha$  est déformé par traction, les systèmes de glissement secondaires ne deviennent actifs que lorsque la direction de traction a nettement dépassé l'axe de symétrie  $[100]$ - $[111]$ . Les expériences sur ces cristaux, exposées dans ce travail, montrent que ce dépassement est indépendant de la température et de la vitesse de déformation et qu'il n'est pas affecté par les vieillissements intermédiaires. Le "glissement facile" dans ces cristaux est accompagné par la propagation de bandes de Lüders et ne peut pas être distingué du palier. Si deux bandes de Lüders correspondant à différents systèmes de glissement se rencontrent, elles forment une barrière infranchissable l'une pour l'autre jusqu'à ce que la contrainte appliquée atteigne la valeur à laquelle se propage le glissement secondaire. Une explication de la consolidation des systèmes latents est proposée sur ce principe.

## EINFACHES UND DOPPELTES GLEITEN IN ALPHA-MESSING KRISTALLEN

Wenn ein Einkristall aus alpha-Messing durch Zugbeanspruchung verformt wird, kommt die doppelte Gleitung erst dann völlig in Gang, wenn die Zugachse die  $[100]$ - $[111]$  Symmetrielinie merklich "überschritten" ("overshot") hat. Versuche an hier beschriebenen Kristallen zeigen, dass der Betrag der Überschreitung (overshoot) von der Temperatur und dem Verformungsgrad wirklich unabhängig ist und weiterhin durch eingeschobene Spannungs-Alterungsbehandlungen nicht beeinflusst wird. Die Leicht-Gleitung (easy glide) wird bei diesen Kristallen von der Wanderung Lüderssche Linien entlang der Probe begleitet und kann so nicht von der plastischen Dehnung unterschieden werden. Wenn zwei Lüderssche Linien auf verschiedenen Gleitsystemen zusammentreffen, bildet jede der beiden ein Hindernis für die Wanderung der anderen, das so lange undurchdringbar ist, bis die angelegte Spannung die Grösse erreicht hat, bei der normalerweise doppelte Gleitung auftritt. Auf Grund der vorliegenden Ergebnisse wird eine Erklärung für die latente Verfestigung und das Überschreiten (overshoot) vorgeschlagen.

## INTRODUCTION

This paper describes an investigation into the cause of the "overshoot" of the crystal orientation across the  $[100]$ - $[111]$  symmetry line during tensile deformation of alpha-brass single crystals. According to the usual theory of the deformation of single crystals in tension,<sup>1</sup> slip should occur on one system (the *primary* system) until the orientation of the crystal reaches the symmetry line. Beyond this point slip should occur equally on both the primary system and a second system (the *conjugate* system), causing the orientation to move along the symmetry line towards  $[211]$ . This theory agrees with early observations on copper<sup>2</sup> and aluminium,<sup>1,3</sup> but not with those on certain alloys. Results on the latter show that the crystal continues to slip almost entirely on the primary system after the orientation has reached the symmetry line,<sup>4-7</sup> causing the orientation to overshoot

this line, i.e., to continue moving towards  $[101]$ , the direction of primary slip. After a certain amount of this additional primary slip the conjugate system suddenly becomes active and further slip then concentrates itself on this system. The amount of overshoot is greatest for crystals containing 30 per cent zinc in copper;<sup>2</sup> this alloy was therefore chosen for the present experiments.

Previous work on the tensile deformation of alpha-brass has shown that during the initial horizontal part of the plastic stress-strain curve (called *easy glide*) the extension is not uniform along the gauge length and that the slip lines cluster together.<sup>8</sup> It follows that an orientation measurement taken during easy glide is not necessarily representative of the whole specimen. However, during the stage of strong linear hardening, which occurs between the stages of easy glide and of conjugate slip, the total extension and orientation are uniform along the sample. The experiments of von Göler and Sachs<sup>2</sup> showed that the plastic strain calculated from the change of orientation appears to be less than that measured directly. They attributed this difference to

\* Received January 4, 1955.

† Department of Physical Metallurgy, University of Birmingham, England.

‡ Formerly, Professor of Physical Metallurgy, University of Birmingham, England. Now at the Atomic Energy Research Establishment, Metallurgy Division, Harwell, England.

some conjugate slip assumed to occur during the period in which primary slip is predominant. However, for samples with initial orientations near  $[100]$  the amount of such conjugate slip needed to account for the discrepancy would be enough to produce a marked drift of the orientation towards  $[110]$ , the direction of conjugate slip. Because this drift has not been observed, doubt exists on this point. Furthermore, Maddin<sup>9</sup> did not observe any such conjugate slip in his metallographic studies of stretched brass crystals. He noticed a similar but much smaller discrepancy between the measured extension and that calculated from the measured change in orientation, which he attributed to cross-slip. Because of these differences of behavior and interpretation, a comparison of the measured and calculated extensions was included in the present investigation.

Two theories have been proposed to explain the overshoot phenomenon. The first, due to Koehler,<sup>10</sup> supposes that vacancies produced by dislocations moving in the primary slip planes migrate to nearby zinc atoms, thereby reducing alloy hardening near the active slip plane. After a certain amount of primary slip the alloy hardening is completely removed on these planes but still remains on the conjugate planes. Thus, slip does not start on the conjugate system until the applied shear stress on this exceeds that on the primary system by the same amount as the critical shear stress of brass exceeds that of copper. This explanation is consistent with experimental results for the effect of zinc content on the amount of overshoot. To test the theory further, samples of the same initial orientation can be strained at various temperatures and rates of strain to determine whether changes in the mobility of vacancies influence the amount of overshoot; a crystal strained in liquid air, for example, should show a smaller overshoot than one extended at room temperature.

The second theory, formed by the present writers at the beginning of this study, supposes that the difficulty in starting the conjugate slip is due to locking of the dislocations of the conjugate system by atmospheres of solute atoms, dislocations on the active primary slip planes having been freed from their atmospheres during the initial slip. This theory is consistent with the observation of a yield point in alpha brass crystals.<sup>11</sup> It can be tested further by extending a crystal until its orientation has crossed the symmetry line, so that the conjugate system carries the largest resolved shear stress, but not so far as to activate the conjugate system; if the crystal is then aged, to form atmospheres on all the dislocations, and strained again, slip ought then to occur preferentially on the conjugate system.

It will be noticed that in both of these theories the cause of overshoot is ascribed to some process of *softening* (vacancies, and release from atmospheres, respectively) which occurs on the primary planes, during the initial slip, but not on the conjugate planes. These theories thus diverge from the usual view<sup>12</sup> that overshooting is evidence for *latent hardening*, i.e., for a

positive hardening process on the conjugate system. The investigation described below has been mainly concerned with testing these theories.

## EXPERIMENTAL METHOD

The 70-30 brass was made from oxygen-free high-conductivity copper (99.99 per cent) and high-purity zinc (99.999 per cent), which were melted together in an alundum-lined crucible, chill cast, and then drawn to 1.5 mm diameter wire. Pieces of this wire, 12 cm long, were grown into single crystals under argon by the Andrade and Roscoe fusion method,<sup>13</sup> being supported in silica quills and coated with graphite during growth. To verify that the graphite had no appreciable effect on the mechanical properties of these crystals, a few crystals were grown in moulds of powdered alumina; the latter gave the same stress-strain curves and showed the same ageing behavior as the former. After growth, all crystals were homogenized under argon for five days at 850°C, air-cooled in silica quills, and etched in dilute nitric acid. After wire loops, for mounting in the testing machine, had been soldered or brazed on its ends, giving a working length of 3.5 cm for the tensile experiment, each crystal was finally electropolished using 8 per cent hypophosphoric acid in water.

Analyses were made of the finished specimens. Spectrographic analysis gave the following percentages of impurities: Fe, 0.01 to 0.04; Cd, Ni, Pb, Sn, each <0.01; As, <0.003; Sb, <0.002; Bi <0.001; Al, Mn, not detected. A detailed chemical analysis of one specimen showed that the copper content was constant to within 0.3 per cent along its gauge length. Chemical analyses on all specimens gave copper contents ranging from 70.7 to 72.3 per cent.

The tensile experiments were made on a hard machine of the Polanyi<sup>14</sup> type, with a normal strain rate of  $4.2 \times 10^{-5}$  per second. The orientations of specimens were measured *in situ* during the tensile experiments by means of the back-reflection Laue method. To ensure that the initial orientation was uniform along the gauge length, each specimen was first examined by back-reflection with an X-ray beam collimated into a line segmented into five parts. In the early experiments frequent orientation measurements were made during deformation, but in the later ones it proved sufficient to make one measurement (at three points along the gauge length) after 0.2 per cent primary extension and another after 4 per cent extension on the conjugate system.

In all experiments at room temperature the point at which conjugate slip began was determined by continual microscopical examination (at 15X) of the deforming specimen during the period of linear hardening, after easy glide. A change in the slope of the load-extension curve always occurred at the start of conjugate slip.

Annealing of specimens at temperatures below 300°C was done on the tensile machine, using a bath of silicone oil. Annealing at 720°C was done elsewhere, with the

specimen suspended vertically inside a brass sleeve and sealed off in silica under argon.

## RESULTS

### a. Distribution of Primary Slip

To study the distribution of primary slip along the gauge length, and to examine the relation between the extension and the change of orientation, three crystals were strained on each of which fine silica hairs had been attached with Canada balsam at six places along the gauge length. During each experiment the distances between successive hairs were measured and also calculated (assuming single slip) from the changes of orientation measured at points midway between hairs. In every case where the distribution of slip lines between two hairs was uniform, the measured and calculated extensions proved to be equal.

During the period of easy glide, slip concentrated itself into one or more Lüders bands, outside which very few slip bands were observed. As extension continued through the easy-glide stage the Lüders bands moved along the gauge length. Figure 1 gives a series of photographs, taken in rapid succession during easy glide after an overall extension of 6 per cent, which show a Lüders band moving through a section of the specimen. In Fig. 2 the local extensions between adjacent silica hairs are compared with the overall extension of the crystal. In this diagram the letters A, B, C, D, E, refer, in order, to successive sections along the gauge length. Had the crystal extended uniformly the curves of the individual extensions would all be superimposed along the broken line inclined at 45 degrees. This figure, together with Fig. 3, shows in fact that a Lüders band started in section A and moved along the gauge length, that the local tensile strain within the Lüders band was the same as the overall strain at the end of easy glide, and that, when the Lüders band filled the entire gauge length, the easy glide ended. Easy glide in this material is thus indistinguishable in these respects from the phenomenon of "yield elongation" observed in soft steels when the



FIG. 1. A sequence of photographs at 30 $\times$  showing a Lüders band moving through a section of the crystal. The pictures were taken in rapid succession while easy glide was in progress, after an overall extension of 6 per cent.

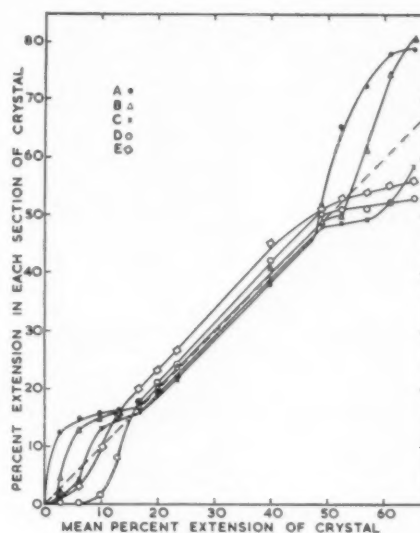


FIG. 2. The percent extension measured locally between adjacent silica hairs, on crystal no. 2, at various values of the mean extension. The letters A, B, C, D, E, refer to successive sections, between hairs, along the specimen.

upper yield point is overcome; it is thus an indication, not of an absence of work hardening, but of a process of propagation of slip through a material of constant properties. The dispersion of the curves of the individual extensions (Fig. 2), which occurs at the end of the period of linear hardening, shows that conjugate slip also spreads along the specimen in the form of a Lüders band. Although earlier investigators have reported a strong tendency for slip lines to cluster together in

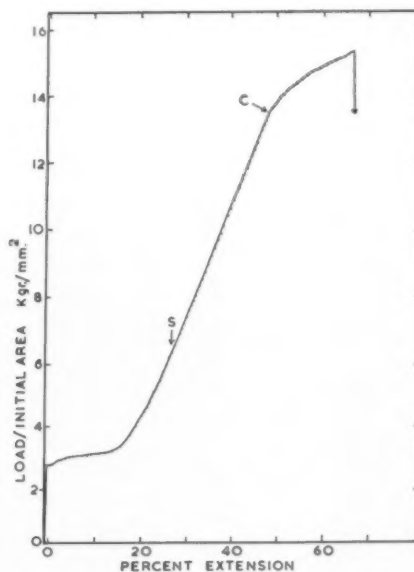


FIG. 3. The load-extension curve of crystal no. 2. The arrows lettered S and C denote arrival at the symmetry line, and the start of conjugate slip, respectively.



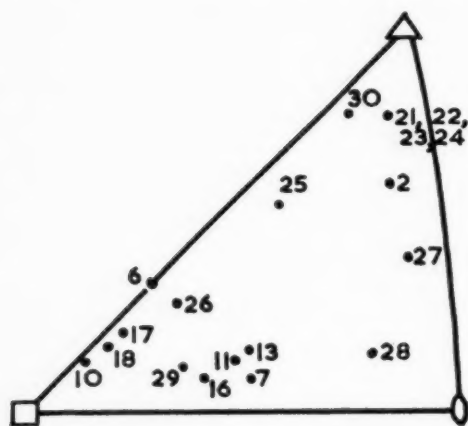


FIG. 4. The initial orientations of the tensile axes of the tested crystals.

alpha-brass, Lüders bands of primary slip do not appear to have been reported previously for this material.

#### b. Effects of Temperature and Rate of Strain on Overshooting

Five specimens, the initial orientations of which are shown in Fig. 4, were strained under the following conditions:

Specimen number:	21	22	23	24	25
Temperature of straining, °C:	-190	-190	+20	+200	-190
Rate of straining, sec <sup>-1</sup> :	$4.2 \times 10^{-5}$	$10^{-2}$	$4.2 \times 10^{-5}$	$4.2 \times 10^{-5}$	$10^{-2}$

Stress-strain curves for the first four of these specimens, which all had very similar orientations, are shown in Fig. 5. The curves show a discontinuity at the start of conjugate slip, in accord with the higher resolved shear stress at which the conjugate system succeeds the primary one. It will be noticed that specimens strained at -190°C, at +20°C, and at different rates of strain, all showed practically the same amount of overshoot, which disagrees with the theory that the overshoot is caused by the migration of vacancies.\* The results on specimen no. 25 confirmed those on specimen no. 22.

#### c. Ageing Experiments

Specimen 11, whose load-extension curve and changes of orientation are shown in Fig. 6, was aged for two hours at 200°C at each of the points marked on the diagram. Specimen 7 was extended until the orientation had crossed the symmetry line and was then aged at 200°C for twelve hours and at 250°C for two hours. In both cases slip continued, after ageing, on the primary

\* Recent experiments of the same type, by Heather M. Murphy and E. A. Calnan (Acta Met., 1955, in press), have also led to the conclusion that overshoot in alpha-brass is not caused by the migration of vacancies.

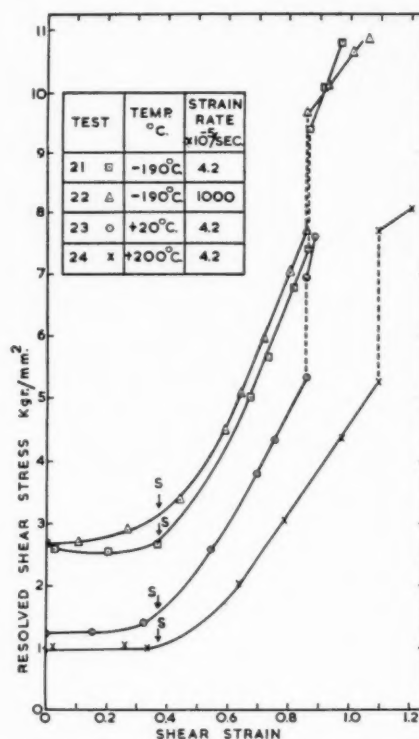


FIG. 5. The resolved shear stress supported by the active slip system at various total strains, measured on crystals of similar orientations at various temperatures and rates of straining. For simplicity, a smooth curve is drawn for the crystal strained at 200°C which does not show the repeated yielding that occurred throughout the extension.

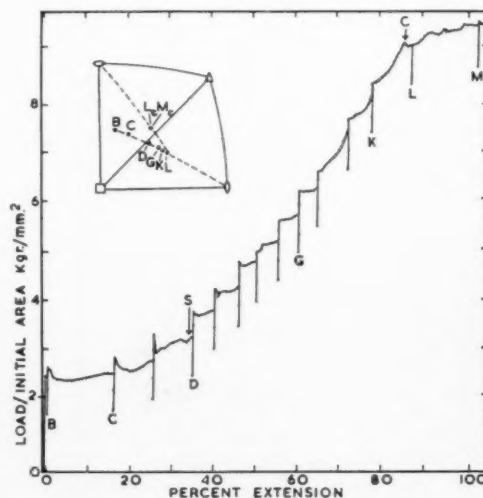


FIG. 6. The orientation of, and load supported by, specimen no. 11 at various stages during tensile deformation. The specimen was aged for two hours at 200°C at each point marked on the load-extension curve. The letters on the stereographic projection refer to orientations measured after reaching corresponding stages on the load-extension curve. The subscript *c* denotes the orientation measured inside the Lüders band of conjugate slip.

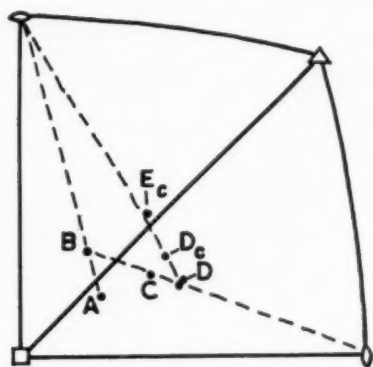


FIG. 7. Changes of orientation, A to E, during the extension of specimen no. 17. The specimen was annealed for four hours at 720°C at the point B.

system, and the conjugate system remained inactive until the normal amount of overshoot had occurred. Thus the overshoot does not appear to be caused, directly at least, by atmospheres locking dislocations on the conjugate system.

#### d. Annealing Experiments

Several specimens were annealed at 720°C at stages during their deformation. Those annealed at the end of easy glide did not recrystallize, and on subsequent straining they showed a new period of easy glide, similar in length to that of an unstrained crystal. With one such crystal (specimen 16) five periods of easy glide were obtained in this way. Specimen 17 was interesting, for it crossed the symmetry line during the initial period of easy glide, but did not reach the orientation at which conjugate slip normally begins. After annealing for four hours at 720°C a normal amount of easy glide and overshoot again occurred, but it took place on the *conjugate* system, not the primary one; this is shown in Fig. 7. It is thus possible to induce conjugate slip, once the symmetry line has been crossed, in a specimen which has been extended in easy glide and then thoroughly annealed.

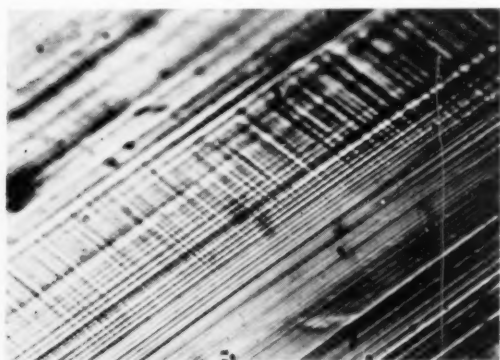


FIG. 8. A typical band of secondary slip, observed at the end of easy glide. The primary slip direction lies within 10 degrees of the plane of the photograph. 720 $\times$ .

Specimens extended beyond easy glide into the region of linear hardening usually recrystallized on annealing at 720°C. In one case recrystallization occurred at only one end of the specimen. This end was cut off, a new grip was soldered on, and after electropolishing the specimen was strained again. It showed a period of easy glide, but this occurred at a resolved shear stress of 2.2 kgm/mm<sup>2</sup> and was only one-third of the normal length. Thus, although crystals of alpha-brass can be fully recovered after extensions up to the end of easy glide, by annealing at 720°C, after larger extensions they either recrystallize or recover only partially.

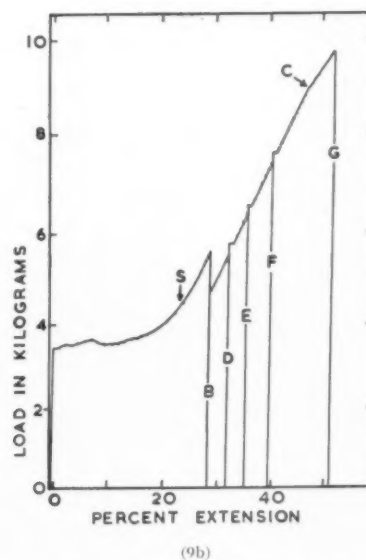
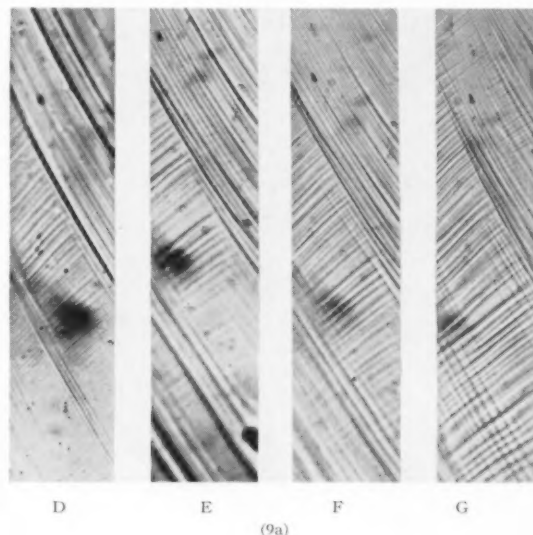


FIG. 9. (a) Photographs (270 $\times$ ) taken at a given place on a crystal after extensions to the points marked D, E, F, G, in the load-extension curve (Fig. 9b). The specimen was electropolished after extension to the point B.

### e. Observations of Slip Lines

To examine the suggestion of von Göler and Sachs<sup>2</sup> that some conjugate slip occurs during the stage of linear hardening, before the Lüders band of conjugate slip starts, several crystals were studied in detail microscopically. In all cases some bands of secondary slip could be seen, very faintly, just after the end of easy glide. Measurement of the orientation of the slip traces showed that the active slip plane in these bands was that of the conjugate system. A typical example is shown in Fig. 8; here the conjugate slip cuts across primary slip lines that had been active during easy glide. In one specimen these bands were first detected some 7 degrees *before* the crystal orientation had reached the symmetry line.

To study the mode of slip further during the stage of linear hardening some crystals were electropolished after reaching the beginning of this stage and then strained and examined again. Figure 9 shows photographs of the bands of conjugate slip developed in a given area on a specimen at the various stages indicated along the load-extension curve. While this specimen was hardening linearly more conjugate slip developed within the band of conjugate slip, but the band itself did not widen appreciably until the main conjugate slip began in the form of a Lüders band. It was observed that bands of conjugate slip became linked together by conjugate slip lines as the boundary of the Lüders band progressed up to them; whereas those still beyond the Lüders band remained clearly separated by regions purely of primary slip.

The existence of these bands of conjugate slip raises the point whether the extension, as calculated from the changes of orientation on the assumption of single slip, agrees with the directly measured value. Figure 10, in which the calculated and measured values are compared for several specimens, shows in fact that they agree.

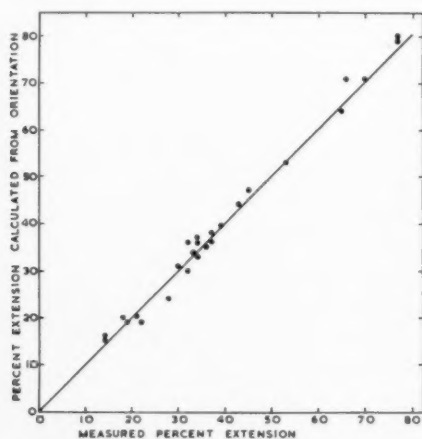


FIG. 10. The extension calculated from the change of orientation, assuming single slip, as a function of the measured extension. The values given are all taken during the period of linear hardening, after easy glide.

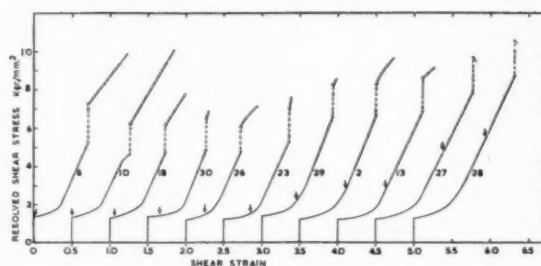


FIG. 11. The resolved shear stress supported by the active slip system at various total strains, measured on crystals extended at room temperature. The number on each curve denotes the specimen whose initial orientation is shown in Fig. 4.

The earlier observations of von Göler and Sachs on this point are thus not confirmed.

### f. Effect of Initial Orientation on the Amount of Overshoot

Several specimens were extended to determine whether the amount of overshoot depended on the initial orientation. The resulting stress-strain curves are given in Fig. 11; in these, the arrival at the symmetry line is shown by an arrow. It will be seen that the amounts of easy glide and overshoot do not vary very much with the initial orientation. Specimens 6 and 10, whose initial orientations lay on the symmetry line, were particularly interesting since the Lüders bands formed in different parts of their gauge lengths involved slip in one or other of the two symmetrically disposed slip systems. When two such bands involving different systems met they refused to propagate through one another, apart from a few intersections between their outriding slip bands. Only when the applied stress was increased to the level at which the Lüders bands of conjugate slip normally form did these mutually obstructing Lüders bands pass through one another. The results on specimen 6, in which three Lüders bands were formed, are shown in Fig. 12.

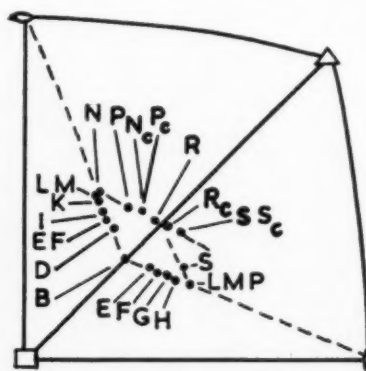


FIG. 12. Changes of orientation of two adjacent sections of specimen no. 6, whose initial orientation lay at point B. The points B to S denote successive orientations developed during the deformation.

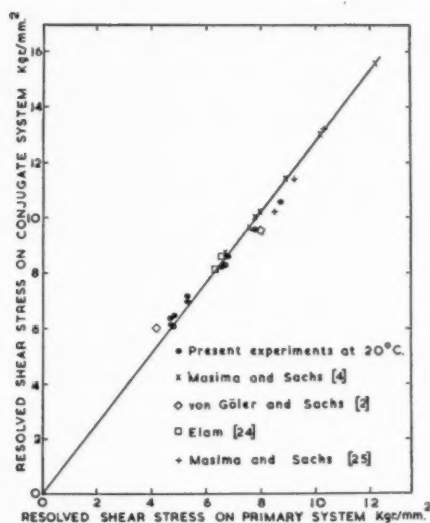


Fig. 13. The resolved shear stress on the conjugate system, at the start of conjugate slip, as a function of the resolved shear stress on the primary system, at the same point.

These results prove the reality of latent hardening, in the sense that the slip lines of the one system experience difficulty in breaking through the active slip lines of the other one. The vacancy and atmosphere theories, on the other hand, which suppose that overshooting is caused by softening processes on the active slip planes, but not the latent ones, would require the Lüders bands to pass through one another without difficulty.

A measure of latent hardening is provided in Fig. 13, in which the hardening on the conjugate slip system is compared with that on the primary system. For each system the hardening is measured by the shear stress acting on it at the point where conjugate slip begins. The room temperature results of the present experiments and those of previous investigators all lie along the straight line  $\sigma_c = 1.28\sigma_p$ , where  $\sigma_c$  and  $\sigma_p$  are the shear stresses acting on the conjugate and primary systems, respectively, at the start of conjugate slip. A relation of this type has been used previously by Masima and Sachs.<sup>4</sup>

#### DISCUSSION

This work has shown that overshooting in alpha-brass crystals is due to the difficulty which slip on the conjugate system experiences in cutting through the active primary slip lines, thus confirming the old hypothesis of latent hardening, and is not due to softening processes localized in the active primary slip lines.

There is evidence in other materials that active slip systems experience difficulty in cutting through one another. Honeycombe<sup>15</sup> observed in crystals of pure aluminium oriented for double slip that a roughly chequered pattern of slip lines was formed, in each element of which slip occurred substantially on only one system. Likewise, Pratt<sup>16</sup> showed that when two slip

systems are equally favoured, in sodium chloride crystals, although slip occurs initially on both systems one system usually becomes predominant on further deformation. Further evidence on aluminium crystals was provided by Paxton and Cottrell<sup>17</sup> who showed that after slip had been made to occur, by plastic twisting, on systems inclined to those used in tensile deformation, the stress for further tensile slip was sharply increased.

It thus appears that localized latent hardening, in the sense that an active slip plane provides locally a barrier to slip on an intersecting system, may be a general phenomenon. In order for this localized effect to make itself felt as an overall latent hardening, giving rise to overshooting, it is necessary that when the symmetry line is reached there should be an unequal distribution of slip between the primary and conjugate systems, such that the mean free path between the obstructing slip lines of the other system is appreciably longer in the planes of the primary system than in those of the conjugate one.

This condition is satisfied most completely in materials that show a yield phenomenon, since in these the nucleation of a slip line is much more difficult than its growth, so that the initially formed slip lines of the primary system become very long, thus creating at the beginning of deformation a highly anisotropic pattern of slip which, through the effect of localized latent hardening, tends to be self-perpetuating. Consistent with this view is the fact that overshooting has been observed in crystals of materials that show a yield phenomenon independently of whether the latter is caused by solute atoms, as in alpha brass<sup>11</sup> and iron,<sup>18</sup> or by work-softening, as in pure aluminium after a preliminary deformation at a low temperature.<sup>19,20</sup>

The argument developed above suggests that, contrary to the usual view, overshooting should be regarded as a normal characteristic of the plastic deformation of crystals, and that the intriguing feature is that it ever should be absent. Even in crystals of pure aluminium overshooting occurs if work-softening is present,<sup>20</sup> or if, as Chen and Mathewson<sup>21</sup> showed, a tapered specimen is used so that deformation spreads along the gauge length rather in the manner of a Lüders band. Absence of overshoot is, from the present point of view, an indication of an exceptionally turbulent mode of plastic deformation in which so many barriers to primary slip are formed, e.g., by localized slips on intersecting systems, that the localized latent hardening due to such barriers is as severe on the primary system as on the conjugate one. There is evidence for this severe hardening on the primary system in the fact that the specimens reported in the literature not to have shown overshooting are in general those which, in spite of initial orientations favourable for single slip, had very little easy glide and work-hardened rapidly.

Indirect evidence for the lesser turbulence of slip in brass crystals as compared to that in aluminium is to be found in Fig. 11. The various crystals there repre-



sented, though of widely varying orientation (see Fig. 4), all have closely similar stress-strain curves. This is to be contrasted with the striking dependence on initial orientation of the rate of hardening of crystals of pure aluminium.<sup>26</sup> This dependence is usually held to be the result of the varying incidence of local conjugate slip at early stages of the deformation, in amounts depending on the initial orientation. The annealing studies reported here strongly suggest that up to the end of easy glide the brass crystals were devoid of conjugate slip, and the similarity of the curves of Fig. 11 implies that the restriction of conjugate slip, when it does start, to discrete bands limits its capacity to cause work-hardening.

The reluctance of active slip lines to intersect one another is understandable since dislocation lines cut through one another only with difficulty when this leads to the formation of jogs on them.<sup>22</sup> The energy of a jog increases with increasing spacing of the partial dislocations which form the complete dislocation; this spacing in turn increases as the specific energy of the fault between the partial dislocations decreases. An indication of the stacking fault energy is provided by the tendency to form annealing twins in the metal. Because very few annealing twins are formed in aluminium, and because the tendency to form annealing twins increases when zinc is added to copper,<sup>28</sup> the stacking fault energy should decrease in passing from aluminium to copper to brass. Latent hardening, and the tendency towards overshooting, should increase in the same order.

#### ACKNOWLEDGMENTS

This work was made possible by the award of an Athlone Fellowship to one of us (G. R. P.) and by the

provision of laboratory facilities and equipment by the University of Birmingham. During the course of the work we had the benefit of several useful discussions with Professor R. Maddin and other colleagues. The brass wire was prepared by Dr. G. W. Ardley.

#### REFERENCES

1. G. I. Taylor and C. F. Elam, *Proc. Roy. Soc.* **A108**, 28 (1925).
2. F. von Göler and G. Sachs, *Z. Phys.* **55**, 581 (1929).
3. R. Karnop and G. Sachs, *Z. Phys.* **41**, 116 (1927).
4. M. Masima and G. Sachs, *Z. Phys.* **50**, 161 (1928).
5. G. Sachs and J. Weerts, *Z. Phys.* **62**, 473 (1930).
6. E. Osswald, *Z. Phys.* **83**, 55 (1933).
7. C. F. Elam, *Proc. Roy. Soc.* **A116**, 694 (1927).
8. H. L. Burghoff, *Trans. A.I.M.E.* **137**, 214 (1940).
9. R. Maddin, C. H. Mathewson, and W. R. Hibbard, Jr., *Trans. A.I.M.E.* **185**, 527 (1949).
10. J. S. Koehler, *Acta Met.* **1**, 508 (1953).
11. G. W. Ardley and A. H. Cottrell, *Proc. Roy. Soc.* **A219**, 328 (1953).
12. E. Schmid and W. Boas, *Kristall Plastizität* (Julius Springer, Berlin, 1935), p. 148.
13. E. N. da C. Andrade and R. Roscoe, *Proc. Phys. Soc.* **41**, 160 (1937).
14. M. Polanyi, *Z. Tech. Phys.* **6**, 121 (1925).
15. R. W. K. Honeycombe, *J. Inst. Metals* **80**, 45, 491 (1951).
16. P. L. Pratt, *Acta Met.* **1**, 103 (1953).
17. H. W. Paxton and A. H. Cottrell, *Acta Met.* **2**, 3 (1954).
18. J. H. Auld and G. B. Greenough, *Acta Met.* **2**, 209 (1954).
19. R. J. Stokes and A. H. Cottrell, *Acta Met.* **2**, 341 (1954).
20. R. J. Stokes, private communication.
21. N. K. Chen and C. H. Mathewson, *Trans. A.I.M.E.* **191**, 653 (1951).
22. A. H. Cottrell, *Dislocations and Plastic Flow in Crystals* (Clarendon Press, Oxford, 1953).
23. W. R. Hibbard, Jr., J. C. Liu, and S. F. Reiter, *Trans. A.I.M.E.* **188**, 1020 (1950).
24. C. F. Elam, *Proc. Roy. Soc.* **A115**, 148 (1927).
25. M. Masima and G. Sachs, *Z. Phys.* **54**, 666 (1928).
26. K. Lücke and H. Lange, *Z. Metall.* **43**, 55 (1952).

# THE HEATS OF FORMATION IN THE SYSTEMS TITANIUM-ALUMINIUM AND TITANIUM-IRON\*

O. KUBASCHEWSKI and W. A. DENCH†

A calorimeter has been constructed for the determination of exothermic heats of alloying. The heats of formation of iron-aluminium alloys determined with this apparatus agree closely with those obtained by Oelsen and Middel using quite a different method. The heats of formation of FeTi and in the Ti-Al system were also measured, but with Fe<sub>2</sub>Ti and Ti-Sn alloys reaction was incomplete. A few representative heats of formation in kcal/g-atom are as follows:

Fe <sub>0.7</sub> Al <sub>0.3</sub>	-3.8	Ti <sub>0.75</sub> Al <sub>0.25</sub>	-5.9	Ti <sub>0.25</sub> Al <sub>0.75</sub>	-8.75
Fe <sub>0.5</sub> Al <sub>0.5</sub>	-6.0	Ti <sub>0.65</sub> Al <sub>0.35</sub>	-7.5		
Fe <sub>0.3</sub> Al <sub>0.7</sub>	-6.8	Ti <sub>0.5</sub> Al <sub>0.5</sub>	-9.6	Fe <sub>0.5</sub> Ti <sub>0.5</sub>	-4.85
Fe <sub>0.25</sub> Al <sub>0.75</sub>	-6.6	Ti <sub>0.42</sub> Al <sub>0.58</sub>	-9.9		

The probable errors are discussed and estimated to be of the order of 1.5 to 2.5 per cent.

Using the heats of formation of the Ti-Al alloys, and the free energies in the Ti-O system previously determined, the possibility of producing Ti-Al alloy from TiO<sub>2</sub> and excess aluminium has been discussed, and it was found that alloys containing up to 43 per cent Ti could be made relatively free of oxygen.

## CHALEURS DE FORMATION DANS LES SYSTÈMES TITANE-ALUMINIUM ET TITANE-FER

Un calorimètre a été construit pour la détermination des chaleurs de mélange exothermiques. Les chaleurs de formation des alliages fer-aluminium obtenues avec cet appareil concordent avec celles d'Oelsen et Middel obtenues par une autre méthode. Les chaleurs de formation de Fe-Ti et du système Ti-Al ont été mesurées, mais par contre, dans le cas de Fe<sup>\*</sup>Ti et des alliages Ti-Sn, la réaction était incomplète. Quelques chaleurs de formation caractéristiques en kcal/g-atome sont données ci-dessous:

Fe <sub>0.7</sub> Al <sub>0.3</sub>	-3.8	Ti <sub>0.75</sub> Al <sub>0.25</sub>	-5.9	Ti <sub>0.25</sub> Al <sub>0.75</sub>	-8.75
Fe <sub>0.5</sub> Al <sub>0.5</sub>	-6.0	Ti <sub>0.65</sub> Al <sub>0.35</sub>	-7.5		
Fe <sub>0.3</sub> Al <sub>0.7</sub>	-6.8	Ti <sub>0.5</sub> Al <sub>0.5</sub>	-9.6	Fe <sub>0.5</sub> Ti <sub>0.5</sub>	-4.85
Fe <sub>0.25</sub> Al <sub>0.75</sub>	-6.6	Ti <sub>0.42</sub> Al <sub>0.58</sub>	-9.9		

Les erreurs probables sont discutées et de l'ordre de 1, 5 à 2, 5%.

A l'aide des chaleurs de formation des alliages Ti-Al et des énergies libres du système Ti-O, la possibilité de produire des alliages Ti-Al à partir de TiO<sub>2</sub> est étudiée et il est montré que les alliages jusqu'à 43% Ti peuvent être obtenus pratiquement sans oxygène.

## DIE BILDUNGSWÄRMEN DER SYSTEME TITAN-ALUMINIUM UND TITAN-EISEN

Zur Bestimmung der bei der Legierungsbildung freiwerdenden Wärme wurde ein Kalorimeter entwickelt. Die mit diesem Apparat bestimmten Bildungswärmen von Eisen-Aluminium-Legierungen zeigen eine sehr gute Übereinstimmung mit den von Oelsen und Middel auf eine ganz andere Weise gefundenen Werten. Die Bildungswärmen von FeTi und die des Systems Ti-Al wurden ebenfalls gemessen; die Reaktionen verliefen jedoch bei Fe<sub>2</sub>Ti und den Ti-Sn-Legierungen unvollständig. Einige charakteristische Bildungswärmen in kcal/gatom sind wie folgt:

Fe <sub>0.7</sub> Al <sub>0.3</sub>	-3.8	Ti <sub>0.75</sub> Al <sub>0.25</sub>	-5.9	Ti <sub>0.25</sub> Al <sub>0.75</sub>	-8.75
Fe <sub>0.5</sub> Al <sub>0.5</sub>	-6.0	Ti <sub>0.65</sub> Al <sub>0.35</sub>	-7.5		
Fe <sub>0.3</sub> Al <sub>0.7</sub>	-6.8	Ti <sub>0.5</sub> Al <sub>0.5</sub>	-9.6	Fe <sub>0.5</sub> Ti <sub>0.5</sub>	-4.85
Fe <sub>0.25</sub> Al <sub>0.75</sub>	-6.6	Ti <sub>0.42</sub> Al <sub>0.58</sub>	-9.9		

Die möglichen Fehler werden diskutiert; eine Abschätzung ergibt einen Fehler in der Größenordnung von 1.5 bis 2.5%.

Auf Grund der Bildungswärmen der Ti-Al-Legierungen und der freien Energien im System Ti-O, die schon früher bestimmt wurden, wurde die Möglichkeit einer Herstellung von Ti-Al-Legierungen aus TiO<sub>2</sub> und einem Überschuss an Aluminium diskutiert. Es wurde festgestellt, dass eine Herstellung von ziemlich sauerstoff-freien Legierungen bis zu einem Ti-Gehalt von 43% möglich ist.

## INTRODUCTION

In view of the possible technical application of titanium-aluminium and titanium-iron alloys, it was considered useful to know their heats of formation. Since the experimental methods so far used for the thermochemical investigation of alloy systems<sup>1</sup> did not

appear to be particularly suitable for the systems in question, a new method of determination was devised.

## EXPERIMENTAL METHOD

### Apparatus

In principle, a mixture of the powders of the two component metals is heated by a small furnace within a calorimeter until alloying takes place. The electrical

\* Received January 4, 1955.

† Metallurgy Division, National Physical Laboratory, Teddington, England.

energy supplied is measured and subtracted from the total heat evolved.

A sketch of the apparatus is shown in Fig. 1.

The compacted powder mixture (A) is suspended by a 0.25 mm molybdenum wire within the furnace. This consists of a molybdenum winding (B) insulated by alumina bushes (C) from the molybdenum framework (D), surrounded by ten radiation screens of 0.03 mm nickel foil (E). The radiation screens are separated by protuberances made by indenting with a pin. The furnace hangs on a 1 mm molybdenum wire, and is enclosed in a hollow cylindrical aluminium block (F) the lid of which is fastened by four brass studs (G). Two gas outlet holes (H) pass through the lid. The block is suspended by linen threads (J) within a cylindrical brass vacuum-container (K) fitted with an O-ring seal (L). The container is connected to a rotary vacuum pump and a McLeod gauge by a tube (M) which is shielded from direct radiation by a brass bridge (N). This tube also holds the container which is immersed in a water bath, thermostatically controlled at  $25^{\circ}\pm 0.01^{\circ}\text{C}$  by a toluene temperature regulator. One end of the furnace winding is joined to the molybdenum framework, the other end is connected by a steel terminal (O) to 0.5 mm copper wire, which is carried by a silica tube through the lid of the aluminium block. The furnace and block are earthed to the brass container by 0.5 mm copper wire. Ten 0.25 mm copper-Eureka thermocouples in series have their hot junctions at representative positions on the surface of the aluminium block, six on the wall and two each on the top and bottom. The soft-soldered junctions are clamped to the surface by a copper washer and brass screw (P), from which they are electrically insulated by a folded piece of thin mica. The cold junctions are similarly clamped to a brass block

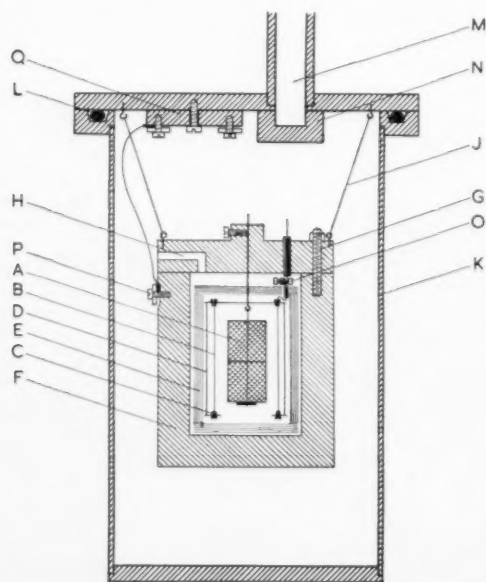


FIG. 1. Calorimeter.

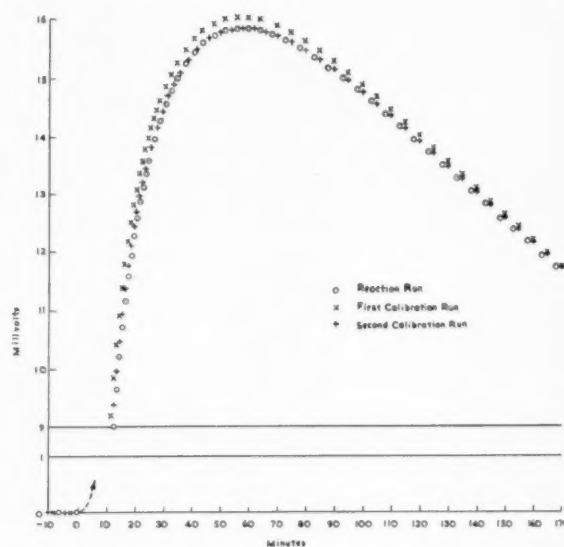


FIG. 2. Potential difference/time curve for a titanium-aluminum alloy with 43.8% Al by weight.

(Q) attached to the lid of the vacuum container, through which the thermocouple and furnace leads are taken by waxed rubber seals. Access to the specimen is obtained by successively lowering the thermostat bath and the main parts of the vacuum container, aluminium block, and radiation screens. Power is applied to the furnace through a watt-hour meter at about 30 volts A. C. and 3.5 amp. The potential difference of the thermocouple is measured on a deflection potentiometer.

### Preparation of Specimens

A titanium powder of -120 mesh was analysed and shown to have the following average composition: 98.3 per cent Ti, 0.35 Ca, 0.09 Mg, 0.3 Fe+Al+Si, 0.3 O<sub>2</sub>, 0.1 N<sub>2</sub>, and 0.5 H<sub>2</sub>. The hydrogen was removed by heating the powder to 800°C *in vacuo*, so as to bring the purity to 98.8 per cent Ti.

The aluminium powder (-200 mesh) contained 99.9 per cent Al according to analysis. The remaining 0.1 per cent was probably mainly surface oxygen.

The iron powder (-120 mesh) contained 0.015 per cent C, <0.001 Si, 0.05 Mn, 0.005 S, and <0.005 Cu, Ni, Cr. The oxygen content, however, was appreciable, and the powder was therefore reduced by heating for one-half hour to 850°C in a stream of hydrogen purified over copper turnings (250°C), silica gel, P<sub>2</sub>O<sub>5</sub>, and magnesium turnings (620°C). After degassing in a vacuum, the slightly sintered powder was ground in an agate mortar. The gas content after deoxidation and degassing was: 0.066 per cent O<sub>2</sub>, 0.006 N<sub>2</sub>, and 0.0006 H<sub>2</sub>.

After weighing out, the powders were mixed for 17 hours in a rotary mixer, then made into compacts (15 mm diameter, 15 mm long) under a load of 5 to 10 tons, two compacts being required for each charge.

### Procedure

The unreacted compacts are weighed and loaded into the calorimeter, which is immersed in the thermostat bath and evacuated to 0.003 mm Hg pressure. When a uniform temperature has been attained within the calorimeter, the furnace is switched on, the input watt-hours being measured. Within 3-5 minutes the compacts are heated to the temperature at which the reaction starts. This temperature has been established by preliminary runs in a separate arrangement. The start of the reaction is indicated by a change in the electrical resistance of the furnace winding, and by a slight evolution of gas. At this point the furnace is switched off. The reaction increases the temperature of the compacts by several hundred degrees. The temperature of the aluminium block rises, and the thermocouple-potential is measured until a maximum value is reached after about one hour.

On the following day, when the calorimeter is again at a uniform temperature of 25°C, an amount of electrical energy is put into the furnace which, it is estimated, will raise the block to the same maximum temperature as in the reaction run: that is, an amount of energy equal to the electrical energy introduced to initiate the reaction plus the heat evolved during alloying. One to three of these calibration runs may be necessary before an exact repeat of the potential-difference/time curve of the reaction run is obtained. Figure 2 shows the potential-difference/time plot for the reaction run, and the

TABLE I. Experimental results and their accuracy.

Composition		Heat of formation in cal/g-atom	Accuracy in cal/g-atom
in weight %	in atomic %		
82.85 Fe, 17.15 Al	70.0 Fe, 30.0 Al	-3760	±220
75.65 Fe, 24.35 Al	60.0 Fe, 40.0 Al	-4750	±190
75.65 Fe, 24.35 Al	60.0 Fe, 40.0 Al	-4900	±200
67.45 Fe, 32.55 Al	50.0 Fe, 50.0 Al	-6000	±185
50.1 Fe, 49.9 Al	33.3 Fe, 66.7 Al	-6250	±280
45.3 Fe, 54.7 Al	28.6 Fe, 71.4 Al	-6860	±160
40.85 Fe, 59.15 Al	25.0 Fe, 75.0 Al	-6670	±160
95.0 Ti, 5.0 Al	91.45 Ti, 8.55 Al	-2260	±240
90.0 Ti, 10.0 Al	83.55 Ti, 16.45 Al	-4390	±230
90.0 Ti, 10.0 Al	83.55 Ti, 16.45 Al	-4030	±230
85.0 Ti, 15.0 Al	76.15 Ti, 23.85 Al	-5720	±240
80.0 Ti, 20.0 Al	69.25 Ti, 30.75 Al	-6940	±220
80.0 Ti, 20.0 Al	69.25 Ti, 30.75 Al	-7130	±210
76.0 Ti, 24.0 Al	64.1 Ti, 35.9 Al	-7380	±230
75.0 Ti, 25.0 Al	62.8 Ti, 37.2 Al	-7870	±200
65.0 Ti, 35.0 Al	51.1 Ti, 48.9 Al	-9410	±240
65.0 Ti, 35.0 Al	51.1 Ti, 48.9 Al	-9730	±240
60.0 Ti, 40.0 Al	45.8 Ti, 54.2 Al	-9600	±230
60.0 Ti, 40.0 Al	45.8 Ti, 54.2 Al	-9540	±240
56.2 Ti, 43.8 Al	41.95 Ti, 58.05 Al	-9620	±200
55.0 Ti, 45.0 Al	40.75 Ti, 59.25 Al	-9980	±220
55.0 Ti, 45.0 Al	40.75 Ti, 59.25 Al	-9600	±240
37.2 Ti, 62.8 Al	25.0 Ti, 75.0 Al	-8950	±260
37.2 Ti, 62.8 Al	25.0 Ti, 75.0 Al	-8680	±260
46.18 Ti, 53.82 Fe	50.0 Ti, 50.0 Fe	-4840	±280
46.18 Ti, 53.82 Fe	50.0 Ti, 50.0 Fe	-4870	±290
46.18 Ti, 53.82 Fe	50.0 Ti, 50.0 Fe	-4600	±290
46.18 Ti, 53.82 Fe	50.0 Ti, 50.0 Fe	-4900	±280
30.02 Ti, 69.98 Fe	33.33 Ti, 66.67 Fe	(-4360)	see text
30.02 Ti, 69.98 Fe	33.33 Ti, 66.67 Fe	(-4140)	see text
30.02 Ti, 69.98 Fe	33.33 Ti, 66.67 Fe	(-4430)	see text

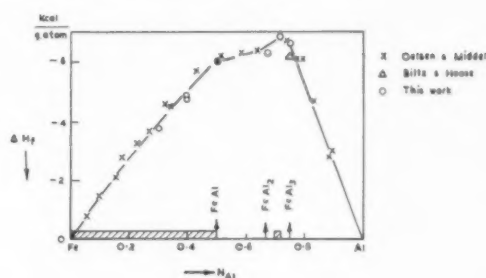


FIG. 3. Heats of formation in the system iron-aluminium.

first and second calibration runs of the 43.8 wt. per cent Al-Ti alloy as an example.

The difference between the input electrical energy in the reaction- and calibration-runs is then the energy evolved by the reaction.

### RESULTS

In this way, the heat of formation at various compositions has been determined in the systems: iron-aluminium, titanium-aluminium, and titanium-iron. The results are given in Table I and Figs. 3 and 4. The estimation of the errors indicated in Table I will be discussed below.

#### Iron-Aluminium

Several alloys of this system have been investigated in order to compare the results with those of other investigators. Oelsen and Middel<sup>2</sup> measured the heats of formation by mixing the molten metals in a calorimeter at room temperature. When the heat contents of the molten components were subtracted from the total heat effect, the heat of formation was obtained. Biltz and Haase<sup>3</sup> measured the heat of formation of FeAl<sub>3</sub> as the difference between the heat of solution of the alloy and

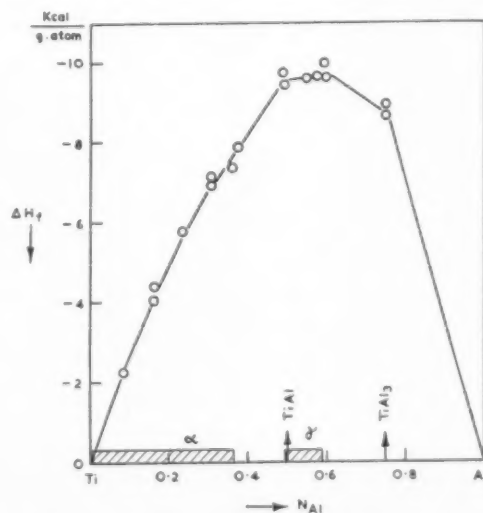


FIG. 4. Heats of formation in the system titanium-aluminium.



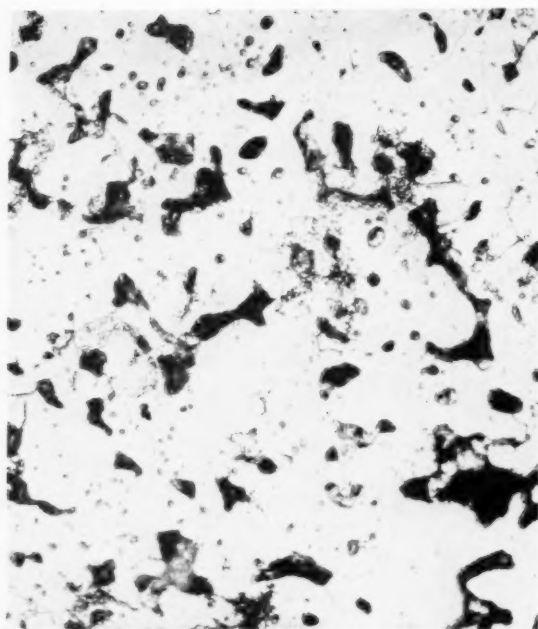


FIG. 5. Ti-Al, 20% Al: after reaction. 500X.

of the parent metals using hydrochloric acid as the solvent and the calorimetric fluid.

In the present experiments, reaction started at about 660°C, i.e., the melting temperature of aluminium. The results of seven measurements are given in Table I together with the estimated errors and are compared with the earlier results of Oelsen and Middel, and Biltz and Haase in Fig. 3. In view of the experimental ac-



FIG. 6. Ti-Al, 35% Al: after reaction. 150X.

curacy, which is not better than  $\pm 10$  per cent in either of the two sets of earlier measurements, the agreement is considered to be good, and increases confidence in the present method. A discrepancy of *ca* 300 cal between Oelsen's and the present work at high iron contents will be discussed further below.

### Titanium-Aluminium

These reactions also started at about 660°C. The compacts kept their shape even after reaction was complete. The results of 17 experiments are given in Table I and plotted in Fig. 4. The line was drawn so as to be consistent with the phase diagram determined by Bumps, Kessler and Hansen.<sup>4</sup>

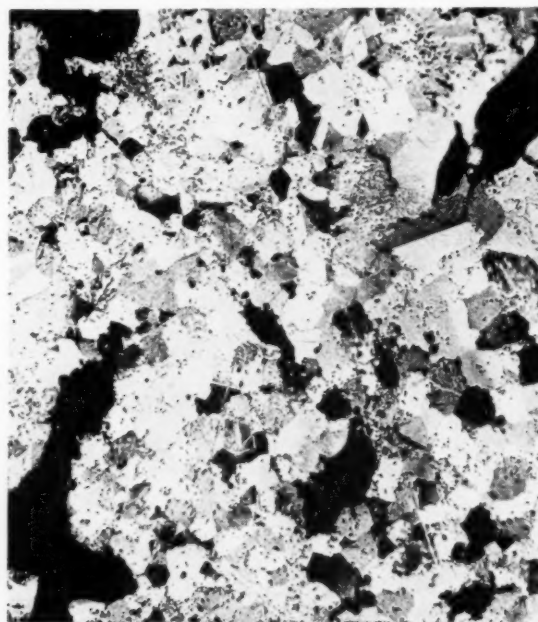


FIG. 7. Ti-Al, 40% Al: after reaction. 150X.

As with the iron-aluminium alloys there is a curvature in the solid solution range indicating an increase of the (negative) partial heat of solution of aluminium,  $\Delta\bar{H}_{Al}$ , with aluminium content. The minimum heat of formation was found in the  $\gamma$  phase when saturated with Al ( $N_{Al}=0.585$ ). The compound  $TiAl_3$  is clearly distinguished on the heat-concentration curve.

### Titanium-Iron

At room temperature two compounds  $TiFe$  and  $TiFe_2$ , exist, but no extensive homogeneity ranges.<sup>5</sup> Equi-atomic mixtures of iron and titanium reacted at about 1090°C, the eutectic temperature. From the four determinations given in Table I a heat of formation of  $TiFe$  of  $-4850 \pm 150$  cal/g-atom is obtained. For  $TiFe_2$  the values are less negative. This appeared to be improbable in view of the high melting-point maximum at this

composition. The alloys formed were therefore studied by the X-ray method. The equiatomic alloy was shown to consist virtually entirely of FeTi, some traces of Fe<sub>2</sub>Ti being also present. The N<sub>Fe</sub>=0.667 alloy, however, consisted essentially of about equal parts of FeTi and  $\alpha$ Fe, and only a small quantity of Fe<sub>2</sub>Ti. Under the conditions of the experiments, Fe<sub>2</sub>Ti was thus not formed quantitatively, and the heats of formation shown in Table I are therefore numerically much too low. Some compositions in the heterogeneous FeTi-Fe<sub>2</sub>Ti and Fe<sub>2</sub>Ti-Fe ranges were also investigated, and again, the heat of formation per g-atom was only slightly more negative than corresponded to the proportion of FeTi present in the final alloys.

### Titanium-Tin

Compacts of tin and titanium powders (with 10, 30 and 60 per cent Sn) were heated up to 1000°C. No heat effect was observed, and subsequent micro-examination indicated that very little alloying had occurred. The heat of formation is therefore probably much less negative than that of any other alloy investigated.

### CORRECTIONS AND ACCURACY

Errors in the heats of formation may arise from (1) the experimental measurement, (2) impurity effects, and (3) incomplete reaction.

(1a) Most of the errors arising from the actual measurement have been eliminated by the exact reproduction of the potential-difference/time curve in the calibration runs, which were carried out after each individual reaction run. Thus the main error comes from the accuracy of the watt-hour meter. This was calibrated by the Electricity Division of the National Physical Laboratory and was accurate to within 0.4 per cent. Since the heats of formation in Table I were obtained as differences between the energy inputs in the reaction and calibration runs, the maximum error was worked out for each heat value individually. On an average, this turned out to be about  $\pm 1$  per cent, but increased up to  $\pm 2$  per cent with the less negative values.

(1b) The specimen, after reacting at high temperatures ( $\gg 1000^\circ\text{C}$ ) cooled rapidly. Its temperature during the period of potential-difference readings had, however, not attained room temperature. The temperature of the specimen was estimated to be between  $90^\circ\text{C}$  and  $60^\circ\text{C}$  during this period. The specific heats of the alloys investigated are not known. As a rule, the changes in atomic heat on alloying are very small, if not negligible. It can safely be said that the necessary corrections would not amount to more than  $\pm 25$  cal/g-atom.

(2) Purities of the metals used were given above. It has generally been overlooked in earlier calorimetric work of a similar kind that the impurities may be transferred to the baser metal evolving a relatively high

amount of additional heat. In the present work with metals of known purity corrections may be applied. In the case of iron-aluminium, for instance, one would expect the oxygen and nitrogen in the iron to be passed to the aluminium during the reaction. The amount of this heat may be calculated from the analysis of the iron and the heats of formation of Fe<sub>3</sub>N, AlN, Fe<sub>3</sub>O<sub>4</sub>, and Al<sub>2</sub>O<sub>3</sub>. It follows that  $-176$  cal/g-atom Fe must be subtracted from the heats of formation in the Fe-Al system. This correction was not applied by Oelsen and Middel<sup>2</sup> who used "commercially pure iron" in their investigation in the same system. This easily accounts for the differences, still existing between their and the present heats of formation, particularly at high iron contents. In order to account for this difference one may assume that Oelsen's iron contained about 0.12 per cent oxygen plus nitrogen, but in view of the relative inaccuracies of the two methods this is no more than a very rough estimate.

For the Fe-Ti system it was calculated that  $-158$  cal/g-atom Fe must be subtracted from the heats of formation observed. A corresponding calculation for the Ti-Al system is difficult. The data for the free energies in the titanium-oxygen system<sup>6</sup> and of alumina<sup>1</sup> imply that oxygen would be passed from aluminium to titanium at high titanium contents, and in the reverse direction at high aluminium contents. The respective corrections are:  $-15$  cal/g-atom Al to be added for titanium-rich alloys, and  $-80$  cal/g-atom Ti to be subtracted for aluminium-rich alloys. Since the temperature of reaction was not known, however, no correction has been applied, but the calculated values have been added to the values for the inaccuracies in column 4 (Table I).

These values for the inaccuracy of the individual heats were obtained by adding the inaccuracies discussed in (1a) and (1b), and, for Fe-Al and Fe-Ti, half the value of the correction (2).

(3) Incompleteness of reaction may be a major source of error in this type of calorimetric work, as was already shown above for the reaction of  $2\text{Fe} + 1\text{Ti}$ . It is therefore essential that completeness of reaction should be ascertained. X-ray and microscopic methods have been employed. Representative examples of micrographs are shown in Figs. 5-7. These were taken from sections through Ti-Al specimens after reaction. The specimens are, of course, porous, but the etched surfaces give essentially the same pictures as were obtained after long annealing to  $1000^\circ\text{C}$ - $1350^\circ\text{C}$  by Bumps, Kessler and Hansen<sup>4</sup> (*q.v.*). If, for instance, an alloy Ti:Al = 1:1 had not reacted completely, but, say 5 per cent consisted of an equivalent mixture of TiAl<sub>3</sub> and  $\alpha$ Ti-Al this would show clearly in the micrographs. The corresponding correction would, however, be small: the heat of formation would be 110 cal numerically too low, that is 1.2 per cent. It was concluded from the combined X-ray and micrographic evidence that the error of possible incompleteness of reaction was well within the other

errors given, and no additional inaccuracy-value has been added to the values in column 4 (Table I).

### PRODUCTION OF TITANIUM-ALUMINIUM ALLOYS

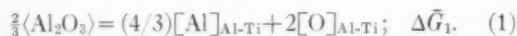
It may be of some interest to show how the thermochemical data of alloy formation may be used to approach a practical problem, such as the production of titanium-aluminium alloys by the reduction of titanium dioxide by aluminium.

The free-energy/composition curve of the titanium-oxygen system was established by Kubaschewski and Dench<sup>6</sup> at 1000°C, and the heats of formation of the titanium-aluminium alloys (Fig. 4) may be taken to be equal to their free energy of formation at the same temperature, i.e. the changes in atomic heat ( $\Delta C_p$ ) and in entropy ( $\Delta S$ ) on alloying are assumed to be zero. The errors introduced by this simplification will be discussed further below.

With the present thermochemical data one may calculate the oxygen contents of aluminium-titanium alloys depending on their composition, at 1000°C. The authors are aware that, in practice, one would go to much higher temperatures, and, in fact, the thermite reaction is not isothermal at all. Data for liquid Ti-Al alloys and for the free energy of Ti-O solutions at higher temperatures are, however, not available, and the following calculation may be taken as an outline of the mode of calculation rather than a final assessment for practical application.

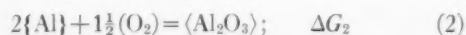
In the following calculations the accepted thermodynamic terminology will be used, as given, for instance, by Kubaschewski and Evans.<sup>1</sup> The bar over the symbol  $\Delta\bar{G}_i$  denotes the free-energy change on dissolving 1 mole,  $i$ , in a theoretically infinite amount of an alloy of given composition. Various types of brackets are used to indicate states of aggregation, i.e., (solid), {liquid}, (gaseous), and dissolved: [solute]<sub>solvent</sub>.

If TiO<sub>2</sub> reacts with an excess of molten aluminium, the reaction may be written as



This formulation neglects the possible interaction of alumina with titanium oxides. However, the percentage of Ti<sub>2</sub>O<sub>3</sub> dissolved in Al<sub>2</sub>O<sub>3</sub> cannot be great under equilibrium conditions, and, in this percentage, would not affect the free energy of alumina by more than, say, 2 or 3 kcal. The heat of formation of Al<sub>2</sub>TiO<sub>5</sub> from its component oxides is not known, but if it were even as high as that of Al<sub>2</sub>SiO<sub>5</sub>,<sup>1</sup> it would not be stable in the presence of excess aluminium.

In order to calculate the equilibria of reaction (1) the free energies of the following basic reactions are required:



The free energy of formation of alumina is given by<sup>1</sup>

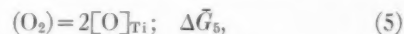
$$\Delta G_2 = -407,440 - 8.05T \log T + 106.1T.$$

The value for the free energy of solution of aluminium in the Al-Ti alloys,  $\Delta\bar{G}_3$ , may be obtained from Fig. 4 by drawing the tangent at any point of the curve. This tangent will intersect the ordinate at  $N_{\text{Al}}=0$  and  $\Delta\bar{H}_{\text{Ti}}$  for  $\langle\text{Ti}\rangle = [\text{Ti}]_{\text{Al-Ti}}$ , and at  $N_{\text{Al}}=1.0$  and  $\Delta\bar{H}_{\text{Al}}$  for  $\langle\text{Al}\rangle = [\text{Al}]_{\text{Al-Ti}}$ , where the composition of Ti-Al is that of the point of contact of the tangent to the  $\Delta H$ - $N$  curve. Since the entropy of formation of the Ti-Al alloys is neglected, we have  $\Delta\bar{H}_{\text{Ti}} \sim \Delta\bar{G}_{\text{Ti}}$  and  $\Delta\bar{H}_{\text{Al}} \sim \Delta\bar{G}_{\text{Al}}$ . In order to correct the last free-energy value for the solution of liquid aluminium in the alloys, the free energy of fusion of aluminium,  $\Delta G_f = 2500 - 2.68T$ , is introduced, and

$$\Delta\bar{G}_3 \sim \Delta\bar{H}_{\text{Al}} - \Delta G_f$$

is obtained, where  $\Delta\bar{H}_{\text{Al}}$  is derived from the curve in Fig. 4 in the manner described.

Thirdly, the partial free energy of oxygen in the Ti-Al alloys,  $\Delta\bar{G}_4$ , is required. Since this has not been determined directly, it must be derived in another way, which is somewhat involved. The partial free energy of solution of oxygen in the binary titanium-oxygen alloys at 1000°C,



is known from the work of Kubaschewski and Dench.<sup>6</sup> The partial free energy of titanium in the Ti-Al alloys



was shown in the preceding paragraph to be obtainable from Fig. 4, and to be  $\Delta\bar{G}_6 = \Delta\bar{G}_{\text{Ti}} \sim \Delta\bar{H}_{\text{Ti}}$ .

The connection between  $\Delta\bar{G}_5$  and  $\Delta\bar{G}_6$  with  $\Delta\bar{G}_4$  is as follows.

In the presence of aluminium, the integral free energy of the titanium-oxygen alloys is reduced by a certain amount which may be denoted  $\Delta G^*$ . An integral free energy may be split up, according to Lewis, into two terms involving the partial free energies of the components,

$$\Delta G^* = N_{\text{O}}\Delta\bar{G}_{\text{O}}^* + N_{\text{Ti}}\Delta\bar{G}_{\text{Ti}}^*, \quad (7)$$

where  $N_{\text{O}}$  and  $N_{\text{Ti}}$  are the atomic fractions of oxygen and titanium in the binary alloy. On the other hand,  $\Delta G^*$  may be obtained by an integration of  $\Delta\bar{G}_{\text{Ti}}^*$  according to a modified form of the Duhem-Margules equation, namely

$$\Delta G^* = N_{\text{O}} \int_0^{N_{\text{Ti}}} \frac{\Delta\bar{G}_{\text{Ti}}^*}{N_{\text{O}}^2} dN_{\text{Ti}}. \quad (8)$$

For a given composition of titanium-aluminium,  $\Delta\bar{G}_{\text{Ti}}^*$  ( $=\Delta\bar{G}_6$ ), i.e., the reduction in free energy of titanium in the titanium-oxygen alloys owing to the presence of the aluminium, is constant. Equation (8) may thus be



TABLE II. Oxygen content of aluminium-titanium alloys produced from titania and excess aluminium at 1000°C.

$N_{Ti}$	Weight % Ti	$-\frac{1}{2}\Delta G_2$	$(4/3)\Delta G_3$	$-2\Delta G_6$	$-\Delta G_5$	Weight % O per 100% Ti	Weight % O in alloy
0-0.25	0-37.3	202,800	0	70,000	272,800	0.01	0.003
0.25-0.42	37.3-43.8	202,800	-7,750	29,100	224,350	0.3	0.1-0.13
0.42-0.51	43.8-64.9	202,800	-13,500	16,900	206,200	6.2	2.7-4.0
0.51-0.64	64.9-76.0	202,800	-21,200	4,800	186,400	12.0	7.8-9.1
0.75	84.2	202,800	-23,600	3,400	182,600	13.5	11.4

written for the binary Ti-O alloys as

$$\Delta \bar{G}^* = (1 - N_{Ti}) \Delta \bar{G}_{Ti}^* \int_0^{N_{Ti}} \frac{dN_{Ti}}{(1 - N_{Ti})^2} \\ = (1 - N_{Ti}) \Delta \bar{G}_{Ti}^* \frac{1}{1 - N_{Ti}} = \Delta \bar{G}_{Ti}^*.$$

It follows then from equations (7) and (8) that

$$\Delta \bar{G}_{Ti}^* = N_O \Delta \bar{G}_O^* + N_{Ti} \Delta \bar{G}_{Ti}^*; \quad \text{i.e.,} \\ \Delta \bar{G}_O^* = \Delta \bar{G}_{Ti}^* = \Delta \bar{G}_6.$$

Since  $\Delta \bar{G}_O^*$  represents the reduction in free energy from  $\frac{1}{2}\Delta \bar{G}_5$  to  $\frac{1}{2}\Delta \bar{G}_4$ , we now find for the unknown free energy of the solution of oxygen in the Ti-Al alloy

$$\Delta \bar{G}_4 = \Delta \bar{G}_5 - 2\Delta \bar{G}_6. \quad (9)$$

With this, all the required basic free energies are known to calculate the equilibria of reaction (1). Equilibrium in reaction (1) is established when

$$(4/3)\Delta \bar{G}_3 - \frac{2}{3}\Delta G_2 + \Delta \bar{G}_4 = 0 \quad (10)$$

or, inserting equation (9),

$$(4/3)\Delta \bar{G}_3 - \frac{2}{3}\Delta G_2 - 2\Delta \bar{G}_6 + \Delta \bar{G}_5 = 0. \quad (11)$$

In Table II, the first three terms of Eq. (11) were calculated for various compositions of aluminium-titanium from the curve in Fig. 4, and the free-energy equation of alumina. The resulting free-energy value,  $\Delta \bar{G}_5$ , was used to find in the curve in Kubaschewski and Dench's paper<sup>6</sup> the corresponding oxygen concentration, which was then reduced for the actual amount of titanium present in the titanium-aluminium alloy: last column. It is seen that these percentages increase discontinuously at certain compositions. These discontinuities correspond to the breaks in the  $\Delta H$ - $N$  curve, Fig. 4. They would not be expected to occur with molten titanium-aluminium alloys, for which the  $\Delta H$ - $N$  and  $\Delta G$ - $N$  curves should be continuous.

It is seen from Table II that, according to the present calculation, titanium-aluminium alloys with up to 43 per cent Ti by weight may be produced at 1000°C, with very little oxygen. For higher concentrations of titanium the equilibrium contents of oxygen increase rapidly with concentration.

The calculation involves the inaccuracy of the free-energy equation for  $Al_2O_3$  which is about  $\pm 2$  kcal/mole,

and its possible reduction by the uptake of  $Ti_2O_3$  in solution which was estimated above to be not more than 3 kcal/mole. The  $\Delta H$  curve of Ti-Al in Fig. 4 is accurate within  $\pm 150$  cal, but the differentiation, i.e., the drawing of tangents, would magnify this error. The neglect of the entropies of reactions (3) and (6) may result in an error of about  $\pm 1$  kcal in each  $\Delta \bar{G}_3$  and  $\Delta \bar{G}_6$ . The total error in  $\Delta \bar{G}_5$ , arising from these sources, is thus estimated to be of the order of  $\pm 6$  kcal. As may be seen from the  $\Delta \bar{G}_5$  curve in the earlier paper<sup>6</sup> this inaccuracy would not affect the oxygen percentages to a significant extent, but there is an additional source of error which is mostly neglected in recent considerations of this kind—e.g., the de-oxidation equilibria in liquid steel. In deriving the free energy of reaction (1), those for oxygen and aluminium in the ternary alloys were obtained from those in the respective binary alloys with titanium. There is, however, a mutual effect of oxygen and aluminium on their activities in the ternary alloys which was, as usual, disregarded in the calculations above. For the deoxidation of steel this point was discussed by Richardson,<sup>7</sup> for instance. Fortunately, the two effects largely compensate each other, but it is not possible to estimate the extent of the residual effect on the values of  $\Delta \bar{G}_5$ . The resulting discrepancy may be of the same order as that observed between theoretical and experimental values for the deoxidation of liquid steel (see Richardson<sup>7</sup>). Such a discrepancy would, however, not impair the value of general principles involved in the present evaluation.

It has been mentioned that, in practice, the process would presumably be carried out in the form of a thermite reaction, and that the alloys would be molten during reaction. In fact, the temperature increase, calculated from the heats of formation of  $TiO_2$  and  $Al_2O_3$ , and from the specific heats of the substances involved, is about 1200°C for a 40 per cent Ti alloy, to which is added the temperature increase due to the ignition. One may expect from general experience that the minimum in the heat of formation of titanium-aluminium alloys shifts towards equiatomic composition in the liquid state. The conditions for the production of liquid Ti-Al may therefore be somewhat more favourable. In fact, Cuelleron and Pascaud<sup>8</sup> have made from titania and aluminium, using various fluxes, by a thermite-type reaction alloys containing 40-48 per cent Ti and oxygen of the order of 1 per cent by weight. In the most favourable case, these authors claim a composition of



65 per cent Ti and 0.02 per cent oxygen. Although the calculations above contain a number of simplifying assumptions and are for 1000°C only, the latter figures appear to be a little doubtful, and would require checking. In addition, the violent thermite-type reaction would lead to a product in which segregation is incomplete; that is,  $\text{Al}_2\text{O}_3$  inclusions, which are not easily removed, would be found in the metal.

Nevertheless, a less violent reaction, in which true equilibrium could be established, should yield titanium-aluminium alloys with considerable percentages of titanium and a very low oxygen content. In practice, alloys are required that are much lower in aluminium. In view of the high price of titanium, it should be an economical advantage to add to titanium a titanium-aluminium alloy of, say, 40 per cent Ti rather than pure aluminium.

#### ACKNOWLEDGMENTS

The work described in this paper has been carried out as part of the General Research Programme of the

National Physical Laboratory, and this paper is published by permission of the Director of the Laboratory.

The authors wish to acknowledge assistance received from Mr. B. B. Argent (B. Met.) during his period at the N.P.L. as a vacation student.

#### REFERENCES

1. O. Kubaschewski and E. L. Evans, *Metallurgical Thermochemistry* (Butterworth-Springer, London, 1951).
2. W. Oelsen and W. Middel, *Mitt. KWI Eisenforschung Düsseldorf*, **19**, 1 (1937).
3. W. Biltz and C. Haase, *Z. anorg. allg. Chem.* **129**, 141 (1923).
4. E. S. Bumps, H. D. Kessler, and M. Hansen, *J. Metals* **4**, 609 (1952).
5. R. J. van Thyne, H. D. Kessler, and M. Hansen, *Trans. Am. Soc. Metals* **44**, 974 (1952).
6. O. Kubaschewski and W. A. Dench, *J. Inst. Metals* **82**, 87 (1953).
7. F. D. Richardson, *J. Iron and Steel Inst.* **166**, 137 (1950).
8. J. Cuélleron and C. Pascaud, *Compt. rend.* **233**, 745 (1951).

# ÜBER DIE ABHÄNGIGKEIT DER KORNGRENZENAUSSCHEIDUNG VON DER ORIENTIERUNG DER BENACHBARTEN KRISTALLE\*

W. GRUHL und D. AMMANN†

Es wird die Abhängigkeit der Stärke der Korngrenzenausscheidung von der Orientierungsdifferenz der benachbarten Kristalle an Proben mit Fasertextur nach [001] von Kupfer-Nickel-Mangan und Kupfer-Beryllium gemessen. Dabei wird beobachtet, dass mit steigendem Orientierungswinkel die Breite der Korngrenzenausscheidung bis zu einem flachen Maximum bei 45° zunimmt. Die Kurve der relativen Korngrenzenenergie erreicht ihr Maximum bereits bei einem Orientierungswinkel von 21°. Eine Abhängigkeit der Stärke der Ausscheidung von der Richtung der Korngrenze kann nicht festgestellt werden. Dagegen ist der Fall, dass zwei gleiche, niedrig indizierte Ebenen aufeinander liegen und die Korngrenze zu diesen Ebenen parallel verläuft, als Sonderfall anzusehen.

## ON THE DEPENDENCE OF GRAIN BOUNDARY PRECIPITATION ON THE ORIENTATION OF SURROUNDING CRYSTALS

The dependence of the rate of grain boundary precipitation on the orientation difference of the neighboring crystals is measured in copper-nickel-manganese and copper-beryllium specimens with [001] fibre axes. It can be shown that with increasing difference and orientation the breadth of the grain boundary precipitation increases to a flat maximum at 45°. The curve of relative boundary energy reaches the maximum at an orientation angle of 21°. No dependence of the precipitation rate on the grain boundary direction can be found. Similar index planes coincide.

## SUR LA RELATION ENTRE LA PRÉCIPITATION INTERGRANULAIRE ET L'ORIENTATION DES CRISTAUX VOISINS

Par mesure de la relation entre l'importance de la précipitation aux joints de grains et les différences d'orientation des cristaux voisins sur des éprouvettes présentant une texture fibreuse [001] en alliages Cu-Ni-Mn et Cu-Be, il est montré que l'épaisseur des précipités croît avec la différence d'orientation jusqu'à un maximum plat pour 45°. Par contre, l'énergie superficielle atteint son maximum pour une différence d'orientation de 21°. Aucune relation entre la précipitation et la direction des joints de grains. Par contre, le cas de deux plans identiques de faible indice avec une frontière parallèle à ces plans est à considérer comme cas particulier.

Bereits vor mehreren Jahren haben P. J. E. Forsyth, G. J. Metcalfe, R. King und B. Chalmers<sup>1</sup> darauf hingewiesen, dass die Stärke der diskontinuierlichen Ausscheidung an den Korngrenzen offenbar von der gegenseitigen Orientierung der benachbarten Kristalle abhängig ist, da die unter dem Mikroskop beobachteten dunklen Zonen an manchen Korngrenzen stark, an anderen nur schwach ausgebildet sind. Insbesondere zeigt sich häufig, dass sich die Stärke der Ausscheidung an Stellen, an denen Zwillingsstreifen ein benachbartes Korn berühren, mehrmals sprunghaft ändert. Diese Beobachtung ist später u.a. an Kupfer-Beryllium<sup>2,3</sup> und auch an dem hexagonalen Zink-Kupfer (2% Cu)<sup>4</sup> bestätigt worden. P. J. E. Forsyth, G. J. Metcalfe, R. King und B. Chalmers<sup>1</sup> vermuten, dass die Korngrenzenausscheidung umso stärker ist, je verschiedener die an der Korngrenze nebeneinander liegenden Körner orientiert sind. Sie nehmen an, dass die Stärke der Ausscheidung durch den Grad der Fehlordnung des Gitters in der nächsten Umgebung einer Korngrenze bestimmt wird.

Diese Vermutung hat nach allem, was uns heute über die Vorgänge bei der Keimbildung der Ausscheidung bekannt ist, einen hohen Grad der Wahrscheinlichkeit, doch fehlt bisher der experimentelle Nachweis.

\* Received January 22, 1955.

† Giesserei-Institut der Rhein.-Westf. Technischen Hochschule, Aachen, Germany.

Es erschien deshalb interessant, einen Versuch zur Messung der Ausscheidungsstärke in Abhängigkeit von der Orientierung zu unternehmen.

Bereits R. Smoluchowski und Mitarbeiter<sup>5</sup> hatten in ihren Arbeiten über die Orientierungsabhängigkeit der Korngrenzendiffusion erkannt, dass die räumliche Behandlung des Problems erheblich vereinfacht wird, wenn man an Proben mit Fasertextur arbeitet, bei denen alle Körner eine kristallografische Richtung gemeinsam haben. An Stelle von 3 Freiheitsgraden der kristallografischen Orientierung bleibt dann nur einer, der Orientierungswinkel  $\theta$  übrig. Führt man die Versuche an Stengelkristallen, wie sie in der Transkristallisationszone einer gegossenen Probe auftreten, durch, so verlaufen die Korngrenzen mit grosser Näherung senkrecht zur Stengelrichtung, die zugleich Faserachse der Textur ist, so dass bei einem zur Stengelrichtung senkrechten Anschliff die Richtung der Korngrenze nur noch durch einen Winkel  $\varphi$  angegeben werden kann. Damit lässt sich die Breite der Ausscheidungszone als Funktion  $b = f(\theta, \varphi)$  darstellen.

Die Versuche wurden an einer Kupfer-Nickel-Mangan-Legierung (30% Ni, 30% Mn, 40% Cu)<sup>6</sup> sowie an Kupfer-Beryllium (1,8% Be)<sup>7,2,3</sup> durchgeführt, die beide eine deutliche diskontinuierliche Ausscheidungsform zeigen.‡ Bei beiden Legierungen bereitete die

‡ Versuche an AlMg (5% Mg) scheiterten wegen der geringen Breite der Ausscheidungszone, eine Kupfer-Zinn-Nickel-Legierung

Herstellung eines einwandfreien Gussgefüges aus Stengelkristallen keine Schwierigkeit.

#### VERSUCHE MIT KUPFER-NICKEL-MANGAN

Nach dem Vergiessen zeigte diese Legierung ein Gefüge mit sehr unterschiedlichem Korndurchmesser. Neben sehr grossen Körnern, die besonders in der Randzone bis zu 6 mm Durchmesser aufwiesen, waren zahlreiche kleine (bis herab zu 0,1 mm Durchmesser) zu sehen, so dass eine röntgenografische Orientierungsbestimmung einer grösseren Zahl benachbarter Kristalle nicht möglich war. Im Gusszustand zeigte das Gefüge jedoch deutliche Dendriten, die die Orientierung der Körner einwandfrei erkennen liessen. Laue-Rückstrahlungsaufnahmen an mehreren grossen Kristallen zeigten, dass die Wachstumsrichtung der Dendriten der [001]-Richtung der Körner entsprach. Im Längsschliff verliefen die Dendriten genau senkrecht zur zylindrischen Probenachse, die [001]-Richtung war zugleich Stengel- und Faserachse, wie dies bei den kubisch flächenzentrierten Metallen der Fall ist.<sup>8</sup> Die Streuung der Fasertextur betrug max.  $\pm 10^\circ$ , um diesen Betrag wich die [001]-Richtung der Körner höchstens von der Stengelerichtung ab. Von der Probe wurde nun ein Querschliff senkrecht zur Stengelrichtung angefertigt und das Gefüge eines grösseren Bereiches fotografisch festgehalten. Anschliessend wurde entsprechend den Angaben von O. Dahl und K. L. Dreyer<sup>6</sup> zur Erzielung der Ausscheidungen zunächst ein 24 stündiges Lösungsglühen im Salzbad bei  $800 \pm 5^\circ\text{C}$  vorgenommen, die Probe in Wasser abgeschreckt und dann 4 Stunden bei  $400^\circ\text{C}$  im Salzbad ausgelagert. Nach erneutem Anschleifen wurde dieselbe Stelle des Gefüges, in dem jetzt die Dendriten verschwunden waren, dafür jedoch an den Korngrenzen deutliche Ausscheidungen auftraten, bei derselben Vergrösserung erneut fotografiert und die Orientierung der Körner durch Übertragung der

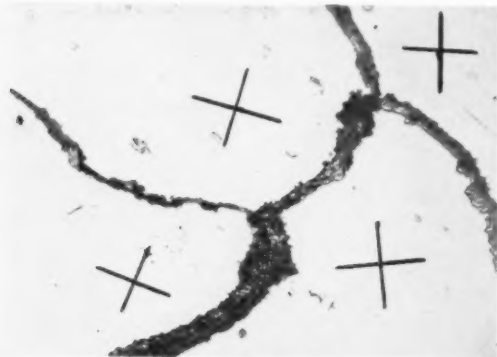


BILD 1. Korngrenzenausscheidung bei Kupfer-Nickel-Mangan  $V = 520$ . Die [100]-Richtung der Körner ist mit eingezeichnet.

ung (14% Sn, 3% Ni, Rest Cu) ergab infolge des zu feinen Transkristallisationsgefüges keine Möglichkeit der röntgenografischen Orientierungsbestimmung. Eine Zink-Kupfer-Legierung (2% Cu Rest Zn) zeigt nach dem Vergiessen nur Ringfasertextur<sup>9</sup> und war deshalb unbrauchbar.

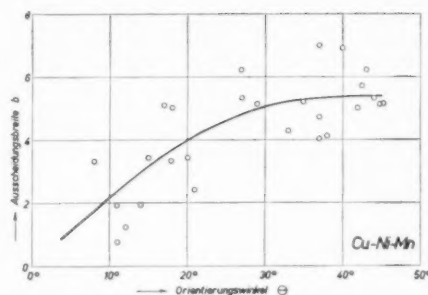


BILD 2. Abhängigkeit der Breite der Korngrenzenausscheidung von der Orientierungsdifferenz bei Kupfer-Nickel-Mangan.

Dendritenrichtung aus der vorigen Aufnahme festgelegt. Ein Vergleich der beiden Bilder zeigte, dass im Verlauf der Wärmebehandlung nur eine relativ geringfügige Verschiebung der Korngrenzen stattgefunden hatte, so dass die einzelnen Körner stets zu identifizieren waren. Die Orientierungswinkel konnten dann aus den Aufnahmen auf  $\pm 1^\circ$  genau ermittelt werden.

Bild 1 zeigt das Gefüge der Kupfer-Nickel-Mangan-Legierung nach der vorgenommenen Wärmebehandlung. Der Anschliff erfolgte senkrecht zur Faserachse. Man sieht, dass die Breite einer Ausscheidungszone an ein und derselben Korngrenze recht unterschiedlich ist. Zur Ausmessung wurde das Gefüge bei 780 facher Vergrösserung auf die Mattscheibe des Mikroskops geworfen und die Ausscheidungsbreite  $b$  aus mehreren Messungen gemittelt. In Bild 1 ist die [100]-Richtung der Körner, wie sie sich aus der Übertragung ergab, durch Kreuze gekennzeichnet.

Bild 2 zeigt die Abhängigkeit der Stärke der Korngrenzenausscheidung von dem Orientierungswinkel  $\theta$  bei der Kupfer-Nickel-Mangan-Legierung. Die Ausscheidungsbreite  $b$  ist hier in mm bei 780 facher Vergrösserung angegeben. Da als Faserachse die [001]-Richtung vorliegt, haben wir eine 4 zählige Symmetrie, bei der der Winkel  $\theta$ , der die Orientierungsdifferenz angibt, einen Höchstwert von  $45^\circ$  annehmen kann. Naturgemäss streuen die einzelnen Werte stark, doch zeigt sich eine deutliche Zunahme der Stärke der Ausscheidung mit wachsender Orientierungsdifferenz, wobei die gemittelte Kurve einen Höchstwert bei  $\theta = 45^\circ$  erreicht. Die erhebliche Streuung der Werte ist teilweise wohl auf Ungenauigkeiten bei der Ausmessung der Ausscheidungsbreite zurückzuführen, da diese im Verlauf ein und derselben Korngrenze Unterschiede bis zu 100% aufwies (vgl. Bild 1). Auf weitere Ursachen für die Streuung der Werte wird bei den Messungen an Kupfer-Beryllium noch hingewiesen.

#### VERSUCHE MIT KUPFER-BERYLLIUM

Eine Legierung mit 1.75% Be zeigte nach dem Vergiessen ziemlich gleichmässige Stengelkristalle, deren Durchmesser jedoch 2 mm nur vereinzelt überstieg. Ebenso wie bei Kupfer-Nickel-Mangan zeigten sich im Gusszustand deutliche Dendriten nach [100]. Ein



BILD 3. Ausscheidung an den Korngrenzen und im Korninneren bei Kupfer-Beryllium. Die Orientierung der Körner ist an den Ätzstreifungen deutlich zu erkennen.  $V=530$ .

Versuch, die Dendritenrichtung ebenso wie bei Kupfer-Nickel-Mangan zur Orientierungsbestimmung heranzuziehen, scheiterte jedoch daran, dass nach einem 24 stündigen Diffusions- und Lösungsglühen bei  $820 \pm 5^\circ\text{C}$  im Salzbad und nachfolgender Wasserabschreckung eine erhebliche Verschiebung der Korngrenzen stattgefunden hatte, so dass die ursprünglichen Körner nicht mehr zu erkennen waren. Hier ergab sich jedoch eine andere Möglichkeit zur Orientierungsbestimmung. Nach 4 stündigem Anlassen auf  $400^\circ\text{C}$  im Salzbad zeigte sich an den Korngrenzen eine deutliche diskontinuierliche, daneben im Korninneren eine kontinuierliche Ausscheidung, wie sie bereits früher festgestellt worden war.<sup>3</sup> Durch mehrfaches Ätzpolieren wurden auf den Kornflächen Ätzstreifungen erzielt, die zweifellos durch eine orientierte Ausscheidung der  $\gamma$ -Phase auf bestimmten kristallografischen Ebenen hervorgerufen werden. Diese Streifen verlaufen zum Teil in einer Richtung, teils stehen sie senkrecht aufeinander. Eine an mehreren grösseren Körnern vorgenommene Bestimmung der Orientierung dieser Streifen durch Laue-Rückstrahlungsaufnahmen ergab, dass sie stets parallel zu der  $[100]$ -Richtung verlaufen. Die Orientierung der Körner konnte hierdurch einwandfrei erkannt werden. Bild 3 zeigt das Gefüge einer solchen Probe mit Ausscheidungs-zonen an den Korngrenzen und streifigen Ausscheidungen im Korninneren, die die  $[100]$ -Richtung der Körner angeben. Die Schliiffläche verläuft senkrecht zur Faserachse.

Die Abweichung des Korngrenzenverlaufes der Stengelkristalle von der Achse der zylindrischen Probe wurde aus einem Längsschliff mit max.  $\pm 15^\circ$  gemessen. Die Streuung der  $[001]$ -Richtung einzelner Körner von der Faserachse betrug nach den Röntgenaufnahmen max.  $\pm 8^\circ$ . Zur Auswertung wurde eine grössere Anzahl von Gefügeaufnahmen verschiedener Stellen derselben Probe bei 530 facher Vergrösserung hergestellt und die Ausmessung des Orientierungswinkels  $\theta$  mittels eines Winkelmessers auf  $1^\circ$ , die der Ausscheidungsbreite mittels einer Schublehre auf 0.1 mm genau gemessen,

wobei letztere, die allerdings bei Kupfer-Beryllium kaum schwankte, gemittelt wurde.

Zusätzlich wurde noch der die Richtung einer Korngrenze angegebende Winkel  $\varphi$  ermittelt und die Ausscheidungsbreite auch in Abhängigkeit von diesem gemessen. Analog zu der von W. Shockley und R. T. Read<sup>9</sup> bei ihren Berechnungen verwendeten Definition der Korngrenzenrichtung wurde  $\varphi$  in der Weise gemessen, dass eine Tangente an die Korngrenze gelegt und ausserdem eine mittlere  $[100]$ -Richtung mit dem Winkel  $\theta/2$  zu den beiden  $[100]$ -Richtungen der benachbarten Körner gebildet wurde.  $\varphi$  wurde zwischen diesen beiden Richtungen gleichfalls auf  $1^\circ$  genau gemessen.

Bild 4 zeigt die Abhängigkeit  $b$  von  $\theta$  bei Kupfer-Beryllium. Die Ausscheidungsbreite  $b$  ist hier in mm bei 530 facher Vergrösserung angegeben. Wie man sieht, streuen die Werte auch hier nicht unerheblich, doch dürfte der direkte, bei Kupfer-Nickel-Mangan durch die starken Unterschiede in der Breite der Ausscheidungen hervorgerufene Messfehler hier in Fortfall kommen, da die Ausscheidung entlang ein und derselben Korngrenze bei Kupfer-Beryllium ziemlich gleichmässig stark war (vgl. Bild 3). Die gestrichelt eingezeichnete Kurve ergibt sich aus einer genauen Mittelung der Messwerte, die ausgezogene Kurve gibt den tatsächlichen Wert für  $b$  wieder, der durch den Nullpunkt gehen muss, da ja bei der Orientierungsdifferenzkeine Korngrenze und damit auch keine Korngrenzenausscheidung existiert. Man sieht, dass die Abweichung beider Kurven nur bei kleinen Orientierungsdifferenzen merklich wird. Ansonsten ist ebenso wie bei der Kupfer-Nickel-Mangan-Legierung ein deutlicher Anstieg der Ausscheidungsbreite mit zunehmender Orientierungsdifferenz zu beobachten, bei  $45^\circ$  tritt wiederum ein flaches Maximum der Kurve auf.

Auffällig sind die hier trotz genauester Ausmessung auftretenden starken Streuungen der einzelnen Werte. P. J. E. Forsyth, G. J. Metcalfe, R. King und B. Chalmers<sup>1</sup> vermuten, dass die Richtung der Korngrenze einen Einfluss auf die Stärke der Ausscheidung hat. Aus diesem Grunde wurde die Abweichung der einzelnen Messpunkte von der ausgezogenen Kurve in Bild 4 in Abhängigkeit von dem Winkel  $\varphi$ , der die Richtung der Korngrenze zu der mittleren  $[100]$ -Richtung der benachbarten Körner angibt, gemessen. Der Winkel  $\varphi$

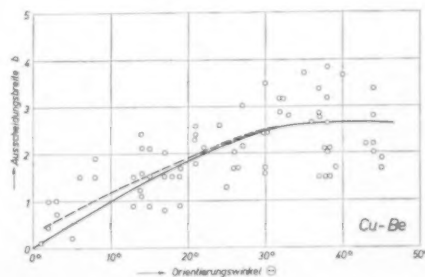


BILD 4. Abhängigkeit der Breite der Korngrenzenausscheidung von der Orientierungsdifferenz bei Kupfer-Beryllium.



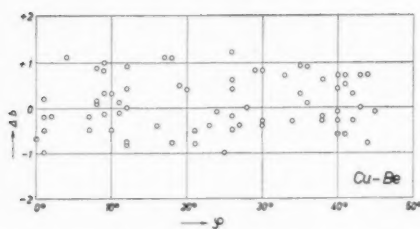


BILD 5. Abweichung der Ausscheidungsweite in Abhängigkeit von dem Richtungswinkel  $\varphi$  der Korngrenze.

kann ebenso wie  $\theta$  bei der vorliegenden 4 zähligen Symmetrie einen Höchstwert von  $45^\circ$  annehmen. In Bild 5 ist diese Abhängigkeit  $b$  von  $\varphi$  dargestellt. Wie man sieht, hat die Richtung der Korngrenze offensichtlich keinen Einfluss auf die Grösse der Streuungen und damit auch keinen Einfluss auf die Breite der Ausscheidung. In Bild 6 ist eine Korngrenze gezeigt, die in ihrem Verlauf sämtliche Werte für  $\varphi$  von  $0-45^\circ$  annimmt; die Ausscheidungsweite ist hier unverändert.

Eine weitere mögliche Ursache für die Streuungen wäre die Tatsache, dass die Korngrenzen nicht immer genau senkrecht zur Schliffebene verlaufen. Die gemessenen Abweichungen von  $\pm 15^\circ$  würden im Grenzfall folgende Korrektur des gemessenen  $b$ -Wertes erforderlich machen:

$$b_{\text{wahr}} = b_{\text{gemessen}} \cdot \cos 15^\circ = \text{ca. } 0.97 b_{\text{gemessen}}$$

Die maximalen Abweichungen dürfen hiernach nur  $+3\%$  betragen, liegen tatsächlich jedoch erheblich höher.

Für die Abweichung der gemessenen Kurve von der tatsächlichen bei kleinen Werten für  $\theta$  ist offenbar die Tatsache verantwortlich, dass die Fasertextur keineswegs ideal war, sondern Streuungen von max.  $\pm 8^\circ$  aufwies. Damit können die kristallografischen Längsachsen zweier Körner im Grenzfall um  $16^\circ$  gegeneinander geneigt sein. Setzt man einfach voraus, dass sich aufeinander senkrecht stehende Orientierungsdifferenzen vektoriell addieren lassen, so muss diese Orientierungsdifferenz von  $\theta' = \text{max. } 16^\circ$  zu dem in der Schliff-



BILD 6. Korngrenzenausscheidung bei veränderter Richtung einer Korngrenze bei Kupfer-Beryllium.  $V = 530$ .

ebene gemessenen  $\theta_{\text{gem}}$  nach den Regeln des rechtwinkligen sphärischen Dreiecks zur tatsächlichen Orientierungsdifferenz  $\theta$  entsprechend:

$$\cos \theta = \cos \theta_{\text{gem}} \cdot \cos \theta'$$

führen. Es werden so maximale Abweichungen von  $\theta$  bis zu  $16^\circ$  bei  $\theta_{\text{gem}} = 0$  und solche bis zu ca.  $2^\circ$  bei  $\theta_{\text{gem}} = 45^\circ$  auftreten. Diese Überlegung erklärt ohne weiteres die beobachteten Abweichungen bei kleineren Orientierungsunterschieden, insbesondere auch die Tatsache, dass die genau gemittelte, in Bild 4 gestrichelte Kurve von der wahren, ausgezogenen nach oben abweicht. Eine Verschiebung des Messpunktes nach rechts zu etwas grösseren Winkeln hin würde sie der ausgezogenen Kurve näher bringen. Diese im Rahmen einer Fehlerabschätzung wohl durchaus zulässige einfache Addition der Orientierungsunterschiede, die auf der Voraussetzung beruht, dass sich eine dreidimen-

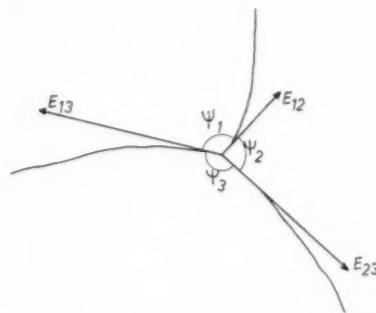


BILD 7. Schema zur Messung der relativen Korngrenzenenergie.

sionale Fehlorientierung nicht anders auswirkt als eine zweidimensionale, zeigt jedenfalls, dass für die Abweichung bei kleinen Winkeln die Streuung der Fasertextur verantwortlich ist und erhärtet die Richtigkeit des Verlaufes der ausgezogenen Kurve, die durch den Nullpunkt geht.

Die bei grossen Orientierungsdifferenzen beobachteten Streuungen sind schon im Hinblick auf den flacher werdenden Verlauf der Kurve in der Nähe des Maximums durch Winkelstreuungen nicht zu klären. Auf ihre Ursache wird im folgenden noch eingegangen.

Die zahlreichen Gefügaufnahmen der Kupfer-Beryllium-Legierung erlaubten zusätzlich noch die Messung der relativen Korngrenzenenergie als Grenzflächenenspannung, wie sie in ähnlicher Weise erstmals von C. G. Dunn und F. Lionetti<sup>10</sup> an Eisen mit 3% Si sowie von K. T. Aust und B. Chalmers<sup>11</sup> an Blei und Zinn und von A. P. Greenough und R. King<sup>12</sup> an Silber durchgeführt wurde. An einer Stelle des Gefüges, an der drei Korngrenzen zusammenstossen, stellen sich im Falle des Gleichgewichtes zwischen diesen bestimmte Winkel ein, die von dem Energieverhältnis der drei Korngrenzen abhängig sind. In Bild 7 ist dieser Fall schematisch dargestellt. Da die Summe der drei Vektoren im Gleichgewichtsfall Null ist, gilt die

Beziehung:

$$\frac{E_{23}}{\sin\psi_1} = \frac{E_{13}}{\sin\psi_2} = \frac{E_{12}}{\sin\psi_3}$$

An einer Anzahl von Gefügestellen, an denen drei Korngrenzen zusammenstossen, wurden die Winkel  $\psi_1$ ,  $\psi_2$  und  $\psi_3$  genau ausgemessen und so drei Relativwerte für die Energie der drei Korngrenzen erhalten. Zwar war bei der 24 stündigen Homogenisierungsglühung bei 820°C nicht darauf geachtet worden, ob diese auch zur Winkelkonstanz geführt hatte, doch lässt die Beobachtung, dass die Korngrenzen sich bei der Glühung so stark verschoben hatten, dass das ursprüngliche Gefüge nicht mehr zu erkennen war, mit grosser Wahrscheinlichkeit auf eine weitgehende Einstellung des Gleichgewichtes schliessen. In Bild 8 sind nun die erhaltenen Wertetripel ausgehend von einem Maximalwert, der für eine Korngrenze, an der der Orientierungswinkel  $\theta=45^\circ$  betrug, gleich 1 gesetzt wurde, so aufgetragen, dass sich eine möglichst geschlossene Kurve ergab. Man kann auf diese Weise die relative Korngrenzenenergie in Abhängigkeit von der Orientierung erkennen. Die Kurve verläuft zunächst ausgehend von dem Wert 0 ziemlich steil ansteigend und erreicht bei einem Wert für  $\theta$  von annähernd  $21^\circ$  ihren Höchstwert, der sich bei grösseren Orientierungswinkeln nicht mehr verändert. Dieser Kurvenverlauf der relativen Korngrenzenenergie stimmt recht gut mit den Ergebnissen anderer Autoren,<sup>10,11,12</sup> insbesondere von K. T. Aust und B. Chalmers<sup>11</sup> für das kubisch flächenzentrierte Blei bei einer Fasertextur nach [001] überein, auch dort wurde ein Maximalwert der Korngrenzenenergie bei  $\theta=22^\circ$  gemessen. Analog hierzu hatten R. Smoluchowski und Mitarbeiter<sup>5</sup> beobachtet, dass von einem kritischen Orientierungswinkel  $\theta_{kr}=22^\circ$  ab eine merkliche Bevorzugung der Korngrenzen bei der Diffusion von Zink bzw Silber in Kupfer stattfindet. In Bild 8 ist zum Vergleich auch die Kurve der Ausscheidungsbreite  $b$  aus Bild 4 gestrichelt in dem Massstab mit eingezeichnet, dass der Höchstwert von  $b$  auch dem der Korngrenzenenergie  $E$  entspricht. Man sieht, dass beide Kurven in ihrem Verlauf nicht übereinstimmen, da die Kurve der Ausscheidungsbreite wesentlich flacher verläuft und

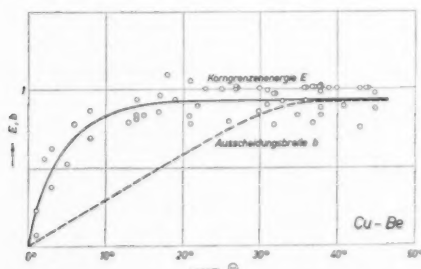


BILD 8. Relative Korngrenzenenergie von Kupfer-Beryllium in Abhängigkeit von der Orientierungsdifferenz. Die Kurve der Ausscheidungsbreite ist aus Bild 4 gestrichelt mit eingezeichnet.

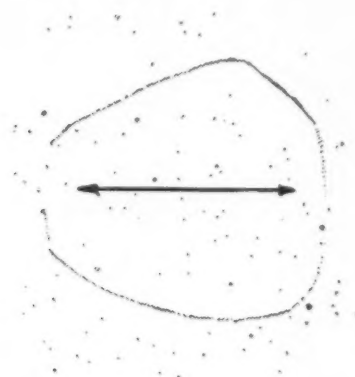


BILD 9. Korngrenzenausscheidung bei Kupfer-Beryllium an einem von einem anderen völlig umschlossenen Kristall. Der Pfeil gibt die vermutliche Faserrichtung an. (Nach P. J. E. Forsyth, G. J. Metcalfe, R. King und B. Chalmers.)

erst bei einem Orientierungswinkel  $\theta$  von etwa  $40^\circ$  ihr Maximum erreicht.

#### DEUTUNG DER ERGEBNISSE

Die Versuche haben deutlich gezeigt, dass die Korngrenzenausscheidung umso stärker ist, je verschiedener die benachbarten Kristalle an der betreffenden Korngrenze orientiert sind. Damit wird die Vermutung von P. J. E. Forsyth, G. J. Metcalfe, R. King und B. Chalmers<sup>1</sup> auch experimentell bestätigt. Im Gegensatz zu der Vermutung dieser Autoren konnte jedoch bei Proben mit Fasertextur keine Abhängigkeit der Stärke der Korngrenzenausscheidung von der Richtung der Korngrenze festgestellt werden. W. Shockley und R. T. Read<sup>9</sup> hatten errechnet, dass der Korngrenzenwinkel  $\varphi$  einen Einfluss auf die Korngrenzenenergie bei gleichem Orientierungswinkel  $\theta$  haben müsste, und zwar ergab sich rechnerisch für ein primitiv kubisches Gitter eine Abweichung bis max. 40%. Tatsächlich konnte ein solcher Einfluss bisher auch bei den Messungen der Korngrenzenenergie selbst<sup>10,11,12</sup> nicht beobachtet werden, ebenso zeigten die Versuche von R. Smoluchowski und Mitarbeitern,<sup>5</sup> dass  $\varphi$  keine Wirkung auf die Geschwindigkeit der Korngrenzendiffusion hat. Die vorliegenden Versuche bestätigen daher die Richtigkeit der experimentellen Befunde.

Trotzdem ist die Beobachtung von P. J. E. Forsyth, G. J. Metcalfe, R. King und B. Chalmers<sup>1</sup> über den Einfluss der Richtung der Korngrenze als real anzusehen. In Bild 9 ist eine Aufnahme dieser Autoren von Kupfer-Beryllium gezeigt, in der ein Korn von einem anderen völlig umwachsen ist. Deutlich erkennt man, dass hier nur bei einer ganz bestimmten Richtung der Korngrenze eine Ausscheidung fehlt, während in allen anderen Richtungen eine deutliche und ziemlich gleichmässig starke Ausscheidung zu sehen ist. Offenbar haben hier beide Körner eine Hauptrichtung, möglicherweise [100], gemeinsam. Diese gemeinsame Richtung verläuft hier quer zum Schlibbild, entsprechend dem

eingezeichneten Pfeil. Die Ebenen senkrecht zur dieser Richtung haben die gleichen Indices, sind jedoch um unbekannte Winkel gegeneinander verdreht. Bei der vorliegenden Versuchsanordnung wurde dieser Fall nicht erfasst, hier lagen alle Korngrenzen etwa parallel zur Faserachse. Es wird vermutet, dass ein Sonderfall dann vorliegt, wenn gerade zwei niedrig indizierte Ebenen parallel zueinander liegen und die Korngrenze zusätzlich parallel zu diesen Ebenen verläuft. Eine grundsätzliche Abhängigkeit der Ausscheidungsstärke von dem Korngrenzenwinkel  $\varphi$  ist jedoch mit Sicherheit nicht festzustellen.

Um die Ergebnisse selbst zu verstehen, muss man zunächst einmal überlegen, von welchen Faktoren die gemessene Ausscheidungsbreite  $b$  überhaupt abhängig ist. Es sind dies einmal die Keimbildungshäufigkeit und zum anderen die Geschwindigkeit des Wachstums der gebildeten Ausscheidungskeime. Beides wird von der Korngrenzenenergie sowie von der Stärke und Zahl der an einer Korngrenze vorhandenen Gitterstörstellen und Versetzungen beeinflusst. Dabei ist jedoch anzunehmen, dass die Keimbildungsgeschwindigkeit wesentlich stärker beeinflusst wird als die Wachstumsgeschwindigkeit. Wie Messungen der Ausscheidungsgeschwindigkeit an  $\alpha$ -Eisen<sup>13</sup> und Kupfer-Beryllium<sup>3</sup> in verformtem und unverformtem Zustand gezeigt haben, wird durch eine nach dem Abschrecken vorgenommene Kaltverformung die zur Keimbildung erforderliche Inkubationszeit erheblich herabgesetzt, während der weitere Ausscheidungsverlauf, also das Keimwachstum sogar leicht verzögert erscheint. Das verformte Gitter ist infolge einer erhöhten Zahl von Versetzungen den unmittelbar an einer Korngrenze liegenden Gitterbereichen, in denen sich die Korngrenzenausscheidung abspielt, recht ähnlich; man kann daher für den vorliegenden Fall zumindest voraussetzen, dass die Geschwindigkeit des Keimwachstums nur unwesentlich verändert und gegenüber der Keimbildungshäufigkeit vernachlässigt werden kann. Betrachtet man weiterhin das Wesen der diskontinuierlichen Ausscheidung, die ja nach anfänglicher Keimbildung in einem spontanen Zerfall des Muttergitters in die beiden Gleichgewichtsphasen besteht, wobei nach U. Dehlinger<sup>14</sup> dieser Zerfall sich autokatalytisch in das Kristallinnere fortpflanzt, so erkennt man leicht, dass die Geschwindigkeit des Fortpflanzens wohl kaum von der Orientierungsdifferenz der Körner abhängig sein kann, da sich dieser Vorgang ja sehr rasch von der Korngrenze entfernt. Unter dieser Annahme einer konstanten Wachstumsgeschwindigkeit der dunklen Ausscheidungszonen wird aber deren gemessene Breite  $b$  zu einer Funktion des Zeitpunktes, an dem die erste Keimbildung stattgefunden hat. Dass die Keimbildung ausschlaggebend für die Ausscheidung ist und gerade an den Korngrenzen besonders erleichtert wird, zeigen u.a. auch die Untersuchungen von A. von Wiedebach-Nostitz<sup>15</sup> an Zink-Silber- sowie von W. Gruhl<sup>4</sup> an Zink-Kupfer-Legierungen; hier findet die Ausscheidung der  $\epsilon$ -Phase bei tiefen Temperaturen, bei

denen eine Keimbildung im Inneren der Körner noch nicht möglich ist, in Form der diskontinuierlichen Ausscheidung an den Korngrenzen statt, bei höheren Temperaturen ist die kontinuierliche Ausscheidung vorherrschend.

Nach R. Becker<sup>16</sup> ist nun die Keimbildungshäufigkeit für die Bildung einer zweiten Phase durch die Beziehung

$$I \approx \text{prop. exp} \left( -\frac{Q+A}{RT} \right)$$

gegeben, worin  $Q$  die Aktivierungswärme für die Diffusion,  $A$  die Keimbildungsarbeit,  $R$  die allgemeine Gaskonstante und  $T$  die absolute Temperatur bedeuten. Berücksichtigt man nun im vorliegenden Fall noch die Korngrenzenenergie und betrachtet diese als Erhöhung des an einer Korngrenze vorhandenen spezifischen Energiezustandes des Gitters gegenüber dem im Inneren der Kristalle, so wird sich die für eine Keimbildung aufzuwendende Arbeit um diesen Energiebetrag  $E'$  vermindern. Man erhält somit für die Keimbildungshäufigkeit

$$I \approx \text{prop. exp} \left( -\frac{(Q+A)-E'}{RT} \right).$$

Damit lässt sich die mit zunehmendem Orientierungswinkel  $\theta$  wachsende Breite der Ausscheidungszonen erklären, da ja der Betrag von  $E'$  mit  $\theta$  ansteigt und bei steigender Keimbildungshäufigkeit  $I$  auch der Beginn der Keimbildung früher einsetzt. Nach dem Unterbrechen der Auslagerung in einem bestimmten Zeitpunkt erscheinen dann diejenigen Zonen am breitesten, an denen die Keimbildung am frühesten eingesetzt hat.

Der in Bild 8 dargestellte Verlauf der relativen Korngrenzenenergie  $E$  und der gemessenen Ausscheidungsbreite  $b$  stimmt mit den vorhergehenden Überlegungen jedenfalls bis zu einem Orientierungswinkel  $\theta = 21^\circ$  überein. Bis zu diesem Orientierungswinkel wird die Struktur der Korngrenzen recht befriedigend durch das Versetzungsmodell, wie es von J. M. Burgers<sup>17</sup> und W. L. Bragg<sup>18</sup> vorgeschlagen wurde, wiedergegeben. Für grössere Werte von  $\theta$  bleibt die Korngrenzenenergie konstant, während die Ausscheidungsbreite noch weiter zunimmt. In diesem Bereich hat nach R. Smoluchowski<sup>19</sup> das Inselmodell von N. F. Mott<sup>20</sup> Gültigkeit; nach dieser Vorstellung wechseln entlang einer Korngrenze Inseln, in denen die Gitter der benachbarten Kristalle relativ gut aufeinander passen mit solchen Gebieten ab, in denen eine schlechte Passung, die nicht ohne weiteres durch eine einfache Versetzungsstruktur überbrückt werden kann, vorhanden ist. Offenbar ist im Gültigkeitsbereich des Mott'schen Inselmodells nun nicht mehr ausschliesslich die Korngrenzenenergie für die Erhöhung der Keimbildungshäufigkeit massgebend. Betrachtet man jedoch eine Stelle, an der eine schlechte Passung der benachbarten Gitter vorliegt, so haben wir hier ein Gebiet, an dem gleichsam beide Gitter zusammenhanglos aufeinander liegen. Beide Gitter haben eine

vollständige Oberfläche, durch die sie voneinander getrennt sind. Nach R. Becker<sup>16</sup> wird die Bildung eines Keims nun wesentlich durch seine Grenzflächenspannung gegenüber der ihn umgebenden Mutterphase erschwert. Dadurch, dass bereits vor der Bildung des Ausscheidungskeimes an der Korngrenze selbst eine freie Grenzfläche des Muttergitters vorliegt, wird die aufzuwendende Grenzflächenenergie zweifellos stark herabgesetzt und damit nach den Ansätzen von R. Becker<sup>16</sup> sowohl die Keimbildungsarbeit  $A$  als auch die kritische Keimgröße erniedrigt. Es werden sich somit Keime vorzugsweise an den Stellen schlechter Passung bilden. Je verschiedener nun die Orientierung der Körner ist, desto zahlreicher und grösser werden auch die Gebiete schlechter Passung, so dass die gesamte Keimbildungshäufigkeit entlang einer Korngrenze ansteigt. Mit dieser Überlegung wird die Beobachtung, dass die Breite der Ausscheidungszonen mit steigendem Orientierungswinkel auch nach dem Erreichen eines Höchstwertes der Korngrenzenenergie bei ca.  $21^\circ$  noch weiter ansteigt, wohl verständlich.

Die Betrachtung der Ausscheidungsbreite als Funktion des Zeitpunktes, in dem die Keimbildung an der betreffenden Stelle vor sich gegangen ist, lässt auch eine Erklärung für die insbesondere bei grossen Orientierungswinkeln beobachtete starke Streuung der Messwerte (vgl. Bild 4) zu. Der Zeitpunkt einer ersten Keimbildung wird im einzelnen durch statistische und thermische Schwankungen bestimmt, lediglich sein wahrscheinliches Eintreffen wird durch die Keimbildungshäufigkeit  $I$  wiedergegeben. Betrachtet man zusätzlich noch die Keimbildungsverhältnisse, insbesondere im Gültigkeitsbereich des Mott'schen Inselmodells, so

wird auch die Keimbildungsarbeit, je nachdem wie nun die Passung der Gitter innerhalb einzelner, submikroskopischer Bereiche ist, sehr verschieden starken Schwankungen unterworfen sein, ihre Verminderung in Abhängigkeit von der Orientierung erhält damit gleichfalls einen rein statistischen Charakter. Damit findet die beobachtete starke Streuung der einzelnen Werte eine Erklärung.

Herrn Professor Dr. G. Wassermann, Clausthal, sei für die Anregung zu dieser Arbeit sowie für zahlreiche Diskussionen herzlich gedankt.

#### LITERATUR

1. P. J. E. Forsyth, G. J. Metcalfe, R. King, und B. Chalmers, *Nature* **158**, 875 (1946).
2. A. G. Guy, C. S. Barrett, und R. F. Mehl, *Met. Techn.* 1948, Techn. Publ. Nr. 2341.
3. W. Gruhl und G. Wassermann, *Metall* **5**, 93 und 141 (1951).
4. W. Gruhl, *Metall*, **9**, 353 (1955).
5. M. R. Achter und R. Smoluchowski, *J. Appl. Phys.* **22**, 126 (1951); R. Flanagan und R. Smoluchowski, *J. Appl. Phys.* **23**, 785 (1952).
6. O. Dahl und K. L. Dreyer, *Z. Metallk.* **45**, 342 (1954).
7. H. Bumm, *Z. Metallk.* **29**, 30 (1937).
8. vgl. G. Wassermann, "Texturen metallischer Werkstoffe" (Berlin, 1939).
9. W. Shockley und R. T. Read, *Phys. Rev.* **75**, 692 (1949); *Phys. Rev.* **78**, 275 (1950).
10. C. G. Dunn und F. Lionetti, *Trans. A.I.M.E.* **185**, 125 (1949).
11. K. T. Aust und B. Chalmers, *Proc. Roy. Soc.* **201**, 210 (1950); *Proc. Roy. Soc.* **204**, 359 (1951).
12. A. P. Greenough und R. King, *J. Inst. Met.* **79**, 415 (1951).
13. W. Gruhl, *Z. Metallk.* **41**, 178 (1950).
14. U. Dehlinger, *Z. Metallk.* **29**, 401 (1937).
15. A. von Wiedebach-Nostitz, *Z. Metallk.* **37**, 56 (1946).
16. R. Becker, *Z. Metallk.* **29**, 245 (1937).
17. J. M. Burgers, *Proc. Phys. Soc.* **52**, 23 (1940).
18. W. L. Bragg, *Proc. Phys. Soc.* **52**, 54 (1940).
19. R. Smoluchowski, *Phys. Rev.* **87**, 482 (1952).
20. N. F. Mott, *Proc. Phys. Soc.* **60**, 391 (1948).



## ÜBER DIE IDEALEN ORIENTIERUNGEN EINER WALZTEXTUR\*

JOHANNA GREWEN und G. WASSERMANN†

Eine vergleichende Untersuchung der Walztextur einer Aluminiumfolie mit dem Texturgoniometer ergab, dass die Textur an allen Stellen der Folie ungefähr gleich ist, dass jedoch hinsichtlich der Einzelheiten Unterschiede bestehen. Auch die Lage der Maxima der Belegungsdichte unterliegt einer Streuung und ist schon in den vier Quadranten einer Polfigur nicht übereinstimmend. Es wird untersucht, wie sich dieser Befund auf die Deutung der Textur mit Hilfe von idealen Orientierungen auswirkt.

Die idealen Orientierungen, die für gewalztes Aluminium und andere kubisch-flächenzentrierte Metalle innerhalb der letzten dreissig Jahre vorgeschlagen worden sind, werden besprochen und mit den (111)-Polfiguren der vorliegenden Untersuchung verglichen. Nahezu alle diese Orientierungen sind mit der Polfigur annähernd in Übereinstimmung, aber keine wird den experimentellen Ergebnissen wirklich gerecht.

Die bisherige Annahme idealer Orientierungen mit einer Kristallebene parallel der Walzebene und einer Kristallrichtung parallel der Walzrichtung erscheint daher für die Beschreibung von Walztexturen nicht geeignet.

Es wird eine neue Beschreibung vorgeschlagen, nach der die Polfigur aus einer Überlagerung mehrerer Fasertexturen (die in Bezug auf die Rotation um die Faserachse beschränkt sind) besteht. Es werden für Aluminium zwei Faserachsen [111] und eine Faserachse [100] angenommen und die sich daraus ergebenden theoretischen Polfiguren konstruiert.

Das Ergebnis stimmt mit den experimentellen Resultaten sehr gut überein. Es können auf diese Weise nicht nur die Lagen der Maxima beschrieben werden, sondern insbesondere auch die bei der bisherigen Methode ganz unberücksichtigt gelassenen Streulagen.

### ON THE IDEAL ORIENTATIONS OF A ROLLING TEXTURE

A comparative study of the rolling texture of aluminium foil by means of the texture goniometer has shown that the texture is nearly the same everywhere in the foil. There are, however, differences in details. Also, the location of the orientation maxima shows scattering, and differs in the four quadrants of the same pole figure. An investigation was made as to the manner in which this variation affects the interpretation of the texture by means of ideal orientations.

The ideal orientations proposed for rolled aluminium and other f.c.c. metals during the last 30 years are discussed and compared with the (111) pole figure of the present investigation. Nearly all of these orientations are in approximate agreement with the pole figure, but none gives a true picture of the experimental results.

Therefore, the former assumption of ideal orientations in the form of a crystal plane parallel to the rolling plane and a crystal direction parallel to the rolling direction appears unsuitable as a description of rolling textures.

A new description is proposed according to which the pole figure consists of a composition of several fibre textures, the latter being restricted as to the rotation around the fibre axis. For aluminium, two fibre axes [111] and one fibre axis [100] are suggested, and the resulting theoretical pole figures are constructed.

The result is in very good agreement with the experimental findings. This method permits a description of the location of the maxima and, in particular, the orientation spread which could not be considered in earlier procedures.

### SUR LES ORIENTATIONS IDÉALES DES TEXTURES DE LAMINAGE

Une étude de la texture de laminage d'une feuille d'aluminium montre que, bien que la texture soit sensiblement la même en tous les points, il existent cependant dans le détail des différences. C'est ainsi que la position des maximums de densité présente une dispersion et ne coïncide pas dans les quatre cadrans d'une figure polaire. Il est montré comment cette observation influe sur l'interprétation de la texture.

Les orientations idéales qui ont été proposées au cours des trente dernières années pour l'aluminium laminé et les autres métaux cubiques à faces centrées sont discutées et comparées avec les figures de pôles (111) de cette recherche.

Toutes ces orientations sont sensiblement en coïncidence, mais aucune ne correspond réellement aux résultats expérimentaux.

Les hypothèses actuelles pour les orientations idéales (plan cristallin parallèle au plan de laminage et direction cristalline parallèle à la direction de laminage) ne paraissent pas appropriées à la description des textures de laminage. Il est proposé de décrire celles-ci par la superposition de plusieurs textures de fibres (se limitant à une rotation autour de l'axe de la fibre). Pour l'aluminium, les figures polaires sont construites en prenant comme axes de fibre [111] et [100].

Le résultat correspond très bien à l'expérience et, de cette façon, non seulement la position des maximums peut être expliquée, mais aussi la dispersion, contrairement aux méthodes antérieures.

\* Received August 10, 1954; in revised form October 15, 1954.

† Institut für Metallkunde der Bergakademie Clausthal, Clausthal-Zellerfeld, Deutschland.

## EINLEITUNG

Die Kristallorientierungen in verformten und rekristallisierten Blechen sind in den meisten Fällen so kompliziert, dass eine genaue Bestimmung und Darstellung der Textur nur mit Hilfe der stereographischen Projektion in Form von Polfiguren möglich ist. Daneben hat man sich stets bemüht, sogenannte "ideale Orientierungen" aufzufinden, d.h. einzelne Kristallorientierungen, derart, dass eine bestimmte Kristallfläche der Blechebene parallel und eine in dieser Fläche liegende kristallographische Richtung als parallel der Walzrichtung angegeben wird.

Durch eine solche Vereinfachung will man eine Grundlage für das Verständnis und die Deutung der Entstehung der Texturen von Blechen schaffen, ohne die komplizierten, nach Richtung und Ausmass sehr verschiedenen Streuungen berücksichtigen zu müssen. Weiterhin ist es mit Hilfe der idealen Orientierungen möglich, die Texturen von Blechen auf einfache und anschauliche Weise mit Hilfe von Worten zu beschreiben.

Die idealen Orientierungen lassen sich nun durchaus nicht immer leicht und sicher bestimmen. Während z.B. über die ideale Orientierung der als "Würfellage" bekannten Rekristallisationstextur kein Zweifel bestehen kann, ist das Auffinden idealer Orientierungen bei den Rekristallisations- und Walztexturen von Blechen in den meisten anderen Fällen recht schwierig und unsicher. Dies rührt daher, dass entweder die Maxima der Belegungsdichte in der Polfigur nicht sehr ausgeprägt sind, oder dass sich nicht alle Maxima mit den Flächenpolen eines Einkristalles zur Deckung bringen lassen.

Für eine möglichst sichere Bestimmung der idealen Orientierungen sollten folgende Voraussetzungen erfüllt sein:

1. muss die Anisotropie des untersuchten Materials möglichst gross sein, so dass sich die Bereiche maximaler Belegungsdichte scharf ausprägen und möglichst eng begrenzt sind. Dies wird am ehesten bei einem Werkstoff mit hohem Verformungsgrad verwirklicht sein. Diese Voraussetzung ist bei den meisten der in der Literatur beschriebenen Texturen erfüllt.

2. muss die Bestimmungsmethode so genau sein, dass sich die Bereiche maximaler Belegungsdichte auch wirklich präzise bestimmen und abgrenzen lassen. Dies ist durch die Verwendung des Geiger-Müller-Zählrohres zur Texturbestimmung heute möglich. Das früher verwendete photographische Verfahren ist dagegen recht ungenau und erfüllt diese Voraussetzung nur unzureichend.

3. wird vorausgesetzt, dass die Polfiguren reproduzierbar sind, d.h. dass die Belegungsdichte an denselben Stellen immer die gleiche ist. Dieser Punkt ist jedoch noch weitgehend unklar, denn die Möglichkeit einer Streuung der Belegungsdichte ist unseres Wissens bisher weder untersucht noch überhaupt diskutiert worden.

## EXPERIMENTELLE ERGEBNISSE

Die Frage nach der Streuung der Textur innerhalb eines Bleches war Gegenstand einer Untersuchung, über die ausführlich an anderer Stelle berichtet wurde.<sup>1</sup> An hartgewalzter Aluminiumfolie von  $37\mu$  Dicke und 94,6% Walzgrad wurden Texturbestimmungen vorwiegend für die (111)-Flächen durchgeführt. Zum Zwecke genauer Vergleichbarkeit und Zuordnung der Polfigur zu jeweils einer bestimmten Stelle des Materials wurden dem Vergleich nur die äusseren Zonen der Polfigur, wie sie nach Decker, Asp und Harker<sup>2</sup> mit dem Durchstrahlverfahren aufgenommen werden können, zugrunde gelegt.

Es zeigte sich, dass Proben, die an verschiedenen Stellen, (jedoch immer in der Mitte der Folienbreite) der Folie entnommen worden waren, zwar in grossen Zügen, nicht aber in den Details der Textur miteinander übereinstimmten. Die kleinen Differenzen in den Polfiguren waren auch dann vorhanden, wenn die untersuchten Stellen in der Folienrolle nur 6 mm voneinander entfernt waren, und sie vergrösserten sich andererseits nicht oder nur sehr wenig, wenn die Proben aus verschiedenen Rollen (hergestellt aus verschiedenen Stranggussabschnitten) stammten.

Bei Texturen, die mit dem Geiger-Müller-Zählrohr bestimmt wurden, ist bereits bekannt,<sup>3</sup> dass die Polfiguren nicht völlig symmetrisch sind, d.h., die Belegungsdichte in den vier Quadranten ist nicht übereinstimmend, die Ebenen Blechnormale-Walzrichtung und Blechnormale-Querrichtung sind keine Spiegelebenen. Dies wurde auch an der untersuchten Aluminiumfolie festgestellt.

Zu einer Übersicht über die in der Folie vorherrschende Textur gelangt man am besten, wenn man jede Polfigur über die vier Quadranten mittelt und überdies eine Mittelung über sämtliche, an verschiedenen Proben aufgenommenen Polfiguren vornimmt.

Die Untersuchung war für die äusseren Zonen<sup>2</sup> der Polfigur (Durchstrahlung) an 17 verschiedenen Proben, für die inneren Zonen<sup>4</sup> (Rückstrahlung) an 3 Proben vorgenommen worden. Die aus den Polfiguren aller dieser Proben durch Mittelung und Vervielfachung gewonnene Polfigur für die (111)-Flächen zeigt die Abb. 1. Die Abb. 2 gibt eine von einer Einzelbestimmung herrührende, durch Spiegelung vervierfachte Polfigur der (200)-Flächen wieder (Cu-Strahlung).

Eine weitere Auswertung der Ergebnisse dieser Untersuchung sei hier bezüglich der Frage vorgenommen, wie sich Streuungen auf die Lage der Belegungsmaxima auswirken und welche Schlüsse aus der Lage dieser Maxima auf die idealen Orientierungen der Walztextur des Aluminiums gezogen werden können.

Eine Durchsicht der Polfiguren der Einzelbestimmungen zeigte, dass in den einzelnen Polfiguren die Maxima keineswegs immer an denselben Stellen liegen, auch ihre Lage ist vielmehr Streuungen unterworfen. Dies gilt bereits für die einzelne Polfigur in sich, denn

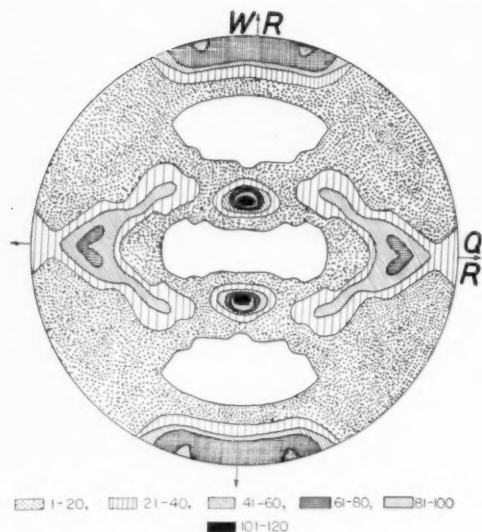


ABB. 1. Polfigur der (111)-Flächen einer um 94,6% gewalzten Aluminiumfolie, gemittelt und vervierfacht.

bei Vervielfachung der Lagen einer Polfigur durch Spiegelung kommen die Stellen höchster Intensität nicht alle zur Deckung. So ist es nicht verwunderlich, dass auch die Maxima, die von verschiedenen Proben stammen, nicht miteinander zur Deckung kommen. Natürlich sind bezüglich der Lage der Maxima ganz bestimmte Gebiete bevorzugt. Wenn man aber alle in den 17 Polfiguren der äusseren Zonen und in 3 Bestimmungen für die Mitte der Polfiguren gefundenen Maxima in einem Quadranten zusammenfasst, wie dies für die (111)-Polfigur in Abb. 3 geschehen ist, so erkennt man, dass die Streuung doch bemerkenswert gross ist.

#### DIE IDEALE ORIENTIERUNGEN

Zur Entscheidung der Frage, ob trotz der Streuung bestimmte Lagen als bevorzugt bezeichnet werden

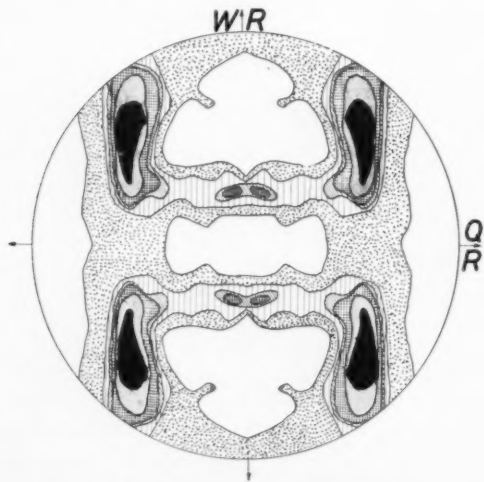


ABB. 2. Polfigur der (200)-Flächen einer um 94,6% gewalzten Aluminiumfolie, Einzelbestimmung, vervierfacht.

können, sei zunächst erörtert, welche idealen Orientierungen für Aluminium von früheren Beobachtern angegeben worden sind.

Man kann feststellen, dass die Resultate der zahlreichen Untersuchungen der Walztextur kubisch-flächenzentrierter Metalle in grossen Zügen recht gut übereinstimmen, obwohl zu den meisten dieser Bestimmungen das photographische Verfahren benutzt wurde. Im einzelnen sind aber doch Unterschiede vorhanden, die dazu führten, dass die von den verschiedenen Beobachtern gemachten Angaben über die idealen Orientierungen nicht oder nicht immer übereinstimmen und im Laufe der Zeit Verbesserungsvorschlägen unterlagen. Dabei ist zunehmend die Tendenz erkennbar, anstelle der in früheren Jahren angegebenen, einfach indizierten Flächen und Richtungen kompliziertere, höher indizierte Orientierungen als ideale Lagen anzunehmen.

Dies gilt auch für die Walztextur des Aluminiums, das gerade in letzter Zeit mehrfach erneut untersucht wurde, ohne dass sich eine einheitliche Auffassung

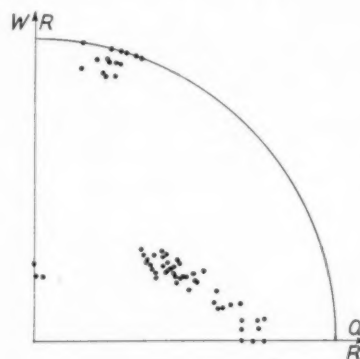


ABB. 3. Punkte maximaler Belegung der (111)-Flächen auf Grund von sieben Einzelbestimmungen in den äusseren Zonen und drei Bestimmungen in der Mitte.

über die auftretenden idealen Orientierungen herausbildete.

In der Tabelle I sind die von verschiedenen Forschern für gewalztes Aluminium angegebenen idealen Orientierungen zusammengestellt. Abb. 4 zeigt für die Angaben der Tabelle I die Flächenpole.

In einer ganzen Reihe von Bestimmungen aus den Jahren 1923/33 war festgestellt worden, dass die Walztextur des Aluminiums in der Hauptsache durch die Orientierung (011)  $[2\bar{1}1]$  beschrieben werden kann.<sup>5,6</sup> Andere Forscher fanden, dass eine bessere Beschreibung der Textur dadurch möglich sei, dass man daneben noch eine zweite ideale Lage, nämlich (112)  $[\bar{1}11]$  angab.<sup>7,8</sup> v. Göler und Sachs<sup>8</sup> wiesen dann darauf hin, dass diese doppelte Lage auch durch eine einzige Orientierung, nämlich (135)  $[\bar{5}33]$  beschrieben werden könne. Auch diese ideale Lage wurde mehrfach bestätigt.<sup>6</sup>

Einen von der (135)  $[\bar{5}33]$ -Lage etwas abweichenden Vorschlag machten weiterhin Barrett und Steadman,<sup>9</sup>

TABELLE I. Ideale Orientierungen der Walztextur des Aluminiums.

1. Lage		2. Lage		3. Lage		erste Beobachter	
Walzebene	Walzrichtg.	Walzebene	Walzrichtg.	Walzebene	Walzrichtg.		
(011)	$[\bar{2}\bar{1}1]$					H. Mark u. K. Weissenberg (1923) <sup>5</sup>	
(011)	$[\bar{2}\bar{1}1]$	(112)	$[\bar{1}\bar{1}1]$			F. Wever (1923) <sup>7</sup>	
(135)	$[\bar{5}33]$					Frhr. v. Göler u. G. Sachs (1927) <sup>8</sup>	
(135)	$[\bar{2}\bar{1}1]$					C. S. Barrett u. F. W. Steadman (1942) <sup>9</sup>	
mittlerer Walzgrad							
(011)	$[\bar{2}\bar{1}1]$	(112)	$[\bar{1}\bar{1}1]$	(100)	$[001]$	H. J. Wallbaum (1951) <sup>10</sup>	
hoher Walzgrad							
(112)	$[\bar{1}\bar{1}1]$	(100)	$[011]$				
96% Walzgrad							
(011)	$[\bar{2}\bar{1}1]$	(112)	$[\bar{1}\bar{1}1]$	(100)	$[001]$	K. Lücke (1954) <sup>11</sup>	
99,99% Walzgrad							
(112)	$[\bar{1}\bar{1}1]$	(100)	$[011]$	(011)	$[\bar{2}\bar{1}1]$		
(479)	$[\bar{9}47]$					F. W. Custers (1941) <sup>12</sup> an 47% Fe-Ni	
(7 12 22)	$[\bar{8}45]$					Hu Hsun, P. R. Sperry, u. P. A. Beck (1952) <sup>3</sup>	

die eine (135)  $[\bar{2}11]$ -Orientierung als ideale Lage angeben.

Auf Grund von neueren Untersuchungen nach dem photographischen Verfahren gaben Wallbaum<sup>10</sup> und Lücke<sup>11</sup> an, dass im gewalzten Aluminiumblech neben den bekannten Lagen (011)  $[\bar{2}11]$  und (112)  $[\bar{1}\bar{1}1]$  noch die Würfellage (100)  $[001]$  vertreten sei. Bei sehr hohem Walzgrad trat die (011)  $[\bar{2}11]$ -Lage zurück und die Würfellage verschwand völlig. (112)  $[\bar{1}\bar{1}1]$  war jetzt am stärksten vertreten. Es soll daneben die Lage (100)  $[011]$  neu gebildet werden.

Von den höher indizierten idealen Lagen ist zunächst die sogenannte Z-Orientierung ( $Z = \text{Zwischen}$ ) zu nennen, die Custers<sup>12</sup> an einer 47% igen Eisen-Nickellegierung gefunden hat, die aber auch für Aluminium diskutiert worden ist.<sup>3,11</sup> Diese Lage entspricht einer (479)  $[\bar{9}47]$ -Orientierung.

Eine weitere hochindizierte Lage, die als ideale Orientierung nach (7 12 22)  $[\bar{8}45]$  angegeben wird, fanden Hsun Hu, Sperry und Beck.<sup>3</sup>

Trägt man diese im Laufe von drei Jahrzehnten vorgeschlagenen idealen Orientierungen gemeinsam in

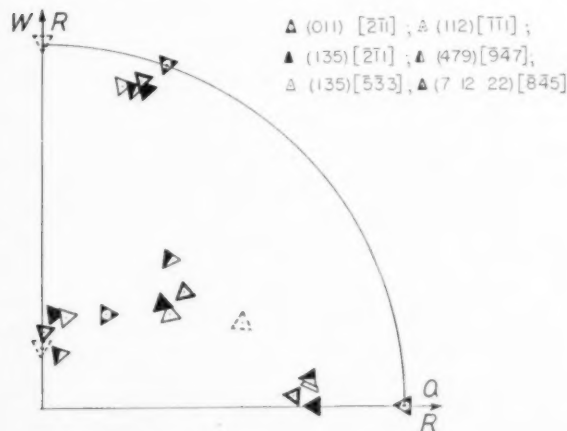


ABB. 4. Ideale Orientierungen nach Vorschlag verschiedener Beobachter.

eine Polfigur ein, wie dies (mit Spiegelung an den Symmetrieebenen des Bleches) in Abb. 4 geschehen ist, so erkennt man, dass sie zwar bis zu einem gewissen Grade voneinander abweichen, dass aber ihre Flächenpole doch in ganz bestimmten, verhältnismässig engen Gebieten der Polfigur ausstechen und das dies dieselben Gebiete sind, die auch von den experimentell gefundenen Maxima der Belegungsdichte, wie sie Abb. 3 zeigt, eingenommen werden. Man kann sagen, dass keine der idealen Lagen dem Befund widerspricht, andererseits aber auch, dass keine als völlig befriedigend noch repräsentativ für die Polfigur bezeichnet werden kann. Die idealen Lagen überdecken vielmehr etwa den Streubereich der Maxima.

Eine Durchsicht unserer experimentell gefundenen Polfiguren zeigt ferner, dass stets ein oder zwei Maxima mit den Flächenpolen einer idealen Lage gut übereinstimmen, dass aber weitere Flächenpole der idealen Orientierung nicht mit einem Maximum der Belegungsdichte zur Deckung gebracht werden können. Eine vollständige Übereinstimmung der Maxima einer einzelnen Polfigur mit allen Polen einer idealen Lage konnte jedenfalls in der vorliegenden Untersuchung nicht gefunden werden. Dies kommt z.B. auch in den von Hsun Hu, Sperry und Beck<sup>3</sup> wiedergegebenen Polfiguren deutlich zum Ausdruck. Es stimmt die von diesen Autoren angenommene ideale Orientierung (7 12 22)  $[\bar{8}45]$  in Fig. 1 ihrer Veröffentlichung nur mit dem starken Maximum nahe der Blechnormalen gut überein. Die anderen Flächenpole der idealen Orientierung weichen dagegen von den Stellen maximaler Belegung deutlich ab.

Dieses Ergebnis führt zu dem Schluss, dass der Versuch der Beschreibung einer Walztextur durch Annahme einer bestimmten Kristallfläche parallel zur Walzebene und einer bestimmten Kristallrichtung parallel zur Walzrichtung dem tatsächlichen Aufbau der Textur nicht entspricht und aufgegeben werden sollte. Dazu kommt noch, dass die Angabe hoch indizierter Flächen und Richtungen dem Bestreben,



durch solche idealen Orientierungen eine anschauliche Beschreibung der Textur zu geben, wenig gerecht wird, und dass solche hochindizierten Flächen so schwach mit Atomen besetzt sind, dass auch ihr Wert für die Deutung der Textur in Frage gestellt ist.

#### VERSUCH EINER BESCHREIBUNG MIT HILFE VON FASERTEXTUREN

Die Tatsache, dass einzelne Richtungen der idealen Lagen immer wieder mit Stellen besonders dichter Belegung zur Deckung kommen, lässt vermuten, dass es nur bestimmte Kristallrichtungen sind, die sich in bestimmte Richtungen des Bleches einstellen. Es wurde daher versucht, eine Beschreibung der Walztextur mit Hilfe von Fasertexturen zu geben und zwar derart, dass eine Überlagerung mehrerer Fasertexturen angenommen wird. Solche Fasertexturen brauchen allerdings nicht wie bei Drähten vollständig zu sein, d.h. es braucht nicht eine Rotation der möglichen Kristallorientierungen um die Faserachse um  $360^\circ$  stattzufinden, sondern es könnte eine unvollständige Fasertextur, bei der eine Rotation jeweils nur um bestimmte Winkelbereiche stattfindet, vorliegen.\* Es erhebt sich natürlich die Schwierigkeit, dass an sich jede Kristallrichtung als Faserachse fungieren könnte und damit die Zahl der Möglichkeiten unübersehbar gross sein würde. Da ja aber bei Drähten im allgemeinen einfach indizierte Richtungen als Faserachse auftreten, schien es naheliegend, zu versuchen, ob

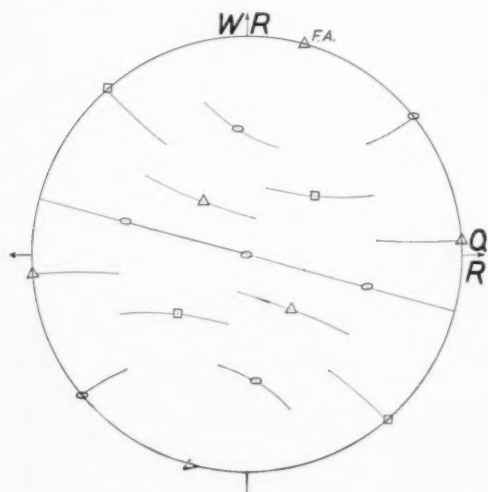


ABB. 5. Erste [111]-Faserachse zur Beschreibung der Walztextur des Aluminiums mit Flächenpolen für die (111)-, (100)-, und (110)-Flächen. Rotation der Faserachse um  $\pm 30^\circ$ . (F. A. = Faserachse.)

\* Es sei darauf hingewiesen, dass von Glocker<sup>13</sup> schon vor langer Zeit ein Auswertungsverfahren für Texturaufnahmen angegeben wurde, das auf der Annahme beruhte, dass in gewalzten Blechen Fasertexturen auftreten. Allerdings ging auch dieses Verfahren von der alten Vorstellung aus, dass die ausgezeichnete Richtung (Faserachse) parallel zur Walzrichtung liegen muss. Die Streuung wurde als teilweise Rotation um die Walzrichtung (Faserachse) gedeutet.

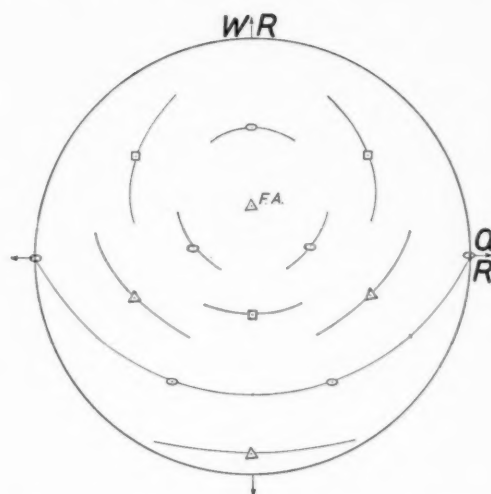


ABB. 6. Zweite [111]-Faserachse zur Beschreibung der Walztextur des Aluminiums. Rotation der Faserachse um  $\pm 30^\circ$ .

nicht auch bei Blechen eine Deutung der Textur mit Hilfe niedrig indizierter Faserachsen möglich ist, zumal in den Polfiguren der (111)- und (100)-Flächen ja ausgeprägte Maxima auftreten. So wurden für den Versuch einer solchen Beschreibung Faserachsen nach [111] und [100] gewählt. Betrachtet man die Abb. 1, so sieht man (und dies kommt auch in den Polfiguren von Hsun Hu, Sperry und Beck zum Ausdruck), dass am stärksten ausgeprägt und am wenigsten streuend die beiden Gebiete maximaler Belegung nahe der Walzrichtung und nahe der Normalrichtung sind. Das Maximum nahe der Querrichtung ist, wie unsere Untersuchungen ergaben, häufig nur sehr schwach ausgebildet und zudem viel stärker streuend. Auch in der Polfigur der Würfelflächen (vergl. Abb. 2) ist ein ausgeprägtes Maximum zu bemerken. Es wurde in-

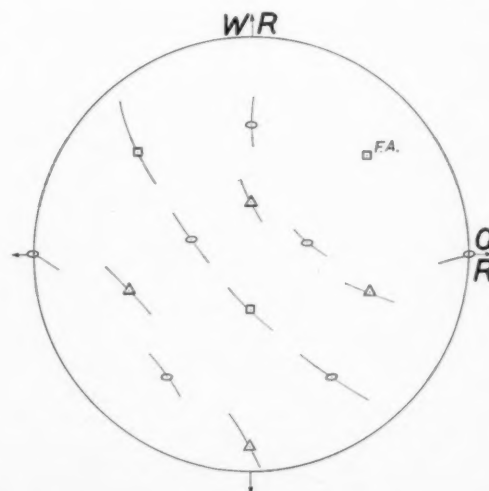


ABB. 7. [100]-Faserachse zur Beschreibung der Walztextur des Aluminiums. Rotation der Faserachse um  $\pm 15^\circ$ .

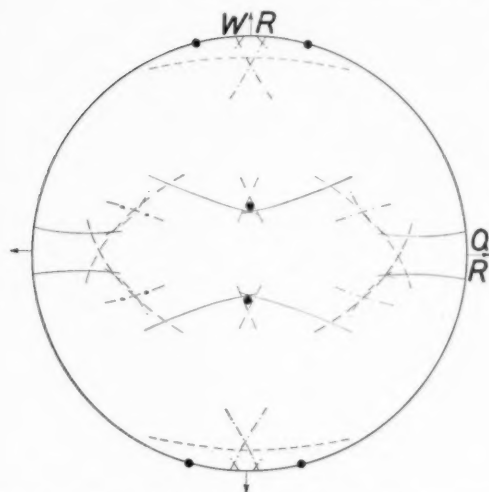


ABB. 8. Auf Grund der Annahme von drei Faserachsen konstruierte Polfigur der (111)-Flächen. (● = Faserachsen.)

folgedessen versucht, unter den folgenden Annahmen Polfiguren zu konstruieren:

1. eine Faserachse nach  $[111]$  liegt in der Blechebene,  $15^\circ$  gegen die Walzrichtung gedreht. ( $\alpha = 0^\circ$ ,  $\beta = 15^\circ$ .) Die Abb. 5 zeigt diese Faserachse und die Flächenpole für (111), (100) und (110).

2. Eine zweite Faserachse  $[111]$  liegt in der Ebene Blechnormale-Walzrichtung um  $25^\circ$  gegen die Normalrichtung geneigt. Diese Lage ist in Abb. 6 dargestellt ( $\alpha = 65^\circ$ ,  $\beta = 0^\circ$ ).

3. Eine dritte Faserachse ist nach  $[100]$  orientiert. Ihre Lage und die zugehörigen Flächenpole für die (111), (100) und (110)-Eben ist aus Abb. 7 ersichtlich ( $\alpha = 20^\circ$ ,  $\beta = 48^\circ$ ).

Diese drei ausgezeichneten Richtungen stellen nun aber insofern keine vollständigen Faserachsen dar, als eine Rotation um  $360^\circ$  nicht zulässig ist. Es handelt

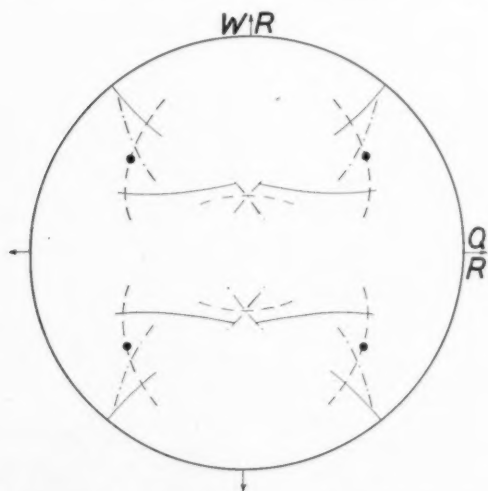


ABB. 9. Auf Grund der Annahme von drei Faserachsen konstruierte Polfigur der (100)-Flächen. (● = Faserachse.)

sich vielmehr um unvollständige Fasertexturen. Bei den beiden  $[111]$ -Faserachsen erfolgt um die in Abb. 5 und 6 gezeigten Lagen eine Rotation (Streuung) um  $\pm 30^\circ$ , d.h. also um  $60^\circ$ . Bei der Dreizähligkeit dieser Achsen ist also ein Bereich von  $3 \times 60 = 180^\circ$  bestrichen, dazwischen befinden sich nicht belegte Lücken von je  $60^\circ$ . Bei der  $[100]$ -Faserachse wurde um die in Abb. 7 gezeichnete Lage eine Rotation von  $\pm 15^\circ$  angenommen. Die Vierzähligkeit dieser Achse ergibt dann belegte Bereiche von  $4 \times 30 = 120^\circ$ . Dazwischen liegen vier Lücken der Belegung von je  $60^\circ$ .

Auf Grund der vorstehend gemachten Annahmen über den Aufbau der Walztextur aus Fasertexturen wurden nun die Polfiguren für die Flächen (100), (111) und (110) konstruiert. Das Ergebnis ist in den Abb. 8, 9 und 10 wiedergegeben. Durch Vergleich der Abb. 8 mit Abb. 1 erkennt man, dass für die (111)-Polfigur die

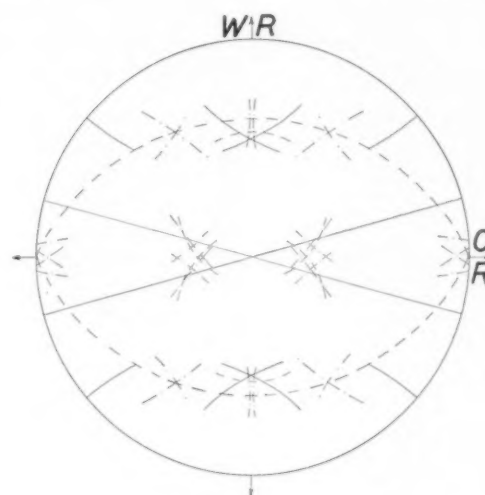


ABB. 10. Auf Grund der Annahme von drei Faserachsen konstruierte Polfigur der (110)-Flächen.

Übereinstimmung zwischen der konstruierten Polfigur und der experimentell gefundenen überraschend gut ist. Dasselbe ergibt sich für die Würfflächen bei Vergleich der Abb. 9 mit Abb. 2 oder mit der Abb. 2 der Arbeit von Hsun Hu, Sperry und Beck.<sup>3</sup> Für die (110)-Flächen liegt in der Literatur eine Polfigur von v. Göler und Sachs<sup>8</sup> aus dem Jahre 1925 vor. Die Abb. 10 zeigt mit ihr befriedigende Übereinstimmung. Abb. 11 gibt die bei der vorliegenden Untersuchung aufgenommenen Polfigur der (110)-Flächen wieder (Mo-Strahlung). Man erkennt beim Vergleich von Abb. 10 und 11, dass auch für die Dodekaederflächen eine sehr gute Übereinstimmung zwischen der konstruierten und der experimentell bestimmten Polfigur vorhanden ist.

Natürlich werden nicht nur genau die Orientierungen vorhanden sein, die durch die in den Abb. 8, 9 und 10 gezeichneten Kreisbögen gekennzeichnet sind. Man muss vielmehr noch zusätzlich mit Streulagen rechnen, die folgendermassen zustande kommen: Es

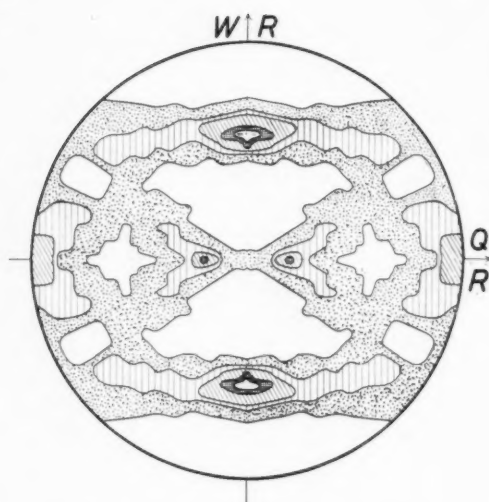


Abb. 11. Polfigur der (110)-Flächen einer um 94,6% gewalzten Aluminiumfolie, Einzelbestimmung, vervierfacht.

wird eine Abweichung der ausgezeichneten Richtungen der einzelnen Kristalle von der Faserachse vorhanden sein, wie sie auch bei den Texturen von Drähten mehr oder weniger festzustellen ist. Damit erweitern sich die Striche der Abb. 8, 9 und 10 zu Bändern. Aus Gründen der Deutlichkeit wurde hier auf eine solche Darstellung verzichtet. Man kann sich jedoch vorstellen, dass auf diese Weise Polfiguren mit verschiedenen Belegungsdichten erhalten werden können.

Entsprechend der Schwankung der Belegungsmaxima innerhalb desselben Bleches wird natürlich auch die Orientierung der Faserachsen selbst in gewissen Grenzen schwanken. Ebenso wird die Streuung, die durch unvollständige Rotation um die Faserachsen entsteht, gewissen Schwankungen unterworfen sein. Sehr erheblich werden diese Streuungen allerdings nicht werden, da die in grossen Zügen festgestellte Gleichheit der Polfiguren ein- und desselben Materials oder auch verschiedener Metalle gleicher Struktur sonst nicht vorhanden sein könnte.

Die hier vorgenommene Schilderung des Aufbaues einer Walztextur mit Hilfe unvollständiger Fasertexturen ist vielleicht nicht anschaulicher als die Angabe von idealen Lagen der bisherigen Art, zweifellos ist sie aber viel leistungsfähiger. Die bisher gebräuchlichen idealen Orientierungen gingen von der Voraussetzung aus, dass sämtliche Maxima der Polfigur mit Flächenpolen der idealen Orientierungen in Übereinstimmung waren. Die vorliegende Untersuchung hat gezeigt, dass schon diese Annahme, wenn nicht in allen, so doch in vielen Fällen nicht erfüllt ist. Überdies ist zu bedenken, dass schon das Operieren mit den bisherigen idealen Orientierungen eine Vereinfachung und

Idealisierung der Polfigur bedeutet, die der Wirklichkeit nur annähernd entspricht, denn ein wesentlicher Teil der Flächenpole sticht in der Polfigur an Orten aus, die von den Maxima mehr oder weniger weit entfernt sind.

Dem gegenüber haben die neuen idealen Orientierungen den Vorzug, dass sämtliche rechnerisch festgestellten Maxima der Belegungsdichte, wie sie durch die zugrunde liegende Annahme von Faserachsen zustande kommen, tatsächlich mit den experimentell gefundenen Orten maximaler Belegungsdichte übereinstimmen. Darüberhinaus aber führt die neue Darstellung auch zu einer weitgehend vollständigen Übereinstimmung an all den Stellen der Polfigur, die von Orten maximaler Belegung entfernt sind. Ein weiterer Vorteil ist, dass nach Festlegung der Faserachsen die Polfigur jeder beliebigen Flächenart konstruiert werden kann. Damit ergibt sich auch die Möglichkeit, zu kontrollieren, ob die Polfiguren verschiedener Flächenarten tatsächlich einander entsprechen.

Ob das hier gegebene Bild des Aufbaues einer Walztextur mit Hilfe von Faserachsen mehr ist, als eine bloss Beschreibung, ob also dieser Aufbau ursächlich zusammenhängt mit der Entstehung der Textur und ob sich auf diese Weise ein neuer Weg zum Verständnis der Texturbildung eröffnen wird, kann heute noch nicht gesagt werden. Es sei jedoch darauf hingewiesen, dass die Beschreibung der (110)-Walzlage des Eisens durch eine bevorzugte Streuung in Form einer Rotation um die Walzrichtung schon früher angenommen wurde.<sup>6</sup> Auch die Walztexturen von Magnesium und anderen hexagonalen Metallen lassen sich als vollständige, die des Zinks als unvollständige Fasertextur nach [0001] beschreiben.<sup>6</sup> Vor allem wird es zunächst notwendig sein, weitere experimentelle Ergebnisse zu gewinnen.

Der Deutschen Forschungsgemeinschaft sei für die Unterstützung dieser Arbeit bestens gedankt.

#### LITERATUR

1. J. Grewen u. G. Wassermann, Z. f. Metallkde. **45**, 570 (1954).
2. B. F. Decker, E. T. Asp, u. D. Harker, J. Appl. Phys. **19**, 388 (1948).
3. Hu Hsun, P. R. Sperry, u. P. A. Beck, Trans. A.I.M.E. **194**, 76 (1952).
4. L. G. Schulz, J. Appl. Phys. **20**, 1030 (1949).
5. H. Mark u. K. Weissenberg, Z. f. Phys. **14**, 328 (1923).
6. vergl. z. B., G. Wassermann, Texturen metallischer Werkstoffe (Springer, Berlin, 1939).
7. F. Wever, Z. f. Phys. **5**, 69 (1923); Mitt. KWI Eisenforschung **28**, 69 (1924).
8. Frhr. v. Göler u. G. Sachs, Z. f. Phys. **41**, 873 (1927).
9. C. S. Barrett u. F. W. Steadman, Trans. A.I.M.E. **147**, 57 (1942).
10. H. J. Wallbaum, Z. f. Metallkde. **42**, 371 (1951).
11. K. Lücke, Z. f. Metallkde. **45**, 86 (1954).
12. F. H. Custers, Physica **8**, 771 (1941).
13. R. Glocker, Z. f. Metallkde. **16**, 181 (1924); Z. f. Phys. **31**, 386 (1925).

# A GROWTH MECHANISM FOR MERCURY WHISKERS\*

G. W. SEARS

Very fine whiskers of solid mercury can be grown by condensation of mercury vapor on a glass surface. It is demonstrated that the whiskers have a single imperfection, an axial screw dislocation, which accounts for their morphology. The whiskers are nucleated on tiny crystalline regions in the glass surface which present the end of a screw dislocation.

## UN MÉCANISME DE CROISSANCE DES BARBES DU MERCURE

De très petites barbes de mercure solide peuvent croître par condensation de la vapeur sur une surface de verre. Il est montré que ces barbes n'ont comme seule imperfection qu'une dislocation vis axiale, ce qui explique leur morphologie. Ces barbes ont pour germe de petites régions cristallines à la surface du verre où se trouve l'extrémité d'une dislocation vis.

## EIN WACHSTUMSMECHANISMUS FÜR QUECKSILBER IN HÄRCHENARTIGER AUFWACHSUNG (WHISKERS)

Eine sehr feine härchenartige Aufwachsung (whiskers) von festem Quecksilber kann durch Kondensation von Quecksilberdampf auf einer Glasscheibe gezüchtet werden. Es wird gezeigt, dass die einzelnen Härchen (whiskers) nur eine einzige Unregelmässigkeit haben, eine axiale Schraubenversetzung, welche ihre Entstehung erklärt. Die Härchen entstehen durch Keimwirkung auf kleinen kristallinen Gebieten der Glasoberfläche, die das Ende einer Schraubenversetzung darstellen.

In 1921 Volmer and Estermann<sup>1</sup> reported the formation of tiny platelets of mercury by the condensation of mercury vapor upon a blown glass surface at  $-63.5^{\circ}\text{C}$ . The platelets of mercury grew to a length of about 0.3 mm and were so thin that they underwent ceaseless Brownian motion. The mercury vapor pressure in the closed evacuated chamber was controlled by regulating the temperature of mercury in a reservoir. Platelets were observed to grow in about two minutes when the reservoir was held at  $-10^{\circ}\text{C}$ . This pressure of mercury vapor was 1600 times the vapor pressure at  $-63.5^{\circ}\text{C}$ .

The growth rate of platelets in their large dimension was a thousandfold greater than could be accounted for by direct impingement and condensation of mercury atoms upon the advancing plane from the vapor phase. Volmer and Estermann concluded that the impinging mercury atoms were adsorbed on the solid surface and the adsorbed atoms migrated over the surface until they either evaporated or were incorporated into the solid lattice.

Langmuir<sup>2-5</sup> has concluded from studies of interaction of gases with solid surfaces that gas molecules striking a solid surface are temporarily adsorbed before they are re-evaporated. Impingement, temporary adsorption and re-evaporation is the general mechanism for reflection of gas molecules at a solid surface.

Since detailed theories of the growth of perfect crystals<sup>6,7,8</sup> and of imperfect crystals<sup>9</sup> have since been developed, it seemed desirable to repeat the experiments of Volmer and Estermann and examine the phenomena in more detail. The author<sup>10</sup> has described some new results briefly in which very fine whiskers of solid mercury have been grown 0.01 micron in radius and 1

to 2 mm in length. The present paper presents a detailed growth mechanism for these whiskers.

## EXPERIMENTAL

The initial experiments were carried out using the vessel illustrated in Fig. 1. The liquid mercury which supplied the vapor for crystal growth was contained in reservoir, R. The crystals were grown on the condensation finger, F. The reservoir was filled with a few milliliters of liquid mercury and sealed onto a vacuum system

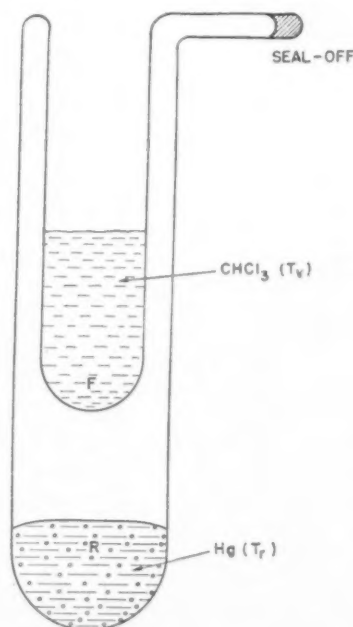


FIG. 1. Original Crystal Grower.

\* Received December 9, 1954.

† General Electric Research Laboratory, Schenectady, N. Y.



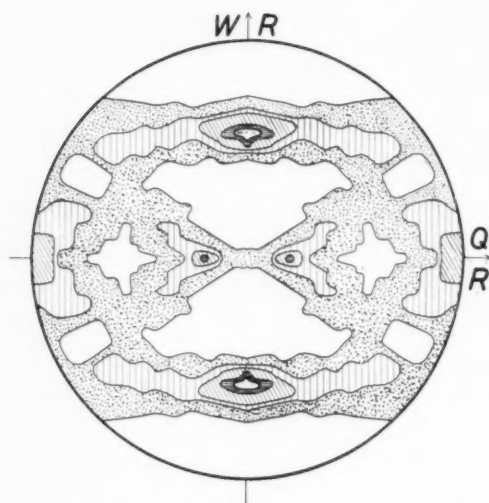


Abb. 11. Polfigur der (110)-Flächen einer um 94,6% gewalzten Aluminiumfolie, Einzelbestimmung, vervierfacht.

wird eine Abweichung der ausgezeichneten Richtungen der einzelnen Kristalle von der Faserachse vorhanden sein, wie sie auch bei den Texturen von Drähten mehr oder weniger festzustellen ist. Damit erweitern sich die Striche der Abb. 8, 9 und 10 zu Bändern. Aus Gründen der Deutlichkeit wurde hier auf eine solche Darstellung verzichtet. Man kann sich jedoch vorstellen, dass auf diese Weise Polfiguren mit verschiedenen Belegungsdichte erhalten werden können.

Entsprechend der Schwankung der Belegungsmaxima innerhalb desselben Bleches wird natürlich auch die Orientierung der Faserachsen selbst in gewissen Grenzen schwanken. Ebenso wird die Streuung, die durch unvollständige Rotation um die Faserachsen entsteht, gewissen Schwankungen unterworfen sein. Sehr erheblich werden diese Streuungen allerdings nicht werden, da die in grossen Zügen festgestellte Gleichheit der Polfiguren ein- und desselben Materials oder auch verschiedener Metalle gleicher Struktur sonst nicht vorhanden sein könnte.

Die hier vorgenommene Schilderung des Aufbaues einer Walztextur mit Hilfe unvollständiger Fasertexturen ist vielleicht nicht anschaulicher als die Angabe von idealen Lagen der bisherigen Art, zweifellos ist sie aber viel leistungsfähiger. Die bisher gebräuchlichen idealen Orientierungen gingen von der Voraussetzung aus, dass sämtliche Maxima der Polfigur mit Flächenpolen der idealen Orientierungen in Übereinstimmung waren. Die vorliegende Untersuchung hat gezeigt, dass schon diese Annahme, wenn nicht in allen, so doch in vielen Fällen nicht erfüllt ist. Überdies ist zu bedenken, dass schon das Operieren mit den bisherigen idealen Orientierungen eine Vereinfachung und

Idealisierung der Polfigur bedeutet, die der Wirklichkeit nur annähernd entspricht, denn ein wesentlicher Teil der Flächenpole sticht in der Polfigur an Orten aus, die von den Maxima mehr oder weniger weit entfernt sind.

Dem gegenüber haben die neuen idealen Orientierungen den Vorzug, dass sämtliche rechnerisch festgestellten Maxima der Belegungsdichte, wie sie durch die zugrunde liegende Annahme von Faserachsen zustande kommen, tatsächlich mit den experimentell gefundenen Orten maximaler Belegungsdichte übereinstimmen. Darüberhinaus aber führt die neue Darstellung auch zu einer weitgehend vollständigen Übereinstimmung an all den Stellen der Polfigur, die von Orten maximaler Belegung entfernt sind. Ein weiterer Vorteil ist, dass nach Festlegung der Faserachsen die Polfigur jeder beliebigen Flächenart konstruiert werden kann. Damit ergibt sich auch die Möglichkeit, zu kontrollieren, ob die Polfiguren verschiedener Flächenarten tatsächlich einander entsprechen.

Ob das hier gegebene Bild des Aufbaues einer Walztextur mit Hilfe von Faserachsen mehr ist, als eine bloss Beschreibung, ob also dieser Aufbau ursächlich zusammenhängt mit der Entstehung der Textur und ob sich auf diese Weise ein neuer Weg zum Verständnis der Texturbildung eröffnen wird, kann heute noch nicht gesagt werden. Es sei jedoch darauf hingewiesen, dass die Beschreibung der (110)-Walzlage des Eisens durch eine bevorzugte Streuung in Form einer Rotation um die Walzrichtung schon früher angenommen wurde.<sup>6</sup> Auch die Walztexturen von Magnesium und anderen hexagonalen Metallen lassen sich als vollständige, die des Zinks als unvollständige Fasertextur nach [0001] beschreiben.<sup>6</sup> Vor allem wird es zunächst notwendig sein, weitere experimentelle Ergebnisse zu gewinnen.

Der Deutschen Forschungsgemeinschaft sei für die Unterstützung dieser Arbeit bestens gedankt.

#### LITERATUR

1. J. Grewen u. G. Wassermann, Z. f. Metallkde. **45**, 570 (1954).
2. B. F. Decker, E. T. Asp, u. D. Harker, J. Appl. Phys. **19**, 388 (1948).
3. Hu Hsun, P. R. Sperry, u. P. A. Beck, Trans. A.I.M.E. **194**, 76 (1952).
4. L. G. Schulz, J. Appl. Phys. **20**, 1030 (1949).
5. H. Mark u. K. Weissenberg, Z. f. Phys. **14**, 328 (1923).
6. vergl. z. B., G. Wassermann, Texturen metallischer Werkstoffe (Springer, Berlin, 1939).
7. F. Wever, Z. f. Phys. **5**, 69 (1923); Mitt. KWI Eisenforschung **28**, 69 (1924).
8. Frhr. v. Göler u. G. Sachs, Z. f. Phys. **41**, 873 (1927).
9. C. S. Barrett u. F. W. Steadman, Trans. A.I.M.E. **147**, 57 (1942).
10. H. J. Wallbaum, Z. f. Metallkde. **42**, 371 (1951).
11. K. Lücke, Z. f. Metallkde. **45**, 86 (1954).
12. F. H. Custers, Physica **8**, 771 (1941).
13. R. Glocker, Z. f. Metallkde. **16**, 181 (1924); Z. f. Phys. **31**, 386 (1925).

## A GROWTH MECHANISM FOR MERCURY WHISKERS\*

G. W. SEARS

Very fine whiskers of solid mercury can be grown by condensation of mercury vapor on a glass surface. It is demonstrated that the whiskers have a single imperfection, an axial screw dislocation, which accounts for their morphology. The whiskers are nucleated on tiny crystalline regions in the glass surface which present the end of a screw dislocation.

### UN MÉCANISME DE CROISSANCE DES BARBES DU MERCURE

De très petites barbes de mercure solide peuvent croître par condensation de la vapeur sur une surface de verre. Il est montré que ces barbes n'ont comme seule imperfection qu'une dislocation vis axiale, ce qui explique leur morphologie. Ces barbes ont pour germe de petites régions cristallines à la surface du verre où se trouve l'extrémité d'une dislocation vis.

### EIN WACHSTUMSMECHANISMUS FÜR QUECKSILBER IN HÄRCHENARTIGER AUFWACHSUNG (WHISKERS)

Eine sehr feine härchenartige Aufwachsung (whiskers) von festem Quecksilber kann durch Kondensation von Quecksilberdampf auf einer Glasscheibe gezüchtet werden. Es wird gezeigt, dass die einzelnen Härchen (whiskers) nur eine einzige Unregelmässigkeit haben, eine axiale Schraubenversetzung, welche ihre Entstehung erklärt. Die Härchen entstehen durch Keimwirkung auf kleinen kristallinen Gebieten der Glasoberfläche, die das Ende einer Schraubenversetzung darstellen.

In 1921 Volmer and Estermann<sup>1</sup> reported the formation of tiny platelets of mercury by the condensation of mercury vapor upon a blown glass surface at  $-63.5^{\circ}\text{C}$ . The platelets of mercury grew to a length of about 0.3 mm and were so thin that they underwent ceaseless Brownian motion. The mercury vapor pressure in the closed evacuated chamber was controlled by regulating the temperature of mercury in a reservoir. Platelets were observed to grow in about two minutes when the reservoir was held at  $-10^{\circ}\text{C}$ . This pressure of mercury vapor was 1600 times the vapor pressure at  $-63.5^{\circ}\text{C}$ .

The growth rate of platelets in their large dimension was a thousandfold greater than could be accounted for by direct impingement and condensation of mercury atoms upon the advancing plane from the vapor phase. Volmer and Estermann concluded that the impinging mercury atoms were adsorbed on the solid surface and the adsorbed atoms migrated over the surface until they either evaporated or were incorporated into the solid lattice.

Langmuir<sup>2-5</sup> has concluded from studies of interaction of gases with solid surfaces that gas molecules striking a solid surface are temporarily adsorbed before they are re-evaporated. Impingement, temporary adsorption and re-evaporation is the general mechanism for reflection of gas molecules at a solid surface.

Since detailed theories of the growth of perfect crystals<sup>6,7,8</sup> and of imperfect crystals<sup>9</sup> have since been developed, it seemed desirable to repeat the experiments of Volmer and Estermann and examine the phenomena in more detail. The author<sup>10</sup> has described some new results briefly in which very fine whiskers of solid mercury have been grown 0.01 micron in radius and 1

to 2 mm in length. The present paper presents a detailed growth mechanism for these whiskers.

### EXPERIMENTAL

The initial experiments were carried out using the vessel illustrated in Fig. 1. The liquid mercury which supplied the vapor for crystal growth was contained in reservoir, R. The crystals were grown on the condensation finger, F. The reservoir was filled with a few milliliters of liquid mercury and sealed onto a vacuum system

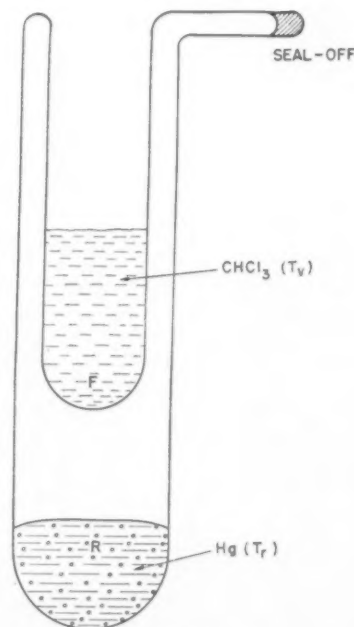


FIG. 1. Original Crystal Grower.

\* Received December 9, 1954.

† General Electric Research Laboratory, Schenectady, N. Y.

via a seal-off constriction. The vacuum line consisted of a two-stage diffusion pump backed by a mechanical pump. Since there was mercury vapor throughout the system, no liquid air trap was used. The pressure was measured with a McLeod gauge.

The vessel was evacuated 24 hours before sealing off. It and the mercury were torched for about an hour in the early stages of evacuation. The McLeod gauge indicated a permanent gas pressure of about  $10^{-6}$  mm at seal-off. This pressure insured that molecular flow was operative between the mercury reservoir and the finger. After the vessel was sealed off, it was ready for use in an indefinite number of experiments.

In later experiments the vessel shown in Fig. 2 was used. The vessel had the additional feature that not only the pressure of mercury vapor over the finger was controlled, but also the vapor temperature was controlled. In addition to the reservoir, R, and a finger, F, there was a built-in dewar, A, to control the temperature of condensing mercury vapor. The reservoir was filled with mercury. The crystal grower was evacuated, baked and sealed-off according to the same schedule as the vessel of Fig. 1. In crystal growth experiments in the final vessel, three temperatures were controlled. The condensation temperature,  $T_c$ , was established at  $-63.5^\circ\text{C}$  by a bath of partially frozen chloroform in the condensation finger. The temperature of the mercury vapor,  $T_v$ , was controlled by an acetone bath in the built-in dewar, A. The reservoir temperature,  $T_R$ , was controlled by immersion in an acetone bath contained in a separate dewar flask. The temperatures of the acetone baths was controlled manually. Dry ice frag-

ments were added to lower the temperature and copper strips were introduced to raise the temperature. The mercury crystals were observed with a  $5\times$  magnifier through a port, P. To measure whisker lengths a low power telescope, which superimposed a scale on the image, was used.

For crystal growth, temperatures  $T_R$ ,  $T_v$ , and  $T_c$  were adjusted in that order. The reservoir temperature,  $T_R$ , was then slowly allowed to rise until crystal formation was observed.  $T_c$  was always held at  $-63.5^\circ\text{C}$ .

## RESULTS

### A. Crystal Form

When the vapor temperature,  $T_v$ , was  $25^\circ\text{C}$ , all crystals were thin platelets in agreement with Volmer and Estermann.<sup>1</sup> The platelets ranged up to 0.3 mm in length and their thickness has been estimated at  $\sim 0.03\mu$ .

It has been found for the first time that for  $T_v = -50^\circ\text{C}$ , all crystals were whiskers. The whiskers ranged up to 1 to 2 mm in length and were  $\sim 0.01\mu$  in radius.

For  $-50^\circ\text{C} < T_v < 25^\circ\text{C}$  a mixture of whiskers and platelets was observed to form simultaneously. The fraction of each was apparently a smoothly varying function of  $T_v$ .

### B. Supersaturation Ratios

If  $p_0$  is the vapor pressure of solid mercury at the whisker temperature and  $p$  is the actual pressure of mercury vapor, the *supersaturation ratio*,  $\alpha$ , is defined by the equation

$$\alpha = \frac{p}{p_0} \quad (1)$$

For  $T_v = -50^\circ\text{C}$ , the first whiskers appeared at a supersaturation ratio of about a hundred. If  $T_v = 25^\circ\text{C}$ , the first platelets appeared at a supersaturation ratio of about 1600. This latter observation agreed well with that of Volmer and Estermann.<sup>1</sup> When the supersaturation ratio was increased over the appearance value, the crystal population increased.

### C. Appearance Kinetics

When the reservoir temperature,  $T_R$ , was such as to furnish a mercury vapor pressure less than a critical pressure to nucleate and grow crystals, no crystals would appear in a very long time. If  $T_R$  was allowed to rise until the critical supersaturation was reached, crystals began to appear in a few minutes. If  $T_R$  was held constant, the number of crystals per unit area of finger surface stayed sensibly fixed over a long period. A further temperature increase gave rise to an increase in crystal population in 10 or 20 minutes. A new fixed temperature was accompanied by a cessation in the appearance of new crystals. The free-energy change

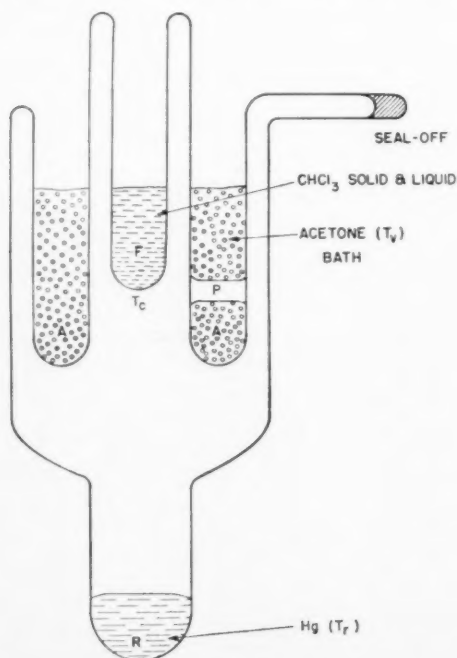


FIG. 2. Final Crystal Grower.

driving nucleation and growth is controlled by the supersaturation of mercury vapor over the cold finger.

The appearance kinetics for both platelets and whiskers were alike, although they appeared under differing  $T_V$  and  $T_R$ . The concentration of crystals was dependent on  $T_R$  and not on time for a fixed  $T_V$ . The crystal population on the condensation finger was static for a given mercury pressure independent of the time allowed for growth. It was estimated roughly for  $T_c = -63.5^\circ\text{C}$  and  $T_V = 25^\circ\text{C}$ , that the crystal population was a thousand times larger for a vapor pressure of  $4.2 \times 10^{-5}$  mm than for  $1.9 \times 10^{-5}$  mm Hg.

#### D. Growth Characteristics

In a typical experiment the whiskers were first observed as tiny dots on the condenser finger. As the whiskers grew longer they began to bend in Brownian motion. Each whisker reached some length in about thirty minutes which is designated as its terminal length. The terminal lengths for the most part ranged from .25 to 1.25 mm with a very few whiskers attaining lengths of 2.5 mm. The longest whiskers made their appearance at the highest supersaturations. The whisker remained at constant radius throughout the axial growth to terminal length. At the attainment of terminal length, the axial growth rate abruptly diminished to an immeasurable rate. Just as abruptly, the radial growth started. The radial growth was indicated by a cessation of Brownian motion followed by the cyclic appearance of interference colors, blue through red. The rate of change of interference colors offers a precise technique for measuring radial growth rate. It has been impossible to make more than a rough measurement of axial growth rate.

A selected crystal is visible under an arbitrary illumination if viewed through a small solid angle. If the observation and illumination directions are fixed, a given whisker appears and disappears occasionally.

The whiskers in Brownian motion were observed to deflect at the thin ends by about 0.1 mm in 1.0 mm length. The platelets moved so that the normal to the platelet remained in one plane. It was observed that certain prominent whiskers appeared at the same location in successive experiments on a given condensation surface. These whiskers were either unusually long or unusually bright.

#### DISCUSSION

It is known from electron microscopic evidence<sup>10</sup> that a glass surface is for the most part smooth like a liquid surface, but that tiny crystalline regions are scattered here and there in the vitreous whole. It is proposed that solid mercury nucleates on crystalline regions which present exposed screw dislocation ends. The screw dislocation in the crystallite is transposed to a screw dislocation in mercury and the mercury crystal grows out from the glass in the form of a whisker. The whisker will be

bounded parallel to the axis by low index or closed-packed planes since these have the lowest surface energy and will give it the minimum free energy.

This discussion will present the syntheses of the preceding mechanism from experimental evidence and the consequences of this mechanism. The arguments proceed from calculations of whisker radius and growth rate. These are presented below.

#### A. Whisker Radius

The bending, which a whisker undergoes in Brownian motion, can be used to estimate the radius of the whisker. If the average deflection of the end of a whisker is  $\bar{\delta}$ , its average kinetic energy  $\bar{E}$  is given by

$$\bar{E} \sim \frac{1}{2} K \bar{\delta}^2, \quad (2)$$

where  $K$  is the Hooke's law constant for deflection of the whisker and  $\bar{\delta}^2$  is approximated for  $\delta^2$ . The principle for equipartition of energy states that the average thermal energy per particle per degree of freedom for a harmonic oscillator is  $kT$  where  $k$  is the molecular gas constant. We write

$$\bar{E} = kT \quad (3)$$

since only one degree of freedom is observed.  $T$  is the absolute temperature of the whisker.

The Hooke's law constant,  $K$ , can be evaluated from elastic theory. A circular cross section is assumed although it will be shown in a later section that the whisker has a polygonal cross section. If  $r$  is the whisker radius,  $l$  is the whisker length and  $E$  is Young's modulus for solid mercury, it can be written that

$$K = \frac{3\pi r^4 E}{4l^3}. \quad (4)$$

If Eqs. (2), (3) and (4) are combined, it may be written that

$$kT = \frac{1}{2} \frac{3\pi r^4 E}{4l^3} \bar{\delta}^2. \quad (5)$$

Equation (5) is solved for  $r$ :

$$r = \left\{ \frac{8l^3 kT}{3\pi E \bar{\delta}^2} \right\}^{\frac{1}{2}}. \quad (6)$$

It will be recalled  $l = 1$  mm and  $\bar{\delta} = 0.1$  mm. Young's modulus is  $10^{11}$  dynes/cm<sup>2</sup> for mercury.<sup>11</sup> The whisker radius is found to be about 0.01 microns.

#### B. Growth Rate

When a whisker is formed at a reservoir temperature of  $-30^\circ\text{C}$ , the time lapse until appearance of a full size whisker is about 20 minutes. The time between the first sign of a whisker and its attainment of a length of 1 mm is about 10 minutes. The average growth rate is,



therefore, about  $1.5 \times 10^{-4}$  cm/sec. The mass rate of impingement,  $\dot{W}$ , of mercury atoms on the whisker end is given by

$$\dot{W} = \pi r^2 p \left( \frac{m}{2\pi kT} \right)^{1/2}, \quad (7)$$

where  $r$  is the whisker radius,  $p$  is the pressure of mercury over the whisker,  $m$  is the mass of a mercury atom,  $k$  is the molecular gas constant, and  $T$  is the absolute temperature of the vapor phase. If it is assumed that every atom which strikes the whisker end is incorporated into the mercury lattice and if the whisker radius is constant, it can be written that

$$\pi r^2 \rho \dot{l} = \dot{W}, \quad (8)$$

where  $\dot{l}$  is the rate of length increase and  $\rho$  is the density of solid mercury. By combining Eqs. (7) and (8) and solving for  $\dot{l}$  it is found that

$$\dot{l} = \frac{p}{\rho} \left( \frac{m}{2\pi kT} \right)^{1/2}. \quad (9)$$

The vapor pressure of mercury at  $-30^\circ\text{C}$  is about  $7 \times 10^{-6}$  mm Hg. The growth rate calculated from Eq. (4) is given by

$$\dot{l}_{\text{calc}} = 3 \times 10^{-8} \text{ cm/sec} \quad (10)$$

The actual growth rate is 5000 times the calculated growth rate. If the assumption of a constant whisker radius had not been made, the calculated growth rate would have been even smaller and the discrepancy between calculated and measured growth rates would have been larger.

The calculated growth rate is based on the hypothesis that only mercury atoms striking the advancing whisker end contribute to axial growth. The discrepancy between measured and calculated growth rates demonstrates that mercury atoms striking elsewhere on the mercury and/or glass surface are contributing to axial growth.

### C. Surface Nucleation

Consider now the nucleation of a new mercury layer on the surface of a low index plane. The nucleation rate,  $\dot{N}$ , in nuclei/cm<sup>2</sup>/sec for surface nucleation is given by

$$\dot{N} = B e^{-\Delta f^*/kT}, \quad (11)$$

where  $\Delta f^*$  is the free energy of formation of a critical-sized surface nucleus and  $10^{22} > B > 10^{18} \text{ sec}^{-1}$ . It can be shown that

$$\Delta f^* = \frac{\pi a \sigma^2 M}{\rho R T \ln \alpha}, \quad (12)$$

where  $\sigma$  is the surface free energy of solid mercury,  $M$  is the gram atomic weight of mercury,  $R$  is the molar gas constant,  $a$  is the interlayer spacing for mercury, and  $\alpha$  is the supersaturation ratio.

The surface nucleation rate necessary to account for an axial growth rate of  $1.5 \times 10^{-4}$  cm/sec can be calculated, if it is assumed that each new layer grows to full size instantaneously.

A layer of mercury is about  $3 \times 10^{-8}$  cm thick. It is necessary to nucleate 5000 layers per second. Since the whiskers are 0.01 micron in radius, their end area is  $3 \times 10^{-12} \text{ cm}^2$  and the nucleation rate needed to allow a growth rate of  $1.5 \times 10^{-4}$  cm/sec is

$$\dot{N} \cong 2 \times 10^{15} \text{ nuclei/cm}^2/\text{sec}. \quad (13)$$

Equation (8) is combined with the logarithmic form of Eq. (7) and solved for  $\ln \alpha$ .

$$\ln \alpha = \frac{\pi a \sigma^2 M}{\rho k R T^2 \ln \frac{B}{\dot{N}}}. \quad (14)$$

Equation (10) is solved for  $\sigma$  with the constants  $B = 10^{20} \text{ sec}^{-1}$ ,  $\sigma = 500 \text{ ergs/cm}^2$ . The value of supersaturation necessary to cause a growth rate of  $1.5 \times 10^{-4}$  cm/sec is

$$\alpha = p/p_0 = 10^{24}. \quad (15)$$

It might be argued that for such a large nucleation rate, significant error might be involved in the use of Eq. (15). However, the magnitude of the discrepancy between the calculated supersaturation ratio of  $10^{24}$  and the measured ratio of  $10^2$  to  $10^3$  for the growth rate in question leaves no doubt that the axial growth mechanism does not involve nucleation of new layers. Even to nucleate a single surface nucleus per cm<sup>2</sup> per sec would require a supersaturation ratio of  $4 \times 10^6$ .

### D. Axial Growth Mechanism

Since it has been established that the axial growth rate cannot be accounted for by homogeneous two-dimensional nucleation, it must be postulated that a permanent growth step is exposed in the advancing face. This is equivalent to the statement that the whisker contains an axial screw dislocation.

The phenomenal growth rate still must be rationalized. It has already been postulated on thermodynamic grounds that a whisker is bounded by low index faces parallel to its axis. Since two-dimensional nucleation cannot occur on these faces, a mechanism is provided for rapid axial growth. Mercury atoms impinge on the sides of the whisker, are adsorbed, and migrate to the advancing end, where they are incorporated into the crystal lattice. If it is assumed that all atoms within a distance,  $\lambda_z$ , of the end contribute to the axial growth, then it can be written that

$$2\pi r \lambda_z + \pi r^2 = 5000 \pi r^2. \quad (16)$$

Ignoring the second term of the left side of equation (16) and solving for  $\lambda_z$

$$\lambda_z = 2500r. \quad (17)$$

It has been calculated that  $r=0.01$  micron, so that  $\lambda_z=0.025$  mm. The quantitative expression for the axial growth rate is then given by

$$l = \frac{2\lambda_z}{r} \frac{p}{\rho} \left( \frac{m}{2\pi kT} \right)^{\frac{1}{2}} \quad (18)$$

Burton, Cabrera and Frank<sup>9</sup> have shown theoretically that an atom adsorbed on a solid surface has a finite life time,  $\tau_s$ , before evaporation. It is presumed that the ad-atom does not in the meanwhile encounter a growth site where it is incorporated into the solid lattice. The average distance an ad-atom moves between adsorption and evaporation is called the mean displacement of adsorbed molecules. This distance is just  $\lambda_z$  which was introduced in Eq. (16).

In any condensation process the net condensation rate is the difference between the impingement rate and the evaporation rate. In the preceding calculations, it has been assumed that the evaporation rate can be neglected. This approximation is justifiable for the high supersaturation ratios used, from 70 upwards, since the supersaturation ratio is equal to the ratio of impingement rate to evaporation rate.

Since a mercury whisker must have a higher evaporation rate than bulk mercury at the same temperature, it must be proved that the vapor pressure,  $p_w$ , of a whisker does not exceed the vapor pressure of bulk mercury by a large factor. If  $p_0$  is the vapor pressure of bulk mercury at temperature,  $T$ ,

$$\ln \frac{p_w}{p_0} = \frac{2\gamma M}{\rho r RT}, \quad (19)$$

where  $\gamma$  is the surface free energy of solid mercury,  $M$  is the atomic weight,  $\rho$  is the density,  $r$  is the fiber radius and  $R$  is the gas constant. Assuming  $\gamma=500$  ergs/cm<sup>2</sup> as a reasonable value, it is calculated that  $p_w/p_0 \approx 2$  for  $r=0.01\mu$ .

The minimum ratio of  $p/p_w$  is 50, where  $p$  is the pressure of mercury in the vapor phase, and the neglect of evaporation is justified. The increase of vapor pressure associated with the presence of an axial screw dislocation is only 1 per cent of the bulk vapor pressure,<sup>12</sup> so this contribution is entirely negligible.

### E. Nucleation

The final mercury whisker appears to be a perfect crystal except for an axial screw dislocation. The result could have arisen by two possible mechanisms. The original nucleus contained a screw dislocation, or the original nucleus was a perfect crystal and a screw dislocation was introduced later. The available evidence supports the former mechanism.

It has already been shown that mercury cannot surface-nucleate on mercury at an appreciable rate for the experimental supersaturations used. It follows that it would be even more difficult to nucleate on a perfect

foreign crystal, and most difficult on a vitreous surface. Beyersdorf<sup>13</sup> has published electron photomicrographs of fractured glass showing crystallites ranging from 0.002 to 0.02 $\mu$  in diameter. The crystallites with emergent screw dislocations would offer sites where solid mercury could nucleate. The mercury nuclei would have built-in screw dislocations necessary for rapid growth. The crystallites without a screw dislocation would be ineffective.

Mercury nuclei might also form at the steps bounding terraces; however, no repeatable step would form and growth would cease under the supersaturation used experimentally.

It should be pointed out that the postulated mechanism predicts the repetitive formation of whiskers at a given site under like conditions. Experimentally it has been observed that certain distinctive whiskers form repeatedly at a given site on the finger. These whiskers are distinguished by their length, direction of growth, or brightness.

### F. Radial Growth

It is now necessary to rationalize the cessation of rapid axial growth at constant radius and the initiation of a normal radial growth rate when a terminal length is reached. Since homogeneous surface nucleation is excluded, it must be assumed that new layers can be nucleated at the substrate-mercury corner at the base of each whisker.

Since the end of a whisker is a sink for adsorbed mercury atoms, the surface concentration of ad-atoms will vary over the surface and will be a minimum at the whisker end. Conversely, if a whisker was evaporating, the surface concentration would be a maximum at the emergent screw dislocation.

If  $\tau_s$  is the mean lifetime of an adsorbed mercury atom, and  $\sigma^*$  is the surface concentration in equilibrium with mercury vapor of pressure,  $p$ ,

$$\sigma^* = \frac{p\tau_s}{(2\pi mkT)^{\frac{1}{2}}} \quad (20)$$

It can be shown that, if  $\sigma(x)$  is the steady state surface concentration at coordinate  $x$  on a fiber, where  $x=0$  is taken at the free whisker end,

$$\sigma - \sigma_0 = (\sigma^* - \sigma_0)e^{-x/\lambda_z} \quad (21)$$

Here  $\sigma_0$  is the ad-atom concentration in equilibrium with the whisker. At the whisker end,  $x=0$  and  $\sigma=\sigma_0$ . Away from the end, Eq. (21) may be simplified since  $\sigma^* \gg \sigma_0$ .

$$\sigma = \sigma^*(1 - e^{-x/\lambda_z}) \quad (22)$$

As a whisker grows long,

$$\sigma \rightarrow \sigma^* \quad (23)$$

at its base. The original mercury crystal grew radially to the whisker radius at a critical pressure  $p$ , but not

at a pressure below  $p$ . Hence the whisker should again begin to grow radially by the intermediation of the substrate whisker corner when the surface concentration approaches  $\sigma^*$ , if the whisker radius is less than the radius of the crystallite upon which it grew. Such whiskers should grow only a few multiples of  $\lambda_z$  long. Experimentally, many whiskers are observed fulfilling this length requirement. The other extreme is the situation where the whisker and crystallite radii are nearly equal. Radial growth over the vitreous glass requires a higher surface concentration than  $\sigma^*$ . Such whiskers are probably represented by those which are observed with lengths up to 1 to 2 mm. When the mercury pressure in the system is raised by increasing the reservoir temperature, these whiskers may also thicken radially. Intermediate cases would involve radial growth partly over crystallite and partly over vitreous glass. These would grow to intermediate length.

### G. Surface Diffusion

In a previous section a value of 0.025 mm has been calculated for the mean free path of a mercury atom adsorbed on a mercury surface. This value is estimated for the planes parallel to the whisker axis. It is reasonable that these planes are rhombohedral (100) planes. The (100) planes present the closest packing, a 3.00 Å interatomic spacing, and should have the lowest surface free energy. This habit should give the thermodynamically most stable crystal. An adsorbed atom on the rhombohedral (100) plane would be expected to be bonded to four atoms in the adsorbent plane, but at 3.47 Å separation instead of 3.00 Å, since the interatomic distance of atoms in adjacent (100) planes is the former.

Burton, Cabrera and Frank<sup>9</sup> have derived equations by which the mean surface displacement can be estimated. They demonstrated that

$$\lambda_z = a \cdot \exp\left(\frac{W_s' - U_s}{2kT}\right), \quad (24)$$

where  $U_s$  is the activation energy for transfer of an adsorbed molecule between neighboring adsorption sites,  $W_s'$  is the energy of evaporation from adsorbed layer to the vapor,  $a$  is the interatomic spacing, and  $k$  is the molecular gas constant. Mackenzie<sup>16</sup> has calculated that  $U_s$  is only about 10 per cent of  $W_s'$  using Lennard-Jones forces. Equation (25) is modified accordingly.

$$\lambda_z = a \cdot \exp\left(\frac{0.9W_s'}{2kT}\right). \quad (25)$$

If  $\phi_1$  is the bond energy of 3.47 Å interatomic separation and  $\phi_2$  is the bond energy for 3.00 Å separation, the value of  $W_s'$  may be written

$$W_s' = 4\phi_1 \quad (26)$$

and the heat of evaporation may be written

$$\Delta H = 3\phi_1 + 3\phi_2. \quad (27)$$

There is no information available on the energy ratios  $\phi_1/\phi_2$  other than  $\phi_1/\phi_2 = p > 1$ . Combining Eqs. (25), (26), and (27), it may be written that

$$\lambda_z = a \cdot \exp\left(\frac{3.6p}{6(p+1)} \cdot \frac{\Delta H}{RT}\right). \quad (28)$$

Introducing the values  $\lambda_z = 2.5 \times 10^{-3}$  cm,  $a = 3.00$  Å,  $\Delta H = 15,000$  cal/mole into Eq. (28) and solving for  $p$ , it is found that

$$p = \phi_1/\phi_2 = 1.13. \quad (29)$$

### H. Mechanical Strength

It has been theoretically predicted that perfect crystals should deform elastically to much higher strains than have been observed for real crystals.<sup>17</sup> The weakness of actual crystals is interpreted as evidence for the presence of edge dislocations which move under small stress and cause plastic rather than elastic deformation.

Since the sole imperfection of a mercury whisker is an axial screw dislocation, it is expected that the whisker should exhibit theoretical strength. No attempt has been made to investigate this property. However, whiskers of iron<sup>14</sup> and zinc sulfide<sup>15</sup> have been grown—presumably by the same mechanism. The strength of both iron and zinc sulfide whiskers is approximately the predicted theoretical strength for perfect crystals.

### I. Mercury Platelets

The mechanism for the growth of mercury platelets has not been elucidated. There is some indication that mercury may nucleate on certain heterogeneities as supercooled liquid. At some critical size the droplet freezes, catalyzed by the same heterogeneity upon which it formed. The solid nucleus then is presumed to have two fast-growing directions so that a platelet is formed.

### ACKNOWLEDGMENT

I am pleased to acknowledge valuable discussions with and encouragement from D. Turnbull and J. H. Hollomon in the explanations presented herein.

### REFERENCES

1. M. Volmer and I. Estermann, *Z. Physik* **7**, 13 (1921).
2. I. Langmuir, *Phys. Rev.* **2**, 329 (1913).
3. I. Langmuir, *Phys. Rev.* **4**, 377 (1914).
4. I. Langmuir, *J. Amer. Chem. Soc.* **37**, 1139 (1915).
5. I. Langmuir, *Proc. Nat. Acad. Sci.* **3**, 141 (1917).
6. J. Frenkel, *J. Phys. U.S.S.R.* **9**, 392 (1945).
7. I. N. Stranski, *Z. Physik Chem.* **136**, 259 (1928).
8. W. Kossel, *Nachr. Ges. Wiss. (Göttingen)*, 1927, p. 135.
9. W. Burton, N. Cabrera, and F. C. Frank, *Phil. Trans. Roy. Soc.* **243**, 299 (1951).
10. G. W. Sears, *Acta Metal.* **1**, 457 (1953).
11. Landolt-Bornstein, vol. 1, 5th ed., Suppl. 3, p. 26 (Julius Springer, Berlin 1935).
12. E. W. Hart, Private communication.
13. K. Beyersdorf, *Glas und Hochvakuum Technik* **2**, 8 (1952).
14. G. W. Sears, A. Gatti, and R. L. Fullman, *Acta Met.* **2**, 727 (1954).
15. W. W. Piper and W. L. Roth, *Phys. Rev.* **92**, 503 (1953).
16. A. J. MacKenzie, Thesis, University of Bristol (1951).
17. L. Bragg and W. M. Lomer, *Proc. Roy. Soc. (Lond.)* **A196**, 171 (1949).

## A MECHANISM OF WHISKER GROWTH\*

G. W. SEARS†

Fine whiskers of zinc, cadmium, silver, and cadmium sulfide have been grown on pyrex and quartz glass substrates by vapor deposition. The maximum supersaturation ratio at which whiskers can be grown is in good correspondence with the calculated supersaturation at which two-dimensional nucleation occurs. This correspondence offers support for the generality of the growth mechanism first proposed for mercury whiskers.

### SUR UN MÉCANISME DE LA CROISSANCE DES BARBES

Des barbes fines de zinc, de cadmium, d'argent et de sulfure de cadmium ont été formées sur un support en pyrex ou en quartz par condensation de vapeur. Le maximum du rapport de sursaturation auquel ces barbes peuvent grandir est en bon accord avec la sursaturation calculée pour une germination à deux dimensions. Cet accord montre la généralité du mécanisme de croissance proposé pour les barbes du mercure.

### EIN WACHSTUMSMECHANISMUS FÜR HÄRCHENARTIGE AUFWACHSUNGEN (WHISKERS)

Feine härchenartige Aufwachsungen (whiskers) aus Zink, Kadmium, Silber und Kadmiumsulfid wurden durch Abscheidung aus der Dampfphase auf Pyrex- und Quarzglas hergestellt. Das maximale Übersättigungsverhältnis, bei dem die Härchen (whiskers) gezüchtet werden können, steht in guter Übereinstimmung mit der berechneten Übersättigung, bei der zweidimensionale Keimbildung auftritt. Diese Übereinstimmung ist eine Stütze für die Allgemeingültigkeit des Wachstumsmechanismus<sup>1</sup>, der zunächst für härchenartige Quecksilberaufwachsungen (whiskers) vorgeschlagen wurde.

It has been reported<sup>1</sup> that solid mercury may be condensed from the vapor phase in the form of very thin whiskers. A detailed mechanism has been proposed<sup>2</sup> which rationalizes the growth behavior.

The postulates, however, are not restricted to the growth of mercury crystals. They should be valid for the growth of crystalline substances in general. This paper reports attempts to grow whiskers of a number of other materials by application of the proposed concepts of crystal growth. Whiskers have been grown for all substances investigated—zinc, cadmium, silver and cadmium sulfide—by condensation from the super-saturated vapor phase.

### EXPERIMENTAL

The crystal growth experiments were carried out in the apparatus shown in Fig. 1. The crystal growth vessel, *G*, was an evacuated tube containing the material under investigation. The vessel was provided with an eyelet at one end so that it could be suspended in the furnaces. The vessels were constructed of pyrex for zinc and cadmium. Quartz glass vessels were used for cadmium sulfide and silver.

The growth vessel and its crystalline charge were thoroughly outgassed prior to sealing off. The vessel was attached at one end to a vacuum system via a seal-off constriction. The other end was attached by a second constriction to a distillation train. This train consisted of three chambers in series joined by constrictions.

The material under investigation was introduced into the first chamber. The system was evacuated and the

growth vessel and the remaining distillation chambers were heavily torched. When a pressure of  $10^{-6}$  mm Hg, as measured by ion gauge, was reached with the system hot the torching was stopped. After the system had cooled off, a furnace was placed around the first chamber and the bulk of the crystals were distilled to the second chamber. The residue was sealed off.

This procedure was followed for each distillation until finally the growth vessel was sealed off from the vacuum line. An eyelet was sealed onto one end and the growth vessel was ready for use.

The furnaces,  $F_1$  and  $F_2$ , were tubular with nichrome windings. Furnace  $F_2$  was open at both ends and  $F_1$  was open at one end. The furnace temperatures,  $T_1$  and  $T_2$ , were controlled by chromel-alumel thermocouples con-

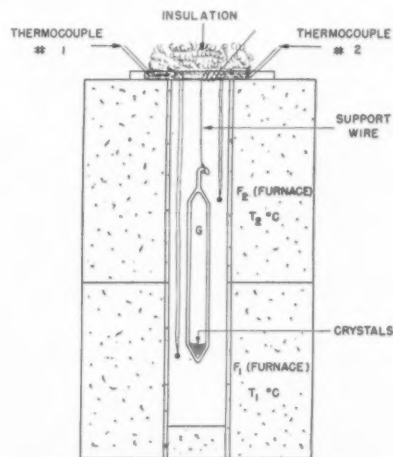


FIG. 1.

\* Received December 9, 1954.

† General Electric Research Laboratory, Schenectady, New York.



nected to a pair of Brown-Honeywell temperature controllers. Their hot junctions were located at the upper and lower ends of the vessel,  $G$ .

Before starting an experiment, the temperatures were adjusted so that  $T_2 > T_1$ . A temperature difference of about 250°C was used to insure complete distillation of the crystals to the bottom of  $G$ .

The vessel was then removed from the furnaces and the temperatures were adjusted for growth, i.e.,  $T_1 > T_2$ . The vessel was reinserted and in about 30 minutes was removed for examination under a stereoscopic microscope.

### RESULTS

Whiskers have been grown of cadmium, zinc, silver and cadmium sulfide. The critical condition in each case was that the supersaturation ratio be maintained below a value characteristic of the material. For slightly higher supersaturation ratios, almost no whiskers were produced. For much higher supersaturation ratios, only massive crystals were produced.

Cadmium whiskers were formed in profusion by operating at  $T_1 = 330^\circ\text{C}$  and  $T_2 = 250^\circ\text{C}$ . This corresponded to an initial supersaturation ratio of about 20.<sup>3</sup> The pressure of cadmium in the vessel was about 200 $\mu$ . The whiskers ranged up to 1 mm in length and were quite thin in cross section. They appeared in a few instances to be in barely perceptible Brownian motion, when observed at 60 $\times$  magnification. Zinc whiskers were grown by operating with  $T_1 = 375^\circ\text{C}$  and  $T_2 = 350^\circ\text{C}$ . This gave a supersaturation of about three and corresponds to a vapor pressure of about 20 $\mu$ .<sup>3</sup> The whiskers were practically indistinguishable from the cadmium whiskers in their appearance.

The silver whiskers were grown by operating between  $T_1 = 940^\circ\text{C}$  and  $T_2 = 850^\circ\text{C}$ . The vapor pressure level was 1 $\mu$  and the supersaturation ratio was about ten.<sup>3</sup> These crystals were much shorter than those of zinc and cadmium. The largest whiskers were only 0.1 mm in length. However, as they were grown at a much lower vapor pressure for about the same length of time, their shorter length is not surprising.

Cadmium sulfide was grown with  $T_1 = 810^\circ\text{C}$  and  $T_2 = 800^\circ\text{C}$ . While no vapor pressure data appear to have been published, it can be estimated from its distillation rate that the vapor pressure ranges from 10–100 $\mu$ . Its supersaturation ratio is probably less than two.

Other types of crystals were grown in each experiment in which whiskers were grown, for example ribbons of CdS, thin hexagons of Cd, and thin triangular platelets of Zn, Cd and Ag, which were attached to the vessel at one vertex. Since the purpose of the experiment was to demonstrate if whiskers could be grown under predictable conditions, these observations are not presently considered.

It was very frequently observed for all materials that there was a minute bright spot at the base end of the many whiskers.

### DISCUSSION

It has been proposed<sup>2</sup> that mercury whiskers nucleate on tiny crystalline regions on a glass surface which present an emergent screw dislocation. The nucleation occurs with the assistance of the step at supersaturations far less than necessary for two-dimensional nucleation of even mercury on mercury. It is postulated that the nucleus with a built-in screw may grow axially at low supersaturations by the action of the dislocation. However, radial growth cannot occur because the supersaturation is below the critical value for two-dimensional nucleation. When a whisker grows long enough thickening occurs. It is proposed that under these conditions the screw step no longer depletes the concentration of adsorbed atoms at the base of the whisker. Thickening is then presumed to occur by intermediation of the crystallite-mercury corner in two-dimensional nucleation. Mercury whiskers have also been observed on quartz glass.<sup>4</sup> The same considerations are presumed to be valid.

In the present discussion, consideration will be given only to early stages of whisker growth, since all that is observed is the presence or absence of whiskers in the distillate. If the growth concepts are correct, the critical condition for whisker growth is the absence of two-dimensional nucleation, or at least a low surface nucleation rate.

The relation between supersaturation ratio,  $\alpha$ , and surface nucleation rate,  $\dot{N}$ , is given by

$$\ln \alpha = \frac{\pi a \sigma^2 M}{\rho k T^2 R \ln B / \dot{N}}, \quad (1)$$

where  $B = 10^{20} \text{ sec}^{-1}$ ,  $a$  is the interlayer spacing,  $\rho$  is the density,  $\sigma$  is the surface free energy,  $M$  is the molecular weight,  $k$  is Boltzmann's constant,  $R$  is the molar gas constant, and  $T$  is the absolute temperature. Only the surface free energy,  $\sigma$ , is subject to uncertainty. In the absence of better information the value for the surface tension of the liquid metal was used for the surface free energy of the solid. The critical supersaturation was calculated for the formation of one surface nucleus/cm<sup>2</sup>/sec. In Table I are listed the calculated critical supersaturations for two-dimensional nucleation,  $\alpha_{\text{calc}}^*$ , and the experimentally estimated upper limit,  $\alpha_{\text{mess}}^*$ , for the growth of whiskers.

It should be pointed out that the critical supersaturation,  $\alpha_{\text{calc}}^*$ , is very sensitive to changes in the growth

TABLE I.

Sub- stance	$\alpha_{\text{calc}}^*$	$\alpha_{\text{mess}}^*$	$T_2^\circ\text{C}$	$\rho$ (gms cm <sup>3</sup> )	$\sigma$ (ergs cm <sup>2</sup> )	$\alpha \times 10^3$ cm
Cd	24	~20	250°	8.65	630 <sup>5</sup>	2.80 <sup>7</sup>
Zn	7	~3	350°	7.14	750 <sup>5</sup>	2.47 <sup>7</sup>
Ag	4	~10	850°	10.50	1140 <sup>5,6</sup>	2.04 <sup>7</sup>
CdS	small	≤ 2	800°	4.82	—	—

\* Surface tension of solid Ag.

temperature,  $T_2$ . Since the surface free energy should be relatively constant with temperature, the critical supersaturation,  $\alpha_{\text{calc}}^*$ , should increase rapidly with decreasing temperature of growth.

It will be noticed that the experimentally estimated supersaturation for the growth of whiskers is less than or approximately equal to the calculated supersaturation for growth by two-dimensional nucleation. Above these experimental supersaturations the growth of massive crystals, which presumably involves surface nucleation, occurs experimentally and whiskers do not grow.

It is expected that CdS has a lower surface free energy than silver. Since the growth occurs at about the same temperature, the value of  $\ln \alpha$  will be smaller for CdS. On this basis, it is expected that the critical supersaturation ratio for surface nucleation of CdS is less than four. This is in agreement with the small estimated experimental supersaturation.

With few possible exceptions Brownian motion was not observed at room temperature for the longest whiskers ( $\sim 1$  mm) under  $60\times$  magnification. It has been shown<sup>2</sup> that the radius,  $r$ , of a whisker which undergoes Brownian motion can be calculated by

$$r = \left( \frac{8l^3 kT}{3\pi E \bar{\delta}^2} \right)^{1/3}, \quad (2)$$

where  $l$  is the whisker length,  $k$  is the molecular gas constant,  $T$  is the absolute temperature,  $E$  is Young's modulus and  $\bar{\delta}$  is the average deflection of the whisker end. In the present instance  $\bar{\delta} \leq 10^{-4}$  cm,  $l = 10^{-2}$  cm,  $E \approx 10^{11}$  dynes/cm<sup>2</sup>. This calculation demonstrates that  $r \geq 0.1\mu$ . Direct observation at  $60\times$  magnification places an upper limit ( $r < 2\mu$ ) on the radii.

## CONCLUSIONS

It appears that the growth mechanism proposed for mercury whiskers may be applied to describe the growth of other crystalline whiskers. The critical condition for growth of whiskers seems to be that the supersaturation ratio must be maintained below some critical value characteristic of the material. In the proposed growth mechanism it is assumed that this supersaturation is the critical value for homogeneous surface nucleation.

## REFERENCES

1. G. W. Sears, *Acta Met.* **1**, 457 (1953).
2. G. W. Sears. To be published.
3. S. Dushman, *Vacuum Technique* (John Wiley, New York, 1949), pp. 746-752.
4. G. W. Sears. To be published.
5. T. R. Hogness, *J. Amer. Chem. Soc.* **43**, 1621 (1921).
6. E. R. Funk, H. Udin, and J. Wulff, *A.I.M.E.* **191**, 1207 (1951).
7. C. S. Barrett, *Structure of Metals*, 1st ed. (McGraw-Hill Co., New York, 1943).

## RELATION ENTRE LES STRUCTURES ET LES PROPRIETES DES ALLIAGES ALUMINIUM-ARGENT PENDANT LE DURCISSEMENT STRUCTURAL\*

B. BELBEOCH et A. GUINIER†

Les variations de dureté pendant le durcissement structural de Al-Ag sont mises en corrélation avec la variation de la structure étudiée par diffusion des rayons X aux petits angles.

La transition entre durcissement à froid et durcissement à chaud correspond à l'apparition sur les diagrammes de nombreuses traînées longues et floues caractéristiques de la présence de très petits précipités de  $AlAg_2$ .

Pendant le durcissement à chaud la dureté augmente quand les grains de précipité se développent, les traînées devenant courtes et intenses, puis diminue quand les précipités sont devenus gros et parfaits, la diffusion tendant à disparaître.

Pendant le durcissement à froid les diagrammes présentent des anneaux: l'alliage contient des "zones G.P."

Cependant l'évolution des zones révélée par les rayons X n'est pas à première vue en corrélation directe avec celle de la dureté. Le diamètre des anneaux de diffusion diminue constamment quand le revenu se poursuit, alors que les variations de la dureté sont réversibles au cours de certains traitements thermiques (en particulier phénomènes de réversion).

On peut admettre que le durcissement est lié aux zones de petites dimensions. Celles-ci sont masquées sur le diagramme par les zones volumineuses. Cette hypothèse est vérifiée par des mesures d'intensités de diffusion en valeur absolue.

### RELATION BETWEEN STRUCTURES AND PROPERTIES DURING AGE HARDENING IN $AlAg$ ALLOYS

The variations of hardness during the age hardening of an Al-Ag alloy are correlated with the structure variations studied with small-angle X-ray scattering.

The transition between cold-hardening and warm-hardening corresponds to the appearance on the X-ray patterns of many long and blurred streaks which are characteristic of very small  $AlAg_2$  precipitates.

During warm-hardening the hardness increases with the growth of the precipitates and the streaks become short and intense. When the precipitates have become large and perfect, the scattering vanishes.

During cold-hardening, the patterns have rings, the alloy containing "G.P. zones."

However, the evolution of the zones as revealed by X-rays is not directly correlated with the variation of hardness. The diameter of the rings on the patterns decreases steadily as the annealing progresses, while the hardness variations are reversible with some thermal treatments (particularly reversion).

It might be concluded that the hardening is determined by zones of very small size. These are masked on the patterns by larger zones. The conclusion is verified by measurements of absolute diffuse intensity.

### ZUSAMMENHANG ZWISCHEN STRUKTUR UND EIGENSCHAFTEN VON ALUMINIUM-SILBER-LEGIERUNGEN BEI DER AUSHÄRTUNG

Der Härteverlauf und die durch Kleinwinkelstreuung beobachteten strukturellen Veränderungen während der Aushärtung werden miteinander verglichen.

Beim Übergang von der Kalt- zur Warmaushärtung treten auf den Röntgenaufnahmen zahlreiche lange Streifen mit geringer Intensität auf, die für das Vorhandensein von sehr kleinen Ausscheidungen von  $AlAg_2$  charakteristisch sind.

Die Härte steigt bei der Warmaushärtung wenn sich die Ausscheidungen entwickeln, die Streifen werden kurz und nehmen an Intensität zu; sie geht, wenn die ausgeschiedene Phase Gestalt annimmt, wieder zurück, die Streuung verschwindet.

Während der Kaltaushärtung zeigen die Röntgenaufnahmen Ringe: Die Legierung enthält "G.P.-Zonen."

Das Auftreten der Zonen, das aus dem Röntgenbild ersichtlich wird, steht auf den ersten Blick in keiner direkten Beziehung zu den Härteeffekten. Bei fortschreitender Rückbildung geht der Durchmesser der ringförmigen Beugungserscheinungen kontinuierlich zurück bis auch die Härte im Verlaufe von bestimmten Wärmebehandlungen (insbes. Rückbildung) rückbildbar wird.

Man möchte annehmen, dass die Härtesteigerung an Zonen mit sehr kleinen Abmessungen gebunden ist. Sie sind auf den Röntgenaufnahmen durch voluminöse Zonen überdeckt. Diese Hypothese wird durch absolute Intensitätsmessungen belegt.

La structure cristallographique des alliages  $AlAg$  pendant le durcissement est maintenant assez bien connue grâce à de nombreuses études aux rayons X.

Nous nous référons particulièrement au travail récent de Walker et Guinier<sup>1</sup> (dénotté ici W. G.) qui a été restreint à l'étude de la diffusion aux faibles angles.

Sans donner ici la description détaillée des phénomènes observés, rappelons que la conclusion la plus importante de cette étude est l'existence de deux types de diagrammes correspondant à deux types de structure bien distincts:

Le "diagramme à anneau" (Fig. 1a) est caractéristique de la présence dans la solution solide de "zones." Dans le cas de Al-Ag les zones sont formées par des

\* Received November 29, 1954.

† Conservatoire des Arts et Métiers, Paris, France.

rassemblements d'atomes d'argent en noyaux quasi-sphériques, les atomes ne quittant pas sensiblement les noeuds du réseau de la matrice. Le noyau riche en argent est entouré d'une auréole appauvrie en argent.

Le "diagramme à traînées" (Fig. 1b). Les traînées issues du centre prouvent l'existence de petites plaquettes très minces parallèles aux plans (111) de la solution solide. Ces plaquettes ont la structure du précipité  $AlAg_2$  cristallisant dans le système hexagonal avec plus ou moins de défauts d'empilement.

D'un autre côté les propriétés mécaniques et physiques de ces alliages aluminium-argent ont été étudiées en détail par Köster et ses collaborateurs.<sup>2</sup> Leur conclusion générale est qu'il existe deux processus d'évolution, l'un se produisant aux basses températures de revenu, l'autre aux températures plus élevées. Cette dualité est particulièrement nette dans l'évolution de la dureté:

d'où les dénominations de "durcissement à froid" (Kaltaushärtung) et "durcissement à chaud" (Warmaushärtung).

Il est très tentant en rapprochant les études de la structure et des propriétés physiques de faire l'hypothèse que le *phénomène de durcissement à froid est provoqué par les zones et que le durcissement à chaud est dû à la présence de précipités*.

Cette idée s'appuie sur le fait que les domaines correspondant aux durées et températures de revenu des deux stades pour la variation de dureté semblent à première vue en bonne concordance avec ceux fournis par la diffusion des rayons X. Cependant comme nous le verrons plus tard des difficultés apparaissent si on essaie de confronter de plus près l'évolution des diagrammes.

Il nous a paru important d'établir de façon indiscutable une relation entre structure et propriétés mécaniques dont l'importance théorique est évidente. On pouvait penser qu'une partie des difficultés de l'interprétation provenait de ce que les études aux rayons X de W. G.<sup>1</sup> avaient été faites sur des alliages à 20% en poids d'argent, alors que la majeure partie des résultats du laboratoire Köster portaient sur des alliages à 38% en poids d'argent (13% atomique).

Nous avons donc repris l'étude de W. et G. sur l'alliage même dont s'était servi Köster\* et nous nous sommes efforcés de reproduire les cycles des traitements thermiques décrits dans les articles de Köster et de ses Collaborateurs de façon à disposer d'éléments de comparaison indiscutables.

Nous donnerons ici seulement les résultats de nos expériences de rayons X sans décrire les techniques qui sont identiques à celles de W. G.

#### COMPARAISON DES TRANSITIONS ENTRE LES DEUX TYPES DE STRUCTURE ET LES DEUX TYPES DE DURCISSEMENT

Le premier point à établir est la coïncidence des transitions entre les deux types de structure et les deux processus d'évolution des propriétés. A cet effet nous avons choisi la dureté à cause de la netteté des phénomènes. Köster représente l'ensemble de ses mesures par un réseau de courbes "isochrones".<sup>3</sup> Chacune des courbes (Fig. 2) correspond à la variation de dureté en fonction de la température de revenu pour une durée donnée de revenu (1/2 h, 1 h, 3 h, 6 h, etc. . . .)

On voit, principalement pour les courtes durées, que chaque courbe comprend deux maximums. La dureté de l'alliage augmente d'abord avec la température puis décroît et pour les températures plus élevées subit une deuxième augmentation bien plus forte que la première. Ce sont respectivement les durcissements *à froid* et *à chaud* et nous définirons les points de transition par les temps et température de revenu correspondant aux

\* Nous remercions très vivement le Professeur W. Köster d'avoir bien voulu nous envoyer des échantillons d'alliages préparés dans son laboratoire.



FIG. 1(a). Diagramme à anneau: alliage recuit 1/2 h. à 160°C (agrandi 4 fois).

FIG. 1(b). Diagramme à traînées: alliage recuit 16 h. à 156°C (agrandi 4 fois).



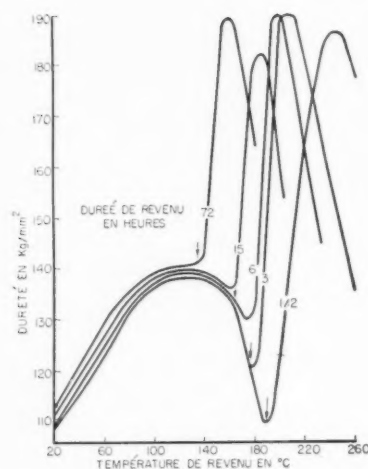


FIG. 2. Variation de la dureté en fonction de la température de revenu pour différentes durées de revenu. Les flèches indiquent l'apparition des trainées. (D'après le travail de W. Köster et F. Braumann, Z. Metallk. 43, 194 (1952).

minimums des courbe isochrones.<sup>3</sup> Nous avons reproduit dans la Fig. 2 quelques unes des courbes de Köster.

Par diagrammes de rayons X, nous avons suivi l'évolution isotherme des alliages en prenant des séries de diagrammes après des recuits de durée croissante à une température donnée. On trouve d'abord un diagramme à anneau. Quand le temps de revenu augmente le diamètre de l'anneau diminue, en même temps que son intensité augmente.

Au bout d'un certain temps apparaît le second type de diagramme avec des trainées issues du centre du diagramme. Le tableau suivant donne le temps au bout duquel apparaissent ces trainées c'est-à-dire le début de la seconde structure.

Si on rapproche ces résultats des courbes de Köster on constate qu'il y a une coïncidence satisfaisante des transitions entre les deux stades de durcissement constatés aux rayons X, et fournis par les mesures de dureté.

Il serait illusoire de chercher une trop grande précision dans ces déterminations car l'on sait<sup>4</sup> que la cinétique du durcissement peut être influencée par l'état du métal et qu'il y a dans tout échantillon des portions à réseau perturbé dont le vieillissement peut être plus ou moins en avance sur le reste du métal. Ainsi sur certains diagrammes l'anneau et des trainées sont visibles simultanément. Pour certains clichés on ne voit pas de trainées bien qu'on soit dans la région de durcissement à chaud: nous avons obtenu des diagrammes sans trainées

TABLEAU I.

Température de revenu	Temps au bout duquel apparaissent les trainées
130°	72 h
156°	8 h
175°	2 h 30-3 h
185°	1/2 h

pour des échantillons recuits pendant 1 heure à 200°: Il faut remarquer (W. G.) que les trainées apparaissent sur le diagramme quand un des cristaux irradiés a un axe [111] à peu près normal aux rayons incidents. Il peut se faire quand les cristaux sont assez gros que cette condition ne soit réalisée pour aucun des cristaux de l'échantillon.

On peut donc considérer comme nettement établi la présence de zones pendant le durcissement à froid, et de précipités pendant le durcissement à chaud.

## RELATION ENTRE LA STRUCTURE ET LA DURETE

Nous allons maintenant mettre en corrélation les variations d'aspect du diagramme et les variations de la dureté dans chacun des deux stades en commençant par le cas du durcissement à chaud, qui est le plus net.

### 1. Cas du Durcissement à Chaud

Considérons une série de revenus isochrones, par exemple d'une durée de 72 h à diverses températures au dessus de 130°, début du deuxième stade.

Voici l'aspect des diagrammes obtenus en faisant varier la température, ainsi que les duretés correspondantes lues sur les courbes de Köster.

TABLEAU II. Isochrone 72 h.

Température de revenu	Aspect	Dureté en kg/mm²	Structure
130°	Anneau intense et nombreuses trainées longues et floues	142	Plaquettes minces de précipité se développant
154°	Anneau presque complètement disparu. Nombreuses trainées courtes très intenses et très nettes	188	
170°	Pratiquement plus de diffusion	172	Gros précipités plus parfaits

On constate qu'au début du durcissement à chaud c'est-à-dire sur la branche ascendante de la courbe de dureté les trainées sont longues et floues correspondant à des précipités très petits.<sup>5</sup> Elles s'intensifient progressivement et deviennent plus courtes et nettes quand on atteint le maximum de dureté, les précipités sont alors plus nombreux et plus gros. Sur la branche descendante de la courbe elles disparaissent: les précipités sont alors trop volumineux pour donner naissance à une diffusion centrale perceptible.

Ainsi dans le second stade, la dureté augmente quand les précipités sont encore petits et décroît quand ils ont atteint une certaine taille et une certaine perfection. La même corrélation existe pour d'autres durées de revenu.

Il faut aussi rapprocher ces données de celles fournies par les diagrammes de diffraction aux grands angles, comme par exemple ceux qui ont été établis par Glocker<sup>6</sup> sur monocristaux.

Ces diagrammes révèlent des régions de diffusion linéaires disposées le long des axes [111] du réseau

TABLEAU III.

Isotherme 150°—Résultats par diagrammes de Laue et Goniomètre Schiebold-Sauter		Isotherme 156°—Diffusion aux petits angles	
Durée de revenu	Aspect des diagrammes	Durée de revenu	Aspect des diagrammes
après recuit à 545° et trempe	pas de trainées	après trempe	anneau
après revenu de 1 h	naissance des trainées	après revenu de 1 h	anneau
après revenu de 10 h	trainées intenses	après revenu de 8 h	anneau rétréci et trainées longues
après revenu de 2 jours	taches du réseau hexagonal sur les trainées	après revenu de 16 h	anneau très rétréci et longues trainées
après revenu de 6 jours	augmentation de l'intensité des taches	après revenu de 3 jours	trainées courtes et intenses
après revenu de 36 jours	augmentation de l'intensité des taches et forte diminution de l'intensité des trainées	durée supérieure à 3 jours	diminution de la diffusion

réciroque du cristal de solution solide qui produisent sur le cliché des trainées dirigées suivant ces axes. Glocker a suivi l'évolution des diagrammes le long d'isothermes et non d'isochrones.

Nous confrontons dans le tableau III les résultats de Glocker et nos résultats obtenus par diffusion centrale à des températures très voisines.

Les trainées observées par Glocker sont évidemment en corrélation avec les précipités c'est-à-dire avec le processus de durcissement à chaud. On a montré<sup>7</sup> qu'elles sont dues aux défauts d'empilement des plans (111) qui passent progressivement de l'arrangement cubique de la solution solide à l'arrangement hexagonal du précipité AlAg<sub>2</sub>. Ces imperfections sont importantes surtout au début de l'apparition des précipités quand ceux-ci sont très petits. Ces régions perturbées forment alors de nombreux obstacles à la propagation des dislocations et provoquent l'augmentation considérable de la dureté.

Quand les précipités deviennent plus gros ils deviennent d'une part plus rares, et d'autre part plus parfaits puisque, dans les clichés de Glocker, les diffusions anormales disparaissent. Il y a alors moins d'obstacles à la propagation des dislocations et la résistance mécanique diminue. C'est ce que montrent à la fois l'examen des Tableaux II et III concernant les résultats de diffusion centrale, et l'examen des résultats de Glocker du Tableau III.

Il est un point sur lequel il est nécessaire d'insister afin d'éliminer une source de confusions regrettables. Glocker a conclu, à juste titre, de ses expériences résumées dans le Tableau III et aussi d'expériences sur la réversion des alliages AlAg que les diffusions qu'il observe en forme de trainées n'ont rien à voir avec le durcissement à froid. De cela il conclut, et là est la confusion, "les trainées de Guinier-Preston n'ont rien à voir avec le durcissement à froid."

Or comme nous l'avons vu précédemment les trainées observées par Glocker, de même que celles vues en diffusion centrale sont caractéristiques du durcissement à chaud. Par contre les "zones G. P." qui sont sphériques dans le cas de l'AlAg se traduisent non pas par des

trainées mais par des anneaux, elles sont bien caractéristiques du durcissement à froid.

La confusion est provoquée par un rapprochement injustifié entre les alliages AlAg et AlCu.

Dans l'alliage AlCu il se trouve que les "zones G. P." caractéristiques du durcissement à froid ont une forme bien différente de celles de l'alliage AlAg. Ce sont des zones plates. Ces zones provoquent sur les diagrammes des trainées de diffusion anormale dirigées suivant les axes [100]. Ces trainées pour AlCu sont en corrélation avec le durcissement à froid. Elles correspondent aux anneaux des diagrammes AlAg, la différence d'aspect du diagramme traduisant les différences de forme des zones dans les deux cas. On ne doit pas assimiler ces "trainées Guinier-Preston" données par les alliages AlCu avec les trainées qu'ont observées Glocker, et d'autres auteurs aussi, sur les monocristaux d'AlAg; celles-ci sont dues aux imperfections de structure des précipités se développant pendant le durcissement à chaud. Une étude détaillée de l'ensemble des diagrammes montre d'ailleurs que les trainées dues aux imperfections du réseau n'ont qu'une ressemblance superficielle avec les trainées traduisant le forme extérieure des zones.

Nous pouvons donc conclure que l'ensemble des observations sur la structure des alliages Al-Ag pendant le deuxième stade du durcissement forme un tout cohérent, et en donne une image qui fournit une explication satisfaisante de l'évolution de la dureté.

## 2. Cas du Durcissement à Froid

Par contre les phénomènes sont beaucoup moins clairs dans le premier stade et de sérieuses difficultés se présentent.

Si l'on fait subir aux échantillons des traitements de revenus isochrones (pendant 1/2 heure, par exemple) à température croissante, la courbe de dureté (Fig. 3) montre que celle-ci croît, passe par un maximum pour une température de 130° et décroît ensuite pour retrouver sa valeur initiale à 185°, température à laquelle débute le second stade de durcissement. Köster a montré que du point de vue de la dureté on retrou-

vait cette isochrone en faisant subir à un même échantillon un cycle de chauffages successifs de 1/2 heure à températures croissantes.<sup>8</sup> Après un recuit à 545° qui homogénéise l'alliage on trempe l'échantillon dans l'eau à 18°. Puis on le porte successivement pour 1/2 heure à 80°C, 100°C, 130°C, 160°C, 175°C, 185°C, avec interruption par trempe à l'eau à 18°C après chacun des revenus de 1/2 heure. C'est ce traitement thermique que nous avons adopté car il permet en effet de faire les diagrammes de rayons X sur le même échantillon ce qui diminue les chances d'erreurs. Les différents clichés sont pris dans les mêmes conditions de fonctionnement du tube à rayons X et avec le même temps de pose. Les résultats des diagrammes ne suivent pas à première vue ceux concernant la dureté: On constate que jusqu'à 185°, température à laquelle apparaissent les traînées, tous les diagrammes comportent un anneau, de diamètre continuellement décroissant.

Nous mesurons les diamètres des anneaux par enregistrement au micro-densitomètre. Quand on trempe l'échantillon après l'avoir homogénéisé à 545°, l'état de l'alliage est assez mal défini car le diamètre de l'anneau varie d'une manière importante avec la rapidité de la trempe. (Les variations du diamètre peuvent atteindre 20%), mais ces variations du diagramme initial n'influent pas de façon systématique sur les diagrammes suivants.

Pour deux séries nous avons obtenu les résultats suivants:

TABLEAU IV.

Températures de revenu	Diamètres en mm	
	I	II
après trempe, à partir de 545°	32.5	34
1/2 h 80°	34	34
1/2 h 100°	33.5	34
1/2 h 130°	31.5	33.5
1/2 h 160°	27	27
1/2 h 175°	23	20
1/2 h 185°	apparition des traînées	
g: grandissement de l'enregistrement	9.8	10

L'évolution des diagrammes est donc différente de celle de la dureté. Après revenu à 100° et 160° la dureté est la même: or la structure révélée par les rayons X n'est pas la même puisque le diamètre de l'anneau a diminué nettement. L'opposition est encore plus nette si on compare l'échantillon après trempe après homogénéisation à 545°C et après revenu à 185°C.

De l'identité des duretés, Köster avait conclu que l'alliage retrouvait la structure initiale. Ce n'est certainement pas rigoureusement exact puisque les diagrammes de rayons X aux petits angles sont différents: d'une part un anneau de grand diamètre et d'intensité faible et de l'autre un anneau intense et de très faible diamètre, avec des traînées. Du point de vue structural l'alliage contient donc dans le premier cas des zones de faible

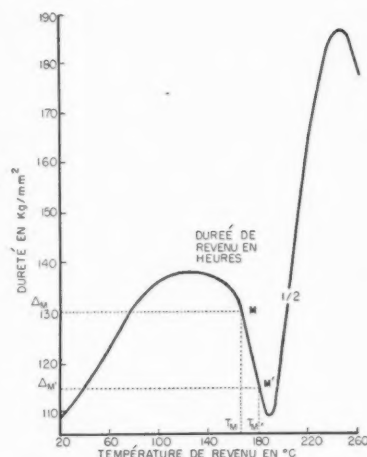


FIG. 3. Variation de la dureté en fonction de la température de revenu pour l'isochrone 1/2 heure.

dimension, et dans le second cas des zones plus volumineuses et quelques précipités.

Examinons la courbe de la Fig. 3, l'isochrone 1/2 h. Sur la branche descendante de la courbe de dureté, Köster a trouvé que l'alliage se comportait comme s'il existait un état d'équilibre réversible. Par exemple, si partant d'un état représenté par le point *M* (température  $T_M$  dureté  $\Delta_M$ ) on chauffe l'alliage pendant 1/2 heure à une température  $T_{M'}$  correspondant à l'état représenté par le point *M'* la dureté diminue de  $\Delta_M - \Delta_{M'}$ . Si l'on reporte l'alliage pour 1/2 heure à la température  $T_M$  la dureté reprendra la valeur  $\Delta_M$ . Par contre les diagrammes ne sont pas réversibles. Le diamètre de l'anneau diminue quand on porte l'alliage de  $T_M$  à  $T_{M'}$  l'alliage étant maintenu 1/2 heure à  $T_{M'}$ , et diminue encore, légèrement il est vrai quand on reporte l'alliage à la température  $T_M$  pendant 1/2 heure.

De deux traitements produisant donc une augmentation apparente du diamètre des zones, l'un provoque une augmentation et l'autre une diminution de la dureté.

Ces phénomènes sont une manifestation des propriétés de réversion que l'alliage AlAg présente dans le stade du durcissement à froid.

Un alliage durci par revenu à 130° redevient mou après un très court recuit à 200° et retrouve sa dureté après un nouveau recuit à 130°. L'opération peut être répétée plusieurs fois de suite.\* Cette réversibilité n'apparaît pas sur les diagrammes de diffusion aux faibles angles. L'anneau caractéristique du premier chauffage à 130° décroît très faiblement de diamètre au cours du recuit à 200° et décroît encore par nouveau chauffage à 130°.

On a donné pour d'autres alliages durcissants une explication simple de la réversion: les zones qui provoquent le durcissement à froid ne sont pas stables à une température de l'ordre de 200°. Elles se redissolvent donc à 200° et se reforment à nouveau si on réchauffe

\* Communication personnelle de Mr. le Professeur W. Köster.

l'alliage à une température plus basse, provoquant le second durcissement après réversion.

Cette théorie est directement confirmée par les diagrammes de rayons X, dans le cas de l'alliage AlCu: les traînées caractéristiques des zones G.P. disparaissent par réversion et réapparaissent lors du second durcissement.<sup>10</sup>

Or l'aspect des clichés de diffusion aux petits angles pour l'aluminium-argent ne semble pas, à première vue confirmer cette théorie.

Doit-on alors admettre que zones et durcissement à froid ne sont pas cause et effet? Pour tenter de lever ces difficultés nous avons cherché à déterminer la structure de l'alliage *quantitativement* sans nous contenter de la description qualitative de la nature des zones qui avait été donnée par W. G.

#### ETUDE QUANTITATIVE DE LA STRUCTURE DES ALLIAGES CONTENANT DES ZONES

Nous mesurons en valeur absolue l'intensité diffusée aux faibles angles en comparant celle-ci à l'intensité du faisceau direct. En admettant un modèle de structure pour la zone compatible avec la répartition de l'intensité diffusée en fonction de l'angle, on arrive à déduire la proportion d'atomes d'argent ségrégés au cours des différents traitements thermiques et cette donnée supplémentaire nous permettra de proposer une explication concernant l'évolution de l'alliage.

Dans la série des expériences quantitatives, un seul échantillon a été utilisé. Nous lui faisons subir le cycle de chauffages successifs décrit précédemment et nous l'examinons après l'avoir trempé de la température de revenu (successivement 80°, 100°, 130°, 160°, 175°, 185°) à la température de l'eau à 18°.

L'échantillon est irradié à la même place et les conditions de fonctionnement du tube sont maintenues constantes. Le faisceau direct dont la section au niveau du film est un étroit rectangle de 1 mm sur 0.2 mm était affaibli par une lame de cuivre de 0.265 mm d'épaisseur de façon à ramener le noircissement dû au faisceau direct au même ordre de grandeur que celui de l'anneau de diffusion.

Les densités photographiques étant inférieures à l'unité nous admettons qu'elles sont proportionnelles aux intensités de rayons X reçus, les intensités étant relevées par enregistrement des clichés au micro-densitomètre.

Nous mesurons pour chaque cliché le rapport  $G_M/I$ ;  $T_M$  étant l'intensité diffusée au maximum de l'anneau à l'angle de diffusion  $\epsilon_M$ , après avoir soustrait la diffusion à vide;  $I$  est l'intensité du faisceau direct.

Nous prenons pour mesure de l'intensité du faisceau direct  $I$ , la moitié de l'intensité maximum enregistrée sur la trace du faisceau direct. En effet celle-ci ayant un profil approximativement triangulaire, tout se passe comme si l'intensité était uniforme et égale à  $I$  sur une trace de même largeur que la trace enregistrée.

TABLEAU V.

Températures de revenu	$\frac{T_M}{I}$	$\epsilon_M$ radians
Homogénéisation 545°	1.22	0.017
130°	2.42	0.0163
160°	4.6	0.014
175°	3.38	0.0118

Pour une série de mesures nous avons obtenu les résultats suivants en faisant subir à l'échantillon le cycle décrit précédemment.

Soient:

$I_0$  l'intensité incidente sur l'échantillon (c'est-à-dire l'énergie tombant sur 1 cm<sup>2</sup> d'échantillon placé perpendiculairement au faisceau de rayons X).

$S_0$  surface irradiée sur l'échantillon.

$S_1$  surface irradiée sur le piège.

$K_{AlAg}$  facteur d'absorption de l'échantillon.

$K_{Cu}$  facteur d'absorption du cuivre.

$h$  épaisseur de l'échantillon.

$r$  distance échantillon-film.

Du rapport  $T_M/I$  nous pouvons déduire le pouvoir diffusant de l'alliage  $i(\epsilon)$  c'est-à-dire le rapport de l'intensité diffusée par cm<sup>2</sup> de l'alliage à l'intensité diffusée par un électron libre  $I_e$ . La formule de Thomson relative à l'intensité diffusée par un électron à une distance  $r$  de l'échantillon est, pour les faibles angles,

$$I_e = \frac{7.9 \times 10^{-26} \cdot I_0}{r^2}.$$

L'intensité diffusée par l'alliage est alors,  $S_0 h$  étant le volume de l'échantillon

$$T_M = \frac{S_0 h \cdot i(\epsilon_M) \cdot K_{AlAg} \cdot 7.9 \times 10^{-26} \cdot I_0}{r^2}. \quad (1)$$

Pour le faisceau direct, écrivons la conservation de l'énergie sur toute section du faisceau par exemple immédiatement après l'échantillon et juste avant le piège.

On a alors:

$$I_0 K_{AlAg} S_0 = I S_1 K_{Cu}^{-1}. \quad (2)$$

Des relations (1) et (2) on tire  $i(\epsilon_M)$  en fonction de  $T_M/I$

$$i(\epsilon_M) = \frac{T_M}{I} \frac{r^2}{S_1 h} \frac{K_{Cu}}{7.9 \times 10^{-26}}$$

soit numériquement avec  $r = 10$  cm

$$K_{Cu} = 4 \cdot 10^{-6}$$

$$h = 0.005 \text{ cm}$$

$$S_1 = 0.002 \text{ cm}^2$$

$$i(\epsilon_M) = 0.5 \times 10^{27} \frac{T_M}{I}. \quad (3)$$



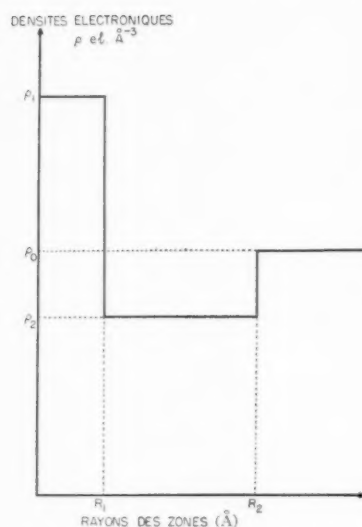


FIG. 4. Schéma d'une zone. Répartition de la densité électronique en fonction du rayon des zones.

Nous allons maintenant évaluer  $i(\epsilon_M)$  théoriquement d'après un modèle de structure déterminé.

#### Evaluation de $i(\epsilon_M)$

Nous prendrons comme modèle de structure pour la zone celle donnée par W. G. Le schéma (Fig. 4) consiste en un noyau de densité électronique  $\rho_1$  riche en argent, entouré d'une coquille de densité électronique  $\rho_2$  inférieure à la densité électronique moyenne  $\rho_0$ . On doit avoir,  $V$  étant le volume de la zone.

$$\rho_0 V = \int_{\text{zone}} \rho dV$$

c'est-à-dire :

$$(\rho_1 - \rho_2)R_1^3 = (\rho_0 - \rho_2)R_2^3. \quad (3 \text{ bis})$$

Dans le calcul de l'intensité diffusée, W. G. considèrent qu'elle peut être évaluée par la diffusion de 2 sphères :

- une sphère  $R_1$  de densité électronique  $(\rho_1 - \rho_2)$
- une sphère  $R_2$  de densité électronique  $-(\rho_0 - \rho_2)$ .

Soit  $N$  le nombre de zones par  $\text{cm}^3$ ; l'amplitude diffusée est alors<sup>9</sup>

$$A(\epsilon) = N^{\frac{1}{2}} \left[ (4/3)\pi R_1^3 (\rho_1 - \rho_2) \exp\left(-\frac{4\pi^2}{10\lambda^2} \epsilon^2 R_1^2\right) - (4/3)\pi R_2^3 (\rho_0 - \rho_2) \exp\left(-\frac{4\pi^2}{10\lambda^2} \epsilon^2 R_2^2\right) \right]. \quad (4)$$

Soient  $C_0, C_1, C_2$ , les concentrations atomiques en argent des trois régions considérées. Soient :

$Z_{Al}$  = nombre atomique de l'aluminium  $Z_{Al} = 13$   
 $Z_{Ag}$  = nombre atomique de l'argent  $Z_{Ag} = 47$   
 $a$  : paramètre de la maille,  $a = 4 \text{ Å}$ . Il y a 4 atomes par maille.

La densité électronique est liée à la concentration par la formule suivante :

$$\rho \text{ el. } \text{Å}^{-3} = \frac{4Z_{Al}(1-C) + 4Z_{Ag}C}{a^3}. \quad (5)$$

En faisant successivement  $C = C_0, C_1, C_2$  on obtient les densités électroniques des trois régions, noyau, auréole, milieu homogène.

De la relation (3 bis) on tire :

$$\begin{aligned} \frac{4}{a^3} \cdot (4/3)\pi R_1^3 (C_1 - C_2) \\ = (4/3)\pi R_2^3 (C_0 - C_2) \cdot \frac{4}{a^3} = n \quad (6) \end{aligned}$$

On voit que,  $C_2$  étant faible,  $n$  représente approximativement le nombre d'atomes d'argent rassemblés dans le noyau.

L'expression (4) devient alors

$$\begin{aligned} A(\epsilon) &= N^{\frac{1}{2}} n (Z_{Ag} - Z_{Al}) \\ &\times [\exp(-k\epsilon^2 R_1^2) - \exp(-k\epsilon^2 R_2^2)] \\ \text{avec } k &= \frac{4\pi^2}{10\lambda^2}. \quad (7) \end{aligned}$$

Et l'intensité diffusée  $i(\epsilon)$  qui est telle que  $i(\epsilon) = A^2(\epsilon)$  devient

$$i(\epsilon) = N n^2 (Z_{Ag} - Z_{Al})^2 \times [\exp(-k\epsilon^2 R_1^2) - \exp(-k\epsilon^2 R_2^2)]^2. \quad (8)$$

À l'angle de diffusion  $\epsilon_M$ , l'intensité diffusée maximum est alors  $i(\epsilon_M)$  et son expression doit être égale à la valeur expérimentale :

$$\begin{aligned} i(\epsilon_M) &= 0.5 \times 10^{27} \cdot \frac{T_M}{I} = N n^2 (Z_{Ag} - Z_{Al})^2 \\ &\times [\exp(-k\epsilon_M^2 R_1^2) - \exp(-k\epsilon_M^2 R_2^2)]^2. \end{aligned}$$

Si nous déterminons  $R_1$  et  $R_2$  nous pouvons alors étudier les variations de  $N n^2$  au cours des traitements thermiques.

#### Détermination des rayons $R_1$ et $R_2$

Le choix des rayons doit être fait de façon à faire coïncider le mieux possible les courbes d'intensité observées et théoriques. Nous comparerons plutôt les amplitudes pour simplifier les calculs.

Nous utiliserons deux relations.

1. la valeur de l'angle de diffusion pour le modèle considéré doit coïncider avec l'angle du maximum observé, qui est donné mathématiquement par:

$$\left(\frac{di(\epsilon)}{d\epsilon}\right)_{\epsilon=\epsilon_M} = 0 \text{ soit } \left(\frac{dA(\epsilon)}{d\epsilon}\right)_{\epsilon=\epsilon_M} = 0 \quad (9)$$

Posons  $R_1/R_2 = u$ . La relation (9) fournit

$$\exp[k\epsilon_M^2(R_1^2 - R_2^2)]$$

$$= u^2 = \exp\left[k\epsilon_M^2 R_1^2 \left(1 - \frac{1}{u^2}\right)\right], \quad (10)$$

$$A(\epsilon_M) = N^{1/2} n (Z_{Ag} - Z_{Al}) (1 - u^2) \exp(-k\epsilon_M^2 R_1^2). \quad (11)$$

2. La deuxième relation exprime simplement l'allure de la courbe de l'amplitude en fonction de l'angle de diffusion. Nous caractérisons la forme de la courbe par sa largeur  $l$ , rapport de son aire à son ordonnée maximum

$$l = \frac{\int_0^{\epsilon_0} A d\epsilon}{A(\epsilon_M)} \quad (12)$$

$\epsilon_0$  est la valeur pour laquelle l'amplitude reprend pratiquement la valeur 0.

La largeur est alors fournie très simplement, à la fois expérimentalement et par le calcul. De (7) (11) et (12), on tire:

$$l = \frac{1}{2} (\pi/k)^{1/2} \frac{\exp(k\epsilon_M^2 R_1^2)}{R_1(1+u)}. \quad (13)$$

La relation (10) s'écrit:

$$R_1^2 = \frac{2u^2 Lu}{k\epsilon_M^2(u^2 - 1)}. \quad (14)$$

En éliminant  $R_1$  entre (13) et (14), on obtient:

$$f(u) = \frac{8u^2(1+u)Lu}{(u-1)\exp\left(\frac{4u^2 Lu}{u^2 - 1}\right)} = \pi \cdot \left(\frac{\epsilon_M}{l}\right)^2. \quad (15)$$

De chacune des courbes représentant la variation de l'amplitude en fonction de l'angle de diffusion nous évaluons la largeur  $l$ , et par conséquent  $\pi(\epsilon_M/l)^2$ . Nous traçons  $f(u)$  en faisant varier  $u$  de 0 à 1 et nous déterminons graphiquement la valeur de  $u$  correspondant à chaque valeur de  $\pi(\epsilon_M/l)^2$ . De chaque valeur de  $u$  nous calculons la valeur de  $R_1$  par la relation (14).

La mesure de  $l$  est assez délicate. Il faut déterminer la valeur de  $\epsilon$  pour laquelle l'amplitude atteint pratiquement la valeur zéro. D'autre part pour  $\epsilon$  très voisin de 0 il faut extrapoler la courbe  $A(\epsilon)$  car la largeur du piège ne permet pas d'atteindre le centre du diagramme; on arrive près du centre à  $\epsilon = 0.005$  radian.

Les résultats numériques sont les suivants:

TABLEAU V.

Températures de revenu	$f(u)$	$u$	$R_1 \text{ \AA}$	$R_2 \text{ \AA}$
trempe	1.25	0.37	26	70
130°	1.51	0.46	30	65
160°	1.59	0.49	37	75
175°	1.57	0.48	44	92

Nous avons indiqué dans ce tableau les valeurs fournies par le calcul lorsqu'on trempe l'échantillon ayant subi l'homogénéisation à 545°. Néanmoins nous rappelons que cet état est mal défini.

Des relations (6) et (11) nous tirons les valeurs du produit  $Nn$ , nombre par  $\text{cm}^3$  d'atomes d'argent ségrégués et de  $N$ , nombre de zones par  $\text{cm}^3$ .

$$Nn = \frac{i(\epsilon_M)}{(Z_{Ag} - Z_{Al})^2 (1 - u^2)^2 \exp(-2k\epsilon_M^2 R_1^2) \cdot \frac{16\pi}{3a^3} \cdot R_1^3 (C_1 - C_2)} \quad (16)$$

$$N = \frac{i(\epsilon_M)}{(Z_{Ag} - Z_{Al})^2 (1 - u^2)^2 \exp(-2k\epsilon_M^2 R_1^2) \cdot \left(\frac{16\pi}{3a^3}\right)^2 \cdot R_1^6 (C_1 - C_2)^2} \quad (17)$$

avec

$$i(\epsilon_M) = 0.5 \times 10^{27} \frac{T_M}{I}$$

$$Z_{Ag} - Z_{Al} = 34 \text{ et } a = 4.$$

La proportion d'argent ségréguée, c'est-à-dire le rapport entre l'argent rassemblé dans les noyaux des zones par unité de volume, à celui existant dans le même

volume avant traitement thermique est:

$$p = (4/3) \pi R_2^3 N. \quad (18)$$

TABLEAU VI.

Températures de revenu	$Nn$	$n = \frac{16\pi}{3a^3} R_1^3 (C_1 - C_2)$	$N$	$p$
trempe	0.27	$\frac{10^{21}}{C_1 - C_2}$	0.6	$\frac{1}{(C_1 - C_2)^2}$
130°	0.57	$\frac{10^{21}}{C_1 - C_2}$	0.85	$\frac{1}{(C_1 - C_2)^2}$
160°	0.64	$\frac{10^{21}}{C_1 - C_2}$	0.5	$\frac{1}{(C_1 - C_2)^2}$
175°	0.27	$\frac{10^{21}}{C_1 - C_2}$	0.1	$\frac{1}{(C_1 - C_2)^2}$

Les résultats concernant  $Nn$ ,  $n$ ,  $N$  et  $p$  sont réunis dans le tableau suivant:

Il faut signaler que les chiffres du Tableau VI ne peuvent être considérés que comme des ordres de grandeur étant donné le caractère schématique du modèle adopté et le manque de précision des mesures effectuées.

Pour obtenir les valeurs numériques du nombre de zones, il faut choisir les valeurs des concentrations  $C_1$  et  $C_2$ . On peut admettre que l'auréole est très pauvre en argent c'est-à-dire  $C_2$  voisin de 0. Quant aux noyaux enrichis il est logique de penser qu'ils contiennent encore de l'aluminium puisque même dans le précipité d'équilibre il y a deux atomes d'argent pour un d'aluminium. Si nous adoptons  $C_1 = 0.5$  on voit qu'au maximum, il y aurait 40% des atomes d'argent ségrégés. Dès le début de la formation des zones une proportion considérable d'atomes d'argent est ségrégée. C'est un résultat important qui avait déjà obtenu sur l'alliage aluminium-cuivre.

Mais sans préciser la valeur de  $C_1 - C_2$ , et simplement en admettant qu'elle varie peu pendant le durcissement, le tableau VI montre que le nombre de zones croît d'abord avec la température puis décroît. Il en est de même pour le nombre d'atomes d'argent ségrégés. Donc quand le revenu se poursuit à des températures supérieures à 130°C, il y a disparition de nombreuses petites zones d'argent et seul un nombre relativement faible est susceptible de se développer. Il y a donc comme phénomène essentiel à partir de 130° et quand le revenu se poursuit jusqu'à 185°, dissolution des petites zones. Or ces petites zones sont beaucoup plus efficaces quant à la dureté de l'alliage que les quelques zones volumineuses subsistantes. D'où la décroissance de la dureté au cours du durcissement à froid après qu'on ait dépassé le stade où les petites zones sont développées au maximum qui se place aux environs de 130°.

Les atomes d'argent libérés à 185°C par dissolution des zones sont disponibles pour se déposer autour des germes de précipité si la température croît: c'est le processus de durcissement à chaud. Si au contraire on

porte à nouveau l'alliage à une température inférieure (130°, par exemple) les atomes d'argent pourront reformer des petites zones et un nouveau durcissement à froid se produire. Pendant ce temps les quelques zones volumineuses qui subsistaient à 185° resteront inchangées ou se développeront encore légèrement.

Mais on doit rendre compte, pour justifier cette explication de la réversion, du fait que les nouvelles petites zones reformées après réversion ne sont jamais visibles sur les diagrammes. La raison en est que le pouvoir diffusant des zones croît très rapidement avec leur diamètre si bien que dans un mélange de zones de différents diamètres les petites zones ne produisent pas d'effet visible auprès de la diffusion des grosses zones. Un calcul simple permet de préciser ce point: soit une zone de rayons  $R_1$ ,  $R_2$  et une zone de rayon moitié  $R_1/2$  et  $R_2/2$ ; l'intensité diffusée par la première à l'angle de diffusion maximum, est

$$i_M = n^2 (Z_{Ag} - Z_{Al})^2 \times [\exp(-k\epsilon_M^2 R_1^2) - \exp(-k\epsilon_M^2 R_2^2)^2]$$

l'intensité diffusée par la deuxième est:

$$i_M' = n'^2 (Z_{Ag} - Z_{Al})^2 \times \left[ \exp\left(-k\epsilon_M'^2 \frac{R_1^2}{4}\right) - \exp\left(-k\epsilon_M'^2 \frac{R_2^2}{4}\right) \right]$$

ou

$$n' = \frac{n}{8}$$

et  $\epsilon' = 2\epsilon$  on a donc finalement

$$i' = \frac{i}{64} = 0.01i.$$

Si donc il se forme un nombre égal de zones ( $R_1$ ,  $R_2$ ) et de zones ( $R_1/2$ ,  $R_2/2$ ) l'intensité diffusée par les petites n'est que 1.5% de l'intensité diffusée par les

plus grosses. *Il est pratiquement impossible d'espérer déceler le large anneau de la petite zone à côté du petit anneau de la grosse zone.*

### CONCLUSION

Ainsi une étude détaillée des diagrammes de rayons X nous a ramenés à une explication du durcissement à froid proche de celle adoptée pour l'alliage AlCu, et voisine également des idées émises par Köster. Le durcissement à froid serait dû à la présence de petites zones qui ne sont pas stables à haute température et se redissolvent pour la plupart. Certaines seulement subsistent après avoir grossi suffisamment.

Les difficultés de la corrélation des propriétés physiques avec les diagrammes de rayons X viennent de ce que les rayons X sont beaucoup plus sensibles aux zones volumineuses, alors que les propriétés physiques dépendent principalement des zones plus petites. Aussi la structure déduite directement des diagrammes n'est pas susceptible d'expliquer l'évolution des propriétés mécaniques. Il faut, en se basant sur les modèles de rassemblement d'atomes révélés par les rayons X, admettre des structures qui ne sont pas en contradiction avec les observations mais ne sont pas directement prouvées.

Il se trouve que cette difficulté ne se rencontre pas avec l'alliage aluminium-cuivre. En effet dans ce cas à cause de la forme des zones (plaquettes) et aussi de leur structure (le réseau de la matrice est distordu à cause

de la différence des diamètres atomiques entre l'aluminium et le cuivre), les zones même très petites sont décelables aux rayons X. D'autre part les zones ne peuvent pas augmenter de dimensions sans changer de structure. Ainsi les rayons X permettent de suivre directement l'évolution des zones qui sont responsables du durcissement à froid. Il n'en est pas de même pour l'aluminium-argent mais nous pensons qu'il s'agit d'une simple modification des conditions de l'expériences et non d'une différence fondamentale du processus de ségrégation des atomes.

### REFERENCES

1. A. H. Geisler et J. K. Hill, *Acta Cryst.* **1**, 238 (1948); A. Guinier, *Acta Cryst.* **5**, 212 (1952); C. S. Barrett et A. H. Geisler, *J. Appl. Phys.* **11**, 733 (1940); C. B. Walker et A. Guinier, *Acta Met.* **1**, 568 (1953).
2. W. Köster et F. Braumann, *Z. für Metall.* **43**, 193 (1952); W. Köster, H. Steinert, et J. Scherb, *Z. für Metall.* **43**, 202 (1952); R. Glocker, W. Köster, J. Scherb, et G. Ziegler, *Z. für Metall.* **43**, 208 (1952); G. Ziegler, *ibid*, 213; U. Dehlinger et H. Knapp, *ibid*, 223.
3. W. Köster et F. Braumann, *Z. für Metall.* **43**, 194 (1952).
4. R. Graf et A. Guinier, *Compt. Rend. Acad. Sc.* **238**, 2175 (1954); **238**, 819 (1954).
5. P. P. Ewald, *Proc. Phys. Soc. Lond.* **52**, 67 (1940).
6. R. Glocker, W. Köster, J. Scherb, et G. Ziegler, *Z. für Metall.* **43**, 210 (1952); (Tableaux 1-2-3).
7. C. S. Barrett, *Structure of Metals* (McGraw-Hill, New York, 1954), p. 259.
8. W. Köster et F. Braumann, *Z. für Metall.* **43**, 199 (1952) (fig. 15b).
9. A. Guinier, *X-Ray Crystallographic Technology* (Hilger, London, 1952), p. 266.
10. V. Gerold, *Z. für Metall.* **45**, 593 (1954).



# CONSTANTES ELASTIQUES ET FROTTEMENT INTERIEUR DE L'ALUMINIUM POLYGONISE\*

J. FRIEDEL, C. BOULANGER et C. CRUSSARD†

L'aluminium polygonisé à gros grains présente, à haute température, une forte baisse du module d'Young accompagnée d'un frottement intérieur élevé. La baisse du module est attribuée à la mise en mouvement des parois de polygonisation. Son étalement sur une large intervalle de température ainsi que la chaleur d'activation complexe qui la régit semblent indiquer la superposition de plusieurs phénomènes de relaxation: sans doute microfluage et diffusion des dislocations hors de leurs plans de glissement ("climb"). Cette interprétation suppose que dans l'aluminium l'énergie de formation des crans ("jogs") est de l'ordre de 0.7 à 1 eV.

## ELASTIC MODULUS AND INTERNAL FRICTION OF POLYGONIZED ALUMINIUM

In polygonised coarse-grained aluminium, one can observe at elevated temperature a strong drop of Young's modulus, while the internal friction reaches high values. The drop of modulus is attributed to displacements of the dislocation walls of the polygonised structure. The fact that it spreads over a large temperature interval, as well as the complex activation energy of the phenomenon, seems to prove that it is due to the joint contribution of several relaxation mechanisms: probably microcreep and climb of dislocations. According to this explanation, the energy of jog formation on dislocations should be about 0.7 to 1 eV, in aluminium.

## ELASTIZITÄTSKONSTANTEN UND INNERE REIBUNG BEI POLYGONISIERTEM ALUMINIUM

In grosse Körner polygonisiertes Aluminium zeigt bei hohen Temperaturen einen sehr starken Abfall des Young Moduls, der von einer Erhöhung der inneren Reibung begleitet wird. Der Abfall des Moduls wird dem Beginn der Bewegung der Grenzflächen der Polygone zugeschrieben. Seine Auswirkung über einen grossen Temperaturintervall, sowie die zusammengesetzte Aktivierungswärme, die die Bewegung lenkt, scheinen zu zeigen, dass eine Überlagerung von mehreren Erscheinungen der Relaxation vorliegt: Es sind dies ohne Zweifel das Mikrofließen und die Diffusion der Versetzungen aus ihren Gleitebenen heraus ("climb"). Diese Deutung setzt voraus, dass beim Aluminium die Bildungsenergie der Fehlstellen ("jogs") in der Grössenordnung von 0.7 bis 1.0 eV liegt.

### 1. INTRODUCTION

On sait que des parois de polygonisation se déplacent par glissement sous des contraintes suffisantes; ce type de mouvement, prédit par Bragg<sup>1</sup> puis par Shockley, a été clairement mis en évidence par Parker et Washburn.<sup>2</sup> Les récentes expériences de Betteridge<sup>3</sup> peuvent s'interpréter dans ce sens, en admettant que les dislocations présentes, arrangées en parois, subissent sous des contraintes très faibles un certain microfluage. Les expériences décrites dans cet article fournissent l'occasion de préciser les conditions dans lesquelles s'opère ce microfluage.

### 2. RESULTATS EXPERIMENTAUX

#### 2-1. Traitement de Polygonisation

Les expériences ont porté sur des fils de 0.4 mm de diamètre d'aluminium ou d'alliages à base d'aluminium dont la composition est reportée dans le Tableau I.\* Ces fils sont d'abord recuits à une température voisine du solidus de façon à obtenir un gros grain, de l'ordre du diamètre du fil; puis ils sont écrouis en les enroulant sur un cylindre de 4 mm de diamètre, déformation faible qui ne dépasse pas l'écrouissage critique; de cette façon

\* Received November 17, 1954.

† Institut de Recherches de la Sidérurgie, Saint-Germain-en-Laye, France.

\* Ces alliages ont été aimablement fournis par le service de Recherches de la Société Pechiney.

un chauffage d'une heure à 50°C au-dessous de la température du premier recuit les polygonise.

Des diagrammes Laue effectués par transmission (Fig. 1a) montrent un astérisme important, ce qui prouve que le métal n'a pas recristallisé. Des diagrammes en retour à grande distance mettent en évidence la fragmentation de cet astérisme (Fig. 1b) due à la polygonisation; celle-ci subsiste sans changement lors de traitements ultérieurs à température même légèrement supérieure à celle où elle a été obtenue.

L'examen aux rayons X montre que, dans un grain, la désorientation entre blocs voisins est de l'ordre de 10'. La distance  $X$  entre dislocations sur les parois de polygonisation est donnée par  $b/X = 10' = 3.10^{-3}$  rad

TABLEAU I. Composition des alliages d'aluminium utilisés.

Désignation	Composition				
	Si %	Fe %	Cu %	Mg %	Ca %
Al 99.995	0.0022	0.0015	0.001		
Al 99.96	0.012	0.018	0.010		
Al-Si 0.15	0.15				
Al-Mg 0.4				0.4*	
Al-Cu 0.4	0.005	0.01	0.41		
Al-Cu I	0.01	0.01	1.04		
Al-Cu 3	0.005	0.01	3.12		
Al-Mg 4	0.020	0.009		4.0*	
Al-Ca 0.7	0.04	0.02			0.74
Al-Ca 2.4	0.04	0.02			2.36

\* Une correction a été faite pour tenir compte de l'oxydation superficielle du Mg.

( $b \approx 3.10^{-8}$  = une distance interatomique);  $X$  est donc de l'ordre de  $10^{-6}$  cm. Ceci permet de calculer directement la taille  $l$  des blocs de polygonisation, s'ils sont équiaxes: une coupe par un plan perpendiculaire à l'axe d'enroulement (Fig. 2), montre que le bobinage sur le cylindre de diamètre  $d$ , suivi de recuit, a laissé par  $\text{cm}^2$   $1/l$   $X = 2/bd$  dislocations d'un signe en excès; d'où  $l \approx bd/2X \approx 5.10^{-4}$  cm pour  $d = 0.4$  cm, en accord avec le nombre de sous-grains que l'on peut déduire des points de la figure 1b. Des valeurs du même ordre ont été observées par Hedges et Mitchell<sup>4</sup> sur le bromure d'argent ( $l \approx 10^{-3}$  cm;  $X \approx 10^{-4}$  cm).

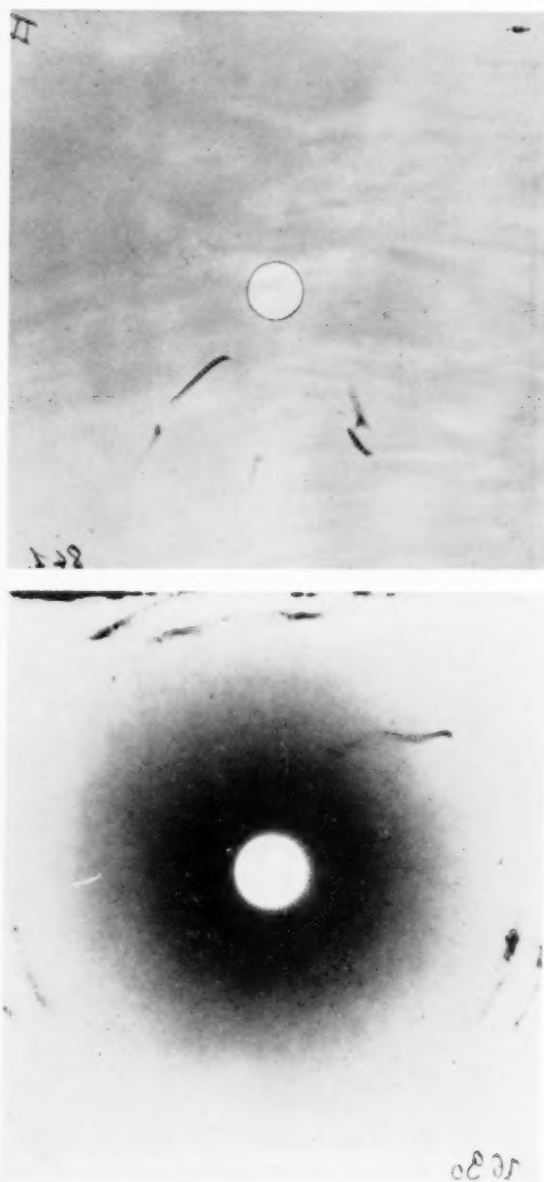


FIG. 1. Clichés Laue d'aluminium polygonisé.  
(a) par transmission; (b) en retour, à 12 cm.

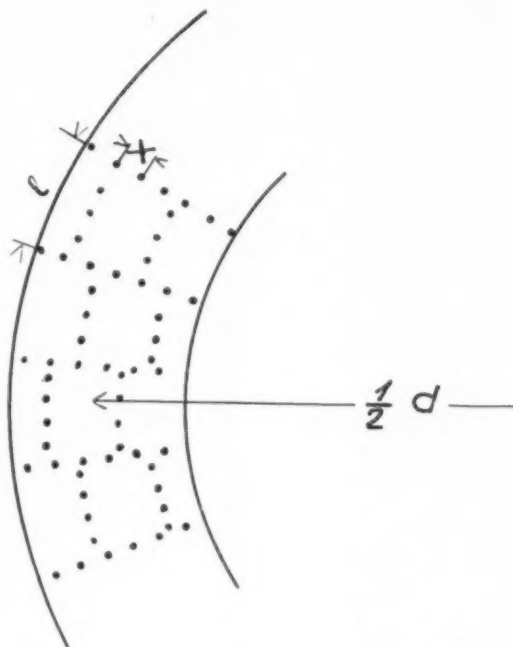


FIG. 2. Calcul de la taille  $l$  des blocs polygonisés.

La dimension des sous-grains observée dans nos éprouvettes est voisine de celle de la "structure mosaïque" des métaux recristallisés. Elle suggère que les arêtes des blocs sont constituées par les dislocations de la structure mosaïque initiale du cristal avant écrouissage.

Nous noterons que Cahn<sup>5</sup> a observé sur des monocristaux d'aluminium très pur et après flexion une polygonisation assez différente, en lamelles parallèles qui coalescent à haute température en sous-grains beaucoup plus gros que les nôtres, atteignant le dixième de millimètre d'épaisseur. La Fig. 3 compare schématiquement des blocs polygonisés de ces deux types et un bloc de la structure mosaïque initiale. Deux raisons concourent probablement à cette différence:

(a) les cristallites de Cahn étaient produits par écrouissage critique. La finesse des taches Laue [cf. (6), (7)] et les faibles limites élastiques<sup>8</sup> indiquent dans ce cas une structure mosaïque de grande taille  $l \geq 10^{-3}$  cm. Nos cristallites proviennent au contraire de fils fortement écrouis dont la recristallisation doit laisser subsister un grand nombre de dislocations, formant une structure mosaïque plus fine et complexe. Cette différence est soulignée par l'étude de Lacombe sur les cristallites insulaires.

(b) les cristallites de Cahn sont déformés avec un soin extrême; leur orientation est choisie de façon qu'un seul système de glissement entre en jeu. Les boucles de dislocations créées sont probablement grandes et se réarrangent assez facilement en grandes parois parallèles formées de dislocations-coins, ce qui correspond à leur configuration la plus stable. Dans nos expériences au contraire, les cristallites étant orientés au hasard, leur

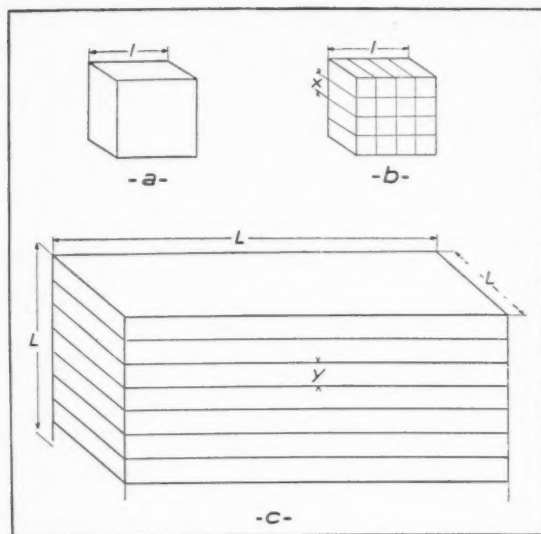


FIG. 3. Schémas de blocs mosaïques et polygonisés. (a) structure mosaïque; (b) polygonisation observée ici; (c) polygonisation de Cahn.  $l \approx 10^{-3}$  à  $10^{-4}$  cm;  $X \approx 10^{-3}$  cm;  $L \approx 10^{-1}$  cm;  $L' \approx 10^{-2}$  cm;  $V \approx 10^{-3}$  cm.

déformation a mis en jeu plusieurs systèmes de glissement, comme le prouve le fait que l'astérisme produit un étalement non seulement dans la direction de flexion, mais aussi dans une direction perpendiculaire (ce qui

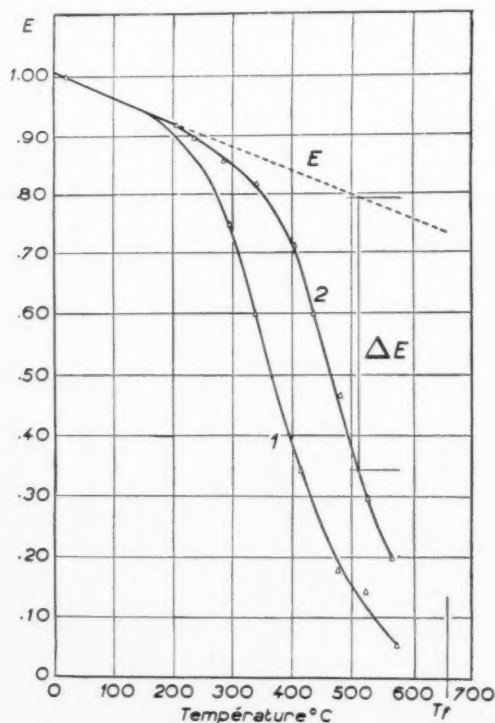


FIG. 4. Variation du module d'Young de l'aluminium 99.96% polygonisé. 1: 1 cycle en 48 min; 2: 1 cycle en 15 sec. Trait pointillé: extrapolation  $E$  de la variation de basse température;  $\Delta E$ : anomalie du module.

peut être dû aussi à des torsions parasites); les parois de polygonisation qui en résultent après recuit peuvent donc être composées de plusieurs sortes de dislocations; elles peuvent avoir des orientations plus quelconques et coalescent mal.

Les fils polygonisés ont été comparés à des fils "recristallisés," c'est-à-dire enroulés à l'état écroui, puis recuits dans les mêmes conditions que les premiers, ce qui produit une structure recristallisée à gros grains.

## 2-2. Module d'Young

Les fils, enroulés en ressorts à boudin, ont été essayés dans l'appareil déjà décrit par l'un de nous,<sup>9</sup> légèrement modifié pour pouvoir décrire des cycles très lents. Rappelons que le fil est déformé par des flexions alternées faibles (déformation maxima  $\approx 10^{-5}$ ) et lentes (1 cycle

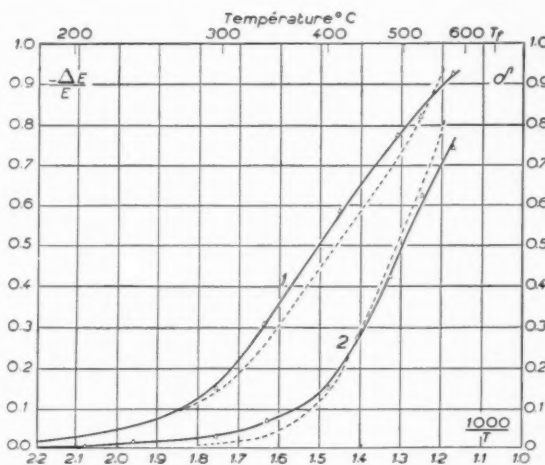


FIG. 5. Anomalie relative  $-\Delta E/E$  du module et frottement intérieur  $\delta$  pour l'aluminium 99.96% polygonisé. Traits pleins:  $-\Delta E/E$ ; traits pointillés:  $\delta$ . 1: 1 cycle par 48 min; 2: 1 cycle par 15 sec.

en 4 sec; en 15 sec; en 48 min). Le module d'Young et le frottement intérieur ont été mesurés à des températures  $T$  allant de l'ambiante à la température de fusion  $T_f$ .

La figure 4, pour l'aluminium 99.96%, montre que le module d'Young s'écarte au-dessus de 200–300°C, de sa variation lente et linéaire des basses températures, et baisse assez brusquement jusqu'à environ le 1/10ème de la valeur extrapolée à partir des basses températures. On obtient les mêmes valeurs du module au chauffage et au refroidissement, tant que la température de 640°C n'est pas dépassée (Fig. 7).

La variation du module dépend de la fréquence. Mais les courbes donnant  $-\Delta E/E$  ( $E$  valeur extrapolée des basses températures,  $\Delta E$  anomalie) en fonction de  $1/T$  ne correspondent pas à une chaleur d'activation unique: elles se resserrent aux hautes températures (Fig. 5) comme si l'anomalie comprenait deux parties régies par des chaleurs d'activation différentes, de l'ordre de 35 à 40 Kcal/mole à basse température (vers 300° à 350°C

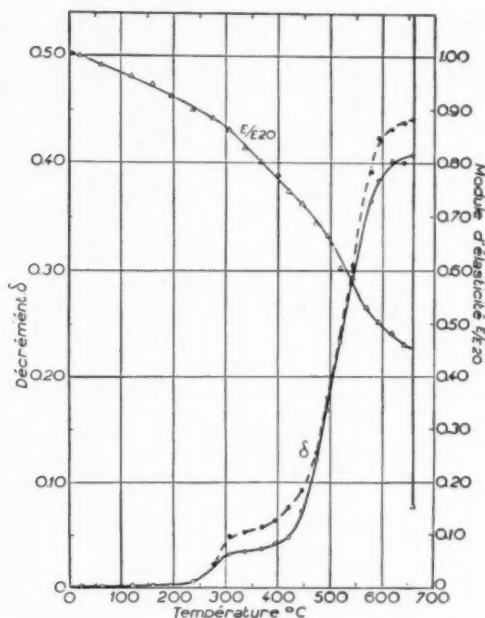


FIG. 6. Frottement intérieur de l'aluminium 99.995 partiellement polygonisé pour 1 cycle en 4 sec et 2 amplitudes. (a) trait plein: amplitude nulle (extrapolation); (b) trait pointillé: amplitude de la déformation  $10^{-5}$ . On a reporté aussi la variation du module  $E/E_{20}$ .

pour 1 cycle par 15 sec) et de 55 à 60 Kcal/mole à plus haute température (vers 500° à 550°C pour 1 cycle par 15 sec).

Les autres alliages d'aluminium utilisés donnent des résultats analogues avec de petites différences dans l'état de polygonisation, la température de début de l'anomalie et la chaleur d'activation.

On n'a pu décider expérimentalement si ces différences proviennent d'une action des différentes impuretés sur l'état de polygonisation ou sur la mobilité des parois une fois formées. Chaque élément a toutefois son action propre. Les résultats obtenus avec les alliages Al-Cu sont très voisins de ceux obtenus avec l'aluminium 99.96%. Le silicium et le magnésium semblent gêner la polygonisation, et les différences entre les courbes dans les états recristallisés et polygonisés sont faibles. Dans les alliages Al-Ca, les grains sont plus fins, la polygonisation moins nette et l'amortissement toujours fort; l'anomalie du module commence environ 100 degrés plus bas et la chaleur d'activation est plus faible; enfin l'anomalie subsiste en grande partie dans l'état "recristallisé."

Enfin dans l'aluminium 99.997% et pour les cycles les plus lents, le module semble pratiquement s'annuler aux hautes températures: des contraintes infimes suffisent à produire une déformation plastique. Ceci est dû sans doute à une migration des joints de grains, qui a été effectivement observée dans ce cas par les traces qu'elle laisse sur la surface du fil.

### 2-3. Frottement Intérieur

Le frottement intérieur  $\delta$  prend de fortes valeurs et devient critique ( $\delta \approx 1$ ) ou même parfois hypercritique à hautes températures. La figure 5, pour l'aluminium 99.96, montre qu'il prend en fait des valeurs voisines de  $-\Delta E/E$  et un peu supérieures à celles-ci, surtout pour les cycles rapides. Il faut cependant remarquer que la mesure de frottements hypercritiques est peu précise, et celle du module correspondant difficile à interpréter. La figure 6 montre que, pour les cycles rapides,  $\delta$  augmente un peu avec l'amplitude des déformations, surtout aux hautes températures.

### 2-4. Aluminium Recristallisé

Des mesures ont été faites sur de l'aluminium 99.96 recristallisé à gros grain (de façon à éviter le glissement visqueux de Kê aux joints de grains). Les Figs. 7 et 8 montrent que, pour 1 cycle en 15 secondes, l'on observe audessus de 300° à 400°C une anomalie de module  $-\Delta E$  et un frottement intérieur  $\delta$  croissant avec la température et plus faibles que pour l'aluminium polygonisé:  $\delta$  et  $-\Delta E/E$  sont de l'ordre de quelques dixièmes seulement au voisinage du point de fusion.

Une polygonisation incomplète, qui n'affecte que certains grains, donne des résultats intermédiaires entre ceux des métaux recuits et polygonisés (Figs. 7 et 8). La Fig. 8 souligne le parallélisme entre la chute du module et l'augmentation du frottement intérieur.

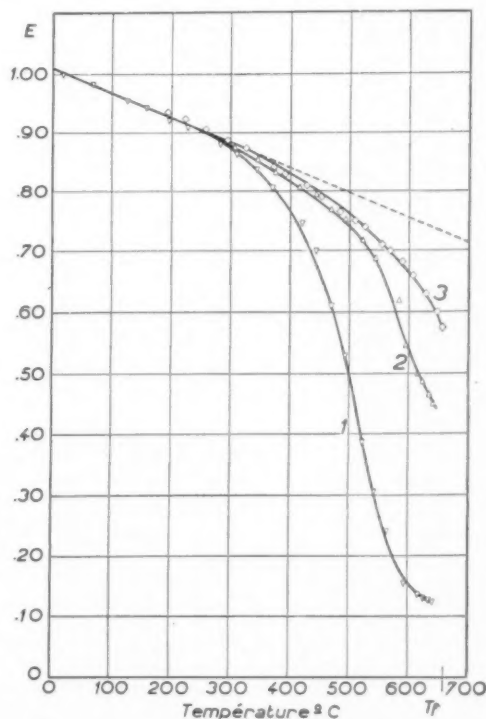


FIG. 7. Variation du module d'Young de l'aluminium 99.96. 1: polygonisé; 2: polygonisation imparfaite; 3: recristallisé.



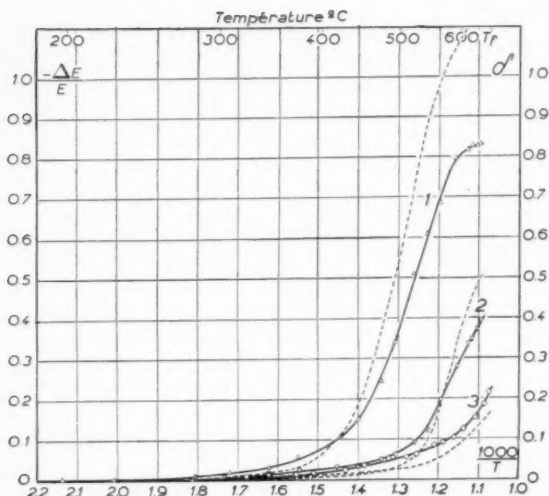


FIG. 8. Frottement intérieur  $\delta$  et anomalie relative  $-\Delta E/E$  du module dans l'aluminium 99.96. 1: polygonisé; 2: mélange de grains polygonisés et recuits; 3: recristallisé. Trait plein  $-\Delta E/E$ . Trait pointillé  $\delta$ .

Une description plus complète des résultats expérimentaux sera publiée prochainement.<sup>9</sup>

### 3. INTERPRETATION DES RESULTATS. BAISSSE DU MODULE D'YOUNG A HAUTE TEMPERATURE

Comme la taille des grains est de l'ordre du diamètre du fil, on est dans les conditions de "monocristal" de Kê,<sup>10</sup> et la forte baisse du module d'Young observée à haute température ne peut pas être attribuée à un glissement visqueux aux joints de grains, sauf, partiellement, dans les alliages Al-Ca à grains fins, où l'anomalie de viscosité intergranulaire subsiste effectivement dans les fils recuits.

La baisse du module s'explique en fait de façon satisfaisante si l'on admet que les dislocations des parois de polygonisation se déplacent facilement à haute température par glissement et diffusion sous l'action des contraintes appliquées.

Ces déplacements sont élastiques si les arêtes et les sommets des blocs de polygonisation sont bloqués. Nous justifions ce point après avoir calculé l'anomalie prévue (par. 3).

Un blocage progressif des parois quand la température décroît peut expliquer la disparition de l'anomalie de module aux basses températures; il donne lieu à une hystérésis qui s'accompagne de frottement intérieur. Nous interprétons ce blocage en termes de microfluage et de diffusion des dislocations (par. 4).

#### 3-1. Baisse du Module

La présence dans le cristal d'un système d'arcs de dislocations fixés à leurs extrémités et mobiles dans un plan sous l'action d'une force  $\sigma b$  due aux contraintes appliquées produit un cisaillement supplémentaire

(Fig. 9, cf.<sup>8,11</sup>)

$$\Delta\epsilon = NAb = N^2b/12\rho = N^2\sigma/6\mu\alpha(X), \quad (1)$$

si  $A$  est l'aire décrite par l'arc  $PQ$  de longueur  $l$ ,  $\rho$  son rayon de courbure,  $\mu$  le module de cisaillement et qu'il y a  $N$  tels arcs par unité de volume. Enfin,  $\alpha(X) \simeq (2\pi)^{-1} \times \text{Ln}(2X/b)$  est un facteur voisin de l'unité, dans le cas présent où les dislocations sont distantes de  $X \simeq 10^{-5}$  cm sur les parois.

Les déformations  $\Delta\epsilon$  sont élastiques, car elles sont réversibles et proportionnelles aux contraintes  $\sigma$ . Le déplacement des arcs de dislocation produit donc un abaissement des modules élastiques. Le calcul de cette anomalie demande que l'on connaisse les relations exactes de  $\sigma$  et  $\Delta\epsilon$  avec les contraintes appliquées et la déformation macroscopique du cristal. Ces relations dépendent d'un certain nombre de facteurs: nature des contraintes appliquées (flexion, torsion); répartition des systèmes de glissement des arcs de dislocation; nature de leur déplacement (glissement, diffusion). Si l'on se limite à une contrainte de flexion  $\sigma_e$  et si l'on suppose des systèmes de glissement répartis au hasard dans le cristal,\* un calcul simple de moyenne donne pour les déformations du cristal  $\Delta\epsilon_g$ ,  $\Delta\epsilon_d$  produites respectivement par le glissement des arcs de dislocation et leur diffusion perpendiculairement à leurs plans de glissement:

$$\Delta\epsilon_g = \frac{2}{3}\Delta\epsilon_d \simeq \frac{N^2\sigma_e}{48\alpha(X)\mu}. \quad (2)$$

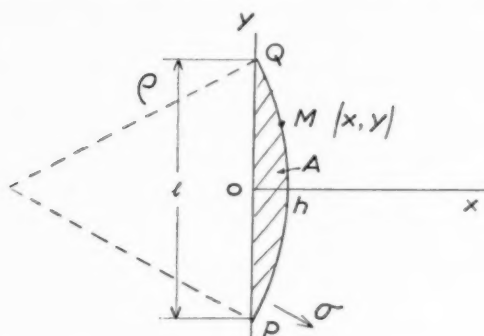
On peut se rendre compte qualitativement des raisons pour lesquelles les coefficients de proportionnalité de  $\Delta\epsilon_g$  et  $\Delta\epsilon_d$  avec  $\sigma_e$  sont inférieurs au rapport entre  $\Delta\epsilon$  et  $\sigma$  (formule 1); il est en effet évident que  $\Delta\epsilon_g$  et  $\Delta\epsilon_d$  sont inférieurs à  $\Delta\epsilon$ , et  $\sigma$  plus petit que  $\sigma_e$ . En outre,  $\Delta\epsilon_d$  est supérieur à  $\Delta\epsilon_g$  du fait que les moyennes opérées sur  $\sigma$  dans les deux cas sont différentes: en effet, si  $\Sigma$  est le tenseur des contraintes appliquées et  $\mathbf{n}$  le vecteur normal au plan où se déplace l'arc de dislocations, on a  $\sigma b = (\mathbf{n}\Sigma\mathbf{b})$ ; le vecteur de Burgers  $\mathbf{b}$  est normal à  $\mathbf{n}$  pour le glissement, tandis que dans la diffusion, l'angle entre les deux vecteurs varie de 0 à  $\pi/2$ .

Si donc seuls les glissements sont permis (d'après l'équation (2), l'anomalie  $\Delta\epsilon_g$  du module d'Young sera donnée par

$$\frac{\Delta\epsilon_g}{\epsilon} = -\frac{\Delta\epsilon_g}{E + \Delta\epsilon_g} \simeq -\frac{N^2}{18}, \quad (3)$$

où  $\epsilon$  et  $E$  sont la déformation et le module du cristal parfait;  $E + \Delta\epsilon_g$  est le module mesuré ( $\Delta\epsilon_g$  négatif).

\* Il faut remarquer que, si tous les plans de glissement étaient inclinés à  $45^\circ$  sur l'axe du fil,  $\Delta\epsilon_g$  serait double de la valeur donnée par l'équation (2). Le cas réel doit se situer entre ces deux extrêmes, car la polygonisation a été obtenue par une flexion qui a introduit des glissements inclinés sur l'axe d'un angle pas très éloigné de  $45^\circ$  (sans compter ceux produits par les torsions parasites). Mais la valeur exacte du coefficient de l'équation (2) n'a pas de répercussion important dans la suite.

Fig. 9. Arc PQ de dislocation sous l'action d'une contrainte  $\sigma$ .

Aux températures assez hautes pour que les arcs puissent *diffuser*, le déplacement des arcs de dislocation peut s'analyser en un glissement et une diffusion normalement au plan de glissement; les déformations correspondantes  $\Delta\epsilon g$  et  $\Delta\epsilon d$  s'ajoutent car elles sont dues, pour chaque arc, à des composantes différentes du tenseur des déformations. D'où pour l'anomalie  $\Delta E$  du module d'Young:

$$\frac{\Delta\epsilon g + \Delta\epsilon d}{\epsilon} = -\frac{\Delta E}{E + \Delta E} \sim -\frac{N^2}{7} \quad (4)$$

Pour des blocs de polygonisation de taille  $l$  (Fig. 3b) dont les arêtes sont fixes mais les parois mobiles,  $N \simeq (l^2 X)^{-1}$  si les dislocations sont distantes de  $X$  sur les parois; donc

$$N^2 \simeq l/X.$$

Comme  $X \ll l$ , les déformations dues au déplacement des dislocations sont beaucoup *plus fortes* que celles du cristal parfait, et les modules élastiques deviennent très petits. Les valeurs de  $l$  et  $X$  mesurées au paragraphe 2-1 donnent  $l \simeq 50X$ , donc  $(E + \Delta E)/E \simeq 1/8$  si les dislocations peuvent diffuser: le module du cristal polygonisé n'est plus qu'environ le dixième du module du cristal parfait, en bon accord avec l'expérience.

L'équation (3) donne, pour la même valeur de  $l/X$ ,  $(E + \Delta E)/E \simeq 1/4$ : la majeure partie de l'anomalie peut s'obtenir par simple glissement des dislocations.

Il est intéressant de noter pour finir que l'anomalie de module n'est pas liée à la taille des arcs de dislocation, mais seulement à leur arrangement géométrique. Elle serait en particulier beaucoup plus forte pour une *polygonisation en lamelles* du type observé par Cahn pour laquelle on aurait, si les arêtes des blocs sont fixes et les parois mobiles,  $Nl^2 \simeq L^2/L'Y$ , pour des lamelles de tailles  $L$ , d'épaisseur  $L'$  et des dislocations distantes de  $Y$  sur les parois (Fig. 3c). Avec des valeurs raisonnables  $L \simeq 10^{-1}$  cm,  $L' \simeq 10^{-2}$  cm et  $Y \simeq 10^{-3}$  cm, on aurait ainsi  $(E + \Delta E)/E \simeq 10^{-3}$ .

Inversement, pour la structure mosaïque d'un métal recristallisé (Fig. 3a) l'anomalie doit être faible:  $N^2 \simeq 1$  et si les dislocations peuvent diffuser,  $-\Delta E/E \simeq 1/7$ .

On observe effectivement une anomalie de cet ordre à haute température dans divers métaux (Mg, Al, Cu, Ag, cf.<sup>25</sup>). La Fig. 8 donne l'anomalie que nous avons obtenue pour l'aluminium 99.96. Une anomalie de même ordre, quoique plus faible a été observée dès la température ordinaire dans le cuivre et l'argent recristallisés imparfaitement recuits<sup>11-14</sup>, où les nuages d'impuretés n'ont probablement pas eu le temps de se former, du fait de leur diffusion assez lente dans ces métaux. Comme dans ce cas seuls les glissements sont possibles, on devrait s'attendre à ce que l'anomalie soit déterminée par l'équation (3), et atteigne ainsi 5%; en fait, l'anomalie observée n'atteint que 1 à 2%. Une bonne partie des dislocations de la structure mosaïque semble donc bloquée, soit par les atomes d'impuretés qui ont eu le temps de diffuser, soit parce que ce sont des "barrières de Cottrell"<sup>7</sup> qui sont spécialement stables dans ces métaux.<sup>15</sup>

Enfin quand l'éprouvette est *partiellement polygonisée*, la Fig. 7 montre que, comme on doit s'y attendre, l'anomalie de module est intermédiaire entre celles des métaux recristallisés et polygonisés. C'est probablement aussi ce qui s'est produit dans les monocristaux "anormaux" de germanium étudiés par Baker, Slifkin et Marx:<sup>23</sup> l'état initial était probablement polygonisé et les recuits successifs ont amené une recristallisation progressive qui a réduit l'anomalie. Si cette interprétation est exacte, une mesure aux rayons X de la taille des blocs polygonisés permettrait, à l'aide des considérations du paragraphe 4-2, de déduire de la température de baisse du module l'énergie de liaison des impuretés aux dislocations dans le germanium.

### 3-2. Stabilité de la Structure Polygonisée

Pour que les déplacements que nous venons d'analyser puissent se produire de façon réversible, il faut que la structure polygonisée soit stable.

A température suffisante pour que les précipités soient dissous, que les nuages d'impuretés soient mobiles et que les crans diffusent sous l'action des contraintes appliquées, les seuls points d'ancrage possibles pour les arcs de dislocation sont les *points triples* qu'ils forment entre eux. Ceux-ci doivent être assez stables si, comme semble l'indiquer la taille des blocs polygonisés, leurs arêtes sont constituées par les dislocations de la structure mosaïque initiale avant écrouissage (cf. par. 2-1.). Celle-ci, ayant résisté à une longue histoire de traitements thermiques, doit être particulièrement stable: ses points triples sont en équilibre sous la tension de ligne et un certain nombre des arcs sont probablement des barrières de Lomer Cottrell.<sup>7</sup> Les points triples les plus instables, c'est-à-dire ceux qui se déplacent le plus facilement (par glissement ou diffusion) sous l'action des contraintes appliquées, disparaissent sans doute lors des premières oscillations; leur nombre doit être faible, car la structure polygonisée ne présente aucun grossissement apparent lors de ces oscillations.

On peut d'ailleurs noter qu'aux températures assez basses pour que les dislocations ne puissent diffuser, les sommets des blocs polygonisés sont fixés, en majeure partie, du fait que les plans de glissement des arêtes et des dislocations de parois qui les entourent n'ont le plus souvent aucune direction commune. Un sommet de bloc peut en effet glisser si quatre systèmes de dislocations (les trois arêtes et les dislocations des parois) ont au moins une direction commune de glissement. Un calcul simple montre que, dans le système cubique à faces centrées, la probabilité d'une telle configuration est  $\frac{1}{32} \approx \frac{1}{3}$  si les systèmes de dislocation ont des plans de glissement répartis au hasard. Les considérations précédentes réduisent cette proportion.

#### 4. FROTTEMENT INTERIEUR ET BAISSSE DE MODULE AUX TEMPERATURES INTERMEDIAIRES

##### 4-1. Relaxation

L'anomalie de module disparaît progressivement à basse température (Fig. 4 et 5) par suite sans doute d'un blocage des parois. Le frottement intérieur  $\delta$  indépendant de l'amplitude qui accompagne cette baisse d'anomalie est sans doute lié à un phénomène de relaxation.

Les variations de  $\delta$  et de  $-\Delta E/E$  mesurées (Figs. 4 et 5) ne peuvent cependant pas correspondre à un mécanisme de relaxation unique. Des calculs classiques<sup>16</sup> montrent que dans ce cas la chute de module (entre 1% et 99% de relaxation) se ferait dans un intervalle de température  $\Delta T$  beaucoup plus réduit:  $\Delta T \approx (kT/U) \log 100$ , soit environ  $100^\circ$  pour les températures  $T$  et les chaleurs d'activation  $U$  observées; le frottement intérieur présenterait un pic très fort, de même largeur, centré à la température où le module est relaxé de moitié, et dont le maximum serait d'environ:

$$\frac{\pi}{2} \frac{\Delta E}{[E(E+\Delta E)]^{\frac{1}{2}}}, \text{ soit } \frac{9\pi}{4(10)^{\frac{1}{2}}} \approx 2.2$$

pour  $(E+\Delta E)/E \approx 1/10$ .

L'étalement de la baisse de module sur un plus grand intervalle de température semble indiquer que *plusieurs* mécanismes de relaxation entrent en jeu, dotés de chaleurs d'activation différentes. C'est ce que semble indiquer aussi la variation de  $\Delta E/E$  avec la fréquence (Fig. 5). La baisse de module s'étale évidemment dans l'échelle des fréquences en même temps que dans celle des températures; il lui correspond un pic de frottement intérieur affaibli et élargi.

Nous proposons de relier la relaxation aux "basses" températures ( $300^\circ$  à  $500^\circ$ ) au glissement des dislocations par microfluage, les nuages d'impuretés bloquant toutes les parois à température assez basse. La relaxation à "haute" température ( $500^\circ$  à  $600^\circ$ ) est attribuée à la diffusion des dislocations hors de leurs plans de

glissement. Nous allons montrer que ces deux types de mécanismes ont des chaleurs d'activation raisonnables et que leur relaxation doit s'étager dans la zone des températures observées. Le frottement intérieur total, trop complexe, ne sera pas étudié. Nous montrerons ailleurs<sup>9</sup> que le pic de frottement interne  $\delta$  est déplacé vers les hautes températures quand plusieurs mécanismes de relaxation de chaleurs différentes et voisines agissent simultanément. Ceci pourrait expliquer la croissance continue observée pour  $\delta$  avec la température.\*

##### 4-2. Microfluage

###### Diffusion des impuretés

Appliquant les considérations de Cottrell<sup>7</sup> sur le microfluage de Chalmers,<sup>17</sup> nous supposons que les dislocations sont entourées de nuages d'impuretés qu'elles doivent entraîner dans leur déplacement.

Cette interprétation semble raisonnable pour les raisons suivantes: 1°—L'anomalie dépend peu de la nature et de la concentration des impuretés et est indépendante des conditions de chauffe; elle varie par contre avec la vitesse des déformations. Ceci exclut la possibilité d'expliquer l'anomalie en invoquant une libération progressive à haute température, par dissolution de précipités.

2°—Le long recuit de polygonisation à  $600^\circ\text{C}$  a permis la formation de nuages appréciables autour de chaque arc de dislocation: même dans l'aluminium 99.997, pour la densité de dislocation réalisée ici, on dispose d'une centaine d'atomes d'impuretés par longueur atomique  $b$  de dislocation.

3°—Les contraintes  $\sigma$  sont faibles ( $5 \cdot 10^6$  dynes/cm<sup>2</sup> au maximum à basse température,  $5 \cdot 10^5$  dynes/cm<sup>2</sup> à haute température) et les déformations lentes: pour 1 cycle en 15 secondes, la vitesse moyenne de déplacement des dislocations est  $v \approx 4hv \approx 3 \cdot 10^{-6}$  cm/sec, car la flèche prise par les arcs de dislocation (Fig. 9) est  $h \approx l^2/8\rho \approx l^2\sigma/\mu b \approx 10^{-5}$  cm. Ces valeurs sont inférieures aux conditions limites établies par Cottrell pour le microfluage:

$$\sigma_c = 28\lambda kTcb^{\frac{1}{2}}$$

$$v_c = 4D/\lambda$$

$c$  est ici la concentration des impuretés,  $D$  leur coefficient de diffusion et  $\frac{1}{2}\lambda = \text{const.}$   $T^{-1}$  la distance maximum de trainage du nuage derrière la ligne de dislocation (distance au-delà de laquelle la dislocation est arrachée au nuage). L'impureté prépondérante ici est vraisemblablement le fer;  $\lambda \approx 15b$  est une valeur raisonnable dans ce cas.<sup>24</sup> Avec  $D \approx 10^{-10}$  cm<sup>2</sup> sec<sup>-1</sup> et  $c \approx 10^{-5}$ , pour l'aluminium le plus pur, ceci donne  $\sigma_c \approx 10^7$  dynes/cm<sup>2</sup> et  $v_c \approx 10^{-8}$  cm/sec<sup>-1</sup>.

\* Sur la Fig. 6, la croissance de  $\delta$  avec la température se fait en deux étapes: il semble que dans ce cas, on ait effectivement séparé les mécanismes de "basse" et de "haute" température (microfluage et diffusion). Les raisons de ce comportement seront discutées dans un autre article.<sup>9</sup>

### Température de relaxation

Le frottement dû au trainage du nuage est proportionnel à la vitesse.<sup>7</sup> L'élément situé au centre de l'arc de dislocation, de coordonnées  $(h, 0)$  sur la Fig. 9, se déplace donc en suivant une équation du type:

$$P \frac{\partial x}{\partial t} + Q \frac{\partial^2 x}{\partial y^2} = \sigma b, \quad (6)$$

où  $\sigma b$  est la force appliquée dans le plan de glissement;  $Q = \frac{1}{2} \mu b^2 \alpha$  est la tension de ligne, et  $P$  le coefficient de frottement de la dislocation. Le terme d'inertie est négligeable dans ces mouvements lents.<sup>18</sup> D'après l'équation (1), pour de petits déplacements,  $\partial^2 x / \partial y^2 = 1/\rho = 8h/l^2 = 12\Delta\epsilon/Nl^2b$ ; l'équation (6) se met donc aisément sous la forme

$$\sigma = \frac{6\alpha\mu}{Nl^3} \Delta\epsilon + \frac{3}{2} \frac{P}{Nl^2b^2} \frac{\partial \Delta\epsilon}{\partial t}, \quad (7)$$

car le cisaillement dans le plan de glissement dû au déplacement d'une dislocation est  $\Delta\epsilon/N = \frac{2}{3}lbx$ .

Introduisant la contrainte de flexion  $\sigma_e$  et la déformation moyenne  $\Delta\epsilon g$  due au glissement des parois, le calcul de moyennes du paragraphe 3-1 permet d'écrire

$$\sigma_e = \frac{18E}{Nl^3} \Delta\epsilon g + \frac{12P}{Nl^2b^2} \frac{\partial \Delta\epsilon g}{\partial t}, \quad (8)$$

$\Delta\epsilon g$  représente la fraction de la déformation totale qui est déphasée par rapport à  $\sigma$ , d'un angle  $\varphi$ , déterminé d'après (8) par

$$tg \varphi = 2\pi\nu x - \frac{2}{3} \frac{P}{E} \frac{l^2}{b^2} = \omega\tau_\sigma \quad (9)$$

en appelant  $\tau_\sigma$  le temps de relaxation à  $\sigma = \text{Cte}$ . Or on sait<sup>16</sup> qu'en introduisant le temps de relaxation à déformation constante

$$\tau_\epsilon = \tau_\sigma \frac{E + \Delta E g}{E} = \tau_\sigma \frac{1}{1 + \frac{Nl^3}{18}}$$

on doit trouver le maximum du frottement intérieur à une température  $T_1$  pour laquelle

$$2\pi\nu(\tau_\epsilon\tau_\sigma)^{1/2} = 1. \quad (10)$$

En portant dans cette équation les valeurs trouvées ci-dessus pour  $\tau_\sigma$  et  $\tau_\epsilon$ , et en tenant compte de ce que d'après Cottrell,<sup>7</sup>  $P = 7c\lambda^2 kT/b^3 D$ , avec  $D = D_0 \exp(-U_1/kT)$ , on trouve:

$$T_1 = \frac{U_1}{k \left[ \ln \left( 3D_0 E b^5 \left( 1 + \frac{Nl^3}{18} \right)^{1/2} \right) - \ln(28\pi\lambda^2 kT_1 l^2 c\nu) \right]} \quad (11)$$

Dans le cas de nos essais sur l'aluminium, si  $T_1$  est de l'ordre de 650°K, cette équation peut s'écrire

$$T_1 \simeq U_1 / k \ln(D_0 Z_1 / 14 l^2 c\nu), \quad (12)$$

où  $Z_1 = (1 + Nl^3/18)^{1/2}$  varie entre 1 et 2 quand on passe du métal recristallisé aux métaux polygonisés, ou écrouis.

Les valeurs  $U_1 \simeq 35$  Kcal/mole et  $D_0 \simeq 1$  pour la diffusion du fer donnent, avec  $l = 5 \cdot 10^{-4}$  cm et  $c = 10^{-4}$ ,  $T_1 \simeq 320$  et 450°C pour  $\nu = 1$  cycle en 48 minutes et 15 secondes, respectivement. Ces valeurs de  $T_1$  et de  $U_1$  sont en accord satisfaisant avec l'expérience pour l'anomalie de module aux basses températures (par. 2-2). Les formules (11) et (12), où  $l$  intervient au carré, montrent que les impuretés jouent probablement plus sur  $T_1$  par leur action sur la taille de la polygonisation que directement par leur concentration. Enfin une certaine dispersion est à prévoir sur la taille  $l$  des blocs polygonisés. Celle-ci doit contribuer à l'étalement de la baisse de module et du frottement intérieur, mais ne peut l'expliquer entièrement: une dispersion raisonnable de  $l$ , dans le rapport de 1 à 10 par exemple, étale  $T_1$  sur 120° seulement.

Les Figs. 7 et 8 montrent que la température de blocage des parois est sensiblement la même que l'éprouvette soit polygonisée ou recristallisée. Ceci doit être dû à ce que la taille  $l$  des blocs polygonisés est la même que celle de la structure mosaïque du métal recristallisé.

### 4-3. Diffusion

Le frottement intérieur de haute température est lié à une baisse de module pourvue d'une forte chaleur d'activation. Nous proposons de l'attribuer à la diffusion des dislocations des parois hors de leurs plans de glissement. Nous montrons que cette diffusion donne lieu à une relaxation dans une zone de températures et avec une chaleur d'activation convenables, et que d'autres mécanismes, tels que la création d'atomes interstitiels, peuvent être négligés.

#### Chaleur d'activation

Comme nous l'avons signalé au paragraphe 3-1, on peut étudier séparément les déformations dues au glissement et à la diffusion des dislocations perpendiculairement à leurs plans de glissement. Sous l'action de la force  $\sigma b = (b \Sigma n)$  due au tenseur  $\Sigma$  des contraintes appliquées, un arc de dislocation prend par diffusion une certaine courbure  $\rho$  dans le plan  $n$  perpendiculaire à son plan de glissement.

Si  $U_2$  est l'énergie d'activation et  $\alpha$  un coefficient de fréquence pour la diffusion d'une longueur  $b$  de dislocation sur une distance atomique, la vitesse de diffusion d'un arc de dislocation peut évidemment s'écrire, aux faibles contraintes  $\sigma$  et aux températures élevées con-



sidérées ici :

$$\frac{\partial x}{\partial t} = ab\nu_0 [\exp(-U_2/kT)] \left( \sigma b - \frac{1}{2} \frac{\mu b^2 \alpha}{\rho} \right) b^2/kT, \quad (13)$$

$\nu_0$  est la fréquence des vibrations atomiques et  $\mu b^2 \alpha / 2\rho$  la force due à la tension de ligne. Cette équation peut se mettre sous la forme (7) avec  $P = kT / a\nu_0 b^3 \exp(U_2/kT)$  et donne donc lieu à un phénomène de relaxation avec une chaleur d'activation  $U_2$ . Il reste à préciser les valeurs de cette chaleur  $U_2$  et du coefficient  $a$ .

Nous montrons à la fin de ce paragraphe que les contraintes sont assez faibles et les températures assez élevées pour que les concentrations de crans et de lacunes soient celles de l'équilibre thermique. Mott<sup>19</sup> a remarqué que dans ce cas  $U_2$  est la somme de trois termes : l'énergie  $U_{fc}$  de formation des crans ; celles  $U_{fl}$  et  $U_{dl}$  de formation et de déplacement d'une lacune.

La diffusion des dislocations se fait en effet par absorption ou émission de lacunes par les crans. A la fin d'une émission ou au début d'une absorption, le cran doit être décroché de la lacune pour être dans un état stable. Le cran ne peut ici se décrocher par glissement de la lacune qui l'a émise<sup>20</sup> car il serait rappelé à sa position initiale par la tension de ligne et ne serait donc pas dans un état stable. C'est donc, comme l'a proposé Mott, la lacune qui doit se décrocher du cran en sautant dans une des 11 positions réticulaires voisines. La fréquence d'émission d'une lacune par un cran soumis à une force  $\tau b^*$  sera donc

$$11\nu_0 \exp(-F_{fl} - F_{dl} + \tau b^*)/kT,$$

si  $F_{fl}$  et  $F_{dl}$  sont les énergies libres de formation et de déplacement d'une lacune ; la fréquence d'absorption en sens inverse sera

$$11\nu_0 \exp(-F_{fl} - F_{dl} - \tau b^*)/kT.$$

Si  $F_{fc}$  est l'énergie libre de formation des crans, leur concentration sera  $\exp(-F_{fc}/kT)$ . La vitesse de diffusion d'un élément de dislocation sous contrainte  $\tau$  faible, s'écrit donc

$$\frac{\partial x}{\partial t} = 22\nu_0 b [\exp(-F_{fc} - F_{fl} - F_{dl})/kT] \tau b^3/kT. \quad (14)$$

Les remarques suivantes permettent de passer des énergies libres  $F$  aux énergies internes  $U$  correspondantes.  $F_{fc}$  est dû presque uniquement à des distorsions élastiques, dans un métal comme l'aluminium où les dislocations sont peu décomposées.<sup>20</sup> Il est donc proportionnel aux modules élastiques  $\mu$ ,  $E$  (qui décroissent de façon à peu près linéaire quand la température croît) et au volume atomique (qui croît comme  $1 + 3\alpha T$ , si  $\alpha$  est

\* La force s'exerçant sur la dislocation à l'endroit du cran,  $\tau b$ , est la différence entre la force due à l'action de la contrainte extérieure, soit  $\sigma b$ , et celle due à la tension de ligne. Nous en avons tenu compte dans l'équation (13).

le coefficient d'expansion linéaire du métal). On a donc

$$F_{fc} = U_{fc} + T \partial F_{fc} / \partial T \simeq U_{fc} [1 + (dE/E_0 dT - 3\alpha)T],$$

si  $E_0$  est la valeur du module extrapolée à 0°K.

En appliquant le même raisonnement à la fraction  $l$  d'origine élastique de l'énergie  $F_{fl}F + \delta l$ , l'équation (14) se met sous la forme (13) avec

$$\left. \begin{aligned} U_2 &= U_{fl} + U_{dl} + U_{fc} \\ \text{et} \\ a &= 22 \exp[-\{U_{fc} + l(U_{fl} + U_{dl})\} \\ &\quad \times (dE/E_0 dt - 3\alpha)/k]. \end{aligned} \right\} \quad (15)$$

$U_{dl}$  doit être un peu inférieure à l'énergie de déplacement d'une lacune dans un métal parfait, donc  $U_{fl} + U_{dl}$  un peu inférieure à l'énergie  $U_d$  de self-diffusion. Dans l'aluminium,  $U_d$  est probablement voisin de 40 kcal/mole, en accord avec les chaleurs d'activation mesurées dans le fluage et la rupture.<sup>21</sup> Des valeurs  $U_{fc}$  assez faibles, de l'ordre de 15 à 20 kcal/mole, rendent donc compte des chaleurs  $U_2$  observées. On en déduit des énergies libres de formation de cran  $F_{fc}$  un peu inférieures : environ 15 kcal/mole à température ordinaire, car  $3\alpha = 0.7 \cdot 10^{-4}$ ,<sup>28</sup> et  $dE/E_0 dT = 4.7 \cdot 10^{-4}$  d'après Sutton,<sup>29</sup> en accord avec les résultats de la figure 4 (cf. aussi<sup>26</sup>). Cette valeur est en bon accord avec celle calculée par Seeger à l'aide d'un modèle de Peierls-Nabarro.<sup>20</sup>

Par analogie avec ce qui se passe pour la self diffusion (cf.<sup>23,27</sup>) il est raisonnable de supposer qu'une fraction  $l$  assez forte de l'énergie  $F_{fl} + F_{dl}$  est d'origine élastique. Ceci conduit à des coefficients de fréquence  $a$  assez élevés.\* Les valeurs raisonnables  $l = 0.6$ ,  $U_{fc} = 20$  kcal/mole et  $U_{fl} + U_{dl} = 35$  kcal/mole donnent, avec l'équation (15),  $a \simeq 2 \cdot 10^5$ , valeur que nous utiliserons dans ce qui suit.

#### Température de relaxation

On déduit facilement de l'équation (13), mise sous la forme (7), l'équation reliant la contrainte extérieure  $\sigma_e$  à la déformation due à la diffusion  $\Delta \epsilon d$ . On trouve ainsi :

$$\sigma_e = \frac{12E}{Nl^3} \Delta \epsilon d + \frac{8P}{Nl^2} \frac{\partial \Delta \epsilon d}{\partial t}.$$

Aux températures envisagées, les nuages de Cottrell n'opposent pas de résistance au déplacement des dislocations ; nous pouvons raisonner comme au paragraphe 4-2, à condition de considérer qu'à la déformation en phase avec  $\sigma_e$ , ici  $\epsilon + \Delta \epsilon g$ , se superpose une déformation  $\Delta \epsilon d$  dont le déphasage  $\varphi$  est déterminé par l'équation précédente. Il se trouve que  $\varphi$  et  $\tau_e$  ont la même valeur que dans l'équation (9). Mais  $\tau_e$  est donné ici par

$$\tau_e = \tau_\sigma \frac{E + \Delta E g + \Delta E d}{E + \Delta E g} = \tau_\sigma \frac{1 + Nl^3/18}{1 + Nl^3/7}.$$

\* Le coefficient de fréquence  $a$  est lié à l'entropie d'activation  $\Delta S = k \ln(a)$ .

En raisonnant comme dans le cas du microfluage, on trouve que le pic de frottement intérieur se produit à une température

$$T_2 = U_2 / k \ln \frac{3a\nu_0 E b^5}{4\pi\nu T_2^2} \left( \frac{1 + Nl^3/7}{1 + Nl^3/18} \right)^{1/2}, \quad (16)$$

soit, pour l'aluminium, avec  $a = 2 \cdot 10^5$  et  $T_2$  de l'ordre de  $800^\circ\text{K}$ ,

$$T_2 \simeq U_2 / k \ln [6 \cdot 10^4 z_2 / \nu l^2], \quad (17)$$

où  $z_2 = [(1 + Nl^3/7)/(1 + Nl^3/18)]^{1/2}$  est égal à 1 pour la structure mosaïque et à 1.5 pour les métaux écrouis ou polygonisés.

La valeur  $U_2 \simeq 55$  kcal/mole donne pour  $T_2$  des valeurs en bon accord avec l'expérience:  $T_2 = 475^\circ\text{C}$  pour 1 cycle en 48 minutes et  $600^\circ\text{C}$  pour 1 cycle en 15 secondes.

#### Equilibre des lacunes et des crans

L'équation (13) suppose que les crans et les lacunes gardent leurs concentrations d'équilibre lors de la déformation. Ceci se justifie du fait que la déformation est lente, la température élevée et l'énergie de formation de crans assez faibles.

1°—Lors de la diffusion, les crans se déplacent le long des lignes de dislocation et s'annihilent assez rapidement par rencontre avec des crans de signe contraire.

Mais de nouveaux crans se reforment assez facilement pour maintenir une concentration voisine de l'équilibre.

La fréquence  $\nu_a$  d'annulation des crans sera en effet au plus égale à leur vitesse,  $a\nu_0 b [\exp(-U_{f1} - U_{d1})/kT] \sigma b^3/kT$ , divisée par leur distance moyenne  $l' = b \exp(U_{fc}/kT)$ . Un couple de crans se crée d'autre part si une lacune se trouve sur la ligne de dislocation et se décompose en deux crans. La fréquence  $\nu_c$  d'un tel événement par arc  $l'$  de dislocation sera de l'ordre de  $(l'/b) \nu_0 [\exp(-U_{f1} - 2U_{fc})/kT] b \text{ grad}(\ln c)$ , pour une concentration  $c = b/l'$  de crans et si les lacunes sont en équilibre thermique. Les fréquences  $\nu_a$  et  $\nu_c$  sont égales si la distance entre crans diffère de leur distance d'équilibre  $l'$  d'une quantité  $\delta l'$  telle que

$$\frac{\delta l'}{l'} = \frac{l' \partial c}{c \partial x} = \frac{a \sigma b^3}{kT} \exp(U_{fc} - U_{d1})/kT,$$

pour  $a \simeq 20$ ,  $U_{fc} \simeq U_{d1} \simeq 15$  kcal/mole, et  $\sigma b^3 \ll kT$ , ce rapport est bien inférieur à l'unité, donc la concentration des crans voisine de l'équilibre.

2°—Les lacunes sont elles aussi en équilibre thermique, parce que les crans sont assez rapprochés pour se fournir mutuellement toutes les lacunes nécessaires à leur diffusion. Le temps  $\tau$  mis par une lacune pour passer d'un cran qui l'émet à un cran voisin qui l'absorbe est en effet  $\tau = \int_0^{l'} dx/v$ , si  $l'$  est la distance entre crans et  $v = \nu_0 b^2 (\text{grad}(\ln c) / \exp(-U_{d1}/kT))$  la vitesse des lacunes à la concentration  $c$ . Si  $c_1$  et  $c_2$  sont les concentra-

tions des lacunes au voisinage des deux crans, on a, pour un régime permanent où le flux  $v_c$  de lacune est indépendant de la position,

$$\tau^{-1} = [2(c_2 - c_1)/(c_1 + c_2)] \nu_0 \exp(-U_{d1} - 2U_{fc})/kT.$$

La fréquence de formation d'une lacune sur un cran,  $\nu_0 [\exp(-U_{f1} - U_{d1})/kT] (\sigma b^3/kT)$ , sera de l'ordre de  $\tau^{-1}$  si

$$2 \frac{c_2 - c_1}{c_2 + c_1} = \frac{\sigma b^3}{kT} \exp(2U_{fc} - U_{f1})/kT.$$

Ces déviations relatives de concentrations sont très faibles, car  $\sigma b^3 \ll kT$  et  $U_{f1} > 2U_{fc}$ .

#### Autres mécanismes possibles

La diffusion des dislocations peut aussi se faire par émission et absorption d'atomes interstitiels. Mais ce mécanisme est négligeable aux températures considérées ici, car les atomes interstitiels ont une énergie de création beaucoup plus forte que les lacunes.

D'autre part une paroi de dislocations purement vis ne peut glisser que si les crans qu'elle contient absorbent ou émettent des lacunes (Fig. 10a). Une telle paroi ne commence donc à glisser qu'à haute température, avec une chaleur d'activation égale à  $U_2$  (définie au début du paragraphe 4-3).

Mais ces parois sont en nombre négligeable. Sur toutes les parois qui ne sont pas purement vis, en effet, les crans se déplacent aisément par glissement, et ne gênent donc pas le glissement des arcs de dislocation (Fig. 10b). Leur concentration est seulement un peu modifiée: elle devient plus forte près de A que près de B quand l'arc de la figure b se déplace vers la droite. Il en résulte une force qui s'oppose au glissement des parois. Mais il est facile de montrer que cette force thermodynamique est

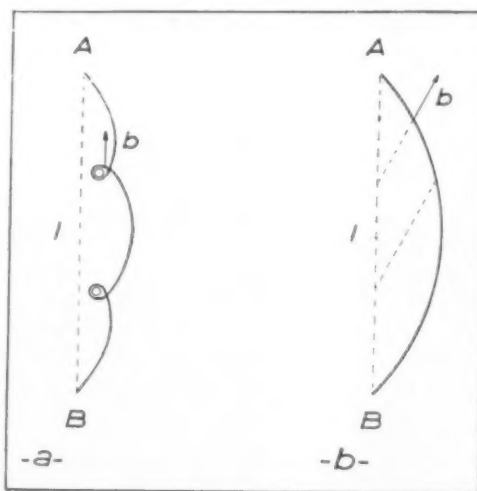


FIG. 10. (a) arc de dislocation-vis dont les crans diffusent. (b) arc de dislocation non vis dont les crans glissent.

négligeable dans les petits déplacements étudiés ici quand le vecteur de Burgers  $b$  fait avec la ligne  $AB$  un angle supérieur au degré. La proportion de parois dont le glissement est bloqué est donc de l'ordre de  $10^{-4}$ .

#### *Frottement interne dans l'aluminium écroui*

Notons pour finir que les températures de relaxations  $T_1$  et  $T_2$  relatives au microfluage et à la diffusion croissent toutes les deux avec la longueur "libre"  $l$  des arcs de dislocation.

La baisse de module et les pics de frottement interne doivent donc s'observer à plus basse température dans un métal écroui, où les longueurs  $l$  sont certainement plus courtes. Kê<sup>20</sup> observe effectivement un pic de frottement intérieur à 250°C dans un aluminium 99,99 fortement écroui et pour  $\nu = 1 \text{ sec}^{-1}$ . Si ce pic est dû au glissement des dislocations par microfluage, l'équation (12) donne pour longueur des arcs "libres" de dislocation la valeur raisonnable  $l \approx 2 \cdot 10^{-6} \text{ cm}$ . A plus haute température, la diffusion des dislocations entraîne sans doute un réarrangement par "revenu" de toute la structure écrouie et un frottement interne non reproductible.

#### 5. RESUME ET CONCLUSION

L'utilisation d'un hystérésimètre d'un nouveau genre décrit ailleurs,<sup>9</sup> nous a permis de suivre jusqu'au point de fusion les variations du module d'Young et du frottement intérieur de fils d'aluminium, "pur" ou légèrement allié.

Ces mesures ont mis en évidence à haute température une baisse anormale du module d'Young accompagnée d'hystérésis élastique. Pour les éprouvettes à gros grains bien recristallisés, la baisse relative de module et l'élévation corrélative de frottement intérieur apparaissent au-dessus de 300 à 400°C et croissent lentement jusqu'à des valeurs voisines de 0.2 près du point de fusion. Pour des éprouvettes à grains de même grosseur mais polygonisés, le module décroît rapidement à partir de 300° à 400°C et atteint vers 600°C environ un dixième de la valeur observée pour les grains bien recristallisés; le frottement intérieur croît parallèlement jusqu'à des valeurs voisines de l'unité.

Pour expliquer ce comportement à haute température, nous supposons que les parois des sous-grains produits par la polygonisation sont composées de bouts de dislocations parallèles, ancrés à leurs extrémités; sous l'action d'une contrainte, l'ensemble de ces dislocations se déplace (par glissement et diffusion) comme si elles constituaient une membrane élastique fixée sur son pourtour; ces déplacements produisent une petite déformation supplémentaire qui explique la chute du module.

Quand la température décroît, les parois sont sans doute progressivement bloquées, ce qui réduit l'anomalie de module et produit une certaine hystérésis.

L'étalement du frottement intérieur et de la baisse de module sur un assez grand intervalle de température ainsi que les chaleurs d'activation complexes observées semblent indiquer que le blocage se fait en plusieurs temps. Dans cette hypothèse, quand la température décroît, les arcs de dislocation commencent par ne plus pouvoir diffuser hors de leurs plans de glissement; puis leur glissement même est empêché par la faible mobilité des nuages d'impuretés qui les entourent. Si cette interprétation est exacte, la chaleur d'activation de 35 kcal/mole observée à basse température est celle de diffusion des impuretés; celle de haute température, voisine de 55 à 60 kcal/mole, est la somme de l'énergie de self diffusion  $U_D$  et de l'énergie de formation des crans  $U_{fc}$ .

Avec  $U_D = 40 \text{ kcal/mole}$ , on aurait ainsi  $U_{fc} = 15 - 20 \text{ kcal/mole}$ , en accord avec les prévisions théoriques.

Les diagrammes de rayons X permettent d'évaluer la dimension des sous grains des parois de polygonisation et des bouts de dislocations qui les constituent. On peut ainsi calculer la valeur maxima de la baisse du module ainsi que les températures de relaxation des deux mécanismes de blocage. On trouve un bon accord avec l'expérience.

Ces recherches jettent donc des lueurs nouvelles sur le mouvement des dislocations dans les réseaux aux températures moyennes ou élevées; elles permettent de distinguer les mouvements par glissement et par diffusion, et d'atteindre ainsi l'énergie de formation des crans; elles confirment le rôle de frein que jouent les nuages d'impuretés. Elles permettent ainsi de préciser les notions de "mobilités" et de "flexibilité" des dislocations qui jouent un rôle essentiel dans le fluage des métaux aux températures élevées.

En passant, on obtient des données quantitatives sur les dimensions des sous-grains, qui donnent des aperçus intéressants sur la polygonisation (par. 2-1); celle-ci ne se produit pas du tout de la même façon dans un grain d'un métal polycristallin, plus ou moins parfait et écroui par des glissements multiples, que dans un monocristal déformé avec précaution.

#### REFERENCES

1. W. L. Bragg, Proc. Phys. Soc. **52** (1940).
2. E. R. Parker and J. Washburn, Trans. A.I.M.E. **194**, 1076 (1952).
3. W. Betteridge, N.P.L. Conference on Creep and Fracture (1954).
4. J. M. Hedges and J. W. Mitchell, Phil. Mag. **44**, 233 (1953).
5. C. W. Cahn, J. Inst. Met. **76**, 121 (1949).
6. A. Guinier and Tennevin, Physica **15**, 1 (1949).
7. A. H. Cottrell, *Dislocations and Plastic Flow* (Oxford, 1953).
8. N. F. Mott, Phil. Mag. **43**, 1151 (1952).
9. C. Boulanger, C. R. Acad. Sci. **233**, 722 (1951). Rev. Métallurgie (à publier).
10. T. S. Kê, Phys. Rev. **71**, 533 (1947).
11. J. Friedel, Phil. Mag. **44**, 444 (1953).
12. W. Koster and W. Rauscher, Z. Metallk. **39**, 111 (1948).
13. G. Bradfield and F. Pursey, Phil. Mag. **44**, 437 (1953).
14. A. D. W. Smith, J. Inst. Met. **79**, 477 (1952).

15. A. Seeger and G. Schock, *Acta Met.* **1**, 519 (1953).
16. C. Zener, *Elasticity and Anelasticity of Metals* (Chicago, 1948).
17. B. Chalmers, *Proc. Roy. Soc.* **156A**, 427 (1936).
18. J. S. Koehler, *Imperfections in Nearly Perfect Crystals* (New York, 1952).
19. N. F. Mott, *Comm; privée* (1954).
20. A. Seeger, *Conférence de Bristol et comm. privée* (1954).
21. C. Crussard and J. Friedel, *N.P.L. Conference on creep and fracture* (1954).
22. T. S. Kê, *Trans. A.I.M.E.* **188**, 575, 581 (1950).
23. G. S. Baker, L. M. Slifkin, and J. W. Marx, *J. Appl. Phys.* **24**, 1331 (1953).
24. J. Friedel, *A publier*.
25. W. Koster, *Z. Metallk.* **39**, 145 (1948).
26. A. D. LeClaire, *Acta Met.* **1**, 438 (1953).
27. F. S. Buffington and M. Cohen, *Acta Met.* **2**, 660 (1954).
28. N. F. Mott and H. Jones, *Metals and Alloys* (Oxford, 1936).
29. P. M. Sutton, *Phys. Rev.* **91**, 816 (1953).



# ELECTRON TRANSPORT IN COPPER AND DILUTE ALLOYS AT LOW TEMPERATURES. I\*

D. K. C. MACDONALD AND W. B. PEARSON†

The electrical resistance of copper is noteworthy in showing a minimum at very low temperatures ( $\sim 10^\circ\text{K}$ ). This phenomenon has been traced to the presence of very small quantities of certain specific metallic solutes, and a corresponding remarkable variation of thermoelectric power has been observed in these dilute alloys. Detailed experimental studies of a wide range of alloys are presented in this and a companion paper, and the problems involved in preparing such very dilute alloys and interpreting the findings are discussed.

## MOUVEMENT DES ÉLECTRONS DANS LE CUIVRE ET SES ALLIAGES DILUÉS À BASSE TEMPÉRATURE. I

La résistance électrique du cuivre présente un minimum remarquable à très basse température ( $\sim 10^\circ\text{K}$ ). Ce phénomène a été relié à la présence de très faibles quantités de certains éléments dissous de caractère métallique et une variation également remarquable du pouvoir thermo-électrique a été observée dans ces alliages. L'étude expérimentale est présentée dans ce mémoire et le suivant et les difficultés dans la préparation de ces alliages très dilués et dans l'interprétation des résultats sont exposées.

## ELEKTRONENWANDERUNG IN KUPFER UND VERDÜNNTEN LEGIERUNGEN BEI TIEFEN TEMPERATUREN. I

Der elektrische Widerstand von Kupfer ist insofern beachtenswert, als er bei sehr tiefen Temperaturen ( $\sim 10^\circ\text{K}$ ) einen Minimalwert zeigt. Diese Erscheinung wurde auf die Gegenwart von sehr kleinen Mengen gelöster Teilchen mit spezifisch metallischer Natur zurückgeführt. Weiterhin wurde in diesen verdünnten Legierungen eine entsprechend bemerkenswerte Veränderung der Thermokraft festgestellt. Ins einzelne gehende experimentelle Untersuchungen für eine grosse Anzahl von Legierungen werden in dieser und einer gleichzeitig erscheinenden Veröffentlichung mitgeteilt. Ferner werden die Schwierigkeiten bei der Herstellung solcher sehr verdünnten Legierungen und die Auslegung der Ergebnisse diskutiert.

### 1. INTRODUCTION

Our choice of copper as a subject for study in this field stems from the previous discovery of a minimum in its electrical resistance at low temperatures.<sup>1,2</sup> In earlier work spectrographic examination‡ failed to reveal any significant difference between "pure" specimens of copper which did, and did not, exhibit the resistive minimum. Later, very sensitive spectrographic measurements, for which we are indebted to Dr. A. E. Douglas of these laboratories, showed faint traces of lead and tin as impurities which were considered as significantly different in content between the specimens. As, in our opinion, no satisfactory theory was then available to guide the research, although several had been published, it was felt that the only reasonable experimental approach was to start a systematic examination of dilute alloys of copper, in particular investigating effects of valency and atomic size of solute and beginning with the elements lead and tin. In the present paper, after discussing sources of materials used and certain experimental difficulties in preparation of the alloys, we report in detail measurements of electrical resistivity and thermoelectric force at low temperatures for dilute alloys of copper with silver, gold, nickel and tin. These results have been referred to briefly in earlier publications by us.<sup>3-8</sup> The monovalent impurities gold

and silver do not give rise to a resistance minimum in copper and do not greatly influence the thermoelectric force when present in very dilute solid solution. (Although it is of interest that copper in gold<sup>9</sup> does produce a resistive minimum.§) This is in marked contrast to the effects produced by small amounts of a heterovalent impurity such as tin (as also gallium, indium, silicon, germanium, lead and bismuth). Nickel as solute plays an intermediate role, although it probably does not give rise to a minimum as large as .2 per cent of the residual resistance.

The results of electrical resistance and thermoelectric force measurements reported in this paper are in general agreement with the earlier work of Borelius, Keesom, Johansson and Linde<sup>10,11</sup> on thermoelectric power, and with that of Linde<sup>12,13</sup> and Mendoza and Thomas<sup>14</sup> on electrical resistance.

The use of very low temperatures (used generally to denote the temperature region extending down from liquid hydrogen ( $20^\circ\text{K}$ )) is particularly advantageous when investigating electron scattering in solids since at these temperatures the thermal vibrations of the lattice are almost entirely damped out, and we may then readily detect small effects which would certainly be swamped at higher temperatures.|| Furthermore, by dealing with very dilute alloys containing perhaps only

\* Received November 2, 1954.

† Division of Physics, National Research Council, Ottawa, Canada.

‡ By courtesy of Atomic Energy Research Establishment, Harwell, and Dr. F. M. Brewer of Oxford.

§ In view of this now rather surprising result, these earlier experiments<sup>9</sup> are being repeated by us.

|| Many of the alloys dealt with in the present work would be regarded as "high conductivity" copper if investigated at room temperature only.

$10^{18}$  specific impurity atoms per cc, it is possible to investigate scattering effects which may be quite different from those produced by higher impurity concentrations, say  $\sim 1$  at. % (i.e.,  $\sim 10^{21}$  impurity atoms/cc), which have been commonly used in the past. On the other hand, the considerable difficulties of our investigation in working at these very low concentrations have revealed many experimental problems in obtaining and handling copper of sufficient basic purity and in producing alloys of known and uniform solute content. These are discussed further below.

One further aspect which appears of possible importance in investigations of electron scattering at low temperatures, where the sensitivity is relatively great, is the scattering to be expected by "frozen-in" lattice imperfections. Under these conditions scattering contributions due to lattice vacancies, grain boundaries, and dislocations may be appreciable and variable from specimen to specimen, and in very dilute alloys we might well expect significant effects due to the segregation of solute atoms about these imperfections to relieve lattice strain since the more dilute the alloy the greater will become the *fraction* of solute atoms which may ultimately be "trapped" in this way. In general, of course, such effects would be expected to be most pronounced when the effective radii of solute and solvent atoms are somewhat different.<sup>15</sup>

In addition to the experimental problems, it may be pointed out that the theoretical interpretation of the behavior of copper at low temperatures presents considerable difficulties. We have suggested elsewhere (e.g., ref. 6) that while the modern electron transport theory as developed by such workers as Bloch, Fröhlich, Wilson and Mott, appears to be reasonably adequate for the interpretation of isothermal electrical resistance measurements, yet this is not the case when we try to interpret experiments under a thermal gradient, i.e., measurements of thermoelectric force and thermal conductivity. However, if we *accept* the broad predictions of the conventional theory for thermoelectric force, then (cf. ref. 5) it appears inescapable that the conduction electrons in metallic copper must be regarded as far from ideally free since in particular the thermoelectric power of pure copper rises positively from the lowest temperatures.<sup>1</sup> On the other hand, from the evidence of magnetic susceptibility and electrical conductivity in this metal, it appears certain that the *d*-band is to be regarded as full and that consequently conduction is due simply to the *s*-electrons. Furthermore, our thermoelectric experiments show that, in terms of current theory, remarkable scattering effects may be exhibited by very small amounts of impurity (in particular, an apparent dependence on electron energy at least some 50 to 100 times greater than, for example, unscreened ionic scattering could account for). The minimum in the electrical resistivity of copper at 10 to 20°K is similarly dependent on surprisingly low concentrations of specific impurities and we present here the detailed experi-

mental data on this phenomenon with tin as solute. From the theoretical point of view, the influence of such small solute contents contrasts strongly with the usually accepted model of a well-behaved metal and in fact this behavior is more reminiscent of the effects of impurity on the properties of a semiconductor.

It should also be noted that Mendoza and Thomas<sup>14</sup> found that the resistance of "pure" copper (which showed no minimum around 10°K) started to rise rapidly below 0.25°K. Thus the resistivity of "pure" copper at very low temperatures also awaits satisfactory interpretation.

## 2. SOURCE OF MATERIALS

In this work we have used samples of pure high-conductivity copper from various sources. In particular, we have used: (1) an old supply of Hilger spectrographically-pure copper (Laboratory No. 1184), specimens of which were found to have a residual resistance  $R_{4.2^\circ\text{K}} / (R_{273^\circ\text{K}} - R_{4.2^\circ\text{K}}) \approx 2.5 \times 10^{-3}$  for the annealed metal. This was used to make the earlier alloys in small 1 gm melts. Microscopical examination of this copper suggested that the rods had been prepared by powder metallurgical methods and that while the metal was probably free from other metallic elements as impurities, it was generally concluded that appreciable quantities of oxygen were present (we may note that the solubility limit of oxygen is variously quoted as 0.001 to 0.002 wt. % at 500°C and 0.007 wt. % at 1050°C.)

(2) Spectrographically-pure copper from Messrs. Johnson, Matthey and Mallory of somewhat higher residual resistance than (1) above.

(3) A copper bar (referred to here as JTH copper) of unknown primary origin which on the basis of residual resistance measurements was the copper of highest

TABLE I.

(1) Hilger Copper No. 11184	
Analysis given by Adam Hilger Ltd.:	
Oxygen—0.016%	
Spectroscopic analysis showed:	
Fe—0.0005%*	
Ag, As, Bi, Mg, Pb, S and Sn present as "trace". Copper by difference 99.983% or excluding oxygen 99.999%.	
(2) Johnson Matthey and Mallory Co. Copper:	
Spectrographic analysis by the makers showed:	
Ag, Ni, Pb, Ga and Fe present as "trace."	
(3) JTH Copper (2):	
Chemical analysis showed 0.002% Fe. Spectrographic analysis showed the presence of Fe and traces of Ca, Al and Mg.	
(4) American Smelting and Refining Co. Copper:	
Sample analyses of this copper have been published by Smart and Smith. <sup>16</sup>	

\* Chemical analysis carried out in this laboratory showed up to 0.004% Fe present in a sample of this copper.

overall purity, showing  $R_{4.2^\circ\text{K}}/(R_{273^\circ\text{K}} - R_{4.2^\circ\text{K}}) \approx 2.3 \times 10^{-3}$ . Another similar bar gave a resistance ratio of  $\sim 2.8 \times 10^{-3}$ .

Results of spectrographic examination of these three copper samples carried out partly by us are given in Table I.

(4) High purity electrolytic copper was also obtained from the American Smelting and Refining Company, and was examined both before and after its final vacuum melting in graphite. (For details of preparation see Smart and Smith.)<sup>16</sup>

Of the solute metals used, tin, nickel and silver were of Johnson Matthey "spec-pure" quality, and gold of 99.99% purity was obtained from the Royal Canadian Mint. The graphite used was of special spectroscopic purity from the National Carbon Company and contained variously traces of calcium, magnesium and silicon.

### 3. ALLOY PREPARATION

In the earliest experiments, because of the relatively small quantities of Hilger copper available, alloys were prepared in 1 gm melts under vacuum in small alumina crucibles, while some melts were made in graphite crucibles of the highest purity. The solute to be melted was placed in a small hole drilled in the copper rod. However, the larger quantity of JTH copper available permitted melts of  $\sim 50$  gm to be made in alumina crucibles *in vacuo* or under hydrogen which was then pumped off while the alloy was still molten.

In the small melts the crucible was heated while suspended in a tungsten coil heater in a pyrex tube to act as a vacuum enclosure, while the large melts were made in a "mullite" tube resistance furnace of standard design,<sup>17</sup> evacuated when cold to  $10^{-6}$  mm Hg. The large melts were stirred by an alumina rod operating through an O-ring seal. In all cases the alloys were solidified and cooled in the crucible. The ingots were then removed, cleaned of alumina, generally cold-worked to some degree to accelerate homogenization, and given an homogenizing anneal of at least several hours, slightly below the solidus temperature. Samples were then rolled in carefully cleaned rollers with about 90% reduction in area to 0.1 mm thickness, and cut into strips some 2 mm in width. These strips were annealed variously in helium or *in vacuo* to recrystallize them. In later work this was usually for about 14 hours at  $\sim 530^\circ\text{C}$ , although in the earlier work with the 1 gm melts the temperatures were higher and annealing times shorter. The alloy strips prepared in this way were used for determination of electrical resistivity at  $4.2^\circ\text{K}$  (liquid helium boiling under atmospheric pressure) and at  $273.2^\circ\text{K}$  (the ice point) or continuously between these temperatures, and for measurement of thermoelectric force in the range  $4.2^\circ\text{K}$  to  $\sim 60^\circ\text{K}$ . Measurements were made by methods standard in this laboratory (see, for example, references 5 and 18).

A very slight amount of iron contamination would

have a profound effect on the low temperature thermoelectric force (cf. Borelius *et al.*<sup>10,11</sup> confirmed by the present investigations), as well as increasing the residual resistance significantly and causing a resistance minimum; consequently particular care was taken to remove any possible traces of iron picked up in cutting or rolling, before annealing the specimens. This was done by "picking" the strips immediately before sealing up for the anneal; this treatment also diminished the surface oxide layer that the specimens acquired while awaiting treatment.

### 4. THE EXPERIMENTAL PROBLEM

As a result of our initial series of experiments of which short notes were published,<sup>3,4</sup> we realized that it was necessary to distinguish clearly between vacuum-melted alloys and those melted under hydrogen or in graphite. In the first case, owing to the presence of oxygen in Hilger and JTH copper, solute was removed from solid solution as oxide; and in the second case insoluble oxide impurities were reduced and entered the copper in solid solution.

In the following sections an attempt is made to assess the effects of these and other factors on the electrical properties of the very dilute alloys so that modification of the electrical properties of copper due to small specific solute atom additions can be properly specified and understood.

#### Effective Solute Concentration

A knowledge of the effective solute concentration is necessary to assess the experimental data. In the case of "oxygen-containing" alloys (vacuum-melted alloys of copper containing oxygen), the use of nominal compositions is not possible and leads to inconsistent results primarily due to partial solute removal as an insoluble oxide phase. Spectrographic analysis of the alloys is also unsuitable as it determines both the solute present in solid solution and that removed as an insoluble oxide phase. The only satisfactory method of determining the effective solute concentration appears to be the measurement of residual impurity resistivity at low temperature. We have used this method generally in examining the variation with solute concentration of the size of the resistance minimum and the thermoelectric power. It is clearly not possible to use "oxygen-containing" alloys to determine the variation of resistivity with concentration at very great dilution, although at larger solute concentrations (cf. Linde,<sup>12,13</sup>  $\sim 0.5$  or 1 at. % solute), the ratio of solute removed as oxide to solute present in solid solution becomes negligibly small because of the small oxygen content of the copper.

In the case of reduced alloys, spectrochemical analysis can be used effectively (e.g., Figs. 11, 12 and 13) as all the solute is now present in solid solution and, excluding the effects of indigenous impurities, the variation of resistivity with concentration for specific solute

TABLE II. Residual resistivity  $R_{4.2^\circ}/(R_{273^\circ} - R_{4.2^\circ})$ .

Nominal composition	Annealed in tube furnace. Sealed in pyrex capsule in 4/5 atmos. helium	Annealed in tube furnace. Sealed in pyrex capsule in vacuum	Annealed <i>in vacuo</i> by passage of an electric current. Surrounded by tube with cool walls
.0022 at. % tin	$16.3 \times 10^{-3}$	$14.3 \times 10^{-3}$	$9.9 \times 10^{-3}$
.008 at. % tin	$28.2 \times 10^{-3}$	$26.4 \times 10^{-3}$	$14.5 \times 10^{-3}$
.027 at. % tin	$56.8 \times 10^{-3}$	$55.6 \times 10^{-3}$	$11.5 \times 10^{-3}$

additions can thus be determined. However, it must be noted that the relative accuracy of the spectroscopic analyses is not high and it has been found necessary to develop special techniques to obtain reproducible results from the very small samples available when the solute concentration is also very small. Differences between nominal and analysed composition are apparently the result of solute volatilization during alloy preparation and processing (*vide infra*).

#### Solute Loss by Evaporation

In general, the tendency is to observe a low resistivity in relation to nominal solute composition. This is due to two causes: solute loss by evaporation and solute removal from solid solution as an insoluble oxide phase. Loss by evaporation was particularly serious if alloys were annealed *in vacuo* by passage of an electric current while enclosed in a pyrex tube having relatively cool walls, as this condition favored continuous evaporation and condensation of the solutes.

The residual resistance values shown in Table II illustrates clearly the loss by evaporation during annealing under these conditions, compared to annealing in a sealed tube heated in a resistance furnace. In this case the walls of the sealed capsule are at approximately the same temperature as the specimen and continuous evaporation and condensation of solute does not take place. This method of annealing has been used for alloys reported in the present work. Table II shows that, as expected, there was slightly more tin loss when the specimen was enclosed in an evacuated tube than when enclosed with 4/5th of an atmosphere pressure of helium at the annealing temperature.

In more concentrated alloys the loss of solute during annealing may be expected to be a much smaller relative percentage than in the case of dilute alloys.

#### Influence of Oxygen

Oxygen was undoubtedly present up to or beyond the solubility limit in the Hilger and JTH copper. The extent to which an oxide phase containing solute can exist in equilibrium in the solid state will depend on the form of the isothermal section of the ternary equilibrium diagram for the system Cu-M-O at any given temperature. In particular the position of the point X in the schematic isothermal section for the copper-rich corner of such a system shown in Fig. 1 will determine the

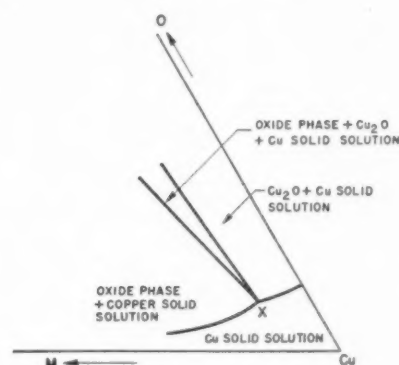


FIG. 1. Copper-rich corner of an isothermal section in a hypothetical alloy system Cu-metal-oxygen.

maximum extent to which the solute, M, can be removed from solid solution as oxide. In general, when the free energy of formation of the MO oxide phase is considerably larger than that of  $\text{Cu}_2\text{O}$ , it is to be expected that X will be located very close to the Cu-O edge of the ternary section.

The presence of oxygen, *per se*, in our Hilger and JTH copper does not appear to cause any significant scattering in samples annealed at  $530^\circ\text{C}$ . Thus polycrystalline samples from these sources give residual resistances which are lower by a factor of about 3 than that of oxygen-free pure copper obtained from the American Smelting and Refining Company.

#### Homogeneity and Metal Texture, etc.

Tests of alloy homogeneity have been made by taking two different parts of the original ingot, homogenizing, rolling and annealing them separately and then measuring resistivity and thermoelectric force. Good agreement between individual experiments has been obtained, indicating that the heat treatments given were adequate.

The effects of micro-inhomogeneities in the specimens due to coring during solidification have been studied by omitting the original homogenization treatment. This had little effect on the conductivity measurements as might well be expected from the type of average involved in making such an experiment, but led to very variable results for thermoelectricity which may readily be ascribed to the sensitive character of the parameter measured and to the local Peltier effects which will arise from such micro-inhomogeneities.

The alloy strips whose electrical properties were measured show a preferred orientation or texture (cf. Burgers and Sandee)<sup>19</sup> developed in the final annealing treatment following the rolling of the specimen. In order to see whether this texture had any significant influence on the resistivity and/or thermoelectric force, a number of pieces were cut in pairs taken from copper-tin and copper-silver alloys parallel to, and perpendicular to,



rolling direction. It was found after annealing that the resistivity of each specimen was essentially the same although it was notable that the resistivity of all specimens cut parallel was slightly *greater* than those cut perpendicular to the rolling direction. The small difference amounted to an absolute value of the residual resistance  $\sim 5 \times 10^{-4}$ .

The resistivity of a few specimens was then measured soon after 90 to 95% reduction of cross-sectional area by cold-rolling. While on the one hand the over-all residual resistivity increased very markedly from that of the annealed specimens, there was no observable difference between specimens cut parallel to, and perpendicular to, the rolling direction.

In view of the great difference in effective dimension of the grain boundaries in the two directions,<sup>20</sup> we confidently conclude that grain boundaries in themselves can generally have no appreciable influence on the scattering in the range of temperatures and electron mean free paths investigated by us. Furthermore, the electron mean free path in samples of JTH or Hilger copper is  $\sim 10^{-2}$  mm at 4.2°K so that in none of the specimens investigated (having a cross-section of some  $0.1 \times 2$  mm) can the specimen size appreciably affect the electron scattering. Some experiments on single crystals are being carried out to confirm in greater detail this and other observations. (See, e.g., Pearson.<sup>21</sup>)

#### Graphite-Melted Alloys and Alloys Melted under Hydrogen

Some melts of copper and alloys have been made in graphite or under hydrogen (subsequently pumped off before the melt solidifies) in order to remove the oxygen content of the copper. However, it is found in the case of melts in "spectrographically pure" graphite crucibles or in alumina crucibles with added graphite, that the residual resistivity of pure copper is increased by  $\sim 7 \times 10^{-3}$ . The same behavior is found for graphite-melted copper obtained from the American Smelting and Refining Company. It seems unlikely that this is due to scattering by the very small amount of carbon retained in solid solution since pure copper melted under hydrogen showed a similar increase of resistivity. It is more probable that the changes of resistivity and thermoelectric force found after melting in graphite are due to reduction of the oxides of traces of metallic impurities so that the *metals* enter solid solution. This problem is discussed in detail in §4(a).

### 4. EXPERIMENTAL RESULTS AND DISCUSSION

#### (a) Copper-Silver Alloys

The variation of residual resistivity with concentration is shown in Fig. 2. No trace of resistance minimum is found for measurements down to 4.2°K and corresponding thermoelectric force measurements (Fig. 3) show a slightly negative power at low temperatures,

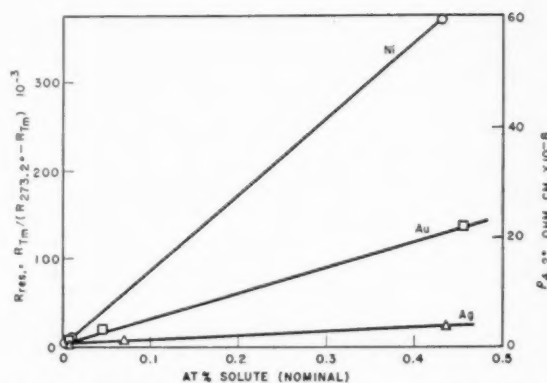


FIG. 2. Variation of residual resistivity with nominal solute concentration for dilute alloys of silver, gold and nickel in copper. In calculating  $\rho_{4.2^\circ\text{K}}$  we have taken the resistivity of copper as 1.724 ohm cm at 293°K. The alloys were *not* prepared under reducing conditions.  $T_m$  is the temperature at which the resistance minimum occurs.

becoming positive above  $\sim 14^\circ\text{K}$ , although of course the precise transition point will depend on solute concentration corresponding, essentially, to the onset of significant thermal scattering (e.g., cf.<sup>5</sup>).

#### (b) Copper-Gold Alloys

The results of residual resistivity and thermoelectric force measurements (Figs. 2 and 3) are very similar to those of copper-silver alloys. While copper as solute in gold produces a resistive minimum (cf. Templeton and MacDonald<sup>9</sup>), no trace of a minimum is found for gold as a solute in copper. The rather slight change of thermoelectric force compared, for example, to that found in copper-tin is to be readily expected for the case of a homovalent solute and we may consequently infer that silver and gold are both essentially homovalent with copper at low temperatures.

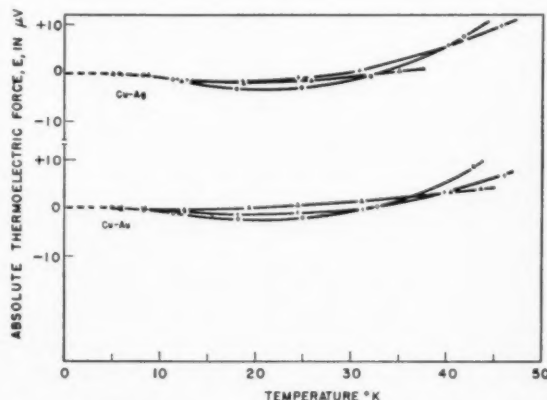


FIG. 3. Absolute thermoelectric force of dilute copper-silver and copper-gold alloys as a function of temperature. Cu-Ag Alloys:  $\circ$  Cu+0.0064 at.% Ag.  $+$  Cu+0.072 at.% Ag.  $\triangle$  Cu+0.44 at.% Ag. Cu-Au Alloys:  $\circ$  Cu+0.0065 at.% Au.  $+$  Cu+0.046 at.% Au.  $\triangle$  Cu+0.46 at.% Au. The compositions quoted are "nominal" solute additions. The alloys were *not* prepared under reducing conditions.

## (c) Copper-Nickel Alloys

Figure 2 shows also the variation of resistivity with concentration for nickel as solute. Nickel appears to give rise to little or no resistive minimum in copper at  $\sim 10^\circ\text{K}$ . The thermoelectric force becomes progressively more negative with increasing nickel content, Fig. 4, and indeed by the time we have reached 0.4 at.% the thermoelectric power, at even so high a temperature as  $70^\circ\text{K}$ , is no longer approximately the same as that of pure copper, and it is possible that some significant change in the lattice characteristic temperature,  $\theta$ , has occurred. Good agreement is found with the results of Borelius, Keesom, Johansson and Linde<sup>10</sup> for alloys of high nickel concentration. For comparison with other alloys, we also show variations of  $S_{15^\circ\text{K}}$  (*vide infra*) with  $R_{\text{res}}$  in Fig. 5.

The increase of residual resistivity per atomic per cent solute calculated for nickel and gold as solute is not greatly different from that found by Linde<sup>13</sup> from measurements down to  $83^\circ\text{K}$  on alloys having higher solute concentrations, but the value for silver as solute is only about half of that found by Linde. Apart from the diagrams given, we have not quoted detailed values for the increase of residual resistivity found for these solutes as our investigations of very dilute alloys, relying on nominal composition only, are not expected to give results as accurately as measurements on more concentrated alloys where the solute concentration can be determined analytically with precision.

## (d) Copper-Tin Alloys

For copper-tin alloys, and others to be discussed in a later paper, which all show a characteristic and remarkable variation with concentration of the absolute thermoelectric power,  $S$ , and size of the resistance minimum, we adopt the following method for comparison of these properties. We discuss  $S$  at  $15^\circ\text{K}$  (sub-

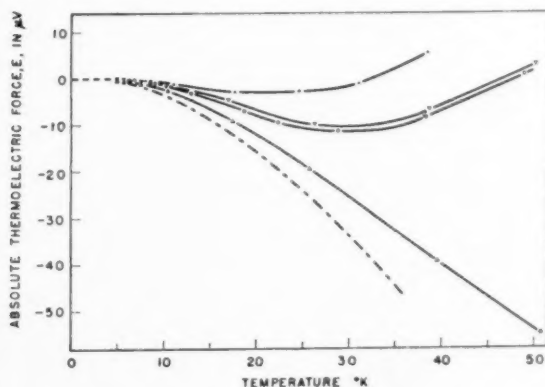


FIG. 4. Absolute thermoelectric force of copper-nickel alloys as a function of temperature. + Copper;  $\nabla$  Cu+0.0044 at.% Ni;  $\circ$  Cu+0.01 at.% Ni;  $\triangle$  Cu+0.44 at.% Ni; ---- Cu+1.12 at.% Ni (from Borelius *et al.*). The compositions quoted are "nominal" solute additions. The alloys were *not* prepared under reducing conditions.

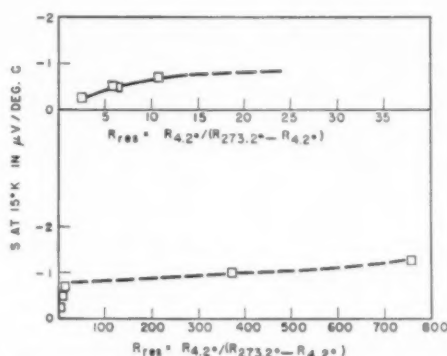


FIG. 5. The absolute thermoelectric power of dilute solid solutions of nickel in copper as a function of the residual resistivity of the alloys. Note different abscissae scales. The alloys were *not* prepared under reducing conditions.

sequently referred to as " $S_{15^\circ\text{K}}$ ") where, on the one hand, the thermoelectric power has grown sufficiently large to be readily measurable\* and, on the other, the temperature is still low enough so that thermal scattering is generally much smaller than residual scattering. Furthermore, in this region,  $E$  is found to be nearly linear with temperature for the alloys studied. In the case of the resistance minimum we take, as a measure of its size,  $(R_{4.2^\circ\text{K}} - R_{T_m})/R_{T_m}$  (subsequently referred to as " $R_{\text{min}}$ "). This follows our earlier method of assessing the size of the minimum,<sup>6</sup> although we have since found that there is some appreciable variation in the temperature at which the minimum occurs. We have, however, verified that the "cusp-like" variation of  $R_{\text{min}}$  with concentration (Figs. 6 and 14) is not due simply to variation of  $T_m$ , the temperature at which the minimum occurs, but is indeed due to the relative size of the minimum. We have also plotted  $(RT_m - 6^\circ - RT_m)/RT_m$  and  $(dR/dT)/RT_m$  (for the approximately linear increase of  $R$  just below  $T_m$ ) against solute concentration with very similar results to those shown in Figs. 6 and 14.

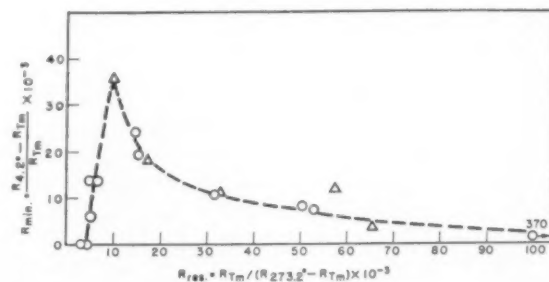


FIG. 6. The relative size of the resistance minimum as a function of the residual resistivity of dilute solid solutions of tin in copper. The alloys were *not* prepared under reducing conditions.  $\circ$  Alloys made from JTH copper;  $\triangle$  Alloys made from Hilger copper.

\* Bearing in mind that  $S$  must ultimately vanish with  $T \rightarrow 0$  in accordance with the Third Law of Thermodynamics.

TABLE III.

Copper		Residual resistance	Resistance minimum	$S_{15^\circ\text{K}}$
		$R_{\text{res}} = R_{Tm} / (R_{273.2^\circ} - R_{Tm})$	$R_{\text{min}} = (R_{4.2^\circ} - R_{Tm}) / R_{Tm}$	$\mu\text{V}/^\circ\text{K}$
JTH containing oxygen		$\sim 2.5 \times 10^{-3}$	0	-0.3
JTH (1)				
H <sub>2</sub> reduced		$9.5 \times 10^{-3}$	$38.0 \times 10^{-3}$	-10.2
JTH (2)				
H <sub>2</sub> reduced		$11.2 \times 10^{-3}$	$31.8 \times 10^{-3}$	-8.8
American Smelting and Refining Company	Electrolytic, from nitrate bath			-0.4
	After melting and casting in graphite	$9.8 \times 10^{-3}$	$5.3 \times 10^{-3}$	-3.5

The remarkable and unexpected variation of thermoelectric force and size of resistance minimum of copper-tin alloys with solute concentration, together with the experimental difficulties already discussed, have previously prevented a satisfactory interpretation of the results of the investigations. The oxygen contained in JTH and Hilger copper leads to a partial removal of tin added as solute when the alloys are melted and isothermally annealed. The difficulty arising from the presence of oxygen can be overcome by melting the alloys in reducing conditions in graphite or under hydrogen (see, for instance, Alkins and Hallows<sup>22</sup>), but it has the great disadvantage that *other* traces of impurity which were present in the copper as oxides and so did not contribute to electron scattering, are now also reduced, enter solid solution, and thus contribute to scattering. This leads to an increase of  $R_{\text{res}}$  for the JTH or Hilger copper (isothermally annealed at 530°C) by a factor of  $\sim 4$ , while at the same time a resistance minimum appears together with a large negative absolute thermoelectric power at 15°K, Table III.

These effects appear to be due to the presence of traces of iron entering into solid solution, particularly as it is known that this element scatters conduction-electrons strongly (Linde) and that only  $\sim .003$  at. % Fe in solid solution can change the absolute thermoelectric power of copper at 15°K from  $\sim 0$  to  $\sim -11$   $\mu\text{V}$  per degree.<sup>11</sup> We find, for instance, that  $\sim .054$  wt. % iron gives a value of  $S_{15^\circ\text{K}} = -15.5$   $\mu\text{V}/^\circ\text{C}$  and of  $R_{\text{min}} = 121 \times 10^{-3}$ . We have detected the presence of iron spectroscopically, and chemical analyses show the presence of  $\sim .002\%$  in JTH copper and  $\sim .004\%$  in Hilger copper. Further confirmation of this analysis comes from residual resistivity measurements of hydrogen-reduced alloys made with JTH copper and containing .0023 and .054 wt. % of added iron.  $R_{\text{res}}$  is then found to extrapolate back to  $\sim 11 \times 10^{-3}$  for hydrogen reduced JTH copper containing no added iron in agreement with actual measurements of 9.8, 11.15, and  $10.9 \times 10^{-3}$  for three samples of copper in this state. Taking  $2.5 \times 10^{-3}$  for  $R_{\text{res}}$  of the pure JTH copper (obtained for this copper containing oxygen) and using the variation of added iron concentration with  $R_{\text{res}}$ , we then deduce  $\sim .002$  wt. % iron as the intrinsic iron content of hydrogen reduced JTH copper.

If reduced copper or alloys are annealed at temperatures higher than  $\sim 530^\circ\text{C}$ ,  $R_{\text{res}}$  is found to increase

still further, indicating the presence now in solid solution of traces of other impurities such as lead or bismuth which have negligible solubility\* at 530°C. As, however, all alloys discussed in this paper were annealed at  $\sim 530^\circ\text{C}$  after rolling, the presence of traces of these impurities is not important.

### (e) Copper-Tin Alloys Containing a Little Oxygen

Equilibrium diagram considerations show that it may indeed be possible for the presence of oxygen to remove tin from solid solution in such a manner that an essentially linear rise of  $R_{\text{res}}$  with increasing nominal tin content, will still be evinced. It appears that the apparently low scattering found by us due to tin in solid solution in copper<sup>4</sup> must be attributed to this cause and also perhaps to evaporation of tin during the preparation and annealing treatments given to those alloys. As already noted, the only effective means of determining the amount of tin *actually* present in solid solution in dilute alloys containing oxygen is by measurement of residual resistivity. Accordingly, in Figs. 6 and 7 we show the variation of  $R_{\text{min}}$  and  $S_{15^\circ\text{K}}$  with  $R_{\text{res}}$  for polycrystalline copper-tin alloys, and these curves may be accepted as the *true* behavior of copper-tin alloys in the *absence of other metallic impurities in solid solution*. The curves previously published<sup>6</sup> were prepared from a combination of data obtained on "oxygen-containing" and reduced alloys.

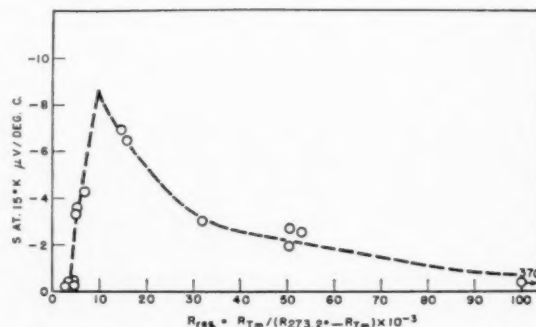


FIG. 7. The absolute thermoelectric power at 15°K of dilute solid solutions of tin in copper as a function of the residual resistivity of the alloys. The alloys were *not* prepared under reducing conditions.

\* Cf. MacDonald and Pearson.<sup>23</sup>

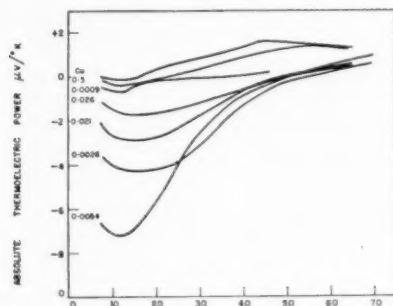


Fig. 8. Absolute thermoelectric power of dilute solid solutions of tin in copper as a function of the temperature. The alloys were *not* melted under reducing conditions. The figures refer to the nominal tin content of the alloys in atomic per cent.

The remarkable feature of Figs. 6 and 7 is the rapid increase of size of  $R_{\min}$  and  $S_{15^\circ\text{K}}$  up to an effective concentration of  $\sim 0.004$  at. % tin ( $R_{\text{res}} = 10^{-2}$ ) followed by a subsequent decrease with increasing tin content. Correspondingly, the absolute thermoelectric force,  $E$ , attains its largest negative value (at  $\sim -50^\circ\text{K}$ ) for alloys having a solute concentration  $\sim 0.004$  at. %. Figure 8 shows that the absolute thermoelectric power,  $S$ , of these dilute alloys (although differing greatly from that of pure copper at low temperatures), approaches the same value as pure copper at higher temperatures,  $\sim 70^\circ\text{K}$ .<sup>\*</sup> Consequently measurements made at room temperature (or indeed down to liquid nitrogen temperatures) will reveal none of the interesting behavior of very dilute copper-tin alloys.

Some theoretical implications of these findings have been discussed by us elsewhere and will be summarised in the following paper. Here we wish only to draw

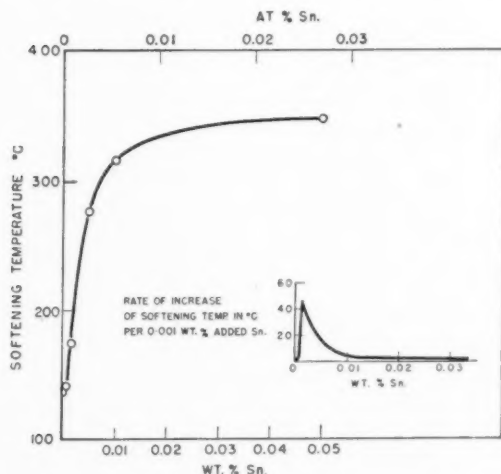


Fig. 9. Variation of "softening temperature" (see footnote to text) with tin content of dilute solid solutions of tin in copper. After Smart and Smith.<sup>26</sup> Insert: Rate of increase of softening temperature as a function of tin content for the same alloys.

<sup>\*</sup> Hence the usefulness of such alloys against pure copper as low temperature thermocouples.<sup>24,25</sup>

attention specifically to the similarity in the change of electrical properties of these very dilute solid solutions with that found by Smart and Smith<sup>26</sup> for the variation of "softening temperature"† with concentration for very dilute solid solutions of tin in oxygen-free pure copper (Fig. 9). The rapid initial increase and subsequent saturation of the increase in softening temperature suggests a location of tin atoms about particular sites such as lattice defects and grain boundaries in copper, rather than an entirely random distribution throughout the bulk of the metal.‡ If, on first adding tin to copper, the tin atoms locate themselves at the grain boundaries or near lattice defects until these special sites become "saturated" and if thereafter the tin atoms distribute themselves randomly throughout the grains, we may have an explanation of the variation of softening temperature with concentration shown in Fig. 9.

The correlation of mechanical and electrical properties suggests a possible common origin for the remark-

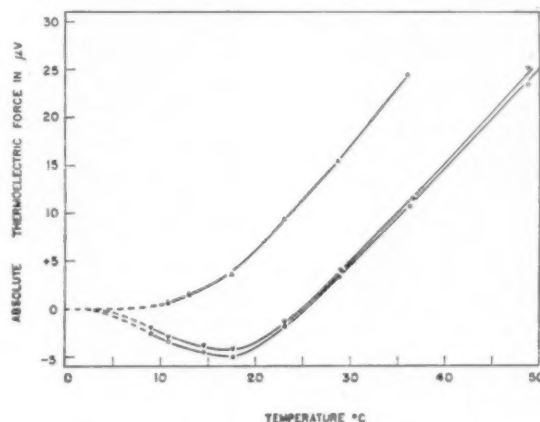


Fig. 10. Absolute thermoelectric force as a function of temperature for:  $\Delta$  Pure silver (upper curve);  $\Delta$  Silver+0.0065 at. % Au (middle curve);  $\circ$  Silver+0.0069 at. % Cu (lower curve).

able variation of  $R_{\min}$  and  $S_{15^\circ\text{K}}$  with concentration. This is made more probable when it is noticed that in the specimens used for electrical measurements, the critical tin concentration corresponds very crudely, to about an order of magnitude, with that required for an unimolecular layer along the grain boundaries of the specimen.

A consideration of all of the factors involved does not at present, however, necessarily lead to the conclusion that the *fundamental* origin of the resistance minimum itself is to be found in a segregation of solute atoms to grain boundaries or lattice defects, but rather that this may be contributory to the unexpected variation of  $R_{\min}$  and  $S_{15^\circ\text{K}}$  with solute concentration in certain dilute

† Softening temperature is an arbitrary measurement determined under the same conditions for all alloys. It is taken as the half-hard point on annealing curves of samples reduced 75% by cold drawing, and it is generally reproducible to  $\pm 2^\circ\text{C}$ .<sup>16</sup>

‡ The diminution of entropy due to aggregation of tin atoms would then be compensated by energy gained through relief of lattice strains.



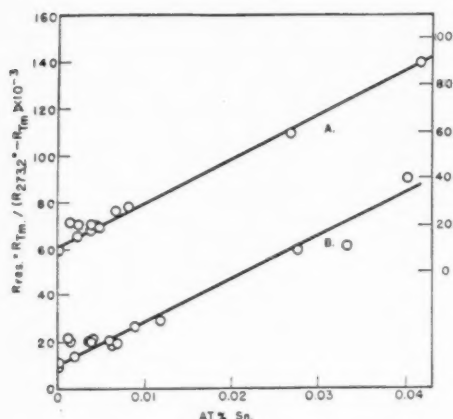


FIG. 11. Dilute solid solutions of tin in copper. A: Variation of residual resistivity with nominal solute concentration (right-hand scale). B: Variation of residual resistivity with spectroscopically analysed composition (left-hand scale).

copper alloys. Experiments are being made on single crystals to test this suggestion. The origin of the resistance minimum is still not adequately understood, although we have found it to depend specifically on the presence of certain heterovalent solute atoms.

The segregation of solute atoms about lattice imperfections suggests that the relative radii of solvent and solute might be of some importance in impurity scattering in very dilute alloys. We have accordingly measured the absolute thermoelectric force of the homovalent alloys, copper in silver and gold in silver, each containing  $\sim 0.0065$  at.% solute. The differences of radii of solvent and solute are approximately 11% for silver-copper and zero for silver-gold. The absolute thermoelectric force given by each alloy is, however, practically the same (Fig. 10).

#### (f) "Reduced" Copper-Tin Alloys

Hydrogen-reduced alloys were originally prepared so that all the added tin would be present in solid solution and spectroscopic analysis could be reliably used to

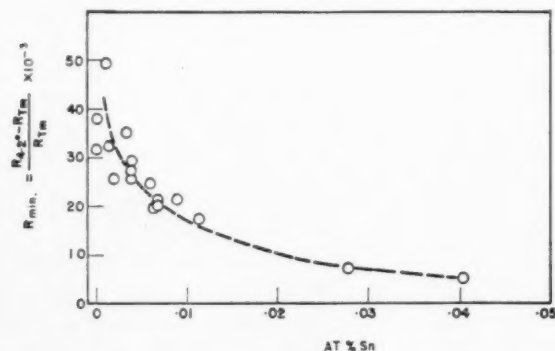


FIG. 12. The relative size of the resistance minimum of dilute solid solutions of tin in copper as a function of the analysed tin content for alloys melted under reducing conditions.

give the effective solute concentration. However, as already noted, this treatment reduced *other* impurities originally present as oxides, and the alloys actually investigated (after cold-rolling to strips and annealing at  $\sim 530^\circ\text{C}$ ), appear to be ternary solid solutions of added tin solute and  $\sim 0.0025$  at.% iron impurity. Although we cannot at present offer a complete interpretation of the behavior of these alloys, the electrical properties appear to be of some considerable interest. In Fig. 11 we show variation of  $R_{res}$  with nominal and analysed composition. As the solute concentration has been determined analytically, we can calculate the increase of residual resistivity per atomic per cent tin and find  $2.90 \times 10^{-6}$  ohm cm in good agreement with  $2.85 \times 10^{-6}$  ohm cm obtained by Linde.<sup>13</sup> The electron scattering cross section of tin in these dilute alloys is  $\sim 5 \times 10^{-16}$  cm<sup>2</sup>. Figures 12 and 13 give the variation of  $R_{min}$  and  $S_{15^\circ\text{K}}$  with analysed tin content, and Figs. 14 and 15 the variation of  $R_{min}$  and  $S_{15^\circ\text{K}}$  with  $R_{res}$ .

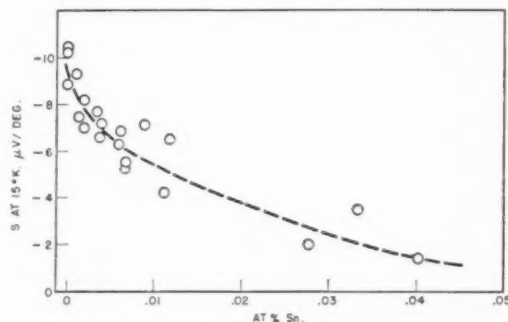


FIG. 13. The absolute thermoelectric power at  $15^\circ\text{K}$  of dilute solid solutions of tin in copper as a function of the analysed tin content for alloys melted under reducing conditions.

It can be seen from Fig. 11 that the tin which was added and iron which was already present in the copper appear to scatter independently, although there is a small anomalous rise of  $R_{res}$  with tin additions of .001 to .005 at.% tin, which might perhaps be the result of some long range electron-interaction of solute atoms. These findings are also generally confirmed in reduced alloys with gallium, indium, silicon and germanium as solutes.<sup>23</sup> In view of this additivity of scattering, the decline of  $R_{min}$  and  $S_{15^\circ\text{K}}$  with added tin content up to  $\sim 0.007$  at.% tin is puzzling. (At higher tin contents the curves suitably transposed in  $R_{res}$  follow closely those of Figs. 6 and 7.)

The variation of  $R_{min}$  and  $S_{15^\circ\text{K}}$  with  $R_{res}$  in these ternary alloys can not be explained. The curves shown in Figs. 14 and 15 normalised to the same residual resistivity as the oxygen-containing alloys (i.e., allowing for scattering due to reduced impurities) fit rather exactly the variation of  $R_{min}$  and  $S_{15^\circ\text{K}}$  with  $R_{res}$  of pure copper-tin alloys, Figs. 6 and 7. On the other hand, detailed variation of  $R_{min}$  with  $R_{res}$ , say, shown as a function of added tin content in Fig. 16 (together with the behavior shown in Figs. 12 and 13) suggests strongly

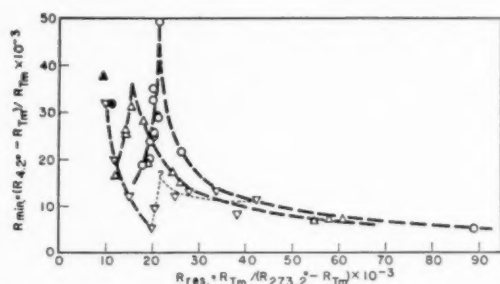


FIG. 14. The relative size of the resistance minimum of dilute solid solutions of tin in copper as a function of the residual resistivity of the alloys. The alloys were melted under reducing conditions.  $\nabla$  Alloys made with Hilger copper and melted in graphite.  $\triangle$  Alloys made with JTH copper (1) and melted under hydrogen.  $\circ$  Alloys made with JTH copper (2) and melted under hydrogen.  $\blacktriangle$ ,  $\bullet$  JTH copper (1) and (2) melted under hydrogen.

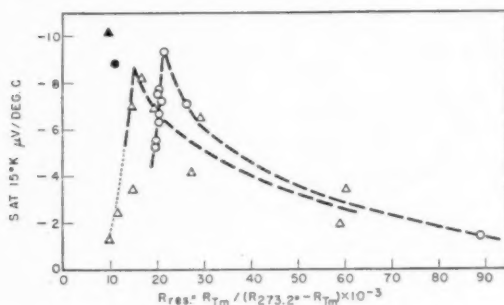


FIG. 15. The absolute thermoelectric power at 15°K of dilute solid solutions of tin in copper as a function of the residual resistivity of the alloys. The alloys were melted under hydrogen.  $\triangle$  Alloys made with JTH copper (1).  $\circ$  Alloys made with JTH copper (2).  $\blacktriangle$ ,  $\bullet$  JTH copper (1) and (2).

the removal of iron from solid solution on addition of tin, either as iron or as an iron-tin compound. If iron separated from solid solution as the element, coherent precipitation of iron<sup>27</sup> on annealing at 530°C might explain the anomalous rise of  $R_{res}$  at concentrations less than  $\sim 0.007$  at. % tin. However, further experiments have shown that this is not the case. We have prepared

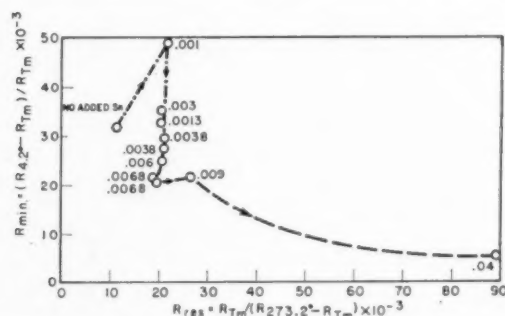


FIG. 16. Dilute solid solutions of tin in copper made in reducing conditions under hydrogen. Variation of the relative size of the resistance minimum with residual resistivity considered in relation to increasing tin content of the alloys. The figures give the spectroscopically analysed tin content of the alloys in atomic per cent.

dilute ternary alloys with tin and iron additions and the presence of a small amount of tin does not lead to a markedly reduced iron solubility due to precipitation of metallic iron nor, when the iron and tin additions are roughly equivalent, to the precipitation of an iron-tin compound. We seem therefore at present to be left only with the possibility of some long-range interaction between the iron and tin atoms,\* which is particularly puzzling in view of the apparently independent scattering of the added tin atoms and impurities in the de-oxidized copper matrix.

## SUMMARY

We wished to investigate the effects of electron-scattering in very dilute copper alloys with specific solutes at low temperatures where the thermal scattering becomes negligible. However, the sensitivity of the method was found to be such that numerous problems arose in the handling of the alloys and in obtaining "pure" copper, as it was found that impurity contents as low as  $\sim 10^{18}$  atoms/cc could greatly modify its properties, and lead to results which at first sight are apparently random. We believe, however, that we have now provided a satisfactory explanation for most of the effects encountered so that the results reported here for copper-silver, copper-gold, copper-nickel and copper-tin alloys and in the following paper for copper-gallium, copper-indium, copper-silicon, copper-germanium, copper-lead and copper-bismuth alloys may be reliably accepted and used for theoretical interpretation of electron-scattering processes in very dilute copper alloys.

## ACKNOWLEDGMENT

We wish to thank Dr. J. S. Dugdale for his interest in this work and Mr. F. W. Richardson and Miss D. M. Pester for their excellent technical assistance and enthusiasm, and Mr. W. Stockdale for carrying out chemical and spectroscopical analyses.

## REFERENCES

1. D. K. C. MacDonald, Proc. Internat. Conf. Low Temp. Physics, (Oxford, 1951), p. 58.
2. R. Berman and D. K. C. MacDonald, Proc. Roy. Soc. (Lond.) A211 122 (1952).
3. D. K. C. MacDonald, Phys. Rev. **88**, 148 (1952).
4. D. K. C. MacDonald and W. B. Pearson, Phys. Rev. **88**, 149 (1952).
5. D. K. C. MacDonald and W. B. Pearson, Proc. Roy. Soc. (Lond.) A219, 373 (1953).
6. D. K. C. MacDonald and W. B. Pearson, Phil. Mag. vii 45, 491 (1954).
7. D. K. C. MacDonald, Physica **19**, 841 (1953).
8. D. K. C. MacDonald and W. B. Pearson, Acta Met. **1**, 242 (1953).
9. D. K. C. MacDonald and I. M. Templeton, Phil. Mag. vii 42, 432 (1951).
10. G. Borelius, W. H. Keesom, C. H. Johansson, and J. O. Linde, Proc. Acad. Amsterdam **33** (1) 32 (1930).

\* The interaction envisaged would more probably be an electron scattering interaction than one leading specifically to any ordering of the iron and tin atoms.

11. G. Borelius, W. H. Keesom, C. H. Johansson, and J. O. Linde, Proc. Acad. Amsterdam **35** (1) 25 (1932).
12. J. O. Linde, Ann. Phys. (5) **10**, 52 (1931).
13. J. O. Linde, Ann. Phys. (5) **15**, 219 (1932).
14. E. Mendoza and J. G. Thomas, Phil. Mag. vii **42**, 291 (1951).
15. W. Hume-Rothery, *The Structure of Metals and Alloys*, 2nd ed. (The Institute of Metals, London, 1950).
16. J. S. Smart and A. A. Smith, Trans. A.I.M.M.E. **143**, 272 (1941).
17. W. Hume-Rothery, J. W. Christian, and W. B. Pearson, *Metallurgical Equilibrium Diagrams* (The Institute of Physics, London, 1952).
18. D. K. C. MacDonald and W. B. Pearson, Proc. Roy. Soc. (Lond.) **A221** 534 (1954).
19. W. G. Burgers, and J. Sandee, Physica **9**, 996 (1942).
20. M. Cook and T. Ll. Richards, J. Inst. Met. **67**, 203 (1941).
21. W. B. Pearson. To be published, 1955.
22. W. S. Alkins and A. P. C. Hallows, J. Inst. Met. **56**, 125 (1935).
23. D. K. C. MacDonald and W. B. Pearson, Acta Met. (in following paper).
24. T. M. Dauphinee, D. K. C. MacDonald, and W. B. Pearson, J. Sci. Instrum. **30**, 399 (1953).
25. W. B. Pearson, J. Sci. Instrum. **31**, 444 (1954).
26. J. S. Smart and A. A. Smith, Trans. A.I.M.M.E. **166**, 144 (1946).
27. J. Reekie, T. S. Hutchinson, and F. E. Hetherington, Proc. Phys. Soc. **B66**, 1101 (1953).

# ELECTRON TRANSPORT IN COPPER AND DILUTE ALLOYS AT LOW TEMPERATURES. II\*

D. K. C. MACDONALD AND W. B. PEARSON†

Following an earlier paper in this journal, detailed low temperature measurements are presented on the anomalous resistive minimum and thermoelectric power of very dilute copper alloys with B group metal solutes.

The problems of theoretical interpretation which should be of considerable importance in the general electron theory of metals are summarised.

## MOUVEMENT DES ÉLECTRONS DANS LE CUIVRE ET SES ALLIAGES DILUÉS À BASSE TEMPÉRATURE. II

Comme suite au précédent mémoire, la résistance électrique et le pouvoir thermo-électrique à très basse température ont été mesurés pour des solutions très diluées de métaux du groupe B dans le cuivre.

Les difficultés de l'interprétation théorique qui doit être de grande importance pour la théorie électronique des métaux sont résumées.

## ELEKTRONENWANDERUNG IN KUPFER UND VERDÜNNTEN LEGIERUNGEN BEI TIEFEN TEMPERATUREN. II

Im Anschluss an eine frühere Veröffentlichung in dieser Zeitschrift wird über genauere Tief-Temperatur-Messungen des anomalen Widerstandsminimums und der Thermokraft von sehr stark verdünnten Kupfer-Legierungen (Kupfer mit Metallen der Gruppe B) berichtet.

Die Probleme der theoretischen Deutung, welche eigentlich von beachtlicher Bedeutung für die allgemeine Elektronentheorie der Metalle sein sollten, werden zusammengefasst.

### INTRODUCTION

In a previous paper<sup>1</sup> dealing with dilute alloys of silver, gold, nickel and tin in copper, we have discussed fully the materials and methods used and the experimental difficulties encountered, particularly in relation to the presence in the parent copper of small quantities of iron and oxygen.

In the present paper we report the influence of small quantities of a series of B-group metal solutes on the residual resistance ratio ( $R_{res}$ ), size of the resistance minimum ( $R_{min}$ ) and absolute thermoelectric force at 15°K ( $S_{15°K}$ ) (for discussion of these quantities see the previous paper<sup>1</sup>), in order to examine specifically the effects of heterovalent solutes of increasing valency difference. As discussed in (1) we use  $R_{res}$  as a measure of solute concentration while for alloys reduced in hydrogen we have also examined the variation of  $R_{res}$  with nominal solute concentrations.

### SOURCE OF MATERIAL

Of the metals used as solutes, gallium and indium of 99.9% purity and bismuth and lead of 99.99% purity were obtained from Messrs. Johnson, Matthey and Company. Germanium, of 99.999% purity, was obtained through the kindness of the General Electric Research Laboratories, Schenectady, while silicon, of 99.9% purity, was obtained from the British Thomson-Houston Company.

\* Received November 2, 1954.

† Division of Physics, National Research Council, Ottawa, Canada.

### EXPERIMENTAL OBSERVATIONS

Figures 1 to 4 show the variation of  $R_{res}$  with nominal concentration of gallium, indium, silicon and germanium as solutes, for alloys melted under reducing conditions.

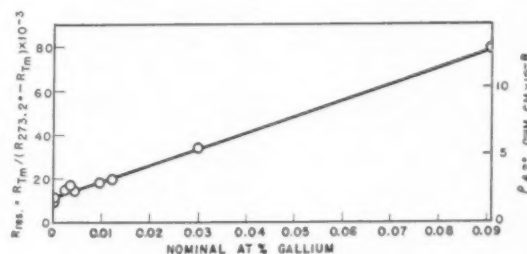


FIG. 1. The residual resistivity of dilute solid solutions of gallium in copper as a function of nominal gallium content of the alloys. The alloys were melted under hydrogen. In calculating  $\rho_{4.2°K}$  we have taken the resistivity of copper as 1.724 ohm cm at 293°K.

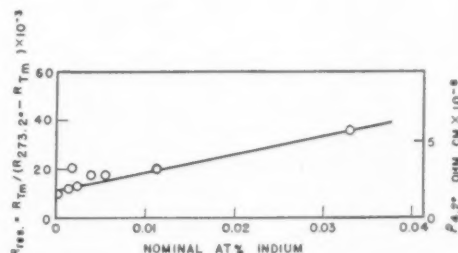


FIG. 2. The residual resistivity of dilute solid solutions of indium in copper as a function of nominal indium content of the alloys. The alloys were melted under hydrogen. In calculating  $\rho_{4.2°K}$  we have taken the resistivity of copper as 1.724 ohm cm at 293°K.



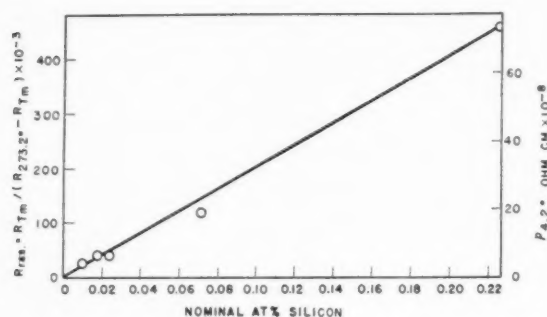


FIG. 3. The residual resistivity of dilute solid solutions of silicon in copper as a function of nominal silicon content of the alloys. The alloys were melted under hydrogen. In calculating  $\rho_{4.2}^{\circ}\text{K}$  we have taken the resistivity of copper as 1.724 ohm cm at 293°K.

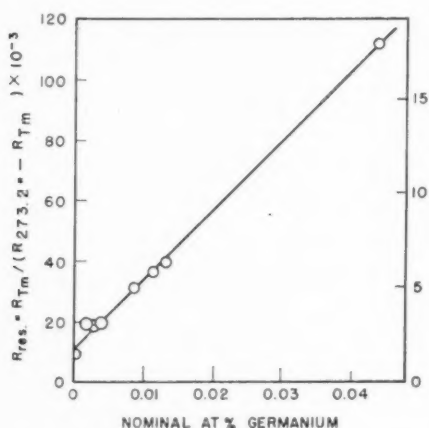


FIG. 4. The residual resistivity of dilute solid solutions of germanium in copper as a function of nominal germanium content of the alloys. The alloys were melted under hydrogen. In calculating  $\rho_{4.2}^{\circ}\text{K}$  we have taken the resistivity of copper as 1.724 ohm cm at 293°K.

We have not been able to carry out satisfactory quantitative spectrochemical analyses of the solutes gallium, indium and germanium, although, in the case of alloys made under reducing conditions, we have determined the *relative* ratios of solutes present in the actual resistance specimens and found in general good agreement with the ratios of nominal solute concentration. The actual *presence* of the specific added solute has been verified by spectrochemical analysis in all specimens examined.

As we have only been able to use nominal values of solute concentrations in these very dilute alloys, we shall not quote precise scattering cross sections (or the equivalent increase of resistivity caused by the addition of 1 at. % solute) except to say that our findings are in general agreement with those of Linde<sup>2</sup> obtained from alloys of higher solute concentration.

We show the variation of  $R_{\min}$  and  $S_{15}^{\circ}\text{K}$  with  $R_{\text{res}}$  in Figs. 5 to 12 for alloys with gallium, indium, germanium and bismuth as solutes. The behavior of copper-lead alloys is similar to that of copper-bismuth alloys.

However, as the variation of  $S_{15}^{\circ}\text{K}$  and  $R_{\min}$  with  $R_{\text{res}}$  for the lead alloys is rather less self-consistent than was found for copper-bismuth, we have not thought it worth while to reproduce the results of these observations.

Gallium, indium and germanium as solutes behave qualitatively in a similar fashion to tin as solute.<sup>1</sup> That is to say,  $R_{\min}$  and  $S_{15}^{\circ}\text{K}$  show "cusp-like" variation at a critical solute concentration, at which the size of the resistance minimum saturates, while the thermoelectric force,  $E$ , in very dilute alloys decreases to a minimum

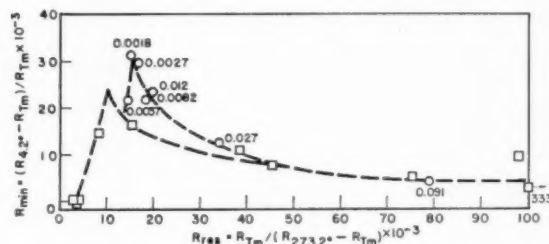


FIG. 5. The relative size of the resistance minimum of dilute solid solutions of gallium in copper as a function of the residual resistivity of the alloys.  $\circ$  Alloys melted under hydrogen.  $\square$  Alloys *not* melted under reducing conditions. The figures refer to the nominal gallium content of the alloys which were melted under reducing conditions.

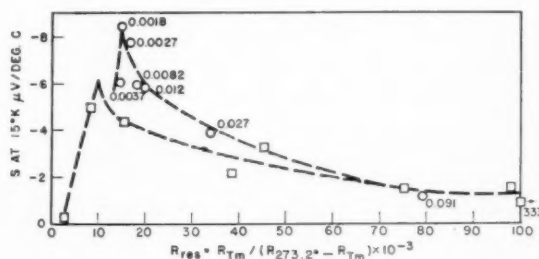


FIG. 6. Absolute thermoelectric power at 15°K of dilute solid solutions of gallium in copper as a function of the residual resistivity of the alloys.  $\circ$  Alloys melted under hydrogen.  $\square$  Alloys *not* melted under reducing conditions. The figures refer to the nominal germanium content of the alloys which were melted under reducing conditions.

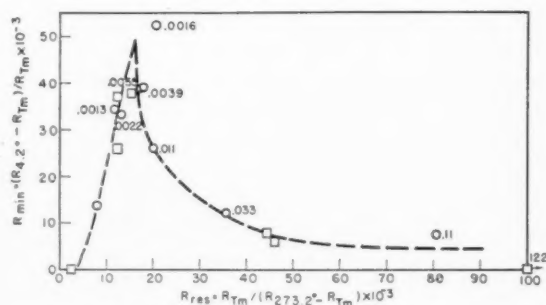


FIG. 7. The relative size of the resistance minimum of dilute solid solutions of indium in copper as a function of the residual resistivity of the alloys.  $\circ$  Alloys melted under hydrogen.  $\square$  Alloys *not* melted under reducing conditions. The figures refer to the nominal indium content of the alloys which were melted under reducing conditions.

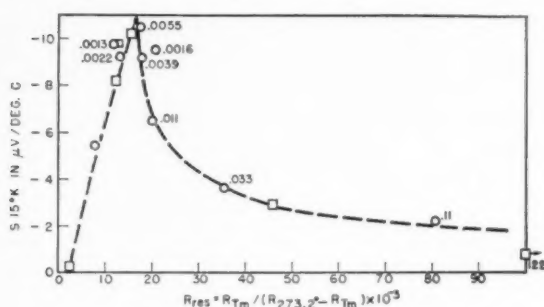


Fig. 8. Absolute thermoelectric power at 15°K of dilute solid solutions of indium in copper as a function of the residual resistivity of the alloys.  $\circ$  Alloys melted under hydrogen.  $\square$  Alloys not melted under reducing conditions. The figures refer to the nominal indium content of the alloys which were melted under reducing conditions.

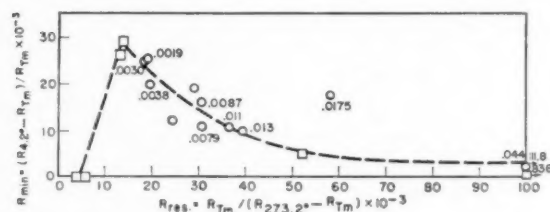


Fig. 9. The relative size of the resistance minimum of dilute solid solutions of germanium in copper as a function of the residual resistivity of the alloys.  $\circ$  Alloys melted under hydrogen.  $\square$  Alloys not melted under reducing conditions. The figures refer to the nominal germanium content of the alloys which were melted under reducing conditions.

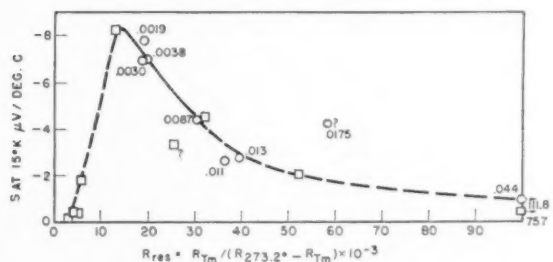


Fig. 10. Absolute thermoelectric power at 15°K of dilute solid solutions of germanium in copper as a function of the residual resistivity of the alloys.  $\circ$  Alloys melted under hydrogen.  $\square$  Alloys not melted under reducing conditions. The figures refer to the nominal gallium content of the alloys which were melted under reducing conditions.

value in the region of 50°K, and then rises again so that the absolute thermoelectric power,  $S$ , at  $\sim 70^\circ$  is not very different from that of pure copper. From the few copper-silicon alloys that we have examined, it appears that silicon as solute also behaves similarly to gallium, indium, germanium and tin. Lead and bismuth, however, as solutes behave rather differently. The equilibrium concentration in solid solution in copper at  $\sim 550^\circ\text{C}$  is effectively zero as observed from the residual resistivity and the absolute thermoelectric force (Fig. 13) in alloys quenched from that temperature. At higher

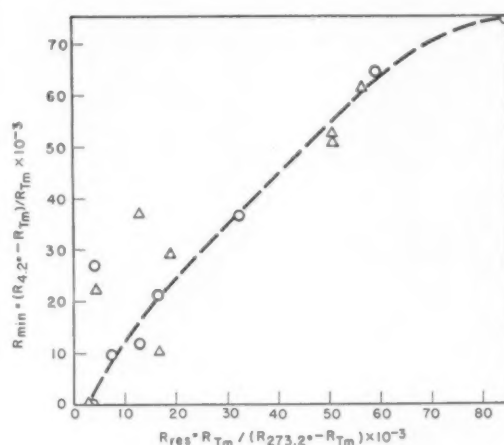


Fig. 11. The relative size of the resistance minimum of dilute solid solutions of bismuth in copper as a function of the residual resistivity of the alloys.  $\circ$  Alloys containing approximately 0.002 at.% bismuth quenched from various temperatures.  $\triangle$  Alloys containing approximately 0.015 at.% bismuth quenched from various temperatures.

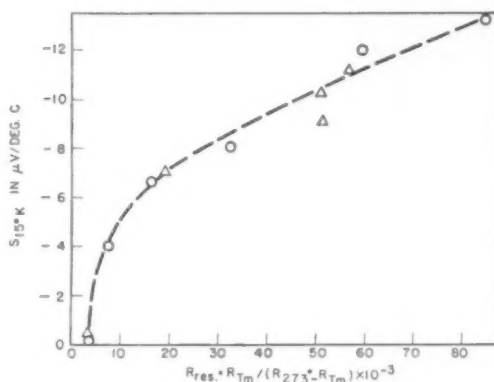


Fig. 12. Absolute thermoelectric power at 15°K of dilute solid solutions of bismuth in copper as a function of the residual resistivity of the alloys.  $\circ$  Alloys containing approximately 0.002 at.% bismuth quenched from various temperatures.  $\triangle$  Alloys containing approximately 0.015 at.% bismuth quenched from various temperatures.

temperatures, on the other hand, there is a rapid increase in the relative equilibrium solubility and we have examined the variation of  $R_{\min}$  and  $S_{15^\circ\text{K}}$  by quenching alloys from successively higher temperatures. Although we have not yet reached a critical concentration limiting the increase of  $R_{\min}$  and  $S_{15^\circ\text{K}}$  with  $R_{\text{res}}$ , the shape of the curves shown in Figs. 11 and 12 appears characteristic of a different behavior for lead and bismuth as solutes compared to gallium, indium, silicon, germanium and tin.\*

\* It is possible that, in these alloys which have been quenched from temperatures greater than the normal annealing temperature of  $530^\circ\text{C}$ , other solutes such as, for instance, oxygen, are also entering solid solution to an increasing extent and contributing to the observed thermoelectric force and the size of the resistance minimum.

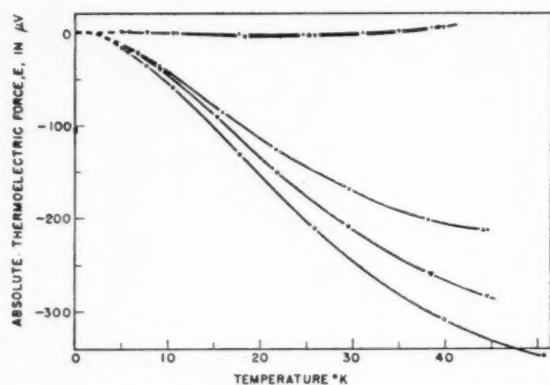


FIG. 13. Absolute thermoelectric force of dilute solid solutions of bismuth in copper as a function of temperature. An alloy containing approximately 0.015 at. % bismuth has been quenched from the following temperatures ( $\pm 5^\circ\text{C}$ ):  $\nabla$   $550^\circ\text{C}$ .  $\times$   $705^\circ\text{C}$ .  $\blacktriangledown$   $860^\circ\text{C}$ .  $\circ$   $1000^\circ\text{C}$ .  $+$  Pure copper sample.

The similarity of gallium, indium, silicon, germanium and tin on the one hand, and lead and bismuth on the other hand, when they are present as solutes in very dilute solid solution in copper is further demonstrated in Figs. 14–16, where we plot the actual size of the resis-

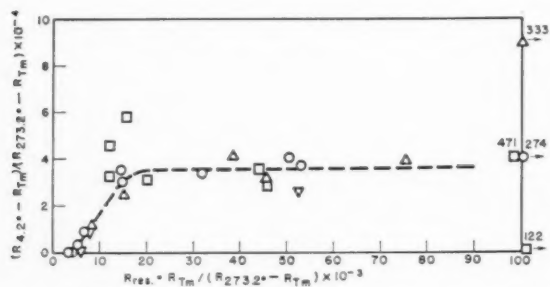


FIG. 14. Variation of  $(R_{4.2^\circ} - R_{T_m}) / (R_{273.2^\circ} - R_{T_m})$  with residual resistivity for dilute alloys of copper. The alloys were *not* melted under reducing conditions.  $\triangle$  Cu-Ga alloys.  $\square$  Cu-In alloys.  $\nabla$  Cu-Ge alloys.  $\circ$  Cu-Sn alloys.

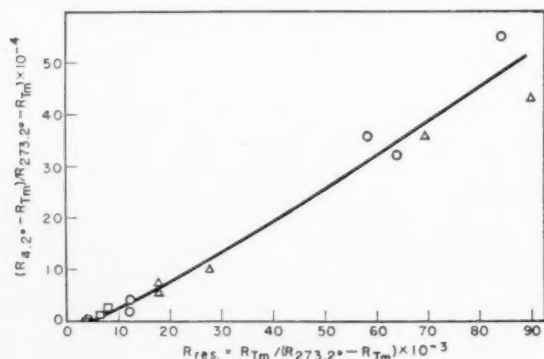


FIG. 15. Variation of  $(R_{4.2^\circ} - R_{T_m}) / (R_{273.2^\circ} - R_{T_m})$  with residual resistivity for solid solutions of lead in copper. The alloys have been quenched from various temperatures.  $\triangle$ ,  $\circ$  Alloys containing approximately 0.015 at. % lead melted respectively under hydrogen and *in vacuo*.  $\square$  Alloys made from Hilger copper.

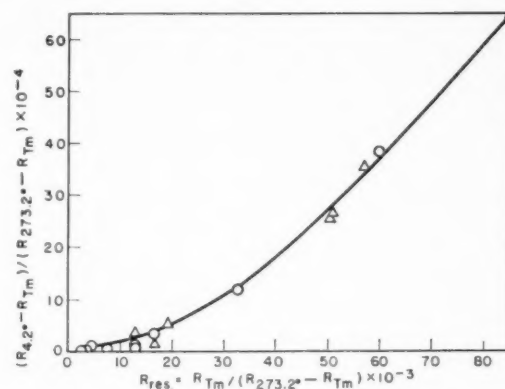


FIG. 16. Variation of  $(R_{4.2^\circ} - R_{T_m}) / (R_{273.2^\circ} - R_{T_m})$  with residual resistivity for solid solutions of bismuth in copper. The alloys have been quenched from various temperatures.  $\circ$  Alloys containing approximately 0.002 at. % bismuth.  $\triangle$  Alloys containing approximately 0.015 at. % Bismuth.

tance minimum as  $(R_{4.2^\circ} - R_{T_m}) / (R_{273.2^\circ} - R_{T_m}) \times 10^{-4}$  against residual resistivity. With gallium, indium, germanium or tin as solutes, the size of the minimum increases rapidly with increase of residual resistivity and then appears to *saturate* in size around  $R_{res} \sim 15 \times 10^{-3}$ . This is generally true for the “reduced” as well as the “oxygen-containing” alloys, although in Fig. 14 we have plotted measurements of “oxygen-containing” alloys only so that they refer to the specific added solute without the added complication of other metallic solutes in solid solution. In the copper-lead and copper-bismuth alloys the size of the minimum increases at a similar rate to that found with the other solutes up to  $R_{res} \sim 15 \times 10^{-3}$ , but then continues to increase at an even greater rate as  $R_{res}$  increases. Indeed, no evidence of saturation was found up to a residual resistance as high as  $R_{res} = 85 \times 10^{-3}$ .

#### DISCUSSION OF ELECTRICAL PROPERTIES OF DILUTE COPPER ALLOYS

As first proposed by us,<sup>3</sup> later examined in more detail<sup>4</sup> and further evinced in the present paper, it seems inescapable, from the evidence shown in Figs. 17 to 23

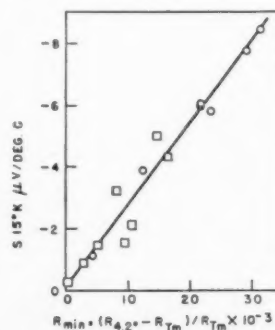


FIG. 17. Variation of the absolute thermoelectric power at  $15^\circ\text{K}$  as a function of the relative size of the resistance minimum for dilute solid solutions of gallium in copper.

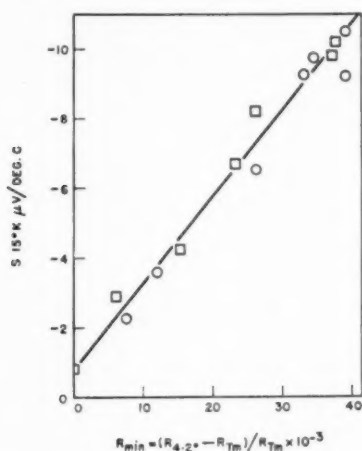


FIG. 18. Variation of the absolute thermoelectric power at 15°K as a function of the relative size of the resistance minimum for dilute solid solutions of indium in copper.

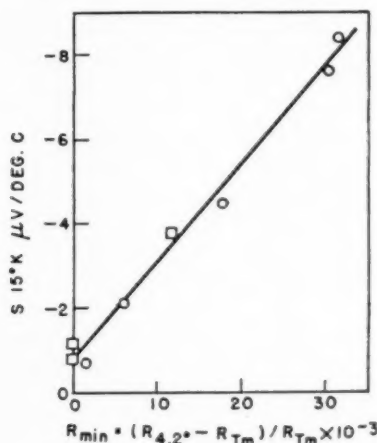


FIG. 19. Variation of the absolute thermoelectric power at 15°K as a function of the relative size of the resistance minimum for dilute solid solutions of silicon in copper.

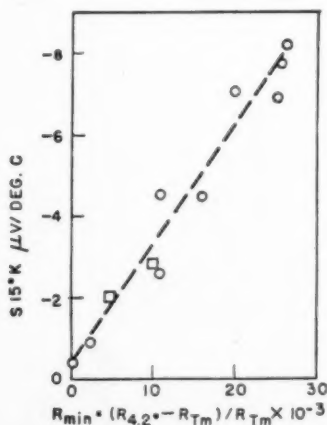


FIG. 20. Variation of the absolute thermoelectric power at 15°K as a function of the relative size of the resistance minimum for dilute solid solutions of germanium in copper.

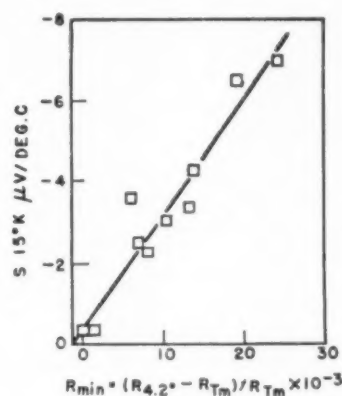


FIG. 21. Variation of the absolute thermoelectric power at 15°K as a function of the relative size of the resistance minimum for dilute solid solutions of tin in copper.

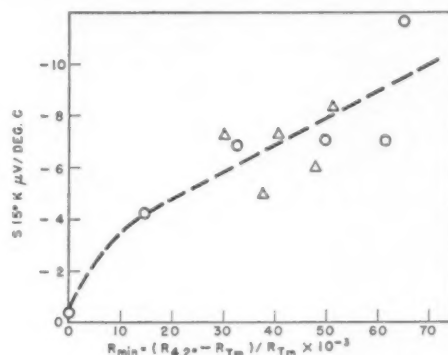


FIG. 22. Variation of the absolute thermoelectric power at 15°K as a function of the relative size of the resistance minimum for dilute solid solutions of lead in copper.

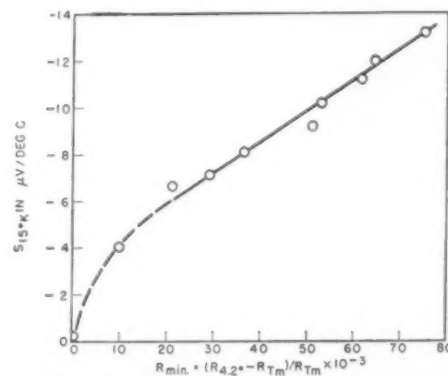


FIG. 23. Variation of the absolute thermoelectric power at 15°K as a function of the relative size of the resistance minimum for dilute solid solutions of bismuth in copper.

for variation of  $R_{min}$  with  $S_{15°K}$ ,\* that the minimum of electrical resistance and the remarkable variation of

\* The variation of  $R_{min}$  with  $S_{15°K}$  for copper-tin alloys shown in MacDonald and Pearson<sup>4</sup> was plotted from our earlier results, and was taken from the smoothed curves for variation of  $R_{min}$  and  $S_{15°K}$  with  $R_{res}$ . The present figure is plotted from later measurements of  $R_{min}$  and  $S_{15°K}$  each made on the same alloy specimen, and is to be preferred to the earlier data.



thermoelectric power in a range of dilute copper alloys *must* be regarded as having a common physical origin. If, then, we try to interpret the thermoelectric data in terms of the current theory of metals as developed by Bloch, Sommerfeld, Fröhlich, Mott and others, we are forced to assume<sup>3,4,5</sup> that the electron-scattering due to these solutes must be intensely energy-dependent, for which as yet no fundamental explanation is forthcoming. However, if such highly energy-dependent scattering *were* present, it could indeed also furnish a possible source for a resistive minimum and the theoretical suggestions of Korringa and Gerritsen<sup>6</sup> might also be considered in this light. On the other hand, we may well suspect that the current electron-theory is inadequate in one or more respects and rather recently there has been interest<sup>7-12\*</sup> in the effect first suggested by Gurevich,<sup>13</sup> namely, a possible "dragging" of the conduction-electrons by the phonons responsible for lattice heat conduction under a thermal gradient. This would then, in general, give rise to a thermoelectric power which would only become important at low temperatures (e.g., references 9, 10) and thus accord qualitatively with the observations. It is very difficult, however, to see why this effect should depend so very markedly on very dilute impurity concentrations and, more specifically, why it should not also be present in the *pure* metal depending, as it does, on lattice-electron scattering. If, however, these difficulties *were* resolved we should then hope to see rather directly that a corresponding lack of thermal equilibrium in the inverse electron-lattice scattering of a conductivity measurement—the possible importance

of which was first realised by Peierls—would give rise to the corresponding anomalous resistive-minimum.†

The theoretical situation is still far from clear and we cannot at all be sure that the true source of these remarkable phenomena has yet even been indicated; a rather difficult feature appears to be the specifically selective nature of the solutes responsible. It seems most probable, however, that the solution, when obtained, will be of great interest in many respects in the field of metallurgy and the electron theory of metals.

#### ACKNOWLEDGMENT

We wish to thank Dr. J. S. Dugdale for his interest in this work and Mr. F. W. Richardson and Miss D. M. Pester for their excellent technical assistance and enthusiasm, and Mr. W. Stockdale for carrying out chemical and spectroscopical analyses.

#### REFERENCES

1. D. K. C. MacDonald and W. B. Pearson, *Acta Met.* **3**, 000 (1955).
2. J. O. Linde, *Ann. Physik, Ser. 5* **15**, 219 (1932).
3. D. K. C. MacDonald and W. B. Pearson, *Proc. Roy. Soc. (Lond.)* **A219**, 373 (1953).
4. D. K. C. MacDonald, *Physica* **19**, 841 (1953).
5. D. K. C. MacDonald and W. B. Pearson, *Phil. Mag.* **vii** **45**, 491 (1954).
6. J. Korringa and A. N. Gerritsen, *Physica* **19**, 457 (1953).
7. H. P. R. Frederikse, *Phys. Rev.* **92**, 248 (1953).
8. F. Blatt, Private communication.
9. D. K. C. MacDonald, *Physica* (1954)—Special issue of Amsterdam International Semi-Conductor Conference. See also *Rapp. 10<sup>e</sup> Cons. Solvay* (1954).
10. D. K. C. MacDonald, W. B. Pearson, and G. K. White, *Bull. Int. Inst. Refrig. (Grenoble Conference)* (1954).
11. C. Herring, *Phys. Rev.* **96**, 1163 (1954).
12. P. G. Klemens, *Austral. J. Phys.* **7**, 520 (1954).
13. L. Gurevich, *J. Phys. U.S.S.R.* **9**, 477 (1945); **10**, 67 (1946).

\* We are grateful to Messrs. Herring, Klemens and Blatt for letting us read their manuscripts before publication.

† Such a proposal has already been made informally by Dr. G. K. White of these laboratories.

## LETTERS TO THE EDITOR

### Some Observations of Dislocation Sites in Polygonized Silicon-Iron Crystals\*

The character of polygonized boundaries in bent and annealed single crystals has been summarized by Cottrell<sup>1</sup> and recently by Forty<sup>2</sup> in terms of the Burgers-Bragg model of a low-angle boundary<sup>3</sup> consisting of edge dislocations arranged in rows perpendicular to the slip plane and slip direction. Observations of etching effects which can be interpreted as locating the site of individual edge dislocations in such a boundary have also been summarized by Forty.<sup>2</sup> Perhaps the most striking are the photomicrographs of Vogel, Pfann, Corey and Thomas<sup>4</sup> and the more recent ones of Oberly<sup>5</sup> and Gilman as reported by Fisher.<sup>6</sup> Dunn and Daniels<sup>7</sup> also noted etching effects on polygonized silicon-iron crystals which had been bent about a  $\langle 112 \rangle$  axis and observed on a  $\{112\}$  plane. This note describes further observations of Dunn and Daniels' crystals examined after the same (and in some cases the original) metallographic preparation at higher magnification.

Figure 1 illustrates the  $\langle 112 \rangle$  edge dislocation observed in the  $\{112\}$  plane of a body-centered-cubic structure having a Burgers vector of  $1/2$  a  $\langle 111 \rangle$  or in the case of  $3\frac{1}{4}\%$  silicon-iron,  $2.47 \times 10^{-8}$  cm. Figure 2 shows the  $\{112\}$  surface of a crystal 0.025 inch thick bent around a radius of 0.635 cm and annealed 24 hours at  $950^\circ\text{C}$ . The polygonized boundaries are generally parallel to  $\{111\}$  planes, i.e., are for the most part symmetrical, but they are often branching or discontinuous. A scattering of individual etch pits aligned nearly perpendicular to the main boundaries suggests the location of the active slip planes which from observations of slip lines are  $\{110\}$ .<sup>7</sup> Etch pit counts indicate an average dislocation density of  $3 \times 10^4$  which corresponds to an angle of 2.5 minutes.<sup>†</sup> The average measured polygon width is  $3.4 \times 10^{-4}$  cm. These measurements correspond to a calculated bend radius of

0.65 cm, which checks quite well with the 0.635 cm used.

Figure 3 illustrates a branching boundary in specimen P-2 of Dunn and Daniels<sup>7</sup> after bending around a 1.7 cm radius and a four-hour anneal at  $1300^\circ\text{C}$ . From the dislocation density the symmetrical boundary supports angles of 2.6 minutes and 1.65 minutes before and after the branch, respectively. The branch is an asymmetrical boundary at an angle of approximately 55 degrees. The treatment of asymmetrical boundaries by Read<sup>3</sup> suggests

$$\frac{1}{D} = \frac{\theta}{b_{111}} \left( \sin 35^\circ + \frac{b_{111}}{b_{110}} \cos 35^\circ \right),$$

assuming that the  $b_{110}$  type dislocation with a Burgers vector  $a\sqrt{2}$  in magnitude can form from vacancy segregation in the  $(110)$  plane. On this basis with  $D$  measured as  $8.2 \times 10^{-5}$  cm,  $\theta$  for the branch becomes 0.955 minute,

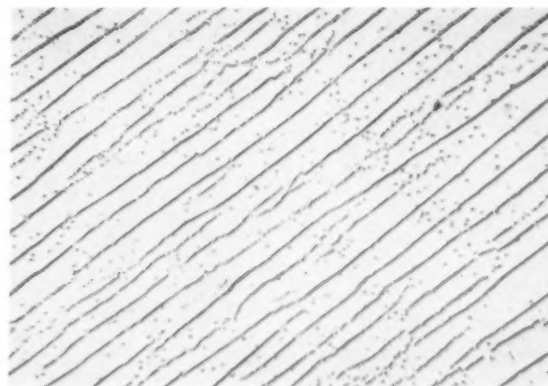


FIG. 2.  $\{112\}$  surface of crystal bent around  $[121]$  axis and annealed 24 hours at  $950^\circ\text{C}$ . Sub-boundaries parallel to  $\{111\}$  plane. 2000X, oblique illumination, chrome-acetic acid electro etch.

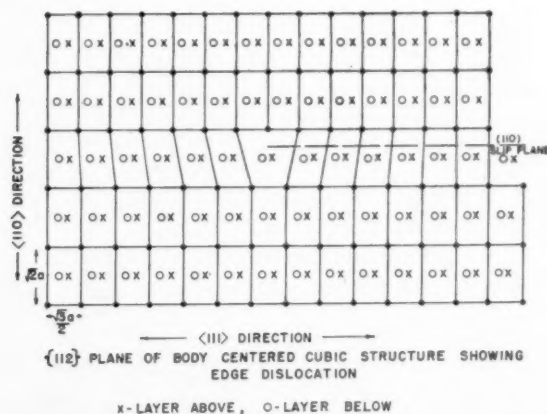


FIG. 1.  $\{112\}$  plane of body-centered-cubic structure showing edge dislocation.



FIG. 3. Similar specimen to Fig. 2, but annealed four hours at  $1300^\circ\text{C}$ . 10000X, chrome-acetic acid electroetch.



FIG. 4. Same as Fig. 3; different area. 2000X.

which corresponds to  $2.60 - 1.65 = 0.95$  minute required by a strain-free junction.

On the basis of this and other analyses, it will be assumed that the etch pits shown locate individual edge dislocations which, from the geometry of the specimen and the deformation, are perpendicular to the plane of observation.

Figure 4 shows one end of a polygonized boundary from the same specimen which consists entirely of a

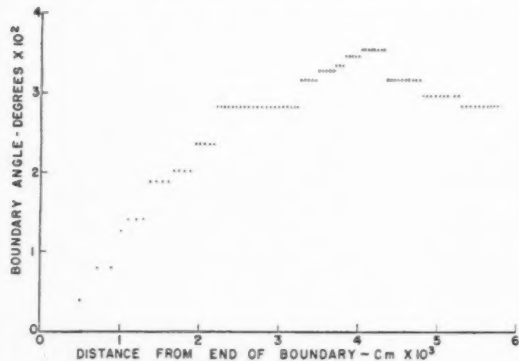


FIG. 5. Variation in angle along sub-boundary in Fig. 4.



FIG. 6. Same as Fig. 3; different area. 1500X.

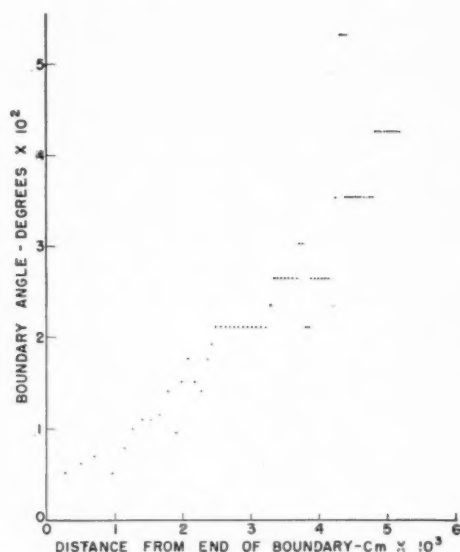


FIG. 7. Variation in angle along sub-boundary in Fig. 6.

resolvable sequence of pits, with both ends terminating within the crystal. The dislocation density and the calculated angle between sub-grains are not uniform along the boundary, as shown in Fig. 5. A similar heterogeneous boundary is shown in Fig. 6 and analyzed in Fig. 7. This variable dislocation array implying a variable angle between polygons requires additional elastic strain and a resulting unstable transition configuration. This configuration can be stabilized by the migration of the dislocations to adjacent boundaries or by their migration along the boundary to form a uniform spacing which traverses the crystal. This transition boundary provides an open end for dislocation migration which is responsible in part for the increase in polygon or lamellar width that has been observed to occur on annealing at high temperatures.<sup>7</sup>

In one corner of this specimen sub-boundaries ( $\sim 1^\circ$ ) were initially present in the unbent crystal and reacted during annealing with the polygonization boundaries as



FIG. 8. Same as Fig. 3; different area.

shown in Fig. 8. As the polygonized boundary approaches the higher angle sub-boundary, the dislocation density of the former decreases and the latter changes direction near the junction in a manner that shortens the lower angle boundary and lengthens the higher angle boundary. If the edge dislocations and the polygon boundaries remain perpendicular to the plane of observation, it is postulated that the dislocations are migrating down the polygon boundary into the higher angle sub-boundary which might eventually remove the polygon boundary and result in the growth of polygon width.

Additional work is planned and in progress to further explore the role of sub-boundaries and polygonization in recovery and recrystallization.

C. G. DUNN

General Electric Company  
Pittsfield, Massachusetts

W. R. HIBBARD, JR.

General Electric Company  
The Knolls  
Schenectady, New York

#### References

1. A. H. Cottrell, *Dislocations and Plastic Flow in Crystals* (Oxford Press, London, 1953).
2. A. J. Forty, "Direct Observations of Dislocations in Crystals," *Advances in Phys.* **3**, No. 9, 1 (1954).
3. W. T. Read, Jr., *Dislocations in Crystals* (McGraw-Hill, New York, 1953).
4. F. L. Vogel, W. G. Pfann, H. E. Corey, and E. E. Thomas, *Phys. Rev.* **90**, 489 (1953).
5. J. J. Oberly, *J. Metals* (Sept. 1954) 1025.
6. J. C. Fisher, A.S.M. Symposium on Imperfections, Oct. 1954.
7. C. G. Dunn and F. W. Daniels, *Trans. A.I.M.E.* **191**, 147 (1951).

\* Received December 29, 1954.

† For a symmetrical boundary  $\theta \cong b/D$ , where  $b$  is the Burgers vector and  $D$  is the distance between dislocations.

#### Comments on "Formation Energies of Vacancies in Copper and Gold" by C. J. Meechan and R. R. Eggleston\*

In a recent paper, Meechan and Eggleston<sup>1</sup> have given data on the temperature variation of the resistance of samples of pure copper and gold. From these data they have inferred the existence of vacancies in both metals at high temperatures and have given values for the activation energies of formation of these. It will be shown below that the validity of the argument used is in doubt and that the figures quoted should be treated with reserve.

The basic assumption made in<sup>1</sup> is that, for a pure metal, the resistance due to thermal vibration is a quadratic function of temperature and that any excess resistance at high temperatures can be ascribed to vacancies. However, the justification for using such a quadratic function is based on an equation given by Mott and Jones<sup>2</sup> as an approximation valid for temper-

atures that are not too high. The basic equation given by Mott and Jones is

$$\frac{d}{dT} \left( \ln \frac{R}{T} \right) = 2\alpha\gamma, \quad (1)$$

where  $R$  is the resistance at absolute temperature  $T$ ,  $\alpha$  is the volume expansion coefficient and  $\gamma$  is Gruneisen's constant. Assuming  $2\alpha\gamma$  to be independent of temperature, (1) can be integrated to give

$$RaTe^{2\alpha\gamma T} \cong T(1 + 2\alpha\gamma T) \quad (2)$$

and the last approximation is used in reference 1. However,<sup>2</sup>  $2\alpha\gamma \cong 2 \times 10^{-4}$ , so that for the highest temperature considered, viz. 1200°K, this approximation is only valid to within about 3 per cent and at least two extra terms must be taken in the expansion of the exponential to attain an accuracy of 1 in 10<sup>4</sup> which seems to be the order claimed in reference 1. Even at 500°C, at least one extra term is necessary. Furthermore, though few data are available for the variation of  $\gamma$  with temperature,  $\alpha$  certainly increases with  $T$ . For copper,  $\alpha$  increases from  $50.1 \times 10^{-6}/^\circ\text{C}$  at 100°C to  $57.9 \times 10^{-6}/^\circ\text{C}$  at 800°C (cf. Borelius,<sup>3</sup> who uses  $\alpha$  to denote the linear expansion coefficient). Therefore,  $R$  should be represented by at least a cubic, and possibly a quartic, function of  $T$ . We have fitted cubic curves to the  $R$ - $T$  values for both copper and gold and find that it is possible to fit the results reasonably well over the whole temperature range. The ranges of deviations are from -38 to +21 for copper and from -43 to +38 for gold, while the r-m-s. deviations are 18 for copper and 19 for gold (all figures in units of  $10^{-5}$  ohm). These errors seem to be of the same order of magnitude as those quoted in reference 1 as being within experimental error, but in each case the coefficient of  $T^2$  is found to be negative so that a theoretical interpretation is not straightforward. Use of a quartic approximation should reduce the deviations and could easily reverse the sign of the  $T^2$  term.

A better approach would seem to be to plot  $\ln(R_{\text{mms}}/T)$  as a function of  $T$ , as has been done in the figure. In both cases, for  $T > 200^\circ\text{C}$  the curves are smooth with a slowly increasing gradient, but the low temperature points appear to be anomalous. Further,

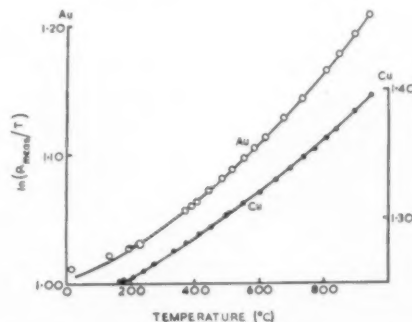


Fig. 1. Plots of  $\ln(R_{\text{mms}}/T)$  against temperature for gold (left-hand scale) and copper (right-hand scale).



TABLE I.

Temperature		0°	200°	400°	600°	800°	900°
Copper	Slope of curve $2\alpha\gamma$	1.91*	2.01*	1.66	1.84	2.08	2.66
	Slope of curve $2\alpha\gamma$			2.09*	2.19*	2.27*	
Gold	Slope of curve $2\alpha\gamma$	2.55*	2.75†	2.89†	[3.05]**	3.00	3.38
						[3.21]	

\* Values of  $\alpha$  from ref. 3.† Values of  $\alpha$  from International Critical Tables.

\*\* Figures in brackets are extrapolated values.

the gradients are always slightly less than the corresponding value of  $2\alpha\gamma$  (see Table I) but approach this value at the higher temperatures. This smaller gradient and possibly the anomalous points at low temperature may be accounted for qualitatively if we assume that  $R_{\text{meas}}$  includes a residual resistance  $R_0$  not due to thermal motion. Then

$$\ln(R_{\text{meas}}/T) = \ln(R + R_0)/T \\ = \ln(R/T) + \ln(1 + R_0/R), \quad (3)$$

where  $R$  is the resistance due to thermal motion [as in Eqs. (1) and (2)]. We may take  $R_0 \ll R$  for  $T > 300^\circ\text{K}$  so that the second term is approximately  $R_0/R$ . Therefore, since  $R$  is dominated by a term proportional to  $T$ ,  $\ln(R_{\text{meas}}/T)$  includes a term proportional to  $1/T$  which could reduce the gradient of the  $\ln(R_{\text{meas}}/T)$  vs  $T$  curve below the value of  $2\alpha\gamma$  and cause the deviations at low temperatures. Alternatively, a better evaluation of  $\gamma$  as a function of  $T$  might remove the discrepancy.

It can be seen therefore that there are at least two methods of expressing the results given in reference 1 without introducing a vacancy contribution to the resistivity. Thus, while it is not the intention of this letter to deny the existence of vacancies, we do wish to point out that, at least until the variation of  $2\alpha\gamma$  with  $T$  is known accurately, the figures quoted in reference 1 for the activation energy of formation of vacancies and for their probable concentration at the melting point should be treated with caution.

J. F. NICHOLAS

Division of Tribophysics  
Commonwealth Scientific & Industrial  
Research Organization  
Melbourne, Australia

## References

1. C. J. Meechan and R. R. Eggleston, *Acta Met.* 2, 680 (1954).
2. N. F. Mott and H. Jones, *Properties of Metals and Alloys* (London, 1936), p. 268.
3. G. Borelius, *Handbuch der Metallphysik* 1 (1) (Leipzig, 1935), p. 224.

\* Received January 26, 1955.

### Some Observations on the Relationship Between Vacancies, Recovery and Precipitation in Al-Mg Alloys\*

Recent work<sup>1,2</sup> on the plastic deformation of high purity aluminium-magnesium alloys at relatively high

temperatures (200°C) has indicated that the presence of magnesium in solid solution retards the climb of dislocations out of their slip planes. At first sight these results seem to contradict the observations that we have made on the effect of magnesium on the recovery of cold-worked aluminium. In this case we find that the time for complete recovery of hardness or of X-ray line breadth, prior to the beginning of recrystallization, is decreased considerably by 0.1% magnesium and that further additions of magnesium up to 2.9% have little additional effect. Besides this the activation energy for these recovery processes is decreased by magnesium which agrees with the earlier findings of Varley.<sup>3</sup> We also find that for a given amount of cold work (20% cold reduction) the fractional increase in electrical resistivity increases linearly with magnesium content from about 0.3% for super-purity aluminium to 1.4% for an aluminium - 2.9% magnesium alloy. Furthermore, the fraction of the increase in electrical resistivity brought about by cold-working which is annealed out during recovery increases from about 30% for super-purity



FIG. 1. Aluminium - 3.6% magnesium annealed and then reheated at 100°C for 2000 hours. 250X.



FIG. 2. Aluminium - 3.6% magnesium cold-worked 20%, reheated at 100°C for 2000 hours. 250X.

aluminium to almost 100% for the 2.9% magnesium alloy. Following Seitz,<sup>4</sup> these results can be explained if it is assumed that the large magnesium atoms are acting as traps for the vacancies produced by cold-working. Support for these conclusions was obtained by the fact that the density increased by 0.02% after annealing the cold-worked 2.9% magnesium alloy. The vacancies so formed will thus aid the climb of dislocations out of their slip plane during a recovery anneal and thus decrease the time for complete recovery. With high temperature deformation, however, the excess vacancies will be annealed out as fast as they form and so the recovery process will be controlled by dislocations alone and in this case the recovery process will be hindered by the magnesium atoms, as found by McLean and Farmer<sup>1</sup> and Rachinger.<sup>2</sup>

Many workers<sup>5,6,7,8</sup> have shown that when aluminium-magnesium alloys containing more than 3% magnesium are cold-worked by quite small amounts, the rate of precipitation at the grain boundaries is markedly increased (see Figs. 1 and 2); precipitation on slip planes is only observed after quite high amounts of cold work, i.e., 40% cold reduction. From the evidence discussed above magnesium-vacancy pairs are produced after cold-working and it is likely that these will diffuse faster than magnesium atoms alone. When a magnesium-vacancy pair reaches a high-angle grain boundary the vacancy will be annihilated, thus leaving the extra magnesium atom at the grain boundary. In this way the rate of precipitation at high-angle boundaries will be increased by cold work.

It is hoped to publish a full account of these results later.

E. C. W. PERRYMAN

Aluminium Laboratories Limited  
Kingston, Canada  
(Present Address)  
Deep River, Ontario, Canada

#### References

1. D. McLean and M. H. Farmer, *J. Inst. Metals* **83**, 1 (1954).
2. W. A. Rachinger, *J. Inst. Metals* **81**, 718 (1952).
3. P. C. Varley, *J. Inst. Metals* **75**, 1037 (1948-49).
4. F. Seitz, *Advances in Physics* **1**, 43 (1952).
5. E. C. W. Perryman and S. E. Hadden, *J. Inst. Metals* **77**, 207 (1950).
6. P. Brenner and W. Roth, *J. Inst. Metals* **74**, 159 (1948).
7. E. H. Dix, Jr., *Trans. A.I.M.M.E.* **137** (1940).
8. P. Brenner and G. J. Metcalfe, *J. Inst. Metals* **81**, 261 (1953).

\* Received February 15, 1955.

#### Approximate Steady-State Configuration of a Dislocation Mill\*

Frank and Read<sup>1</sup> have shown how a segment of dislocation lying in a slip plane and pinned at both ends can generate an indefinite number of dislocation loops when a critical shear stress is exceeded. A loop-source

of this type is known as a Frank-Read source. A simpler configuration, in which the dislocation segment is pinned only at one end, the other extending to infinity or to the surface of the crystal, also was described by Frank and Read. Orowan has termed it a dislocation mill. Upon application of a shear stress, the dislocation segment of a dislocation mill will rotate about its fixed end, winding itself up into a spiral. Neglecting all dissipative effects, the approximate shape of the steady state spiral can be determined.

The assumptions to be made are as follows: (a) there is no dissipation of energy, (b) the energy of a moving dislocation is equal to  $Gb^2/2(1-v^2/c^2)^{1/2}$  per unit length, independent of the character of the dislocation (edge or screw) and of its acceleration,<sup>2</sup> and (c) interaction of different turns of the spiral is neglected.

Consider a circle of radius  $r$  with center at the origin of the spiral. Let the acute angle between the spiral and the circle at their point of intersection be  $\phi$ . Consider the energy that leaves the circle when the spiral makes a complete revolution. It is

$$E_1 = [Gb^2/2(1-v^2/c^2)^{1/2}] \cdot 2\pi r \cdot \cos\phi,$$

where  $v$  is the velocity of the dislocation segment normal to itself. The energy supplied within the circle in the same length of time is

$$E_2 = b\tau \cdot \pi r^2.$$

Equating, and making use of the fact that  $\sin\phi = v/\omega r$  where  $\omega$  is the (constant) angular velocity of the spiral, the velocity of the dislocation at a radial distance  $r$  is

$$v^2/c^2 = [(Gb/r\tau)^2 - 1][(Gb/r\tau)^2(c/\omega r)^2 - 1]^{-1}.$$

If this expression is valid for all  $r$ , it must be valid in particular for  $r_1 = Gb/\tau$ , for which

$$v^2/c^2 = 0 \cdot [(c/\omega r_1)^2 - 1]^{-1} \neq 0.$$

In other words, the angular velocity must be  $\omega = c/r_1 = c\tau/Gb$ . Putting this value of  $\omega$  in the expression for  $v^2/c^2$ ,

$$v^2/c^2 = [(Gb/r\tau)^2 + 1]^{-1}.$$

Thinking of the spiral as being stationary for the moment, the increment of radius  $dr$  corresponding to an increment in angle  $d\theta$  is  $dr/r d\theta = \tan\phi = Gb/r\tau$  and the equation of the spiral in polar coordinates is  $r = (Gb/\tau)\theta$ . The spiral is, then, an Archimedes spiral with a spacing of turns  $\Delta r = 2\pi(Gb/\tau)$ , which is  $4\pi$  times the critical radius of curvature at the center of the spiral.

The time required for one rotation of the spiral is  $\Delta t = 2\pi/\omega = 2\pi Gb/c\tau$  and the relative velocity of the two portions of the crystal is  $V = b/\Delta t = c\tau/2\pi G$ .

The separation of successive turns of the spiral probably is a fair approximation to the spacing of dislocation loops dynamically generated from a Frank-Read source. Fisher, Hart, and Pry,<sup>3</sup> in discussing dynamic loop generation, assume this spacing to be  $2\pi$  times the critical radius of curvature, rather than  $4\pi$

times it. Moreover, as pointed out by Leibfried,<sup>4</sup> they underestimated the back-stress at the center of a dislocation loop by a factor of  $\pi$ . These two factors, one of 2 for the loop spacing and one of  $\pi$  for the back-stress, act in opposite senses. Together they reduce the estimated number of dislocation loops that are generated in a single dynamic burst from about 300 to about 40. This change is not important to the discussion of dynamic loop generation, and the possibility still remains that dislocations may be generated at Frank-Read sources in bursts of a hundred loops or so at a time.

J. C. FISHER

Metallurgy and Ceramics Research Department  
General Electric Company  
Schenectady, New York

#### References

1. F. C. Frank and W. T. Read, *Phys. Rev.* **79**, 722 (1950).
2. F. C. Frank, *Proc. Phys. Soc. A* **62**, 307 (1949).
3. J. C. Fisher, E. W. Hart, and R. H. Pry, *Phys. Rev.* **87**, 958 (1952).
4. G. Leibfried. Private communication.

\* Received February 25, 1955.

#### Tensile Tests on Silicon Whiskers\*

Since the study of metal whisker growth by Compton, Mendizha and Arnold,<sup>1</sup> several workers have performed mechanical tests on whiskers which revealed their exceptionally high strength.<sup>2,3,4</sup> These tests were somewhat qualitative, since, although the strains were measured rather accurately, the stresses could not be. All mechanical tests on whiskers reported in the literature so far and of which the author is aware, have been bending tests, in which the stress withstood by whiskers before kinking was calculated from the strain (radius of curvature) and the elastic modulus. Now, theoretically, when elastic strains become large, deviations from the linearity of Hooke's law are expected. Hence, a computation of stress based on Hooke's law cannot be accurate here and a tensile test is clearly indicated.

Difficulties in manipulating whiskers of the order of 1 micron or less in diameter have been overcome by gripping the ends of the whisker in beads of diphenyl carbazide on loops of 1½-mil wire. By passing a current through the loop, a little diphenyl carbazide is melted (m.p. = 173°C) to form a minute bead which encloses the wire. A whisker to be tested is brought up to this

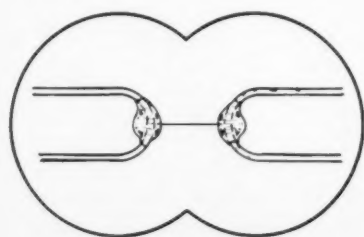


FIG. 1.

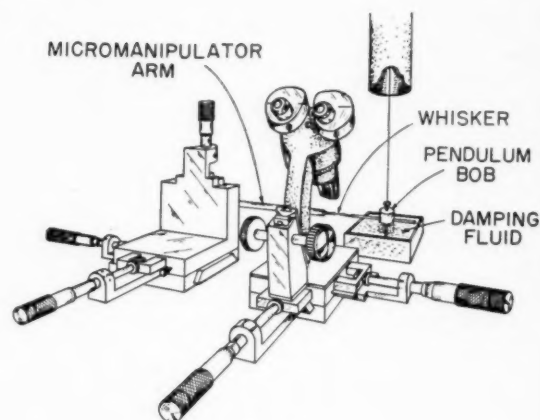


FIG. 2.

bead and is sucked in when the bead is molten. A view of a whisker under tension is sketched in Fig. 1 and an over-all sketch of the apparatus is shown in Fig. 2. The forces needed are of the order of hundredths of a gram, and are conveniently obtained by displacing a long, light pendulum from its equilibrium position using a micromanipulator. A whisker is first connected to the bead mounted on the micromanipulator and its other end is then connected to a similar bead mounted on the pendulum bob. The pendulum bob is provided with fins which dip into a conducting damping fluid (saturated salt water, thickened with cellulose gum). This completes the electrical circuit for melting the diphenyl carbazide and also provides damping against transient drafts and vibrations. The bob weighs 33 gm when dipped in the fluid, and the pendulum length is 330 cm, which gives .01 gm tensile force on the whisker per millimeter displacement of the bob. The accuracy of the force measurement is better than 1/2% for displacements greater than 4 mm (which includes most whiskers tested).

After whiskers are fractured, the stubs are mounted for electron-microscopic determination of their diameters. The diameter can be easily determined to better than 1/2% at any point, but it varies slightly along the length of the whisker and one can not be certain that the measured diameter is the smallest present. The fracture stress is thus known to about 2 per cent, and if errors are inherent in the measurement of the diameter, the true fracture stress will be still higher than the calculated result. Several whiskers of length greater than 1 mm were tested a second time by reconnecting the longer stub after fracture. The fracture stress in the second test was usually somewhat larger than in the first, though in one case it was very nearly the same. This would result from nonuniformity of cross section along the length of the whisker, the thinnest section fracturing first. If the pendulum oscillated excessively during loading (as would happen occasionally if the whisker were not aligned with the center of gravity of the bob) the whisker would have to bend rather ab-

ruptly at the beads and would fracture there at somewhat lower stresses than those needed to break the whisker near its center.

The maximum fracture stress found so far for silicon was  $390 \text{ kg/mm}^2$ , which is 2.03% of the Young's Modulus for the  $\langle 111 \rangle$  direction<sup>6</sup> ( $19.22 \times 10^3 \text{ kg/mm}^2$ ).<sup>†</sup> This result is based on the assumption of a circular cross section. If the whiskers are not nearly round, far more variation in apparent diameter would be expected along the observed length. At any rate, the cross section would almost certainly be smaller than that calculated assuming a circle, and our derived fracture stress would still be conservative.

No necking down of a whisker has ever been observed. Although no accurate measurements of tensile strain have so far been made (due to the relatively short lengths of the whiskers tested so far), it could easily be seen that the maximum strains obtained were not over 3 per cent.

R. L. EISNER

Metallurgy Department  
Westinghouse Research Laboratories  
East Pittsburgh, Pennsylvania

#### References

1. K. G. Compton, A. Mendizza, and S. M. Arnold, *Corrosion* **7**, 327 (1951).
2. C. Herring and J. K. Galt, *Phys. Rev.* **85**, 1060 (1952).
3. W. W. Piper and W. L. Roth, *Phys. Rev.* **92**, 503 (1953).
4. G. W. Sears, A. Gatti, and R. L. Fullman, *Acta Met.* **2**, 727 (1954).
5. E. R. Johnson and J. A. Amick, *J. Appl. Phys.* **25**, 1204 (1954).
6. H. J. McSkimin, W. L. Bond, E. Buehler, and G. K. Teal, *Phys. Rev.* **83**, 1080 (1951).

\* Received March 16, 1955.

† The value of Young's modulus listed for silicon in the A.S.M. Metals Handbook (1948) is incorrect and should be about  $23 \times 10^6$  psi rather than  $16 \times 10^6$ . The value listed here was derived from reference 6.

#### Variation of the Yield Point with Temperature in $\text{AuCu}_3$ \*

Polycrystalline wires of  $\text{AuCu}_3$ , 0.010 in. in diameter, were first annealed at  $900^\circ\text{C}$  for three hours to assure uniform grain size, and then annealed for 15–24 hours at various temperatures ranging from  $200^\circ$  to  $900^\circ\text{C}$ . After quenching, stress-strain curves were determined in a simple continuous loading machine. The yield point was taken as the stress corresponding to the bend in the stress-strain curve. Figure 1 represents the plot of the yield points so obtained as a function of heating temperature  $T$ . Discontinuities at  $395^\circ$ ,  $590^\circ$  and  $850^\circ\text{C}$  are easily discernible. The first discontinuity corresponds to the order-disorder transformation; the second and third are linked to the transformations in the disordered state recently reported.<sup>1</sup> Also, the so-called rate of strain-hardening of these alloys, defined as  $d\sigma/d\epsilon$ , where  $\sigma$  is stress and  $\epsilon$  is strain, has been determined. Its dependence on the temperature of annealing is represented in Fig. 2. As in the case of the yield points, discontinuities were detected at the temperatures previously cited. A

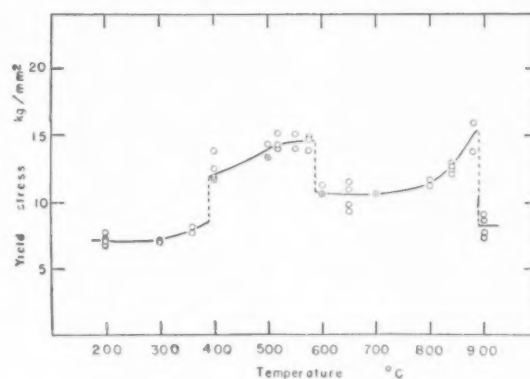


FIG. 1.

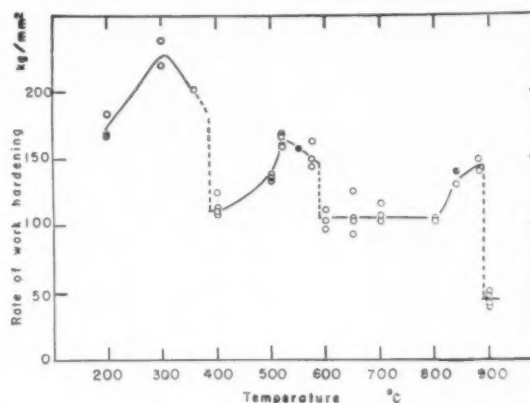


FIG. 2.

full discussion of these phenomena will be published later.

This work was supported by the Office of Naval Research.

G. C. KUCZYNSKI  
M. DOYAMA

Department of Metallurgy  
University of Notre Dame  
Notre Dame, Indiana

#### Reference

1. G. C. Kuczynski and M. Doyama, *Bull. Am. Phys. Soc.* Berkeley Meeting, December 28, 1954.

\* Received April 23, 1955.

#### ERRATUM

The Influence of Grain Boundaries on the Nucleation of Secondary Phases

*Acta Metallurgica* **3**, 72 (1955)

P. J. Clemm and J. C. Fisher

The first and third equations which appear below Fig. 5 on p. 72 should read as follows:

$$a = 3 \{ 2\phi(1-k^2) - K[1-k^2 - (K^2/4)]^{1/2} - K/\sqrt{8} \}$$

$$c = 2 \{ 4(\pi/3 - \delta) + kK[1-k^2 - (K^2/4)]^{1/2} \}$$

In each case the term  $K/\sqrt{8}$  was mistakenly printed as  $K/\sqrt{8} K$ .



## SOME CURRENT PAPERS IN OTHER JOURNALS

### Acta Crystallographica, Vol. 8

Part 4, April, 1955 (Partial Contents).

The X-ray anomalous reflexions from diamond. J. A. Hoerni and W. A. Wooster.

The crystal structure of  $Mn_2Sb$ . L. Heaton and N. S. Gingrich.

The crystal structures of  $P_4S_{10}$  and  $P_4S_7$ . A. Vos and E. H. Wiebenga.

On the crystal structure of the  $\zeta$ -phase in the silver-zinc system and the mechanism of the  $\beta$ - $\zeta$  transformation. G. Bergman and R. W. Jaross.

Formation and identification of thallium single crystals. K. D. Alexopoulos.

The lattice of rhombohedral sulfur. J. D. H. Donnay.

Al-Th intermetallic compounds. II. P. B. Braun and J. H. N. van Vucht.

Part 5, May, 1955 (Partial Contents).

The theory of Kikuchi patterns. Y. Kainuma.

A magneto-X-ray study of magnetite at 78°K. S. C. Abrahams and B. A. Calhoun.

The diffraction of X-rays by a cylindrical lattice. II. E. J. W. Whittaker.

The diffraction of X-rays by a cylindrical lattice. III. E. J. W. Whittaker.

The crystal structure of  $RhSe_2$ . S. Geller and B. B. Cetlin.

Polymorphism in one dimension. C. J. Schneer.

Einige Beispiele für die Ortskorrelation der Elektronen in Kristallstrukturen. K. Schubert.

### Journal of the Institute of Metals, Vol. 83

Part 8, April, 1955,

Intercrystalline fracture of beta-brasses containing aluminium. E. C. W. Perryman.

The effect of zirconium and titanium on the intercrystalline-cracking tendency of beta-brasses. E. C. W. Perryman and R. J. Goodwin.

The system uranium-tungsten. D. Summers-Smith.

The interactions of static stress and corrosion with aluminium alloys. F. A. Champton.

Specific-heat measurements on aluminium-4% copper and aluminium-4% copper-tin alloys. I. J. Polmear and H. K. Hardy.

The slip-band extrusion effect observed in some aluminium alloys subjected to cyclic stresses. P. J. E. Forsyth and C. A. Stubbington.

Part 9, April, 1955.

Inhomogeneous deformation in rolling and wire-drawing. B. B. Hundy and A. R. E. Singer.

Deformation and annealing textures in thorium. R. E. Smallman.

Preliminary note on the creep properties of internally oxidized copper alloys. J. W. Martin and G. C. Smith.

The sintering, fabrication, and properties of thorium. M. D. Smith and R. W. K. Honeycombe.

Some observations on the creep of pre-strained aluminium. G. R. Wilms.

### Journal of Metals, Vol. 7

June, 1955 (Partial Contents).

Reaction rate study of the dissolution of cuprite in sulphuric acid. M. E. Wadsworth and J. R. Woodward.

Solid state diffusion in the reduction of magnetite. J. O. Edstrom and G. Bitsianes.

Intermediate phases in the Cr-Mo-Co system at 1300°C. J. B. Darby, Jr. and P. A. Beck.

### Archiv für das Eisenhüttenwesen

Heft 3, März, 1955 (Partial Contents).

Bestimmung des Schmelzbereichs einiger technischer Ferrolegierungen. H. Brendecke und F. Pawlek.

Genaue Mikro-Schnellanalyse von Gasen. H. Feichtinger.

Untersuchungen über das Aufkohlungs- und Umwandlungsverhalten und die Schlagzähigkeit von unlegierten und legierten Einsatzstählen. H. Krainer, M. Kroneis und R. Gattringer.

Untersuchung von Umwandlungsvorgängen und Seigerungserscheinungen in Nickelstählen mit Magnetitsuspension. K. H. v. Klitzing.

Ätzverfahren für hochlegierte Chrom- und Chrom-Nickel-Stähle zum Nachweis von Austenit, Ferrit, Sigma-Phase und Karbiden. F. Braumann und G. Pier.

Erzeugung von magnetischen Vorzugsrichtungen durch inhomogene Spannungen bei Magnetostruktions-Werkstoffen. E. Houdremont und O. Rüdiger.

Die Beeinflussung der Inisilizierung von Stahl durch weitere Legierungselemente. E. Fitzer.

Erfahrungen mit Zählrohrgeräten für Röntgen-Feinstrukturuntersuchungen und-Emissionsspektalanalyse. H. Möller und V. Hauk.

Heft 4, April, 1955.

Probenahme in sedimentären Eisenerz-Lagerstätten. H. Kolbe.

Der Angriff eisengesättigter Zinkschmelzen auf manganhaltiges Eisen. H.-J. Wiester und D. Horstmann.

Die Bestimmung kleiner Aluminiumgehalte im Stahl. W. Werz und A. Neuberger.

Die Bestimmung des Bors im Stahl. H. G. Short.

Kennzeichnung der Spröbruchneigung von Stählen durch Messung der Fließspannung, Reißspannung und Brucheinschnürung an dreiaxial beanspruchten Proben. A. Kochendörfer und C. Rohrbach.

Spannungs- und Verzerrungszustand an der Grenzfläche zweier Kristalle. H. Möller und F. Brasse.

# SELF-DIFFUSION IN DILUTE BINARY SOLID SOLUTIONS\*

R. E. HOFFMAN, D. TURNBULL and E. W. HART†

The coefficient of self-diffusion of silver,  $D_{Ag}$ , has been measured as a function of the atom fraction  $X$  of the substitutional solutes Pb, Cu, Al or Ge. In general, the results can be described by an equation of the form  $D_{Ag} = D_{Ag}^0 \exp(bX)$ , where  $b$  is a temperature dependent constant greater than zero. However, a linear relation  $D_{Ag} = D_{Ag}^0(1+bX)$  is somewhat more satisfactory for the Ag-Pb and Ag-Cu solutions. The coefficient of self-diffusion of lead in infinitely dilute solution of Pb in Ag was found to be  $D_{Pb} = 0.22 \exp(-38,100/RT) \text{ cm}^2\text{sec}^{-1}$ , and at  $1000^\circ\text{K}$ ,  $D_{Pb} \sim 13D_{Ag}^0$ .

The self-diffusion coefficients of the solvent and solute ( $D_1$  and  $D_2$ , respectively) are, to a certain degree, interrelated and a formal theory for this interrelationship is developed on the basis of a lattice vacancy mechanism. It is supposed that the solvent atoms diffuse at a different rate within disturbed regions, immediately surrounding solute atoms, than outside them. If  $D_2 > D_1$ , it follows from our formal theory that the movement of the regions is the primary mechanism for bringing solvent atoms into them and  $D_1 = (1-\alpha X)D_1^0 + \alpha XD_2$ , where  $\alpha$  is the number of effective solvent-vacancy exchanges within the region during the period in which its center moves one lattice spacing. The experimental results on lead are entirely consistent with this theory with  $\alpha \sim 11$ .  $D_2$  values are not available for the other solutes.

Overhauser and Lazarus have developed different theories relating the rates of diffusion of solvent atoms within the disturbed regions to the interatomic forces. Both theories predict effects much smaller than observed, except that Overhauser's is in fair agreement with the results for Cu and Pb additions.

## AUTODIFFUSION DANS LES SOLUTIONS SOLIDES BINAIRES DILUÉES

Le coefficient d'autodiffusion de l'argent  $D_{Ag}$  a été mesuré en fonction de la concentration atomique  $X$  des atomes en substitution Pb, Cu, Al, ou Ge. En général, ces résultats peuvent être exprimés par une expression de la forme  $D_{Ag} = D_{Ag}^0 \exp(bX)$  où  $b$  est une constante positive dépendant de la température. Néanmoins, une relation linéaire  $D_{Ag} = D_{Ag}^0(1+bX)$  est plus satisfaisante pour les solutions Ag-Pb et Ag-Cu. Le coefficient d'autodiffusion du plomb  $D_{Pb}$ , dans une solution infiniment diluée de Pb dans Ag est égale à  $0.22 \exp(-38,100/RT) \text{ cm}^2\text{sec}^{-1}$  et ainsi à  $1,000^\circ\text{K}$ , on a  $D_{Pb} \sim 13D_{Ag}^0$ . Les coefficients d'autodiffusion du solvant et du soluté ( $D_1$  et  $D_2$  respectivement) ne sont pas indépendants et une théorie de leur relation est établie dans l'hypothèse de la diffusion par les lacunes. Il est admis que les atomes du solvant diffusent à une vitesse différente dans les régions perturbées entourant les atomes dissous. Si  $D_2 > D_1$ , il résulte de cette théorie que le mouvement de ces régions perturbées est le mécanisme fondamental pour porter les atomes du solvant au région perturbées et  $D_1 = (1-\alpha X)D_1^0 + \alpha XD_2$ , où  $\alpha$  est le nombre des permutations effectives lacunes-atomes du métal de base pendant le temps où le centre de la région perturbée se déplace d'une maille. Les résultats expérimentaux pour le plomb sont en accord avec cette théorie en prenant  $\alpha \sim 11$ . Il n'y a pas de valeur de  $D_2$  connue pour les autres solutés.

Overhauser et Lazarus ont développé des théories différentes pour relier aux forces interatomiques les vitesses de diffusion du solvant dans les régions perturbées. Ces deux théories prévoient des effets beaucoup plus faibles que ceux observés, bien que celle de Overhauser soit en bon accord avec les résultats obtenus pour des additions de Cu et Pb.

## DIE SELBSTDIFFUSION IN VERDÜNNTEN BINÄREN MISCHKRYSTALLEN

Der Selbstdiffusionskoeffizient von Silber,  $D_{Ag}$ , wurde als Funktion des atomaren Anteils  $X$  der Substitutionsmischkristalle von Pb, Cu, Al oder Ge gemessen. Im allgemeinen können die Ergebnisse durch eine Gleichung der Form  $D_{Ag} = D_{Ag}^0 \exp(bX)$ , beschrieben werden, wobei  $b$  eine temperaturabhängige Konstante grösser als null ist. Für die Ag-Pb und Ag-Cu Mischkristalle ist jedoch eine lineare Gleichung  $D_{Ag} = D_{Ag}^0(1+bX)$  etwas befriedigender. Der Selbstdiffusionskoeffizient von Blei,  $D_{Pb}$ , in sehr stark verdünnter Lösung von Pb in Ag wurde gefunden zu  $D_{Pb} = 0.22 \exp(-38,100/RT) \text{ cm}^2\text{sec}^{-1}$ , und für  $1000^\circ\text{K}$ :  $D_{Pb} \sim 13D_{Ag}^0$ .

Die Selbstdiffusionskoeffizienten des lösenden, und des gelösten Stoffes ( $D_1$  bzw.  $D_2$ ) stehen bis zu einem gewissen Grad in Beziehung zu einander. Eine formale Theorie für diese Zwischenbeziehungen wird auf der Grundlage eines Leerstellenmechanismus' entwickelt. Es wird vermutet, dass die Atome des Lösungsmittels innerhalb der gestörten Bezirke, die die gelösten Atome unmittelbar umgeben, in einem anderen Ausmass diffundieren als ausserhalb davon. Wenn  $D_2 > D_1$  ist, so folgt aus unserer formalen Theorie, dass die Bewegung der Bezirke den primären Mechanismus darstellt, der die lösenden Atome in diese Bezirke bringt. Weiterhin ist  $D_1 = (1-\alpha X)D_1^0 + \alpha XD_2$ , dabei ist  $\alpha$  die Anzahl der effektiven Wechsel zwischen die lösenden Atome und die Leerstellen innerhalb der Regionen während der Periode, in der ihr Zentrum sich um einen Gitterplatz weiterbewegt.

Die experimentellen Ergebnisse bei Blei sind mit dieser Theorie gänzlich in Übereinstimmung mit einem  $\alpha \sim 11$ .  $D_2$ -Werte für die anderen gelösten Stoffe sind nicht zu erhalten.

Overhauser und Lazarus haben verschiedene Theorien entwickelt, bei denen sie das Mass der Diffusion von lösenden Atomen innerhalb der gestörten Bereiche auf interatomare Kräfte zurückführen. Beide Theorien sagen weit kleinere Effekte als beobachtet voraus, ausser dass die Theorie von Overhauser in ziemlich guter Übereinstimmung mit den Ergebnissen für Cu und Pb Zusätze ist.

\* Received January 17, 1955.

† Metallurgy Research Department, General Electric Company, Schenectady, New York.

\* This work was supported by the United States Atomic Energy Commission under Contract No. W-31-109-Eng-2.

## INTRODUCTION

A previous note<sup>1</sup> described the results of measurements of the self-diffusion coefficient of silver,  $D_{Ag}$ , in silver-lead alloys in the range 0–1.3 atom per cent lead and in the temperature range 700–825°C. It was found that:

1. At a given lead concentration, the activation energy,  $Q$ , defined by the relation

$$D_{Ag} = D_0 \exp(-Q/RT) \quad (1)$$

was the same, within experimental error, as the activation energy for self-diffusion in pure silver, and

2. At a given temperature, the concentration dependence of  $D_{Ag}$  was given approximately by the relation

$$D_{Ag} = D_{Ag}^0 (1 + bX), \quad (2)$$

where  $D_{Ag}^0$  is the self-diffusion coefficient in pure silver,<sup>2</sup>  $X$  is the atom fraction of lead, and  $b$  is a temperature-dependent parameter, given by the relation

$$b = 10.5 \exp(5000/RT). \quad (3)$$

It was pointed out that these results could not be accounted for simply on the basis of an increase in the equilibrium number of free lattice vacancies; rather, it was hypothesized that the lead atoms took part directly in the transport of silver, perhaps by some sort of interchange mechanism catalyzed by lattice vacancies. If this hypothesis is correct, then the parameter  $b$  of Eq. (2) should be related to the self-diffusion of lead in these alloys.

The purposes of the present investigation were

1. to measure the effects of other solute additions on  $D_{Ag}$ ;
2. to measure the rate of self-diffusion of lead in silver-lead alloys to determine whether there is a rapid lead-silver interchange.

## EXPERIMENTAL

Binary silver alloys containing lead, copper, germanium and aluminum in various concentrations were vacuum melted and cast into 1/2 in. ingots. The ingots were subsequently swaged to 3/8 in. diameter, solution treated, quenched and cut into 1/4 in. long samples, the end samples being used for chemical analysis. Each sample was ground on 4/0 paper until the two faces were flat and parallel and then etched lightly to clean the surfaces.

Radioactive silver,  $Ag^{110}$ , of high specific activity was obtained from the United States Atomic Energy Commission; radioactive lead,  $Pb^{210}$  (RaD), was obtained from the Canadian Atomic Energy Commission, Ltd. Thin layers ( $<1\mu$ ) of the appropriate isotope were electroplated on one face of the samples from conventional plating baths. For the most part, the diffusion

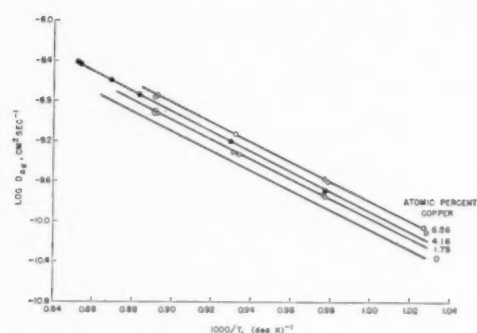
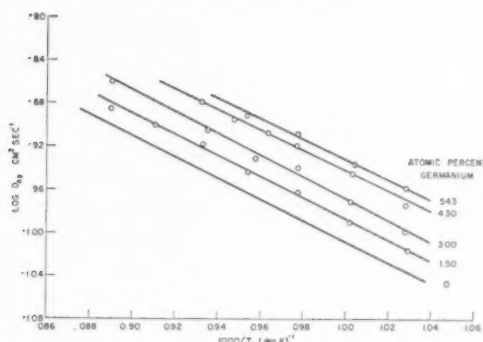
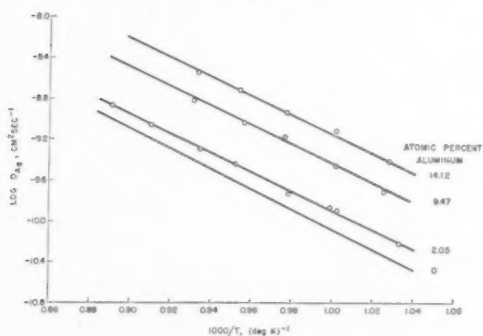
specimens consisted of single 1/4 in. samples with the plated faces exposed. However, for all measurements of  $D_{Pb}$  and for measurements of  $D_{Ag}$  in the high-aluminum samples, "sandwich-type" specimens were prepared by sintering together two identical samples with the isotope at the interface.

The diffusion anneals were carried out in furnaces in which the temperature was held constant to within  $\pm 2^\circ\text{C}$ , with the samples enclosed in evacuated quartz tubes. Subsequent to diffusion, the samples were carefully mounted in a lathe, reduced in diameter to remove surface diffusion effects, and then sectioned in the conventional manner. The activity of the sections was measured with a thin (30 mg/cm<sup>2</sup>) glass window Geiger-Müller tube in conjunction with a Tracerlab Autoscaler. Diffusion coefficients were calculated from the slopes of the straight lines obtained by plotting the logarithm of the specific activity *versus* the square of the penetration depth.

Because of the radioactive daughters of  $Pb^{210}$ , a special procedure had to be adopted for measuring the activity of the lead isotope. The following procedure was suggested to us in a private communication by Dr. N. H. Nachtrieb of the Institute for the Study of Metals, The University of Chicago.  $Pb^{210}$  decays to  $Bi^{210}$  by the emission of very weak beta and gamma radiation with a half-life of 22 years.  $Bi^{210}$  in turn decays to  $Po^{210}$  by emitting a 1.17 MEV beta particle with a 5.0-day half-life and  $Po^{210}$  decays to stable  $Pb^{206}$  by the emission of a 5.3 MEV alpha-particle and weak gamma radiation with a half-life of 140 days. Since gamma radiation is counted in a Geiger-Müller tube with much less efficiency than beta radiation and since the 30 mg/cm<sup>2</sup> window absorbs the alpha radiation of  $Po^{206}$  and the beta radiation from  $Pb^{210}$ , only the  $Bi^{210}$  beta radiation will be measured from a mixture of the three isotopes. Immediately after sectioning, the total amount of bismuth in a given section is made up partly of bismuth which diffused into that section and partly of bismuth which was formed there by decay of  $Pb^{210}$ . However, after a period of 25–30 days after sectioning, essentially all the bismuth which arrived in the section by diffusion will have decayed and the bismuth activity will then be directly proportional to the amount of  $Pb^{210}$  that diffused into the section. Therefore, in all the lead diffusion experiments, the counting was delayed until 30 days after sectioning.

## RESULTS

Measurements of  $D_{Ag}$  have been made on Ag-Cu alloys containing up to 6.7 atomic per cent Cu, on Ag-Ge alloys containing up to 5.4 atomic per cent Ge, and on Ag-Al alloys containing up to 14.1 atomic per cent Al. For each composition, the measurements extended over a temperature range of about 150°C. Graphs of  $\log D_{Ag}$  *versus* reciprocal absolute temperature are shown in Figs. 1–3. For each composition, the data

FIG. 1. The temperature dependence of  $D_{Ag}$  in Ag-Cu alloys of various compositions.FIG. 2. The temperature dependence of  $D_{Ag}$  in Ag-Ge alloys of various compositions.FIG. 3. The temperature dependence of  $D_{Ag}$  in Ag-Al alloys of various compositions.

were fitted to an equation of the form

$$D = D_0 \exp(-Q/RT)$$

by the method of least squares. Values of  $D_0$  and  $Q$  for each composition, including the previously published data for the Ag-Pb alloys<sup>1</sup> and for diffusion in pure silver,<sup>2</sup> are given in Table I.

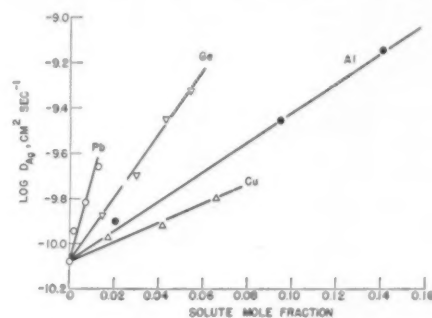
The linear dependence of  $D_{Ag}$  on solute concentration,  $X$ , that was used to describe the data for the Ag-Pb alloys<sup>1</sup> was also found to give a satisfactory description of the data for Ag-Cu. However, for both the Ag-Ge and Ag-Al alloys, a relation of the form

$$D_{Ag} = D_{Ag}^0 \exp(bX) \quad (4)$$

TABLE I. Frequency factor,  $D_0$ , and activation energy,  $Q$ , for silver self-diffusion in various solid solutions.

Solute	Atom per cent	$D_0$ , $\text{cm}^2\text{sec}^{-1}$	$Q$ , kcal/gm-atom
—	0.00	0.724	45.5
Pb	0.21	0.22	42.5
	0.71	0.89	44.7
	1.30	0.70	43.5
	4.16	1.84	46.6
Cu	6.56	0.51	43.5
	1.50	0.55	44.0
	3.00	1.59	45.3
	4.30	1.89	44.5
Al	5.43	2.18	44.2
	2.05	0.25	42.5
	9.47	0.83	42.9
	14.1	0.73	41.2

gave a decidedly better fit of the data. Actually Eq. (4) also may be used to describe, within experimental error, the data for Ag-Pb and Ag-Cu, although in both cases the linear relation is somewhat better. Graphs of  $\log D_{Ag}$  at 1000°K versus  $X$  for the various solutes are shown in Fig. 4. The values of  $b$ , as determined by fitting the data either to Eq. (2) or Eq. (4) are given in Table II.

FIG. 4. The dependence of  $D_{Ag}$ , at  $T=1000^\circ\text{K}$ , on solute concentration for Pb, Cu, Al and Ge additions.

The self-diffusion coefficient of lead,  $D_{Pb}$ , has been measured in pure silver and in several dilute Ag-Pb alloys in the temperature range 700°–825°C. The data are plotted in Fig. 5 as  $\log D_{Pb}$  versus reciprocal absolute temperature, and the least-squares values for  $D_0$  and  $Q$  are given in Table III. The relative magnitudes of  $D_{Ag}$  and  $D_{Pb}$  are shown in Fig. 6, where  $\log D_{Ag}$  and  $\log D_{Pb}$ , both at 1000°K, are plotted as functions of lead concentration.

From the deviations of the experimental points from the least-squares line, it is estimated that the probable

TABLE II. Values of the parameter  $b$  for  $T=1000^\circ\text{K}$ .

Solute	$b$ , Eq. (2)	$b$ , Eq. (4)
Pb	129	86.0
Cu	11.4	10.2
Ge	—	32.7
Al	—	15.1



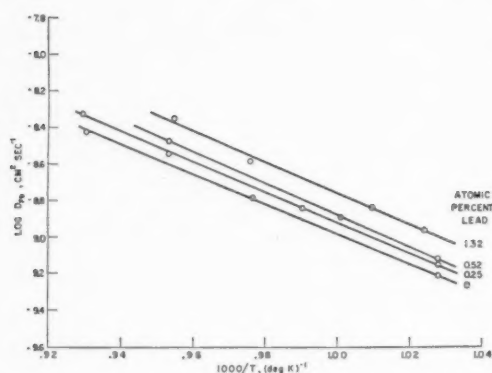


FIG. 5. The temperature dependence of  $D_{Pb}$  in pure silver and Ag-Pb alloys of various compositions.

TABLE III. Frequency factor,  $D_0$ , and activation energy,  $Q$ , for the diffusion of lead in silver-lead alloys.

Atom fraction Pb	$D_0$ , $\text{cm}^2\text{sec}^{-1}$	$Q$ , kcal/gm-atom
0	0.22	38.1
0.25	0.22	37.8
0.52	0.38	38.7
1.32	0.46	38.5

error in the magnitude of the diffusion coefficients is less than 10 per cent. The activation energies are probably accurate to within  $\pm 2$  kcal/gm-atom.

### THEORY

In order to interpret our results, it is necessary to develop the theory for the interrelation of the motion

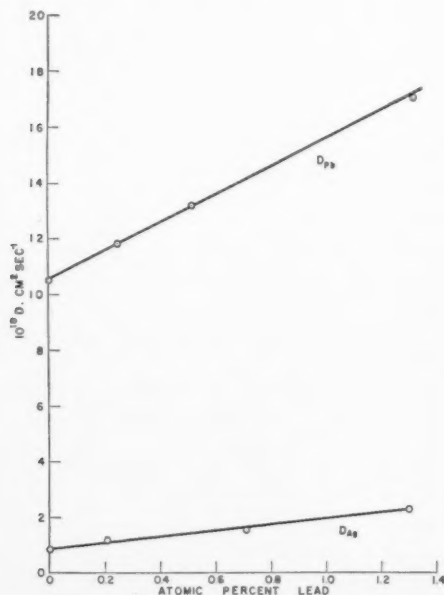


FIG. 6. The concentration dependence of  $D_{Pb}$  and  $D_{Ag}$  in Ag-Pb alloys at 1000°K.

of the solute and solvent atoms. Overhauser<sup>3</sup> and Lazarus<sup>4</sup> have already put forth theories relating the exchange frequency of solvent atoms with vacancies in the vicinity of the solute atom to the interatomic forces, but neither has grappled with the problem of formally relating the fundamental exchange frequencies (e.g., solute-vacancy, solvent-vacancy in or not in the vicinity of the solute) to the observable diffusion coefficient (either of solute or solvent). We shall develop some conclusions about the proper solution of this problem.

A detailed treatment assuming the lattice vacancy mechanism for diffusion will be given, then we shall point out in general how the treatment should be modified for other mechanisms of diffusion.

### The Diffusion Coefficient $D_2$ of Solute Atoms in Infinitely Dilute Solution

Let:

$D_1$  and  $D_2$  be the self-diffusion coefficients of solvent and solute atoms respectively;

$\nu_1^0$  = the frequency of exchange of a lattice vacancy with a solvent atom remote from a solute atom;

$\nu_1'$  = the exchange frequency of a lattice vacancy and solvent atom in the immediate vicinity of a solute atom;

$\nu_2$  = the exchange frequency of a solute atom and lattice vacancy;

$x_v^0$  = the fraction of vacant lattice sites in solid solution elements remote from any solute atoms;

$x_v'$  = the fraction of vacant lattice sites in the immediate vicinity of the solute atoms.

We must define more precisely the meaning of "immediate vicinity of the solute atom." Surrounding each solute atom there will be a disturbed region,  $m$  coordination shells in radius, in which  $|\nu_1' - \nu_1^0|$  and  $|x_v' - x_v^0|$  are appreciably greater than zero. We suppose that  $|\nu_1' - \nu_1^0|$  and  $|x_v' - x_v^0|$  are greatest for  $m=1$  but do not know over how many shells the disturbance extends. To simplify our treatment we shall assume arbitrarily that the disturbed region is only one coordination shell in radius; hence  $\nu_1'$  and  $x_v'$  are single-valued corresponding to  $m=1$ .

A lattice vacancy in the first coordination shell of a solute atom has for its nearest neighbors one solute atom, four solvent atoms that are, and seven solvent atoms that are not, nearest neighbors to the solute. Diffusion of the solute atom is a two step process: first, exchange of a solute atom with the vacancy, and second, exchange of the vacancy with a neighboring solvent atom. Thus irrespective of the magnitude of the solute-vacancy exchange frequency a solvent atom must jump into the vacancy after its exchange with the solute before a solute diffusion jump is completed. The frequency  $f_2$  of these solute atom diffusion jumps will then be the product of the solute-vacancy exchange frequency, vacancy concentration, and the probability  $p_1$  that the

vacancy in the solute atom coordination shell will exchange with a solvent atom.

Evidently,

$$p_1 = \frac{4\nu_1' + 7\nu_1^0}{4\nu_1' + 7\nu_1^0 + \nu_2} \quad (5)$$

Therefore,\*

$$f_2 = \frac{\nu_2(4\nu_1' + 7\nu_1^0)x_v'}{4\nu_1' + 7\nu_1^0 + \nu_2} \quad (6)$$

The self-diffusion coefficient  $D_2$  of the solute atom is

$$D_2 = (1/6)\lambda^2 f_2 = (1/6) \frac{\lambda^2(4\nu_1' + 7\nu_1^0)x_v'\nu_2}{(4\nu_1' + 7\nu_1^0 + \nu_2)} \quad (7)$$

If  $\nu_2 \gg \nu_1' \gg \nu_1^0$  the rate of solute diffusion is governed by the rate of exchange of vacancies with solvent atoms in the first solute coordination shell and Eq. (7) reduces to

$$D_2 = (2/3)\nu_1'^2 x_v' \quad (7a)$$

Similarly, if  $\nu_2 \gg \nu_1^0 \gg \nu_1'$ , the rate of solute diffusion is governed by the rate of exchange of vacancies with solvent atoms outside the solute coordination shell, and then

$$D_2 = (7/6)\nu_1^0 \lambda^2 x_v' \quad (7b)$$

On the other hand, if  $(4\nu_1' + 7\nu_1^0) \gg \nu_2$ , the rate of solute diffusion is controlled by the solute-vacancy exchange frequency, and

$$D_2 = (1/6)\nu_2 \lambda^2 x_v' \quad (7c)$$

### Self-Diffusion Coefficient of the Solvent

The distortion of the lattice by solute atoms will also produce an effect on the rate of solvent self-diffusion so long as either  $\nu_1' \neq \nu_1^0$  or  $x_v' \neq x_v^0$ . A rigorous formal description of this effect is very complicated, but we may gain some insight into the problem by considering some simple limiting cases.

First, we investigate the situation where the solute atoms are assumed to be stationary. We again suppose that the disturbed region surrounding each solute atom includes only the first coordination shell in which the solvent self-diffusion coefficient is  $D_1'$ . The self-diffusion coefficient of the solvent in all other regions is taken to be that of the pure solvent,  $D_1^0$ . The total volume fraction of the disturbed solvent,  $V$ , is given by:

$$V \cong qX,$$

where  $q$  is the number of solvent atoms in each disturbed region and  $X$  is the atom fraction of the solute.

Now the observed self-diffusion coefficient of the solvent,  $D_1$ , is the resultant coefficient of a duplex

\* Equation (6) is based on the arbitrary assumption that the time required for one interchange between the vacancy and solvent atom corresponds to the time necessary to randomize the position of the vacancy about the solute atom.

system consisting of (assumed) stationary spherical regions of diffusivity  $D_1'$  embedded in a matrix of diffusivity  $D_1^0$ . The corresponding problems for the diffusion of heat and electricity have been solved by Maxwell<sup>5</sup> and Lord Rayleigh<sup>6</sup> and these solutions have recently been reviewed and extended by Landauer.<sup>7</sup> Applied to our material transport problem, Landauer's result is

$$4D_1 = (3V-1)D_1' + (2-3V)D_1^0 \pm \{[(3V-1)D_1' + (2-3V)D_1^0]^2 + 8D_1'D_1^0\}^{1/2} \quad (9)$$

where the sign of the third term is chosen so that  $D_1$  is always positive. For the special case where  $D_1' \gg D_1^0$  and  $V \rightarrow 0$ , Eq. (9) reduces to:

$$D_1 = D_1^0(1+3V). \quad (9a)$$

If solute atoms move, the Landauer equation is no longer strictly applicable and there is an additional "moving-solute effect" on  $D_1$ . We shall now investigate the contribution of the "moving-solute effect" by assuming that the "stationary-solute effect" is negligible. Let the time required to complete one solute diffusion jump be  $\tau_2 = 1/f_2$ , where  $f_2$  is defined by Eq. (6). The total number of solvent-vacancy exchanges,  $n_1'$ , within the first solute coordination shell during the time  $\tau_2$  is

$$n_1' = 4\nu_1' x_v' / f_2 \quad (10)$$

However, there is some upper limit,  $k$ , to the number of these exchanges that constitute effective diffusion jumps, where  $k$  is of the order of the number of atoms in the distorted region. When  $n_1' \gg k$ , the distribution of solvent atoms in the disturbed regions will have been completely randomized before the solute diffusion jump is completed. Although we have been unable to derive analytically an expression for the number,  $\alpha$ , of solvent-vacancy exchanges in the disturbed region, in the time  $\tau_2$ , that actually contribute to solvent diffusion, a relation that we can justify only on the basis that it gives the proper limits is

$$\alpha = k[1 - \exp(-4\nu_1' x_v' / f_2 k)] \quad (11)$$

The total number of effective solvent diffusion jumps, per unit time, in a specimen containing  $N$  atoms, is then

$$n_1 = (1-\alpha X)N x_v^0 \nu_1^0 + N X \alpha f_2 \quad (12)$$

It follows that the observed self-diffusion coefficient of the solvent is

$$D_1 = (1-\alpha X)D_1^0 + \alpha X D_2 \quad (13)$$

For the case  $4\nu_1' x_v' \gg f_2 k$ , Eq. (13) becomes

$$D_1 = (1-kX)D_1^0 + kX D_2 \quad (13a)$$

We have considered only the limiting cases where one or the other of the two effects (fixed-solute or moving-solute) can be ignored. From Eq. (13) it is evident that the condition under which the moving solute effect will be negligible is that  $D_2 \cong D_1^0$ . The fixed solute effect will

be negligible when the number,  $n_e$ , of external solvent atoms that enter the disturbed region in time  $\tau_2$  is appreciably smaller than  $\alpha$ . Since

$$n_e = 7\nu_1^0 x_v' / f_2, \quad (14)$$

the required condition for a negligible fixed solute effect is that

$$7\nu_1^0 x_v' / f_2 \ll \alpha. \quad (15)$$

At the present time, we are unable to propose how to combine the contributions from the two effects in intermediate cases.

Equation (9), derived by considering only the solute atoms as stationary, predicts a linear dependence of  $D_1$  on  $X$  for  $X$  small and  $D_1' \gg D_1^0$ . For larger  $X$  and  $D_1' > D_1^0$ ,  $D_1$  increases at a rate greater than given by a straight line relation.

Equation (13), derived by considering only the moving-solute effect, demands that  $D_1$  vary linearly with  $X$ . However, (13) is strictly valid only for solutions so dilute that the probability that disturbed regions will impinge on each other is negligible. In solution elements where the regions have impinged, the solvent-vacancy exchange frequency is probably accentuated. Hence,  $D_1$  in more concentrated solutions will be greater than is predicted by Eq. (13).

### Other Diffusion Mechanisms

Irrespective of the diffusion mechanism, it is always possible in principle that the solvent self-diffusion will be facilitated in disturbed regions surrounding solute atoms. There will be an effect, analogous to that already proposed for the vacancy mechanism, on the solvent diffusion due to the motion of these regions.

Now assume that the direct interchange of solvent atoms (by any mechanism) is unaffected at any point by solute atoms. Then, if the solute diffuses by an interstitial mechanism, its motion, however rapid, will not affect the rate of solvent self-diffusion. However, if the solute diffuses by a mechanism of direct interchange (with solvent atoms), the solvent self-diffusion coefficient will be described by Eq. (13) with  $\alpha$  unity.

### Theories of Overhauser<sup>3</sup> and Lazarus<sup>4</sup>

Overhauser has developed a theory for the effect of solute atoms on solvent self-diffusion based on the assumption that the potential energy barrier opposing solvent diffusion is changed by local elastic strains arising from the size disparity of solute and solvent atoms. The energy barrier shift was assumed to be due to changes in the ion-ion repulsive interaction effected by the introduction of local strain. This interaction was represented by the Born-Mayer expression:

$$U = H \exp(-r/\rho), \quad (16)$$

where  $r$  is the interatomic distance and the constants

$H$  and  $\rho$  are chosen to describe the measured elastic constants of the pure solvent.

Assuming as an approximation that all solvent atom sites are equivalent (i.e., the traverse of a diffusing atom is completely random irrespective of the position of the solute atoms), Overhauser obtains, by performing a space average over solute atom positions:

$$D_1 = D_1^0 \exp(bX), \quad (17)$$

where

$$b = \left( \frac{128\pi}{45} \right) \left( \frac{gK}{kT} \right)^2 \left( \frac{a}{r_0} \right)^3 + \left( \frac{32\pi\gamma}{3} \right) \left( \frac{gK}{kT} \right) (1-3\lambda); \quad (17a)$$

$$K = \left( \frac{3}{2} \right)^{1/2} H \left( \frac{a}{\rho} \right) \exp \left( - \frac{3^{1/2} a}{2^{3/2} \rho} \right); \quad (17b)$$

$$\gamma = 2(1-2\mu)/(1+\mu); \quad (17c)$$

$$\lambda = \exp[-(2-3^{1/2})a/2^{3/2}\rho]; \quad (17d)$$

$g$  is a measure of the size disparity between solute and solvent atoms that Overhauser deduced from the difference in lattice parameters of the atoms in their pure crystals,  $a$  is the lattice parameter of the pure solvent,  $\mu$  is Poisson's ratio, and  $r_0$  is the cutoff distance, usually set equal to  $a$ , introduced to prevent the strain from going to infinity at the center of an impurity atom. Overhauser's assumption of the equivalence of sites may be a fair approximation for relatively concentrated solutions but is certainly inadmissible in the limit of dilute solutions.

Lazarus<sup>4</sup> has also developed a theory relating  $\nu_1'$  to the interatomic forces. He assumes that  $\nu_1'$  is single-valued and different from  $\nu_1^0$  only in the first coordination shell of the solute atom. It is supposed that the activated state for diffusion is produced by a half-unit shear of the cell containing the diffusing atom and lattice vacancy.  $\nu_1'$  is then calculated from the microscopic shear modulus evaluated according to the method of Fuchs.<sup>8</sup> In addition, the theory gives the vacancy concentration,  $x_v'$ , in the solute coordination shell.

Also assuming parallel addition of the solution elements, Lazarus obtains for very dilute solutions:

$$D_1 = D_1^0 [1 - 4X + 4X \exp(\Delta E/kT)], \quad (18)$$

where  $\Delta E = E_1 - E_1'$ .  $E_1$  and  $E_1'$  are the energies required to move a solvent atom into a vacancy when it is remote from, and in the first coordination shell of, the solute atom, respectively.  $E_1$  and  $E_1'$  are directly proportional to the corresponding microscopic shear moduli. Formally, Eq. (18) is equivalent to our Eq. (13) when it is assumed that  $4\nu_1' x_v' \ll f_2 k$ .

## COMPARISON BETWEEN THEORY AND EXPERIENCE

## Comparison with Our Formal Theory

Since a complete comparison of the present theory with experience requires a knowledge of the diffusion coefficients of both solvent and solute, this discussion will be restricted largely to the results from the silver-lead alloys.

As already noted, the dependence of  $D_{Ag}$  on  $X_{Pb}$  is best fitted by a linear relation, with a slope  $b=129$  at  $1000^\circ\text{K}$ . Also, at  $T=1000^\circ\text{K}$  and at infinite dilution of lead,  $D_{Pb}/D_{Ag}\cong 13$ .\* By comparing Eqs. (2) and (13) we see that

$$\alpha = b / \left( \frac{D_2}{D_1^0} - 1 \right). \quad (19)$$

Hence the description of the observed effect of lead on  $D_{Ag}$  solely in terms of the moving solute effect would require that  $\alpha \cong 11$ . On the other hand, since  $D_2/D_1^0 = f_2/\nu_1^0 x_v^0$ , it follows that  $n_e \ll \alpha$  so long as  $x_v'$  is not appreciably larger than  $x_v^0$ . It therefore appears that the fixed-solute effect may be negligible in the Ag-Pb alloys.

If the major contribution to the enhancement of  $D_{Ag}$  by lead does arise from moving-solute effect, and if the disturbed region does not extend significantly beyond the first coordination shell of the lead atoms, then in order that  $\alpha \cong 11$ , it is also necessary that  $4\nu_1' \gg f_2/x_v'$  (see Eq. 11). Furthermore, it may be seen from Eq. (7) that if  $4\nu_1' \gg f_2/x_v'$ , then also  $4\nu_1' \gg \nu_2$ , which implies that the rate of self-diffusion of lead in Ag-Pb solutions is mainly controlled by the frequency of the exchange of lead atoms with vacancies (i.e.,  $D_2$  is given by Eq. 7c).

In any event, there is not the one-to-one correspondence, suggested in our first note,<sup>1</sup> between the number of lead diffusion jumps and the number of silver diffusion jumps facilitated by lead atoms. Rather, it seems clear that a single lead atom facilitates the diffusion jumps of several silver atoms in its vicinity.

Since we have no data on the rate of diffusion of Cu, Ge, and Al in the corresponding silver alloys, we cannot calculate  $\alpha$  but we can examine the dependence of  $D_{Ag}$  on  $X$  for these alloys. For  $X \gtrsim 0.03$ , a linear relation between  $D_{Ag}$  and  $X$  does describe satisfactorily the data for all solutes. In the Ag-Ge and Ag-Al alloys, this dependence is not linear over the entire concentration range, but can be described by an exponential relation. This exponential dependence is, of course, not unique. As already noted, a greater than linear increase of  $D_1$  with  $X$  can be qualitatively accounted for on the assumption that the solvent-vacancy exchange frequency is larger in volume elements where the disturbed regions around the solute atoms overlap than within isolated disturbed regions.

\* The ratio  $D_{Pb}/D_{Ag}$  varies between 10 and 14 in temperature range  $700^\circ\text{--}800^\circ\text{C}$ .

## Comparison of Experimental Results with the Theories of Overhauser and Lazarus

In order to compare the results with the theory of Overhauser, we have calculated values of  $b$  from Eq. (17a) and compared these with the experimental values (Table III). In making these calculations, we have chosen  $\mu=0.37$ ,<sup>9</sup>  $a=4.076 \text{ \AA}$ ,<sup>10</sup>  $D=2.00(10)^{-6}$  ergs/ion pair, and  $\rho=0.166 \text{ \AA}$ . Rather than estimate the parameter  $g$  from the lattice constants of the pure elements, we calculate it from the equation derived by Eshelby<sup>11</sup>

$$\frac{3\Delta a}{a} = 16\pi(1+\gamma)gX, \quad (20)$$

relating  $g$  to the change in lattice parameter of silver,  $\Delta a$ , effected by the introduction of atom fraction  $X$  of solute. Using the lattice parameter data of Raub and von Polaczek-Witteck<sup>12</sup> for Ag-Pb, Owen and Rogers<sup>13</sup> for Ag-Cu, Foote and Jette<sup>14</sup> for Ag-Al and Owen and Rowlands<sup>15</sup> for Ag-Ge, we obtain the following values:  $g_{Pb} = +8.1(10)^{-3}$ ,  $g_{Cu} = -3.92(10)^{-3}$ ,  $g_{Al} = -1.33(10)^{-3}$ ,  $g_{Ge} = +2.8(10)^{-4}$ . Further, instead of making the assumption that  $r_0 = a$ , we shall put the comparison between theory and experiment on a relative basis by choosing  $r_0$  so that  $b_{calc} = b_{exp}$  for copper and assuming that  $r_0$  is the same ( $2.17 \text{ \AA}$ ) for the other systems. The results of the final calculation for  $T=1000^\circ\text{K}$  are shown in Table IV. Evidently the Overhauser theory

TABLE IV. Comparison of values of  $b$  for  $1000^\circ\text{K}$  from experiment ( $b_{exp}$ ) and calculated from Overhauser's theory ( $b_{th}$ ).

Solute	$b_{exp}$	$b_{th}$
Cu	10.2	10.2
Pb	86.0	72
Ge	32.7	0.40
Al	15.1	0.2

satisfactorily describes the effect of dissolved lead or copper on the self-diffusion coefficient of silver, but the effects of dissolved germanium and aluminum are about two orders of magnitude larger than calculated on the basis of Overhauser's theory. We conclude that the simple strain energy theory of solid solutions is much too limited in its scope to describe adequately the diffusion behavior of all binary solid solutions. Electronic disturbances, not predictable by the simple strain the-

TABLE V. Comparison of values of the parameter  $\beta = [(D_{Ag}/D_{Ag}^0) - 1]$  at  $1000^\circ\text{K}$  from experiment,  $\beta_{exp}$ , and calculated from Lazarus' theory,  $\beta_{th}$ .

Solute	$X$	$\beta_{exp}$	$\beta_{th}$
Pb	0.01	1.3	0.24
Cu	0.05	0.7	-0.11
Ge	0.05	4.1	0.89
Al	0.05	1.1	0.38



ory, may accompany solution and have an important effect on the rate of diffusion of solvent atoms.

Table V compares the experimental values,  $\beta_{\text{exp}}$ , of the parameter  $\beta = [(D_{\text{Ag}}/D_{\text{Ag}}^0) - 1]$  at 1000°K with the values  $\beta_{\text{th}}$  calculated on the basis of Lazarus' theory. The effects predicted by his theory are, in the case of Al, Ge and Pb, less than observed by a factor of 3 to 5. Also the observed influence of copper on  $D_{\text{Ag}}$  is opposite in direction to that predicted by Lazarus' theory. However, Lazarus' theory is one order of magnitude closer to agreement with experience on aluminum and germanium additions than is Overhauser's.

In summary, no theory has yet been developed that adequately relates for all alloys the effect of solute atoms on the self-diffusion coefficient of the solvent to the interatomic forces.

#### ACKNOWLEDGMENT

We are pleased to acknowledge the assistance of H. Brandhorst, J. D. Smith and especially M. W. Ranney on the experimental measurements. We have profited greatly from numerous discussion with A. W.

Overhauser. Also we are grateful to D. Lazarus for sending us a copy of his paper in advance of publication.

#### REFERENCES

1. R. E. Hoffman and D. Turnbull, *J. Appl. Phys.* **23**, 1409 (1952).
2. L. Slifkin, D. Lazarus, and T. Tomizuka, *J. Appl. Phys.* **23**, 1032 (1952).
3. A. W. Overhauser, *Phys. Rev.* **90**, 393 (1953); **91**, 246A (1953).
4. D. Lazarus, *Phys. Rev.* **93**, 973 (1954); A.S.M. Seminar on Imperfections, Chicago (1954), to be published.
5. J. C. Maxwell, *Electricity and Magnetism*, Vol. 1, Third Ed. (Oxford Press, London, 1914).
6. Lord Rayleigh, *Phil. Mag.* **34**, 481 (1892).
7. R. Landauer, *J. Appl. Phys.* **23**, 779 (1952).
8. K. Fuchs, *Proc. Roy. Soc. (Lond.)* **151**, 585 (1935); **153**, 622 (1936); **157**, 444 (1936).
9. E. Schmid and W. Boas, *Plasticity of Crystals* (F. A. Hughes, London, 1950).
10. R. W. G. Wyckoff, *Crystal Structures* (Interscience Publishers, New York, 1951).
11. J. D. Eshelby, *J. Appl. Phys.* **25**, 255 (1954).
12. E. Raub and A. von Polaczek-Witteck, *Z. Metallk.* **34**, 93 (1942).
13. E. A. Owen and J. Rogers, *J. Inst. Metals* **57**, 257 (1935).
14. F. Foote and E. R. Jette, *Trans. A.I.M.E.* **143**, 151 (1941).
15. E. A. Owen and V. W. Rowlands, *J. Inst. Metals* **66**, 361 (1940).

## BiMn "SPIRE" GROWTHS INDUCED BY A MAGNETIC FIELD\*

B. W. ROBERTS†

BiMn "spires" or columns of highly oriented ferromagnetic BiMn crystallites have been found to grow out of a mixture of molten Bi and particles of Mn metal. The growth direction is along an applied magnetic field and has occurred both perpendicular to and against the gravitational field. A first mechanism for formation postulates the enhancement of the nucleation probability at the tip of a spire by the high magnetic field present. The second mechanism requires the formation of ferromagnetic BiMn particles throughout the molten Bi volume. These particles are then pulled to the spire tip, where they are aligned and subsequently grow by size preference.

### CROISSANCE EN SPIRALE DE Bi-Mn PRODUITE PAR UN CHAMP MAGNÉTIQUE

Une texture basaltique de cristaux ferro-magnétiques Bi-Mn fortement orientés peut se produire à partir d'un mélange de Bi fondu et de particules de Mn. La direction de croissance est parallèle au champ magnétique appliqué et peut se produire aussi bien perpendiculairement que parallèlement au champ de la pesanteur. Un premier mécanisme explique cette formation par l'accroissement de la germination à l'extrémité d'une spire par le champ magnétique appliqué, tandis que le second fait appel à la formation de particules Bi-Mn ferromagnétiques dans le volume fondu, ces particules étant ensuite attirées par la pointe de la spire où elles seraient alignées et où elles pourraient grossir.

### DURCH EINWIRKUNG EINES MAGNETISCHEN FELDES HERVORGERUFENES NADELWACHSTUM BEI BiMn ("SPIRE" GROWTH)

Aus einer Mischung von geschmolzenem Bi und Teilchen aus Mn-Metall wachsen BiMn "Nadeln" ("Spires") oder Säulen aus sehr gut orientierten ferromagnetischen BiMn-Kristallen. Die Wachstumsrichtung liegt in Richtung des angelegten magnetischen Feldes und trat sowohl senkrecht zum als auch gegen das Gravitationsfeld auf. Ein erster Bildungsmechanismus setzt eine erhöhte Keimbildungsmöglichkeit an der Spitze der Nadeln voraus, hervorgerufen durch das starke magnetische Feld. Der zweite Mechanismus verlangt die Bildung von ferromagnetischen BiMn-Teilchen im gesamten geschmolzenen Bi. Diese Teilchen werden dann an die Spitze der Nadel gezogen, wo sie anschliessend durch Grössenauslese wachsen.

## INTRODUCTION

An interesting magnetic growth phenomenon has been observed in two cases during the low-temperature diffusion formation of BiMn alloy. BiMn "spires" or columns of highly oriented crystallites have grown out of a central mass of elements both against and perpendicular to the gravitational field, but in both cases along an imposed magnetic field. The diffusion temperature lies between the melting point of Bi (271°C) and the modified Curie temperature of BiMn (360°C ↑ and 340°C ↓). The magnetic moments in BiMn are found to be parallel to the  $c_0$  axis above 84°K up to the Curie temperature.

### First Case: Growth Perpendicular to Gravity

A pressed rod, 3/8 inch in diameter and 1 inch long, composed of Bi and Mn powders was sealed into an evacuated pyrex tube and supported horizontally inside a small resistance furnace which in turn was suspended in a 1500±300 oersted permanent magnet field. The furnace was held at 315°±10°C for 25 hours. After the pyrex tube was broken open and the annealed powder rod removed, several columns of BiMn particles, hereafter called spires, were noticed on the end of the pressed rod. One spire about 0.5 cm in length and eight or ten

shorter single spires had grown out along the lines of the imposed magnetic field and at the same time perpendicular to the gravitational field. A single spire had a diameter of roughly 0.5 mm.

The largest group of spires is shown in Fig. 1 at a magnification of 35X after being positioned between the poles of a small permanent magnet. The depth of field was small so that all regions are not in focus. The individual spires had sharp projections pointing out radially from each column center at random positions along the length. The projections appear to favor pointing at one another.

An X-ray rotation picture was taken of a single spire which appeared in all respects like those composing the group in Fig. 1. This X-ray picture showed a single crystal-type pattern with the spots elongated several degrees. All of the elongated and discontinuous reflections observed index on the BiMn pattern, and indicate the  $c_0$  axis to lie along the length of the spire. Continuous X-ray lines are found to be Bi. BiMn is hexagonal with the NiAs structure, and Bi has a rhombohedral structure. The spires are coated with Bi and this is fortunate since finely divided BiMn is pyrophoric and larger-size grains absorb moisture readily.

Since the spires align themselves along lines of magnetic force and have been shown by X-ray means to be BiMn with the  $c_0$  axis pointing along the length, there is little doubt that highly oriented BiMn alloy has been formed by the influence of an imposed magnetic field.

\* Received December 9, 1954.

† Metallurgy Research Department, General Electric Research Laboratory, Schenectady, New York.

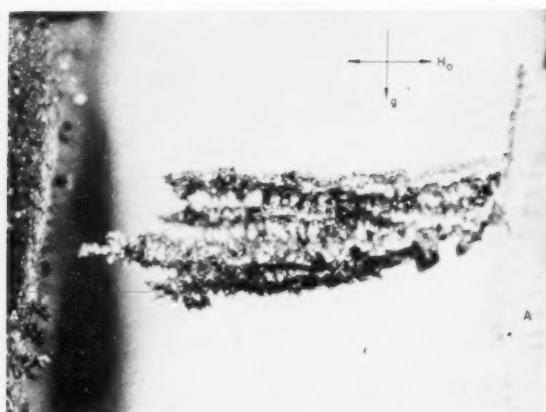


FIG. 1. BiMn "spires" grown perpendicular to gravitational field. 35X. A=small magnet poles. Figure reduced to one-third.

It is also unusual in that a large mass of material has been transported by diffusion away from a central mass.

### Second Case: Growth Against Gravity

Stock Bi and electrolytic Mn powders which passed through a 100-mesh screen were sealed into a pyrex tube about 1 inch in diameter after mixing. This tube was wrapped with Nichrome tape and asbestos in order to maintain a temperature of  $315^{\circ}\pm 10^{\circ}\text{C}$  for about 26 hours in the gap of a large permanent magnet.\* Figure 2 shows the arrangement in the magnet and the position of the spires which were situated in a nearly homogeneous magnetic field of  $8700\pm 200$  oersteds and grew from two globules of Bi metal which did not react completely with the Mn present in the end of the tube. The spires reached the enclosing pyrex wall in several instances after growing vertically about 1 cm. The outer surfaces were not as irregular as those found in the first case, shown in Fig. 1, but did show parallel striations running around the spire. No record was made of the external appearance, but the metallographs shown in Fig. 3 illustrate cross sections of a Bi globule, showing the arrangement of BiMn crystallites in the spires.

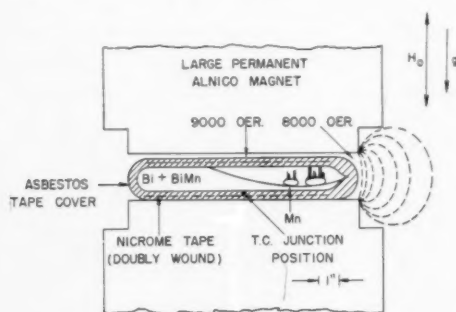
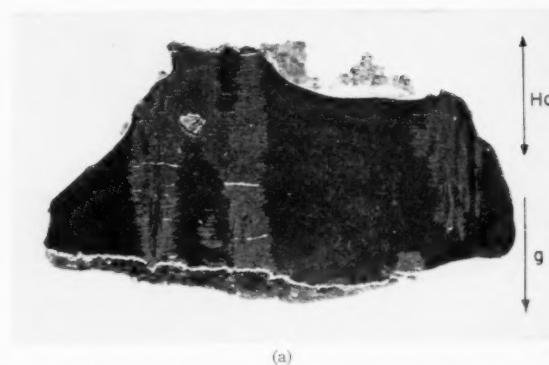
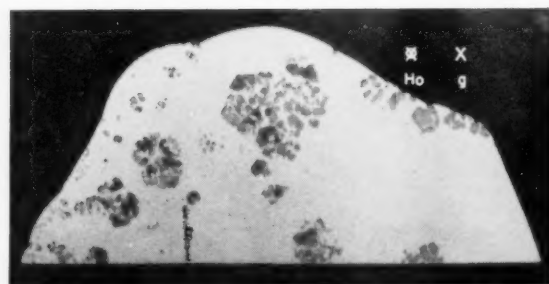


FIG. 2. Experimental arrangements for spire growth against gravity.

\* Through the courtesy of Dr. William Whittamore of Brookhaven National Laboratory. See RSI 22, 73 (1951).



(a)



(b)

FIG. 3. (a) Cross section of Bi globule, sectioned parallel to axis of spires. (10X, 0.1 per cent Nital swab etch.) (b) Cross section of Bi globule, sectioned perpendicular to axis of spires. 10X.

Figure 3a shows a cross section of the spires when the plane of sectioning is parallel to the spire axes. Lighter-colored BiMn crystallites are situated in an array of platelets perpendicular to the spire axes and these are seen to pass from the base of the Bi globule out through the top. The spire in the background center extended about 1 cm until it touched the pyrex tube wall. It has been broken off by handling. In the section shown it is seen that the Bi matrix exists along the center of several of the spires. In Fig. 3b this is more clearly shown to be the general case since each spire is seen to be made of crystallites which are roughly circular in cross section and which do not come into contact at the center, but have the Bi matrix (light area in this metallograph) forming channels between.

Close examination shows that in many cases the roughly circular particles have straight edges which intersect at about 120 degrees. This reflects the hexagonal crystal structure of BiMn since the section is roughly perpendicular to the  $c_0$  axis of the observed crystallites. Even the smallest groups of cross-sectioned particles seen have a wall of Bi matrix dividing the crystallite columns. Considering the two sections through the BiMn spires, it is seen that the shape of most particles are flattened ellipsoids of revolution which have a sharp outer edge. At the center of a spire some of the particle edges are "squared-off," as shown in Fig. 4. This blunt inner edge of the spheroids would appear to be connected with the direction of impingement of new crystallites or the rapid depletion of Mn

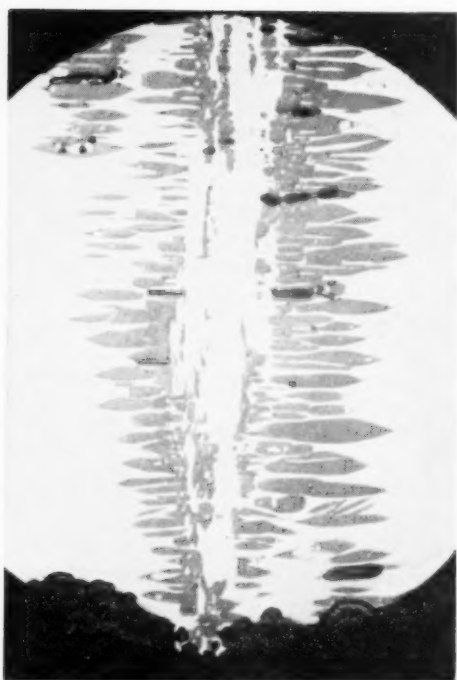


FIG. 4. Area of Fig. 5a photographed at 100 $\times$  to show detail of spire growth. Figure reduced to one-half.

from the solution in the inner channel. The sample matrix was made up of many large Bi grains which appeared to be randomly oriented.

When BiMn grains have been smoothly polished, either dry or with alcohol as a lubricant to help prevent water reacting with the surface, it has been found that the magnetic domains are clearly visible<sup>1</sup> when observed through a microscope with the Nicol prisms nearly crossed. The domains appear as black and white stripes, or, in certain orientations, as light grey to dark grey stripes of varying intensities. This effect was first observed grossly with polarized light by Kerr<sup>2</sup> on large surfaces of polycrystalline iron.

The pattern of the domains gives direct evidence as to the orientation of the BiMn crystallite at the surface section. Figure 5a shows several patterns observed on the same grain when the polarized light entered the surface and was scattered back nearly parallel in both cases to the  $c_0$  axis. This surface is the same as shown in Fig. 3b. Three pattern types are visible. The lower left corner shows a zig-zag or "rick-rack" pattern which in many places makes abrupt turns of about 120 degrees. Above this region the domains have a fern-like arrangement which frequently deviates to the zig-zag design. On the right-hand edge the domains appear to have parallel edges and interlock in an extended maze. It is evident in all of these designs that the domain or Bloch walls seek an equilibrium configuration in which they are equally spaced.

Figure 5b shows the polarized light pattern observed

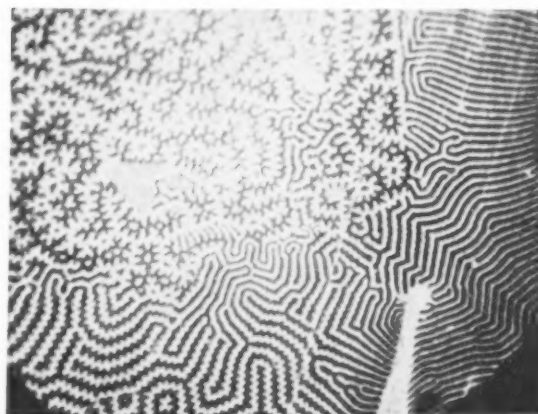
when the  $c_0$  axis is roughly parallel to the plane of sectioning. The domains are seen to lie approximately along the  $c_0$  and magnetic axes. There are irregularities as the domain approaches the top edge of the crystallite which have not been explained. The domains propagate through crystallite boundaries. In the lower right-hand corner a grain is shown with parallel domain boundaries. The Kerr effect, however, is a minimum under this condition so that the relative reflected light intensities are small and it is thus difficult to see.

The domain patterns bear out the observed direction of the magnetic axis and the X-ray evidence for the orientation of the  $c_0$  axis.

#### POSSIBLE EXPLANATIONS OF THE BiMn SPIRES

We have described two independent experiments in which Bi and Mn atoms have moved over many atomic distances while guided by a magnetic field and at the same time not have been affected by the presence of the earth's gravitational field.

A first thought might be that the elements in question have condensed from the vapor phase in an inhomogeneous magnetic field. This postulate was tested ex-



(a)



(b)

FIG. 5. (a) Polarized light patterns observed when section surface is perpendicular to  $c_0$  axis. 500 $\times$ . Figure reduced to one-half. (b) Polarized light patterns observed when section surface is roughly parallel with  $c_0$  axis. 500 $\times$ . Figure reduced to one-third.



perimentally by placing a small permanent magnet with a field of 3000 to 4000 oersteds between two piles of Mn and Bi powders all suitably held in an evacuated pyrex bulb. The assembly was placed in a furnace and held at 315°C for 48 hours. At the end of this time, no magnetic formations were observed on the poles of the magnet. The obvious explanation of this lack of reaction is the very low vapor pressures present at 315°C. For Mn, the pressure is  $10^{-12}$  micron, and for Bi it is  $10^{-6}$  micron. Both values are extrapolated from Dushman.<sup>3</sup>

All evidence points instead to diffusion of the Mn into the Bi and then the formation of the spires by a series of steps.

It is pictured that Mn atoms from the Mn powder upon which the molten Bi globules rest have diffused into the Bi. When a certain concentration of Mn is built up on the Bi globule, precipitation of BiMn will occur. The Mn concentration necessary for precipitation would appear to be low since Guillaud<sup>4</sup> has observed the ferromagnetic BiMn hysteresis transformation nearly across the Bi-Mn phase diagram. Guillaud's last point of measurement was on a sample which contained 2 atomic per cent Mn. This sample had been prepared by bringing the elements down slowly from 900°C to 440°C. Thus, it is possible that on the order of only 1 atom per 100 may be required in solution for precipitation of BiMn alloy.

It is probable that BiMn particles will first nucleate and precipitate at the lower surfaces of the Bi globules since the Mn will diffuse through the base and initially have the greatest concentration there. The first particles thus formed will be situated at random about the globule base.

The experiments have shown that the spires have continued to propagate in rough columns through the molten Bi along the lines of an applied magnetic field. Now a magnetic particle in a homogeneous magnetic field will be subjected to no translational force. It will be aligned with the magnetic field. A magnetic particle in an inhomogeneous field, however, will have a force exerted upon it such that it will be pulled to the region of greatest magnetic flux.

When a BiMn particle above the critical size\* necessary to exhibit ferromagnetic properties is formed and oriented with the field, it will have at the poles a magnetic field  $H_{\text{end}}$ :

$$H_{\text{end}} = H_0 + (4\pi - N)I_s,$$

where  $H_0$  is the applied external field,  $N$  is the shape demagnetization factor which varies between zero and  $4\pi$ , being zero along the axis for the case of a long, thin needle and  $4\pi$  for a flat disc with the direction of magnetization perpendicular to the disc.  $I_s$  is the saturation magnetization. Therefore, at the end of any BiMn particle in the Bi matrix, a larger inhomogeneous field is found than that originally impressed on the sample.

\* The critical size is estimated to be a particle with ten atoms on a side.

Two possible methods of spire formation in the matrix can be visualized. The first is to have volume nucleation of BiMn particles which are above the critical size and thus ferromagnetic. These particles are then pulled to the region of highest magnetic flux which is near the end of another oriented BiMn particle. Here they would be pulled into contact with the existing surface and aligned with the field present:  $H_{\text{end}}$ . The new particle would in turn become the tip of a spire which would be the attractive point for the next particle to enter the region.

A second mode of spire formation involves the enhancement of the nucleation probability at the spire tip. We will calculate the energy difference per unit volume of a particle of BiMn which is situated in the molten Bi far from a ferromagnetic particle and of one placed at the tip of a spire where the existing field includes both  $H_0$  and the pole field of the ferromagnetic BiMn particle.

Evidence for the initial shape of a BiMn particle is not available. If it were an infinitely thin disc,  $N$  would equal  $4\pi$  and the additional field would be zero. The initial form is probably close to a sphere where  $N$  would be  $4\pi/3$ , so that  $H_{\text{end}} = H_0 + (8/3)\pi I_s$ .

The magnetic domain patterns (Fig. 5) show an alternating arrangement of domain orientation at the surface of a particle which did not exist at the time of formation. The crystallites were single-domain initially, and then the domains rearranged when  $H_0$  was removed or after the lateral growth was large enough to cause shape energies to require more than one domain to be present.

Now consider the energy per unit volume of a single domain BiMn particle in the matrix:

$$E_{\text{Bi}} = -H_0 I_s,$$

and the same particle at the end of a spire with  $N=0$ ,

$$E_{\text{end}} = -H_0 I_s - 4\pi I_s^2.$$

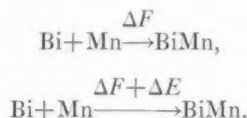
The difference of these energies is:

$$\Delta E = -4\pi I_s^2 = -\frac{B_s^2}{4\pi} \quad (B_s = 4\pi I_s),$$

and since the ferric induction ( $B_s$ ) for BiMn is about 8000 gauss,<sup>4</sup> the last equation yields about  $-5 \times 10^6$  ergs/cc  $\approx -0.1$  gm-cal./cc, depending upon the initial value of  $N$  and the stage of spire growth. The longer a spire becomes, the more it approximates a long, thin rod, so that the magnetic energy ( $-B_s^2/4\pi$ ) will be approached as the spires grow. Thus, the BiMn particle would prefer to exist in the ferromagnetic phase at the tip of a spire rather than as the elements in solid solution or a BiMn particle below the critical size for ferromagnetism. This energy would aid nucleation of the two elements or the enlargement of BiMn particles

which were floating in solution with sizes smaller than the critical size.

We may schematically show the proposed interaction of the magnetic energy in these equations:



where  $\Delta F$  is the free energy of formation. The additional increment of magnetic energy will drive the alloying reaction to completion only if the system of Mn, Bi, and BiMn alloy is near equilibrium and within the energy limit given by  $\Delta E$ . There is very little thermodynamic information available on this reaction. It is known that the product once formed is stable (in the absence of oxygen or water) up to 445°C, and that the alloy forms with only 2 atomic per cent Mn present in the Bi solution.<sup>3</sup> If the amount of Mn necessary was very much less—say, on the order of a fraction of 1 per cent—then near-equilibrium conditions may have existed under the experimental arrangement. A source of Mn was present and the temperature was low.

It has been observed experimentally that molten Bi wets particles of BiMn. In addition, all of the spires appear to have channels of Bi matrix running along their length. This suggests capillary action for the method of transport of material along the spires away from the central mass. From the following equation we may compute the approximate height to which Bi would be pulled in a capillary:

$$mgh = 2\pi r\gamma,$$

where  $\gamma$  is the surface tension. Since  $m = \pi r^2 h d$ , this yields  $h^2 = 2\gamma / r d g$ , where  $h$  is the height to which the Bi is pulled,  $r$  is the radius of the capillary,  $d$  is the density of molten Bi, and  $g$  is the acceleration due to gravity. Using for the Bi surface tension,  $\gamma = 388$  dynes/cm (Handbook of Chemistry and Physics, 1953),  $r = 0.005$  cm,  $d = 9.8$  gm/cm<sup>3</sup>, and  $g = 980$  cm/sec<sup>2</sup>,  $h$  is found to be about 5.7 cm. This height is nearly six times as great as the height observed in the spire growths.

The crystallites are found to grow, after formation and alignment at a spire tip, to a size on the order of mils. The photomicrograph of Fig. 4 also shows that the edges of particles facing the channels are blunt, while those growing out into the matrix are pointed. We may explain the initial growth as that of preferential size; in other words, very small particles would be absorbed onto the surface of larger particles due to surface energy differences. The blunt edges on the inner BiMn particles may be simply due to the lesser quantity of Mn or BiMn diffusing up the thin Bi channels as compared to the large amount diffusing out of the volume from which the outer pointed particles may absorb new material. The preferred crystallographic direction of growth is in the basal plane.

## CONCLUSION

Two cases of growth of columns of BiMn alloy along an imposed magnetic field have been observed during low-temperature diffusion experiments. These spires are found to be made up of highly oriented BiMn crystallites with their crystal and magnetic axes aligned closely with an applied magnetic field. The columns are separated by thin walls of Bi which are held in place by surface tension.

In order to explain the growth of these spires away from the central mass of material through which their component materials have traveled, consideration of the influence of the imposed magnetic field seems imperative. One mechanism for formation is schematically shown in Fig. 6a. It is postulated that the large anisotropic magnetic field existing at the end of a spire contributes an energy on the order of 0.1 gm-cal/cc in excess of the free energy of formation. This additional energy would enhance the probability of nucleation of a BiMn particle at the spire tip. It is also possible that BiMn particles which are below the critical size to exhibit ferromagnetism would be caused to grow above this limit in the spire tip vicinity. For this mechanism to operate one would need only the imposed field and a source of new Mn atoms or subcritical BiMn particles to propagate the growth. New material would be supplied by diffusion through the molten Bi. This mechanism would require conditions near equilibrium for the reaction and for this no definite data are available. Equilibrium here implies uniformity of Mn concentration in the molten Bi.

A second possible mechanism would require the formation throughout the Bi volume of small crystallites of BiMn alloy which are above the critical size and thus ferromagnetic. These particles would be pulled by the force created by the inhomogeneous field acting on the magnetic poles to the point of greatest magnetic flux which exists at the spire ends. This is schematically shown in Fig. 6b.

The latter mechanism requires that the ferromagnetic

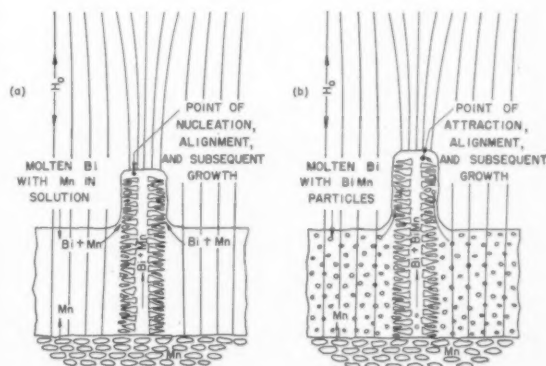


FIG. 6. (a) Schematic drawing of localized nucleation and formation of a BiMn spire. (b) Schematic drawing of volume nucleation and formation of a spire.

particles would not immediately coalesce to larger-size particles with less surface energy since greater difficulty would be had in traversing the Bi channels to the tip of a spire where they would be attracted, aligned, and subsequently grow in size.

The magnetic energy nucleation mechanism would appear to be the better explanation of these BiMn spire growths; however, since it is necessary that conditions near equilibrium prevail during formation, the existence of equilibrium should be demonstrated. Insufficient data exist to establish clearly the state of the system during the spire growth formation.

Growth of the spires from the base as has been demonstrated<sup>5</sup> for tin "whiskers" was not considered here because of the much larger diameter and consequent greater mass.

#### ACKNOWLEDGMENTS

Many helpful talks with D. Turnbull are acknowledged. C. P. Bean has given generously of his time in discussing the magnetic aspects of this phenomenon. The metallographs were skillfully prepared by Miss Jean Hurd and E. F. Koch. I. S. Jacobs carefully read the manuscript.

#### REFERENCES

1. B. W. Roberts and C. P. Bean, *Phys. Rev.* **96**, 1494 (1954).
2. John Kerr, *Phil. Mag.* **169**, 321 (1877).
3. Saul Dushman, *Scientific Foundations of Vacuum Techniques* (John Wiley, New York), p. 750.
4. Charles Guillaud, Thesis, Strasbourg, 1943. *J. Phys. et le radium*, **12**, 223 (1951).
5. S. E. Koonce and S. M. Arnold, *J. Appl. Phys.* **24**, 365 (1953).

# A METHOD FOR THE MEASUREMENT OF ELASTIC RELAXATION, AND ITS USE FOR DETERMINATION OF THE SOLUBILITY OF CARBON IN $\alpha$ -IRON

E. LINDSTRAND\*

A new method is developed for measuring elastic relaxation. The samples are in the form of spirals, which are twisted through a certain angle and then released. The course of creep is registered photographically, and thus the magnitude of the elastic after-effect is found. The method is applied to the determination of the solubility of carbon in  $\alpha$ -iron. The specimens are made so large that the carbon in solution can be determined directly by weighing, which is a considerable advantage of the method. First, the relation between carbon content and after-effect was determined. Supersaturated samples were then quenched from different temperatures, and thus the solubility limit was obtained between 400 and 700°C. The results deviate both from earlier investigations using the torsional pendulum method, and also considerably from the results obtained by calorimetric methods. The latter need correction, partly because of the recently discovered precipitation of  $\text{Fe}_2\text{C}$  at lower temperatures. The equilibrium between this carbide and carbon in solution is also discussed.

Une nouvelle méthode est développée pour le mesurage du relâchement élastique. Les échantillons, qui sont en spirales, sont tordus un certain angle et ensuite relâchés. Le cours de glissement est enregistré photographiquement, et de cette manière on trouve la grandeur de la répercussion. La méthode est appliquée à la détermination de la solubilité de carbone en fer- $\alpha$ . Les échantillons ont une grandeur permettant la détermination du carbone en dissolution directement par pesage, fait constituant un grand avantage de la méthode. Premièrement la relation entre contenu de carbone et répercussion a été déterminée. Des échantillons sursaturés furent ensuite refroidis brusquement de différentes températures, et de cette manière la limite de la solubilité a été obtenue entre 400 et 700°C. Les résultats devient, et des résultats antérieurs obtenus en utilisant la méthode de pendule de torsion, et de ceux obtenus par méthodes calorimétriques. Celles-ci doivent être corrigées entre autre à cause de la précipitation de  $\text{Fe}_2\text{C}$  à des températures plus basses, trouvée récemment. L'équilibre entre ce carbide et fer en dissolution est de même discuté.

Es ist eine neue Methode für die Messung der elastischen Nachwirkung entwickelt worden. Die Proben sind spiralförmig und werden um einen gewissen Winkel gedreht und dann ausgelöst. Der Kriechverlauf wurde photographisch registriert, und in dieser Weise findet man die Grösse der elastischen Nachwirkung. Die Methode ist auf die Bestimmung der Löslichkeit von Kohlenstoff in  $\alpha$ -Eisen angewandt. Die Proben sind so gross, dass der Kohlenstoff in Lösung direkt durch Wägung bestimmt werden kann, was ein grosser Vorteil dieser Methode ist. Zuerst wurde das Verhältnis zwischen Kohlenstoffhalt und Nachwirkung bestimmt. Übersättigte Proben wurden von verschiedenen Temperaturen abgeschreckt, und in dieser Weise die Löslichkeitsgrenze zwischen 400 und 700°C erhalten. Die Resultate unterscheiden sich sowohl von Untersuchungen, mit der Torsionspendel-Methode ausgeführt, als auch wesentlich von den Resultaten, die auf kalorimetrischem Wege erhalten wurden. Diese müssen u.a. korrigiert werden infolge der kürzlich entdeckten Ausscheidung von  $\text{Fe}_2\text{C}$  bei niedrigen Temperaturen. Das Gleichgewicht zwischen diesem Karbid und Kohlenstoff in Lösung wird auch besprochen.

## 1. INTRODUCTION

Earlier determinations of the solubility of carbon in  $\alpha$ -iron by calorimetric methods<sup>1</sup> and by relaxation methods<sup>2,3</sup> have given results which differ appreciably. In the present work the solubility has been determined from the elastic relaxation, measured by a new method proposed by Professor Borelius. The samples are in the form of spirals, which are twisted through a certain angle. They are then released, and the extension due to the elastic after-effect, which in simple cases diminishes exponentially, is measured as a function of time. The course of creep is registered photographically, and the spirals are held at a temperature where the time constant has a convenient value. Thus for C in  $\alpha$ -Fe,  $-5^\circ\text{C}$  gives 33 seconds. Compared with earlier measurements where the damping of torsional oscillations has been observed, this method has some advantages. The samples can be made so large that the carbon content may be determined by weighing, and the relaxation is ob-

served more directly, which makes it easier to discover and remove certain sources of errors. The apparatus developed by the present writer has also been used for a determination of the solubility of nitrogen in  $\alpha$ -iron, published preliminarily by Åström and Borelius<sup>4</sup> and more fully by Åström (11).

## 2. APPARATUS FOR MEASURING THE ELASTIC RELAXATION

The wires for the samples were made of technically pure iron from Sandvikens Jernverks AB and contained small impurities of Si, Mn, P, S, N, and C. The diameter of the wire was 2.5 mm, the inner diameter of the spirals 28 mm, and the weight about 200 g. The free space between two consecutive windings was 1.3 mm. During measurements the upper ends of the spirals are fixed as shown in Fig. 1, while the lower are free. The sample is mounted in a refrigerator, through the bottom of which an extension of the spiral protrudes via a liquid seal trap. On the extension a small mirror is mounted, and under this a pair of wings which submerge in oil. During measurements the spiral is twisted through a

\* Received November 24, 1954.

† Royal Institute of Technology, Department of Physics, Stockholm, Sweden.



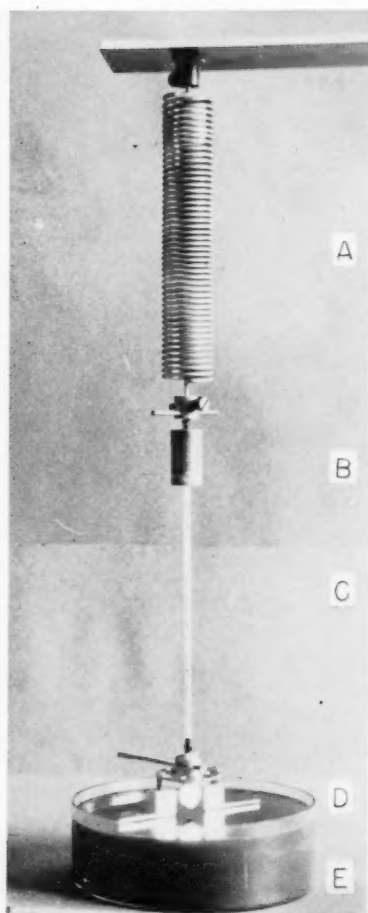


FIG. 1. A spiral with accessories, removed from the refrigerator. A. Sample. B. Part of the liquid seal trap. C. Extension, passing through bottom of refrigerator. D. Mirror. E. Damping equipment.

certain angle, which can be read on a protractor. It is held in this position for a sufficiently long time and then released. The first oscillations are rapidly damped by the oil, and after that the course of relaxation is registered photographically using an apparatus developed at this laboratory by Johansson and Larris.<sup>5</sup> An illuminated slit with a rotating sector shutter placed in front of it gives a flash each second. The slit is projected on a strip of film (Fig. 2) by the mirror and a lens. In order

to facilitate counting the spots, the slit is moved up and down periodically.

### 3. HEAT TREATMENT

The furnace for heat treatment was of the resistance type with three separate windings. By regulating the current in the different sections, the temperature could be held within  $\pm 0.5^\circ\text{C}$  over a distance of 20 cm. The voltage was kept constant with two a-c voltage stabilizers in series. The specimens were put into a vertical Pythagoras tube  $40 \times 1000$  mm, which could be evacuated and filled with hydrogen or argon. The temperature was measured by a thermocouple in a quartz tube, which was inserted in the furnace tube through its upper end.

A typical heat treatment could consist of the following procedures. The sample was purified from carbon and nitrogen in an atmosphere of moist hydrogen for about 24 hours, at a temperature of  $720^\circ\text{C}$ . The spiral was then brought down into the lower, cool part of the furnace tube, taken out and weighed. As a check the elastic after-effect was sometimes measured, and it was found to be about 2 per cent of that at maximum carbon content. This background is corrected for in the calculation of the after-effect. Carburization took place in an atmosphere of dry hydrogen, which had been passed over toluene. By variation of the velocity and duration of the gas stream, the carbon content could be given any desired value. The time of carburization varied between 5 and 20 hours. The sample was then once more allowed to cool down in the furnace and was weighed. In a third heat treatment the spiral was heated to  $710^\circ\text{C}$  and kept there for a half to one hour, after which it was quenched in a 10 per cent NaOH-solution.

This relatively complex heat treatment is necessary in order to avoid any oxidation which would, if it occurred, make the results of weighing meaningless. The heat treatment described above was performed when the relation between carbon content and after-effect was to be calculated. For the later determination of the solubility where no weighing was involved, a simpler heat treatment could be employed.

### 4. INTRODUCTORY INVESTIGATIONS

Before any attempts were made to determine the solubility curve, some measurements were carried out to test the workability of the method.



FIG. 2. A film strip, which shows the course of relaxation of a spiral, containing 0.0065 wt % carbon. The light-spot enters from the left, and in the right end, the exposure has been interrupted for about five minutes.

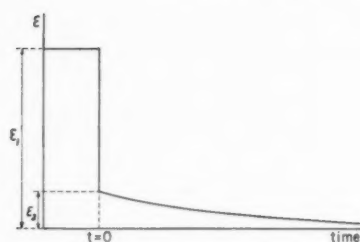


FIG. 3. The angle of torsion as a function of time.

If the lower, free end of the spiral is twisted to an angle  $\epsilon_1$  and released, the residual deflection  $\epsilon$  as a function of time in uncomplicated cases, such as shown in Fig. 3, can be expressed by the formula

$$\epsilon = \epsilon_2 e^{-t/\tau_s} \quad (1)$$

where  $\epsilon_2$  denotes the initial after-effect,  $\tau_s$  the relaxation time constant for strain when stress is kept constant, and  $t$  the time from the moment of release. In Fig. 4 the logarithm of the quotient  $\epsilon/\epsilon_1$  is plotted against time. The figure refers to an ordinary sample after carburization. The later part of the curve is a straight line, in conformity with Eq. (1), and it has a time constant of 33 seconds. If the line is extended to the time zero, that is, to the moment the spiral is released, this gives an initial value  $\epsilon_2/\epsilon_1$ . This value is taken as a measure of the strength of the after-effect.

The first part of the experimental curve, however, deviates from the straight line. If one takes the difference between values of  $\epsilon/\epsilon_1$  from the curve and those from the dashed extension of the straight line and plots them in a new logarithmic diagram, another straight line is found with a time constant of 6 seconds. This is the relaxation time for nitrogen at the same temperature. The sample must have been charged with nitrogen, and this must have occurred in some process after the decarburization, as no significant elastic relaxation was observed at that stage.

In the earlier measurements of after-effects<sup>2,3</sup> the wires were put under a torsional strain, while in the

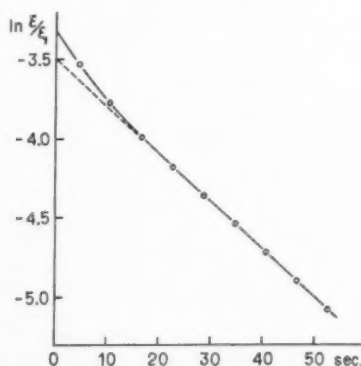


FIG. 4. The logarithm of the elastic relaxation as a function of time. Total angle of torsion 88°. Measuring temperature  $-4.5^\circ\text{C}$ . Quenched from  $660^\circ\text{C}$ .

present experiments they are bent. Though in the latter case the strain is not constant over the cross section, this should not alter the elastic after-effect. This was also verified experimentally. A spiral, on which measurements had been made, was drawn to such dimensions that it could be used as a torsion wire in the same apparatus. The relaxation was found to be the same irrespective of whether the sample was a spiral or a torsion wire.

To test the influence of the measuring temperature, this has been varied between  $-10$  and  $+20^\circ\text{C}$ . As expected, the relaxation time varied exponentially with the inverted value of the absolute temperature but the total after-effect was the same at all temperatures. These measurements give an activation energy of about 79 000 Ws/mol (19 000 cal/mol). Wert<sup>6</sup> has found the value 19 800 cal/mol.

Investigations were also made on the influence of the oil damping, total angle of torsion, time of carburization and texture, and they all gave results which agree with the general theory of relaxation and similar experiments made earlier.

#### 5. RELATIONSHIP BETWEEN CARBON CONTENT AND AFTER-EFFECT

The initial after-strain  $\epsilon_2/\epsilon_1$  was determined for a number of spirals which as described above had been charged at  $705^\circ\text{C}$  with varying amounts of carbon

TABLE I.

Sample	wt % C	$\epsilon_2/\epsilon_1$	K
8	0.0022	0.0026	116
5	0.0038	0.0044	117
1	0.0041	0.0046	113
(3	0.0049	0.0043	88)
4	0.0067	0.0082	123
2	0.0145	0.0167	115
10	0.0154	0.0189	123

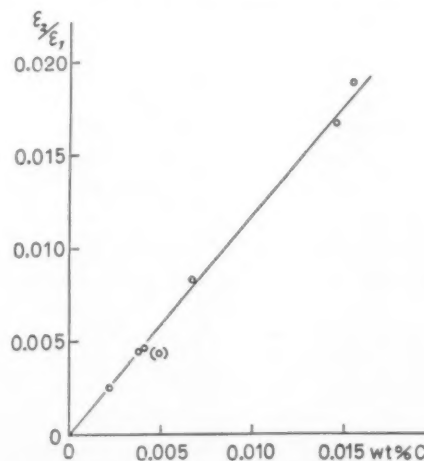


FIG. 5. The elastic after-effect as a function of carbon content. The slope of the line gives the proportionality constant.

below the solubility limit, and quenched in NaOH-solution. The carburization time varied between 5 and 20 hours. The results are given in Table I, and plotted in Fig. 5. Within the limits of error there appears to be proportionality between elastic after-effect and carbon content. The proportionality constant  $K = (\epsilon_2/\epsilon_1)/[c]$  is found to be 118, if  $[c]$  is expressed in weight parts.

## 6. DETERMINATIONS OF SOLUBILITY

For the determining of the solubility limit some of the charged samples were kept for about half-an-hour at suitable temperatures in order to attain equilibrium between solution and carbide, and were then quenched in NaOH-solution and measured. One difficulty that arises in these experiments as well as in those under section 5 is the influence of the small, undesired amount of nitrogen in solution, already discussed in section 4. This influence fixes the lower limit of accurate measurements to 0.002 wt % carbon. The results are found in Table II.

TABLE II.

Sample	$t(^{\circ}\text{C})$	$\frac{1000}{T}$	$\epsilon_2/\epsilon_1$	$\ln z$	wt % c
7 a	713	1.013	0.0232	-6.99	0.0197
2 a	660	1.072	0.0154	-7.41	0.0130
10 a	606	1.138	0.0109	-7.78	0.0092
2 b	568	1.189	0.0080	-8.06	0.0068
10 b	534	1.239	0.0059	-8.37	0.0050
4 a	499	1.294	0.0042	-8.69	0.0036
3 a	468	1.349	0.0032	-8.98	0.0027
1 a	444	1.393	0.0026	-9.19	0.0022

## 7. DISCUSSION OF RESULTS FROM THIS INVESTIGATION

The results are best shown in a logarithmic equilibrium diagram, that is a diagram where the logarithm of concentration is given as a function of the reciprocal of the absolute temperature. As a measure of the concentration we use the atomic ratio  $z = \text{C}/\text{Fe}$ . The values for the solubility taken from Table II are then found to form a straight line marked  $\text{Fe}_3\text{C}$  in Fig. 6. This line is described by the empirical formula

$$\ln z = -6080 \frac{1}{T} - 1.3. \quad (2)$$

From thermodynamic considerations, e.g. Ref. (1), the following equation is derived for the equilibrium of solution

$$\ln z = -\frac{L}{R} \frac{1}{T} + \frac{\Delta S}{R}, \quad (3)$$

where  $L$  denotes the heat of solution, and  $\Delta S$  is explained below.

The total increase of entropy involved in the solution of 1 mol carbide consists of two parts; one that is due to disordered distribution in the solution, and can be

described by Gibbs' formula, and another that is due to ferromagnetic effects and denoted by  $\Delta S$  in Eq. (3).

Identification of the two equations, (2) and (3), gives  $L = 50\,500$  Ws/mol and  $\Delta S = -1.3 R$ . Both values are in good agreement with the experimental results from the calorimetric investigation (1) ( $L = 52\,400$  Ws/mol,  $\Delta S = -1.3 R$ ).

The samples have been quenched from temperatures between 400 and 700°C, where cementite ( $\text{Fe}_3\text{C}$ ) is in equilibrium with carbon in solution. It is, however, also of interest to study the phase diagram at lower temperatures. Below 230°C the phase that appears in equilibrium with carbon in solution is, as recently found, not cementite but  $\text{Fe}_2\text{C}$ . Data relating to this carbide can be derived from experiments made in this laboratory by O. Krisement.<sup>7</sup> He measured the evolution of heat during precipitation of  $\text{Fe}_2\text{C}$  at temperatures about 200°C. From his data and Eq. (3) it is possible to calculate the solubility limit, if one can estimate the value of  $\Delta S$ , when 1 mol  $\text{Fe}_2\text{C}$  precipitates. From thermodynamic considerations (1) it is probable that  $\Delta S$  is zero if none of the components has a Curie point above the equilibrium temperature. At 200°C this is true for  $\text{Fe}_3\text{C}$  (Curie point 190°C), and we make the assumption that it is true for  $\text{Fe}_2\text{C}$  too. Then  $\Delta S$  only depends on the amount of  $\alpha\text{-Fe}$  that is used to form carbide. This amount of  $\alpha\text{-Fe}$  depends of course on whether 1 mol  $\text{Fe}_3\text{C}$  or  $\text{Fe}_2\text{C}$  is formed. The calculation of  $\Delta S_{\text{Fe}_2\text{C}}$  involves so many uncertain factors, however, that we can only estimate  $\Delta S_{\text{Fe}_2\text{C}}$  and  $\Delta S_{\text{Fe}_3\text{C}}$  to be of the same order of magnitude, and we put them equal. Anyhow, some small difference in the  $\Delta S$ -values does not have any appreciable influence on the final results.

Figure 6 shows the phase diagram, derived from this work and Krisement's measurements on  $\text{Fe}_2\text{C}$ . The heat of solution,  $L'$ , for  $\text{Fe}_2\text{C}$  is found to be 37 000 Ws/mol. An independent determination of this figure, derived from measurements of the heat of formation of  $\text{Fe}_2\text{C}$  and  $\text{Fe}_3\text{C}$  by Browning, De Witt and Emmet<sup>8</sup> confirms the value given above.

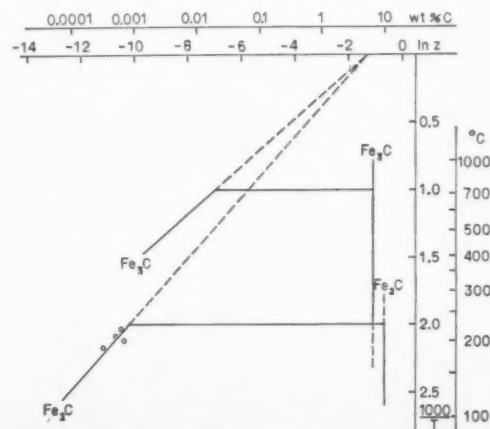


Fig. 6. Part of the logarithmic equilibrium diagram Fe-C, obtained from this investigation and Krisement's measurements.

## 8. DISCUSSION OF THE DEVIATION FROM EARLIER MEASUREMENTS

Dijkstra<sup>2</sup> and Wert<sup>3</sup> used the damping of torsional oscillations to determine the solubility of carbon in  $\alpha$ -iron. Dijkstra obtained the proportionality constant  $K$  between after-effect and carbon content in an indirect way, via resistance measurements. His results on polycrystalline material show a wide scattering, and  $K$  varies between 140 and 350. The mean value is about 200, and this figure has been used in later investigations, e.g. by Wert. Dijkstra's measurements on single crystals, however, have given much more constant values of  $K$ , and from these it is possible to calculate the  $K$ -value for a polycrystalline sample with disordered orientation of the crystal axis. Thus  $K=172$  is obtained, which differs considerably from the value 118 that is found in the present investigation.

In spite of the considerable difference in the  $K$ -values the agreement between the final results, as can be seen from Fig. 7, is fairly good, especially at higher temperatures. It looks as if some unknown effect makes it impossible to compare directly the  $K$ -values, derived from the two different methods. If a similar undesired nitrogen absorption as mentioned under 6 has taken place also in these earlier determinations of  $C$  in  $\alpha$ -Fe, using the torsional pendulum method, this nitrogen would have caused an error in the results. It is, in fact, difficult to decide from the measurements with the pendulum method whether an increase in the height of the peak in the damping-temperature diagram is due to carbon or nitrogen in solution. This is a probable explanation of the fact that the damping measurements have given a somewhat higher solubility at low temperatures.

The calorimetric measurements made by Borelius and Berglund<sup>1</sup> in this laboratory have given a solubility that is only about half as large as that found by relaxation methods. In these measurements the samples were quenched from different temperatures between 300

and 700°C, and the evolution of heat due to precipitation was then measured at about 100°C. In the calorimetric calculations it was assumed that the same carbide, cementite, precipitates at the equilibrium temperatures and at the measuring temperature. Present knowledge of  $Fe_3C$  shows that this is not the case. One must assume two different carbides, which affects the result in two ways. The heat of solution will have another value, and the carbon remaining in solution at the measuring temperature cannot be neglected.

For calculation of solubilities from calorimetric data the heat of solution of  $Fe_3C$ , 37 000 Ws/mol, must be used instead of the value 50 200 Ws/mol, valid for  $Fe_3C$  at the measuring temperature. This will increase the solubility values by 35 percent.

The neglect of the carbon remaining in solution at the measuring temperature compared with the amount of carbon that precipitates at the equilibrium temperature is permissible if the precipitate is  $Fe_3C$  but not if it is  $Fe_2C$ . The carbon in solution in equilibrium with  $Fe_2C$  at the measuring temperature (130°C) is 0.0004 at. %, while, for instance, at the lowest equilibrium temperature (350°C) used in the calorimetric measurements, a solubility of only 0.0010 at. % carbon is found, so that the correction here is rather large.

In Fig. 7, the mean value of the original calorimetric results is shown by a dashed line. The horizontal marks give the upper and lower limits of the experimental values, corrected with regard to the two facts mentioned above. At higher temperatures the divergence is still rather large, and the probable explanation is an insufficient rate of quenching in the calorimetric experiments, where the samples were cylinders with 18 mm diameter. Even if one assumes the cooling medium to be perfect—that is to say, if the surfaces were held at 0°C, the inner parts would have been cooled too slowly. With the knowledge of heat conductivity<sup>9</sup> and precipitation speeds, measured by Wert,<sup>10</sup> it can, for instance, be expected that about half the carbon content will precipitate during quenching, if the initial temperature is above 600°C. At initial temperatures below 450°C the precipitation will be very small, however.

## ACKNOWLEDGMENT

The author wishes to express his gratitude to Professor G. Borelius for suggesting this investigation and for his advice in the course of the work.

## REFERENCES

1. Borelius and Berglund, *Arkiv för fysik* **4**, 173 (1951).
2. Dijkstra, *Philips Research Report* **2**, 357 (1947).
3. Wert, *J. Metals* **10**, 1242 (1950).
4. Åström and Borelius, *Acta Met.* **2**, 547 (1954).
5. Johansson and Larris, *Arkiv f. Mat., Astr. och Fysik* **31B**, No. 2 (1944).
6. Wert and Zener, *Phys. Rev.* **76**, 1169 (1949).
7. Krisement, *Arkiv för fysik* **7**, 353 (1953).
8. Browning, De Witt, and Emmet, *J. Am. Chem. Soc.* **72**, (1950).
9. Carslaw and Jaeger, *Conduction of Heat in Solids* (Oxford, 1947).
10. Wert, *J. Appl. Phys.* **20**, 943 (1949).
11. Åström, *Arkiv för fysik* **8**, 495 (1954).

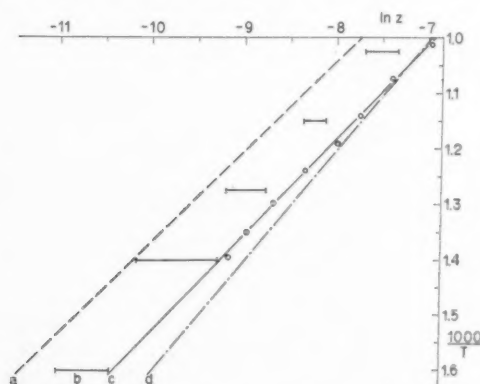


FIG. 7. The signs denote (a) Dashed line: calorimetric measurements by Borelius and Berglund; (b) horizontal marks: upper and lower limit of the experimental values from the calorimetric measurements, corrected according to the discussion in the present work; (c) fully drawn line and circles: results from the present investigation; (d) line of dots and dashes: measurements by Dijkstra and Wert.



## AN INTERFEROMETRIC STUDY OF GRAIN BOUNDARY GROOVES IN TIN\*

H. MYKURA†

An interferometric study of grain-boundary grooves in thermally etched tin has shown that the mechanism of groove formation by surface diffusion is not operative in this case. Owing to the shape and method of support of the specimen used, grain-boundary groove formation by a mechanism depending on simultaneous grain-boundary sliding and migration occurred. Some of the boundaries so formed are considered to have reached the equilibrium dihedral angle in the grooves. From dihedral-angle measurements and a published value of the surface-free energy of tin, a value of  $160 \pm 40$  erg  $\text{cm}^{-2}$  for the grain-boundary free energy of large-angle grain boundaries in pure tin is obtained. However, the result is liable to systematic errors due to surface contamination of the specimens by oxygen.

### ETUDE INTERFÉROMÉTRIQUE DES DÉPRESSIONS AUX JOINTS DE GRAINS DANS L'ÉTAIN

Une étude interférométrique des dépressions aux joints de grains dans l'étain après chauffage sous vide à haute température a montré que la diffusion en surface n'est pas le mécanisme de la formation de ces dépressions. Du fait de la forme de l'échantillon et de la méthode de suspension, cette formation se produit par glissement et déplacement simultanés du joint de grain. Certaines des frontières ainsi formées semblent avoir atteint le dièdre d'équilibre. A partir des mesures de ces dièdres et de l'énergie de surface de l'étain, il a été obtenu une valeur de  $160 \pm 40$  erg.  $\text{cm}^{-2}$  pour l'énergie du joint de grain pour une frontière à grand angle. Néanmoins, ce résultat est sujet à une erreur systématique par suite de la contamination de la surface par l'oxygène.

### EINE INTERFEROMETRISCHE UNTERSUCHUNG DER FURCHENBILDUNG AN DEN KORNGRENZEN DES ZINNS

Eine interferometrische Untersuchung der Furchen an den Korngrenzen von thermisch geätztem Zinn hat gezeigt, dass im vorliegenden Fall die Ausbildung der Furchen nicht durch Oberflächendiffusion vorsichgeht. Als Folge der Gestalt und der Art der Probenanbringung entstanden die Furchen an den Korngrenzen gleichzeitig durch Korngrenzengleiten und Korngrenzenwanderung. Von einigen so gebildeten Korngrenzen kann angenommen werden, dass sie den Gleichgewichtswinkel zwischen den beiden Seiten der Furche erreicht haben. Für die freie Energie von "Grosswinkelkorngrenzen" in reinem Zinn wurde aus den experimentell bestimmten Werten der Winkel zwischen den beiden Flächen der Furchen und einem bekannten Wert der freien Oberflächenenergie des Zinns ein Wert von  $160 \pm 40$  erg.  $\text{cm}^{-2}$  berechnet. Das Ergebnis ist jedoch von systematischen Fehlern beeinträchtigt, die durch die Oberflächenverunreinigung der Probe durch Sauerstoff hervorgerufen werden.

## INTRODUCTION

The formation of grain-boundary grooves on a metal surface when it is heated in an inert atmosphere (thermal etching) has been known for some time and has been investigated in detail by Chalmers, King and Shuttleworth,<sup>1</sup> who give references to previous work on this topic. The cause of groove formation is the surface free energy of the grain boundary, the angle at the base of the groove (the dihedral angle) being determined by the local equilibrium of the surface tension forces of the grain boundary and the metal surface.<sup>1,2</sup> The equations relating the equilibrium dihedral angle to the grain boundary and surface free energies involved have been given by Herring.<sup>3</sup> If the factors depending on crystallographic orientation in Herring's equations are neglected, the equilibrium condition becomes the simple Neumann triangle as for liquids, and the ratio of grain-boundary free energy to surface free energy can be evaluated from dihedral-angle measurements. Most of the work on thermal etching has been on copper and silver, and in those

cases the mechanism of groove formation is usually considered to be the migration of individual atoms along the surface away from the boundary.

The grain-boundary grooves produced by thermal etching are easily seen during microscopic examination and several techniques for the measurement of groove profiles have been developed. The original method, used by Smith,<sup>2</sup> Bailey and Watkins,<sup>4</sup> and Greenough and King,<sup>5</sup> consists of cutting a section through the specimen, usually normal to both surface and grain boundary. The section cutting techniques are laborious, and precautions have to be taken to prevent damage to the surface in cutting and polishing the sections. King<sup>5</sup> has developed an optical reflexion technique, which is essentially a microscopic angle collimator. This method will not give the groove profile, but only the maximum angle on each side of the groove. For the measurements of groove angles the technique is rapid and convenient (c.f. Buttner, Udin and Wulff<sup>6</sup>).

The use of interferometric methods has several times been suggested for the study of grain-boundary grooves, but because of the large wedge angles which occur, it had not been used successfully. Developments in interference microscopy have now made the inter-

\* Received January 26, 1955.

† University College of the West Indies, Jamaica, British West Indies.

ferometric method practicable.<sup>7</sup> The method has several advantages over the sectioning method: it is much less laborious, permits observations along the whole length of a boundary and is nondestructive. The particular interferometric technique used in these experiments has been described in detail elsewhere.<sup>7,8</sup> To test its performance, some preliminary experiments were done with copper. Measurements on grain-boundary grooves in copper (thermally etched in argon or hydrogen atmospheres), using the orthodox sectioning techniques, have been reported by Bailey and Watkins.<sup>4</sup> The groove profiles measured interferometrically appeared similar to those obtained by sectioning and gave a value of  $159^\circ \pm 3^\circ$  for the dihedral angle, while Bailey and Watkins give values of  $158^\circ$  and  $160^\circ$ .

#### THERMAL ETCHING OF TIN

The material used was "Chempur" tin, whose main impurities are: Sb 0.0032%, P 0.0021%, Bi 0.0008%, Cu 0.0006%, As 0.0005%. The flat surface for microscopic examination was produced by casting some molten tin onto a clean, preheated glass plate and prising off the globule after cooling. The globules were cut into specimens having a flat surface of about one cm<sup>2</sup>. Each specimen was sealed into a glass ampoule in an (ideally) oxygen-free atmosphere for heat treatment. Two methods were used to try to obtain an inert atmosphere. In the first, the ampoule was partly filled with anhydrous alcohol; the alcohol was then evaporated by pumping with a water pump and gentle heating, and the ampoule sealed when all the alcohol had vaporised. In the second method the ampoule was evacuated by an oil diffusion pump and sealed after half an hour's pumping.

For heat treatment the ampoules were suspended in reflux condenser vapour baths of ethyl benzoate and methyl salicylate, giving temperatures of  $213^\circ \pm 1^\circ\text{C}$  and  $223^\circ \pm 1^\circ\text{C}$ , respectively, i.e.,  $19^\circ\text{C}$  and  $9^\circ\text{C}$  below the melting point of tin. The ethyl benzoate proved quite satisfactory, and specimens were heat-treated at  $213^\circ\text{C}$  for various times up to 250 hours. The methyl salicylate was less stable and had to be replaced every 12 hours; specimens were heat-treated intermittently for times up to 50 hours.

Surface free energy effects, such as groove formation, can be greatly altered by very small amounts of impurity if preferential adsorption at the surfaces occurs. The tin is liable to contamination during melting and casting, and also during heat treatment, if the atmosphere in the ampoule is not inert. Using clean glassware for the melting and casting of the specimen, the only likely source of contamination is atmospheric oxygen. Microscopic examination of specimens before heat treatment showed very slight but definite oxide formation on the back of specimens, i.e., the surface exposed to the atmosphere during cooling after casting; the front surface appeared clean. All specimens, whether

sealed off under vacuum or alcohol vapour, showed some surface oxidation after heat treatment. As the ampoules could not be made sufficiently oxygen-free to prevent the formation of oxide during heat treatment, some were sealed off with a higher gas pressure to see how the amount of oxide affected the results.

The distribution of the oxide formed on the surface during heat treatment was far from uniform. The oxide was in the form of specks, varying in size from about  $3\mu$  downwards. Some areas were almost clear of specks while others were completely covered. The shape of these areas suggests that oxidation during heat treatment took place mainly on oxide nuclei formed during casting. The oxide film on those specimens sealed off at a higher residual oxygen pressure was visible to the naked eye as a yellow to purplish tarnish; it formed during the first hour of heat treatment and then remained constant. Through the courtesy of Dr. Wilman, some of the specimen surfaces were examined by electron diffraction. The photographs showed sharp rings due to SnO and spots due to metallic tin, indicating that the surface was partly covered by crystallites of oxide.

The globules cast to give a flat specimen surface were often single crystals. To provide an adequate number of grain boundaries for examination, the globules were cut with wire cutters to give separate specimens. During heat treatment several new grains formed in the plastically deformed region and grew until all the deformed material had recrystallised. At the temperatures used, the time required for recrystallisation is short compared with the length of heat treatment. However, long after recrystallisation is complete and an apparently stable grain structure has been reached, further grain-boundary migration can occur. Attempts at the measurement of the rate of grain-boundary groove formation are therefore liable to errors from this cause. A slowly migrating boundary usually leaves a series of scars and can be identified as such during microscopic examination.

#### GRAIN-BOUNDARY GROOVE MEASUREMENTS

The specimens were removed from the heat treatment ampoules when cold, and examined microscopically—first at low power to determine the general grain configuration, then each boundary with a 4 mm objective. Interferograms were taken at selected points, usually at grain-boundary intersection (i.e., grain corners) and at one or more points along each boundary; a drop of oil placed on the specimen provided the interferometric reference surface.<sup>9</sup> Groove profiles and dihedral angles were evaluated from enlarged prints by methods described in detail elsewhere.<sup>8</sup>

The profiles of the grain-boundary grooves in tin were found to be quite different from those in copper or silver. In almost all cases the grooves were highly asymmetrical and the grain surfaces on either side of

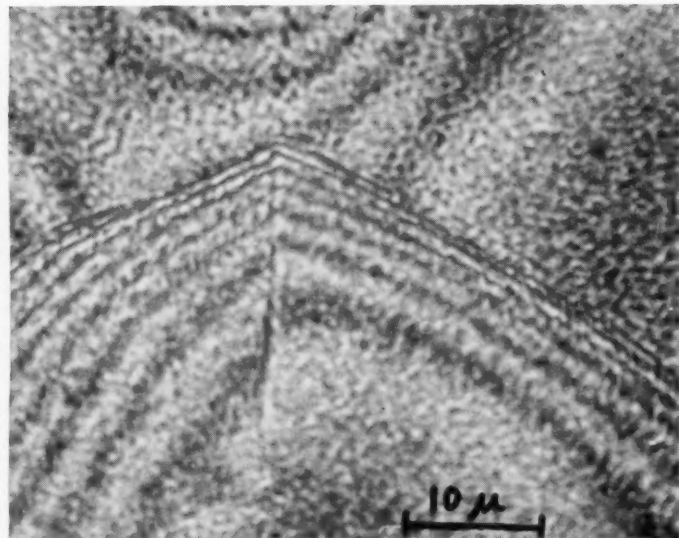
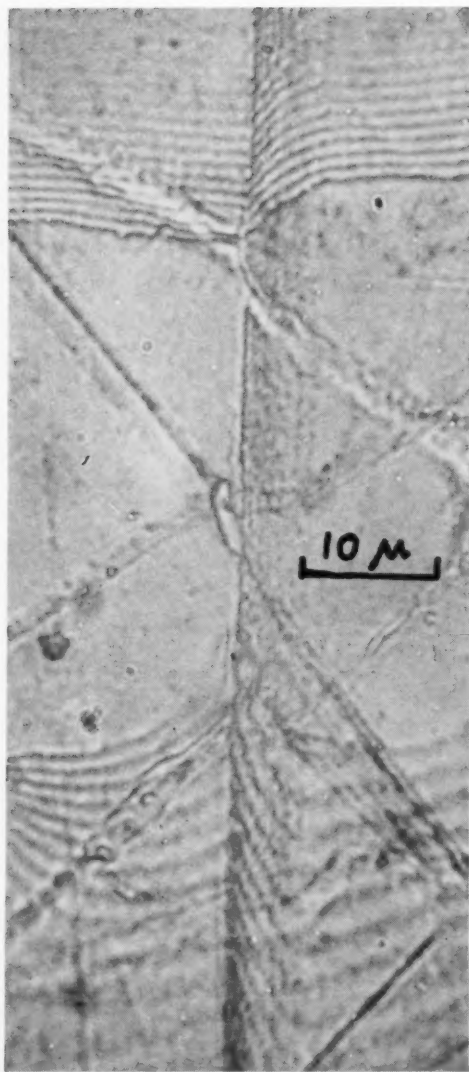


FIG. 2

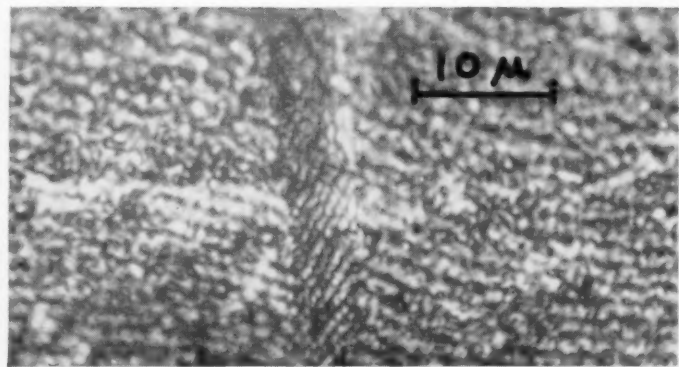


FIG. 4

PLATE I—FIG. 1. A type I grain-boundary groove in tin with interference fringes crossing the boundary at top and bottom. Scars show that grain-boundary migration has occurred over the curved part of the surface, total boundary migration =  $5\mu$ . From scratches crossing the boundary, sliding along the surface over a distance of  $4.3\mu$  occurred. From difference of height, boundary sliding perpendicular to the surface =  $4\frac{1}{2}$  fringes =  $0.8\mu$ .

FIG. 2. Interferogram of a three-boundary-intersection. For exanation of boundary movement see Fig. 3. Grain *A* is 6 fringes above the level of grains *B* and *C*. Boundaries *AB* and *AC* form type I grooves. Fringes on grains *B* and *C* are due to curvature of the oil reference surface.

FIG. 4. A type II boundary in one of the more heavily oxidised specimens. A small strip of the surface free of visible oxide crosses the boundary without any change in groove profile. (All interferograms were taken through N.A. 0.85 lens with mercury green light; height difference between successive fringes =  $\lambda/2n = 0.18$  microns.)

the boundary were on different levels, indicating that grain-boundary sliding in a direction normal to the surface had occurred. Often there were also discontinuities in scratches crossing the boundary, showing that boundary sliding parallel to the surface had also taken place. Figure 1 is an example of a groove showing simultaneous grain-boundary migration and grain-boundary sliding. Unlike the copper grain boundary grooves, the depths of the tin grooves showed little correlation with the length of heat treatment. For instance, one groove attained a depth of six fringes ( $=1.1\mu$ ) after 7 hours at  $213^\circ\text{C}$ , while another after 100 hours at the same temperature was less than one quarter of a fringe deep. Further, in any one specimen the depth of grooves could vary over the whole observed range down to immeasurably small. Figure 2 is an interferogram of grain corners in a specimen heat-treated 28 hours at  $213^\circ\text{C}$ . The two migrating boundaries have developed deep grooves and a scar marking the locus of the junction is clearly visible, while the stationary boundary can only just be seen. Figure 3 explains the boundary movements in Fig. 2.

The tin grooves were classified into three groups on the basis of their appearances (Fig. 5). In grooves of type I, the profile on one side of the boundary was similar to that of normal grooves, while the other side was quite flat and undisturbed. The wedge angle near the boundary was usually within the limits  $13^\circ \pm 2^\circ$  and there were always slight scars showing that the boundary had migrated over the curved surface. The type II grooves consisted of a steep rise on one side of the boundary, usually of negligible curvature and wedge angle between 10 and 20 degrees. The rise terminated at a sharp edge where the surface became flat. The other side was quite flat in some cases, but in others the surface rose and curved smoothly to become flat. as Type III grooves consisted of a step at the boundary that was too steep to be resolved. The height of the step could be determined from the order of the fringes or (less accurately) with the fine focus adjustment of the microscope. Often there was no measurable surface curvature beside the step, but some specimens, particularly those heat treated for longer times, had profiles like type I and type II with a step at the boundary in addition. The division between type II and type III was rather arbitrary, as the boundaries were classed

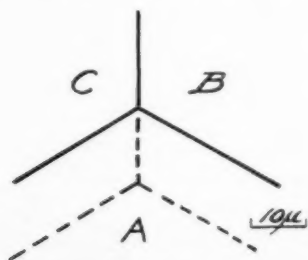


FIG. 3. Boundary migration in Fig. 2. Initial position of boundaries: broken lines; final position: solid lines.

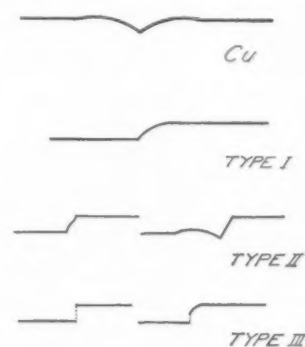


FIG. 5. Typical grain-boundary grooves observed with copper (Cu) and tin (types I, II and III) specimens. Vertical scale exaggerated.

as type III if the profile could not be resolved completely, and the maximum wedge angle resolvable by the interference method used was about 25 degrees. In specimens heat-treated for times up to 25 hours the frequency of occurrence of the three types of grooves was about equal, but with longer heat treatment times type III grooves predominated. With a number of boundaries the groove profile varied, in extreme cases changing from type I to type II. Usually, grain-boundary sliding with a rotational component took place in such cases.

There was no difference in general appearance of the grooves between the less and more heavily oxidized specimens. Owing to the discontinuous nature of the oxide-covered patches, individual boundaries could be examined on clear and oxide-covered areas and there was no difference in shape of groove in such cases (see also Fig. 4). This was unexpected and it is assumed that the clear areas of the specimen were covered with an invisible layer of oxide, so thin that it did not obscure the reflections from metallic tin in the electron diffraction tests. In analysing the groove-angle measurements, boundaries on specimens in all stages of oxide contamination were taken together. The general appearance of grooves heat-treated at  $223^\circ\text{C}$  was similar to that at  $213^\circ\text{C}$ . Little change of groove shape with temperature is to be expected. The  $223^\circ\text{C}$  grooves were therefore included with  $213^\circ\text{C}$  as they are too few to yield a significant average value taken alone.

Sixty boundaries in specimens heat-treated at  $213^\circ\text{C}$  and 10 in specimens heat-treated at  $223^\circ\text{C}$  were examined, though most of the type III grooves and some of the type II grooves were not photographed. Dihedral angles evaluated from the interferograms were as follows:

Type I grooves: 24 measurements on 14 different boundaries gave a mean dihedral angle of  $166\frac{1}{2}^\circ \pm 2^\circ$ , only three measurements being outside the limits  $167^\circ \pm 3^\circ$ .

Type II grooves: 16 measurements on 12 separate boundaries gave a mean dihedral angle of  $162\frac{1}{2}^\circ \pm 4^\circ$ , individual values ranging from 154 to 176 degrees.



Type III grooves: fringes not resolved, but dihedral angles less than 160 degrees.

#### THE METHOD OF GRAIN-BOUNDARY GROOVE FORMATION

As the tin groove profiles are very different from those found in copper or silver, it may be assumed that the mechanism of formation also differs. The fact that the surfaces of different grains were on different levels when deep grooves were observed and that no grooves were observed when the two grains were on the same level, suggests that grain-boundary sliding was important in the formation of these grooves and that surface diffusion played a minor part.

Grain-boundary sliding in tin has been studied by Puttick and King.<sup>10</sup> In the experiments described here the forces causing grain-boundary sliding were presumably due to the weight of the specimen. As each specimen was supported at very few points, there must have been shearing stresses across some of the boundaries. The specimens contained very few grains, so there can have been little interlocking between grains to support these stresses. Some unsuccessful attempts were made to reduce the amount of grain-boundary sliding by shaping the ampoules to support the specimens more evenly and so to reduce the shear forces acting across the boundaries.

The condition for local equilibrium at the intersection of a grain boundary with a surface is independent of

the mechanism by which such equilibrium is attained. If changes in surface topography by surface diffusion can take place only very slowly, an approach towards equilibrium by grain-boundary migration and sliding may occur. A grain-boundary meeting a surface at an inclination tends to migrate to meet the surface more nearly at right angles. If at the same time there is a shearing stress across the boundary, the combined effect of surface tension and external stress, together with some diffusion, can produce a grain-boundary groove with equilibrium dihedral angle and a profile like that of the observed type I grooves (Fig. 6). If the shearing stress caused grain-boundary sliding in the opposite direction, boundary migration towards the normal would be prevented and a profile like that of type II grooves developed; in this an approach towards equilibrium dihedral angles would however necessitate a considerable amount of metal transfer by diffusion. Type III profiles would be expected to occur if grain-boundary sliding is the dominant factor during heat treatment.

If the type I and II grooves were formed by the proposed mechanism, the direction and curvature of the boundaries immediately below the surface should be as shown in Fig. 6. To check this, some specimens were dismembered into their separate grains by the mercury immersion technique<sup>10</sup> and in others normal sections were cut. While the boundary directions were mainly as expected, the grains were so distorted at the relevant points during dismembering or cutting that no definite conclusions could be drawn.

#### THE GRAIN-BOUNDARY FREE ENERGY OF TIN

The measurement of the equilibrium dihedral angle of a grain-boundary groove gives the ratio of grain boundary to surface free energies, if the variations of surface free energy with crystallographic orientation are neglected. Few experimental data are available on the orientation dependence of surface free energy, but in taking the average of a large number of readings, the effect is thought to cancel out.<sup>6</sup> The grain-boundary free energy of boundaries between grains of small orientation difference is known to increase with increasing orientation difference, while for large orientation differences the surface free energy is nearly constant.<sup>12</sup> Low-energy grain boundaries are statistically rare in a number of boundaries between randomly oriented grains, and the mean surface free energy evaluated from a number of randomly oriented boundaries will give the value for large-angle boundaries.

The type III boundaries were obviously not in equilibrium and can be neglected in deriving a value of the grain-boundary free energy. The measured dihedral angle values of type II grooves had a very wide spread, and while there may have been some approach towards equilibrium, this is unlikely to have been reached by many boundaries. From the proposed mechanism of

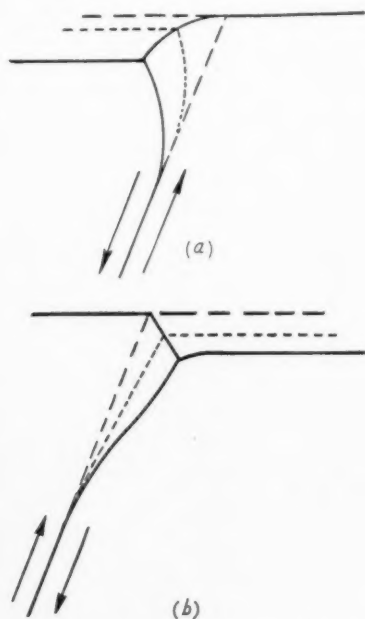


FIG. 6 (a) and (b) Possible mechanism of tin groove formation by boundary sliding and migration. Initial position: broken lines; intermediate position: dotted; final position: solid lines. Direction of applied shear stress indicated by arrows. Vertical scale exaggerated.

formation the type I grooves are the most likely to attain equilibrium, and the very small spread of the measured values indicates that a close approach to the equilibrium groove angle has been reached. Taking the mean dihedral angle of type I grooves,  $D=166\frac{1}{2}^\circ$ , as the best equilibrium value and using the equation  $E_B/E_S=2 \cos(D/2)$ , the ratio of grain boundary to surface free energy  $E_B/E_S=0.235\pm0.035$ . Owing to the oxide contamination of the surface,  $E_S$  in this case must be taken to refer to such contaminated surfaces, but  $E_B$  will refer to pure tin boundaries, as there was no contamination inside the specimens. A value of  $E=685 \text{ erg cm}^{-2}$  for tin has been obtained by Greenhill and McDonald<sup>11</sup> using the wire-pulling technique. This result has only been published as a short note. It is difficult to estimate the degree of surface cleanliness of the specimens used and the reliability of the result, but this is probably no better than the dihedral-angle measurements reported here. If it is assumed that the tin specimens in these two experiments suffered from similar surface contamination, the two results can be combined to give a value for the grain-boundary free energy of pure tin of  $160\pm40 \text{ erg cm}^{-2}$ .

Chalmers<sup>12</sup> has derived a value for the grain-boundary free energy of tin by an entirely different method, using the variation of grain-boundary free energy with orientation difference of the grains. The value obtained

$100 \text{ erg cm}^{-2}$ , is sufficiently close to the value derived from grain-boundary groove measurements to lend credence to both results, though each depends on a number of unverified assumptions.

#### ACKNOWLEDGMENTS

The author wishes to thank Mr. R. King for supplying some high purity tin and for encouragement and comment, Dr. H. Wilman for the electron diffraction tests and comment and the authorities of the University College of the West Indies for research facilities.

This paper is based on a thesis accepted by the University of London for the Ph.D. degree.

#### REFERENCES

1. B. Chalmers, R. King, and R. Shuttleworth, *Proc. Roy. Soc. A* **193**, 465 (1948).
2. C. S. Smith, *T.A.I.M.E.* **175**, 15 (1948).
3. C. Herring, in *The Physics of Powder Metallurgy* (1951).
4. G. L. J. Bailey and H. C. Watkins, *Proc. Phys. Soc.* **B63**, 350 (1950).
5. A. P. Greenough and R. King, *J. Inst. Metals* **79**, 415 (1951).
6. F. H. Buttner, H. Udin, and J. Wulff, *J. Metals* **5**, 313 (1953).
7. H. Mykura, *Proc. Phys. Soc.* **B67**, 281 (1954).
8. H. Mykura, Ph.D. Thesis (London, 1954).
9. S. Tolansky and M. Omar, *Nature, (Lond.)* **170**, 81 (1952).
10. K. Puttick and R. King, *J. Inst. Metals* **80**, 537 (1952).
11. E. B. Greenhill and S. R. McDonald, *Nature (Lond.)* **171**, 37 (1953).
12. B. Chalmers, *Progress in Metal Physics* **3**, 293 (1952).

## SELF-DIFFUSION OF GOLD IN GOLD-NICKEL ALLOYS\*

A. D. KURTZ, B. L. AVERBACH, and MORRIS COHEN†

The self-diffusion rate of gold in gold-nickel alloys was measured as a function of composition and temperature in the region of complete solid solubility, using an autoradiographic method to trace the diffusion of  $\text{Au}^{198}$ .

The diffusion data reveal no anomalies that correlate with the miscibility gap. However, the  $D_{\text{Au}}^*$ ,  $D_{\text{Ni,Au}}^*$  and  $Q_{\text{Au}}^*$  values show maximum deviations from the linear averages of the pure metal values in the composition range corresponding to the minimum in the solidus curve.

### AUTODIFFUSION DE L'OR DANS LES ALLIAGES OR-NICKEL

La vitesse d'autodiffusion de l'or dans les alliages or-nickel dans le domaine de solubilité totale a été mesurée par autoradiographie avec  $\text{Au}^{198}$  en fonction de la composition et de la température.

Les constantes de diffusion ne montrent aucune anomalie en relation avec la lacune de miscibilité. Par contre, l'écart de  $D_{\text{Au}}^*$ ,  $D_{\text{Ni,Au}}^*$  et  $Q_{\text{Au}}^*$  par rapport à la variation linéaire entre les valeurs correspondant aux deux métaux purs, présente un maximum pour le minimum du solidus.

### DIE SELBSTDIFFUSION VON GOLD IN GOLD-NICKEL LEGIERUNGEN

Mit Hilfe einer autoradiografischen Methode, die es gestattet, die Spur von  $\text{Au}^{198}$  bei der Diffusion zu verfolgen, wurde das Mass der Selbstdiffusion von Gold in Gold-Nickel Legierungen in Abhängigkeit von der Zusammensetzung und der Temperatur im Bereich völliger Mischkristallbildung gemessen.

Die Ergebnisse über die Diffusion zeigen keine Anomalien, die mit der Mischungslücke in Widerspruch stehen. Im Zusammensetzungsbereich, der dem Minimum in der Soliduskurve entspricht, zeigen jedoch die  $D_{\text{Au}}^*$ ,  $D_{\text{Ni,Au}}^*$  und  $Q_{\text{Au}}^*$  Werte maximale Abweichungen von den linearen Mitteln der reinen Metalle.

## 1. INTRODUCTION

Relatively few measurements have been made of self (radioactive) diffusion coefficients in an alloy system as a function of composition. Although such data are worth while in themselves, the present work on gold-nickel alloys was undertaken with broader objectives in mind. This system exhibits a miscibility gap below  $840^\circ\text{C}$ ; above this temperature, a complete series of face-centered-cubic solid solutions exists. There are suitable radioactive isotopes for the determination of the self-diffusion coefficients for both gold and nickel, and the thermodynamic activities have been measured by Seigle.<sup>1</sup> Thus this system appears quite appropriate for an experimental test of the equation proposed by Darken<sup>2</sup> and Le Claire,<sup>3</sup> which relates the self-diffusivities  $D_{\text{Au}}^*$  and  $D_{\text{Ni}}^*$ , the interdiffusion coefficient  $\bar{D}$ , and the thermodynamic driving force for interdiffusion.

The first step in this sequence of experiments involved the determination of  $D_{\text{Au}}^*$  as a function of composition and temperature, and these data are reported here.

## 2. EXPERIMENTAL METHOD

### Specimen Preparation

Alloys were prepared from fine gold (99.96) and vacuum-cast nickel (99.986) by induction melting in alumina crucibles under an argon atmosphere, and arranging for directional solidification from the bottom.

The ingots were machined into  $\frac{1}{2}$ -inch diameter rods, sealed in evacuated Vycor tubes, and annealed for about one week at  $925$  to  $1000^\circ\text{C}$ . After this treatment, the grain size was approximately 4 mm, which was sufficiently coarse to avoid undue grain-boundary diffusion. The faces of  $\frac{3}{8}$ -inch thick disc specimens were surface-ground on fine abrasive papers and a film of  $\text{Au}^{198}$  about 100A thick was deposited by evaporation on the exposed faces of various alloy compositions. This amount of gold was too small to have a material effect on the chemical composition of the base alloy.

A disc-specimen of identical composition was then welded to the radioactive face. Welding was accomplished by hot pressing in a stainless steel cylinder under an argon atmosphere. Satisfactory welds were obtained in one hour at  $850^\circ\text{C}$ . The diffusion anneals were of the order of 6 to 14 days, and the temperatures were controlled to  $\pm 1^\circ\text{C}$ .

### Autoradiographic Method

The penetration of the radioactive tracer was determined by an autoradiographic method.<sup>4</sup> The diffusion samples were sectioned at an angle of about 3 degrees to the original interface, the selected angle depending on the extent of penetration. Eastman No-screen X-ray film was placed next to the sectioned surface and exposed for times ranging from five minutes to one hour. Microdensitometer traces were obtained for each autoradiogram; by selecting a suitable amplification factor on the microphotometer, it was possible to distinguish differences in density between points 0.04 cm apart in the radiogram, corresponding to a

\* Received December 16, 1954; in revised form April 2, 1955.

† Department of Metallurgy, Massachusetts Institute of Technology, Cambridge, Massachusetts.

distance of 0.002 cm in the sample for a sectioning angle of 3 degrees. The blackening was converted to relative intensity, and the self-diffusion coefficient was determined from the intensity *versus* distance curve. The isotope  $\text{Au}^{198}$  decays to  $\text{Hg}^{198}$  by emitting a  $\beta$ -particle (0.96 mev). There is a subsequent emission of a  $\gamma$ -ray (0.41 mev), but only the  $\beta$ -ray was recorded in the autoradiogram since the emulsion was insensitive to  $\gamma$ -rays of this wavelength.

In determining the self-diffusion coefficient by autoradiography it is advisable to make a correction for the intensity originating beneath the surface. At a surface making an angle,  $\alpha$ , with the original interface, it is shown in the appendix that the observed intensity is given as a function of the distance,  $l$ , along the interface (see Fig. 1) by the equation:\*

$$\frac{I(l)}{I_0} = \frac{\exp(\mu l \tan \alpha + \mu^2 D t)}{2} [1 - \text{erf}(z_0)], \quad (1)$$

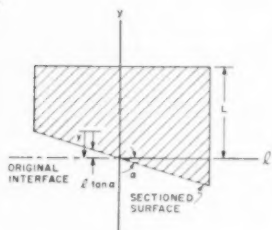


FIG. 1. Geometry of sectioned couples.

where

- $l$  = distance along the original interface,
- $I(l)$  = intensity corresponding to a given value of  $l$ ,
- $I_0$  = a constant including the initial intensity at the interface,
- $D$  = diffusion coefficient,
- $t$  = diffusion time,
- $\mu$  = mean linear absorption coefficient,

and

$$z_0 = \left( \frac{l^2 \tan^2 \alpha}{4Dt} + \mu l \tan \alpha + \mu^2 D t \right)^{1/2}$$

The quantity,  $l \tan \alpha$ , is the distance from the original interface to various positions at the surface of the oblique section. It is also shown in the appendix that for reasonably large values of  $\mu$  the slope of a plot of  $\ln[I(l)/I_0]$  vs  $(l \tan \alpha)^2$  is given by

$$-\frac{1}{4Dt} \left( 1 + \frac{2}{\mu l \tan \alpha} \right).$$

The absolute value of the slope is thus larger than  $1/4Dt$  and dependent on  $l$ , but at sufficiently large

\* The correction term previously published<sup>1</sup> contains an error.

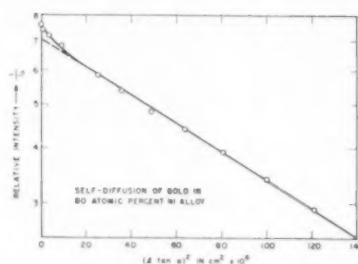


FIG. 2. Autoradiographic intensity curve.

values of  $\mu l \tan \alpha$ , the correction term becomes negligible and the slope becomes constant.

A typical plot of  $\log[I(l)/I_0]$  vs  $(l \tan \alpha)^2$  is shown in Fig. 2 for an alloy containing 80 atomic per cent nickel. At small values of the abscissa, the curve deviates from a straight line and exhibits a steeper slope, as indicated by the expression above. At larger values of the abscissa, the slope is constant and thus equal to  $-1/4Dt$ . Diffusion coefficients were obtained by utilizing the slope of the straight line portion of such plots.

Because the isotope  $\text{Au}^{198}$  decays with a half-life of only 2.7 days, a strict time schedule had to be maintained in order to obtain suitable autoradiograms. This necessitated the use of initial activities of the order of  $10^4$  millicuries per gram.

### 3. RESULTS

The self-diffusion coefficients of gold,  $D_{\text{Au}}^*$ , in various gold-nickel alloys at a series of temperatures are shown in Fig. 3. It is evident that the diffusion coefficients are smooth functions of composition with some tendency toward a maximum at 20 atomic per cent nickel. No anomaly appears at 70–80 atomic

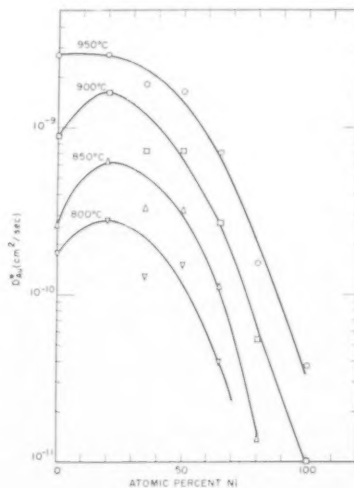


FIG. 3. Self-diffusion of gold in gold-nickel alloys.



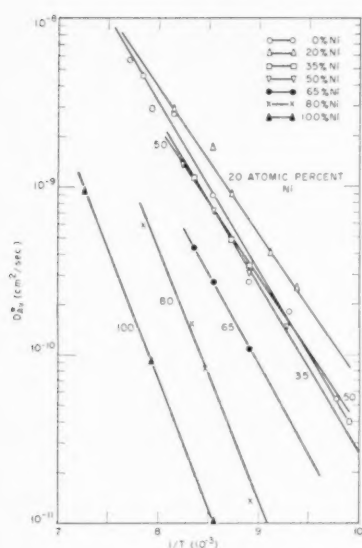


FIG. 4. Effect of temperature on self-diffusion of gold in gold-nickel alloys.

per cent nickel, the composition at the top of the miscibility gap.

Figure 4 shows that the diffusion data are consistent with the customary relationship

$$D_{Au} = D_{0,Au} \exp(-Q_{Au}/RT),$$

and the values for  $D_{0,Au}$  and  $Q_{Au}$  are given in Table I. There are minima in  $D_{0,Au}$  and  $Q_{Au}$  in the neighborhood of 20–50 atomic per cent nickel, as plotted in Fig. 5.

#### 4. DISCUSSION OF RESULTS

Although the self-diffusion coefficients,  $D_{Au}$ , (Fig. 3) appear to have maximum values near 20 atomic per cent nickel, the maximum deviation from linear average of the pure metal values lies at about 50 atomic per cent. This is approximately where the maximum lowering of the melting-point occurs, relative to the average (linear) melting-point of the pure metals. In a rough way, the self-diffusion coefficients seem to correlate with the melting-point variations as a function of composition.

TABLE I. Frequency factors and activation energies for self-diffusion of gold in gold-nickel alloys.

At. % Ni	$D_{0,Au}$ (cm <sup>2</sup> sec <sup>-1</sup> )	$Q_{Au}$ (cal/mol)
0	0.26	45,300
20	0.05	40,200
35	0.063†	42,700†
50	0.091	43,400
65	0.51†	48,800†
80	1.1	60,500
100	2.0	65,000

† Determined by Reynolds<sup>8</sup> in a related investigation.

TABLE II. Entropies of self-diffusion of gold in gold-nickel alloys

At. % Ni	$\nu$ (10 <sup>12</sup> /sec)	$a$ (10 <sup>-8</sup> cm) at 20°C	$\Delta S$ (cal/deg. mol) calculated from $D_{0,Au}$
0	3.56	4.07	7.6
20	3.60	3.97	4.4
35	3.78	3.90	4.8
50	4.17	3.82	5.5
65	4.40	3.73	8.6
80	5.82	3.64	9.9
100	7.85	3.56	10.6

The correlation of the diffusivities with the melting temperature is inherent in many of the recent interpretations of self-diffusion data.<sup>6,7,8</sup> Following Zener<sup>6</sup> the self-diffusivity of substitutional atoms in face-centered-cubic metals may be written as:

$$D = a^2 \nu \exp(\Delta S/R) \exp(-\Delta H/RT), \quad (2)$$

where

$a$  = lattice parameter,

$\nu$  = frequency of vibration,

$\Delta S$  = entropy of activation for self-diffusion,

$\Delta H$  = enthalpy of activation for self-diffusion,

$R$  = gas constant, and

$T$  = diffusion temperature.

Thus, the experimental values (Table I) of  $D_{0,Au}$  correspond to the  $[a^2 \nu \exp(\Delta S/R)]$  and  $Q_{Au}$  is equivalent to  $\Delta H$ . Using the Debye frequency for  $\nu$ , the entropies of diffusion were calculated and listed in Table II. The  $\nu$  values given in Table II were computed by Averbach<sup>9</sup> from experimental data on the excess relative entropy of mixing.<sup>1</sup> The values for the diffusion entropy calculated from  $D_{0,Au}$  are all positive.

Zener<sup>6</sup> has interpreted self-diffusion data in terms of the fraction,  $\lambda$ , of the free energy of activation required for the jumping of an atom from one site to an adjacent

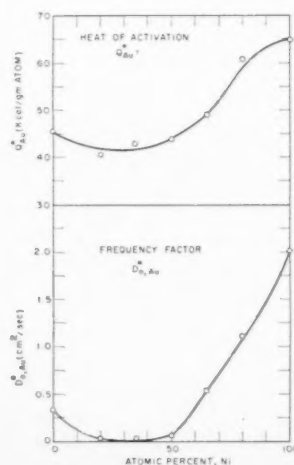


FIG. 5. Self-diffusion of gold in gold-nickel alloys.

vacant site and the fraction,  $(1-\lambda)$ , required for the formation of the vacant site. The entropy is then estimated to be:

$$\Delta S = \lambda \beta (\Delta H / T_m), \quad (3)$$

where  $\beta = d(E/E_0)/d(T/T_m)$ ,  $E$  is Young's modulus,  $E_0$  is Young's modulus at 0°K, and  $T_m$  is the melting temperature. The coefficient  $\beta$  arises from an attempt to estimate the temperature coefficient of the free energy associated with the straining of the lattice during the elementary diffusion jump.

The value of  $\beta$  for gold is listed<sup>6</sup> as 0.31 and a value of  $\beta = 0.42$  was obtained from data on Young's modulus for nickel.<sup>10</sup> A linear average of these values was used for the intermediate alloys. The  $\lambda$ -quantities calculated from Eq. (3) are listed in Table III. Zener has concluded on empirical grounds that the best value for  $\lambda$  in face-centered-cubic metals is 0.55.

TABLE III. Fraction of activation energy for jump of gold atom in self-diffusion in gold-nickel alloys.

At. % Ni	$\lambda^{(6)}$	$K^{(7)}$	$\lambda^{(7)}$
0	0.70	0.052	0.88
20	0.40	0.039	0.57
35	0.38	0.037	0.58
50	0.42	0.035	0.64
65	0.56	0.037	0.88
80	0.54	0.045	0.82
100	0.67	0.046	0.80

A similar approach was used by Buffington<sup>7</sup> except that the temperature-dependence of the lattice spacing as well as of the elastic constants is also considered. The diffusion equation becomes:

$$D = a^2 \nu \exp \left[ \frac{KE_0 a_0^3 \lambda (\varphi - 3\alpha)}{R} \right] \exp \left[ \frac{-KE_0 a_0^3}{RT} \right], \quad (4)$$

where

$a$  = lattice parameter,

$$\varphi = -\frac{1}{E_0} \left( \frac{dE}{dT} \right); \quad E_0 = \text{Young's modulus}$$

extrapolated to 0°K,

$$\alpha = \frac{1}{a_0} \left( \frac{da}{dT} \right); \quad a_0 = \text{lattice parameter}$$

extrapolated to 0°K,

$K$  = constant.

Suitable values of the parameters  $\varphi$  and  $\alpha$  are not always available even for pure metals, and in the case of gold-nickel alloys it was necessary to use a linear average of the best data on the pure metals. The constant  $K$  for each composition can be computed from the measured activation energy ( $Q_{Au}^* = KE_0 a_0^3$ ) and the quantity  $\lambda$ , which has the same significance as in

Eq. (3), can then be evaluated from the measured frequency factor  $D_{0,Au}$ . The quantities  $K$  and  $\lambda$  derived from Eq. (4) are tabulated in Table III; Buffington selected the values  $K = 0.051$  and  $\lambda = 0.64$  as the most probable for face-centered-cubic metals.

The assumptions entering into the formulation of Eqs. (3) and (4) are applicable to the case of self-diffusion in a pure metal, but discrepancies may be expected when these equations are used for the case of self-diffusion in an alloy. In addition, the parameters listed in Table V involve estimates of the values of  $\beta$ ,  $\varphi$ ,  $\alpha$ , and  $E_0$  for solid solutions, and thus only qualitative agreement can be anticipated. Nevertheless, the scatter in the resulting  $\lambda$  and  $K$  quantities for gold-nickel alloys is no worse than that obtained for similar calculations based on the published self-diffusivities in pure metals.

These treatments assume that the displacements of the barrier atoms involved in the elementary jump of a given atom into a neighboring vacancy are the same for each atom, and that the elastic energy at the saddle point can be described in terms of a macroscopic elastic modulus. This simple situation does not prevail when more than one kind of atom participates in the diffusion act. In addition, entropy changes arising from a modification of the vibrational spectrum when the atom is at the saddle point are also neglected. When the diffusing atom is jammed between the barrier atoms there is a negative contribution to the entropy arising from the reduced amplitude of vibration of the jumping atom and the barrier atoms. This effect is partially compensated by the increased amplitudes in the vacancy created by the diffusing atom. However, with atoms of greatly different sizes, as in the gold-nickel system,<sup>9</sup> these effects may not cancel and the poorest compensation would be expected near the 50 atomic per cent composition. While the rough outlines of these interpretations may be useful here as a basis for discussion, considerable refinement will be required before they can be applied with confidence to the process of self-diffusion in alloys.

## 5. SUMMARY

The self-diffusion coefficient for gold has been determined as a function of composition and temperature in the gold-nickel system. The diffusion data reveal no anomalies that correlate with the miscibility gap. However, the  $D_{Au}^*$ ,  $D_{0,Au}^*$  and  $Q_{Au}^*$  values show maximum deviations from the linear averages of the pure metal values in the composition range corresponding to the minimum in the solidus curve. The entropies of diffusion are positive and are qualitatively consistent with recent interpretations.

## 6. ACKNOWLEDGMENTS

The authors are grateful to the Wright Air Development Center for sponsoring this investigation (under

Contract AF 33(038)-23281, Scope I) and to G. Pishenin, E. Keplin, and V. Czerniszow for their assistance with the experimental phases of the program. They would also like to acknowledge the aid received on several occasions from H. C. Gatos, V. Griffiths, and J. E. Reynolds. The cooperation of the Brookhaven National Laboratory in providing the gold isotope is also greatly appreciated.

The research represents a portion of a thesis submitted by A. D. Kurtz in partial fulfillment of the requirements for the degree S.M. in Metallurgy at the Massachusetts Institute of Technology, August, 1952.

#### APPENDIX

When the quantity  $1/\mu$  is not negligibly small compared to the diffusion distance,  $y$ , it is necessary to take into account the intensity arising from regions in the sample beneath the autoradiographic surface. Assuming an average linear absorption coefficient,  $\mu$ , the contribution from each infinitesimal layer to the intensity observed at the surface must be computed. Introducing the parameters shown in Fig. 1, if the intensity at a given point in the sample is  $I(y)$ , the contribution of all such regions to the surface intensity,  $I(l)$ , is:

$$I(l) = \int_{l \tan \alpha}^{\infty} I(y) \exp[-\mu(y - l \tan \alpha)] dy, \quad (\text{A-1})$$

where  $l$  is a distance along the original interface,  $y$  is the diffusion distance, and  $y - l \tan \alpha$  is the absorption length for radiation originating at  $y$ .

The solution of the diffusion equation appropriate to the present boundary condition is

$$I(y) = \frac{I_0}{(4\pi Dt)^{1/2}} \exp\left(-\frac{y^2}{4Dt}\right), \quad (\text{A-2})$$

where  $I_0$  is the constant,  $D$  is the diffusion coefficient, and  $t$  is the diffusion time. One obtains

$$\frac{I(l)}{I_0} = \frac{\exp(\mu l \tan \alpha)}{(4\pi Dt)^{1/2}} \int_{l \tan \alpha}^{\infty} \exp(-y^2/4Dt - \mu y) dy. \quad (\text{A-3})$$

The integration gives Eq. (1) in the text:

$$\frac{I(l)}{I_0} = \frac{\exp(\mu l \tan \alpha + \mu^2 Dt)}{2} [1 - \text{erf}(z_0)]. \quad (\text{A-4})$$

For large values of  $z_0$ ,

$$\frac{I(l)}{I_0} = \frac{\exp(-l^2 \tan^2 \alpha / 4Dt)}{(4\pi z_0)^{1/2}} \left(1 - \frac{1}{2z_0^2} + \frac{3}{(2z_0^2)^2} \dots\right). \quad (\text{A-5})$$

Neglecting all but first powers of  $z_0$ ,

$$\ln \frac{I(l)}{I_0} = -\frac{(l \tan \alpha)^2}{4Dt} - \frac{1}{2} \ln(4\pi z_0). \quad (\text{A-6})$$

For values of  $(l \tan \alpha / 2\mu Dt)^2 \ll 1$ ,

$$\ln \frac{I(l)}{I_0} = -\frac{(l \tan \alpha)^2}{4Dt} - \frac{1}{2} \ln \left(1 + \frac{l \tan \alpha}{\mu Dt}\right) + \text{constant} \quad (\text{A-7})$$

and the slope of a plot of  $\ln[I(l)/I_0]$  vs  $(l \tan \alpha)^2$  becomes the expression given in the text.

#### REFERENCES

1. L. L. Seigle, M. Cohen, and B. L. Averbach, *J. Metals* **4**, 1320 (1952).
2. L. S. Darken, *Trans. A.I.M.E.* **175**, 184 (1948).
3. A. D. LeClaire, *Progress in Metal Physics* (Interscience Publishers, New York, 1949) Vol. I, Chap. 7.
4. H. Gatos and A. D. Kurtz, *J. Metals* **6**, 616 (1954).
5. J. E. Reynolds, *Diffusion in Gold-Nickel Alloys*. Sc.D. thesis, Department of Metallurgy, Massachusetts Institute of Technology.
6. C. Zener, *Imperfection in Nearly Perfect Crystals* (John Wiley, New York, 1952) Chap. 11.
7. F. S. Buffington and Morris Cohen, *Acta Met.* **2**, 660 (1954).
8. A. D. Le Claire, *Acta Met.* **1**, 438 (1953).
9. B. L. Averbach, P. A. Flinn, and M. Cohen, *Acta Met.* **2**, 92, (1954).
10. W. Köster, *Z. Metallk.* **39**, 1 (1948).

## SUR LA PRECIPITATION D'OXYDE $\text{Fe}_3\text{O}_4$ DANS LES PELLICULES D'OXYDATION DU FER AUX TEMPERATURES ELEVEES\* \*\*

J. PAIDASSI†

L'étude de la trempe des pellicules formées par oxydation directe du fer dans l'air ou de celles résultant de la réoxydation des pellicules précédentes après détachement de leur support métallique nous a conduit aux conclusions suivantes:

1. Le précipité de  $\text{Fe}_3\text{O}_4$  qui peut s'observer dans la couche de FeO de ces pellicules se forme seulement au cours de leur refroidissement par décomposition de la phase de protoxyde.

2. Il est d'autant plus difficile d'empêcher cette décomposition que la température d'oxydation ou de réoxydation est plus élevée. Quand cette température est supérieure à  $980^\circ\text{C}$ , les trempes les plus énergiques sont impuissantes à prévenir un début de précipitation.

3. La teneur en oxygène des phases FeO riches en oxygène, est le facteur prépondérant de leur instabilité au cours d'un refroidissement rapide (par trempe) ou assez rapide (refroidissement dans l'air).

Quand les pellicules précédentes sont refroidies dans l'air la précipitation de  $\text{Fe}_3\text{O}_4$  dans la couche de protoxyde présente un certain nombre de particularités que, compte tenu des résultats antérieurs, et moyennant quelques hypothèses simples, il est possible d'expliquer.

### THE PRECIPITATION OF $\text{Fe}_3\text{O}_4$ IN SCALES FORMED BY OXIDATION OF IRON AT ELEVATED TEMPERATURES

The study of the quenching of scales formed by direct oxidation of iron in air or of those resulting from the oxidation of existing films after detachment from their metallic support leads to the following conclusions:

(1) The precipitation of  $\text{Fe}_3\text{O}_4$  which can be observed in the layer of FeO of the scales forms only during their cooling down by decomposition of the monoxide.

(2) It is more difficult to prevent this decomposition if the temperature of oxidation or re-oxidation is very high. When this temperature is above  $980^\circ\text{C}$ , the most energetic quenching does not prevent the beginning of precipitation.

(3) The concentration of oxygen in FeO rich in oxygen is the predominating factor in their instability during rapid cooling, whether by quenching or by cooling in air.

When the former scales are cooled in air the precipitation of  $\text{Fe}_3\text{O}_4$  in the layer of monoxide presents a certain number of peculiarities which can be explained by taking into account previous results and making some simple hypothesis.

### ÜBER DIE AUSSCHIEDUNG DES OXYDES $\text{Fe}_3\text{O}_4$ IN DEN OXYDATIONSHÄUTCHEN DES EISENS BEI ERHÖHTEN TEMPERATUREN

Durch eine Untersuchung des Abschreckverhaltens von Häutchen, die entweder durch unmittelbare Oxydation des Eisens an Luft oder durch erneute Oxydation der zunächst vorhandenen Filme nach Ablösen von ihrer metallischen Unterlage gebildet worden waren, kamen wir zu folgenden Schlüssen:

1. Die Ausscheidung von  $\text{Fe}_3\text{O}_4$ , die man in der aus FeO bestehenden Grundmasse dieser Häutchen beobachten kann, bildet sich nur während der Abkühlung und zwar durch eine Entmischung der Protoxydphase.

2. Es ist darüberhinaus schwieriger diese Entmischung zu verhindern, wenn die Temperatur der Oxydation oder der erneuten Oxydation sehr hoch ist. Wenn diese Temperatur über  $980^\circ\text{C}$  liegt, ist es selbst bei schroffem Abschrecken nicht möglich, die beginnende Ausscheidung zu unterdrücken.

3. Der Sauerstoffgehalt der sauerstoffreichen FeO-Phasen ist der für ihre Instabilität bei sehr schneller (durch Abschrecken) oder beschleunigter (durch Abkühlen an Luft) Abkühlung verantwortliche Faktor.

Wenn sie oben erwähnten Häutchen an Luft abgekühlt werden, zeigt die Ausscheidung des  $\text{Fe}_3\text{O}_4$  in der Grundmasse des Protoxydes einige Besonderheiten, die auf Grund der obigen Versuche und unter Annahme einer einfachen Hypothese erklärt werden können.

### INTRODUCTION

On sait<sup>1,2,3</sup> que des pellicules d'oxydation formées à la surface du fer dans l'intervalle  $610^\circ\text{--}1000^\circ\text{C}$  et refroidies dans l'air sont constituées par la superposition de trois couches continues et compactes. De la face

externe en contact avec l'atmosphère à la face interne adhérente au fer-support, ce sont successivement: une couche de  $\text{Fe}_2\text{O}_3$ , une couche de  $\text{Fe}_3\text{O}_4$  et une couche de FeO, couches dont les épaisseurs relatives ont été précisées par ailleurs.<sup>3</sup> De plus, lorsque les pellicules ont été obtenues à des températures supérieures à  $800^\circ\text{C}$  environ, on observe dans la zone externe de la couche de FeO, une précipitation fine d'oxyde  $\text{Fe}_3\text{O}_4$ . L'aspect micrographique de cette zone est représenté

\* Cette recherche a fait l'objet du contrat n° 3 entre l'auteur et le "Consejo de Investigación Científica" de l'Université de Concepcion,

\*\* Received January 11, 1955.

† L'Université de Concepción, Chile.



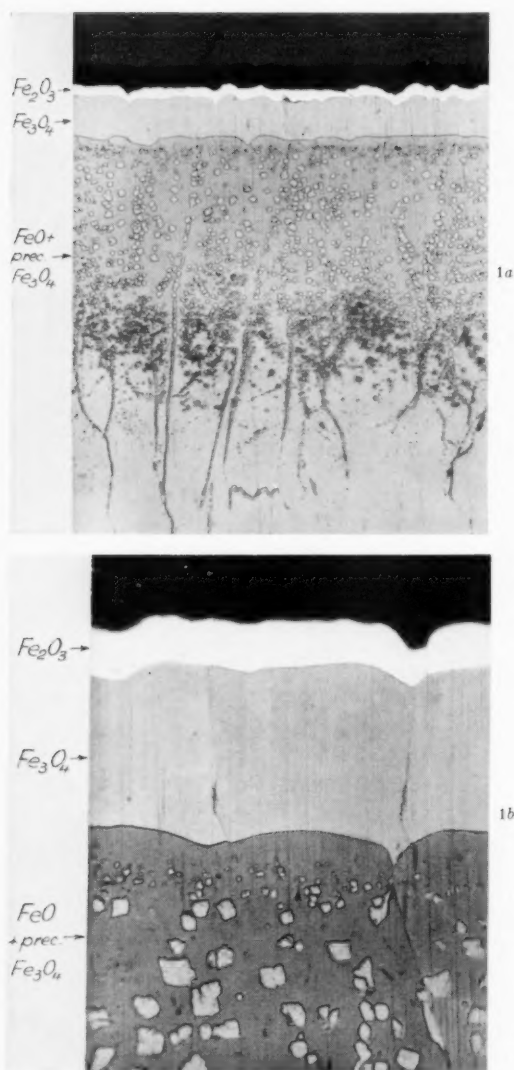


FIG. 1a et 1b. Partie externe de la coupe d'une pellicule d'oxydation sur support de fer: 950°C—4 heures (300X et 1250X).

sur les clichés 1(a) et 1(b) qui ont été obtenus sur une pellicule formée par oxydation du fer pendant 4 heures à 950°C et refroidie dans l'air. En partant de l'interface  $\text{Fe}_3\text{O}_4/\text{FeO}$ , on observe aux différents niveaux de la couche de protoxyde:

- Une bande étroite d'oxyde  $\text{FeO}$  exempt de précipité.
- Une zone à précipité dense de  $\text{Fe}_3\text{O}_4$  uniformément dispersé dans les cristaux columnaires de  $\text{FeO}$ .
- Une zone de filaments, où la densité de précipitation, est plus faible et où les granules de  $\text{Fe}_3\text{O}_4$  sont généralement disposés en alignements.

L'ensemble constitue ce que nous appellerons désormais la "couche mixte." Une telle couche peut être caractérisée, en plus de son épaisseur totale, par

l'épaisseur de la bande supérieure privée de précipité et par la dimension maximum des particules de  $\text{Fe}_3\text{O}_4$  dans la zone à précipité.

Une couche mixte présentant des caractères analogues peut également s'observer lorsque les pellicules précédentes sont détachées de leur support métallique, réoxydées au dessus de 800°C environ\* et laissées se refroidir dans l'air.<sup>3,4</sup> Mais dans ce cas sauf pour les durées très courtes de réoxydation, la couche protoxyde résiduelle se trouve envahie dans sa quasi totalité par le précipité à l'exception d'une bande étroite longeant chacune des deux interfaces  $\text{FeO}/\text{Fe}_3\text{O}_4$  de l'échantillon. De plus les particules de  $\text{Fe}_3\text{O}_4$  sont plus régulièrement dispersées dans la matrice de  $\text{FeO}$ , que dans le cas antérieur.

Bien que l'existence de cette couche mixte ait été signalée à plusieurs reprises et en particulier par Bénard et Coquelle,<sup>1</sup> aucune explication n'avait été fournie jusqu'à maintenant des causes de sa formation. Si les lois de la diffusion permettent en effet de justifier la succession des couches d'oxydes compacts  $\text{Fe}_2\text{O}_3$ ,  $\text{Fe}_3\text{O}_4$  et  $\text{FeO}$  dans l'ordre indiqué par l'expérience, elles ne peuvent que difficilement expliquer la formation d'un domaine diphasé avec dispersion d'une phase dans une autre. Elles semblent de plus en contradiction avec l'existence d'un étroit domaine privé de précipité, au voisinage immédiat de l'interface  $\text{FeO}/\text{Fe}_3\text{O}_4$ . Ces difficultés ne semblaient pouvoir être levées qu'en introduisant l'hypothèse d'une formation du précipité de  $\text{Fe}_3\text{O}_4$  au cours du refroidissement, soit dans le domaine des températures supérieures à 570°C par suite d'une réaction de précipitation proeutectoïde, soit aux températures inférieures à 570°C par suite de la décomposition du protoxyde suivant l'équation de Chaudron:



Dans le présent travail, où nous avons fait varier de façon systématique les conditions de refroidissement des pellicules après l'oxydation à haute température, nous nous proposons de démontrer qu'effectivement le précipité de  $\text{Fe}_3\text{O}_4$  ne se forme qu'au refroidissement par décomposition de la phase protoxyde. L'étude du mécanisme même de cette précipitation fera l'objet d'une publication ultérieure.

## RESULTATS EXPERIMENTAUX

I. Une première série d'expériences a été réalisée en refroidissant brusquement depuis la température de formation jusqu'à l'ambiante, des pellicules d'oxydation adhérent au métal.

Les pellicules étaient obtenues en oxydant dans l'air des plaquettes de fer Armco, soigneusement préparées. Cette préparation comprenait dans l'ordre suivant:

\* Au cours d'une telle réoxydation des couches superposées de  $\text{Fe}_2\text{O}_3$  et de  $\text{Fe}_3\text{O}_4$ , continues et compactes, croissent aux dépens de la phase  $\text{FeO}$ .

un polissage aux papiers émeri jusqu'au (000), un lavage dans plusieurs bains successifs de toluène et enfin un recuit de longue durée dans l'hydrogène pur et sec à  $900^\circ\text{C}$  ou  $1000^\circ\text{C}$  suivant les cas. Dans nos expériences la température d'oxydation a été de  $850^\circ$ ,  $900^\circ$  et  $1000^\circ\text{C}$ , la durée d'oxydation variant de quelques minutes à plusieurs heures. Seules les pellicules présentant tous les caractères morphologiques d'une pellicule non décollée à la température de l'expérience étaient retenues, l'apparition d'une solution de continuité au niveau de l'interface métal/oxyde en cours d'oxydation modifiant en effet complètement la constitution de la pellicule.

L'étude micrographique des échantillons trempés a montré que la couche de protoxyde des pellicules formées à  $850^\circ$  et  $900^\circ\text{C}$  était d'apparence homogène. Par contre la couche de protoxyde des pellicules formées à  $1000^\circ\text{C}$ , présentait dans sa partie externe un précipité très fin de  $\text{Fe}_3\text{O}_4$ . Nous proposons de le désigner "*précipité de trempe*" afin de le distinguer du précipité habituellement observé après refroidissement lent.

Ces résultats permettent de conclure qu'il existe une température critique telle que dans toute pellicule formée à une température supérieure, il soit impossible d'éviter, même en faisant appel aux trempes les plus énergiques, la présence d'un précipité de  $\text{Fe}_3\text{O}_4$  dans la zone externe de la couche de protoxyde. Cette température critique se situe entre  $900^\circ$  et  $1000^\circ\text{C}$ .

II. Dans une seconde série d'expériences, les conditions d'apparition du *précipité de trempe* ont été déterminées non plus sur des pellicules d'oxydes adhérent encore à leur support métallique mais sur des pellicules soumises à une réoxydation par l'air à des températures variées après avoir été séparées de leur support métallique. Dans la majorité des essais on soumettait à la réoxydation une pellicule provenant de l'oxydation du fer pendant 4 heures à  $900^\circ\text{C}$ , l'épaisseur de la couche de protoxyde étant dans ces conditions de l'ordre de  $500\mu$ . Des réoxydations de ces pellicules standard ont été opérées à six températures échelonnées de  $850^\circ$  à  $1000^\circ\text{C}$ , chaque traitement se terminant par un refroidissement brusque jusqu'à l'ambiante. Ces expériences ont montré que les échantillons réoxydés à  $950^\circ\text{C}$  et au-dessous présentaient après trempe une couche de protoxyde rigoureusement exempte de précipité, tandis que dans les échantillons oxydés à  $980^\circ\text{C}$  et au-dessus, le protoxyde était le siège d'une précipitation fine de  $\text{Fe}_3\text{O}_4$  en dépôt d'une trempe énergétique. On retrouve donc ici sur les phases  $\text{FeO}$  de pellicules préparées dans des conditions différentes cette notion de température critique mise en évidence dans la première série d'expériences, avec l'avantage cette fois de pouvoir resserrer l'intervalle qui inclut la température critique  $T_c$ . Nous admettrons qu'en première approximation  $T_c = 960-970^\circ\text{C}$ .

Il est nécessaire de signaler que dans les expériences effectuées sur pellicules réoxydées l'observation et l'interprétation étaient rendues plus délicates par la

présence dans la région externe du protoxyde d'un précipité primaire de  $\text{Fe}_3\text{O}_4$  formé au cours du refroidissement qui mettait fin à la préparation de la pellicule standard de départ.

Ce précipité primaire se redissout dans la matrice de  $\text{FeO}$  dans les premiers instants du traitement de réoxydation et ce n'est que pour des durées de réoxydation très brèves, au moins aux températures les plus élevées, qu'il en subsiste après la trempe finale. Sa morphologie particulière permet toutefois de le distinguer du *précipité secondaire de trempe*.

Ces observations nous ont permis d'autre part de déterminer l'ordre de grandeur de la vitesse d'homogénéisation de la phase protoxyde aux différentes températures. Cet ordre de grandeur est fourni en effet par la vitesse de dissolution du précipité primaire de  $\text{Fe}_3\text{O}_4$  dans la matrice de protoxyde à différentes températures. A titre d'exemple, une pellicule standard refroidie lentement et présentant par conséquent une zone précipitée pourra devenir homogène, après un traitement de réoxydation de 30 minutes à  $800^\circ\text{C}$ , de 5 minutes à  $900^\circ\text{C}$  et de 2 minutes seulement à  $1000^\circ\text{C}$ . Au dessous de  $750^\circ\text{C}$  la vitesse de dissolution du précipité dans la matrice se ralentit considérablement puisqu'un séjour de 24 heures à cette température ne suffit pas à faire disparaître les granules de  $\text{Fe}_3\text{O}_4$ . Ces observations se trouvent illustrées par les figures 2, 3, et 4 ci-jointes.

La micrographie de la figure 2 montre l'aspect que possède après trempe dans l'eau salée à  $-5^\circ\text{C}$ , le côté externe d'une pellicule standard ( $900^\circ\text{C}-4$  heures), réoxydée durant 3 min. 45 sec. à  $950^\circ\text{C}$ . On note que la couche de  $\text{FeO}$  est micrographiquement homogène, ce qui prouve:

1—Que le séjour de l'échantillon à  $950^\circ\text{C}$  durant 3 min. 45 sec. a été suffisant pour dissoudre en totalité le précipité initial de l'échantillon de départ.

2—Qu'une phase protoxyde oxydée dans l'air à  $950^\circ\text{C}$  reste à cette température homogène micrographiquement.

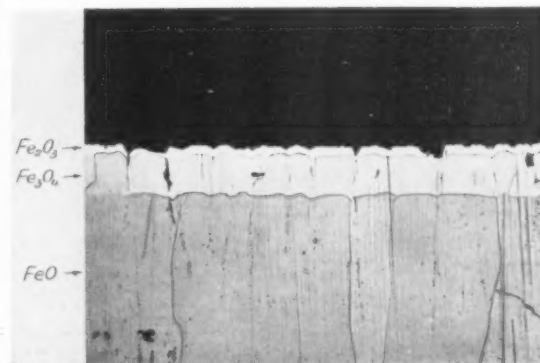


FIG. 2. Pellicule standard ( $900^\circ\text{C}-4$  h.) détachée de son support de fer, réoxydée dans l'air à  $950^\circ\text{C}$  durant 3 min. 45 sec. et trempée finalement dans l'eau ( $350\times$ ).

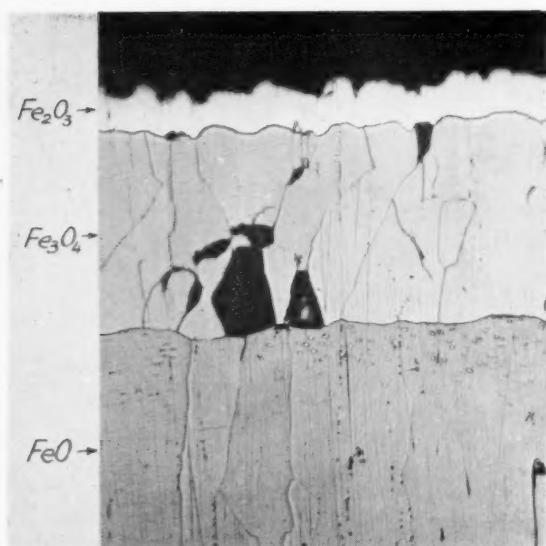


FIG. 3. Pellicule réoxydée dans l'air à 950°C durant 7 min. 30 sec. et trempée finalement dans l'eau (400X). Les taches sombres visibles dans la couche de  $\text{Fe}_3\text{O}_4$  correspondent à des arrachements d'oxyde produits au cours du polissage.

La micrographie de la figure 3 représente de même une pellicule réoxydée pendant 7 min. 30 sec. à 950°C et trempée dans l'eau salée à -10°C. Les quelques particules de précipité qui s'observent encore dans le voisinage de l'interface  $\text{FeO}-\text{Fe}_3\text{O}_4$  doivent être considérées comme le résidu de la dissolution du précipité initial au cours de la réoxydation.

La micrographie de la figure 4(a) montre d'autre part une pellicule réoxydée à 980°C pendant 3 min. 45 sec. et trempée dans l'eau salée à -5°C. Un précipité apparaît dans la couche de protoxyde de cette pellicule. Un examen sous plus fort grossissement (fig. 4b) révèle que ce précipité est constitué d'une part par des grosses particules constituant le résidu du précipité initial incomplètement dissous et d'autre part par des particules extrêmement fines à peine perceptibles même sous les plus forts grossissements du *précipité de trempe*.

#### DISCUSSION ET CONCLUSIONS

Les expériences précédemment décrites permettent d'affirmer sans aucun doute que dans les pellicules formées par oxydation directe ou réoxydation, à des températures inférieures à la température critique, le précipité qui s'observe dans la couche de protoxyde, (si on fait abstraction des résidus éventuels du précipité primaire) résulte de la décomposition de cette phase au cours du refroidissement. Le processus de diffusion, dont la couche de  $\text{FeO}$  est le siège au cours de l'oxydation du fer ou d'échantillons d'oxyde  $\text{FeO}$  homogène dans l'air, n'est donc pas compliqué par la présence d'une phase  $\text{Fe}_3\text{O}_4$  dispersée.

Pour ce qui est des pellicules préparées par oxydation directe ou réoxydation aux températures supérieures

à la température critique, on pourrait se demander par contre si le *précipité de trempe* n'est pas déjà formé dans la matrice de  $\text{FeO}$  à la température de formation, puisqu'une trempe aussi vigoureuse soit-elle, ne permet pas de s'en affranchir. L'examen de la figure 5 montre cependant qu'il n'en est rien. En effet on voit dans cette micrographie l'aspect du précipité de trempe dans une phase protoxyde oxydée à l'air à 1000°C et trempée de cette température. La structure est du type Widmanstätten, ce qui est un argument en faveur d'une formation quasi-instantanée de  $\text{Fe}_3\text{O}_4$  au cours du refroidissement.

On se trouve donc conduit à admettre que l'instabilité de la phase protoxyde, présente dans les pellicules réoxydées, augmente en même temps que la température de réoxydation. Pour les températures de réoxydation supérieures à la température critique  $T_c$ , cette instabilité devient telle que les trempes les plus énergiques sont impuissantes à éviter une décomposition partielle de la phase  $\text{FeO}$  au cours du refroidissement.

Si l'on rapproche ceci du fait que dans tous les diagrammes d'équilibre fer-oxygène proposés, la solubilité de l'oxygène dans la phase protoxyde augmente dans l'intervalle 570°-1000°C, de façon uniforme avec la température, on est amené à conclure que

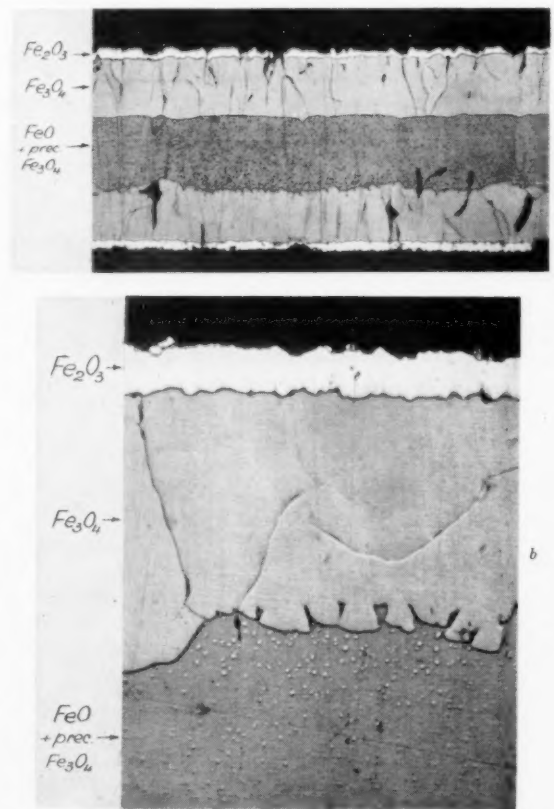


FIG. 4a et 4b. Pellicule réoxydée dans l'air à 980°C durant 3 min. 45 sec. et trempée finalement dans l'eau. Fig. 4a (150X); Fig. 4b (750X).

l'instabilité des phases FeO au refroidissement varie dans le même sens que leur teneur en oxygène. Ceci conduit à introduire pour les phases FeO une notion de teneur critique en oxygène  $c_c$ , définie comme suit: dès que la teneur en oxygène de la phase FeO dépasse  $c_c$ , cette phase ne peut être refroidie sans se décomposer partiellement et cela, même dans le cas où le refroidissement est réalisé par trempe énergétique.

Si nous admettons que les concentrations aux interfaces d'une pellicule d'oxydation sont données par les concentrations d'équilibre des phases correspondantes en contact, la valeur de  $c_c$  est donnée par l'abscisse du point d'intersection de l'horizontale correspondant à la température critique  $T_c$  avec la courbe donnant la concentration de saturation en oxygène de FeO, dans le diagramme d'équilibre Fe—O. En adoptant le diagramme Fe—O établi par Bénard<sup>5</sup> on trouve:  $c_c = 24.3\%$ . Il y a lieu de noter que la netteté avec laquelle les phases FeO se subdivisent en phases trempables et non trempables tendrait à laisser supposer que l'inclinaison réelle de la courbe-limite du côté de l'oxygène du faisceau de stabilité de la phase FeO dans le diagramme d'équilibre Fe—O, pourrait être plus accentuée dans l'intervalle  $900^\circ\text{--}1000^\circ\text{C}$ , que celle qui a été indiquée par la plupart des auteurs ayant établi cette courbe.

Par ailleurs, de nombreuses particularités des pellicules trempées ou refroidies dans l'air, conduisent à admettre que pour chacun de ces deux modes de refroidissement, le phénomène de décomposition des phases FeO présente une insensibilité relative, vis à vis de la vitesse de refroidissement, la teneur en oxygène étant ainsi en première approximation le seul facteur dont dépend l'instabilité au refroidissement des phases FeO riches en oxygène, étudiées dans ce travail.

Les résultats généraux qui viennent d'être exposés permettent enfin d'interpréter moyennant quelques hypothèses simplificatrices complémentaires, certaines particularités présentées par les couches mixtes des pellicules d'oxydation refroidies dans l'air, en particulier:

a. L'existence d'un liseré sans précipité, contre l'interface  $\text{FeO}/\text{Fe}_3\text{O}_4$ , et d'épaisseur sensiblement indépendante de la température et de la durée d'oxydation.

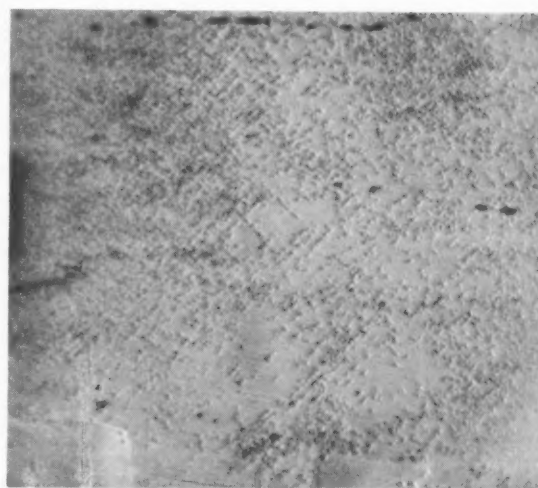


FIG. 5. Phase FeO, oxydée à l'air à  $1000^\circ\text{C}$  et trempée à partir de cette température (1000X).

b. L'augmentation progressive en fonction de la température d'oxydation (ou de réoxydation) de la dimension maxima des particules du précipité de  $\text{Fe}_3\text{O}_4$ .

c. Le fait que l'épaisseur de la couche mixte d'une pellicule sur support de fer croît paraboliquement en fonction de la durée dans le cas d'une oxydation isotherme.

#### REMERCIEMENTS

Je tiens en terminant à adresser mes remerciements au "Consejo de Investigación Científica" de l'Université de Concepcion (Chili) pour les fonds qu'il m'a accordé et grâce auxquels cette recherche a pu être réalisée.

Je remercie également Monsieur J. Bénard, Professeur à la Faculté de Sciences de Paris, en liaison avec lequel a été poursuivi ce travail, pour les nombreuses et fructueuses discussions et échanges de vue sur la question.

#### BIBLIOGRAPHIE

1. J. Bénard et O. Coquelle, *Rev. Metallurgie* **43**, 113 (1946).
2. J. Paidassi, *Boletín Soc. Chilena de Química* **3**, 55 (1951).
3. J. Paidassi, *Boletín Soc. Chilena de Química* **5**, 46 (1953).
4. Mme A. Michel, J. Bénard, et G. Chaudron, *Bull. Soc. Chim. France* **11**, 175 (1944).
5. J. Bénard, *Colloque Etat Solide*, C.N.R.S. (Paris, 1948), p. 80.



# MARKER MOVEMENTS IN TITANIUM-MOLYBDENUM DIFFUSION COUPLES AND THE ZENER THEORY OF $D_0$ \*

P. G. SHEWMON† and J. H. BECHTOLD‡

Marker movements have been found and their rates measured in diffusion couples of pure titanium *versus* pure molybdenum. Ti-Mo alloys are body centered cubic (b.c.c.) in the temperature range studied, 1400–1640°C. The marker movements imply a vacancy mechanism of diffusion in the b.c.c. transition metals which contradicts the prediction of Zener and LeClaire of a ring mechanism of diffusion. The anomalies which lead to the prediction of a ring mechanism are discussed, and an alternative explanation consistent with a vacancy mechanism is given.

## MOUVEMENTS DES REPÈRES DANS LA DIFFUSION DES COUPLES Ti-Mo ET LA THÉORIE DE ZENER DE $D_0$

En étudiant la diffusion dans les couples titane pur-molybdène pur, les mouvements des repères ont été observés et leurs vitesses mesurées. Les alliages Ti-Mo sont cubiques centrés dans l'intervalle de température étudié 1400–1640°. Les mouvements des repères sont le corollaire d'une diffusion par les lacunes, ce qui est en contradiction avec le mécanisme par rotation prévu par Zener et Le Claire pour les métaux de transition cubiques centrés. Les anomalies qui avaient conduit à ce mécanisme par rotation sont discutées et il est donné une autre explication en harmonie avec le mécanisme de diffusion par les lacunes.

## ÜBER DIE MARKIERUNGSBEWEGUNG BEI DER DIFFUSION ZWISCHEN Ti UND Mo UND DIE ZENER THEORIE VON $D_0$

In Diffusionsprobenpaaren—reines Titan gegen reines Molybdän—wurden Markierungsbewegungen festgestellt und deren Wanderungsausmass gemessen. Im untersuchten Temperaturbereich, 1400–1640°, haben die Ti-Mo Legierungen ein kubisch-raumzentriertes Gitter. Bei den kubisch-raumzentrierten Übergangsmetallen erfordert die Markierungs-wanderung einen Leerstellenmechanismus der Diffusion, der jedoch mit der Vorhersage von Zener und LeClaire über einen Ringmechanismus der Diffusion in Widerspruch steht. Die Anomalien, die zur Vorhersage eines Ringmechanismus<sup>1</sup> führen, werden diskutiert; weiterhin wird eine Alternativerklärung in Übereinstimmung mit einem Leerstellenmechanismus gegeben.

### INTRODUCTION

Zener,<sup>1</sup> and more recently LeClaire,<sup>2</sup> has proposed that diffusion takes place by a ring mechanism in body centered cubic transition metals. These predictions have been based on a correlation between the entropy of activation for self diffusion,  $\Delta S$ , and the temperature, dependence of the elastic constants. If this prediction is true there should be no marker movements or Kirkendall effect in body-centered-cubic metals and compounds. To date the only published study of marker movements in a b.c.c. lattice is the work of Landergren and Mehl using beta-brass.<sup>3</sup> These authors found a small but definite marker movement. Since the predictions of a ring mechanism were made by correlating self diffusion data, it was thought that marker movements should also be studied in a terminal solid solution or an isomorphous system of b.c.c. metals. A study of diffusion in body-centered-cubic titanium-molybdenum alloys\* was therefore undertaken and marker movements have been found. This again contradicts the predictions of Zener and LeClaire. The purpose of this paper is to report the marker movements and to propose an explanation for this shortcoming of the Zener theory.

\* Received January 12, 1955.

† Carnegie Institute of Technology, Pittsburgh; formerly, Westinghouse Research Laboratories.

‡ Westinghouse Electric Corporation, Research Laboratories, East Pittsburgh, Pennsylvania.

\* The Ti-Mo system is isomorphous b.c.c. at all temperatures above 885°C.<sup>4</sup>

### EXPERIMENTAL PROCEDURE AND RESULTS

Sandwich type diffusion couples were made by resistance butt welding a 0.58 in. diameter cylinder of pure molybdenum between two cylinders of pure titanium of the same diameter. Three thin strips of thorium oxide, approximately 0.001×0.010×0.60 in., were put in each interface to serve as markers. After welding, the specimens were machined cylindrical, and paralleled flats 0.25 in. wide were ground on each side of the specimens. The couples were then given a stress relief anneal by heating for one hour in vacuum at 1240°C. Following this the flats were given a metallographic polish, and the positions of the markers were individually measured relative to a mark outside the diffusion zone. All distance measurements were made with a Kodak Contour Projector, and were reproducible to within  $\pm 0.0002$  in. The specimens were next annealed in a vacuum furnace at  $10^{-5}$  to  $10^{-6}$  mm Hg at temperatures from 1400 to 1640°C. After annealing, 0.025 in. of metal was removed from the flats to eliminate the effects of surface diffusion and vapor transport, the flats were again polished, and the position of the markers individually determined.

Measurements were made on different couples after diffusion anneals at one of five different temperatures. In each couple the markers were found to move toward the titanium. The movements ranged from 0.0107 in. to 0.0017 in. The movements are given in Table I.

TABLE I. Marker movements in molybdenum-titanium diffusion couples.

Spec. no.	Diffusion temp. (°C)	Diffusion time (minutes)	Marker movement (inches)
Direct Measurement			
A-7*	1470	4135	$10.7 \times 10^{-3}$
I-7*	1515	482	$1.7 \times 10^{-3}$
A-9	1605	380	$8.9 \times 10^{-3}$
C-3	1640	120	$6.8 \times 10^{-3}$
I-6	1640	120	$2.5 \times 10^{-3}$
	1640	413	$5.5 \times 10^{-3}$
I-5	1400	3228	$2.6 \times 10^{-3}$
C-2	1400	3228	$4.9 \times 10^{-3}$
Diffusion Curve Method			
A-7	1470	4135	$10 \times 10^{-3}$

\* The A- and C-specimens were made with arc melted duPont sponge titanium. The I-specimens were made with iodide titanium.

In a few cases the thoria markers were large enough to interfere with diffusion near the markers. This interference could easily be detected metallographically and the movement of these markers was not recorded. If the markers had not interfered with diffusion, the scatter between the movements of the different markers was always less than  $\pm 20$  per cent.

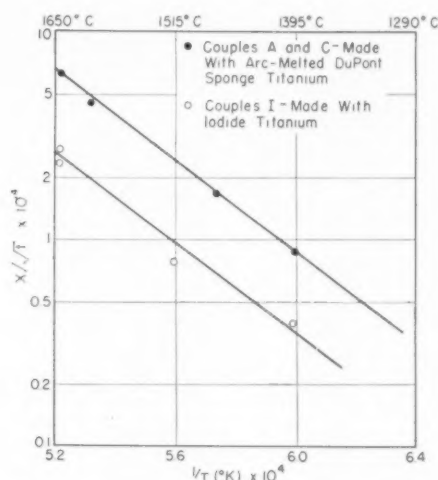
The marker movement in a given couple can be measured in two independent ways. The marker movements given above were obtained by direct measurement. The second method has been termed the "diffusion curve method" by da Silva and Mehl.<sup>5</sup> It has been used in several investigations and is reported to give more reproducible results than direct measurement.<sup>6,7</sup> The technique is based on the observation that the original interface coincides with the Matano interface.\* Thus the final distance between the thoria markers and the Matano interface is the distance which the markers have moved during diffusion. The position of the markers is determined when the specimen is sectioned for chemical analysis.

The marker movement was checked by the diffusion curve method in one specimen, A-7. The movement was  $10 \times 10^{-3}$  in. The value obtained by direct measurement was  $10.7 \times 10^{-3}$  in. This check is well within experimental error since the final position of the markers could only be determined to within a thousandth of an inch in the machining operation.

In Table I it is seen that the marker movement in specimen C-3, after 120 minutes at 1640°C was  $6.8 \times 10^{-3}$  in., yet the movement in I-6 after 120 minutes at 1640°C was only  $2.5 \times 10^{-3}$  in. These two specimens were annealed at the same time so that the time and temperature of diffusion for the two specimens are exactly the

\* If the concentration of one component in atom per cent,  $c$ , is plotted against diffusion distance, the Matano interface is defined by the equations:

$$x=0, \quad \int_0^{100} xdc=0,$$

FIG. 1.  $\log(x/(t)^{1/2})$  versus  $1/T$ .

same. The difference between the two movements is therefore much too large to be experimental error.

The internal consistency of marker movement data can be checked<sup>5,6,7</sup> by using the equation

$$x = B(t)^{1/2} \exp(-A/RT), \quad (1)$$

where  $A$  and  $B$  are constants independent of time and temperature,  $T$  is the absolute temperature,  $t$  is the time,  $R$  is the gas constant, and  $x$  is the marker movement. In Fig. 1 the data from Table I are plotted as  $\log x/(t)^{1/2}$  versus  $1/T$ . It is found that the data for the A- and C-specimens fall on one straight line and the data for the I-specimens fall on another, i.e., the data fall into two separate groups. The slopes of the two lines are approximately the same, but for a given time and temperature the marker movement found in the I-specimens is roughly one-third that found in the A- and C-specimens. The only difference between these two groups of specimens is that the I-series were made with iodide titanium while the A- and C-series were made with arc-melted duPont sponge titanium. This indicates that the marker movements within a given set of specimens are consistent but impurities increase the rate of marker movement.

## DISCUSSION

If marker movement is observed in metallic diffusion couples, it implies that diffusion must take place by either a vacancy or an interstitial mechanism. For an isomorphous solid solution of transition elements, the interstitial mechanism can be ruled out because of the large amount of energy required to form an interstitial atom.<sup>8</sup> Therefore the observation that marker movements occur in b.c.c., Ti-Mo diffusion couples, establishes that diffusion takes place primarily by a vacancy mechanism, at least in this system, and by implication in all b.c.c. solid solutions of transition metals.

When Zener<sup>1</sup> originally made his analysis of  $D_0$  for self-diffusion he worked with the equations

$$D = D_0 e^{-\Delta H/RT}, \quad (2)$$

$$D_0 = a^2 \nu e^{\Delta S/R}, \quad (3)$$

$$\left(\frac{\Delta S}{R}\right) = \lambda \left(\frac{\Delta H}{RT_m}\right) \frac{d(\mu/\mu_0)}{d(T/T_m)}, \quad (4)$$

where  $a$  is the interatomic distance,  $\nu$  is the vibrational frequency of the atoms,  $\mu$  is an appropriate elastic constant (Zener used Koster's<sup>9</sup> data for Young's modulus),  $\mu_0$  is  $\mu$  extrapolated to 0°K,  $T_m$  is the melting point of the metal,  $\Delta S$  is the entropy of activation for diffusion,  $\Delta H$  is the heat of activation for diffusion, and  $\lambda$  an experimentally determined constant.

By plotting  $\ln(D_0/a^2\nu)$  versus

$$\frac{\Delta H}{\mu_0 R} \frac{d\mu}{dT},$$

Zener found that  $\lambda \approx 0.55$  for f.c.c. metals and  $\lambda \approx 1$  for b.c.c. metals. From this difference in  $\lambda$  for the two types of lattices he suggested that diffusion might take place by different mechanisms in the two types of metals. A ring mechanism would probably have a higher  $\Delta S$  than a vacancy mechanism; also, the vacancy mechanism is fairly well established for f.c.c. metals. Therefore he suggested that diffusion in b.c.c. metals takes place by a ring mechanism.

LeClaire<sup>2</sup> has extended Zener's theory by trying to correlate the different parts of  $\Delta S$  and  $\Delta H$  with other physical properties. For a vacancy mechanism  $\Delta S$  and  $\Delta H$  can each be broken up into two parts, the first associated with the formation of a vacancy, ( $\Delta S_1$  and  $\Delta H_1$ ), and the second associated with the migration of an atom from an equilibrium site into an adjacent vacancy, ( $\Delta S_2$  and  $\Delta H_2$ ). LeClaire takes equation (3) and develops it into:

$$D_0 = a^2 \nu \exp \left[ \Delta S_1 - (\Delta H - k_1 L_s) \right. \\ \left. \times \left( \frac{1}{\mu} \frac{d\mu}{dT} - \frac{1}{\rho} \frac{d\rho}{dT} \right) \right] / R, \quad (5)$$

where  $L_s$  is the heat of sublimation,  $\rho$  is the density and  $k_1$  is defined as the ratio  $\Delta H_1/L_s$ .

LeClaire could not find any physical property with which to correlate  $\Delta S_1$  but he did show that it should be positive and of the order of 1-2 cal/mole°K. He further reasons that near a vacancy  $\mu$  and  $(T_m/\mu_0)d\mu/dT$  will be less than the bulk values. If we use the bulk values for the elastic constants instead of the correct values this will tend to add a spurious negative entropy of activation. He assumed that  $\Delta S_1$  would be equal to this spurious negative contribution and simplified his equation by setting  $\Delta S_1 = 0$ . Upon solving for  $k_1$ , he found it to be positive and equal to 0.215 for all f.c.c.

metals for which self diffusion data are available. For the b.c.c. data ( $\alpha$  Fe and some approximate data for W),  $k_1$  is negative. Negative values of  $k_1$  have no physical significance so he concluded that the b.c.c. data would not fit the vacancy mechanism equation.

Using much the same type of reasoning he develops for a ring mechanism the equation

$$R \log N_r = R \log \frac{D_0}{a^2 \nu} + \Delta H \left( \frac{1}{\mu} \frac{d\mu}{dT} - \frac{1}{\rho} \frac{d\rho}{dT} \right), \quad (6)$$

where  $N_r$  is the "number of distinct rings, each of  $r$  atoms, whose rotation can effect a migration of the atom in any one direction." Solving for  $N_r$  one finds  $N_r \leq 0.2$  for the f.c.c. data and  $N_r > 2$  for the b.c.c. data. Since  $N_r$  must be greater than one, he concludes that the b.c.c. data are consistent with a ring mechanism and the f.c.c. data are not.

In Eqs. (2) to (5) one has a correlation which not only fits the more recent diffusion data quite well, but is selective enough to rule out older data which have since been proved inaccurate. Nevertheless, the conclusions drawn from these equations about the mechanism of diffusion in b.c.c. metals seems to be incorrect.

Zener<sup>10</sup> has pointed out that the entropy associated with the formation of a vacancy,  $\Delta S_1$ , should be larger in b.c.c. metals than in f.c.c. metals, and that this factor has been left out in the development and interpretation of the equations given above. This difference in  $\Delta S_1$  for the two types of lattices can be seen from the following considerations.  $\Delta S_1$  is given by<sup>11</sup>

$$\Delta S_1 = +ZR \ln \frac{\nu}{\nu^*}, \quad (7)$$

where  $Z$  is the number of nearest neighbors,  $\nu$  and  $\nu^*$  are the frequency of vibration of atoms in the bulk metal, and next to a vacancy, respectively. In an f.c.c. lattice the nearest neighbors of a vacancy are nearest neighbors of each other, while in a b.c.c. lattice the nearest neighbors of a vacancy are not nearest neighbors of each other. Therefore, the atoms around a vacancy in a b.c.c. lattice will relax, or move their equilibrium position toward the vacancy, more than the atoms around a vacancy in an f.c.c. lattice. This increased relaxation will give a larger value of  $\nu/\nu^*$  in a b.c.c. lattice, thus giving a larger  $\Delta S_1$ .

If we hypothesize that (1) diffusion occurs by a vacancy mechanism in b.c.c. and f.c.c. transition metals, (2)  $\Delta S_1(\text{f.c.c.}) = 0$ , as LeClaire did, but  $\Delta S_1(\text{b.c.c.}) > 0$ , and (3) the relationship between  $\Delta S_2$  and the elastic constants is the same in b.c.c. and f.c.c. metals, then  $\Delta S(\text{b.c.c.})$  will be greater than  $\Delta S(\text{f.c.c.})$ , ( $\Delta S = \Delta S_1 + \Delta S_2$ ). This explains the larger values of  $\lambda$  for b.c.c. metals in Zener's work, without assuming a ring mechanism. The negative values of  $k_1$  (Eq. 5), which led LeClaire to suggest a ring mechanism for b.c.c.

metals can also be explained quite satisfactorily with these hypotheses. If  $\Delta S_1 > 0$  is inserted in Eq. (5) along with the data for alpha-iron (see LeClaire's paper),  $k_1 = 0$  if  $\Delta S_1 = 1.36$  cal/mol $^\circ$ K, and, if  $k_1 = 0.215$ , as it did for the f.c.c. data with  $\Delta S_1(\text{f.c.c.}) = 0$ , one obtains  $\Delta S_1(\text{b.c.c.}) = 5.36$  cal/mol $^\circ$ K.  $k_1 = 0.215$  is a reasonable value for alpha iron and gives  $\Delta S_2 = \Delta S - \Delta S_1 = 7.94$  cal/mol $^\circ$ K. This value of  $\Delta S_2$  is positive as Zener's theory requires, and is roughly equal to  $\Delta S = \Delta S_2$  for the f.c.c. metals listed by LeClaire. Finally, inspection of Eq. (6) shows that the only requirement for  $N_v > 1$  is a relatively large  $\Delta S$ , which is again consistent with the above hypotheses. Therefore, the hypotheses given above will account for each of the anomalies which led Zener and LeClaire to the questionable prediction of a ring mechanism for diffusion in b.c.c. metals, while these hypotheses have no effect on the general correlation between  $D_0$  and  $d\mu/dT$ .

Buffington and Cohen<sup>12</sup> have recently extended Zener's theory of  $D_0$  in a manner similar to LeClaire's. These authors believe that diffusion occurs by a vacancy mechanism in b.c.c. metals, which is in agreement with the work reported here. One of the constants evaluated by these authors,  $\lambda$ , is quite similar to the  $\lambda$  in Zener's theory. Their observation that  $\lambda(\text{b.c.c.}) > \lambda(\text{f.c.c.})$  is the same as Zener's and thus is consistent with the hypotheses given above.

#### SUMMARY

Marker movements have been observed and their rates measured in diffusion couples of b.c.c. Ti versus

b.c.c. Mo. This implies a vacancy mechanism of diffusion which contradicts the predictions of Zener and LeClaire that diffusion occurs by a ring mechanism in b.c.c. transition metals. It has been hypothesized that the entropy of formation of a vacancy is greater in a b.c.c. lattice than in an f.c.c. lattice, and that diffusion occurs by a vacancy mechanism in b.c.c. metals. It is then shown that these hypotheses are consistent with the anomalies which led Zener and LeClaire to predict a ring mechanism of diffusion in body centered cubic metals.

#### ACKNOWLEDGMENT

The authors would like to thank Dr. C. Zener for many helpful discussions, and Mr. W. Platte for welding the diffusion specimens.

#### REFERENCES

1. C. Zener, *J. App. Phys.* **22**, 372 (1951).
2. A. D. LeClaire, *Acta Met.* **1**, 438 (1953).
3. U. S. Landergren and R. F. Mehl, *J. Metals* **5**, 153 (1953).
4. M. Hansen, E. Kamen, H. Kessler, and D. McPherson, *Trans. A.I.M.E.* **191**, 881 (1951).
5. C. daSilva and R. F. Mehl, *Trans. A.I.M.E.* **175**, 184 (1948).
6. U. S. Landergren, Ph.D. Thesis, Carnegie Institute of Technology, Pittsburgh, Pennsylvania, May 1953.
7. G. T. Horne and R. F. Mehl. To be published in *Trans. A.I.M.E.*
8. F. Seitz, *Phase Transformations in Solids* (J. Wiley, New York, 1951), p. 115.
9. W. Koster, *Z. Metallk.* **39**, 1 (1948).
10. C. Zener, Private communication.
11. N. F. Mott and R. W. Gurney, *Electronic Processes in Ionic Crystals* (Oxford Press, London, 1940), p. 30.
12. F. S. Buffington and M. Cohen, *Acta Met.* **2**, 660 (1954).



## ACTIVITY OF ALUMINUM IN LIQUID Ag-Al, Fe-Al, Fe-Al-C, AND Fe-Al-C-Si ALLOYS\*

J. CHIPMAN† and T. P. FLORIDIS‡

Experimental data on the distribution of aluminum between liquid iron and silver at 1600°C are presented. The effects of carbon and silicon in the iron are shown.

Recent data of Hillert on the cell:



are extrapolated to obtain the activity of aluminum in liquid Ag-Al solutions. This and the distribution data lead to values for the activity coefficient of aluminum in liquid iron.

In the infinitely dilute solution in pure iron,  $\gamma_{\text{Al}}^\circ = 0.031$  at 1600°. The value of  $\log \gamma_{\text{Al}}$  increases almost linearly with the concentration of Al, C, or Si.

The solubility of graphite in iron decreases with increasing aluminum content.

### ACTIVITÉ DE L'ALUMINIUM DANS LES ALLIAGES LIQUIDES Ag-Al, Fe-Al, Fe-Al-C, ET Fe-Al-C-Si

Les auteurs rapportent les résultats expérimentaux sur la répartition de l'aluminium entre le fer liquide et l'argent à 1600°, ainsi que les effets du carbone et du silicium dans le fer.

Les résultats récents de Hillert sur la cellule:



sont extrapolés pour obtenir l'activité de l'aluminium dans les solutions liquides Ag-Al. Ces résultats et la répartition ci-dessus conduisent au coefficient d'activité de l'aluminium dans le fer liquide.

Pour les solutions infiniment diluées dans le fer pur,  $\gamma_{\text{Al}}^\circ = 0.031$  à 1600°. La valeur de  $\log \gamma_{\text{Al}}$  croît presque linéairement avec la concentration en Al, C, ou Si.

La solubilité du graphite dans le fer décroît avec les teneurs croissantes en aluminium.

### DIE AKTIVITÄT VON ALUMINIUM IN FLÜSSIGEN Ag-Al, Fe-Al, Fe-Al-C UND Fe-Al-C-Si LEGIERUNGEN

Über die Verteilung von Aluminium in flüssigem Eisen und Silber bei 1600° werden experimentelle Untersuchungen mitgeteilt. Der Einfluss des Kohlenstoffs und des Siliziums werden beschrieben.

Die kürzlich von Hillert für die Anordnung



mitgeteilten Ergebnisse werden extrapoliert, um die Aktivität von Aluminium in flüssigen Ag-Al Lösungen zu erhalten. Dies und die Verteilungsergebnisse führen zu den Werten der Aktivitätskoeffizienten von Aluminium in flüssigem Eisen.

In der unendlich verdünnten Lösung im reinen Eisen ist  $\gamma_{\text{Al}}^\circ = 0.031$  bei 1600°. Der Wert des  $\log \gamma_{\text{Al}}$  steigt fast linear mit der Konzentration von Al, C oder Si.

Die Löslichkeit von Graphit in Eisen nimmt mit steigendem Aluminiumgehalt ab.

## INTRODUCTION

In the application of thermodynamics to the study of reactions occurring in liquid metals, it frequently happens that the greatest uncertainty in a calculation attaches to the question of the activity of a minor component. Attempts to calculate the equilibrium constant for the deoxidation of liquid steel with aluminum have been subject to this uncertainty. The earliest study of the activity coefficient of aluminum in liquid iron was made by Chipman<sup>1</sup> who measured the distribution ratio of aluminum between liquid iron and liquid silver at 1600°C. It was assumed that the activity of aluminum in the liquid silver layer was equal to its mole fraction, an assumption which is

not justified and which has been shown to be a source of substantial error.

An important contribution was made by Chou,<sup>2</sup> who showed that the activity of aluminum in liquid silver could be estimated by the following steps: (1) The activity of silver in silver-lead alloys was calculated from the phase diagram and the known heat of fusion of silver. (2) From experimental data on the distribution of silver between lead and aluminum<sup>3</sup> the activity coefficient of silver in aluminum was determined over a wide range of compositions. (3) The activity coefficient of aluminum in these solutions was calculated by means of the Gibbs-Duhem equation.

The data on distribution of aluminum between liquid silver and liquid iron were then used to determine its activity in the latter solution. These calculations were repeated and elaborated by J. F. Elliott,<sup>2</sup> who showed that the activity coefficient of aluminum in dilute solutions in liquid iron,  $\gamma_{\text{Al}}^\circ$  is in the neighborhood of 0.04 at 1600°.

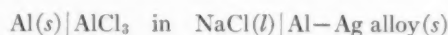
\* Received April 20, 1955.

† Professor of Metallurgy, Massachusetts Institute of Technology.

‡ Graduate Student, Department of Metallurgy, Mass. Institute of Technology.

## ACTIVITY OF ALUMINUM IN LIQUID SILVER

Recently Hillert<sup>4</sup> has determined the activity of aluminum in solid aluminum-silver alloys at various concentrations and temperatures up to 527°C by electromotive force measurements of the cell:



These new measurements provide a more direct means for estimating the activity of aluminum in liquid silver than was found in the indirect calculations of Chou and Elliott. Data on alloys in the terminal solid solution field are given in Table I. The emf at 820°K and the temperature coefficient in the range 642–820°K provide the basis for the calculated values at 1052°K shown in the fourth and fifth columns of the table. This temperature marks a peritectic of the system in which the solid solution,  $N_{\text{Al}}=0.175$  is in equilibrium with the liquid,  $N_{\text{Al}}=0.212$ . Interpolation in the data for  $\log \gamma_{\text{Al}}$  in line A of Fig. 1 gives  $\log \gamma_{\text{Al}}=-1.18$  and  $a_{\text{Al}}=0.0116$ . In the equilibrium liquid phase  $a_{\text{Al}}$ , relative to solid Al, has the same value; but relative to liquid Al a correction is needed which is readily obtained from the heat of fusion. When this is done, it is found that for  $N_{\text{Al}}=0.212$ ,  $a_{\text{Al}}=0.0134$  and  $\log \gamma_{\text{Al}}=-1.20$ , all in the liquid state.

The sixth column gives the solidus temperature of each alloy. The seventh shows the composition of the equilibrium liquid phase, assuming a straight-line liquidus rather than curved as in Hansen's<sup>5</sup> diagram. The final column is  $\log \gamma_{\text{Al}}$  in the liquid phase at the liquidus temperature.

To find values of  $\gamma_{\text{Al}}$  at higher temperatures, information on the heat of mixing would be highly desirable. The large values reported by Kawakami<sup>6</sup> may have suffered from the heat of the reaction of aluminum with oxygen dissolved in the silver. For this reason they are discarded and the correction to 1600° is based on the assumption that  $\log \gamma$  is inversely proportional to absolute temperature. Resultant activity coefficients at 1600°C are shown in line C. The value of  $\log \gamma_{\text{Al}}$  at infinite dilution previously deduced from the calculations of Chou and Elliott is shown at the point E. A recalculation by Floridis,<sup>7</sup> using different methods of extrapolation, gave the point F. The new values of line C must be considered the more reliable.

TABLE I. Calculations from Hillert's data on the cell:  
 $\text{Al}(s) | \text{AlCl}_3 \text{ in } \text{NaCl}(l) | \text{Al}-\text{Ag}(s)$ .

$N_{\text{Al}}$	$E$ (mv) 820°K	$\frac{dE}{dT} \times 10^3$ mv/deg	$E$ , calc 1052°K	$\log \gamma_{\text{Al}}$ 1052°K	Solidus $T^\circ\text{K}$	Liquidus $N_{\text{Al}}$	$\log \gamma_{\text{Al}}$
0.185	105	10.2	129	-1.12			
0.140	126	12.3	154	-1.36	1093	0.170	-1.35
0.100	144	14.6	178	-1.56	1138	0.120	-1.53
0.053	170	20.8	218	-1.85	1183	0.070	-1.71

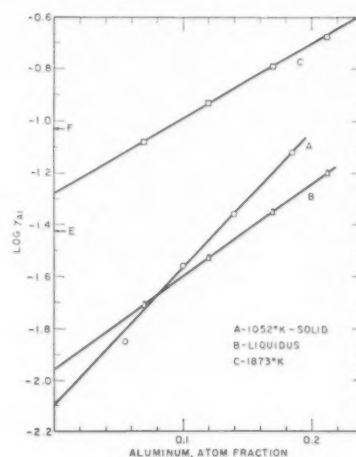


Fig. 1. Activity coefficient of aluminum in silver-aluminum alloys; data of M. Hillert, extrapolated.

## DISTRIBUTION OF ALUMINUM BETWEEN IRON AND SILVER

The primary purpose of this study was to apply the method of distribution of aluminum between iron and silver to a determination of the effect of carbon and silicon on the activity coefficient of aluminum in liquid iron. As a preliminary study, it was deemed advisable to recheck the data previously reported.<sup>1</sup>

The experimental equipment was extremely simple. A Vycor tube, 38 mm OD, was fitted with a brass head which permitted introduction of argon for protection against oxidation and was provided with an opening for sampling and for temperature measurement. Melts were made in 25 mm OD alundum thimbles. The charge was heated by induction and consisted of 50 grams each of electrolytic iron and silver, and varying amounts of aluminum, graphite, and silicon. In one series of runs graphite crucibles were used to assure carbon saturation. Temperatures were measured with a platinum, platinum 10 per cent rhodium thermocouple protected by a thin silica tube, which was immersed in the bath only for about 40–60 seconds for each measurement. Melts were held at  $1600 \pm 10^\circ\text{C}$  for 45 minutes after which samples of each liquid phase were withdrawn by suction, using a silica tube of 3 mm ID.

The experimental results are shown in Table II where the analytical data are expressed as atomic per cent. Figure 2 shows the mole fraction of aluminum in the two layers. Line A, for carbon-free iron, shows good agreement between old and new data. Line B is for approximately 1 per cent C, average 4.15 atom per cent. Line C for carbon saturation is more strongly curved than the others because of decreasing carbon solubility with increasing aluminum.

TABLE II. Chemical analysis of phases in equilibrium at 1600°C, Atom %.

Heat No.	Silver Layer			Iron Layer			
	Al	Si	Fe	Al	Si	C	Ag
2	0.47	—	1.43	0.80	—	—	0.44
3	2.41	—	1.49	3.77	—	—	0.48
4	9.94	—	2.07	14.47	—	—	0.89
6	24.35	—	2.99	33.30	—	—	2.33
7	30.33	—	4.62	39.93	—	—	3.47
21	26.90	—	5.74	35.01	—	—	3.69
29	6.73	—	2.53	9.54	—	—	0.89
30	14.00	—	2.42	18.58	—	—	1.30
8	6.01	—	1.54	4.88	—	18.35	0.07
9	16.25	—	2.59	15.51	—	14.08	0.46
11	28.15	—	2.80	29.69	—	9.28	1.93
12	27.75	—	3.48	26.15	—	13.13	3.11
13	32.60	—	4.06	36.11	—	7.89	2.03
31	2.35	—	0.74	1.73	—	19.44	0.03
32	27.00	—	3.07	27.00	—	10.08	3.93
34	7.31	—	1.33	4.90	—	18.80	0.16
16	2.94	—	1.87	4.08	—	3.88	0.23
18	18.56	—	3.63	23.75	—	3.53	1.45
20	30.34	—	4.66	36.68	—	3.72	2.65
22	1.98	—	1.92	2.24	—	5.38	0.14
24	10.04	—	1.51	11.78	—	4.74	0.83
25	18.01	—	2.15	21.69	—	3.65	1.27
33	10.44	—	2.67	13.00	—	4.15	0.65
35	8.61	0.14	0.90	4.40	13.19	9.71	0.01
36	9.57	0.85	0.78	3.71	23.08	4.45	0.18
37	10.96	2.81	0.94	3.65	33.25	2.17	0.36
38	10.28	7.82	1.49	3.46	38.16	0.70	0.48

## ACTIVITY OF ALUMINUM IN LIQUID IRON

At equilibrium the activity of aluminum is the same in the iron and silver layers, therefore:

$$\frac{N_{Al}^{(Ag)}}{N_{Al}^{(Fe)}} = \frac{\gamma_{Al}^{(Fe)}}{\gamma_{Al}^{(Ag)}}$$

The value of  $\gamma_{Al}^{(Ag)}$  from Fig. 1 and the distribution ratio determine the activity coefficient in liquid iron. In Fig. 3,  $\log \gamma_{Al}^{(Fe)}$  is plotted against  $N_{Al}^{(Fe)}$  for the carbon-free and carbon-saturated solutions. Since all subsequent discussion pertains only to solutions in liquid iron, the superscript (Fe) will be dropped, and the activity coefficient in binary Fe-Al alloys will be designated  $\gamma'_{Al}$ . In the dilute, carbon-free solution at concentrations up to  $N=0.2$ , the activity coefficient

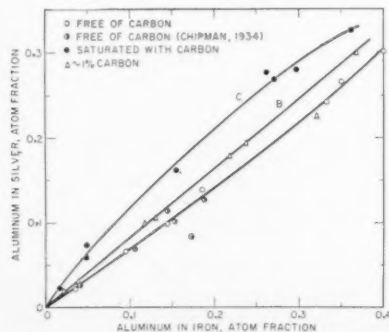


FIG. 2. Distribution of aluminum between liquid iron and silver at 1600°.

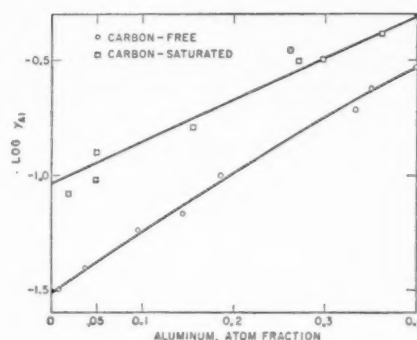


FIG. 3. Activity coefficient of aluminum in iron at 1600°.

of aluminum is given by the equation:

$$\log \gamma'_{Al} = -1.51 + 2.60 N_{Al}$$

## EFFECT OF CARBON ON ACTIVITY OF ALUMINUM

If  $\gamma_{Al}$  represents the activity coefficient of aluminum in Fe-Al-C solution and  $\gamma'_{Al}$  that in a binary Fe-Al solution of the same aluminum concentration, the effect of the carbon may be expressed in the coefficient  $\gamma_{Al}^{(C)}$  defined by the equation:

$$\log \gamma_{Al}^{(C)} = \log \gamma_{Al} - \log \gamma'_{Al}$$

In Fig. 4,  $\log \gamma_{Al}^{(C)}$  is plotted against the atom fraction of carbon.

## EFFECT OF SILICON ON ACTIVITY OF ALUMINUM

In a similar way the effect of silicon in Fe-Al-C-Si alloy will be expressed in the coefficient  $\gamma_{Al}^{(Si)}$  defined by the equation:

$$\log \gamma_{Al}^{(Si)} = \log \gamma_{Al} - \log \gamma'_{Al} - \log \gamma_{Al}^{(C)}$$

Figure 5 shows the values of  $\log \gamma_{Al}^{(Si)}$  for the four alloys which contained silicon. The similarity of the effects of carbon and silicon are evident. The greater curvature at high concentrations of silicon may be due in part to an interaction effect in the silver layer where the atom fraction of silicon was as high as 0.08.

## SOLUBILITY OF CARBON IN LIQUID Fe-Al ALLOYS

From the results of the runs carried out in graphite crucibles, it was possible to determine the solubility of carbon in liquid iron-aluminum alloys at 1600°C. In Fig. 6, the logarithm of the atom fraction of carbon is plotted against the atom fraction of aluminum; a straight line is obtained which, when extrapolated to zero mole fraction of aluminum, gives the solubility of carbon in liquid iron at 1600°C, which is in agreement with the value previously reported.<sup>8</sup> The equation

$$\log N_C = -0.68 - 1.17 N_{Al}$$

may be considered valid for the range up to 0.36 atom fraction of aluminum in iron.

## DISCUSSION

The effect of one solute upon the activity coefficient of another, in the infinitely dilute solution, is expressed by the interaction parameter:

$$\epsilon_2^{(3)} = \partial \ln \gamma_2 / \partial N_3 = \partial \ln \gamma_3 / \partial N_2 = \epsilon_3^{(2)}.$$

The foregoing data and plots establish the following values of several such parameters:

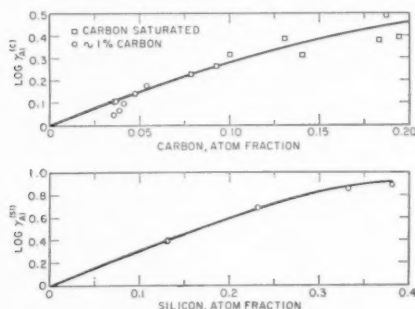
$$\epsilon_{Al}^{(Al)} = +6.0 \quad (\text{Fig. 3}),$$

$$\epsilon_{Al}^{(C)} = +6.7 \quad (\text{Fig. 4}),$$

$$\epsilon_{Al}^{(Si)} = +6.9 \quad (\text{Fig. 5}).$$

These are of an order of magnitude not very different from those of other solutes in iron which have little or no intersolute attractive forces. Apparently the principal forces are those between solute and solvent atoms, and the positive parameters are the result of competition for iron atoms in the nearest-neighbor shells.

The effect of aluminum on the activity coefficient of carbon is shown by its effect on the solubility of graphite.



FIGS. 4 (above) and 5 (below). Effects of carbon and silicon on activity coefficient of aluminum.

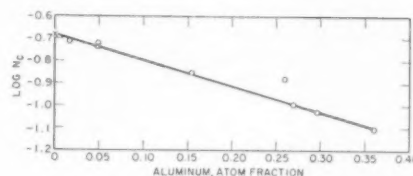


FIG. 6. Solubility of graphite in Fe-Al-C alloys.

From Fig. 6 it is seen that  $\partial \ln \gamma_C / \partial N_{Al} = +2.7$  in the range  $N_{Al} = 0-0.36$  and for carbon saturation. This, however, is not the value for  $\epsilon_C^{(Al)}$  which must equal  $\epsilon_{Al}^{(C)}$  or  $+6.7$ . The solubility line shown in Fig. 6 probably increases in steepness with increasing aluminum and decreasing carbon concentrations.

## ACKNOWLEDGMENTS

The authors express their thanks to the Office of Naval Research for sponsorship and to the Hellenic Chemical Products and Fertilizer Co., Ltd. for a fellowship grant.

## REFERENCES

1. J. Chipman, *Trans. A.S.M.* **22**, 385 (1934).
2. (a) Y. H. Chou, Doctorate Thesis, Carnegie Institute of Technology (1947).
2. (b) Y. H. Chou and J. F. Elliott. Unpublished.
3. R. Lorentz and F. Erbe, *Z. Anorg. Chem.* **183**, 311 (1929).
4. M. Hillert, Master's Thesis, Department of Metallurgy, Massachusetts Institute of Technology (1954).
5. M. Hansen, *Der Aufbau der Zweistofflegierungen* (J. Springer, Berlin, 1936), pp. 1-4.
6. M. Kawakami, *Sci. Rep. Tohoku Imp. Univ.* **16**, 521 (1930).
7. T. Floridis, Master's Thesis, Department of Metallurgy, Massachusetts Institute of Technology (1954).
8. J. Chipman, R. M. Alfred, L. W. Gott, R. B. Small, D. M. Wilson, C. N. Thomson, D. L. Guernsey, and J. C. Fulton, *Trans. A.S.M.* **44**, 1215 (1952).



## SOME OBSERVATIONS ON THE INTERNAL FRICTION OF POLYCRYSTALLINE ALUMINIUM DURING THE EARLY STAGES OF CREEP\*

G. B. BROOK† and A. H. SULLY‡

Measurements of internal friction at strain amplitudes of less than  $10^{-5}$  have been made during the tensile creep at constant load of super- and commercial-purity aluminium wires at room temperature, 250°C and 350°C. On loading, an increase in internal friction occurred and this was partially recovered during the primary creep stage in 1 to 2 hours at 350°C, 4 to 8 hours at 250°C and about 2 to 20 hours at room temperature (the stresses used at room temperature were too small to cause creep). The component of internal friction due to deformation remained constant during the next few hours and at 350°C was proportional to the applied stress. On unloading, almost complete recovery occurred. There was also evidence of a slight decrease in grain-boundary damping during creep and this has been interpreted tentatively as resulting from a decrease in "grain-boundary roughness." The internal friction due to deformation was only partially recovered without stress. At room temperature a maximum in internal friction occurred with increasing load and appeared to be a result of the rate of recovery exceeding that of the increase in internal friction due to deformation.

Commercial-purity aluminium behaved similarly at 350°C, a much higher stress being required to produce the same effects. At low stresses no recovery occurred.

X-ray observations suggested that the recovery of very high internal frictions at high stresses was accompanied by some polygonisation.

The results are discussed qualitatively in terms of dislocation theory.

### SUR LE FROTTEMENT INTERNE DE L'ALUMINIUM POLYCRISTALLIN PENDANT LES PREMIÈRES PÉRIODES DU FLUAGE

Des mesures de frottement interne pour des déformations inférieures à  $10^{-5}$  ont été effectuées au cours du fluage à charge constante sur des fils d'aluminium de pureté commerciale et de haute pureté à température ordinaire, à 250° et à 350°. Au moment de la mise en charge, il se produit un accroissement du frottement interne qui disparaît pendant le premier stade du fluage, à 350° entre 1 heure et 2 heures, à 250° entre 4 et 8 heures, et à la température ordinaire entre 2 et 20 heures. (A la température ordinaire, les contraintes sont trop faibles pour entraîner un fluage.) La partie du frottement interne due à la déformation restait constante au cours des quelques heures suivantes et, à 350°, était proportionnelle à la contrainte appliquée. Au moment de la décharge, une restauration presque complète se produit. Il se produisait également pendant le fluage une faible diminution dans l'amortissement intercrystallin et il est proposé d'expliquer ceci par une diminution de la "rugosité du joint de grain." Le frottement interne dû à la déformation n'est que partiellement restauré en l'absence de contraintes. A la température ordinaire, il se produit un maximum dans le frottement interne avec l'augmentation de la charge qui semble dû à une restauration plus rapide que l'accroissement du frottement interne dû à la déformation.

L'aluminium de pureté commerciale se comporte de la même façon à 250°, mais pour les mêmes effets, une contrainte plus élevée est nécessaire. Pour les faibles contraintes, il n'y a pas restauration.

L'examen aux rayons X indique que la restauration du frottement interne très élevé pour les fortes contraintes, est accompagnée de polygonisation.

Les résultats sont discutés qualitativement dans le cadre de la théorie des dislocations.

### EINIGE BEOBACHTUNGEN ÜBER DIE INNERE REIBUNG VON POLYKRISTALLINEM ALUMINIUM WÄHREND DER FRÜHEN STADIEN DES KRIECHENS

An Drähten aus Reinstaluminium und Aluminium in handelsüblicher Reinheit wurden während des Spannungskriechens bei konstanter Last bei Raumtemperatur, 250 und 350°C Messungen der inneren Reibung bei einer Verformungsamplitude kleiner als  $10^{-5}$  vorgenommen. Bei der Belastung stieg die innere Reibung. Sie erholte sich teilweise während der frühen Stadien des Kriechens und zwar in 1 bis 2 Stunden bei 350°C, in 4 bis 8 Stunden bei 250°C und in ungefähr 2 bis 20 Stunden bei Raumtemperatur (die bei Raumtemperatur verwendeten Spannungen waren zu gering, um ein Kriechen zu bewirken). Die der Verformung zugehörige Komponente der inneren Reibung blieb während der nächsten wenigen Stunden konstant; sie war bei 350°C proportional der angelegten Spannung. Bei der Entlastung trat eine annähernd vollständige Erholung auf. Ausserdem hatte es den Anschein, als ob während des Kriechens ein geringer Abfall in der Korngrenzenspannung auftreten würde. Diese Erscheinung wurde versuchsweise durch eine Abnahme der "Korngrenzenrauigkeit" erklärt. Ohne Spannung erholte sich die durch die Verformung hervorgerufene innere Reibung nur teilweise. Bei Raumtemperatur trat mit steigender Last ein Maximum der inneren Reibung auf. Dieses Maximum scheint durch denjenigen Anteil der Erholung verursacht zu werden, der über die Zunahme der auf Deformation zurückzuführenden inneren Reibung hinausgeht.

Handelsübliches Aluminium verhielt sich bei 350°C ähnlich; es wurde jedoch eine wesentlich höhere Spannung benötigt, um die gleichen Effekte zu erzielen. Bei niedrigen Spannungen trat keine Erholung auf.

Röntgenbeobachtungen liessen die Vermutung zu, dass bei sehr hohen Spannungen die Erholung einer sehr grossen inneren Reibung von einer geringen Polygonisation begleitet wurde.

Die Ergebnisse werden auf Grund der Versetzungstheorie diskutiert.

\* Received January 13, 1955.

† Fulmer Research Institute, Stoke Poges, Bucks.

‡ British Steel Castings Research Association, Sheffield, formerly Fulmer Research Institute, Stoke Poges, Bucks.

## I. INTRODUCTION

In recent years the measurement of the internal friction of metals has been used increasingly as a means of following atomic movements especially in diffusion and deformation. Progress in this field has been described in three comprehensive reviews: by Zener<sup>1</sup> on anelastic phenomena, and more recently by King and Chalmers<sup>2</sup> on grain-boundary phenomena and by Nowick<sup>3</sup> whose review is complementary to that of King and Chalmers.

However, it is desirable to mention a few relevant papers together with more recently published work.

Various workers<sup>3-8</sup> using copper,  $\alpha$ -brass, and 80/20 nickel chromium have shown that internal friction passes through a maximum with increasing strain, but these authors did not specify the time which elapsed between the deformation and the internal friction measurement. Since recovery of internal friction produced by cold work<sup>9</sup> is known to occur rapidly even at room temperature in iron, aluminium, copper and  $\alpha$ -brass, it is desirable that internal friction measurements should be made concurrently with measurements of strain. Such measurements have been made by Boulanger<sup>8</sup> on an 80/20 nickel-chromium alloy. He found that if the internal friction was measured one minute after deformation, its variation with strain was similar in form to that of the stress-strain curve. After 100 hours at 20°C and 400 hours at 100°C, appreciable recovery had occurred and the residual friction showed a maximum at a relatively low strain comparable with that observed in the earlier investigations.

In the work to be described, measurements of internal friction have been made in aluminium concurrently with the progress of longitudinal creep at constant load. The internal friction was measured by making the specimen a torsional pendulum with a frequency of about 1 cps. Under these conditions the decrement was not amplitude-sensitive over a range of strain amplitude  $2 \times 10^{-6}$  to  $10^{-5}$ .

Whilst this work was in progress Maringer<sup>10</sup> published a brief account of experiments on similar lines using

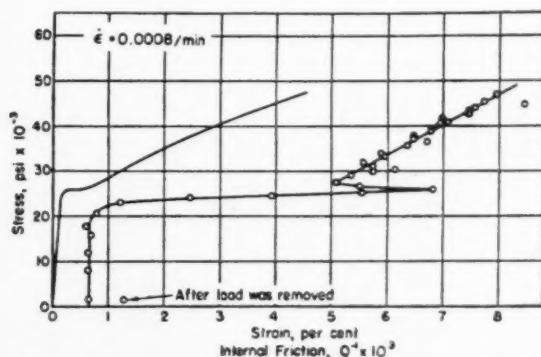


FIG. 1. Variation of internal friction (expressed as  $Q^{-1} = 1/\pi$  X decrement) with stress during tensile test of molybdenum wire (Maringer<sup>10</sup>).

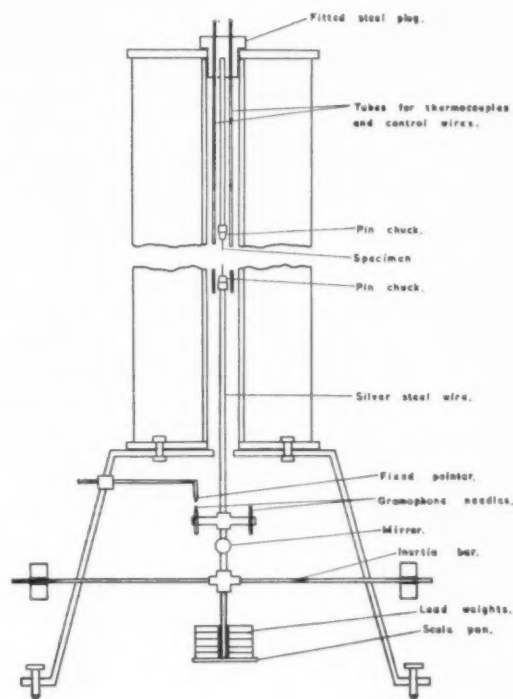


FIG. 2. Modified Kê apparatus for measurement of creep and internal friction.

molybdenum wires at room temperature. The internal friction was determined at a frequency of about 1 cps whilst the specimen was extended at constant rate. No change was observed until just before or at the yield point, at which time a large increase in internal friction occurred (Fig. 1). This fell during yielding but rose again during strain-hardening at an approximately constant rate which was dependent on the strain rate.

## II. EXPERIMENTAL

## (i) Apparatus

The modified Kê apparatus for measuring damping capacity and creep extension is shown diagrammatically in Fig. 2.

The furnace was bolted to a steel tripod with adjustable feet. It consisted of a silica tube 1 in. in bore evenly wound with Nichrome wire except at the ends where the turns were spaced more closely so as to give a uniform temperature over the central 8 in. of the tube, the gradient over this length being less than 2°C. An a-c bridge thermostat connected to a platinum resistance thermometer adjacent to the windings enabled the temperature to be controlled to  $\pm 2^\circ\text{C}$ . Six holes were drilled in the steel plug, closing the top of the furnace and by opening and closing these the temperature gradient could be controlled. Usually three had to be kept closed and this was done by inserting two

thermocouples and a silica tube containing a piece of wire which received the same heat treatments as the specimen.

The specimen wire was 15 cm long and 0.9 mm (0.036 in.) diameter and was attached at either end to 80/20 nickel-chromium alloy grips to a silver steel rod which was rigid in comparison to the specimen. The upper rod was held rigidly in a steel plug fitting tightly into the top of the furnace. The lower rod was attached to an aluminium disc carrying two gramophone needles. The distance of one needle from a fine point secured to the frame was measured by means of a travelling telescope to  $\pm 0.001$  cm, thus enabling the extension to be measured to  $\pm 0.01\%$ . A small concave mirror attached to the steel rod focussed an image of a thin line on to a scale 3 meters away. Attached to the end of the rod was an inertia bar 8 cm long carrying two small adjustable steel weights at the end. Oscillations of the inertia bar were started by energising two electromagnets placed near the inertia weights.

The specimen was loaded by means of slotted lead weights. These weighed 10 g each and were machined from a cylinder of antimonial lead,  $\frac{7}{8}$  in. diameter. Alternate weights were pinned to ensure accurate location. The maximum stress which could be applied was 530 g/sq mm. (756 lb/sq in.). The frequency of oscillation could be varied by adjusting the position of the inertia weights along the bar; but, as it was virtually impossible to do this during a test without the risk of accidentally straining the specimen, this was not attempted. The added load also affected the moment of inertia of the assembly but as the load corresponding to

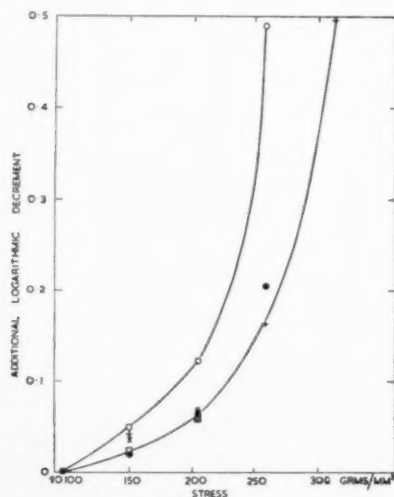


Fig. 3. Range of stress-decrement curves for super-purity aluminium at 350°C.

Symbol	No.
+	4
○	6
●	7
×	8
□	9

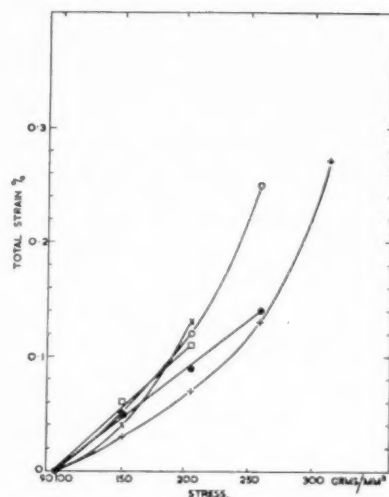


Fig. 4. Stress-total strain curves for the specimens of Fig. 3.

Symbol	No.
+	4
○	6
●	7
×	8
□	9

a stress of 350 g/mm<sup>2</sup> was only the equivalent of moving the inertia weights 1 mm along the bar, no compensation was necessary.

The most satisfactory grips consisted of two small, flat 80/20 nickel-chromium alloy plates with U-shaped grooves. Pin chucks were less satisfactory.

The two materials used were super-purity aluminium (>99.9% aluminium) and a synthetic commercial purity aluminium with 0.2% iron and 0.15% silicon (>99.6% aluminium). Both were cold drawn to 0.09 mm (0.036 in.) diameter with a final reduction in area of 98%.

## (ii) Experimental Procedure

A piece of cold-drawn wire was mounted with a 15 cm length between the grips. This was placed in the furnace and annealed for one hour at 450°C, which was the lowest temperature at which the preferred orientation of the wire was removed on recrystallisation. The resulting grain size was about 0.01–0.03 cm for super-pure aluminium and 0.001 cm for commercially pure aluminium. X-ray Laue photographs consisted of sharp, undistorted spots. It was not possible to carry out the heat treatment at 450°C, with the inertia bar attached, without some measurable creep occurring and distortions of the X-ray diffraction spots. The inertia bar was therefore attached at room temperature subsequent to annealing and the temperature then raised to that of the test at which the specimen was held until the damping capacity remained constant, a matter of about 15 minutes. As a matter of convenience, the specimen was normally held at temperature

over-night. In all cases, even at the highest temperature used ( $350^{\circ}\text{C}$ ), no measurable creep was observed under the weight of the inertia bar and the fixing rod. In making internal friction measurements, the frequency of oscillation was of the order of 1 cps and so the logarithmic decrement could be obtained by the visual observation of the amplitude of every  $n$ th vibration, where  $n$  was chosen according to the decrement. The amplitudes were plotted on semi-logarithmic paper against the ordinal number of vibrations. A straight line plot was obtained, thus showing that, within the accuracy of measurement, the logarithmic decrement was independent of amplitude. The maximum scale deflection of 1 cm corresponded to a maximum surface strain of  $10^{-5}$  and the decrement was constant over the strain range  $2 \times 10^{-6}$  to  $10^{-5}$ . Below a strain amplitude of  $2 \times 10^{-6}$  the decrement could not be measured with sufficient accuracy.

Measurements of damping and longitudinal extension were made after each increment of load and after various intervals of time after the maximum load had been applied. Experiments were terminated at various stages of the creep curve and X-ray Laue photographs of the wire taken.

### III. CHANGES IN INTERNAL FRICTION DURING LOADING AND DURING CREEP AT CONSTANT LOAD

The general effect of loading was to increase the logarithmic decrement. The measurement of this increment was, however, complicated by the fact that the additional decrement was rapidly recovered at all temperatures both in super-purity and in commercial purity aluminium, especially at higher stresses. A significant fall in decrement occurred between successive increments of load whether or not creep was occurring. Consequently the load was increased at regular intervals with several measurements of decrement between increments and with strain measurements immediately

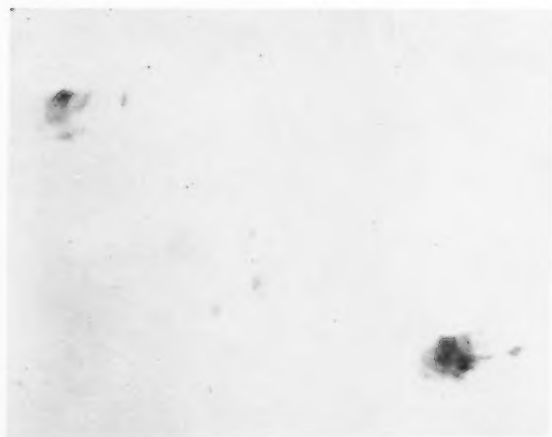


FIG. 5. Part of Laue photograph from specimen of high purity aluminium unloaded after 11 minutes at  $258 \text{ g/mm}^2$  at  $350^{\circ}\text{C} \times 5$ .

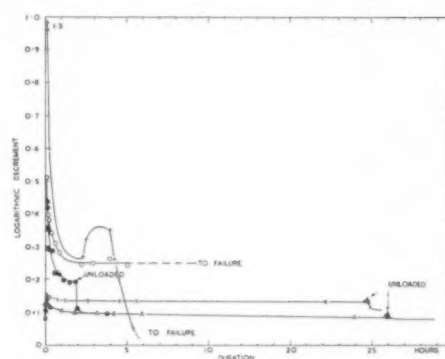


FIG. 6. Variation of decrement of super-purity aluminium during primary creep at  $350^{\circ}\text{C}$ .

Symbol	No.	Stress g/mm <sup>2</sup>	Initial	Decrement Maximum	Constant
+	4	313	0.094	1.3	?
○	6	258	0.122	0.511	0.248
×	8	204	0.085	0.151	0.135
△	10	150	0.086	0.148	0.095
●	14	258	0.101	0.437	0.190

before and after successive increments of load. The actual measurement of logarithmic decrement at  $250^{\circ}\text{C}$  and at  $350^{\circ}\text{C}$  could be accomplished in only 10 seconds and no change of decrement could in general be detected within this period of time the plot of amplitude against vibration number being linear. Occasionally, however, at high stresses such plots exhibited an abrupt change of slope. These events were relatively rare and were not reproducible. The scatter between successive measurements of decrement during the period in which it was decreasing between load increments was always appreciable and, after the first hour, the mean of five measurements was taken.

### Experiments at $350^{\circ}\text{C}$

On loading at  $350^{\circ}\text{C}$  the increases in strain and decrement were approximately proportionate to load up to  $204 \text{ g/mm}^2$  and the fall at constant load was slight. Above this stress up to a maximum of  $313 \text{ g/mm}^2$  equal increments of load produced successively larger increments of strain and of decrement. Figure 3 shows the range of decrement measurements at each load and Fig. 4 the corresponding strains.

Specimens unloaded and removed from the furnace immediately after loading were examined by X-rays. The effect of the deformation on the Laue diffractions naturally varied from grain to grain but the general effect of the application of the higher stresses was to enlarge the diffraction spots which also showed a diffuse substructure with short asterisms (Fig. 5). At the lower stresses only a slight diffuseness with no substructure was observed.

When creep was allowed to occur by maintaining the load, the decrement decreased to a constant value over a short period of time—usually about one to two hours.



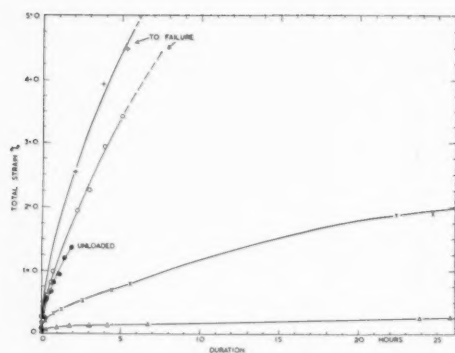


FIG. 7. Creep curves corresponding to Fig. 6.

Symbol	No.	Stress g./mm <sup>2</sup>
+	4	313
○	6	258
×	8	204
△	10	150
●	14	258

Decrement-time and strain-time curves for experiments at 350°C are shown in Figs. 6 and 7. Curve 4 at 313 g/mm<sup>2</sup> was the only one in which the decrement fell to an appreciably lower value than the annealed specimen before loading. It is doubtful whether a constant decrement would have been attained for this specimen since the rate of strain was very high and led to early failure. The decrease in this case was not continuous and the decrement fell and rose again. After fracture, strain etching of the wire was visible and slip bands could be seen with the naked eye. X-ray

FIG. 8. Part of Laue photograph from specimen of high-purity aluminium after failure in 6-22 hours at 313 g/mm<sup>2</sup> at 350°C.5X.FIG. 9. Part of Laue photograph from specimen of high-purity aluminium after failure in 6-22 hours at 258 g/mm<sup>2</sup> at 350°C.5X.

examination showed that the deformation had caused large asterisms, each of which was completely fragmented into fine sharp spots with little trace of diffuse background (Fig. 8). This indicated that complete polygonisation\* had occurred.

The decrement-time curves of the two specimens stressed at 258 g/mm<sup>2</sup> (Specimens 6 and 14, Figs. 6 and 7) showed less scatter than the specimen at 313 g/mm<sup>2</sup> (Specimen 4) and the decrement reached a constant value within one to two hours. At this time,

FIG. 10. Part of Laue photograph from specimen of high-purity aluminium unloaded after 1.8 hours at 258 g/mm<sup>2</sup> at 350°C.5X.

\* The term "polygonisation" is used throughout in its generalized sense, meaning the formation within the original crystals of smaller undistorted crystals of closely similar orientation.

specimen 14 was unloaded when the decrement fell instantaneously to a value a little below that before loading. In Laue photographs of these two specimens, the asterisms showed some polygonisation (Figs. 9 and 10). The individual spots in the asterisms were finer than in the specimen tested at  $313 \text{ g/mm}^2$  (Fig. 8) and there was more continuous background, especially in the specimen unloaded after two hours.

The rise in decrement of specimen 10 at  $150 \text{ g/mm}^2$  was also small, and fell in a rather longer period than the two hours required at higher stresses to the original value before loading. On unloading, after a slight rise, it fell to a value of 0.077, which is below the initial value of 0.086 by about the same amount as the decrease in decrement which occurred between two hours and the time at which the specimen was unloaded. This suggests that the apparent complete recovery of the additional decrement was the result of some change which occurred between two and 24 hours. The decrement before loading is due mainly to grain-boundary

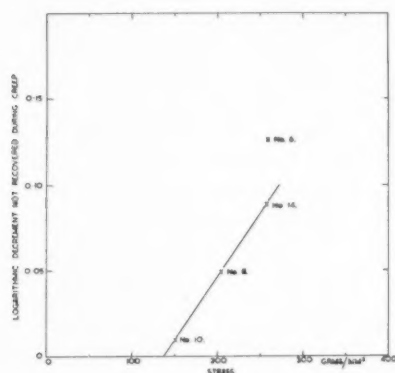


Fig. 11. Relationship between creep stress and unrecovered decrement in super-purity aluminium during creep at  $350^\circ\text{C}$ .

effects and the decrease of the decrement to less than the original value after unloading suggests some change in grain boundary conditions. X-ray examination of this specimen revealed no asterisms and only a diffuse spreading of individual Laue diffractions.

At all but the highest and lowest stresses the increase in decrement as a result of the deformation did not completely recover during creep after loading. As is shown by Fig. 11, there is a roughly linear relationship between the stress and the residual constant decrement.

Several experiments were also carried out at  $350^\circ\text{C}$  on aluminium of commercial purity in which polygonisation would not be expected to occur. The results were much the same as in the super-purity material with the difference that appreciably higher stresses were required to produce corresponding effects in the commercial purity material. Figure 12 shows the variation of strain with stress and time during loading and with time after loading for two tests at  $476 \text{ g/mm}^2$  and  $421 \text{ g/mm}^2$ . The former test was almost identical

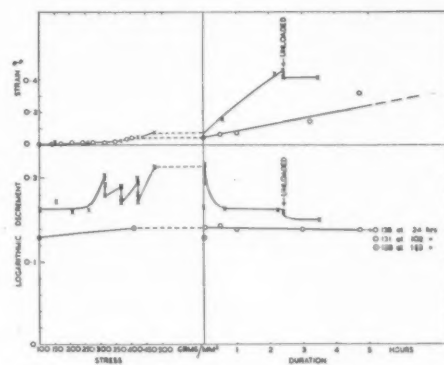


Fig. 12. Creep and decrement curves for commercial-purity aluminium at  $476 \text{ g/mm}^2$  (X) and  $421 \text{ g/mm}^2$  (O) at  $350^\circ\text{C}$ .

with the test on super-purity material at a stress of  $204 \text{ g/mm}^2$ . At a stress of  $421 \text{ g/mm}^2$  and at lower stresses the decrement at first increased slightly and recovery occurred gradually over the next 120 hours. There is evidence, however, that this apparent recovery was the result of changes in background damping. No signs of polygonisation were detected by X-ray examination.

#### Experiments at $250^\circ\text{C}$

At  $250^\circ\text{C}$  the changes in internal friction and in the appearance of Laue photographs during loading and during creep at constant load were similar to those observed at  $350^\circ\text{C}$ . Figure 13 shows a typical variation of creep and decrement in a test at  $403 \text{ g/mm}^2$  at  $250^\circ\text{C}$ . A constant value of decrement was reached in about six to eight hours. This constant value of decrement was not reproducible from specimen to specimen and was sometimes lower than the initial value before loading. X-ray examination of wires unloaded at the maximum damping after loading revealed some asterisms with intensity maxima whilst those unloaded in the region of constant decrement showed some sharp spots in asterisms and a sharper sub-structure in the intensity maxima.

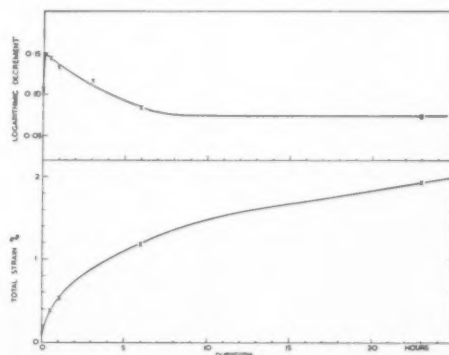


Fig. 13. Creep and decrement curves for high-purity aluminium at  $403 \text{ g/mm}^2$  at  $250^\circ\text{C}$ .

### Experiments at Room Temperature

The experiments at 250°C and 350°C suggested that the fall in internal friction after loading and during creep might be associated with the development of polygonisation as revealed by X-rays. Further measurements were therefore made at room temperature in the expectation that the internal friction developed by strain would not recover or would recover much more slowly. This expectation was not fulfilled even at stresses below that required to produce creep.

The results of measurements made during loading on specimens loaded at room temperature are illustrated by Fig. 14. The decrement increased on loading from an original value of  $1.55 \times 10^{-3}$  and rapid recovery occurred between each increment of load. Two sets of loadings are shown in Fig. 14. The maximum damping corresponded to a decrement of  $10.5 \times 10^{-3}$ . This was attained at fairly low loads, and recovery then became so rapid that this peak value could not be reached by subsequent increases of stress. The recovery of decrement was

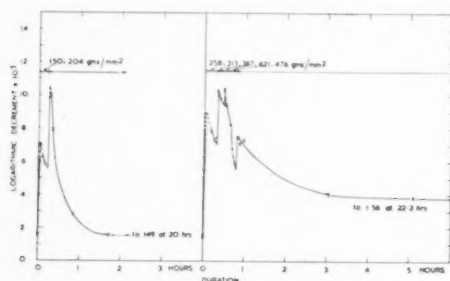


FIG. 14. Effect of stress on the decrement of high-purity aluminium at 11°C.

complete. In the first example shown in Fig. 14, recovery was substantially complete 1.7 hours after loading to 204 g/mm<sup>2</sup> while in the second case after loading to 476 g/mm<sup>2</sup>, the initial value of decrement was recovered in 22.2 hours. The plastic strain was 0.19% at the lower and 0.33% at the higher stress, at neither of which was creep detected. The additional decrement on loading rapidly recovered and a further slight rise on unloading was also recovered. The recovery was complete as far as could be ascertained with this technique of measurement where apparatus losses were probably of the order of  $10^{-3}$ . It may well be that there is a residual decrement of about  $10^{-5}$  as found by other authors.

A cold-drawn wire of the same purity, tested for comparison, had a decrement of  $12.1 \times 10^{-3}$ . Over the same range of applied stress, this remained constant to within  $\pm 0.7 \times 10^{-3}$ .

The X-ray pattern of the annealed wire after unloading showed a slight diffuseness of the Laue diffractions but no asterisms.

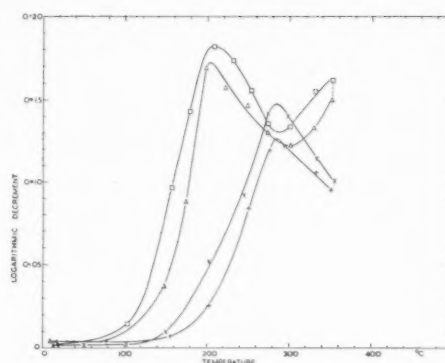


FIG. 15. Variation of decrement with temperature for high- and commercial-purity aluminium before and after primary creep. X High-purity aluminium before deformation; + High-purity aluminium after deformation; □ Commercial-purity aluminium before deformation; Δ Commercial-purity aluminium after deformation. [High-purity aluminium extended 1.36% in 1.82 hours at 258 g/mm<sup>2</sup>. Commercial-purity aluminium extended 0.44% in 2.87 hours at 476 g/mm<sup>2</sup>.]

### IV. THE RECOVERY OF INTERNAL FRICTION AFTER DEFORMATION WITHOUT LOAD

In certain experiments, the specimens were unloaded immediately after measurements of decrement and strain had been made during loading, and the process of recovery followed without the influence of stress (or more correctly under the influence of a low stress of 96 g/mm<sup>2</sup> due to the inertia assembly) (Fig. 16).

The rate at which the decrement decreased was at first greater than under the higher stresses. After one hour, the rate at which the decrement decreased became very small and over the next 20 hours there was a slow fall to below the initial value of decrement, by the same amount in each case. It is believed that only partial recovery of the internal friction introduced by deformation occurred and that the slow decrease over the next 16 to 20 hours was a decrease in grain-boundary internal friction. The evidence for this is given in the next section but further investigation is required to confirm it.

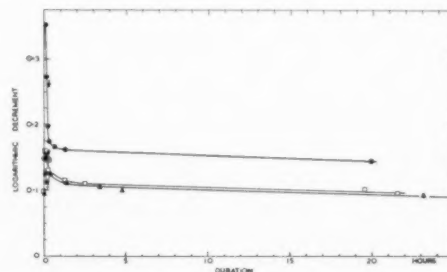


FIG. 16. Variation in decrement of high-purity aluminium during recovery after deformation at 350°C. (The arrows represent the time at which unloading took place.)

Symbol	No.	Stress g/mm <sup>2</sup>	Initial	Decrement Maximum	Final
●	7	258	0.149	0.355	0.142
□	9	204	0.100	0.160	0.094
▲	11	150	0.096	0.127	0.090

### V. EFFECT OF DEFORMATION ON THE GRAIN BOUNDARY DAMPING PEAK

At 250°C and 350°C, the initial decrement before loading was almost entirely due to grain-boundary effects<sup>11</sup> and these were far greater than the changes introduced by the deformation. Hence, it was desirable to see if any changes in grain-boundary damping occurred which might be misinterpreted as changes due to deformation within the grains. In particular it was necessary to see if recovery of the additional internal friction was complete or whether a small decrement remained which was masked by variations in boundary damping.

The grain-boundary damping peak was obtained for aluminium of both purities on heating to the temperature of deformation, 350°C. The specimens were loaded and allowed to creep until a constant decrement was obtained (two hours). After unloading, the decrement was allowed to decrease to a constant value to avoid complications due to further changes with time and the decrement-temperature curve obtained on cooling (Fig. 15). The corresponding creep and decrement-time curves are 14 in Figs. 6 and 7 and that at 476 g/mm<sup>2</sup> in Fig. 12. At 350°C the decrement after unloading was somewhat less than before loading and on cooling both curves lay below those for the annealed materials. Both peaks were lowered but there was no significant shift in the temperatures of the peaks which agree well with values obtained by Kê.<sup>11,12</sup>

At lower temperatures, where the contribution of grain-boundary effects was low, the curve after deformation crossed the other and there was a residual increase in the decrement at room temperature. This amounted to 0.001 to 0.002, which is about the accuracy of measurement at 350°C and would not be detected in the presence of the high grain-boundary decrement.

Two significant facts emerge from this. First, there was a decrease in grain-boundary damping within the first two hours of creep both for pure and impure aluminium and, secondly, that complete recovery did not occur at 350°C, but there remained a small additional decrement of the order of the accuracy of measurement at 350°C.

### VI. DISCUSSION

#### (i) Comparison with Work of Other Authors

The only published work with which these experimental results may be strictly compared is that of Maringer.<sup>10</sup> Despite the disparity in material, his results for molybdenum at room temperature reproduced in Fig. 1 show the same features as those for aluminium at the same temperature. The constant internal friction at stresses below the yield of molybdenum was naturally not observed in annealed aluminium but this did occur in cold-drawn wire. The rapid rise at or immediately before yielding is comparable with the rise for annealed aluminium as

each increment of load was added. Immediately after the yield, the stress in molybdenum remained approximately constant and during this period the internal friction fell rapidly, as occurred at constant load in aluminium. The apparatus used in the work on aluminium did not allow the maintenance of a constant strain rate so that no results for aluminium comparable with the linear stress-internal friction relationship in molybdenum are available. The small peaks superimposed on the linear portion of Maringer's curve are similar to those observed at high constant loads in aluminium at 350°C. The fall in internal friction after unloading the molybdenum wire also accords with the observations reported here. It would be interesting to know if the internal friction after unloading decreased further with sufficient time.

Most other work on the effect of deformation on internal friction has been carried out at high frequencies and shows a strain amplitude dependence over the range  $10^{-7}$  to  $10^{-5}$ .<sup>7,13</sup> Kê<sup>14</sup> has observed amplitude-sensitive curves in partly recrystallised aluminium-0.5% copper alloys at 1 cps. This corresponded to a maximum in the decrement at a particular amplitude, which he interprets as a relaxation process resulting from the movement of dislocations dragging impurity atoms by which they are anchored. The observance of a maximum in decrement on loading is consistent with the observations of Boulanger and other authors. Recovery appears to occur more readily in aluminium than in the 80/20 nickel-chromium alloy so that at the higher stresses, at which the rate of increase in internal friction is lower, the high rate of recovery leads to an apparent peak. The observations in aluminium differ from those in copper, nickel-chromium, etc., in that the maximum occurs at a lower stress and strain. Our observation that in aluminium recovery is apparently complete may not be significant as changes in decrement less than  $10^{-3}$  cannot be detected in the apparatus used. The maxima of  $10^{-2}$  are of the same order as those observed in copper<sup>6,7</sup> at high frequencies. A cold-drawn aluminium wire maintained a constant decrement of  $12 \times 10^{-2}$  under the same conditions.

#### (ii) Discussion in Terms of Dislocation Theory

First of all, it is necessary to distinguish between contributions to the measured internal friction resulting from deformation and grain-boundary effects, respectively.

At room temperature the contribution of the latter to the initial decrement is small. However, at 250°C and 350°C the decrement is largely of grain-boundary origin,<sup>11</sup> the peak for super-purity aluminium of the grain size used being 285°C. It has been shown that the effect of deforming both super- and commercial-purity aluminium at 350°C is (1) to introduce an additional internal friction which is partly recovered if the load is maintained and almost fully recovered a



short time after the removal of the load and (2) to lower the grain-boundary friction slightly, resulting in a lowering but not a displacement of the peak. The loss of some grain-boundary friction was also observed at low stresses. This suggests a slow decrease in boundary damping and explains why the final decrement at 250°C was often lower than the initial value. At this temperature, owing to the rapid fall of decrement with temperature, the difference between the two curves is much greater than at 350°C, as can be seen from Fig. 15.

Three reasons have been advanced for the lowering of a grain-boundary peak. The first possible cause is grain growth to a size approaching the size of the specimen.<sup>11,12</sup> As this would also involve a shift of the peak and the whole curve to a higher temperature this can be ruled out. Microscopical evidence also confirmed that the grain size did not increase materially during the course of the tests in the present case. The second is an increase in the amount of impurities, which is unlikely. Thirdly, it may be a consequence of the removal of submicroscopic irregularities at grain boundaries. There is evidence<sup>2</sup> that grain-boundary movement is inhibited by small irregularities which then deform slowly to allow creep at a diminished rate and that grain-boundary internal friction measurements at high temperatures (400–450°C in aluminium) include a contribution resulting from the deformation of those irregularities. Marsh<sup>13</sup> has recently derived an expression for the height of the grain-boundary internal friction peak which includes a factor that is a measure of "grain-boundary roughness." He finds that a decrease in roughness may be expected to decrease the height of the damping peak and this appears to be the most likely explanation of the lowering of grain-boundary peaks observed in the present work. The initial decrement of the annealed material at 250°C and 350°C consists of two components, the larger due to grain-boundary flow with a small component due to plastic deformation of grain-boundary irregularities. If this be accepted, the slight overall decrease in internal friction which occurred during the first 25 hours of creep is due to a decrease in grain-boundary roughness. A slight decrease observed overnight before loading probably occurs by the same mechanism as a result of the weight of the inertia bar. However, more detailed work is required on this point. It is clear, however, that grain-boundary effects cannot be expected to account for more than a slight decrease in internal friction during the first 20–24 hours of creep.

Although the effect of deformation on internal friction has been known for many years, the mechanism by which it occurs is still a matter of conjecture and any attempt at explanation of the results of this work is somewhat speculative.

A qualitative interpretation can be made if it be assumed the magnitude of the additional internal friction is a measure of the number of active dislocations. Maringer<sup>16</sup> and Hasiguti and Hirai<sup>6</sup> used this

concept to explain their results. In the annealed metal, the dislocations present are lightly bound either by mutual interaction or by anchoring to impurity atoms as proposed by Cottrell in such a way that the small cyclic stresses involved in making decrement measurements are too small to free the dislocations. Some internal friction probably arises from the oscillation of dislocations about their mean position but this is probably of the order  $10^{-6}$  and not detectable by this technique.

The increase in damping and rapid recovery at room temperature were associated with stresses which led to plastic strains of the order of 0.1–0.3 per cent but which were not sufficiently high to cause continuing creep. Tentatively the increase in damping is ascribed to the movement of dislocations which become unblocked under the influence of the applied stress. At the strains observed it may be assumed that some slip has occurred. It is not clear whether the observed increase in damping is due to frictional losses resulting from the movement of dislocations in the slip plane freed during the deformation or whether movement of these is blocked and the frictional loss is due to the freeing of additional dislocations which are almost but not quite freed from locking impurities by the applied stress. The former explanation is more likely since the latter would imply an amplitude-sensitive decrement and this was rarely observed.

The rapid recovery of the additional decrement implies a rapid decrease in the number of mobile dislocations and the re-establishment of a stable array which could not be disturbed by the cyclic stress. The dislocation density could be reduced by passage of dislocations out of the material, by mutual annihilation of dislocations of equal and opposite Burgers vectors, by trapping by impurity atoms or by stabilization by mutual interaction.

At 250°C and 350°C the internal friction would rise on loading for the same reason as at room temperature. The number of dislocations freed or activated will, however, be greater and consequently so would the rise in decrement. At a stress of 204 g/mm<sup>2</sup> and below the rise was relatively small whilst at 258 g/mm<sup>2</sup> and above the rise was disproportionately greater. In the same way the initial rate of recovery was much greater at higher stresses. This suggests that both on loading and in the initial stages of creep, an additional mechanism operates at the higher stresses. The X-ray observations provide a clue to this. At the lower stresses no asterisms were observed, but only a general diffuseness of each reflection with little or no change occurring within the first 24 hours. At the higher stresses small asterisms with one or more diffuse intensity maxima were visible immediately after loading. After two hours and more definitely after 24 hours, some evidence of polygonisation was observed. It is possible that this may have been detected at an earlier stage with a more sensitive X-ray technique.

A tentative explanation of these results may be that at the lower stresses deformation occurred as a result of the freeing of bound dislocations already present whereas at the higher stresses where greater deformations were observed Frank-Read sources were also activated. At the lower stresses, recovery occurred by the same means as those postulated at room temperature with the addition that trapping of dislocations by impurity atoms is aided by the higher diffusion rates at elevated temperatures. The higher stresses are sufficient to activate Frank-Read sources leading to a much larger increase in decrement and presumably conditions are then favourable for polygonisation or cell-formation to occur and this additional process allowed more rapid immobilisation of dislocations.

At 350°C the component of internal friction due to deformation did not entirely recover but decreased to a constant value proportional to the creep stress (Fig. 11). This component of decrement subsequently remained constant, the further slight decrease in decrement being attributed to a decrease in grain boundary roughness. This constant decrement signifies an approximately constant activation of dislocations during the early stages of secondary creep as might be expected. On unloading the rapid and almost complete recovery of this decrement is consistent with the formation of a stable array of dislocations.

Commercial-purity aluminium at 350°C behaved in a similar manner to the purer material but a much higher stress was required for similar effects. Polygonisation was not observed. At a sufficiently low stress, recovery of deformation decrement did not occur under stress (though some grain-boundary decrease probably occurred). This suggests that at a sufficiently low stress and in the presence of sufficient impurity atoms, it is possible for the applied stress to release only such

dislocations as are required to maintain secondary creep. In fact in these cases no primary creep or strain-hardening could be detected.

#### ACKNOWLEDGMENT

The authors wish to acknowledge the assistance of Mr. B. A. Hatt in carrying out the X-ray work.

#### REFERENCES

1. C. Zener, *Elasticity and Anelasticity of metals* (University of Chicago Press, Chicago, Ill., 1948).
2. R. King and B. Chalmers, *Progress in Metal Physics* **1**, 127 (1949).
3. A. S. Nowick, *Progress in Metal Physics* **4**, 1 (1953).
4. C. Zener, H. Clarke, and C. S. Smith, *Trans. A.I.M.M.E.* **147**, 90 (1942).
5. A. W. Lawson, *Phys. Rev.* **60**, 330 (1941).
6. R. R. Hasiguti and T. Hirai, *J. Appl. Phys.* **22**, 1084 (1951).
7. J. Weertman and J. S. Koehler, *J. Appl. Phys.* **24**, 624 (1953).
8. C. Boulanger, *Comptes rend. (Paris)* **226**, 1170 (1948).
9. W. Köster *et al.*, *Z. Metallk.* **29**, 116 (1937); **30**, 345 (1938); **32**, 282 (1940). *Archiv. Eisenhütten* **14**, 271 (1940-1).
10. R. E. Maringer, *J. Appl. Phys.* **24**, 1525 (1953).
11. T. S. Kê, *Phys. Rev.* **71**, 533 (1947).
12. T. S. Kê, *J. Appl. Phys.* **20**, 274 (1949).
13. A. S. Nowick, *Symposium on Plastic Deformation of Crystalline Solids* (Pittsburgh, 1950), p. 155.
14. T. S. Kê, *Science Record* **3**, 61 (1950).
15. K. J. Marsh, *Acta. Met.* **2**, 530 (1954).
16. R. E. Maringer. Private communication.

#### Note Added in Proof

Since this paper was prepared, similar work by Köster and Stotte (*Z. Met.* **45** (1954) 356) has been published. They investigated the effect of plastic deformation on the internal friction of polycrystalline  $\alpha$ -brass at frequencies of 300-1000 cps by an electromagnetic technique which enabled the first measurements to be made about 10 seconds after loading. Their results were generally similar to those reported above.

# ACTIVATION ENERGIES FOR CREEP OF CADMIUM, INDIUM, AND TIN\*

R. E. FRENKEL,† O. D. SHERBY,‡ and J. E. DORN†

It is shown that the total plastic strain for high temperature creep of cadmium, indium and tin under constant load is a function of  $t \cdot e^{-\Delta H/RT}$ , where  $t$ =time under stress,  $\Delta H$ =activation energy for creep,  $R$ =gas constant and  $T$ =absolute temperature. The activation energies for these metals were found to be 21,000, 16,500 and 21,000 calories per mole, respectively.

## ENERGIE D'ACTIVATION POUR LE FLUAGE DU CADMIUM, DE L'INDIUM ET DE L'ÉTAIN

Il est montré que la déformation plastique totale lors du fluage à haute température du cadmium, indium et étain sous charge constante est une fonction de  $t \cdot e^{-\Delta H/RT}$  où  $t$  est la durée du maintien sous charge,  $\Delta H$  l'énergie d'activation pour le fluage,  $R$ =la constante des gaz parfaits et  $T$  la température absolue. Les énergies d'activation pour ces métaux sont respectivement égales à 21.000, 16.500 et 21.000 cal/mol.

## DIE AKTIVIERUNGSENERGIEN FÜR DAS KRIECHEN VON KADMIIUM, INDIUM UND ZINN

Die plastische Gesamtverformung beim Kriechen von Kadmium, Indium und Zinn bei hohen Temperaturen unter konstanter Belastung ist eine Funktion von  $t \cdot e^{-\Delta H/RT}$ . Es bedeutet dabei:  $t$ =Zeit unter Spannung,  $\Delta H$ =Aktivierungsenergie für das Kriechen,  $R$ =Gaskonstante und  $T$ =absolute Temperatur. Die Aktivierungsenergien für diese Metalle wurden zu 21.000, 16.500 bzw. 21.000 cal/mol. bestimmt.

### INTRODUCTION

The results of several investigations<sup>1,2</sup> have revealed that the total strain during high-temperature creep of relatively pure metals can be correlated by the functional relationship

$$\epsilon = f(\theta), \quad \sigma = \text{constant}, \quad (1)$$

where

$\epsilon$ =total plastic strain,  
 $\theta = t e^{-\Delta H/RT}$ ,  
 $t$ =duration of test,  
 $e$ =base of natural logarithms,  
 $R$ =gas constant,  
 $T$ =absolute temperature,  
 $\Delta H$ =activation energy,  
 $\sigma$ =stress (or load).

For the pure metals of Fe, Au, Cu, Al, Pb, and Zn whose activation energies for self-diffusion and creep are fairly accurately known, the activation energy for high temperature creep agreed quite well with that for self-diffusion.<sup>2</sup> Analyses of Roberts' data<sup>3</sup> revealed that the activation energy for creep of Mg was about 31,000 cal/mole; recently Shewmon and Rhines<sup>4</sup> have shown that the activation energy for self-diffusion in Mg is about 32,000 cal/mole. Such coincidence between the activation energies suggests that the rate-controlling process for high temperature creep is that of self-diffusion and thus lends partial support to Mott's dislocation-climb model for high temperature creep.<sup>5</sup> But inasmuch as the comparison of the energies for high-temperature creep and self-diffusion is currently limited to only seven of the metallic elements, additional confirmation of the universality of their identity for

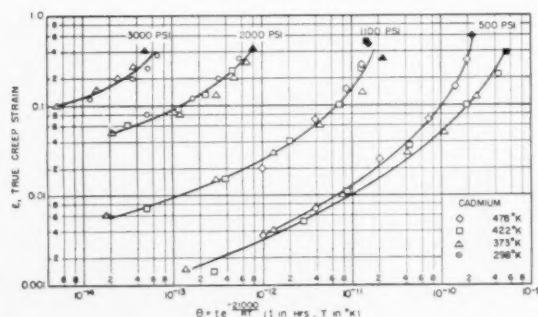


FIG. 1. Correlation of creep strain-time data for cadmium at various stresses.

\* Received January 17, 1955.

† Department of Physical Metallurgy, University of California, Berkeley, California.

‡ Institute of Engineering Research, University of California, Berkeley, California.

TABLE I. Purity and preparation of material for creep testing.

Material	Purity, (At. No.) per cent	Preparation	Heat treatment	Grain size, grains/cm
Cd (48)	99.96	Cast ingot cold rolled to 0.10 inch sheet, then machined into specimen blanks	2.5 hours at 553°K	24-30
In (49)	99.86	Cast ingot cold rolled to 0.10 inch sheet, then machined into specimen blanks	1.5 hours at 333°K	10-15
Sn (50)	99.94	Cast ingot cold rolled to 0.10 inch sheet, then machined into specimen blanks	2.0 hours at 478°K	20

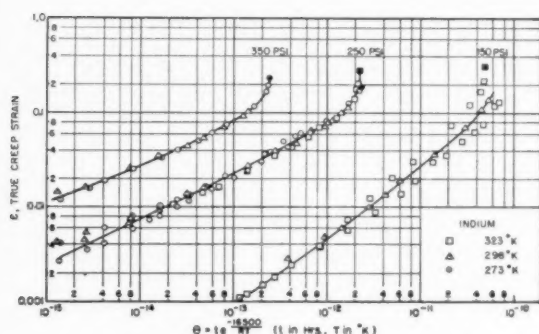


FIG. 2. Correlation of creep strain-time data for indium at various stresses.

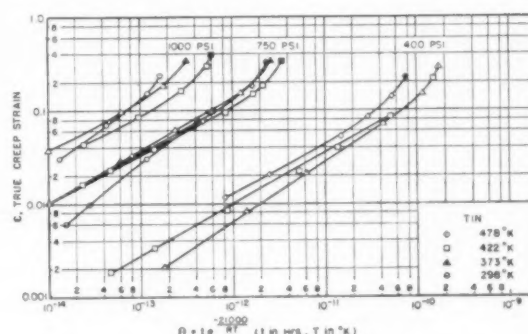


FIG. 3. Correlation of creep strain-time data for tin at various stresses.

other elements is desirable. Consequently the activation energies for creep of Cd (48), In (49), and Sn (50) were determined for the purpose of comparing them with the known activation energies for self-diffusion in these metals.

#### EXPERIMENTAL TECHNIQUES AND RESULTS

The creep tests were conducted under constant load conditions. Strain was measured by means of a rack and pinion extensometer sensitive to  $10^{-4}$  for a two-inch gage length specimen. Temperature was maintained constant within  $\pm \frac{1}{2}^{\circ}\text{C}$ .

The purity of the materials and their preparation for test are given in Table I. In view of the previous extensive investigations, only a few creep tests were considered to be required to reaffirm the nominal validity of Eq. (1) for the present investigation. As shown by the correlations presented in Figs. 1 to 3, Eq. (1) appears to be valid for the metals and conditions of test employed here. In order to illustrate more effectively the uniformity of the activation energy for creep that was obtained in these investigations, the logarithm of the time to reach strains of 0.04 and strains of 0.10 were plotted as a function of the reciprocal of the absolute temperature as shown in Fig. 4. Since the slopes of these lines times 2.303 give  $\Delta H/R$ , the corresponding activation energies were readily calculated as shown on each line. Although the data for In exhibit excellent internal consistency, some scatter

was obtained in the calculated activation energies for Sn and Cd. In view of the well-known scatter normally encountered in the creep behavior of various specimens from the same original material, the variations in the activation energies obtained here were not considered to be excessive. Over the range of conditions studied the following activation energies were obtained:

Metal	$\Delta H$ for creep cal/mole
Cd	$21,000 \pm 2,000$
In	$16,500 \pm 500$
Sn	$21,000 \pm 2,000$

These activation energies were found to be insensitive to stress, strain, and temperature over the ranges of these variables that were investigated.

#### DISCUSSION

The activation energies for creep of Cd, In, and Sn, as obtained in this investigation, are compared with previously reported activation energies for self-diffusion in Table II.

These correlations appear to be good with the exception of the newly reported data for Sn. Partial confirmation of the nominal validity of the reported activation

TABLE II. Activation energies for self-diffusion and creep of cadmium, indium and tin.

Element	Direction	Self-diffusion data		Reference	Creep data (This investigation) $\Delta H$ (Activation energy) cal/mole
		$D_0$ (Frequency factor) $\text{cm}^2/\text{sec}$	$\Delta H$ (Activation energy) cal/mole		
Cd	$\parallel C$	$5 \times 10^{-2}$	18,200	6	21,000
	$\perp C$	$1.0 \times 10^{-1}$	19,100		
In		1.02	17,900	7	16,500
Sn	$\parallel C$	$1.2 \times 10^{-5}$	10,500	8	21,000
	$\perp C$	$3.7 \times 10^{-8}$	5,900		

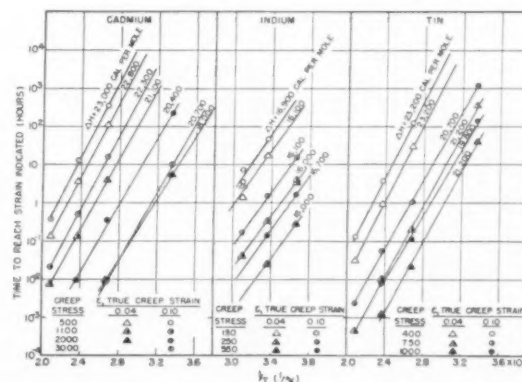


FIG. 4. Logarithm of time to reach  $\epsilon=0.04$  and 0.10 at various stresses versus reciprocal of absolute temperature for cadmium, indium and tin.



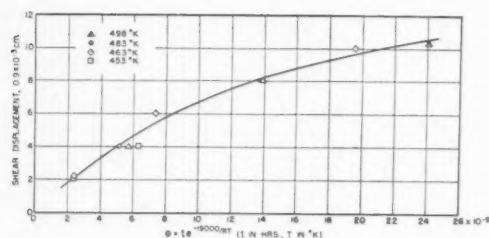


FIG. 5. Correlation of shear displacement-time data for tin by the relation  $\epsilon = f(\theta)$  under a stress of 21.3 psi. (Data of Puttick and King.<sup>9</sup>)

energy for creep of Sn is obtained from the data of Puttick and King<sup>9</sup> on grain-boundary shearing in Sn. Investigations on Al have shown that the activation energy for grain boundary shearing is practically the same as that for creep.<sup>10</sup> As shown in Fig. 5, analyses of Puttick and King's data give an activation energy of 19,000 cal/mole for grain boundary shearing of Sn. The discrepancy between  $\Delta H$  creep and  $\Delta H$  self-diffusion for tin is rather perturbing, particularly since Fensham's techniques in evaluating the tin self-diffusion data appear excellent. However, certain questions may be raised with regard to the diffusion data. Firstly, the frequency factor  $D_0$  appears anomalous. Most values of  $D_0$  for self-diffusion in metals<sup>11,12</sup> range between  $10^{-1}$  to 10, whereas the experimental values of  $D_0$  for tin are very much lower (Table II). Dienes<sup>12</sup> has shown that such low values of  $D_0$  yield very large negative entropies of activation when Zener's theoretical expression<sup>13</sup> for  $D_0$  is used. And, Zener has suggested that negative entropy values are attributable to inaccuracies in experiments or presence of inhomogeneities which provide short circuiting diffusion paths. Secondly, it has been shown that the activation energies for self-diffusion in tin do not correlate well with other diffusion data when plotted *versus* the respective absolute melt-

ing temperatures, whereas the activation energy for creep of tin correlates reasonably well.<sup>14</sup> It is therefore believed that the self-diffusion data for tin might be in error. However, further experimentation will be necessary to clarify this issue.

### CONCLUSIONS

1. The total plastic strain for high temperature creep of Cd, In and Sn under constant load appears to be a function of  $t e^{-\Delta H/RT}$ , where  $t$  is the duration of test,  $R$  the gas constant,  $T$  the absolute temperature and  $\Delta H$  is the activation energy.

2. The activation energies for high temperature creep of Cd, In and Sn were found to be 21,000, 16,500 and 21,000 cal/mole respectively.

3. Whereas the activation energies for creep of Cd and In agreed well with those for self-diffusion, that for creep of Sn was found to be greater than the reported values for self-diffusion. It was thought that the latter discrepancy might be attributable to difficulties in determining the activation energies for self-diffusion in Sn.

### REFERENCES

1. O. D. Sherby and J. E. Dorn, Trans. A.I.M.E. **194**, 959 (1952).
2. O. D. Sherby, R. L. Orr, and J. E. Dorn, Trans. A.I.M.E. **200**, 71 (1954).
3. Discussion of Paper by C. S. Roberts, Trans. A.I.M.E. **200**, 690 (1954).
4. P. G. Shewmon and F. N. Rhines, Trans. A.I.M.E. **200**, 1021 (1954).
5. N. F. Mott, Proc. Phys. Society, **64B**, 729 (1951).
6. E. S. Wadja, G. A. Shirn, and H. B. Huntington, Acta Met. **3**, 39 (1955).
7. R. E. Eckert and H. G. Drickamer, J. Chem. Phys. **20**, 13 (1952).
8. P. J. Fensham, Austr. J. Sci. Res. **3**, 91 (1950).
9. K. E. Puttick and R. King, J. Inst. Metals **80**, 537 (1952).
10. B. Fazan, O. D. Sherby, and J. E. Dorn, Trans. A.I.M.E. **200**, 919 (1954).
11. G. J. Dienes, J. Appl. Phys. **21**, 1189 (1950).
12. G. J. Dienes, J. Appl. Phys. **22**, 848 (1951).
13. C. Zener, J. Appl. Phys. **22**, 372 (1951).
14. J. E. Dorn, J. Mechanics and Physics of Solids, **3**, 85 (1954).

## STACKING FAULTS IN COLD WORKED ALPHA-BRASS\*†

B. E. WARREN and E. P. WAREKOIS‡

Stacking faults on the (111) planes of a face-centered cubic metal produce a broadening of the X-ray peaks, and also peak shifts from which the stacking fault probability can be directly determined. Measurements were made of the (111), (200), (222) and (400) reflections from cold worked filings of  $\alpha$  brass of composition 90-10, 80-20, 70-30, and 65-35. The stacking fault probability increases with increasing zinc content, reaching  $\alpha=0.039$  for the composition 65-35. Root-mean-square strains and coherent domain sizes were obtained from the peak broadening. An appreciable part of the particle size broadening results directly from stacking faults. The root-mean-square strains are of the order of the yield stress divided by Young's modulus, and the product of strain and domain size is approximately a constant of the order of 1A. It is suggested that the intersection of stacking faults on different (111) planes is an important part of the work-hardening in  $\alpha$ -brass.

### DÉFAUTS D'EMPLIAGE DANS LE LAITON $\alpha$ ÉCROUÍ

Les défauts d'empilage sur les plans (111) d'un métal cubique à faces centrées produisent un élargissement ainsi qu'un déplacement des raies X d'où l'on peut déduire la probabilité de ces défauts. Les mesures ont été effectuées pour les raies (111) (200) (222) (400) de la limaille de laiton  $\alpha$  de composition 90/10, 80/20, 70/30, 65/35. La probabilité d'un défaut d'empilage croît avec la teneur en zinc atteignant  $\alpha=0,039$  pour 65/35. La racine carrée de la moyenne du carré des déplacements et les dimensions des domaines cohérents ont été déterminées à partir de l'élargissement. Une partie notable de l'élargissement dû aux dimensions des domaines cohérents résulte des défauts d'empilage. La racine carrée de la moyenne du carré de déplacement est de l'ordre de la limite élastique divisée par le module de Young, tandis que le produit du déplacement par les dimensions des domaines cohérents est une constante de l'ordre de 1 Å. L'intersection des défauts d'empilage dans les différents plans (111) serait une partie importante de la consolidation des laitons  $\alpha$ .

### STAPELFEHLER IN KALTVERFORMTEM ALPHA MESSING

Durch Stapelfehler auf den (111)-Ebenen eines kubischraumzentrierten Metalles wird eine Verbreiterung der Röntgenlinien und eine Verlagerung ihrer Maxima verursacht, aus der die Stapelfehler Wahrscheinlichkeit direkt bestimmt werden kann. An kaltverformten  $\alpha$ -Messing Feilspänen (Ms 90, 80, 70 und 65) wurden die (111)-, (200)-, (222)- und die (400)-Reflexe aufgenommen. Die Wahrscheinlichkeit, dass Stapelfehler auftreten, nimmt mit steigendem Zinkgehalt zu und erreicht bei der Zusammensetzung von Ms 65 einen Wert von  $\alpha=0.039$ . Die Wurzel aus den mittleren Quadrat der Verzerrung und die Grösse der Kohärenzbereiche wurde aus den Linienbreite berechnet. Ein merklicher Anteil der Teilchengrößenverbreiterung wird direkt durch die Stapelfehler verursacht. Die Wurzel aus den mittleren Quadrat der Verzerrung liegt in der Größenordnung der Streckgrenzenspannung dividiert durch den Young'schen Modul. Das Produkt aus der Verzerrung und der Korngrösse ist annähernd konstant und liegt in der Größenordnung von 1A. Es wird vermutet, dass die Durchsetzung von Stapelfehlern auf verschiedenen (111)-Ebenen einen bedeutenden Anteil der Verfestigung ausmacht.

### I. INTRODUCTION

Cold work in a metal broadens the X-ray powder pattern peaks. It is usually assumed that the broadening results from two effects:

1. a reduction in the size of the coherently diffracting domains, and
2. distortions within the coherent domains.

With modern methods the broadening from the two effects can be separated, and mean domain sizes and mean square strains determined. In addition to these two effects, Barrett<sup>1</sup> has suggested that in a face-centered cubic material such as  $\alpha$ -brass, cold work may produce stacking faults on the (111) planes.

If we represent a close packing of spheres in terms of close-packed hexagonal layers, there are three sets of positions A, B, C for the atoms in each layer. The sequence ABCABC produces the FCC packing, while

the sequence ABABAB produces the hexagonal close-packed structure. In the FCC packing if the  $m$ th layer is A and the  $(m+1)$ th layer is B, slip on the (111) plane might shift everything above the  $m$ th layer as indicated in Fig. 1 so that the  $(m+1)$ th layer becomes C. We say that a stacking fault has been introduced between the  $m$ th and the  $(m+1)$ th layer. The single stacking fault has produced 4 layers in the hexagonal close packed sequence.

Paterson<sup>2</sup> has shown that stacking faults on the (111) planes of an FCC material produce a line broadening and also a small peak shift. The peak shift is particularly important because it allows a direct determination of the stacking fault probability independent of particle size and distortion broadening. The pertinent equations for the effect of stacking faults can be obtained and extended by a simpler method than that used by Paterson by following certain procedures introduced by Méring.<sup>3</sup> The treatment is given in the next section for stacking faults occurring at random on one set of (111) planes.

\* Received January 1, 1955.

† Research sponsored by the U. S. Atomic Energy Commission.

‡ Massachusetts Institute of Technology, Cambridge, Massachusetts.

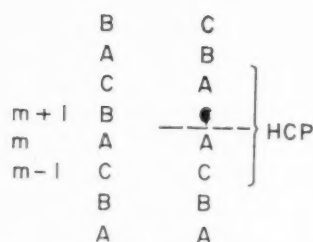


FIG. 1. Close-packed layers. Left, normal FCC sequence. Right, stacking fault between  $m$ th and  $(m+1)$ th layer.

## II. EFFECT OF STACKING FAULTS IN FCC SAMPLE

Let  $\mathbf{a}_1\mathbf{a}_2\mathbf{a}_3$  be the cubic axes and  $hkl$  the corresponding indices. In terms of one set of (111) planes, introduce hexagonal axes  $\mathbf{A}_1\mathbf{A}_2\mathbf{A}_3$  with  $\mathbf{A}_1\mathbf{A}_2$  in the plane and  $\mathbf{A}_3$  normal to the plane. Let  $HKL$  be the indices corresponding to the hexagonal axes. The transformation equations are

$$\begin{aligned} \mathbf{A}_1 &= -\mathbf{a}_1/2 + \mathbf{a}_2/2 + 0 & H &= -h/2 + k/2 + 0 \\ \mathbf{A}_2 &= 0 - \mathbf{a}_2/2 + \mathbf{a}_3/2 & K &= 0 - k/2 + l/2 \\ \mathbf{A}_3 &= \mathbf{a}_1 + \mathbf{a}_2 + \mathbf{a}_3 & L &= h + k + l \end{aligned} \quad (1)$$

For the first two cubic powder pattern lines (111) and (200), the corresponding hexagonal indices are given in Table I.

To perform a summation over layers, we let  $\mathbf{r}_m$  be the position of atom  $m_1m_2$  in layer  $m_3$ ,  $\mathbf{r}_m = m_1\mathbf{A}_1 + m_2\mathbf{A}_2 + m_3\mathbf{A}_3/3 + \delta(m_3)$ . The intensity is given by

$$I = I_e f^2 \sum_m \sum_{m'} \exp[2\pi i/\Lambda (\mathbf{s} - \mathbf{s}_0) \cdot (\mathbf{r}_{m'} - \mathbf{r}_m)], \quad (2)$$

where  $\mathbf{s}$  and  $\mathbf{s}_0$  are unit vectors in the directions of the diffracted and primary beams. Let  $N_1$  and  $N_2$  be the number of repetitions in the  $\mathbf{A}_1$  and  $\mathbf{A}_2$  directions, and introduce the abbreviation

$$\psi^2 = I_e f^2 \frac{\sin^2 \frac{\pi}{\Lambda} (\mathbf{s} - \mathbf{s}_0) \cdot N_1 \mathbf{A}_1}{\sin^2 \frac{\pi}{\Lambda} (\mathbf{s} - \mathbf{s}_0) \cdot \mathbf{A}_1} \frac{\sin^2 \frac{\pi}{\Lambda} (\mathbf{s} - \mathbf{s}_0) \cdot N_2 \mathbf{A}_2}{\sin^2 \frac{\pi}{\Lambda} (\mathbf{s} - \mathbf{s}_0) \cdot \mathbf{A}_2}. \quad (3)$$

The intensity is then given by

$$I = \psi^2 \sum_{m_3} \sum_{m_3'} \exp[2\pi i/\Lambda (\mathbf{s} - \mathbf{s}_0) \cdot ([m_3' - m_3] \mathbf{A}_3/3 + [\delta(m_3') - \delta(m_3)])]. \quad (4)$$

Let  $m_3' - m_3 = m$  and  $\delta(m_3') - \delta(m_3) = \delta_m$ .

Represent the diffraction vector in terms of the continuous variables  $h_1h_2h_3$ , and the vectors  $\mathbf{B}_1\mathbf{B}_2\mathbf{B}_3$  reciprocal to  $\mathbf{A}_1\mathbf{A}_2\mathbf{A}_3$ ,  $(\mathbf{s} - \mathbf{s}_0)/\Lambda = h_1\mathbf{B}_1 + h_2\mathbf{B}_2 + h_3\mathbf{B}_3$ . Introduce the abbreviation  $\phi_m = 2\pi(h_1\mathbf{B}_1 + h_2\mathbf{B}_2 + h_3\mathbf{B}_3) \cdot \delta_m$ . If  $N_m$  is the number of layers having an  $m$ th neighbor, we can replace the double sum of Eq. (4)

with a single sum over  $m$ .

$$I = \psi^2 \sum_{m=-\infty}^{\infty} N_m \langle \exp[i\phi_m] \rangle_m \exp[2\pi i m h_3/3]. \quad (5)$$

The displacement  $\delta_m$  between two  $m$ th neighbors is the sum of the displacements between each intermediate pair of nearest neighbor layers, so that

$$\langle \exp[i\phi_m] \rangle = \langle \exp[i\phi_1] \exp[i\phi_{1-2}] \exp[i\phi_{2-3}] \cdots \rangle.$$

If we assume that the probability of a stacking fault between any two nearest neighbors is independent of all neighboring layers, the average of the product becomes the product of the averages.

$$\langle \exp[i\phi_m] \rangle = \langle \exp[i\phi_1] \rangle^m. \quad (6)$$

For the normal ABCABC sequence, the displacement from one layer to the next is  $\delta_1 = -\mathbf{A}_1/3 + \mathbf{A}_2/3$  and  $\phi_1 = -2\pi(h_1/3 - h_2/3)$ . If a stacking fault intervenes,  $\phi_1' = 2\pi(h_1/3 - h_2/3)$ . From Eq. (3) it follows that the intensity differs significantly from zero only where  $h_1$  and  $h_2$  are closely equal to the integers  $H$  and  $K$ . If  $\alpha$  is the probability of finding a stacking fault between any two neighboring layers, Eq. (6) can be written

$$\langle \exp[i\phi_m] \rangle = [(1-\alpha) \exp[-2\pi i(H-K)/3] + \alpha \exp[2\pi i(H-K)/3]]^m. \quad (7)$$

If  $H-K=3M$ , where  $M$  is an integer, the effect of stacking faults drops out, and we have an ordinary crystalline reflection. For  $H-K=3M \pm 1$ , Eq. (7) becomes

$$\langle \exp[i\phi_m] \rangle = [\frac{1}{2} + (\pm)i(1-2\alpha)\sqrt{3}/2]^m \exp[im\pi],$$

where the  $(\pm)$  choice in sign corresponds to  $3M \pm 1$ . Let  $[\frac{1}{2} + (\pm)i(1-2\alpha)\sqrt{3}/2] = Z \exp[(\pm)i\gamma]$ , where

$$Z = [1 - 3\alpha(1-\alpha)]^{1/2} \quad (8)$$

$$\tan \gamma = \sqrt{3}(1-2\alpha).$$

If we consider both positive and negative values of  $m$ , it is readily shown that for either case

$$\langle \exp[i\phi_m] \rangle = Z^{|m|} \exp[(\pm)i m \gamma + i m \pi].$$

Introducing this result in Eq. (5), and recognizing that  $N_m Z^{|m|}$  is independent of the sign of  $m$ , we obtain

$$I = \psi^2 \sum_{m=-\infty}^{+\infty} N_m Z^{|m|} \cos 2\pi m (h_3/3 + \frac{1}{2} + (\pm)\gamma/2\pi). \quad (9)$$

Equation (9) contains the two principal effects of stacking faults: line broadening and peak shifts. It is equivalent to the equation derived by Paterson from the method of difference equations. If we assume that all layers have the same dimensions  $N_1\mathbf{A}_1$  and  $N_2\mathbf{A}_2$ , and let  $n_i$  be the number of crystals with  $i$  layers, and  $N$  the total number of layers

$$N = \sum_{i=0}^{\infty} i n_i \quad N_m = \sum_{i=|m|}^{\infty} (i - |m|) n_i.$$

The product  $N_m Z^{|m|}$  can then be considered as a Fourier coefficient

$$A_m^{SP} = \frac{1}{N} \sum_{i=|m|}^{\infty} (i - |m|) n_i Z^{|m|},$$

where  $SP$  stands for stacking faults and particle size, and the coefficient  $A_m^{SP}$  is unity for  $m=0$ . With these changes, Eq. (9) is conveniently considered as a cosine Fourier series

$$I = N \psi^2 \sum_{m=-\infty}^{+\infty} A_m^{SP} \cos 2\pi m (h_3/3 + \frac{1}{2} + (\pm)\gamma/2\pi), \quad (10)$$

where the variable is  $(h_3/3 + \frac{1}{2} + (\pm)\gamma/2\pi)$  and  $h_3$  is obtained from the relation  $h_3 |\mathbf{B}_3| = \cos \phi \sin \theta / \Lambda$  where  $\phi$  is the angle between  $\mathbf{B}_3$  and  $H\mathbf{B}_1 + K\mathbf{B}_2 + h_3\mathbf{B}_3$ .

Suppose that the coefficients  $A_m^{SP}$  are determined from the experimental peak shapes and are then plotted as a function of  $m$ . Using the method of Bertaut,<sup>4</sup> the initial slope of the  $A_m^{SP}$ -versus- $m$  curve gives

$$-\left(\frac{dA_m^{SP}}{dm}\right)_{m=0} = \frac{1}{\bar{i}},$$

where  $\bar{i}$  is the average number of layers per crystal.

The variable  $h_3$  which has been used in the preceding discussion is different from that in the Warren and Averbach<sup>5,6</sup> method for separating particle size and distortion broadening by Fourier analysis. In this method each reflection is called  $00l$  and the variable is  $h_3' = 2a_3' \sin \theta / \Lambda$ . The axial length normal to the reflecting planes is  $a_3$ , but a fictitious value  $a_3'$  is usually used to simplify the evaluation of the Fourier coefficients. The harmonic numbers  $m'$  corresponding to the fictitious spacing  $a_3'$  are then conveniently represented by a real distance in the crystal normal to the reflecting planes  $L = m'a_3'$ . In the  $W+A$  analysis the corrected peak shape is represented by the Fourier series

$$I = K \sum_{m=-\infty}^{+\infty} A_m^P A_m^D(l) \cos 2\pi m h_3', \quad (11)$$

where the Fourier coefficient is the product of two coefficients, one representing particle size broadening and the other distortion. If multiple orders are available, the two can be separated by the fact that  $A_m^P$  is independent of order and  $A_m^D(0) = 1$ . Extrapolating to  $l=0$  gives directly  $A_m^P$ . With an approximation\* for  $A_m^D(l)$

$$\ln[A_m^P A_m^D(l)] = \ln A_m^P - 2\pi^2 l^2 \langle Z_m^2 \rangle, \quad (12)$$

\* When coefficients  $A_m^P A_m^D(l)$  are available for several orders,  $A_m^P$  is obtained by extrapolating to  $l=0$ , since  $A_m^P$  is independent of order and  $A_m^D(l) = 1$  for  $l=0$ . If more than two orders are available, the extrapolation can be made against any convenient function of  $l$ , and no approximation is involved. Since linear extrapolations are desirable, it is customary to make the approximation  $A_m^D(l) = \langle \cos 2\pi l Z_m \rangle \rightarrow \exp[-2\pi^2 l^2 \langle Z_m^2 \rangle]$  which is justified for either small values of  $2\pi l Z_m$  or a Gaussian distribution for  $Z_m$ . If more than two orders are available, the extrapolation is independent of the approximation, but when only two orders are available a linear extrapolation against  $l^2$  assumes the correctness of the approximate form for  $A_m^D(l)$ .

TABLE I. Corresponding cubic and hexagonal indices.

$hkl$	$HKL$	$H-K$	$hkl$	$HKL$	$H-K$
111	003	0	200	$\bar{1}02$	1
$\bar{1}\bar{1}\bar{1}$	0 $\bar{0}\bar{3}$	1	020	$\bar{1}\bar{1}2$	2
$\bar{1}\bar{1}1$	$\bar{1}11$	$\bar{2}$	002	012	$\bar{1}$
$\bar{1}1\bar{1}$	101	1			

On a plot of  $\ln[A_m^P A_m^D(l)]$  versus  $l^2$ , the intercept gives the particle-size coefficient  $A_m^P$ , and the slope gives  $\langle Z_m^2 \rangle = L^2 \langle \epsilon_L^2 \rangle / a_3^2$  from which we obtain the mean-square strain normal to the planes and averaged over the distance  $L$ . If the Fourier analysis is carried out by the method of Eqs. (11) and (12) for a sample in which there are stacking faults and true particle size broadening, the initial slope of the  $A_m^P$ -versus- $L$  curve gives

$$-\left(\frac{dA_m^P}{dL}\right)_{L=0} = \frac{1}{\bar{L}} + \frac{3}{2} \frac{\alpha}{d_{111}} \cos \phi, \quad (13)$$

where  $\bar{L}$  is the average size of coherent domains in a direction normal to the reflecting planes, and  $\phi$  is the angle between  $\mathbf{B}_3$  and  $H\mathbf{B}_1 + K\mathbf{B}_2 + h_3\mathbf{B}_3$ . Stacking faults give a broadening which acts like particle size broadening and is included in any measurement of particle size broadening. If we know the stacking fault probability  $\alpha$  we can compute the contribution to the particle size broadening, but from the measured broadening we cannot separate the stacking fault effect from the true particle size broadening.

In addition to line broadening, stacking faults produce a peak shift. The cosine Fourier series represented by Eq. (10) peaks at values of  $h_3$  given by  $h_3 = 2p - \frac{3}{2} - (\pm)3\gamma/2\pi$ , where  $p$  is an integer. If  $\alpha=0$ ,  $\gamma_0 = \tan^{-1}\sqrt{3}$ . If  $\Delta h_3$  is the shift in peak position due to stacking faults,  $\Delta h_3 = -(\pm)(\gamma_\alpha - \gamma_0)\frac{3}{2}\pi$  and for small  $\alpha$  this becomes  $\Delta h_3 = (\pm)3\sqrt{3}\alpha/4\pi$ . Since

$$2 \sin \theta / \Lambda = [ |H\mathbf{B}_1 + K\mathbf{B}_2|^2 + |h_3\mathbf{B}_3|^2 ]^{\frac{1}{2}}$$

with  $H$  and  $K$  constant,  $\Delta 2\theta = 2 \tan \theta \cos^2 \phi \Delta h_3 / h_3$ . Combining these results, we express the peak shift in  $2\theta$  expressed in degrees

$$\Delta(2\theta^\circ) = (\pm) \tan \theta \cos^2 \phi 270\sqrt{3}\alpha / \pi^2 h_3. \quad (14)$$

In terms of cubic indices, the first two reflections on a powder pattern are (111) and (200). Referring to Table I it is seen that for these reflections

$$\begin{array}{ll} 111 & \cos \phi = 1/3 \quad (\pm) = + \quad h_3 = 1 \quad \frac{2}{3} \text{ of planes effective} \\ 200 & \cos \phi = 1/\sqrt{3} \quad (\pm) = - \quad h_3 = 2 \quad \text{all planes effective} \end{array}$$

For (111) and (200) Eq. (14) becomes

$$\begin{array}{ll} (111) & \Delta(2\theta^\circ) = +\alpha \tan \theta 45\sqrt{3} / 2\pi^2 \\ (200) & \Delta(2\theta^\circ) = -\alpha \tan \theta 45\sqrt{3} / \pi^2. \end{array}$$

The effect of stacking faults is to shift (111) outward and (200) inward. For the second orders (222) and (400)



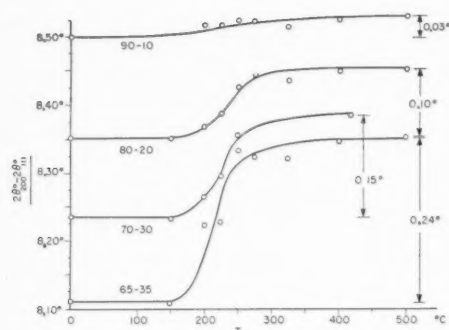


FIG. 2. The  $2\theta$  separation between (111) and (200) for  $\alpha$ -brass filings. Values at the left are for cold-worked material and the other points correspond to successive 1-hour anneals at the temperatures indicated.

the effect is the reverse. Instead of measuring the shift of either peak, it is more accurate to eliminate positioning errors by measuring the decrease in separation of the (111) and (200) peaks recorded on a single run. For 70-30 brass and  $\text{CoK}\alpha$  radiation, this change becomes

$$\Delta(2\theta_{200} - 2\theta_{111}) = -6.2\alpha. \quad (15)$$

Equation (15) allows a direct determination of the stacking fault probability  $\alpha$ , quite independent of line broadening due to particle size and distortion. There are two doubtful points in the use of Eq. (15). It was assumed that the stacking faults occur independently and on only one set of (111) planes. In drastically cold-worked metal the stacking faults probably occur on more than one set of (111) planes, but it is difficult to treat this general case without making specific assumptions. Perhaps it is a good enough approximation to consider that the probability obtained from Eq. (15) on the assumption that stacking faults occur on only one set of (111) planes is actually the sum of the probabilities for the different sets of active (111) planes.

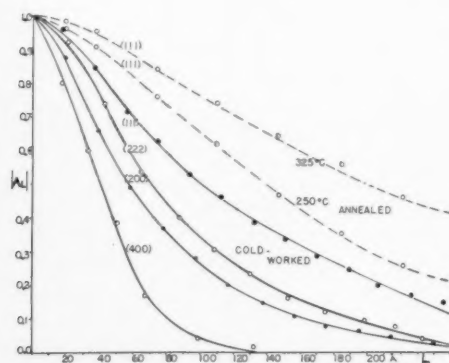


FIG. 3. Fourier coefficients  $A_L$  versus  $L$  ( $\text{\AA}$ ) corrected for instrumental broadening for cold-worked 90-10  $\alpha$  brass. The effect of annealing is shown for the reflection (111).

### III. EXPERIMENTAL RESULTS FOR ALPHA-BRASS

Cold-worked  $\alpha$ -brass shows very strongly all three X-ray effects: distortion broadening, particle size broadening, and stacking fault peak shifts. Measurements were made on four samples of approximate composition 90-10, 80-20, 70-30, and 65-35. The samples were cold-worked by making filings, and these were then pressed into flat-faced briquets. The diffraction patterns were run on a Norelco spectrometer using filtered  $\text{CoK}\alpha$  radiation.

The stacking fault probability was determined from the change in the separation of the (111) and (200) reflections. To minimize positioning errors, the two peaks were recorded on a single run. For heavily cold-worked  $\alpha$ -brass, the (111) and (200) peaks are sharp enough to determine the center of gravity to about  $\pm 0.01^\circ$  in  $2\theta$ . Although the change in the (222)-(400) separation is much greater, the (400) peak is so broad that values obtained from (222)-(400) are actually less accurate.

Figure 2 shows the measured (111)-(200) peak separations for the four compositions. The values at the left represent the cold-worked material, and the other points correspond to successive 1-hour anneals at the temperatures indicated. Since the values at

TABLE II. Stacking fault probability from peak shifts.

Comp.	90-10	80-20	70-30	65-35
$\alpha$	0.005	0.016	0.024	0.039

the right represent normal well annealed material, there is a decrease in the  $(2\theta_{200} - 2\theta_{111})$  separation as a result of cold work. The  $(2\theta_{400} - 2\theta_{222})$  separation shows an increase exactly as predicted by the Paterson theory, and there can be little doubt that we are observing the effect of stacking faults. The effect increases rapidly with increasing Zn content. Most of the effect anneals out in the range 175-250°C. The stacking fault probabilities computed by Eq. (15) for the four cold-worked samples are tabulated below. For the 65-35 sample, the value  $\alpha = 0.039$  corresponds to an average of one stacking fault in every 26 (111) planes, or an average separation between stacking fault planes of  $26d_{111} = 55\text{\AA}$ .

To correlate the stacking fault probability with coherent domain sizes and mean-square strains, a Fourier analysis was made for the four reflections (111), (222), (200), and (400). These were the only pairs of multiple orders which would allow the use of Eq. (12) to separate the broadening due to domain size and strains. Corresponding peaks from well-annealed samples were used to correct for instrumental broadening. The cold-worked and annealed peaks were represented by their Fourier coefficients and the correction for instrumental broadening made by the

method of Stokes.<sup>7</sup> The corrected coefficients are represented as  $A_L$  versus  $L$  where  $L=ma_s$  has the significance of a distance normal to the reflecting planes. For the compositions 90-10 and 65-35 the coefficients are shown by Figs. 3 and 4.

The curves are in the order (111), (222), (200), (400) rather than in the order of  $h^2+k^2+l^2$ , and actually the (200) peak is broader than (222). In earlier studies of  $\alpha$  brass<sup>8,9</sup> it has been assumed that all of the broadening was due to strains, and that the smaller value of Young's modulus in the [100] direction was responsible for the broader (200) and (400) reflections. It now appears that only part of this effect is due to the directional variation in Young's modulus, and a large part is due to the line broadening produced by stacking faults. All four compositions were given successive one hour anneals at 150, 200, 225, 250, 275 and 325°C. The (111) curves for 250°C and 325°C on Figs. 3 and 4 show the effect of annealing.

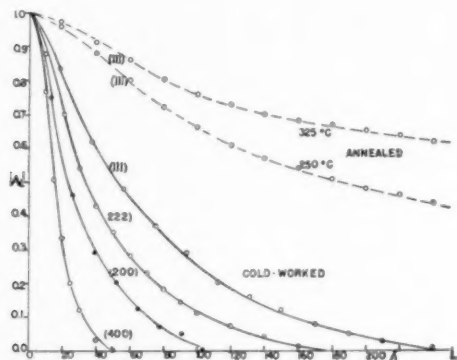


FIG. 4. Fourier coefficients  $A_L$  versus  $L$  ( $\text{\AA}$ ) corrected for instrumental broadening for cold-worked 65-35  $\alpha$  brass. The effect of annealing is shown for the reflection (111).

To separate the broadening due to particle size from that due to strains,  $\ln A_L(l_0)$  was plotted against  $l_0^2 = h^2 + k^2 + l^2$  for various values of  $L$ . By extrapolating to  $l_0 = 0$ , the intercept on the axis of ordinates gives a Fourier coefficient  $A_L^P$  which is due only to particle size and stacking fault broadening. Log plots were made for the two sets of multiple orders (111)-(222) and (200)-(400). The (111)-(222) log plot for cold-worked 65-35 is shown by Fig. 5.

From the intercepts on the log plots, we then made plots of the Fourier coefficients for particle size and stacking fault broadening  $A_L^P$  versus  $L$ . Figure 6 shows such plots for the (111)-(222) and (200)-(400) sets for 65-35 brass. In principle these curves should start as straight lines and then gradually curve upward. In practice there is considerable uncertainty in the values for small  $L$  due to the effect of tails on the diffraction peaks and the correction for distortion broadening. A small hook sometimes appears in the small  $L$  part of the curve, but in general the more accurate the original data, and the more careful the

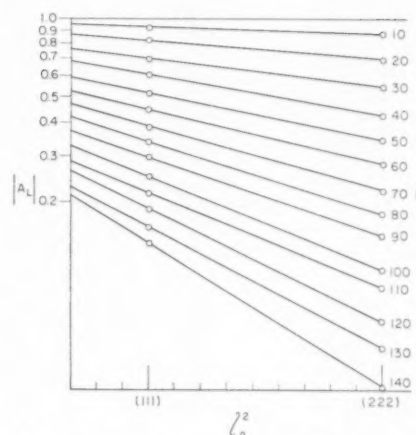


FIG. 5. Plot of  $\log A_L(l_0)$  versus  $l_0^2$  for various values of  $L$  for (111) and (222) of cold-worked 65-35 brass.

Fourier analysis, the smaller the hook. From Eq. (13) the intercept of the initial slope gives an effective mean particle size which includes the effect of true particle size and stacking faults,

$$\frac{1}{L(\text{eff.})} = \frac{1}{\bar{L}} + \frac{3\alpha \cos \phi}{2d_{111}} \quad (16)$$

For cold-worked 65-35 brass, the intercepts of Fig. 6 give average effective dimensions  $\bar{L}_{100} = 62\text{\AA}$  and  $\bar{L}_{111} = 128\text{\AA}$ . These values are not only surprisingly small but no reasonably shaped particle will give this ratio of dimensions. It is seen from Eq. (16) that the measured effective size includes a true size and a fictitious size due to stacking faults  $L_{SF} = 2d_{111}/3\alpha \cos \phi$ . From the measured value of  $\alpha$  for 65-35 we compute  $L_{SF}(100) = 63\text{\AA}$ ,  $L_{SF}(111) = 145\text{\AA}$ . For cold-worked 65-35 brass the effective particle sizes obtained from the peak breadths are due almost completely to the effect of stacking faults. Since the stacking fault contributions come from the measured peak shifts,

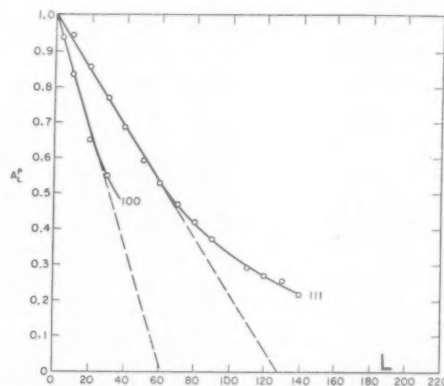


FIG. 6. Plots of  $A_L^P$  versus  $L$  for the [100] and [111] directions for cold-worked 65-35 brass. The intercepts of the initial slopes give the mean particle dimensions  $\bar{L}_{100}$  and  $\bar{L}_{111}$ .

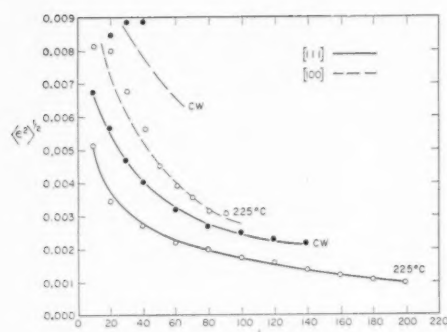


FIG. 7. Root-mean-square averaged strain components  $\langle \epsilon_L^2 \rangle^{1/2}$  as a function of the averaging distance  $L$  for the [100] and [111] directions of cold-worked 65-35 brass filings.

the surprisingly small effective sizes determined from the broadening are given an independent check.

From log plots such as Fig. 5, the slopes give mean square averaged strain components  $\langle \epsilon_L^2 \rangle$ . In terms of columns of length  $L$  normal to the reflecting planes, the components of strain along the column are first averaged over each column and the squares are then averaged over the different columns comprising the sample. The root-mean-square values for the [111] and [100] directions for cold-worked 65-35 brass are shown by Fig. 7. For the [100] direction the *rms* strains are about twice those for the [111] direction. The strain values decrease with increasing distance  $L$  over which the strain is averaged. If this is a real effect it is extremely interesting. It might be due to the strains being extremely inhomogeneous, or it might be that the strains are larger in the smaller particle sizes and as we average over larger values of  $L$  we drop out the contributions from the smaller particles.

The reciprocal stacking fault probability  $\alpha^{-1}$  obtained from the peak shifts, the root-mean-square strain components for an averaging distance  $L=50\text{A}$ , and the effective particle dimensions from the peak broadening are given in Figs. 8 and 9 for 80-20 and 70-30 brass as a function of the annealing temperatures. It is evident that all three effects anneal out in about the same way in the temperature interval.

#### IV. DISCUSSION

For the four cold worked compositions the important numerical results are brought together in Table III. The reciprocal stacking fault probabilities  $\alpha^{-1}$  were obtained from peak shifts by means of Eq. (15), that part of the particle size which is actually due to stacking faults was computed by  $\bar{L}_{SF}(111) = 2d_{111}/(3\alpha \cos \phi_{111})$ , the effective particle sizes  $\bar{L}_{100}$ ,  $\bar{L}_{111}$  were taken from the initial slopes of the  $A_L^P$  versus  $L$  curves, and the root-mean-square strains were arbitrarily taken at  $L=50\text{A}$ .

In  $\alpha$ -brass the stacking fault probability is very low

near the pure copper end, and it is only for increasing zinc content that the stacking fault probability becomes relatively large. The reason for this is not obvious. Perhaps the difference in energy between HCP and FCC packing is reduced by the addition of zinc. In  $\alpha$  Cu-Si, Barrett<sup>10</sup> has found that the stacking faults become prominent only near the high silicon end.

The root-mean-square strains in Table III are of the order of the yield stress divided by Young's modulus  $YS/E=0.005$ . This relation for cold-worked filings has been noticed by other workers, and it probably indicates that in cold-worked filings any appreciable root-mean-square stress above this limiting value relieves itself by further slip.

There is an approximate empirical relation between corresponding particle sizes and stresses. The products  $\bar{L}\langle \epsilon^2 \rangle^{1/2} = \delta$  give fairly constant values of about  $\delta=0.5\text{A}$ . These values of  $\delta$  are of the order of atomic dimensions or of the order of a half dislocation displacement  $\Delta=1.5\text{A}$ . The empirical relationship could be explained by assuming that stacking faults are produced on more than one set of (111) planes. At the intersection of two stacking fault planes there is a misfit of the order of  $\Delta=1.5\text{A}$ . If the misfit is taken up over a dimension of the order of the coherent domain size  $\bar{L}$ , the strains will be of the order  $\delta/\bar{L}$  and this could be considered as the interpretation of the relation  $\bar{L}\langle \epsilon^2 \rangle^{1/2} = \delta$ . The relation could equally well be related to an edge dislocation. In an array of edge dislocations consider the *rms* strain in a cylindrical volume enclosing each dislocation and extending half way to the next dislocation. Dislocation theory gives an expression for the root-mean-square strain in the cylindrical volume which approximates to  $\langle \epsilon^2 \rangle^{1/2} = b/R$  where  $b$  is the Burger's vector and  $R$  is the cylinder radius. If from the two relations for cold worked filings  $\langle \epsilon^2 \rangle^{1/2} = YS/E$  and  $\bar{L}\langle \epsilon^2 \rangle^{1/2} = \delta$ , we eliminate  $\langle \epsilon^2 \rangle^{1/2}$  and set  $\delta=1$ , we obtain  $YS=E/\bar{L}$ . This is very

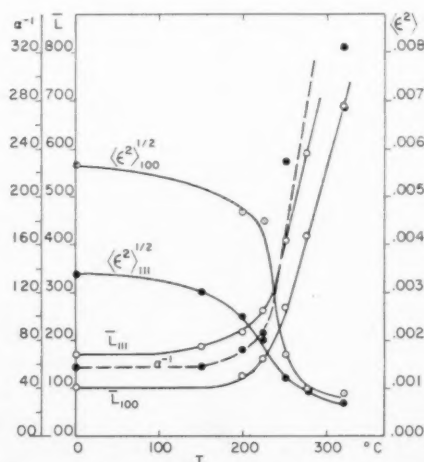


FIG. 8. Values of  $\langle \epsilon_L^2 \rangle^{1/2}$  for  $L=50\text{A}$ ,  $\alpha^{-1}$ , and  $\bar{L}(\text{eff})$  for cold-worked 80-20 brass filings given successive 1-hour anneals at the temperatures indicated.

similar to the relation obtained by W. L. Bragg<sup>11</sup> in his theory of the strength of metals.

If we approximate the strain energy in cold worked  $\alpha$  brass by  $W = \frac{3}{2}E\langle\epsilon^2\rangle$  and use  $E = 9 \times 10^{11}$  dynes/cm<sup>2</sup> and  $\langle\epsilon^2\rangle^{\frac{1}{2}} = 0.007$  from Table III for  $L = 50\text{\AA}$ , we obtain  $W = 0.2$  cal/gm. However the strain values which should be used are those for small  $L$ , and if we had sufficient faith in curves such as Fig. 7 to take values for small  $L$ , the computed strain energy would be several times larger. The energy in the stacking fault planes themselves can be given an upper limit by using some value such as 20 ergs/cm<sup>2</sup> for the twin energy in copper. For 70-30 brass filings the computed upper limit is  $W = 0.1$  cal/gm.

If we assume that  $[110]$  slip takes place on the (111) planes by a zigzag path resulting from a series of half-dislocation displacements, an even number leaves an unfaulted crystal, while an odd number leaves a stacking fault. If the probability of leaving an unfaulted crystal is at least as high as that for a stacking fault, slip must have taken place on at least twice as many planes as those showing stacking faults. Cold-worked 65-35 brass filings show stacking faults on the average every 26 (111) planes, and hence slip must have taken place on the average every 13 (111) planes.

In  $\alpha$ -brass the principal imperfections produced by cold work appear to be stacking faults, and these seem to be the primary cause of most of the X-ray effects. Other dislocation effects such as small-angle grain boundaries and bending must also be present. For stacking faults on more than one set of (111) planes, the misfit at intersecting stacking fault planes should provide the mechanism for locking in the faults. The misfit at intersecting stacking fault planes should also explain a major part of the work hardening in  $\alpha$ -brass.

TABLE III. Results for cold-worked alpha-brass.

Comp.	$\alpha^{-1}$	$\bar{L}_{SP(111)}$	$\bar{L}_{100}$	$\bar{L}_{111}$	$\langle\epsilon_{100}^2\rangle_{100}^{\frac{1}{2}}$	$\langle\epsilon_{111}^2\rangle_{111}^{\frac{1}{2}}$
65-35	26	143 A	62 A	128 A	0.0068	0.0035
70-30	40	234	89	153	0.0067	0.0036
80-20	58	333	100	170	0.0057	0.0034
90-10	200	1100	145	235	0.0033	0.0032

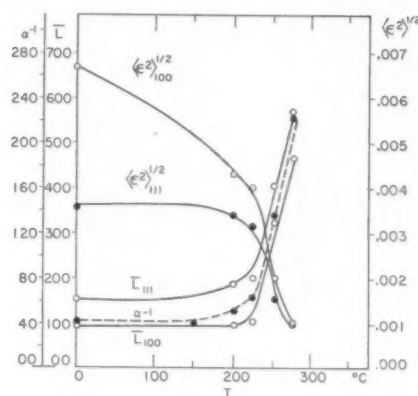


FIG. 9. Values of  $\langle\epsilon^2\rangle^{\frac{1}{2}}$  for  $L = 50\text{\AA}$ ,  $\alpha^{-1}$ , and  $\bar{L}(\text{eff})$  for cold-worked 70-30 brass filings given successive 1-hour anneals at the temperatures indicated.

It has turned out that  $\alpha$ -brass is an interesting material for the study of cold work because stacking faults play an important role and this is one type of dislocation that can be directly detected and measured experimentally.

#### ACKNOWLEDGMENT

We are indebted to Professor B. L. Averbach of the Department of Metallurgy and to Dr. F. H. Wilson of the American Brass Company for some of the samples of  $\alpha$ -brass used in this investigation.

#### REFERENCES

1. C. S. Barrett, *Imperfections in Nearly Perfect Crystals* (John Wiley, New York, 1952), Chap. III.
2. M. S. Paterson, *J. App. Phys.* **23**, 805 (1952).
3. J. Méring, *Acta Cryst.* **2**, 371 (1949).
4. M. F. Bertaut, *Comptes Rendus*, **228**, 492 (1949).
5. B. E. Warren and B. L. Averbach, *J. App. Phys.* **21**, 595 (1950).
6. B. E. Warren and B. L. Averbach, *J. App. Phys.* **23**, 497 (1952).
7. A. R. Stokes, *Proc. Phys. Soc.* **61**, 382 (1948).
8. C. S. Smith and E. E. Stickley, *Phys. Rev.* **64**, 191 (1943).
9. B. E. Warren and B. L. Averbach, *Imperfections in Nearly Perfect Crystals* (John Wiley, New York, 1952), Chap. V.
10. C. S. Barrett, *Trans. AIME J. Metals* **188**, 123 (1950).
11. W. L. Bragg, *Nature* **149**, 511 (1942); *Phys. Soc. Bristol Conf. Report* (1948), p. 26.



# THE LATTICE SPACINGS OF CLOSE-PACKED HEXAGONAL 3/2 ELECTRON COMPOUNDS\*

G. V. RAYNOR and T. B. MASSALSKI†

The lattice spacings of the close-packed hexagonal  $\zeta$ -phase (3/2 electron compound) in the system copper-gallium-germanium have been determined as a function of composition and electron:atom ratio, using alloys quenched from 550°C. The results, with subsidiary experiments on other ternary alloys, show that at a constant electron:atom ratio the axial ratio is itself almost constant. Increase in the number of electrons per atom leads to a marked decrease in axial ratio. These phenomena may be interpreted in terms of an overlap of electrons from the appropriate Brillouin Zone in directions at right angles to the hexagonal axis. Consideration of the ranges of homogeneity of the binary and ternary  $\zeta$ -phases, and comparison of the lattice-spacings along the copper-rich limit of the  $\zeta$ -phase in the ternary system studied with those of the saturated primary solid solution, suggests that the decrease in  $c/a$  required by an increase in the electron:atom ratio is opposed by solute atoms of atomic diameter larger than that of copper, so that a larger overlap is required to stabilise the structure, which is then in general of limited homogeneity range. Further implications of this concept are briefly discussed.

## PARAMÈTRES CRISTALLINS DES COMPOSÉS ÉLECTRONIQUES 3/2 DU SYSTÈME HEXAGONAL COMPACT

Les paramètres cristallins des phases hexagonales  $\zeta$  (composés 3/2) dans le système cuivre-gallium-germanium ont été déterminés en fonction de la composition et de la concentration électronique pour des alliages trempés à 550°. Les résultats complétés par des expériences sur d'autres alliages ternaires montrent que, à concentration électronique constante, le rapport  $c/a$  est lui-même presque constant. L'accroissement du nombre d'électrons par atome conduit à une nette diminution de ce rapport. Ces phénomènes peuvent être expliqués par la superposition des zones de Brillouin perpendiculairement à l'axe hexagonal. L'examen des domaines d'homogénéité des phases  $\zeta$  binaire et ternaire et la comparaison des paramètres cristallins le long de la frontière côté cuivre de la phase  $\zeta$  dans le système ternaire étudié avec ceux de la solution solide primaire saturée indiquent que la diminution de  $c/a$  résultant de l'accroissement de la concentration électronique est compensée par les atomes dissous d'un diamètre atomique supérieur à celui du cuivre, aussi une plus grande superposition des zones de Brillouin est-elle nécessaire pour stabiliser la structure qui a alors en général un domaine d'homogénéité limité. D'autres conséquences de cette conception sont brièvement discutées.

## DIE GITTERKONSTANTEN VON HEXAGONAL DICHTESTEN KUGELPACKUNGEN MIT DEM ELEKTRONENVERHÄLTNIS 3/2

Die Gitterkonstanten der  $\zeta$ -Phase mit hexagonal dichtester Kugelpackung (Elektronenverhältnis 3/2) des Systems Kupfer-Gallium-Germanium wurden in Abhängigkeit von der Zusammensetzung und dem Verhältnis Elektron:Atom an Legierungen, die von 550°C abgeschreckt worden waren, bestimmt. Die Ergebnisse zeigen zusammen mit ergänzenden Experimenten an anderen ternären Legierungen, dass für ein konstantes Verhältnis Elektron:Atom das Achsenverhältnis ebenfalls konstant ist. Ein Ansteigen der Anzahl von Elektronen pro Atom führt zu einem merklichen Abfall des Achsenverhältnisses. Diese Erscheinungen können auf Grund einer Überlappung der Elektronen der zugehörigen Brillouin Zone unter rechten Winkeln zur hexagonalen Achse erklärt werden. Eine Betrachtung der Homogenitätsbereiche der binären und der ternären  $\zeta$ -Phase, sowie ein Vergleich der Gitterkonstanten entlang der kupferreichen Phasengrenze der  $\zeta$ -Phase im untersuchten ternären System mit jenen der gesättigten festen Lösung, lässt vermuten, dass der Abfall im  $c/a$ -Verhältnis, der durch ein Ansteigen im Elektron:Atom-Verhältnis hervorgerufen wird, durch gelöste Atome mit einem grösseren Atomradius als dem des Kupfers gehemmt wird, so dass zur Stabilisierung der Struktur eine grössere Überlappung benötigt wird. Im allgemeinen hat die Struktur dann einen begrenzten Homogenitätsbereich. Weitere Folgen dieser Auffassung werden kurz diskutiert.

## INTRODUCTION

In the system copper-gallium, the face-centred cubic copper-rich primary solid solution is succeeded, with increasing solute percentage, by  $\frac{3}{2}$  electron compounds, the structures of which differ according to temperature.<sup>1</sup> The appropriate portion of the equilibrium diagram is shown in Fig. 1; the body-centred cubic  $\beta$  phase, which exists over a range of compositions, decomposes eutectoidally at 616°C into the  $\gamma$ -phase and the  $\zeta_1$ -phase. The latter is close-packed hexagonal in

structure, and is of limited homogeneity range as shown. At 475°C the  $\zeta_1$ -phase decomposes eutectoidally into  $\gamma$  and the  $\zeta_2$ -phase; the  $\zeta_2$ -phase is also close-packed hexagonal, and again exists over a narrow range of compositions, with slightly less gallium than in  $\zeta_1$ . Thus, in the composition region close to that corresponding with an electron:atom ratio of 1.5, three separate phases exist. The general dependence of the structures of the binary  $\frac{3}{2}$  electron compounds on atomic size and solute valency has been discussed by Hume-Rothery, Reynolds and Raynor,<sup>2</sup> and it is of considerable theoretical interest to extend the discussion to  $\frac{3}{2}$  electron compounds in ternary systems, in which the

\* Received March 8, 1955.

† Department of Physical Metallurgy, University of Birmingham, Birmingham, England.

atomic size and solute valency factors may be varied from those characteristic of one of the component binary systems to those characteristic of the other binary system. Several copper-rich and silver-rich ternary systems have now been examined in the authors' laboratory, and in particular the constitution of the copper-zinc-gallium alloys has recently been reported.<sup>3</sup> In this work it was found that the copper-gallium  $\zeta_1$ - and  $\zeta_2$ -phases were capable of dissolving only very small quantities of zinc. This behavior contrasts markedly with that of the close-packed hexagonal  $\zeta_2$  electron compound in the copper-germanium system, which is capable of dissolving considerable amounts of zinc.<sup>4</sup> This suggested that some essential difference existed between the copper-gallium  $\zeta_1$ - and  $\zeta_2$ -phases, which are formed in the solid state, and the copper-germanium  $\zeta$ -phase, which is stable from room temperature to the melting point and forms directly from the liquid. Accordingly an examination of equilibrium relationships in the copper-gallium-germanium system was undertaken by the present authors. This work will be reported elsewhere; for our present purpose it is sufficient to note that, at the appropriate temperatures, a close-packed hexagonal series of solid solutions exists between  $\zeta_1(\text{Cu-Ga})$  and  $\zeta(\text{Cu-Ge})$ , and between  $\zeta_2(\text{Cu-Ga})$  and  $\zeta(\text{Cu-Ge})$ . The two phases are thus essentially similar, and to gain information with regard to possible reasons for the narrow homogeneity ranges of  $\zeta_1$  and  $\zeta_2$  as compared with the wide homogeneity range of  $\zeta(\text{Cu-Ge})$ , a series of lattice spacing measurements was made in the homogeneous close-packed hexagonal area of the copper-gallium-germanium isothermal equilibrium diagram corresponding to 550°C. The results of this investigation are reported in the present paper.

#### MATERIALS AND EXPERIMENTAL METHODS

Alloys were prepared from oxygen-free, high conductivity copper supplied by Imperial Chemical Industries Ltd., spectrographically standardised gallium supplied by Messrs. Johnson Matthey & Co. Ltd., and spectrographically standardised germanium from the same source. Weighed quantities of the three metals were melted in argon in small sealed silica capsules, with vigorous shaking; the silica capsules were quenched into cold water to secure rapid chilling. Since the capsules did not in general break on quenching, the alloys could be homogenised for five days at 730° to 740°C without removal. After this treatment, ingots 1 g. in weight were found to have suffered negligible change in weight from that of the component metals; the weight losses recorded varied from 1 part in 3000 to 1 part in 5000. Since the chemical analysis of selected alloys gave compositions identical with the synthetic compositions, the latter have in general been accepted.

After homogenisation and heat-treatment for 15 days at 550°C, all alloys were examined metallographi-

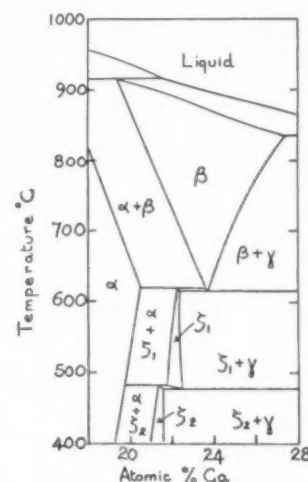


FIG. 1. Partial equilibrium diagram for the copper-gallium alloys.

cally; X-ray specimens were then prepared by filing, and the resulting powder was annealed for relief of strain at the same temperature as that from which the lump was quenched. The powder specimens were also quenched, and after sieving were made into cylinders of diameter 0.02" with the minimum quantity of gum tragacanth. Exposures to copper  $K_\alpha$  radiation were made in a 9 cm camera of the Van Arkel type. High-quality films were obtained, and measured on a Cambridge Universal Measuring Machine. Observed lattice spacings were extrapolated, using the Nelson-Riley function, and the results are recorded in  $A$  units at 18°C. For several selected alloys, the axial ratios were accurately established by the statistical method of Archard.<sup>9</sup> These calculations gave results in excellent agreement with the simpler method of adjusting the axial ratio to give linear Nelson-Riley extrapolations, which was used in the remaining cases.

The constants assumed in the calculations for copper radiation were:

$$\lambda_{\alpha 1}/2 = .7702503 \text{ \AA},$$

$$\lambda_{\alpha 2}/2 = .7721726 \text{ \AA}.$$

#### EXPERIMENTAL RESULTS

In Fig. 2, the area of the equilibrium isothermal section at 550°C which is occupied by the close-packed hexagonal  $\frac{2}{3}$  electron compound is shown; this represents a complete series of solid solutions between  $\zeta_1(\text{Cu-Ga})$  and  $\zeta(\text{Cu-Ge})$ . The points plotted in the homogeneous area represent the compositions of 18 alloys, the lattice spacings of which were measured at room temperature after quenching from 550°C. The compositions were arranged to lie either on lines of constant electron:atom ratio (1.45 and 1.50) or on lines of constant gallium content (5.0 and 14.0 atomic per cent). In addition one alloy lies just within the  $(\alpha + \zeta)$  area, but is so close to the boundary that the lattice spacings corresponding

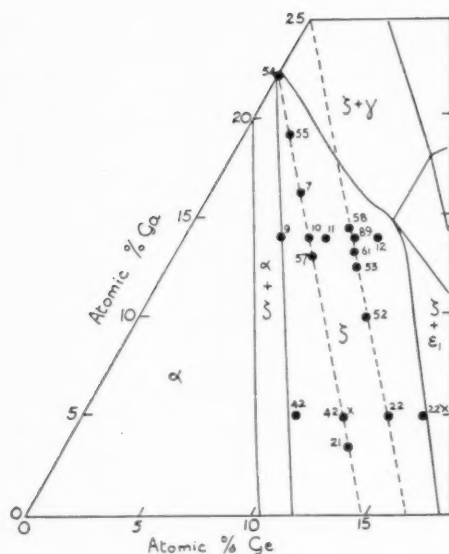


Fig. 2. Compositions of  $\zeta$ -phase alloys studied in copper-gallium-germanium system.

to the diffraction pattern of the hexagonal phase are taken to correspond with those of the most copper-rich alloy along the 14.0 atomic per cent gallium line.

The lattice spacing results may most conveniently be presented in the form of the following diagrams:

Fig. 3: variation of spacings with composition at electron:atom ratio 1.45.

Fig. 4: variation of spacings with composition at electron:atom ratio 1.50.

Fig. 5: variation of spacings with electron:atom ratio at 5 at.% gallium.

Fig. 6: variation of spacings with electron:atom ratio at 14 at.% gallium.

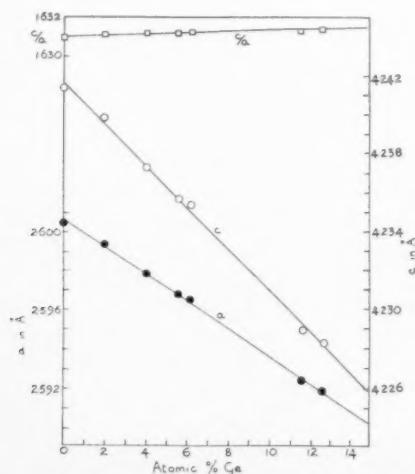


Fig. 3. Variation of spacings with composition at electron:atom ratio 1.45.

The most striking feature of these diagrams is that, although the "c" and "a" lattice spacings decrease considerably on passing from the copper-gallium to the copper-germanium axis of the ternary field at constant electron:atom ratio, the axial ratio "c/a" varies very little with composition at a given electron concentration. When, however, the gallium content is kept constant so that the germanium content and hence the electron:atom ratio varies, the axial ratio "c/a" decreases sharply as the electron:atom ratio rises. This is accomplished partly by a fall in the "c" spacing, but predominantly by a marked increase in the "a" spacing with increasing germanium content. This is shown most strikingly in Fig. 5.

The axial ratio of  $\zeta_1$ (Cu-Ga) at the composition 22.20 atomic per cent of gallium is 1.6310, so that the structure is very nearly ideally close-packed. The lattice spacings of  $\zeta_2$ (Cu-Ga) were also measured, using an alloy of composition 21.50 atomic per cent of gallium quenched from 450°C. For this alloy,  $a = 2.5980$  Å,  $c = 4.2425$  Å, and  $c/a = 1.6330$ . This structure is thus ideally close-packed, and continues the trend observed in the ternary alloys for the axial ratio to increase with decreasing electron:atom ratio.

For comparison with the results described above, it is of interest to know how the axial ratio varies in other ternary systems where the close-packed hexagonal phase based on  $\zeta$ (Cu-Ge) is of wide homogeneity range. Accordingly two additional alloys, one in each of the systems copper-aluminium-germanium and copper-zinc-germanium, were examined; their compositions were calculated to fall close to the aluminium- or zinc-rich limits of the homogeneity range, at an electron:atom ratio of 1.5, and the specimens were quenched from 550°C. The measured spacings were as follows:

System	Composition, At. %				Lattice Spacings Å.		Axial ratio c/a
	Cu	Zn	Al	Ge	a	c	
Cu-Zn-Ge	69.5	20.9	—	9.6	2.6161	4.2522	1.6254
Cu-Al-Ge	77.5	—	17.5	5.0	2.6022	4.2335	1.6269

These figures show that the axial ratios at 1.5 electrons per atom are closely similar to those recorded for the system copper-gallium-germanium, in spite of the fact that, for this electron concentration, the variations of "a" and "c" with composition are different. Thus, when zinc replaces germanium so as to maintain an electron:atom ratio of 1.5, the "c" spacing increases much more rapidly than for the substitution of aluminium or gallium, for which cases the effects are similar. The variation of the "a" spacing on substituting zinc for germanium, again at 1.5 electrons per atom, is also greater than in the other two cases; c/a however is closely similar in all three systems.

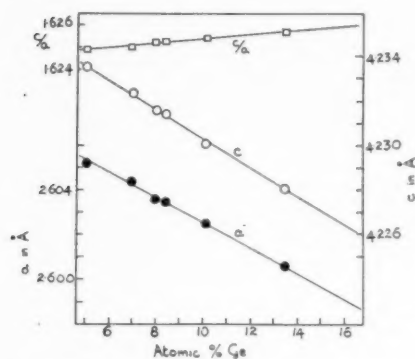


FIG. 4. Variation of spacings with composition at electron:atom ratio 1.50.

### DISCUSSION

The connection between the axial ratio of the close-packed hexagonal structure and the electron-atom ratio, where this falls between 1 and 2, has been discussed in detail by Goodenough;<sup>5</sup> according to these considerations, as the electron:atom ratio is increased, and the Fermi surface within the first Brillouin Zone approaches the bounding planes of the zone, a force of attraction between the Fermi surface and the bounding planes is set up, such that the energy of the structure is lowered by displacement of the appropriate bounding planes towards the origin of  $k$ -space. If the zone walls are not all the same distance from the origin of  $k$ -space, then contraction of the zone in some directions may occur

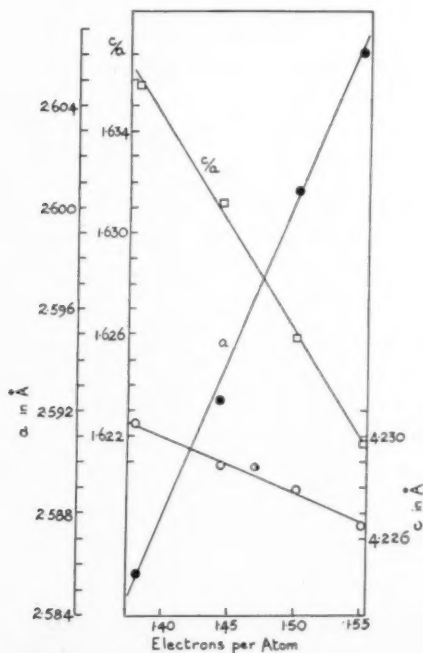


FIG. 5. Variation of spacings with electron:atom ratio at 5 atomic per cent gallium.

before other directions are affected, leading to a change in shape of the Brillouin Zone, and hence a change in the axial ratio of the crystal structure.

Referring to the close-packed hexagonal structure, it is postulated that the axial ratio would assume the ideal value of 1.633 for electron:atom ratios such that the Fermi sphere occupied a relatively small volume within the zone, which is illustrated in Fig. 7. According to Goodenough, and assuming a spherical Fermi surface, the A faces are touched at 1.14 electrons per atom; contact with the B and C faces occurs at 1.36 and 1.67 electrons per atom, while, subject to certain assumptions, overlap across the A faces is expected at approxi-

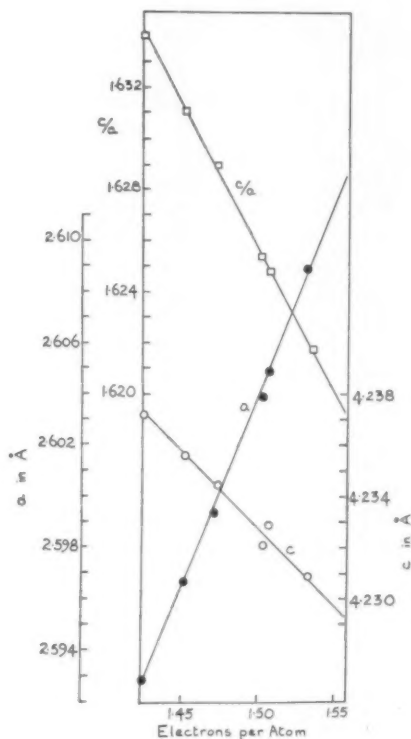


FIG. 6. Variation of spacings with electron:atom ratio at 14 atomic per cent gallium.

mately 1.45 electrons per atom. As the Fermi surface approaches the A faces, movement of these faces inwards leads to an expansion of the "a" spacings in the lattice, while the "c" spacings are relatively unaffected, so that  $c/a$  falls. As the B faces are approached, the "c" spacings in the lattice begin to expand, so that the tendency towards decreasing  $c/a$  is checked, and may be reversed. Before the C faces are touched, overlap across the A faces is initiated, leading to an expansion of the "a" spacings in the lattice and a decrease in  $c/a$  as in the overlap theory of Jones.<sup>6</sup> Goodenough's theory may be summarised in the form of Fig. 8, which shows the expected variation of  $c/a$  in an initially ideally close-packed hexagonal structure with increase of



electron:atom ratio. There is an approximately linear decrease in axial ratio above about 1.4 electrons per atom; for electron:atom ratios of 1.3 to 1.4 Fig. 8 indicates an axial ratio  $>1.633$ , but this depends to some extent on the assumptions made.

The lattice spacings reported in this paper are in good qualitative agreement with Fig. 8. Thus the structure of alloy 42, with the lowest electron:atom ratio studied (1.38), corresponds with an axial ratio of 1.6356. As the electron:atom ratio increases,  $c/a$  decreases linearly (Fig. 5). The point of lowest electron:atom ratio in the  $\zeta$  field corresponds with the copper-rich limit of the  $\zeta$ (Cu-Ge) phase, and the work of Schubert and Brandauer<sup>7</sup> shows that at this electron:atom ratio (1.36) the axial ratio has risen to 1.638, which is in good agreement with the value derived from the present work by extrapolation of the linear graphs of Figs. 3 and 4 to the copper-germanium axis, and assuming that the variation of  $c/a$  in the binary system with composition is again linear. The present results show, therefore, that in the close-packed hexagonal  $\zeta$ -phase of the system copper-gallium-germanium, the variation of  $c/a$  with electron:atom ratio is essentially linear from  $e/a=1.36$  upwards. This value is somewhat lower than that at which the approximately linear  $c/a$  decrease of Fig. 8 begins, and this, taken together with the fact that the decrease in  $c/a$  is attained mainly by marked expansion of the "a" spacing, strongly suggests that overlap of electrons across the A faces of the Brillouin Zone has already occurred at 1.36 electrons per atom. The axial ratio changes are then controlled essentially by variation in the magnitude of this overlap.

Detailed examination of the present results reveals other features of interest. Thus the wide range of homogeneity for  $\zeta$ (Cu-Ge) contrasts strongly with the limited range for  $\zeta_1$ (Cu-Ga). In the former,  $c/a$  may assume the high value of 1.638, while the axial ratio of  $\zeta_1$ (Cu-Ga) is 1.631. As germanium is replaced by gallium, the maximum axial ratio corresponding to the copper-rich limit of the  $\zeta$ -phase progressively falls. In this connection it is of interest to examine the size-factor relationships across the ternary field. The size-

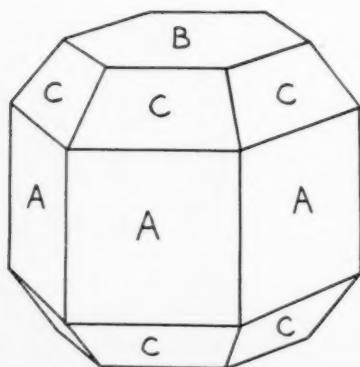


Fig. 7. Brillouin Zone for close-packed hexagonal structure.

factor of germanium with respect to copper is  $-4.15$ . The corresponding size-factor for the complicated gallium structure is, however, difficult to assess. It is generally recognised that the size-factor assessed from the closest distance of approach of atoms in the gallium structure does not enable the alloys of copper, silver and gold with gallium to be adequately correlated with other copper, silver and gold alloys. There is evidence<sup>2</sup> that the effective atomic diameter of gallium in solid solution in copper or silver is larger than this closest distance of approach, while an analysis of lattice-spacing relationships for copper-rich alloys suggests that a value of 2.64 for the effective atomic diameter is appropriate.<sup>8</sup> This corresponds with a size factor of  $+1.7$ .

The axial ratio of the copper-rich limit of the  $\zeta$ -phase thus decreases as the effective size-factor in the ternary system increases. Where the atom of the solute metal is smaller than that of copper, high axial ratios are permitted, but for an effectively larger atom the axial

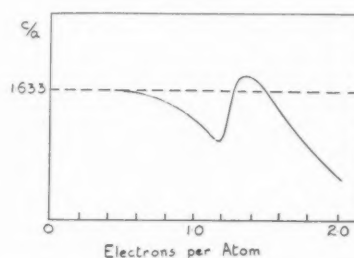


Fig. 8. Variation of axial ratio of close-packed hexagonal structure with electron:atom ratio as suggested by Goodenough.<sup>6</sup>

ratios decrease. The effect of size-factor is illustrated more strikingly at the solute-rich boundary of the  $\zeta$ -phase. As shown in Fig. 2, this boundary occurs at an almost constant electron:atom ratio from the copper-germanium axis to a composition corresponding to approximately 14 atomic per cent gallium, where the effective size factor is very small since the effect of the small germanium atoms present is compensated by the larger gallium atoms. As the gallium content rises further, so that the effective size factor becomes increasingly positive, the solute-rich boundary of the  $\zeta$ -phase moves progressively to smaller electron:atom ratios. It may thus be suggested that the stability of the  $\zeta$ -structure is strongly dependent upon the combined effects of electron:atom ratio and size-factor. The effect of increasing the electron concentration is to decrease the axial ratio; the atomic characteristics of the solute atom may be such as to allow or oppose this decrease. Considering the tetrahedron of atoms formed by three neighbouring basal plane atoms,  $a$ ,  $b$  and  $c$  and the atom  $d$ , in the parallel plane above, which lies above the centre of the triangle formed by them, it will clearly be easier to allow contraction of  $c/a$  if atom  $d$  is replaced by a smaller atom than if it is replaced by a larger one,

especially if short range order exists. In the  $\zeta$ (Cu-Ge) phase, the decrease of  $c/a$  imposed by increasing electron:atom ratio (i.e., increasing overlap across the A planes of the Brillouin Zone) is permitted by the relatively small atomic and ionic diameter of germanium, and a wide homogeneity range results. For the case of the  $\zeta_1$ (Cu-Ge) phase, however, the decrease of  $c/a$  is opposed by the effect of the larger solute atom, the strain energy required to force the structure to assume a lower axial ratio being greater than the lowering of electronic energy due to the displacement of the Brillouin Zone faces. It is for this reason that in binary alloys of silver, copper and gold, close-packed hexagonal  $\frac{3}{2}$  electron compounds of wide homogeneity range are confined to cases where the size-factor is nearly zero or negative.

The form of the copper-rich  $\zeta$ -phase boundary of Fig. 2 may be interpreted on the basis that an increase in the effective size-factor (replacement of germanium by gallium) increases the strain energy necessary to decrease the axial ratio, so that a larger overlap (i.e., a higher electron:atom ratio) is required to overcome this and stabilise the structure. Once the balance has been achieved, however, and the  $\zeta$ -phase is formed, further increase in the electron concentration must be accompanied by decrease in  $c/a$ . The copper-gallium  $\zeta_1$  and  $\zeta_2$  phases represent critical cases. At 1.43 electrons per atom,  $\zeta_2$  is ideally close-packed; slight increase in the electron:atom ratio would require it to decrease its axial ratio, but the additional gallium atoms appear to prevent this, and the phase becomes unstable. At higher temperatures, where lattice strains are accommodated more easily, the  $\zeta_1$  phase is stable, with  $c/a$  decreased to correspond with that required by an electron concentration of 1.445. The phase is again, however, unable to decrease its axial ratio with further gallium additions.

The wide homogeneity range of  $\zeta$ (Cu-Ge) indicates that where the solute atom is small, the decrease of axial ratio required by electron energy considerations is permitted. As shown in Fig. 2, the homogeneity range in the ternary system with gallium remains approximately constant until the effective size factor becomes positive; from this stage onwards, it may be considered that decrease in  $c/a$  is opposed more and more strongly by the solute atoms, leading to instability before the minimum  $c/a$  attainable as a result of the electronic factor can be attained.

During the course of the work, the lattice spacings were measured for four face-centered cubic  $\alpha$  copper-gallium-germanium alloys, the compositions of which lay very close to the  $\alpha/(\alpha+\zeta)$ -phase boundary. These lattice spacings have been plotted in Fig. 9 against the ratio of germanium to gallium atoms in the structure. Also shown are the "a" spacings along the copper-rich boundary of the  $\zeta$ -phase, which is almost parallel to the  $\alpha/(\alpha+\zeta)$  boundary in the phase diagram. These

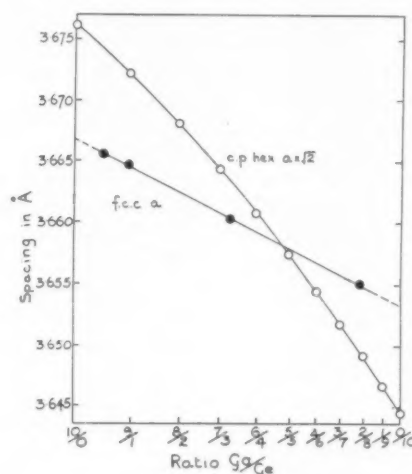


Fig. 9. Comparison of lattice spacings of nearly saturated  $\alpha$  solid solution with a  $\sqrt{2}$  for close-packed hexagonal  $\zeta$ -structure.

have been derived by linear extrapolation of the results of Figs. 3, 4, 5 and 6 to the compositions of the known  $(\alpha+\zeta)/\zeta$ -phase boundary corresponding to various germanium:gallium ratios, and are plotted in Figure 9 multiplied by  $\sqrt{2}$  for direct comparison with the cubic lattice spacings. It is significant that, on the copper-germanium side of the diagram, atoms approach more closely in the basal plane of the hexagonal structure than they do in the cubic structure; at the copper-gallium side, the reverse is true. This comparison supports the view that a larger overlap across the A faces of the Brillouin Zone for the hexagonal structure is required to stabilise this structure for a positive size-factor than for a negative size-factor. Thus for the copper-gallium alloys, the necessary degree of electronic overlap causes expanded "a" spacings for the hexagonal structure. For the copper-germanium alloys, the structure can exist with a smaller overlap; the "a" spacings are thus less expanded, and in fact the interatomic distances in the basal plane are slightly less than those required by electrons entering a nearly full face-centered cubic Brillouin Zone.

#### CONCLUSIONS

The experimental results presented and discussed above show that the axial ratios of the close-packed hexagonal  $\zeta$ -phases in binary and ternary alloys are chiefly determined by the electron:atom ratio. The predominant effect of raising the electron:atom ratio is to increase the "a" spacing, and the results suggest strongly that this is due to the existence of an overlap of electrons over the A faces (parallel to the hexagonal axis) of the appropriate Brillouin Zone. From the form of the homogeneous  $\zeta$ -area in the copper-gallium-germanium phase diagram, and from comparison of lattice spacings in the  $\zeta$ -phase and in the copper-rich face-centered cubic solid solution, it is suggested that the decrease in axial ratio required by an increase in

the electron:atom ratio may take place easily if the solute atom is smaller than that of the solvent, but that if the solute atom is the larger, the required axial ratio decrease is opposed by the rising solute concentration. The stability and range of homogeneity of binary and ternary  $\zeta$ -phases thus depend upon the balance of electronic and atomic size factors, and the present work interprets satisfactorily the previous observations<sup>2</sup> that in binary copper, silver and gold alloys the  $\zeta$ -phases are confined to cases where the size-factor of the solute with respect to the solvent has a very small positive value, or a negative value, and that the  $\zeta$ -phases of wide homogeneity range are in general those corresponding with a negative size-factor.

It now appears probable that the fundamental structure for the  $\frac{3}{2}$  electron compounds is the close-packed hexagonal structure, which will tend to be formed wherever conditions permit. If, however, the decrease in  $c/a$  required by increasing electron:atom ratio is opposed by atomic factors (e.g., too large a positive size-factor), the lattice strain involved in the attempt to adjust the axial ratio to that required by the electron:atom ratio outweighs the lowering of electronic energy, and the phase becomes unstable with regard to alternative phases whose crystal structures

are such that no relative variation of crystallographic axes is possible (e.g., face-centered cubic, body-centered cubic, or  $\gamma$ -brass structures).

#### ACKNOWLEDGMENTS

This work forms part of a general survey of ternary equilibrium diagrams based on copper or silver as solvents, and grateful acknowledgment for financial assistance is made to the Department of Scientific and Industrial Research, the Royal Society, the Chemical Society, and Imperial Chemical Industries, Ltd. One of us (T. B. M.) thanks the University of Birmingham for appointment to a Special Metallurgy Scholarship.

#### REFERENCES

1. W. Hume-Rothery and G. V. Raynor, *J. Inst. Metals* **61**, 205 (1937).
2. W. Hume-Rothery, P. W. Reynolds, and G. V. Raynor, *J. Inst. Metals* **66**, 191 (1940).
3. T. B. Massalski and G. V. Raynor, *J. Inst. Metals* **82**, 539 (1954).
4. P. Greenfield and G. V. Raynor, *J. Inst. Metals* **80**, 375 (1952).
5. J. Goodenough, *Phys. Rev.* **89**, 282 (1953). Ph.D. Dissertation, Dept. of Physics, Univ. of Chicago, 1952.
6. H. Jones, *Proc. Roy. Soc.* **A147**, 400 (1934).
7. K. Schubert and G. Brandauer, *Z. Metallk.* **262** (1952).
8. G. V. Raynor, *Trans. Faraday Soc.* **45**, 698 (1949).
9. G. O. Archard, *Acta Cryst.* **6**, 813 (1953).

# THE ELASTIC INTERACTION OF POINT DEFECTS\*

J. D. ESHELBY†

In an isotropic material it is known that two point defects regarded as centres of dilatation interact with one another only indirectly through the modification of their elastic fields by the surface of the body. In a cubic material there is an additional direct interaction energy equal to the product of the inverse cube of their separation and a function of direction whose average over all angles is zero. This function is evaluated approximately. If in a more refined elastic model we replace each defect by a centre of dilatation plus a small region where the elastic constants differ from those of the matrix there is an additional interaction proportional to the inverse sixth power of the distance between them.

## INTERACTION ÉLASTIQUE DES DÉFAUTS PONCTUELS

Dans un milieu isotrope, il est connu que deux défauts ponctuels, considérés comme des centres de dilatation, ne présentent d'interaction qu'indirectement par la modification de leurs champs élastiques par la surface du corps. Dans un métal cubique, il y a directement une énergie d'interaction complémentaire égale au produit de l'inverse du cube de leur distance et d'une fonction de la direction dont la valeur moyenne est nulle; cette fonction a été estimée. Si dans un modèle plus précis, nous remplaçons chaque défaut par un centre de dilatations plus un petit domaine où les constantes élastiques sont différentes de celles de la matrice, on obtient alors une interaction complémentaire proportionnelle à l'inverse de la sixième puissance de la distance de ces défauts.

## DIE ELASTISCHE WECHSELWIRKUNG VON PUNKTFÖRMIGEN FEHLSTELLEN

Es ist bekannt, dass in einem isotropen Material zwei punktförmige Fehlstellen, die schematisch als Dilatationskernen betrachtet werden, nur indirekt über die Veränderung ihrer elastischen Felder an der Oberfläche des Körpers eine Wechselwirkung aufeinander ausüben. In einem kubischen Material besteht eine zusätzliche direkte Wechselwirkung, die dem reziproken Wert der dritten Potenz ihres Abstandes entspricht und eine Funktion der Richtung, dessen Winkelmittelwert verschwindet. Diese Funktion wird angenähert bestimmt. Wenn wir in einem verfeinerten elastischen Modell jeden Fehlstelle durch ein Dilatationskern plus einer kleinen Region, in der die elastischen Konstanten von der des umgebenden Materials verschieden sind, ersetzen, besteht eine zusätzliche Wechselwirkung, die dem reziproken Wert der sechsten Potenz des Abstandes zwischen ihnen proportional ist.

### 1. INTRODUCTION

The idea of a purely elastic interaction between dislocations and point defects (interstitial and substitutional atoms, lattice vacancies) has proved very useful. Also, when other effects have been allowed for or are negligible, good results can be obtained from an elastic treatment of the interaction of one point defect with another. In the present paper we summarize the known results for the interaction between point defects when they are idealized as centres of dilatation in an isotropic elastic continuum and extend them to the case of cubic anisotropy. For the isotropic case alone we consider the additional interaction when the defects are represented as a superposition of a centre of dilatation and a small region whose elastic constants differ from those of the matrix.

### 2. THE ISOTROPIC CASE

The displacement around a centre of dilatation of strength  $c$  is<sup>1</sup>

$$\mathbf{u} = \mathbf{u}^\infty + \mathbf{u}^I, \quad (1)$$

where

$$\mathbf{u}^\infty = c\mathbf{r}/r^3$$

and  $\mathbf{u}^I$  is the image displacement necessary to satisfy the boundary conditions. In a body with a free surface and Poisson's ratio  $\sigma$  the centre produces a change of volume

$$\Delta V = 4\pi\gamma c, \quad \text{with } \gamma = 3(1-\sigma)/(1+\sigma)$$

made up of a contribution  $4\pi c$  from  $\mathbf{u}^\infty$ , representing a simple radial pushing out of the surface without any dilatation of the medium, and a contribution  $4\pi(\gamma-1)c$  from  $\mathbf{u}^I$  which does involve dilatation.

If external forces or a state of internal stress produce a hydrostatic pressure  $p$  at a centre of dilatation there is an interaction energy

$$E_{\text{int}} = \Delta V p \quad (2)$$

independent of the shear stress<sup>2,3,4</sup> (Cottrell's original expression corresponds to using  $\Delta V^\infty$  instead of  $\Delta V$ ). If we neglect image terms, two centres of dilatation do not interact<sup>5</sup> since each produces a pure shear stress. The indirect interaction via the image terms cannot be calculated in general, but for a large number of defects scattered uniformly through the medium the image terms add up to give practically a uniform dilatation. Thus the interaction energy of one defect with all the others is

$$E_{\text{int}} = K \Delta V \Delta V^I C / \Omega, \quad (2')$$

\* Received March 17, 1955.

† Department of Physical Metallurgy, University of Birmingham, Birmingham, England.



where  $C$  is the atomic concentration of defects,  $\Omega$  the volume per atom,  $K$  the bulk modulus. Combining this with the "self-energy" required to insert each defect in a perfect lattice Friedel<sup>6</sup> has given a good account of the heat and entropy of formation of AuNi alloys.

A familiar elastic model of a point defect is an elastic sphere forced into a hole too small for it. If sphere and matrix have the same elastic constants the results above still hold even if the sphere is not infinitesimal, provided it does not overlap another or intersect the surface of the body. However if its elastic constants ( $\lambda', \mu'$ ) differ from those of the matrix ( $\lambda, \mu$ ) there is an additional interaction with a stress-field. This can be treated separately from the misfit effect, and so we consider a perfectly-fitting inclusion. If surface forces produce a strain  $e_{ij}$  in the homogeneous body, the increase of its elastic energy when the inhomogeneous sphere is introduced is given<sup>4</sup> by the volume-integral

$$\Delta E = \frac{1}{2} \int \{ (\lambda - \lambda') e e' + 2(\mu - \mu') e_{ij} e_{ij}' \} dv \quad (3)$$

taken over the inclusion;  $e_{ij}'$  is the strain in the inclusion. (Repeated suffixes are supposed to be summed over the values 1, 2, 3.  $e = e_{ii}$  is the dilatation.) The interaction energy is

$$E_{\text{int}} = -\Delta E$$

and this is also the interaction energy when  $e_{ij}$  is due to some system of internal stress instead of to surface forces.

We may find the relation between  $e_{ij}'$  and  $e_{ij}$  as follows. If a spherical cavity perturbs a uniform shear  $e_{12}^0$  the surface of the cavity deforms as if it were the surface of a solid sphere which had undergone a shear  $\alpha e_{12}^0$ , where<sup>7</sup>

$$\alpha = (15K + 20\mu) / (9K + 8\mu).$$

If we superimpose an additional shear  $e_{12}^x$  everywhere the shear at infinity is  $e_{12} = e_{12}^0 + e_{12}^x$ . In the hole it is  $e_{12}' = \alpha e_{12}^0 + e_{12}^x$ , but the surface tractions at its surface are equivalent to those on a sphere with uniform shear stress  $\mu e_{12}^x$ . This surface traction can evidently be provided by inserting a sphere with shear modulus  $\mu'$  such that  $\mu' e_{12}' = \mu e_{12}^x$ . A little algebra gives

$$e_{12}' = \mu \alpha e_{12} / (\mu - \mu' + \alpha \mu').$$

In just the same way, starting from the fact that a spherical hole perturbing a uniform dilatation  $e$  undergoes a fractional volume change  $\beta e$  where

$$\beta = (3K + 4\mu) / 4\mu$$

we find

$$e' = K \alpha e / (K - K' + \beta K')$$

for a spherical inclusion of bulk modulus  $K'$  perturbing a uniform hydrostatic pressure. It follows by superposition that  $e_{ij}'$  is uniform in the inclusion and is an

isotropic linear function of the  $e_{ij}$ , say

$$e_{ij}' = A e \delta_{ij} + 2B e_{ij},$$

where  $A$  and  $B$  can be determined from the two special cases. Equation (3) will evidently give

$$\Delta E = \frac{1}{2} \Omega \{ \Lambda e^2 + 2M e_{ij} e_{ij} \},$$

where  $\Lambda$  and  $M$  are functions of  $\lambda, \lambda', \mu, \mu'$  and  $\Omega$  is the volume per atom. The actual expressions for  $\Lambda$  and  $M$  are rather clumsy and not very significant. It is more reasonable to relate them to a macroscopic quantity, the change of an elastic constant with number of defects, just as the strength  $c$  could be related to the macroscopic change of lattice parameter. A reasonably dilute solution of  $n$  defects per unit volume will add an amount  $n \Delta E$  to the normal energy density  $\frac{1}{2} \lambda e^2 + \mu e_{ij} e_{ij}$ , so that the apparent elastic constants will be

$$\lambda_{\text{app}} = \lambda + C \Lambda, \quad \mu_{\text{app}} = \mu + C M$$

if  $C$  is the atomic concentration of defects. For a point defect of strength  $c$  we have  $e_{ij} e_{ij} = 6c^2/r^6$  and so the interaction energy between two defects distant  $r$  apart and producing volume-changes  $\Delta V_1, \Delta V_2$  is

$$E_{\text{int}} = 6\Omega (M_1 \Delta V_2^2 + M_2 \Delta V_1^2). \quad (4)$$

For a pair of interstitials in copper Tucker and Sampson<sup>8</sup> suggest that  $\Delta V \sim 3\Omega$  and Dienes' work<sup>9</sup> gives  $M/\mu \sim 7$ . This gives

$$E_{\text{int}} \sim 10 (a_0/r)^6 \text{ eV}, \quad (5)$$

where  $a_0$  is the lattice parameter. This may well be an over-estimate, but suggests that the interaction may not be negligible in regions where  $r$  is large enough for the elastic theory to be applicable. For a vacancy  $|\Delta V|$  may, perhaps, be about  $\frac{1}{3}$  of  $\Delta V$  for an interstitial, and if  $|M|$  is also smaller than it is for an interstitial this would give a (presumably attractive) interaction energy of a hundredth or a thousandth of (5) or, say, of the order of  $kT(a_0/r)^6$  at room temperature. Stripp and Kirkwood<sup>10</sup> have found a contribution  $0.1kT(a_0/r)^6$  to the free energy from a pair of vacancies, arising from their influence on lattice vibrations. Except at very high temperatures the term (4) may be more important.

Equation (4) implies that two defects with positive  $M_1, M_2$  ("hard spots") will repel each other, the opposite of Crussard's<sup>11</sup> conclusion.

### 3. THE CUBIC CASE

The elastic field (1) may be considered as a solution of the elastic equation when the body forces reduce to three equal crossed "double forces without moment."<sup>7</sup> Formally, the force density is

$$\mathbf{f} = -G \text{grad} \delta(\mathbf{r}). \quad (6)$$

$G$  may be related to  $\Delta V$  by the expression

$$\left\{ \int \mathbf{T} \cdot \mathbf{r} dS + \int \mathbf{f} \cdot \mathbf{r} dv \right\} / 3K$$

for the volume change produced by surface tractions  $\mathbf{T}$  and body forces  $\mathbf{f}$ . In the present case  $\mathbf{T}=0$  (free surface) and

$$\Delta V = -\frac{G}{3K} \int x_i \frac{\partial}{\partial x_i} \delta(\mathbf{r}) dv = -\frac{G}{K}. \quad (7)$$

(Equation (2) of reference 1 is thus incorrect.)

We may likewise take the elastic field of a center of dilatation in a cubic material to be a solution of the appropriate equations with the body-force<sup>(6)</sup>. This leads to the following form for the dilatation:

$$e = D\delta(\mathbf{r}) + F(\mathbf{l})/r^2 + \text{div} \mathbf{u}^T, \quad (8)$$

where  $\mathbf{l} = \mathbf{r}/r$  and

$$\int_{4\pi} F(\mathbf{l}) d\omega = 0. \quad (9)$$

This follows from a previous discussion<sup>4</sup> of the displacement due to a point force. An explicit expression for  $F(\mathbf{l})$  in finite terms is impossible. The volume change is still given by (7) but its splitting into  $\Delta V^\infty$  and  $\Delta V^T$  is more complicated. Evidently the first term in (8) contributes an amount  $D$  to  $\Delta V^\infty$ . The contribution from the second term is zero if the surface of the material is a sphere centred on the imperfection, but is no longer so if, for example, the sphere is indented throughout a region over which  $F(\mathbf{l})$  does not change sign. The contribution is proportional to

$$\lim_{\epsilon \rightarrow 0} \int d\omega \int_0^{r(1)} F(\mathbf{l}) \frac{dr}{r} = \int d\omega F(\mathbf{l}) \log r \quad (10)$$

if the polar diagram of the surface about the defect is  $r=r(\mathbf{l})$ . If a line is drawn through any interior point  $P$  of an ellipsoid meeting its surface in  $A$  and  $B$  then  $AP \cdot PB$  depends only on  $P$  and not on the direction of the line. Thus (10), which can be written

$$\frac{1}{2} \int d\omega F(\mathbf{l}) \log \{r(\mathbf{l})r(-\mathbf{l})\}$$

vanishes in view of (9) for a point defect anywhere within an ellipsoid. Nevertheless, the  $F$ -term can make no contribution to the total volume change produced by a "uniform random" distribution of a large number of defects in a body of any shape. For, by an argument due to Zener<sup>12</sup> or by a generalization of the analytical argument given for the isotropic case<sup>1</sup> it follows that macroscopically there is a uniform shape-independent dilatation. A contribution from the  $F$ -terms would be shape-dependent, and since it vanishes for the ellipsoid it must do so always. It ought to be possible to show directly that (10) vanishes when averaged over all possible positions of the defect.

Equation (2) is still true in the cubic case. For<sup>4</sup> the interaction of a singularity  $S$  with an elastic field  $T$  is

given by the integral

$$\int (p_{ij}^S u_i^T - p_{ij}^T u_i^S) dS_j$$

over a surface enclosing the singularity. If  $S$  can be considered to be due to a density of body-force  $\mathbf{f}^S$  then  $\partial p_{ij}/\partial x_j = -f_i^S$  and the integral becomes

$$-\int f_i^S u_i^T dv,$$

or, in our case,

$$G \int \mathbf{u}^T \cdot \text{grad} \delta(\mathbf{r}) dv = -G \int \delta(\mathbf{r}) \text{div} \mathbf{u}^T dv$$

which in view of (7) is just  $\Delta V$  times the value of  $p$  due to  $T$  at the singularity.

We now try to get an estimate of  $D$  and  $F(\mathbf{l})$ . We have to solve

$$c_{44} \nabla^2 u_1 + (c_{12} + c_{44}) \frac{\partial e}{\partial x_1} + d \frac{\partial^2 u_1}{\partial x_1^2} = G \frac{\partial}{\partial x_1} \delta(\mathbf{r}) \quad (11)$$

and two similar equations, with

$$d = c_{11} - c_{12} - 2c_{44}.$$

By taking the divergence we have

$$(c_{12} + 2c_{44}) \nabla^2 e + d \Sigma_i \frac{\partial^2 u_i}{\partial x_i^2} = G \nabla^2 \delta(\mathbf{r}). \quad (12)$$

Following Leibfried<sup>13</sup> we put  $c_{ij} = c_{ij}^0 + c_{ij}'$  where the  $c_{ij}^0$  are effective isotropic constants found by averaging the  $c_{ij}$  over all orientations; explicitly

$$5c_{11}^0 = 3c_{11} + 2c_{12} + 4c_{44}$$

$$5c_{12}^0 = c_{11} + 4c_{12} - 2c_{44}$$

$$5c_{44}^0 = c_{11} - c_{12} + 3c_{44}.$$

If we write  $\mathbf{u} = \mathbf{u}^0 + \mathbf{u}' + \dots$  and regard the quantities with affixed  $^0$  and  $'$  as of the zeroth and first order we may solve (11) by successive approximation. The zeroth order gives the usual isotropic solution

$$(c_{12}^0 + 2c_{44}^0) e^0 = G \delta(\mathbf{r})$$

$$-4\pi (c_{12}^0 + 2c_{44}^0) \mathbf{u}^0 = G \text{grad}(1/r).$$

Then (12) gives for  $e'$

$$\nabla^2 \left\{ (c_{12}^0 + 2c_{44}^0) e' + (c_{12}' + 2c_{44}') e^0 - \frac{Gd}{8\pi (c_{12}^0 + 2c_{44}^0)} \Pi r \right\} = 0,$$

noting that  $\nabla^2 r = 2/r$  and writing

$$\Pi \equiv \Sigma_i \partial^4 / \partial x_i^4.$$

A solution is evidently given by deleting the  $\nabla^2$ . We must be careful to avoid dropping a delta-function in operating with  $\Pi$  on  $r$ . If we add and subtract the mean value of  $\Pi$  over all angles,

$$\Pi = \frac{3}{5} \nabla^4 + (\Pi - \frac{3}{5} \nabla^4),$$

the first term gives a multiple of  $\delta(\mathbf{r})$  whilst the second term, having zero mean value over angles, does not. We find

$$e = \frac{G}{c_{11}^0} \delta(\mathbf{r}) + \frac{15}{8\pi} \frac{Gd}{(c_{11}^0)^2} \frac{1}{r^7} (x_1^4 + x_2^4 + x_3^4 - \frac{3}{5} r^4). \quad (13)$$

The interaction energy between a pair of defects which produce volume changes  $\Delta V_1, \Delta V_2$  is thus

$$E_{\text{int}} = - \frac{15}{32\pi\gamma^2} \frac{\Delta V_1 \Delta V_2}{\Omega} \frac{a_0^3}{\Omega} \frac{\Omega d}{r^3} \Gamma,$$

where

$$\Gamma = l^4 + m^4 + n^4 - \frac{3}{5} = \frac{2}{5} - 2(l^2 m^2 + m^2 n^2 + n^2 l^2), \quad a_0^3 = 4\Omega$$

if  $(l, m, n)$  are the direction cosines of the line joining the defects. Schmid and Boas<sup>14</sup> have given a stereographic plot of  $l^2 m^2 + m^2 n^2 + n^2 l^2$  from which we can see that  $\Gamma$  has a maximum value of .40 in the 100-direction, a minimum of -.27 in the 111-direction and a value

-.10 in the 110-direction where there is a saddle-point. Thus for any sign of  $d$ ,  $\Delta V_1, \Delta V_2$  there are directions along which the interaction is attractive. These are the 111 directions for metals ( $d$  negative) and like sign of the  $\Delta V$ . For a pair of interstitials in copper with  $\Delta V \sim 3\Omega$  we find

$$E_{\text{int}} \sim 7.5 (a_0/r)^3 \Gamma \text{ eV.}$$

The image interaction (2') still has the same form.  $\Delta V^\infty$  is now the coefficient of  $\delta(\mathbf{r})$  in (13) and thus  $\Delta V^I/\Delta V = (\gamma-1)/\gamma$  as in the isotropic case, provided we form  $\gamma$  from the  $c_{ij}^0$ .

## REFERENCES

1. J. D. Eshelby, *J. Appl. Phys.* **25**, 255 (1954).
2. A. H. Cottrell, *Report on Strength of Solids* (Physical Society London, 1948), p. 30.
3. B. A. Bilby, *Proc. Phys. Soc.* **63A**, 191 (1950).
4. J. D. Eshelby, *Phil. Trans. Roy. Soc.* **244**, 87 (1951).
5. F. Bitter, *Phys. Rev.* **37**, 1526 (1931).
6. J. Friedel, *Advances in Physics* **3**, 446 (1954).
7. A. E. H. Love, *Mathematical Theory of Elasticity* (Cambridge, 1926).
8. C. W. Tucker, Jr. and J. B. Sampson, *Acta Met.* **2**, 433 (1954).
9. G. J. Dienes, *Phys. Rev.* **86**, 228 (1952).
10. K. F. Stripp and J. G. Kirkwood, *J. Chem. Phys.* **22**, 1579 (1954).
11. C. Crussard, *Métaux et Corrosion* **25**, 203 (1950).
12. C. Zener, *Phys. Rev.* **74**, 639 (1948).
13. G. Leibfried, *Z. Phys.* **135**, 23 (1953).
14. E. Schmid and W. Boas, *Plasticity of Crystals* (F. A. Hughes & Co., 1950), p. 192.

## PLASTIC DEFORMATION OF COPPER CRYSTALS UNDER ALTERNATING TENSION AND COMPRESSION\*

M. S. PATERSON†

The strain hardening of high purity copper single crystals during cycles of reversed plastic strain has been studied and shown to depend markedly on the orientation of the crystal. Crystals oriented near  $[100]$  or  $[111]$  show a high rate of strain hardening, while those in the middle of the stereographic triangle or near  $[110]$  show a very low rate of strain hardening, i.e., "easy glide"; in crystals oriented near the  $[100]$ - $[111]$  and  $[100]$ - $[110]$  boundaries, the rate of strain hardening is low at first and later increases, while in those oriented near the  $[110]$ - $[111]$  boundary the rate of strain hardening is more uniform. Similar behaviour was shown in tensile tests, but the easy glide was not as extensive. The importance of small diameter and the unimportance of mishandling of the specimens are discussed in connection with the conditions for the occurrence of easy glide.

Easy glide is shown to be accompanied by very uniform distribution of slip lines, while in crystals oriented nearer  $[111]$  or  $[100]$  and showing rapid strain hardening the slip lines are strongly clustered and sometimes traces of slip on other systems appear between the clusters of main slip lines. X-ray Laue photographs show no asterisms for any crystals after reversed deformation; however, the crystals of high strain hardening give faint Kossel lines while those showing easy glide do not.

An explanation of the observed strain-hardening behaviour in terms of the interaction of dislocations on intersecting planes is proposed.

The Bauschinger effect is clearly demonstrated in the copper single crystals.

### DÉFORMATION PLASTIQUE DES CRISTAUX DE CUIVRE EN TRACTION ET COMPRESSION ALTERNÉES

La consolidation des monocristaux de cuivre de haute pureté au cours des cycles de déformations plastiques alternées est montrée comme dépendant nettement de l'orientation du cristal. Les cristaux orientés au voisinage de  $[100]$  ou  $[111]$  possèdent un coefficient de consolidation élevé, tandis que celui-ci est faible pour ceux situés au milieu du triangle stéréographique ou au voisinage de  $[110]$  ("easy glide"); pour les cristaux au voisinage du côté  $[100]$ - $[111]$  et du côté  $[100]$ - $[110]$ , le coefficient de consolidation est d'abord bas, puis croît ensuite, tandis que pour ceux près du côté  $[110]$ - $[111]$ , ce coefficient est plus uniforme. Un comportement analogue a été observé dans les essais de traction, mais le "easy glide" n'est pas aussi étendu. Le rôle du diamètre de l'éprouvette et le peu d'importance de son alignement sont discutés en fonction des conditions d'apparition du "easy glide."

Le "easy glide" est accompagné d'une répartition très uniforme des lignes de glissement, tandis que, dans les autres cas, les lignes de glissement sont rassemblées en paquet et il apparaît même quelquefois des traces d'un autre système de glissement entre les paquets des lignes principales.

Les diagrammes de Laue ne présentent pas d'astérisme après déformations alternées, tandis que les cristaux à grand coefficient de consolidation présentent de faibles lignes de Kossel, tandis que les autres n'en présentent pas.

L'auteur propose une explication de la consolidation par l'intersection des dislocations. L'existence d'un effet Bauschinger est nettement établie.

### ÜBER DIE PLASTISCHE VERFORMUNG VON KUPFER-KRISTALLEN DURCH WECHSELNDE ZUG- UND DRUCKBEANSPRUCHUNG

Die Verfestigung von sehr reinen Kupfer-Einkristallen durch eine plastische Verformung bei Wechselbeanspruchung wurde untersucht und dabei festgestellt, dass sie in besonders ausgeprägter Weise von der Orientierung der Kristalle abhängig ist. Kristalle mit einer Orientierung nahe  $[100]$  und  $[111]$  zeigen eine sehr starke Verfestigung, während Kristalle, die mit ihrer Orientierung in der Mitte des Orientierungsdreiecks und nahe  $[110]$  liegen, nur eine geringe Verfestigung zeigen, d.h. sie zeigen "Leicht-Gleitung" ("easy-glide"). Bei Kristallen, die nahe den Seiten  $[100]$ - $[111]$  und  $[100]$ - $[110]$  des Orientierungsdreiecks liegen, ist die Verfestigung zunächst gering und steigt später an, während bei Kristallen, die nahe der Dreiecksseite  $[110]$ - $[111]$  orientiert sind, der Verfestigungsverlauf einheitlich ist. Ein gleiches Verhalten zeigt sich beim Zugversuch, jedoch war dabei das Leicht-Gleiten (easy-glide) nicht so ausgeprägt. Im Zusammenhang mit dem Auftreten der Leicht-Gleitung (easy-glide) wird die Bedeutung kleiner Probendurchmesser und der geringe Einfluss einer weniger sorgfältigen Probenbehandlung diskutiert.

Beim Auftreten von Leicht-Gleitung (easy-glide) sind die Gleitlinien sehr einheitlich verteilt, während in Kristallen, die näher bei  $[111]$  oder  $[100]$  orientiert sind, die also eine schnellere Verfestigung zeigen, die Gleitlinien sehr stark zusammengezogen sind und manchmal Gleitspuren auf anderen Systemen zwischen den Anhäufungen der Hauptgleitlinien zeigen. Laue-Aufnahmen zeigen bei keinem Kristall nach der Wechselbeanspruchung Asterismus. Es treten jedoch bei den Kristallen mit starker Verfestigung schwache Kossel-Linien auf, die bei den Kristallen, die ein Leicht-Gleiten zeigen (easy-glide), fehlen.

Auf Grund der Wechselbeziehung von Versetzung auf sich scheidenden den Ebenen wird eine Erklärung für das beobachteten Verfestigungsverhalten vorgeschlagen.

Der Bauschinger-Effekt konnte deutlich in den Kupfer-Einkristallen nachgewiesen werden.

\* Received January 10, 1955.

† Department of Geophysics, The Australian National University, Canberra, Australia.



### I. INTRODUCTION

The study of single crystals under reversed plastic deformation is interesting for several reasons. The strain hardening and the development of the slip pattern can be observed while avoiding the progressive rotation of the crystal orientation, relative to the direction of the stress, that is inevitable in simple tension tests. Observations of the effect of changing the direction of straining should assist the development of dislocation theories of strain hardening. Further, a detailed study of the mechanism of reversed deformation in single crystals is an essential step in understanding the process of fatigue in metals. While fatigue of practical importance occurs under very small strain amplitudes, it should be profitable first to study the grosser processes occurring at larger strain amplitudes.

Orowan's theory of fatigue<sup>1</sup> is based on the strain-hardening of local "plastic" regions under reversed straining. The present work began, in part, as an attempt to provide such data for copper single crystals at comparatively large strain amplitudes; the only previous measurements of this kind were those made by Held<sup>2</sup> on tin. However, the dependence of the strain hardening on the orientation of the copper crystals was soon discovered and the work has largely concentrated on this aspect.

Contrary to the former belief that the strain hardening of a single crystal can be expressed independently of its orientation by the shear stress-slip curve for its active slip system, an initial region of low strain hardening, or "easy glide," has been observed for certain orientations in several face-centered cubic metals, viz.,  $\alpha$ -brass,<sup>3,4</sup> aluminium,<sup>5-8</sup> gold<sup>9</sup> and silver<sup>9,10</sup>. Easy glide has now been observed in tensile tests on copper, very recently by Rosi<sup>10</sup>, and independently in the present work. However, the reversed deformation experiments demonstrate easy glide in copper more spectacularly.

### II PREPARATION OF SPECIMENS

The copper, of 99.999 per cent purity, was supplied by Messrs. Johnson, Matthey and Company. It was cold-drawn to about 1.6 mm diameter and then etched

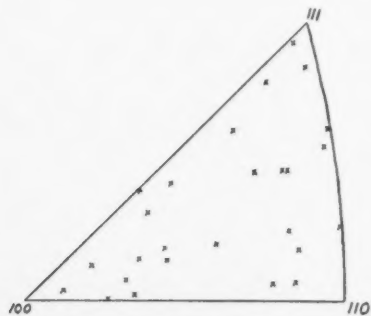


FIG. 1. The orientations of the crystals used in the reversed straining tests.

to remove any impurities from the dies. The single crystals were grown in tubes of spectrographically pure graphite in a vacuum of about  $10^{-4}$  mm Hg by the method of Andrade and Roscoe.<sup>11</sup> Each crystal was of sufficient length to provide two specimens of the same orientation; the cutting was done by nitric acid on a reciprocating thread. The specimens were finally electropolished in an orthophosphoric acid electrolyte. Their orientation was determined by the back-reflection Laue method.

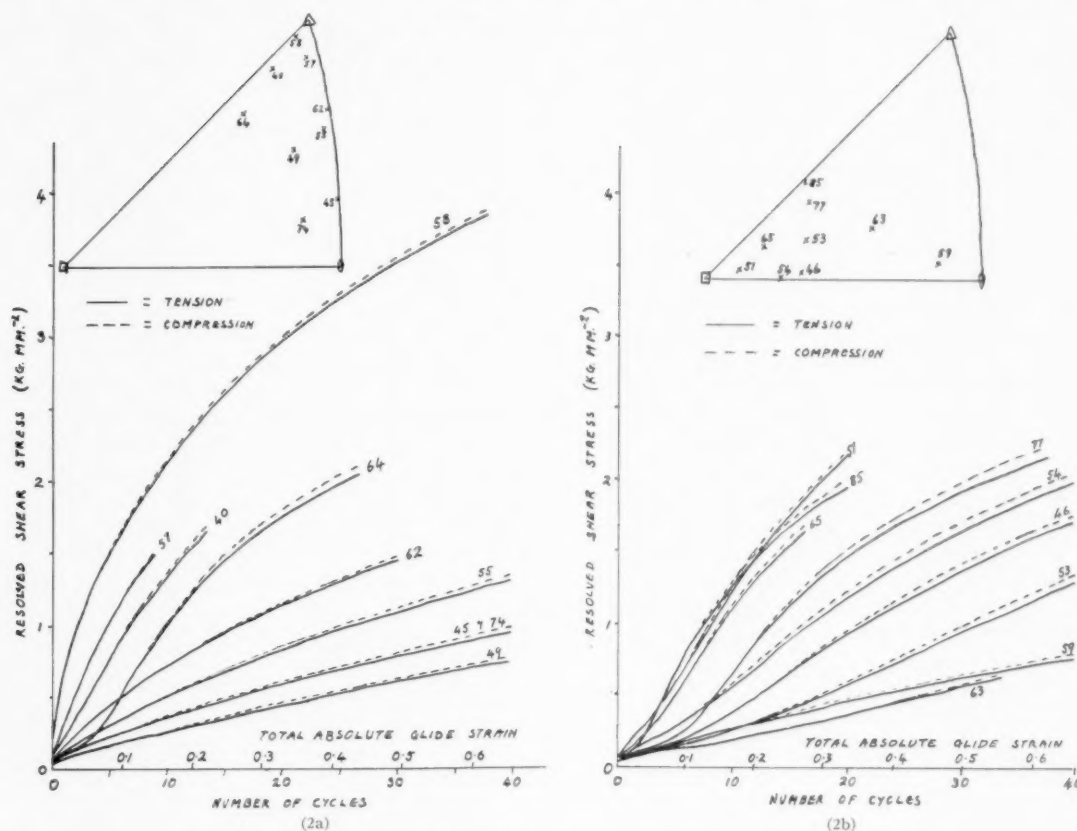
### III. EXPERIMENTAL METHODS

The testing machine is described elsewhere.<sup>12</sup> It was designed to ensure that the specimen chucks were strongly constrained to move axially, thereby minimizing external bending or torsion of the specimen. Also, there was negligible hysteresis in the machine for cycles of load between tension and compression. The load and extension (or relative movement of the chucks) were measured optically with the aid of mirrors attached to rollers. In addition, a microscope was attached to the machine so that the whole length of the specimen could be traversed and the slip pattern observed during the tests.

One of the main difficulties was to develop a method of clamping the specimen firmly without accidentally straining it. Early attempts were made to clamp the ends in V-chucks, after attaching suitable shoulders. Although stress-strain results were obtained in this way which showed the same types of strain hardening as were established in later experiments, there was much scatter since the chucks could not be aligned sufficiently accurately to eliminate distortion of the specimen. However, the following method of "clamping" overcame this difficulty and was used in the experiments described in this paper. A cylindrical steel shoulder was cemented to one end of the specimen with Araldite, the curing being done in a vacuum to avoid oxidizing the electropolished surface of the crystal. This shoulder was clamped in the upper chuck which was of conventional V-groove type. The lower end of the specimen was then dipping into molten "Comsol" solder\* at about 320–350°C, contained in the lower "chuck," which was a hollow block, heated electrically and insulated from the machine by mica washers. On reducing the heating current the solder solidified and firmly gripped the specimen. The load on the specimen was held close to zero during cooling by operating the machine by hand in the direction to compensate for the thermal contraction of the specimen and other heated parts. A stream of nitrogen was directed at the surface of the specimen to prevent oxidation while it was hot.

The free length of the crystals was about 7 mm and the diameter 1.5 mm. This length:diameter ratio seemed

\* 5% Sn, 1.5% Ag, remainder Pb; m.pt. 296°C. Preliminary tests showed negligible creep in this solder under the loads used in the stress-strain tests. "Comsol" was chosen for its creep properties in preference to solders of lower melting point, especially Wood's metal in which creep proved very troublesome.



FIGS. 2. (a) and (b). A selection of the results of the reversed straining tests.

to be the maximum permissible to avoid buckling in the reversed straining tests.

The testing machine was operated manually in a manner to ensure an approximately constant rate of extension of the specimen, of the order of 1 in. per minute; this could not readily be done by means of a motor drive of constant speed since during elastic straining most of the total deflection occurred in the load-measuring springs, while during plastic straining, when the load was changing much less rapidly, most of the deflection was due to extension of the specimen. In the reversed straining tests, the complete stress-strain curves for the first three cycles of deformation were plotted by taking load and extension readings at small intervals, the straining being interrupted momentarily at each reading. Thereafter, only the load at the end of each half-cycle was recorded. The total strain amplitude was increased during strain hardening so that the plastic strain amplitude was constant throughout the test.

In the simple tensile tests, readings were again taken during momentary interruptions in the straining. However, the amount of creep occurring during these interruptions is small and should not appreciably affect the stress-strain curves.

#### IV. REVERSED DEFORMATION EXPERIMENTS

The behavior of high-purity copper crystals in reversed straining was found to be highly dependent on their orientation relative to the specimen axis. The manner in which this is revealed in the strain hardening, the appearance of the slip lines and Laue X-ray photographs is described in the following sections. Later a comparison will be made with the behaviour of similar copper crystals in simple tensile tests.

##### 1. Measurements of Strain Hardening

Using the procedure described in Sec. III, reversed straining tests were done on copper crystals of about twenty five different orientations (Fig. 1); the plastic resolved shear strain amplitude was 0.0083 in all cases. Measurements were usually done on two specimens of the same orientation (see Sec. II), the results from which agreed to within about 5-10 per cent except for some orientations in region B (Fig. 3), where greater scatter seemed to be inherent; the curve that was initially lower was taken to be the better result since the specimen giving the higher result may have been previously damaged.

A selection of the strain-hardening curves is shown in Figs. 2(a) and 2(b). The curves are drawn through the

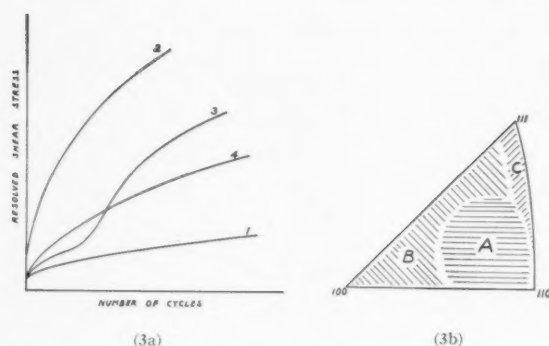


FIG. 3. Schematic representation of the orientation dependence of strain hardening in reversed deformation. Curve 1 is typical for orientation region A; curves 3 and 4 represent transitional types in regions B and C, respectively, which become more like curve 2 as the orientation approaches  $[100]$  or  $[111]$ .

final stresses reached in each half-cycle of strain; the abscissae represent the number of cycles or the equivalent total absolute strain.

The very marked dependence on orientation is seen in these results, and is summarized schematically in Fig. 3. For a crystal oriented in the middle or towards the  $[110]$  corner of the stereographic triangle [region A, Fig. 3(b)], the strain-hardening curve is very flat [type 1, Fig. 3(a)] and almost independent of orientation except for a tendency to be a little higher for orientations near the  $[110]$  corner. On the other hand, for a crystal of approximately  $[111]$  orientation, the strain-hardening curve is very steep (type 2), especially during the first few cycles. From the trend of the results in Fig. 2(b), it appears probable that a crystal of  $[100]$  orientation would also show a strain-hardening curve of type 2. However, in the absence of measurements on crystals of exact  $[111]$  and  $[100]$  orientations, it is not clear whether the strain-hardening curve for  $[100]$  would be quite as steep as for  $[111]$ .

For all intermediate orientations except those near the  $[110]$ - $[111]$  boundary (region B), the strain-hardening curve has two points of inflexion (type 3). The curve is initially of relatively low slope and then

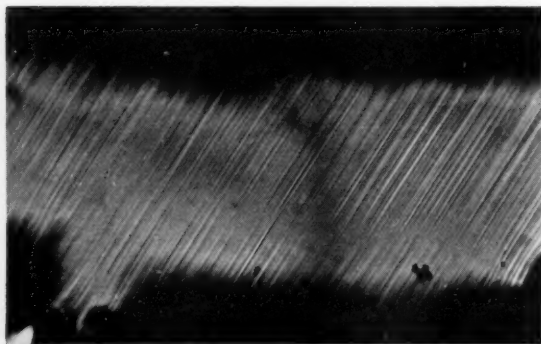


FIG. 4. Slip line pattern in crystal no. 59 in the easy glide region (200X).

rises more steeply; later it tends to flatten out again. The number of cycles at which it bends upwards is less, and the slope of the steep part greater, for orientations nearer the  $[100]$ - $[111]$  boundary; the same trend occurs to a lesser extent for orientations near the  $[100]$ - $[110]$  boundary. Further the minimum slope before the curve bends upwards is greater for orientations nearer the  $[100]$  corner.

For orientations near the  $[110]$ - $[111]$  boundary (region C), the strain-hardening curve has a similar shape to that of the limiting types 1 and 2, but is of intermediate slope (type 4); its steepness is greater for orientations nearer  $[111]$ .

A feature of the strain hardening common to all orientations was the development of a slightly higher yield stress in compression than in tension, independently of whether the first half-cycle was tensile or compressive [Figs. 2(a) and (b)]. This is not thought to be due to a zero drift in the testing machine. Neither does it appear to be due to the development of a buckle in the specimen; when conditions were arranged so that

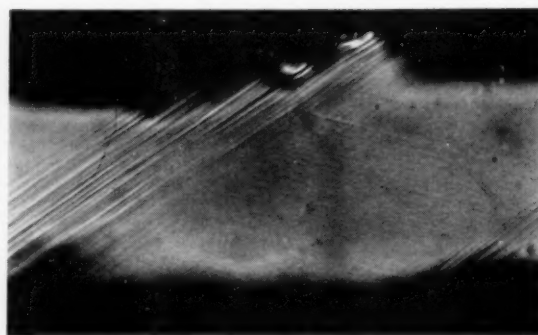


FIG. 5. Clustered primary slip and faint cross-slip in crystal no. 57 near  $[111]$  (200X).

obvious buckling occurred, the discrepancy between tensile and compressive yield stresses was no greater.

## 2. Microscopic Observations

The appearance of the slip lines after reversed straining depended markedly on the orientation of the crystals in a way that could be correlated with the strain-hardening behaviour. Crystals with a low rate of strain hardening showed very uniformly distributed slip on a single system; crystals of high strain-hardening rate showed clustering of slip lines and, frequently, slip on more than one system. In more detail, the observations were as follows:

(a) All crystals with orientations falling within region A and giving strain-hardening curves of type 1 (Fig. 3) showed very uniformly distributed slip on a single system (Fig. 4). No deformation bands of any kind nor any traces of secondary slip were observed. Also, the slip appeared to develop homogeneously over the whole specimen during an experiment.

(b) In crystals with orientations near  $[111]$  or  $[100]$ , corresponding to the highest strain hardening, the prominent slip lines were clustered into bands, between which fine slip lines on both the primary system and a second system were faintly visible. Most of the prominent slip clusters appeared during the early cycles of deformation, after which the main changes were in the general intensity of the slip picture. The final appearance for crystal no. 57, near  $[111]$ , is shown in Fig. 5. Here the second slip plane was identified as that for cross-slip. For crystal no. 51, near  $[100]$ , the secondary traces were either conjugate or cross-slip but the measurements were insufficiently accurate to identify them definitely. Crystal no. 58, which was oriented almost on the  $[111]$ - $[100]$  boundary but close to  $[111]$ , showed two sets of widely separated clusters of prominent slip on different planes, which in some places intersected. These planes were the two on which the maximum resolved shear stress occurred; no cross-slip traces could be identified. The appearance was, therefore, not that of uniformly distributed duplex slip, but rather it suggested independent activity of one or other of the favoured systems in different parts of the crystal (a similar appearance was shown by crystals nos. 54 and 85). It was also particularly noticeable in crystal no. 58 that the boundaries of the clusters of slip were not quite parallel to the slip lines themselves (cf., Lange and Lücke<sup>7</sup>); this suggests that cross-slip probably occurs between the coarse slip clusters but was too fine to be observed.

(c) For crystals oriented in the intermediate regions B and C (Fig. 3), there was a mild clustering of the slip lines, which was more marked for orientations nearer  $[111]$  or  $[100]$ , corresponding to the higher strain-hardening curves. The final appearance of the slip in both orientation regions was similar (Fig. 6 is typical). Traces of slip on a second system between the main clusters were often observed when the clustering was more marked. There was some evidence that for crystals oriented in region B the slip was at first uniformly distributed and later took on a clustered appearance as some lines became more pronounced than others, corresponding to the steeper part of the strain-hardening curves; however, more observations are needed to confirm this.

No kink bands or deformation bands of any type except that described above were observed in crystals of any orientation in these experiments.

### 3. X-Ray Observations

Laue X-ray photographs were taken after each reversed straining test. No asterism or other marked change in the Laue spots was observed for crystals of any orientation. However, Kossel lines were frequently visible (Fig. 7).

Kossel lines<sup>13</sup> are produced by the diffraction of X-rays originating within a crystal, in this case, the

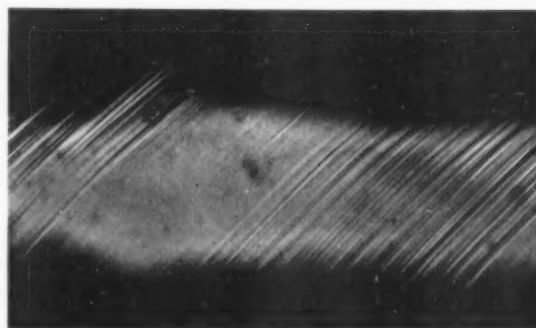


FIG. 6. Clustered slip in crystal no. 77, typical of orientation regions B and C (200X).

fluorescent copper characteristic radiation excited by the incident white radiation from an X-ray tube with a tungsten target. Normally, Kossel lines cannot easily be distinguished from the general background radiation in Laue photographs, but Borrmann<sup>14</sup> obtained very clear Kossel lines in Laue photographs of copper crystals, the surface of which had been roughened and then etched to remove the more disturbed layers. In the present work it was found that fairly clear Kossel lines could also be obtained from copper crystals, of suitable orientation, that had been subjected to reversed straining. This probably indicates that a state of imperfection has been reached in which extinction effects have been substantially reduced but in which there is not yet excessive distortion of the lattice which would cause blurring and consequent loss of contrast of the Kossel lines.

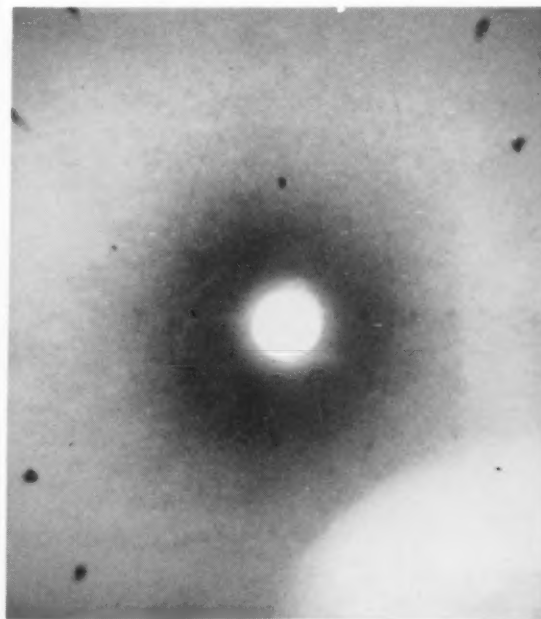


FIG. 7. Kossel lines in Laue X-ray photograph of crystal no. 58; X-ray beam parallel to  $[110]$ .



No Kossel lines were observed in Laue photographs from the crystals before deformation. Also, no Kossel lines were observed after reversed deformation for crystals with orientations within region A (Fig. 3), corresponding to low strain hardening. On the other hand, Kossel lines were clearly visible after reversed deformation for crystals oriented near  $[111]$  and  $[100]$ , showing high strain hardening; faint Kossel lines were obtained for the intermediate orientations (regions B and C, Fig. 3). These observations probably mean that the perfection of crystals showing low strain hardening is not greatly disturbed by the reversed straining, whereas the higher strain hardening is accompanied by greater disturbance of the lattice, as would be expected; in neither case is a large-scale spread of orientation introduced which would give rise to asterisms.

#### 4. Other Observations

The critical shear stresses for the crystals used in the reversed straining and tensile tests are given in Fig. 8 according to orientation. These are the values of stress at which the stress-strain curve begins to depart rapidly from the elastic line;\* values obtained by extrapolating the early linear plastic part of the stress-strain curve to cut the elastic line were about 20 per cent higher. The Schmid law<sup>15</sup> appears to hold in region A of the stereographic triangle (Fig. 3), where the critical shear stress is about  $45 \text{ gm mm}^{-2}$ . However, nearer the  $[111]$ - $[100]$  boundary, the critical shear stresses are higher (the same is true if the extrapolated values are considered). Thus the Schmid law is not obeyed over the whole range of orientations.

The minimum slope of the resolved shear stress-glide curve in the first half-cycle varies like the critical shear stress, with rather more scatter but a greater range. The greatest value is  $30 \text{ kg mm}^{-2}$  for crystal no. 58 oriented near  $[111]$ , compared to an average value of about  $2.5 \text{ kg mm}^{-2}$  for orientations in region A (Fig. 3).

Stress-strain measurements for several cycles of reversed strain similar to those applied to the single crystals

were made on two very coarse-grained polycrystalline specimens of the same copper (grain size about  $\frac{1}{2}$ -1 mm, obtained by annealing the cold-drawn wire). In each case, the stress-strain curves were rather similar in shape, and the rates of strain hardening of similar magnitude, to those obtained from single crystals oriented near  $[111]$ ; the initial yield stresses were rather higher.

A Bauschinger effect was clearly shown by all crystals, taking as its criterion a lower yield stress for straining in the reversed direction than the previously applied stress; in most cases, the yield stress for reversal after the first half-cycle of strain (0.0083 glide) was also less than the initial critical shear stress. Figure 9 shows a typical example. However, if the "yield stress" after reversal was determined by extrapolating the linear plastic part of the cycle to cut the previous elastic line, it was usually nearly equal to the stress previously applied in the first direction (this was also true for the coarse-grained polycrystalline copper). In general, the Bauschinger effect in the single crystals appeared to be of similar magnitude to that in polycrystalline copper. This is further evidence against Heyn stresses (intercrystalline stresses) being the cause of the Bauschinger effect.<sup>16</sup>

A pronounced jerkiness in the rate of deformation during cyclic straining was observed for several crystals near the  $[100]$  orientation; a slight drop in load would accompany an abrupt change in the strain. Lange and Lücke<sup>7</sup> observed a similar effect in the tensile deformation of aluminium crystals oriented near  $[100]$ . The effect in the copper crystals also occurred to a very slight extent for other orientations, but never for those within region A (Fig. 3) except after previous torsion. However, the most pronounced jerky deformation was shown by crystal no. 86b, oriented near  $[110]$ , which had undergone previous torsional strain (see below). Since the stress-strain measurements were not recorded automatically, it was difficult to determine the increment of strain in each jerk but it was probably of an order of magnitude corresponding to a slip of about 1000 Å on one plane.

*Effect of previous torsion.* In order to observe the effect that previous slip on planes other than that normally

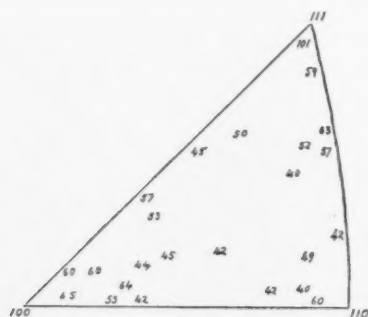


FIG. 8. Critical shear stresses (in  $\text{gm mm}^{-2}$ ) for crystals used in strain-hardening experiments.

\* The value ( $101 \text{ gm mm}^{-2}$ ) for crystal no. 58 oriented near  $[111]$  is somewhat indefinite because of the steepness of its strain-hardening curve.

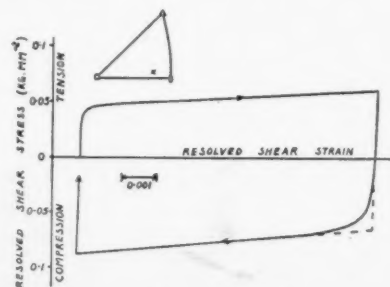


FIG. 9. Stress-strain curves for first cycle of deformation for crystal no. 86a (near  $[110]$ ), showing Bauschinger effect.

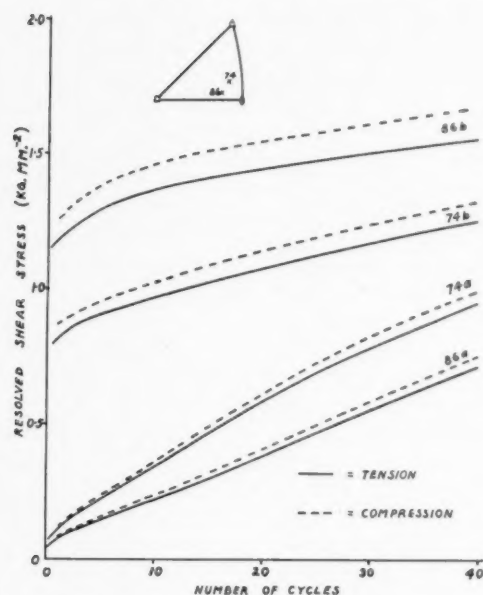


FIG. 10. Effect of prior torsion on strain hardening in reversed deformation. Maximum surface shear strain in torsion was 0.02 for crystal no. 74b and 0.1 for crystal no. 86b.

active in direct stress would have on the rate of strain-hardening of crystals oriented in region A (Fig. 3), two specimens were twisted by amounts corresponding to about 0.02 and 0.1 surface shear strain, respectively, and then twisted back by the same amounts. This was followed by reversed deformation tests, carried out in the usual way. The results of these are given in Fig. 10. For comparison, curves are also given for specimens of the same orientations, cut from the same crystals, but not previously twisted. It is remarkable that the rate of strain hardening is even less after prior torsion than in an undamaged crystal; there is no tendency to strain-harden at the high rate that is characteristic of crystals oriented near  $[111]$  or  $[100]$ , which often show signs of slip on more than one plane.

The final distribution of slip lines resulting from the reversed straining after prior torsion was very uniform, similar to that normally observed for crystals in this orientation region. However, during the first few cycles, the slip pattern developed first in some parts of the specimen and then spread gradually to all parts. This was accompanied by jerky deformation, especially in crystal no. 86b; once, a jerk was actually observed to coincide with the appearance of a new prominent slip line in a previously unmarked area.

#### V. TENSILE TESTS

In order to compare the strain hardening of copper crystals in cyclic straining with that in unidirectional straining, simple tensile tests were carried out for a number of orientations. The method of gripping, the lengths of the specimens and the measuring procedure

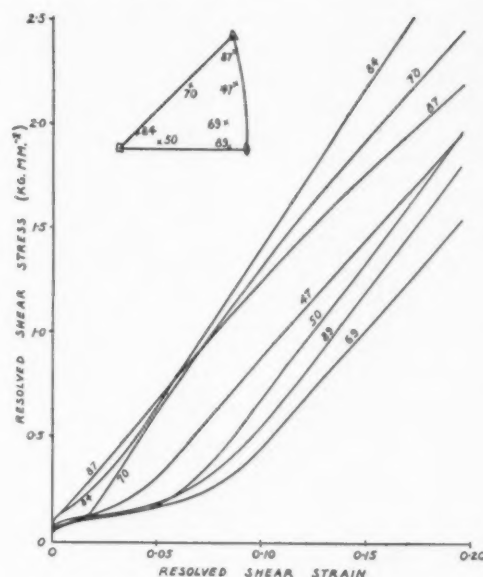


FIG. 11. Shear stress-glide curves from tensile tests.

were identical with those used in the reversed deformation tests. The rigid gripping of the ends of the specimens must lead to very considerable inhomogeneity of strain when the crystal orientation tends to rotate during extension; however, for small strains the effect on the strain hardening should not be serious.

Since these tests were done, an account of similar work on copper has been published by Rosi.<sup>10</sup> While in many respects the two sets of results are similar, it is interesting to compare them and discuss some of the differences, since the method of gripping and the size of the specimens were different.

The results for typical orientations are given in Fig. 11 as resolved shear stress-shear strain curves. These were derived from the tensile stress-strain measurements by the usual method of calculation<sup>17</sup>; in the two cases (no. 70 after 0.08 glide and no. 84 almost from the beginning) where the calculated orientation reaches the  $[100]$ - $[111]$  boundary, Göler and Sachs' method<sup>18</sup> for duplex slip has been used.

As in the reversed deformation tests, there is a pronounced dependence on orientation, mainly due to different behaviour up to strains of about 0.1. For orientations far from the  $[100]$ - $[111]$  boundary, there is a region of low strain hardening extending for several per cent strain, after which the rate of strain hardening is much higher. For the orientations close to  $[100]$ ,  $[111]$  or the  $[100]$ - $[111]$  line, the initial region of low strain hardening is shorter (no. 70) or absent (nos. 84 and 87). However, for all orientations, the rate of strain hardening at the larger strains is of similar magnitude.

Some of the results are plotted as tensile stress-strain curves in Fig. 12, in which are also included Rosi's results [10] for similar orientations. Curve no. 53 is the

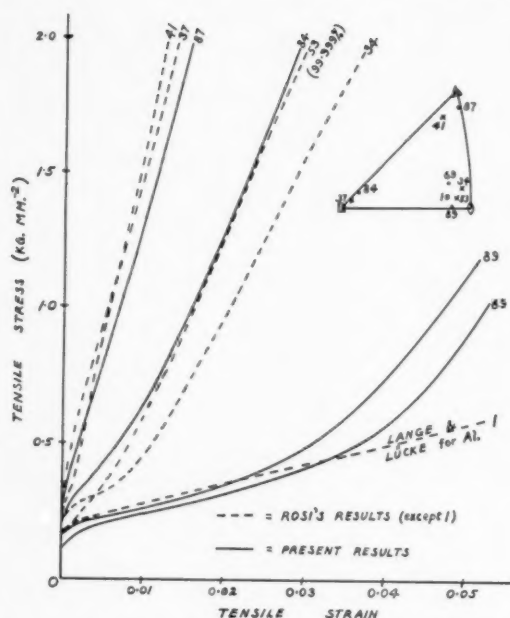


Fig. 12. Comparison of tensile stress-strain curves with those of Rosi<sup>10</sup> and Lange and Lücke.<sup>7</sup>

only one given by Rosi for 99.999 per cent pure copper and should be comparable to curves no. 69 and no. 89 for similar orientations from the present work. However, the region of low strain hardening is of much greater extent in the latter cases than in Rosi's. The other curves from Rosi's paper refer to less pure copper (99.98 per cent). While they are rather similar to the present results for orientations near [111] (nos. 41 and 87) and [100] (nos. 37 and 84), there is again a considerable difference for orientations near [110] (nos. 34 and 69 or 89).

Thus the most striking difference between Rosi's and the present results lies in the greatly extended region of low strain hardening for orientations near [110] in the latter. This is at first surprising in view of the fact that Rosi's specimens were gripped in a manner to minimize the inhomogeneous strain due to lattice rotation whereas in the present work the ends of the specimens were prevented from rotating and the specimens were relatively much shorter. Also, Rosi concludes that higher purity crystals show a shorter region of low strain hardening. However, the explanation may lie in the fact that Rosi's specimens were of greater diameter (9.5 mm compared to 1.5 mm). In this connection, it may be observed that the curve reproduced in Fig. 12 from Lange and Lücke's measurements<sup>7</sup> on high-purity aluminium for an orientation near [110] was obtained from an electropolished crystal of 1.5 mm diameter and shows a very extensive region of low strain hardening.

The distributions of slip lines for the various orientations were similar in most respects to those illustrated by Rosi<sup>10</sup> and Becker and Hobstetter<sup>19</sup> for copper and by Lange and Lücke<sup>7</sup> for high-purity aluminium. The

crystals oriented near [111] and [100] showed strong clustering of the primary slip lines, with slip on other planes (cross-slip or conjugate slip) developed more strongly between the clusters. Crystal no. 70 near the middle of the [100]-[111] boundary did not show clustering of the slip to a marked extent, but the slip lines of the two main systems were fairly intimately intermingled. The crystals near [110] showed very uniformly distributed slip on one plane. This is in contrast to Rosi's conclusion that a mild tendency for clustering of the slip lines existed for orientations away from the [100]-[111] boundary.

The crystals oriented near [110] also showed kink bands, such as illustrated by Rosi<sup>10</sup> and Lange and Lücke.<sup>7</sup> These were probably due to the rigid grips, in agreement with Rosi's observations; their absence in the reversed deformation tests also supports this conclusion. Slip on a second plane sometimes occurred in the kinked regions, as observed in aluminium.<sup>7,21</sup>

"Bands of secondary slip" (cf. Honeycombe<sup>20</sup> and Rosi<sup>10</sup>) were a common feature of deformed crystals of orientations away from [110]. However, no "intimate cross-slip" such as occurs in aluminium<sup>4,7,21,22</sup> was observed in any crystals.

Laue X-ray photographs taken after the tensile tests showed marked asterism for those crystals which contained kink bands, that is, for orientations near [110]. The crystals oriented near [100], [111] or the [100]-[111] boundary showed only slight asterism, although the Laue spots were considerably blurred. This confirms the conclusions of Honeycombe,<sup>20</sup> Lange and Lücke,<sup>7</sup> and others that asterism arises from kink bands. The asterisms from the deformed copper crystals often showed a fine structure (cf. Honeycombe<sup>20</sup>); however, the specimens had been heated to about 350°C for 15 seconds or so when removing them from the testing machine.

Some faint Kossel lines were observed in the Laue photographs. However, they were usually rather broad and, for the orientations near [110], were extremely faint.

## VI. DISCUSSION

The striking contrast between the high rate of strain hardening for crystals oriented near [100] and [111] and the initial low rate for crystals nearer [110] is a feature common to the tensile tests and the cyclic straining tests; that is, in both types of straining, crystals oriented in region A (Fig. 3) show "easy glide."<sup>19</sup> However, whereas in simple tensile straining the region of easy glide ends after a few per cent strain, when the yield stress is still below 0.2 kg mm<sup>-2</sup>, the low rate of strain hardening persists in the reversed straining until the yield stress has been raised to at least 0.8 kg mm<sup>-2</sup>. Thus a change to a high rate of strain hardening (the onset of "turbulent hardening," in Cottrell's graphic terminology<sup>23</sup>) does not always occur when the applied stress exceeds a critical value. The difference in the two

cases must lie in the development of the internal stresses from stuck dislocations; because of the alternation of slip of opposite senses on neighboring active slip planes during reversed straining, the internal stresses in this case probably change sign more frequently in a given distance and so give rise to weaker long-range internal stresses than result for simple tensile straining.

The present experiments throw some further light on the *conditions for the appearance of easy glide*. These have been given as: suitable crystal orientation, careful handling of the crystals, high-purity material, and absence of an oxide layer.<sup>4,5,6,9,23</sup> The present experience with copper confirms the importance of crystal orientation. The copper was also of high purity; however, the role of purity is doubtful in view of Rosi's results<sup>10</sup> and observations on  $\alpha$ -brass.<sup>3,4</sup> The presence of an oxide film on the copper does not seem to matter, since all tests were done in air; even when a visible oxide film was allowed to form it did not appear to affect the results.

An unexpected conclusion is that mishandling of the specimens, such as accidental bending, does not prevent easy glide. Slight damage usually results in the strain-hardening curve in reversed deformation being slightly higher than—but of parallel course to—that for an undamaged specimen. The experiments in which crystals were deliberately distorted in torsion showed that although the yield stress had been considerably raised, the subsequent rate of strain hardening in the reversed straining tests was even lower than in undamaged crystals. (This was in contrast to Paxton and Cottrell's observations<sup>24</sup> that small twists raise the subsequent rate of strain hardening in a tensile test.) However, the high stress-strain curves for polycrystalline specimens suggest that easy glide did not occur in many of the crystals contained in them.

From the evidence given in Sec. V a crystal of smaller diameter probably shows more extensive easy glide. This favours Mott's suggestion<sup>25</sup> that in the region of easy glide most dislocations pass out of the crystal and so do not contribute to the hardening, since in a larger crystal there would be a greater chance of a dislocation meeting an obstacle during its passage through the crystal. If the absence of Kossel lines in the Laue photographs from crystals after easy glide is a reliable indication of higher crystal perfection, this further supports the idea that not many dislocations are trapped in the crystal during easy glide.

The most prominent feature accompanying a high rate of strain hardening, whether in cyclic straining or in simple tensile straining, is the clustering of the primary slip lines, and, frequently, the appearance of other slip lines between these clusters, in spite of the orientation being such that slip on only one set of planes would be predicted. This is in contrast to the very regular distribution of the single set of slip lines resulting from easy glide.

The idea that the high rate of strain hardening (turbulent hardening) arises from the interaction of dis-

locations on intersecting planes<sup>26,27,28</sup> is supported by the observation of traces of slip on more than one set of planes. Although it is only on the primary slip planes that the shear stress component is sufficiently high to cause the movement of large numbers of dislocations (probably due to the catastrophic generation of dislocation loops at Frank-Read sources), the shear stresses effective on some of the other slip planes may also cause the movement of some of the less tightly bound dislocations lying in them; at least, the dislocation segments in these planes will bulge out to some extent and so increase the chance of interaction with dislocations moving in the primary planes. Such an effect will be less for orientations further from the  $[100]$ - $[111]$  and  $[100]$ - $[110]$  boundaries of the stereographic triangle, that is, for orientations nearer the middle of the  $[110]$ - $[111]$  boundary, since here the ratio of the shear stress component on the second most favoured slip plane to that on the primary slip plane is least.

This enables one to give a qualitative explanation of some of the features of the dependence of the strain hardening on orientation in region B. Thus by assuming that dislocations in the conjugate planes<sup>29</sup> interact with those in the primary planes, one can explain the observation that the upward bend in the strain-hardening curve (type 3) occurs at a lower stress for orientations nearer the  $[100]$ - $[111]$  boundary; as the ratio of the resolved shear stress on the conjugate planes to that on the primary planes increases, dislocations on the conjugate planes will be increasingly likely to move (or the dislocation segments to bulge out further) and to interact with dislocations moving on the primary planes. The slope of the steeper part of the strain-hardening curve will also be increased due to the greater number of these dislocation interactions as the relative shear stress component on the conjugate planes is increased.

A similar explanation of the trend of the strain-hardening curves for orientations near the  $[100]$ - $[110]$  boundary is possible in terms of interaction with dislocations in the unpredicted planes<sup>29</sup> instead of the conjugate planes.

The different type of behaviour in region C can now be understood, since no new slip plane is favoured when the  $[110]$ - $[111]$  boundary is approached; only the slip direction changes when this boundary is crossed. Thus the strain-hardening curves (type 4) do not show an upward bend but remain of similar shape to type 1 for region A.

It is interesting to note that increased amounts of cross-slip accompany the increased rate of strain hardening in region C as  $[111]$  is approached; this corresponds to the increasing relative shear stress on the cross-slip planes. However, if these slip lines are due to true cross-slip, involving dislocations having the same Burgers vector as the primary slip, they cannot be associated with hardening resulting from interactions of Lomer-Cottrell type with the dislocations in the primary slip planes. Rather, their presence probably in-



dicates the relief of piling up of screw dislocations in the primary planes.<sup>26</sup> Mott<sup>26</sup> has already suggested that the intersection of screw dislocations may be the mechanism of hardening in the easy glide region. Thus, if the increased amount of cross-slip is evidence that screw dislocations are playing an increasing role in the deformation, it may be that Mott's hardening mechanism for easy glide is still operative in region C but to an increasing degree nearer [111].

Similarly, in region B the part of the strain-hardening curve (type 3) before the upward bend is probably associated with the same mechanism. Here, also, the slope increases as [100] is approached and the relative shear stress component in the cross-slip plane is increased.

No asterisms were observed in the Laue photographs after any of the reversed straining tests; where strong asterisms resulted in the tensile tests, they could be attributed to kink bands. This again shows that the structural features (especially kink bands) that give rise to asterisms are not essential to strain hardening.<sup>26</sup>

#### ACKNOWLEDGMENT

The main part of the design and construction of the apparatus used for the reversed deformation tests was done at the Aeronautical Research Laboratories of the Department of Supply, Melbourne. The author is grateful to the Chief Scientist for the continued use of the apparatus for this work at the Australian National University.

#### REFERENCES

1. E. Orowan, Proc. Roy. Soc. (Lond.) **A171**, 79 (1939).
2. H. Held, Z. Metallk. **32**, 201 (1940).
3. F. v. Göler and G. Sachs, Z. Phys. **55**, 581 (1929).
4. R. Maddin, C. H. Mathewson, and W. R. Hibbard, Trans. A.I.M.E. **175**, 86 (1948); **185**, 527 (1949).
5. G. Masing and J. Raffelsieper, Z. Metallk. **41**, 65 (1950).
6. K. Lücke and H. Lange, Z. Metallk. **43**, 55 (1952).
7. H. Lange and K. Lücke, Z. Metallk. **44**, 183 and 514 (1953).
8. G. Masing and H. Weik, Z. Metallk. **45**, 417 (1954).
9. E. N. daC. Andrade and C. Henderson, Phil. Trans. Roy. Soc. (Lond.) **A244**, 177 (1951).
10. F. D. Rosi, Trans. A.I.M.E. **200**, 1009 (1954); J. Metals (Sept. 1954).
11. E. N. daC. Andrade and R. Roscoe, Proc. Phys. Soc. (Lond.) **49**, 381 (1937).
12. J. Sci. Instrum. In press.
13. R. W. James, The Optical Principles of the Diffraction of X-Rays (London, 1948), pp. 438-452.
14. G. Borrmann, Ann. Phys. **27**, 669 (1936).
15. E. Schmid and W. Boas, The Plasticity of Crystals (Berlin, 1935; Eng. transl., London, 1950), p. 105.
16. R. L. Woolley, Phil. Mag. **44**, 597 (1953).
17. Reference 15, pp. 57 and 105.
18. F. v. Göler and G. Sachs, Z. Phys. **41**, 103 (1927).
19. J. J. Becker and J. N. Hobstetter, Trans. A.I.M.E. **197**, 1231 (1953); J. Metals (Sept. 1953).
20. R. W. K. Honeycombe, J. Inst. Metals (Lond.) **80**, 45 (1951).
21. R. W. Cahn, J. Inst. Metals (Lond.) **79**, 129 (1951).
22. G. J. Ogilvie and W. Boas, Trans. A.I.M.E. **175**, 102 (1948).
23. A. H. Cottrell, Dislocations and Plastic Flow in Crystals (Oxford, 1953), pp. 157-180.
24. H. W. Paxton and A. H. Cottrell, Acta Met. **2**, 3 (1954).
25. N. F. Mott, Phil. Mag. **44**, 741 (1953).
26. N. F. Mott, Phil. Mag. **43**, 1151 (1952).
27. P. Haasen and G. Leibfried, Z. Phys. **131**, 538 (1952).
28. P. Haasen, Z. Phys. **136**, 26 (1953).
29. Terminology of F. D. Rosi and C. H. Mathewson, Trans. A.I.M.E. **188**, 1159 (1950).

## DIFFUSION AND SOLUBILITY OF NITROGEN IN SILICON-IRON\*

D. A. LEAK,<sup>†</sup> W. R. THOMAS<sup>‡</sup> and G. M. LEAK<sup>†</sup>

Internal friction methods have been applied to a ternary alloy of iron, silicon and nitrogen. Two relaxation peaks have been resolved; the existence of a third is somewhat doubtful. The peaks corresponding to jumps of the interstitial nitrogen atoms are connected with sites either (a) identical with those in pure alpha-iron, or (b) in octahedra containing one silicon atom along the tetrad axis. The activation energies for these mechanisms are  $18 \pm 1$  and  $12 \pm 2$  kcal/mole, respectively. Bulk diffusion must take place through the former type of site.

The majority of the nitrogen atoms sit in the silicon sites, at least for the temperature range of the present investigation, 250–1000°C. The solubility of nitrogen in a 3 per cent silicon-alloy has been determined within this temperature range and has been shown to be about an order of magnitude less than for pure alpha-iron. This solubility has been measured for equilibrium with a precipitated nitride. The heat of solution of this nitride is about 8 kcal/g-atom of nitrogen.

## DIFFUSION ET SOLUBILITÉ DE L'AZOTE DANS LES ALLIAGES FER-SILICIUM

La méthode du frottement interne a été appliquée à un alliage ternaire fer-silicium-azote. Deux maximum ont été identifiés; l'existence d'un troisième est toutefois douteuse. Ces maximum correspondent aux sauts des atomes interstitiels d'azote situés soit dans des positions identiques à celles du fer pur, soit dans des positions octaédriques contenant un atome de silicium sur l'axe quaternaire. Les énergies d'activation correspondantes sont  $18 \pm 1$  et  $12 \pm 2$  kcal/mol. La diffusion en volume doit se produire par les positions du premier type.

La plupart des atomes d'azote dissous sont voisins des atomes de silicium du moins dans l'intervalle de température de cette recherche (250–1.000°). La solubilité de l'azote dans un alliage à 3% de silicium a été mesurée dans cet intervalle de température et a été trouvée d'un ordre de grandeur inférieur à celle dans le fer  $\alpha$  pur. La solubilité a été mesurée pour l'état d'équilibre avec un nitrure précipité. La chaleur de dissolution de ce nitrure est de l'ordre de 8 kcal/at. gr. d'azote.

## DIFFUSION UND LÖSLICHKEIT VON STICKSTOFF IN EISEN-SILIZIUM

Eine ternäre Legierung aus Eisen, Silizium und Stickstoff wurde mit Verfahren zur Bestimmung der inneren Reibung untersucht. Es wurden zwei Relaxationsspitzen aufgelöst; die Existenz einer dritten erscheint zweifelhaft. Die Spitzen, die Sprünge der auf Zwischengitterplätzen sitzenden Stickstoffatomen entsprechen, stehen entweder mit Gitterplätzen (a) die mit denen des alpha-Eisens identisch sind oder mit solchen (b) in Oktaedern, die ein Siliziumatom auf der tetraedrischen Achse haben, in Verbindung. Die Aktivierungsenergien für diesen Mechanismus sind  $18 \pm 1$  bzw.  $12 \pm 2$  Kcal/mol. Durch den erstgenannten Typ der Gitterplätze muss eine Massendiffusion stattfinden.

Zu mindestens von 250–1000°, dem Temperaturbereich der vorliegenden Untersuchung, befinden sich die meisten Stickstoffatome auf den Gitterplätzen des Siliziums. Für den untersuchten Temperaturbereich wurde die Löslichkeit von Stickstoff in einer 3% Silizium enthaltenden Eisen-Silizium Legierung bestimmt. Sie ist um eine Größenordnung kleiner als bei reinem alpha-Eisen. Diese Löslichkeit wurde für das Gleichgewicht mit einer Nitriddausscheidung gemessen. Die Lösungswärme dieses Nitrides ist ungefähr 8 Kcal/gatom Stickstoff.

## INTRODUCTION

The effect of carbon and nitrogen on the internal friction observed in alpha iron has been investigated by a number of workers<sup>1</sup> and has been used to follow ageing<sup>2,3</sup> and also to determine the equilibrium solubility of these interstitial impurities.<sup>4</sup> Only a limited amount of work has been carried out with ternary systems, mainly by Fast<sup>5</sup> and Dijkstra<sup>6</sup> and their co-workers. This paper reports work on iron-silicon-nitrogen, one objective being to provide background data for an investigation of the effect of impurities, such as nitrogen, on the magnetic and electrical properties of silicon-iron. The interpretation of the results differs slightly from that of previous workers.

\* Received January 11, 1955.

<sup>†</sup> British Iron and Steel Research Association (Metallurgy General Division) Hoyle Street, Sheffield, England.

<sup>‡</sup> Department of Mines and Technical Surveys, (Metallurgy Division) Atomic Energy Project, Chalk River, Ontario, Canada.

Fast and Meijering<sup>5</sup> in a study of iron-vanadium-nitrogen suggested that the nitrogen atoms (otherwise in free solid solution) contributing to the observed internal friction, tended to be associated with vanadium nitride particles. Two internal friction peaks were observed separated by about 70°C (frequency  $\sim 1$  cps). The lower temperature peak corresponded to that for nitrogen in pure alpha-iron. The higher peak was interpreted as corresponding to nitrogen in abnormal sites. They suggested that the particles introduced abnormal interstices in their vicinity and that the nitrogen atoms tended to lodge there, ultimately combining with vanadium atoms and so coarsening the precipitated particles. Similar earlier work with manganese as the substitutional impurity did not give two well resolved peaks but merely a broadened peak at a temperature only a few degrees higher than for nitrogen in pure alpha-iron. Fast and Dijkstra<sup>7</sup> suggested that this was due to the superposition of two peaks, one

corresponding to jumps of the nitrogen atoms as in pure alpha-iron whilst the second corresponded to jumps to or from sites neighbouring a manganese atom. The results reported here indicate that the higher temperature peak is caused by the jumping of nitrogen atoms around the impurity atom.

Dijkstra and Sladek<sup>6</sup> showed that the presence of 0.5 at.% of these substitutional impurity elements markedly reduced the solubility of nitrogen (in equilibrium with the precipitated impurity nitride or mixed iron-impurity nitride).

Neither Fast nor Dijkstra attempted to calculate diffusion rates under the conditions of their experiments. Their results were interpreted on the basis of the abnormal sites having a lower free energy than the normal alpha-iron lattice sites. This situation is also implicit in the present work where it is suggested that the energy barrier to be overcome in jumping between the abnormal sites is less than that between normal alpha-iron lattice sites. This is, in fact, supported by Dijkstra and Sladek's results which showed a large half peak width for the higher temperature peak.

The solubility considered here is that in equilibrium with a precipitated nitride. This nitride has not yet been characterised. Equilibrium between dissolved nitrogen and a surrounding nitrogen atmosphere has been investigated, for iron containing 3 per cent silicon, by Corney and Turkdogan.<sup>8</sup> They showed that the solubility was about half that for pure alpha-iron. The present work shows a very much reduced solubility in equilibrium with the second phase.

#### TECHNIQUE

This has been described in detail elsewhere.<sup>9,10</sup> Only a brief summary will be given here, to bring out the essential items. This will refer, of course, to an interstitial solute in a body-centered cubic lattice.

The specimen, in the form of a wire or thin strip, is used as a torsional suspension for a freely oscillating system. Internal friction is then observed as the

logarithmic decrement  $\delta$  for resulting decay of free vibrations. This is related to the temperature  $T$  at which the measurement is carried out by

$$\frac{\delta}{\pi} = \Delta \cdot \frac{\omega\tau}{1 + \omega^2\tau^2} \quad (1)$$

where

$$\tau = \tau_0 \exp(Q/RT). \quad (2)$$

This applies to a single relaxation mechanism of relaxation time  $\tau$ ,  $\omega$  is the angular frequency of the free vibrations,  $\Delta$  the relaxation strength of the process,  $Q$  the activation energy for the jump process concerned and  $R$  the gas constant. The diffusion coefficient  $D$  can be related to  $\tau$  for a body-centered cubic lattice, as a random-walk problem

$$D = a^2/36\tau, \quad (3)$$

where  $a$  is the lattice parameter for the solvent. Neglecting variation of  $\Delta$  with  $T$ , then the maximum value of  $\delta$  is obtained when

$$\omega\tau = 1. \quad (4)$$

At this point  $\Delta$  is directly proportional to the amount of interstitial solute taking part in the jump process, that is, the amount of interstitial solute in free solution.

Summarising, the relevant items which can be extracted from internal friction measurements are

- (i) diffusion coefficient of the solute (knowing the frequency  $\omega$  required to give a peak at temperature  $T$ );
- (ii) amount of solute in solution (from the height of the peak);
- (iii) further to item (ii) the decay with time in height of the peak gives an indication of precipitation or ageing.

#### EXPERIMENTAL

Strip specimens of high purity silicon iron were cut, of dimensions about 250×3×1 mm from material prepared by the National Physical Laboratory. The analysis at this stage was as follows: (in wt. %)

Silicon	2.83
Nitrogen	0.001
Oxygen	0.00053
Carbon	0.002
Sulfur	0.004
Aluminum	0.003
Phosphorus	0.003

Specimens were nitrided in ammonia-hydrogen mixtures to give nitrogen levels of about 0.005, 0.01 or 0.05 wt.%. This was carried out by sealing the specimen in a silica reaction tube. After evacuating to remove oxygen, hydrogen and ammonia were introduced to give a total pressure of 25 cm Hg. Nitriding took place at 700°C, at which temperature the total pressure was still less than 1 atmosphere.

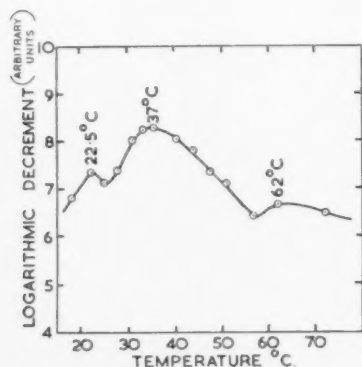


FIG. 1. Typical curve of logarithmic decrement versus temperature. Specimen quenched from 900°C. Frequency of oscillation 1.26 per sec.

For the determination of the diffusion coefficient the following procedure was adopted. Specimens containing about 0.005 to 0.01 wt. % nitrogen were sealed in silica tubes under a vacuum of better than  $1\mu$  Hg pressure. These were then quenched from 900°C or 1000°C into water at 20°C. The silica had to be fractured mechanically at the instant of quenching. This technique avoided oxidation of the specimens and gave specimens containing nitrogen in solution. Immediately after quenching the temperature of the internal friction peak was determined for various frequencies of oscillation.

For the determination of the solubility this method was modified as follows: Specimens containing rather more nitrogen than was in solution at temperature  $T$  were sealed in vacuum in hard glass or silica and quenched from temperature  $T$  into water at 20°C. For a constant  $\omega$ , throughout this series of measurements, the height of the internal friction peak was determined for various quenching temperatures between 200°C and 1200°C. Hard glass was used for quenching temperatures below 800°C. The criterion that a specimen contained more nitrogen than would be in equilibrium

TABLE I.

Frequency of oscillation sec <sup>-1</sup>	Temperature of peaks °C		Diffusion coefficient $\times 10^{16}$ cm <sup>2</sup> sec <sup>-1</sup>	
0.17	—	9	21	0.242
0.79	23	31	—	1.123
0.806	21	30	—	1.147
1.26	22.5	37	62	1.791
2.32	32.5	49	—	3.30
2.88	36	52	—	4.10
5.0	40	63	—	7.11
5.96	—	66.5	92	8.47

solution at temperature  $T$  was that quenching from a temperature greater than  $T$  should give a bigger peak than from the lower temperature. Experience rapidly indicated what specimens should be used for each quenching temperature.

The results of this second series of measurements would thus give the solubility in terms of arbitrary units of logarithmic decrement; in order to get an absolute value it is necessary to know the proportionality constant between  $\Delta$  and the number of interstitial atoms taking part in the jump process. The specimens used were all of the same texture so that the proportionality constant remained unchanged throughout the series of measurements. For a polycrystalline specimen it is not feasible to calculate the proportionality constant. Two methods can be adopted to determine an absolute value for solubility. Firstly, a monocrystalline specimen of known orientation can be loaded with nitrogen and its elastic after-effect determined after quenching. Secondly, chemical analysis of one of the original polycrystalline specimens can be used, provided its nitrogen content falls within the solubility range. This latter method was adopted here.

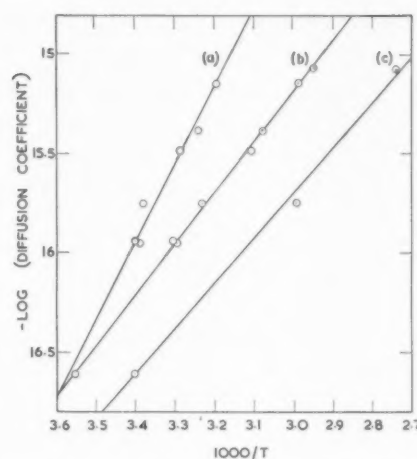


FIG. 2. Diffusion coefficient for nitrogen in 2.83% silicon iron plotted as  $-\log D$  versus  $1000/T$ . Curves (a), (b) and (c) correspond to the three resolved relaxation peaks.

#### DETERMINATION OF DIFFUSION COEFFICIENT

Previous work on the diffusion of nitrogen in pure alpha-iron<sup>11</sup> gave a series of single peaks from which an unambiguous diffusion coefficient could be calculated.

It became apparent immediately the present work was started that the situation with iron-silicon-nitrogen was more complex. In general, two peaks could be resolved, depending upon the frequency of oscillation. In a number of cases a third peak was also observed. Figure 1 is a typical determination with peaks at 22.5°C and 37°C, and possibly at 62°C.

Diffusion coefficients were calculated, for all the observed peaks, in accordance with Eqs. (3) and (4). The results are given in Table I.

From Eq. (3) the relationship between  $D$  and  $T$  is

$$D = D_0 \exp(-Q/RT). \quad (5)$$

The results from Table I are plotted in Fig. 2 as  $-\log D$  versus  $1000/T$ . For a single relationship between  $D$  and  $T$  the slope of the curve in Fig. 2 would give  $Q$  and the intercept at  $1000/T=0$  would give the proportionality constant  $D_0$ . However, Fig. 2 shows that there are two or perhaps three distinct curves corresponding to the distribution of peaks shown in Table I.

#### INTERPRETATION OF DIFFUSION COEFFICIENT DETERMINATIONS

In the case of nitrogen in pure alpha-iron the internal friction measurements correspond to only a single jump mechanism for the interstitial nitrogen to and from sites where all the neighboring atoms were iron. In the case of iron containing 5.5 at.% silicon it is possible to envisage the following interstitial jumps:

(i) to and from sites with all Fe nearest neighbors. This corresponds to the pure iron case (Fe sites).



(ii) to and from sites with one nearest neighbor a Si atom (Si sites).

(iii) from a site with all Fe nearest neighbors to one with a Si neighbor (Fe-Si sites).

(iv) from a site with one Si neighbor to a site with only Fe neighbors (Si-Fe sites).

(v) to and from abnormal sites neighboring particles of the second phase.

(vi) to or from sites with more than one Si neighbor.

By comparison of these results with those for pure alpha-iron<sup>11</sup> it is obvious that curve (a) in Fig. 2 is identical with that for the diffusion of nitrogen in alpha-iron. The activation energy for this process is  $18 \pm 1$  kcal/mol;  $D_0$  is equal to  $3.1 \times 10^{-3}$  cm<sup>2</sup> sec<sup>-1</sup>. Thus this curve (a) can be assumed to correspond to nitrogen atom jumps to and from "Fe sites." In the calculation based on Eqs. (2) and (4) the lattice parameter  $a$  was taken to be  $2.857 \times 10^{-8}$  cm from the work of Jette and Greiner<sup>12</sup> and Farquhar, Lipson and Weill.<sup>13</sup> The alteration of lattice parameter from  $2.861 \text{ \AA}$  for pure iron to  $2.857 \text{ \AA}$  for the silicon-iron alloy, reduces the diffusion coefficient by only 0.6 per cent. This is less than the experimental scatter in the results.

It remains to determine what interstitial jumps give rise to curves (b) and (c) in Fig. 2. Curve (b) will be considered first. Figure 2 shows that the activation energy for the mechanism giving rise to curve (b) is  $12 \pm 2$  kcal/mole.

It has been shown by Jack<sup>14,15</sup> that interstitial nitrogen in the body-centred cubic iron lattice causes a distortion. This can best be visualised by considering an octahedron of iron atoms (Fig. 3). Nitrogen occupies the interstice at the center of this octahedron. The resulting distortion consists of an expansion along the tetrad axis and a contraction along the diad axes. Silicon atoms sitting substitutionally in the iron lattice contract the lattice. Thus, if a silicon atom occupies one of the sites of an iron atom octahedron, along the

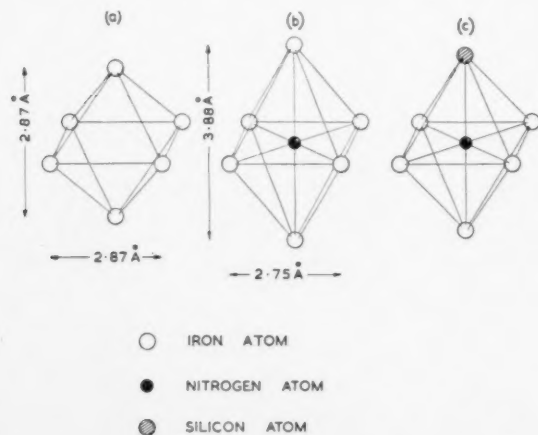


Fig. 3. Octahedral sites in (a) pure alpha-iron, (b) pure alpha-iron plus nitrogen, (c) silicon iron plus nitrogen.

TABLE II

Quenching temperature °C	Frequency of oscillation sec <sup>-1</sup>	Peak heights Arbitrary units		Total solubility Arbitrary units
		Fe sites	Si sites	
300	1.61	—	1.0	1.0
400	1.59	—	1.7	1.7
450	1.16	—	1.4	1.4
500	1.6	—	2.3	2.3
550	2.5	—	3.5	3.5
550	3.9	—	3.2	3.2
600	2.11	—	3.8	3.8
600	1.4	—	4.3	4.3
600	1.16	—	3.6	3.6
650	1.16	0.2	5.3	5.5
700	2.95	—	6.75	6.75
700	1.6	—	4.9	4.9
750	2.13	0.5	6.0	6.5
800	1.72	—	9.5	9.5
800	1.78	0.8	8.3	9.1
900	2.44	0.8	13.0	13.8
900	1.09	0.8	12.8	13.6
900	1.75	2.5	13.0	15.5
950	1.09	1.8	13.5	15.3
1000	1.5	2.75	14.75	17.5
1000	1.83	Total		20.5
1000	1.84	Total		19.5
1100	1.89	Total		18.5
1100	1.89	Total		20
1100	1.69	Total		23
1100	1.75	Total		28
1150	1.86	Total		21
1200	1.67	Total		31

tetrad axis, then the energy of this system, with an interstitial nitrogen atom at the centre, would be less than for an octahedron containing no silicon atom. The expansion required by the interstitial nitrogen atom is partially compensated by the contraction required by the silicon atom; the distortion presented to the surrounding lattice is reduced by the presence of silicon. Thus the nitrogen atoms will prefer to sit in octahedra of which the tetrad axes contain silicon atoms. Considering specifically the internal friction mechanism, under an alternating stress the nitrogen atoms will jump into equivalent sites around the silicon atoms. The activation energy corresponding to jumps for these sites will be less than for Fe-sites due to the energy gained by also accommodating a silicon atom. It is assumed that this type of jump gives rise to curve (b) of Fig. 2 and has been called a Si-site jump.

Calculation of a diffusion coefficient from the jump processes giving rise to the internal friction peaks reported here, assumes that the jump is one step of a random walk problem.<sup>16</sup> This gives rise to Eq. (3). On this basis a diffusion coefficient could be calculated for curve (b) and has, in fact, been carried out in Table I and in the plotting of Fig. 2. The resulting diffusion coefficient is very small in comparison with that for Fe sites. However, there is a strong tendency for nitrogen atoms occupying interstices in octahedra containing silicon atoms to move only through these octahedral sites. The relative scarcity of such octahedra in this dilute alloy (5.5 at.% Si) automatically implies that the nitrogen atoms associated with silicon atoms

will not take part in bulk diffusion to any great extent. In general, they will take part in bulk diffusion only when they have broken away from silicon atoms. They will then contribute to the peaks giving rise to curve (a) in Fig. 2. Thus it may not appear valid to calculate a diffusion coefficient for curve (b) and to arrive at an activation energy for the process. However, the plot in Fig. 2 is equivalent to a plot of  $-\log(\text{constant} \times \text{frequency of oscillation})$  versus  $1/T$ . This in turn is equivalent, from Eqs. (2) and (4), to a plot of  $-\log(\text{constant} \times \text{relaxation time})$  versus  $1/T$ . The slope of curve (b) is thus the activation energy for the jump process involved.

Ferro<sup>17</sup> has recently observed a magnetic after-effect in iron-4% silicon-nitrogen alloys, giving an activation energy of 12 kcal/mole. Presumably this is explainable on the same basis as curve (b) of Fig. 2.

Curve (c) is of doubtful origin. It is suggested that the internal friction peaks giving rise to this curve are due to nitrogen atoms sitting in the vicinity of nitride precipitated particles. This corresponds to Fast and Meijering's treatment<sup>5</sup> of the Fe-V-N system. Further work is needed to determine the origin of these peaks. Sites with two or more Si neighbors will be very rare and will probably not contribute to the measured peaks.

#### DETERMINATION OF SOLUBILITY OF NITROGEN

The height of the internal friction peak is proportional to the number of interstitial solute atoms in random solution. As shown above, for the Fe-Si-N system there are two peaks to be considered. The solubility is the sum of these peak heights. The proportionality between peak height and number of interstitial atoms taking part in the jump process, depends (a) upon the distortion introduced into the lattice by the presence of the interstitial atom, and (b) upon factors common to both jump processes for Fe-sites and Si-sites. It will be seen from the results reported below that the Si-site peak is always much greater than the Fe-site peak. The error introduced by the assumption that the distortions are equal for nitrogen atoms in both sites should not be greater than a few per cent. Since this applies to a small contribution to the total solubility it has been ignored. The accuracy in determination of any point on the solubility curve is probably about  $\pm 5$  per cent. This will be referred to later.

Two major assumptions were made in order to interpret the results: Firstly, that the time taken to measure the internal friction curve did not allow appreciable precipitation to occur during measurement. Work on precipitation will be reported later. For the purposes of the present work each peak was determined more than once. One of the successive determinations was measured only at the peaks. This showed that aging did not introduce a serious error. The second assumption was that the curve of internal friction versus temperature could be analysed quantitatively in

terms of the two jump processes considered. This point will be dealt with forthwith.

The form of the internal friction-temperature curve, Eq. (1), can be rewritten as

$$\frac{\delta}{\pi} = \Delta(P + P^{-1})^{-1}, \quad (6)$$

where

$$P = \omega\tau = \exp\left[\frac{Q}{R}\left(\frac{1}{T} - \frac{1}{T_p}\right)\right] \quad (7)$$

and  $T_p$  is the temperature of the peak. A theoretical curve can thus be fitted to the experimental points, for the major peak corresponding to the Si-sites. The minor peak can then be measured graphically.

#### EXPERIMENTAL RESULTS

These are summarised in Table II. The important errors are as follows:

- (i) the temperature of quenching is known to better than  $\pm 5^\circ\text{C}$  at  $1000^\circ\text{C}$  and  $\pm 2^\circ\text{C}$  at  $300^\circ\text{C}$ . This error is insignificant compared with others, although for quenching temperatures much above  $1000^\circ\text{C}$  the speed of quenching is decidedly variable. As a consequence, no weight is attached to points above  $1000^\circ\text{C}$ .
- (ii) estimation of the background damping.
- (iii) estimation of the best-fit curve.

These latter two errors have been estimated for each temperature of quenching. The total error is less than  $\pm 5$  per cent in the final value for the solubility.

It is significant that there are measurable Fe-site peaks only for high quenching temperatures.

Table II gives solubility in terms of arbitrary units. An absolute value was obtained by nitriding specimens to levels of 0.003, 0.004, 0.006, and 0.008 wt. % N, and then determining the peak height after quenching from  $900$ – $1000^\circ\text{C}$ .

Chemical analysis and internal friction analyses are given in Table III. Chemical analysis was carried out by a modification of the Kjeldahl method.<sup>18</sup>

The final solubility-temperature curve from Tables II and III is given in Fig. 4.

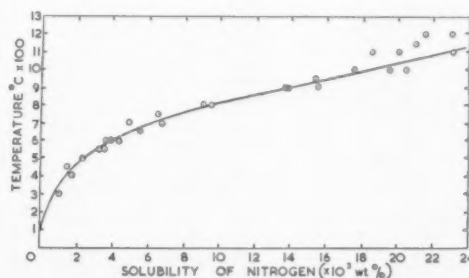


FIG. 4. Solubility of nitrogen in 2.83 wt. % silicon iron in equilibrium with a precipitated nitride.

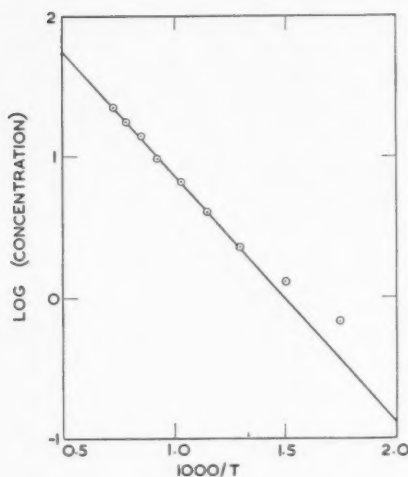


FIG. 5. Data for solubility of nitrogen in silicon iron in the presence of a nitride, in the form of log (concentration) versus  $1000/T$ .

For a perfect solid solution the solubility  $C$  in equilibrium with a precipitated second phase is given by

$$\ln C = -\frac{\Delta H}{RT} + \text{constant}, \quad (8)$$

where  $\Delta H$  is the heat of solution per gram atom of nitrogen. Figure 5 shows a plot of  $\log C$  versus  $1/T$  for the results of Table II.  $\Delta H$  can be calculated from the slope of this curve and is equal to 8 kcal. Thus the solubility  $C$  wt. % is given by

$$\log C = -\frac{4000}{2.3T} - 0.42. \quad (9)$$

#### DISCUSSION

The final solubility curve shown in Fig. 4 is nominally for an alloy containing 2.83 per cent silicon. Obviously for specimens quenched from  $300^\circ\text{C}$  most of the nitrogen is in the form of a precipitated nitride. There is some evidence<sup>19</sup> that this is not silicon nitride  $\text{Si}_3\text{N}_4$ . It is possible that it is a complex iron nitride containing silicon. In other words measurements for low quenching temperatures correspond to alloys containing less than 2.83 per cent silicon in solution. Assuming that  $\text{Si}_3\text{N}_4$  represents the maximum amount of silicon with which nitrogen can combine, then even for an alloy containing 0.01 wt. % nitrogen, this can combine with only 0.015 wt. % silicon. The low quenching temperature measurements were made with alloys containing about 0.01% nitrogen. Thus the error introduced is negligible.

The most significant point is that the solubility of nitrogen in iron is reduced by more than an order of magnitude by the addition of 5.5 at.% of silicon. Almost all the nitrogen atoms in silicon-iron have been

shown to be associated with octahedra containing a silicon atom. This also entails a reduction in the total soluble nitrogen content; this suggests that increase of silicon content might further reduce the nitrogen solubility until nitrogen could no longer be interstitial in silicon-iron. Unfortunately, it may not be practicable to utilize the internal friction technique to investigate this aspect; iron containing more than about 5 wt.% of silicon becomes too brittle to handle by this method.

The results of Corney and Turkdogan<sup>8</sup> showed that the solubility of nitrogen in 2.83 per cent silicon-iron, in equilibrium with 1 atmosphere pressure of nitrogen gas, is about half that for nitrogen in pure alpha-iron at a corresponding temperature. The present results are compatible with this since the precipitated phase in the silicon iron is more stable than iron nitride. Dijkstra<sup>4</sup> suggested that the heats of solution of the two iron nitrides  $\text{Fe}_4\text{N}$  and  $\text{Fe}_{16}\text{N}_2$  were about 8000 cal/g-mole. Borelius,<sup>20,21</sup> however, suggests a heat of solution of about 5500 calories. This would fit equally well with Dijkstra's results. Thus the heat of solution of the present iron-silicon-nitride is some 2000 cal/g-atom of nitrogen greater than that for iron nitride.

Dijkstra and Sladek<sup>6</sup> also investigated the effect of alloying elements on the behavior of nitrogen in iron. Their interpretation of the internal friction curves differs from that given here. The possibility of jumps from Si-sites to Fe-sites (or *vice versa*) corresponds to the jumps postulated by Dijkstra and Sladek for the Fe-Mn-N system. The assumption of the way in which silicon or manganese atoms affect the potential energy of a nitrogen atom in the iron lattice suggests that the energy barrier for jumps from Si- (or Mn-) sites to Fe sites is greater than for jumps in the opposite direction, and is also greater than for Fe-Fe site jumps. Dijkstra and Sladek did not consider Mn-Mn jumps corresponding to Si-Si jumps.

From Equation (1) it becomes immediately apparent that the half-peak width  $\Delta T$  of the internal friction versus temperature curve is given by

$$\Delta T = 2.63 \cdot \frac{R \cdot T_p^2}{Q}, \quad (10)$$

where  $T_p$  is the temperature at which the curve is a maximum. This equation is an approximation, but the error is less than 0.5 per cent for values of  $T_p$  about room temperature and half-peak widths of less than  $50^\circ\text{C}$ . Since this half-peak width is virtually independent of peak height, for a fixed frequency of oscillation, the activation energy for the process is inversely proportional to the half-peak width. Thus the activation energies for the higher-temperature peaks measured both by Dijkstra and Sladek<sup>6</sup> and in the present work are certainly no greater than for Fe-sites. This virtually excludes the mechanism proposed by Dijkstra and Sladek; it also excludes Si-Fe site jumps.

One further aspect of this work has not yet been investigated fully. For low quenching temperatures there is only a negligible peak for Fe-sites. The greater majority of nitrogen atoms sit in Si-sites. As the quenching temperature is raised, the Si-sites peak is raised until at about 700°C a measurable Fe-site peak is observed. This latter peak rises steadily up to 1000°C. For higher quenching temperatures the inaccuracies of the method did not warrant detailed analysis of the peaks. However, the observed tendency was for the Si-site peak to remain roughly constant at a value of 15 (in the arbitrary units of Table II) whilst the Fe-site peak rose steadily. This suggests that the Si-sites are saturated by about 0.015 wt. % nitrogen (0.06 at.%). This suggests that only 1 per cent of the available Si-sites are occupied. This problem can be investigated accurately only by a technique which can resolve the two peaks more accurately—i.e., by the use of a high-frequency method.

### CONCLUSIONS

It has been shown that bulk diffusion of nitrogen in iron containing 2.83 wt. % of silicon is governed by the same diffusion coefficient as in pure alpha-iron. However, the larger part of the nitrogen atoms are closely associated with silicon atoms in the body-centered iron lattice. Below a temperature of about 700°C the number of nitrogen atoms, not associated with silicon atoms, is too small to be detected by the internal friction technique.

The solubility of nitrogen in this alloy in equilibrium with a precipitated nitride has been measured. The silicon alloying content reduces the nitrogen solubility, by comparison with pure alpha-iron, by more than a factor of ten. This solubility is associated with a heat of solution of about 8000 cal/g-atom of nitrogen.

Present evidence suggests that the precipitated phase is not silicon nitride  $\text{Si}_3\text{N}_4$  but is probably a complex iron-silicon-nitride. This problem, together

TABLE III

Quenching temperature °C	Frequency of oscillation sec <sup>-1</sup>	Peak heights		Total in solution Arbitrary units	Chemical analysis wt. %
		Fe-sites	Si-sites		
> 900	1.86	3.4	4.7	8.1	0.008
> 1000	1.86	5.0	4.7	9.7	0.008
900	1.54	0.5	5.3	5.8	0.006
1000	1.63	1.2	4.0	5.2	0.004
950	1.33	0.9	2.1	3.0	0.0026

with an investigation of the mode of precipitation of the nitride is now being studied.

### ACKNOWLEDGMENTS

The authors appreciate stimulating discussions with Dr. K. H. Jack (Kings College Newcastle) and Dr. J. Pearson (BISRA Chemistry Dept.).

### REFERENCES

1. J. L. Snoek, *Physica* **8**, 711 (1941); **9**, 862 (1942).
2. C. A. Wert, *J. App. Phys.* **20**, 943 (1949).
3. S. Harper, *Phys. Rev.* **83**, 709 (1951).
4. L. J. Dijkstra, *Trans. A.I.M.M.E. (J. Metals)* **1**, 252 (1949).
5. J. D. Fast and J. L. Meijering, *Phil. Res. Rep.* **8**, 1 (1953).
6. L. J. Dijkstra and R. J. Sladek, *Trans. A.I.M.M.E. (J. Metals)* **5**, 69 (1953).
7. J. D. Fast and L. J. Dijkstra, *Phil. Tech. Rev.* **13**, 172 (1951).
8. N. S. Corney and E. T. Turkdogan, *B.I.S.R.A. Report MG/A/184/54* (1954). To be published.
9. L. J. Dijkstra, *Phil. Res. Rep.* **2**, 357 (1947).
10. C. A. Wert, *Amer. Soc. Metals Seminar. Modern Research Techniques in Physical Metallurgy*, 225 (1952).
11. W. R. Thomas and G. M. Leak, *Phil. Mag.* **45**, 656 (1954).
12. E. Jette and E. S. Greiner, *Trans. A.I.M.M.E.* **105**, 259 (1933).
13. M. C. M. Farquhar, H. Lipson, and A. R. Weill, *J. Iron Steel Inst.* **152**, 457 (1945).
14. K. H. Jack, *Proc. Roy. Soc. A* **195**, 34 (1948).
15. K. H. Jack, *Proc. Roy. Soc. A* **208**, 200 (1951).
16. J. Polder, *Phil. Res. Rep.* **1**, 5 (1945).
17. A. Ferro, Private communication (1954).
18. B.I.S.R.A. Sub-Committee on Electrical Sheet Methods of Analysis (1954). To be published.
19. W. R. Thomas and G. M. Leak, Unpublished (1954).
20. G. Borelius, *Trans. A.I.M.M.E. (J. Metals)* **3**, 477 (1951).
21. G. Borelius and H. U. Åström, *Acta Met.* **2**, 547 (1954).



## LETTERS TO THE EDITOR

### Isothermal Measurements on the Release of Energy Stored in Cold-Worked Aluminium\*

In the present work the change of the internal energy with time and temperature of deformed high-purity aluminium has been studied by an isothermal calorimetric method. Isothermal measurements of the same kind have previously been reported by Borelius<sup>1</sup> and Borelius, Berglund and Sjöberg<sup>2</sup> on recovery in some metals at 60°C and 100°C. The measurements have now, however, been extended over a larger range of temperature in order to obtain not only recovery but also other relaxation stages.

The calorimetric apparatus was, in principle, the same as that used in earlier investigations with the Borelius type of isothermal microcalorimeter. Owing to the small evolutions of heat, for recovery 0.001–0.03 cal/mole/hr, a number of precautions were made to eliminate or reduce disturbing effects. The specimens, in the shape of small cylinders, 70 mm long and 15 mm in diameter, were prepared from bars of polycrystalline aluminium of a purity of 99.99 per cent. Before cold-working, the samples were annealed and cooled down rather slowly to room temperature. The plastic deformation was made as a compression at room temperature and deformations from some per cent to 45 per cent reduction of the height were used.

The release of stored energy from the cold-worked aluminium was studied by isothermal measurements at successively raised temperatures from 70°C up to 350°C without renewed deformation of the samples. There appeared at different temperatures three different types of rate-of-energy-release-versus-time curves. For the lowest temperatures, below 100°C, hyperbolic curves were always obtained in agreement with Borelius *et al.*<sup>2</sup> Between 180°C and 250°C, however, the measurements gave an exponential relation between rate of energy

and time, and at the highest measuring temperature used, about 350°C, there appeared a maximum followed by an exponential decrease, of a form typical for a nucleation and growth process. The energies released in measurements on a 45 percent deformed specimen are shown in the staple diagram in Fig. 1. The energy values have been obtained by graphical integration of the corrected measuring curves. In this figure the relative Brinell hardness values, measured on the surface of the specimen, have also been plotted.

The first stage in the calorimetric series has been ascribed to recovery. It is distinctly separate from the following as there are measurements between them with practically no evolution of heat. The rate curves for this stage are in agreement with an equation suggested by Borelius<sup>2</sup>

$$\frac{dQ}{dt} = -c.Q. \exp\{-(E-b.Q.)/RT\}, \quad (1)$$

where  $Q$  is the heat still to be given off for full recovery,  $c$  is a constant of the order of the frequency of the atomic vibrations, and  $b$  is a dimensionless number. This equation differs by the factor  $c.Q.$  from a formula for the dissolution of dislocations given earlier by Kuhlmann, Masing and Raffelsieper,<sup>3</sup> having only a constant before the exponential term. Figure 2 shows a typical result of a measurement at 70°C on a slightly deformed specimen. The rate  $dQ/dt$  is plotted against the reciprocal of the time. The curve has been calculated from Eq. (1) with  $c = 8.3 \times 10^{12}$ , which is the atomic frequency for Al,  $b = 15\,000$  obtained from the slope of the first straight part of the curve, and  $E = 26\,700$  cal/mole. From other similar measurements, an average energy of activation for recovery of 28 000 cal/mole was obtained.

As mentioned earlier, in the temperature range 180°C to 250°C exponential curves were obtained. From the

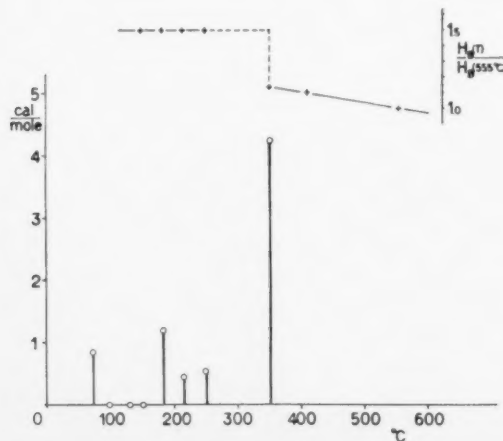


FIG. 1. Energy released by heat treatment of 45% compressed high-purity aluminium and the corresponding hardness values.

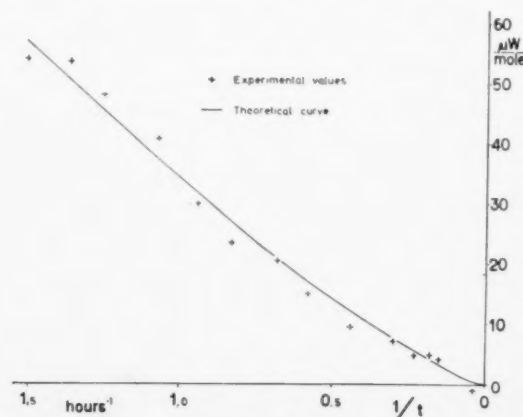


FIG. 2. Rate of energy versus the reciprocal of the time for a slightly deformed high-purity aluminium specimen measured at 70°C.

time constants of the curves for two equally deformed specimens measured at 182.7°C and 205.0°C, an energy of activation of 36 000 cal/mole was calculated, which is in fact the same value as has been ascribed to the self-diffusion effect in aluminium. Further, it was obvious from a microscopic examination that the release of energy at these temperatures, 0.2–1.5 cal/mole, was associated with changes in the substructure of the metal. In order to interpret these results there seem to be two possibilities. One should be that the effect is due to a growth of subgrains, already created during the plastic deformation. The other possible mechanism is a polygonization process.

The results of the calorimetric experiments and the decrease of hardness at about 350°C point to a primary recrystallization process in the specimens at these temperatures. The energy of activation was from measurements at 346.7°C and 353.0°C calculated to 58 000 cal/mole, which value is quite in line with earlier determinations on primary recrystallization. From comparative measurements on specimens, which all had been cold-worked to the same degree, it was found that pre-annealing at about 200°C—that is, in the region of substructure changes—had a marked influence on the recrystallization process.

A more detailed account of results and further discussions will be given elsewhere.<sup>4</sup>

H. U. ÅSTRÖM

Department of Physics  
Royal Institute of Technology  
Stockholm, Sweden

\* Received July 8, 1955.

#### References

1. G. Borelius, *L'état solide*, Inst. Solvay (Bruxelles, 1952), p. 427.
2. G. Borelius, S. Berglund, and S. Sjöberg, *Arkiv f. Fysik* **6**, 143 (1952).
3. D. Kuhlmann, G. Masing, and J. Raffelsieper, *Z. f. Metallk.* **40**, 241 (1949).
4. Hans U. Åström, *Arkiv f. Fysik* (in press), 1955.

#### Effect of Ternary Additions of Silicon and Aluminum on the Ordering Reaction in Iron-Cobalt\*

In recent notes, Oriani<sup>1</sup> and Muldower<sup>2</sup> have commented on the relation between the critical temperature of order,  $T_c$ , and the solidus temperature,  $T_s$ , of a number of alloys. Oriani has observed a correlation between  $T_c$  and  $T_s$  in simple binary alloys of composition  $AB$  and  $AB_3$ . More specifically, he found  $T_c/T_s = 0.63 \pm 0.06$  for alloys of the  $AB$  type and  $T_c/T_s = 0.55 \pm 0.10$  for those of the  $AB_3$  type.

Muldawer has pointed out that when Au is gradually substituted for Ag in the alloys AgZn and AgCd, the ratio  $T_c/T_s$  increases from the values indicated by Oriani to a value of 1.00 at the compositions AuZn

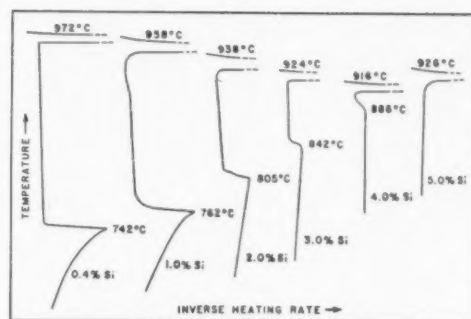


FIG. 1. Inverse rate thermal analysis curves, for alloys containing equal wt. % of Fe and Co, and various wt. % of Si. The upper critical point is the  $\alpha \rightarrow \gamma$  transformation; the lower critical point is related to the ordering reaction.

and AuCd. Muldawer proposed that any generalization concerning the ratio  $T_c/T_s$  should presumably account for the effect of ternary substitutions.

Along somewhat different lines, some data concerning the effect of ternary additions of silicon and aluminum on an alloy containing equal weight percentages of iron and cobalt were obtained. While the substitution of Al and Si in the FeCo structure is not analogous to the replacement of Ag by Au in AgZn or AgCd, it is thought that the effect of the ternary elements on the ordering reaction may be of interest. These data were obtained in the course of unpublished research on the magnetic properties of various ternary Fe-Co alloys.<sup>3</sup>

Figure 1 shows the effect of additions of up to 5 wt % of silicon on inverse-rate thermal analysis curves. The technique employed in obtaining the data was that described by Smith.<sup>4</sup> A heating rate of approximately 2°C per minute was used. The upper transformation temperature indicated is that of longest thermal arrest (on heating) during the  $\alpha \rightarrow \gamma$  phase change. It is seen that increasing silicon contents increase the critical temperature of order and reduce the heat effect due to ordering. At 5.0 wt. % silicon (9.7 at. %) the effect is not discernible, heating either disappeared

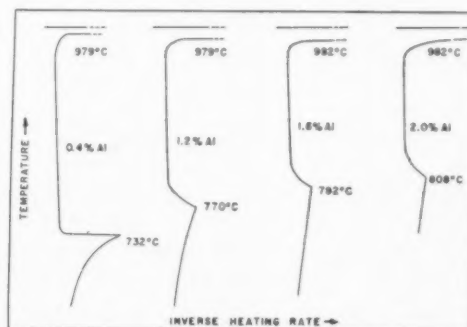


FIG. 2. Inverse rate thermal analysis curves, for alloys containing equal wt. % of Fe and Co and various wt. % of Al. The upper critical point is the  $\alpha \rightarrow \gamma$  transformation; the lower critical point is related to the ordering reaction.

completely, or having been masked by the  $\alpha \rightarrow \gamma$  phase change.

Figure 2 shows the effect of additions of up to 2 wt. % aluminum on inverse-rate thermal analysis curves of similar alloys. In the range of composition investigated, the effect of aluminum on the ordering reaction is similar to that of silicon.

Data of Vogel and Rosenthal<sup>5</sup> indicate that the values of  $T_s$  of the iron-cobalt-silicon alloys investigated decrease with increasing silicon content, and data of Koster<sup>6</sup> indicate the same trend in the iron-cobalt-aluminum alloys. In these cases, then, the ratio  $T_c/T_s$  increases with the ternary addition.

In the present work, no serious effort was made to account for the observed behavior. It might be pointed out however, that both silicon and aluminum form ordered structures with iron, as well as compounds with cobalt.

Incidentally, it was noted that Oriani estimated a value of  $T_c$  for CoFe as approximately 800°C. The actual value is probably about 732°C as obtained by Ellis and Greiner<sup>7</sup> and as reproduced in this laboratory. The change, however, does not appreciably affect Oriani's correlation between  $T_c$  and  $T_s$ .

Acknowledgment is made to the Signal Corps Engineering Laboratory, Fort Monmouth, New Jersey, for support of the work reported herein.

A. J. GRIEST  
J. F. LIBSCH  
G. P. CONARD

Lehigh University  
Bethlehem, Pennsylvania

#### References

1. R. A. Oriani, *Acta Met.* **2**, 343 (1954).
2. L. Muldau, *Acta Met.* **2**, 555 (1954).
3. A. J. Griest, M.S. Thesis, Lehigh University (1951).
4. C. S. Smith, *Trans. A.I.M.E.* **137**, 236 (1940).
5. R. Vogel and K. Rosenthal, *Archiv Eisenhüttenwesen*, **9**, 293 (1935).
6. W. Koster, *Archiv Eisenhüttenwesen* **7**, 263 (1933).
7. W. C. Ellis and E. S. Greiner, *Trans. A.S.M.* **29**, 415 (1941).

\* Received June 1, 1955.

#### Nouvelle Interpretation des Diagrammes a "Side-Bands"

Les diagrammes à "side-bands" ont d'abord été étudiés par Daniel et Lipson<sup>1</sup> et Hargreaves<sup>2</sup> sur des alliages ternaires Cu-Ni-Fe. On en connaît maintenant d'autres exemples.<sup>3,4</sup> Ce type de diagrammes correspond à l'existence dans l'espace réciproque du cristal de paires de satellites disposés symétriquement à petite distance des noeuds du réseau réciproque. La position des satellites est la même autour de chaque noeud, mais leur intensité croît comme le carré de la distance du noeud à l'origine. Prenons comme exemple l'alliage Cu-Ni-Fe étudié par Hargreaves: la phase

cubique homogène n'est stable qu'à haute température (1000°C) et, après trempe et revenu à température modérée (600-800°), la phase unique est remplacée par 2 phases tétraogonales, l'une riche en cuivre et l'autre appauvrie: les deux cristaux ont le même paramètre  $a$  et, pour la première, le paramètre  $c$  est un peu plus grand que  $a$  et pour l'autre un peu plus petit.

Le diagramme à "side-bands" apparaît avant le stade de la séparation de ces deux phases. Il est donc naturel de penser qu'il caractérise un état où les ségrégations sont encore très cohérentes avec le réseau de la matrice. L'interprétation de Daniel et Lipson, et celle plus précise de Hargreaves, sont fondées toutes deux sur l'idée d'une structure *périodiquement modulée* de la solution solide. Des lamelles parallèles aux plans (100) alternativement riches en cuivre et appauvries en cuivre se succèdent régulièrement: Pour les rayons X, tout se passe comme si tous les atomes avaient un facteur de diffusion identique, car les nombres atomiques de Cu, Ni et Fe sont très voisins. On montre que les différents écartements de plans (100) provoqués par les changements de composition doivent produire des "side-bands," conformes à celles qui sont observées. La période de la modulation de la structure déduite de l'écartement des satellites varie suivant les traitements thermiques de 65 à 125 Å.

Un tel modèle de structure périodique soulève de graves difficultés. Comment peut-on expliquer la germination des doubles lamelles à des intervalles réguliers de l'ordre d'une cinquantaine de distances atomiques? Par quel mécanisme de croissance la période de la modulation peut-elle augmenter quand le revenu se produit? La structure primitive devrait complètement disparaître et une nouvelle germination se produirait. Ce n'est pas très vraisemblable, car la variation de l'écartement des "side-bands" est continue.

L'objet de cette note est de signaler que l'hypothèse de la périodicité d'où viennent ces difficultés, n'est pas nécessaire pour rendre compte des diagrammes observés et de proposer un autre modèle de structure. On peut, en effet, rapprocher le phénomène des "side-bands" des diffusions observées au cours du premier stade du durcissement de l'alliage Al-Ag<sup>5</sup>: dans ce cas, des anneaux de diffusion entourent les noeuds du réseau réciproque. On les a expliqués par des *zones* à structure complexe. Chaque zone est formée d'un noyau où se concentrent les atomes d'argent, entourée d'une auréole appauvrie, d'où ces atomes ont migré vers le noyau central. Le point essentiel pour la théorie de la diffraction des rayons X est que le nombre d'atomes d'argent en excès dans le noyau soit égal au nombre d'atomes d'argent marquant dans l'auréole. Les zones sont irrégulièrement distribuées dans la solution solide non modifiée.

Nous admettons que l'alliage Cu-Ni-Fe contient des zones complexes de structure analogue mais en forme de plaquettes parallèles aux plans (100). Une lamelle avec des plans riches en cuivre, donc d'intervalle

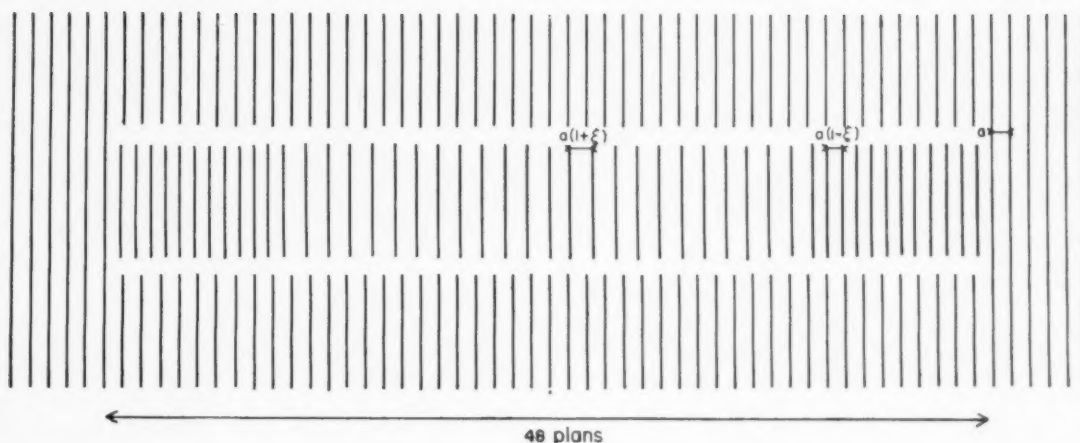


Fig. 1. Schéma d'une zone perturbée insérée dans le réseau normal.

accru, est bordée de chaque côté par une bande appauvrie en cuivre, donc de paramètre inférieur à la normale. La contraction de la bande centrale est exactement compensée par l'expansion de deux bandes latérales, si bien que l'ensemble s'insère dans la matrice sans déformations aux extrémités.

Nous aurions pu supposer aussi une disposition inverse avec une lamelle centrale à paramètre contracté entouré de 2 bandes à paramètre dilaté.

Considérons, par exemple, la zone schématisée suivante (figure 1) les 2 plans d'intervalle  $a(1+\epsilon)$  entourés de deux bandes de  $n$  plans d'intervalle  $a(1-\epsilon)$ , les plans extrêmes de la zone sont confondus avec les plans du cristal régulier de paramètre  $a$ . Un nombre quelconque de telles zones sont incluses dans une suite d'un très grand nombre de plans normaux sans aucune régularité entre elles. Nous supposons que tous les plans ont même pouvoir diffusant. Quand  $\epsilon$  est petit, le calcul de la diffusion produite par la zone conduit au résultat suivant: chaque noeud est entouré d'une paire de bandes symétriques dont le profil est donné par la figure 2 et dont l'intensité est proportionnelle à  $I^2\epsilon^2$ ,  $I$  étant l'ordre du noeud. La zone de structure inverse (au centre plans d'écartement  $a(1-\epsilon)$  bordés par des plans distants de  $a(1+\epsilon)$ ) donne exactement la même figure de diffraction.

La figure de diffraction prévue concorde bien avec les observations. En particulier remarquons que les satellites observés ont toujours une certaine largeur de l'ordre de celle trouvée par les zones de la figure 1 et que le second ordre n'est pas en général observé. Avec l'hypothèse de la structure périodique, au contraire, on prévoit des raies satellites fines: il faut, pour expliquer la largeur observée, ou admettre les variations de période d'un point à l'autre de l'échantillon ou réduire le nombre de périodes de la région modulée, ce qui finalement tend vers la structure de la zone proposée ici.

Le calcul de la figure de diffraction d'une zone perturbée dans le cas général sera publié ailleurs. Nous

citerons ici deux résultats: (1) Pour qu'il apparaisse des satellites nettement détachés du noeud normal, il faut que l'intensité diffusée passe par un minimum nul à l'emplacement du noeud. Ceci exige que dans la décomposition en intégrale de Fourier du déplacement des atomes à partir de la position normale, les coefficients des termes de très grande période soient nuls. C'est ce qui se produit dans le schéma de la figure 1. Par contre, ce ne serait pas le cas pour une zone formée de deux lamelles juxtaposées l'une de  $n$  plans d'intervalle  $a(1+\epsilon)$  et l'autre de  $n$  plans d'intervalle  $a(1-\epsilon)$ . La diffusion produite par une telle zone est une tache dont le maximum coïncide avec le noeud normal: l'expérience permet donc d'éliminer cette structure dans le cas de la décomposition des alliages Cu-Ni-Fe.

(2) Au lieu d'imaginer a priori un modèle et de comparer les diffractions calculées et observées, on peut chercher à déduire directement la structure de la zone des données de l'expérience. Comme dans tout problème de diffraction des rayons X, il n'y a pas une solution unique. Ce qui est seulement possible, c'est de trouver la structure de la zone à centre de symétrie ou d'inversion qui donne les effets de diffusion observés.

Dans la courbe de la figure 2, le rapport de l'écart entre satellite et noeud à la période du réseau réciproque est approximativement égal à l'inverse du nombre total de plans de la zone. Le rapprochement des "side-bands" traduit donc simplement une croissance en épaisseur.

Qualitativement, le processus de la croissance serait le suivant. Le germe de la zone serait un plan (100), par exemple, enrichi en cuivre (en choisissant l'une des deux structures possibles). Les atomes des plans immédiatement voisins sont attirés par ce germe ("up-hill diffusion"): l'origine de cette attraction est la stabilité plus grande, d'une part de la composition enrichie, d'autre part de la composition appauvrie de bandes latérales, puisque la solution solide tend à se décomposer. Par diffusion normale, certains atomes de cuivre passent de la solution solide environnant la



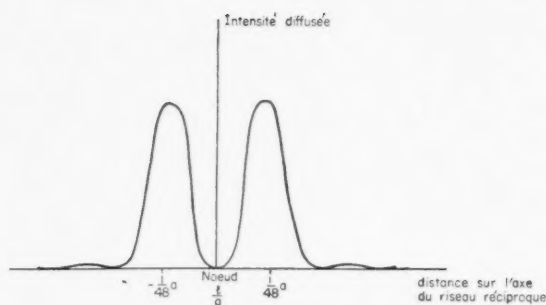


Fig. 2. Variation de l'intensité diffusée le long de l'axe du réseau réciproque normal aux plans de la zone.

zone dans les bandes latérales. Mais ces atomes de cuivre sont en excès par rapport à la composition appauvrie et sont attirés par la bande centrale qu'ils contribuent à épaissir. Ce processus est évidemment d'autant plus lent que les bandes latérales sont plus larges: d'où une taille limite des zones aux températures pas trop élevées. La zone s'accroît quand on augmente les températures de revenu, jusqu'à ce qu'il y ait rupture de cohérence avec la matrice et formation de deux phases à structures cristallines bien caractérisée.

Il apparaît donc, d'après cette analyse, une analogie profonde entre le processus de ségrégation des alliages du type Cu-Ni-Fe et des alliages à durcissement structural bien qu'apparemment les phénomènes de diffraction de rayons X qui les révèlent soient très différents. On voit aussi la possibilité de préciser expérimentalement la structure des zones de ségrégation qui avaient été introduites par les théoriciens (complexes de Dehlinger<sup>7</sup>).

A. GUINIER

Conservatoire des Arts et Métiers  
Paris, France

#### Bibliographie

1. V. Daniel et H. Lipson, Proc. Roy. Soc. A181, 368 (1943); A182, 378 (1944).
2. M. E. Hargreaves, Acta Cryst. 4, 301 (1951).
3. A. H. Geisler et J. B. Newkirk, Trans. A.I.M.E. 180, 101 (1949).
4. J. Manenc, Compt. Rendus. 238, 1817 (1954).
5. C. B. Walker et A. Guinier, Acta Met. 1, 568 (1953).
6. Yin-Yuan Li et R. Smoluchowski, Phys. Rev. 94, 866 (1954).
7. U. Dehlinger et H. Knapp, Zeit f. Metallik. 43, 223 (1952).

\* Received May 24, 1955.

#### Dislocation Densities in Intersecting Lineage Boundaries in Germanium\*

Measurements of linear dislocation densities in intersecting low-angle lineage boundaries in germanium single crystals are described in this letter. The crystals were grown in the [001] direction in a horizontal boat and the lineage boundaries tended strongly to lie in the two {110} planes parallel to the growth direction. It has already been shown, by measurement of etch-pit

spacing and X-ray orientation, that individual boundaries of this type are tilt boundaries consisting of edge dislocations parallel to the growth direction.<sup>1</sup> It is not uncommon for such boundaries to intersect at angles close to 90 degrees, in the form of T's or L's, as viewed in the (001) plane. Such intersections provide a means of testing the grain-boundary theory of edge dislocations, without the need for orientation measurements. Since the sum of the tilt angles,  $\theta$ , encountered in a circuit about the intersection must be zero, the disloca-

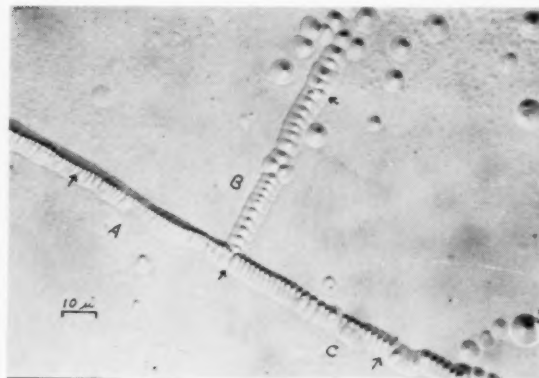


FIGURE 1.

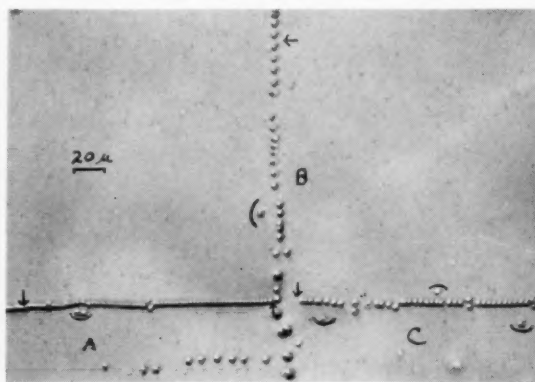


FIGURE 2.

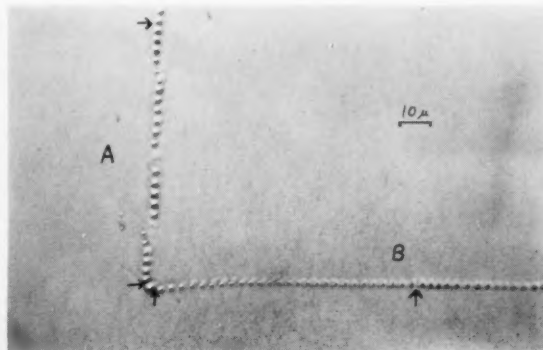


FIGURE 3.

tion densities in the intersecting boundary branches must be simply related. Amelinckx,<sup>2</sup> using equations of Read and Shockley,<sup>3</sup> has already described the case of this relationship, in which the boundary planes have an arbitrary rotation about the [001] axis of a cubic lattice; and he has obtained confirmatory data for rock salt.

The boundaries of the present letter represent a rather ideal case. They may be regarded as lying in  $x$ - or  $y$ -planes of a simple cubic lattice (in the terminology of Read and Shockley) which are parallel to the two {110} planes of the diamond cubic lattice lying parallel to the [001] growth direction. Hence, for each branch,  $\rho = \theta/b$  is the dislocation density, where  $b$  is the Burgers vector,  $(a/2)[110]$  in the germanium lattice. Thus, for an L-intersection,

$$\rho_A + \rho_B = 0, \quad (1)$$

and for a T-intersection,

$$\rho_A + \rho_B + \rho_C = 0, \quad (2)$$

where the subscripts denote the branch of the intersection, and the material in the general vicinity of the boundaries is assumed to be free of macroscopic elastic strain. Since the etchant used, CP-4,<sup>†</sup> does not differentiate edge dislocations with regard to sign, the densest branch in a T-intersection must be chosen by inspection in checking Eq. (2).

In the five T- and three L-intersections for which etch-pit densities were measured, good agreement was found with Eqs. (1) and (2), as shown by the data in Table I. In rows 1 to 5, which are for T-intersections, the densest branch was designated leg A. In each case the same length was counted in each branch. Photomicrographs of boundaries 1, 2, and 7 appear in Figs. 1, 2, and 3, respectively. In making the counts it was difficult to judge whether to include dislocations lying near but not in a boundary. It was noted in several instances that if all such were excluded, the count was usually low for the branch in question, as judged by agreement with Eq. (2). Hence it appears that certain of these dislocations differ in sign. Branch B of Fig. 1 and branches A, B, and C of Fig. 2 contain doublets, to which attention has been called by Oberly.<sup>4</sup> Presumably these are of the same sign as the others in the boundary, as the members of a doublet give the impression of repelling each other.

The agreement between simple theory and experimental observation strongly suggests that the observed boundaries consist entirely of edge dislocations parallel to the growth direction. Had rotations about axes normal to the growth direction been present, then, in general, such agreement could not have been obtained, as such rotations would have produced screw dislocations, presumably revealable by etching,<sup>2</sup> in one branch and edge dislocations, which would be parallel to the view plane and hence invisible, in a perpendicular branch.

TABLE I. Etch-pit density in branches of T- and L-intersections.

Boundary number	Actual length counted (microns)	Etch-pits per 100 microns			
		Branch A	Branch B	Branch C	Branches B+C
1	50	90	40	52	92
2	155	47	14	30	44
3	10	170	120	50	170
4	40	132	67	72	139
5	60	53	43	7	50
6	80	34	33		
7	50	58	58		
8	123	23	23		

Boundary intersections whose branches do not all lie in {110} planes have also been observed in these crystals and are being studied. In general, these are less regular in shape and dislocation density than those shown here, as might be expected.

W. G. PFANN  
L. C. LOVELL

Bell Telephone Laboratories  
Murray Hill, New Jersey

#### References

1. F. L. Vogel, W. G. Pfann, H. E. Corey, and E. E. Thomas, Phys. Rev. **90**, 489 (1953); F. L. Vogel, Acta Met. **3**, 245 (1955).
2. S. Amelinckx, Acta Met. **2**, 848 (1954).
3. W. T. Read and W. Shockley, Phys. Rev. **78**, 275 (1950).
4. J. J. Oberly, J. Metals **6**, 1025 (1954).

\* Received May 31, 1955.

† 15 cc glacial acetic acid, 25 cc HNO<sub>3</sub>, 15 cc 48% HF, plus a few drops of bromine.

#### Internal Deformation Markings in Single Crystals of Cu<sub>3</sub>Au\*

In the course of an extensive study of the mechanism of stress cracking in Cu<sub>3</sub>Au polycrystals and single crystals,<sup>1</sup> it has been demonstrated that copper is preferentially removed from the alloy at specific structural sites by immersion in ferric chloride. Some of the structural sites are associated with growth history, grain boundaries, incoherent twin boundaries and sub-boundaries; other sites are produced by plastic deformations. In either case, the selective removal of copper occurs at sites characterized by imperfections in the crystal structure. The present work concerns deformation structures observed in the body of the crystal as a result of removal of copper along structural paths originating at the surface.

Cu<sub>3</sub>Au single crystals were grown by the Bridgman technique in evacuated quartz tubes. The crystals were homogenized for 300 hours at 850°C and quenched in water. The deformation of the crystals discussed below was approximately 5 per cent.

Figure 1 illustrates the type of preferential attack occurring along surface traces of slip bands after plastic deformation. In this particular crystal, the plane of polish is (114). A similar crystal was strained a few

per cent and immersed in 2 per cent ferric chloride for three months. Following immersion, the crystal was sectioned on a plane parallel to the (111) plane of the slip traces. The structure observed on this plane is shown in Fig. 2. To aid in the analysis of the deformation structure, a set of new slip traces, cutting through

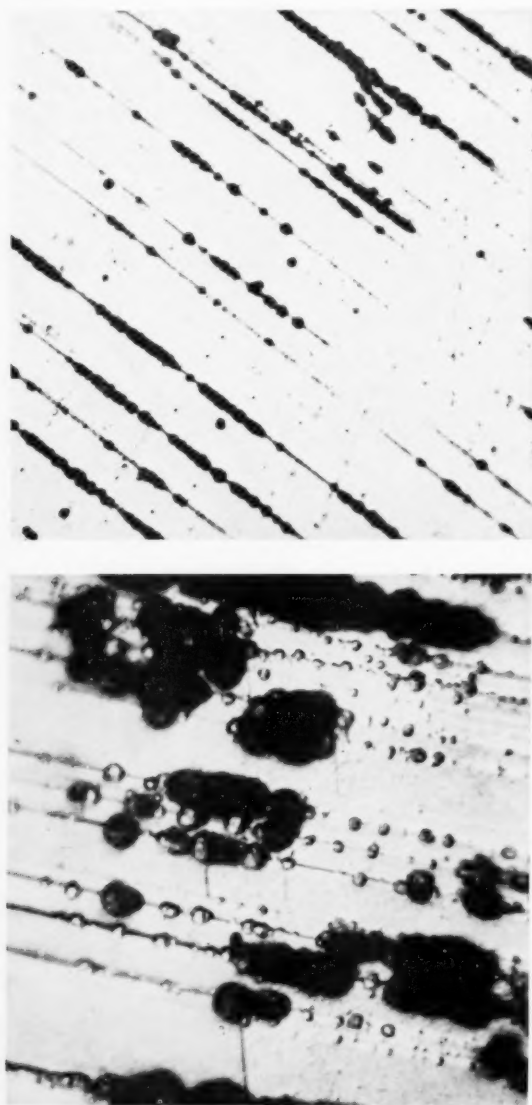


FIG. 1. Preferential attack along slip traces of  $\text{Cu}_3\text{Au}$  in a surface parallel to (114) plane. 200X and 2000X.

the plane of polish, were produced by compressing the polished crystal and these slip bands can be seen in Fig. 3.

In Fig. 1 it is clear that the attack is localized to specific sites lying in the surface traces of the slip bands. In Figs. 2 and 3 corresponding to the (111) plane, it appears that copper has been preferentially removed



FIG. 2. Appearance of cross section parallel to the (111) plane after three months immersion in 2%  $\text{FeCl}_3$  (aq.) 200X.

from two types of structural paths; these are the traces of a second slip plane and curved paths lying in the principal slip plane.

The straight lines at 60 degrees to the new slip traces evidently correspond to a second set of slip planes operating during the initial deformation, and cutting across the primary slip planes. The line of intersection appears as a zone of high activity with respect to the removal of copper as would be anticipated from the local stress associated with a slip plane intersecting the primary slip plane.

In addition to the reacted trace of the second (111) plane, more or less curved traces appear as isolated segments of some length. These curved traces are characteristic of the (111) plane and do not occur on a random plane cut through the crystal, of which Fig. 4 is typical.

That the traces delineated by preferential removal of copper are associated with strained regions is clearly shown in Fig. 5 in which a local indentation was made in the crystal and a random section taken after prolonged immersion. It is evident that strain has penetrated deeply into the crystal and that the structure-dependent



FIG. 3. Cross section parallel to (111) plane with additional slip traces produced subsequent to immersion. 300X.

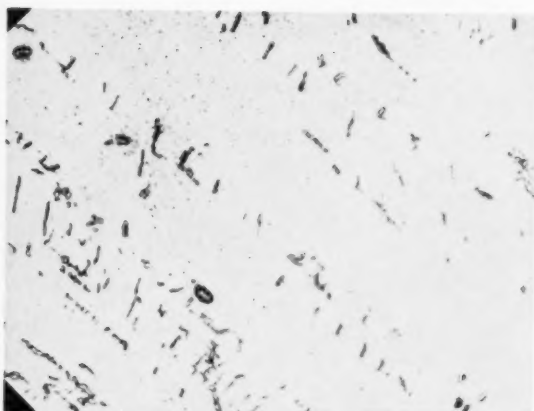


FIG. 4. Random cross section through the deformed crystal after 3 months immersion in ferric chloride 2% (aq.) 300X.

removal of copper is largely confined to this region, except for occasional lines of attack probably associated with the growth structure, which may be seen after suitable etching.

It appears that the simplest interpretation is that these structures correspond to the strained regions along lines of dislocation loops generated during plastic deformation. The fact that only short segments appear is to be expected since the plane of sectioning is not perfectly parallel with (111); furthermore, since copper is removed from a strained region of some volume and in time penetrates into the adjacent crystal of higher perfection if there exists a structural path for the exit of copper ions to the surface, the expected pattern is one of sections of annular rings cut at a shallow angle, which is in accord with Figs. 2 and 3. It might also be expected that there should be some relation between the loops and the principal slip vector which lies along one of the slip traces; however, while there is perhaps a loose connection, it is not clearly evident from the present observations.



FIG. 5. Preferential removal of copper in strained region produced by local indentation after 3 months immersion in ferric chloride (2%) (aq.) 100X.

In conclusion, the evidence suggests that the edge component of dislocations operating in the slip process are rendered visible by the preferential removal of copper in the strained region at surface traces of slip; dislocation loops are similarly observable in the plane of slip after prolonged immersion and progressive removal of copper along the length of the loop.

R. BAKISH†

W. D. ROBERTSON

Hammond Metallurgical Laboratory  
Yale University  
New Haven, Connecticut

#### Reference

1. R. Bakish and W. D. Robertson, submitted to J. Metals, A.I.M.E.

\* Received May 10, 1955.

† Now at Sprague Electric Company, North Adams, Massachusetts.

#### Hardness of Germanium-Silicon Alloys at Room Temperature\*

The preponderance of data on binary metal alloy systems shows that the hardness, yield strength, tensile strength, and rate of strain-hardening of an element increases with the addition of solute atoms. When complete solid solution exists between two metals, a maximum usually occurs in the hardness *versus* concentration curve. Present work on the hardness measurements of germanium-silicon alloys, however, shows some interesting results which deviated from this general observation.

Both germanium and silicon are Group IV elements having a diamond cubic structure. The phase diagram of the germanium-silicon system has been determined by Stöhr and Klemm<sup>1</sup> and was found to have complete solid solubility. The lattice constants of these two elements differ only by four per cent, while those of the alloys follow Vegard's Law closely with a slight negative deviation. Homogeneous germanium-silicon alloys prepared by a method<sup>2</sup> mentioned earlier were used in the hardness measurements. On these alloys, as well as on pure germanium and pure silicon, hardness indentations have been made using a Leitz microhardness tester (Durimet). Figure 1 shows photomicrographs of the indentations taken with 100 gram load. Indentations made with a Knoop hardness indenter usually leave no cracks as shown in Fig. 1 (b). This is true whether the material is germanium, silicon, or germanium-silicon alloy. However, the indentations made with Vickers diamond pyramid indenter always result in cracking at the corners of the indentations as shown in Fig. 1 (a). The cracks are not necessarily formed during the testing because on one occasion, at least, the cracks appeared about two seconds after the load was removed.



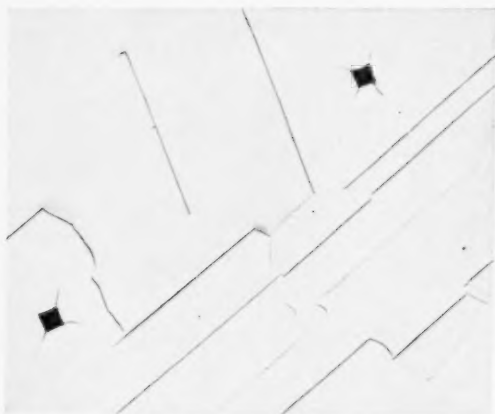


FIG. 1 (a). Vickers hardness indentations on a germanium-silicon alloy of 10 atomic per cent silicon. 100 g load. 250X.

Since hardness numbers are not independent of the load applied to the indenter, a fixed load of 100 g was used to make all the indentations so that alloys of differing hardness could be compared. Loads heavier than 100 g cause chipping and spalling, and render the measurements very difficult. Time of loading was standardized at 15 sec. Surfaces to be tested were etched with an aqueous solution of  $\text{HNO}_3$  and  $\text{HF}$ .

Hardness values as read from such small indentations are scattered widely for each alloy as shown in Fig. 2, which is a plot of hardness *versus* concentration for the germanium-silicon alloys. Each hardness point is an average of a least six hardness indentations. In spite of the large scatter of the data, an interesting fact is that there is no apparent maximum in the hardness-*versus*-concentration curves. Thus, it is to be concluded that silicon is actually softened as the solute atoms of germanium are added.

The hardening of an element by the addition of solute atoms has been explained by Mott and Nabarro<sup>3</sup> and by Cottrell<sup>4</sup> on the basis of interaction between

dislocations and solute atoms. More recently, Fisher<sup>5</sup> has pointed out the influence of short-range order on hardening. In addition, Dorn, Pietrokowsky and Tietz<sup>6</sup> found on some aluminum alloys that part of the solid solution hardening should be attributed to a valency effect. The solute atoms with a larger valence difference from the host element have a greater hardening effect.

The present case in which silicon is softened as the germanium is added cannot be explained on the basis of solution hardening for ordinary metallic systems. In addition, the fact that hardness seems to vary linearly with composition would appear to suggest that the hardness of the alloy at room temperature may be proportional to the number of different kinds of bonds which are present.

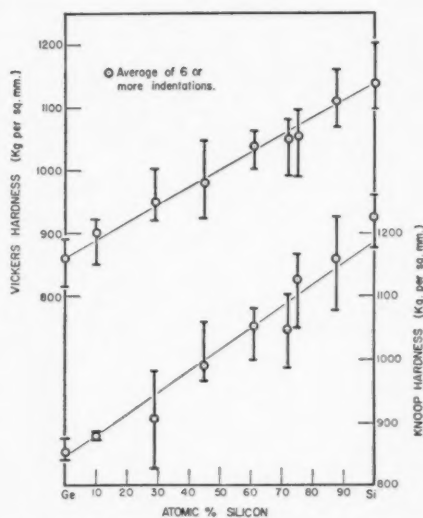


FIG. 2. Indentation hardness of germanium-silicon alloys. 100 g load.

This work was sponsored by the Bureau of Ships under Contract No. NObsr-63180.

C. C. WANG

B. H. ALEXANDER

Sylvania Electric Products, Inc.  
Ipswich, Massachusetts

#### References

1. H. Stöhr and W. Klemm, *Zeit. für anorg. und allgem. Chem.* **241**, 305 (1939).
2. C. C. Wang and B. H. Alexander, A.I.M.E. Symposium on Semiconductors February 15-18, New York, 1954.
3. N. F. Mott and F. R. N. Nabarro, *Report on the Strength of Solids*, Physical Society, London (1948); N. F. Mott, *Imperfections in Nearly Perfect Crystals*, edited by W. Shockley (John Wiley, New York, 1952).
4. A. H. Cottrell, *Report on the Strength of Solids*, Physical Society, London (1948).
5. J. C. Fisher, *Acta Met.* **2**, 9 (1954).
6. J. E. Dorn, P. Pietrokowsky, and T. E. Tietz, *Trans. A.I.M.E.* **188**, 933 (1950).

\* Received May 3, 1955.



FIG. 1 (b). Knoop hardness indentation on a germanium-silicon alloy of 10 atomic per cent silicon. 100 g load. 250X.

## SOME CURRENT PAPERS IN OTHER JOURNALS

### Acta Crystallographica, Vol. 8

Part 8, August 1955 (Partial Contents).

Relations between the phases of structure factors. W. Cochran.  
A generalized treatment of cold work in powder patterns. B. E. Warren.  
Compounds of uranium with the transition metals of the second and third long periods. T. J. Heal and G. I. Williams.  
The determination of the elastic constants of germanium by diffuse X-ray reflexion. S. C. Prasad and W. A. Wooster.

### Archiv für das Eisenhüttenwesen

Heft 6, Juni 1955

Die Verbesserung von Silikasteinen durch Zusatz von Aluminium-Orthophosphat. G. Trömel und K.-H. Obst.  
Zur thermodynamischen Analyse. II. Die Wärmehaltskurve eines Stoffes aus einem einzigen kalorimetrischen Versuch. W. Oelsen, K.-H. Reiskamp und O. Oelsen.  
Spektrochemische Bestimmungen an Tonen und Schamotten. G. Hartleif und H. Kornfeld.  
Beitrag zur photometrischen Bestimmung des Molybdäns im Stahl. J. Bünger.  
Zusammenhang zwischen dem Auftreten von Verformungszwillingen und der Bruchart beim  $\alpha$ -Eisen. H. Buchholtz, F. Braumann und A. Eier.  
Das Dreistoffsystem Eisen-Kobalt-Vanadin. Teil I. Ausbildung des Dreistoffsystems bei gehemmter  $\alpha/\gamma$ -Umwandlung. W. Köster und H. Schmid.  
Ermittlung von Eigenspannungen an wasserabgeschreckten Stahlzylindern. H. Bühler und H. Hendus.  
Einfluss äußerer Spannungen auf die Martensitbildung. W. Schmiedel und H. Lange.

Heft 7, Juli 1955

Über den Werkstoff des Schweißeisen-Zeitalters. E. H. Schulz.  
Die Auflösung von Kohlenstoff in flüssigem Eisen. O. Dahlke und O. Knacke.  
Zur Rückstandsanalyse von Roheisen und Gusseisen. Teil II: Trennung der Isolate. A. Wittmoser und W.-D. Gras.  
Untersuchung der Abschreckalterung weicher unlegierter Stähle mit radioaktiven Isotopen, besonders Kohlenstoff  $C^{14}$ . H.-K. Görlich, H. Goossens und H. Schenck.  
Elektrochemische Untersuchungen der Korrosion von  $\alpha$ -Eisen-Einkristallen in verdünnten Säuren. H.-J. Engell.  
Die Anfangspermeabilität einiger Eisenwerkstoffe bei mechanischer Beanspruchung. W. Jellinghaus und K. Janssen.  
Das Dreistoffsystem Eisen-Kobalt-Vanadin. Teil II. Die Aus-

bildung des Dreistoffsystems bei Gleichgewicht zwischen  $\alpha/\gamma$ -Mischkristallen. W. Köster und H. Schmid.

### Journal of the Institute of Metals, Vol. 83

Part 10, June, 1955.

Presidential address. Maurice Cook.  
The effect of nitrides and ternary intermetallic compounds on the Young's modulus of some aluminium alloys. N. Dudzinski.  
Plastic deformation of aluminium -3.5% copper alloy single crystals. K. M. Carlsen and R. W. K. Honeycombe.  
A three-dimensional faced-centred cubic model for the study of crystal phenomena. P. R. Rowland.  
Tensile properties of some titanium alpha solid solutions up to 600°C. J. W. Suiter.

Part 11, July, 1955.

Creep behaviour at 300°C of a group of precipitation-hardening alloys based on the alpha copper-aluminum phase. J. P. Dennison.  
The equilibrium diagram of the system nickel-titanium. D. M. Poole, and W. Hume-Rothery.  
The solid solubility of chromium carbide,  $Cr_3C_2$ , in titanium carbide. A. Carter.  
A study of the titanium-germanium system in the region 0-11 atomic per cent germanium. (Mrs.) M. K. McQuillan.  
Equilibrium relations at 460°C in aluminium-rich alloys containing 0-7% copper, 0-7% magnesium, and 2.0% silicon. H. J. Axon.  
Mechanical twinning in molybdenum. R. W. Cahn.

Part 12, August, 1955.

The system uranium-titanium. A. G. Knapton.  
Some observations on constitutional changes in copper-aluminium alloys at temperatures below that of the  $\beta \rightleftharpoons \alpha + \gamma_2$  eutectoid. D. R. F. West and D. Lloyd Thomas.

### Journal of Metals, Vol. 7

August, 1955 (Partial Contents).

Some studies of Al-Cu and Al-Zr solid state bounding. S. Storchheim.  
Relation of flake formation in steel to hydrogen, microstructure, and stress. A. W. Dana, Jr., F. J. Shortsleeve, A. R. Troiane.  
Activity of sulphur in liquid Fe-Ni alloys. J. A. Cordier, J. Chipman.  
Production of zirconium diboride from zirconia and boron and carbide. C. T. Baroch, T. E. Evans.  
Continuous ion exchange. R. McNeill, E. A. Swinton, D. E. Weiss.  
On the loss of texture in tapes of a 50 pct Ni-50 pct Fe alloy. S. Spachner, W. Rostoker.

VOL.  
3  
1955

# THEORY OF THE FORMATION OF LATTICE DEFECTS DURING PLASTIC STRAIN\*

H. G. VAN BUEREN†

A simple theory is presented by which a relation between the plastic strain and the concentration of vacancies, interstitials and dislocations is obtained. Dislocations are formed by sources under the action of an applied stress, the other defects by the movement of jogs in the dislocations. The action of a dislocation source under a varying stress is studied, for the case of static as well as of dynamic generation. After the first few per cent of strain, both methods of generation yield the same defect concentrations. By suitable elimination, the influence of workhardening can be left out of the theory. The results apply to zero temperature and plastic strains of 0.05 up to 1. They are compared with the observed critical shear stress, the elementary structure and the resistivity-strain relations in slightly deformed copper.

## THÉORIE DE LA FORMATION DES DÉFAUTS RÉTICULAIRES PENDANT LA DÉFORMATION PLASTIQUE

Il est présenté une théorie simple donnant une relation entre la déformation plastique et la concentration des lacunes, atomes interstitiels et dislocations. Les dislocations sont formées par des sources sous l'action de la contrainte appliquée, tandis que les autres défauts résultent des "jogs" dans les dislocations. L'effet d'une contrainte variable sur une source de dislocations est étudié aussi bien pour la formation statique que dynamique. Après les premiers pourcent de déformation, les deux modes de formation conduisent à la même concentration de défauts. Par un artifice approprié, l'influence de l'écrouissage peut être éliminée de la théorie. Ces conclusions s'appliquent aux déformations à basses températures allant de 0,05 à 1 et elles sont comparées au cisaillement critique, à la structure élémentaire et à la relation résistivité-déformation dans le cuivre faiblement déformé.

## EINE THEORIE DER BILDUNG VON GITTERFEHLSTELLEN BEI DER PLASTISCHEN VERFORMUNG

Es wird eine einfache Theorie beschrieben, durch die die Zusammenhänge zwischen der plastischen Verformung und der Konzentration von Leerstellen, Einlagerungen und Versetzungen gedeutet werden können. Unter der Einwirkung einer angelegten Spannung bilden sich aus den Quellen die Versetzungen; die anderen Fehlstellen entstehen durch die Bewegung der Treppenstufen ("jog-Sprung") in den Versetzungen. Für den Fall der statischen, wie auch für den der dynamischen Wirkung, wird das Verhalten einer Versetzungsquelle bei unterschiedlicher, angelegter Spannung untersucht. Beide Wirkungsweisen führen nach den ersten wenigen Prozenten Verformung zu den gleichen (resultierenden) Fehlstellenkonzentrationen. Durch eine geeignete Eliminierung kann der Einfluss der Verfestigung aus der Theorie eliminiert werden. Die Ableitungen müssten bei niedriger Temperatur und Verformungen zwischen 0.05 und 1 gültig sein. Sie werden mit den beobachteten Werten der kritischen Schubspannung, der Elementarstruktur und den Widerstands-Verformungs-Beziehungen in wenig verformtem Kupfer verglichen.

### 1. INTRODUCTION

It is generally accepted that plastic deformation of crystals, especially of metals, is governed by the action of dislocation sources under the influence of the applied stress. Another well conceived idea is the formation of vacancies and interstitials during deformation by some mechanism connected with the mutual crossing of dislocations. In this paper a theoretical discussion of the detailed processes occurring in deformed crystals is attempted and applied to the case of simple f.c.c. metals such as copper, deformed at very low temperature, where no thermal activation takes place. Section 2 deals with the behaviour of dislocation sources under a varying applied shear stress. It will be shown that the hypotheses of static and dynamic generation of dislocations yield approximately the same results. In section 3 theoretical relations are derived between the concentrations of the various kinds of lattice defects formed during the deformation, and the amount of plastic

strain. In section 4 a comparison is made between the theoretical deductions and the observed phenomena, notably the strain dependence of the electrical resistivity of copper.

### 2. FRANK-READ SOURCE UNDER VARYING STRESS

We consider a dislocation source of length  $l$ . Several kinds of sources have been proposed in literature: the classical Frank-Read source that emits dislocation loops in one atomic plane only, and sources of a more general type, that produce loops on successive atomic planes.<sup>1,2</sup> The following treatment applies to all these sources. The critical shear stress for activation of a source is

$$\tau_1 = \frac{\alpha G b}{l}, \quad (1)$$

where  $G$  is the shear modulus,  $b$  the Burgers vector of the source, and  $\alpha$  a numerical constant of order unity. Let the number of emitted dislocation loops be  $n$  and the area covered by them be  $A$ . This area is determined by the local stress  $\tau$  near the source in the following way.

\* Received February 21, 1955.

† Philips Research Laboratories, N. V. Philips' Gloeilampenfabrieken, Eindhoven, Holland.



Let the density of randomly distributed dislocations in the crystal be  $D_0$ . Presumably these dislocations are arranged in a spatial network, the elements of which can each in their turn act as sources. A loop of area  $A$  has crossed  $AD_0$  dislocations, and has formed  $AD_0$  jogs. The jogs have run a distance of the order  $A^{1/2}$ , and, assuming that the dislocation loop retains its shape on expansion, have left in their wake a number of defects (vacancies or interstitials) which is given by

$$f = \frac{\beta A^{1/2} D_0}{b}, \quad (2)$$

where  $\beta$  is a numerical constant which depends on the shape of the loop and on the efficiency with which the jogs form defects. For a circular loop moving in a field of pure screw dislocations perpendicular to its plane  $\beta = 2/3\pi^{5/2} \approx 0.04$ ; in general  $\beta$  will be smaller, say, 0.02.

It may be argued<sup>2</sup> that in actual cases the efficiency of defect formation is much less, as jogs in successive loops can eliminate each other. However, if the loops follow each other in distances of the order of a thousand atomic distances, this process will not take place. Also, jogs may move along the loop instead of with them, or may perform a combined motion. In order not to produce defects, this motion must conform to rather severe restrictions, which makes it improbable that this effect reduces the efficiency of defect formation appreciably.

Let the mean energy of formation of a defect be  $U$ . It can easily be shown that the energy needed to form these defects in copper for instance, is larger than that involved in the formation of jogs and increases much faster than the latter and than that involved in the elongation of the dislocation line. The energy of defect formation is then the leading factor in the energy-balance governing the expansion of a dislocation loop. Thus, in sufficient approximation, this expansion is associated with the storage of an amount of energy of about  $fU_f$ .

The energy supplied by the local shear stress is simply

$$E = \tau Ab.$$

It is known from various experiments<sup>3</sup> that only part of the supplied energy is stored in a metal in the form of lattice defects which (at low temperature) remain after the deformation, the other part being lost as heat. The fraction retained is  $\lambda E$ , where  $\lambda$  is a numerical constant, its value depending on the method of deformation. The ultimate area reached by a dislocation loop under a shear stress  $\tau$  is thus limited by the equation

$$\lambda \tau Ab = \frac{\beta A^{1/2} D_0}{b} U_f,$$

from which it follows that:

$$A = \left\{ \frac{\lambda \tau b^2}{\beta D_0 U_f} \right\}^2. \quad (3)$$

The emitted loops produce a back-stress at the site of the source. The component of this stress that opposes the local activating shear stress is given by

$$\tau_b = \frac{\gamma n G b}{A^{1/2}}, \quad (4)$$

where  $\gamma$  is a constant of order 0.1, depending on the shape of the loops and on the value of Poisson's ratio. It was silently assumed that all loops reach the same area  $A$ , this is certainly not so. However, on the average the area covered by the loops will indeed be of the order of  $A$  as given by (3).

The time necessary for the loop to attain its final area after the emission has taken place will be very short. Even if the loops run with a velocity of the order of only 1 per cent of that of sound, this time is of the order of  $10^{-8}$  sec. In this time the local shear stress has not changed appreciably, and one can insert in (4) the value of  $A$  which follows from (3). Thus, one finds

$$\tau_b = \frac{\beta \gamma G D_0 U_f n}{\lambda b \tau}. \quad (5)$$

The source will be activated again when the shear stress at the site of the source,  $\tau - \tau_b$ , attains anew the value  $\tau_1$ , i.e., when

$$\tau - \frac{\beta \gamma G D_0 U_f n}{\lambda b \tau} = \frac{\alpha G b}{l}. \quad (6)$$

It is frequently assumed that, according to an hypothesis of Fisher, Hart and Pry,<sup>4</sup> a source once activated continues emitting dislocation loops until the resultant stress at the site of the source has dropped to a value as low as about  $\frac{1}{3}\tau_1$ . This should happen when the dislocations move with approximately the velocity of sound in the material, so that their kinetic energy attains an appreciable value. This *dynamic* generation of dislocations can be opposed to the *static* generation, in which at each activation process only one loop is emitted.

Equation (6) holds for both cases. However, in the case of static generation,  $n$  takes successively the values 1, 2, 3, . . . , whereas in the case of dynamic generation the loops are emitted in sudden bursts, containing  $n_k$  loops at the  $k$ th activation process. The numbers  $n_k$  are limited by the condition that the back stress exerted by these loops alone shall be equal to about  $\frac{2}{3}\tau_1$ , as the stress at the site of the source at the moment of activa-

tion is precisely  $\tau_1$ . According to (5), one has

$$\frac{\beta\gamma GD_0 U_f n_k}{\lambda b \tau_k} \approx \frac{2}{3} \tau_1,$$

or

$$n_k \approx \frac{2 \lambda b}{3 \beta \gamma GD_0 U_f} \tau_1 \tau_k.$$

The number of loops per burst is thus proportional to the activating stress  $\tau_k$ .

We shall show below that after a few per cent of strain, the total number of loops emitted is large—of the order 100—and it is easily demonstrated that even in the case of dynamic generation, the error involved by replacing the discontinuous relation (6) by a continuous relation, is small. There is, then, no difference between the two forms of behavior of dislocation sources and we arrive at

$$n = \sqrt{\frac{\pi}{8} \frac{\alpha l_0^2}{\gamma l^2} \left[ \left( \frac{\tau}{\tau_1} \right)^2 - \frac{\tau}{\tau_1} \right]}, \quad (7)$$

where  $l_0$  stands for the expression

$$l_0 = \left\{ \sqrt{\frac{8 \lambda \alpha}{\pi \beta} \frac{G b^3}{D_0 U_f}} \right\}^{\frac{1}{2}}, \quad (8)$$

and  $\tau_1$  is again equal to  $\alpha G b / l$ .

The physical significance of the quantity  $l_0$  is observed as follows:

In order to activate a source of length  $l$ , the critical semi-circular shape of the dislocation segment must be produced by the acting shear stress. This segment has an area  $\pi l^2 / 8$ ; it contains, according to (2),  $f_{cr} = \beta D_0 / b \cdot (\frac{1}{8} \pi l^2)^{\frac{1}{2}}$  defects. The energy needed to form these defects must be smaller than the supplied energy  $\lambda \alpha G b^2 / l \cdot (\frac{1}{8} \pi l^2)$ ; thus one has:

$$\frac{\beta D_0 U_f}{b} (\frac{1}{8} \pi l^2)^{\frac{1}{2}} < \frac{\lambda \alpha G b^2}{l} (\frac{1}{8} \pi l^2). \quad (9)$$

When this condition is not fulfilled—that is, when

$$l > l_0 = \left\{ \left( \frac{8}{\pi} \right)^{\frac{1}{2}} \frac{\lambda \alpha}{\beta} \frac{G b^3}{D_0 U_f} \right\}^{\frac{1}{2}}, \quad (10)$$

the source cannot be activated. One may thus read for  $l_0$  the maximum length of a dislocation segment that can ever act as a Frank-Read source.

### 3. DENSITY OF DISLOCATIONS, VACANCIES AND INTERSTITIALS

Suppose the number of activated sources of length  $l$  is  $N$  per  $\text{cm}^3$ , and that only one glide system is present (single glide). These sources contribute to the total strain of the material the amount:

$$\epsilon = N b n A. \quad (11)$$

The total number of defects formed by these sources is

$$F = N n \frac{\beta D_0 A^{\frac{1}{2}}}{b}, \quad (12)$$

and the total length of dislocation formed is

$$D = N n \delta A^{\frac{1}{2}}, \quad (13)$$

where  $\delta$  is a numerical constant depending on the shape of the loops. For circular loops,  $\delta = 2\sqrt{\pi}$ ; in general  $\delta$  will be somewhat larger—say  $\delta = 5$ .

In these formulae the dependence on the stress is governed by the quantities  $N$ ,  $n$  and  $A$ . Now these quantities are functions of the local stresses  $\tau$  near the various sources. These local stresses are unknown and their dependence on the applied stress involves the workhardening characteristics of the solid. We therefore want to eliminate  $\tau$  from the expressions (11), (12) and (13). Assuming that  $\tau/\tau_1$  is at least so much larger than unity that in (7), the term  $\tau/\tau_1$  can be neglected in comparison with  $(\tau/\tau_1)^2$  (this assumption holds after the first few per cent of strain), one finds with the help of (3) and (7):

$$F = \sqrt{\frac{\beta^3 \gamma \lambda G D_0^3}{N U_f b^6}} \epsilon^{\frac{3}{2}}, \quad (14)$$

$$D = \delta \sqrt{\frac{\beta N U_f D_0}{\gamma \lambda G b^6}} \epsilon^{\frac{3}{2}}. \quad (15)$$

It is seen that these formulae contain  $l$  only implicitly, viz., in the quantity  $N$ . As  $N$  occurs only as  $N^{\frac{1}{2}}$ , the rise of  $N$  on increasing deformation, when increasingly shorter sources are being activated, has only a minor influence on the magnitudes of  $F$  and  $D$ , and can therefore be neglected. That means that, effectively, the relation between defect concentration and strain is independent of the length of the sources, and one may take for  $N$  the total number of activated sources (of arbitrary length) per  $\text{cm}^3$ . The occurrence of the fourth-degree root has also the important effect that no precise knowledge of the numerical values of the parameters  $\beta$ ,  $\gamma$ ,  $\lambda$ ,  $N$  and  $U_f$  is needed.

Formulae (14) and (15) have been derived under the assumption that single glide occurs. Then the quantity  $D_0$ , the density of crossing dislocations, can be regarded as a constant. However, in multiple glide the "forest" of dislocations crossed by the expanding loops becomes thicker as the deformation proceeds, owing to the dislocations emitted by sources on intersecting glide systems. Suppose there are  $g$  active glide systems; the total number of activated sources being  $N$ , the density of active sources on a given glide plane is then of the order of magnitude

$$\Delta = N d / g \quad (16)$$

sources per  $\text{cm}^2$ , if  $d$  is the mean mutual distance between two active glide planes of one system. It is a simple problem to compute the average number of dislocation zones cut through by a given zone on a certain glide plane. Assuming that all zones have the same area  $A$ , and that the deformation can be considered as homogeneous, this average number is found to be

about:

$$N_i \approx NA^{\frac{1}{2}}, \quad (17)$$

a numerical factor of order unity being neglected. Every zone cut through contains  $n$  dislocations. Thus the total number of dislocations crossed by a given dislocation loop becomes on the average equal to  $D_0A + NnA^{\frac{1}{2}}$ . That is to say, one should, in the case of multiple glide, replace the constant  $D_0$  by

$$D_0' = D_0 + NnA^{\frac{1}{2}}. \quad (18)$$

Taking  $N \approx 10^{11} \text{ cm}^{-3}$ ,  $n = 50$ ,  $A = 10^{-6} \text{ cm}^2$ , values that probably occur after a few per cent of strain (compare next section), it is seen that the second term at the right-hand side of (18) has a value of the order of  $5 \times 10^9 \text{ cm}^{-2}$ . As  $D_0$  only amounts to about  $10^8 \text{ cm}^{-2}$ , this can be neglected. The energy balance describing the expansion of a loop now reads:

$$\lambda \tau A b \approx \frac{\beta N n A^2}{b} U_f, \quad (19)$$

from which it follows that

$$nA = \frac{\lambda \tau b^2}{\beta N U_f} \quad (20)$$

for multiple glide. Thus,

$$\epsilon = N b \cdot nA = \frac{\lambda b^3}{\beta U_f} \tau \quad (21)$$

and from (12) and (18) it follows that

$$F = \frac{\beta N^2}{b} \cdot (nA)^2 = \frac{\lambda^2 b^3}{\beta U_f^2} \tau^2. \quad (22)$$

Hence in the case of multiple glide the relation (14) is replaced by the extremely simple relation

$$F = \frac{\beta}{b^3} \epsilon^2. \quad (23)$$

An expression corresponding to (15) is not so easily derived. We shall not go into this here.

It may be mentioned that neither (21) nor a corresponding expression that can be derived from (3), (7) and (11) can be considered as describing the workhardening characteristics of the material. The quantity  $\tau$  has not a direct physical significance; it is only the mean local shear stress near an activated source and may differ appreciably from the applied shear stress. Further, all results apply only when the influence of thermally activated processes is neglected, that is at very low temperatures.

#### 4. COMPARISON OF THEORY WITH EXPERIMENT

The various expressions occurring in section 3 can be evaluated numerically by inserting appropriate values

for the various constants occurring in them. We shall confine ourselves to the case of copper.

As already mentioned, for the parameters  $\alpha$ ,  $\beta$ ,  $\gamma$  and  $\delta$  one can put:  $\alpha = 1$ ,  $\beta = 0.02$ ,  $\gamma = 0.1$ ,  $\delta = 5$ , with a fair degree of accuracy. The value of  $\lambda$  is very uncertain. From the measurements quoted in<sup>3</sup> it follows that for deformation at room temperature  $\lambda$  is observed to be about 0.05. At very low temperatures this value would probably be found somewhat greater, as then no defects diffuse out of the material. We shall tentatively put  $\lambda = 0.1$ , which means that 10 per cent of the strain energy remains stored in the metal.  $G$  is known to be  $4 \times 10^{11} \text{ dynes/cm}^2$ ,  $b$  is known from the lattice dimensions of Cu to be  $2.5 \times 10^{-8} \text{ cm}$ . The energy of formation of a vacancy is somewhat smaller than 1 eV; that of an interstitial is about 5 eV.<sup>3</sup> As probably many more vacancies than interstitials are formed in view of the large difference in the energy involved, we shall take  $U_f = 2 \text{ eV} \approx 3 \times 10^{-12} \text{ ergs}$ . In single glide, the dislocation density can, as shown above, be put equal to  $D_0$ , the density of originally present dislocations in the network; various authors<sup>6,7</sup> agree that  $D_0 \approx 10^8 \text{ cm}^{-2}$ . The number  $N$  of active Frank-Read sources in a metal can be estimated to be of the order of a few tenths of  $D_0$ <sup>3</sup>—that is, of the order  $10^{11} \text{ cm}^{-3}$ . As said above, the rather large uncertainty in  $N$  does not appreciably influence the results. We thus find, taking the uncertainties into account:

$$F = (0.5 - 1.5) \times 10^4 \epsilon^{3.4} \text{ cm}^{-3}, \quad (24)$$

$$D = (0.5 - 1.5) \times 10^{11} \epsilon^{3.4} \text{ cm}^{-2}, \quad (25)$$

From (8) we find for the length  $l_0$

$$l_0 = (4 - 10) \times 10^{-4} \text{ cm}. \quad (26)$$

From (3), (7) and (8) one can easily deduce that after the first few per cent of strain:

$$A \approx (0.8 - 2) \times 10^{-6} \epsilon^{\frac{1}{2}} \text{ cm}^2 \quad (27)$$

$$n \approx (200 - 500) \times \epsilon^{\frac{1}{2}}. \quad (28)$$

The value of  $l_0$  corresponds to a critical shear stress for the beginning of plastic deformation which is given by:

$$\tau_0 = \frac{\alpha G b}{l_0}.$$

One finds from the theory  $\tau_0 = (1 - 3) \times 10^7 \text{ dynes/cm}^2$ . For pure copper single crystals this stress is observed to be about  $0.1 \text{ kg/mm}^2 = 10^7 \text{ dynes/cm}^2$ .<sup>8</sup>

In the case of multiple glide the relation between the concentration of point defects and the strain follows from (23) to be for copper:

$$F = 1.3 \times 10^{21} \epsilon^2 \text{ cm}^{-3}. \quad (29)$$

With respect to the order of magnitude, during the first few per cent of strain there is not much difference between (24) and (29). On further strain, however,  $F$

increases much faster in multiple glide than in single glide.

The dimensions of the dislocation zones around activated Frank-Read sources are in good agreement with the characteristics of the elementary structure found by Wilsdorf and Kuhlmann-Wilsdorf,<sup>9</sup> if one interprets this structure as the surface markings produced where activated sources, of one glide system only, dissect the surface. The length of these lines as observed on copper and aluminium is a few times  $10^{-3}$  cm, the step height lies between 20 and 100 atomic distances; according to the theory given, after 10 per cent of strain, the length of the elementary lines should be of the order of  $A^{1/2} = 10^{-3}$  cm, and the step height should be on the average equal to  $n \approx 100$  atomic distances. According to the theory, the mutual spacing of the lines should be of the order of  $(NA)^{-1}$  cm, which amounts to a few times  $10^{-5}$  cm, whereas  $(2-5) \times 10^{-6}$  cm was observed for this spacing. However, near the surface the density of activated sources is probably much greater than in the interior.

By far the most important information on the concentrations of lattice defects is obtained by the measurement of the electrical resistivity as a function of the strain. From the work of Jongenburger<sup>10</sup> and Hunter and Nabarro,<sup>11</sup> it follows that one vacancy per  $\text{cm}^3$  in copper contributes  $1.5 \times 10^{-21} \mu\Omega\text{cm}$  to the resistivity, one interstitial atom about three times as much, viz.,  $4.5 \times 10^{-21} \mu\Omega\text{cm}$ , and a density of  $D$  dislocations per  $\text{cm}^2$  the amount of  $0.4 \times 10^{-14} D \mu\Omega\text{cm}$ . Inserting in (24) and (25) yields for the theoretically expected resistivity-strain dependence in single glide:

$$\Delta\rho = (0.02 - 0.05) \times \epsilon^{5/4} + (2 - 8) \times 10^{-4} \epsilon^{3/4}. \quad (30)$$

It follows that the contribution of the dislocations to the resistivity would be very slight and could be neglected.

For multiple glide it can easily be estimated that the contribution of dislocations to the resistivity is also negligible compared to that of the point defects. Thus we have from (29):

$$\Delta\rho \approx 2\epsilon^2. \quad (31)$$

The observed resistivity-strain curves for polycrystalline materials can all be described by a power law of the form

$$\Delta\rho = a\epsilon^r, \quad (32)$$

where  $a$  is about 0.05, and  $r$  lies between 1.2 and 1.5.<sup>12</sup> Blewitt<sup>13</sup> observed the resistivity-strain relation in copper single crystals and found a relation of the form

$$\Delta\rho = 0.01\epsilon^2. \quad (33)$$

He applied large strains of order unity. The value of the coefficient  $a$  in both cases, as well as that of the exponent  $r$  in the case of polycrystals, are in much better agreement with the theory as applied to the case of single glide than with the theory of multiple

glide. This seems at first sight rather unexpected. However, the theory as presented here deals only with the phenomenon of the so-called *fine slip* in slightly deformed metals; the strong sliplines, as observed on most heavier deformed metals are probably formed in another way. They should be considered as more or less accidental effects that are not considered in the above treatment. The number of point defects formed in this manner is presumably much less than the number formed in fine slip (probably the circumstances favouring coarse slip are simply the absence or reduced frequency of formation of point defects). From the occurrence of multiple coarse slip it cannot be concluded that the fine slip, considered locally, also takes place on different glide planes. In the experiments of Kuhlmann and Wilsdorf<sup>9</sup> elementary lines belonging to one glide system only are usually locally observed. Therefore, formula (30) is probably better applied to the actual case than formula (31), especially when the density of the original dislocation network is high. In Blewitt's<sup>13</sup> experiments on single crystals, this density may have been exceptionally low, favoring the occurrence of some kind of multiple fine slip. The low absolute value of the extra resistivity may also be connected with an exceptionally low value of  $D_0$ .

Van Bueren and Jongenburger *loc. cit.* alternately extended and twisted polycrystalline copper and silver wires. They observed that intermediate twisting influenced the resistivity-strain relation on subsequent extension in a very special way: the exponent  $r$  remains constant (except for the first few per cent of strain after the twist), the coefficient  $a$ , however, becomes multiplied by a factor  $m$  which depends on the amount of twist and is 1.3 at a torsional surface strain  $\epsilon_t$  of 0.1. According to Paxton and Cottrell, such a strain causes an increase of the number of homogeneous distributed dislocations by an amount

$$D_t = \frac{\epsilon_t}{rb}, \quad (34)$$

where  $r$  is the radius of the wire (0.25 mm). From this it follows that  $D_t$  after  $\epsilon_t = 0.1$  was  $1.6 \times 10^8 \text{ cm}^{-2}$ . According to (14), the introduction of  $D_t$  homogeneously distributed dislocations has the effect of multiplying the resistivity-strain relation by a factor

$$m = \left( \frac{D_0 + D_t}{D_0} \right)^{3/4},$$

when it is assumed that only point defects contribute to the resistivity. From the known values of  $D_t$  and  $m$ ,  $D_0$  can be calculated; it was found to be  $3.8 \times 10^8 \text{ cm}^{-2}$ , in reasonable agreement with the expectations.

From this and the foregoing it seems that experiment and theory can be made to agree best when it is accepted that dislocations do not contribute more than say 10%



to the low temperature resistivity. This is in contradiction to the result of recovery experiments<sup>12</sup> that indicate that dislocations are responsible for about half of it. This contradiction is at the moment unsolved.\*

## REFERENCES

1. B. A. Bilby, Paper on Bristol Conference on Defects in Crystalline Solids (1954).
2. H. Suzuki, J. Phys. Soc. (Japan) **9**, 531 (1954).
3. G. J. Taylor and H. Quinney, Proc. roy. Soc. **A143**, 307 (1934); L. M. Clarebrough, M. E. Hargreaves, D. Michell, and G. W. West, Proc. roy. Soc. **A215**, 507 (1952).
4. J. C. Fisher, E. W. Hart, and R. H. Pry, Phys. Rev. **87**, 958 (1952).
5. H. B. Huntington and F. Seitz, Phys. Rev. **61**, 311 (1941); H. B. Huntington, Phys. Rev. **61**, 325 (1941); C. J. Meechan and R. R. Eggleston, Acta Met. **2**, 680 (1954).
6. F. Seitz, Advances in Physics **1**, 43 (1952).
7. A. H. Cottrell, *Dislocations and Plastic Flow in Crystals* (Oxford University Press, Oxford, 1953).
8. G. Masing, *Lehrbuch der allgemeinen Metallkunde* (Springer, Berlin, 1950), and many other authors.
9. H. Wilsdorf and D. Kuhlmann-Wilsdorf, Z. angew. Phys. **4**, 361, 409 (1952); Acta Met. **1**, 394 (1953). Paper on Bristol Conference on Defects in Crystalline Solids (1954).
10. P. Jongenburger, Appl. sci. Res. **B3**, 237 (1953); P. Jongenburger, Nature **175**, 545 (1955).
11. S. C. Hunter and F. R. N. Nabarro, Proc. roy. Soc. **A220**, 542 (1953).
12. R. H. Pry and R. W. Hennig, Acta Met. **2**, 318 (1954); C. W. Berghout, unpublished; J. Molenaar and W. H. Aarts, Nature **166**, 609 (1950); M. J. Druyvestyn and J. A. Manintveld, Nature **168**, 868 (1951); H. G. van Bueren and P. Jongenburger, Nature **175**, 544 (1955); W. H. Aarts and R. K. Jarvis, Acta Met. **2**, 87 (1954). A review of all data is given by the author in the Zeitschrift für Metallkunde **46**, 272 (1955).
13. T. H. Blewitt. Private communication.
14. S. Paxton and A. H. Cottrell, Acta Met. **2**, 6 (1954).

\* Note added in proof.—Recent observations by the author on the resistivity change of deformed copper in a magnetic field seem to confirm the conclusion that dislocations are indeed far more effective than concluded above. The only way to explain this is to assume that the theoretical scattering cross-section of dislocations is in error by a factor of 10, as the defect densities computed in (24) and (25) are rather to be regarded as upper limits.

## ON THE EFFECT OF ORDERING UPON THE STRENGTH OF $\text{Cu}_3\text{Au}$ \*

G. W. ARDLEY†

Experiments have been carried out to examine the effect of ordering on the mechanical strength of single crystals of  $\text{Cu}_3\text{Au}$ . It was found that as the disorder→order reaction proceeds the strength is affected in two ways. Firstly, as the degree of long-range order within the anti-phase domains increases the room-temperature strength decreases. Secondly, as the anti-phase domains grow larger the room-temperature strength first increases and then decreases. At the ordering temperature there is an appreciable drop in strength as the alloy passes from the ordered to the disordered state. Above the ordering temperature the strength increases with increasing temperature to a maximum value and then decreases again. The temperature at which this maximum occurs depends upon the applied strain-rate.

### EFFET DE L'ORDRE SUR LA RÉSISTANCE DE $\text{Cu}_3\text{Au}$

Ces expériences avaient pour but d'étudier l'effet de l'ordre sur la résistance mécanique de monocristaux de  $\text{Cu}_3\text{Au}$ . La réaction désordre-ordre a deux effets sur la résistance: 1°—Quand l'ordre à grande distance augmente, la résistance à la température ordinaire diminue. 2°—Quand les domaines en antiphase grossissent, la résistance croît, puis décroît. A la température de Curie, il y a une chute appréciable de la résistance quand l'alliage passe de l'état ordonné à l'état désordonné, mais au-dessus de cette température, la résistance croît avec la température, puis décroît; la température à laquelle le maximum se produit dépend de la vitesse de déformation.

### ÜBER DEN EINFLUSS DES ORDNUNGSVORGANGES AUF DIE FESTIGKEIT VON $\text{Cu}_3\text{Au}$

Es wurde der Einfluss des Ordnungsvorganges auf die mechanische Festigkeit von  $\text{AuCu}_3$ -Einkristallen untersucht und dabei festgestellt, dass der Vorgang Unordnung→Ordnung die Festigkeit auf zweierlei Weise beeinflusst: Erstens nimmt die Festigkeit bei Raumtemperatur mit zunehmendem Fernordnungsgrad in den Antiphasen-Bereichen ab. Zweitens nimmt die Festigkeit bei Raumtemperatur zu und fällt dann wiederum ab, wenn die Antiphasen-Bereiche grösser werden. Bei der kritischen Temperatur, also beim Übergang vom geordneten in den ungeordneten Zustand, wurde ein beträchtlicher Abfall in der Festigkeit festgestellt. Oberhalb der kritischen Temperatur nimmt die Festigkeit bis zu einem Maximalwert zu, um dann wiederum abzufallen. Die Temperatur, bei der dieser Maximalwert auftritt, hängt von der Grösse der angelegten Spannung ab.

### INTRODUCTION

It has been known for some time now that the mechanical strength of an ordering alloy changes as the alloy passes from the disordered to the ordered state. It was thought that in alloys of the  $\text{Cu}_3\text{Au}$  type the ordered structure was always weaker than the disordered one, whilst in alloys of the  $\text{CuAu}$  type the reverse was true<sup>1-5</sup>  $\text{Cu}_3\text{Au}$  remains face-centered-cubic upon ordering but  $\text{CuAu}$  changes from f.c.c. to f.c. tetragonal. This led to the belief that a change in crystal structure upon ordering was necessary to produce an increase in strength.<sup>6,7</sup> In this paper we shall consider only the case of  $\text{Cu}_3\text{Au}$  and it will be shown that one can obtain an increase in strength upon ordering although it is not a permanent increase but rather a transitional one similar to that observed in  $\text{Cu}_3\text{Au}$  by Broom and Briggs,<sup>8</sup> and in  $\text{CuAu}$  by Dehlinger and Graf<sup>9</sup> and Nowack.<sup>1</sup> A complete review of the literature up to 1940 on "age-hardening" in precious metal alloys, together with an extensive bibliography, can be found in the paper by Vines and Wise.<sup>10</sup>

\* Received December 22, 1954.

† General Electric Research Laboratory, Schenectady, New York.

### PREPARATION OF THE CRYSTALS

The alloys were made by melting together known amounts of high purity (99.999%) copper and gold to give the  $\text{Cu}_3\text{Au}$  composition. The copper and gold were first cut into small pieces measuring approximately  $1/8 \times 1/8 \times .040$  in., thoroughly mixed, and then melted together in a graphite crucible under a pressure of less than  $10^{-6}$  mm Hg. Prior to this the crucible had been cleaned and degassed by heating it to  $1300^\circ\text{C}$  for two hours under a high vacuum. Induction heating was used so that the stirring action would help to mix the constituents. The alloy was held molten for about 15 minutes and then allowed to cool to room temperature. To be sure of an homogeneous alloy this procedure—i.e., cutting into small pieces, thoroughly mixing the pieces and then melting them together—was repeated twice more on each ingot before it was cold-swaged down to .100 in. wire. The crystals were grown by the Bridgman method using a lowering rate of  $1''$  per hour. A split graphite mould was used and a pressure of  $10^{-6}$  mm Hg was maintained above the crystals throughout the growth period.

Square crystals were preferred for these experiments and two sizes were used, 1.5 mm and 2.5 mm on a side.

To hold a crystal in the tensile testing machine, a steel grip was brazed to each end of the crystal. This was done by having a U-shaped grip that allowed the crystal to lie between its prongs with only about .001 in. clearance on either side. The crystal and grips were assembled on a flat quartz plate, and a piece of brazing solder was placed at each grip. The whole assembly was put into a horizontal quartz tube and heated to 780°C under a protective atmosphere of hydrogen, whereupon the brazing solder melted and ran down into the gaps between the grips and the crystal, forming a good joint. The solder also ran out along the crystal a little way and formed a meniscus-shaped fillet between the specimen and the end of the grip. This is advantageous because it avoids any sharp discontinuity in cross-section in going from specimen to grip. After brazing, the specimen cooled to room temperature in just a few minutes.

Whenever the specimens were to be annealed for an extended period of time they were sealed into glass tubes under a vacuum, and heated in a resistance furnace. When they were to be annealed for short periods of time they were immersed into a silicone oil bath that was heated by an electric mantle heater. If the surface

of the oil was protected from the atmosphere by passing nitrogen across it, the oil could be heated to as high as 380°C for several days before any serious thermal decomposition occurred.

### EXPERIMENTAL RESULTS I

Before describing the main experimental results there are a few observations on the mode of deformation in  $\text{Cu}_3\text{Au}$  that are worthy of note. Figure 1a shows a reproduction of a load elongation curve for a single crystal of  $\text{Cu}_3\text{Au}$  deformed at room temperature. There are two interesting features to be noticed in this curve: (1) the deformation occurs jerkily at first and then becomes smooth, and (2) the stress does not increase until the jerky flow has ceased. It appears that each drop in load is associated with the formation of a highly localized slip band so that after several of these jerks have occurred, the specimen looks like the one shown in the inset. Further deformation causes more slip bands to appear but from a visual observation they always seem to occur in new parts of the crystal. Within the jerky flow region, therefore, one will always be measuring the strength of undeformed material. The jerky flow is

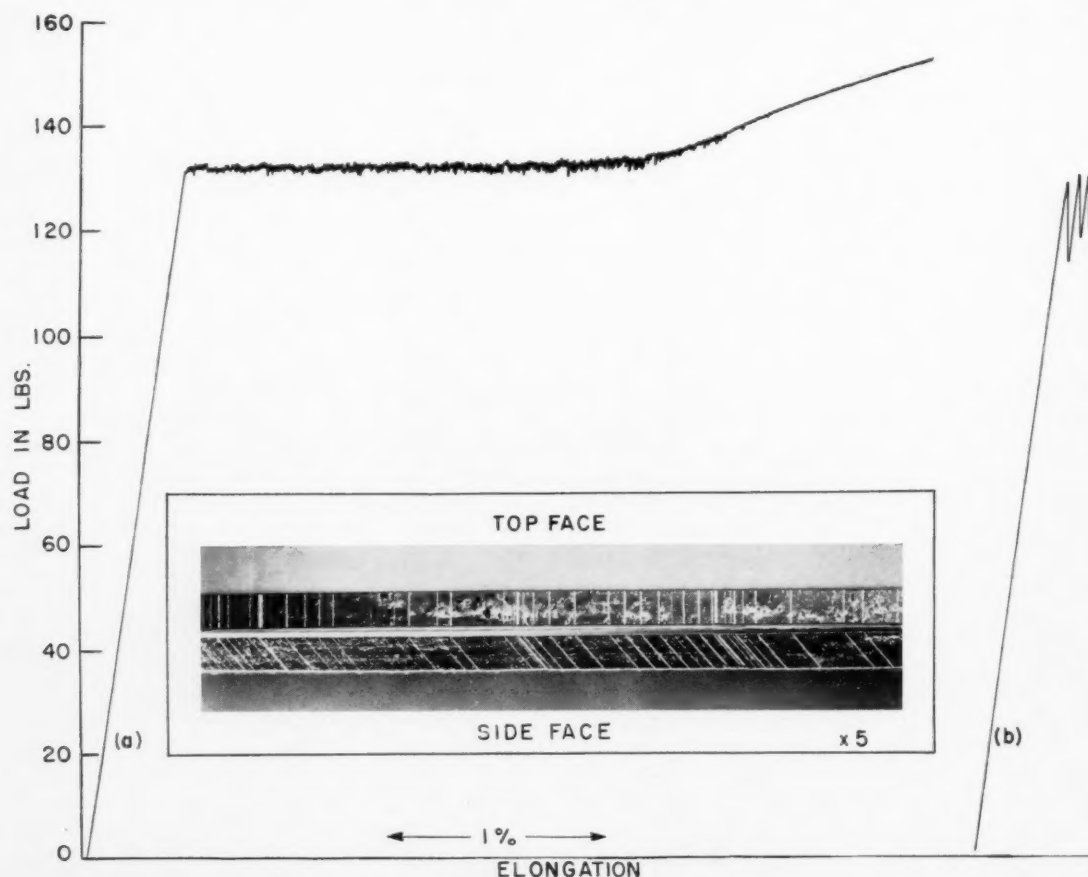


FIG. 1. Typical load-elongation curves showing jerky flow. Inset—slip bands on two faces of a crystal after a small amount of deformation in the jerky range.

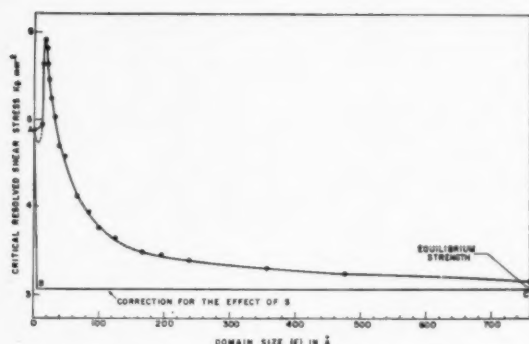


FIG. 2. Room temperature strength *versus* domain size for a single crystal of  $\text{Cu}_3\text{Au}$  ordered at  $350^\circ\text{C}$ . The region above the line ABC represents the contribution to the strength from the anti-phase domain boundaries.

usually much more pronounced than that which is shown in Fig. 1a. The more usual size is like that shown in Fig. 1b.

The observations described above have been separated from the main body of data because as yet they are only of a very preliminary nature. They do bear a strong resemblance however to the observations of Ardley and Cottrell<sup>11</sup> who found similar jerky flow characteristics in  $\beta$ -brass.

## EXPERIMENTAL RESULTS II

The data shown in Fig. 2 are typical of that for the room-temperature strength of a single crystal of  $\text{Cu}_3\text{Au}$  as a function of the anti-phase domain size for an annealing temperature of  $350^\circ\text{C}$ . These data were obtained in the following way. First, the specimen was obtained in the disordered state at room temperature, by heating it to  $420^\circ\text{C}$  for several hours and then quenching it to room temperature in water. The room-temperature resistivity of the specimen was measured potentiometrically and then the specimen was strained in tension to measure its strength. The value obtained for the room-temperature strength of the disordered alloy is denoted by the point A in Fig. 2. To vary the domain size, the specimen was heated to the desired temperature,  $350^\circ\text{C}$  in this case, in an oil bath. The specimen was put into the bath for a short period of time and then it was quenched to room temperature in order to measure its room-temperature resistivity and room-temperature strength. After these measurements had been made the specimen was put back into the oil bath and the annealing treatment continued until the specimen was quenched to room temperature again to measure the new room-temperature resistivity and room-temperature strength for the larger domain size. The sequence of annealing and quenching to room temperature to measure the resistivity and strength was repeated several times until the annealing treatment did not produce any further changes in the strength or resistivity of the specimen. Jones and Sykes<sup>12</sup> have measured the room-temperature resistivity of the disordered

$\text{Cu}_3\text{Au}$  alloy and the value they suggest,  $11.5 \times 10^{-6}$  ohm-cm, was used to check that at the beginning of these experiments, the alloys were indeed disordered. In all cases the room-temperature resistivity of the specimens after the disordering treatment described above—remembering that prior to this treatment the specimens had been rapidly cooled from  $780^\circ\text{C}$ —was within the range  $11.5$  to  $11.6 \times 10^{-6}$  ohm-cm. The domain size after each annealing period was estimated from the room temperature resistivity of the specimen, using the data of the domain size as a function of the resistivity published by Jones and Sykes.<sup>12</sup> Before this could be done, however, two small corrections had to be made. In the present experiments room temperature was about  $10^\circ\text{C}$  higher than the temperature at which Jones and Sykes made their measurements ( $20^\circ\text{C}$ ). The present resistivities were corrected to  $20^\circ\text{C}$ , therefore, using the temperature coefficient of  $10^{-8}$  ohm-cm per  $^\circ\text{C}$ , suggested by Jones and Sykes' Fig. 1.<sup>12</sup> To get curves relating the room-temperature resistivity to the domain size for specimens ordered at  $375^\circ\text{C}$ ,  $350^\circ\text{C}$  and  $325^\circ\text{C}$ , it was necessary to interpolate from Jones and Sykes' data, which are given for specimens ordered at  $376^\circ\text{C}$ ,  $346^\circ\text{C}$  and  $298^\circ\text{C}$ . It was noticed that for large domain sizes the room-temperature resistivity is proportional to the long-range order parameter, and this criterion was adopted to get the resistivity *versus* domain-size curves at  $375^\circ\text{C}$ ,  $350^\circ\text{C}$  and  $325^\circ\text{C}$  (see Fig. 3\*). The values of the domain sizes used in Figs. 2 and 6 were estimated from the measured room-temperature resistivities using Fig. 3.

The critical resolved shear strength of the specimens was measured by straining them in tension on a very hard cantilever beam machine of the Polanyi type.<sup>13</sup> The load and elongation were automatically recorded and an example of the type of curve obtained is reproduced in Fig. 1b. In these tests care was taken to give the specimens as little deformation as possible in order

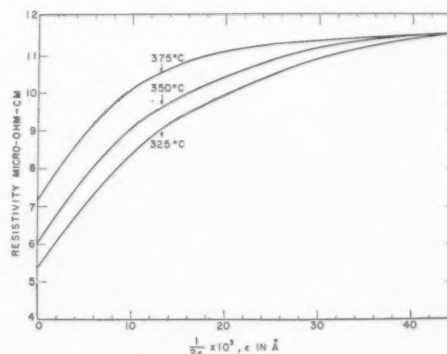


FIG. 3. Resistivity *versus* domain size for annealing temperatures of  $375^\circ\text{C}$ ,  $350^\circ\text{C}$  and  $325^\circ\text{C}$ . Calculated from the data of Jones and Sykes.<sup>12</sup>

\* In the analysis of their data, Jones and Sykes say that the domain sizes they have plotted in their curves are really twice the actual domain sizes. Therefore, in Fig. 3 this factor of 2 has been included.



to avoid any ill effects on subsequent tests due to strain hardening. In general the amount of strain incurred in each test was 0.1 per cent, which is only 1/25 the extent of the jerky flow region (see Fig. 1a).

Returning to Fig. 2, it will be seen that at first the room-temperature strength increases with increasing domain size until it reaches a maximum at around 15–30 Å, then decreases until it reaches an approximately equilibrium value when the domain growth has virtually ended. In this condition the strength of the alloy is less than that of freshly quenched alloys, this observation perhaps being the same as that which led some earlier workers to conclude that ordered alloys are softer than disordered ones.

When the strength reaches its equilibrium value one can regard the specimen as being comprised of very large anti-phase domains the interiors of which have the equilibrium degree of long-range order. If the specimen is now heated to a temperature lower than that at which it had previously been equilibrated, two things can happen. There may be some more domain growth, but if the specimen had been well equilibrated at the higher temperature this growth will be very slow and should be insignificant as far as the strength of the specimen is concerned. More importantly, the degree of order within the domains will increase and any change in the strength brought about by the latest heat treatment can be attributed to this change in the long range order.

To examine this effect some specimens were first equilibrated with respect to the domain growth and the long-range order parameter by holding them at 375°C for a period of seven days. Previous experiment had shown that there was no measurable change in the strength or the resistivity after one day at this temperature. At the end of seven days the specimens were quenched to room temperature and their strengths measured. Subsequently they were equilibrated at a lower temperature and again quenched to room temperature to measure their strength. Equilibration was repeated at successively lower temperatures, ranging from 375°C down to 230°C, the specimens being quenched from each temperature to room temperature in order to measure their room-temperature strength. Below 230°C, the ordering reaction proceeds very slowly and one cannot be sure that the specimens ever reach equilibrium.

The influence of long-range order upon strength is shown in Fig. 4, which gives a plot of the critical resolved shear strength ( $\sigma$ ) versus the long-range order parameter ( $S$ ) and it will be seen that as  $S$  increases the room-temperature strength decreases. The range over which  $S$  can be varied in the Cu<sub>3</sub>Au alloy is very small, i.e., 0.8 to 1.0, and it is difficult to determine any quantitative functional relationship between  $S$  and  $\sigma$ . For this purpose it would be desirable to study the relationship between long-range order and strength on an AB type alloy where  $S$  can be varied all the way from unity to zero, as was done by Green and Brown<sup>14</sup> with  $\beta$ -brass.

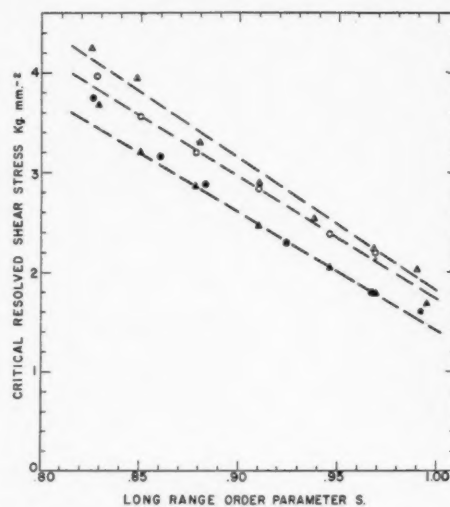


FIG. 4. The variation of the critical resolved shear stress with the long-range-order parameter ( $S$ ). The results from four different specimens are shown in this figure. The values of  $S$  were taken from the curve  $S$  versus temperature published by Keating and Warren.<sup>27</sup>

They showed that the strength increased as  $S$  decreased from unity to 0.5, and then decreased again as  $S$  proceeded from 0.5 to zero.

Qualitatively, it is clear why the strength should rise as the long-range order parameter decreases from unity, both in Cu<sub>3</sub>Au and in  $\beta$ -brass, and why the strength should fall again as the long-range order parameter approaches zero in  $\beta$ -brass.

Consider a long-range ordered crystal made up of a single domain in which the order is perfect, i.e.,  $S = 1$ . If one passes a dislocation appropriate to the ordered crystal of the crystal lattice through this crystal, there will be no change in the atomic arrangement across the slip plane and only a vanishingly small stress will be required.<sup>15,16,17</sup> If, however, there is not quite perfect long-range order in this domain so that some atoms are out of place, the atomic arrangement across the slip plane will be changed after the dislocations have passed through. Energy will be required to do this and the applied stress will have to be raised accordingly. The further  $S$  departs from unity the worse the misarrangement caused by slip will be, and the applied stress will have to be increased proportionately. In effect this is just Fisher's<sup>16</sup> idea for short-range order hardening applied to the case of the departure from perfect long-range order rather than to the case of the departure from a complete random arrangement. Let us consider the disordered alloy for a moment. Fisher<sup>16</sup> has pointed out that when dislocations are passed through a completely disordered alloy the random matching of atoms across the slip plane is re-created behind them. The internal energy of the crystal is not changed, therefore, and consequently the stress required to move the dislocations is small. If there is some short-range order present, how-

ever, it will strengthen the alloy because as the dislocations pass through the crystal the degree of short-range order across the slip plane is reduced to a more nearly random arrangement of higher energy.

Thus, if the arrangement of the atoms in an ordering alloy is changed continuously from a random distribution to the completely ordered distribution we would expect the strength of the alloy to vary in the following way: at first, the strength will increase as the short-range order parameter increases, and then later it will decrease as the fully ordered state is approached.

To evaluate the strength due to the domain size alone, the contribution from the long-range order parameter has to be subtracted. The contribution to the strength from the long-range order alone cannot be determined experimentally over the whole range of  $S$  from zero to unity because of the interference of the domain growth. Therefore, it was decided to follow the strength as  $S$  changed over a limited range and then to assume that the strength would relax from the freshly quenched value (A in Fig. 2) to the equilibrium value (B in Fig. 2) with the same relaxation time. The following procedure was adopted to measure the relaxation times. Specimens were first disordered by heating them to 420°C for 24 hours; then they were transferred to a furnace at 375°C and held there for seven days in order to equilibrate them with respect to both domain growth and long-range order parameter. The specimens were then quenched down to some lower temperature (350°C, 325°C, 300°C or 275°C were used) and their strength followed as a function of time at that lower temperature. The specimens were always strained at room temperature, which meant that the relaxation process was interrupted several times by a quenching treatment. Each time the strength was measured the specimens were deformed a little (approximately .1 per cent tensile strain) but it was assumed that this would not have any serious effects on subsequent measurements. This is a fair assumption to make because it is suspected from previous observations that in the early stages of deformation slip is confined to discrete locations and providing we stay within the so-called "jerky range," we will be measuring the strength of undeformed material. It was found that the relaxation of the strength of the crystals could be related to the time through the simple exponential equation:

$$\frac{\sigma_i - \sigma_t}{\sigma_i - \sigma_f} = 1 - e^{t/\tau(T)},$$

where  $\sigma_i$  is the initial strength,  $\sigma_f$  the final strength,  $\sigma_t$  the strength at the time  $t$ , and  $\tau(T)$  the relaxation time for that particular temperature. The values of  $\tau$  obtained from this relationship were used to construct Fig. 5. The straight line in this figure was drawn to give the best fit to the experimental points by the method of least squares. Bragg and Williams<sup>18</sup> assumed—and the experimental results of Sykes and Evans<sup>28</sup> tend to sup-

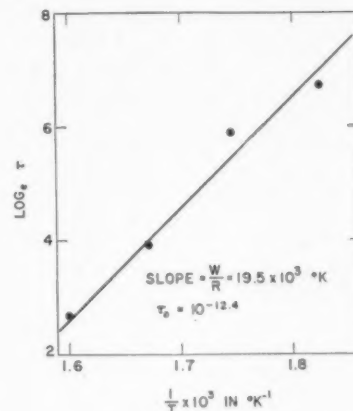


FIG. 5. Relationship between the logarithm of the relaxation time of the strength of a Cu<sub>3</sub>Au single crystal and the reciprocal of the temperature.

port their assumption—that the relaxation time for the ordering process would be related to the temperature through a single activation energy so that  $\tau$  could be written

$$\tau = \tau_0 e^{w/RT}$$

The values suggested for  $\tau_0$  and  $w/R$  by the straight line in Fig. 5, are  $10^{-12.4}$  sec and  $19,500^\circ\text{K}$ , respectively; these are very close to Bragg and Williams' calculated values of  $10^{-12}$  and  $19,000^\circ\text{K}$ . Whilst the agreement here is very good, the quality of the results could undoubtedly be improved by using the electrical resistivity rather than the strength, to follow the course of the relaxation.

Estimates of the relaxation times at 375°C, 350°C and 325°C from Fig. 5 are 4, 14 and 45 seconds, respectively. These are so low that generally by the time the first measurement was taken in the strength-versus-domain-size experiments, the long-range order parameter had essentially relaxed to equilibrium. Under these circumstances the correction to the strength due to the influence of  $S$  degenerates into merely subtracting the equilibrium value of the strength from all the other measurements; this is shown schematically in Fig. 2. This form for the correction cannot be true in the earliest stages of ordering because there the degree of long-range order and the domain growth are intimately connected and any change in one produces an appreciable change in the other. It is worth noting here that on three occasions the strength was observed to decrease a little

TABLE I.

Specimen number	Annealing temperature	Equilibrium strength $\sigma_\infty$ (kg/mm <sup>2</sup> )	$\gamma$ ergs/cm <sup>2</sup>	$l$ Å
1	325°C	2.3	95	3.75
2	325°C	2.25	94	3.75
3	350°C	3.1	98	3.75
4	375°C	3.5	115	6
5	375°C	3.6	104	6

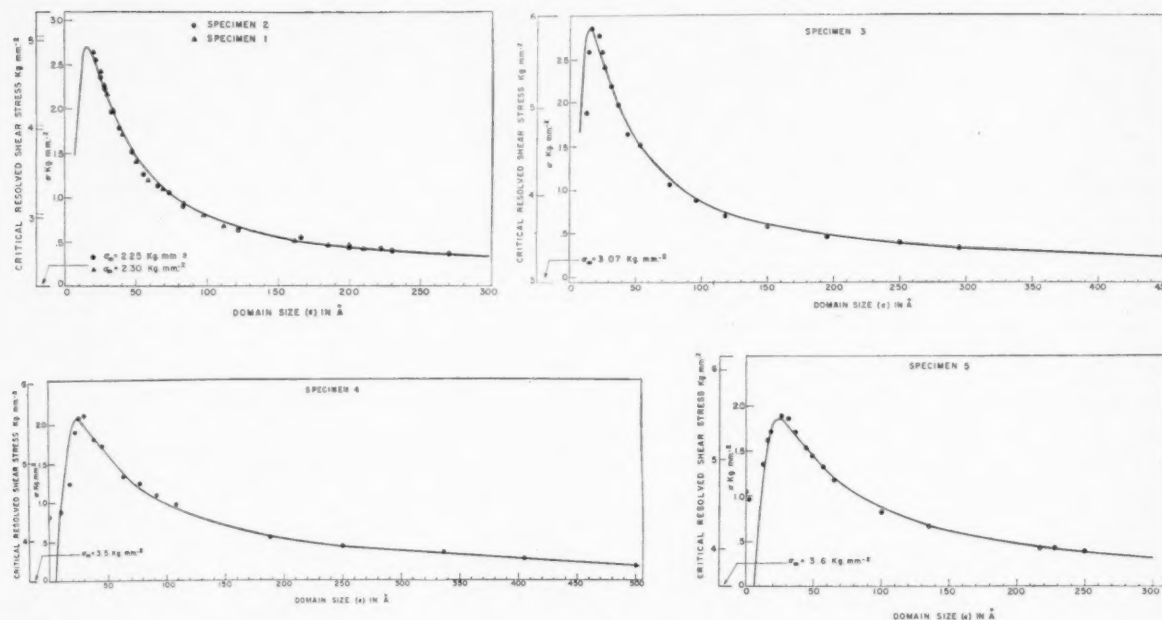


FIG. 6. Room temperature strength versus domain size for annealing temperatures of 375°C, 350°C and 325°C. The left-hand ordinate scale shows the absolute value of the critical resolved shear stress.

—about 5 per cent of the value for freshly quenched specimens—before it began to increase. One of these occasions is recorded in the experimental data of specimen 5 in Fig. 6.

The final data obtained for the strength of an ordered crystal as a function of the domain size for three different annealing temperatures 375°C, 350°C and 325°C, are shown in Fig. 6. The points on these graphs represent the experimental observations whilst the full curve is a plot of the equation

$$\sigma = \frac{\gamma}{\epsilon} \left( \frac{\epsilon - l}{\epsilon} \right)^3, \quad (1)$$

where  $\sigma$  is the resolved shear strength of the crystal,  $\gamma$  the surface energy of a stacking fault in the ordered structure,  $\epsilon$  the anti-phase domain size, and  $l$  the thickness of the anti-phase domain boundaries. This equation was first derived by Cottrell<sup>17</sup> in a slightly different form, by equating the energy of the domain boundaries created during slip to the work done by the applied stress. The model he used is illustrated schematically in Fig. 7. Figure 7a shows an ordered structure containing domain boundaries, before slip; the atoms within the boundaries are thought to be distributed at random. Figure 7b shows the same crystal after it has been slipped a certain distance and it will be seen that the amount of anti-phase boundary has been increased. The energy to do this has to be supplied by the externally applied stress and obviously the more domain boundaries there are—i.e., the smaller the domain size—the larger that stress will have to be. If the crystal is

made up of anti-phase domains whose average diameter is  $\epsilon$ , then it can be shown when the total slip displacement is  $\epsilon/2$ , the amount of anti-phase domain boundary in the slip plane is equal to one half of the total area of the slip plane. Any further slip does not change this ratio so that there is no longer any contribution to the strength from the ordering forces. The energy per unit area of the slip plane due to wrong bonds across the slip plane is therefore  $\gamma/2 \{1 - [(\epsilon - l)/\epsilon]^3\}$  before slip and  $\gamma/2$  after slip. Thus one can write for the work done during slip

$$\sigma \cdot \frac{\epsilon}{2} = \frac{\gamma}{2} \left( \frac{\epsilon - l}{\epsilon} \right)^3, \quad (2)$$

from which Eq. (1) is derived. For  $\epsilon \gg l$ , Eq. (2) reduces

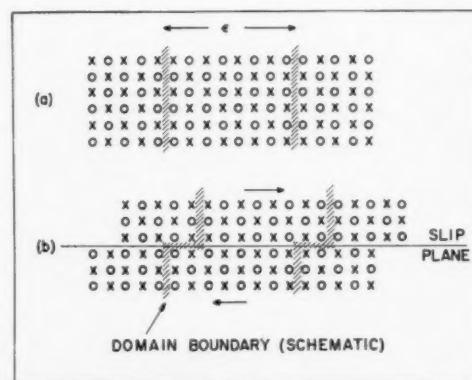


FIG. 7. Schematic illustration of the effect of slip on the anti-phase domain boundaries.

to  $\sigma = \gamma / \epsilon (1 - 3l/\epsilon)$  which is analogous to Cottrell's equation. The values obtained for  $\gamma$  and  $l$ , from the present investigation, range from 94 to 115 ergs per  $\text{cm}^2$  and from one to two atom spacings respectively; see Fig. 6 and Table I. From their X-ray and resistivity measurements, Jones and Sykes<sup>12</sup> also suggest that the domain boundaries are about one or two atom spacings wide. One can estimate the value of  $\gamma$  by considering the energies of the like and unlike bonds in a stacking fault of the ordered structure. Peierls<sup>19</sup> has obtained an expression relating these energies to the critical temperature of the alloy, and using his expression one obtains for  $\gamma$ , when  $S = 1$ , a value of approximately 75 ergs/ $\text{cm}^2$ , which agrees fairly well with the experimentally determined values.

### EXPERIMENTAL RESULTS III

A few experiments were carried out to see how the strength of the  $\text{Cu}_3\text{Au}$  crystals varied above the critical temperature and the results of these experiments are summarized in Figs. 8, 9, and 10. The specimens were first ordered and equilibrated at 300°C and then their strength was measured, at temperature, over the temperature range from 300°C to 680°C. From 300°C to the critical temperature there is a marked increase in strength, presumably due to the decrease of the long-range-order parameter. As the specimen passes through the critical temperature there is a sharp decrease in the strength accompanying the disordering process. This decrease is drawn as a dotted line in Fig. 8 because it was not possible to determine whether it occurred discontinuously or over a finite temperature range. Above the critical temperature the strength increases again until

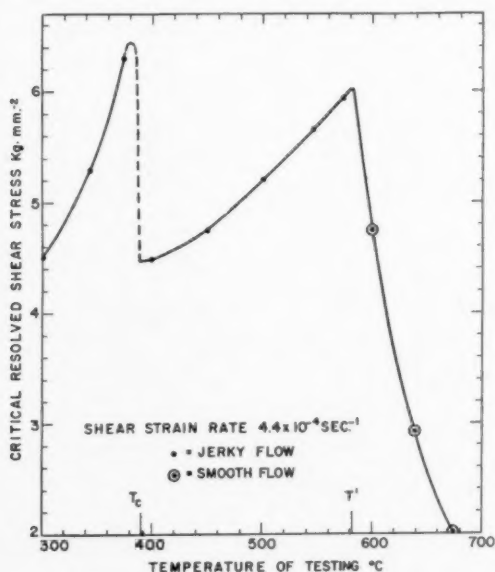


FIG. 8. The critical resolved shear stress versus temperature for a single crystal of  $\text{Cu}_3\text{Au}$ . The crystal was originally ordered at 300°C before these data were taken. Shear strain rate  $4.4 \times 10^{-4} \text{ sec}^{-1}$ .

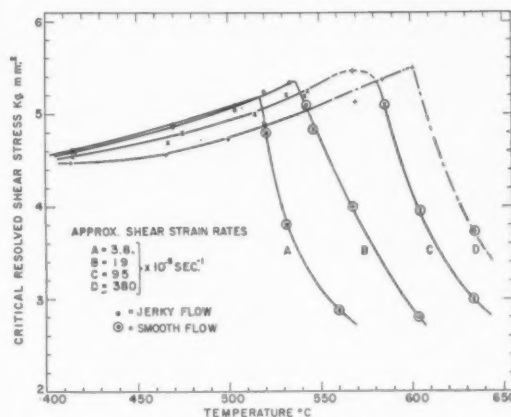


FIG. 9. The critical resolved shear stress versus temperature for different rates of strain. Curve D was obtained from two specimens.

it reaches a maximum value at a temperature  $T'$  and then it decreases again. The position of this maximum was found to be strain-rate dependent, moving to higher temperatures the higher the strain-rate, see Fig. 9. It should be pointed out here that in addition to the change in strength with temperature there are also changes in the shear moduli and for strict comparative purposes one ought to plot strength divided by shear modulus versus temperature rather than just strength versus temperature. However the changes in the shear moduli whilst not negligible, are not large enough to alter the curves of Figs. 8 and 9 appreciably.

Since there is only continuously decreasing short-range order as the temperature is increased above the critical temperature, one cannot attribute the peak at  $T'$  to a similar origin as the one at the critical temperature. However, it has been well established that in certain aging materials such as iron<sup>20,21,22</sup> and aluminum,<sup>23</sup> there is a temperature range over which the strength increases with increasing temperature. In iron this is commonly known as the blue-brittle range, and the increase in strength is thought to be due to strain-aging occurring simultaneously with the deformation.<sup>23</sup> It was thought, therefore, that strain-aging could also be the cause of the peak at  $T'$ , and further evidence to support this point of view arose when two other prominent features of an aging alloy, namely an inverse rate effect (i.e., strength decreases with increasing strain-rate) and a strong yield point, were both found to occur above the critical temperature (see Figs. 9 and 10).

It is not surprising that one observes a yield point and strain-aging in the disordered  $\text{Cu}_3\text{Au}$  alloy because there are three possible mechanisms from which these effects might arise. These are (a) Cottrell locking, where the solute atoms form an atmosphere around the dislocations and pin them,<sup>24</sup> (b) Suzuki pinning, where the solute atoms interact chemically with the stacking faults between the partial dislocations of the face-centered-cubic lattice and pin the dislocations,<sup>25</sup> and (c)



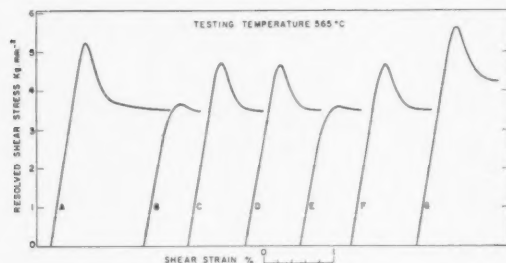


FIG. 10. Showing a yield point and strain-aging in a single crystal specimen of  $\text{Cu}_3\text{Au}$ . Before each test the specimen was rested at  $565^\circ\text{C}$  for the following period of time. (A) 12 hrs; (B) 30 sec; (C) and (D) 1 hr; (E) 15 sec; (F) 3 hrs; (G) 1 hr. Curves A to F were obtained with a shear strain rate of  $3 \times 10^{-4} \text{ sec}^{-1}$  and curve G with a shear strain rate of  $7.5 \times 10^{-4} \text{ sec}^{-1}$ .

Cottrell's<sup>17</sup> development of Fisher's idea,<sup>26</sup> that in an alloy in which there is short-range order, a larger stress is required to start deformation than to maintain it afterwards because the first dislocations to pass across the slip plane produce more disorder than those that follow them. If the deformation is stopped and the short-range order allowed to re-establish itself, the yield point will return and the alloy can be said to have strain-aged. These three mechanisms should apply, of course, to any substitutional solid solution alloy in which short-range order exists, and from this point of view the results obtained on Cu-Zn alloys by Ardley and Cottrell<sup>11</sup> support the findings of the present investigation.

One other observation which is interesting to record is that below the temperature of the second peak,  $T''$ , deformation always occurred discontinuously, whereas above that temperature deformation was smooth. A similar effect was observed in  $\beta$ -brass by Ardley and Cottrell,<sup>11</sup> except that in their case the maximum in the strength-versus-temperature curve, and the transition from jerky flow to smooth flow occurred below the critical temperature.

### CONCLUSIONS

It has been shown that the room-temperature strength of an ordered alloy of  $\text{Cu}_3\text{Au}$  depends on both the degree of long-range order and the anti-phase domain size. It is suggested that this dependence might be predicted by considering the change in bond energies across the slip plane which is brought about by slip.

It is now clear how earlier workers might arrive at different conclusions as to the effect of ordering upon the strength of alloys. Those who had well-ordered alloys would observe a low strength whilst those who had either incomplete ordering or small domain sizes, or

both, would observe a high strength. This is particularly important when comparing the  $\text{Cu}_3\text{Au}$  type alloys with the CuAu types where the ordering rates are so very different. The "transition range" mentioned in the early literature on CuAu alloys is presumably just the period in which noticeable domain growth is occurring.

In view of the large effects the domain size and the long-range-order parameter each have on the properties of ordering alloys, one ought to be careful to separate them when investigating the disorder-order reaction.

In the disordered region, yielding, strain-aging, an inverse strain-rate effect and an inverse temperature dependence of the strength upon temperature have all been observed, thereby forming a picture which is consistent with the current ideas of the effect of solute atoms and their arrangement in the lattice, upon the plastic deformation of alloys.

### ACKNOWLEDGMENTS

I wish to thank Dr. J. C. Fisher and Prof. A. H. Cottrell for their advice and encouragement throughout the course of this work. I would also like to thank Mr. V. J. DeCarlo for helping me to prepare the single crystals.

### REFERENCES

1. L. Nowack, *Z. Metallk.* **22**, 94 (1930).
2. G. Sachs and J. Weerts, *Z. Phys.* **67**, 507 (1931).
3. O. Dahl, *Z. Metallk.* **24**, 107 (1932).
4. O. Dahl, *Z. Metallk.* **28**, 133 (1936).
5. W. Koster, *Z. Metallk.* **32**, 277 (1940).
6. D. Harker, *Trans. A. S. M.* **32**, 210 (1944).
7. C. S. Barrett, *Structure of Metals* (McGraw-Hill, New York, 1952), p. 291.
8. T. Broom and W. R. Biggs, *Phil. Mag.* **45**, 246 (1954).
9. U. Dehlinger and L. Graf, *Z. Phys.* **64**, 359 (1930).
10. R. F. Vines and E. M. Wise, *Age Hardening of Metals* (American Society for Metals, Cleveland, 1940).
11. G. W. Ardley and A. H. Cottrell, *Proc. Roy. Soc.* **A219**, 328 (1953).
12. F. W. Jones and C. Sykes, *Proc. Roy. Soc.* **A166**, 377 (1938).
13. M. Polanyi, *S. Tech. Physik* **6**, 121 (1925).
14. H. Green and N. Brown, *J. Metals* **5**, 1240 (1953).
15. J. S. Koehler and F. Seitz, *J. Appl. Mech.* **14**, A-217 (1947).
16. J. C. Fisher, *Phys. Rev.* **91**, 232 (1953).
17. A. H. Cottrell, *Properties and Microstructure* (American Society for Metals, Cleveland, 1954).
18. W. L. Bragg and E. J. Williams, *Proc. Roy. Soc.* **A145**, 699 (1934).
19. R. Peierls, *Proc. Roy. Soc.* **A154**, 213 (1936).
20. H. Carpenter and J. M. Robertson, *Metals* (Oxford University Press, London, 1939).
21. C. W. MacGregor and J. C. Fisher, *J. Appl. Mech.* **13** (1946).
22. R. L. Kenyon and R. S. Burns, *Age Hardening of Metals* (American Society for Metals, Cleveland, 1939).
23. J. D. Lubahn, *Trans. A. S. M.* **44**, 643 (1952).
24. A. H. Cottrell, *Rept. Bristol Conf., Phys. Soc. London* (1948).
25. H. Suzuki, *Sci. Rep. R. I. T. U.* **A4**, 455 (1952).
26. J. C. Fisher, *Acta Met.* **2**, 9 (1954).
27. D. T. Keating and B. E. Warren, *J. Appl. Phys.* **22**, 286 (1951).
28. C. Sykes and H. Evans, *J. Inst. Metals*, **58**, 255 (1936).

## INTERACTION BETWEEN DISLOCATIONS AND INTERSTITIAL ATOMS IN BODY-CENTERED CUBIC METALS\*

A. W. COCHARDT, G. SCHOEK, and H. WIEDERSICH†

Cottrell and Bilby's theory of the locking of dislocations is extended. The interaction between impurity atoms and dislocations, both edge and screw, is estimated considering the dilation and shear strain associated with carbon atoms in  $\alpha$ -iron and using the observed crystallographic relations between the dislocation line, the slip plane and the lattice. It is found that for both types of dislocations the maximum interaction energy is about 0.75 eV and the saturation concentration near the dislocation about 6 atomic per cent. Carbon atoms occupy preferentially three equivalent positions, 120 degrees apart, around a screw dislocation. Many of them are in the slip plane around an edge dislocation. The elastic energy of a screw dislocation is reduced up to 20 per cent in the presence of a carbon atmosphere.

### INTERACTION ENTRE LES DISLOCATIONS ET LES ATOMES INTERSTITIELS DANS LES MÉTAUX CUBIQUES CENTRÉS

Extension de la théorie du blocage des dislocations de Cottrell et Bilby. L'interaction des atomes étrangers et des dislocations, vis ou coin, est calculée en introduisant la dilatation et la distorsion provoquées par les atomes de carbone dans le fer  $\alpha$  et en utilisant les relations cristallographiques observées entre la ligne de dislocations et le plan de glissement. Il est montré que pour les deux types de dislocations, le maximum de l'énergie d'interaction est de l'ordre de 0,75 e.V. et que la concentration à la saturation au voisinage de la dislocation est de l'ordre de 6% at. Les atomes de carbone occupent de préférence autour d'une dislocation vis trois positions équivalentes à 120° l'une de l'autre. Beaucoup de ces atomes sont autour d'une dislocation coin dans le plan de glissement. L'énergie élastique d'une dislocation vis est réduite de 20% par l'atmosphère de carbone.

### WECHSELWIRKUNG ZWISCHEN VERSETZUNGEN UND EINLAGERUNGATOMEN IN KUBISCH-RAUMZENTRIERTEN METALLEN

Die Theorie von Cottrell und Bilby über die Hemmung von Versetzungen wird erweitert. Unter Berücksichtigung der Aufweitungs- und Scherkräfte, die durch die Kohlenstoffatome in  $\alpha$ -Eisen hervorgerufen werden, sowie den kristallografischen Zusammenhängen zwischen der Versetzungslinie, der Gleitebene und dem Gitter wird die Wechselwirkung zwischen den Verunreinigungsatomen und den Versetzungen, sowohl Stufen- wie auch Schraubenversetzungen, abgeschätzt. Es konnte festgestellt werden, dass für beide Versetzungstypen das Maximum der Wechselwirkungsenergie  $\sim 0.75$  eV und die Sättigungskonzentration nahe der Versetzung  $\sim 6$  At% beträgt. Die Kohlenstoffatome nehmen vorzugsweise drei gleichwertige Lagen ein, die im Abstand von 120° um eine Schraubenversetzung liegen. Viele von ihnen befinden sich in der Gleitebene in der Umgebung einer Stufenversetzung. Die elastische Energie einer Schraubenversetzung wird in Gegenwart einer Kohlenstoffatmosphäre bis zu 20% herabgesetzt.

## INTRODUCTION

Cottrell and Bilby<sup>1</sup> have proposed a theory which explains the yield phenomenon in iron and other body-centered cubic metals. According to their theory interstitial atoms diffuse to dislocations because the strain energy of a crystal is lowered thereby. Each dislocation is, therefore, generally surrounded by a cloud of interstitial atoms which lock it into position. In order to pull a dislocation away from its atmosphere of solute atoms, a relatively high applied stress is needed.

From the calculation of Cottrell and Bilby,<sup>1</sup> it follows that the strain energy of a dislocation is reduced by about 10 per cent when the dislocation is surrounded by a saturated carbon atmosphere. Fisher<sup>2</sup> and Vreeland and Wood,<sup>3</sup> on the other hand, who interpret data on the delayed yield in steel,<sup>4</sup> conclude that this energy difference is only of the order of a few tenths of 1 per

cent. These and other discrepancies were thought to be due to the simplified assumptions made by Cottrell and Bilby. They assumed that an iron unit cell is strained in a hydrostatic manner when it contains a carbon atom. According to this simplified assumption, carbon atoms would segregate only near edge dislocations. Actually, however, as Cottrell and Bilby themselves and Crussard<sup>5</sup> and Nabarro<sup>6</sup> already have pointed out, carbon atoms should diffuse to screw dislocations as well.

The present paper gives a more detailed analysis of the problem. As in the treatment by Cottrell and Bilby, elastic theory of an isotropic continuum is used. This fails near the core of the dislocation where special consideration should be made. Hence, the solution is not exact. However, the present paper considers that the impurity atoms occupy certain interstices which cause a tetragonal distortion of the lattice and it considers the crystallographic relationship between the dislocation line, the slip plane and the positions of the interstitial atoms. The calculation is carried out using carbon in  $\alpha$ -iron as an example.

\* Received March 2, 1955.

† Metallurgy Department, Westinghouse Electric Corporation, East Pittsburgh, Pennsylvania.

# INTERACTION ENERGY BETWEEN DISLOCATIONS AND CARBON ATOMS

The elastic energy,  $U$ , of a body containing a dislocation and a single interstitial atom can be expressed in the form

$$U = U_D + U_C + U_{DC}, \quad (1)$$

where  $U_D$  and  $U_C$  are the energies due to the dislocation and the interstitial atom, respectively.  $U_{DC}$  is the interaction energy between dislocation and interstitial atom. It is the change in elastic energy that occurs when an interstitial atom is transferred from a position in the crystal where the stresses of the dislocation are essentially zero to a position near a dislocation. The energy terms are given by the volume integral of the energy density over the entire body or, if no body forces are present, by a surface integral which expresses the work done by the forces against the internal and external surfaces of the body when the interstitial atom is introduced and when the dislocation is made.<sup>7</sup>

For example, consider the carbon atoms in  $\alpha$ -iron. In order to estimate the interaction energy, it is first necessary to know how the iron lattice is distorted around a carbon atom. Since the exact atomic disarrangement is unknown, we make the simplifying assumption that a unit cell containing a carbon atom is deformed tetragonally as in martensite.\* Williamson and Smallmann<sup>9</sup> have shown that in  $\alpha$ -iron the carbon atoms are in octahedral positions. It is known from X-ray measurements<sup>10</sup> that the mean tetragonal distortion of martensite is proportional to  $n/N$ , where  $n$  is the number of carbon atoms and  $N$  the number of iron atoms. Assuming that this linear relationship applies up to  $n/N=0.5$ , the distortion of a unit cell of iron containing one carbon atom is found. Thereby, we neglect the interaction between the carbon atoms. In this manner the strain tensor  $S_C$  of a unit cell containing one carbon atom is obtained:

$$S_C = \begin{pmatrix} \epsilon_1 & 0 & 0 \\ 0 & \epsilon_2 & 0 \\ 0 & 0 & \epsilon_3 \end{pmatrix}, \quad (2)$$

where

$$\epsilon_1 = 0.38, \quad \epsilon_2 = \epsilon_3 = -0.026 \quad (3)$$

and where we use the rectangular coordinate system of the crystallographic axes. If  $a$  is the lattice parameter, ( $\epsilon_1 a$ ) is the elongation in the 1-direction and ( $\epsilon_2 a$ ) and ( $\epsilon_3 a$ ) are the compressions in the 2- and 3-directions.

In order to estimate the interaction energy  $U_{DC}$ , we expand a unit cell of the crystal near the dislocation line into a tetragonally distorted form. The interaction energy is essentially the work which is done by moving

\* An alternative method would be to treat the carbon atom as an elastic double force<sup>8</sup> acting along one of the axes of the unit cell. This method would be more suitable when the interaction of the carbon atoms is considered. However, under the present assumptions such a method would not be simpler, nor would it lead to appreciably different results.

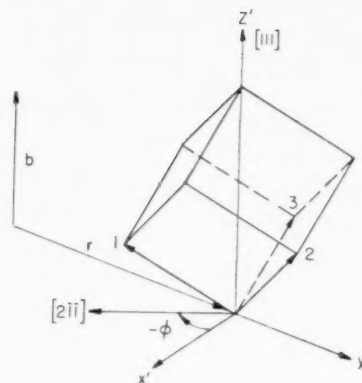


FIG. 1. Coordinate systems for the case of a screw dislocation.

each face of the cell a distance  $d_i$  against the force  $F_i$  which the stress field of the dislocation exerts on it.

$$U_{DC} = + \sum_i F_i d_i. \quad (4)$$

If the stress tensor  $T_D = (\sigma_{ik}^D)$  of the dislocation field is expressed in the same coordinate system as the strain tensor  $S_C = (\epsilon_{ik}^C)$ ,  $U_{DC}$  can be written in the form

$$U_{DC} = - (T_D, S_C) a^3 = - \sum_{ik} \sigma_{ik}^D \epsilon_{ik}^C a^3, \quad (5)$$

where  $a$  is the length of the unit cell. The components of the stress tensor are assumed to be constant along the distance  $a$ .

$U_{DC}$  can now be estimated for a screw dislocation. Consider an iron crystal with a screw dislocation in the  $[111]$ -direction which is the observed slip direction in  $\alpha$ -iron.<sup>11</sup> The line containing the Burgers vector in Fig. 1 represents the dislocation line. At a distance  $r$  there is a unit cell whose axes  $[100]$ ,  $[010]$  and  $[001]$  are defined as 1, 2 and 3 axis, respectively. The right-hand coordinate system  $x'y'z'$  has the same origin as the 1, 2, 3 system but has its  $z'$ -axis parallel to the Burgers vector and the  $y'$ -axis in the direction of the radius vector. The projection of the 1-axis in the  $x'y'$ -plane is the  $[2\bar{1}1]$ -direction and the angle between the  $x'$ -direction and the  $[2\bar{1}1]$ -axis is defined as  $\phi$ .

The strain tensor of a unit cell containing a carbon atom in axis 1 (Fig. 1) is simply given by Eqs. (2) and (3). The stress tensor  $T_D$  of the screw dislocation can be expressed in a simple manner in the coordinate system  $x'y'z'$  (Fig. 1) where it is<sup>12</sup>

$$T_D^{x'y'z'} = \frac{Gb}{2\pi r} \begin{pmatrix} 0 & 0 & 1 \\ 0 & 0 & 0 \\ 1 & 0 & 0 \end{pmatrix}; \quad r > b. \quad (6)$$

Here  $G$  is the shear modulus and  $b = \frac{1}{2}\sqrt{3}a$  the Burgers vector. Transforming  $S_C^{1,2,3}$  into the system  $x'y'z'$ , the two components  $\epsilon_{x'z'}$  and  $\epsilon_{z'x'}$  are found to be

$$\epsilon_{x'z'} = \epsilon_{z'x'} = \frac{\sqrt{2}}{3} (\epsilon_1 - \epsilon_2) \cos \phi. \quad (7)$$

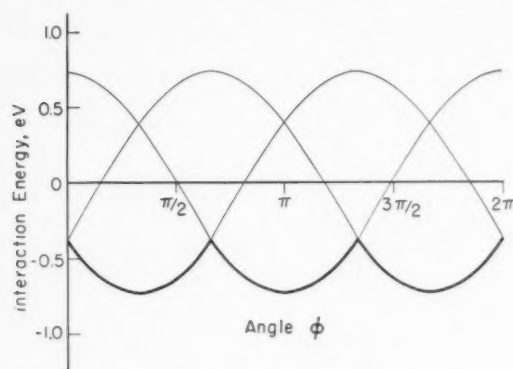


FIG. 2. Interaction energy between a carbon atom and a screw dislocation for each of the three interstitial positions ( $r=b$ ).

The other strain components,  $\epsilon_{ik}$ , do not contribute to  $U_{DC}$  since the corresponding stress components in Eq. (5) are zero. Using Eqs. (5), (6) and (7), the interaction energy is obtained as

$$U_{DC} = A \frac{\cos \phi}{r} \quad r > b, \quad (8)$$

where the constant  $A$  is

$$A = \frac{\sqrt{2} b G a^3}{3\pi} (\epsilon_1 - \epsilon_2).$$

$U_{DC}$  decreases inversely with  $r$  and is zero for a pure dilation ( $\epsilon_1 = \epsilon_2$ ). Equation (8) gives the interaction energy for a carbon atom on axis 1 (Fig. 1). The expressions for the other two cases (carbon atoms on axes 2 and 3) are the same except for a phase difference of  $\pm 120$  degrees due to the trigonal symmetry of a  $\langle 111 \rangle$ -axis. The angular dependence of  $U_{DC}$  for the three cases is shown in curves of Fig. 2. It is seen that there are three equivalent positions of lowest energy at  $\phi = 60, 180$  and  $300$  degrees.

The interaction energy for the nearest carbon atoms at  $r \approx b$  is then  $U_{DC} = 0.75$  eV. By using the elastic equations so close to the dislocation line we certainly overestimate  $U_{DC}$ . According to an estimate by Mott<sup>13</sup>

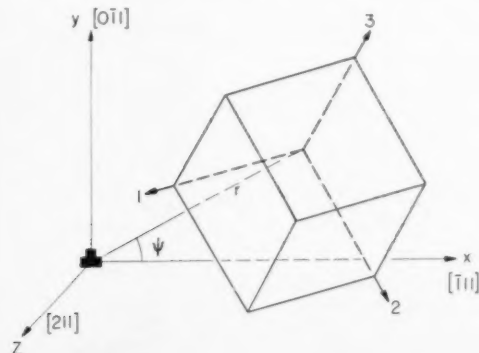


FIG. 3. Coordinate system for the case of an edge dislocation.

and Cottrell,<sup>14</sup> the maximum interaction energy is about 0.5 eV.

The interaction energy of a carbon atom with an edge dislocation is estimated in a similar way. Fig. 3 illustrates the crystallographic relationships. The slip plane ( $xz$ ) is assumed to be the  $(0\bar{1}1)$ -plane which is an observed slip plane in  $\alpha$ -iron with lowest indices.<sup>11</sup> The dislocation line is in the direction  $\langle 211 \rangle$  and the Burgers vector  $b$  in direction  $\langle \bar{1}11 \rangle$ .  $\psi$  is the angle between  $\langle \bar{1}11 \rangle$  and the radius vector from the dislocation to the considered elementary cell.

The stress tensor  $T_D^{x,y,z}$  of an edge dislocation parallel to the  $z$ -axis and with glide plane  $y=0$  is<sup>15</sup>

$$T_D^{x,y,z} = -\frac{D}{r} \begin{pmatrix} -\sin \psi (1 + 2 \cos^2 \psi) & \cos \psi \cos 2\psi & 0 \\ \cos \psi \cos 2\psi & \sin \psi \cos 2\psi & 0 \\ 0 & 0 & -2\nu \sin \psi \end{pmatrix} \quad (9)$$

the extra plane is the half-plane  $x=0$  with  $y>0$ .

The constant  $D$  is

$$D = \frac{Gb}{2\pi(1-\nu)},$$

where  $\nu$  is Poisson's ratio.

The components of the strain tensor  $S_C^{1,2,3}$  are now transformed from the 1, 2, 3 system into the  $x, y, z$  system. This leads to

$$\begin{aligned} \epsilon_{xx} &= \frac{1}{3}(\epsilon_1 + \epsilon_2 + \epsilon_3); & \epsilon_{xy} &= \frac{1}{\sqrt{6}}(\epsilon_3 - \epsilon_2) \\ \epsilon_{yy} &= \frac{1}{3}(\epsilon_2 + \epsilon_3); & \epsilon_{zz} &= \frac{2}{3}\epsilon_1 + \frac{1}{6}(\epsilon_2 - \epsilon_3). \end{aligned} \quad (10)$$

Applying Eq. (5), the interaction energy between a carbon atom and an edge dislocation is then obtained as

$$\begin{aligned} U_{DC} &= -\frac{Da^3}{r} \left\{ \frac{1}{3} \sin \psi (1 + \nu + 2 \cos^2 \psi) (\epsilon_1 + \epsilon_2 + \epsilon_3) \right. \\ &\quad - \frac{1}{2} \sin \psi \cos 2\psi (\epsilon_2 + \epsilon_3) \\ &\quad \left. - \frac{\sqrt{6}}{3} \cos \psi \cos 2\psi (\epsilon_3 - \epsilon_2) + \nu \sin \psi \epsilon_1 \right\}, \quad r > b \quad (11) \end{aligned}$$

Since carbon atoms may occupy positions along axes 1, 2 and 3, there are three sets of constants for the last three terms in Eq. (11). Figure 4 illustrates graphically the  $\psi$ -dependence of  $U_{DC}$  for all three interstitial positions. It shows that the interaction energy is almost constant in the entire half-space below the slip plane if the carbons sit in the positions of lowest energy. There is a slight minimum of  $U_{DC}$  almost in the slip plane. It is further seen from Fig. 4 that, below the slip plane, carbon atoms prefer positions on axis 2 or 3. Similar results are obtained when the  $(xz)$ -plane is assumed to be a  $(112)$ -plane which is another observed slip plane in  $\alpha$ -iron.<sup>11</sup> The only difference is that the minimum of  $U_{DC}$ , which again lies only a few degrees away from the slip plane, is a little more pronounced and all interstitial positions contribute minimum values for  $U_{DC}$  below



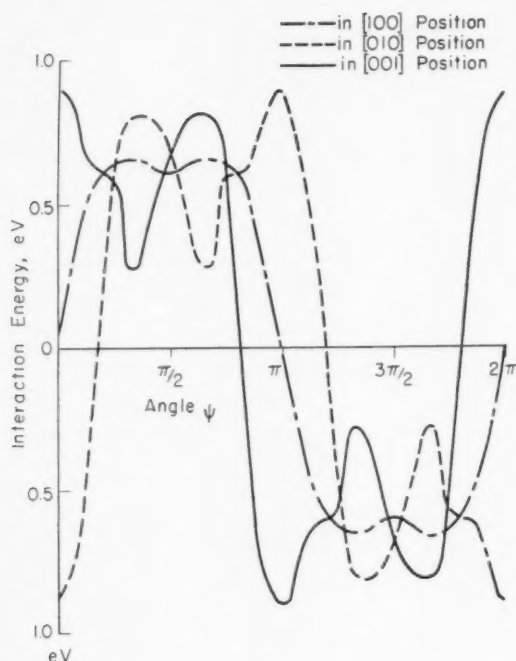


FIG. 4. Interaction energy between a carbon atom and an edge dislocation ( $r=b$ ).

the slip plane. In both cases the interaction energy at  $r=b$  is again about 0.75 eV.

#### SATURATION CONCENTRATION

The number of carbon atoms that can diffuse to a dislocation is limited because, at a certain concentration of carbon near a dislocation, additional carbon segregation no longer reduces the strain energy of the crystal. An estimate of the saturation concentration can be obtained from strain energy considerations. Let us take a volume element near a dislocation which is subjected to the elastic strains  $\epsilon_{ik}^D$  resulting from the dislocation, and assume that this volume element is so small that the strains in it can be considered constant, yet so large that we can speak in terms of concentration of carbon atoms. When carbon atoms diffuse into the energetically most favorable positions of this volume element, the elastic strains are reduced. We shall neglect the interaction between carbon atoms, which is justifiable for small concentrations. (The results of the calculation show that the highest concentration is about 7 atomic per cent). The average strain of the volume element due to the carbon atoms is then proportional to the carbon concentration,<sup>10</sup> and the components of the remaining elastic strain  $\epsilon_{ik}$  are

$$\epsilon_{ik} = \epsilon_{ik}^D - x\epsilon_{ik}^C, \quad (12)$$

where  $(\epsilon_{ik}^C)$  is the strain tensor resulting from the carbon atoms given by Eq. (2) and  $x=2n/N$  expresses the relative concentration of carbon atoms.  $x=1$  means 1 carbon atom per unit cell.

The saturation concentration  $x_s$  is reached when the energy in this volume element is no longer reduced by further segregation of carbon atoms; in other words, if the elastic energy density is denoted by  $u$ ,  $x_s$  is obtained from

$$\frac{\partial u}{\partial x} = 0. \quad (13)$$

Since  $u$  is a homogeneous quadratic function of the strain components  $\epsilon_{ik}$ , it can be written in the form

$$u = u_D + xu_{DC} + x^2u_C. \quad (14)$$

$u_D$  is the elastic energy density due to the dislocation alone; for example, it is

$$u_D = \frac{Gb^2}{8\pi^2r^2} \quad (15)$$

for a screw dislocation;  $u_{DC}$  is simply  $U_{DC}/a^3$ , where  $U_{DC}$  is given by Eq. (8) and (11) and  $u_C$  is the energy density due to the elastic strain of the carbon atmosphere with the concentration  $x=1$ .

$$u_C = G \left\{ \frac{1-\nu}{1-2\nu} (\epsilon_1 + 2\epsilon_2)^2 - 2(2\epsilon_1\epsilon_2 + \epsilon_2^2) \right\}. \quad (16)$$

The saturation concentration  $x_s$  is then derived from Eqs. (13) and (14) as

$$x_s = -\frac{u_{DC}}{2u_C}. \quad (17)$$

Taking the average value of  $u_{DC}$  for all angles, we obtain for the screw dislocation

$$\frac{x_s}{2} = \frac{n}{N} = \frac{b}{r} = 0.06.$$

The result shows that the saturation concentration is about 6 atomic percent one atomic distance away from the dislocation line.

The decrease of the elastic energy of the dislocation due to a saturated carbon atmosphere can be estimated by substituting Eq. (17) into Eq. (14). This leads to an energy density  $u_s$ , which is expressed by

$$u_s = u_D - \frac{u_{DC}^2}{4u_C}. \quad (18)$$

When the elastic energy density is written as a tensor product of the stress and strain tensors, the Schwarz inequality<sup>14</sup> shows that  $u_s \geq 0$ . If the strain tensors of the dislocation and of the carbon atmospheres were similar, the strains of the dislocation could be completely relaxed by a carbon atmosphere and  $u_s$  would become zero.

By inserting numerical values into Eq. (18),  $u_s$  is found to be

$$u_s \approx 0.8 \frac{Gb^2}{8\pi^2r^2}.$$

Thus the strain energy is reduced about 20 per cent when a screw dislocation is surrounded by a saturated carbon atmosphere.

The saturation concentration for an edge dislocation is found by substituting into Eq. (17) the value for  $U_{DC}$  from Eq. (11). This leads to a concentration for the half-space below the slip plane of

$$\frac{x_s}{2} = \frac{n}{N} = 0.07 \frac{b}{r},$$

when the average value of  $U_{DC}$  for the angles below the slip plane is taken. The saturation concentration near an edge dislocation is fairly close to that found near a screw dislocation.

### DISCUSSION

It has been shown that the interaction between a screw dislocation and a carbon atom in  $\alpha$ -iron has about the same strength as the interaction between an edge dislocation and a carbon atom.

The saturation concentration for both types of dislocation has values close to that found by Cottrell and Bilby for an edge dislocation. An essential difference between the results of the present paper and those of Cottrell and Bilby's is that carbon atoms near an edge dislocation are found to be spread out over all angles below the slip plane and are concentrated in the neighborhood of the slip plane rather than at positions just below the dislocation.

If all carbon atoms in a saturated atmosphere were in positions of lowest energy, the reduction of elastic energy would be about 20 per cent for a screw and roughly half as much for an edge dislocation. This means that at absolute zero temperature a dislocation must gain 10 to 20 per cent of its final energy to become free of its atmosphere. However, this energy difference decreases with increasing temperature, as can be seen from the following crude estimate. Carbon atoms are bound to a dislocation line only when their interaction energy is larger than the thermal energy or when  $U_{DC} > \beta kT$ , where  $\beta$  is a factor of the order of 1. The radius  $R$ , of the region in which carbon atoms are bound to the dislocation, is then found from Eq. (8) as

$$R = \frac{A}{\beta kT}$$

for a screw dislocation. If we take  $\beta=1$ , we obtain a radius of  $R=30b$  at room temperature. The number of carbon atoms in this region is about 15 per atomic plane. Since the energy is reduced only in this region, the reduction of the total elastic energy of the dislocation is then only 6 per cent at room temperature.

If we compare the accumulation of carbon atoms around a screw and an edge dislocation, the screw can bind roughly twice as many atoms as an edge dislocation. The reason is that the segregation takes place only below the glide plane of an edge dislocation but all

around a screw dislocation, while the interaction energy per atom is the same in both cases.

As was already mentioned, Fisher<sup>2</sup> has recently concluded from a simple analysis of the mechanism of yielding that the line energy  $\gamma_0$  of a dislocation without a carbon atmosphere is only  $\frac{1}{3}$  per cent larger than the line energy  $\gamma$  of a dislocation surrounded by carbon atoms, whereas, according to Cottrell and Bilby's estimate, the energy increase is about 10 per cent. The discrepancy between these two results, which has already been pointed out by Vreeland and Wood,<sup>3</sup> cannot be explained by the temperature dependence of the ratio  $\gamma/\gamma_0$  nor by assuming the interaction between carbon atoms and screw dislocations to be small—as was ruled out above. It seems, therefore, that the value of  $\gamma_0$ , which Fisher uses, should not be interpreted as the energy of a dislocation without a carbon atmosphere but rather as the energy of a dislocation line at the point where it overcomes the binding force of the carbon atmosphere.

If the dislocation moves away from its atmosphere, the energy increases gradually. Since the binding force is given by the maximum gradient of the energy curve, Fisher's value of  $\gamma_0 - \gamma/\gamma_0 = 3 \times 10^{-3}$  should be associated with the inflection point in this energy curve rather than with the maximum.

### ACKNOWLEDGMENTS

We wish to thank C. Zener, Associate Director of the Westinghouse Research Laboratories, for his helpful criticism. Thanks are also due to several of our colleagues, particularly J. H. Bechtold, G. Comentz, R. Eisner and U. Roesler for discussing with us the present paper.

### REFERENCES

1. A. H. Cottrell and B. A. Bilby, *Proc. Phys. Soc.* **A62**, 49 (1949).
2. J. C. Fisher, "Application of Cottrell's Theory to Delayed Yield in Steel," Submitted to American Society for Metals.
3. T. Vreeland, Jr. and D. S. Wood, "A Comparison Between Dislocation Theory and Experimental Measurements of Delayed Yield in Steel," Technical Report, California Institute of Technology, 1954.
4. D. S. Clark and D. S. Wood, *Proc. A.S.T.M.* **49**, 717 (1949).
5. C. Crussard, *Metaux et Corrosion* **25**, 203 (1950).
6. F. R. N. Nabarro, *Report on Strength of Solids* (London, Phys. Soc., 1948), p. 38.
7. G. Liebfried, *Z. Phys.* **126**, 781 (1949).
8. A. E. Love, *The Mathematical Theory of Elasticity* (New York, 1944).
9. G. K. Williamson and R. E. Smallmann, *Act. Cryst.* **6**, 361 (1953).
10. G. Kurdjumov and E. Kaminsky, *Z. Phys.* **53**, 696 (1929).
11. E. Schmid and W. Boas, *Kristall Plastizität* (Springer-Verlag, Berlin, 1935), p. 90.
12. A. H. Cottrell, *Dislocations and Plastic Flow in Crystals* (Oxford, 1953), p. 36.
13. N. F. Mott, *Imperfections in Nearly Perfect Crystals* (Shockley, Ed.), (New York, 1952), p. 173.
14. A. H. Cottrell, *Dislocations and Plastic Flow in Crystals* (Oxford, 1953), p. 134.
15. A. H. Cottrell, *Dislocations and Plastic Flow in Crystals* (Oxford, 1953), p. 34.
16. E. Madelung, *Die Mathematischen Hilfsmittel des Physikers* (Berlin, 1953), p. 15.

## THE INFLUENCE OF THIN INTERMEDIATE LAYERS ON INTERDIFFUSION IN COPPER-NICKEL COUPLES\*

M. L. MEHTA and H. J. AXON†

Experiments are reported on the chemical diffusion coefficients in the copper-nickel system for the two pure metals and also with the presence of thin (0.00002 in.) intermediate layers of Au, Sn, Zn or Cd.

Au or Zn has small effect whilst Sn or Cd accelerate the rate of diffusion. Sn appears to behave differently from Cd in accelerating the diffusion of nickel into copper and retarding that of copper into nickel.

### INFLUENCE SUR LA DIFFUSION DANS LES COUPLES Cu-Ni DE MINCES COUCHES INTERMÉDIAIRES

Les expériences portent sur les coefficients de diffusion dans le système cuivre-nickel pour les deux métaux purs et en présence de minces couches intermédiaires (0,00002 in.) de Au, Sn, Zn ou Cd.

Au ou Zn ont peu d'effet, tandis que Sn ou Cd augmentent la vitesse de diffusion. Sn semble se comporter différemment que Cd, en augmentant la diffusion du nickel dans le cuivre et en retardant celle du cuivre dans le nickel.

### DER EINFLUSS VON DÜNNEN ZWISCHENSCHICHTEN AUF DIE DIFFUSION ZWISCHEN KUPFER UND NICKEL

Es werden Untersuchungen über die chemischen Diffusionskoeffizienten im System Kupfer-Nickel mitgeteilt und zwar sowohl für die reinen Metalle als auch für die Gegenwart von dünnen Zwischenschichten (0.00002 in.) aus Au, Sn, Zn oder Cd.

Au oder Zn beeinflussen die Diffusion nur gering, während Sn oder Cd die Diffusion beschleunigen. Sn scheint sich dabei anders als Cd zu verhalten, da es die Diffusion von Nickel in Kupfer beschleunigt, die des Kupfer in Nickels jedoch verlangsamt.

Considerable attention has been given to the study of the interdiffusion of copper and nickel, particularly as regards the variation of diffusion coefficient with concentration. The classical study of this system is the analysis by Matano<sup>1</sup> of the results of Grube and Jede<sup>2</sup> which provided the basic method for the examination of this topic and is universally referred to as the Matano method. Perhaps the most recently published work on this topic is due to da Silva and Mehl,<sup>3</sup> who used the Matano method of analysis to evaluate diffusion coefficients in welded diffusion couples of block copper and block nickel at temperatures of 1054 and 947°C, respectively.

There appears to be no published work on the effect of an intermediate layer of a third metal on diffusion in a copper-nickel couple, and the purpose of the present paper is to report the effect of thin electrodeposited layers of gold, tin, zinc and cadmium on the interdiffusion between fully annealed nickel rod and electrodeposited copper.

### EXPERIMENTAL METHODS

The nickel used in the present work was supplied as 0.75 in. dia., rolled and soft annealed bar, from which 4-in. lengths were cut. The nickel starting pieces were faced and centred in a precision lathe and machined between centres to a diameter of 0.6 in. Machining was followed by a final grinding operation using 000 emery paper to give a smooth finish, followed by the careful application of stopping off compound to the machining

centres, degreasing, etching and electrodeposition of either copper or the appropriate intermediate layer of the third metal followed by copper.

The need to electrodeposit copper onto thin layers of tin, zinc and cadmium precluded the direct use of an acid copper-sulfate bath; hence, in all cases the first copper layer was deposited from a conventional cyanide bath to a thickness of 0.002 in., followed immediately by a water swill and further buildup of about 0.1 in. of copper from a conventional acid copper-sulfate bath. All electrodeposition was done on a beaker or small tank scale to facilitate control, the specimens being wired with suitable guard-rings to produce a uniform distribution of deposited metal. Tin, gold, zinc and cadmium layers were deposited from conventional stannate or cyanide baths to a thickness of 0.00002 in.

After the complete electrodeposition treatment the stopping off compound was removed and the specimens were heated together in the same zone of an electrically heated tube furnace through which pure nitrogen was continuously streamed. The specimens were supported in a suitable jig to prevent metallic contact and hence the possibility of the specimens welding together. In view of the intrinsic mechanical weakness of some of the intermediate layers, no machining operation was conducted subsequent to electrodeposition and prior to the diffusion anneal. Similarly, because of the low melting points of some of the metals the diffusion couples were slowly heated from room temperature to the diffusion annealing temperature of 950°C over a period of 30 hours. The slow heating also overcame

\* Received February 24, 1955.

† The University, Manchester, England.

difficulties due to the unequal thermal expansion of the copper and nickel—difficulties which manifested themselves in the separation of copper and nickel when more rapid rates of heating or when thicker deposits of copper were used. Annealing was continued for 140 hours at  $950 \pm 2^\circ\text{C}$  and at the end of this period the specimens were allowed to cool in the furnace. The time required to cool down to room temperature was about 18 hours. In spite of all precautions, some specimens showed blistering after the diffusion anneal. All seriously blistered specimens were discarded, but those which showed only slight blistering were used after the blistered portion had been drilled out.

The annealed specimens were mounted in the lathe between the same centres as originally used in preparing the nickel, and layers were carefully machined off and subjected to chemical analysis for both nickel and copper. A total metal content of less than 99.5 percent by analysis was not accepted. In this way concentration penetration data were obtained which were first plotted on probability paper in the manner described by da Silva and Mehl.<sup>3</sup> This method of plotting showed up the less reliable experimental points and was of great value in constructing the most probable form of the concentration penetration curves shown in Figs. 1 to 5.

#### EXPERIMENTAL RESULTS AND DISCUSSION

Figures 1 to 5 show the concentration penetration curves for the nickel-copper couple and for the other couples which had thin intermediate layers of a third metal. The value of a preliminary screening of the results by a probability paper plot is demonstrated in Fig. 2, in which it can be seen that the point at 12.09 at. % nickel is given little weight because it fell away

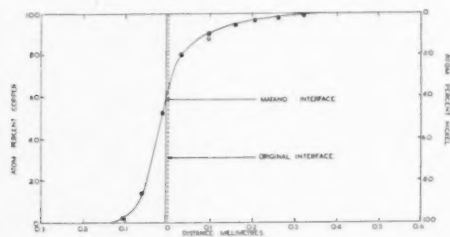


Fig. 1. Concentration penetration curve for simple copper nickel couple.

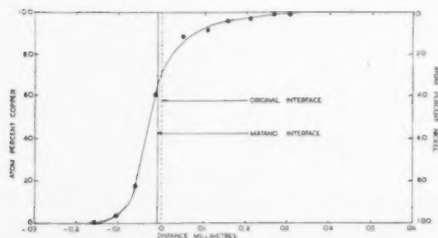


Fig. 2. Concentration penetration curve for copper nickel couple with an intermediate layer of gold.

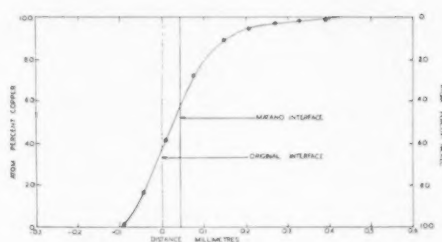


Fig. 3. Concentration penetration curve for copper nickel couple with an intermediate layer of tin.

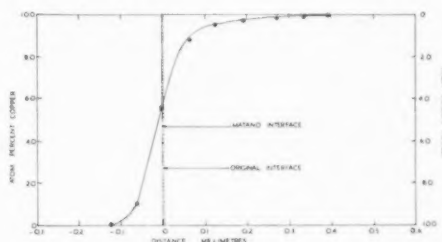


Fig. 4. Concentration penetration curve for copper nickel couple with an intermediate layer of zinc.

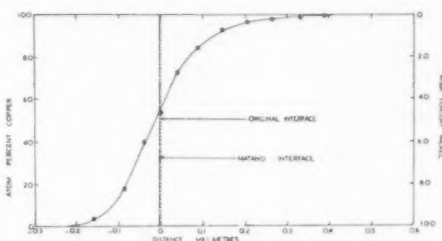


Fig. 5. Concentration penetration curve for copper nickel couple with an intermediate layer of cadmium.

from the probability plot. The concentration penetration curves were analysed by the Matano method to give the variation of diffusion coefficient with composition and the results of this analysis are shown in Figs. 6 to 10, where the values of the diffusion coefficients are probably reliable to within a few percent in the composition range 20 to 80 percent copper, but outside this range too much reliance should not be placed on the results because of the large possibility of error in determining the slope of the concentration penetration curves outside these limits. The magnitude of plotting errors is illustrated in Fig. 9, where two sets of points are plotted. These two sets of points refer to two concentration penetration curves plotted from the same experimental observations.

In discussing these results, attention may first be directed to the plots of diffusion coefficient against concentration which are shown in Figs. 6 to 10. It is to be noted that the diffusion coefficients here reported are the mean or "chemical" diffusion coefficients and take no cognizance of the individual mobilities of the two atomic species, although, as pointed out by Darken<sup>4</sup>



and emphasised by Le Clair,<sup>5</sup> the presence of a Kirkendall effect<sup>6</sup> (as reported by da Silva and Mehl<sup>8</sup> for copper-nickel) necessitates a consideration of the individual mobilities of the two atomic species if diffusion mechanisms are to be discussed in detail. Although it is not possible to evaluate individual diffusion coefficients from the present results, there are, nevertheless, aspects of the concentration penetration curves which underline the desirability of having such information. Thus it will be seen from Figs. 6 to 10 that the presence of thin (0.00002 in.) intermediate layers of gold or zinc exerts little influence on the chemical diffusion coefficients of the copper-nickel system, although a slight retardation may be detected in the composition range 60 to 80 at. % copper. On the other hand the presence of an intermediate layer of tin or of cadmium appears to raise the chemical diffusion coefficient, cadmium being apparently the more effective element.

That Figs. 6 to 10 do not represent the complete picture is indicated by an examination of Figs. 1 to 5, where it can be seen that the concentration penetration curves are reasonably symmetrical about the *original* interface and that the Matano interface moves slightly into the nickel-rich side of the diffusion couple for the

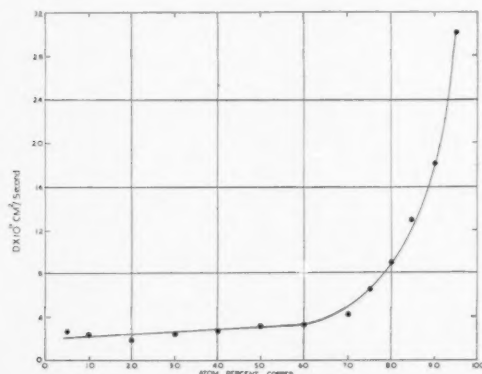


FIG. 6. The variation of diffusion coefficient with concentration in simple Cu-Ni couple.

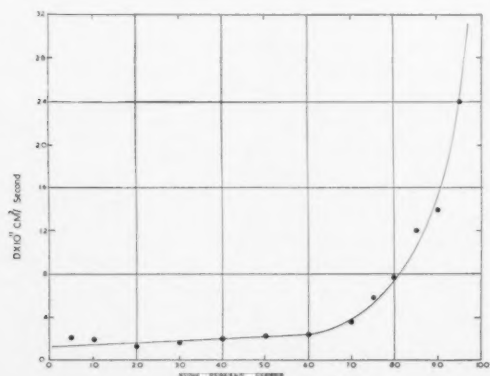


FIG. 7. The variation of diffusion coefficient with concentration in Cu-Ni couple with an intermediate layer of gold.

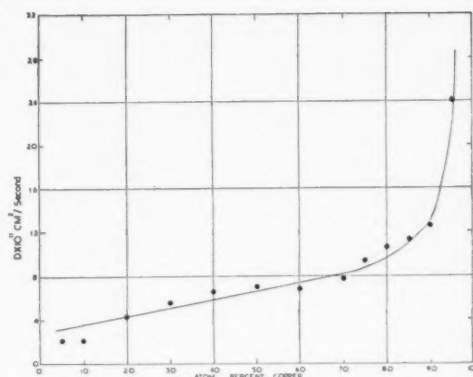


FIG. 8. The variation of diffusion coefficient with concentration for Cu-Ni couple with an intermediate layer of tin.

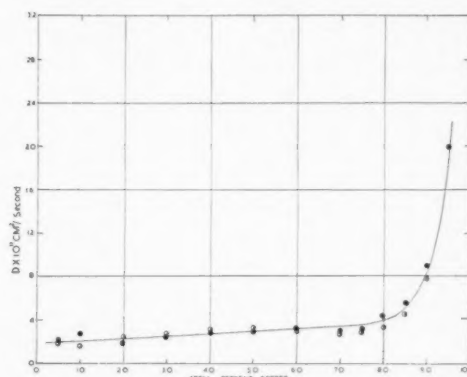


FIG. 9. The variation of diffusion coefficient with concentration for Cu-Ni couple with an intermediate layer of zinc.

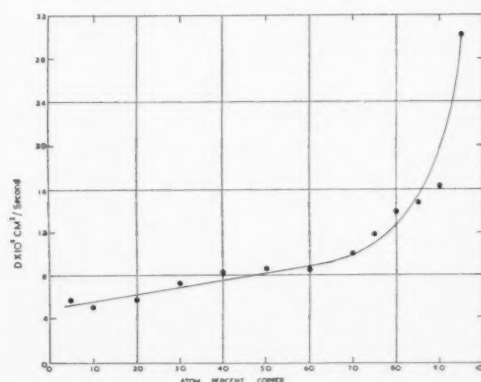


FIG. 10. The variation of diffusion coefficient with concentration for Cu-Ni couple with an intermediate layer of cadmium.

straight copper-nickel system and also in the presence of gold zinc and cadmium intermediate layers, the increased chemical diffusion coefficients in the presence of cadmium being reflected in a larger area between the curve and the Matano interface. A quite different state of affairs is visible in the case of the tin intermediate layer (Fig. 3), where it can be seen that the concentration penetration curve is strongly unsymmetrical about

the *original* interface and that the Matano interface has moved markedly into the copper-rich side of the diffusion couple.

This may be interpreted as indicating a more rapid diffusion of nickel into copper than of copper into nickel. A possible explanation of this observation lies in the production of a semipermeable membrane of material within which the mobility of atoms is modified by the nickel atoms being associated with tin atoms existing either as a nickel tin intermetallic compound or, more probably, as a solid solution region of tin in solid solution in nickel. Examination of the heats of formation of the possible compounds in the nickel-tin-copper system (CuSn 1.8 NiSn 7.5 Ni<sub>3</sub>Sn<sub>2</sub> 7.5 Ni<sub>3</sub>Sn 5.7 kcal/q-atom) suggests that the electrochemical attraction between nickel and tin in solid solution should be strong, and hence the mobility of nickel atoms would be dependent

upon their breaking away from associated tin atoms. Evidence for interatomic attraction in ternary solid solutions has been put forward for the aluminium-magnesium-silicon system<sup>7,8</sup> and it seems that a study of individual atomic mobilities in ternary systems may also reflect the presence of "incipient molecules" in the solid solution.

#### REFERENCES

1. C. Matano, J. Phys. (Japan) **8**, 109 (1933).
2. G. Grube and A. Jede, Z. Elektrochem. **38**, 799 (1932).
3. C. L. C. DaSilva and R. F. Mehl, Trans. A.I.M.M.E. **191**, 155 (1951).
4. L. S. Darken, Trans. A.I.M.M.E. **175**, 184 (1948).
5. A. D. Le Claire, *Progress in Metal Physics*, Vol. 1 (1949); Vol. 4 (1953) (Pergamon Press, London).
6. A. D. Smigelskas and E. O. Kirkendall, Trans. A.I.M.M.E. **171**, 130 (1947).
7. R. B. Hill, and H. J. Axon, J. Inst. Metals **83** (1954-55), 354.
8. T. A. Badaeva, Doklady Akad. Nauk. S.S.S.R. **64**, 533 (1949).

# DIE TEILCHENFORM BEI DER KARBIDAUSSCHIEDUNG AUS DEM $\alpha$ -EISEN\*

W. PITSCH†

Um die Karbidausscheidung aus dem  $\alpha$ -Eisen zu untersuchen, wird aus einer Verbindung von Dämpfungs- und Widerstandsmessungen ein Parameter abgeleitet, welcher nur von der Form der ausgeschiedenen Teilchen abhängt. Dieser Parameter ist der Widerstandskoeffizient  $\beta$ , welcher die durch eine Ausscheidung vom Betrage Eins verursachte Widerstandsänderung angibt. Die Abhängigkeit des Parameters von der Teilchenform wird theoretisch berechnet.

Eine Anwendung der Berechnung auf experimentelle Untersuchungen der Karbidausscheidung zeigt, dass das Karbid sich plattenförmig ausscheidet und dass während der Ausscheidung eine Umformung dieser Platten stattfindet, wobei das Verhältnis "Plattendurchmesser: Plattendicke" abnimmt.

Diese Ergebnisse werden mit elektronenoptischen Beobachtungen verglichen, und es wird das Zenersche Wachstumsgesetz diskutiert.

## THE SHAPE OF PARTICLES DURING PRECIPITATION OF CARBIDE IN $\alpha$ -IRON

Precipitation of carbide in  $\alpha$ -iron is investigated in more detail, combining the two experimental methods of internal friction and electrical resistivity. This combination yields a parameter which is solely dependent on particle shape. The parameter is equal to a coefficient  $\beta$ , which indicates the variation of electrical resistance caused by unit precipitation. The dependence of the parameter on particle shape is theoretically computed.

Using experimental data, the values of the deduced parameter indicate that the precipitated particles are plate-like. Furthermore, during precipitation the ratio "plate-diameter: plate-thickness" decreases, i.e., coagulation takes place.

These results are compared with those of electron micrographs published elsewhere and with Zener's growth law of precipitation.

## FORME DES PRÉCIPITÉS DE CARBURE DANS LE FER $\alpha$

Lors de la précipitation des carbures dans le fer  $\alpha$ , on peut déduire des mesures du frottement interne et de la résistivité un paramètre qui ne dépend que de la forme des particules précipitées; ce paramètre est le changement de résistance dû à une précipitation égale à l'unité. Une application à la précipitation du carbure montre que celui-ci précipite sous forme de plaquettes et que pendant la précipitation, le rapport du diamètre de ces plaques à leur épaisseur diminue.

Ces résultats sont comparés aux observations par microscopie électronique et la loi de croissance de Zener est discutée.

### 1. EINLEITUNG

Bei der Untersuchung von Ausscheidungsvorgängen in übersättigten Mischkristallen misst man im allgemeinen die Änderung einer physikalischen Eigenschaft, etwa den elektrischen Widerstand, die Koerzitivkraft usw., und schliesst daraus auf die Kinetik des Vorganges. Durch eine Verbindung verschiedener Messverfahren ist es möglich, zu weiteren Aussagen über den Ausscheidungsverlauf zu gelangen. (Siehe z.B. Arbeit 10).

In der vorliegenden Arbeit wird gezeigt, wie durch Verbindung zweier geeigneter Messverfahren, mit denen die Ausscheidung gleichzeitig verfolgt wird, die Gestalt der ausgeschiedenen Teilchen untersucht werden kann. Eine solche Verbindung ist möglich, wenn die Messwerte des ersten Verfahrens nur von der ausgeschiedenen Menge  $n_P$  bestimmt werden, während die Messwerte des zweiten Verfahrens ausser von  $n_P$  noch von einem Parameter  $\beta$  abhängen, der die Gestalt der ausgeschiedenen Teilchen angibt, also

$$\begin{aligned}\text{Messwert}_I &= f(n_P), \\ \text{Messwert}_{II} &= f(n_P, \beta).\end{aligned}$$

Der Betrag der Ausscheidung wird nach dem ersten

Verfahren gemessen und der Parameter  $\beta$  als neue Messgrösse aus der zweiten Beziehung bestimmt. Dann ist eine Aussage über die Teilchen möglich, wenn die Abhängigkeit des Parameters von ihrer Form bekannt ist.

### 2. UNTERSUCHUNGSVERFAHREN

Ein Messverfahren der erstgenannten Art ist im Falle einer Nitrid- oder Karbidausscheidung aus dem  $\alpha$ -Eisen die in den letzten Jahren vielfach durch freie Torsions- oder Biegeschwingungen gemessene Dämpfung. Es konnte nämlich gezeigt werden, dass eine solche Dämpfung nur durch gelösten und nicht durch ausgeschiedenen Kohlenstoff verursacht wird.<sup>1</sup> Daher kann während einer Karbidausscheidung aus übersättigter Lösung laufend die Menge  $n_L$  des noch gelösten Kohlenstoffs bestimmt werden. Die ausgeschiedene Menge  $n_P$  ergibt sich dann aus dem anfangs vollständig gelösten Gesamtgehalt  $n_A$  zu  $n_P = n_A - n_L$ . Das gleiche gilt für Stickstoff.

Als zweites Verfahren kann die Widerstandsmessung benutzt werden, denn die Änderung des elektrischen Widerstandes, welche durch eine Karbidausscheidung verursacht wird, hängt nicht nur von der ausgeschiedenen Menge  $n_P$ , sondern auch wesentlich von der Gestalt der Karbidteilchen ab. Über diese Abhängigkeit ist

\* Received May 11, 1955.

† Max-Planck-Institut für Eisenforschung, Düsseldorf, Germany.

bisher quantitativ nichts bekannt, sie muss daher zunächst ermittelt werden.

### 3. ABSCHÄTZUNG DER DURCH EINE KARBIDAUSSCHEIDUNG IM $\alpha$ -EISEN VERURSACHTEN ÄNDERUNG DES ELEKTRISCHEN WIDERSTANDES

Die ausgeschiedenen Karbidteilchen werden im Vergleich zum Eisen als praktisch nicht leitend angesehen, d.h. sie werden wie kleine Isolatoren in einem umgebenden leitenden Gitter behandelt. Dann wird die Änderung des Stromlinienfeldes und daraus die Änderung des Widerstandes berechnet, die bei der Entstehung solcher nicht leitender Einschlüsse auftritt.

An der Oberfläche eines Isolators ist die Normalkomponente der Stromlinien gleich Null, die Strombahnen führen um die Teilchen herum und werden dabei um einen Betrag  $\Delta L$  verlängert (Abb. 1). Ausserdem verringern die im Gitter eingelagerten Isolatoren den leitenden Querschnitt um einen Betrag  $-\Delta F$ . Beide Effekte—die Verlängerung des Stromweges um  $\Delta L$  sowie die Verminderung des leitenden Querschnitts um  $-\Delta F$ , bewirken eine Widerstandserhöhung. Man erhält für diese Widerstandserhöhung, wenn noch der Einfluss einer Menge  $n_L$  gelösten Kohlenstoffs auf den Widerstand des leitenden Gitters mit berücksichtigt wird,

$$\frac{R_{Fe, L, P} - R_{Fe}}{R_{Fe}} = (1 + \alpha n_L) \cdot \left( \frac{\Delta L}{L_0} - \frac{\Delta F}{F_0} \right) + \alpha n_L. \quad (1)$$

In dieser Gleichung ist  $R_{Fe}$  der Widerstand des reinen Eisens,  $R_{Fe, L, P}$  der Widerstand des Eisens, in welchem der Kohlenstoff zum Teil gelöst, zum Teil ausgeschieden ist,  $\alpha = 2,75 [\text{Gew.}\%C]^{-1}$  eine bekannte Grösse,<sup>2</sup>  $L_0$  die ursprüngliche Länge der Strombahnen vor der Ausscheidung und  $F_0$  der ursprüngliche leitende Querschnitt.

Die Berechnung der Ausdrücke  $\Delta L/L_0$  und  $\Delta F/F_0$  soll für kubische Teilchen\* gleicher gemittelter Grösse mit den Kantenlängen  $l_x = l_y = a$  und  $l_z = b$  ausgeführt werden (Abb. 2). Je nach Grösse des Verhältnisses

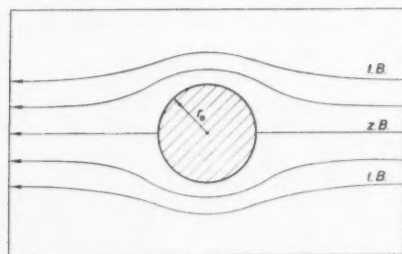


Abb. 1. Der Stromlinienverlauf in der Nähe eines Teilchens mit kreisförmigem Querschnitt (t.B. = tangentielle Strombahn, z.B. = zentrale Strombahn).

\* Dass die besonders gewählte kubische Form keinen wesentlichen Einfluss auf die Abschätzung hat, wurde durch einen Vergleich zwischen einer Abschätzung für Würfel ( $a=b$ ) und einer solchen für Kugeln sichergestellt.

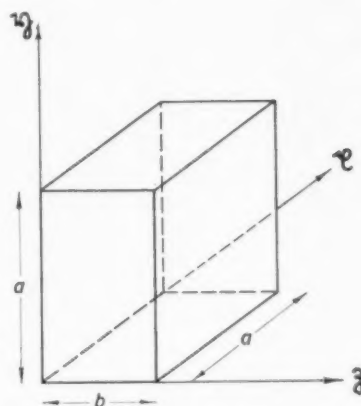


Abb. 2. Kubisches Teilchen mit den Kantenlängen  $l_x = l_y = a$  und  $l_z = b$ .

$a:b$  gilt die Abschätzung für platten-, kugel-, oder stabartige Teilchen. Ausserdem werden die Teilchen als statistisch gleich verteilt angesehen. Dann werden bei der Mittelung über die verschiedenen räumlichen Lagen der Teilchen deren Kanten parallel zu den Achsen eines  $x$ - $y$ - $z$ -Systems gesetzt und für je ein Drittel von insgesamt  $M$  Partikeln die ursprüngliche Stromrichtung  $i$  parallel zur  $x$ -,  $y$ - bzw.  $z$ -Richtung angenommen.

Man erhält die Querschnittsabnahme  $-\Delta F$ , wenn die Zahl  $m$  derjenigen Teilchen, welche eine senkrecht zu  $i$  liegende Fläche  $F$  schneiden oder gerade noch berühren (Abb. 3), mit ihrem eigenen Querschnitt  $\Delta f$  multipliziert wird. So ist z.B. im Falle  $a \geq b$  und  $i \parallel x$

$$m_x = \frac{M a F_0}{3 L_0 F_0} = \frac{M a}{3 L_0} \quad \text{und} \quad \Delta f_x = a \cdot b,$$

also

$$-\Delta F_x = m_x \cdot \Delta f_x = \frac{M a^2 b}{3 L_0}.$$

In gleicher Weise ergibt sich, wenn  $i \parallel y$  bzw.  $i \parallel z$  ist,

$$-\Delta F_y = -\Delta F_z = \frac{M a^2 b}{3 L_0}$$

und daraus

$$-\Delta F = -(\Delta F_x + \Delta F_y + \Delta F_z) = M \frac{a^2 b}{L_0}. \quad (2)$$

Die Längenänderung  $\Delta L$  erhält man, wenn die Zahl  $m'$  der Schnitt- und Berührungspunkte, die eine Bahn des ursprünglichen Stromlinienfeldes mit den Teilchen hat, mit einem gemittelten Betrag  $\bar{\Delta l}$  multipliziert wird, um den eine Strombahn an einem einzelnen Teilchen verlängert wird. Im Falle  $a \geq b$  und  $i \parallel x$  ist (Abb. 4):

$$m'_x = \frac{M a b L_0}{3 F_0 L_0} = \frac{M a b}{3 F_0}.$$



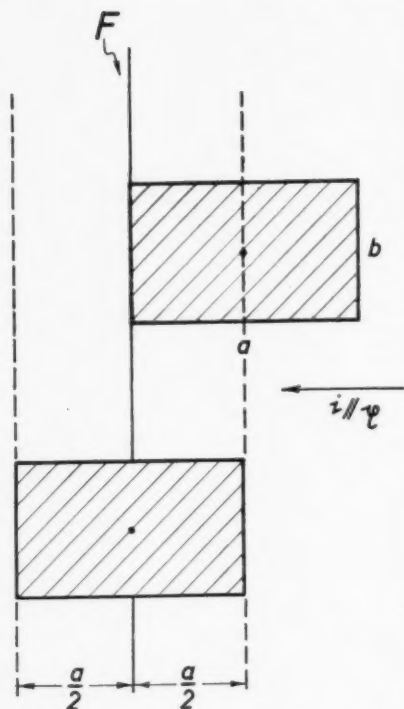


ABB. 3. Schnitt durch ein Teilchen, das die senkrecht zur Stromrichtung  $i$  liegende Fläche  $F$  berührt bzw. schneidet.

Für die Abschätzung von  $\overline{\Delta l}_x$  kann die Ablenkung einer Strombahn, die ein Teilchen tangiert,  $\Delta l_{\min} = 0$  gesetzt werden, während die Ablenkung einer Strombahn, die ein Teilchen zentral trifft,  $\Delta l_{\max, x} = (b/2 + a + b/2) - a = b$  ist (Abb. 5). Als mittlere Ablenkung wird dann  $\overline{\Delta l}_x = \frac{1}{2} \cdot (\Delta l_{\max, x} + \Delta l_{\min}) = b/2$  benutzt,\* und es ist

$$\Delta L_x = m_x' \cdot \overline{\Delta l}_x = \frac{Mab^2}{6F_0}.$$

Ebenso ergibt sich, wenn  $i // y$  bzw.  $i // z$  ist,  $\Delta L_y = Mab^2/6F_0$  bzw.  $\Delta L_z = Ma^3/6F_0$ . Dann ist

$$\Delta L = (\Delta L_x + \Delta L_y + \Delta L_z) = \frac{M}{6F_0} (2ab^2 + a^3). \quad (3)$$

\* Um die Zulässigkeit der gemachten Festsetzungen über  $\Delta l_{\min}$ ,  $\Delta l_{\max}$  und  $\overline{\Delta l}$  zu prüfen, wurde für ein Teilchen mit kreisförmigem Querschnitt der Stromlinienverlauf streng aus der Potentialgleichung  $\Delta \varphi = 0$  mit der Randbedingung  $\partial \varphi / \partial r (r = r_0) = 0$  berechnet ( $r_0$  = Partikelradius,  $r$  = Radialkoordinate) (siehe Abb. 1).

Dabei ergab sich

$$\Delta l_{\max} = r_0 \cdot (\pi - 2) \text{ für die zentrale Bahn (z.B.),}$$

$$\Delta l_{\min} = 0, 1 \cdot \Delta l_{\max} \text{ für die tangentielle Bahn (t.B.),}$$

und für die dazwischen liegenden Werte  $\overline{\Delta l} = \frac{1}{3} \cdot \Delta l_{\max}$ . Da es in erster Linie auf eine qualitative Unterscheidung zwischen platten-, kugel- oder stabartigen Teilchen ankommt, sind die obigen Festsetzungen über  $\Delta l$  also hinreichend genau.

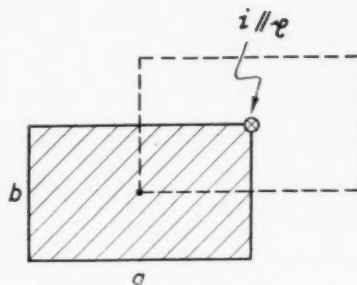


ABB. 4. Schnitt durch ein von der Strombahn  $i$  gerade noch berührtes Teilchen.

Es folgt aus Gleichung (2) und (3)

$$\left( \frac{\Delta L}{L_0} - \frac{\Delta F}{F_0} \right) = \frac{M}{L_0 F_0} \left( \frac{a^3}{6} + \frac{ab^2}{3} + a^2 b \right)$$

und daraus, da das Gesamtvolumen des ausgeschiedenen Karbids  $\Delta V = Ma^2 b$  und das Gesamtvolumen der untersuchten Probe  $V_0 = L_0 F_0$  ist,

$$\left( \frac{\Delta L}{L_0} - \frac{\Delta F}{F_0} \right) = \frac{\Delta V}{V_0} \left( \frac{1}{6} \frac{a}{b} + \frac{1}{3} \frac{b}{a} + 1 \right). \quad (4)$$

Da die Widerstandsänderung in Gleichung (1) in Abhängigkeit von der Karbidmenge  $n_P$  interessiert, ist  $\Delta V$  durch  $n_P$  zu ersetzen. Es ist

$$\Delta V = \frac{G}{\rho} \cdot 4,65 \cdot 10^{-2} n_P \cdot 2 \frac{V_0}{\lambda^3} \quad (5)$$

mit dem Gewicht  $G$  eines Karbidmoleküls, dem spezifischen Gewicht  $\rho$  des Karbids, der Gitterkonstanten des  $\alpha$ -Eisens  $\lambda = 2,86 \text{ \AA}$  und der Menge  $n_P$  des ausgeschiedenen Kohlenstoffs in Gew.%. Während einer Auslagerung bei 90 bis 170°C, wie sie später untersucht wird, scheidet sich der Kohlenstoff als  $\epsilon$ -Karbid aus<sup>3,4</sup>

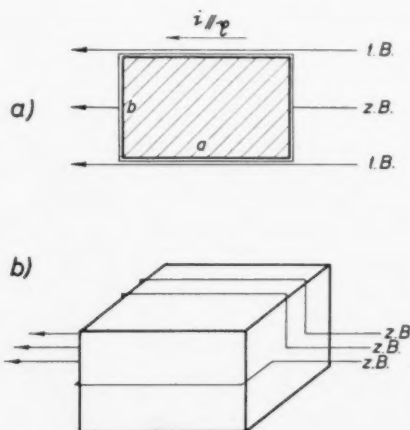


ABB. 5. Vereinfachter Stromlinienverlauf in der Nähe eines kubischen Teilchens (t.B. = tangentielle Strombahn, z.B. = zentrale Strombahn). (a) im Schnitt; (b) perspektivisch.

das nach K. H. Jack<sup>5</sup> eine Zusammensetzung zwischen  $\text{Fe}_2\text{C}$  und  $\text{Fe}_3\text{C}$  hat, die nahe bei  $\text{Fe}_3\text{C}$  liegt. Man kann daher in Gleichung (5) die Werte  $G_{\text{Fe}_3\text{C}} = 179,6 \cdot 1,66 \cdot 10^{-24} \text{g}$  und  $\rho_{\text{Fe}_3\text{C}} = 7,4 \text{ g/cm}^3$  einsetzen und erhält

$$\frac{\Delta V}{V_0} = 0,16 \cdot n_P \quad (6)$$

Aus den Gleichungen (1), (4) und (6) folgt dann schliesslich für den betrachteten Fall  $a \geq b$

$$\frac{R_{\text{Fe}, L, P} - R_{\text{Fe}}}{R_{\text{Fe}}} = (1 + \alpha n_L) 0,16 \cdot \left( 1 + 0,17 \cdot \frac{a}{b} + 0,33 \cdot \frac{b}{a} \right) \cdot n_P + \alpha n_L$$

In gleicher Weise erhält man für den anderen Fall  $a \leq b$

$$\frac{R_{\text{Fe}, L, P} - R_{\text{Fe}}}{R_{\text{Fe}}} = (1 + \alpha n_L) 0,16 \cdot \left( 1,33 + 0,17 \cdot \frac{a}{b} \right) n_P + \alpha n_L$$

Es gilt also allgemein für die relative Widerstandszunahme des Eisens, wenn ein Anteil  $n_L$  des Kohlenstoffs noch gelöst, ein anderer Anteil  $n_P$  als Karbid ausgeschieden ist

$$\frac{R_{\text{Fe}, L, P} - R_{\text{Fe}}}{R_{\text{Fe}}} = \alpha \cdot n_L + \beta \cdot n_P \quad (7)$$

In dieser Gleichung ist  $\beta$  der gesuchte Parameter, der eine Aussage über die Gestalt der ausgeschiedenen Teilchen ermöglicht. Für ihn gilt, wenn man  $\alpha \cdot n_L$  gegen 1 vernachlässigt, da  $0 \leq \alpha \cdot n_L \leq 0,055$  ist (Abb 6):

$$\beta = 0,16 [1 + 0,17 (a/b) + 0,33 (b/a)] [\text{Gew.}\% \text{C}]^{-1} \quad \text{für } a > b, \text{ d.h. für plattenförmige Teilchen,}$$

$$\beta = 0,16 [1,33 + 0,17 (a/b)] [\text{Gew.}\% \text{C}]^{-1} \quad \text{für } a < b, \text{ d.h. für stabförmige Teilchen,} \quad (8)$$

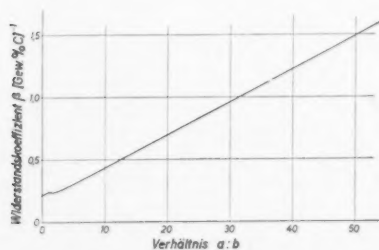


ABB. 6. Der Koeffizient  $\beta$ —der die durch eine Ausscheidung vom Betrage Eins verursachte Widerstandsänderung angibt, theoretisch berechnet für kubische Teilchen mit den Kantenlängen  $l_x = l_y = a$  und  $l_z = b$ , in Abhängigkeit von dem Längenverhältnis  $a:b$ .

$$\beta = 0,24 [\text{Gew.}\% \text{C}]^{-1} \quad \text{für } a = b, \text{ d.h. für körnige Teilchen.}$$

Es folgt das sehr wichtige Ergebnis, dass der Koeffizient  $\beta$  nur von der Form und nicht von der Grösse  $a^2b$  oder der Dispersität  $M/V_0$  der ausgeschiedenen Teilchen abhängt. Die durch die Ausscheidung erzeugte Widerstandszunahme wird nur auf die Form und das Gesamtvolumen der ausgeschiedenen Teilchen zurückgeführt. Die Verbindung Dämpfungs- und Widerstandsmessung gibt also Auskunft über die Form der sich ausscheidenden Karbidteilchen.

Es sei bemerkt, dass in der vorstehenden Abschätzung die Beeinflussung des Widerstandes durch Elektronenstreuung wegen der Grösse der untersuchten Partikel vernachlässigt werden konnte. Ferner wurden, wie in allen bisherigen theoretischen Untersuchungen, etwaige während der Ausscheidung auftretende Gitterverspannungen vernachlässigt.

#### 4. DIE TEILCHENFORM BEI DER KARBIDAUSSCHEIDUNG AUS DEM $\alpha$ -EISEN

Zunächst sollen diese theoretischen Aussagen an bekannten experimentellen Ergebnissen geprüft werden, bei denen die ausgeschiedenen Teilchen direkt lichtmikroskopisch beobachtet werden konnten. Aus Messungen von W. Köster und H. Tiemann<sup>6</sup> geht hervor, dass körniger und lamellarer Zementit den elektrischen Widerstand verschieden beeinflussen. Die Verfasser erhielten eine lineare Abhängigkeit zwischen diesem Karbid und der relativen Widerstandszunahme

$$(R_{\text{Fe}, P} - R_{\text{Fe}}) / R_{\text{Fe}} = \beta_i \cdot n_P$$

Dabei ist  $(R_{\text{Fe}, P} - R_{\text{Fe}})$  die allein durch das Karbid verursachte Widerstandszunahme und

$$\beta_1 = 0,5 \text{ Gew.}\% \text{C}^{-1} \text{ bei lamellarem Zementit,}$$

$$\beta_2 = 0,25 \text{ Gew.}\% \text{C}^{-1} \text{ bei körnigem Zementit.}$$

Ein Vergleich dieser Werte mit der obigen Abschätzung zeigt, dass die Widerstandszunahme des körnigen Zementits recht gut mit der Abschätzung der würfelförmigen Teilchen übereinstimmt. Die Widerstandszunahme des lamellaren Zementits könnte durch plattenförmige Teilchen mit einem Verhältnis  $a:b \approx 15:1$  erklärt werden, jedoch ist es fraglich, ob die für statistisch verteilte Teilchen gemachte Abschätzung bei einer so ausgerichteten Lage der Platten anwendbar ist.

Mit Hilfe der Beziehungen (7) und (8) sollen nun frühere Untersuchungen<sup>2</sup> der Karbidausscheidung aus dem  $\alpha$ -Eisen ausgewertet werden. Es wurden Eisendrähte in feuchtem Wasserstoff gereinigt, 0,0% gedehnt, bei 710°C auf 0,014 bis 0,017 Gew. % Kohlenstoffgehalt aufgeholt, in Wasser abgeschreckt und bei 90 bis 170°C ausgelagert (Zahlentafel I). Während der Auslagerung wurden die Dämpfung  $Q^{-1}$  und der Widerstand  $R$  gleichzeitig gemessen. Damit ist der Wert  $\beta$  nach Gleichung (7) experimentell bekannt, da die Grössen  $n_L$  und  $n_P$  aus der Dämpfungsmessung und das Wider-

ZAHLENTAFEL I. Experimentelle Daten der untersuchten Karbidausscheidung

Anfangskonzentration $n_A$ Gew. % C	Übersättigung* $\Delta n$ Gew. % C	Auslagerungstemperatur $T^\circ\text{C}$	Unterkühlung* $\Delta T^\circ\text{C}$
0,01655	0,0165	90	600
0,01620	0,0160	170	515
0,01475	0,0145	120	550
0,01405	0,0140	149	510

\* Die Unterkühlung und Übersättigung wurde mit Hilfe der in 7) angegebenen Löslichkeitslinie des Kohlenstoffs in  $\alpha$ -Eisen berechnet.)

standsverhältnis  $(R_{Fe,L,P} - R_{Fe})/R_{Fe}$  sowie die Konstante  $\alpha$  unmittelbar ermittelt wurden.

Die sich aus den Experimenten ergebende Abhängigkeit der Grösse  $\beta$  von  $n_P$  ist in Abb. 7 dargestellt. Dazu ist zunächst zu sagen, dass die Abschätzung für würfelförmige Teilchen den Verlauf der  $\beta$ -Kurven nicht erklären kann. Sie ergibt einen zu kleinen und ausserdem konstanten Wert  $\beta = 0,24$  Gew. % C<sup>-1</sup>. Dagegen lassen sich die Kurven vollständig durch folgendes Bild deuten: Das Karbid scheidet sich in Plattenform aus, und mit fortschreitender Ausscheidung nimmt das Verhältnis Plattendurchmesser: Plattendicke =  $a:b$  laufend  $ab$ , weil eine Einförmung der Platten stattfindet. Die Dicke der Platten wächst schneller als ihr Durchmesser.

Wenn man von einem anfänglichen Steilabfall der  $\beta$ -Kurven absieht, bei dem vielleicht Prozesse eine Rolle spielen, welche die Ausscheidung vorbereiten, so ergibt sich aus Abb. 6 und 7 quantitativ folgendes: Unter den vorliegenden Bedingungen findet während der Ausscheidung eine Einförmung der Platten in einem Bereich von etwa  $a:b = 60:1$  bis  $a:b = 25:1$  statt. Nachdem der Ausscheidungsvorgang selbst praktisch beendet ist, tritt eine weitere Koagulation ein, die bis  $a:b = 15:1$  verfolgt wurde.

Ferner sind in Abb. 7 bei gleicher ausgeschiedener Menge  $n_P$  die  $\beta$ -Werte um so grösser, je stärker die Übersättigung ist. Dies erklärt sich vielleicht daraus, dass mit wachsender Übersättigung auch die Keimzahl zunimmt. Es entspricht also der höheren Übersättigung

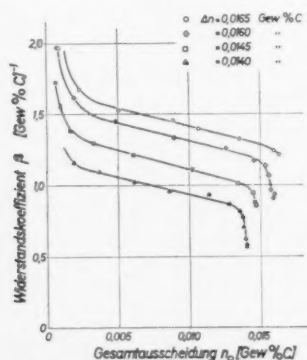


ABB. 7. Der während einer Kohlenstoffausscheidung bei verschieden starker Übersättigung  $\Delta n$  gemessene Koeffizient  $\beta$  in Abhängigkeit vom Betrage der Ausscheidung.

eine grössere Zahl kleinerer Teilchen; die Einförmung ist hier noch nicht so weit fortgeschritten. Eine Änderung der Unterkühlung in einem Bereich zwischen 500 und 600°C scheint darauf keinen merklichen Einfluss auszuüben.

## 5. DISKUSSION

Es ist nun zu fragen, wieweit diese Aussagen über den Ausscheidungsverlauf durch elektronenoptische Beobachtungen geprüft werden können. Es gibt verschiedene Arbeiten, in denen die Karbidausscheidung aus dem  $\alpha$ -Eisen elektronenmikroskopisch untersucht worden ist. Dabei konnte die Gestalt der ausgeschiedenen Teilchen erst nach längeren Glühzeiten mit einiger Sicherheit bestimmt werden, da die Teilchen zu Beginn der Ausscheidung zu klein waren.

J. Radavich und C. A. Wert<sup>8</sup> glaubten die Annahme einer kugeligen Karbidausscheidung im wesentlichen bestätigen zu können, nachdem sie eine Probe mit 0,02 Gew. % übersättigt gelöstem Kohlenstoff 25 min bei 300°C getempert und anschliessend elektronenmikroskopisch beobachtet hatten.

Im Gegensatz dazu hatten J. Trotter, D. McLean und C. J. B. Clews<sup>9</sup> an Proben mit 0,7 Gew. % C, die von 690°C abgeschreckt und eine Stunde bei 250° geglüht worden waren, mit dem Elektronenmikroskop plattenähnliche Karbidausscheidungen gefunden.

Um diese Widersprüche zu klären, wurde schliesslich eine eingehende elektronenoptische Untersuchung der Ausscheidungsvorgänge von A. L. Tsou, J. Nutting und J. W. Menter<sup>3</sup> vorgenommen. Sie verwendeten Eisen, welches neben 0,026 Gew. % C metallische Verunreinigungen von 0,01 Gew. % sowie 0,0057 Gew. % N enthielt. Sie beobachteten u.a. nach einer Glühung bei 700°C, Abschrecken und anschliessender Auslagerung bei 100°C nach 16 h plattenförmige Ausscheidungen mit  $b \approx 500\text{\AA}$  und  $a \approx 2000$  bis  $3000\text{\AA}$  und bei 200°C nach 15 h Platten mit  $b \approx 2500\text{\AA}$  und  $a \approx 7000$  bis  $10\,000\text{\AA}$ . Durch Elektronenbeugungsaufnahmen wurden die ausgeschiedenen Platten als Eisenkarbide nachgewiesen.

Es bleibt die Frage offen, worauf der Unterschied zwischen den elektronenoptischen Beobachtungen zurückgeführt werden kann. Es wäre möglich, dass die von Radavich und Wert beobachteten Zementitpartikel schon weitgehend koaguliert waren und überhaupt wegen ihrer unterschiedlichen Gitterstruktur eine andere Form besitzen als die unterhalb 220°C sich ausscheidenden  $\epsilon$ -Karbideilchen. Andererseits weist Wert auf den zwar geringen Stickstoffgehalt der von Tsou, Nutting und Menter verwendeten Proben hin.<sup>11</sup> Eine umfassende elektronenoptische Untersuchung der Karbidausscheidung aus stickstoffreiem Eisen müsste hier endgültige Klarheit bringen.

Angesichts dieser Unsicherheit lässt sich nur sagen, dass die Ergebnisse der vorliegenden Arbeit mit den letzten elektronenmikroskopischen Beobachtungen qualitativ übereinstimmen. Die quantitative Abweich-

ung der Verhältnisse  $a/b=4$  bis 6 bzw.  $a/b=3$  bis 4 von den eigenen Werten  $a/b \geq 15$  könnte vielleicht auf den Ätzangriff bei der Herstellung der Probenabdrücke zurückgeführt werden. Andererseits ist es durchaus möglich, dass die vorliegende Abschätzung den Widerstandskoeffizienten quantitativ nicht genau wiedergibt.

Schliesslich sollen noch die Aussagen der Ausscheidungstheorie von C. Zener und C. A. Wert<sup>12,13,14</sup> über die Gestalt der ausgeschiedenen Teilchen erörtert werden. Zener und Wert haben für den ausgeschiedenen Bruchteil  $W$  der ausscheidungsfähigen Gesamtmenge ein Zeitgesetz

$$W(t) = \left(\frac{t}{\tau}\right)^k \quad (9)$$

angegeben, das bei längeren Auslagerungszeiten  $t$  in ein Exponentialgesetz

$$W(t) = 1 - \exp\left(-\left(\frac{t}{\tau}\right)^k\right) \quad (10)$$

übergeht. Von den Konstanten  $\tau$  und  $k$  ist nun  $k$  unmittelbar mit der Form der ausgeschiedenen Partikeln verknüpft, indem bei kugelförmiger Ausscheidung  $k=3/2$ , bei stabförmiger  $k=4/2$  und bei plattenförmiger  $k=5/2$  gefordert wird.

Bei den experimentellen Untersuchungen der Karbidausscheidung aus dem  $\alpha$ -Eisen ist das Zeitgesetz (10) zwar allgemein gemessen worden, doch liegen die Exponenten niemals bei  $5/2$ , wie bei plattenförmigen Karbiden zu erwarten wäre; sie liegen bei  $3/2$  und oft sogar deutlich unterhalb  $3/2$ . Abgesehen von den Exponenten  $k < 3/2$ , die in der Theorie grundsätzlich nicht erklärt werden können, wurde auf Grund der experimentellen Ergebnisse eine kugelartige Karbidausscheidung angenommen. Diese Aussage steht mit oben genannten elektronenoptischen Beobachtungen und den eigenen Ergebnissen in Widerspruch.

Um diesen Widerspruch erörtern zu können, muss auf die Ableitung des Zeitgesetzes (9) näher eingegangen werden. Zener . . . 13 leitet dieses Gesetz aus dem 1. Fickschen Diffusionsgesetz ab, dessen Gültigkeit an der Phasengrenze zwischen Karbid und umgebendem Gitter vorausgesetzt wird. Dabei müssen zwei Grössen bekannt sein: die Gleichgewichtskonzentration  $n(S)$  und der Konzentrationsgradient  $\partial n / \partial s (s=S)$  an der Phasengrenze ( $S$  ist eine Linearabmessung des Karbidteilchens,  $s$  die Längenkoordinate in dieser Richtung). Beide Grössen lassen sich nur unter einschränkenden Annahmen angeben.

Die Gleichgewichtskonzentration  $n(S)$  ist abhängig vom Krümmungsradius an der Oberfläche des Teilchens (vgl. Arbeit 15). Im fortgeschrittenen Zustand der Ausscheidung wird diese Abhängigkeit vernachlässigt, und es wird  $n(S)$  gleich der konstanten Gleichgewichtskonzentration  $n(\infty)$  vor einer sehr grossen, ebenen Ausscheidungsfront gesetzt.

Der Konzentrationsgradient  $\partial n / \partial s (s=S)$  lässt sich—unter der Voraussetzung, dass in jedem Augenblick eine stationäre Konzentrationsverteilung im Gitter herrscht—nur für kugelförmiges und eindimensionales Wachstum exakt angeben.

Man erhält dann nach Zener aus dem ersten Fickschen Diffusionsgesetz für die jeweilige Linearabmessung eine Zeitabhängigkeit

$$S(t) \sim t^{1/2} \quad (11)$$

Dieses Gesetz wird für den Radius einer Kugel, eines Zylinders und für die Dicke einer Platte angenommen. Wert versuchte diese Überlegungen auszudehnen,<sup>12</sup> indem er für den Radius einer Platte und für die Länge eines Zylinders willkürlich  $\partial n / \partial s (s=S) = \text{const}$  setzte. Er erhält analog zu Gleichung (11)

$$S(t) \sim t \quad (12)$$

Aus den Gleichungen (11) und (12) ergibt sich für das Volumen  $V$  eines Karbidteilchens

$$V(t) \sim t^k \quad (13)$$

mit  $k_{\text{Kugel}}=3/2$ ,  $k_{\text{Zylinder}}=4/2$  und  $k_{\text{Platte}}=5/2$ . Unter der Voraussetzung, dass während der Ausscheidung keine Keimbildung stattfindet, ist  $W(t) = V(t)/V(\infty)$ , und damit geht Gleichung (13) sofort in Gleichung (9) über.

In der vorstehenden Überlegung erscheint nun vor allem die Ableitung der Gleichung (12) unsicher. Die Gültigkeit der Gleichung würde zur Folge haben, dass—im Gegensatz zu den eigenen Ergebnissen—während einer plattenförmigen Ausscheidung das Verhältnis Plattendurchmesser:Plattendicke zunimmt, und zwar proportional  $t^{1/2}$ . Diese Aussage steht in Widerspruch zu dem thermodynamischen Grundsatz, den energetisch günstigeren Zustand einer möglichst geringen Oberfläche im Vergleich zum Volumen herzustellen. Es ist im Gegenteil zu erwarten, dass an der Plattenkante wegen der stärkeren Krümmung der Oberfläche eine grössere Gleichgewichtskonzentration als vor der Plattenmitte herrschen wird. Dadurch wird das Wachstum gegenüber der Mitte gehemmt, und es ist in Gleichung (12) eher ein Zeitexponent  $\leq \frac{1}{2}$  und damit in Gleichung (13) ein Wert  $k_{\text{Platte}} \leq 3/2$  zu erwarten. Übereinstimmend mit dieser Erwartung wurde bei den oben ausgewerteten Versuchen<sup>2</sup> das Zenersche Wachstumsgesetz (10) mit einem Exponenten 1,15 gefunden. Sonst in der Literatur mitgeteilte höhere Exponenten können z.B. durch eine Keimbildung erklärt werden, die in einem endlichen Zeitbereich stattfindet.<sup>15</sup>

Es sei noch abschliessend bemerkt, dass B. Ilschner<sup>16</sup> auf völlig anderem Wege als Zener und Wert ein Ausscheidungsgesetz abgeleitet hat, in dem der Exponent  $k$  durch die Keimbildung allein bestimmt wird. Dabei können nach längeren Auslagerungszeiten Werte  $1 \leq k \leq 2$  erklärt werden. Die geometrische Form der ausgeschiedenen Teilchen geht in diese Überlegung nicht ein.



Den Herren Professor E. Houdremont und Professor F. Wever danke ich herzlichst für ihr stetes Interesse an der Arbeit. Der Deutschen Forschungsgemeinschaft sei für die materielle Unterstützung gedankt.

#### LITERATUR

1. W. Pitsch u. K. Lücke, Z. Physik **139**, 413 (1954).
2. W. Pitsch u. K. Lücke, Arch. Eisenhüttenw. (im Druck).
3. A. L. Tsou, J. Nutting u. J. W. Menter, J. Iron Steel Inst. **172**, 163 (1952).
4. O. Krisement, Arkiv för Fysik **7**, 353 (1953).
5. K. H. Jack, J. Iron Steel Inst. **169**, 26 (1951).
6. W. Köster u. H. Tiemann, Arch. Eisenhüttenw. **11**, 579 (1931/32).
7. C. A. Wert, Trans. Amer. Inst. Min. Met. Engrs. **188**, 1242 (1950).
8. J. Radavich u. C. A. Wert, J. Appl. Phys. **22**, 367 (1951).
9. J. Trotter, D. McLean u. C. J. B. Clews: Symposium on Metallurgical Applications of the Electron Microscope. Monograph and Report Series No. 8 of the Institute of Metals, S. 75-83, London, 1950.
10. W. Köster u. L. Bangert, Arch. Eisenhüttenw. **25**, 231 (1954).
11. C. A. Wert, Acta Met. **2**, 361 (1954).
12. C. A. Wert, J. Appl. Phys. **20**, 943 (1949).
13. C. Zener, J. Appl. Phys. **20**, 950 (1949).
14. C. A. Wert u. C. Zener, J. Appl. Phys. **21**, 5 (1950).
15. W. Dahl u. K. Lücke, Arch. Eisenhüttenw. **25**, 241 (1954).
16. B. Ilschner, Arch. Eisenhüttenw. **26**, 59 (1955).

## KINETICS OF ORDER-DISORDER TRANSFORMATIONS\*

G. J. DIENES†

A simple theory of the kinetics of order-disorder transformations, based on chemical rate theory, is presented. The theory is constructed entirely in terms of the long range order parameter and reduces to the Bragg and Williams theory at equilibrium. There are several unusual features in the theoretical rate curves. The origin of these characteristics is the order parameter dependence of the energy of ordering. It is shown that ordering must start by fluctuations which are expected to be particularly large for an  $AB_3$  alloy. Thus, the shapes of the ordering curves remind one of nucleation and growth processes, although they are derived entirely from simple rate theory. The theory is shown to be in agreement with the experimentally known qualitative behavior of order-disorder systems. For example, the theory predicts a maximum ordering rate slightly below the critical temperature in agreement with experiment. An improvement of the Bragg and Williams equilibrium theory is also suggested, based on a nonlinear dependence of the ordering energy on the long-range order parameter, which leads to excellent agreement with experiment. The kinetic theory is modified accordingly, resulting in quantitative but not qualitative changes in the predicted rate curves. There are insufficient experimental rate data for a critical quantitative evaluation of the kinetic theory.

### CINÉTIQUE DES TRANSFORMATIONS ORDRE-DÉSORDRE

Il est présenté une théorie simple de la cinétique des transformations ordre-désordre basée sur la théorie des vitesses de réaction. La théorie est exprimée en fonction du paramètre d'ordre à grande distance et conduit, lors de l'équilibre, à la théorie de Williams et Bragg. Les courbes théoriques conduisent à certains aspects inaccoutumés dont l'origine est la relation entre le paramètre d'ordre et l'énergie d'ordre. Il est montré que l'ordre se produit par des fluctuations qui doivent être particulièrement importantes pour un alliage du type  $AB_3$ . Ainsi, la forme des courbes d'établissement de l'ordre est analogue à celle des réactions par germination et croissance, bien que la théorie dérive d'une simple théorie de la vitesse de réaction. Il est montré que cette théorie est en accord qualitatif avec le comportement des systèmes ordre-désordre. C'est ainsi que la théorie prévoit conformément à l'expérience un maximum de la vitesse de mise en ordre, légèrement inférieure à la température critique. Il est suggéré d'améliorer la théorie de Bragg et Williams, en introduisant une relation non linéaire entre l'énergie d'ordre et le paramètre d'ordre à grande distance, ce qui conduit à un excellent accord avec l'expérience. Une modification correspondante de la théorie cinétique altère quantitativement, mais non qualitativement les vitesses de réaction prévues. Les faits expérimentaux sont insuffisants pour une critique quantitative de la théorie cinétique.

### ZUR KINETIK DER ÜBERSTRUKTURBILDUNG

Ausgehend von der chemischen Geschwindigkeitstheorie wird eine einfache Theorie der Kinetik des Umwandlungsvorganges geordnetungeordnet beschrieben. Die Theorie baut völlig auf dem Fernordnungsparameter auf und beschränkt sich auf die Theorie von Bragg und Williams im Gleichgewicht. Die theoretischen Geschwindigkeitskurven zeigen einige ungewöhnliche Eigenheiten. Die Ursache dieser charakteristischen Merkmale liegt in der Abhängigkeit des Ordnungsparameters von der Ordnungsenergie. Es wird gezeigt, dass die Ordnung durch Schwankungen eingeleitet werden muss, die für ein  $AB_3$  Metall besonders gross sein werden. So erinnern die Ordnungskurven an Keimbildung und Wachstumsprozesse, obwohl sie völlig aus der einfachen Geschwindigkeitstheorie abgeleitet sind. Die Theorie zeigt mit dem bekannten experimentellen Verhalten der Systeme mit Überstruktur Übereinstimmung, so z.B. mit der Beobachtung, dass dicht unterhalb der kritischen Temperatur ein Maximum in der Wachstumsgeschwindigkeit auftritt. Weiterhin wird eine Verbesserung der Gleichgewichtstheorie von Bragg und Williams vorgeschlagen, die auf einer nichtlinearen Abhängigkeit der Ordnungsenergie vom Fernordnungsparameter beruht. Dieser Änderungsvorschlag führt zu einer ausgezeichneten Übereinstimmung mit dem Experiment. Dementsprechend wird auch die kinetische Theorie abgewandelt, was quantitative, jedoch nicht qualitative Veränderungen in der vorhergesagten Geschwindigkeitskurven verursacht. Für eine kritische, quantitative Auswertung der kinetischen Theorie liegen nicht genügend experimentelle Daten vor.

### I. INTRODUCTION

The Bragg and Williams theory of order-disorder has survived as a beautifully simple and effective representation of order-disorder phenomena even though it is well known by now that the theory has many shortcomings.<sup>2</sup> The more sophisticated statistical theories, aimed at combining alterations in long and short range order, have given a better understanding of the basic equilibrium problems and have achieved good agree-

ment with experiment in many cases. However, these theories are invariably restricted to considerations of equilibrium and are not concerned with the associated rate phenomena.

The Bragg and Williams theory can be derived from kinetic arguments (as originally done by Gorsky<sup>3</sup>) and the theory is well adapted, as shown by B. and W. to a consideration of relaxation phenomena. In recent years it has been customary to discuss order-disorder transformations in terms of nucleation and growth theory. It has not been found possible to render such theories quantitative. It is attractive to think of order-disorder

\* Received February 28, 1955; in revised form, April 15, 1955.

† Brookhaven National Laboratory, Upton, New York.

transformations, at least for stoichiometric compositions, as a simple exchange reaction in the solid state. On this basis one would construct a kinetic theory along the lines of modern chemical rate theory. This possibility has not been examined in sufficient detail to find out whether the important features of the kinetic phenomena can be described by such a theory without invoking special assumptions of nucleation. Such features will have to be accounted for as sigmoid-shaped rate curves, minimum relaxation times below the critical temperature, apparent experimental agreement with second and third order reactions over various ranges of order, etc.<sup>4</sup>

The purpose of this paper is to examine a simple "chemical" theory of ordering in detail. Since this is essentially an extension of the B. and W. theory, it is constructed entirely in terms of the long-range order parameter. It has not been found possible so far to formulate a satisfactory picture of the kinetics of short-range ordering. It might be added that suitable experiments are not available either. Only the kinetics of long-range order formation has been studied experimentally.

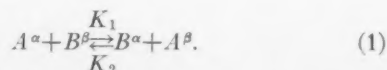
The experimental information concerning the kinetics of long-range order is by no means as sound or extensive as would be desired. The major difficulty is that the connection between the degree of long-range order and the various physical properties which have been used for rate studies is not established clearly either theoretically or experimentally. For further progress it is essential to carry out rate studies directly in terms of the long-range order parameter,  $S$ , as determined from superlattice lines. If some other physical property is used in the rate studies it must be calibrated with respect to X-ray measurements. Even if this is done, however, the possibility still remains that a given physical property may not be a function of  $S$  alone. Thus, the first procedure is much preferred. While there are excellent equilibrium data for a few order-disorder systems, kinetic studies required for quantitative comparison with theory have not been carried out. For the present, therefore, one has to be content with a qualitative comparison of the general features of the kinetic process.

## II. THE BASIC EQUATIONS

Any binary stoichiometric order-disorder system is describable, in the B. and W. scheme, by defining the following quantities. Let there be

$$\begin{aligned} N_B & \text{ B-atoms on } N_B \beta\text{-sites} \\ N_A & \text{ A-atoms on } N_A \alpha\text{-sites} \end{aligned}$$

and designate the number of wrong atoms by  $N_B^\alpha = N_A^\beta$ . The order disorder transformation is describable by the "chemical" equation



The corresponding fractional concentrations are

$$\frac{N_A - X}{N}; \quad \frac{N_B - X}{N}; \quad \frac{X}{N}; \quad \frac{X}{N},$$

where

$$X = N_B^\alpha = N_A^\beta \quad \text{and} \quad N = N_A + N_B.$$

The rate of change of  $X$  with time,  $t$ , can now be written

$$\frac{d(X/N)}{dt} = K_1 \left( \frac{N_A}{N} - \frac{X}{N} \right) \left( \frac{N_B}{N} - \frac{X}{N} \right) - K_2 \left( \frac{X}{N} \right)^2 \quad (2)$$

Let

$$\frac{N_A}{N} = \gamma; \quad \text{then} \quad \frac{N_B}{N} = (1 - \gamma)$$

and rewrite (2) in the form

$$\frac{d(X/N)}{dt} = K_1 \left[ \gamma(1 - \gamma) - \frac{X}{N} + \left( \frac{X}{N} \right)^2 \right] - K_2 \left( \frac{X}{N} \right)^2. \quad (3)$$

At equilibrium  $[d(X/N)/dt] = 0$ , and, therefore,

$$\frac{K_1}{K_2} = K = \frac{X^2/N^2}{\gamma(1 - \gamma) - (X/N) + (X/N)^2}. \quad (4)$$

In terms of the B. and W. long-range order parameter  $S$ , we have

$$X/N = (1 - S)\gamma(1 - \gamma). \quad (5)$$

In terms of  $S$ , therefore, (4) becomes

$$K = \frac{\gamma(1 - \gamma)(1 - S)^2}{S + \gamma(1 - \gamma)(1 - S)^2} \quad (6)$$

or

$$K^{-1} = \frac{S + \gamma(1 - \gamma)(1 - S)^2}{\gamma(1 - \gamma)(1 - S)^2} = \frac{S}{\gamma(1 - \gamma)(1 - S)^2} + 1. \quad (7)$$

Equation (7) is the B. and W. equilibrium condition. B. and W. identify  $K^{-1}$  with  $e^{V/RT}$  and then assume that  $V = V_0 S$ . From the above kinetic argument and conventional rate theory,  $K$  is derived as follows: Let the potential barrier in going from disorder to order be denoted by  $U$ . Let the energy-difference ordered and disordered states be  $V$ . Then

$$\begin{aligned} K_1 &= \nu_1 e^{-(V+U)/RT} \\ K_2 &= \nu_2 e^{-U/RT} \end{aligned} \quad (8)$$

and, therefore,

$$K = K_1/K_2 = \frac{\nu_1}{\nu_2} e^{-V/RT}. \quad (9)$$

This is obviously equivalent to the B. and W. treatment if we let  $\nu_1 = \nu_2$  and following them we assume that  $V = V_0 S$ . Thus, the equilibrium theory is the same

except that one special assumption of the B. and W. theory becomes quite clear, namely, letting  $\nu_1 = \nu_2$ . This amounts to stating that the entropies of activation in the two directions are equal and therefore amounts to neglecting any entropy effects arising from a change in the vibrational spectrum. This deficiency of the B. and W. theory has been pointed out before<sup>5</sup> and some attempts have been made to correct for this.<sup>6</sup> According to our development it is a simple extension of the B. and W. theory to include entropy effects at this stage of the theory. For the present we shall neglect this, as the main features of the kinetic theory are not altered by the inclusion of the entropy term, but we will investigate this point later. In this section, therefore, we proceed with  $\nu_1 = \nu_2 = \nu$ .

One can write now an expression for  $dS/dt$  from Eq. (2) with some assurance, since, according to (8) and (9), the correct equilibrium conditions will be obtained. One gets, using  $V = V_0 S$ ,

$$\frac{dS}{dt} = \nu e^{-U/RT} [\gamma(1-\gamma)(1-S)^2 - e^{-V_0 S/RT} [S + \gamma(1-\gamma)(1-S)^2]]. \quad (10)$$

Equation (10) is the basic kinetic equation embodying the B. and W. formulation. The basic difference between Eq. (10) and an ordinary second-order chemical rate equation is, of course, the dependence of the second exponential term on  $S$ ; that is, the energy of the reaction

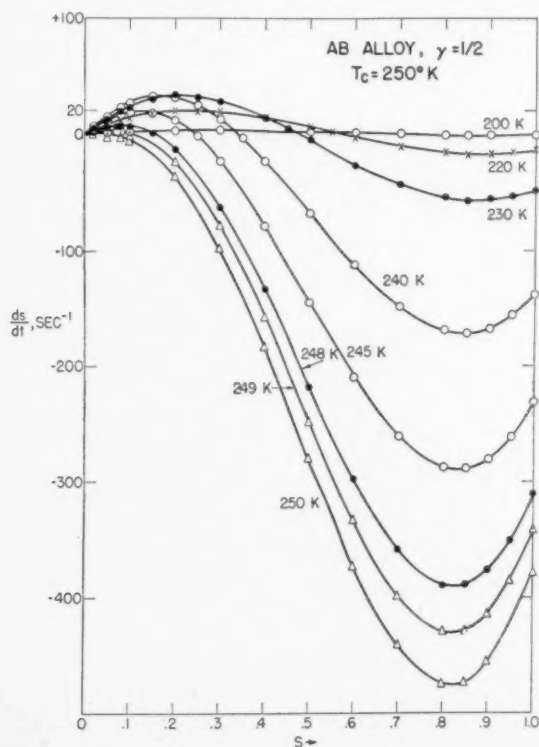


FIG. 1.  $dS/dt$ -versus- $S$  curves for AB alloy.

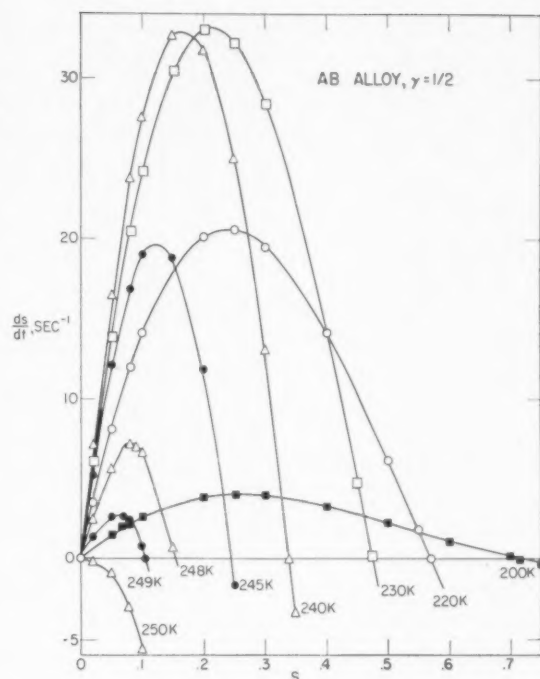


FIG. 2.  $dS/dt$ -versus- $S$  curves for AB alloy in the ordering range. Part of Fig. 1 enlarged (different ordinate).

depends on the amount of reaction which has taken place. As will be shown, this dependence on  $S$  introduces some unusual features into the rate curves.

### III. KINETIC BEHAVIOR

Equation (10) is a mixed algebraic and exponential equation and the characteristics of  $dS/dt$  as a function of  $S$  can only be investigated by numerical calculations. For such computations the following parameters were chosen

$$\begin{aligned} \nu &= 10^{13} \text{ sec}^{-1}, \\ U/R &= 5000 \text{ K}, \\ V_0/R &= 1000 \text{ K}. \end{aligned}$$

#### 1. AB alloy

$dS/dt$  values were calculated as a function of  $S$  at a series of temperatures for the AB case ( $\gamma = \frac{1}{2}$ ). The results are shown in Figs. 1 and 2.\* The equilibrium behavior, as determined from the crossing of the  $dS/dt = 0$  line in Figs. 1 and 2, is, of course, the same as that obtained from the B. and W. theory. (For further discussion, see Sec. IV and Fig. 9.)

Several important points should be noted with respect to the kinetics of ordering for an AB alloy.

(a) The rate at  $S=0$  is always zero. Thus, ordering must start by fluctuations. However, since  $dS/dt$  as a

\* The calculated points are shown in the Figures both for clarity and to indicate the degree of interpolation in drawing the curves.



function of  $S$  has a positive slope at all temperatures below the critical temperature,  $T_c$ , large fluctuations are not required and a long induction period may not occur. The rate theory itself can say nothing about the time scale or temperature dependence of the required fluctuations.

(b) An isothermal  $S$ -versus-time curve can only be constructed at some finite value of  $S$  by numerical integration. If

$$dS/dt = f(S),$$

then,

$$\int_{S_0}^S dS/f(S) = t - t_0, \quad (11)$$

where  $t_0$  is the time required to reach the initial degree of order,  $S_0$ . Changing  $S_0$  is equivalent, of course, to shifting the time scale. Typical curves at 220°K (for an AB alloy of our chosen parameters) are shown in Fig. 3. Typical sigmoid curves are obtained. The shape of these curves reminds one of nucleation and growth processes although the shape of these curves is derived entirely from simple rate theory.

It is quite clear from the discussion so far that, over limited ranges of  $S$ , various simple approximations to the  $S$ -versus- $t$  curves become valid. For example, near the equilibrium value of  $S$ ,  $dS/dt$  is approximately linear in  $S$ , leading to the linear relaxation theory of B. and W. Again, in Dienes<sup>7</sup> experiments on AuCu, a cubic rate equation was found to describe the data for samples, which, by the nature of the experiment, were characterized by relatively high  $S_0$  values. It is evident from Fig. 3 that a cubic approximation will not be a bad one for  $S_0$  values higher than, say, 0.15. Similarly, Rothstein<sup>8</sup> has found that a quadratic approximation is quite satisfactory near  $S_e$  for AuCu<sub>3</sub>. The present treatment renders these approximations reasonable but also shows them to be without fundamental significance.

The  $S$ -versus- $t$  data have been combined in one plot on Fig. 4 (log scale for convenience only,  $S_0 = .02$ ). This figure shows clearly the crossing over of the various

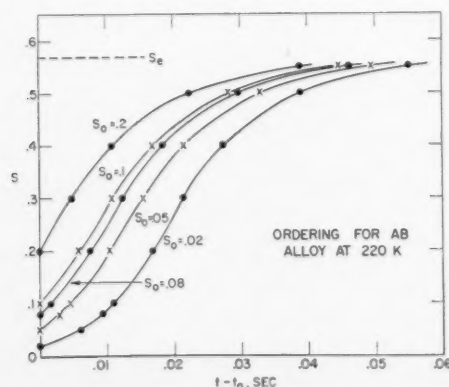


FIG. 3.  $S$ -versus-time curves for AB alloy for different initial values of the order parameter.

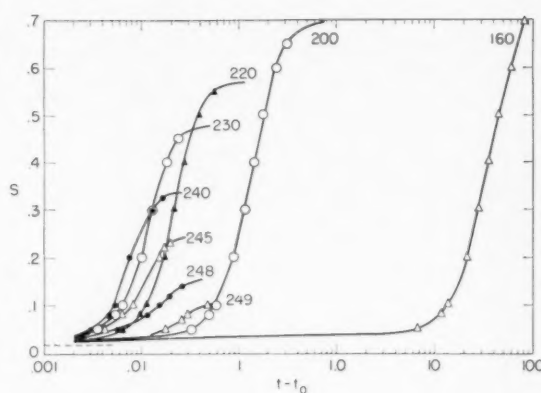


FIG. 4.  $S$ -versus-time curves for AB alloy at various temperatures.

rate curves and the general complex gross behavior arising from the order dependence of  $V$ .

(c) Disorder follows a similar course but starts with a finite slope—i.e., a finite value of  $dS/dt$  at  $S=1$ —which depends only on the temperature. Although there is a maximum disordering rate (see Fig. 1) the change in slope is not great and a truly sigmoid curve is not obtained.

(d) It is clear from Eq. (10) that the temperature dependence is, in general, quite complex because of the presence of two exponential terms,  $U$  and  $V_0S$ . The temperature dependence is simple only for disordering at  $S=1$ . For these initial disordering rates,

$$-dS/dt = \nu e^{-(U+V_0)/RT}. \quad (12)$$

At any other fixed  $S$  value, the disordering rates are not linear in  $1/T$  and may also cross each other. The simple procedure discussed by Parkins, Dienes and Brown<sup>9</sup> is not applicable, and activation energies are not derivable in a simple way from such data.

The temperature dependence of the ordering rates is, of course, also complex. In Fig. 5,  $dS/dt$  is plotted versus  $1/T$  at various fixed values of  $S$ . There is seen to be a maximum rate, or minimum in the relaxation time, as observed experimentally by Siegel<sup>10</sup> for AuCu<sub>3</sub>.<sup>11</sup> This minimum in relaxation time is seen to be a natural consequence of the order dependence of  $V$ . The envelope of the curves in Fig. 5 is given by the temperature dependence of the maximum rate as obtained from Fig. 1. Between 160 and 200K (not shown in Fig. 5) approximate linearity is observed and only very precise data would show the curvature. The corresponding activation energy, however, turns out to be 4180K and is, therefore, a fictitious energy of no physical significance.

## 2. AB<sub>3</sub> alloy

(a) Similar calculations have been done for the AB<sub>3</sub> alloy ( $\gamma = \frac{1}{4}$ ), using the same numerical parameters. It is well known that there is a latent heat of transformation and a discontinuity in the  $S_e$ -versus- $T$  curve in this alloy. The curves of Fig. 6 show this very clearly. It

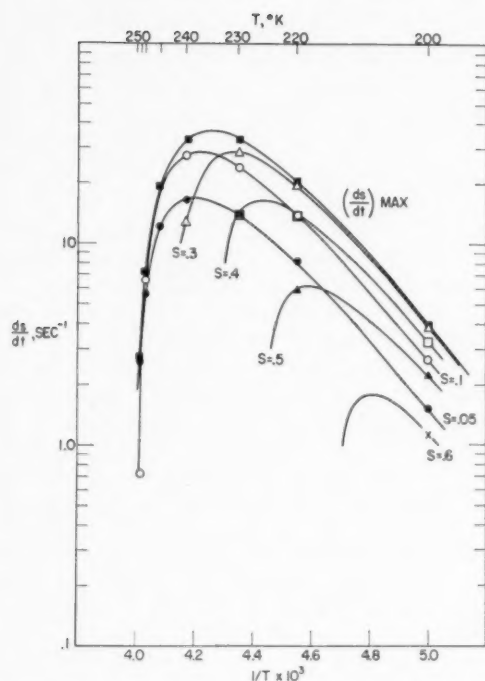
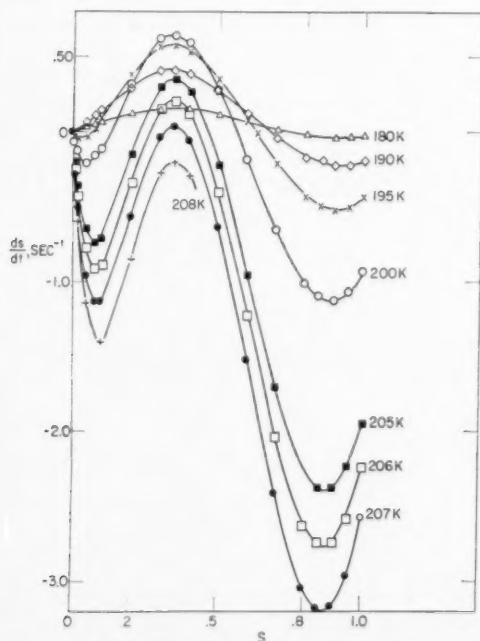
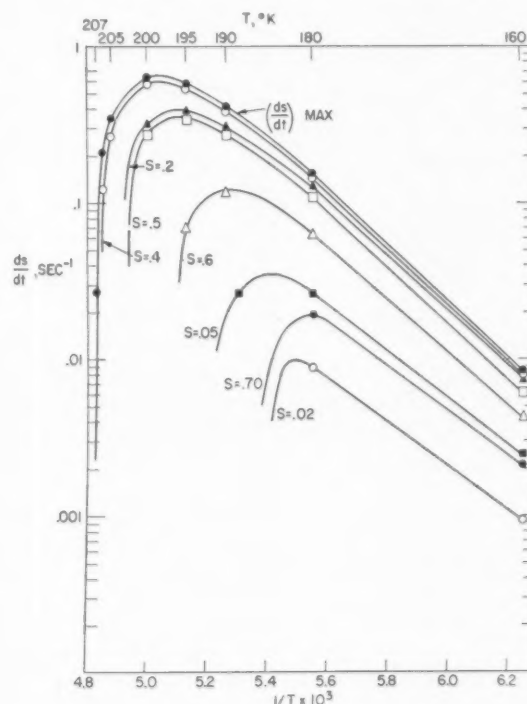


FIG. 5. Rate-versus-temperature characteristics for AB alloy.

is seen that, over quite a large temperature region below  $T_c$ , virtual disordering rates exist for an alloy starting at  $S=0$  for small values of  $S$ . This means that  $S$  has to change discontinuously from  $S=0$  to a finite  $S$  value before ordering can take place. Thus, long induction

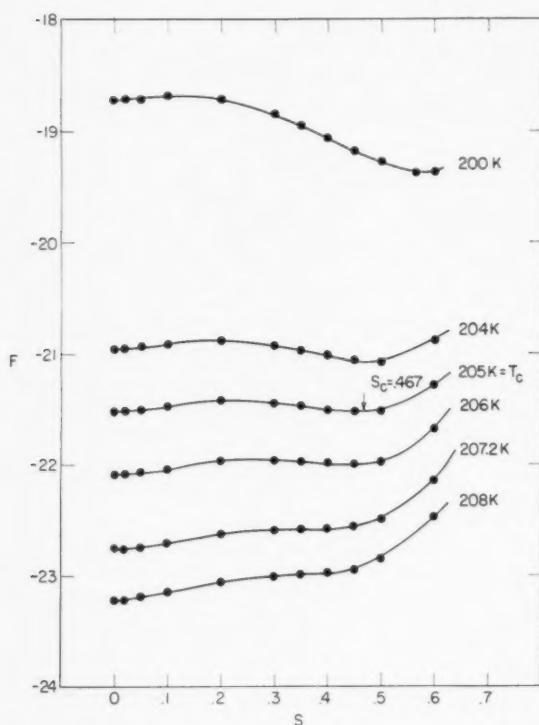
FIG. 6.  $dS/dt$ -versus- $S$  curves for  $AB_2$  alloy.

periods are indicated since large fluctuations are required to start the ordering reactions. In order to relate the characteristics of the  $dS/dt$  curves to the equilibrium  $S$ -versus- $T$  curve, one has to invoke a thermodynamic argument:  $dS/dt=0$  corresponds to maxima or minima in the free energy  $F$  as a function of  $S$ , but only a calculation of  $F$  can tell us about the stability of the various states.  $F$ -versus- $S$  curves were calculated by the method of Nix and Shockley<sup>2</sup> for our example (i.e.,  $V_0/R = 1000K$ ). The results are shown in Fig. 8. From this figure it is clear that 205°K is the critical temperature where the minima in the free energy, at  $S=.467$  and  $S=0$ , are equal. They are separated by an energy barrier, the maximum in  $F$  corresponding to  $dS/dt=0$  at  $S=.23$ . Above  $T_c$ , the thermodynamically stable

FIG. 7. Rate-versus-temperature characteristics for  $AB_3$  alloy.

state is at  $S=0$ , but up to 207.2K there is still a free-energy barrier in going from a finite  $S$  (the upper  $dS/dt=0$ ) to  $S=0$ . Thus, it should be possible to superheat the material up to this temperature. The tangency in the rate curves at  $S=.35$  corresponds to the disappearance of the free-energy barrier at 207.2K and represents the upper limit to superheating. These points are also brought out in the  $S$ -versus- $T$  diagram of Fig. 10 (lower curve), where the discontinuous change in  $S$  corresponds to  $S=.467$ , but where the highest temperature attainable with a finite  $S$  corresponds to  $S=.35$ .

Once the alloy is in the ordering range the  $S$ -versus-time curves are very similar to those presented for the AB alloy. Again, it should be emphasized that the need

FIG. 8. Free energy versus  $S$  for  $AB_3$  alloy.

for fluctuations (nucleation) is a simple consequence of the "chemical" rate theory for this alloy.

(b) The disordering rates in Fig. 6 for small values of  $S$  are of special interest, since sharp maxima in disordering rates are indicated. It should be possible to trace out the corresponding sigmoid integral curves experimentally by quickly raising the temperature of an alloy which is in equilibrium just below  $T_c$ , two degrees or so above  $T_c$ . Such an experiment would be a new and significant test of the theory.

(c) The temperature dependence of the rates for the  $AB_3$  alloy is shown in Fig. 7. The behavior is very similar to that deduced for the  $AB$  alloy. The characteristic maxima in the rates are again observed. The approximately linear region between 160 and 180K gives a spurious activation energy of 4200K.

The theory presented so far applies to stoichiometric compositions of any given  $\gamma$ , i.e., it is assumed that there is an  $\alpha$ - and  $\beta$ -site for every A- and B-atom. The equations, and the definition of  $S$  itself, become modified for nonstoichiometric compositions as discussed in Sec. V.

#### IV. MODIFICATION OF THE BRAGG AND WILLIAMS THEORY

It was pointed out in Sec. II that entropy changes over and above the mixing entropy should be taken into consideration. Since the elastic moduli and the density decrease upon disordering, one expects that the entropy change favors disordering. Let us assume that, analo-

gous to the energy the entropy is proportional to  $S$  and write

$$\frac{dS}{dt} = \nu e^{-U/RT} [\gamma(1-\gamma)(1-S)^2 - e^{-V_0 S/RT} e^{(\Delta\psi/R)S} [S + \gamma(1-\gamma)(1-S)^2]], \quad (13)$$

where  $\Delta\psi/R$  is the additional entropy. Calculations have been carried out for  $\Delta\psi/R=1.000$  and 1.500. It turned out that the resultant equilibrium curves generally showed faster disordering near  $T_c$  than the corresponding B. and W. curves for both  $AB$  and  $AB_3$ . This is in the direction indicated by experiment. The improvement, however, was rather slight, and very large entropies would have to be invoked to yield agreement with experiment.

The rate curves were not appreciably modified. The corresponding curves are very similar to those discussed in Sec. III.

Introduction of an entropy term proportional to  $S$  is, of course, equivalent to making the energy  $V_0$  depend linearly on the temperature. (In this connection see the work of B. Lindner,<sup>12</sup> who discusses a quadratic dependence of energy on  $T$ .)

In order to gain some insight into what experiments suggest, the  $V_0$  values of B. and W. were calculated for  $CuZn$  from the data of Chipman and Warren<sup>13</sup> and for  $AuCu_3$  from the data of Keating and Warren.<sup>14</sup> It was found that neither  $V_0 = V_0'(1-\alpha T)$  nor  $V_0 = V_0' \times (1-\alpha' T^2)$  fitted the experimental data. As a function of  $S$ , however,  $V$  was found to increase with  $S$  considerably faster than proportionally. It appears, therefore, that the B. and W. theory requires modification primarily in the energy term in order to bring it into better agreement with experiment. From what has been said it is also clear that additional term or terms are required in the energy of a power higher than one.

If the same form of the energy function is to hold for  $AB$  and  $AB_3$ , and no latent heat is to be observable in the  $AB$  case, the form of this function is considerably restricted. For the  $AB$  alloy the B. and W. relation reads

$$\ln \frac{1+S}{1-S} = \frac{1}{2} (V_0/RT) S. \quad (14)$$

For small values of  $S$ , expansion of the left-hand side of (14) gives

$$\ln \frac{1+S}{1-S} = 2(S + S^3/3 + S^5/5 + \dots). \quad (15)$$

If the slopes are to match at  $S=0$  and if double intersection (double value of  $S$  at some  $T$ ) is forbidden (no discontinuity in  $S$  as  $f(T)$ ), the energy expanded in terms of  $S$  must start as

$$V = V_0(S + S^3/3 \dots), \quad (16)$$

TABLE I. AB alloy: comparison of experiment with energy relations  $V = V_0 S$  and  $V = V_0(S + \frac{1}{3}S^3)$ 

$S$	Experiment* $T$	$T/T_c$	$V = V_0 S$ $T/T_c$	$V = V_0(S + \frac{1}{3}S^3)$ $T/T_c$
.00	738	1.00000	1.00000	1.00000
.10			.99652	.99984
.20			.98644	.99960
.30			.96932	.99840
.35	733	.99322		
.40			.94416	.99452
.50	723	.97967	.91024	.98612
.56	713	.96612		
.60			.86560	.96960
.67	693	.93902		
.70			.80712	.93892
.72	673	.91192		
.77	653	.88482		
.80			.72820	.88356
.84	613	.83062		
.90			.61140	.77648

\* Chipman and Warren<sup>12</sup> for CuZn.

or some higher power in the second term. The coefficient of  $S^3$ , of course, may be any number less than  $\frac{1}{3}$ . The largest number,  $\frac{1}{3}$ , was chosen here because it leads to the fastest disordering near  $T_c$ .

It seemed worth while, therefore, to investigate a simple modification of the B. and W. theory by applying the relation

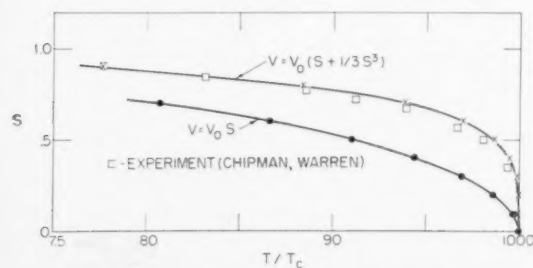
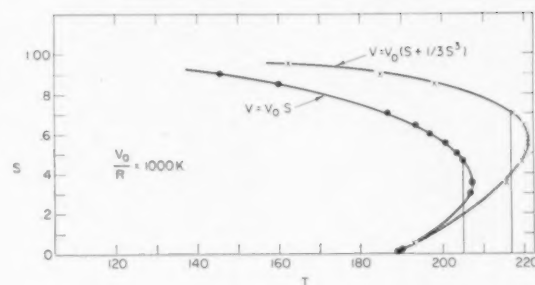
$$V(S) = V_0(S + \frac{1}{3}S^3) \quad (17)$$

to both the AB and  $AB_3$  alloys. The results of this computation for the AB case are shown in Table I and Fig. 9 and are compared with the experimental data and the original B. and W. calculation ( $V = V_0 S$ ). It is clear that the extra term in the energy leads to a much faster change in  $S$  near  $T_c$  and to quite excellent agreement with experiment.

Equation (17) was next applied to the  $AB_3$  case. The complete equation for calculating  $S$  as a function of  $T$  is

$$\ln \left[ \frac{16}{3} \frac{S}{(1-S)^2} + 1 \right] = \frac{V_0}{RT} (S + \frac{1}{3}S^3). \quad (18)$$

The results are shown in Fig. 10. The temperature and  $S$  value at the discontinuity were determined by a free energy versus  $S$  calculation which gave  $S_c = .705$ ,  $T_c = 216.7K$  for  $V_0/R = 1000K$ . This is to be compared

FIG. 9. Equilibrium  $S$  versus  $T/T_c$  for AB alloy. Comparison with experiment on CuZn.<sup>12</sup>FIG. 10. Equilibrium  $S$  versus  $T$  for  $AB_3$  alloy.

with the original B. and W. values of  $S_c = .467$ ,  $T_c = 205K$ . The comparison with the experimental data of Keating and Warren for  $AuCu_3$  is given in Table II and Fig. 11. The improvement over the B. and W. treatment is evident and the agreement with experiment is very satisfactory.

The energy relation of Eq. (17) appears to be an excellent approximation to the experimental data. Thus, this simple modification of the B. and W. theory appears to be very useful. It is worth while, therefore, to investigate the corresponding kinetics based on a relation which is a modified form of Eq. (13), namely,

$$\frac{dS}{dt} = \nu e^{-U/RT} [\gamma(1-\gamma)(1-S)^2 - e^{(-V_0/RT)(S + \frac{1}{3}S^3)} [S + \gamma(1-\gamma)(1-S)^2]]. \quad (19)$$

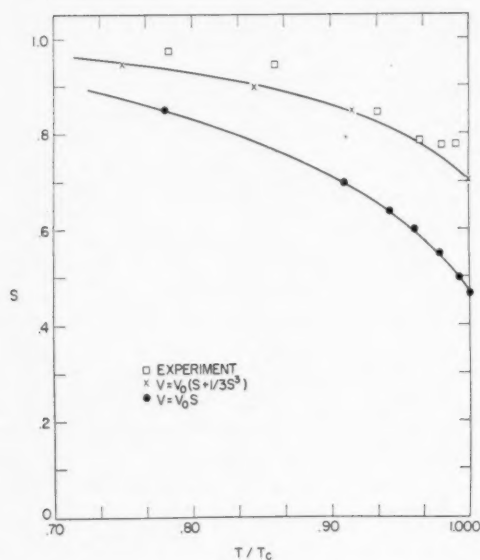
The qualitative features of the  $dS/dt$ -versus- $S$  curves are, of course, the same as before: simply the values of  $S$  at which  $dS/dt = 0$  are now higher. Curves for the AB alloy are therefore not shown. Although qualitatively the same, the changes are more interesting for the  $AB_3$  alloy. The results are shown in Fig. 12. It is clear that the alloy can now be superheated to a value of  $S = .55$ . From this point it disorders as before, with a quite large maximum in the disordering rate near  $S = .2$ . An

TABLE II.  $AB_3$  alloy: comparison of experiment with  $V = V_0 S$  and  $V = V_0(S + \frac{1}{3}S^3)$ 

$S$	Experiment* $T$	$T/T_c$	$V = V_0 S$ $T/T_c$	$V = V_0(S + \frac{1}{3}S^3)$ $T/T_c$
.467			1.0000	
.500			.9928	
.550			.9792	
.600			.9614	
.640			.9438	
.700	667.3(?)	1.0000		
.705				1.0000
.775	660.0	.9891		
	653.0	.9786		
.787			.7809	.9166
.841	623.0	.9336	.7110	.8542
.850				
.900				
.944	573.0	.8587		
.950				.7489
.972	523.0	.7838		

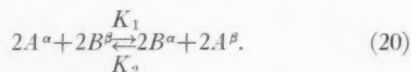
\* Keating and Warren<sup>14</sup> for  $AuCu_3$ .



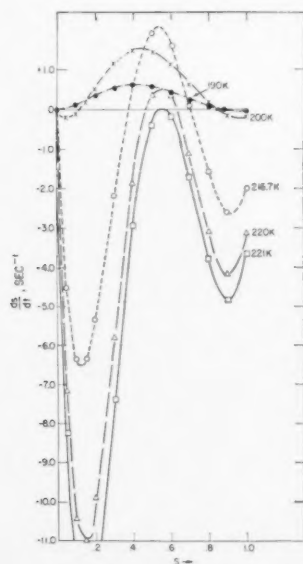
FIG. 11. Comparison of theory and experiment<sup>14</sup> for AuCu<sub>3</sub>.

attempt is being made to trace out experimentally the corresponding integral curves.

It should be noted that if the cooperation of more than two atoms is required to bring about the exchange of right and wrong atoms, the equilibrium properties are not affected by this kinetic change. For example, assume that the "chemical" reaction is



By exactly the same procedure as given in Sec. II, one

FIG. 12.  $dS/dt$ -versus- $S$ -curves for AB<sub>3</sub> alloy using modified B. and W. theory.

obtains

$$\frac{dS}{dt} = \gamma(1-\gamma)\gamma e^{-U/RT} [\gamma^2(1-\gamma)^2(1-S)^4 - e^{-V/RT} [S + \gamma(1-\gamma)(1-S)^2]^2] \quad (21)$$

and at equilibrium

$$e^{1/2(V/RT)} = \frac{S + \gamma(1-\gamma)(1-S)^2}{\gamma(1-\gamma)(1-S)^2}. \quad (22)$$

The details of the kinetics will be changed, of course. However, since the shape of the equilibrium curve is exactly the same, the  $dS/dt=0$  points must remain the same and only the shapes of the curves between these points can be altered.

### V. NONSTOICHIOMETRIC COMPOSITIONS

The above considerations are easily extended to nonstoichiometric compositions in the AB case. For rather small deviations from the ideal AB composition the number of  $\alpha$ - and  $\beta$ -sites will remain fixed, i.e., the excess component is considered to be distributed at random on  $\alpha$ - and  $\beta$ -sites. Thus,

$$\frac{N^\alpha}{N} = \frac{N^\beta}{N} = \frac{1}{2},$$

and  $S$  is defined as

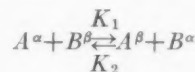
$$S = r_\alpha + r_\beta - 1, \quad (23)$$

where

$$r_\alpha = \frac{N_A^\alpha/N}{N^\alpha/N},$$

$$r_\beta = \frac{N_B^\beta/N}{N^\beta/N}.$$

The chemical equation, with A-atoms in excess (equally valid for excess B-atoms by appropriate change in notation since the problem is completely symmetrical), is



$$\frac{N_A^\alpha}{N} - \frac{X N_B^\beta}{N} - \frac{X N_A}{N} - \frac{N^\alpha}{N} + \frac{X X}{N N}$$

Since A-atoms are in excess,

$$N_A^\alpha = N^\alpha, \quad N_B^\beta = N_B = (1-\gamma)N,$$

and, therefore,

$$\frac{d(X/N)}{dt} = K_1 \left[ \frac{1}{2} - \frac{X}{N} \right] \left[ 1 - \gamma - \frac{X}{N} \right] - K_2 \left[ \gamma - \frac{1}{2} + \frac{X}{N} \right] \left[ \frac{X}{N} \right], \quad (24)$$

and, from Eq. (23),

$$\frac{X}{V} = \frac{1}{2}(1-\gamma) - \frac{1}{4}S. \quad (25)$$

Finally,

$$\frac{dS}{dt} = K_2[\gamma - \frac{1}{2}S][1 - \gamma - \frac{1}{2}S] - K_1[\gamma + \frac{1}{2}S][1 - \gamma + \frac{1}{2}S]. \quad (26)$$

At equilibrium,  $dS/dt=0$ ,

$$K = \frac{K_1}{K_2} = \frac{v_1}{v_2} e^{-V/RT} = \frac{\gamma(1-\gamma) - \frac{1}{2}S + \frac{1}{4}S^2}{\gamma(1-\gamma) + \frac{1}{2}S + \frac{1}{4}S^2} \quad (27)$$

with a maximum value of  $S$  (at  $T=0$ ):

$$S_{\max} = 2(1-\gamma).$$

By evaluating slopes of the two sides of Eq. (27), for  $V = V_0S$  or for  $V = V_0(S + \frac{1}{3}S^3)$  at  $S=0$ , we find for the critical temperature,

$$T_c = \frac{V_0}{R} \gamma(1-\gamma), \quad (28)$$

which is the same relation as that derived by Slater for a slightly different definition of  $S$ .<sup>15</sup>

Calculations have been made with  $V = V_0(S + \frac{1}{3}S^3)$  for  $V_0/R = 1000^\circ\text{K}$  at  $\gamma = .55$  and  $\gamma = .60$ . The results are shown, in Fig. 13 in comparison with the ideal AB case ( $\gamma = .50$ ). It is seen that the equilibrium degree of order decreases at all temperatures as the system departs from stoichiometry.

Rate curves have also been calculated for  $\gamma = .55$  and  $V = V_0S$ . They are qualitatively identical to those for  $\gamma = .50$  but the ordering rates are always less than those for  $\gamma = .50$  for the same  $V_0$  and  $U$ .

Extension of these ideas to nonstoichiometric  $\text{AB}_3$  alloys is straight-forward but laborious since the critical temperature would have to be determined by a free-energy calculation for each composition. In the absence

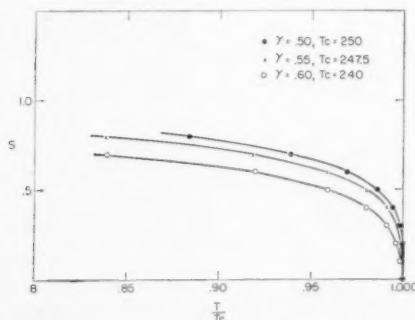


FIG. 13. Equilibrium  $S$  versus  $T/T_c$  for nonstoichiometric AB alloy. The energy relation  $V = V_0(S + \frac{1}{3}S^3)$  was used.

of experimental rate data it was not deemed worth while to carry out the computations at this time.

The present theory is not applicable when phase separation occurs. In that case,  $S$  has to be redefined and a more complicated heterogeneous kinetic theory devised.

## VI. DISCUSSION

The theory presented in the previous sections is a simple and, to a large extent, intuitive one. It focuses attention on the unusual kinetic behavior to be expected theoretically, due to the fact that in an order-disorder system the energy of ordering depends on the amount of order present. The results are in agreement with the experimentally known qualitative behavior of such systems. It is particularly noteworthy that this simple kinetic theory predicts a behavior that is quite similar to what is expected from nucleation and growth, although nucleation is nowhere assumed in the theory. It is a simple consequence of the theory that in certain ranges of the order parameter (particularly for an  $\text{AB}_3$  alloy) large fluctuations are required to initiate ordering.

It is not to be concluded from this study that nucleation and growth may not be the correct mechanism for the ordering of an order-disorder alloy. All one can say is that the simple kinetic theory is capable of describing the known characteristics of these systems without invoking any special assumptions. The theory forms a suitable framework for further quantitative studies and suggests new experiments. Further quantitative experimental and theoretical work will be required for a critical evaluation of these ideas.

## ACKNOWLEDGMENT

The writer is grateful to G. H. Vineyard and D. T. Keating for stimulating discussions.

The work was performed under contract with the U. S. Atomic Energy Commission.

## REFERENCES

1. W. L. Bragg and E. J. Williams, *Proc. Roy. Soc. London* **145A**, 699 (1934); hereafter referred to as "B. and W."
2. For critical review see: F. C. Nix and W. Shockley, *Revs. Modern Phys.* **10**, 1 (1938).
3. W. Gorsky, *Z. Physik* **50**, 64 (1928).
4. References on rate studies to 1950 are given in: F. N. Rhines and J. B. Newkirk, *Trans. ASM* **45**, 1029 (1953); specific papers and more recent work will be referred to at appropriate points.
5. F. Seitz, *Modern Theory of Solids* (McGraw-Hill, New York, 1940), p. 510.
6. D. B. Bowen, *Acta Met.* **2**, 573 (1954).
7. G. J. Dienes, *J. Appl. Phys.* **22**, 1020 (1951).
8. J. Rothstein, *Phys. Rev.* **94**, 1429 (1954).
9. Parkins, Dienes and Brown, *J. Appl. Phys.* **22**, 1012 (1951).
10. S. Siegel, *J. Chem. Phys.* **8**, 860 (1940).
11. For further recent work on this point see: N. W. Lord, *J. Chem. Phys.* **21**, 692 (1953).
12. B. Lindner, *J. Chem. Phys.* **22**, 970 (1954).
13. D. Chipman and B. E. Warren, *J. Appl. Phys.* **21**, 696 (1950).
14. D. T. Keating and B. E. Warren, *J. Appl. Phys.* **22**, 286 (1951).
15. J. C. Slater, *Introduction to Chemical Physics* (McGraw-Hill, New York, 1939), pp. 301-304.

## SOME ANELASTIC PHENOMENA IN ALLOYS OF GOLD AND NICKEL\*

CHOH-YI ANG,<sup>†</sup> J. SIVERTSEN,<sup>‡</sup> and C. WERT<sup>§</sup>

Two relaxation peaks are found in polycrystalline alloys of Au and Ni between room temperature and 600°C. One of these peaks has been identified as the order peak; the origin of the other is uncertain. Both peaks exist in alloys quenched from the solid solution region of the constitution diagram. Upon annealing of these quenched solid solutions both of these peaks disappear; the order peak along with the formation of the mixture phases, the other peak much earlier than this. The kinetics of the disappearance of the order peak are consistent with all measurements of the kinetics of formation of the mixture phases as determined by independent methods. The behavior of the second peak upon quenching and annealing indicates a process which has not been observed before.

### SUR LES PHÉNOMÈNES ANÉLASTIQUES DANS LES ALLIAGES D'OR ET DE NICKEL

Deux maximum de frottement interne sont observés dans les alliages polycristallins d'or et de nickel entre la température ordinaire et 600°. L'un de ces maximum correspond à l'ordre, tandis que l'origine de l'autre est incertaine. Ces deux maximum existent pour les alliages trempés dans le domaine de la solution solide du diagramme d'équilibre; au cours du recuit de ces alliages, les deux maximum disparaissent, le maximum d'ordre lors de la formation du mélange, l'autre beaucoup plus tard. La cinétique de la disparition du maximum d'ordre est en accord avec toutes les mesures obtenues par d'autres méthodes sur la cinétique de la formation d'un mélange de phases, mais le comportement du second maximum indique un processus qui n'a pas encore été observé jusqu'ici.

### EINIGE UNELASTISCHE ERSCHEINUNGEN BEI GOLD-NICKEL LEGIERUNGEN

Zwischen Raumtemperatur und 600°C findet man bei vielkristallinen Gold-Nickel Legierungen zwei Relaxationsspitzen. Eine dieser Spitzen wurde als dem Ordnungsvorgang zugehörig gefunden; die Ursache der anderen ist ungewiss. Beide Spitzen treten bei Legierungen, die aus dem Mischkristallgebiet des Zustandsdiagrammes abgeschreckt worden waren, auf. Beim Anlassen der abgeschreckten Mischkristalle verschwinden beide Spitzen und zwar die Ordnungsspitze mit der Bildung der Mischphase, die andere Spitze wesentlich früher. Die Kinetik des Verschwindens der Ordnungsspitze ist in Übereinstimmung mit allen Messungen der Bildungskinetik der Mischphase, die mit anderen, unabhängigen Methoden durchgeführt wurden. Das Verhalten der anderen Spitze beim Abschrecken und Anlassen weist auf einen Vorgang hin, der bisher nicht beobachtet wurde.

## INTRODUCTION

Certain substitutional alloys exhibit a type of anelastic behavior which seems to be related to a change of order under stress. Whether this change of order is an actual change in the degree of order or merely a change in local spatial configuration of order is not clear. The experimental evidence which would enable one to make a satisfactory picture of the anelastic behavior is rather meager. The effect was first observed by Zener<sup>§</sup> in 70-30  $\alpha$ -brass and was later observed in other alloys systems.<sup>1,2,3</sup> Zener demonstrated the possibility that this relaxation effect is caused by the spatial reorientation under stress of pairs of solute atoms which differ in size from the solvent atoms.<sup>4</sup> Nowick later discussed this relaxation from a more general point of view than Zener's pair-relaxation, but offered no detailed atomistic model.<sup>5</sup> LeClaire and Lomer have more recently devised a quantitative theory of the relaxation.<sup>6</sup> According to this theory the relaxation has its origin in a real change in short-range order under stress. Predictions of the theory are compared in their paper to

experimental data wherever this is possible. While the agreement is satisfactory in the few instances where this can be done, more critical comparisons would be desirable.

The criteria for the existence of this relaxation are not fully established, but in all alloys for which the effect is of large enough magnitude to be observable two conditions have been satisfied. These are (1) a relatively large concentration of one metal in the other and (2) a rather large difference in atomic size of the constituents. All data so far published fit these requirements.

A consideration of these facts led us to believe that a relaxation peak of this type should exist in quenched alloys of gold and nickel. The atomic radii are considerably different (1.44 Å and 1.25 Å, respectively), and alloys of any arbitrarily large concentration can be prepared. Furthermore, we believed that, if anelastic effects in these quenched alloys do exist, they will gradually disappear as the quenched alloys are annealed at temperatures in the mixed phase region (see Fig. 1). The kinetics of this phase separation are known from an earlier investigation.<sup>7</sup>

Accordingly, a number of alloys of various compositions were prepared and studied. The following facts were observed: (1) A relaxation of the type noted above does exist for quenched alloys of gold and nickel. (2)

\* Received March 27, 1955; in revised form June 7, 1955.

<sup>†</sup> Now at P. R. Mallory Company, Indianapolis, Indiana.

<sup>‡</sup> Department of Metallurgy, University of Illinois, Urbana, Illinois.

<sup>§</sup> In this paper, this relaxation will be termed the "ordering relaxation."

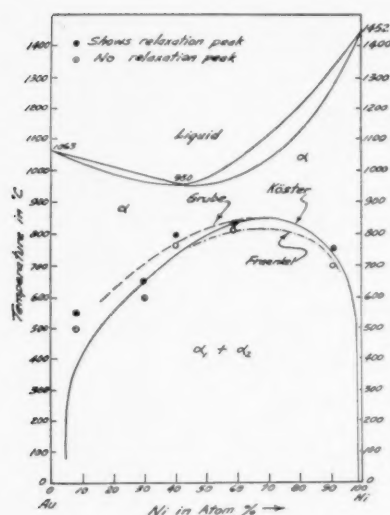


FIG. 1. Constitution diagram for the Au-Ni system. The open and filled circles refer to data obtained in the present investigation.

The effect does disappear if the quenched alloys are annealed in the two-phase region. The disappearance of the relaxation seems simply related to the separation of the quenched solid solution into the mixture phases. (3) Another relaxation peak exists, the origin of which is not known. This appears to be a new relaxation, since its characteristics cannot be reconciled to those of known relaxations which might be expected to exist in these alloys.

## EXPERIMENTAL METHOD

### A. Specimens

A preliminary investigation with an alloy of 40–60 Au-Ni\* established the fact that interesting anelastic effects do exist for these alloys. Then a series of alloys was made up across the constitution diagram with nominal compositions of 8, 30, 40, 59 and 91 per cent nickel. Gold of 99.98 wt. % purity and nickel of 99.92 wt. % purity were used in the preparation of these alloys. The four alloys of lowest nickel content were made by melting together appropriate amounts of the two metals in an electric furnace. An alundum crucible containing the constituent metals was placed inside a

TABLE I. Analyses of alloys

Alloy Number	At. % Au*	At. % Ni*	Designation of alloy
1	92.4	7.7	8%
2	70.3	29.7	30%
3	59.7	40.1	40%
4	41.1	58.9	59%
5	9.1	90.8	91%

\* Samples were analyzed for both gold and nickel.

\* All gold-nickel alloys are expressed in atomic per cent. The designation of an alloy will be made according to its nickel content.

vertical quartz tube connected to a vacuum system. The charge was then melted under vacuum with vigorous manual shaking of the entire vacuum chamber to aid mixing. The high nickel alloy was melted in a high-frequency induction-furnace under an atmosphere of helium.

The five alloys at this stage were in the form of  $\frac{1}{4}$  in. rods about  $1\frac{1}{2}$  in. long. These rods were swaged and drawn to .030 in. dia. wires with numerous intermediate vacuum anneals at 850°C. A final anneal for 10 days at 850°C served to establish a maximum grain-size characteristic of each alloy for this combination of mechanical and thermal treatment. At this time the gold-rich alloys had a grain size of the order of .2 mm; the high nickel alloys had a grain size somewhat smaller than this. Specimens used for anelastic studies were short lengths cut from these wires. The specimens were from 12 to 18 cm long, depending upon their use.

Although there was almost no loss of metal in melting, chemical analysis of each alloy was made to establish the exact composition of each. The results of these analyses are given in Table I.\*\*

### B. Measuring Equipment

Initial measurements of internal friction *versus* temperature were attempted using conventional torsional pendulum equipment used many times before in anelastic measurements (See Figs. 2 and 3, ref. 3). Some promising results were obtained, but they were quite unreplicable because the damping peaks observed disappeared too rapidly. The accurate study of damping in these alloys clearly demanded use of a system with smaller thermal inertia.

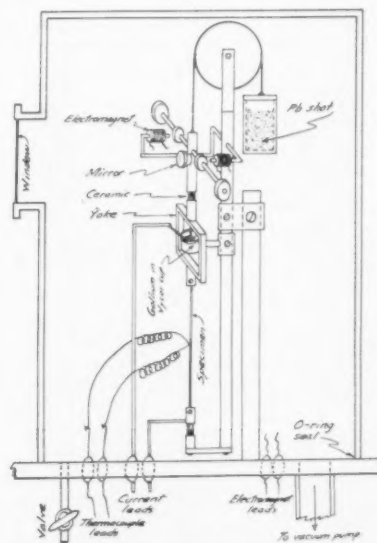


FIG. 2. Torsion pendulum used to make rapid measurements.

\*\* The authors are indebted to the analytical chemistry section of the Westinghouse Research Laboratories for these analyses.



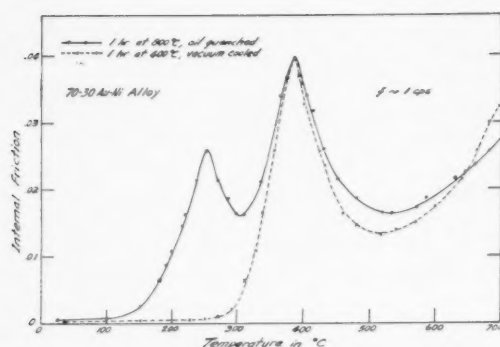


FIG. 3. Damping curves for a quenched and annealed 30 per cent Ni alloy. The ordinate in this and all other damping curves is the tangent of the angle by which the strain lags the stress.

To solve this problem, we constructed an entirely new pendulum (Fig. 2). The desirable features of the better of our older systems (counterbalanced pendulum and evacuated chamber) were retained, but the large thermal inertia of the old furnace was eliminated. This was done by heating the specimen directly with the Joule heat of an alternating current of from 0 to 20 amp. The significant details of this apparatus have been described earlier.<sup>7</sup> The low thermal inertia of this pendulum has been obtained at the expense of some non-uniformity of temperature along the length of the specimen. In spite of this, for application to the present work, it seemed quite satisfactory. A typical measurement made with it is given in Fig. 3. Here are shown the two peaks in the quenched alloy, one at 250°C and the other at 400°C. After an anneal at 400°C for one hour, the lower peak had completely disappeared.

An investigation was made to ascertain the heating rate required to avoid annealing away of this 250°C

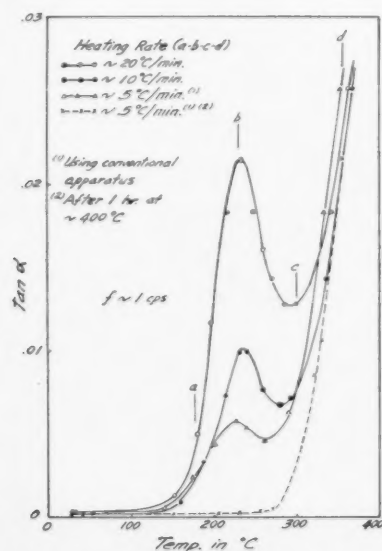


FIG. 4. The effect of heating rate on the lower damping peak for the 30 per cent Ni alloy.

peak during the warm-up period. The results of this study for a specimen of the 30 percent alloy are given in Fig. 4. The 400°C peak is not significantly different for all curves, but the maximum of the 250°C peak is lower the slower is the heating rate. Further measurement showed that a heating rate of 100°C per minute from room temperature directly to 240°C gave the same value as for the topmost curve. Hence it was assumed that for good measurements a heating rate of 20°C/min or greater was adequate.

## RESULTS

Because the experimental results on all alloys follow roughly the same pattern, only data for the 30 per cent Ni alloy will be presented (except for Fig. 9). The data to be shown are actually only a small part of the measurements made even on this alloy. Not only were all measurements repeated several times, but numerous measurements not reported were repeated with small variations in one or several parameters. The results themselves are conveniently divided into four groups: (1) isothermal annealing of quenched specimens, (2) effect of quench temperature, (3) activation energies for the relaxations, and (4) the effect of grain size.

### (1) Isothermal Annealing

Annealing of quenched specimens of all alloys was accompanied by disappearance of both the peaks. Most interesting was the disappearance of the 250°C peak; Fig. 5 shows this effect for the 30 per cent Ni alloy. A specimen of this alloy was quenched from 800°C. A measurement of damping *versus* temperature was then made quickly; this result is Fig. 5A. Curves B, C, and D were obtained after holding the quenched specimen,

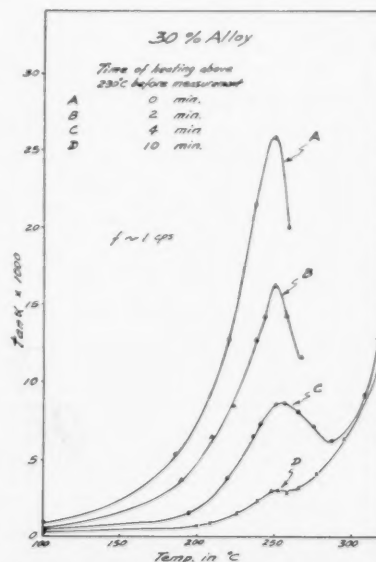


FIG. 5. Disappearance of the lower damping peak following annealing of quenched alloys.

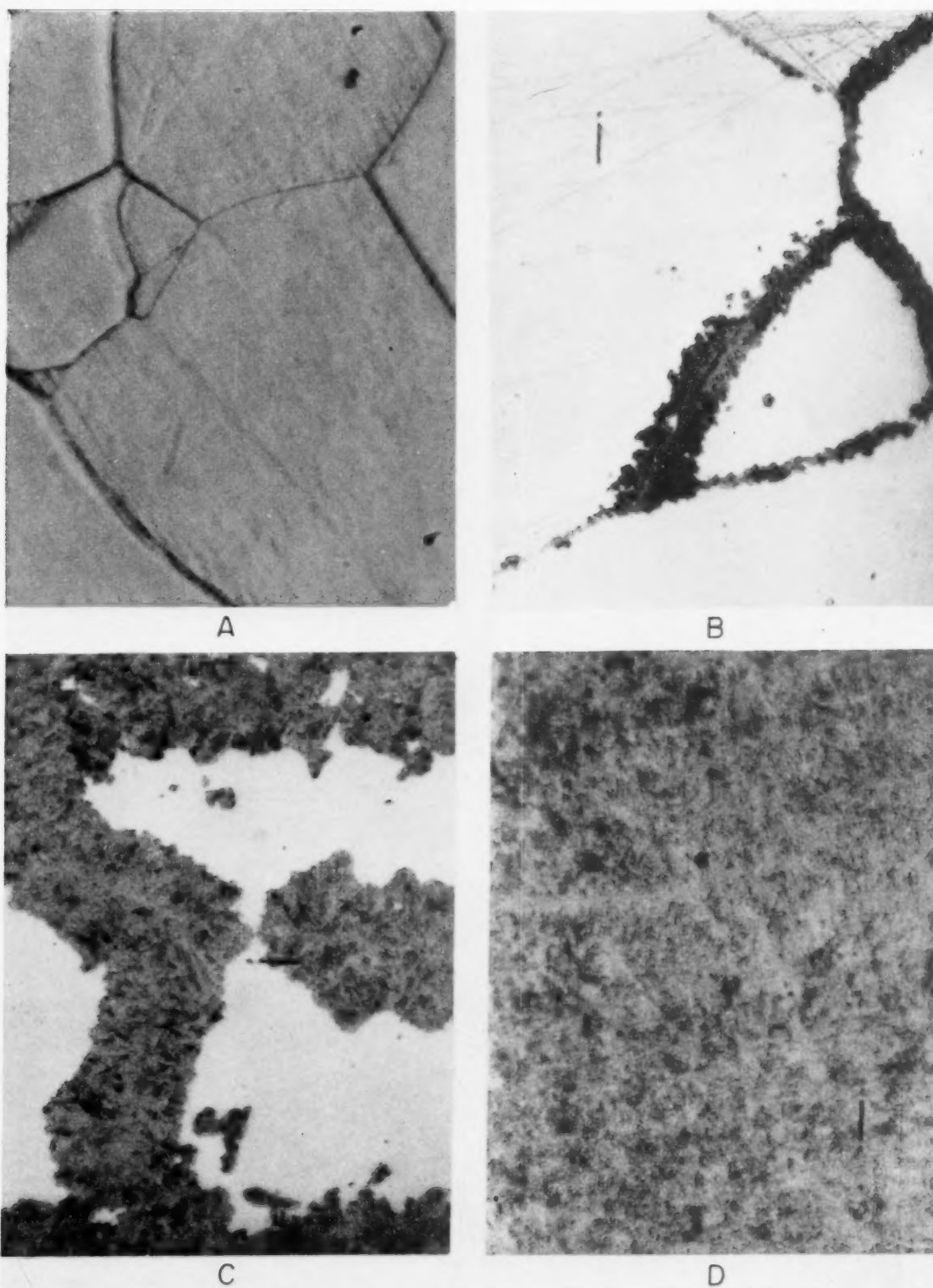


PLATE I.—Fig. 7. Microstructure developed during annealing at 295°C for a quenched alloy. (A) as-quenched, (B) 2520 min., (C) 24,000 min., (D) 135,000 min. All specimens were etched with 1:1 10 percent solutions of KCN and  $(\text{NH}_4)_2\text{S}_2\text{O}_8$  after mechanical polishing. Specimen (A) was further electropolished in 5 per cent KCN solution and etched slightly to remove polishing scratches. 250X.

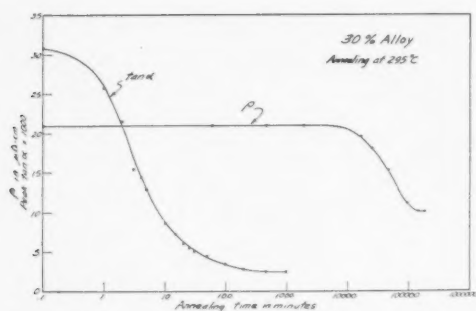


FIG. 6. Effect of isothermal annealing at 295°C on resistivity and damping of a quenched alloy of 30 per cent Ni.

prior to measurement, for 2, 4 and 10 minutes respectively in the neighborhood of 240°C. The chief result of the annealing is seen to be a subsidence of the peak in magnitude. A slight shift in the temperature of the peak is probable during annealing, but this is not a pronounced effect and may be entirely instrumental in origin.

This phenomenon was examined again in a slightly different manner. A specimen was quenched from 950°C (the temperature before quenching is not especially significant as long as it is in the solid solution region). Then it was quickly heated to 295°C (this is the peak position for this quench temperature—see Sec. (2) below.) The damping was measured as a function of time at 295°C. The damping fell quickly from its peak value as is shown in Fig. 6; in one minute it had already decreased considerably, and in 100 minutes it had already reached a steady low value.

The next step was to correlate these data with the process of separation of the quenched solid solution into Ni- and Au-rich regions at 295°C. A standard method of following this process is to observe the drop in electrical resistivity as the phase mixture forms.<sup>7</sup> This was done by measuring the room temperature resistivity at intervals during annealing at 295°C of a quenched 30% alloy. These data are also given in Fig. 6. The resistivity is practically unchanged for some 10<sup>4</sup> minutes, after which it decreases steadily and reaches an essentially constant value in about 10<sup>5</sup> minutes.

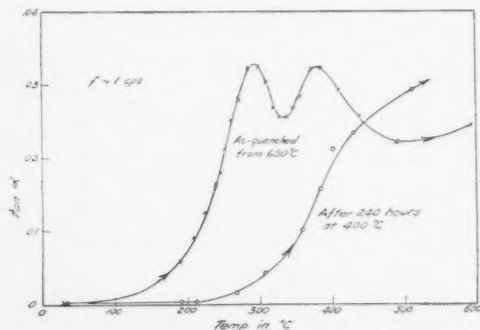


FIG. 8. Behavior of order peak upon annealing at 390°C of a quenched 30 per cent alloy.

Comparison of the curves in Fig. 6 shows that there exists a striking difference in time for annealing away of the two effects. To substantiate our belief that the resistivity change accurately measures the rate of formation of the mixture phase, we made a series of photomicrographs at intervals during annealing. Four of these micrographs were selected for Fig. 7, at intervals of 0, 2500, 24 000 and 135,000 minutes. These micrographs show that changes in  $\rho$  do follow rather well the process of phase separation. Significantly, no difference was seen between the micrograph for the as-quenched specimen and for the specimen after it had annealed for 100 minutes, at which time the damping peak had disappeared. Also, the resistivity change in this first 100 minutes was less than 1 per cent.

The behavior of the 400°C peak was also examined in some detail. That annealing affects this peak too is demonstrated by the data in Fig. 8. Here are presented data for an alloy of 30 per cent Ni quenched from 650°C (just above the phase separation line), then annealed at 400°C for 240 hours. Both peaks are present in the quenched alloy and both have disappeared in the

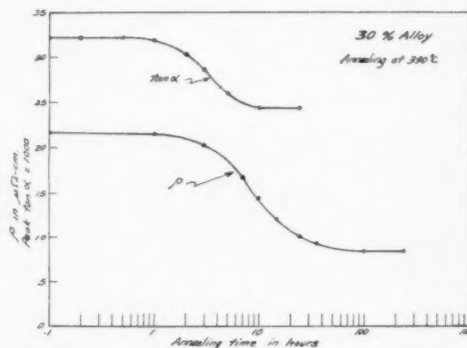


FIG. 9. Effect of isothermal annealing at 390°C on resistivity and order peak.

annealed alloy. The damping at 295°C is seen to have almost completely disappeared during this anneal (according to the kinetics of the disappearance of this peak as given in Fig. 6, it was presumably gone after the first few minutes at 400°C). The damping at 400°C does not fall to such a low value because of the appearance of a generally rising background damping above 300°C. This may well be caused by the myriads of phase boundaries which accompany the formation of the two phases. Micrographs taken for the quenched sample and the annealed sample are indistinguishable from those of Fig. 7A and Fig. 7D, respectively.

The magnitude of this peak and the room temperature resistivity,  $\rho$ , were also measured as a function of annealing time. Such data are plotted in Fig. 9 for an isothermal anneal at 390°C. This peak does disappear along with the general phase separation; unfortunately the damping does not tend to zero as before because of the increase of the background damping. It does seem

reasonable to suppose from the data in Fig. 9, however, that the magnitude of this peak is a simple function of the amount of untransformed solid solution still remaining.

## (2) The Effect of Quench Temperature

Nowick and Sladek have observed that quenching of Ag-Zn alters the relaxation time of the ordering relaxation,<sup>9</sup> in fact, they find tremendous changes in relaxation time,  $\tau$ , which they attribute to the quenching-in of thermally produced vacancies. Because of the relatively narrow solid solution range for the Au-Ni alloys, such experiments are rather limited, but they were attempted. No significant changes were observed for  $\tau$  in the case of the higher peak (the 400°C peak for the

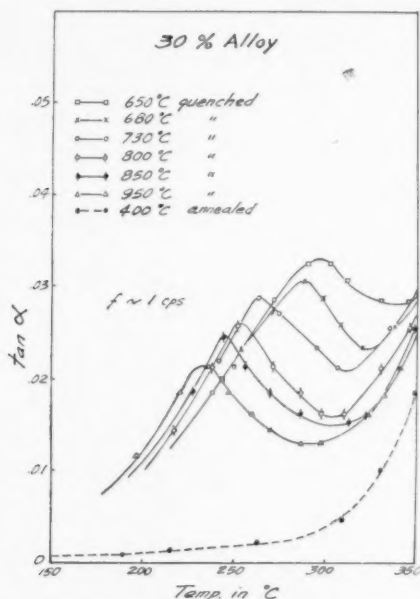


FIG. 10. Position and magnitude of lower peak as a function of quench temperature.

30 per cent alloy). The lower peak, however, was changed both in magnitude and in relaxation time. The results of these studies for the 30 per cent alloy are again typical for all alloys; they are presented in Fig. 10. A study of the data in this figure shows that two generalizations can be drawn: (1) the relaxation time (at a given temperature—say 250°C) decreases as the quench temperature increases. The spread of relaxation times for the data presented is about a factor of 10. (2) The magnitude of the peak decreases somewhat as the quench temperature increases.

It will be noted that the quench temperature of 650°C for this alloy is barely in the solid solution region. The next step was to see how this peak would appear when the specimen was quenched from just below the solubility line, say from 600°C. These data are presented in Fig. 11 along with similar data for the other four

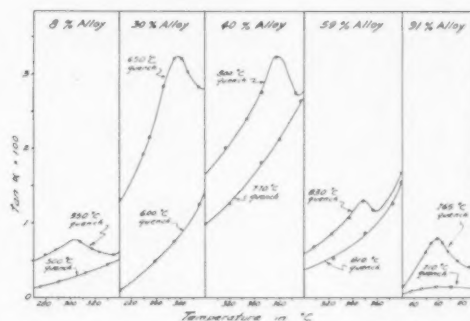


FIG. 11. Behavior of lower peak following quenching in neighborhood of solubility line.

alloys.\* It is observed that peak disappears when the quench temperature is lowered through some critical temperature range for each alloy. If these points are plotted on the constitution diagram for the alloy system, they straddle fairly well the solid solution line (see Fig. 1).

## (3) Heats of Activation

All relaxations which have their origin in movement of atoms seem to be characterized by a relaxation time depending on temperature according to the expression

$$\tau = \tau_0 \exp(\Delta H/RT).$$

In this equation  $\Delta H$ , the heat of activation, has been observed to be of the order of the heat of activation for volume diffusion. Consequently, it is of some value to

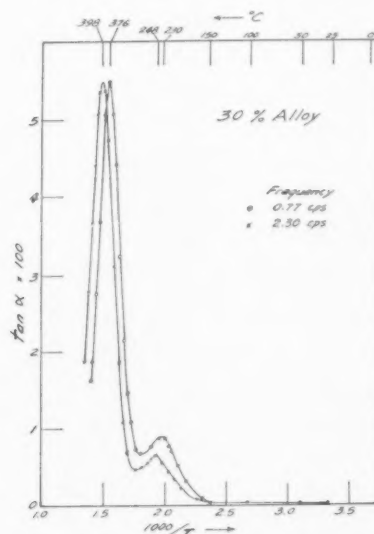


FIG. 12. Shift in position of both peaks with change in pendulum frequency.

\* Each alloy was held for one hour at the temperature specified before quenching. Photomicrographs showed that this was not long enough for phase separation to be complete for the lower temperature of each alloy. For example, structures similar to Fig. 7b were observed for the 30 per cent alloy after one hour at 600°C.



TABLE II. Activation energies of relaxations and of diffusion in alloys of Au and Ni. All values of energy are given in cal/mol. The three columns of values for  $\Delta Q$  are estimated from the curves in Reynolds' thesis.

Alloy	Temp. of lower peak <sup>2</sup>	$\Delta H$ Lower peak	Temp. of higher peak	$\Delta H$ Higher peak	$\Delta Q$ Au in alloy	$\Delta Q$ Ni in alloy	$\Delta Q$ Inter-diffusion
8%	570°K	37,000	670°K	43,500	43,000	47,000	41,500
30%	570°K	37,000	670°K	43,500	41,000	55,000	43,900
40%	625°K	41,000	670°K	43,500	42,000	53,000	42,000
59%	625°K	41,000	670°K	43,500	47,000	36,000	49,000
75%	No Peak		825°K	54,500	55,000	37,000	105,000
91%	330°K	22,000	925°K	60,000	65,000	46,000	100,000

\* Quench conditions of Fig. 10.

measure the heats of activation for these relaxations.  $\Delta H$  for the 400°C peak may be easily calculated from measurements of peak shift in temperature with a known change in frequency. Data obtained for the 30 per cent alloy are presented in Fig. 12. The heat of activation calculated for this relaxation is 43,500 cal/mol.

For the lower peak this method presents some problems. As is clear from Fig. 11, the peak has partially disappeared on the second measurement at 2.3 cps. It is not apparent then that this method is clearly applicable to this peak, especially if a slight shift in peak position accompanies the gradual disappearance of the peak. However, disregarding this possibility and normalizing the magnitudes of both curves, we did make a calculation of the heat of activation. The value obtained for this alloy with quench conditions was 32,000 cal/mol.

There is an independent method of checking the correctness of these values. This is the comparisons of these calculations with the values which can be read off the empirical curve of Wert and Marx for  $\Delta H$  versus peak temperature for 1 cps (10). The values of 43,500 and 32,000 fit well on this curve, indicating (1) that the two relaxations seem for these alloys to fit into the general scheme of all the other relaxations, and (2) that the method of calculation is rather good for both. It is conceivable, of course, that neither statement is correct and that the agreement is simply fortuitous, but this seems rather unlikely.

No further measurements of  $\Delta H$  were made using the two-frequency method, but the method of Wert and Marx was assumed to be correct. The value of  $\Delta H$  was then computed for all alloys from knowledge of the peak positions at 1 cps. These values of  $\Delta H$  are presented in Table II along with values of the activation energies for diffusion in these alloys as determined by Reynolds.<sup>11</sup> Because variations in quenching temperature affect the position of the lower peak by an amount sufficient to cause a variation in  $\Delta H$  of several Kcal, only two significant figures are given for this peak.

Because the behavior of both peaks for the 91 per cent alloy is peculiar an additional alloy at 75 per cent Ni was prepared to see if the trend in temperature of the two peaks could be determined. For this alloy only one peak was observed. This is tentatively called the *high-temperature peak*.

#### (4) The Effect of Grain Size

It is important to find out if either of these two peaks is the grain-boundary peak. To check this point a series of specimens of the 30 per cent alloy were prepared covering a wide range of grain size. The wire with smallest grains had equiaxed grains about .005" in diameter. An intermediate grain size was about .025" and a large grain specimen had grains extending across the .030" wire and about .1" long. Some small differences in the height of the peaks were observed, but they were much smaller than one would expect for such a large difference in grain size and were in the wrong direction. No shift in peak position with grain size was observed. Thus we believe that neither of the peaks is the grain boundary peak.

### DISCUSSION

#### (1) General Discussion

If the experimental results presented in the last section are to be of any value, they must be interpreted in such a way as to show the details of the processes that are taking place in the alloys during the various heat treatments. This interpretation is especially difficult since proposals of the nature of the relaxation must be made at the same time. The best that can be done is to devise an explanation which will be consistent with the experimental observations of this investigation as well as other experimental facts. In this last category the following information must be included: (a) the results of Flinn, Averbach and Cohen on X-ray studies of gold and nickel,<sup>12</sup> and (b) the measurements of Reynolds on diffusion in the alloys.<sup>11</sup>

The only two relaxations which have been reported up to now for substitutional alloys are the grain-boundary relaxation and those arising from changes in local order—the ordering peak. Always the grain-boundary relaxation has been observed to be located in temperature slightly above the latter peak indicating that its activation energy is slightly higher than that for the latter. Furthermore, the evidence in  $\alpha$ -brass strongly indicates that the activation energy for the ordering peak is closely the same as that for interdiffusion in the alloy (or to the diffusion of Zn as corrected from the data on chemical diffusion).<sup>13</sup>

The first impulse we had on observing the appearance of the two peaks (as in Fig. 2) was to assume that the peaks at 400°C and 250°C (for the 30 per cent alloy) were indeed the grain-boundary relaxation and the ordering relaxation, respectively. However, following through with this assumption leads to inconsistencies with the X-ray data<sup>12</sup> and the diffusion data<sup>11</sup> which cannot be resolved. Furthermore, testing this hypothesis by observing which peak disappears for a single crystal was not possible because we were unable to make a single crystal. By long heat treatment, however, we did produce rather large grain samples by grain growth, and by reheating a sample of mixed phase material just over the phase boundary we obtained samples of fine grain. Since neither peak was much different for the two kinds of samples we conclude that neither of these peaks is the grain-boundary peak. We now suppose that the grain-boundary peak must lie at temperatures even higher than 400°C. It is reasonable to believe that it is not seen when one goes to higher temperatures (as in Fig. 2) because the formation of the mixture phases in the grain boundaries at high temperatures hardens them so as to prevent their moving under stress.

## (2) The High Temperature Peak

It is now possible to suppose that the peak at 400°C is the ordering peak. With this supposition, it can be shown that the data obtained for this alloy are consistent with the results of other experiments on these alloys. This will be done in the following paragraphs.

The activation energy for this relaxation is seen from Table II to correspond fairly well to that for diffusion in the alloys. The four alloys of lowest Ni content fit fairly well the activation energies either for Au in the alloy or for interdiffusion, but whether the data are accurate enough so that a positive distinction between the two can be made is not certain. At any rate, calling this relaxation the ordering peak is consistent with present thought of its relationship to diffusion as proposed by Le Claire<sup>13</sup> and Nowick.<sup>2</sup>

The X-ray data of Flinn, Averbach and Cohen showed that the separation of the quenched solid solution into the Au- and Ni-rich phases was a heterogeneous reaction. The untransformed part of the material retained its quenched structure of short-range order.<sup>12,14</sup> Since the magnitude of the damping peak ought to be about linear with the volume of untransformed material, the peak ought then to disappear at the same rate as

the volume of mixed phases material increases. This is seen from Fig. 9 to be the case since the damping peak and the resistivity (which is qualitatively a volume property) decrease together.

## (3) The Low-Temperature Peak

The source of the low-temperature peak cannot be described in terms of any relaxation so far known to exist in such substitutional alloys. The fact that it anneals out rather rapidly even as low as 300°C indicates that it has little to do with the reaction in which the mixed phase structure is formed. In the one hour required for its disappearance (as is shown in Fig. 6) the resistivity and X-ray measurements show no measurable change.<sup>14</sup> Changes which occur when the temperature is varied are not so large as have been observed for other alloys,<sup>9</sup> but they are not to be neglected in any interpretation of the effect.

There are several possible sources from which the damping effects noted here might arise, but since no conclusive statements about them can be made, it seems that no useful purpose will be served by discussing them at this time. The one thing which is amply clear from the data presented is that the damping per individual event must be large, since the presence or absence of the state which gives rise to the damping effect does not effect the X-ray or resistance measurements to a marked extent.

## ACKNOWLEDGMENT

This work was sponsored in part by the Office of Ordnance Research, U. S. Army. It represents a portion of a thesis submitted by Choh-Yi Ang in partial fulfillment of the requirements for the degree Ph.D. in Metallurgical Engineering at the University of Illinois, February, 1954.

## REFERENCES

1. C. Zener, *Elasticity and Anelasticity of Metals*, University of Chicago Press, 1948.
2. A. Nowick, *Phys. Rev.* **88**, 925 (1952).
3. C. Wert, *Modern Research Techniques in Physical Metallurgy*, ASM (1953) 225.
4. C. Zener, *Physical Review*, **71**, 34 (1947).
5. A. Nowick, *Progress in Metal Physics*, Vol. 4, Interscience Publ. Inc. (1953), 1.
6. A. Le Claire and W. Lomer, *Acta Met.* **2**, 731 (1954).
7. W. Koster and W. Damohl, *Z. Metallk.* **28**, 248 (1936).
8. Choh-Yi Ang and C. Wert, *J. Appl. Phys.* **25**, 1061 (1954).
9. A. Nowick and R. Sladek, *Acta Met.* **1**, 113 (1953).
10. C. Wert and J. Marx, *Acta Met.* **1**, 131 (1953).
11. J. B. Reynolds, Thesis, M.I.T., 1953.
12. P. Flinn, B. Averbach and M. Cohen, *Acta Met.* **1**, 664 (1953).
13. A. D. Le Claire, *Phil. Mag.* **42**, 673 (1951).
14. Private information.

## THE DIFFUSIVITY OF HYDROGEN IN NICKEL\*

M. L. HILL and E. W. JOHNSON†

The diffusivity of hydrogen in nickel was determined at 380°C to 1000°C from nonsteady rates of hydrogen evolution from 0.3 to 0.5 in. dia. cylinders. The specimens were prepared by heating in H<sub>2</sub> at various temperatures above 600°C and pressures above 1 atm. Evolution rates into a vacuum were determined from (1) the rate of pressure increase in a known collecting volume, and (2) the pressure drop across a constriction in the gas transfer line. The measured diffusivity  $D$  varies only with temperature, indicating (1) that the evolution rate is diffusion-controlled, and (2) that the diffusivity is independent of both solute concentration and method of specimen preparation. The results are well represented by  $D = 0.00447 \text{ cm}^2 \text{ sec}^{-1} \exp(-8600 \text{ cal}/RT)$ .

A combination of the present  $D_0$  value with the theoretical expression of Wert and Zener for lattice diffusion yields a negative entropy of activation  $\Delta S$ . This is explained by the hypothesis that the diffusing hydrogen particles do not perceptibly distort the metal lattice, and that  $\Delta S$  is determined mainly by the change of vibrational frequency of the diffusing particles as they jump between adjacent sites. The value of  $\Delta S$  calculated from available charge density data is negative and agrees sufficiently well with the experimental  $\Delta S$  value to confirm strongly the hypothesis of interstitial lattice diffusion.

### LA DIFFUSIBILITÉ DE L'HYDROGÈNE DANS LE NICKEL

La diffusibilité de l'hydrogène dans le nickel est déterminée entre 380 et 1000°C, à l'aide des vitesses de dégagement de l'hydrogène à partir de cylindres de 0,3 à 0,5 in.  $\phi$ . Les éprouvettes ont été préparées par chauffage dans l'hydrogène, à diverses températures supérieures à 600° et sous des pressions supérieures à une atm. Les vitesses de dégagement dans le vide ont été déterminées 1° à partir des vitesses d'augmentation de pression dans un volume collecteur connu et 2° par la chute de pression à travers un diaphragme dans la conduite de gaz. La diffusibilité mesurée  $D$  varie seulement avec la température, ce qui montre que 1° la vitesse de dégagement est régie par la diffusion et que 2° la diffusibilité est indépendante de la concentration et de la méthode de préparation des éprouvettes. Les résultats sont bien représentés par  $D = 0.00447 \text{ cm}^2 \text{ sec}^{-1} \exp(8600 \text{ cal}/RT)$ .

Une comparaison de cette valeur  $D_0$  avec l'expression théorique de Wert et Zener de la diffusion réticulaire conduit à une entropie d'activation  $\Delta S$  négative. Ceci s'explique en admettant que les particules d'hydrogène diffusantes ne perturbent pas sensiblement le réseau et que  $\Delta S$  est déterminé surtout par le changement de la fréquence des vibrations des particules diffusantes lors des sauts. La valeur de  $\Delta S$  calculée à partir des densités de charge connues est négative et s'accorde suffisamment bien avec la valeur expérimentale pour confirmer l'hypothèse de la diffusion en insertion.

### DIE DIFFUSIONSFÄHIGKEIT VON WASSERSTOFF IN NICKEL

Die Diffusionsfähigkeit von Wasserstoff in Nickel wurde für einen Temperaturbereich von 380 bis 1000°C aufgrund der wechselnden Beträge von Wasserstoff, der aus Zylindern von 0.3 bis 0.5 in. Durchmesser entwickelt wurde, bestimmt. Die Proben wurden durch eine Erhitzung in Wasserstoff bei verschiedenen Temperaturen über 600°C und Drücken über 1 atm vorbereitet. Das Mass der Gasentwicklung im Vakuum wurde aus folgenden Daten bestimmt: (1) aus dem Mass der Druckzunahme in einem bekannten Sammelvolumen und (2) aus dem Druckabfall in einer Verengung der Gasleitung. Die gemessene Diffusionsfähigkeit  $D$  verändert sich nur in Abhängigkeit von der Temperatur und zeigt somit (1) dass das Mass der Gasentwicklung durch die Diffusion kontrolliert wird und (2) dass die Diffusionsfähigkeit sowohl von der Lösungskonzentration als auch von der Methode der Probenherstellung unabhängig ist. Die Ergebnisse werden durch die Beziehung  $D = 0.00447 \text{ cm}^2 \text{ sec}^{-1} \exp(-8600 \text{ cal}/RT)$  gut dargestellt.

Eine Kombination des vorliegenden  $D_0$  Wertes mit den theoretischen Ausdrücken von Wert und Zener für die Gitterdiffusion ergibt eine negative Aktivierungsentropie. Dies wird dadurch erklärt, dass die diffundierenden Wasserstoffteilchen das Metallgitter nicht merklich verzerren und dass  $\Delta S$  in der Hauptsache durch den Wechsel der Vibrationsfrequenz der diffundierenden Teilchen, der durch das Hin- und Herspringen der Teilchen zwischen benachbarten Gitterplätzen hervorgerufen wird, bestimmt wird. Der Wert von  $\Delta S$ , der aus Werten der Ladungsdichten berechnet wurde, ist negativ und stimmt recht gut mit dem experimentellen Wert von  $\Delta S$  überein. Damit ist auch eine starke Unterstützung für die Hypothese der Diffusion auf Zwischengitterplätzen gegeben.

The diffusion of hydrogen in metals is well known to be considerably faster than that of other alloy elements. The bulk diffusivity is therefore more accurately measurable down to low temperatures, where it is sometimes found to behave anomalously. One anomaly in iron-hydrogen alloys has been discussed.<sup>1</sup> The anomalies are

apparently largely responsible for the frequent conclusion that the hydrogen is situated elsewhere than in the lattice interstices.<sup>2,3,4</sup>

Hydrogen in nickel was chosen for the present study because of its apparent freedom from anomalous behavior. The diffusivity is, as will be shown, consistent with the hypothesis of interstitial lattice accommodation of the alloyed hydrogen.

Previous determinations of hydrogen diffusion rates

\* Received November 4, 1954; in revised form April 28, 1955.

† Westinghouse Research Laboratories, East Pittsburgh, Pennsylvania.

have utilized both steady and nonsteady rate measurement methods. The steady-state methods have usually been permeation measurements, in which the hydrogen is introduced at one side of a metal membrane and is withdrawn and measured at the opposite side. The permeation flux is then proportional to the difference between the square roots of the respective hydrogen pressures and also to the reciprocal of the membrane thickness, indicating (1) that hydrogen diffuses as single atoms or ions, and (2) that the permeation rate is controlled by volume diffusion. The proportionality constant  $P$ , termed the permeability, is related to the diffusivity  $D$  by

$$P = KD \quad (1)$$

in which  $K$  is the solubility constant as defined by Sieverts' law:

$$C = Kp^{1/2} \quad (2)$$

Here,  $C$  is the hydrogen solubility in equilibrium with hydrogen gas at the partial pressure  $p$ . The evaluation of  $D$  from steady-state permeation data thus requires an auxiliary knowledge of  $K$ .

An evaluation of  $D$  independent of  $K$  is obtained from nonsteady rate measurements. The Fick's law equation solution for gas evolution from finite cylinders into a vacuum, following a brief initial diffusion period  $t_0$ , has been given<sup>1</sup> as

$$\log\left(\frac{\bar{C}}{C_0}\right) = -0.25 - Dt\left(\frac{4.29}{a^2} + \frac{10.05}{b^2}\right) \quad (\text{for } t > t_0), \quad (3)$$

in which  $\bar{C}$  is the average solute concentration at time  $t$ ,  $C_0$  is the initial concentration, specified as uniform throughout the specimen at  $t=0$ ,  $a$  is the specimen length, and  $b$  the diameter. The logarithm of the evolution rate is then given by

$$\log\left(-\frac{d\bar{C}}{dt}\right) = \text{const.} - Dt\left(\frac{4.29}{a^2} + \frac{10.05}{b^2}\right) \quad (\text{for } t > t_0). \quad (4)$$

Hence the diffusivity can be determined from the slope of a plot of either  $\log\bar{C}$  or  $\log(-d\bar{C}/dt)$  vs  $t$ . In this connection it is convenient to define a "diffusing time"  $\tau$  such that

$$D\tau\left(\frac{4.29}{a^2} + \frac{10.05}{b^2}\right) = 1. \quad (5)$$

Hence

$$\frac{d \log \bar{C}}{dt} = \frac{d \log(-\partial \bar{C} / \partial t)}{dt} = -\tau^{-1}. \quad (6)$$

It is readily seen that  $\tau$  is just the time interval  $(t_2 - t_1)$  for  $\bar{C}$  to fall to 1/10 its value at any time  $t_1$  following  $t_0$ . The diffusivity is then calculable from the specimen dimensions and observed values of  $\tau$  with the aid of Eq. (5).

## EXPERIMENTAL

The nickel employed in the present investigation was commercially pure metal of the chemical analysis:

% Ni	% C	% Fe	% Mn	% Cu
99.55	0.08	0.036	0.235	0.01

One-half inch diameter hot-rolled and annealed bars were machined into cylindrical specimens of the dimensions given in Table I.

Initial charging of the specimens with hydrogen was by heating in hydrogen gas under either of two sets of conditions. Specimens of Group A were "thermally" charged with up to 16.7 ml./100 g hydrogen by saturating for 15 hours at 1 atm. and 1150 to 1400°C. Specimens of Group B were annealed at 1000°C for two hours and then "pressure" charged with up to 48 ml/100 g by saturating for 18 hours at 600°C under pressures of up to 67 atm. The pressure charging apparatus was similar to that of Hobson and Sykes.<sup>5</sup> Hydrogen losses from the specimens during cooling and storage were minimized by water quenching from the charging temperature and storing in liquid nitrogen.

Hydrogen evolution rates were determined in the modified analytical apparatus sketched in Fig. 1. Each specimen was mechanically sanded, washed in acetone, and admitted to the evacuated apparatus through the mercury lift. It was then moved by means of a magnet into the heated fused silica furnace tube. Temperature calibration of the latter was by means of a calibrated chromel-alumel thermocouple having its hot junction imbedded in a dummy specimen in the evacuated furnace tube.

The gas evolved from the specimen was drawn through the 0.2 mm dia. pyrex orifice or constriction C and through cold trap No. 1. It was then compressed by the collecting pumps (diffusion pump No. 1 and the Toepler pump) into the calibrated room temperature collecting volume bounded by the Toepler pump and mercury cutoffs Nos. 4, 7, and 8, and optionally No. 6. The constriction could also be by-passed, if desired, by opening cutoff No. 2.

The constriction and thermocouple vacuum gauges served as a gas flowmeter. The pressure reading of ther-

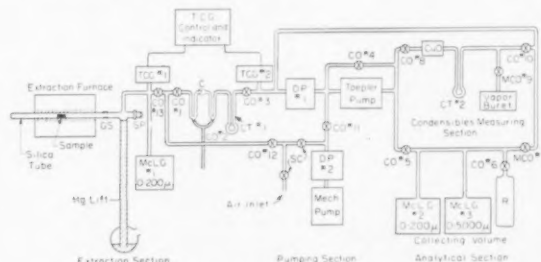


FIG. 1. Apparatus.—CO: mercury cut-off; MCO: manometer cutoff; CT: cold trap; GS: graded seal (silica pyrex); C: constriction; DP: diffusion pump; McL. G: McLeod gauge; SC: stopcock; SP: sample port (standard taper stopper); TCG: thermocouple gauge; R: reservoir (calibrated volume).



mocouple gauge No. 2 was always negligible compared with that of No. 1, permitting a determination of the flow rate from the reading of gauge No. 1 alone. The envelope of the latter was continuously immersed in ice water, and the output potential of the gauge was automatically recorded. Static calibration of the gauge was with tank hydrogen, using McLeod gauge No. 1. The flow rate through the constriction was such that the pressure of tank hydrogen originally placed in the furnace tube decreased exponentially with time, indicating molecular flow. The time  $\tau'$  for the pressure to fall to 1/10 its original value was 9.0 minutes.

At the end of each extraction the gas was analyzed by copper oxide oxidation and fractional freezing, combined with a separate moisture determination from the pressure rise in cold trap No. 1 on heating. Approximately 99 per cent of the evolved gas was hydrogen, the remainder being CO, CO<sub>2</sub>, and N<sub>2</sub>.

During each extraction it was possible to measure the pressure  $p$  in the collecting volume, as well as the pressure  $p'$  registered by thermocouple gauge No. 1 and McLeod gauge No. 1. The diffusing time was then determined as follows: The net rate of pressure change in the furnace tube,  $dp'/dt$ , is proportional to the difference between the respective rates of gas evolution from the specimen and gas flow through the constriction. The former rate is given by Eq. (4) and the latter is proportional to  $p'$ . Hence

$$dp'/dt = (\text{const.})e^{-2.3t/\tau} - 2.3p'/\tau' \quad (7)$$

The solution of Eq. (7) for the condition  $p'=0$  when  $t=0$  is

$$p' = \text{const.}(e^{-2.3t/\tau} - e^{-2.3t/\tau'}) \quad (8)$$

With the usual rapid transfer of gas through the collecting pumps, the rate of pressure rise in the collecting volume,  $dp/dt$ , is proportional to the flow rate through the constriction and therefore to  $p'$ . Hence, from Eq. (8)

$$dp/dt = \text{const.}(e^{-2.3t/\tau} - e^{-2.3t/\tau'}) \quad (9)$$

A considerable simplification is now obtained from the fact that when  $\tau$  is several times  $\tau'$ , the quantity

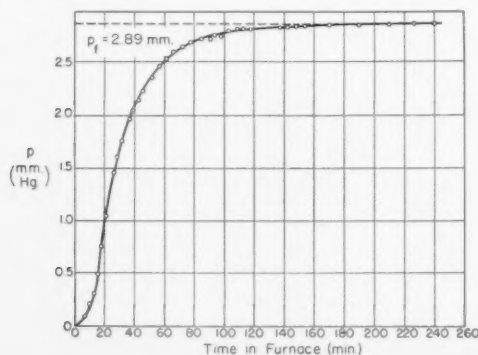


FIG. 2. Accumulation curve: Pressure of gas (99.6% H<sub>2</sub>) collected from 0.50 in. dia. X 0.63 in. nickel cylinder at 621°C.

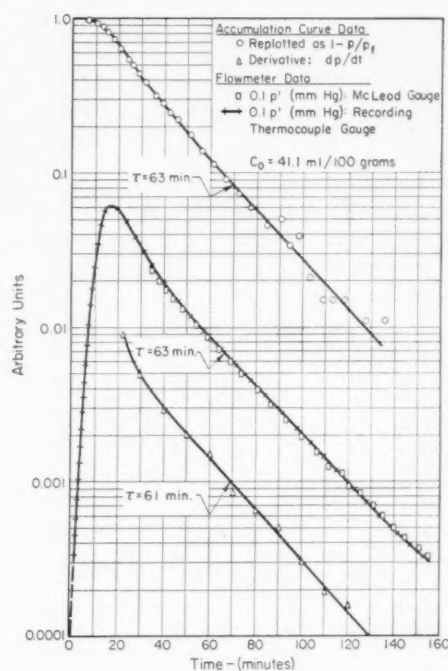


FIG. 3. Evolution of gas (99.5% H<sub>2</sub>) from 0.50 in. dia. X 0.633 inch cylinder at 621°C.

$(e^{-2.3t/\tau} - e^{-2.3t/\tau'})$  increases from zero to a maximum at relatively low values of  $t$ , following which it closely approximates  $e^{-2.3t/\tau}$ . The fractional error of this approximation is less than 5 per cent when  $t$  is greater than  $\tau$  and when  $\tau$  is 2.3 or more times  $\tau'$ . Under these conditions either  $p'$  or  $dp/dt$  can be satisfactorily approximated as  $(\text{const.})e^{-2.3t/\tau}$ . Hence a line of slope  $-\tau^{-1}$  should result from a plot of either  $\log p'$  or  $\log (dp/dt)$  vs  $t$ . The time dependence of  $p'$  is thus the same as that of  $-dC/dt$  (Eq. 4), and the gas flow rate through the constriction can be conveniently used as a direct measure of the evolution rate.

The solution of Eq. (9) for the conditions  $p=0$  when  $t=0$ ;  $p=p_f$  when  $t=\infty$  is

$$1 - \frac{p}{p_f} = \frac{\tau}{\tau - \tau'} \left( e^{-2.3t/\tau} - \frac{\tau'}{\tau} e^{-2.3t/\tau'} \right). \quad (10)$$

The maximum value of  $1 - p/p_f$  occurs at  $t=0$ , following which a plot of  $\log(1 - p/p_f)$  rapidly becomes linear with the slope  $-\tau^{-1}$ . Hence the variation of  $1 - p/p_f$  with time is the same as that of  $C$  (Eq. 3), and, to a first approximation,  $p$  can be taken as a direct measure of the amount of hydrogen extracted from the specimen.

The conformance of the experimental data to the above relationships is shown in Figs. 2 and 3, which were obtained in a typical run at 621°C. Figure 2 is a  $p$  vs  $t$  "accumulation" curve, showing the determination of  $p_f$ . The resulting values of  $\log(1 - p/p_f)$  are plotted versus  $t$  as the circles in Fig. 3. These are seen to define a

TABLE I. Conditions and results of evolution rate measurements

Group A								
Diameter (in.)	Length (in.)	Charging temp.* (°C)	C <sub>0</sub> (ml/100 g)	Evolution temp. (°C)	$\tau$ (min)	$D \times 10^6$ (cm <sup>2</sup> /sec)	Av.	Deviation %
0.50	1.11	1351	15.7	380	404	6.2	6.35	$\pm 2.5$
0.50	0.57	1400	16.7	380	310	6.5		
0.50	1.11	1282	14.5	477	186	13	13	0
0.31	0.78	1180	12.4	477	78	13		
0.50	0.53	1400	16.4	528	117	17		
0.31	0.38	1400	16.2	575	29	28		
0.50	1.11	1351	15.6	621	70	35		
0.31	0.78	1180	12.3	669	24	41	42	$\pm 2.3$
0.50	0.68	1400	—	669	50	43		
0.50	1.11	1282	14.5	814	32.5	79		
0.50	1.11	1282	14.5	930	20	120		
Group B								
		Charging Press.** (atm.)						
0.50	0.65	67.1	—	380	348	6.1		
0.50	0.62	67.1	46.2	528	124	17		
0.50	0.43	67.3	47.8	575	70	25		
0.50	0.63	67.1	41.1	621	63	34		
0.50	0.64	67.3	43.2	669	51	42	42	0
0.50	0.43	67.3	47.8	669	41	42		
0.50	0.64	28.1	32.0	718	38	56	54.5	$\pm 2.7$
0.50	0.42	28.1	32.4	718	32.5	53		
0.50	0.64	67.3	42.0	765	31	69	68	$\pm 1.5$
0.50	0.42	67.3	44.2	765	25.5	67		
0.50	0.64	67.3	44.6	850	22.5	95		
0.50 <sup>a</sup>	0.63	28.1	33.0	986	14	150		

\* All Group A specimens were charged at 1 atm. H<sub>2</sub> pressure.

\*\* All Group B specimens were charged at 600°C.

<sup>a</sup> Run made without 0.2 mm constriction in flow line.

straight line at the larger values of  $t$  in accordance with Eq. (10).

Values of  $dp/dt$  were determined graphically from the slope of the "accumulation" curve in Fig. 2, and are plotted as the triangles in Fig. 3. The resulting value of  $\tau$  agrees reasonably well with that from the  $\log(1 - p/p_f)$  curve, but is probably not as accurate due to the difficulty of precisely determining  $dp/dt$ .

A semilogarithmic plot of  $p'$  vs  $t$  is shown as the middle curve of Fig. 3. Here the squares represent the readings of McLeod gauge No. 1, and the solid curve corresponds to the continuously recorded output of thermocouple gauge No. 1. The resulting value of  $\tau$  agrees well with that from the  $\log(1 - p/p_f)$  plot.

Of the various above methods of evaluating  $\tau$ , that based on the continuous measurement of  $p'$  was preferable because (1) the results were obtained directly from a plot of the data themselves rather than from small differences between large quantities, and (2) the continuous recording of the thermocouple gauge output avoided the need for repeated manual operation of a McLeod gauge. The superior precision of the method is indicated by the small scatter of the  $p'$  readings at large values of  $t$ .

The only run in which the flow rate was too large to permit using the constriction was at 986°C. Here a satisfactory value of  $\tau$  (14 min) was obtained from  $p'$  readings with cutoff No. 2 open.

## RESULTS

The experimental curves from all runs were similar to those in Figs. 2 and 3, indicating (1) that hydrogen in nickel conforms to the conventional diffusion laws, and (2) there is no perceptible variation of the diffusivity with concentration.

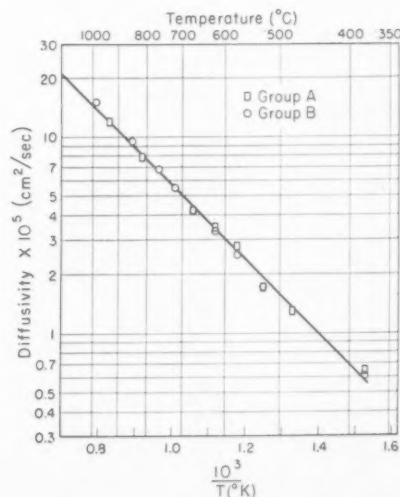


FIG. 4. Diffusivity of hydrogen in nickel.

The conditions and results of all runs are given in Table I. Average values of  $D$  and mean deviations are listed for those cases in which two runs within either Group A or Group B were conducted at the same temperature. The highest such mean deviation,  $\pm 2.7$  per cent, is considered to approximate the experimental precision.

The results are plotted as  $\log D$  vs  $1/T$  in Fig. 4, in which the Group A and Group B data are represented by squares and circles, respectively. Only the average value of  $D$  is plotted for each pair of runs within a group conducted at the same temperature. The straight line indicates that  $D$  conforms to

$$D = D_0 \exp(-E_d/RT) \quad (8)$$

in which

$$D_0 = 4.47 \times 10^{-3} \text{ cm}^2/\text{sec}; \quad E_d = 8600 \text{ cal/mole.}$$

The maximum error is considered such that  $D_0$  may be as high as  $6.2 \times 10^{-3} \text{ cm}^2/\text{sec}$ , for which  $E_d$  is 9250 cal, or as low as  $3.8 \times 10^{-3} \text{ cm}^2/\text{sec}$ , for which  $E_d$  is 8270 cal.

The present method of determining  $D$  is based on the assumption that the evolution rate is entirely diffusion-controlled. This point was checked with experiments on specimens of different sizes and shapes, in accordance with a previous discussion.<sup>1</sup> The results (Table I and Fig. 4) indicate that the calculated diffusivity varies randomly with specimen dimensions, thus confirming the assumption of diffusion-controlled evolution. Additional confirmation is obtained from the reasonable agreement of the present results with those of Euringer (Table II), whose specimens had a diameter only 1/25 that of most of the specimens examined here.

The use of two different charging methods distinguishing Groups A and B was based on a previous finding in iron of a slight variation of the diffusivity with the conditions of prior hydrogen charging. The fact that all data from both Group A and Group B are represented by a single line in Fig. 4 indicates that the diffusivity of hydrogen in nickel is independent of the method of specimen preparation.

The possible existence in nickel of "residual" or slowly diffusing hydrogen of the kind previously found in iron<sup>1</sup> was checked by vacuum fusion analysis of two extracted specimens. No significant amount of hydrogen was found, indicating that all of the hydrogen had diffused at the single values of  $D$  reported herein.

## DISCUSSION

For comparing the present results with previous rate data, "literature" values of  $D$  were calculated from available permeabilities and solubilities with the aid of Eq. (1). The solubility data covering the broadest temperature range are those of Sieverts<sup>6</sup> and Lucke-meyer-Hasse and Schenk.<sup>7</sup> These data were averaged graphically to yield the empirical relationship:

$$K = 1.04 \times 10^{-5} T^{1.93} \quad (9)$$

(for  $K$  in  $\text{atm}^{-1} \text{ml}/100\text{g}$ ,  $T$  in  $^\circ\text{K}$ ). A combination of the resulting values of  $K$  with published values of  $P$  yielded reasonably linear plots of  $\log D$  vs  $1/T$ , but the corresponding values of  $E_d$ , and particularly  $D_0$ , varied considerably from one set of permeability data to the next. These constants are listed in Table II.

The only case found in the literature in which  $D$  was determined from nonsteady evolution rates is the work of Euringer<sup>13</sup>, whose specimens were 0.5 mm dia. wires. Lieser and Witte<sup>14</sup> have more recently measured nonsteady absorption by 6 mm dia. nickel spheres, but their results differ substantially from the previous data. The present results should be more accurate than any of the previous data in view of their covering a broader temperature range.

The question as to whether or not the hydrogen diffuses interstitially should be resolvable from a comparison of  $D_0$  with the results of theoretical calculations for a simple lattice model. Such a model has been treated by Wert and Zener.<sup>15</sup> Substitution of the present values of  $E_d$  and  $D_0$  into their equations (8) and (5) yielded  $-3$  e.u. as the molar entropy of activation  $\Delta S$ . A modified computational method<sup>16</sup> yielded  $-1.6$  e.u. Both calculations are based on the assumption that hydrogen occupies octahedral interstices in the nickel lattice.

The negative entropy of activation can be reconciled with the interstitial diffusion hypothesis if  $\Delta S$  is assumed to be the sum of a lattice contribution,  $\Delta S_l$ , and a vibrational contribution,  $\Delta S_v$ . The former is always positive, as pointed out by Zener,<sup>17</sup> because of the lattice distortion accompanying movement of the solute particle through the potential energy saddle point between adjacent sites. With hydrogen diffusion this distortion may well be negligible, particularly if the

TABLE II. Literature values of  $D_0$  and  $E_d$  for hydrogen in nickel

Investigator	Ref.	Primary data	Temp. range ( $^\circ\text{C}$ )	$D_0$ ( $\text{cm}^2/\text{sec}$ )	$E_d$ (kcal)
Ham	(8)	Permeability	376-600	0.015	10.6
Smithells and Ransley	(9)	Permeability	248-400	0.023	10.8
Borelius and Lindblom	(10)	Permeability	200-550	0.017	10.8
Hendricks and Ralston	(11)	Permeability	478-798	0.0011	8.4
Lombard	(12)	Permeability	458-598	0.20	14.8
Euringer	(13)	Evolution Rate	85-165	0.0037	9.0
Lieser and Witte	(14)	Absorption Rate	400-600	0.001	5.5
Present research		Evolution Rate	380-986	0.0045	8.6

diffusing particles are positive ions, or protons. The major component of  $\Delta S$  is then  $\Delta S_v$ .

The vibrational entropy contribution  $\Delta S_v$  originates from the change of vibrational frequency of the solute particle as it moves along a given jump path. From the statistical mechanical expression for the entropy of a harmonic oscillator,<sup>18</sup>  $\Delta S_v$  is readily approximated as:

$$\Delta S_v = R \ln(\nu/\nu')^n, \quad (10)$$

in which  $\nu$  is the frequency at the interstitial site,  $\nu'$  is the frequency at the potential energy saddle point, and  $n$  is the number of vibrational modes affected by the frequency change. It is here assumed that the diffusing particle retains its vibrational freedom in both the  $y$ - and  $z$ -directions as it jumps in the  $x$ -direction. Hence  $n$  is 2.

An estimate of  $\Delta S_v$  is obtainable from the assumption that the hydrogen exists and diffuses as protons. Its potential energy,  $V$ , is then the ionic charge multiplied by the electrostatic potential. The respective frequencies  $\nu$  and  $\nu'$  are proportional to the second derivatives of  $V$  at the two locations considered.<sup>19</sup> The sum of these second derivatives at each location, or the Laplacian of  $V$ , is proportional to the electron charge density in accordance with Poisson's equation.<sup>20</sup> As the diffusing particle moves from the potential energy minimum to the saddle point, the sign of the second derivative of its potential energy in the jump direction,  $\partial^2 V/\partial x^2$ , is reversed, and the charge density increases. These two effects combine to yield a value of  $\nu'$  substantially greater than that of  $\nu$ , and hence a negative value of  $\Delta S_v$ .

A preliminary calculation, based on available charge density data for  $\text{Cu}^+$ ,<sup>21</sup> yielded approximately 1.65 as the ratio  $\nu'/\nu$ , from which  $\Delta S_v$  is seen to be  $-2.0$  e.u. The agreement of this approximate theoretical result with the experimental  $\Delta S$  value,  $-1.6$  e.u., seems reasonable. Hence the observed value of  $D_0$  is entirely consistent with the hypothesis that hydrogen in nickel is accommodated in the lattice interstices.

### CONCLUSIONS

From the above data and calculations the following conclusions are considered warranted:

(1) The evolution of hydrogen from nickel is a diffusion-controlled process obeying conventional diffusion kinetics in the temperature range  $380^\circ$  to  $1000^\circ\text{C}$ . There is no perceptible variation of the diffusion coefficient  $D$  with concentration in the range  $0$ – $50$  ml/100 g, nor is there any evidence that the diffusivity varies with thermal history in the manner previously found in iron.

(2) The diffusivity as a function of temperature is represented by Eq. (8) in which  $D_0 = 4.47 \times 10^{-3}$   $\text{cm}^2/\text{sec}$  and  $E_d = 8600$  cal/mole. The value of  $D_0$  is in good accord with the hypothesis that the hydrogen is situated predominantly within and diffuses among the octahedral interstices of the nickel lattice.

(3) The experimentally determined entropy of activation is negative, suggesting that the diffusion is accompanied by little, if any, lattice distortion.

### ACKNOWLEDGMENT

The writers are grateful to Dr. C. Zener for many helpful and informative discussions that aided greatly in the preparation of this paper.

### REFERENCES

1. E. W. Johnson and M. L. Hill, *Acta Met.* **3**, 99 (1955).
2. D. P. Smith, *Hydrogen in Metals*, University of Chicago Press, 1948.
3. J. H. Andrew and H. Lee, Symposium on Internal Stresses in Metals and Alloys, Inst. of Metals (London, 1948), p. 265.
4. C. A. Zapffe, *Materials and Methods* **32** (October, 1950), p. 58.
5. J. D. Hobson and C. J. Sykes, *J. Iron and Steel Inst.* **169**, 209 (1951).
6. A. Sieverts, Krumbhaar W. and E. Jurissh, *Z. physik. Chem.* **77**, 591 (1911).
7. L. Luckemeyer-Hasse and H. Schenck, *Arch. Eisenhüttenwesen* **6**, 209 (1932).
8. W. R. Ham, *J. Chem. Phys.* **1**, 476 (1932).
9. C. J. Smithells and Ransley, C. E., *Proc. Roy. Soc. (London)* **A157**, 292 (1936).
10. G. Borelius and J. Lindblom, *Ann. d. Physik.* (4) **82**, 201 (1927).
11. C. B. Hendricks and R. R. Ralston, *J. Amer. Chem. Soc.* **51**, 3278 (1929).
12. V. Lombard, *Compt. Rend.* **177**, 116 (1923).
13. G. Euringer, *Z. Physik* **96**, 37 (1935).
14. K. H. Lieser and H. Witte, *Z. für phys. Chem.* **202**, 21 (1954).
15. C. Wert and C. Zener, *Phys. Rev.* **76**, 1169 (1949).
16. E. W. Johnson and M. L. Hill, "Theory of Hydrogen Solution and Diffusion in Metals." Paper given at 127th Meeting of the American Chemical Society, Cincinnati, April 1955. To be published.
17. C. Zener, *Symposium on Imperfections in Nearly Perfect Crystals*, National Research Council (J. Wiley and Sons, New York, 1952), p. 289.
18. W. P. Allis and M. A. Herlin, *Thermodynamics and Statistical Mechanics* (McGraw-Hill, New York, 1952), p. 211.
19. S. Glasstone, *Theoretical Chemistry* (Van Nostrand, New York, 1944), p. 29.
20. J. C. Slater and N. H. Frank, *Introduction to Theoretical Physics* (McGraw-Hill, New York, 1933), p. 212.
21. D. R. Hartree and W. Hartree, *Proc. Roy. Soc. (Lond.)* **A157**, 490 (1936).



# A SURFACE STRUCTURE OBSERVED ON ELECTROLYTICALLY POLISHED ZINC\*

K. F. HULME†

A structure which can be produced on the surfaces of zinc specimens polished electrolytically in 20 per cent aqueous chromium trioxide solutions is described. Similar structures have been reported previously on electropolished metal surfaces. An account is given of various experiments performed to establish the significance of the structure. The results show that the structure is not a revelation of an internal substructure or "mosaic" of the metal but is closely associated with the electropolishing process. A possible explanation is given which has relevance to the theory of electropolishing and electrode processes.

## UNE STRUCTURE SUPERFICIELLE OBSERVÉE SUR LE ZINC POLI ÉLECTROLYTIQUEMENT

Il est décrit une structure observée à la surface d'échantillons de zinc polis électrolytiquement dans une solution aqueuse à 20% de trioxide chromique. Des structures analogues ont déjà été signalées sur des surfaces polies électrolytiquement et il est rendu compte des diverses expériences entreprises pour donner l'explication de cette structure. Les résultats montrent qu'elle ne correspond pas à une sous-structure du métal, ni à la structure mosaïque, mais qu'elle est étroitement liée au mécanisme du polissage électrolytique. Une explication possible est donnée liée à la théorie du polissage électrolytique.

## EIN OBERFLÄCHENGEFÜGE BEI ELEKTROLYTISCH POLIERTEM ZINK

Es wird ein Gefüge beschrieben, das auf der Oberfläche von Zinkproben durch Elektropolieren mit 20% igem wässrigen Chromtrioxyd erzeugt werden kann. Ähnliche Gefüge wurden schon früher an elektrolitisch polierten Metalloberflächen beobachtet. Es werden verschiedene Untersuchungen mitgeteilt, die zur näheren Kennzeichnung des Gefüges ausgeführt wurden. Die Ergebnisse zeigen, dass das Gefüge kein innermetallisches Subgefüge oder "Mosaik" ist, es steht vielmehr in engem Zusammenhang mit dem elektrolitischen Poliervorgang. Eine mögliche Erklärung, die auch für die Theorie des Elektropolierens und die anodische Auflösung von Bedeutung ist, wird gegeben.

### 1. INTRODUCTION

Whilst polishing single crystals of zinc electrolytically in 20 per cent aqueous solutions of chromium trioxide as part of another investigation it was noticed that quite frequently surfaces were obtained which appeared iridescent to the naked eye; to obtain the polish required it was necessary to repolish using a higher current density. High-power microscopical examination of a surface showing this iridescence revealed detail on the surface in the form of parallel lines with a remarkably constant spacing of approximately one micron. A photograph of such a surface, which after polishing had been immersed for a short time in dilute hydrochloric acid, is shown in Fig. 1; the etchant has produced hexagonal pits and the floor of these may be taken as parallel to the basal plane (0001) or nearly so. We infer that the lines run across the surface in a crystallographically determined direction (parallel to the trace of the basal plane on the surface). The iridescence of the surface is attributable to this regular surface detail causing the surface to act as a poor diffraction grating.

Surface structures similar in appearance but with a smaller spacing (400 Å to 1400 Å) have been reported on electrolytically polished surfaces of aluminium and its alloys by workers using electron microscope techniques.<sup>1-7</sup> Jouty<sup>7</sup> has also observed by optical microscopy a similar structure on a copper surface polished

in phosphoric acid solution. Bussy and Chaudron have suggested that the polishing process may be revealing a substructure of the metal in the form of inhomogeneous impurity distribution; on the other hand, Brown and Honeycombe<sup>2</sup> and Bucknell, Geach and Welsh<sup>3</sup> have favoured the interpretation that the structure is not a structure of the metal but a product of the electropolishing process. It was known that the polishing of zinc in 20 per cent CrO<sub>3</sub> solution could reveal as a surface profile inhomogeneous impurity distribution of another type often present in single crystals grown from the melt.<sup>22</sup> (Examples of this substructure

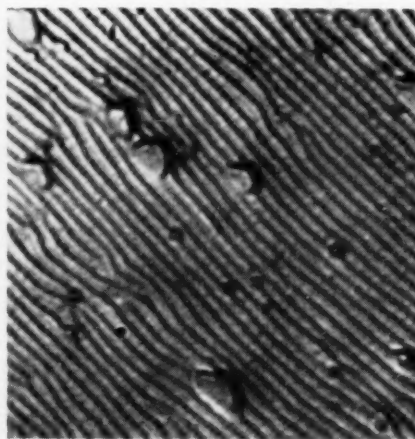


Fig. 1. Optical micrograph of zinc single crystal surface after electropolish and light etch. 3600X.

\* Received May 19, 1955.

† H. H. Wills Physical Laboratory, University of Bristol, Bristol, England. (Now at the Radar Research Establishment, St. Andrews Rd., Gt. Malvern, Worcs., England.)

have been recorded by Straumanis,<sup>8</sup> Buerger<sup>9</sup> and Smialowski.<sup>10</sup> An explanation of its origin has been given by Rutter and Chalmers.<sup>11</sup> The impurity is concentrated into the walls of hexagonal rods or into lamellae; the dimensions of the structure are approximately 0.05 mm.) An investigation of the structure on zinc polished in 20 per cent  $\text{CrO}_3$  was therefore undertaken to clarify its significance; there was the convenience in this case that the spacing of the structure was large enough for useful observation with the optical microscope. The experiments soon showed that the structure is not directly connected with any substructure of the crystal on which it appears but is closely associated with the electrode process during polishing.

## 2. EXPERIMENTAL STUDIES

### 2.1. The Appearance of the Structure on Various Samples of Zinc and Its Dependence on the Crystallographic Orientation of the Surface.

The structure has been observed after polishing on single crystals, on polycrystalline zinc obtained from an ingot (both of 99.99+ per cent purity) and on a zinc 3 per cent cadmium alloy cast in a graphite boat. To produce the structure current densities in the range 20 to 60 ma/cm<sup>2</sup> were found to be effective. The electrolyte was a 20 per cent aqueous solution of commercial chromium trioxide maintained at 8°–12°C by a glass cooling coil through which tap water was passed; the cathode was a cylindrical sheet of aluminium. The patterns observed were not commonly so perfect as that shown in Fig. 1. Figure 2, showing the structure on twin and matrix in a single crystal, illustrates the more usual form that the structure takes. On the basal plane (0001) of a single crystal, obtained by cleavage, the structure was in the form of either "rosettes" (Fig. 3) or a maze pattern (Fig. 4); it was found that the "rosettes" were shallow saucer-shaped depressions in the surface.

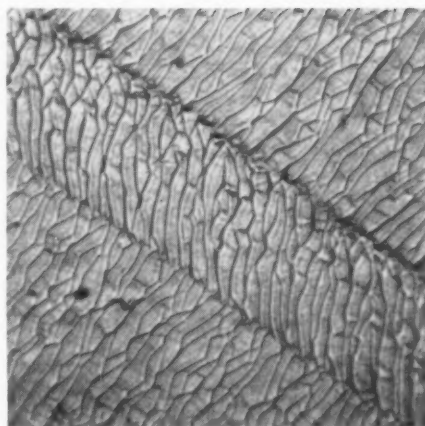


Fig. 2. The structure on twin and matrix in a single crystal. 650X.

A systematic study of the appearance on surfaces of different crystallographic orientation on the same specimen was made. For this experiment a single crystal rod of 8 mm diameter, the end of which had been made approximately hemispherical, was used. The structure was produced by the normal method on the end terminated by the hemisphere, and the rest of the crystal was etched in the standard crystallographic etching reagent for zinc.<sup>12</sup> The crystal was held in a small two-circle goniometer on the stage of an inverted microscope and its orientation was found with the aid of the reflections from the etched portion. By adjusting the goniometer scales, surfaces of known crystallographic orientation on the hemispherical end were presented to the microscope for examination. The results are summarized in Fig. 5.

The significance of the black lines which delineate the structure was investigated on a single crystal which had been prepared so that the spacing of the lines was large. (It was shown in an experiment described below that the spacing of the lines depended on the current density used during the preparation; by using a low



Fig. 3. "Rosette" obtained on electropolished cleavage plane 1150X.

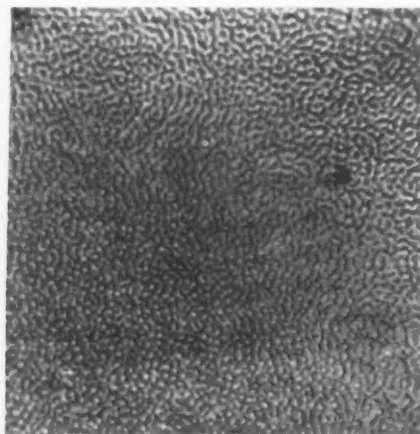


Fig. 4. Maze on electropolished cleavage plane. 1150X.

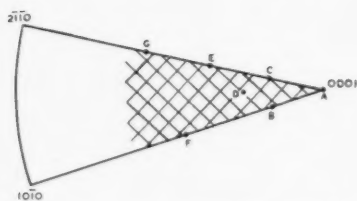


FIG. 5. For surfaces corresponding to the shaded area on the standard stereographic projection the structure on the hemisphere was in the form of lines with trend parallel to the trace of the basal plane on the surface. Otherwise there were areas of either (i) smooth polish—i.e., no visible detail, or (ii) rough attack with some indication of lines parallel to the trace of a plane ( $h k i 0$ ) on the surface. The values of the spacing of the pattern at the positions on the hemisphere corresponding to the points A, B, C, D, E, F, G were respectively 2.1, 2.0, 2.7, 2.9, 2.9, 2.7, 2.3  $\mu$ .

current density a large spacing was obtained on this specimen.) The light profile technique<sup>13</sup> was used to show that the lines were steps on the surface (see Fig. 6). Using the value of the profile sensitivity obtained by calibration on a steel ball of radius 0.5 mm it was deduced that the inclination of the approximately planar areas between the steps to the mean surface was  $\sim 3$  degrees; the inclination of the basal plane to the surface was known to be nearly 20 degrees. The tilt of the approximately planar areas was such that the normal to them would lie intermediate in direction between the normals to the mean surface and to the basal plane.

### 2.2. The Relationship between Spacing and Current Density

It was established that successive polishing treatments of the same single crystal specimen using the same current density did produce the structure with approximately the same spacing at a selected point on the specimen surface. In each treatment fresh electrolyte was used and care was taken that the temperature

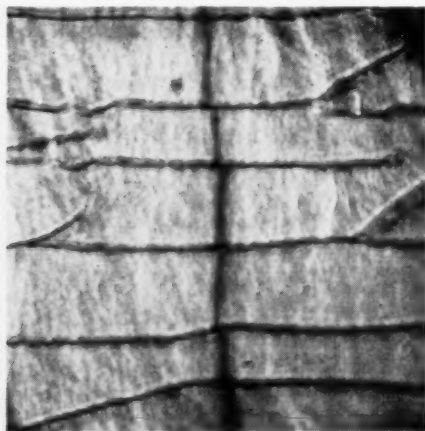


FIG. 6. Tolansky light profile superposed on structure of large spacing. The sidesteps of the black vertical profile line at the horizontal dark lines of the structure indicate that the latter are steps on the surface. 1700 $\times$ .

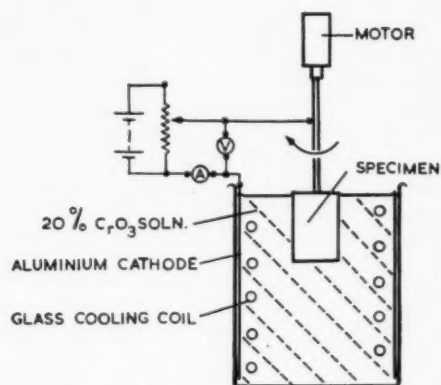


FIG. 7. Schematic diagram of electropolishing apparatus.

of the electrolyte at the start was the same to within  $\pm 0.2^\circ\text{C}$ . The specimen was rotated during the electrolysis. Rotation had been found to be helpful in producing a uniformly good polish and its use was continued in these experiments in the belief that it would help to produce a uniformly bad polish; the rate of rotation was kept constant at  $72 \pm 10$  rev/min. Each electrolysis was allowed to proceed for the same length of time; the length of time was chosen so that the mean depth of material removed was several times the spacing of the structure. Before each electrolysis the specimen was immersed for several seconds in aqua regia to remove all traces of its previous surface detail. A diagrammatic sketch of the apparatus used in this experiment and the one described below is given in Fig. 7. The spacings were measured using a microscope and eyepiece micrometer. The objective used was a 1.8 mm oil immersion type. The results of eight successive electro-

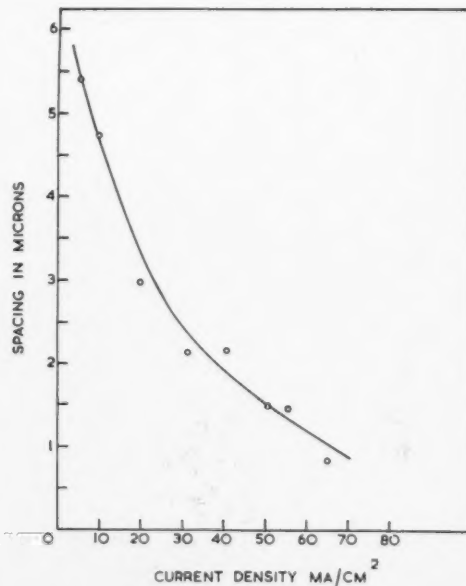


FIG. 8. Plot of spacing of structure against current density used during polishing.

lyses indicated that under these conditions the spacings obtained were constant to within  $\pm 10$  per cent.

Using the same method and observing the same precautions, the relationship between the current density and the observed spacing of the structure was determined. In this experiment, however, the duration of each electrolysis was chosen so that at the end of each electrolysis the same amount of charge had passed through the solution. The results are shown graphically in Fig. 8.

It will be seen that the measured spacings vary by a factor of six. The lower limit of spacing that can be measured accurately is determined by the resolving power of the microscope; the lowest point plotted on the graph is somewhat unreliable because the spacing is approaching the resolving limit of the microscope. At current densities much above those used for the lowest point in the graph the surface appears detailless, i.e., a good polish is obtained.

### 2.3. The Polarization of the Zinc Electrode in 20 Per Cent $\text{CrO}_3$ Solution

Because of the relevance to a possible explanation of the structure which is given below, the anodic polarization curve for zinc in 20 per cent aqueous chromic acid solution was measured for current densities in the range in which the structure is observed. The zinc electrode used was a polycrystalline cylinder of diameter 1.5 cm.

In order to make the conditions comparable in the two experiments the cylinder was rotated about its axis in this experiment at the same rotation rate as that used when the relationship between spacing and current density was investigated. A potentiometer was used to measure the difference of potential between the anode and a 0.1 N calomel electrode from which a Luggin probe was

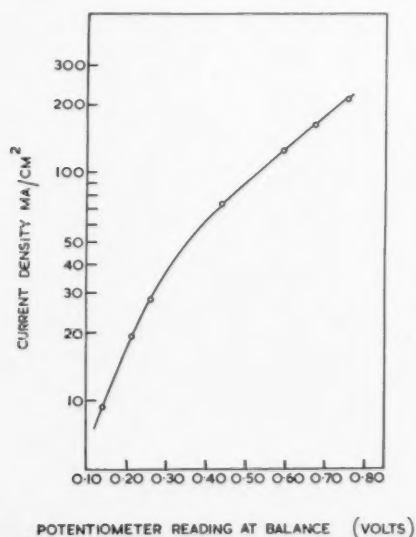


Fig. 9. Plot of anodic potential of zinc electrode in 20 per cent aqueous  $\text{CrO}_3$  solution against current density.

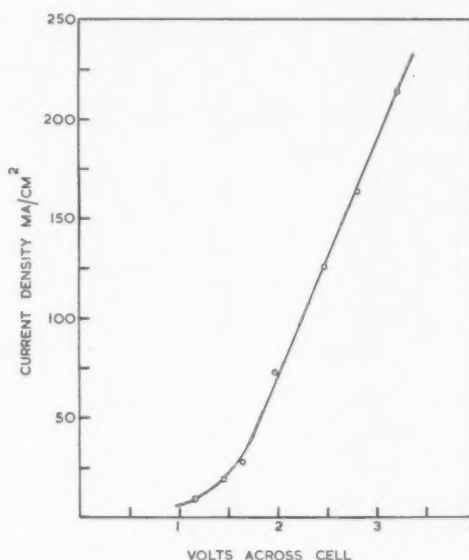


Fig. 10. Plot of current density over anode against total voltage across cell.

led; the tip of the probe was at a mean distance of about 0.25 mm from the rotating anode (the cylinder did not rotate perfectly axially). The results are shown in the graph of Fig. 9. Each point represents the mean of eight observations. Figure 10 is a graph of the total voltage across the cell against the current density at the anode.

The potentiometer reading at balance was markedly affected by the rate of rotation. At a current density of  $117 \text{ mA/cm}^2$  its values were 0.1–0.3, 0.56, 0.43, when the rates of rotation were 0, 72/min, 144/min. It was deduced that there was considerable concentration polarization present. An approximate value for the conductivity of the solution was obtained by traversing the tip of the Luggin probe across the electrolyte; by measuring the potentials obtained and from a knowledge of the geometry of the system and the current through the solution it was deduced that  $\sigma = 0.30 \text{ mho cm}^{-1}$ .

### 3. DISCUSSION

From the above experiments we conclude that the observed structure is certainly not a "substructure" of the zinc or a revelation of a Darwin mosaic structure.<sup>14</sup> If it were, the most obvious interpretation consistent with the observed directions of the structure would be a lamination parallel to the basal plane with constant spacing; but this is incompatible with the spacings observed at various orientations on the hemisphere. The fact that the spacing of the structure is a function of the current density used during electrolysis substantiates this conclusion.

The structure is best thought of as semicrystallographic etching with the scale determined by the electrode processes in some way. We are familiar with the fact that when a crystal is immersed in a suitable rea-



gent the attack can take place so as to reveal crystallographic planes in the crystal attacked. Some etching reagents, however, do produce curved pits, the faces of which are only approximations to crystallographic planes. When etch-pits with planar faces are produced, we may infer that there are very marked differences in the reactivity of surfaces with different crystallographic orientations, whereas rounded pits indicate much smaller differences of reactivity.

It would appear that the surface produced when zinc is anodically attacked in 20 per cent  $\text{CrO}_3$  solution contains in many cases areas which approximate to the basal plane (0001) of the crystal.

A possible explanation of what determines the observed spacings of the structure will now be given. Agar and Hoar<sup>15</sup> have shown that the current density distribution over electrodes of various shapes is determined by the ratio of a characteristic dimension of the electrode, " $a$ ", to " $k$ ", the product of the electrical conductivity of the solution  $\sigma$  and the slope of the electrode polarization curve  $dE/dJ$  ( $E$ =polarization voltage at current density  $J$ ). Wagner<sup>16</sup> has recently calculated current density distributions for some simple geometrical cases. When the electrode has a triangular profile the characteristic length " $a$ " is the amplitude of the profile (see Fig. 11). If the electrode polarization

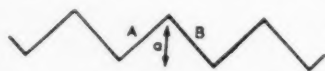


Fig. 11. Triangular electrode profile.

were zero the distribution of current over such an electrode profile would be determined solely by the solution of Laplace's equation  $\nabla^2\phi=0$  in the electrolyte with  $\phi=\text{constant}$  at the electrode surface and  $J=\sigma \text{ grad } \phi$ . (Here  $\phi$ =electric potential; we assume other electrodes to be remote and the conductivity of the metal electrode to be infinitely large.) This solution would give infinitely large current densities at the tips of the profile. Polarization voltages increase with increasing current density, and the consequence of the existence of finite polarization at the electrode is that the current is distributed more uniformly than in the case of zero polarization. Thus, when  $a \gg k$  (polarization relatively unimportant) the current density is very non-uniform being concentrated on the tips of the profile, but when  $a \ll k$  (polarization important) the current density is nearly uniform over the profile, being still greatest at the tips. In the first case, the profile is rapidly smoothed out during anodic dissolution, whereas in the latter case the profile is only changed slowly. It is suggested that the spacing of the structure described above is determined by the value of  $\sigma(dE/dJ)$  operative during the electropolishing process. The attack will tend to create a surface profile owing to the different reactivities of crystallographically different surfaces, but as the profile amplitude increases towards

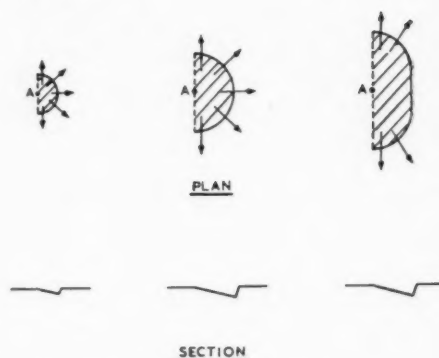


Fig. 12. Three stages in the development of attack on a surface after nucleation at the point A. An increasing area of the basal plane (shown as shaded in the plan and inclined at about  $20^\circ$  to the mean surface in the sectional view) is revealed as attack proceeds.

" $k$ ", the tendency for the non-uniform current distribution to smooth it out becomes greater. The profile amplitudes is thus stabilized at a definite value determined by the magnitude of " $k$ ". A possible sequence of events after the start of the attack at some singularity in the surface of the crystal (perhaps a small precipitate or some other phase in the crystal or even a dislocation) is shown in Fig. 12. At first attack proceeds to reveal a semicircle of the basal plane (we will talk of the basal plane for simplicity although we mean an approximation to the basal plane). But as the depth of the pit becomes greater, the increasing inhomogeneity of the current distribution causes the rate of dissolution at the bottom of the pit to decrease and further growth of the pit will be mainly by sideways extension as shown in the diagram. Some evidence of shapes of this sort is often found in the pattern (see Fig. 2).

If these ideas are correct we can give an explanation of why the pattern differs in perfection on different specimens (compare Fig. 1 with Fig. 2). Where the mean distance between nucleation sites for attack is large compared with the spacing, comparatively perfect line patterns would be expected; but with a large number of nucleation points, considerable interference between the pits generated by neighbouring points would be anticipated and the observed structure would be more complex.

The theory is attractive on qualitative grounds, but it is difficult to bring the observed spacings into rigorous quantitative comparison with the measured values of  $\sigma$  and  $dE/dJ$ . The following considerations are relevant to this comparison and to the question of whether a surface profile will be retained.

(1) The current distribution over a profile needed for this surface profile to be retained is sensitive to the geometry of the profile. For a triangular profile with sharp corners a uniform distribution over the plane faces suffices (it need not have the same value on faces A and B in Fig. 11). Whereas for a sine-wave profile

TABLE I.

Current density ma/cm <sup>2</sup>	10	20	30	40	50	60
Spacing 10 <sup>-4</sup> cm	4.65	3.32	2.48	1.89	1.51	1.27
$\sigma(dE/dJ)$ cm	3.12	1.72	1.33	1.25	1.12	1.13
$\gamma$	1.49 10 <sup>-4</sup>	1.93 10 <sup>-4</sup>	1.87 10 <sup>-4</sup>	1.52 10 <sup>-4</sup>	1.35 10 <sup>-4</sup>	1.13 10 <sup>-4</sup>

there is a variety of different distributions that satisfy the requirement.

(2) The current distribution over a surface profile is determined by  $a/k$  and by the dependence of the reaction rate on the crystallographic orientation of the surface, for the profile necessarily exposes various orientations. The relative importance of these two factors will determine at what fraction of the critical length the amplitude is such that the profile is stable. As Wagner<sup>17</sup> points out, different crystallographic surfaces will have different effective values of " $k$ ". Engell<sup>18</sup> has recently demonstrated the different electrochemical reactivities of different crystallographic faces on  $\alpha$ -iron single crystals. These differences can be interpreted in terms of the theoretical treatment of polarization at metal electrodes given by Lorenz.<sup>19</sup>

(3) The measured values of the polarization include considerable concentration polarization. In considering the effect on a surface profile we need only take account of those components of the polarization operative at the surface or in a layer of thickness of the same order as the profile amplitude. Concentration polarization would then be largely irrelevant when considering surface profiles of the magnitude observed above.

(4) The profiles produced at different current densities may not be geometrically similar and this would make an exact comparison more difficult because the spacing is not then proportional to the amplitude (which should more properly be compared with  $\sigma(dE/dJ)$ ).

(5) It is possible that the value of  $\sigma$  in the immediate neighbourhood of the surface is different from the value in the bulk electrolyte.

As a crude approximation it is true that the spacing is equal to  $\gamma \cdot \sigma \cdot (dE/dJ)$  where  $\gamma$  is a constant. The validity of this approximation is shown in Table I.

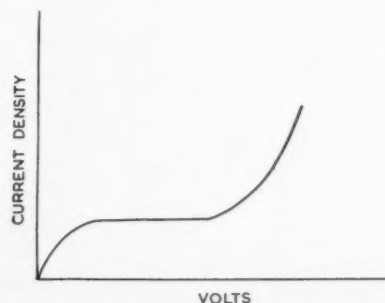


FIG. 13. Step-like polishing curve.

In conclusion, we should like to suggest how the explanation of the structure offered above might be modified when considering polishing processes in which diffusion and not conduction is the factor responsible for surface smoothing.

It will be seen that the polarization curve for zinc polishing in 20% CrO<sub>3</sub> is not of the type characterized by a step of constant current density (see Fig. 13). This latter shape of curve is thought to indicate that the diffusion to the anode of uncharged molecules ("acceptors") needed for the electrode reaction is the rate-determining process.<sup>20</sup> The polishing mechanism can then be described according to Wagner<sup>17</sup> by diffusion of acceptors according to  $\nabla^2 c = 0$ , with  $c = 0$  at the electrode; the treatment is thus formally similar to that when electric potentials are involved. The distribution of current over a surface profile is now determined by the solution of the diffusion problem, and the critical length  $\sigma(dE/dJ)$  has no significance. But some at least of the patterns observed by Jouty<sup>7</sup> and the electron microscopists<sup>1-6</sup> mentioned above were produced in electropolishing baths with step-like polarization curves. If these observations are to be brought into line with a theory of the same type as outlined above, we must seek a critical length for the diffusion-controlled processes. We note that the critical length  $\sigma(dE/dJ)$  is the length of path in the solution perpendicular to the mean surface in which the potential drop is the same as the potential drop at the electrode due to polarization; for the potential drop in the path length  $X$  in the solution is  $J \cdot X / \sigma$  and in the polarization layer is  $(dE/dJ) \cdot J$ . It is perhaps reasonable to regard as the critical length for a diffusion-controlled process that path length in which the acceptor suffers the same change in free energy as the change in free energy it causes when it reaches the electrode. The acceptor molecules will not change their electrostatic potential energy if they are uncharged, but their Gibbs free energy will change because of the change in concentration of acceptors according to the equation,  $g = RT \log c$ , where  $c$  = concentration in moles/cc. The change of energy in path length  $X$  is then  $\Delta g = (RT/c)(dc/dx)X$  where  $dc/dx$  is the concentration gradient normal to the mean surface. Equating this to the change of energy when the acceptor reaches the anode and enables a mole of ions of valence  $z$  to enter the solution, and using the fact that  $J = z \cdot F \cdot D \cdot dc/dx$ , we obtain for the critical length

$$X = \frac{z^2 F^2 D \cdot c}{RT} \cdot \frac{dE}{dJ} \sim 10^2 c \frac{dE}{dJ}$$

Again the relevant portion of  $dE/dJ$  is that operative at or close to the electrode. According to Wagner,<sup>17</sup> the value of  $c$  at the electrode surface may be vanishingly small, compared with the value in the bulk solution.

If the theory outlined above is correct, then it would appear that the consideration of critical lengths is important to a complete understanding of electropolishing processes. In view of the variety of complex behaviours of electropolishing baths it is improbable that other factors can be ignored. However, viscous films on the anode would seem to be less directly relevant by-products of the anodic reaction helping only to prevent hydrodynamic disturbance of the concentration gradients in a diffusion-controlled process. Similarly, thin films of metal oxide or salt on the electrode are not a *sine qua non* of electropolishing processes. Rowland<sup>21</sup> has demonstrated this by electropolishing noble metals in molten alkali chlorides at 950°C; at this temperature there are no stable compounds of the noble metals to form a film. It would be interesting to know whether all electropolishing reagents are capable of producing regular surface profiles of the type described above.

#### ACKNOWLEDGMENTS

The author would like to thank Professor F. C. Frank for his continued interest, much helpful discussion, criticism and advice, and Mr. N. S. Hush of the Chemis-

try Department of this University for suggestions on electrochemical points. Some of the zinc used was very kindly donated by the Imperial Smelting Corporation, Avonmouth, Bristol.

The author is indebted to the University of Bristol for a maintenance grant.

#### REFERENCES

1. G. L. Bucknell and G. A. Geach, *Nature* **164**, 231 (1949).
2. A. F. Brown and R. W. K. Honeycombe, *Phil. Mag.* **42**, 1146 (1951).
3. G. L. Bucknell, G. A. Geach, and N. C. Welch, *Research* **5**, 289 (1952).
4. P. Bussy and G. Chaudron, *Comptes Rendues* **236**, 2323 (1953).
5. P. A. Jacquet, *Comptes Rendues* **237**, 1248 (1953).
6. P. Bussy, *Comptes Rendues* **238**, 247 (1954).
7. R. Jouty (Marseilles), Private communication.
8. M. E. Straumanis, *Z. für anorg. u. allgem. Chemie* **180**, 1 (1929).
9. M. J. Buerger, *Z. für Krist.* **89**, 195 (1934).
10. M. Smialowski, *Z. für Metallkunde* **29**, 133 (1937).
11. J. W. Rutter and B. Chalmers, *Can. J. Phys.* **31**, 15 (1953).
12. C. S. Barrett, *Structure of Metals*, 2nd ed. (London, McGraw-Hill, 1953), p. 194.
13. S. Tolansky, *Nature* **169**, 445 (1952).
14. C. G. Darwin, *Phil. Mag.* **43**, 800 (1922).
15. J. N. Agar and T. P. Hoar, *Disc. Far. Soc.* **1**, 158 (1947).
16. C. Wagner, *J. Electrochem. Soc.* **98**, 116 (1951).
17. C. Wagner, *J. Electrochem. Soc.* **101**, 225 (1954).
18. H. J. Engell, *Naturwiss.* **42**, 124 (1955).
19. W. Lorenz, *Z. für Naturforschung* **9a**, 716 (1954).
20. J. Edwards, *J. Electrodeposits Tech. Soc.* **28**, 137 (1952).
21. P. R. Rowland, *Nature* **171**, 931 (1953).
22. K. F. Hulme, *Acta. Met.* **2**, 812 (1952).

# AN X-RAY EXAMINATION OF CRYSTALLOGRAPHIC TRANSFORMATIONS IN INDIUM-RICH SOLID SOLUTIONS WITH THALLIUM, LITHIUM AND LEAD\*

A. MOORE,† J. GRAHAM,† G. K. WILLIAMSON‡, and G. V. RAYNOR†

The progress with temperature of the crystallographic transformations in indium-thallium (f.c.t.;  $c/a > 1 \Rightarrow$  f.c.c.) and indium-lead (f.c.t.;  $c/a > 1 \Rightarrow$  f.c.t.;  $c/a < 1$ ) solid solutions has been studied using polycrystalline specimens. The transitions are diffusionless; in the former case a metastable two-phase field is defined only on heating, while the latter shows the co-existence of two phases both on heating and cooling. Variations in the electron concentration affect the nature of the transformation. The addition of 0.7 at. % lithium to an alloy containing 20.7 at. % thallium prevents the tetragonal to cubic transformation from taking place with a mechanism involving macroscopic shear. Conclusive evidence regarding the order of either transformation could not be obtained; a suggestion is made with respect to the general occurrence of second order transformations in the solid state.

## ETUDE PAR RAYONS X DES TRANSFORMATIONS DES SOLUTIONS DE THALLIUM, LITHIUM ET PLOMB DANS L'INDIUM

Pour des éprouvettes polycristallines, les transformations dans les alliages indium-thallium (f.c.t.;  $c/a > 1 \Rightarrow$  f.c.c.) et indium-plomb (f.c.t.;  $c/a > 1 \Rightarrow$  f.c.t.;  $c/a < 1$ ) ont été étudiées en fonction de la température. La transition a lieu sans diffusion; dans le premier cas, un domaine métastable à deux phases n'existe que lors chauffage, tandis que le second montre la coexistence de deux phases, tant au chauffage qu'au refroidissement. Des variations dans la concentration électronique modifient la nature de la transformation; 0,7 at. % de lithium, ajoutés à un alliage à 20,7 at. % de thallium, empêchent la transformation tétragonale cubique de se produire par un mécanisme comportant un cisaillement macroscopique. Aucune conclusion n'a pu être obtenue sur l'ordre de ces deux réactions; quelques idées sont avancées sur l'apparition des transformations de second ordre à l'état solide.

## EINE RÖNTGENOGRAFISCHE UNTERSUCHUNG DER KRISTALLOGRAFISCHEN UMWANDLUNG IN INDIUM-REICHEN MISCHKRISTALLEN MIT THALLIUM, LITHIUM UND BLEI

An polykristallinen Proben aus Indium-Thallium (tetr.flz.;  $c/a > 1 \Rightarrow$  kub. flz.) und Indium-Blei (tetr.flz.;  $c/a > 1 \Rightarrow$  tetr. flz.;  $c/a < 1$ ) wurde der Verlauf der kristallografischen Umwandlungen in Abhängigkeit von der Temperatur untersucht. Die Umwandlungen sind diffusionslos. Im erstgenannten Falle konnte nur bei der Erhitzung ein metastabiles Zweiphasengebiet definiert werden, während im anderen Falle sowohl bei der Erhitzung als auch bei der Abkühlung zwei Phasen neneinander festgestellt werden konnten. Veränderungen in der Elektronenkonzentration beeinflussen die Natur der Umwandlung. Eine Zugabe von 0.7 At. % Lithium zu einer Legierung mit 20.7 At. % Thallium verhindert, dass die Umwandlung tetragonal-kubisch nach einem Mechanismus verläuft, der ein makroskopisches Scheren mit sich bringt. Ein schlüssiger Beweis über die Ordnung der Umwandlung konnten nicht erbracht werden; unter Berücksichtigung der normalerweise im festen Zustand auftretenden Umwandlung zweiter Art wurde eine Annahme gemacht.

## INTRODUCTION

The binary solid solutions of indium containing ~22 at. % thallium and ~13 at. % lead undergo a crystallographic transformation with change of temperature.<sup>1,2</sup> On heating, the transformation in the former case is from face-centred-tetragonal (f.c.t.) of  $c/a > 1$  to face-centred-cubic (f.c.c.); in the latter, f.c.t. of  $c/a > 1$  transforms to f.c.t. of  $c/a < 1$ . Research on these transformations has already been reported,<sup>3-9</sup> but most of the work has been of a metallographic nature, aimed at defining a simple mechanism descriptive of the transformation and consistent with the shear markings on external faces. As Geisler<sup>5</sup> pointed out, however, such a mechanism may be quite irrelevant to the actual processes occurring in the transforming crystal; the various shear processes may occur in consequence of the trans-

formation and only to relieve stresses developed during its course. This latter interpretation of the significance of the shear markings, however, does not receive wide support.

For single crystals of indium-thallium alloys, the topographical markings are consistent with a double shear process.<sup>7,8</sup> As far as can be experimentally determined,<sup>8</sup> these two shear processes are simultaneous. The surface topography of polycrystalline specimens shows sets of parallel-sided bands traversing grains and intersecting similar bands in a given grain. In previous work<sup>8</sup> it has been suggested that each of these sets can be regarded as representing a region in which the "first" shear is on the same {110} plane but in opposite (110) directions in neighbouring bands. The "second" shear subdivides the main bands, but these finer bands may not always be resolved. The fine bands are f.c.t. twins of which two sets are possible in each main band. In single crystal studies the movement of the boundary interface between the sheared and the unsheared regions

\* Received April 29, 1955.

† Department of Physical Metallurgy, University of Birmingham, England.

‡ Formerly I. C. I. Fellow, University of Birmingham, England.



can be controlled by varying a temperature gradient in the crystal. This movement is subject to  $\sim 2^\circ\text{C}$  hysteresis. Polycrystalline specimens have been reported<sup>1</sup> to show similar effects, the shear process initiating at random centres and proceeding spontaneously with temperature.

The work reported here was undertaken to decide whether either transformation could be represented in terms of transitions through a two-phase field in an equilibrium diagram, and thus to deduce the order of the transformation. For the case of indium-thallium Guttman has stated that a two-phase region does not exist, but his experimental evidence, as reported, is not entirely conclusive and the thermodynamic significance of a single line which separates two single-phase fields in the equilibrium diagram was not fully discussed.

#### PREPARATION OF ALLOYS

Alloys were prepared from spectrographically pure indium\* and thallium,\* and lead of  $>99.99\%$  purity. The metals were melted and cast in sealed pyrex tubes *in vacuo*. To ensure uniformity of composition in the cast ingot, the alloys were vigorously shaken for four to five minutes at approximately  $20^\circ\text{C}$  above the melting point, and then quenched into water. Homogenisation in the solid state was attained by swaging to 50 per cent of the original cross section and subsequently heating *in vacuo* at  $120^\circ\text{C}$  for five days. Alloys intended for diffractometer studies were cast as 4 gm ingots, while those for X-ray photography were cast as 1 gm ingots. In no case did the casting losses exceed 1 percent by weight. The maximum difference between the intended and analysed compositions was 0.1 at. %.

#### EXPERIMENTAL DETAILS

The transformations were followed accurately in an inert atmosphere at elevated temperatures using a Geiger-counter diffractometer with  $\text{CuK}\alpha$  radiation, and also by precision lattice-parameter measurements based on conventional film techniques using  $\text{CoK}\alpha$  radiation. Alloys in cold worked, quenched, and annealed states were examined. In the diffractometer investigation alloy specimens could be maintained automatically within  $\pm 0.5^\circ\text{C}$  of predetermined temperatures for long periods. Temperature gradients throughout the specimen were too small to be detected.<sup>10</sup>

Specimens for use in the diffractometer were prepared by filing the entire homogenised ingot. The specimens were formed as discs by partially sintering filings at room temperature under a pressure of 10 tons/sq. inch. An annulus 1/16 inch wide was removed from the periphery for analysis. Specimens for film studies were prepared from wire (dia. 0.015 inch) extruded at  $20^\circ\text{C}$ .

Diffractometer observations were confined to the profiles of the  $\{111\}$  and the  $\{200\}$  reflections. These

reflections were chosen for their sharpness and relatively high peak intensities which enabled a rapid and relatively accurate determination of lattice parameters to be made. The line profiles were such that both the  $a$  and  $c$  parameters could be obtained on the calibrated diffractometer to an accuracy of about  $\pm 0.002$  kx units. Within these limits the  $\text{K}\alpha_2$  component has been found to have a negligible effect on the profile of the  $\{200\}$   $\text{K}\alpha_1$  reflection. This is particularly important when a geometrical analysis must be made of the  $\{200\}$  reflection, as in the case where the  $(002)$  and  $(200)$  reflections partially overlap.

The procedure used in analysing the  $\{200\}$  reflections, which may contain one, two, or three component reflections corresponding respectively to the existence of a cubic phase only, a tetragonal phase only or a mixture of both, was as follows. Provided that the profiles of the  $(002)_t$ \* and  $(200)_t$  reflections are known from observations at lower temperatures where overlapping of these reflections does not occur, the  $(002)_t$  component can be drawn with little or no ambiguity. Similarly, and using the "multiplicity" relation that exists between  $(002)_t$  and  $(200)_t$  reflections the  $(200)_t$  component may also

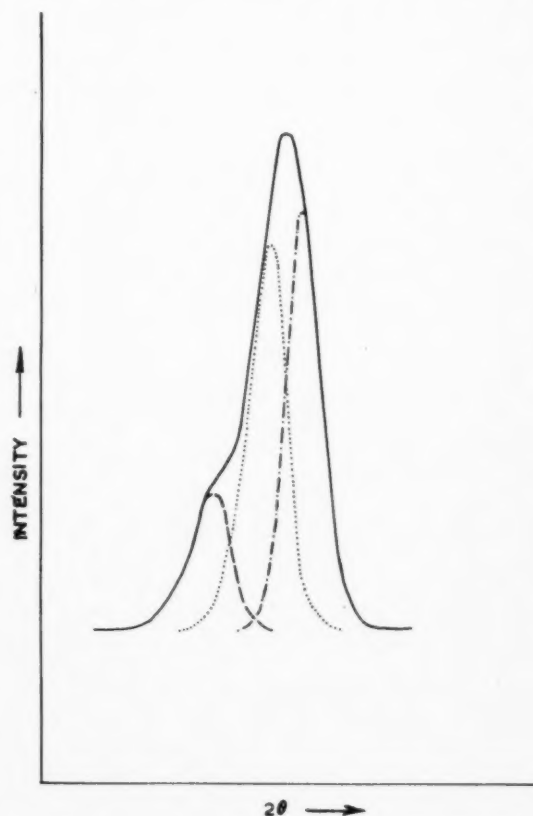


FIG. 1. Geometrical resolution of an observed  $\{200\}$  profile. —observed profile; --- $(002)$  tetragonal profile; —·— $(200)$  tetragonal profile; ····· $(200)$  cubic profile.

\* Suffixes  $t$  and  $c$  are assigned to reflections of the same type from f.c.t. and f.c.c. structures respectively.

\* Supplied by Messrs. Johnson, Matthey and Co., Ltd., London.

be constructed. Any intensity present in the  $\{200\}$  reflection, other than that which can be accounted for by the presence of a tetragonal phase, is attributed to the presence of a cubic phase. By further analysis the profile and position of the  $(200)_c$  reflection may be obtained.

# I

## EXPERIMENTAL OBSERVATIONS: INDIUM-THALLIUM SYSTEM

Figures 2, 3 and 4 show the progress of the crystallographic change from a f.c.t. structure to a f.c.c. structure in terms of lattice parameters plotted against temperature for three alloys of composition 19.0 at.%, 20.4 at.%, and 21.7 at.% thallium respectively. In each case the dotted portions refer to observations on the original cold-worked alloy; the solid line refers to the annealed alloy on heating from room temperature, and the link chain to the reverse change of f.c.c. to f.c.t. Figures assigned to the plotted points give the time in hours at which the specimen was maintained at temperature before any observations were made.

Certain general features are common to the three alloys:

(a) The relaxation with increasing temperature of the tetragonal structure towards cubic is not a continuous process; there is a marked discontinuity in the slope of the  $a$  and  $c$  parameter curves. From this point the cubic

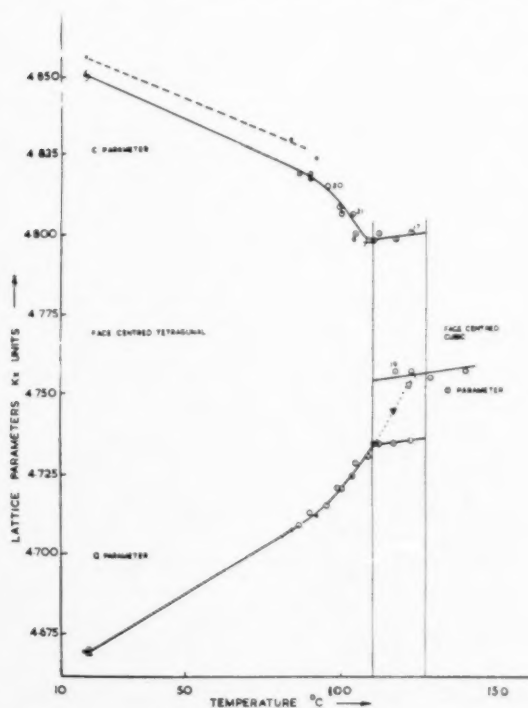


FIG. 2. Variation of lattice parameters with temperature for an indium-19 at.% thallium alloy. ● heating worked specimen; ○ heating annealed specimen; ▽ hypothetical parameter deduced from the unresolved  $(200)_c$  and  $(200)_t$  reflections.

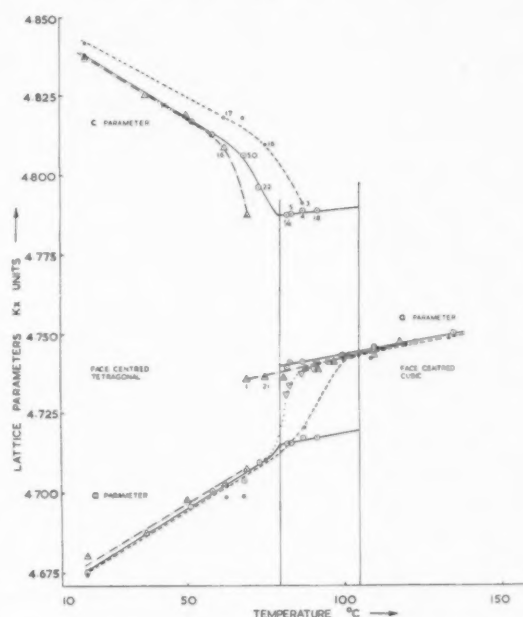


FIG. 3. Variation of lattice parameters with temperature for an indium-20.4 at.% thallium alloy. ● heating worked specimen; ○ heating annealed specimen; ▽ cooling from  $>80^\circ\text{C}$ ; ▽ hypothetical parameter deduced from the unresolved  $(200)_c$  and  $(200)_t$  reflections on heating an annealed specimen.

structure is found to co-exist with the tetragonal structure. The temperature at which the last trace of the tetragonal structure disappears has been assessed as that where the parameter- $vs$ -temperature curve corresponding to the combined profiles of the  $(200)_c$  and  $(200)_t$  reflections becomes a tangent to the  $a_c$  parameter- $vs$ -temperature curve.

(b) The reverse process of f.c.c. to f.c.t. does not proceed through a similar two phase region to that observed on heating; the variation in parameters of the tetragonal phase is almost identical to the converse process on heating.

(c) For an alloy which had been annealed at a given temperature to produce two phases, it was found that on decreasing the temperature, there was no change in the proportion of phases present. On reheating, the transformation, as far as could be detected, proceeded without hysteresis after the higher temperature was regained. In particular, the alloy containing 20.4 at.% thallium, when cooled through  $15^\circ\text{C}$  from  $100^\circ\text{C}$  did not show any change in the proportion of phases present even after 100 hours. There was, however, a slight thermal contraction.

(d) Diffractometer and film observations both showed the  $\{111\}$  and  $\{222\}$  reflections to be remarkably sharp throughout the transformation. For reasons discussed in the following section, it was necessary for the similarity of  $(111)_c$  and  $(111)_t$  spacings to be studied accurately. Any factor affecting line breadths is more easily detected at high Bragg angles and for this purpose the

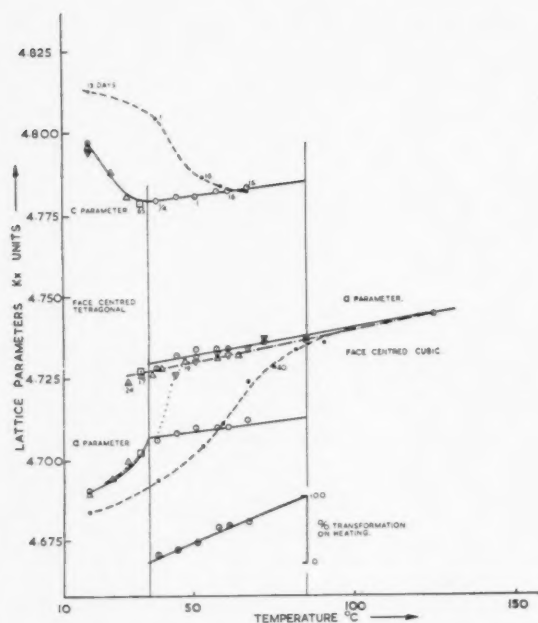


FIG. 4. Variation of lattice parameters with temperature for an indium-21.7 at.% thallium alloy. ● heating worked specimen; ○ heating annealed specimen; △, □ cooling from  $>36^{\circ}\text{C}$ ; ▽ hypothetical parameter deduced from the unresolved (200) cubic and (200) tetragonal reflections on heating an annealed specimen.

study was made on the  $\{333\}$  reflection at  $\theta \sim 79^{\circ}$  using monochromatic  $\text{CoK}\alpha$  radiation. Film measurements showed the half-peak width ( $\beta_1$ ) to vary with temperature (see Table 1). (The measured value was not corrected for instrumental broadening.)

(e) Cold-working increases the  $c/a$  ratio of the tetragonal phase. In the case of the 21.7 at.% alloy the  $c$  parameter increases by  $\sim 0.5$  per cent, while the  $a$  parameter decreases by  $\sim 0.25$  per cent (see Fig. 4). For alloys of lower thallium content this effect was less marked and absent in pure indium. Further, the appearance of the cubic phase, on heating, can be delayed by approximately  $20^{\circ}\text{C}$  by cold-working the specimen.

#### DISCUSSION

It has been assumed<sup>1</sup> that the transformation in the indium-thallium system is of the second order,\* and is

\* The concept of a second order transformation was introduced by Ehrenfest<sup>11</sup> to explain the so-called  $\lambda$ -point transition in liquid helium, a transformation which originally<sup>12</sup> could not be treated thermodynamically as one of the first order. A transformation is of the first, second, or higher order, if the first, second, or higher derivatives of the Gibbs free energy, with respect to temperature and pressure are discontinuous between the two phases. The distinction between the various orders of transformation is artificial, but equations can be calculated from this concept which explain thermodynamic relations in the  $\lambda$ -point transition. Consequences of the theory are, that in a second order phase change there is a discontinuity in the specific heat- $vs$ -temperature relation, but no latent heat; and that the atomic volumes of the two phases are continuous. Stout<sup>13</sup> has shown that for a two-component system the two co-existing phases must be of the same composition, but

TABLE I.

Temperature $^{\circ}\text{C}$	$\ast(333)\beta_1$	Structure
$20^{\circ}$	$44'$	f.c.t.
$72^{\circ}$	$27'$	f.c.t.
$90^{\circ}$	$35'$	f.c.t.+f.c.c.
$114^{\circ}$	$37'$	f.c.c.

\* The decrease in line breadth for the tetragonal structure on heating to  $72^{\circ}\text{C}$  is a real effect.

diffusionless, proceeding entirely by shear; and prior to the present investigation, no two-phase region had been observed, except where definite temperature gradients existed. The existence of a two-phase region has now been clearly demonstrated by the diffractometer study. Further evidence has been obtained from a Debye-Scherrer film of an alloy containing 22.5 at.% thallium at  $20^{\circ}\text{C}$ , which shows three  $\{400\}$  reflections. These could be due to the co-existence of a cubic and tetragonal phase. Parameter measurements of the tetragonal phase from this film agree, within the limits of experimental error, with the extrapolation of values obtained with the diffractometer for the corresponding parameters in the temperature range  $140^{\circ}$ – $40^{\circ}\text{C}$ .

It is of interest to consider the nature of the transformation in the light of these results. In view of the high rate at which the transformation of f.c.t. to f.c.c. in the system indium-thallium proceeds, diffusion is unlikely and the compositions of the co-existing phases are thus the same. Absence of a composition difference between the co-existing phases, is consistent with a transition of the second order; it is thus important to examine the other criterion, involving equality or otherwise of the atomic volumes of these phases. The calculation of atomic volumes for the respective phases from the unit cell dimensions, while indicating that there is a difference of 0.5 per cent, cannot be conclusive, as this value lies just within that expected from errors in film measurement. The relative spacings of the  $\{111\}$  planes in the tetragonal and cubic phases, however, depend critically upon the order of transformation, and a simple calculation, assuming equality of  $(111)_c$  and  $t$  spacings, shows conclusively that the atomic volumes of the two co-existing phases cannot be equal (see Appendix). Visual estimation of line breadths on a film of a two-phase alloy indicated that the common  $\{111\}$  series of reflections was the sharpest of the pattern. This is in agreement with two-phase films in the system copper-manganese, where a similar cubic-tetragonal transformation occurs.<sup>14</sup> Quantitatively, it can be shown that, for the atomic volumes of f.c.t. with  $c/a=1.015$  and f.c.c. structures to be equal, the difference in  $(111)$  spacings must be 0.00014 kx units. This figure corre-

this does not necessarily imply that a comparatively wide two-phase region cannot exist. Since in such a two-phase region the co-existing phases are of the same composition, the lever rule will not apply; it seems necessary to postulate that the chemical free energies of the two phases must be equal.

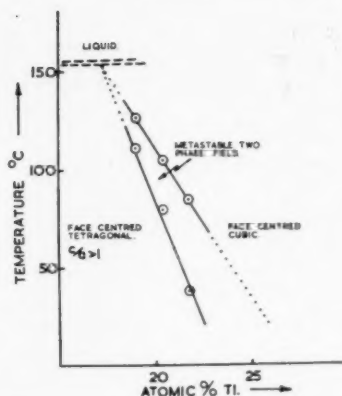


FIG. 5. Modified portion of indium-thallium phase diagram.

sponds to an increase in line breadth of 2.5 minutes of arc in the  $\{333\}$  reflection at  $\theta \sim 79^\circ$ , assuming there to be no inherent difference in the line profiles of the tetragonal and cubic structures.

Table I, however, shows the difference between the half-peak widths of the cubic and tetragonal reflections. The observed broadening of the  $\{333\}$  reflection may be due to particle size, the presence of microstresses, faulting, or a combination of these factors. Until a strict analysis of line-broadening can be made, no conclusive deduction regarding the order of the transformation is possible from the consideration of the breadth of  $\{111\}$  reflections.

If the transformation is of the second order, the chemical free energies of the two phases are regarded as equal, so that the two phases could co-exist in any relative proportions. The fact that there is a range of compositions and temperatures over which these phases exist in reproducible proportions (see Fig. 5) suggests either that the chemical free energies of the co-existing phases are not equal, or that the internal strain and surface energy factors are always reproducible. This latter possibility is unlikely; on this evidence, therefore, the transformation appears to have first-order characteristics. In this case, if true equilibrium is attained, the equilibrium phases must differ in composition. It has been mentioned above that diffusion must play an insignificant part in the mechanism of the transformation; and the phases that are observed to take part in the transition must necessarily be, therefore, metastable, and the free-energy curves of the two phases co-existing during the transition must be very nearly coincident and close to the tangent defining the first order equilibrium two phase field.

Because of the metastable nature of the phases formed, the representation of the two-phase field deduced from the above results in an equilibrium diagram is impossible. Nevertheless the presence of an equilibrium two-phase field is demanded by thermodynamic considerations.

The driving force for the phase changes is not well

understood. If an activation energy process is postulated to explain the facts, it must be a function of the percentage transformation. The system is almost analogous to the martensite transformation in steels, where an activation energy is postulated, but where the transformation is halted before going to completion. In martensite, it is assumed that the retarding force is provided by the locking up of stresses in the hard transformed phase; but although this is unlikely in the present case, where the material is a soft metal at temperatures near its melting point, microstresses may be present and influence the transformation.

It is difficult, also, to reconcile the wide two-phase region in the temperature diagrams (Figs. 2, 3, and 4) with the small temperature hysteresis observed by other workers<sup>1,8</sup> between the appearance and disappearance of surface markings for both poly- and single crystal specimens. To obtain any agreement, it must be assumed that the appearance of shear markings on heating coincides with the commencement of the two-phase region.

## II

### INTRODUCTION

It was suggested by other work in this laboratory that the nature of the above transformation could be affected by electron concentration. On general considerations a decrease in electron concentration would permit a greater degree of relaxation of the tetragonal structure before transformation began. In the limit the transformation could be expected to occur as a phase change of the second or higher order.

To test this hypothesis the transformation has been re-examined for an alloy of composition 20.7 at.% thallium, containing 0.7 at.% lithium. The X-ray examination has been supplemented by a metallographic study at various temperatures.

### EXPERIMENTAL OBSERVATIONS

#### (i) X-ray examination.

The course of the transformation f.c.t.  $\rightarrow$  f.c.c. is shown in Fig. 6, where lattice parameters are plotted against temperature. The parts of the curves shown in full have been deduced without ambiguity from the experimental observations made on heating. The variation of the parameters of both the cubic and tetragonal structures within the two-phase fields cannot be deduced without ambiguity from the experimental observations of line profiles, because of the absence of a marked point of inflexion in the observed  $\{200\}$  profile (see Part I). Two alternative interpretations of the line profiles for the continuation of the transformation are given by the dotted portions. It is to be noted that the two courses are fundamentally different: in one case a continuous relaxation of the degree of tetragonality without the appearance of any cubic phase is assumed, while the other involves the assumption that the be-



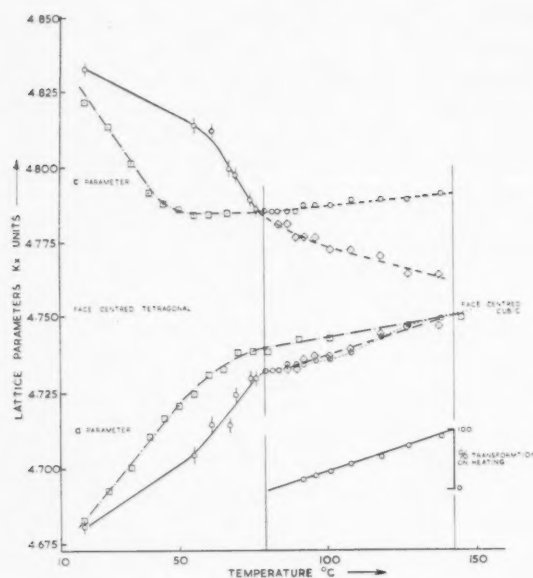


FIG. 6. Variation of lattice parameter with temperature for an indium-20.7 at.% thallium-0.7 at.% lithium alloy.  $\diamond$  heating annealed specimen;  $\square$  cooling from 142°C;  $\odot$ ,  $\diamond$  two possible courses for the continuation of the transformation above 79°C (see text); in the case  $\odot$  a hypothetical parameter deduced from the unresolved 200 cubic and 200 tetragonal reflections.

haviour is similar to that of the binary alloy. On cooling (link chain—Fig. 6) the transformation proceeds in a different manner (cf. Fig. 3) from that observed in the binary alloy.

On heating, and assuming a behaviour similar to that of the binary alloy, the values of the  $a$  parameters in the two-phase region have been assumed to lie on the tangents to either end of the curve corresponding to the hypothetical parameter calculated from the combined profiles of the  $(200)_c$  and  $(200)_t$  reflections. From the relative intensities of the  $(200)_c$  and  $(002)_t$  reflections, the proportion of each phase present within the two-phase region has been calculated, and found to vary linearly with temperature (see Fig. 6).

As shown in Fig. 6, the  $c$  parameter of the tetragonal phase remains approximately constant on cooling from 79° to 55°C. In this temperature range it is impossible to resolve geometrically the  $(200)_c$  and  $(200)_t$  reflections so the hypothetical parameter corresponding to  $(200)_c$  and  $t$  is plotted. It is significant that within this range (where the  $c$  parameter is constant) the breadth of the  $(200)_c$  and  $t$  reflection increases by 8 per cent over its value at higher and lower temperatures; and secondly, that the extrapolation of the tetragonal  $a$  parameter from the two-phase region defined on heating, intersects the hypothetical  $a$  parameter, defined on cooling, at 55°C, the temperature at which the  $c$  parameter, on cooling, begins to increase (see Fig. 11). Both these observations imply that a tetragonal and a cubic structure co-exist on cooling in the range 79°–55°C, and the latter

supports the view that these structures co-exist on heating in the range 80°–105°C.

It appears probable, therefore, that in the change from f.c.t. to f.c.c. for this ternary alloy there exists a range of co-existence of the tetragonal and cubic phases both on heating and cooling. The alternative explanation, that the process is a continuous relaxation complicated by structure imperfections, is however, not excluded.

On either view, certain features exist that are in common with the binary alloy.

(a) The  $a$  and  $c$  parameters increase and decrease, respectively, with increasing temperature.

(b) At the temperature (80°C) corresponding to the appearance of the cubic phase in the binary alloy, there is a marked change in the slope of the parameter- $vs$ -temperature curves.

#### (ii) Metallographic examination.

From the X-ray observations it is obvious that there is a difference, probably a fundamental one, between the transformation of f.c.t. to f.c.c. in the binary and ternary alloys based on 20.7 at.% thallium. To obtain further evidence for this view the respective alloys were examined metallographically at elevated temperatures.

Two specimens, approximately 0.25 inch cubes, were mounted side by side in a solid plastic body 2 in. dia.  $\times$  0.5 in. thick, containing a heating element 0.25 in. beneath the specimens. Temperatures of the specimens were indicated by a thermocouple embedded in the

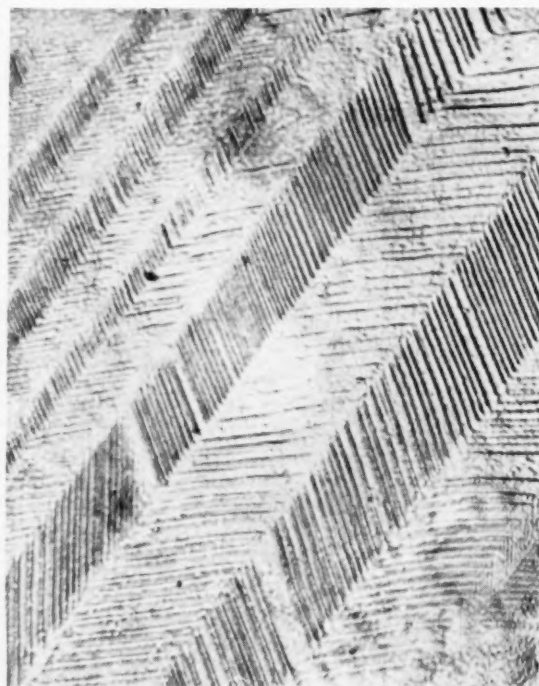


FIG. 7. Micrograph of indium-20.4 at.% thallium alloy showing fine lamellae in ill-defined main bands (1600 $\times$ ).

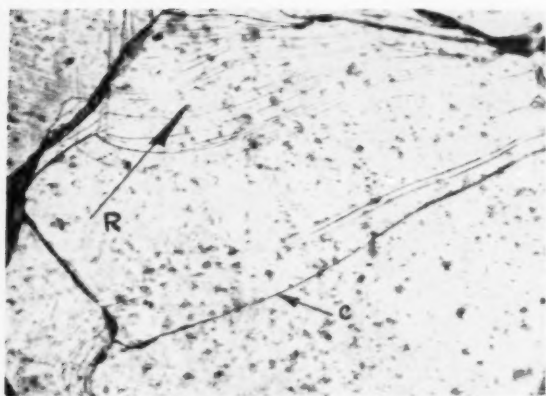


Fig. 8. Surface cracks (*R*) and new grain boundary (*C*) developed during a heating and cooling cycle on an indium-20.4 at.% thallium alloy (140X).

centre of one of them. No measurement of the temperature gradients through the specimens, or assessment of the temperature at the free surface, was made: the aim was to compare the behaviour of the binary and ternary alloys. The alloys initially examined had been chill cast, worked 50 per cent, annealed for five days at 120°C, and furnace-cooled to room temperature. Metallographic surfaces were obtained by careful hand-polishing as far as 3/0 emery paper and finally by electropolishing.<sup>1</sup> Examination at room temperature showed the familiar shear markings associated with the transformation f.c.t.  $\rightleftharpoons$  f.c.c. to exist only in the binary alloy (Fig. 7). It is to be noted that the outlines of the main bands are irregular as suggested by Geisler.<sup>5</sup> The ternary alloy showed no trace of such markings. On heating, the intensity of the shear markings in the binary alloy gradually decreased but even at 140°C faint traces were visible. This effect was probably due to an oxide skin. In the range 120°–140°C cracks, (see *R*, Fig. 8) appeared on the visible surface of the binary alloy, radiating from certain grain boundary corners; this was not a general effect throughout, although other cracks appeared running approximately parallel to other grain boundaries. On subsequent cooling within the range

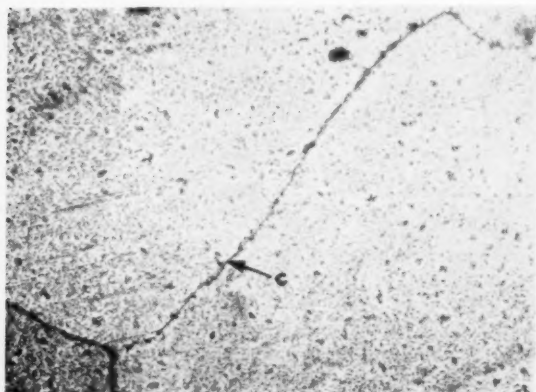


Fig. 9. As Fig. 8 after slight repolishing (140X).

140°–125°C, what seemed to be further cracks suddenly appeared (see *C*, Fig. 8). After cooling in still air, the surface was repolished slightly, and re-examination showed (Fig. 9) complete absence of the cracks (*R*) which had formed on heating. However the surface marks (*C*) that appeared on cooling were found to be new grain boundaries. This experiment was repeated after quenching the surfaces of the alloys from 140°C with alcohol. Cracking similar to that previously described was observed, together with a certain redistribution of grain boundaries (Fig. 10). From the parallelism of shear markings in grains before and after their boundaries had moved (Fig. 10) it was concluded that recrystallisation as such had not occurred. (All photomicrographs have been taken at 20°C.) This behaviour is similar to that observed in aluminium<sup>15</sup> during high-temperature annealing and which has been attributed to stress-induced boundary migration. In the case of the ternary alloy the initial surface topography remained unaltered throughout the various treatments described

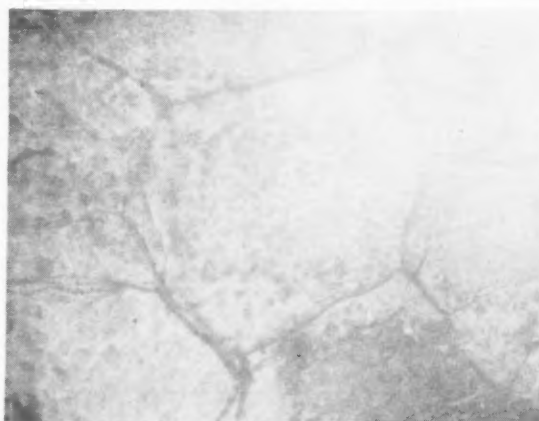


Fig. 10. Grain-boundary movement which instantaneously occurred in cooling an indium-20.4 at.% thallium alloy (140X).

above. Only in one case, after cooling in still air, were any traces of shear markings observed. In this instance the markings were localised in one spot, and were considerably finer and more widely spaced than for the corresponding binary case. To improve the contrast the same surface was repolished and etched. These markings or others similar could not, however, be reproduced.

These results, while inconclusive regarding the existence of a shear process in the ternary alloy do emphasize the profound effect upon the mechanism of the transformation f.c.t.  $\rightleftharpoons$  f.c.c. in indium-thallium alloys of the slight addition of lithium.

#### DISCUSSION

As mentioned above, there are two possibilities for the course of the transformation in the ternary alloys. If the forward process (f.c.t. to f.c.c.) does occur as a simple, but not necessarily complete, relaxation towards cubic, it would be expected that it would be reversible

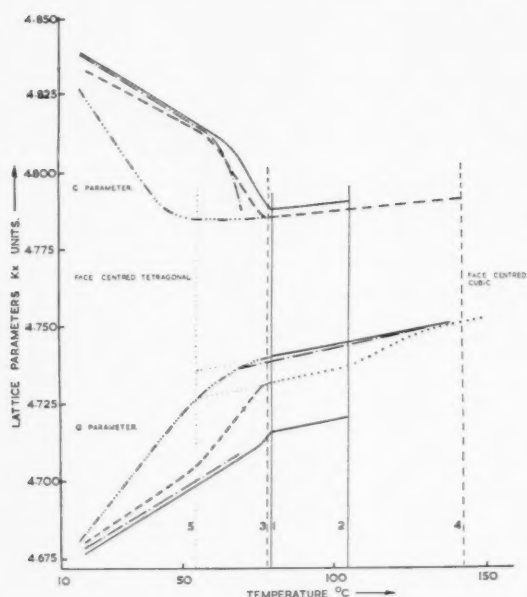


FIG. 11. Comparison of parameter-temperature curves for the alloys indium-20.4 at. % thallium; and indium-20.7 at. % thallium-0.7 at. % lithium. — In·Tl heating; — In·Tl cooling; — In·Tl·Li heating; — In·Tl·Li cooling from 142°C; ..... hypothetical parameter deduced from the unresolved (200) cubic and (200) tetragonal reflections in In·Tl·Li on heating above 79°C; 1—2, In·Tl metastable two-phase field-heating; 3—4, In·Tl·Li metastable two-phase field-heating; 3—5, In·Tl·Li metastable two-phase field-cooling. Composition: In·Tl 20.4 at. % Tl, In·Tl·Li 20.7 at. % Tl, 0.7 at. % Li.

with temperature. Since, however, the reverse process is different from the forward process, this mechanism of a pure relaxation is doubtful. Nevertheless, the metallographic evidence clearly suggests that the mechanism of the change f.c.t.  $\rightleftharpoons$  f.c.c. is either a relaxation, or a process involving shear of only very small magnitude.

The relevant lattice spacing-*vs*-temperature curves for the alloys used in the metallographic study are superimposed in Fig. 11. With regard to the second possibility the following factors are significant:

(a) In both cases, the *c* parameter decreases in a similar manner with temperature, a cubic phase appearing when the *c* parameter reaches approximately 4.78 kx units. Further decrease in the *c* parameter does not occur.

(b) In the ternary alloy, the *a* parameter of the tetragonal phase relaxes to within 0.008 kx units of the value of the cubic parameter, while for the binary case, relaxation proceeds only to within 0.025 kx units.

Within the region where two phases co-exist, the ternary and binary alloy parameters show similar trends, though the metallographic evidence points to a profound difference. The possible shear process appears to be greatly affected by the almost complete relaxation of the tetragonal *a* parameter to that of the cubic structure before the phase transforms. As there is no

metallographic evidence for shear in the ternary system, it must be assumed either that conditions favour movement of individual atoms across the interface, rather than movement of the whole interface between the two phases, or that relaxation of the *c* parameter to the cubic parameter occurs, initiating from random centres. It is difficult to imagine how this latter process occurs without macroscopic shear.

After cooling through the two-phase field, both the *a* and *c* parameters of the tetragonal phase vary steadily with falling temperature. The mechanism for this growth of tetragonality is not at present understood, but the nature of the parameter curves suggests that this mechanism is the reverse of that for the decay in tetragonality on heating, but subject to a severe hysteresis.

### III

#### EXPERIMENTAL OBSERVATIONS—INDIUM-LEAD

A phase diagram for the system indium-lead in the range 12–14 at. % lead, and 20°–145°C has been drawn from observations made on specimens at various temperatures (Fig. 12). In contrast with the previous systems, overlapping of the reflections from the respective phases did not normally occur. Consequently, the identification of slight traces of a second phase was simple. However, crossing a phase boundary sometimes resulted in line-broadening, particularly of the two (200) reflections, of sufficient magnitude to prevent quantitative analysis. In every case, the line-broadening was eliminated, and the original state regained by pressing the specimen under 10 tons sq in. at room temperature. As with the system indium-thallium, the transformation proved to be irreversible with temperature within the two-phase region as detailed below:

- (a) 12.7 at. % lead irreversible in ranges 61.5°–20°C; 93°–61.5°C; 120°–91°C; 120°–20°C.
- (b) 13.2 at. % lead irreversible in the range 60°–40°C.

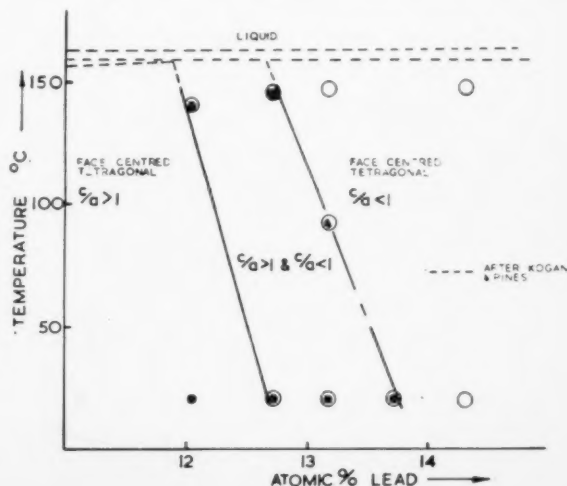


FIG. 12. Modified portion of indium-lead phase diagram.

In each case, the higher-temperature condition was attained in less than five minutes, this being the minimum time in which any specimen could be examined. On cooling the high-temperature structures in the ranges detailed above, no variation in the proportion of phases occurred within 13 hours. There was one exception to this generalisation. An alloy of 12.7 at.% lead, annealed at 139 °C for 17 hours, partially transformed on furnace cooling to room temperature. Examination after 15 minutes showed the (200) reflections to be so broadened that they appeared together as a plateau above the "background." Resting the specimen for one week resulted in considerable refinement of these broadened reflections. This condition persisted without alteration for one month. Only after working was the original state regained (Fig. 13). Throughout these treatments, the half-peak widths of the {111} and (002) reflections remained constant. In a similar experiment, an alloy containing 12.0 at.% lead was furnace-cooled from 135 °C (i.e., just within the two phase region) to 20 °C. The proportion of the phase of axial ratio less than unity decreased, as evidenced by a decrease in

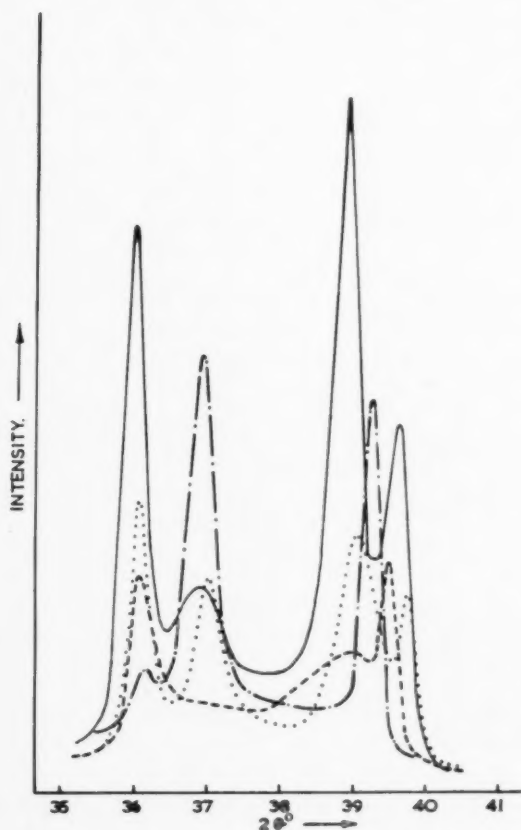


Fig. 13. Intensity profiles of an alloy indium-12.7 at.% lead. The reflections, with increasing  $\theta$ , are (002),  $c/a > 1$ ; (200),  $c/a < 1$ ; (200),  $c/a > 1$ ; (002),  $c/a < 1$ . — cold worked—at 20 °C; --- after 1 hr. at 140 °C; - - - after 15 mins. at 20 °C—previously furnace cooled from 140 °C; ..... after resting at 20 °C for 4 days and 1 month.

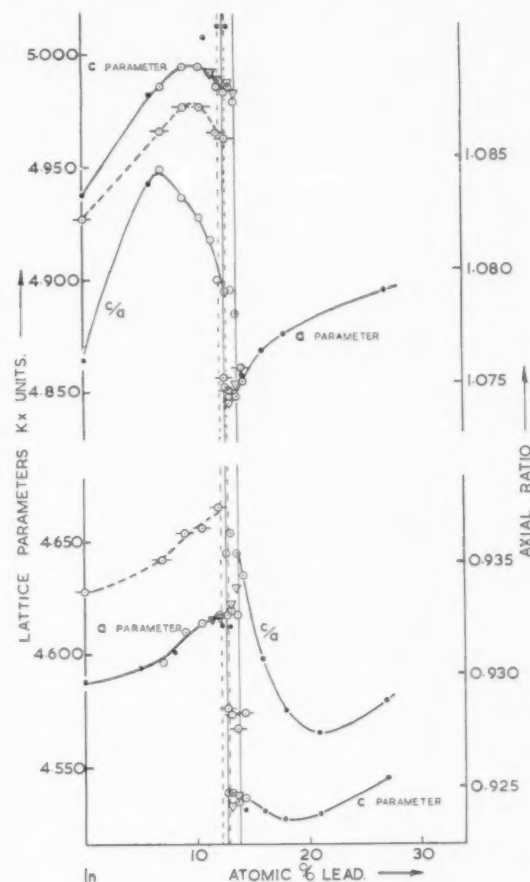


Fig. 14. Parameter-composition curves, indium-lead system. ● after Tyzack and Raynor; ○ diffractometer; △ film; ○—135 °C isotherms; || boundary of two phase field at 20 °C—cold worked specimen; || boundary of two phase field at 135 °C.

intensity of the (002) reflection, which remained sharp. However, the (200) reflection of this phase broadened and became indistinguishable from the background. This state persisted even on quenching to  $-185^{\circ}\text{C}$ , and resting at this temperature for 16 hours. Again, throughout these treatments, the common {111} reflection remained sharp.

By a Debye-Scherrer technique, using  $\text{CoK}\alpha$  radiation, the entire diffraction pattern up to the {333} reflection was examined using specimens in the form of extruded wire for which the grain size was varied by suitable annealing treatments. Such specimens were examined after cooling to room temperature at various rates. By varying the history of specimens containing between 13.0 and 13.7 at.% lead, structures could be obtained at 20 °C consisting of a mixture of the two tetragonal phases in any proportion. Usually the patterns were such that those reflections with  $h = \pm k$  were sharp, while all other observed reflections were considerably broadened. Even alloys which had transformed completely from one structure to the other



gave the spotty reflections characteristic of large grain size.

As it was impossible to traverse the two-phase region on heating or cooling in the diffractometer studies, the variation of the parameters with temperature could not be investigated in its entirety. Detailed information regarding the transformation could be conveniently obtained only from the isothermal variation of parameters with composition (Fig. 14).

### DISCUSSION

As pointed out by previous workers<sup>2,16</sup> indium-lead alloys consisting of two phases are easily obtained. Experimentally, it has been impossible to decide with sufficient accuracy whether the co-existing phases had the same atomic volumes, so that the question of the order of this transformation must be left in doubt. Differences would be expected, however, in the behaviour of the lattice spacings as functions of composition within the two-phase region, for transformations of the first and second order. The parameters are constant within an equilibrium first-order, two-phase field, but for a second-order change the spacings of both phases would vary, while maintaining the atomic volumes equal. Even if equilibrium can be assumed, the two-phase field is too narrow to permit a detailed lattice spacing study and the evidence obtained so far is inconclusive.

The change in atomic volume on transformation has been calculated from the parameter measurements at 135°C and 20°C for a fixed composition. At the former temperature, the change is  $-0.25\%$ , while at the latter it is  $+0.3$  per cent, on passing from the phase with  $c/a > 1$  to that of  $c/a < 1$ . This suggests that at an intermediate temperature, the atomic volumes would be equal, and the transformation could then proceed as a phase change of the second order. The numerical basis of this conclusion, however, is just on the limits of experimental accuracy.

The variation of the proportions of the two co-existing phases with previous history indicates that their respective free-energy values are almost identical in the two-phase region. The irreversibility of the transformation within the two-phase region, as investigated under varying conditions, again suggests, as in indium-thallium alloys, that diffusion is not the governing factor of the transformation. Micrographs show a similar transformed structure to the indium-thallium alloys.<sup>16</sup>

Throughout the experiments, the condition of the alloy obtained by severely working each specimen at room temperature was taken as standard, since it was reproducible, regardless of the previous thermal history of the specimen and in most cases, gave sharp diffraction lines. The only exception was an alloy in the centre of the two-phase field, in which the (200) reflection was slightly broadened. (cf. Fig. 14.)

The broadened reflections have not yet been quanti-

tatively explained; it seems probable, however, that they are due, not to a layer fault, but to a type of imperfection involving displacements of atoms from the lattice sites.

From the plot of parameters against composition, it appears that the  $c$  parameter goes through a maximum at 10 at.% lead. This is at variance with previous work,<sup>2</sup> which indicated that the  $c$  and  $a$  parameters, and  $c/a$  increased continuously with the addition of lead, until the onset of the transformation. This point is significant, since it provides a common link with similar transformations in other indium-rich solid solutions,<sup>1,17-19</sup> where the transformation is always preceded by a decrease in  $c$  parameter. The discrepancy mentioned above has been thoroughly investigated using a film technique. It is probable that in the earlier work, calculations based on too few X-ray reflections, led to inaccurate axial ratio values for the composition range 6-12 at.% lead.

### CONCLUSIONS

(i) In the system indium-thallium there is a finite range of co-existence of the two phases in the transformation f.c.t.  $\rightarrow$  f.c.c. As it is unlikely that the reaction can be of the second order the structures observed in the two-phase region must result from an approximation to conditions demanded in a first-order transformation. Since no evidence for diffusion has been obtained, the phases observed are necessarily metastable.

(ii) For each of the binary alloys of indium-thallium, and possibly for the ternary alloy indium-thallium-lithium, there is a specific range of tetragonality that is not adopted. The degree of relaxation of the tetragonal structure before transforming to cubic depends upon electron concentration. The greater degree of relaxation towards cubic, obtained by decreasing the electron concentration, permits the transformation to proceed with no apparent macroscopic shear.

(iii) In the system indium-lead, a two-phase field is found between two tetragonal phases. Determinations of atomic volumes suggest that the transformation may be second order, at least over a limited temperature range. The pronounced effect of grain size and thermal history, usually irrelevant in determining phase boundaries, show the importance of small energy factors in determining the constitution actually adopted.

(iv) The requirement of continuous atomic volumes for second-order phase changes is so rigorous, that it seems unlikely that such changes will be of wide occurrence. Even where the conditions are approximately fulfilled, alteration of any variable may be enough to disturb the delicate thermodynamic balance.

### ACKNOWLEDGMENTS

We wish to acknowledge the award of a D.S.I.R. maintenance allowance (A.M.) and a of Hackett Research Studentship awarded by the University of Western Australia (J. G.). We are particularly indebted to Miss J. Witcomb for help in much of the experimental

work. Grateful acknowledgement is made for financial assistance from the Royal Society and Imperial Chemical Industries Limited.

#### APPENDIX

Proof that cubic and tetragonal structures of equal (111) spacings cannot have equal atomic volumes.

Let the lattice spacings of the cubic and tetragonal phases be represented by  $a_c$  and  $a_t$ ,  $c_t$  respectively.

From the condition that the {111} spacings are equal

$$1/a_c d_{111}^2 = 1/a_t d_{111}^2 \quad \text{i.e.,} \quad 2/a_t^2 + 1/c_t^2 = 3/a_c^2 \quad (1)$$

Assuming that the atomic volumes are also equal, then

$$a_c^3 = a_t^2 c_t \quad (2)$$

From Eqs. (1) and (2)

$$a_t^6 + 6a_t^4 c_t^2 - 15a_t^2 c_t^4 + 8c_t^6 = 0,$$

i.e.,

$$a_t = \pm c_t, \quad \text{or} \quad a_t = \sqrt{-8c_t^2}$$

The only real tetragonal phase which can satisfy Eqs. (1) and (2) has unit axial ratio.

#### REFERENCES

1. L. Guttman, Trans. A. I. M. E. **188**, 1472 (1950).
2. C. Tyzack and G. V. Raynor, Trans. Faraday Soc. **50**, 675 (1954).
3. J. S. Bowles, C. S. Barrett and L. Guttman, Trans. A. I. M. E. **188**, 1478 (1950).
4. A. H. Geisler and D. L. Martin, (Discussion to 3) Trans. A.I.M.E. **191**, 1057 (1951).
5. A. H. Geisler, Acta Met. **1**, 260 (1953).
6. Z. S. Basinski and J. W. Christian, Acta Met. **1**, 759 (1953).
7. Z. S. Basinski and J. W. Christian, Acta Met. **2**, 101 (1954).
8. Z. S. Basinski and J. W. Christian, Acta Met. **2**, 148 (1954).
9. S. Makarov, Izvest. Akad. Nauk. S. S. S. R. Otdel Khim. Nauk. **485** (1950).
10. G. K. Williamson and A. Moore. To be published in J. Sci. Insts.
11. P. Ehrenfest, Leiden Comm. Suppt. No. 75(b) (1933).
12. A. J. Rutgers and G. A. Wouthuysen, Physica **4**, 515 (1937).
13. J. W. Stout, Phys. Rev. **74**, 605 (1948).
14. Z. S. Basinski and J. W. Christian, J. Inst. Metals **80**, 659 (1951-52), and private communication.
15. P. A. Beck and P. R. Sperry, J. Appl. Phys. **21**, 150 (1950).
16. W. S. Kogan and P. B. Pines, Doklady Akad. Nauk. S.S.S.R. **87**, 771 (1952).
17. C. Tyzack, Ph.D. Thesis, University of Birmingham (1953).
18. W. Betteridge, Proc. Phys. Soc. **50**, 519 (1938).
19. C. G. Fink, E. R. Jette, S. Katz and F. J. Schnettler, Trans. Electrochem. Soc. **88**, 229 (1945).

# CRYSTALLOGRAPHIC RELATIONSHIPS IN AGED COPPER-BERYLLIUM ALLOYS\*

J. S. BOWLES† and W. J. McG. TEGART‡

The precipitation of CuBe from copper-beryllium  $\alpha$  solid solutions involves a transformation from a face-centered cubic ( $F$ ) to a body-centered cubic ( $B$ ) structure. The habit plane of the relief effects produced on polished surfaces by this transformation has been determined. It is not a simple lattice plane but is close to  $\langle 110 \rangle_F$ . The association between variants of the habit plane and variants of the orientation relationship has been found to be such that a variant of the habit plane is associated with that variant of the  $\langle 100 \rangle_B$  pole which lies in the same stereographic triangle.

With these results the precipitation reaction has been analysed using the geometrical theory developed for martensitic transformations by Bowles and Mackenzie.<sup>1,2,6</sup> The theory then predicts the orientation relationship determined by Guy.<sup>11</sup>

## RELATIONS CRISTALLOGRAPHIQUES DANS LES ALLIAGES CUIVRE-GLUCINIUM

La précipitation de CuBe à partir des solutions solides cuivre-glucinium comporte une transformation du système cubique à faces centrées ( $F$ ) dans le système cubique centré ( $B$ ). Le plan d'habitat des reliefs sur une surface polie produits par cette transformation a été déterminé; ce n'est pas un plan simple mais il est voisin de  $\langle 110 \rangle_F$ . Le rapport entre les variantes du plan d'habitat et les variantes de la relation d'orientation est tel qu'une variante du plan d'habitat est alliée à la variante du pôle  $\langle 100 \rangle_B$  qui appartient au même triangle stéréographique.

A l'aide de ces résultats la précipitation est analysée par la théorie géométrique développée pour les transformations martensitiques par Bowles et Mackenzie.<sup>1,2,6</sup> La théorie prévoit les orientations observées par Guy.<sup>11</sup>

## ÜBER DIE KRISTALLOGRAFISCHEN ZUSAMMENHÄNGE BEI AUSGELAGERTEN KUPFER-BERYLLIUM LEGIERUNGEN

Die Ausscheidung von CuBe aus  $\alpha$  Mischkristallen des Systems Kupfer-Beryllium ist gleichbedeutend mit einer Umwandlung einer kubisch-flächenzentrierten ( $F$ ) in eine kubisch-raumzentrierte ( $B$ ) Struktur. Es wurde die Habitusebene der Reliefwirkungen bestimmt, die diese Umwandlung auf polierten Flächen hinterlässt. Die Habitusebene ist keine einfache Gitterebene, sie liegt jedoch nahe bei  $\langle 110 \rangle_F$ . Der Zusammenhang zwischen Veränderungen der Habitusebene wie auch der Orientierungsbeziehung ist derart, dass eine Änderung der Habitusebene von der Änderung desjenigen  $\langle 100 \rangle_B$ -Poles begleitet wird, der im gleichen Bestimmungsdreieck liegt.

Mit diesen Ergebnissen wurden die Ausscheidungsreaktionen auf Grund der geometrischen Theorie der Martensitumwandlung von Bowles und Mackenzie.<sup>1,2,6</sup> analysiert. Die Theorie sagt dann die von Guy<sup>11</sup> bestimmte Orientierungsbeziehung voraus.

### 1. INTRODUCTION

Although the details of the atomic mechanisms of martensitic transformations have not yet been elucidated, the phenomenological theory of the over-all atomic displacements has been developed to the point where accurate predictions can be made of habit planes, orientation relationships and the homogeneous strains accompanying the transformations.<sup>1-4</sup> For the diffusion-controlled transformations no such quantitative theory exists. X-ray studies have disclosed a wealth of information about intermediate structural states produced during these transformations, but no quantitative theory of the crystallographic relations has yet been derived. Some time ago the suggestion was made by Bowles and Barrett<sup>5</sup> that, during the stage of "coherence," the geometry of the atomic processes involved in diffusion-controlled transformations may be identical with that involved in martensitic transformations.

At the time this suggestion was made, the only experimental evidence available to support it was the general similarity of the orientation relationships produced by the two kinds of transformation. However, the recent developments in the phenomenological theory of martensitic transformations enable a more satisfactory test to be made of the merits of this idea. If the geometry of the processes involved in the two kinds of transformation is identical, then the theory developed for martensitic transformations should be capable of predicting the geometrical features of diffusion-controlled transformations. The work to be described in this paper was carried out to test the validity of the predictions of the theory for the precipitation of CuBe from copper-beryllium  $\alpha$  solid solutions.

This particular precipitation process was selected for two reasons. First, the lattice transformation involved is f.c.c.  $\rightarrow$  b.c.c.; the theory for this case has been worked out in detail<sup>6</sup> and shown to yield predictions consistent with observation for a number of martensitic transformations. Second, the precipitation of CuBe is accompanied by the production of visible relief effects on the surfaces of polished specimens. These relief effects

\* Received May 2, 1955.

† C.S.I.R.O., Division of Tribophysics, University of Melbourne, Carlton, N.3., Victoria, Australia; now New South Wales University of Technology, High Street, Kensington, N.S.W., Australia.

‡ C.S.I.R.O., Division of Tribophysics, University of Melbourne, Carlton, N.3., Victoria, Australia.

have been described as similar to those produced by martensitic transformations<sup>7,8</sup> and, in the present work, they are interpreted as having a similar origin. It is proposed that the relief effects arise as a direct consequence of the net change in shape accompanying the formation of plate-shaped crystals of CuBe.

The phenomenological theory<sup>1,2</sup> has been developed from the proposal that the total atomic displacements produced by martensitic transformations can be described consistently by means of a homogeneous strain which is composed of an invariant plane strain and a small dilatation, followed by a shear, which is part of a twinning shear in the final lattice but which occurs inhomogeneously. It has been shown that these conditions determine the total strain, and hence the orientation relationship, in terms of a single parameter,  $\theta$ . In applying the theory to a particular transformation, it is necessary to evaluate  $\theta$  by calculating the variation of the habit plane with  $\theta$  and determining that value, if any, for which the predicted and observed habit planes agree. The predicted habit plane variation for face-centered cubic to body-centered cubic transformations has already been derived<sup>6</sup> so it remains to determine the habit plane of copper-beryllium, i.e., the plane of the relief effects, and to evaluate  $\theta$ .

The experimental work is described in §§2, 3. This consisted of determining the general indices of the habit plane and of finding which variant of the habit plane is associated with a particular variant of the precipitate orientation. In §4 these results are used to evaluate  $\theta$  and the orientation relationship is then determined by substitution in the equations developed elsewhere.<sup>6</sup> The predicted orientation relationship is compared with that measured by Guy.<sup>11</sup>

The notation used in this paper is the same as that used previously.<sup>1,2,6</sup>

## 2. EXPERIMENTAL METHODS

The alloys used were prepared from oxygen-free high conductivity copper (>99.98 wt. % copper) with traces (<0.005 wt. %) of lead, tin, nickel and iron, and a copper-beryllium mother alloy (95.85 wt. % copper, 4.14 wt. % beryllium) supplied by Brush Beryllium Corporation. Initially the melting procedure described by Guy, Barrett and Mehl<sup>12</sup> was followed but later the alloys were prepared by melting the mother alloy and the copper together in silica under an atmosphere of purified nitrogen. The solidified rods were swaged down from 12 mm diameter to 7–8 mm diameter with intermediate anneals at 800–850°C.

The alloys used were restricted to the range 1.80–1.95 wt. % beryllium since it was found that relief effects were not produced in specimens containing smaller concentrations of beryllium.

To avoid grain-boundary precipitation during the ageing treatments, all the experiments were performed on single crystals. Crystals made by the Bridgman technique were found to be badly cored, and therefore

repeated zone melting was used to produce more homogeneous crystals. The specimens, sealed under nitrogen in a silica tube, were passed through a small coil fitted in the centre of a tube furnace. The coil was maintained above the liquidus temperature and the furnace at 800°C. After zone melting the specimens were maintained at 800°C for three days and then water-quenched. The single crystals produced in this way were not cored but only small lengths of uniform composition could be obtained.

Specimens were cut from the single crystals with a jeweller's hacksaw, lapped on carborundum paper and then polished with diamond dust. They were then carefully electropolished in an orthophosphoric acid electrolyte<sup>10</sup> for one half to three quarters of an hour to obtain a strain-free surface. Mechanically polished specimens were found to be unsuitable for studying the relief effects because discontinuous precipitation occurred in the deformed surface layer during ageing. Specimens were aged at temperatures ranging from 250°C to 330°C for periods of 15 minutes to 24 hours to determine the optimum conditions for the development of relief effects. The habit plane of the relief effects was determined by plotting the zone normal to each trace direction into a single stereographic triangle and determining the common point of intersection of all zones.<sup>13</sup> The directions of the relief effects in a given set varied slightly, but the trace measurements were reproducible to within 3 degrees.

The orientations of the parent crystals were determined, both before and after ageing, from back reflection Laue and oscillating crystal photographs. In spite of the care taken in preparation of the crystals, the diffraction spots were diffuse even before ageing. However, the orientations determined prior to ageing are considered to be accurate to within  $\pm 1^\circ$ .

In the aged specimens the spots were much more diffuse, reflections occurring over a range of several degrees. For this reason the determination of the complete pole figure of the precipitate axes was not attempted. However, in connection with the problem of finding out which variant of the habit plane is associated with a particular variant of the orientation relationship, the locations of those  $\langle 100 \rangle_B^*$  poles which occur in the neighbourhood of  $\langle 100 \rangle_F^*$  poles were determined. Owing to the slight uncertainty in the matrix orientation after ageing, the positions of these  $\langle 100 \rangle_B$  poles were determined relative to the original positions of the  $\langle 100 \rangle_F$  poles. Oscillating crystal photographs taken with filtered or monochromatic copper radiation were used for this purpose. Even in specimens aged for 20 hours the reflections from the precipitate were very weak and exposures of about 3 or 14 hours were needed for filtered and monochromatic radiation respectively.

For the correlation of habit plane and orientation relationship variants, the directions of the relief effects

\* The suffices *B* and *F* are used to denote the body-centered cubic (CuBe) and face-centered cubic ( $\alpha$ ) phases respectively.



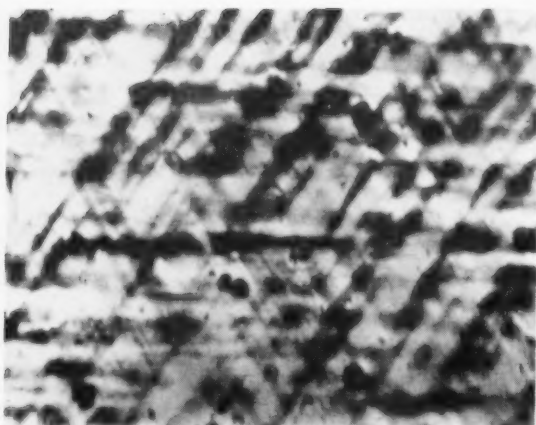


FIG. 1. Relief effects produced on electropolished surface of copper-beryllium single crystal by ageing for 4 hours at 285°C. 100X.

and the locations of  $\langle 100 \rangle_B$  poles were measured using specimens aged at 285°C for 20 hours. Stereographic projections were constructed showing the orientations, relative to the parent crystal, of the  $\langle 100 \rangle_B$  axes and of those variants of the habit plane capable of producing the observed relief effects. As will be described in the next section, these projections indicate a unique association of habit plane variants and of variants of the  $\langle 100 \rangle_B$  poles.

### 3. EXPERIMENTAL RESULTS

It was found that the relief effects developed best in specimens containing 1.80–1.95 weight per cent beryllium at 285°C. Relief effects were not observed outside the range 260° to 330°C for ageing periods of four hours. On ageing at 285°C faint relief effects became visible after an hour and three quarters and were clearly developed after four hours. A typical photomicrograph of the relief effects is shown in Fig. 1.

The results of the habit plane determination are shown in Fig. 2; the mean normals to 28 traces in six different specimens passed through the region indicated. It will be noted that the habit plane is not a plane of low in-

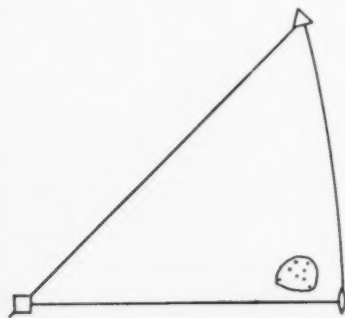


FIG. 2. Results of habit plane determination. Each spot represents a determination from a specimen surface; the range of orientations within which the habit plane is most likely to lie is defined by the rough circle.

dices; a similar conclusion was reached by Guy, Barrett and Mehl.<sup>12</sup> When the trace normals were plotted on the stereographic projection, it was noted that several variants of the habit plane could be associated with each trace. This multiplicity makes it difficult to determine the habit plane more accurately, for the mean traces used in the determinations may actually be derived from more than one variant. Under these conditions, it is not surprising that attempts to improve the accuracy of the determination by using traces on two surfaces<sup>14</sup> were not successful.

Although relief effects were visible in specimens aged for four hours at 285°C, X-ray reflections from the precipitate were not detected until after about 20 hours. Metallographic examination of specimens aged at 285°C revealed a striated structure parallel to the relief effects (Fig. 3). After 24 hours at 285°C the discontinuous precipitation of a nodular constituent was observed (Fig. 4.)

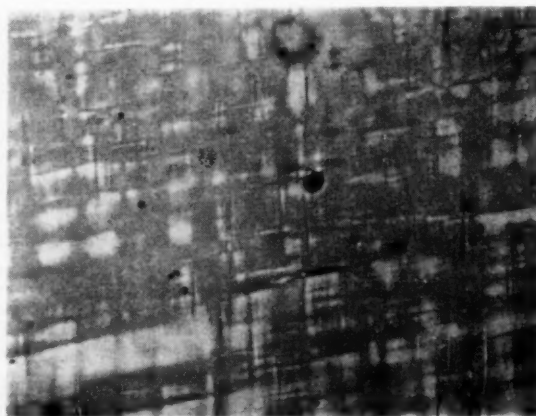


FIG. 3. Striated structure in crystal aged 19 hours at 285°C. Etched with ammonia-hydrogen peroxide reagent. 100X.

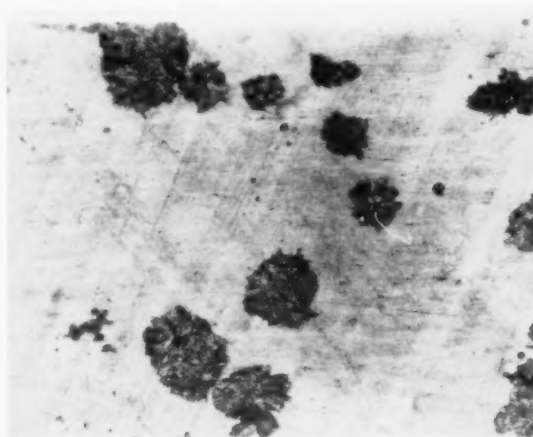


FIG. 4. Discontinuous precipitation in crystal aged 100 hours at 285°C. Etched with ammonia-hydrogen peroxide reagent. 100X.

The data obtained for the correlation of habit plane and orientation relationship variants are shown in Figs. 5(a) and 5(b). The interpretation of these data involves a knowledge either of the approximate orientation relationship or of the "correspondence"<sup>2</sup> between the initial and final lattices. Guy<sup>11</sup> has shown that the orientation relationship is such that one of the  $\langle 100 \rangle_B$  axes is in the neighbourhood of a  $\langle 100 \rangle_F$  axis whilst the other two  $\langle 100 \rangle_B$  axes are near  $\langle 110 \rangle_F$  axes. In this respect the copper-beryllium orientation relationship is similar to those observed in the various iron alloys. This means that in any specimen there are as many variants of the precipitate orientation as there are  $\langle 100 \rangle_B$  poles near  $\langle 100 \rangle_F$  poles and, further, that when the orientation relationship is known, a particular variant of the precipitate orientation can be specified by describing the location of that one of its  $\langle 100 \rangle_B$  poles which is near a  $\langle 100 \rangle_F$  pole.

The association of habit plane and orientation relationship variants can therefore be specified in terms of the relative positions of the habit plane and the relevant  $\langle 100 \rangle_B$  pole. It is necessary to find from the data of Figs. 5(a) and 5(b) a particular combination of a variant of the habit plane and a variant of the  $\langle 100 \rangle_B$  pole, which, when repeated by the symmetry operations of the parent crystal, generates all the other observed  $\langle 100 \rangle_B$  poles and habit planes. Such a combination is found by systematic trial and error. For example, it might be proposed that a  $\langle 100 \rangle_B$  pole observed at  $[u \ v \ w]_F$  is associated with an observed habit plane variant  $(h \ k \ l)_F$ . If another  $\langle 100 \rangle_B$  pole is observed at  $[u-w \ v \ u]_F$ , then for the proposed association to be valid, another habit plane must occur at  $(h-l \ k \ h)_F$  and so on.

In the specimens examined a given trace could usually be attributed to several variants of the habit plane. Accordingly, all variants of the habit plane capable of producing the observed traces have been plotted in Figs. 5(a) and 5(b). This does not imply that all the variants plotted are really present but there is no reason to suppose that each trace is produced by a single variant of the habit plane. Another complication is the possibility that a habit plane variant could escape detection if its orientation relative to the specimen surface were such that the surface was not tilted at all or was only tilted through a very small angle.

Notwithstanding this uncertainty in the number of habit plane variants present, the trial and error analysis of the data in Fig. 5(a) leads to the unique result that a variant of the habit plane is associated with that variant of the  $\langle 100 \rangle_B$  pole which lies in the same stereographic triangle. If we denote the variants of the habit plane and precipitate by the indices of the form  $\{1, 10, 12\}_F$  and  $\{1, 1.3, 20\}_F$  respectively, then this result states that a variant of the habit plane at  $(1, 12, 10)_F$  is associated with the variant of the precipitate at  $[1, 20, 1.3]_F$ . The trial and error analysis of the data in Fig. 5(b) leads to two results, one of which is in agreement with the result of Fig. 5(a), and another which

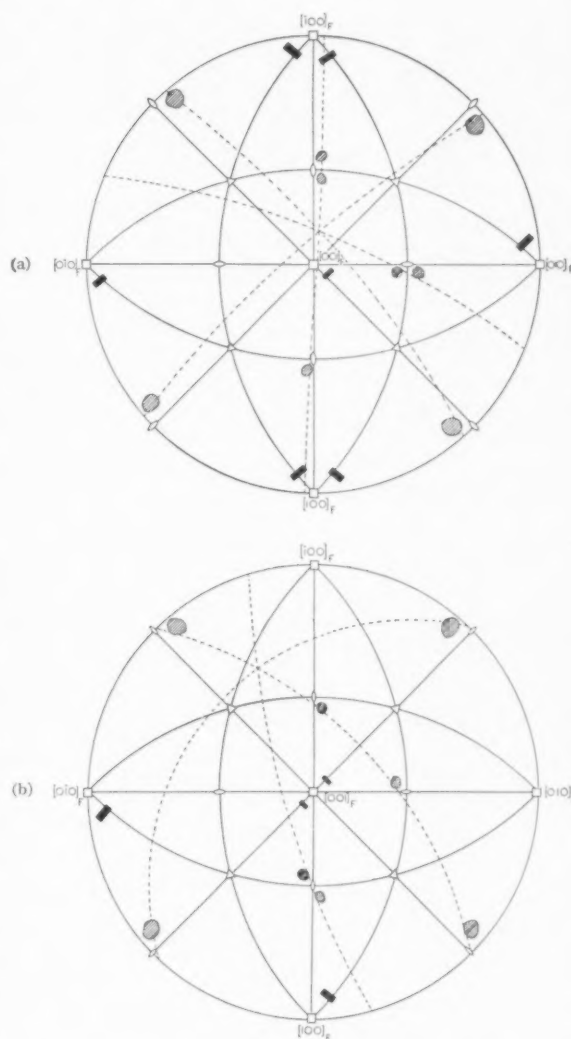


Fig. 5. Stereographic projection of the data obtained to determine the association of variants of the habit plane and variants of the precipitate orientation. The dotted great circles are the normals to the observed traces and the cross-hatched areas are the habit plane variants capable of producing these traces. The filled rectangles indicate the locations where  $\langle 001 \rangle_B$  poles were observed.

states that a variant of the habit plane at  $(1, 12, 10)_F$  is associated with that variant of the  $\langle 100 \rangle_B$  pole at  $[20, 1.3, 1]_F$ . Such a result is not unexpected in view of the uncertainty in the number of habit plane variants present, but agreement of one of the results with the unique result of Fig. 5(a) strongly suggests that this is the correct association.

#### 4. COMPARISON OF THEORY AND EXPERIMENT

In applying the theory of the transformation from face-centered cubic to body-centred cubic lattices<sup>6</sup> to the transformation in copper-beryllium alloys, the assumptions involved are that the lattice correspond-

ence is described by the relation

$$[B; y] = \begin{bmatrix} 1 & 0 & 1 \\ 1 & 0 & 1 \\ 0 & 1 & 0 \end{bmatrix} [F; x] \quad (1)$$

and that the twinning plane (the plane of the slip inhomogeneity) is  $(112)_B$ .

The theory involves a variable parameter  $\theta = (a_B/a_F)\delta$ , where  $a_B$  and  $a_F$  are the lattice parameters of the final and initial structures respectively, and  $\delta$  is a dilatation which must be within a few per cent of unity for the theory to be applicable. The predicted variation of habit plane with  $\theta^2$  is shown in Fig. 6. The first step in applying the theory is to determine  $\theta^2$  by finding that value for which the predicted and observed habit planes agree. Since at this stage it is not known which variant of the experimental habit plane is to be compared with the predicted habit planes, it is assumed provisionally that the experimental habit plane lies in the stereographic triangle  $[010]_F$ ;  $[011]_F$ ;  $[111]_F$ . On this assumption the experimental habit plane agrees well with the predicted habit planes for  $\theta^2 = 0.59$  to  $0.60$ . This assumption will only be justified if the subsequent analysis predicts the association between habit plane and orientation relationship variants that has been found in the present investigation. Specifically the requirement is that the predicted orientation relationship be such that the  $[001]_B$  axis, which is generated from the  $[010]_F$  axis [Eq. (1)] lies in the same triangle as the habit plane. Since this implies that the habit plane lies in a triangle containing  $[010]_F$ , the assumed location of the habit plane is not an impossible one.

Having derived the value of  $\theta^2$  the next step is to see whether the implied value of the unknown dilatation  $\delta$  is close to unity. The values of  $\delta = \theta / (a_B/a_F)$  for  $\theta^2 = 0.59$  and  $\theta^2 = 0.60$  are shown in Table I. The values labelled  $\delta_{\text{actual}}$  have been calculated from the lattice parameters,  $a_F = 3.57\text{\AA}$ ,  $a_B = 2.69\text{\AA}$ ,  $(a_B/a_F)^2 = 0.568$ ,<sup>15</sup> whilst for those labelled  $\delta_{\text{corrected}}$ , an attempt has been made to take into account the possibility that the beryllium

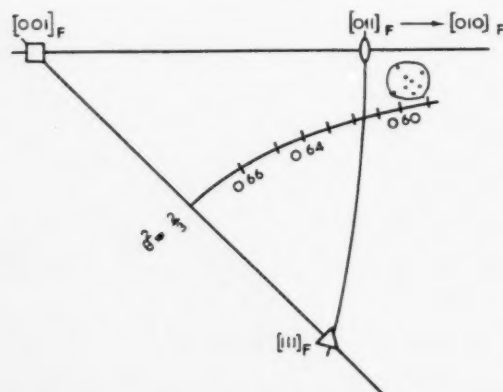


FIG. 6. Stereographic projection showing the predicted variation of habit plane with  $\theta^2$ , and the experimentally determined habit plane region.

TABLE I. Values of  $\delta$  for Cu-Be transformation

	$\theta^2 = 0.59$	$\theta^2 = 0.60$
$\delta_{\text{actual}}$	1.019	1.028
$\delta_{\text{corrected}}$	0.988	0.996

atoms segregate prior to the transformation. For this purpose the relation<sup>16</sup>

$$a_F = (3.608 - 0.003 \times C)\text{\AA} \quad (2)$$

where  $C$  is the concentration of beryllium in atomic per cent, has been used to calculate the value of  $a_F$  for 50 at. % beryllium, whence  $(a_B/a_F)^2 = 0.605$ . All the values of  $\delta$  are within a few per cent of unity, as required, and  $\delta$  could be exactly unity for a critical degree of segregation of beryllium atoms.

The orientation relationship is defined by the theory in terms of an invariant line strain  $S$ . This strain differs from the "total strain"<sup>11</sup> which generates the final lattice in its observed orientation, only by a dilatation  $1/\delta$  which does not affect the orientation relationship. Since equations describing the strain  $S$  were derived earlier,<sup>6</sup> the application of the theory to the copper-beryllium transformation merely involves substituting the derived value of  $\theta$  into these equations. Some simplifications arise in the present case because the axial ratio of the final body-centred lattice is unity and Eqs. (4.7), (4.9) and (4.10) of reference [6] become:

$$\cos \alpha = (2 - 3\theta^2)^{1/2} / \theta, \quad (3)$$

(LSL)

$$= \begin{bmatrix} 1, & -\theta^2 \cos \alpha \sin \omega / 2, & \theta^2 \sin \alpha / 2 \\ 0, & \sqrt{3} \theta^2 \cos \omega, & (\theta^2 \cos \alpha \cos \omega - 2\theta \sin \omega) / \sqrt{3} \\ 0, & \sqrt{3} \theta^2 \sin \omega, & (\theta^2 \cos \alpha \sin \omega + 2\theta \cos \omega) / \sqrt{3} \end{bmatrix} \quad (4)$$

and

$$\cos \omega = (4\theta + 3) / 2\sqrt{3}(1 + \theta). \quad (5)$$

The basis  $L$  to which the strain  $S$  is referred is related to the basis  $F$ , defining the f.c.c. unit cell, by the transformation

$$(LTF) = \begin{bmatrix} \sin \alpha / \sqrt{2}, & -\sin \alpha / \sqrt{2}, & \cos \alpha \\ \cos \alpha / \sqrt{2}, & -\cos \alpha / \sqrt{2}, & -\sin \alpha \\ 1/\sqrt{2}, & 1/\sqrt{2}, & 0 \end{bmatrix}. \quad (6)$$

The values of  $\alpha$  and  $\omega$  for  $\theta^2 = 0.59$  and  $0.60$  are given in Table II.

Of the four possible solutions which can be obtained for (LSL) by combining positive and negative values of  $\alpha$  and  $\omega$ , it is only necessary to consider the  $(\alpha+, \omega+)$

TABLE II. Values of  $\alpha$ ,  $\omega$  and  $k$  for the Cu-Be transformation

	$\theta^2 = 0.59$	$\theta^2 = 0.60$
$\cos \alpha$	0.624364	$1/\sqrt{3}$
$\cos \omega$	0.991433	0.992030
$k(\alpha+, \omega+)$	0.250255	0.276393
$k(\alpha+, \omega-)$	0.749745	0.723607

and  $(\alpha+, \omega-)$  solutions; the other two are variants of these. Further, the  $(\alpha+, \omega-)$  solution involves a much greater fraction,  $k$ , of the twinning shear than the  $(\alpha+, \omega+)$  solution (Table II) and thus might be expected to be less favoured from an energetic point of view. In fact, calculation with the  $(\alpha+, \omega-)$  solution leads to an orientation relationship which is incompatible with the experimental observations and thus we consider only the  $(\alpha+, \omega+)$  solution. The values of  $k$  have been calculated from Eq. (4.15),<sup>6</sup> which in the present case reduces to

$$1 + 2k = (2 - 3\theta^2)^{1/2} (3 - 4\theta^2)^{1/2} / \theta. \quad (7)$$

The  $(\alpha+, \omega+)$  solution for  $\theta^2 = 0.59$  is

$$(\mathbf{L}\mathbf{S}\mathbf{L}) = \begin{bmatrix} 1; & -0.143875; & 0.230434 \\ 0; & 1.013155; & 0.095013 \\ 0; & 0.133476; & 0.907123 \end{bmatrix}. \quad (8)$$

The orientation relationship produced by this strain is most conveniently described by the transformation matrix  $(\mathbf{F}\mathbf{T}\mathbf{B})$  describing the relative positions of the bases  $\mathbf{F}$  and  $\mathbf{B}$ . It follows from Eq. (1) that the axes  $[100]_B$ ,  $[010]_B$  and  $[001]_B$  are generated from  $[101]_F$ ,  $[10\bar{1}]_F$  and  $[010]_F$  respectively. The columns of the matrix  $(\mathbf{F}\mathbf{T}\mathbf{B})$  are therefore unit vectors in the directions  $(\mathbf{F}\mathbf{T}\mathbf{L})(\mathbf{L}\mathbf{S}\mathbf{L})(\mathbf{L}\mathbf{T}\mathbf{F})[101]_F$ , etc. Thus, for  $\theta^2 = 0.59$

$$(\mathbf{F}\mathbf{T}\mathbf{B}) = \begin{bmatrix} 0.694027; & 0.715100; & 0.083419 \\ -0.145274; & 0.025617; & 0.989060 \\ 0.705139; & -0.698553; & 0.121662 \end{bmatrix}. \quad (9)$$

Similarly for  $\theta^2 = 0.60$

$$(\mathbf{F}\mathbf{T}\mathbf{B}) = \begin{bmatrix} 0.691563; & 0.716416; & 0.092133 \\ -0.151348; & 0.019003; & 0.988298 \\ 0.706282; & -0.697414; & 0.121570 \end{bmatrix}. \quad (10)$$

The orientation of  $[001]_B$  relative to the basis  $\mathbf{F}$  is given by the last column of  $(\mathbf{F}\mathbf{T}\mathbf{B})$ . It will be noted that

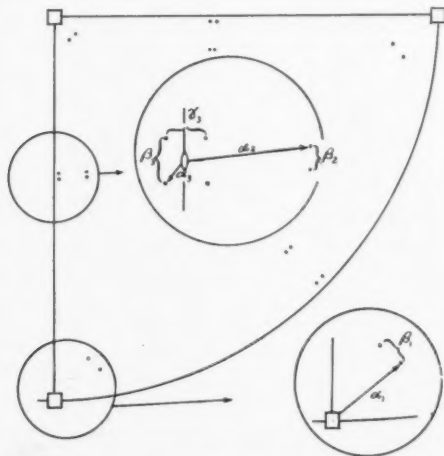


FIG. 7. Stereographic projection of the predicted orientation relationship. The values of the angles indicated are listed in Table III.

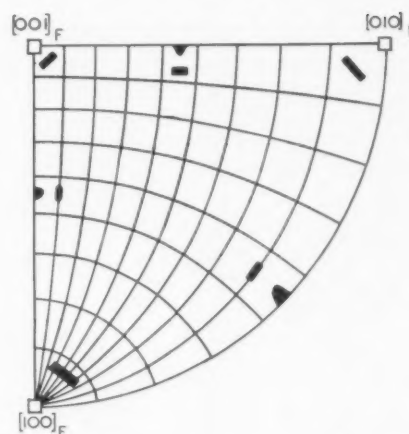


FIG. 8. Stereographic projection showing the orientation relationship determined by Guy.<sup>11</sup> The filled rectangles indicate the locations where  $(001)_B$  poles were observed.

in both cases  $[001]_B$  lies in the stereographic triangle  $[010]_F$ ;  $[011]_F$ ;  $[111]_F$ , thereby confirming the validity of the provisional assumption made earlier. The theory thus predicts the observed association between habit plane variants and variants of the orientation relationship.

The pole figure predicted by the theory is shown in Fig. 7, the numerical values of the angles indicated being given in Table III. For comparison the pole figure determined by Guy<sup>11</sup> using a 1.75 percent beryllium alloy is reproduced in Fig. 8. It can be seen that the predicted orientation relationship reproduces all the essential features of the observed pole figure. Perhaps the most striking feature is the interpretation that is provided for the symmetry of the pole spreading. The arcs in the observed pole figure arise from the merging of groups of two (or four) poles belonging to different variants; this merging can be attributed to plastic deformation in the matrix, for the observed regions of intensity would be reproduced within experimental error if the predicted poles were spread uniformly over a range of about 1 to 1½ degrees. Another possible origin for the pole spreading is variation of  $\theta^2$ . As can be seen from Fig. 7 and Table III, variation of  $\theta^2$  changes the angles of separation of the pairs of poles; this could also account for the lack of precision of the habit plane determination.

TABLE III. Values for the angles of the predicted orientation relationship

Angle	$\theta^2 = 0.59$	$\theta^2 = 0.60$
$\alpha_1$	8.49	8.77
$\beta_1$	3.10	2.39
$\alpha_2$	8.36	8.71
$\beta_2$	0.90	1.20
$\alpha_3$	1.60	1.32
$\beta_3$	1.32	1.53
$\gamma_3$	2.95	2.17



The orientation relationship predicted for  $\theta^2=0.60$  has the property that  $[111]_F \parallel [201]_B$ . This relation was found by Neerfeld and Mathieu<sup>16</sup> in specimens of iron-30 percent nickel and of 18-8 stainless steel, transformed in tension. Neerfeld and Mathieu assumed that the additional relation  $[\bar{1}01]_F \parallel [010]_B$  also held. For the  $\theta^2=0.60$  orientation, these directions are 1.32 degrees apart. It is possible that the orientation studied by Neerfeld and Mathieu was actually that corresponding to  $\theta^2=0.60$ . For this case there is no parallelism of simple rational lattice planes, but the irrational planes  $(1,1,\sqrt{3})_F$  and  $(1+\sqrt{3}, 1-\sqrt{3}, 2)_B$  are parallel.

## 5. DISCUSSION

The present investigation has shown that the geometrical features of the precipitation of CuBe are described consistently by the phenomenological theory that was developed for martensitic transformations. It should be noted that this theory does not impose any restrictions on the transformation mechanism other than the specification of the over-all atomic displacements involved.\* It does not imply that the transformation mechanism involves homogeneous strains nor even that whole planes of atoms are moved without segregation or ordering of solute atoms, as suggested by Geisler.<sup>17</sup>

Recent discussions<sup>8,17,18</sup> of the significance of double strain descriptions in relation to mechanism have been complicated by conflicting interpretations of the nature of the relief effects produced by transformations. Geisler<sup>8</sup> considers that there is no change of shape inherently associated with the lattice transformation, but that the observed change of shape arises as a result of slip caused by transformation stresses. Since transformation stresses presumably arise from an inherent shape change, the view that the relief effects are due both to the inherent shape change and to slip seems much more reasonable. He proposes that the slip simulates a homogeneous strain, and that this strain is responsible for the observed tilting of polished surfaces about their intersections with the habit plane. The only homogeneous strains that can be simulated by slip on a single slip system are shears on the slip plane in the slip direction. Since a simple shear rotates planes about their intersections with the shear plane, surfaces will be rotated about their intersections with the habit plane only when the intersection of habit plane and slip plane lies in the specimen surface. For all other surfaces the martensite plate would become tipped up out of the surface. This limitation can be overcome by invoking double slip, but, since the homogeneous strains involved in the transformation have dilatational components, no combination of slip processes can simulate such strains.

\* Strictly, the phenomenological theory describes the correspondence between lattice points in the initial and final lattices. This correspondence defines the over-all atomic displacements involved in the lattice transformation, but does not include the atomic displacements due to diffusion.

For the relief effects in copper-beryllium, Geisler, Mallery and Steigert<sup>19</sup> favour the interpretation, suggested by Guinier and Jacquet<sup>9,10</sup> that the relief effects result from mechanical slip on the  $\{110\}_F$  planes of the matrix due to the formation of Guinier-Preston zones parallel to the  $\{100\}_F$  planes. They examined the pole figure of Guy and claimed it to be in excellent agreement with the Nishiyama relationship,  $(111)_F \parallel (101)_B$ ;  $[\bar{1}01]_F \parallel [010]_B$ . The discrepancy between the measured angle of approximately 8 degrees for  $\alpha_1$  and the angle of 9.73 degrees, predicted from the Nishiyama relationship, was attributed to experimental error, while the spreading of the poles was regarded as arising from plastic deformation of the matrix, produced by transformation stresses. They proposed that blocks of the matrix become rotated about that  $\langle 110 \rangle_F$  direction lying in the plane of the relief effects. This suggestion is incompatible with the results of the present investigation for it implies that, when the  $[001]_B$  axis lies in the stereographic triangle  $[010]_F$ ;  $[011]_F$ ;  $[111]_F$ , the habit plane is in the neighbourhood of  $(101)_F$ , instead of  $(011)_F$  as determined experimentally.

It is clear that Geisler's proposal, that the relief effects can be attributed to slip alone, is not consistent with observation. Instead, the change in shape produced by the transformation must be regarded as the resultant of the strain describing the distortion of the initial lattice into the final lattice, and the slip inhomogeneity. Such an interpretation of the relief effects is in no way incompatible with Geisler's views on the mechanism of transformations. Geisler pointed out that since relief effects are produced both by diffusion-controlled and martensitic transformations, it is not necessary to postulate any fundamental difference in transformation mechanism to explain their origin. He therefore proposed that the classical mechanism of diffusion-controlled transformations could be extended to cover martensitic transformations. According to this mechanism, the atoms move independently of each other, one at a time, under the influence of thermal activation. To overcome the difficulty that, in some cases at least, the growth of martensite plates seems to be independent of thermal activation, Geisler visualized the atomic movements as being "well organized, one atom pulling the others."<sup>8</sup> Such a mechanism can be reconciled with our interpretation of the relief effects. In the early stages of the growth of the new crystal the individual atomic displacements would simply be those described by the homogeneous strain that converts the initial lattice into the final lattice. At a certain stage of growth the stresses arising from this mode of transformation could produce slip, as Geisler suggests, thus modifying the change of shape caused by the "homogeneous" mode of transformation.

However, there is no evidence that the slip inhomogeneity arises from slip occurring after the generation of the new structure and it is quite possible that the slip inhomogeneity is an inherent feature of the trans-

formation mechanism. Indeed, a mechanism that produces the slipped state directly seems more probable than one that produces a highly stressed product which then slips.

In contrast to Geisler's views, other workers<sup>4,20-22</sup> have attempted to develop growth mechanisms for martensitic transformations in which the atomic displacements are produced by the spontaneous movement of transformation dislocations. The striking similarity between martensitic transformations and mechanical twinning provides strong evidence in favour of such mechanisms. Martensitic transformations and mechanical twinning are both accompanied by homogeneous strains and in both processes the new crystals are plate-shaped and produced in time intervals of the order of a few microseconds; both processes can be induced by plastic deformation and the audible click that accompanies twinning in certain metals is also a feature of many martensitic transformations. These common characteristics suggest that the two processes occur by similar mechanisms. Further, as pointed out by Orowan,<sup>23</sup> the existence of lens-shaped lamellae in twinning (and martensitic transformations) implies the presence of dislocations as a simple geometrical corollary. The amount of shear across a lamella is proportional to its thickness and thus where the thickness changes, even by one lattice spacing, the amount of shear changes discontinuously by a small amount. This discontinuous change must be provided by a dislocation situated at the step. An explanation of mechanical twinning in terms of dislocations has been provided by the "pole mechanism" of Cottrell and Bilby<sup>24</sup> and it seems attractive to consider similar mechanisms for martensitic transformations.<sup>21</sup> In such dislocation mechanisms, it should be possible to include the slip inhomogeneity as an integral feature of the process.

If we accept the hypothesis of a dislocation mechanism for martensitic transformation then, with a view to developing a general theory applicable both to diffusion-controlled and martensitic transformations, it becomes of interest to consider the possibility that diffusion-controlled transformations also occur by a dislocation mechanism. On the existing evidence there is no reason to reject this possibility. If a dislocation mechanism is operative in martensitic transformations in which the plates grow very rapidly, then the propagation of the transformation dislocations must occur spontaneously. However, this is not an essential feature of a dislocation mechanism and there is no reason why the propagation of transformation dislocations should not be spontaneous in some transformations and require thermal activation in others. If

thermal activation is required the rate of growth will be a function of temperature and the new crystals will grow at an observable rate. In precipitations, where a change of composition is involved, a further possibility exists for here it is possible that the rate of propagation of the transformation dislocations is governed by the rate at which the required concentration of solute atoms can be assembled at the advancing interface.

The concept of a common dislocation mechanism for diffusion-controlled and martensitic transformations leads to a ready interpretation of the results of the present investigation. If the geometry of the atomic processes involved in the two kinds of transformation is the same, then it is not surprising that the phenomenological theory developed for martensitic transformations should be capable of predicting the geometrical features of a typical diffusion-controlled transformation like the precipitation of CuBe.

This speculation concerning the possible role of dislocation mechanisms in diffusion-controlled transformations is, of course, intended to apply only to the early stages of growth (the so-called stage of "coherent" growth). After a non-coherent interface has been produced, growth can occur by the accretion of individual atoms and the shape assumed by the growing crystal will be determined mainly by considerations of interfacial energy.

#### REFERENCES

1. J. S. Bowles and J. K. Mackenzie, *Acta Met.* **2**, 129 (1954).
2. J. K. Mackenzie and J. S. Bowles, *Acta Met.* **2**, 138 (1954).
3. M. S. Wechsler, D. S. Lieberman and T. A. Read, *Trans. A.I.M.E.* **197**, 1503 (1953).
4. H. Suzuki, *Sci. Rep. R.I.T.U.* **A6**, 30 (1954).
5. J. S. Bowles and C. S. Barrett, *Progress in Metal Physics* **3**, 1 (1952).
6. J. S. Bowles and J. K. Mackenzie, *Acta Met.* **2**, 224 (1954).
7. L. Northcott, *J. Inst. Met.* **59**, 225 (1936).
8. A. H. Geisler, *Acta Met.* **1**, 260 (1953).
9. A. Guinier and P. A. Jacquet, *Rev. Met.* **41**, 1 (1944).
10. A. Guinier and P. A. Jacquet, *Nature* **155**, 695 (1945).
11. A. G. Guy, *Gen. Elec. Rev.* **49**, 28 (Aug. 1946).
12. A. G. Guy, C. S. Barrett and R. F. Mehl, *Trans. A.I.M.E.* **175**, 216 (1948).
13. J. S. Bowles, *Trans. A.I.M.E.* **191**, 44 (1951).
14. C. S. Barrett, *Structure of Metals*, 2nd ed. (London, McGraw-Hill, 1953), p. 42.
15. S. Miyatani, *J. Phys. Soc. Japan* **4**, 181 (1949).
16. H. Neerfeld and K. Mathieu, *Arch. Eisenh.* **20**, 69 (1949).
17. A. H. Geisler, *Acta Met.* **2**, 639 (1954).
18. Z. S. Basinski and J. W. Christian, *Acta Met.* **1**, 759 (1953).
19. A. H. Geisler, J. H. Mallery and F. E. Steigert, *Trans. A. I. M. E.* **194**, 307 (1952).
20. M. Cohen, E. S. Machlin and V. G. Paranjpe, *Thermodynamics in Physical Metallurgy* (Cleveland, Ohio, A. S. M., 1950), p. 242.
21. B. A. Bilby, *Phil. Mag.* **44**, 782 (1953).
22. Z. S. Basinski and J. W. Christian, *Phil. Mag.* **44**, 791 (1953).
23. E. Orowan, *Dislocations in Metals* (New York, A.I.M.E., 1954), p. 116.
24. A. H. Cottrell and B. A. Bilby, *Phil. Mag.* **42**, 573 (1951).

# THE HEATS OF FORMATION OF SOME TRANSITION METAL SILICIDES\*

D. A. ROBINS and I. JENKINS†

A method is described for determining the heats of formation of highly stable metal silicides and data are given for the following compounds:— $\text{Ti}_5\text{Si}_3$ ,  $\text{TiSi}$ ,  $\text{TiSi}_2$ ,  $\text{Zr}_5\text{Si}_3$ ,  $\text{ZrSi}$ ,  $\text{ZrSi}_2$ ,  $\text{ThSi}_2$ ,  $\text{V}_5\text{Si}_3$ ,  $\text{Ta}_5\text{Si}_3$ ,  $\text{TaSi}_2$ ,  $\text{MoSi}_2$ , and  $\text{WSi}_2$ . The highest heats of formation are those of compounds containing Group IVa metals and, in general, the disilicides are not as stable as compounds containing a lower percentage of silicon. An analysis of the bond lengths in the disilicides is carried out and a comparison is made between the heats of formation data and changes in the character of the metal bonding.

## CHALEURS DE FORMATION DE QUELQUES SILICIURES DES MÉTAUX DE TRANSITION

Il est décrit une méthode pour la détermination des chaleurs de formation de siliciures très stables et les valeurs correspondant aux composés suivants sont données:  $\text{Ti}_5\text{Si}_3$ ,  $\text{TiSi}$ ,  $\text{TiSi}_2$ ,  $\text{Zr}_5\text{Si}_3$ ,  $\text{ZrSi}$ ,  $\text{ZrSi}_2$ ,  $\text{ThSi}_2$ ,  $\text{V}_5\text{Si}_3$ ,  $\text{Ta}_5\text{Si}_3$ ,  $\text{TaSi}_2$ ,  $\text{MoSi}_2$  et  $\text{WSi}_2$ . Les chaleurs de formation les plus élevées correspondent aux métaux du groupe IVa et, en général, les disiliciures ne sont pas aussi stables que les composés comportant un pourcentage plus faible de silicium. La longueur de la liaison dans les disiliciures est étudiée et les chaleurs de formation sont comparées aux changements dans le caractère de la liaison des atomes de métal.

## DIE BILDUNGSWÄRMEN EINIGER SILIZIDE VON ÜBERGANGSMETALLEN

Zur Bestimmung der Bildungswärmen von sehr stabilen Metallsiliziden wird eine Methode beschrieben. Für folgende Verbindungen werden die Ergebnisse mitgeteilt:  $\text{Ti}_5\text{Si}_3$ ,  $\text{TiSi}$ ,  $\text{TiSi}_2$ ,  $\text{Zr}_5\text{Si}_3$ ,  $\text{ZrSi}$ ,  $\text{ZrSi}_2$ ,  $\text{ThSi}_2$ ,  $\text{V}_5\text{Si}_3$ ,  $\text{Ta}_5\text{Si}_3$ ,  $\text{TaSi}_2$ ,  $\text{MoSi}_2$  und  $\text{WSi}_2$ . Die höchsten Bildungswärmen haben Verbindungen, die Metalle der Gruppe IVa enthalten. Die Disilizide sind im allgemeinen nicht so stabil wie die Verbindungen mit einem niedrigeren Siliziumgehalt. Eine Analyse der Bindungslänge in Disiliziden und ein Vergleich zwischen den Bildungswärmen und den Veränderungen im Charakter der metallischen Bindung werden durchgeführt.

## 1. INTRODUCTION

The increasing need for materials having high strength at elevated temperatures has directed attention to the high melting point carbides, borides and silicides of the transition metals. Little information is available, however, on the basic properties and characteristics of many of these compounds and particularly is this the case for borides and silicides.

The present paper describes a method which has been developed for the determination of the heats of formation of these compounds from their elements when the reaction is highly exothermic. The silicides which are likely to be of greatest interest are those of the metals in Groups IVa, Va and VIa of the periodic table and approximate values for the heats of formation of a number of these compounds have been obtained.

## 2. EXPERIMENTAL WORK

Preliminary work had shown that when a bar composed of a mixture of molybdenum and silicon powders, in the proportions corresponding to  $\text{MoSi}_2$ , was heated at one end so that the powders reacted, the heat produced was sufficient to promote reaction in the adjacent portion of the bar. By this means the whole bar could be converted into the disilicide. The property of highly exothermic reactions of this type to be self-propagating has been used in the present investigation for the measurement of the heats of formation of a number of metal silicides.

\* Received April 6, 1955.

† Communication from the Staff of the Research Laboratories of The General Electric Company, Ltd., Wembley, England.

## 2.1. Materials

The silicon powder used in the present investigation had been prepared from a 50/50 silicon-aluminium alloy which was crushed to powder and the aluminium extracted with 50 per cent hydrochloric acid. The major impurity was aluminium (0.1 per cent), and traces of boron and iron were each less than 0.01 per cent.

The various metals used in the preparation of the silicides were all in the form of powder and, with the exception of thorium, the impurity content in every case was less than 0.5 per cent. The thorium contained 98.7 per cent thorium, 0.15 per cent iron, a trace of silicon and the balance thorium oxide. The titanium and zirconium powders were prepared from the corresponding hydride, the degassing treatment being carried out just prior to their use. The niobium powder contained traces of the elements C, Ta, Ti, Si and Fe, and the chromium powder had been prepared electrolytically and was given a degassing treatment. The molybdenum and tungsten powders were of the quality used in the lamp and valve industries (less than 0.1 per cent impurity).

## 2.2. Apparatus

The reaction chamber, which is shown in Fig. 1, consisted of an outer steel cylinder closed at one end; into the opposite end was screwed a steel plug from which was suspended a steel base plate. A compacted rondel of mixed metal and silicon powder (approx. 10 mm dia and 20 mm high and pressed at about 20 tons/sq in.) was weighed and supported on the steel base by a thin disc of the same mixture which had already been

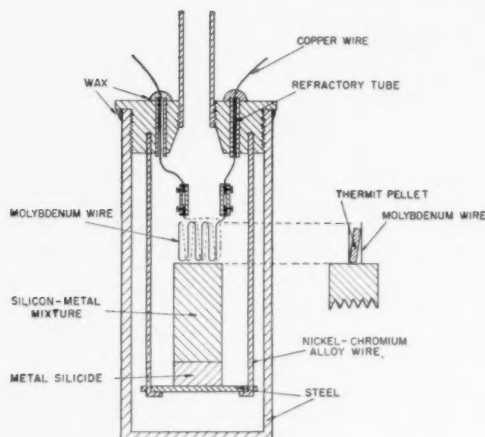


FIG. 1. The reaction chamber.

reacted. In this way, the metal silicon mixture was prevented from coming into contact with any material with which it might react. A coil heater, made from 0.2 mm dia molybdenum wire, was suspended just above the top of the compact and a weighed pellet, 8 mm in diameter, of a mixture of degassed chromium oxide and aluminium powder (thermit mixture) was placed inside the coil, which itself was connected to an outside electrical source. The reaction chamber was made vacuum tight using a fixed quantity of wax (1 g) and could be evacuated to a pressure of  $10^{-4}$  mm of mercury via a glass tap placed immediately above the reaction chamber. A Dewar flask filled with 600 mls of water at a temperature of 1–2 degrees below that of the temperature of the room was placed around the reaction chamber and temperature changes were followed using a Beckman thermometer.

In order to remove sources of error, the top of the Dewar flask was enclosed with an asbestos cover during each experiment, the stirrer was run at a constant speed and the positions of the stirrer, thermometer and reaction chamber in relation to the water level remained unaltered.

### 2.3. Technique

The reaction chamber, containing a weighed compact of mixed powders in the proportions to form a given metal silicide, was evacuated. After stirring the water in the Dewar flask for one-half hour, the rate of the rise in temperature, due to gain of heat from the room, was determined. The glass tap was then closed and a current was passed through the molybdenum heater. The current flowing and the potential across the heater were measured on calibrated instruments, as also was the time during which the current flowed. From this information the heat added to the system by the heater could be determined. This heat was sufficient to ignite the thermit pellet which, in turn, melted the molybdenum heater, thus breaking the electrical

circuit. The high temperature produced locally was sufficient to initiate reaction of the pressed compact of mixed powders and this reaction then proceeded throughout the whole compact. To facilitate the rapid dispersion of the heat produced, two seconds after the breaking of the electrical circuit 99.8 per cent argon was added to the reaction chamber through the glass tap until atmospheric pressure was reached, the tap then being closed. Temperature readings were taken throughout the experiment (Fig. 2) and from these results the temperature rise, produced by the combined effects of the electric current, thermit mixture and the reaction under examination, was found.

The heat of formation of a given silicide could be determined, knowing the heat of reaction of the thermit mixture, the weight of the thermit pellet, the electrical energy added, the weight of the metal-silicon compact under examination, the water equivalent of the apparatus and the rise in temperature produced during an experiment.

The method of measurement of the heat of formation so far described was only applicable to a limited number of the silicides of the metallic elements under examination since, in many cases, the heat liberated on reaction was not sufficient to ensure that the whole of the compact was converted to the silicide. In order to extend the measurements to silicides which had lower heats of formation, the method was modified where necessary in the following way. In place of the single rondel of metal-silicide mixture previously used composite rondels

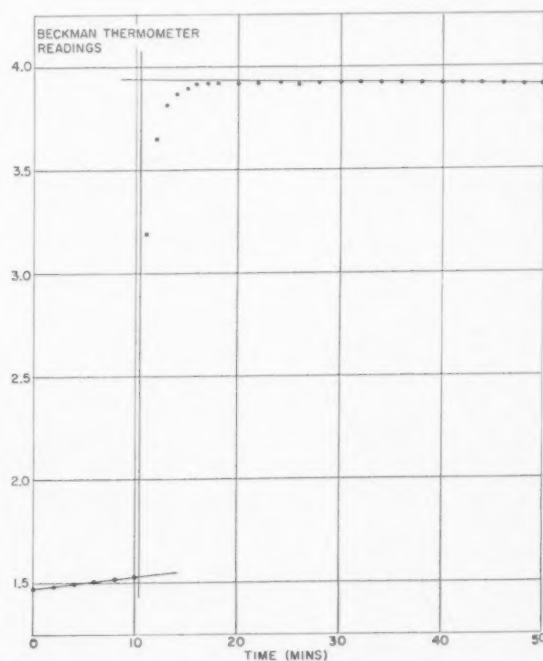


FIG. 2. Typical temperature/time curve from which the corrected temperature rise was obtained. Room temperature, 22.1°C; starting temperature, 20.8°C; corrected temperature rise, 2.415°C.



were prepared. A compact of metal-silicon mixture approx. 8.0 mm dia and 15 mm high was pressed from the material under examination and weighed. This compact was then surrounded by pressed zirconium-silicon mixture of the composition 79.6 per cent zirconium, 20.4 per cent silicon by weight which, according to Lundin, McPherson and Hansen,<sup>1</sup> corresponded to the compound  $Zr_6Si_5$ . This composite pellet was weighed and set up in the apparatus as previously described, the high heat of reaction of the Zr/Si mixture, which had been determined independently (Table III), ensuring that the inner compact reacted completely. Knowing the heat produced by the Zr/Si mixture in addition to that by the thermit pellet and the molybdenum heater, the heat due to the silicide under examination could be calculated. No difficulty was experienced in removing the outer shell for an examination of the inner silicide, there being little adhesion between the two zones after reaction.

#### 2.4. Calibration of Apparatus

To determine the water equivalent of the apparatus, it was assembled as for a heat of formation determination except that no thermit pellet was included and in place of a metal-silicon compact a reacted compact of Zr/Si was substituted. A known current was passed through the molybdenum heater for a measured time whilst the chamber was under a static vacuum and then argon was added as previously described. Knowing the electrical energy added and the rise in temperature of the system which this produced (taken from a graph of the temperature changes), the water equivalent of the system was calculated and found to be 695 mls (Table I). Any changes in the water equivalent of the apparatus in different experiments, due to small differences in size of the compacts examined and variations in the specific heats of the silicides, were considered to be negligible.

Some difficulty was experienced in preparing a thermit mixture suitable to operate under high vacuum conditions since, if a comparatively unstable metal oxide was used then, on reaction, the pellet disintegrated due to the decomposition of the oxide. An oxide of low stability was necessary, however, to give a heat of reaction with aluminium high enough to initiate the metal silicon reaction.  $Cr_2O_3$  degassed at 800°C *in vacuo* before use was found to work satisfactorily provided excess aluminium was present above that neces-

TABLE I. The water equivalent of the apparatus

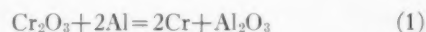
Temp. rise (°C.)	Elec. energy added (cal.)	∴ Water eq. (ml.)
1.21	848	701
1.27	885	696
2.45	1690	690
4.23	2935	694
1.67	1156	692
Average of 695		

TABLE II. The heat of reaction of the thermit mixture

Temp. rise (°C)	∴ Total heat evolved (cal.)	Elec. energy added (cal.)	∴ Heat from thermit (cal.)	Wt. of thermit (g.)	∴ Heat of re- action (cal./g.)
1.165	812	157	655	1.157	566
1.72	1195	433	762	1.357	562
1.30	903	78	825	1.460	565
2.26	1561	103	1458	2.573	567
Average value—565					

sary to form  $Al_2O_3$  so that on reaction a molten pellet was readily produced. The composition of the mixture used was 66.4 per cent by weight of  $Cr_2O_3$  and 33.6 per cent by weight of aluminium powder which had been degassed at 300°C in a vacuum prior to use, i.e., 90 per cent  $(Cr_2O_3 + 2Al) + 10$  per cent Al. The heat of reaction of the mixture prepared by grinding the constituents together was measured in the apparatus already described, the reaction being started by passing a current through a molybdenum heater containing a small weighted pellet of thermit mixture. This pellet was resting upon a larger pressed and weighed compact of thermit mixture and the heat produced from the known quantity of reactants was measured.

The heat produced by the thermit mixture was found to be 565 cal/g (Table II). The heats of formation of  $Cr_2O_3$  and  $Al_2O_3$  are 269.5 and 400 kcal/g mol respectively<sup>2</sup> and therefore the heat of reaction corresponding to the equation:



is 130.5 kcal/g mol. This value is in good agreement with the heat of reaction of the thermit mixture, the value 565 cal/g being equivalent to 129 kcal/g mol, assuming that the excess aluminium does not take part in the reaction.

#### 3. EXPERIMENTAL RESULTS

The heats of formation of various metal silicides determined in this investigation are summarized in Table III. Data obtained during the determination of

TABLE III. Heat of formation values

Compound	Method used*	Heat of formation						
		kcal/g mol X(-1)			kcal/g atom Si X(-1)			
					Average			
Ti <sub>2</sub> Si <sub>3</sub>	A	137	140	139	45.7	46.7	46.3	46.2
TiSi	A	30.9	31.1	31.3	30.9	31.1	31.3	31.0
TiSi <sub>2</sub>	A	32.0	32.0	32.8	16.0	16.0	16.4	16.1
Zr <sub>2</sub> Si <sub>3</sub>	A	147	146	147	49.0	48.7	49.0	48.8
"ZrSi <sub>2</sub> "	A	205	204	201	41.0	40.8	40.2	40.7
		201	205	204	40.2	41.0	40.8	
ZrSi	A	35.1	35.3	35.4	35.1	35.3	35.4	35.3
ZrSi <sub>2</sub>	A	35.0	37.0	35.4	17.5	18.5	17.7	17.9
ThSi <sub>2</sub>	B	42.5	42.6	39.9	21.2	21.3	20.0	20.8
V <sub>2</sub> Si	B	35.8	40.0	35.0	35.8	40.0	35.0	36.9
Ta <sub>2</sub> Si <sub>3</sub>	B	78.7	74.1	74.7	26.2	24.7	24.9	25.3
TaSi <sub>2</sub>	B	26.6	28.7	27.9	13.3	14.5	14.0	13.9
"MoSi <sub>2</sub> "	B	45.7	46.9	47.9	22.9	23.5	23.9	23.4
MoSi <sub>2</sub>	A	31.2	31.6	31.2	15.6	15.8	15.6	15.7
WSi <sub>2</sub>	B	22.3	20.1	24.4	11.2	10.1	12.2	11.2

\* A no zirconium-silicon shell around compact. B compact enclosed in zirconium-silicon mixture ("ZrSi<sub>2</sub>").

TABLE IV. Typical data obtained during heat of formation experiments

Silicide under exam.	Temp. rise (°C)	Total heat evolved (cal)	Elec. energy (cal)	Heat from thermit (cal)	Heat from "ZrSi <sub>3</sub> shell (cal)	Heat from silicide (cal)	Wt. of spec. (g)	Heat of formation (kcal/g mol)
Ti <sub>5</sub> Si <sub>3</sub>	3.16	2200	57	93	—	2050	4.832	137
Ti <sub>5</sub> Si <sub>3</sub>	3.65	2540	56	62	—	2422	3.592	140
Ti <sub>5</sub> Si <sub>3</sub>	2.80	1946	57	20	—	1869	4.343	139
V <sub>2</sub> Si	1.945	1352	61	38	803	450	1.633	35.8
V <sub>2</sub> Si	2.24	1557	64	39	978	476	1.545	40.0
V <sub>2</sub> Si	2.44	1696	137	13	995	551	2.049	35.0

the heats of formation of Ti<sub>5</sub>Si<sub>3</sub> and V<sub>2</sub>Si are given in Table IV as typical of the quantities of heat evolved at each stage of the experiment.

Attempts were made to determine the heats of formation of a number of silicides not included in Table III but, due to the lower reactivity of the metal-silicon mixture, complete reaction could not be obtained without using a disproportionately large amount of zirconium-silicon mixture in the following cases: VSi<sub>2</sub>, Nb<sub>2</sub>Si, NbSi<sub>2</sub>, Cr<sub>3</sub>Si, CrSi<sub>2</sub>, W<sub>3</sub>Si<sub>2</sub>. It is possible that in the case of the chromium silicides that their low melting points prevented the reactions from proceeding throughout the body of the pressed compact.

An examination of the silicides formed was carried out by taking X-ray diffraction photographs of the powders; the results are summarized in Table V. In all cases, except for Zr<sub>5</sub>Si<sub>3</sub>, Mo<sub>3</sub>Si<sub>2</sub> and possibly ZrSi, the purity of the silicides formed suggested that the values obtained for their heats of formation are at least approximately correct. The thorium oxide detected in the thorium disilicide sample was already present in the thorium powder used in its preparation. Conflicting data on the silicides present in the zirconium-silicon system have been published<sup>1,3</sup> and it is interesting to note that the purity of the compound corresponding to the composition Zr<sub>6</sub>Si<sub>5</sub> was greater than that corresponding to ZrSi. The major phase produced in each case was identical however, and corresponded to the data

given for ZrSi.<sup>3</sup> It seems possible, therefore, that this compound contains less silicon than the proposed formula would suggest.

A source of slight error was the formation of an extremely thin yellow-brown deposit on the walls of the reaction chamber after each experiment. No loss in weight of the compounds could be detected after reaction, but X-ray examination showed the film to be silicon monoxide produced, presumably, either by the combination of silicon with oxygen from the decomposition of Cr<sub>2</sub>O<sub>3</sub> or from an oxide film already present on the silicon powder.

The reproducibility and accuracy of the results obtained for very exothermic reactions is considerably greater than for those reactions where composite compacts were used since, in the latter case, the heat produced by the silicide under examination was only a small part of the total heat evolved (Table IV). Any error introduced due to the corrections applied for the electrical energy added and the heat from the thermit pellet are considered to be very small.

#### 4. HEATS OF FORMATION AND BOND LENGTHS

It can be seen that the heat of formation of the disilicides increases with increasing atomic weight in the Groups IVa and Va of the periodic table but not in Group VIa where molybdenum disilicide has the

TABLE V. X-ray examination of reacted compacts

Nominal composition (Wt. %)	Compound expected	Phases found
Metal Silicon		
74.0	Ti <sub>5</sub> Si <sub>3</sub>	Only Ti <sub>5</sub> Si <sub>3</sub> detected
63.1	TiSi	TiSi + a trace of TiSi <sub>2</sub>
46.1	TiSi <sub>2</sub>	TiSi <sub>2</sub> + traces of TiSi and silicon
84.4	Zr <sub>5</sub> Si <sub>3</sub>	Zr <sub>5</sub> Si <sub>3</sub> + 10 to 20% additional phases
79.6	Zr <sub>6</sub> Si <sub>5</sub>	Compound corresponding to data published for ZrSi <sup>3</sup>
76.5	ZrSi	Compound corresponding to data published for ZrSi <sup>3</sup> + up to 10% ZrSi <sub>2</sub>
61.9	ZrSi <sub>2</sub>	ZrSi <sub>2</sub> + a trace of silicon
80.5	ThSi <sub>2</sub>	Mainly ThSi <sub>2</sub> and some ThO <sub>2</sub>
78.4	V <sub>2</sub> Si	One unidentified predominant phase
91.5	Ta <sub>5</sub> Si <sub>3</sub>	Ta <sub>5</sub> Si <sub>3</sub> + trace of other phases
76.3	TaSi <sub>2</sub>	Only TaSi <sub>2</sub> detected
83.7	Mo <sub>3</sub> Si <sub>2</sub>	MoSi <sub>2</sub> + Mo <sub>3</sub> Si <sub>2</sub> + molybdenum
63.1	MoSi <sub>2</sub>	MoSi <sub>2</sub> + slight trace of Mo <sub>3</sub> Si <sub>2</sub>
76.6	WSi <sub>2</sub>	Only WSi <sub>2</sub> detected

TABLE VI. Crystal structure of disilicides

Silicide	Crystal system	$a_0$	Lattice parameters A $b_0$	$c_0$	Atomic positions	Ref. No.
TiSi <sub>2</sub>	ortho-rhombic	8.236	4.773	8.523	Ti(8): (0,0,0; $\frac{1}{2}, \frac{1}{2}, 0$ ; $\frac{1}{2}, 0, \frac{1}{2}$ ; $0, \frac{1}{2}, \frac{1}{2}$ ) + 0,0,0; $\frac{1}{4}, \frac{1}{4}, \frac{1}{4}$ . Si(16): (0,0,0; $\frac{1}{2}, \frac{1}{2}, 0$ ; $\frac{1}{2}, 0, \frac{1}{2}$ ; $0, \frac{1}{2}, \frac{1}{2}$ ) + $x, 0, 0$ ; $x, 0, 0$ ; $\frac{1}{4} + x, \frac{1}{4}, \frac{1}{4}$ ; $\frac{1}{4} - x, \frac{1}{4}, \frac{1}{4}$ . ( $x = 4/12$ )	(8)
ZrSi <sub>2</sub>	ortho-rhombic	3.72	14.61	3.67	Zr(4): $0, y, \frac{1}{4}$ ; $0, \bar{y}, \frac{3}{4}$ ; $\frac{1}{2}, \frac{1}{2} + y, \frac{1}{2}, \frac{1}{2} - y, \frac{3}{4}$ . $y = 0.104$ Si(8) $y$ for Si' = 0.439 $y$ for Si'' = 0.750	(9) (13)
VSi <sub>2</sub>	hexagonal	4.562		6.359	V(3): $\frac{1}{2}, 0, 0$ ; $0, \frac{1}{2}, \frac{1}{2}$ ; $\frac{1}{2}, \frac{1}{2}, \frac{2}{3}$ . Si(6): $x, 2x, 0$ ; $2\bar{x}, x, \frac{1}{3}$ ; $x, x, \frac{2}{3}$ ; $\bar{x}, 2\bar{x}, 0$ ; $2x, x, \frac{1}{3}$ ; $\bar{x}, x, \frac{2}{3}$ . ( $x = 1/6$ )	(8)
NbSi <sub>2</sub>	hexagonal	4.785		6.576	As for VSi <sub>2</sub>	(8)
TaSi <sub>2</sub>	hexagonal	4.773		6.552	As for VSi <sub>2</sub>	(8) (10)
CrSi <sub>2</sub>	hexagonal	4.422		6.351	As for VSi <sub>2</sub>	(8)
MoSi <sub>2</sub>	tetragonal	3.200		7.861	Mo(2) 0,0,0; $\frac{1}{2}, \frac{1}{2}, \frac{1}{2}$ . Si(4) 0,0, $x$ ; 0,0, $\bar{x}$ ; $\frac{1}{2}, \frac{1}{2}, \frac{1}{2} + x$ ; $\frac{1}{2}, \frac{1}{2}, \frac{1}{2} - x$ ( $x = 1/3$ )	(8)(11) (12)
WSi <sub>2</sub>	tetragonal	3.212*		7.831*	As for MoSi <sub>2</sub>	(8) (11) (12)

\* Due to conflicting data in the literature on the lattice constants of WSi<sub>2</sub>, the values for the sample prepared in this investigation were accurately determined and found to be:  $a = 3.2123 \pm 0.0005\text{Å}$ ,  $c = 7.8313 \pm 0.0005\text{Å}$ .

highest value. There is also, in general, a decrease in stability in going from Group IVa to VIa. An attempt has been made to correlate these results with the available structural data on the disilicides.

From published information concerning the atomic positions of the silicon and metal atoms in the crystal lattice (Table VI), the length and number of the bonds between metal-metal atoms, metal-silicon atoms and

TABLE VII. The number and length of the bonds between atoms in the disilicides

Silicide	Metal-metal bonds		Metal-silicon bonds		Silicon-metal bonds		Silicon-silicon bonds	
	No.	Length Å	No.	Length Å	No.	Length Å	No.	Length Å
TiSi <sub>2</sub>	4	3.194	6 4	2.750 2.535	3 2	2.750 2.535	3 2	2.750 2.535
ZrSi <sub>2</sub>	2	3.55	2(Si') 4(Si') 4(Si'')	3.04 2.69 2.82	2(Si') 4(Si') 4(Si'')	3.04 2.69 2.82	2(Si') 4(Si') 4(Si'')	2.55 3.34 2.61
VSi <sub>2</sub>	4	3.114	6 4	2.634 2.496	3 2	2.634 2.496	3 2	2.634 2.496
NbSi <sub>2</sub>	4	3.245	6 4	2.764 2.591	3 2	2.764 2.591	3 2	2.764 2.591
TaSi <sub>2</sub>	4	3.233	6 4	2.756 2.582	3 2	2.756 2.582	3 2	2.756 2.582
CrSi <sub>2</sub>	4	3.061	6 4	2.554 2.472	3 2	2.554 2.472	3 2	2.554 2.472
MoSi <sub>2</sub>	4	3.200	10	2.616	5	2.616	5	2.616
WSi <sub>2</sub>	4	3.212	10	2.618	5	2.618	5	2.618

TABLE VIII. Bond numbers calculated from the bond lengths

Silicide	Metal-metal bonds			Metal-silicon bonds			Silicon-metal bonds			Silicon-silicon bonds		
	No. of bonds	Bond No.	total bond No.	No. of bonds	Bond No.	total bond No.	No. of bonds	Bond No.	total bond No.	No. bonds	Bond No.	total bond No.
TiSi <sub>2</sub>	4	.12	.5	6	.38	5.7	3	.38	2.8	3	.21	1.6
				4	.87		2	.87		2	.49	
ZrSi <sub>2</sub>	2	.08	.2	2(Si')	.20	5.4	2(Si')	.20	3.5	2(Si')	.46	1.0
				4(Si')	.78		4(Si')	.78		4(Si')	.02	
				4(Si'')	.48		4(Si'')	.48	1.9	4(Si'')	.36	1.4
VSi <sub>2</sub>	4	.08	.3	6	.40	5.1	3	.40	2.5	3	.42	2.4
				4	.68		2	.68		2	.56	
NbSi <sub>2</sub>	4	.12	.5	6	.38	5.3	3	.38	2.6	3	.20	1.4
				4	.75		2	.75		2	.39	
TaSi <sub>2</sub>	4	.12	.5	6	.40	5.4	3	.40	2.7	3	.21	1.4
				4	.78		2	.78		2	.40	
CrSi <sub>2</sub>	4	.07	.3	6	.46	5.2	3	.46	2.6	3	.45	2.5
				4	.63		2	.63		2	.62	
MoSi <sub>2</sub>	4	.09	.4	10	.56	5.6	5	.56	2.8	5	.35	1.8
WSi <sub>2</sub>	4	.09	.4	10	.57	5.7	5	.57	2.9	5	.35	1.8

silicon-silicon atoms have been calculated (Table VII).

For covalent and metallic bonding, Pauling has proposed the following empirical formula relating variations in bond length with the number of shared electron pairs making up that bond (bond number):<sup>4</sup>

$$R_1 - R_n = 0.3 \log n \quad (2)$$

where  $n$  is the bond number,  $R_1$  and  $R_n$  are the bond lengths for bond numbers of 1 and  $n$  respectively. Using this formula, together with values of the single bond radius calculated by Pauling,<sup>4</sup> the bond numbers corresponding to the various bond lengths have been calculated. By summation the apparent total valency of the individual atoms have been found (Table VIII).

The results show that there is little or no bonding between metal atoms in the disilicides examined, the metal-metal bonding in the metal prior to combination with silicon having been replaced by strong metal-silicon bonding. It is also apparent that the calculated values for the valency of the metal atoms are all in the range 5-6 and are often not in keeping with their accepted valencies. This would suggest that the nature of the bond in the pure metal from which the single bond radius has been calculated is different from that formed in the disilicide. The silicon-silicon bond distances are considered to be determined very largely by the stronger metal-silicon bonding.

The relationship between the calculated values for the apparent valency of the metal atoms in the disilicides and the heat of formation data will be considered in more detail. The results being compared are summarized in Table IX which also contains approximate limits for the heats of formation of the less stable disilicides

estimated from the lack of reactivity of the metal-silicon mixtures.

Consider firstly TiSi<sub>2</sub>. The apparent valency of 5.7 for the titanium atoms in TiSi<sub>2</sub> has been calculated from Eq. (2) using the value of 1.324 Å for the single bond radius as given by Pauling for metallic Ti<sup>4</sup>. Since the maximum possible valency for Ti is four, it is apparent that the character of the bonding in the disilicide is different from that in the metal. Let the true single bond radius of titanium in TiSi<sub>2</sub> be  $R_1'$  and the bond numbers corresponding to the bond lengths 2.750 Å and 2.535 Å (Table VII) be  $A$  and  $B$  respectively then from (2).

$$R_1' = 0.3 \log A + R_A = 0.3 \log B + R_B \quad (3)$$

Also to fulfil the valency conditions (Table VII)

$$6A + 4B = 4 \quad (4)$$

TABLE IX

Silicide	Heat of formation (kcal/g mol of SiX(-1))	Apparent total valency of metal atoms (from Table VIII)	Max. number of bonding electrons
TiSi <sub>2</sub>	16.1	5.7	4
ZrSi <sub>2</sub>	17.9	5.4	4
VSi <sub>2</sub>	Less than c. 10	5.1	5
NbSi <sub>2</sub>	Less than c. 12	5.3	5
TaSi <sub>2</sub>	15.9	5.4	5
CrSi <sub>2</sub>	Probably less than 12	5.2	6
MoSi <sub>2</sub>	15.7	5.6	6
WSi <sub>2</sub>	11.2	5.7	6



Solving Eqs. (3) and (4)

$$A = 0.264 \quad B = 0.603 \quad R_1' = 1.202A$$

As an alternative approach to that of assuming a constant value for the single bond radius for the different bond lengths, it has been assumed that the bond numbers are simple fractions.<sup>5</sup> Using values of  $\frac{1}{3}$  and  $\frac{1}{2}$  corresponding to bond lengths of 2.750 and 2.535 Å then the single bond radius,  $R_1$ , is found to be 1.271 and 1.182 Å respectively and it can be seen that the value obtained in the previous paragraph lies between these two values.

Pauling has shown that the single bond radius of a given transition element is approximately linearly dependent on the  $d$ -character of the s.p.d. hybrid bond orbitals and has suggested the following equation for the transition elements in the first long period<sup>6</sup>:

$$R_1 = 1.825 - 0.043z - (1.600 - 0.100z)\delta \quad (5)$$

where  $z$  is the atomic number - 18 and  $\delta$  is the fraction of  $d$ -character.

Similar equations have been prepared for the heavier transition elements. Applying Eq. (5) to the limiting values 1.271 and 1.182 Å calculated for the single bond radius of titanium in titanium disilicide, the percentage of  $d$ -character of the bonds is found to be 32 and 39 per cent respectively. The percentage of  $d$ -character of the bonds in metallic titanium calculated using the value of 1.324 Å for  $R_1$  in Eq. (5) is 27 per cent. Although the quantitative analysis given above may not be fully justified due to the approximate nature of the basic equations, the general result, that a considerable increase in the  $d$ -character of the titanium bonds has taken place due to combination with silicon, is apparent. It is suggested that the high heat of formation of  $\text{TiSi}_2$  is at least in part associated with this change in the character of the bonding.

The apparent total valency of the zirconium atom in  $\text{ZrSi}_2$  is also considerably greater than the maximum possible true valency of 4 (Table IX) and, as with  $\text{TiSi}_2$ ,  $\text{ZrSi}_2$  has a high heat of formation. However, the apparent increase in valency is not as great as for titanium in  $\text{TiSi}_2$ , although the heat of formation is a little higher.

In Group Va the apparent valencies of the elements, calculated from the bond lengths in the disilicides, increases with increasing atomic number, the value for vanadium being 5.1 (Table IX). It would seem likely, therefore, that for vanadium the character of the bonding is similar to that in the free metal. For niobium and tantalum, however, the higher apparent valency values obtained suggest that an increase in the  $d$ -character of the bond has taken place. This increase is greater for tantalum than for niobium but is not as large as that found for titanium in  $\text{TiSi}_2$ . These results follow the

same form as the heat of formation data,  $\text{TaSi}_2$  having a lower heat of formation than  $\text{TiSi}_2$  but being more stable than vanadium or niobium disilicides.

It is difficult to correlate the heats of formation and the bond lengths for the disilicides of the Group VIA elements since it is likely that the valency in the metallic state increases with increasing atomic number.<sup>7</sup> The apparent total valency of the metal atoms given in Table IX have been calculated using Pauling's values of the single bond radius which in turn were obtained by assuming a constant metal valency of 5.78. For these elements the  $d$  character of the s.p.d. hybrid bond orbitals is already larger than for the elements in Groups IVA and Va<sup>6</sup> and it is possible, therefore, that other factors have a more important effect on the heats of formation.

## 5. CONCLUSIONS

The method developed for determining the heats of formation of highly exothermic reactions has been applied to a number of the silicides of the transition metals. The data obtained have shown that the lower silicides are in most cases more stable than the disilicides and that the highest heats of formation are to be found in Group IVA.

An analysis of the bond lengths in the disilicides has shown that the metal-metal bonding originally present in the metal has been replaced by strong metal-silicon bonding.

Some correlation has been found between the heats of formation data and the metal-silicon bond lengths for the disilicides of Group IVA and Va metals.

## ACKNOWLEDGMENTS

The authors would like to thank Mr. H. P. Rooksby and Dr. E. A. D. White for the X-ray examination of the various samples.

## REFERENCES

1. C. E. Lundin, D. J. McPherson and M. Hansen, *Trans. A.S.M.* **45**, 901-914 (1953).
2. O. Kubaschewski and E. Evans, *Metallurgical Thermochemistry* (Butterworth-Springer, Ltd., 1951).
3. R. Kieffer, F. Benesovsky, and R. Machenschalk, *Z. Metallk.* **45**, 493-498 (1954).
4. L. Pauling, *J. Amer. Chem. Soc.* **69**, 542-553 (1947).
5. L. Pauling, A. M. Soldate, *Acta Cryst.* **1**, 212-216 (1948).
6. L. Pauling, *Proc. Roy. Soc.* **196**(A), 343-362 (1949).
7. W. Hume-Rothery, H. M. Irving, R. J. P. Williams, *Proc. Roy. Soc.* **208**(A), 431-443 (1951).
8. H. J. Wallbaum, *Z. Metallk.* **33**, 378-381 (1941).
9. St. V. Naray-Szabo, Z. Krist., **97**(A) 223-228 (1937).
10. H. Nowotny, H. Schachner, R. Kieffer and F. Benesovsky, *Monatshefte Chemie* **84**, 1-12 (1953).
11. W. H. Zachariasen, *Z. physik. Chem.* **128**, 39-48 (1927).
12. H. Nowotny, R. Kieffer and H. Schachner, *Monatshefte Chemie*, **83**, 1243-1252 (1952).
13. H. Schachner, H. Nowotny and H. Kudielka, *Monatshefte Chemie* **85**, 1140-1153 (1954).

## LETTERS TO THE EDITOR

### On Pore Formation during Diffusion\*

In his article in the March, 1955 issue of *Acta Metallurgica*,<sup>1</sup> J. A. Brinkman attributes porosity formation in diffusion specimens primarily to the action of tensile stresses in the diffusion zone. While it has not always been recognized that mechanical stresses influence the formation of pores during diffusion, it seems to us that the nucleation and growth picture is not essentially changed by taking this fact into consideration. The presence of elastic strain energy modifies the expression for the bulk free energy change upon formation of a void, but does not alter the general form of the equations. Therefore, even in the presence of stress, a critical pore size exists which must be exceeded in order for the nucleus to be stable. This critical size will depend upon the excess vacancy concentration, as well as the magnitude of the stresses in the diffusion zone. It is impossible to consider stress alone, and ignore the existence of a non-equilibrium concentration of defects in the diffusion zone, when it is exactly this lack of equilibrium which generates the stresses under consideration.

The important question still remains: to what extent must the concentration of vacancies in the diffusion zone exceed the equilibrium concentration before porosity appears? This question could be given at least an approximate answer if something were known about the size and nature of the heterogeneous nuclei around which the vacancies condense. We find it difficult to believe Brinkman's idea that voids are homogeneously nucleated by microcracking. First, the average stress level in the diffusion zone is probably three orders of magnitude lower than his assumed value. According to Price,<sup>2</sup> alpha-brass elongates at the rate of about 10 per cent per minute at 800°C under a tensile load of 1000 psi. Brass sheets in which extensive porosity formed throughout during dezincification underwent a linear shrinkage of 3 per cent in 15 minutes at 800°C, corresponding to a strain rate of 0.2 per cent per minute.<sup>3</sup> Dezincification was roughly half complete in this time. These data suggest that the average tensile stress in the diffusion zone must be quite small, of the order of  $1000/50 = 20$  psi during most of the diffusion period. Even making allowances for very high stress concentrations, which are really not likely at such an elevated temperature and low strain rate, it is not plausible that the cleavage strength of  $10^5$  or  $10^6$  psi will be anywhere reached. Second, we have frequently observed in dezincified commercial brass sheets that pores form throughout the entire specimen. Photomicrographs illustrating this behavior can be found in the March, 1955 issue of *Acta Metallurgica*.<sup>3</sup> The voids in the center of these sheets must have nucleated and grown in the presence of a compressive stress, since the center of the sheet is always in compression, while the outer layers are

in tension. This observation is evidence that a tensile stress is not necessary for the nucleation of porosity in diffusion specimens.

As Seitz has already pointed out, a vacancy supersaturation of 100 or 1000 times the normal equilibrium concentration would be necessary in order to obtain homogeneous nucleation of voids at an observable rate in a metal. Previous estimates<sup>4</sup> have indicated that voids actually form in commercial metals and alloys when the vacancy concentration is about 1 per cent above normal, which suggests that the pores are nucleated by some impurity or imperfection already present in the matrix, somewhat in the manner that fog is nucleated by dust particles in the atmosphere. More careful experiments which we have recently completed prove that in so-called "high-purity" brass the degree of vacancy supersaturation necessary for visible pore formation is almost vanishingly small, probably less than 0.01 per cent. Voids are seen to a considerable depth within the brass after removal of only a small amount of zinc from the surface. When this same material is zone-refined, however, practically no pores form within the body of the specimen, even upon complete dezincification. These experiments prove beyond any reasonable doubt that the porosity is heterogeneously nucleated. Also, we have an obvious clue to the nature of the "dust" in this alloy upon which vacancies condense to form pores. Commercial high-purity brass is prepared from electrolytic copper and pure zinc melted in the conventional manner, in air under a charcoal cover. Although the resulting alloy is quite free from metallic impurities, it contains almost 0.3 per cent of oxygen. This fact was not appreciated until the experiments described above led us to perform a series of vacuum fusion analyses on the brass. According to these, the oxygen content of the as-received material is 0.284 wt.%. After zone-purifying in vacuum this is reduced to 0.072 per cent. Apparently the impurities which nucleate voids in alpha-brass are oxide particles, probably zinc oxide.

The above remarks are intended to apply strictly only to the formation of porosity in diffusion couples. Recent experiments have shown that voids may also form in homogeneous metals deformed at elevated temperatures.<sup>5,6</sup> Tensile stress may play a larger role in the direct nucleation of porosity under such conditions by the mechanism proposed by Brinkman. Here again, however, an alternative explanation is possible in terms of the generation of an excess vacancy concentration by plastic flow, and subsequent precipitation of holes.

L. SEIGLE  
R. RESNICK

Sylvania Electric Products, Inc.  
Atomic Energy Division  
Bayside, New York

## References

1. J. A. Brinkman, *Acta Met.* **3**, 140 (1955).
2. W. B. Price, "Symposium on Effect of Temperature on Properties of Metals," A.S.M.E.-A.S.T.M. (1931), p. 340.
3. R. W. Balluffi and L. L. Seigle, *Acta Met.* **3**, 170 (1955).
4. R. W. Balluffi, *Acta Met.* **2**, 194 (1954).
5. J. N. Greenwood, D. R. Miller and J. W. Suiter, *Acta Met.* **2**, 250 (1954).
6. J. Herenguel and M. Scheidecker, *Rev. Metall.* **48**, 179 (1951).

\* Received June 10, 1955.

### On the Mechanism of Pore Formation during Diffusion\*

In their letter,<sup>1</sup> Seigle and Resnick attempt to show that (1) the presence of mechanical stresses eliminates neither the need for an excess vacancy concentration for void growth nor the dependence of the critical void size on the magnitude of this excess concentration, and (2) the microcracking mechanism proposed by the author<sup>2</sup> for nucleation of voids in Kirkendall experiments cannot be correct. We propose to show here that they have offered no satisfactory arguments in support of either of these conclusions.

In attempting to substantiate the first conclusion, they argue that one cannot consider stress alone as the factor which determines critical pore size. They offer two arguments in support of the second conclusion: (a) the average stress level in the diffusion zone cannot be as great as we have postulated, and (b) the center of a sheet specimen is always in compression and voids are formed there as well as in the outer layers.

Let us consider their argument leading to conclusion (1). It is agreed that, even in the presence of stress, a critical pore size exists which must be exceeded in order for the nucleus to be stable. It is also true that the critical size will depend on any deviation of the defect concentration from its equilibrium value, as well as on the magnitude of the stresses in the diffusion zone. However, if the deviations are sufficiently small and the stresses are as great as we have proposed, this dependence is negligible compared with the dependence on the stress, and one can consider the critical pore size to depend only on the stress. Thus, it may very well be possible to consider stress alone, and ignore the existence of a nonequilibrium concentration of defects in the diffusion zone. Furthermore, it is the author's belief that any minute deviations of the vacancy concentration in the diffusion zone from its equilibrium value are more likely to be negative than positive. Here the equilibrium value of the vacancy concentration is defined as that concentration of vacancies existing in a pore-free crystal subjected to the same stress as that present in the diffusion zone. Their conclusion that the deviations must be positive is true in the case of a pore-free crystal, since there is a net flow of vacancies into (or interstitials away from) the stressed region, resulting in an unbalance between the rates of creation and annihilation of defects within the region. In the case of

stressed crystal with pores present, however, the presence of the pores tends to create an unbalance in the opposite sense, which will be the dominant effect whenever the stress is relaxing as a result of the growth of pores. Thus it becomes possible for pore growth to occur in the presence of a tensile stress even when the vacancy concentration is below its equilibrium value.

We shall consider next argument (a) leading to conclusion (2). Seigle and Resnick attempt to show that stresses of the magnitude which we postulated cannot be established in the diffusion zone by citing the experimental data of Price,<sup>3</sup> in which a macroscopic stress was applied to a polycrystalline specimen of alpha-brass at 800°C. It is now generally believed that the inability of a polycrystalline metal to withstand large macroscopic stress concentrations, as observed by Price, is a result of the viscous behavior of the grain boundaries, while the critical shear stress for slip is rather insensitive to temperature, generally remaining finite up to the melting point, and essentially independent of the rate of deformation.<sup>4</sup> Thus, it should be impossible to maintain large stress concentrations in polycrystalline specimens at high temperatures by the application of stress on a macroscopic scale. The stresses resulting from the annihilation of vacancies or the production of interstitials at dislocations, on the other hand, in a Kirkendall experiment are built up locally on an atomic scale within each grain and cannot relax by grain boundary viscous flow. Probably the mechanism by which relaxation would occur, if slip were impossible, would be the diffusional mechanism considered by Herring.<sup>5</sup> If one calculates, by use of Herring's theory, the stress which will be established in the diffusion zone at a temperature of 800°C and a strain rate of 0.2 per cent per minute, the actual conditions described by Seigle and Resnick, one obtains a stress somewhat greater than  $10^9$  dynes/cm<sup>2</sup>, the value assumed by the author. Therefore it seems reasonable to assume that a stress order of magnitude greater than that quoted by Price can exist under these conditions, even though the deformation rate is smaller. Since the yield stress of the material is determined, presumably, by the most easily activated Frank-Read generators in any region of applied stress, one might expect that such localized stress application on an atomic scale would in general exhibit higher values for the yield stress. Furthermore, the occurrence of multiple slip requires a higher stress than single slip, and higher biaxial than uniaxial stresses are required to initiate slip. These three factors indicate that the local stress concentrations occurring in Kirkendall experiments are probably somewhat greater than the high temperature critical shear stress for slip of the material, and that argument (a) therefore is probably not correct.

In argument (b), offered in substantiation of conclusion (2), Seigle and Resnick state that the center of the sheet is always in compression, while the outer layers are in tension. We pointed out that the stressed region undergoing plastic deformation at any time is



narrow, and that it moves away from the Kirkendall interface. One should expect it to end up eventually in the center of the sheet, and the outer layers to be in compression. This is evident when one considers that the region in tension is that region in which the time rate of depletion of the zinc concentration is greatest, while the region in compression is that in which this quantity is least. If one solves the problem of diffusion out of a slab to obtain this quantity, it becomes evident that the final state of the specimen is one in which the center is in tension and the outer layers are in compression.

The more recent experimental data presented by Seigle and Resnick are of considerable interest. However, it is not apparent that they support the concept of existence of an excess vacancy concentration or that they tend to invalidate the microcracking nucleation mechanism proposed by the author. It was pointed out by the author<sup>2</sup> that the presence of impurity particles could act as stress concentration centers and thereby appreciably affect the process of pore nucleation.

J. A. BRINKMAN

North American Aviation, Inc.  
Nuclear Engineering and  
Manufacturing  
Downey, California

#### References

1. L. Seigle and R. Resnick, *Acta Met.* **3**, *supra*.
2. J. A. Brinkman, *Acta Met.* **3**, 140 (1955).
3. W. B. Price, "Symposium on Effect of Temperature in Properties of Metals," A.S.M.E.-A.S.T.M. (1931), p. 340.
4. E. Orowan, *Rep. Prog. Phys.* **XII**, 228-229 (1949).
5. C. Herring, *J. Appl. Phys.* **21**, 437 (1950).

\* Received July 1, 1955.

#### Abnormal After-Effect of Twisted Metal Wires upon Heating\*

When metal wires are subjected to a plastic deformation in torsion, they ordinarily untwist partially after the applied torque is released. There are a few exceptions to this rule. C. S. Barrett<sup>1</sup> has plastically twisted iron and zinc wires and found that after the torque was released the wires may, for a short time, twist further when their oxide layer is removed. A similar anomalous after-effect has been observed in this laboratory when metal wires were heated after they had been subjected to a plastic deformation in torsion.

The apparatus is schematically described in Fig. 1. A wire is clamped between two steel pin vises inside a glass tube flushed with helium. The upper pin vise is rigidly mounted while the lower one is free to rotate. An electric motor rotates a platform on which two electromagnets are located. After the platform has rotated a constant amount (450 degrees) and the wire has been twisted to about 2 per cent surface shear strain, the electromagnet is turned on. This lowers the soft iron pins and releases the wire. Torsion vibrations are prevented by the vanes immersed in silicone fluid

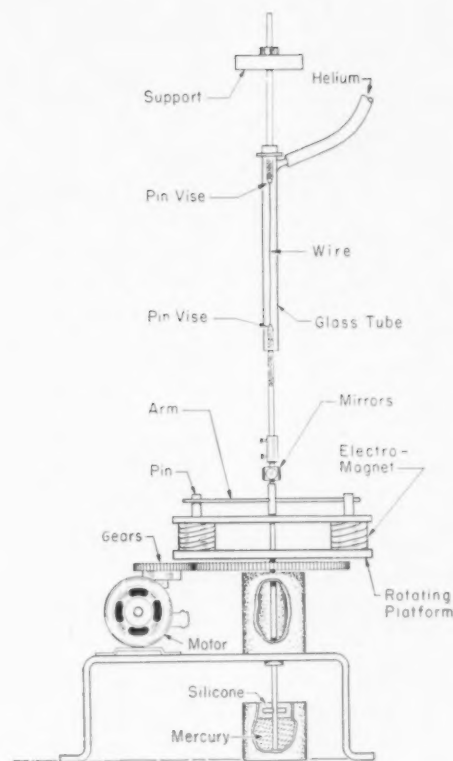


FIG. 1. Schematic drawing of wire twisting apparatus.

which damp the system critically. The silicone fluid floats on mercury inside a copper container. The wire can be heated up in a few seconds by passing a high amperage current through it. This is accomplished by connecting the copper container and the upper brass rod to a low voltage source. The angle of twist is measured on a semi-circular scale by a light beam reflected from the mirrors.

Measurements were made on polycrystalline high-purity aluminum, copper and silver wires and on commercial Nichrome-V wires (diameter 50 mil, gage length 10 inches) which were annealed in helium for 15 minutes at 300, 900, 330, and 950°C, respectively. Each wire was annealed a second time inside the apparatus before testing in order to remove stresses that may have been produced when the wire was placed in the apparatus. Three wires of each material were twisted clockwise and three counterclockwise.

A wire was twisted, released, and its anelastic behavior measured at room temperature for 29 minutes. The aluminum, copper, silver, and Nichrome wires were then rapidly heated up and kept at 300, 400, 300, and 700°C, respectively. Again, the angle of twist was measured as a function of time. The results are seen in Fig. 2. Each curve represents the average of the data on the six wires. The positive values of the ordinate stand for twist in the direction of initial loading, the negative values for untwist. The zero mark of



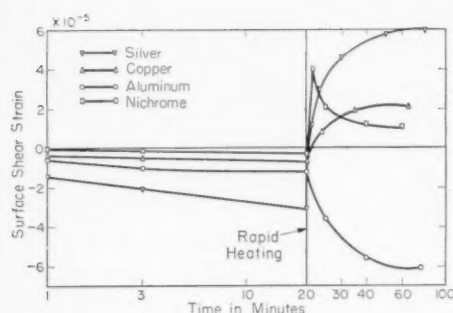


FIG. 2. Results of measurements.

the ordinate indicates the position of the wire to which it elastically sprang back after the applied torque was released.

It is seen that no abnormal after-effect is observed with the aluminum wires which untwist at room temperature (the first 20 minutes) and continue to untwist at high temperature. The copper and silver wires behave differently since they untwist at room temperature and then reverse when heated up. The effect is more pronounced in silver where the amount of further twist approaches 0.1 per cent surface shear strain. The most peculiar effect is observed with the Nichrome wires. As all the other wires, they exhibit a normal after-effect at room temperature. However, when heated up, they first twist further by a relatively large amount for a short time and then gradually untwist.

It may be that these phenomena can be explained in a way similar to that with which C. S. Barrett has explained his effects. Dislocations pile up under the oxide layer near the surface as a result of the plastic deformation. When the metal is heated, the stress needed for the dislocations to break through the oxide layer becomes smaller than the stress at the spearhead of the dislocation pile. Dislocations will then break through to the surface, and the wire will twist further, as is the case in copper and silver. In aluminum this does not occur probably because of the much stronger oxide layer. The behavior of the Nichrome is more complex.

A. W. COCHARDT

Westinghouse Research Laboratories  
East Pittsburgh, Pennsylvania

## References

1. C. S. Barrett, *Acta Met.* 1, 2 (1953).

\* Received July 14, 1955.

### Dislocation Glide as an Aid to Precipitation at Low Temperatures\*

Turnbull has pointed out that precipitation from solid solution often occurs so rapidly at low temperatures that

it cannot be explained by volume diffusion.<sup>1</sup> He has shown that, during cellular precipitation, a lamellar structure of precipitate and reoriented matrix grows as a spherulitic composite, separated from the original matrix by a grain boundary. Diffusion along the outward-moving grain boundary drains solute from the matrix and delivers it to growing lamellae of precipitate.

Diffusion of solute along single dislocations also can drain solute from the matrix and deliver it to a precipitate particle that is in contact with the dislocation. Turnbull pointed out also that, if dislocations were to glide during this process, much more of the matrix could be reached and drained of solute, allowing considerable precipitation to occur through the agency of only a few dislocations.<sup>2</sup> It occurred to us that the free energy of precipitation is available as a driving force for dislocation glide under these circumstances.

We believe that dislocation glide at low temperatures, with the free energy of precipitation as a driving force, may be important in (1) the precipitation of the essentially two-dimensional precipitates that often form early in the precipitation process; in (2) precipitation hardening, which in this process is caused by the work-hardening that results from precipitation-induced dislocation motion, multiplication, and tangling; and possibly in (3) recovery from radiation damage, where the "precipitation" is the formation of vacancy or interstitial layers, or is recombination.

J. C. FISHER

J. H. HOLLOMON

General Electric Research Laboratory  
Schenectady, New York

## References

1. D. Turnbull, *Acta Met.* 3, 55 (1955).
2. D. Turnbull, "Diffusion Short Circuits and their Role in Precipitation," *Defects in Crystalline Solids*, The Physical Society (London), 1955.

\* Received July 26, 1955.

## ERRATUM

Dislocation Densities in Intersecting Lineage Boundaries in Germanium

*Acta Metallurgica* 3, 513 (1955)

W. G. Pfann and L. C. Lovell

On p. 513, line 15, column 1, read " $(a/2[110])$ " instead of " $(a/2[110])$ ".

## SOME CURRENT PAPERS IN OTHER JOURNALS

### Acta Crystallographica, Vol. 8

Part 9, September, 1955 (Partial Contents)

- On the relations between structure and morphology of crystals. II. P. Hartman and W. G. Perdok.  
On the relations between structure and morphology of crystals. III. P. Hartman and W. G. Perdok.  
Growth features on crystals of long-chain compounds. I. S. Amelinckx.  
La methode statistique en cristallographie. I. E. F. Bertaut.  
La methode statistique en cristallographie. II. E. F. Bertaut.  
A classification of cylindrical lattices. E. J. W. Whittaker.  
The structure of Guinier-Preston zones. I. The Fourier transform of the diffuse intensity diffracted by a Guinier-Preston zone. K. Toman.  
The crystal structure of  $\beta$ -PuSi<sub>2</sub>. O. J. C. Runnalls and R. R. Boucher.  
A study of the atomic scattering factor for aluminium. G. S. Parry.  
Precession camera settings. D. J. Fisher.  
Symmetry relations between structure factors. J. Waser.  
The accuracy of structures determined by powder methods, with reference to the Ag-Zn  $\zeta$  structure. I. G. Edmunds.

### Archiv für das Eisenhüttenwesen

Heft 7, Juli 1955 (Partial Contents)

- Über den Werkstoff des Schweisseisen-Zeitalters. E. H. Schulz.  
Die Auflösung von Kohlenstoff in flüssigem Eisen. O. Dahlke und O. Knacke.  
Zur Rückstandsanalyse von Roheisen und Gusseisen. Teil II: Trennung der Isolate. A. Wittmoser und W. D. Gras.  
Untersuchung der Abschreckalterung weicher unlegierter Stähle mit radioaktiven Isotopen, besonders Kohlenstoff C<sup>14</sup>. H.-K. Görlich, H. Goossens und H. Schenck.  
Elektrochemische Untersuchungen der Korrosion von  $\alpha$ -Eisen-Einkristallen in verdünnten Säuren. H.-J. Engell.  
Die Angangsporeabilität einiger Eisenwerkstoffe bei mechanischer Beanspruchung. W. Jellinghaus und K. Janssen.  
Das Dreistoffsystem Eisen-Kobalt-Vanadin. Teil II. Die Ausbildung des Dreistoffsystems bei Gleichgewicht zwischen  $\alpha/\gamma$ -Mischkristallen. W. Köster und H. Schmid.  
Heft 8, August 1955 (Partial Contents)  
Johann Georg Ludolph Blumhof und seine Enzyklopädie der Eisenhüttenkunde. H. Dickmann.  
Die photometrische Bestimmung von Niob und Tantal im Stahl. A. Eder.  
Graphische Verfahren der röntgenographischen Verformungsmessung. G. Kemnitz.  
Industrielle Anwendungsmöglichkeiten der röntgenographischen Spannungsmessung. A. Schaal.  
Vergleich röntgenographisch und mechanisch gemessener Verformungen an Gusseisen. V. Hauk.  
Das Verhalten der Oberflächenschichten und die elastischen Konstanten von Stahl mit 0,43% C bei Spannungsmessung mit Röntgenstrahlen. H. Hendus und C. Wagner.  
Veränderungen im Gefügebau von Chrom-Nickel-Molybdän-Stählen bei langzeitiger Beanspruchung im Zeitstandversuch bei 500°.

Elektronenmikroskopische Untersuchung der Gefügeveränderungen eines Chrom-Nickel-Molybdän-Stahles unter Langzeitiger Zugbeanspruchung bei 500°. G. Wever und A. Schrader.  
Das Zustandsschaubild Eisen-Eisenphosphid Fe<sub>2</sub>P-Wolframphosphid WP-Wolfram. R. Schneider und R. Vogel.  
Stabilisierungsvorgänge an Dauermagneten. I. Titz, F. Raidl und H. Krainer.

### Journal of the Institute of Metals, Vol. 84

Part 1, September, 1955

- A further study of the oxidation of titanium and its alloys at high temperatures. A. E. Jenkins.  
Textures in face-centered cubic metals and alloys. R. E. Smallman.  
Intermediate precipitates in aged binary alloys of aluminium with cadmium, indium or tin. (Miss.) J. M. Silcock.  
The structural ageing characteristics of ternary aluminium-copper alloys with cadmium, indium or tin. (Miss.) J. M. Silcock, T. J. Heal and H. K. Hardy.

### Journal of Metals, Vol. 7

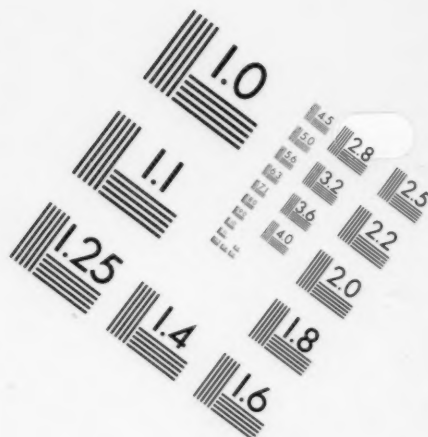
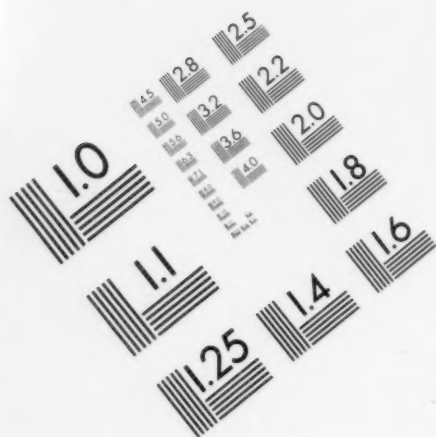
No. 9, September, 1955

- Ordering and magnetic heat treatment of the 50 pct Fe-50 pct Co alloy. R. C. Hall, G. P. Conrad, and J. F. Libsch.  
Further observations on yield in single crystals of iron. H. W. Paxton and I. J. Bear.  
Diffusion of Co<sup>60</sup> and Fe<sup>55</sup> in cobalt. H. W. Mead and C. E. Birchenall.  
Grain boundary diffusion of nickel into copper. S. Yukawa and M. J. Sinnott.  
Bainite reaction in a plain carbon steel. H. I. Aaronson and C. Wells.  
Diffusion of zinc and copper in alpha- and beta-brasses. R. Resnick and R. W. Balluffi.  
Thermal conductivity of vanadium and certain vanadium alloys. J. L. Weeks and K. F. Smith.  
Kinetics and mechanism of the oxidation of molybdenum. M. Sinnad and A. Spilners.  
Contribution to mathematics of zone melting. L. Burris, Jr., C. H. Stockman and I. G. Dillon.  
Instability of a smooth solid-liquid interface during solidification. D. Walton, W. A. Tiller, J. W. Rutter, and W. C. Winegard.  
Some aspects of slip in germanium. R. G. Treuting.  
Bauschinger effect in creep and tensile tests on copper. J. D. Lubahn.  
Zirconium-columbium diagram. B. A. Rogers and D. F. Atkins.  
Lineage structure in aluminum single crystals. A. Kelly and C. T. Wei.  
Microcalorimetric investigation of recrystallization of copper. P. Gordon.  
Method of determining the diffusivity of gas in metal: oxygen in chromium. D. Caplan and A. A. Burr.  
Relationship between recovery and recrystallization in super-purity aluminum. E. C. W. Perryman.  
On the casting, rolling and annealing textures of chromium. W. H. Smith.  
Temperature gradient zone melting. W. G. Pfann.  
Phase equilibria in the system FeO-Fe<sub>2</sub>O<sub>3</sub>-SiO<sub>2</sub>. A. Muan.



**NATIONAL  
MICROGRAPHICS  
ASSOCIATION**

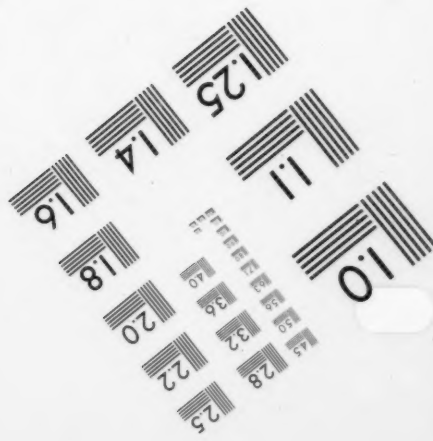
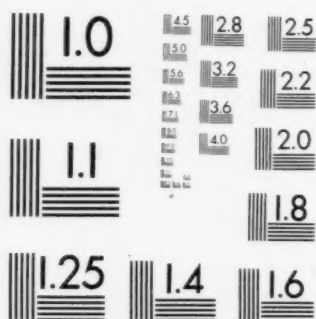
MS303-1980



Centimeter



Inches



# PERGAMON PRESS INC.



MICROFORMS INTERNATIONAL  
MARKETING CORPORATION  
FAIRVIEW PARK, ELMSFORD, NEW YORK 10523



**PRODUCED AT**  
**MIMC MICROFORMS LABORATORY**  
**ELMSFORD, NEW YORK**